

# Petroleum Engineering

Principles, Calculations, and Workflows



**Moshood Sanni**

---

Geophysical Monograph Series

## Geophysical Monograph Series

- 185 **Indian Ocean Biogeochemical Processes and Ecological Variability** Jerry D. Wiggert, Raleigh R. Hood, S. Wajih A. Naqvi, Kenneth H. Brink, and Sharon L. Smith (Eds.)
- 186 **Amazonia and Global Change** Michael Keller, Mercedes Bustamante, John Gash, and Pedro Silva Dias (Eds.)
- 187 **Surface Ocean–Lower Atmosphere Processes** Corinne Le Quèrè and Eric S. Saltzman (Eds.)
- 188 **Diversity of Hydrothermal Systems on Slow Spreading Ocean Ridges** Peter A. Rona, Colin W. Devey, Jérôme Dymont, and Bramley J. Murton (Eds.)
- 189 **Climate Dynamics: Why Does Climate Vary?** De-Zheng Sun and Frank Bryan (Eds.)
- 190 **The Stratosphere: Dynamics, Transport, and Chemistry** L. M. Polvani, A. H. Sobel, and D. W. Waugh (Eds.)
- 191 **Rainfall: State of the Science** Firat Y. Testik and Mekonnen Gebremichael (Eds.)
- 192 **Antarctic Subglacial Aquatic Environments** Martin J. Siebert, Mahlon C. Kennicut II, and Robert A. Bindshadler (Eds.)
- 193 **Abrupt Climate Change: Mechanisms, Patterns, and Impacts** Harunur Rashid, Leonid Polyak, and Ellen Mosley-Thompson (Eds.)
- 194 **Stream Restoration in Dynamic Fluvial Systems: Scientific Approaches, Analyses, and Tools** Andrew Simon, Sean J. Bennett, and Janine M. Castro (Eds.)
- 195 **Monitoring and Modeling the Deepwater Horizon Oil Spill: A Record-Breaking Enterprise** Yonggang Liu, Amy MacFadyen, Zhen-Gang Ji, and Robert H. Weisberg (Eds.)
- 196 **Extreme Events and Natural Hazards: The Complexity Perspective** A. Surjalal Sharma, Armin Bunde, Vijay P. Dimri, and Daniel N. Baker (Eds.)
- 197 **Auroral Phenomenology and Magnetospheric Processes: Earth and Other Planets** Andreas Keiling, Eric Donovan, Fran Bagenal, and Tomas Karlsson (Eds.)
- 198 **Climates, Landscapes, and Civilizations** Liviu Giosan, Dorian Q. Fuller, Kathleen Nicoll, Rowan K. Flad, and Peter D. Clift (Eds.)
- 199 **Dynamics of the Earth's Radiation Belts and Inner Magnetosphere** Danny Summers, Ian R. Mann, Daniel N. Baker, and Michael Schulz (Eds.)
- 200 **Lagrangian Modeling of the Atmosphere** John Lin (Ed.)
- 201 **Modeling the Ionosphere-Thermosphere** Joseph D. Huba, Robert W. Schunk, and George V. Khazanov (Eds.)
- 202 **The Mediterranean Sea: Temporal Variability and Spatial Patterns** Gian Luca Eusebi Borzelli, Miroslav Gacic, Piero Lionello, and Paola Malanotte-Rizzoli (Eds.)
- 203 **Future Earth – Advancing Civic Understanding of the Anthropocene** Diana Dalbotten, Gillian Roehrig, and Patrick Hamilton (Eds.)
- 204 **The Galápagos: A Natural Laboratory for the Earth Sciences** Karen S. Harpp, Eric Mittelstaedt, Noémi d'Ozouville, and David W. Graham (Eds.)
- 205 **Modeling Atmospheric and Oceanic Flows: Insights from Laboratory Experiments and Numerical Simulations** Thomas von Larcher and Paul D. Williams (Eds.)
- 206 **Remote Sensing of the Terrestrial Water Cycle** Venkat Lakshmi (Ed.)
- 207 **Magnetotails in the Solar System** Andreas Keiling, Cairtriona Jackman, and Peter Delamere (Eds.)
- 208 **Hawaiian Volcanoes: From Source to Surface** Rebecca Carey, Valerie Cayol, Michael Poland, and Dominique Weis (Eds.)
- 209 **Sea Ice: Physics, Mechanics, and Remote Sensing** Mohammed Shokr and Nirmal Sinha (Eds.)
- 210 **Fluid Dynamics in Complex Fractured-Porous Systems** Boris Faybishenko, Sally M. Benson, and John E. Gale (Eds.)
- 211 **Subduction Dynamics: From Mantle Flow to Mega Disasters** Gabriele Morra, David A. Yuen, Scott King, Sang Mook Lee, and Seth Stein (Eds.)
- 212 **The Early Earth: Accretion and Differentiation** James Badro and Michael Walter (Eds.)
- 213 **Global Vegetation Dynamics: Concepts and Applications in the MC1 Model** Dominique Bachelet and David Turner (Eds.)
- 214 **Extreme Events: Observations, Modeling and Economics** Mario Chavez, Michael Ghil, and Jaime Urrutia-Fucugauchi (Eds.)
- 215 **Auroral Dynamics and Space Weather** Yongliang Zhang and Larry Paxton (Eds.)
- 216 **Low-Frequency Waves in Space Plasmas** Andreas Keiling, Dong-Hun Lee, and Valery Nakariakov (Eds.)
- 217 **Deep Earth: Physics and Chemistry of the Lower Mantle and Core** Hidenori Terasaki and Rebecca A. Fischer (Eds.)
- 218 **Integrated Imaging of the Earth: Theory and Applications** Max Moorkamp, Peter G. Lelievre, Niklas Linde, and Amir Khan (Eds.)
- 219 **Plate Boundaries and Natural Hazards** Joao Duarte and Wouter Schellart (Eds.)
- 220 **Ionospheric Space Weather: Longitude and Hemispheric Dependences and Lower Atmosphere Forcing** Timothy Fuller-Rowell, Endawoke Yizengaw, Patricia H. Doherty, and Sunanda Basu (Eds.)
- 221 **Terrestrial Water Cycle and Climate Change Natural and Human-Induced Impacts** Qijuhong Tang and Taikan Oki (Eds.)
- 222 **Magnetosphere-Ionosphere Coupling in the Solar System** Charles R. Chappell, Robert W. Schunk, Peter M. Banks, James L. Burch, and Richard M. Thorne (Eds.)
- 223 **Natural Hazard Uncertainty Assessment: Modeling and Decision Support** Karin Riley, Peter Webley, and Matthew Thompson (Eds.)
- 224 **Hydrodynamics of Time-Periodic Groundwater Flow: Diffusion Waves in Porous Media** Joe S. Depner and Todd C. Rasmussen (Auth.)
- 225 **Active Global Seismology** Ibrahim Cemen and Yucel Yilmaz (Eds.)
- 226 **Climate Extremes** Simon Wang (Ed.)
- 227 **Fault Zone Dynamic Processes** Marion Thomas (Ed.)
- 228 **Flood Damage Survey and Assessment: New Insights from Research and Practice** Daniela Molinari, Scira Menoni, and Francesco Ballio (Eds.)
- 229 **Water-Energy-Food Nexus – Principles and Practices** P. Abdul Salam, Sangam Shrestha, Vishnu Prasad Pandey, and Anil K Anal (Eds.)
- 230 **Dawn–Dusk Asymmetries in Planetary Plasma Environments** Stein Haaland, Andrei Rounov, and Colin Forsyth (Eds.)
- 231 **Bioenergy and Land Use Change** Zhangcai Qin, Umakant Mishra, and Astley Hastings (Eds.)
- 232 **Microstructural Geochronology: Planetary Records Down to Atom Scale** Desmond Moser, Fernando Corfu, James Darling, Steven Reddy, and Kimberly Tait (Eds.)
- 233 **Global Flood Hazard: Applications in Modeling, Mapping and Forecasting** Guy Schumann, Paul D. Bates, Giuseppe T. Aronica, and Heiko Apel (Eds.)
- 234 **Pre-Earthquake Processes: A Multidisciplinary Approach to Earthquake Prediction Studies** Dimitar Ouzounov, Sergey Pulinet, Katsumi Hattori, and Patrick Taylor (Eds.)
- 235 **Electric Currents in Geospace and Beyond** Andreas Keiling, Octav Marghitu, and Michael Wheatland (Eds.)
- 236 **Quantifying Uncertainty in Subsurface Systems** Céline Scheidt, Lewis Li, and Jef Caers (Eds.)

Geophysical Monograph 237

---

**Petroleum Engineering**  
*Principles, Calculations, and Workflows*

Moshood Sanni

This Work is a co-publication of the American Geophysical Union and John Wiley and Sons, Inc.



**WILEY**

This Work is a co-publication between the American Geophysical Union and John Wiley & Sons, Inc.

This edition first published 2019 by John Wiley & Sons, Inc., 111 River Street, Hoboken, NJ 07030, USA and the American Geophysical Union, 2000 Florida Avenue, N.W., Washington, D.C. 20009

© 2019 the American Geophysical Union

All rights reserved. No part of this publication may be reproduced, stored in a retrieval system, or transmitted, in any form or by any means, electronic, mechanical, photocopying, recording, or otherwise, except as permitted by law. Advice on how to obtain permission to reuse material from this title is available at <http://www.wiley.com/go/permissions>

### **Published under the aegis of the AGU Publications Committee**

---

Brooks Hanson, Executive Vice President, Science  
Lisa Tauxe, Chair, Publications Committee

For details about the American Geophysical Union visit us at [www.agu.org](http://www.agu.org).

### **Wiley Global Headquarters**

111 River Street, Hoboken, NJ 07030, USA

For details of our global editorial offices, customer services, and more information about Wiley products visit us at [www.wiley.com](http://www.wiley.com).

### **Limit of Liability/Disclaimer of Warranty**

While the publisher and authors have used their best efforts in preparing this work, they make no representations or warranties with respect to the accuracy or completeness of the contents of this work and specifically disclaim all warranties, including without limitation any implied warranties of merchantability or fitness for a particular purpose. No warranty may be created or extended by sales representatives, written sales materials, or promotional statements for this work. The fact that an organization, website, or product is referred to in this work as a citation and/or potential source of further information does not mean that the publisher and authors endorse the information or services the organization, website, or product may provide or recommendations it may make. This work is sold with the understanding that the publisher is not engaged in rendering professional services. The advice and strategies contained herein may not be suitable for your situation. You should consult with a specialist where appropriate. Neither the publisher nor authors shall be liable for any loss of profit or any other commercial damages, including but not limited to special, incidental, consequential, or other damages. Further, readers should be aware that websites listed in this work may have changed or disappeared between when this work was written and when it is read.

### **Library of Congress Cataloging-in-Publication Data**

ISBN: 9781119387947

Cover Design: Wiley

Cover Image: © Petroleum System, Sanni (2018)

Set in 10/12pt Times New Roman by SPi Global, Pondicherry, India

10 9 8 7 6 5 4 3 2 1

# CONTENTS

---

Preface .....	vii
Acknowledgments .....	ix
<b>1 Petroleum System and Petroleum Engineering.....</b>	<b>1</b>
<b>2 Petroleum Reservoir Rock Properties.....</b>	<b>17</b>
<b>3 Reservoir Fluid Properties .....</b>	<b>65</b>
<b>4 Equations of States.....</b>	<b>103</b>
<b>5 Formation Evaluation.....</b>	<b>121</b>
<b>6 Formation Testing.....</b>	<b>181</b>
<b>7 Fluid Flow in Reservoirs .....</b>	<b>211</b>
<b>8 Well Test Analysis.....</b>	<b>243</b>
<b>9 Reservoir Inflow Performance.....</b>	<b>327</b>
<b>10 Well Production System .....</b>	<b>369</b>
<b>11 Production System Analysis.....</b>	<b>397</b>
<b>12 Reservoir Material Balance.....</b>	<b>421</b>
<b>13 Decline Curve Analysis.....</b>	<b>451</b>
<b>14 Secondary and Tertiary Recovery Methods .....</b>	<b>459</b>
<b>Index.....</b>	<b>503</b>

## PREFACE

---

Petroleum engineering problems, like most earth science problems, can be considered mainly to be inverse problems that can be ill-posed with nonunique solutions. In order to reduce uncertainty in calculated parameters, integrated workflows that combine one or more approach for diagnosis; validation, and parameter calculation must be considered.

The objective of this book is to create a unified resource that will enable petroleum engineers to solve basic to advanced petroleum engineering problems using a step-by-step approach by integrating prevailing methods in the petroleum industry to create workflows.

This book is based on my years of experience in research, training, product support, application development, and consultancy services, with most of the material evolving from training graduates and professionals in the oil and gas industry. This resource is compiled to provide

trainees and experienced petroleum engineers with fundamental and advanced understanding of the principles, calculations, and workflows required to solve petroleum engineering problems.

This book will appeal to a broad community of earth scientist and engineers working in the oil and gas industry: students who want to understand direct application of petroleum engineering principles in solving real petroleum engineering problems; consultants who want to solve problems with reduced uncertainty; professionals as reference material for day-to-day petroleum engineering problem solving; software developers to understand mathematical and graphical methods required for specific and general petroleum engineering application development.

**Moshood Sanni**

## ACKNOWLEDGMENTS

---

I would like to thank all the people I have worked and interacted with during my career in the oil and gas industry. They have all contributed to enriching me. Every question asked during training, discussion with colleagues, queries from clients, and criticism from all has helped in shaping this book.

My sincere appreciation to Dr. Lekan Aluko, Director and Principal Consultant at PetroVision Energy Services, for entrusting me with training and mentoring of clients and staff, where interactions have helped me appreciate prevailing methods and workflows in the oil and gas industry.

My gratitude to Aisha Ogbeche (PetroVision) for her valuable suggestions and time taken to review this book.

I would like to thank my colleagues at PetroVision: Dr. Umar Ngala, Dr. Onochie Obidi, Ebube John-Nwosu, Uche Eze, Tanuja Rawatlal, Thy Ngo, Reza Nazaria,

Dabeer Ulhasan, and Houshang Mansouri for their comments and assistance during the compilation of this book. I would also like to thank Olayiwola Fasokun and Dr. Olakunle Ogunrewo for their valuable comments during revision of this book.

My sincere appreciation to Wiley's editorial staff, Kathryn Corcoran, Karthiga Mani, Kari Capone, Dr. Rituparna Bose, and Wiley's production staff Danielle LaCourciere for their editorial, management, and production support.

I would like to thank my wife (Bola), kids, mum, and my entire family for their sacrifice and time I have taken from them travelling to deliver courses, staying awake to improve my course material, and putting this book together.

Finally, I would like to dedicate this book to the memory of my father Sanni, A.O.



# Petroleum System and Petroleum Engineering

Petroleum can be used to describe naturally occurring semisolid, liquid, and gas composed of organic compounds. Petroleum types include bitumen, crude oil, and natural gas. The term petroleum can also be used to describe naturally occurring crude oil and its derivatives. In this book, petroleum will mean bitumen, oil, and gas, while derivatives of petroleum will be referred to as petroleum products. The properties of petroleum reservoir fluids are discussed in Chapter 3.

The primary function of a petroleum engineer is to find economical and environmentally acceptable ways of producing petroleum fluids. In order for a petroleum engineer to achieve this objective, the factors affecting the ability of a reservoir to hold fluids, the flow of single and multiphase fluid through the reservoir, the production system at low and high pressure, the reservoir rock and fluid interaction must be well understood. In recent times, environmental considerations have played a crucial role in petroleum exploration and production activities. As such, petroleum engineers are expected to seek technology with minimum environmental damage. Operational activities in the petroleum industry at exploration and production activities are expected to conform to stringent environmental regulations in most parts of the world.

## 1.1. THE PETROLEUM ENGINEER

Petroleum engineers, based on roles and responsibilities, can generally be classified as either reservoir engineers or production engineers.

Reservoir engineers have the primary function of optimizing petroleum/hydrocarbon recovery from subsurface reservoirs. The roles of a reservoir engineer vary depending on the life of a reservoir/field, company, division/

department within the company, and size of company. Some of the primary functions of a reservoir engineer include, but are not limited to: estimation of hydrocarbons in place; estimating recoverable hydrocarbon; creating hydrocarbon recovery profiles with time; optimization of hydrocarbon recovery; working in a multidisciplinary team to build reservoir models.

Production engineers are responsible for managing the interface between the reservoir and the well. They are responsible for deciding how best to combine reservoir drive mechanisms for production, well completion, and production tubing design in order to optimize hydrocarbon production. Other tasks that fall within the scope of production engineers include: downhole data monitoring; production optimization; identifying how best to harness energy in the production system; diagnosis of production problems; recommending solutions to production problems; and planning and management of remedial and workover operations.

## 1.2. ROLES OF THE PETROLEUM ENGINEER IN THE FIELD LIFE CYCLE

Finding new fields is the main objective of the exploration phase in the oil and gas field life cycle. Exploration begins with acquisition and interpretation of seismic data to find potential petroleum traps through identification of structural characteristics that could form petroleum traps.

The role of a reservoir engineer during the exploration phase is to test the exploration hypothesis using well testing procedures and other petroleum engineering techniques if the exploration well discovers hydrocarbon. Crucial roles of reservoir engineer at this stage include: design and implementation of well test program; reservoir

deliverability assessment using acquired data from rock and fluid samples to understand if discoveries have properties for commercial exploitation.

During drilling operations at the exploration stage or for appraising the discovered area, the role of the reservoir engineer is to give guidance to ensure minimal damage is done to the wellbore during drilling operations. Some of the advice would include desirable overbalance pressure, impact of drilling operation on well deliverability, methods of mitigating impact of drilling on formation damage, well placement for optimized hydrocarbon recovery, and advice on well geometry in multiple compartment reservoirs, where the combined effect of reservoir compartmentalization and well geometry have significant impact on overall well and reservoir deliverability.

During the production phase, when the field is producing at maximum or optimized capacity, the role of the petroleum engineer is to give guidance to ensure that hydrocarbon can flow to the surface through production tubing. Some of the advice during production will be based on understanding well conditions such as skin effect and stimulation, and potential flow assurance problems such as wax, hydrate, asphaltene, and scales, which have significant impact on well deliverability. Understanding potential flow assurance problems is very important during production and well start-ups.

During field engineering operations, the role of reservoir engineers will vary from company to company. However, important functions will include: selection of field equipment that can achieve desirable job objectives; acquisition of field data that meet desirable quality level; and quality control of field data and interpretation of acquired data.

### 1.3. ORIGIN OF PETROLEUM

One of the most widely accepted theories on the origin of petroleum is the organic theory of petroleum formation. The organic theory states that petroleum originates from marine life, which includes single celled organisms (*planktons*) and complex organisms such as fishes and crustaceans. These organisms, which contain carbon, die and accumulate in water rich environments and ocean floors. Following accumulation of sediment over millions of years, deposited marine organisms became buried under kilometers of sediments. Under increased pressure and temperature due to overburden formation pressure from layers of sediments and organic matter, a mixture of organic chemical compounds called *kerogen* is formed. At high temperature in the earth's crust, *kerogen* releases hydrocarbons, which then migrate towards the surface where they are either trapped in reservoir rocks before

reaching the surface or escape to the surface and lose volatile constituents to yield bitumen and tar.

### 1.4. PETROLEUM SYSTEM

The geological concept, components, and process describing the formation, migration, and storage of hydrocarbons constitute a *petroleum system*. Components of a working petroleum system define the requirements for the formation of a petroleum resource, which includes: petroleum source rock, migration pathway, reservoir rock, seal, and traps (structural and stratigraphic).

The following summarizes the requirement for the formation of petroleum resources:

- An environment that ensures burial and preservation of dead marine tissues;
- the presence of a permeable migration path for movement of hydrocarbon from source rock to reservoir rocks;
- rock with capacity to store fluid and characterized seal to ensure preservation of hydrocarbon over geological time and appropriate structures to trap hydrocarbon.

#### 1.4.1. Petroleum Source Rocks

Source rocks are rocks rich in organic matter that can generate hydrocarbon when subjected to sufficiently high temperature. Source rocks are produced through *lithification*, a complex process involving deposition of unconsolidated grains of sediment to form consolidated rock. Source rocks approximately consist of about 90–99% mineral matter and 1–10 % organic matter, which are of marine and terrestrial origin. The organic matter in source rocks consists of *kerogen*, which is the organic fraction preserved in the sediments, and *bitumen*, which is the organic fraction that is soluble in organic solvent. A very important characteristic of source rock is the *total organic content*, which is the organic richness of a rock represented as weight percent of organic carbon (from *kerogen* and *bitumen*), and gives a qualitative indication of petroleum potential.

*Kerogens* are described as *Type I*, which is of marine algae origin and likely to produce light oil and some gas; *Type II*, which is of mixed marine plant and animal microorganism origin and most likely produce crude oil and natural gas; and *Type III*, which is of land plant origin and most likely to produce primarily gas.

**1.4.1.1. Petroleum Source Rock Formation.** The formation of source rock requires that conditions exist for conservation of organic matter over geological time with a significant supply of organic matter. Other important requirements include: sedimentation of particles (silt and clay) containing organic debris; increasing

overburden pressure; and poor oxygen supply to minimize degradation of dead matter through oxidation.

**1.4.1.2. Petroleum Generation from Source Rock.** The requirement for release of petroleum from source rock is temperature. The earth's interior is characterized by a temperature increase with depth. The change in temperature of the earth's interior per unit depth change is called *geothermal gradient*. Large quantities of hydrocarbons are formed around a depth of 1–2 km, with oil generation reaching peak at 3 km (Fig. 1.1). Gas dominates depth between 4 and 6 km due to the high temperature, which leads to cracking of oil to form gas (Fig. 1.1). At deeper formation depth, greater than 6 km, kerogen becomes carbonized and is no longer able to produce hydrocarbons.

### 1.4.2. Petroleum Migration

This is the process of the movement of hydrocarbon from source rock to reservoir rock that occurs over geological time. With increased overburden pressure at high temperature, source rocks become compressed and pore space between grains reduces, expelling hydrocarbons to zone of lower pressure. This first stage is called *primary migration*. Expelled hydrocarbons from source rock further migrate vertically by buoyancy. Hence, the presence of a migration path – permeable rock – is a very important requirement for petroleum migration. This second process of migration is called *secondary migration*. Hydrocarbons are less dense than water and will migrate upwards through water saturated rock until they encounter an impermeable rock, which serves as a trap. In these traps, gas, oil, and water are separated according to their density, with gas at the top followed by oil then water where the three phases exist.

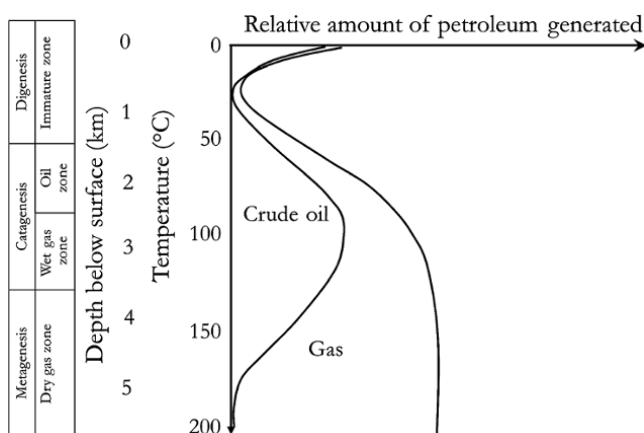


**Figure 1.1** Stages of petroleum generation. Adapted from [Tissot and Welte, 1984; Selley, 1998].

### 1.4.3. Reservoir Rock

Important characteristics of reservoir rock are porosity and permeability. Reservoir rocks must be porous to enable them to hold hydrocarbon and permeable to allow the flow of hydrocarbon.

*Porosity* is related to the fraction of void in a reservoir rock relative to reservoir bulk volume while *permeability* relates to the interconnectivity of pore spaces and is the characteristic of the reservoir to allow fluid flow under a pressure gradient. Where reservoir rocks are impermeable or have low permeability; hydraulically induced fractures or acidizing to dissolve impermeable rocks, such as limestone, dolomite, and calcite cement, between the sediment grains can be used to improve pore space interconnectivity to enable production of hydrocarbons.

Almost all reservoir rocks are sedimentary, formed by settling and accumulation of mineral and/or organic particles. The two most common petroleum reservoir rocks are sandstones and carbonates (limestones and dolomites). Sandstones and limestones show a wide variety of textures and are deposited in a variety of environments. Igneous (formed from cooling magma) and metamorphic (formed from previously existing rocks by extreme pressure, temperature, time, and chemical action) textures are usually made of closely interlocking minerals and, as such, are usually impermeable. However, hydrocarbon accumulations have been found within and around igneous rock, with their natural process of formation considered to be through *biotic* and *abiotic* processes.

### 1.4.4. Seal Rock

A reservoir must have an impervious seal or cap rock that ensures that hydrocarbons are preserved over geological time. Cap rocks are mostly sedimentary due to their ability to deform under stress, unlike igneous and metamorphic rocks. Though cap rock can have pore spaces, the absence of interconnected pores (permeability) ensures the hydrocarbon does not escape from reservoirs. Common reservoir seals include shales, clay, chalk, and evaporates.

### 1.4.5. Traps

The seal–reservoir interface must be configured to contain hydrocarbons. There are three main types of seal–reservoir configuration that ensure containment of hydrocarbons.

- *Structural traps*, which are due to folding and faulting of the earth's strata, leading to the formation of domes, anticlines, and folds. The majority of the world hydrocarbon reservoir (about 78%) is characterized by structural traps (Fig. 1.2).

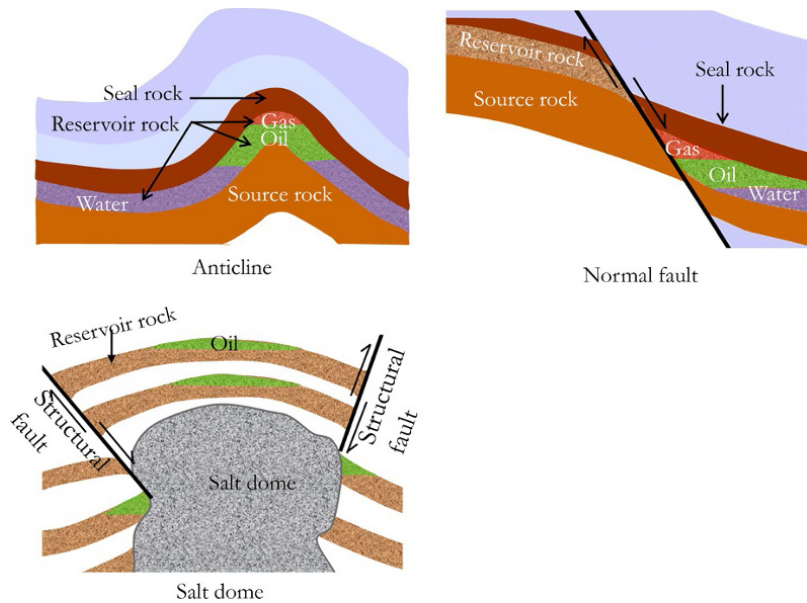


Figure 1.2 Structural traps.

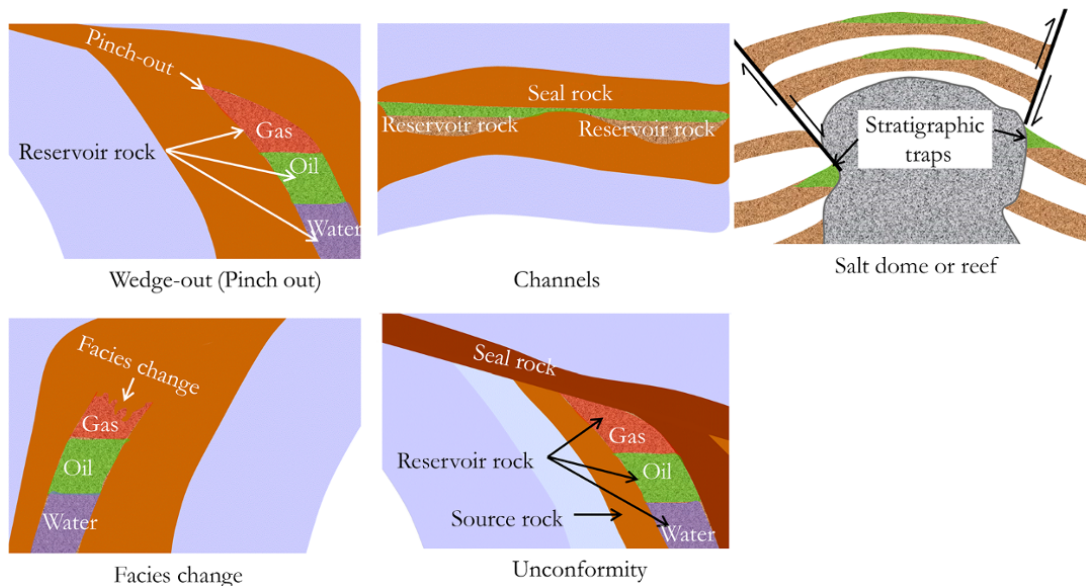


Figure 1.3 Stratigraphic traps.

- *Stratigraphic traps*, which occur due to lateral and/or vertical variations in reservoir properties such as lithology of reservoir rock; permeability; porosity, and thickness. About 13% of the world reservoir is characterized by this kind of trap (Fig. 1.3).

- There is also the possible combination of structural and stratigraphic traps. About 9% of the world reservoir is characterized by this kind of trap.

The chances of all the petroleum systems elements existing together is low, which explains the high risk associated with finding hydrocarbon during exploration.

### 1.5. PETROLEUM RESERVOIRS

In a reservoir containing gas, oil, and water the fluid distribution is primarily due to the density difference, with gas at the top of the reservoir followed by oil then water (Fig. 1.4).

At any given depth in a reservoir, the pressure in the pore space occupied by the fluid is due to the combined pressure exerted on pore space by the fluid column at the depth of consideration and the overbearing rocks at that depth. The pressure effect of fluid column weight and rock matrix pressure is termed *overburden pressure*.

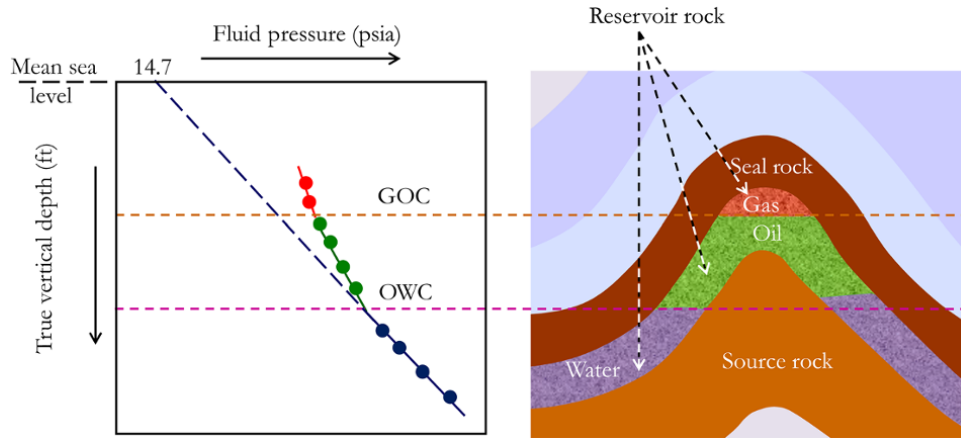


**Figure 1.4** Reservoir fluid zones in a normally pressurized petroleum reservoir.

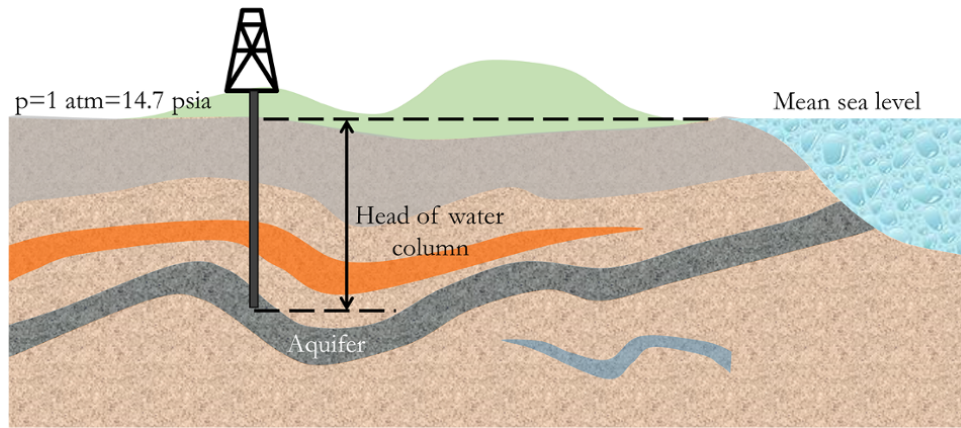


**Figure 1.5** Aquifer in hydraulic communication with the surface (normally pressure aquifer).

Measurement and analysis of formation fluid pressure at different depths is important and can be used to determine hydrocarbon fluid zones in a reservoir (Fig. 1.4).

### 1.5.1. Reservoir Fluid Zones

Formation fluid pressure at any given depth is primarily controlled by formation water pressure in hydraulic communication with the other fluid in the reservoir. The formation fluid pressure at any depth within the fluid column can be defined as:

$$p_j = G_j z_j + C_j \quad (1.1)$$

where  $p_j$  is fluid formation pressure in fluid zone  $j$ ,  $G_j$  is gradient of fluid  $j$ ,  $z_j$  is depth in fluid zone  $j$ , and  $C_j$  is constant of gradient equation for fluid  $j$ . Hence, the formation water pressure at any depth can be defined as:

$$p_{\text{water}} = G_{\text{water}} z_{\text{water}} + C_{\text{water}} \quad (1.2)$$

where the water column has some form of hydraulic connection to the surface,  $C_{\text{water}} = 14.7$  psia and

extrapolation of the water gradient line to the surface will be 14.7 psia (1 atm), which is atmospheric pressure (Fig. 1.5).

$G_{\text{water}}$  is the water gradient and is dependent primarily on the composition and temperature of water. The gradient of fresh water, defined by  $\frac{dp_{\text{water}}}{dz_{\text{water}}}$ , is 0.433 psi/ft. The value of gradient for North Sea water is approximately 0.45 psi/ft (salinity of 35,000 ppm) and approximately 0.59 psi/ft for Dead Sea with water (salinity of 330,000 ppm). When the value of  $C_{\text{water}}$  is 14.7 psia, the water zone is said to be *normally pressured*; when the value is greater than 14.7 psia, the water zone is said to be *overpressured*; and when the value is less than 14.7 psia, the water zone is said to be *underpressured*.

An abnormally pressured (underpressured or overpressured) reservoir would only occur when there is an hydraulic seal between the aquifer and the surface. An overpressured reservoir can arise due to uplift of a trapped reservoir after migration, while an underpressured reservoir will be due to downthrow of a reservoir after

migration. The effect of temperature on confined (trapped) formation fluid can also create an abnormal pressured reservoir. Other processes that have been reported to cause abnormal reservoir pressure include: osmosis, buoyancy, phase changes, and differential depletion across compartments with common aquifer.

Gradients of oil and gas are less than that of water due to lower densities. The pressure in the gas and oil zones, respectively, at any given depth can be expressed as:

$$p_{\text{gas}} = G_{\text{gas}}z_{\text{gas}} + C_{\text{gas}} \quad (1.3)$$

$$p_{\text{oil}} = G_{\text{oil}}z_{\text{oil}} + C_{\text{oil}} \quad (1.4)$$

Typical values of fluid gradients are: 0.01–0.1 psi/ft for gas; 0.23–0.35 psi/ft for oil, and as high as 0.39 psi/ft for heavy oil; and 0.43–0.5 psi/ft for water.

For a reservoir with gas, oil, and water zones as shown in Fig. 1.4, at the gas–oil contact (GOC) if the fluid zones are in hydraulic communication, it is expected that the reservoir in pristine state will be in equilibrium and  $p_{\text{gas}}$  will be equal to  $p_{\text{oil}}$ . Hence, solving equations (1.3) and (1.4) with  $p_{\text{gas}} = p_{\text{oil}}$ , depth value which is equal to the GOC is determined. The oil–water contact (OWC) is determined in similar approach by solving equations (1.4) and (1.3) with the condition  $p_{\text{oil}} = p_{\text{water}}$ .

From equations (1.3) and (1.4), with  $p_{\text{gas}} = p_{\text{oil}}$ , the GOC is given as:

$$\text{GOC} = z_{\text{gas}} = z_{\text{oil}} = \frac{C_{\text{gas}} - C_{\text{oil}}}{G_{\text{oil}} - G_{\text{gas}}} \quad (1.5)$$

From equations (1.4) and (1.2), with  $p_{\text{oil}} = p_{\text{water}}$ , the OWC is given as:

$$\text{OWC} = z_{\text{oil}} = z_{\text{water}} = \frac{C_{\text{oil}} - C_{\text{water}}}{G_{\text{water}} - G_{\text{oil}}} \quad (1.6)$$

The “OWC” determined from gradient analysis, equation (1.6), is actually the free water level (FWL), which is the depth at which water saturation approaches 1 and the pressure of the oil phase is the same as that of water (zero capillary pressure). Actual OWC is defined as the depth at which water saturation approaches 1 with the existence of capillary pressure. The difference between FWL and OWC is discussed in Chapter 2 and Chapter 6. In order to distinguish between OWC and FWL, equation (1.6) is redefined as FWL instead of OWC:

$$\text{FWL} = \frac{C_{\text{oil}} - C_{\text{water}}}{G_{\text{water}} - G_{\text{oil}}} \quad (1.7)$$

### Exercise 1.1 Reservoir Fluid Zones

Given the formation pressure measurements and reservoir fluid density at different true vertical depths (relative to mean sea level) from a reservoir with gas, oil, and water zones in Table 1.1:

**Table 1.1** Formation Pressure and Fluid Data.

True vertical depth subsea, TVDSS (ft)	Formation pressure (psia)	Fluid	Reservoir fluid density (lb/ft <sup>3</sup> )
6,967.00	3,765.47	Gas	14.4
7,624.00	3,896.00	Oil	37.4
8,936.00	4,432.64	Water	64.8

Determine the gas–oil contact and free water level. Determine if reservoir is normally pressured or abnormally pressured.

### Solution Steps.

*Step 1:* convert reservoir fluid density in lb/ft<sup>3</sup> to fluid gradient in psi/ft by dividing by 144 (144 in<sup>2</sup> ≡ 1 ft<sup>2</sup>).

*Step 2:* calculate  $C_{\text{fluid}}$ :  $C_{\text{water}}$ ,  $C_{\text{gas}}$ , and  $C_{\text{oil}}$  using equations (1.2), (1.3), and (1.4), respectively.

*Step 3:* calculate GOC and FWL using equations (1.5) and (1.7), respectively.

*Step 4:* using the value of  $C_{\text{water}}$ , infer if the reservoir is normally or abnormally pressured.

### Solution.

Calculating  $C_{\text{water}}$  using equation (1.2):

$$p_{\text{water}} = G_{\text{water}}z_{\text{water}} + C_{\text{water}}$$

Making  $C_{\text{water}}$  the subject of the formula:

$$C_{\text{water}} = p_{\text{water}} - G_{\text{water}}z_{\text{water}}$$

Substituting  $p_{\text{water}}$ ,  $G_{\text{water}}$ , and  $z_{\text{water}}$  into the above:

$$C_{\text{water}} = 4,432.64 - 0.45 \times 8,936 = 411.44 \text{ psia}$$

$C_{\text{gas}}$ , and  $C_{\text{oil}}$  are also calculated in similar way using equations (1.3) and (1.4), respectively.

The calculated fluid gradients and  $C_{\text{fluid}}$  for each zone are summarized in Table 1.2.

Calculating the GOC and FWL using equations (1.5) and (1.7), respectively:

$$\text{GOC} = \frac{3,068.77 - 1,915.88}{0.260 - 0.100} = 7,218.11 \text{ ft}$$

$$\text{FWL} = \frac{1,915.88 - 144.44}{0.45 - 0.26} = 7,906.53 \text{ ft}$$

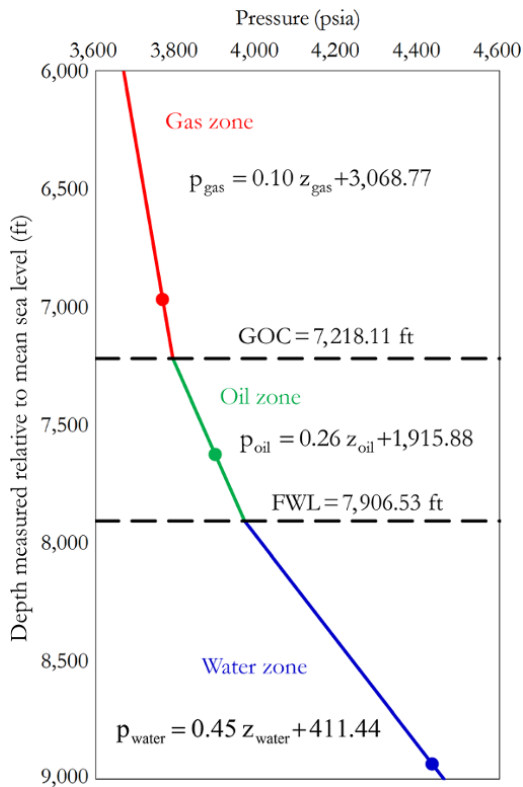
The reservoir aquifer is abnormally pressured (over-pressured) because  $C_{\text{water}}$  is greater than 14.7 psia (1 atmosphere).

Fig. 1.6 shows a graphical presentation of solution to Exercise 1.1.

It is convenient to plot depth on a reversed vertical axis and pressure on horizontal axis to enhanced visualization (Fig. 1.6) considering that depth increases vertically downwards. However, for gradient equations, it is best

**Table 1.2** Summary of Solution to Exercise 1.1.

TVDSS (ft)	Formation pressure (psia)	Fluid	Fluid density (lb/ft <sup>3</sup> )	Fluid gradient (psi/ft)	C <sub>fluid</sub> (psia)
6,967.00	3,765.47	Gas	14.4	0.100	3,068.77
7,624.00	3,896.00	Oil	37.4	0.260	1,915.88
8,936.00	4,432.64	Water	64.8	0.450	411.44


**Figure 1.6** Reservoir fluid zones for Exercise 1.1.

to express depth as an independent variable and pressure as dependent variable, as shown in equations (1.1), (1.2), (1.3), and (1.4), and as illustrated in Fig. 1.6. This ensures that fluid gradient is the coefficient of  $z$  (depth) and  $C_{\text{fluid}}$  can be easily used to determine if the reservoir is normally pressured or abnormally pressured. Use of pressure–depth profiles for reservoir characterization is discussed in detail in Chapter 3 (Wireline Formation Testing).

### 1.5.2. Reservoir Hydrocarbon Volumes

One of the primary functions of a petroleum engineer is determining the volume of hydrocarbons in reservoirs. The volume of hydrocarbon in a reservoir is expressed in terms of stock tank condition, which is the condition representing surface pressure and temperature. This

makes sense considering that for sales and comparison it will be appropriate to have fixed conditions. Also, crude oil is stored, metered, and sold at surface conditions. Original oil in place (OOIP) can be expressed as:

$$\text{OOIP}(\text{m}^3) = \frac{\text{GRV} \times \text{N/G} \times \phi \times (1 - S_{\text{wc}})}{B_{\text{oi}}} \quad (1.8)$$

Equation (1.8) may be called OIP (oil in place), STOIP (stock tank oil in place) or STOIIP (stock tank oil initially in place).

Equation (1.8) can be expressed in an engineering oil field (EOF) unit as:

$$\text{OOIP}(\text{stb}) = \frac{7,758 \times \text{GRV} \times \text{N/G} \times \phi \times (1 - S_{\text{wc}})}{B_{\text{oi}}} \quad (1.9)$$

$B_{\text{oi}}$  is the formation volume factor at initial reservoir condition while  $\frac{1}{B_{\text{oi}}}$  represents the shrinkage factor at initial reservoir condition.  $B_{\text{oi}}$  in equations (1.8) and (1.9) converts oil volume at reservoir condition to stock tank (surface) condition.  $\text{N/G}$  (net-to-gross ratio) defines the fraction of the gross rock volume (GRV) that is reservoir rock. The product of GRV and  $\text{N/G}$  give the *net rock volume*, which is the volume that contains economically producible hydrocarbons.

In a similar way, original gas in place is expressed in metric units, in terms of  $B_{\text{gi}}$  (initial gas formation volume factor), as:

$$\text{OGIP}(\text{m}^3) = \frac{\text{GRV} \times \text{N/G} \times \phi \times (1 - S_{\text{wc}})}{B_{\text{gi}}} \quad (1.10)$$

and, also in metrics units, in terms of  $Z_i$  (initial gas compressibility factor) as:

$$\text{OGIP}(\text{m}^3) = \text{GRV} \times \text{N/G} \times \phi \times (1 - S_{\text{wc}}) \frac{T_s p_i}{T_f p_s Z_i} \quad (1.11)$$

$$T_s = (273 + 15)\text{K}$$

$$p_s = (101.35\text{Kpa})$$

OGIP is expressed in EOF units as:

$$\text{OGIP}(\text{MMscf}) = \frac{43,560 \times \text{GRV} \times \text{N/G} \times \phi \times (1 - S_{\text{wc}})}{B_{\text{gi}}} \quad (1.12)$$

and, also in EOF units, in terms of  $Z_i$  as:

$$\begin{aligned} \text{OGIP}(\text{MMscf}) &= 43,560 \times \text{GRV} \times \text{N/G} \times \phi \\ &\quad \times (1 - S_{\text{wc}}) \frac{T_s p_i}{T_f p_s Z_i} \quad (1.13) \\ T_s &= (460 + 60) \text{R} \\ p_s &= 14.65 \text{psia} \end{aligned}$$

Table 1.3 summarizes parameters and their units for hydrocarbon in place calculations.

**1.5.2.1. Reservoir Hydrocarbon Volume Estimates.**

Where reservoir hydrocarbon volumes are conclusively determined using decisively known values of parameters in OOIP and OGIP equations without any room for random variation, this approach is called *deterministic* hydrocarbon in place calculation. In such volume calculations, a given reservoir property input will always produce the same output. Hydrocarbon in place can also be determined using a range of reservoir property values in the form of probability distributions, such that hydrocarbon

in place is thus determined in some form of probability distribution. This approach is called *stochastic* hydrocarbon in place calculation. In the stochastic calculation, reservoir properties are randomly sampled from distribution over a number of specified times to generate possible outcomes. The most common approach for stochastic hydrocarbon in place calculation is to use a *Monte Carlo method*, which is a wide class of computerized algorithms that uses repeated random sampling for calculations.

**1.5.2.2. Gross Rock Volume Calculation.** *Gross rock volume (GRV)* is an important input for hydrocarbon volume in place calculations. Methods for calculating rock volume from contour maps involves representing the entire volume as stripes of frustums (Fig. 1.7).

Gross rock volume can be calculated using the *trapezoidal (average end-area) method*, which is expressed as:

$$\text{GRV} = \sum_{i=1}^n \frac{h_i}{2} (A_{i-1} + A_i) \quad (1.14)$$

**Table 1.3** Parameters and Units for Hydrocarbon in Place Calculations.

Nomenclature	Parameter	Equation (1.8)	Equation (1.9)	Equations (1.10) and (1.11)	Equations (1.12) and (1.13)
		units	units	units	units
<b>GRV</b>	gross rock volume	m <sup>3</sup>	acre-feet	m <sup>3</sup>	acre-feet
<b>N/G</b>	Net-to-Gross Ratio	fraction	fraction	fraction	fraction
<b>φ</b>	porosity	fraction	fraction	fraction	fraction
<b>S<sub>wc</sub></b>	connate water saturation	fraction	fraction	fraction	fraction
<b>B<sub>oi</sub></b>	initial oil formation volume factor	m <sup>3</sup> /m <sup>3</sup>	bbl/stb		
<b>B<sub>gi</sub></b>	initial gas formation volume factor			m <sup>3</sup> /m <sup>3</sup>	ft <sup>3</sup> /scf
<b>T<sub>s</sub></b>	base temperature, std condition			K	R
<b>T<sub>f</sub></b>	formation temperature			K	R
<b>p<sub>s</sub></b>	base pressure, std condition			kPa	psia
<b>p<sub>i</sub></b>	initial reservoir pressure			kPa	psia
<b>Z<sub>i</sub></b>	gas compressibility factor at p <sub>i</sub>			fraction	fraction

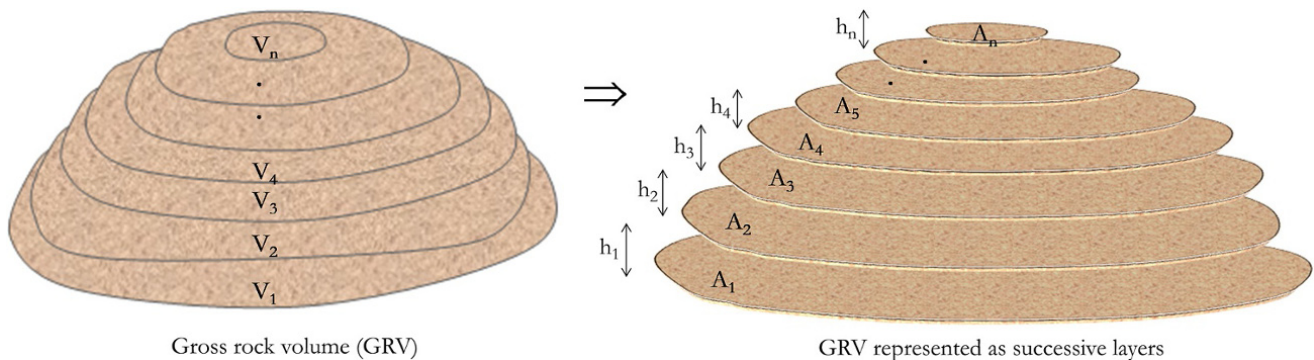


**Figure 1.7** Representation of gross rock volume as frustums for volumetric calculations.



where  $A_i$  is the area of the end section,  $h_i$  is the distance between sections  $A_i$  and  $A_{i-1}$ .

Another method is the *prismoidal method*, which is expressed as:

$$GRV = \sum_{i=1}^n \frac{h_i}{3} (A_{i-1} + A_i + \sqrt{A_{i-1} \times A_i}) \quad (1.15)$$

**Exercise 1.2 Hydrocarbon Volume Calculation**

Using the information provided in Fig. 1.8, calculate the deterministic OOIP in stock tank barrels (stb) using

the trapezoidal and prismoidal rock volume calculation methods given that:  $\phi = 0.21$ ;  $N/G = 1$ ;  $S_{wc} = 0.13$  and  $B_o = 1.5 \text{ bbl/stb}$ .

**Solution Steps.**

*Step 1:* determine the approximate number of square grids within the OWC contour line and other contour lines above the OWC, up to the reservoir top. Square grids can be refined smaller to improve the accuracy of the area to be determined from the number of square grids (Fig. 1.9).

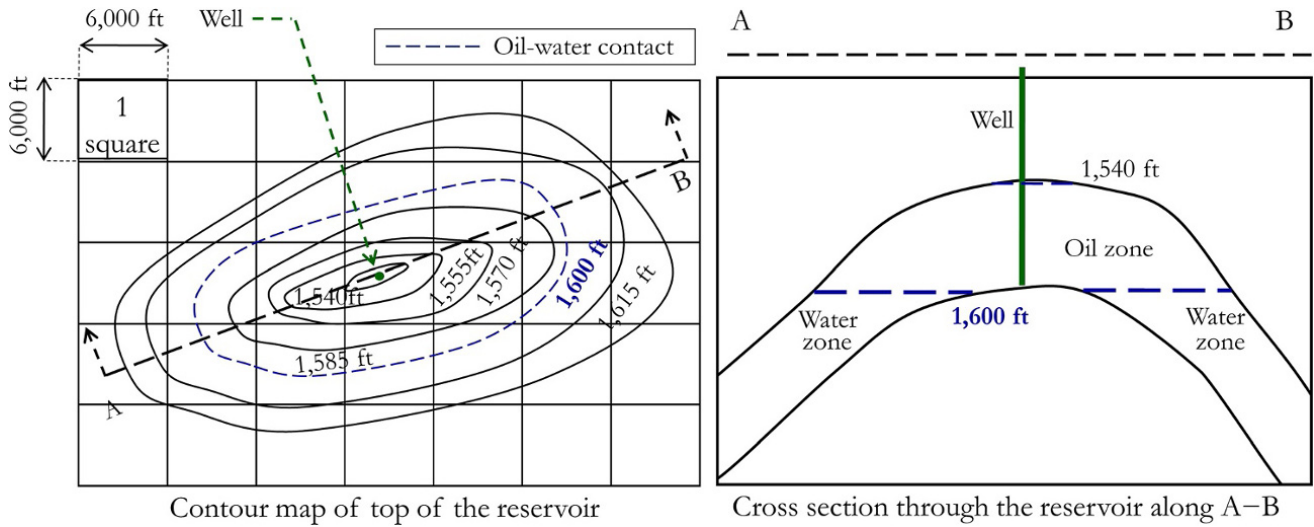


**Figure 1.8** Contour map of the top of the reservoir and the cross-section through A-B.

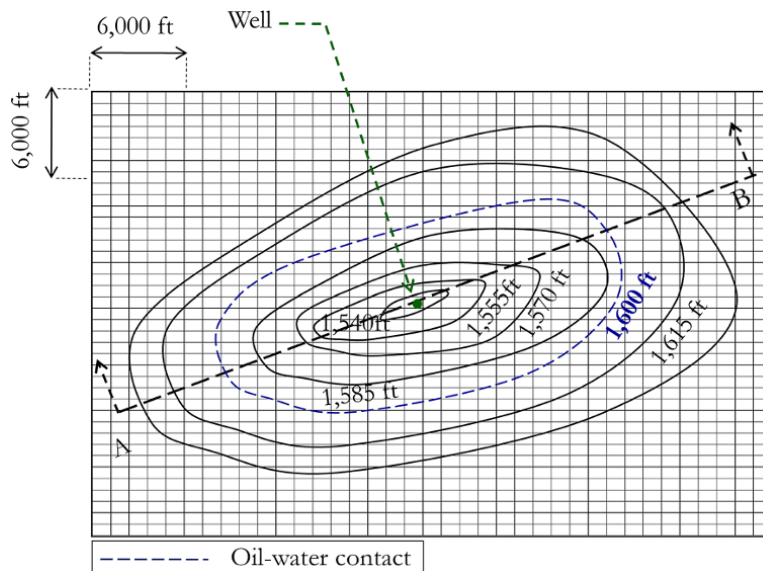


**Figure 1.9** Refined square grids for more accurate area calculation.

*Step 2:* determine cross-sectional area of the OWC and the remaining contour lines above the OWC, up to the reservoir top by multiplying the number of square grids (N) by the area of a single square grid.

*Step 3:* determine gross rock volume over net reservoir interval using equations (1.14) and (1.15).

*Step 4:* determine the OOIP using equation (1.9).

**Solution.**

Table 1.4 summarizes the gross rock volume calculation for Exercise 1.2.

Gross rock volume:

*Using the trapezoidal method*

$$GRV (ft^3) = 5.78E + 09ft^3$$

$$GRV(acre-ft) = 5.78 \times 10^9 (ft^3) \times 2.29568 \times 10^{-5} \left( \frac{acre-ft}{ft^3} \right) = 1.33 \times 10^5 (acre-ft)$$

$$OOIP(stb) = \frac{7,758 \times GRV \times N/G \times \phi \times (1 - S_{wc})}{B_{oi}}$$

$$OOIP(stb) = \frac{7,758 \times 1.33 \times 10^5 \times 1 \times 0.21 \times (1 - 0.13)}{1.5} = 1.25 \times 10^8 stb$$

*Using the prismoidal method*

$$GRV (ft^3) = 5.65E + 09ft^3$$

$$GRV(acre-ft) = 5.65 \times 10^9 (ft^3) \times 2.29568 \times 10^{-5} \left( \frac{acre-ft}{ft^3} \right) = 1.30 \times 10^5 (acre-ft)$$

$$OOIP(stb) = \frac{7,758 \times GRV \times N/G \times \phi \times (1 - S_{wc})}{B_{oi}}$$

$$OOIP(stb) = \frac{7,758 \times 1.30 \times 10^5 \times 1 \times 0.21 \times (1 - 0.13)}{1.5} = 1.23 \times 10^8 stb$$

**1.5.2.3. Net-to-Gross Ratio.** The *net-to-gross ratio* (N/G or NTG) can refer to a wide range of definitions. It may refer to *sand net-to-gross* (NTG<sub>sand</sub>), *reservoir net-to-gross* (NTG<sub>res</sub>) or *pay net-to-gross* (NTG<sub>pay</sub>).

*Sand net-to-gross ratio:* this is the ratio of sand interval(s) to the entire gross interval of interest (Fig. 1.10), where sand interval(s) can be defined as interval(s) of *clean sandstone lithology*, often determined using a limiting *shale fraction* (V<sub>sh</sub>) cutoff.

*Reservoir net-to-gross ratio:* this is the ratio of the hydrocarbon bearing rock interval(s) that has desirable reservoir properties to the entire gross interval of interest (Fig. 1.10). Desirable reservoir properties are porosity and permeability, as they determine the capacity of the reservoir to store and flow hydrocarbon, respectively.

*Pay net-to-gross ratio:* this is the ratio of net pay-to-gross rock interval (Fig. 1.10), where net pay is reservoir interval(s) that contain hydrocarbons that can be produced economically. Net pay intervals must exceed a defined minimum porosity, permeability, and hydrocarbon saturation called *cutoffs*. Generalized values of cutoffs for petrophysical properties as presented in some literature are meaningless; since the pay intervals are intervals that can be produced economically as such, cutoff values must be measured under dynamic conditions or analogues that have similar fluid, rock, and rock-fluid properties. The recovery of oil, for instance, does not depend on permeability only but on viscosity and thickness of interval. Hence, a heavy oil would have a higher permeability cutoff than a light oil. Also, pay interval would depend on current technology and economic parameters to define what can be produced economically. Intervals considered uneconomical today may become economical in the future. This also means that cutoffs can change with time.

The concept of using a pay interval should only be considered in recovery calculation methods that cannot discriminate between producible and nonproducibile intervals. In reservoir simulation where a geological model (*geomodel*) is used directly in the simulation without upscaling petrophysical properties, an approach very common in recent times, pay interval, net-to-gross and cutoffs should be avoided. This is because reservoir

**Table 1.4 Gross Rock Volume Calculation for Exercise 1.2.**

Contour depth, z (ft)	N = No. of 600 × 600 ft squares	A <sub>i</sub> (ft <sup>2</sup> ) = N × 6000 × 6000	h <sub>i</sub> (ft) = z <sub>i</sub> - z <sub>i-1</sub>	V <sub>i</sub> (ft <sup>3</sup> ) using equation (1.14)	V <sub>i</sub> (ft <sup>3</sup> ) using equation (1.15)
1,600	7.1	2.56E+08			
1,585	4.5	1.62E+08	15	3.13E+09	3.11E+09
1,570	1.9	6.84E+07	15	1.73E+09	1.68E+09
1,555	0.7	2.52E+07	15	7.02E+08	6.76E+08
1,540	0.1	3.60E+06	15	2.16E+08	1.92E+08
GRV = ΣV <sub>i</sub> =				5.78E+09	5.65E+09

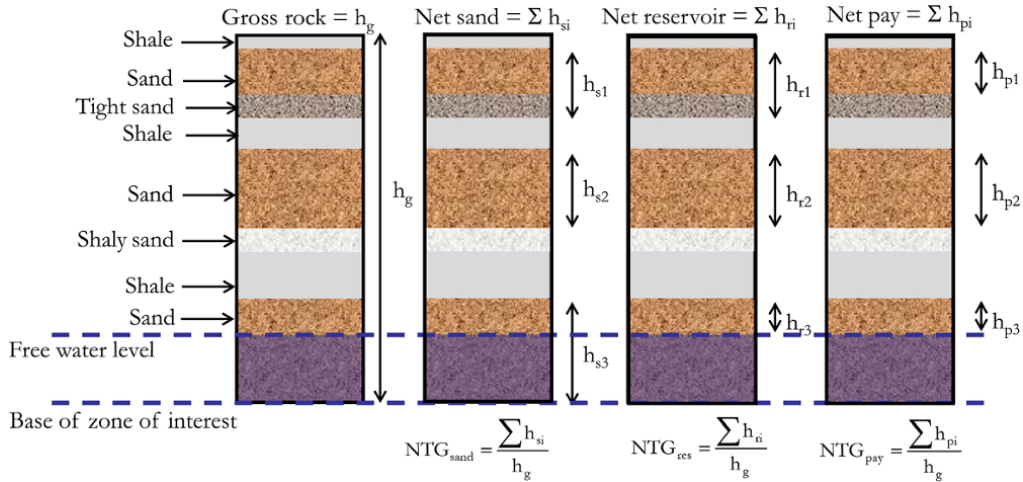


Figure 1.10 Schematic illustration of different definitions of net-to-gross ratios.

simulation would handle appropriately intervals that can contribute to flow or otherwise.

Petroleum resource can generally be classified as: *prospective*, *contingent*, and *reserves* in order of their increasing chance of commerciality (Fig. 1.11). These categories of petroleum resources are a subset of the *total petroleum initially-in-place* (Fig. 1.11) [SPE-PRMS, 2008].

### 1.6. PETROLEUM RESOURCE CLASSIFICATION

Petroleum resource estimation and classification falls into the discipline of reservoir engineering. However, support from other discipline, such as geologist, geophysics, petrophysicist, facility design engineers and economists, is required and important.

#### 1.6.1. Prospective Resources

Based on the chances of commercialization, prospective resources are ranked lowest amongst the different petroleum resources. Prospective resources (*prospect*) are estimated petroleum quantities associated with a

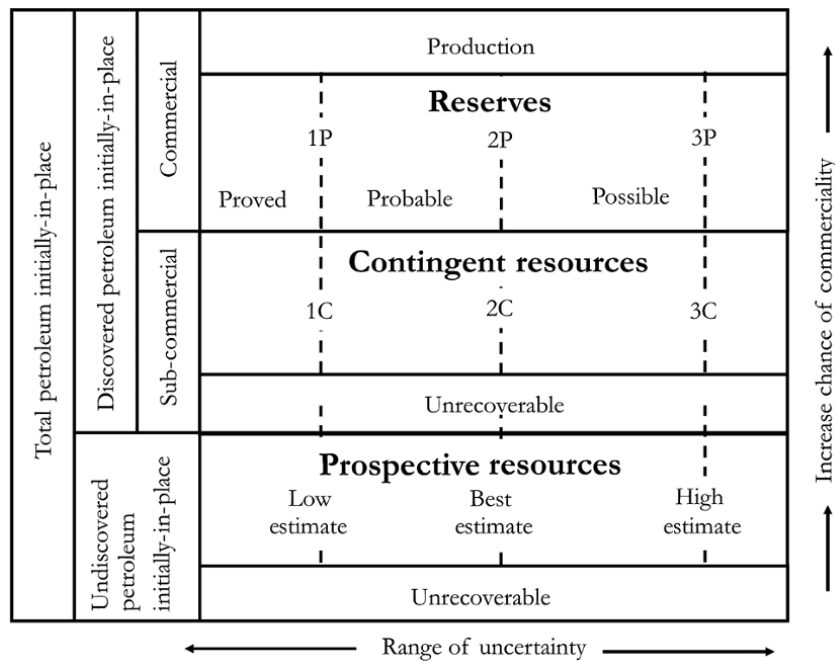


Figure 1.11 Petroleum resource classification [SPE-PRMS, 2008].

development plan, at a given date, considered potentially recoverable from undiscovered accumulation.

Based on uncertainty and level of confidence, prospective resources can be classified as: *low estimate*; *best estimate*, and *high estimate* (Fig. 1.11). Estimation of each category of prospective resources can be by *scenario-based approach*, with different deterministic cases, or by *stochastic approach* discussed in Section 1.5.2.1.

### 1.6.2. Contingent Resources

Contingent resources are estimated petroleum quantities associated with a development plan, at a given date, considered potentially recoverable from discovered accumulation but not commercial due to one or more contingencies [SPE-PRMS, 2008]. Contingent resources rank next after prospective resources in order of increasing chance of commercialization (Fig. 1.11).

Based on uncertainty and level of confidence, contingent resources can be classified as: 1C (with at least 90% probability of quantity been recoverable), 2C (with at least 50% probability of quantity been recoverable), and 3C (with at least 10% probability of quantity been recoverable).

### 1.6.3. Reserves

Reserves can be defined as estimated petroleum quantities anticipated to be commercially recoverable by application of development projects, to known discovered accumulations from a given date forward under defined conditions [SPE-PRMS, 2008].

Reserve are associated with development option(s) and, hence, for a resource to be classified as reserve, it is expected that there must exist a resolute intention to develop resources within a reasonable time frame, typically five years [SPE-PRMS, 2008].

Criteria that must be met for petroleum resources to be classified as reserve include:

- resources must be discovered (presence of a well);
- resource must be commercially recoverable with exiting technology;
- there must be commercially recoverable remaining reserve based on a development plan at the effective date of the evaluation.

#### 1.6.3.1. Reserve Classification Based on Uncertainty.

Based on the uncertainty and the level of confidence in the amount of commercially recoverable resources, reserves can be described as: 1P(Proved); 2P(Proved + Probable), and 3P(Proved + Probable + Possible) where:

*Proved reserve* is the estimated petroleum quantity anticipated to be commercially recoverable by

application of development projects with a high level of confidence (at least with 90% confidence).

*Probable reserve* is the estimated petroleum quantity that, when added to the proved reserved, is anticipated to be recoverable by application of development projects with at least 50% confidence.

*Possible reserve* is the estimated petroleum quantity that, when added to the proved and probable reserve, is anticipated to be recoverable by application of development projects with at least a 10% confidence.

The proved petroleum reservoir volume must be limited to identified hydrocarbon levels such as hydrocarbon down to (HDT) the lowest known hydrocarbons, where hydrocarbon–water contact (HWC) is absent. Formation pressure logs analysis (gradient analysis) remains one of the most reliable sources of fluid contacts, as discussed in Chapter 6. It is important the fluid contacts from the gradient analysis of formation pressure logs are checked for consistencies with well log analysis such as neutron density for gas–oil contact and resistivity log for hydrocarbon–water contact. Analysis of open hole well logs and formation pressure logs are discussed in Chapters 5 and 6, respectively.

The use of seismic attributes for proved reserve volumetric calculation requires that such attributes are well defined in the reservoir and correlated to well properties. Seismic attributes alone without well correlation cannot be used for proved reserve estimation.

**1.6.3.2. Reserve Categorization Based on Development Status.** Based on development status, reserves can be classified as *developed reserve* and *undeveloped reserves*.

(i) *Developed reserves* are reserves that are expected to be recovered from the existing well and facility. Developed reserve may be further categorized based on production status as *producing reserve* – where reserve is expected to be recovered from the existing completion interval, which is open to production, at the time of reserve estimation – and *nonproducing reserve* – where there is existing facility to recover reserve however they are not producing due to wells shut-in or inability of wells/facility to produce [SPE-PRMS, 2008].

(ii) *Undeveloped reserves* are reserves that are expected to be recovered from new wells within an undrilled compartment, or from an existing well that requires a major workover or requires major expenditure for recompletion [SPE-PRMS, 2008].

### 1.6.4. Reserve Estimation Methods

Acceptable methods for reserve estimation include one or a combination of the methods described here.

#### 1.6.4.1. Volumetric Method for Reserve Estimation.

This method is based on equations (1.8)–(1.13) to determine in place volume, which will then be multiplied by a recovery factor determined from relative permeability data, reservoir performance methods or analogue field data. Volumetric methods require gross rock volume, net-to-gross ratio, initial/connate water saturation, porosity, fluid formation volume factor, and recovery factor.

*Gross rock volume (GRV)*: can be determined from a combination of well and seismic data; the geophysicist creates depth maps with the reservoir top and base from which GRV is calculated. Creation of depth maps involves *well-to-seismic tie* processes and mapping horizon from seismic analysis. Seismic data are reasonably reliable for assessment of areal extent, geometry, and structural properties of the reservoir. Uncertainty with use of seismic data for reserve estimation is generally high.

Seismic data on their own are poor in the prediction of porosity, NTG, and  $S_{wc}$ . However, by correlating seismic attributes with well data and properties, the reliability of seismic data for predicting reservoir properties can be improved. Reserve estimation requires accuracy for valuation, repeatability for comparison, and transparency, which may not be met by use of seismic data without correlating with well data.

*Net-to-gross ratio (NIG or NTG)*: is the ratio of net reservoir (with porosity and permeability) to total gross thickness of interest; it can be determined along the well from analysis of well logs (Chapter 5). The geologist creates property correlations between the wells and delineates the reservoir into different geologic units. Across each geological unit in the reservoir, geostatistical techniques and depositional models can be used to distribute properties across each geological unit and the entire reservoir model. Seismic attributes derived from high quality seismic data can be used in geological extrapolation of reservoir properties across each geological unit using geostatistical techniques such as *kriging* and *cokriging*.

*Porosity*: open hole well log interpretation with calibration against core porosity, determined under stressed conditions or corrected for stress effect, can be used to determine porosity along the well. In a similar way to NTG distribution, by correlating properties across the well for different geological units and then using geostatistical techniques, porosity can be distributed across the entire reservoir model. Seismic attributes derived from high quality seismic data are important in porosity distribution.

*Initial connate water saturation ( $S_{wc}$ )*: capillary pressure data and  $S_{wc}$  calculated along the well from the open hole log are used to derive *saturation-height function* (Section 2.5.7) for each facies (rock type). Derived saturation-height function is then used in populating water saturation in the entire reservoir model. Distribution of

water saturation away from the well must be based on capillary pressure relationship for each rock type (facies) rather than by geostatistical extrapolation.

#### 1.6.4.2. Performance-based Approach for Reserve Estimation.

These methods involve use of production histories with a model (simulation or analytical) to model reservoir system, predict reservoir performance, and recoverable and unrecoverable hydrocarbon volumes. Methods that can be described as performance based include:

- **Material balance**: this involves representing different reservoir section as “tanks” and using conservation of mass principles and fluid properties to model reservoir systems, energy for fluid production, and volume left in the reservoir for a given volumetric withdrawal. The concept of material balance for reservoir performance prediction is discussed in Chapter 12.

- **Reservoir simulation**: this involves dividing the reservoir into grid cells (finite element or finite volume), with each cell serving as a simple material balance “tank”, and using combination of material balance, flow in porous media, and fluid equation to predict flow of reservoir fluids through porous media, reservoir deliverability, and recoverable and unrecoverable hydrocarbon volumes.

- **Well test analysis**: this involves analysis of pressure and rate measurement with *well test interpretation models* to predict reservoir performance. Well test interpretation models are analytical models derived from a combination of mass continuity equation, Darcy’s law and equation of state. These interpretation models can be used to simulate bottomhole well pressure response for a given rate history. Well test analysis also gives either minimum connected volume when full reservoir boundaries have not been reached during testing or in place volume when full boundaries have been reached during well testing. Analysis of well test data is discussed in Chapter 8.

- **Production decline curve analysis**: this approach involves using declining mathematical equations such as exponential, harmonic or hyperbolic functions as reservoir or field performance response. Use of the production decline curve method for reserve estimation involves finding the best decline model that matches production history, then using the model to predict future production and recoverable and unrecoverable hydrocarbon volumes. Use of production decline models for reservoir performance prediction is discussed in Chapter 13.

**1.6.4.3. Analogue.** Analogies to other reservoirs may be considered for obtaining properties for resource and reserve calculation where they have similar geological characteristic, geological location, and reservoir rock and fluid characteristics.

The choice of method for estimating reserves generally depends on maturity of assets, availability and quality of data, and the experience and familiarity of the engineer with the different resource estimation methods.

### 1.6.5. Use of Seismic Data for Petroleum Resource Calculation

With rigorous interpretation, seismic data are important for characterization of reservoir features such as dip, faulting, and reliable gross thickness. The use of seismic data for petroleum resource estimation requires in-depth support from the geologist and geophysicist, as most reservoir engineers may not be familiar with seismic interpretation methods. Seismic interpretation often depends significantly on experience and judgement.

Using seismic data for determining reservoir properties used for volumetric calculation is only reliable, when there are well data to correlate with seismic data. Where there are no well data to correlate seismic attributes, analogues with reasonable assumptions are often preferred to seismic derived properties alone for volumetric properties determination.

### 1.6.6. Resource Estimation at Different Stages of Life Cycle

**1.6.6.1. Prospect.** Prospect (*prospective resources*) are considered potentially recoverable hydrocarbon volumes associated with a development plan that targets currently undiscovered resources. Geologists and geophysicists using theories, seismic data, regional or near-field correlation will be involved in determining the probability of finding petroleum as part of *prospect risking and ranking*.

When geologists identify the possibility of petroleum being found in a particular area, likely petroleum volumes and the recoverable amount of petroleum in the reservoir, field or concession are calculated using mapped structure.

The only resource volume calculation method for a prospect is the volumetric approach described by equations (1.8)–(1.13) with properties taken from analogue, correlation with nearby fields, and valid assumptions. GRV can be determined from seismic data but petrophysical properties should not be determined from seismic data due to the absence of well data to correlate seismic attributes at this stage. A prospect must satisfy the following criteria before it can be termed a prospect: (i) presence of a trapping mechanism; (ii) porosity and permeability; and (iii) a matured source rock that can generate hydrocarbon. Hence, the probability that a prospect has a reservoir with trapped hydrocarbon (probability of success) is, therefore, a product of probability of area of interest having a trap, reservoir rock, and mature source rock. This probability of success can be expressed as:

$$pr_{\text{success}} = pr_{\text{trap}} \times pr_{\text{reservoir}} \times pr_{\text{source}} \quad (1.16)$$

Equation (1.16) assumes constituent probabilities are independent of each other.

**1.6.6.2. Discovery.** When a well has been drilled and hydrocarbon is found, the well becomes a *discovery well*. Petrophysical properties can then be obtained along the well using well log interpretation techniques. Correct fluid formation volume factor and other fluid properties can be determined from analysis of fluid samples recovered from the well. At this stage, a well test may be carried out, with analysis of well test data giving an understanding of the potential deliverability of the well and reservoir boundaries in the case of an extended well test.

At this point, initial volumetric calculations at the prospective stage can be updated with increased confidence as well log properties are available. At this stage if there are seismic attributes, from high quality seismic data, they can be correlated with well properties and used for property distribution away from the well. Resource volume calculation options that can be considered include: volumetric; well test to get minimum connected volume (which is a proved volume) or hydrocarbon initially in place if pressure diffusion has reached the entire reservoir boundaries; and material balance if full reservoir boundaries have been reached by pressure diffusion to ensure depletion. Reservoir simulation can also be used to match test data and predict reservoir performance with respect to recoverable and unrecoverable hydrocarbon resources.

**1.6.6.3. Appraisal.** Generally, one or more additional wells will be drilled to appraise discovered petroleum resources. More than one well improves the understanding of the structure of the reservoir, lateral continuity of properties, the ability to correlate properties between wells, and to delineate the reservoir into different geologic units. Core samples may be acquired during drilling of appraisal well(s). Core samples are then analyzed for petrophysical properties such as porosity, permeability, capillary pressure, and relative permeability (Chapter 2). Calibration of porosity with well log data improves confidence in the calculated porosity; capillary measurements are useful for predicting water distribution in the reservoir; relative permeability gives an indication of flow of different phases in the presence of others. Relative permeability models can be used to determine a range of recoverable petroleum from initially in place volume.

The appraisal stage of the field development should provide enough information for a development strategy of the field, if the field is to be developed. Petroleum resources determined at this stage can be reserve or contingent resources. Where resource is classified as reserve, then reservoir, field or concession will proceed to

development. If the resource is considered contingent, then development maybe considered in the future when it is either economically feasible (for economic contingent resource) or technically feasible (for technical contingent resource).

**1.6.6.4. Development Stage.** As additional wells are drilled for production at the *initial development stage*, information acquired from newly drilled wells will provide more information on the structure and properties of the reservoir. Pressure and rate measurements at this stage can be used to monitor the well and reservoir. Also, additional information will help improve models, optimizing the development plan based on reservoir response. The initial development stage can be considered as a *build-up stage* of production profile (Fig. 13.1). Since the resource is at the development stage, it must have satisfied criteria for a reserve (can be produce commercially) and, therefore, the interest at the development stage is remaining reserve. At this stage, with increased information, reserve estimate and category may change.

When the field is at the *full field development stage*, where the reservoir or field has produced at an extended plateau or produced a significant volume from the reservoir and dynamic reservoir response is understood, material balance, well test analysis (specifically deconvolution), and reservoir simulation can be used to improve reservoir performance characterization and reserve estimate. Also, at this stage, based on an understanding of the reservoir or field, reservoir and well management decisions – such as increasing production with infill drilling; arresting decline if the field is in decline; well workovers to improve production; supplementing reservoir energy with methods such as such water or gas injection to improve reservoir deliverability; use of artificial lift to improve well deliverability – may be considered. Of interest at this stage, too, is available reserve, which is how much more can be further recovered economically. Also at this stage, with increased information, reserve estimate and category may change.

### 1.6.7. Reserve Reporting and Audit

It is important that a reserve report gives the information for which it is meant for. A reserve report maybe

created for the various stakeholders of the petroleum resource(s), which may include: potential investors; existing investors; company executives; financial institutions; government agencies; and regulatory bodies.

Depending on the end use, typical information expected in a reserve report includes:

- reserve quantities (proven, probable, and possible);
- rate prediction from reserves;
- net present value and future value of reserves.

It is also important that reserve estimation goes through an audit process. A reserve audit process involves a review of the data and interpretation methods used for reserve estimation. The reserve audit process provides an independent opinion, different from that of the parties involved in the estimation, on rationality of estimated reserves.

## REFERENCES

- Selley, R.C., 1998. *Elements of Petroleum Geology*, 2nd edn. New York, Sydney, Tokyo, Toronto: Academic Press.
- SPE-PRMS, 2008. *Petroleum Resources Management System*. Society of Petroleum Engineers (SPE).
- Tissot, B. and Welte, D., 1984. *Petroleum Formation and Occurrence*, 2nd edn. New York, Tokyo, Berlin, Heidelberg: Springer-Verlag.

## BIBLIOGRAPHY

- Amyx, J.M., Bass, D.M., and Whiting, R., 1960. *Petroleum Reservoir Engineering – Physical Properties*. New York: McGraw-Hill.
- Chilingar, G., Buryakovsky, L., Eremenko, N., and Gorfunkel, M., 2005. *Geology and Geochemistry of Oil and Gas*, 1st edn. Oxford: Elsevier.
- Hyne, N., 2012. *Nontechnical Guide to Petroleum Geology, Exploration, Drilling and Production*, 3 edn. Tulsa, OK: PennWell Corp.
- Protter, M. and Protter, P., 1988. *Calculus with Analytic Geometry*, 4th edn. Boston Portola Valley: Jones and Bartlett Publishers.
- Venkatramaiah, C., 1996. *Textbook of Surveying*. Universities Press (India) Limited.
- Worthington, P. and Cosentino, L., 2005. The role of cut-offs in integrated reservoir studies. *SPE Reservoir Evaluation & Engineering*, **8**(04), 276–290.

## 2

### Petroleum Reservoir Rock Properties

Petroleum (oil and gas), also referred to as hydrocarbons, occurs naturally in pore spaces of sedimentary rocks which can be sandstones or carbonates (limestone or dolomite). Pore spaces between grains (matrix) serve the purpose of petroleum fluid storage while the interconnectivity of the pore space enables flow of petroleum fluids during production. Sandstone reservoirs, which can be consolidated or unconsolidated, store petroleum fluids mainly in pore spaces between grains (matrix), while carbonate reservoirs store petroleum fluids in pore spaces between grains (matrix) and fissures (natural fractures).

For petroleum fluids in reservoirs to be economical, the rock must have pore space to ensure the accumulation of petroleum fluid and connected pore spaces to allow flow of petroleum fluid under pressure differential. In *conventional reservoirs*, such as sandstone and carbonate reservoirs, these connected pore spaces exist naturally and relate directly to reservoir permeability. In *unconventional reservoirs*, such as shale bearing gas and/or shale bearing oil, the pore spaces are not connected and, therefore, there is a need to induce connection of pore spaces through hydraulic fracturing for petroleum fluid to flow.

Reservoir rock properties can be determined from analysis of *core samples*, which are cylindrical formation rock samples taken through the well section using a core bit with a hollow center. The setup for coring includes a core barrel, which holds the core, and a core catcher, which grips the core when breaking core away from undrilled section to prevent rock from dropping out of the drill string. Core sample length can range from less than a meter to about 100 meters. Cores may be further cut to smaller lengths for transportation. Extracted cores can have diameters in the range of few millimeters to over 150 mm.

In the laboratory, core samples are further processed (cutting and trimming) to suit laboratory use and setups. Laboratory studies on core samples can be grouped as: *routine core analysis (RCAL)* and *special core analysis (SCAL)*.

Routine core analysis includes measurement of basic rock properties such as porosity, permeability, grain density, and water saturation. Special core analysis includes a list of core measurements other than routine core analysis, which would include capillary pressure, relative permeability (steady and unsteady state), compressibility (rock and pore volume), and electrical properties. SCAL often refers to measurements that are dependent on fluid saturation, wettability, and fluid–rock interaction. The most common SCAL measurements are capillary pressure and relative permeability. SCAL measurements are very important in field performance prediction and reservoir hydrocarbon recovery. SCAL results may vary over field life and vary from reservoirs and fluids due to their dependence on wettability. Well logs are also another important approach for determining rock properties. This approach is covered in detail under *Formation Evaluation* (Chapter 5). Formation evaluation involves determination of physical and chemical properties of rocks and fluid content using well logs (information obtained from the borehole).

#### 2.1. POROSITY

Porosity characterizes the capability of a reservoir to store fluid due to presence of voids (Fig. 2.1). The porosity of a rock sample can be defined as the ratio of pore volume to bulk volume of the sample.



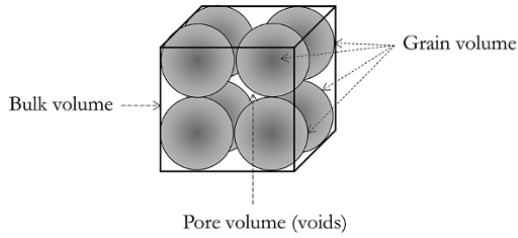


**Figure 2.1** Bulk, grain, and pore volume.

$$\text{Porosity} = \phi = \frac{V_p}{V_b} \quad (2.1)$$

$$\text{Porosity} = \phi = \frac{V_b - V_{gr}}{V_b} \quad (2.2)$$

$$\text{Porosity} = \phi = \frac{V_p}{V_{gr} + V_p} \quad (2.3)$$

where  $V_p$  = pore volume;  $V_b$  = bulk volume and  $V_{gr}$  = grain volume.

### 2.1.1. Absolute and Effective Porosity

Absolute (total) porosity relates to the ratio of total pore space to the bulk volume. Due to cementation (precipitation of binding materials between rock grains) over geological time, pore spaces may become isolated (unconnected) and, as such, they do not contribute to recoverable fluid volume. The primary interest of reservoir engineering is recoverable hydrocarbon, which mostly resides in connected pore volume. In recent times, however, unconnected volume, especially in unconventional reservoirs, has become increasingly important as it can be recovered by creating multiple hydraulic fractures. Defining porosity based on only interconnected pores space (excluding voids that are not connected) gives effective porosity. Effective porosity is hence defined as the ratio of the interconnected pore volume to the bulk volume of a material.

### 2.1.2. Porosity Determination

The determination of porosity from equations (2.1), (2.2) or (2.3) requires the measurement of at least two of  $V_b$ ,  $V_{gr}$  or  $V_p$ .

**2.1.2.1. Bulk Volume Measurement.** The simplest and most direct method of determining the bulk volume of a core sample is by linear measurement of the diameter and length of the core sample (Fig. 2.2); the volume is calculated using the geometric volume formula for a solid cylinder. This method is prone to error, especially when the core sample is characterized by irregularities.



**Figure 2.2** Linear bulk volume measurement.

The bulk volume for a cylindrical core sample can be defined as:

$$V_b = \frac{\pi d^2 l}{4} \text{ in consistent units} \quad (2.4)$$

The displacement method is a more accurate method for determining the bulk volume of a core sample. The approach involves using a liquid as a displacement fluid to determine the volume of the sample. The core sample is first dried weighed in air ( $W_{dry}$ ) then saturated with a liquid such as water to ensure any pore spaces are filled. The core sample can be freed of excess water by gently touching the surface with saturated filter paper. The saturated core sample is then weighed in air and the weight recorded ( $W_{sat}$ ). The saturated specimen is then submerged in same liquid used in saturating the core and the core is weighed while still submerged and weight recorded ( $W_{sub}$ ). The difference between weight of the saturated core sample in air and that when submerged in the liquid is the weight of the displaced liquid (*Archimedes' principle*). The volume of the displaced liquid, and hence the bulk volume of the core sample, is determined. Strong wetting liquids are preferable for displacement due to their ability to saturate the core properly.

Another method is to coat the core sample directly with paraffin wax to prevent liquid from saturating the core and then measure the volume of the liquid displaced by the paraffin coated core. Displaced volume equals bulk volume directly.

Mercury can also be used for bulk volume determination. Due to the strongly nonwetting characteristics of mercury, core pores will not be penetrated and, therefore, the displaced mercury volume is the bulk volume of core. The use of mercury ensures that rock properties remain unaltered. The use of mercury, like paraffin coating, does not require the core to be saturate with fluid.

**2.1.2.2. Grain Volume Measurement.** The most obvious method of determining grain volume requires weighing the core sample and dividing its mass by the grain density to give grain volume. Considering that core samples may not be of uniform rock or mineral type, determining representative density for the core may be erroneous, hence the volume determined using this method may not be reliable.

Another method is crushing the core sample and measuring the mass of the grains and the volume of the crushed grains (by measuring the volume of liquid displaced by the crushed grains). By crushing core samples, isolated pores are released. Hence, when  $V_{gr}$  measured by this approach is combined with  $V_b$  using equation (2.2), absolute porosity can be calculated.

The most accurate method of porosity determination is using *Boyle's Law porosimeter* (gas expansion method). This process involves expanding an inert gas such as helium or nitrogen from a reference cell into another cell containing the core sample, called the sample chamber, as shown in Fig. 2.3 and Fig. 2.4.

The initial pressure–volume condition of the porosimeter (Fig. 2.3) is defined as:

$$P_{initial} V_{initial} = P_{ch} (V_{ch} - V_{gr}) + P_{ref} V_{ref} \quad (2.5)$$

The final pressure–volume condition of the porosimeter (Fig. 2.4) after equilibrating  $V_{ch}$  and  $V_{ref}$  is defined as:

$$P_{final} V_{final} = P_{equil} (V_{ref} + V_{ch} - V_{gr}) \quad (2.6)$$

Since the number of moles of the entire system remains unchanged, applying Boyle's law to the initial and final conditions of the porosimeter setup (Fig. 2.3 and Fig. 2.4),  $P_{initial} V_{initial}$  in equation (2.5) is equal to  $P_{final} V_{final}$  in equation (2.6).

$$P_{ch} (V_{ch} - V_{gr}) + P_{ref} V_{ref} = P_{equil} (V_{ref} + V_{ch} - V_{gr}) \quad (2.7)$$

Making  $V_{gr}$  the subject of the formula, grain volume is hence expressed as:

$$V_{gr} = \frac{V_{ref} (P_{equil} - P_{ref}) + V_{ch} (P_{equil} - P_{ch})}{P_{equil} - P_{ch}} \text{ in consistent units} \quad (2.8)$$

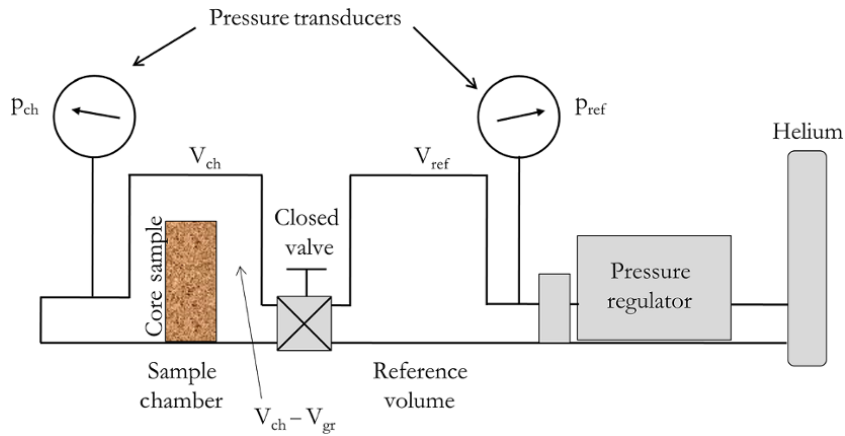


Figure 2.3 Initial porosimeter condition.

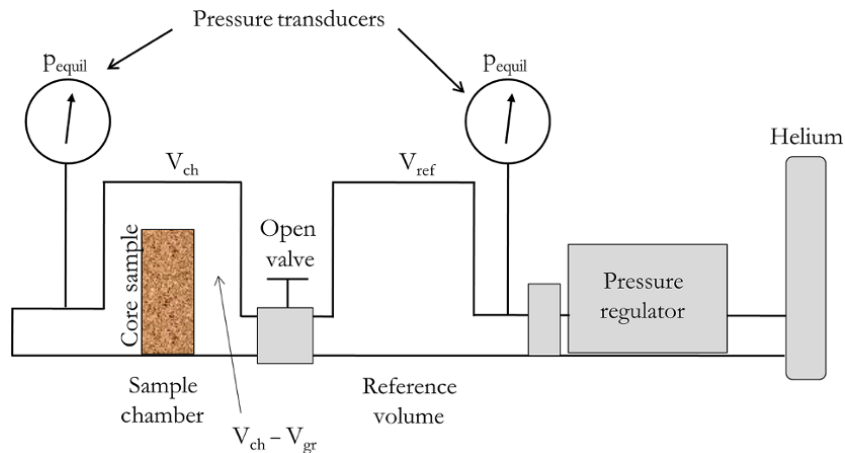


Figure 2.4 Final (equilibrium) porosimeter condition.

where  $p_{ch}$  is the initial pressure of the chamber,  $p_{ref}$  is the initial pressure of the reference cell,  $p_{equil}$  is the final (equilibrium) pressure of the system,  $V_{ch}$  is the volume of the chamber,  $V_{gr}$  is the volume of the grains, and  $V_{ref}$  is the volume of the reference cell.

**2.1.2.3. Pore Volume Measurement.** The simplest method of determining pore volume involves directly saturating the core with fluid such as water or oil and using the mass difference method to determine the volume of fluid required to fully saturate the core sample, as shown in equation (2.9).

$$V_p = \frac{W_{sat} - W_{dry}}{\rho_{liq}} \quad (2.9)$$

where  $\rho_{liq}$  is the density of liquid used in saturating core sample. With  $V_p$  determined, porosity can then be calculated using equation (2.1).

Another method for determining pore volume is the *retort method*, which is based on a summation of the fluid samples recovered from a pristine core sample from the formation. This method requires that core samples must be handled correctly to prevent loss of fluid.

$$V_p = V_o + V_w + V_g. \quad (2.10)$$

where  $V_o$  is the volume of oil recovered from the sample,  $V_w$  is the volume of water recovered from the sample, and  $V_g$  is the volume of gas recovered from the sample.

This method requires two samples (best taken adjacent to each other). Mercury is injected at high pressure into one of core samples; the volume of mercury absorbed under pressure is measured and the gas volume in the core (core gas) sample is thus determined. The adjacent sample is heated to high temperature so oil and water can evaporate and the fluid samples are then condensed and measured. The total volumes of gas, oil, and water are summed to obtain the total  $V_p$ . This method is quick but could be faced with challenges of accurate recovery and measurement of fluid from core sample.

### Exercise 2.1 Example of the Displacement Method for Calculating Porosity

A core sample was sent to the laboratory as part of the core analysis. The sample was cleaned and dried, then saturated with water. The saturated core sample was further submerged in water and the apparent weight in water was measured. The following data obtained from the saturation experiment.

$$W_{dry} = 110.35 \text{ g}$$

$$W_{sat} = 135.83 \text{ g}$$

$$W_{sub} = 20.00 \text{ g}$$

- Determine  $V_b$ ,  $V_p$ , and the porosity.
- What kind of porosity value was determined from this experiment?

### Solution Steps.

*Step 1:* determine  $V_b$  and  $V_p$ .

*Step 2:* calculate porosity.

### Solution.

Weight of water displaced ( $W_{wtr}$ ) by water saturated core sample =  $W_{sat} - W_{sub}$   
 $= 135.83 - 20 = 115.83 \text{ g}$ .

Volume of water displaced ( $V_{wtr}$ ) equals bulk volume of core sample ( $V_b$ ).

This implies that:

$$V_{wtr} = V_b = \frac{W_{wtr}}{\rho_{liq}} = \frac{115.83}{1} = 115.83 \text{ cm}^3$$

Using equation (2.9):

$$V_p = \frac{W_{sat} - W_{dry}}{\rho_{liq}} = \frac{135.83 - 110.35}{1} = 24.48 \text{ cm}^3$$

Using equation (2.1):

$$\phi = \phi_{eff} = \frac{V_p}{V_b} = \frac{24.48}{115.83} = 0.22 = 22\%$$

The porosity calculated is effective porosity because only connected pore space could have been saturated by water.

### Exercise 2.2 Example of Boyle's Law Porosimeter Method for Calculating Porosity

The core sample from Exercise 2.1 was dried and placed in a porosimeter. A Boyle's law porosity experiment was carried out and the following data obtained.

$$p_{ch} = 0.00 \text{ psig}$$

$$p_{ref} = 50.00 \text{ psig}$$

$$p_{equil} = 31.39 \text{ psig}$$

$$V_{ch} = 120.00 \text{ cm}^3$$

$$V_{ref} = 50.00 \text{ cm}^3$$

$V_{gr}$  = volume of grain

Determine grain volume ( $V_{gr}$ ) and core porosity using  $V_b$  calculated in Exercise 2.1

What kind of porosity is calculated?

**Solution.**

Using equation (2.8):

$$V_{gr} = \frac{V_{ref}(p_{equil} - p_{ref}) + V_{ch}(p_{equil} - p_{ch})}{p_{equil} - p_{ch}}$$

$$V_{gr} = \frac{50.00(31.39 - 50.00) + 120.00(31.39 - 0)}{31.39 - 0} = 90.34 \text{ cm}^3$$

$$\phi = \phi_{eff} \frac{V_b - V_{gr}}{V_b} = \frac{115.83 - 90.34}{115.83} = 0.22 = 22\% = \phi_{eff}$$

The porosity calculated is effective porosity because only connected pore space could have been penetrated by the gas during experiment.

**Exercise 2.3** Example of Water Displacement Method Using Crushed Core Sample

Core sample from above experiment was crushed and grains poured in graduated cylinder of water which originally measured a volume of 100 cm<sup>3</sup> and final volume of 184.56 cm<sup>3</sup> after adding crushed core sample.

Determine the volume of sand particles and porosity from this experiment using V<sub>b</sub> from Exercise 2.1. What kind of porosity is determined in this experiment?

Crushed grain volume, V<sub>gr</sub> = V<sub>gr\_crush</sub> = 84.56 cm<sup>3</sup>

Bulk volume, V<sub>b</sub> = 115.83 cm<sup>3</sup>

**Solution.**

$$\phi = \phi_T = \frac{V_b - V_{gr\_crush}}{V_b} = \frac{115.83 - 84.56}{115.83} = 0.27 = 27\%$$

Porosity calculated is total porosity because actual grain (which excludes unconnected pore spaces) was used for determining porosity.

**Exercise 2.4** Example of Unconnected Porosity Calculation

Using the above experiments, determine unconnected porosity.

**Solution.**

Unconnected porosity φ<sub>uncon</sub> is:

$$\phi_{uncon} = \phi_T - \phi_{eff} = 27 - 22 = 5\%$$

For practical integration of core porosity data with the reservoir model, it is important porosity measurement is carried out under conditions similar to *in situ* reservoir conditions. It is advisable to always measure porosity under confinement pressure that equals the reservoir overburden pressure. Alternatively, correction can be

carried out on porosity measurement not carried out under confinement pressure.

**2.2. PERMEABILITY**

Permeability defines the capability of the rock to allow fluid to flow under a pressure gradient and is characterized by the connectivity of pore spaces. Hence, any reliable method for determining the permeability of a core sample would generally involve fluid flowing at a known rate through porous material under measured differential pressure.

**2.2.1. Henry Darcy's Experiment**

*Darcy's law*, although originally based on empirical observation, can be derived from the *Navier Stokes equation* for an incompressible Newtonian fluid flowing slowly through a rigid permeable medium under isothermal and steady-state conditions.

Henry Darcy's experiment carried out in 1856 [Hubbert, 1956], when investigating water filtration for a municipal supply in Dijon, France, showed that for a pack of porous bed (Fig. 2.5) the flow velocity of water can be expressed as:

$$q = \frac{Q}{A} = K \frac{h_1 - h_2}{L} \tag{2.11}$$

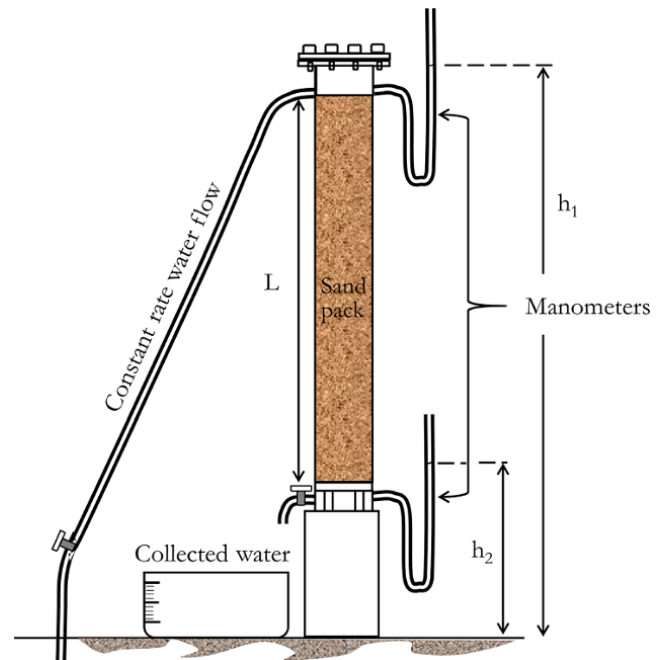


**Figure 2.5** Henry Darcy's experimental setup for vertical flow [Hubbert, 1956. *Darcy's Law and the Field Equation of the Flow of Underground Fluids. Transactions AIME, Volume 207, pp. 222–239.*].

where  $Q$  is the constant volumetric flow rate of water,  $A$  is the cross-sectional area of the sand pack,  $L$  is the height of the sand pack,  $h_1$  is the height of manometer 1,  $h_2$  is the height of manometer 2,  $K$  is a constant of proportionality that characterizes the sand pack, and  $q$  is the constant flow velocity of water  $\left(\frac{Q}{A}\right)$

Even though the original Darcy experiment was for a sand pack, the law has been extended to reservoir rock type which is often compact. The law was further modified to account for the effect of fluid viscosity; as such Darcy's law is expressed as:

$$\frac{Q}{A} = -\frac{k}{\mu} \frac{dp}{dL} \text{ for linear flow.} \quad (2.12)$$

where the difference in manometer height (which is a measurement of pressure) is replaced explicitly with pressure and the effect of viscosity included in the equation (2.11). Darcy's Law shows the relationship between rate of fluid transfer as a function of pressure gradient when  $Q$  is the flow rate ( $\text{cm}^3/\text{s}$ ),  $k$  is the permeability (Darcy),  $A$  is the cross-sectional area ( $\text{cm}^2$ ),  $\mu$  is viscosity (cp),  $p$  is pressure (atm), and  $L$  is the length (cm)

### 2.2.2. Darcy's Law for Liquids

Integrating equation (2.12) between  $p_1$  and  $p_2$  over the length of the sand sample yields:

$$\begin{aligned} \frac{Q}{A} \int_0^L dL &= -\frac{k}{\mu} \int_{p_1}^{p_2} dp = -\frac{k}{\mu} (p_2 - p_1) = \frac{k}{\mu} (p_1 - p_2) \Rightarrow \frac{Q}{A} L \\ &= \frac{k}{\mu} (p_1 - p_2) \Rightarrow \frac{Q}{A} = \frac{k \Delta p}{\mu L} \\ \frac{Q}{A} &= \frac{k \Delta p}{\mu L} \text{ for linear flow.} \end{aligned} \quad (2.13)$$

From equation (2.13), 1 Darcy unit is therefore the permeability of a medium that allows flow velocity of 1 cm/s for a fluid of 1cp subjected to a pressure gradient of 1 atm/cm. When measuring permeability with a liquid or gas, a subscript representing the phase is often added to permeability ( $k$ ). As such,  $k_{\text{Liq}}$  (or  $k_{\text{Liquid}}$ ) represents liquid permeability and  $k_{\text{g}}$  (or  $k_{\text{gas}}$ ) represents gas permeability. This is important, because when gas is used for permeability measurement, there is a need to convert gas permeability to the equivalent liquid permeability. Also when gas is used for permeability measurement, there is need to modify Darcy's equation to account for gas compressibility.

It is more common to express permeability as millidarcy (mD) rather than Darcy because most reservoir rocks are

less than 1 Darcy. The SI unit for permeability is  $\text{m}^2$ . The relationship between the different units of permeability is:

$$1 \text{ Darcy} = 0.987 \times 10^{-8} \text{ cm}^2 = 0.987 \times 10^{-12} \text{ m}^2$$

In engineering oil field (EOF) units, Darcy's law for linear flow can be expressed as:

$$\frac{Q}{A} = -1.127 \times 10^{-3} \frac{k}{\mu} \frac{dp}{dL} \quad (2.14)$$

or

$$\frac{Q}{A} = 1.127 \times 10^{-3} \frac{k \Delta p}{\mu L} \quad (2.15)$$

where  $Q$  is constant rate flow (bbl/d),  $k$  is permeability (mD),  $A$  is cross-sectional area ( $\text{ft}^2$ ),  $\mu$  is viscosity (cp),  $p$  is pressure (psi), and  $L$  is length (ft).

Where the effect of elevation and inclination on Darcy's experimental setup is considered (Fig. 2.6), the equation for fluid flow from top to bottom becomes:

$$\begin{aligned} \frac{Q}{A} L &= \frac{k}{\mu} [(p_1 + \rho g z) - (p_2 + \rho g(z - L \sin \theta))] \\ \frac{Q}{A} &= \frac{k}{\mu L} (p_1 - p_2 + L \rho g \sin \theta) \end{aligned} \quad (2.16)$$

and when flow is from bottom to the top it becomes:

$$\begin{aligned} \frac{Q}{A} L &= \frac{k}{\mu} [(p_2 + \rho g(z - L \sin \theta)) - (p_1 + \rho g z)] \\ \frac{Q}{A} &= \frac{k}{\mu} \left( \frac{p_2 - p_1}{L} - \rho g \sin \theta \right) \\ \frac{Q}{A} &= \frac{k}{\mu L} (p_2 - p_1 - L \rho g \sin \theta) \end{aligned} \quad (2.17)$$

**2.2.2.1. Permeability Measurement.** The most common method for core permeability measurement is based on the *Hassler experimental setup* (Fig. 2.7). Different laboratories have their own modification of the *Hassler Cell*. However, the principles are the same. The core sample is placed in a rubber sleeve and pressure ranging from a few hundred to thousands of psi is exerted to hold the sleeve and to ensure flow is axial to core length. Liquid or gas (nitrogen or air) at constant rate is then forced thorough the core sample in the Hassler Cell and pressure drop across the core sample is measured. The experiment is repeated multiple times.

Fluid rate is measured with a flow meter and the corresponding pressure drop across the cell measured with a transducer. For an incompressible fluid (liquid experiment), a plot of  $\frac{Q}{A}$  against  $\frac{dp}{dL}$  will yield a straight line with

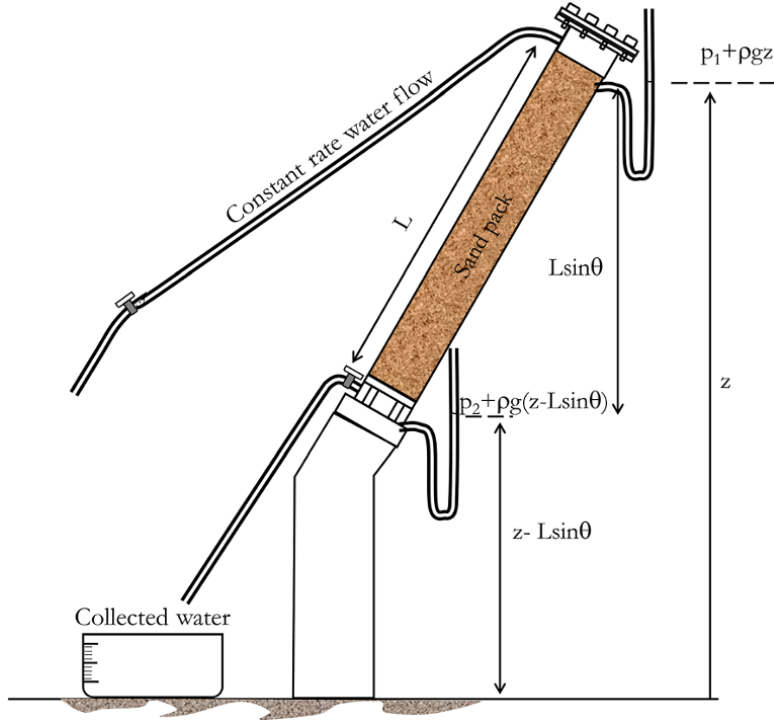


**Figure 2.6** Henry Darcy's experimental setup for inclined flow [Hubbert, 1956. Darcy's Law and the Field Equation of the Flow of Underground Fluids. *Transactions AIME*, Volume 207, pp. 222–239].

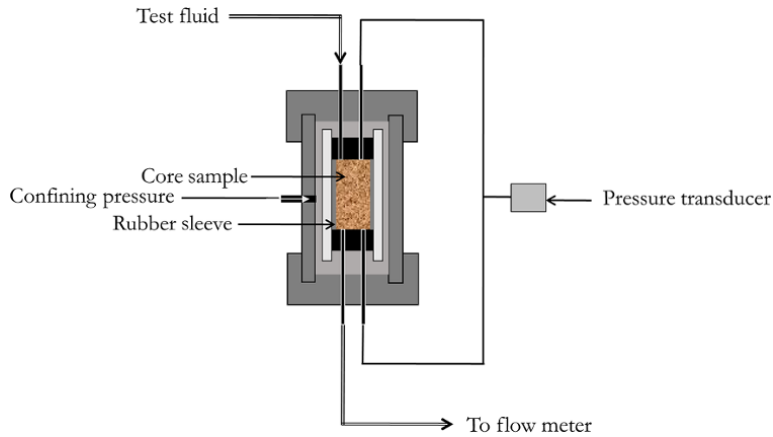


**Figure 2.7** Hassler Cell for permeability measurement.

slope  $\frac{k}{\mu}$  (fluid mobility) (Fig. 2.8), from which  $k$  is determined using the viscosity of the fluid determined from fluid experiments or supplied from published property tables.

For Darcy's unit,  $k = \text{Darcy}$ ,  $Q = \text{cm}^3/\text{s}$ ,  $dp = \text{atm}$ ,  $A = \text{cm}^2$ ,  $L = \text{cm}$ ,  $\mu = \text{cp}$ .

**Exercise 2.5** Permeability Calculation from Core Experiment

Using the experimental setup in Fig. 2.9, determine core permeability with a flow of water given the following:  $\mu = 1 \text{ cp}$ ;  $L = 85 \text{ cm}$ ;  $r_{\text{core}} = 3 \text{ cm}$ ;  $\Delta p = 10 \text{ atm}$ ;  $Q = 0.05 \text{ cm}^3/\text{s}$ .

**Solution.**

$$A = \pi r^2 = \pi \times 3^2 = 28.274 \text{ cm}^2$$

from equation (2.13),  $\frac{Q}{A} = \frac{k \Delta p}{\mu L}$ .

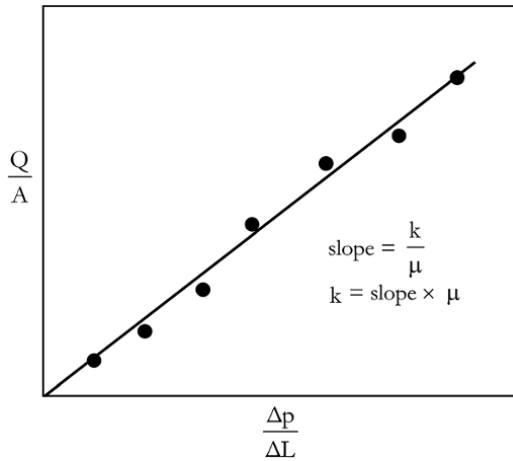


Figure 2.8 Permeability calculation from experiment.

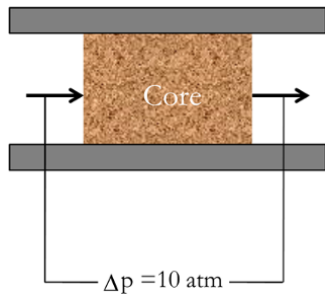


Figure 2.9 Setup for Exercise 2.5.

Substituting parameters:

$$\frac{0.05}{28.274} = \frac{k \cdot 10}{185} \Rightarrow$$

$$k = 0.015 \text{ Darcy}$$

$$k = 15 \text{ mD}$$

**Exercise 2.6** Permeability Calculation in Inclined Core Sample

Consider a core sample with setup above (Fig. 2.10); calculate core permeability with water flowing downwards, given the following:  $\theta = 30^\circ$ ;  $\mu = 1 \text{ cp}$ ;  $\rho = 1 \text{ g/cm}^3$ ;  $L = 100 \text{ cm}$ ;  $r_{\text{core}} = 3.84 \text{ cm}$ ;  $p_2 = 3 \text{ atm}$ ;  $p_1 = 1.5 \text{ atm}$ ;  $g = 980 \text{ cm/s}^2$ ;  $Q = 0.01 \text{ cm}^3/\text{s}$ .

**Solution.**

$$A = \pi r^2 = 3.1416 \times 3.84^2 = 46.325 \text{ cm}^2$$

$$\rho g L \sin \theta = 1 \left( \frac{\text{g}}{\text{cm}^3} \right) \times 980 \left( \frac{\text{cm}}{\text{s}^2} \right) 100(\text{cm}) \sin(30)$$

$$= 98,000 \left( \frac{\text{g}}{\text{s}^2 \text{cm}} \right)$$

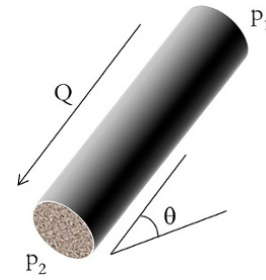


Figure 2.10 Inclined core sample.

$$\rho g L \sin \theta = 1 \left( \frac{\text{g}}{\text{cm}^3} \right) \times 980 \left( \frac{\text{cm}}{\text{s}^2} \right) 100(\text{cm}) \sin(30) = 49,000$$

$$49,000 \left( \frac{\text{g}}{\text{s}^2 \text{cm}} \right) = 4,900 \text{ Pa} = 0.04835 \text{ atm}$$

Therefore,  $\rho g L \sin \theta = 0.04835 \text{ atm}$ .

Substituting  $\rho g L \sin \theta$  above into equation (2.17):

$$\frac{0.01}{46.325} = \frac{k}{1 \times 100} (3 - 1.5 - 0.0485)$$

$$k = 0.014872 \text{ Darcy} = 15 \text{ mD}$$

**2.2.3. Darcy's Law for Gas**

The use of gas for permeability determination leads to a modification of Darcy's law. Due to the compressible nature of gas, volume and, therefore, flow rate are pressure dependent.

Gas rate is always measured at standard condition (pressure of 1 atm and temperature of 60 °F), hence the final Darcy's equation for gas will be written in standard cubic centimeter (sc).

For isothermal gas injection during core experiments  $Q_1 p_1 = Q_2 p_2$  where subscripts 1 and 2 represent inlet and outlet conditions, respectively, for any given pressure,  $p$ , with gas rate,  $Q$ .

Also,  $Q_p = Q_{sc} p_{sc}$ , where subscript 'sc' represents standard condition.

Making  $Q$  the subject of the formula

$$Q = \frac{Q_{sc} p_{sc}}{p}$$

and substituting  $Q = \frac{Q_{sc} p_{sc}}{p}$  into equation (2.12) gives:

$$\frac{Q_{sc}}{A} dL = - \frac{k p dp}{\mu p_{sc}}$$

Integrating between core inlet and outlet boundary conditions

$$\frac{Q_{sc}}{A} \int_0^L dL = - \frac{k}{p_{sc}} \int_{p_1}^{p_2} \frac{p dp}{\mu}$$

$$\frac{Q_{sc}}{A} L = \frac{k}{p_{sc} \mu_{av}} \frac{p_1^2 - p_2^2}{2}$$

$$\frac{Q_{sc}}{A} = \frac{k}{\mu_{av}} \frac{p_1^2 - p_2^2}{2L p_{sc}}$$

In Darcy's unit  $p_{sc} = 1$  atm, hence the above equation becomes:

$$\frac{Q_{sc}}{A} = \frac{k}{\mu_{av}} \frac{(p_1^2 - p_2^2)}{2L} \quad (2.18)$$

where  $\mu_{av}$  is average gas viscosity in cp.

The nonlinearity of pressure in Darcy's equation for gas is discussed in detail under *Fluid Flow in Reservoir* (Chapter 7) and *Well Test Analysis* (Chapter 8).

Gas at low rate and low pressure drop has been shown to give an overestimation of permeability because gas molecules, unlike liquid molecules, do not adhere to pore surfaces hence leading to a *slippage effect*. This slippage, which characterizes permeability dependence on pressure, is called the *Klinkenberg effect*. Therefore, a correction is required for permeability measured with gas. This correction is called the *Klinkenberg correction*. This phenomenon is important at laboratory scale for correcting gas measured permeability but is rarely applicable for reservoir simulation and prediction purposes.

The steps for correcting gas measured permeability involve plotting calculated gas permeability ( $k_g$ ) against  $\frac{1}{p_{mean}}$  and determining true permeability ( $k_\infty$  or  $k_{Liq}$ ) from extrapolation of the measured data on a straight line to the point where  $\frac{1}{p_{mean}} = 0$  (which is infinite mean pressure), as shown in Fig. 2.11. The mean pressure ( $p_{mean}$ ) is defined as  $p_{mean} = \frac{p_1 + p_2}{2}$ . The factor derived from the slope of the plot, defined as "b", is dependent on molecular weight and size; it is called the *Klinkenberg slippage function*. The true permeability also called *liquid permeability* or *Klinkenberg corrected permeability*, represents the true permeability for the experiment using fully saturated incompressible fluid (liquid).

During the Klinkenberg experiment, flow through core sample can be carried out under either constant mass flow rate or constant differential pressure.

### Exercise 2.7 Example of Gas Permeability Calculation with the Klinkenberg Correction

Cleaned, polished, and dried core sample with diameter 3.8 cm and length 11 cm was used for permeability measurement. Injection using nitrogen with average viscosity of 0.018 cp was carried out on the core sample in a Hassler Cell at a constant rate of 13.54 scc/s with constant hydraulic confining pressure applied on rubber sleeves round the

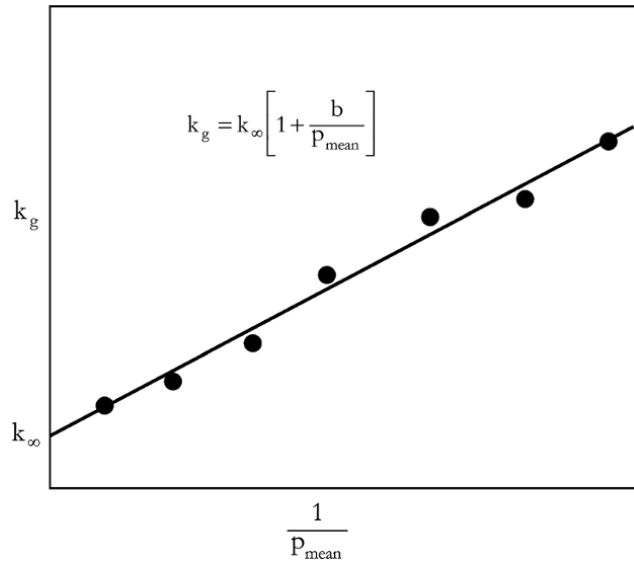


**Figure 2.11** Gas permeability determination with the Klinkenberg correction.

**Table 2.1** Gas Permeability Experimental Data.

Injection pressure $p_1$ (atm)	Pressure drop across core $p_1 - p_2$ (atm)
1.04	0.012
1.41	0.012
2.30	0.009
3.40	0.009
4.00	0.009

core sample. Injection pressure and pressure drop across the core sample were measured; gas flow rate was measured.

Determine the Klinkenberg corrected permeability ( $k_\infty$ ) and the Klinkenberg correction factor, b. The results from the experiment is given in Table 2.1.

### Solution Steps.

*Step 1:* calculate  $p_2$  (discharge pressure downstream the core).

*Step 2:* calculate  $p_1^2 - p_2^2$  using pressure drop and injection pressure.

*Step 3:* determine  $k_g$  for each experimental run.

*Step 4:* determine  $p_{mean}$  using  $\left(\frac{p_1 + p_2}{2}\right)$  then calcu-

late  $\frac{1}{p_{mean}}$ .

*Step 5:* plot various determine  $k_g$  with corresponding

$\frac{1}{p_{mean}}$ .



Step 6: extrapolate line fit to  $\frac{1}{p_{mean}} = 0$ , vertical axis intercept is  $k_{\infty}$ ; from slope calculate b.

**Solution.**

The solution to Exercise 2.7 is summarized in Table 2.2.

The plot of  $k_g$  against  $\frac{1}{p_{mean}}$  is shown in Fig. 2.12.

Comparing the Klinkenberg correction equation:

$$k_g = k_{\infty} \left( 1 + \frac{b}{p_{mean}} \right) \tag{2.19}$$

with the equation of the line in Fig. 2.12:

Intercept of vertical axis = 3.0241 =  $k_{\infty}$ .

Slope = 16.435 =  $k_{\infty}b$

Making b the subject of the formula:

$$b = \frac{16.435}{k_{\infty}} = \frac{16.435}{3.0241} = 5.435$$

Therefore,  $k_{\infty} = 3.0$  Darcy and  $b = 5.44$

**Table 2.2** Solution to Exercise 2.7.

$p_1$ (atm)	$p_1 - p_2$ (atm)	$p_2$ (atm)	$p_1^2 - p_2^2$	$k_g$ (Darcy)	$\frac{p_1 + p_2}{2}$	$\frac{1}{p_{mean}}$
1.04	0.012	1.03	0.0248	19.051	1.03	0.967
1.41	0.012	1.40	0.0337	14.031	1.40	0.712
2.30	0.009	2.29	0.0413	11.442	2.30	0.436
3.40	0.009	3.39	0.0611	7.735	3.40	0.295
4.00	0.009	3.99	0.0719	6.574	4.00	0.250

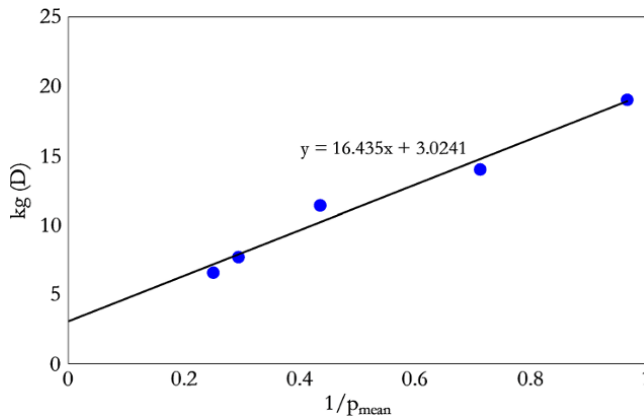


**Figure 2.12** Plot of  $k_g$  against  $\frac{1}{p_{mean}}$ .

**2.2.4. Non-Darcy Flow**

Another deviation from Darcy flow is caused by inertial effects that are due to acceleration of fluid at the pore throats and deceleration at pore bodies. Non-Darcy flow is prominent at high fluid velocity. It is characterized by

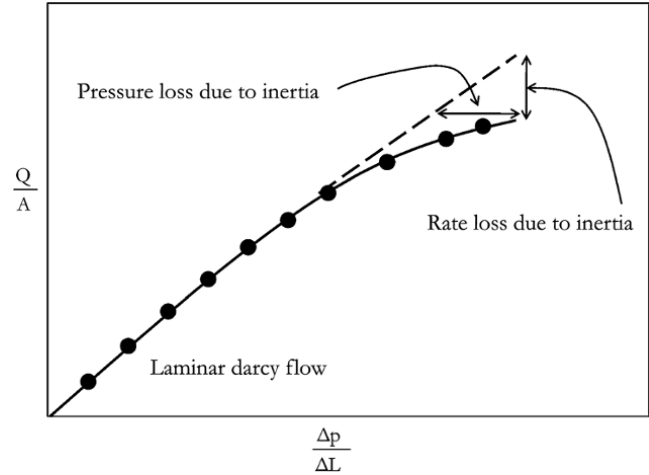


**Figure 2.13** Effect of turbulence (inertia).

the *non-Darcy coefficient* or *Forchheimer parameter*, which accounts for the nonlinear behavior of the pressure drop as a function of fluid velocity (Fig. 2.13). The Darcy equation accounting for the inertia effect, also called the *Forchheimer equation*, is expressed as:

$$-\frac{dp}{dL} = \frac{\mu V}{k} + \beta \rho V^2 \tag{2.20}$$

where  $\beta$  is the non-Darcy coefficient,  $\rho$  is the density of the fluid, and  $V$  is the velocity of the flowing fluid.

The effect of turbulence (inertia) has a significant effect in reservoir simulation involving gas and or gas condensate, especially in vertical wells where the velocity of the flowing stream from reservoir to tubing is high. Equation (2.20) can be expressed in terms of mass flux ( $G$ ) using the relationship:  $G = \rho V$ .

Where  $V$  is flow velocity defined as  $V=Q/A$

Substituting  $V = \frac{G}{\rho}$  into equation (2.20)

$$-\frac{dp}{dL} = \frac{\mu G}{k\rho} + \frac{\beta G^2}{\rho} \tag{2.21}$$

Expressing  $\rho$  as function of pressure:  $\rho = \frac{pM}{ZRT}$  and substituting into equation (2.21)

$$-\frac{pdp}{dL} \frac{M}{ZRT} = \frac{\mu}{k} G + \beta G^2$$

$$-pdp \frac{M}{ZRT} = \left( \frac{\mu}{k} G + \beta G^2 \right) dL$$

where  $M$  is molecular weight,  $R$  is the universal gas constant,  $T$  is temperature, and  $Z$  is a compressibility factor.

Integrating between  $p_1$  and  $p_2$  over the length of the sand sample ( $L$ ) yields:

$$-\frac{M}{ZRT} \int_{p_1}^{p_2} p dp = \left( \frac{\mu}{k} G + \beta G^2 \right) \int_0^L dL$$

$$\begin{aligned}\frac{M}{ZRT} \frac{(p_1^2 - p_2^2)}{2} &= \left(\frac{\mu}{k}G + \beta G^2\right)L \\ \frac{(p_1^2 - p_2^2)M}{2ZRTL} &= \frac{\mu}{k}G + \beta G^2 \\ \frac{(p_1^2 - p_2^2)M}{2ZRTL G} &= \frac{\mu}{k} + \beta G\end{aligned}\quad (2.22)$$

Hence, permeability and the non-Darcy coefficient can be determined using equation (2.22).

### Exercise 2.8 Non-Darcy Flow Experiment using Packed Sand

The inlet of the horizontally placed cylinder of packed sand is connected to an air supply flow line that continuously supplies air at controlled and measured rate. The outlet position is designed to allow air passing through the packed bed to escape into the atmosphere. The injection pressure and pressure drop across the packed column of sand were measured.

Determine the permeability and the non-Darcy coefficient ( $\beta$ ) of the packed bed of sand given:  $M = 28.97 \text{ g/mol}$ ;  $T = 299.75 \text{ K}$  ( $26.75 \text{ }^\circ\text{C}$ );  $L = 30 \text{ cm}$ ;  $D = 3 \text{ cm}$ ;  $R = 82.05746 \text{ cm}^3 \text{ atm K}^{-1} \text{ mol}^{-1}$ , and  $p_2 = 1 \text{ atm}$ .

Results from the experiment are given in Table 2.3.

#### Solution Steps.

Step 1: determine  $p_1$  (inlet pressure upstream the packed sand),  $p_1 = \Delta p + p_2$ .

Step 2: determine  $p_{\text{Average}}$ :  $p_{\text{Average}} = \frac{(p_1 + p_2)}{2}$ .

Step 3: determine average fluid density,

$$\rho_{\text{Average}} = \frac{p_{\text{Average}} M}{Z_{\text{Average}} RT}$$

Where  $Z_{\text{Average}}$  is average compressibility factor over pressure  $p_1$  and  $p_2$ , and given in Table 2.3.

Step 4: determine  $p_1^2 - p_2^2$ ,  $G$  and  $\frac{(p_1^2 - p_2^2)M}{2ZRTL G}$ .

Step 5: plot  $\frac{(p_1^2 - p_2^2)M}{2ZRTL G}$  against  $G$ .

Step 6: determine  $k$  and  $\beta$ .

**Table 2.3** Non-Darcy Experiment Data.

$\Delta p$ (atm)	$Q$ ( $\text{cm}^3/\text{s}$ )	$Z_{\text{Average}}$	$\mu$ (cp)
0.092	0.265	0.994	0.01803
0.125	0.305	0.979	0.01803
0.147	0.327	0.968	0.01803
0.173	0.351	0.956	0.01803
0.206	0.378	0.944	0.01803
0.226	0.391	0.933	0.01803
0.258	0.414	0.921	0.01803
0.285	0.428	0.909	0.01802
0.328	0.450	0.893	0.01802

#### Solution.

The solution to Exercise 2.8 is summarized in Table 2.4.

The plot of  $\frac{(p_1^2 - p_2^2)M}{2ZRTL G}$  against  $G$  is shown in Fig. 2.14.

Comparing Fig. 2.14 with equation (2.22):

$$\frac{(p_1^2 - p_2^2)M}{2ZRTL G} = \frac{\mu}{k} + \beta G,$$

The intercept of the vertical axis =  $2.897 \times 10^{-4} = \frac{\mu}{k}$

Where  $\mu$  is average viscosity from Table 2.3 which is 0.01803 cp.

Hence,  $k = 0.01803/2.897 \times 10^{-4} = 62 \text{ Darcy}$ .

Slope =  $1.746 \times 10^3 = \beta$

Therefore,  $k = 62 \text{ Darcy}$  and  $\beta = 1.75 \times 10^3 \text{ cm}^{-1}$ .

### 2.2.5. Averaging Reservoir Permeability

In simple or complex reservoir modelling where there is permeability variation, the effective permeability of the system or region of interest will be a form of permeability average. Selecting the correct averaging technique is important in reservoir modelling.

**2.2.5.1. Parallel Stratified Linear Flow.** Consider a stratified formation with layer permeability of  $k_1, k_2, \dots, k_n$ , thicknesses  $h_1, h_2, \dots, h_n$ , cross-sectional area  $A_1, A_2, \dots, A_n$ , with all layers having equal length and width (Fig. 2.15).

$$Q = -\frac{\bar{k}}{\mu} A_T \frac{\Delta p}{L}$$

where  $\bar{k}$  is effective permeability and  $A_T$  is the total cross-sectional areas of the stratified formation in the direction of fluid flow.

For stratified sand:

$$Q = Q_1 + Q_2 + \dots + Q_n$$

**Table 2.4** Solution to Exercise 2.8.

$p_1$ (atm)	$p_{\text{Average}}$ (atm)	$\rho_{\text{Average}}$ ( $\text{g}/\text{cm}^3$ )	$p_1^2 - p_2^2$ ( $\text{atm}^2$ )	$G = \rho_{\text{Average}} V$ $G = \rho_{\text{Average}} \frac{Q}{A} \frac{(p_1^2 - p_2^2)M}{2ZRTL G}$ ( $\text{g s}^{-1} \text{ cm}^{-2}$ )	$\frac{(p_1^2 - p_2^2)M}{2ZRTL G}$
1.0920	1.0460	1.239E-03	0.192	4.65E-05	8.180E-02
1.1250	1.0625	1.278E-03	0.266	5.52E-05	9.657E-02
1.1470	1.0735	1.306E-03	0.316	6.04E-05	1.059E-01
1.1730	1.0865	1.339E-03	0.376	6.65E-05	1.161E-01
1.2060	1.1030	1.376E-03	0.454	7.36E-05	1.284E-01
1.2260	1.1130	1.405E-03	0.503	7.77E-05	1.362E-01
1.2580	1.1290	1.444E-03	0.583	8.46E-05	1.468E-01
1.2850	1.1425	1.480E-03	0.651	8.96E-05	1.569E-01
1.3280	1.1640	1.535E-03	0.764	9.77E-05	1.717E-01

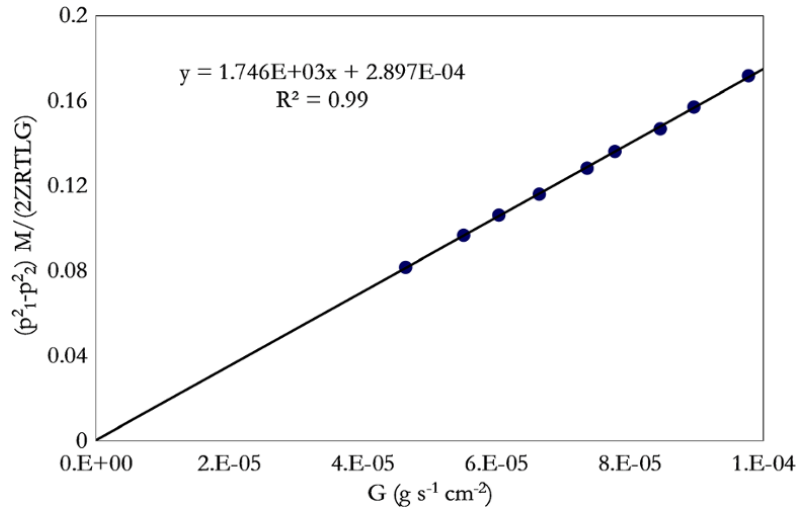


Figure 2.14 Plot of  $\frac{(p_1^2 - p_2^2)M}{2LRTG\mu}$  against  $G$ .

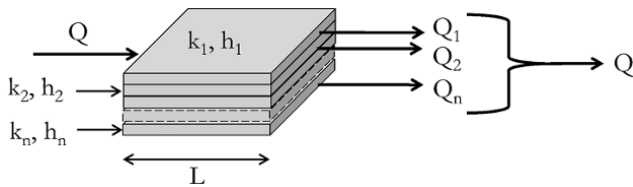


Figure 2.15 Stratified linear flow.

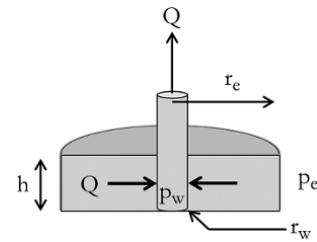


Figure 2.16 Single layer homogeneous radial flow.

$$Q = -\frac{\bar{k}}{\mu} A_T \frac{\Delta p}{L} = -\frac{k_1}{\mu} A_1 \frac{\Delta p}{L} - \frac{k_2}{\mu} A_2 \frac{\Delta p}{L} - \dots - \frac{k_n}{\mu} A_n \frac{\Delta p}{L}$$

$$-\frac{\bar{k}}{\mu} A_T \frac{\Delta p}{L} = -\sum_{i=1}^n \frac{k_i}{\mu} A_i \frac{\Delta p}{L} = -\frac{\Delta p}{\mu L} \sum_{i=1}^n k_i A_i$$

$$-\frac{\Delta p}{\mu L} \bar{k} A_T = -\frac{\Delta p}{\mu L} \sum_{i=1}^n k_i A_i \Rightarrow \bar{k} A_T = \sum_{i=1}^n k_i A_i \Rightarrow \bar{k} = \frac{\sum_{i=1}^n k_i A_i}{A_T}$$

$$A_T = \sum_{i=1}^n A_i$$

$$\bar{k} = \frac{\sum_{i=1}^n k_i A_i}{\sum_{i=1}^n A_i} = \frac{\sum_{i=1}^n k_i h_i}{\sum_{i=1}^n h_i} \quad (2.23)$$

Therefore, for parallel stratified sand with linear flow, effective permeability can be represented with a thickness-weighted arithmetic mean.

**2.2.5.2. Parallel Stratified Radial Flow.** For a single layer homogeneous radial flow (Fig. 2.16):

$$A = 2\pi r h$$

$$\frac{Q}{A} = -\frac{k dp}{\mu dr} \Rightarrow \frac{Q}{2\pi r h} = -\frac{k dp}{\mu dr}$$

$$dp = -\frac{Q\mu}{2\pi k h} \frac{dr}{r}$$

Integrating between reservoir boundary conditions (reservoir extent and wellbore):

$$\int_{p_w}^{p_e} dp = -\frac{Q\mu}{2\pi k h} \int_{r_w}^{r_e} \frac{dr}{r} \Rightarrow p_e - p_w = \Delta p = -\frac{Q\mu}{2\pi k h} \ln \frac{r_e}{r_w}$$

Hence, for parallel stratified radial flow (Fig. 2.17):

$$\Delta p = -\frac{Q\mu}{2\pi k h} \ln \frac{r_e}{r_w} \Rightarrow Q = -\frac{\Delta p 2\pi \bar{k} h}{\mu \ln \frac{r_e}{r_w}}$$

$$Q = Q_1 + Q_2 + \dots + Q_n$$

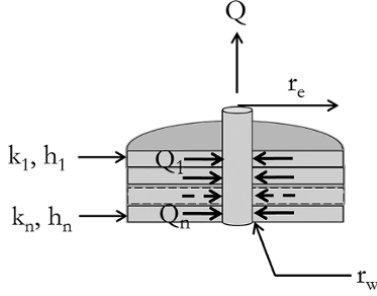


Figure 2.17 Stratified radial flow.

$$Q = -\frac{\Delta p 2\pi}{\mu \ln \frac{r_e}{r_w}} \bar{k} h = -\frac{\Delta p 2\pi}{\mu \ln \frac{r_e}{r_w}} k_1 h_1 - \frac{\Delta p 2\pi}{\mu \ln \frac{r_e}{r_w}} k_2 h_2 \dots - \frac{\Delta p 2\pi}{\mu \ln \frac{r_e}{r_w}} k_n h_n$$

$$\text{where } h = \sum_{i=1}^n h_i$$

$$\bar{k} h = k_1 h_1 + k_2 h_2 + \dots + k_n h_n = \sum_{i=1}^n k_i h_i$$

$$\bar{k} = \frac{\sum_{i=1}^n k_i h_i}{h} = \frac{\sum_{i=1}^n k_i h_i}{\sum_{i=1}^n h_i}$$

This last equation shows that equation (2.23) is valid for both stratified linear and radial flow.

**2.2.5.3. Serial Stratified Linear Flow.** Considering stratified formations arranged in series (Fig. 2.18):

$$\begin{aligned} \Delta p &= \Delta p_1 + \Delta p_2 + \dots + \Delta p_n \\ \Delta p &= -\frac{Q\mu L}{kA} = -\frac{Q\mu L_1}{k_1 A} - \frac{Q\mu L_2}{k_2 A} \dots - \frac{Q\mu L_n}{k_n A} \\ -\frac{Q\mu L}{A \bar{k}} &= -\frac{Q\mu L_1}{A k_1} - \frac{Q\mu L_2}{A k_2} \dots - \frac{Q\mu L_n}{A k_n} \\ \frac{L}{\bar{k}} &= \sum_{i=1}^n \frac{L_i}{k_i} \Rightarrow \\ \bar{k} &= \frac{L}{\sum_{i=1}^n \frac{L_i}{k_i}} \end{aligned} \quad (2.24)$$

Therefore, for serial stratified sand with linear flow, effective permeability can be represented with harmonic mean.

**2.2.5.4. Serial Stratified Radial Flow (Radial variation in permeability).** Considering radially stratified formation in series (Fig. 2.19)

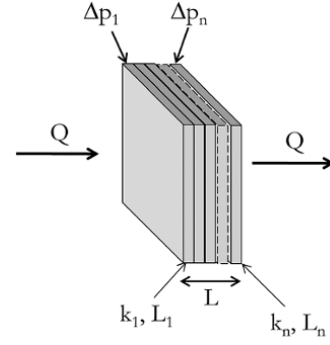


Figure 2.18 Serial stratified linear flow.

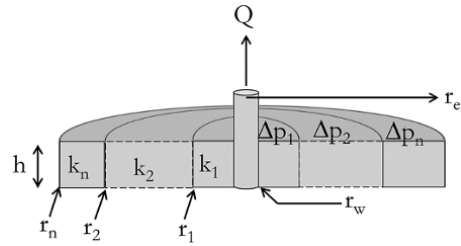


Figure 2.19 Radial variation in permeability.

$$\begin{aligned} \Delta p &= -\frac{Q\mu}{2\pi \bar{k} h} \ln \frac{r_e}{r_w} \\ \Delta p &= -\frac{Q\mu}{2\pi k h} \ln \frac{r_e}{r_w} = -\frac{Q\mu}{2\pi k_1 h} \ln \frac{r_1}{r_w} - \frac{Q\mu}{2\pi k_2 h} \ln \frac{r_2}{r_1} \dots \\ &\quad - \frac{Q\mu}{2\pi k_n h} \ln \frac{r_n}{r_{n-1}} = -\frac{Q\mu}{2\pi h} \sum_{i=1}^n \frac{\ln \frac{r_i}{r_{i-1}}}{k_i} \\ &\quad - \frac{Q\mu \ln \frac{r_e}{r_w}}{2\pi h \bar{k}} = -\frac{Q\mu}{2\pi h} \sum_{i=1}^n \frac{\ln \frac{r_i}{r_{i-1}}}{k_i} \\ \bar{k} &= \frac{\ln \frac{r_e}{r_w}}{\sum_{i=1}^n \frac{\ln \frac{r_i}{r_{i-1}}}{k_i}} \end{aligned} \quad (2.25)$$

**2.2.5.5. Geometric Mean for Randomly Distributed Formation.** Most reservoirs have randomly distributed permeability, hence there is justification for nonlinear average techniques such as geometric mean. Geometric averaging is a common method of estimating average permeability from smaller-scale samples. The problem with this approach for upscaling reservoir permeability or averaging reservoir permeability is sensitivity to sample permeability for a small sample size. This means that with

few low permeability samples, geometric average would give low permeability. However, in reality, this may not be true considering that, for randomly distributed permeability, fluid will follow through a path of connected high permeability (path of least resistance). Geometric mean should, therefore, be used with caution.

Geometric mean for randomly distributed formation (Fig. 2.20) is expressed in equation (2.26):

$$k = \sqrt[n]{k_{h1} \cdot k_{h2} \cdot k_{h3} \dots k_{hn}} \quad (2.26)$$

Various modifications of geometric mean for permeability determination have been proposed in the literature.

Other nonlinear averaging techniques used for reservoir upscaling include arithmetic-harmonic average and harmonic-arithmetic average (Fig. 2.21 and Fig. 2.22, respectively). These methods are common and justified considering upscaled reservoir permeability should lie between the harmonic (low bound mean) and arithmetic mean (upper bound mean):  $k_{\text{Harmonic}} < k_{\text{Harmonic-Arithmetic}} < k_{\text{Arithmetic-Harmonic}} < k_{\text{Arithmetic}}$ .

In reservoir simulation it is advisable to use different permeability averaging techniques and check averaged

permeability distribution of the upscaled model with a bench marks. Bench marks can include running streamline simulations to check which averaging method gives a comparable result with a geological model (fine grid model), checking which averaging methods best predicts water break through where relative permeability is known, or comparing which averaging techniques gives average permeability closest to average permeability from well test analysis within the radius of investigation.

In recent time, upscaling properties in a geological model to properties in reservoir simulation is becoming uncommon, as geological models with their properties can be used directly for reservoir simulation, due to enhanced software and hardware computing capabilities.

### 2.3. EFFECTIVE CONFINING PRESSURE DEPENDENCE OF POROSITY AND PERMEABILITY

It is very important that porosity and permeability measurements are carried out under stress conditions that reflect reservoir condition where possible. Porosity and permeability measured under stress is very important in calibrating porosity and permeability derived from other methods, as well as for reliable prediction of well and reservoir performance. Where porosity and permeability are measured at atmospheric conditions or a confining pressure different from that of the reservoir, correction should be applied to determined correct stressed porosity and

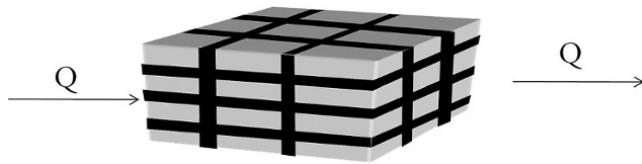


Figure 2.20 Random permeability distribution

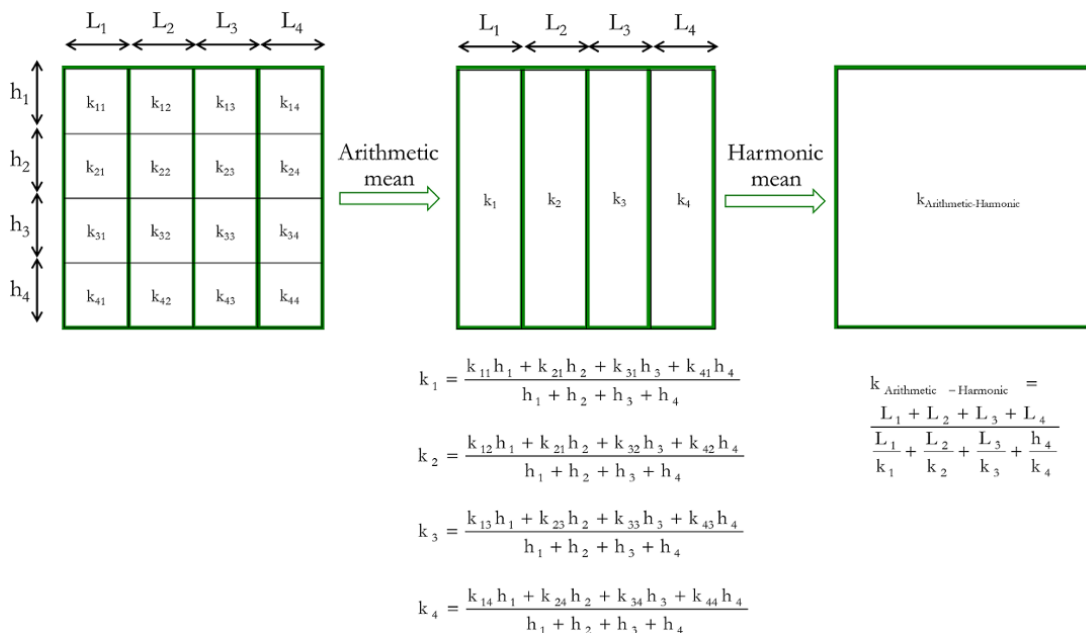
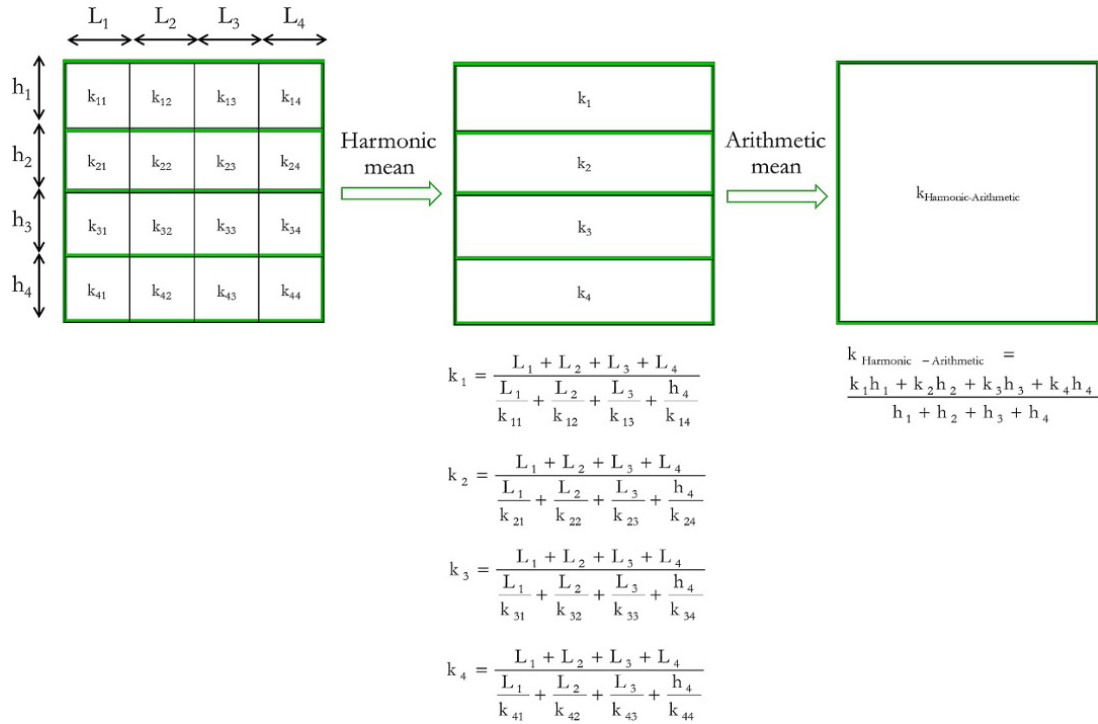


Figure 2.21 Arithmetic-harmonic permeability averaging.



**Figure 2.22** Harmonic-arithmic permeability averaging.

permeability values using stress-dependent porosity and permeability models.

Most predictions of change in porosity and permeability due to confining stress is based on *power law* or *exponential law* relationships. *Dong et al.* (2010) showed that power law gives a better prediction of effective confining pressure dependence of porosity and permeability.

Based on exponential law relationship, porosity and permeability under confining pressure,  $p_e$ , are expressed as equations (2.27) and (2.28), respectively

$$\phi = \phi_0 \exp[-\beta(p_e - p_0)] \quad (2.27)$$

$$k = k_0 \exp[-\gamma(p_e - p_0)] \quad (2.28)$$

where  $\phi_0$  and  $k_0$  are porosity and permeability measured at atmospheric condition ( $p_0$ ), respectively;  $\beta$  and  $\gamma$  are the porosity and permeability *exponential material constants*, respectively.

Based on power law relationship, porosity and permeability under confining pressure,  $p_e$ , are expressed as equations (2.29) and (2.30), respectively

$$\phi = \phi_0 \left( \frac{p_e}{p_0} \right)^{-q} \quad (2.29)$$

$$k = k_0 \left( \frac{p_e}{p_0} \right)^{-p} \quad (2.30)$$

$q$  and  $p$  are the porosity and permeability *power material constants*, respectively.

Material constants ( $\beta$ ,  $\gamma$ ,  $q$  and  $p$ ) can be determined from core samples with measurements at different pressure or taken from analogous reservoirs.

## 2.4. WETTABILITY

Wettability is an important measurement, though not directly used for reservoir performance prediction but very useful as it affects other rock–fluid measurements.

Wettability is defined as the preference of a liquid to adhere, contact, spread on a solid preferentially to another immiscible fluid present. This degree of spread or contact is defined by contact angle (Fig. 2.23).

Typical values of contact angles and interfacial tension are shown in Table 2.5.

There are commonly used terminologies in petrophysics and reservoir engineering that relate to wettability or are affected by wettability. They include:

**Drainage** This is the reduction in wetting phase saturation. Initial trapping of oil is a drainage process called *primary drainage*. In this process oil (nonwetting phase) displaces water (wetting phase), therefore causing a reduction in water (wetting phase) saturation. Other drainage processes that occur in the reservoir include: gas (nonwetting) phase displacing oil (wetting) by the gas cap expansion process or gas injection process; re-vaporization of condensate

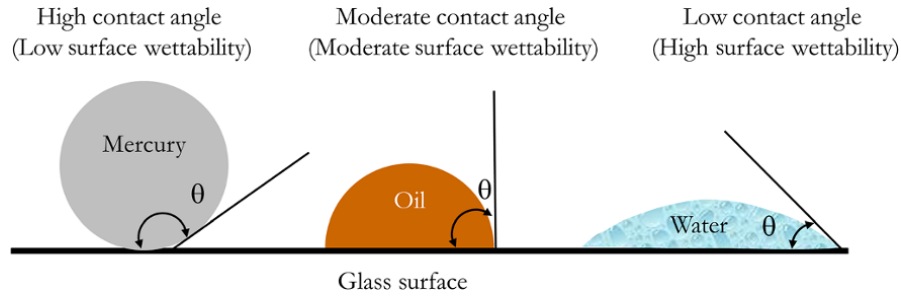


Figure 2.23 Wetting of mercury, oil, and water on a glass surface in the presence of air.

Table 2.5 Typical Values of Contact Angles and Interfacial Tensions.

Wetting phase	Nonwetting phase	T and p conditions	$\theta$ (°)	$\sigma$ (dynes/cm)
Brine	Oil	Reservoir	30	25–30
Brine	Oil	Laboratory	30	48
Brine	Gas	Reservoir	0	72
Brine	Gas	Laboratory	0	50
Oil	Gas	Reservoir	0	4
Gas	Mercury	Laboratory	130–140	480

during buildup causing displacement of condensate (wetting phase) by gas (nonwetting phase).

**Imbibition** This is the increase in wetting phase saturation. Imbibition processes in the reservoir include: water (wetting phase) displacing oil (nonwetting phase) due to water influx from an aquifer or water flooding; water (wetting phase) displacing gas (nonwetting phase) due to gas depletion; oil (wetting phase) displacing gas (nonwetting phase) during gas cap invasion by oil due to tilting or shrinkage of the gas cap; condensate dropout where condensate (wetting phase) displaces gas (nonwetting phase) during drawdown or production test.

**Irreducible Water Saturation ( $S_{wir}$ )** Irreducible water saturation is the minimum water saturation that can be achieved during oil or gas displacement of water in a water-saturated core sample. Irreducible water saturation may vary from one experiment to another, as it depends on the final drive pressure when flowing oil or gas is used for displacement, or the maximum centrifugal rotation speed for centrifuge displacement.  $S_{wir}$  corresponds to the water saturation value at which water relative permeability tends to zero.

**Connate Water Saturation ( $S_{wc}$  or  $S_{wi}$ )** Connate water saturation, also called initial connate water saturation, is the water saturation in a reservoir *in situ*, at pristine state. This is water saturation at the end of primary drainage process. Connate water saturation in hydrocarbon-bearing sand, except the transition

zone, is irreducible water saturation at the end of primary drainage.

**Residual Oil ( $S_{or}$ )** Residual oil saturation is the minimum oil saturation after gas or water displacement, either in the reservoir or in a laboratory core sample. This is oil saturation that cannot be removed further through flooding. At the laboratory scale, this value varies along the core length at the end of a test. It is common for the value at the core outflow face (which is also used for calculating the final value of  $k_{ro}$ ) to be used. Also, average value or  $S_{or}$  along the core length at the end of the test can be used to define  $S_{or}$  for a given test.

**Remaining Oil Saturation** Remaining oil saturation defines oil saturation at any time during the production life of a reservoir.

**Hysteresis** This is dependence of capillary pressure on saturation path and history.

### 2.4.1. Wettability Measurement

Common methods for determining wettability of reservoir rock samples are: contact angle measurement; the *Amott–Harvey technique* [Amott, 1959]; the U.S. Bureau of Mines (USBM) test [Anderson, 1986a, 1986b]; and Craig’s Wettability Criteria [Craig, 1971].

**2.4.1.1. Contact Angle.** The concept of using the contact angle in defining wettability is summarized using Fig. 2.23 and in Table 2.5. Values for contact angles for different reservoir rock samples are: 105–180° for oil-wet; 75–105° for neutral-wet and 0–75° for water-wet.

**2.4.1.2. Amott–Harvey Technique.** This procedure is described in Fig. 2.24. The process involves flooding the core plug to connate water saturation ( $S_{wc}$ ) with oil, often using a centrifuge. The core plug is then subjected to spontaneous formation brine imbibition, by immersing in brine, to determine spontaneous water saturation,  $S_{spw}$ .  $\Delta S_{ws}$  is then determined using:  $\Delta S_{ws} = S_{spw} - S_{wc}$ .

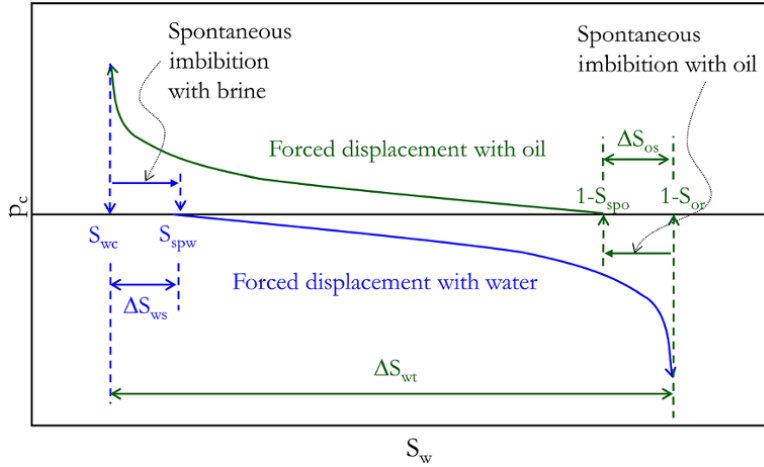


Figure 2.24 Typical  $p_c$  against  $S_w$  from the Amott–Harvey wettability experiment.

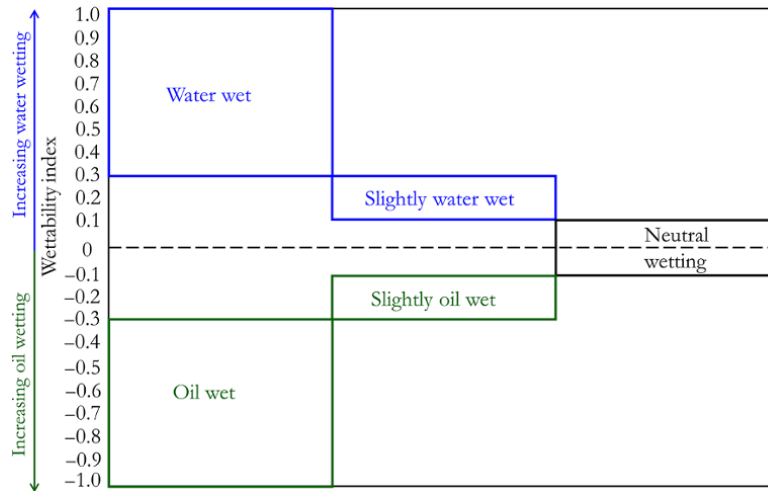


Figure 2.25 Amott–Harvey wettability index chart.

The core plug with oil and water at  $S_{wc}$  is then centrifuged to  $S_{or}$  using water (forced displacement of oil with water). The volume of water used for forced displacement is noted.

Total change in  $S_w$  ( $\Delta S_{wt}$ ) is then determined by addition of the results from the spontaneous and forced portions of the test:  $\Delta S_{wt} = 1 - S_{or} - S_{wc}$ .

The core plug with  $S_{or}$  and  $S_{wc}$  is then immersed in oil for spontaneous oil imbibition and the volume of oil spontaneously ( $\Delta S_{os}$ ) imbibed is determined using:  $\Delta S_{os} = 1 - S_{or} - (1 - S_{spo}) = S_{spo} - S_{or}$ .

This is then followed by forced displacement of water with oil using a centrifuge to  $S_{wc}$ .

Total change in oil saturation ( $\Delta S_{ot}$ ) is determined by adding the volumes from spontaneous imbibition with

forced displacement.  $\Delta S_{ot}$  and  $\Delta S_{wt}$  should be approximately the same.

The Amott–Harvey wettability Index ( $WI_{\text{Amott-Harvey}}$ ) of the core plug is then determined using:

$$\text{Displacement by water ratio} : \delta w = \frac{\Delta S_{ws}}{\Delta S_{wt}} \quad (2.31)$$

$$\text{Displacement by oil ratio} : \delta o = \frac{\Delta S_{os}}{\Delta S_{wt}} \quad (2.32)$$

$$\text{Amott-Harvey Wettability Index} : WI_{\text{Amott-Harvey}} = \delta w - \delta o \quad (2.33)$$

From  $WI_{\text{Amott-Harvey}}$  calculated, the wettability of the core sample is then determined using Fig. 2.25, which shows wettability and corresponding WI.



**Exercise 2.9** Wettability Determination Using the Amott–Harvey Method

Determine the wettability of a sample given the forced displacement data of a core sample from Amott–Harvey in Table 2.6.

**Solution Steps.**

*Step 1:* plot  $p_c$  against  $S_w$  for forced displacement with water and oil (Fig. 2.26).

*Step 2:* determine  $\Delta S_{ws} = S_{spw} - S_{wc}$ ;  $\Delta S_{wt} = 1 - S_{or} - S_{wc}$ ;  $\Delta S_{os} = 1 - S_{or} - (1 - S_{spo}) = S_{spo} - S_{or}$  from graph (Fig. 2.26).

*Step 3:* calculate  $\delta_w$ ,  $\delta_o$  and  $WI$ .

*Step 4:* determine the wettability of the sample using the Amott wettability index table/chart.

**Table 2.6** Forced Displacement Test Data from Amott–Harvey Experiment.

Forced displacement with water		Forced displacement with oil	
$S_w$	$p_c$ (psi)	$S_w$	$p_c$ (psi)
0.90	-82.51	0.15	98.60
0.88	-53.59	0.16	80.69
0.84	-28.49	0.17	62.77
0.81	-13.67	0.22	47.94
0.76	-7.80	0.27	36.69
0.71	-5.93	0.33	28.10
0.66	-3.63	0.41	18.60
0.57	-2.17	0.49	13.12
0.52	-1.21	0.64	5.31
0.29	0.00	0.77	0.65

$p_c$  is the capillary pressure in psi (discussed in detail in Section 2.5).

**Solution.**

$$\Delta S_{ws} = S_{spw} - S_{wc} = 0.29 - 0.15 = 0.14$$

$$\Delta S_{wt} = 1 - S_{or} - S_{wc} = 0.9 - 0.15 = 0.75$$

$$\Delta S_{os} = (1 - S_{or}) - (1 - S_{spo}) = 0.9 - 0.77 = 0.13$$

$$\delta_w = \frac{\Delta S_{ws}}{\Delta S_{wt}} = \frac{0.14}{0.75} = 0.1867$$

$$\delta_o = \frac{\Delta S_{os}}{\Delta S_{wt}} = \frac{0.13}{0.75} = 0.1733$$

$$WI_{Amott-Harvey} = \delta_w - \delta_o = +0.01$$

Based on the Amott wettability index (Fig. 2.25), this correspond to neutral wettability as  $WI_{Amott-Harvey}$  lies between  $-0.1$  and  $+0.1$ .

**2.4.1.3. USBM (U.S. Bureau of Mines) Test.** This method, which is outlined in Fig. 2.27 is similar to the Amott–Harvey approach. It involves displacing oil to  $S_{or}$  followed by displacing to  $S_{wc}$ . Capillary pressure associated with centrifuge speed is plotted against average water saturation ( $S_w$ ) during the displacement process. The USBM method, although similar to the Amott–Harvey technique, does not require measurement of saturation change during spontaneous water and oil imbibition. The USBM wettability index ( $WI_{USBM}$ ) is defined as:

$$WI_{USBM} = \log\left(\frac{A_1}{A_2}\right) \tag{2.34}$$

The USBM wettability criteria are defined as follows: for water-wet,  $WI_{USBM}$  is close to a value of 1; for neutral

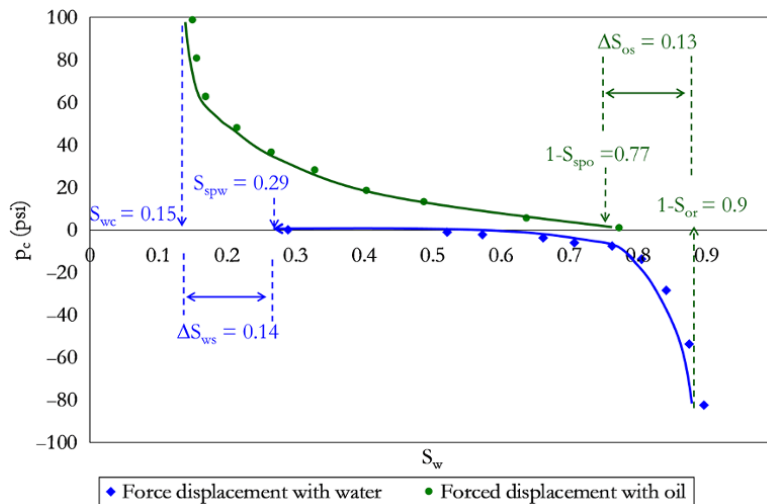


**Figure 2.26**  $p_c$  against  $S_w$  plot for Exercise 2.9.

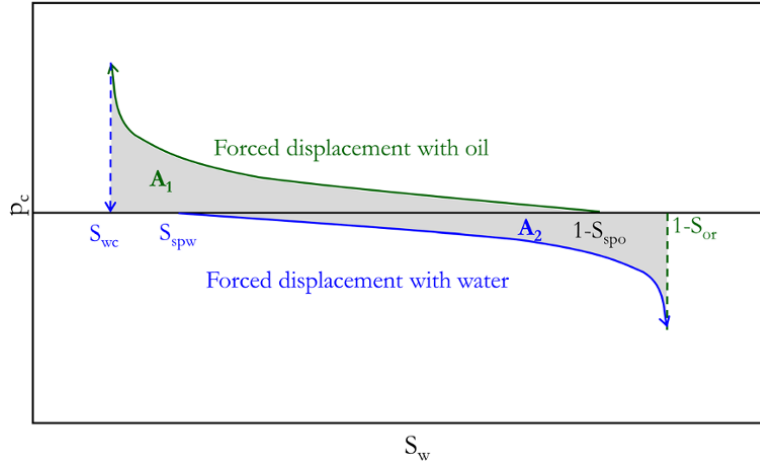


Figure 2.27 Typical  $p_c$  against  $S_w$  the from USBM wettability experiment.

Table 2.7 Determination of  $A_1$  and  $A_2$  Using Numerical Integration.

Forced displacement with oil			Forced displacement with water		
$S_{wj}$	$p_c(S_{wj})$	$\Delta A_1 = (\Delta S_w/2) \times [p_c(S_{wj-1}) + p_c(S_{wj})]$	$S_{wj}$	$p_c(S_{wj})$	$\Delta A_2 = (\Delta S_w/2) \times [p_c(S_{wj-1}) + p_c(S_{wj})]$
0.15	98.60		0.90	-82.51	
0.16	80.69	0.531	0.88	-53.59	1.477
0.17	62.77	0.949	0.84	-28.49	1.391
0.22	47.94	2.490	0.81	-13.67	0.742
0.27	36.69	2.111	0.76	-7.80	0.471
0.33	28.10	2.091	0.71	-5.93	0.377
0.41	18.60	1.763	0.66	-3.63	0.216
0.49	13.12	1.314	0.57	-2.17	0.258
0.64	5.31	1.381	0.52	-1.21	0.087
0.77	0.65	0.403	0.29	0.00	0.141
$A_1 = \Sigma \Delta A_1 =$		13.034	$A_2 = \Sigma \Delta A_2 =$		5.159

wettability,  $WI_{USBM}$  is close to a value of 0; and for oil-wet,  $WI_{USBM}$  is close to value of -1.

**Exercise 2.10** Wettability Determination Using the USBM Method

Determine the wettability of a core sample by the USBM method using the data provided in Table 2.6.

**Solution Steps.**

Step 1: plot  $p_c$  against  $S_w$  for both forced displacement with water and oil as shown in Fig. 2.26 and Fig. 2.27.

Step 2: determine  $A_1$  and  $A_2$  using numerical integration techniques such as *Trapezoidal rule* or *Simpson rule* (Table 2.7).

Step 3: determine  $WI_{USBM}$  using  $WI_{USBM} = \log\left(\frac{A_1}{A_2}\right)$  from equation (2.34).

**Solution.**

Key calculation steps in calculating  $A_1$  and  $A_2$  is summarized in Table 2.7.

$$WI_{USBM} = \log\left(\frac{13.034}{5.159}\right) = 0.4$$

Based on the USBM wettability index this corresponds to neutral wettability, as  $WI_{USBM}$  is close to 0.

Note: both the Amott–Harvey and USBM are common methods for wettability determination and show significant differences in results for core samples with near neutral wettability properties.

**2.4.1.4. Craig’s Wettability Criteria.** These wettability criteria, defined based on relative permeability model parameters, can be summarized as:

- water-wet:  $S_{wi} > 0.25$ ;  $S_w$  at  $k_{rw} = k_{ro} > 0.5$ ;  $k'_{rw} < 0.3$
- oil-wet:  $S_{wi} < 0.15$ ;  $S_w$  at  $k_{rw} = k_{ro} < 0.5$ ;  $k'_{rw} > 0.5$

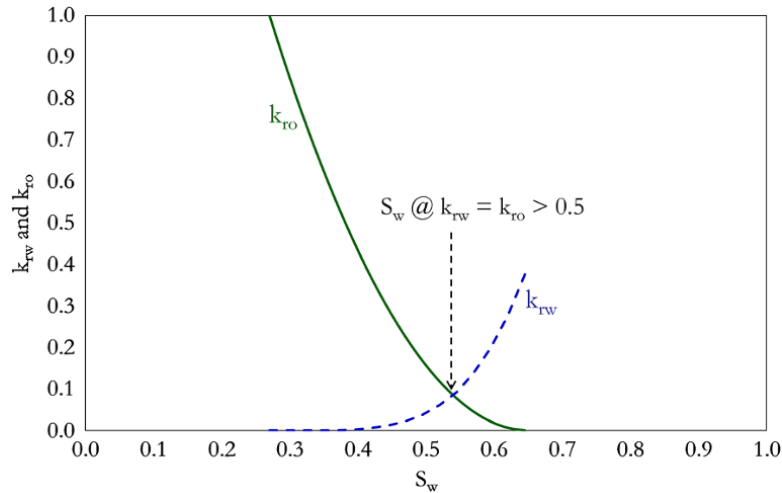


Figure 2.28 Example of relative permeability model for a water-wet rock sample.

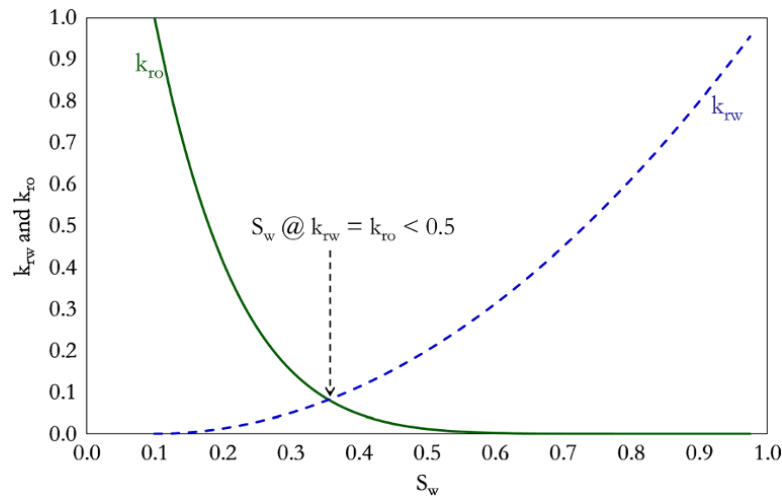


Figure 2.29 Example of relative permeability model for an oil-wet rock sample.

where  $S_{wi}$  is initial (connate) water saturation,  $k_{rw}$  is water relative permeability as a function of water saturation ( $S_w$ ),  $k'_{rw}$  is maximum water relative permeability, and  $k_{ro}$  is oil relative permeability.

Use of Craig’s wettability criteria to define wettability is illustrated in Fig. 2.28 and Fig. 2.29 for water-wet and oil-wet rock samples respectively.

Concept and modelling reservoir relative permeability are discussed in Section 2.6.

The different wettability measurement approach are summarized in Table 2.8.

### 2.5. CAPILLARY PRESSURE

In order for a fluid to displace another fluid in porous media, a threshold pressure called the *capillary pressure* is required. During migration of hydrocarbon from source

rock into a reservoir trap, this threshold pressure (capillary pressure) must be exceeded for oil (nonwetting phase) to displace water (wetting phase) (Fig. 2.30a) and also to enable oil to be trapped around water (Fig. 2.30b). When the reservoir is in equilibrium, capillary pressure exists as a discontinuous pressure across the interface of trapped oil (nonwetting phase) and water (wetting phase), as shown in Fig. 2.30b. Hence, a threshold pressure (capillary pressure) which is equal to this discontinuous pressure across the interface of oil and water is required, in order to remove trapped oil from pores wetted by water (Fig. 2.30c).

Capillary pressure, therefore, assists or resists the displacement of one fluid by another in a porous media. Capillary pressure determination in an important SCAL measurement for determination of initial reservoir fluid distribution, reservoir fluid trapping, and cap-rock seal capacity.

**Table 2.8** Summary of Wettability Measurement Approach/Criteria.

	Oil-wet	Neutral-wet	Water-wet
Contact angle (°)	105–180	75–105	0–75
Amott–Harvey wettability index	–1.0 to –0.3	–0.3 to 0.3	0.3 to 1.0
USBM wettability index	about –1	about 0	about 1
Craig’s Criteria	$S_{wi} < 0.15$ ; $S_w$ at $k_{rw} = k_{ro} < 0.5$ ; $k'_{rw} > 0.5$	$0.15 < S_{wi} < 0.25$ ; $S_w$ at $k_{rw} = k_{ro} \approx 0.5$ ; $0.3 < k'_{rw} < 0.5$	$S_{wi} > 0.25$ ; $S_w$ at $k_{rw} = k_{ro} > 0.5$ ; $k'_{rw} < 0.3$

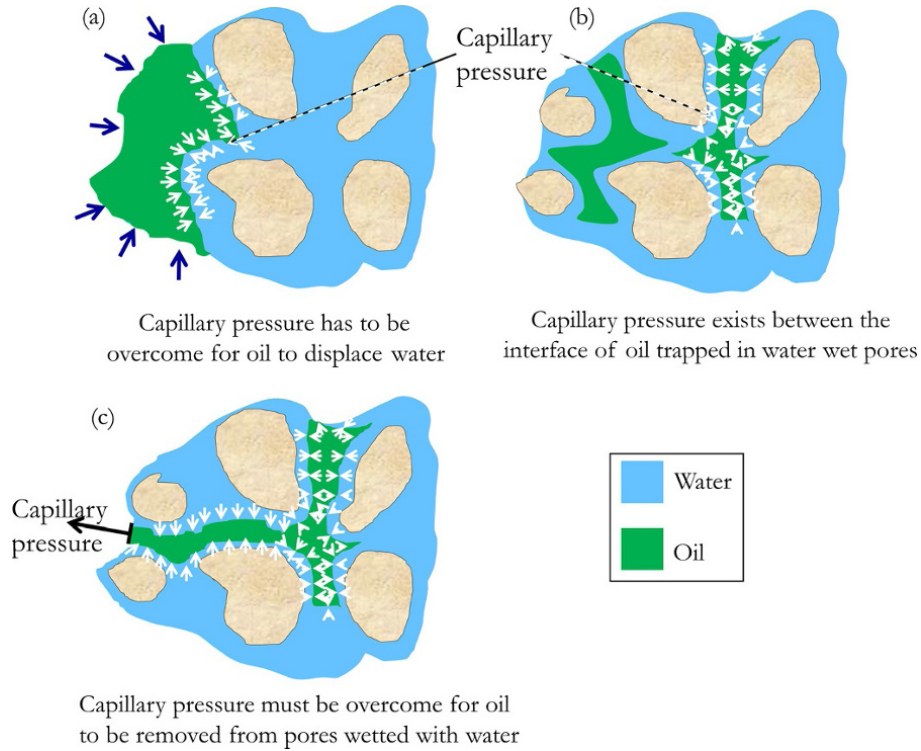


**Figure 2.30** Capillary pressure in reservoir rock.

**2.5.1. Capillary Tube Analogy of Porous Media**

Porous media can be modelled as bundles of capillary tubes with varying diameters, where tube diameter is synonymous with pore throat diameter. Using this concept of porous media behaving like capillary tubes, the effect of the capillary on fluid displacement and distribution of the fluid can be explained. Fig. 2.31 illustrates how capillary pressure assists water to rise in the core sample and capillary tube by spontaneous displacement of air.

Fig. 2.32 shows water (wetting phase) rising and displacing air (nonwetting phase).

When the interface is in equilibrium:

force exerted by wetting face – force exerted by nonwetting face = force acting at interface:

$$p_{nw}A_{nw} - p_wA_w = \sigma \cos\theta(2\pi r) \quad (2.35)$$

where  $p_{nw}$  is the pressure exerted by the nonwetting phase,  $A_{nw}$  is the area of the nonwetting phase,  $p_w$  is the pressure exerted by the wetting phase,  $A_w$  is the area of the wetting phase,  $\sigma$  is the interfacial tension (fluid property), and  $\theta$  is the contact angle, which is the wettability characteristic (rock–fluid property).

From equation (2.35):

$$(p_{nw} - p_w)\pi r^2 = \sigma \cos\theta(2\pi r) \quad (2.36)$$

But capillary pressure ( $p_c$ ) can be defined as:

$$p_c = p_{nw} - p_w \quad (2.37)$$

Substituting equation (2.37) into equation (2.36):

$$p_c = \frac{2\sigma \cos\theta}{r} \quad (2.38)$$

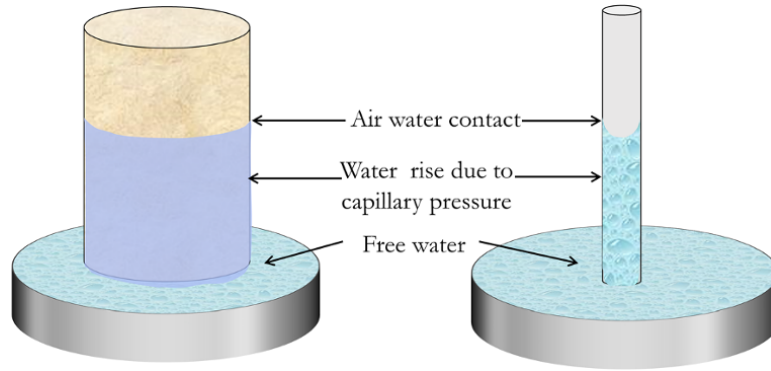


**Figure 2.31** Capillary pressure assisting water to rise in core sample and capillary tube (displacement of air by water).

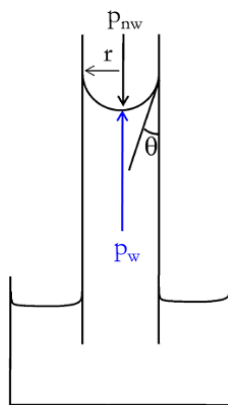


**Figure 2.32** Rising of wetting liquid in circular tubes.

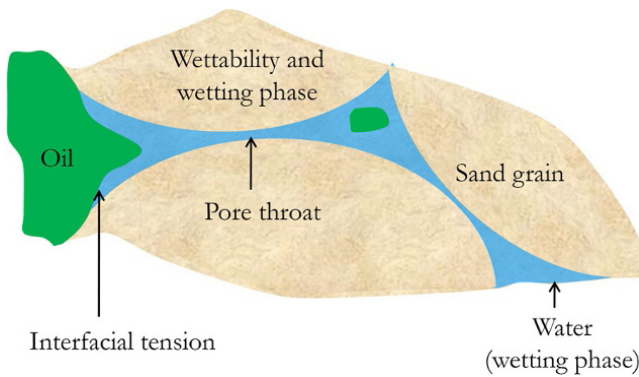


**Figure 2.33** Capillary pressure in water-wet reservoir rock.

Therefore, using the capillary tube analogy, capillary pressure ( $p_c$ ) can be defined by equation (2.38).

The expression in equation (2.38) is also called *Laplace's equation*. Capillary pressure depends on interfacial tension, pore throat size (capillary or confinement radius), and wettability (Fig. 2.33).

Fig. 2.34 further illustrates the dependence of capillary pressure (and rise of water level) on capillary tube radius in capillary tubes or interconnectivity of pore spaces (permeability) in reservoir rock. This implies that capillary pressure is high in a low permeability reservoir and is, hence, the reason why capillary pressure in shale or shaly reservoirs is high.

### 2.5.2. Capillary Pressure and Fluid Distribution

A more useful expression of capillary pressure is relating it to height of fluid column. This is important in understanding fluid distribution in reservoirs. Fig. 2.35 shows water displacing air (gas) in a capillary tube and water displacing oil in capillary tube.

From equation (2.37):

Capillary pressure = pressure of nonwetting phase – pressure of wetting phase:

$$p_c = p_{nw} - p_w$$

Thus, for an oil-water system (considering water-wet),  $p_c = p_o - p_w$ .

Gas is always the nonwetting phase in both oil-gas and water-gas systems. Hence for a gas-oil system (oil as wetting phase),  $p_c = p_g - p_o$ . For a gas-water system (water-wet),  $p_c = p_g - p_w$ .

#### 2.5.2.1. Gas-Water System with Water Displacing Air.

From Fig. 2.35a

$$p_{w1} = p_{w2} + \rho_w g h_w \tag{2.39}$$

$$p_{g1} = p_{g2} + \rho_g g h_w \tag{2.40}$$

$\rho$  is the density where the subscript g is gas, w is water, and o is oil.

But  $p_{w1} = p_{g1}$  (absence of capillary pressure at horizontal interface); thus, combining equations (2.39) and (2.40):

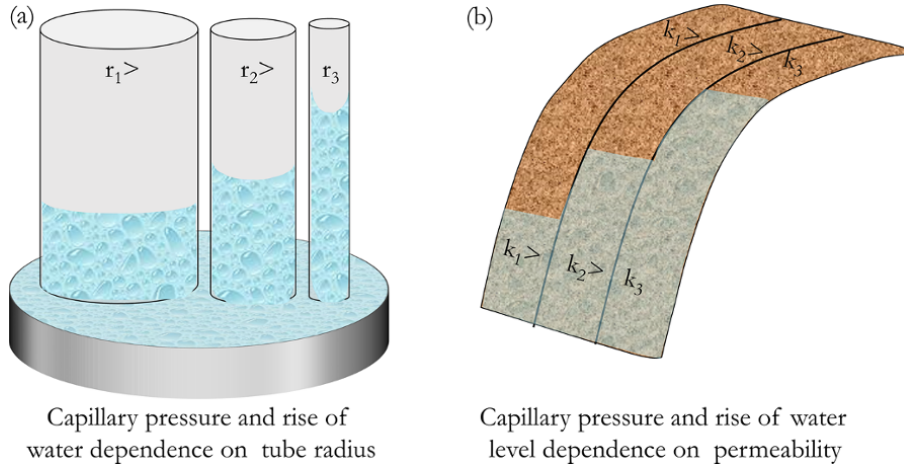


**Figure 2.34** Effect of capillary tube radius and interconnectivity of pore spaces (permeability) on rising of water level.

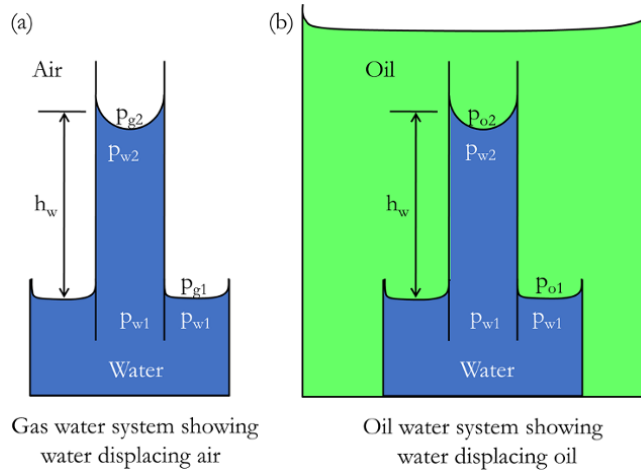


**Figure 2.35** Capillary pressure assisting fluid displacement in a capillary tube.

$$p_{w2} + \rho_w g h_w = p_{g2} + \rho_g g h_w$$

$$p_{g2} - p_{w2} = (\rho_w - \rho_g) g h_w$$

Hence

$$p_c = (\rho_w - \rho_g) g h_w \text{ in consistent units} \quad (2.41)$$

An example of consistent unit is CGS units, with  $p_c = \text{dynes/cm}^2$ ;  $\rho = \text{gm/cm}^3$ ;  $g = \text{cm/sec}^2$ ;  $h_w = \text{cm}$ .

Equation (2.41) can be expressed in engineering oil field (EOF) units as:

$$p_c = \frac{(\rho_w - \rho_g) h_w}{144} \text{ in EOF units} \quad (2.42)$$

In EOF units,  $p_c = \text{psi}$ ;  $\rho = \text{lb/ft}^3$ ;  $h_w = \text{ft}$

**2.5.2.2. Oil-Water System with Water Displacing Oil.**  
From Fig. 2.35b

$$p_{w1} = p_{w2} + \rho_w g h_w \quad (2.43)$$

$$p_{o1} = p_{o2} + \rho_o g h_w \quad (2.44)$$

But  $p_{w1} = p_{o1}$  (absence of capillary pressure at horizontal interface), so combining equations (2.43) and (2.44):

$$p_{w2} + \rho_w g h_w = p_{o2} + \rho_o g h_w$$

$$p_{o2} - p_{w2} = (\rho_w - \rho_o) g h_w$$

Hence

$$p_c = (\rho_w - \rho_o) g h_w \text{ in consistent units} \quad (2.45)$$

$$p_c = \frac{(\rho_w - \rho_o) h_w}{144} \text{ in EOF units} \quad (2.46)$$

A generalized equation for capillary pressure can be written as:

$$p_c = \frac{(\rho_w - \rho_{HC})h_w}{144} \quad (2.47)$$

where  $\rho_{HC}$  is the density of hydrocarbon fluid in contact with water in the reservoir.

Distribution of oil and water is influenced by the balance of imbibition capillary pressure and gravity. This balance of force is responsible for the creation of a transition between the oil and water zones. This transition zone also exists at a gas–oil interface; however, it is less than that between oil and water. Capillary pressure is dependent on saturation path and history. Fig. 2.36 illustrates the difference between the capillary pressure curve for the drainage and imbibition process. This phenomenon of capillary pressure dependence on saturation path and history is called *hysteresis*.

A comparison of capillary pressure effect on gas–water reservoirs and oil–water reservoirs shows a smaller transition in gas–water reservoirs compared with oil–water reservoirs (Fig. 2.37). This smaller transition region is due to a larger density contrast between gas and water compared with oil and water.

Fig. 2.36 and Fig. 2.37 shows that in a hydrocarbon-water reservoir, water saturation decreases with increasing height above free water level (FWL). FWL corresponds to  $p_c = 0$  (Fig. 2.36).

From equation (2.46), height above FWL is defined as:

$$h_{FWL} = h_w = \frac{144p_c}{(\rho_w - \rho_o)} \quad (2.48)$$

Height above the oil–water contact (OWC) is:

$$h_{OWC} = h_{FWL} - OWC \quad (2.49)$$

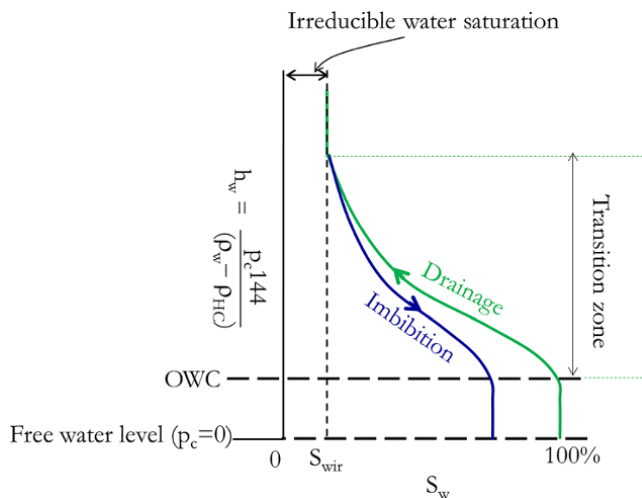


**Figure 2.36** Capillary pressure effect on the distribution of oil and water in a reservoir.

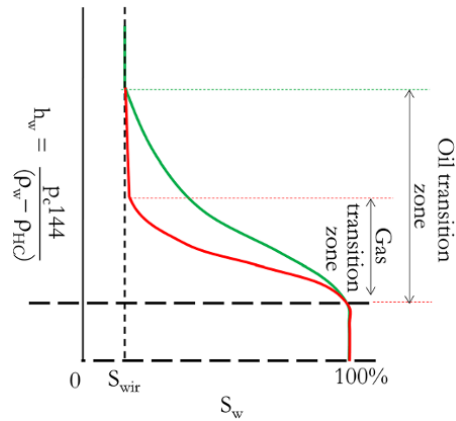


**Figure 2.37** Comparison of transition zone in oil–water and gas–water reservoirs.

By substituting equation (2.48) into equation (2.49), height above OWC becomes:

$$h_{OWC} = \frac{144p_c}{(\rho_w - \rho_o)} - OWC \quad (2.50)$$

Formation thickness between specific intervals  $h_1$  and  $h_2$  with capillary pressure of  $p_{c1}$  and  $p_{c2}$  respectively is expressed as:

$$h_2 - h_1 = \frac{144(p_{c2} - p_{c1})}{(\rho_w - \rho_o)} \quad (2.51)$$

Average water saturation over interval  $h_1$  and  $h_2$  is expressed as:

$$\bar{S}_w = \frac{\int_{h_1}^{h_2} S_w dh}{(h_2 - h_1)} \quad (2.52)$$

**Exercise 2.11** Capillary Pressure and Water–Oil Distribution in Reservoirs

Given the data from a capillary pressure experiment on a core sample from an oil reservoir in Table 2.9 and also given  $\rho_w = 64 \text{ lbs/ft}^3$  and  $\rho_o = 45 \text{ lbs/ft}^3$ :

Determine water saturation at a depth of 170 ft above the OWC.

Determine water saturation 100 ft above the FWL.

Given that the top oil bearing column to the OWC is 270 ft, calculate average water saturation over the oil-bearing zone.

**Solution Steps.**

*Step 1:* make a table and plot of  $h_w$  against  $S_w$  using equation (2.48).

- Step 2: determine the OWC.
- Step 3: use equation (2.49) to determine  $h_{FWL}$  for a depth of 170 ft above the OWC and read  $S_w$  from  $h_w$  against  $S_w$  to determine  $S_w$  for Question 1.
- Step 4: read  $h_{WFL}$  on  $h_w$  against  $S_w$  to determine  $S_w$  for Question 2.
- Step 5: using equation (2.52) to determine  $\bar{S}_w$  either by using numerical integration or finding the area formed by  $h_w$  against  $S_w$  over interval  $h_1$  and  $h_2$ .

**Solution.**

The height above FWL calculation is summarized in Table 2.10.

The plot of  $h_w$  against  $S_w$  is shown in Fig. 2.38

The FWL is the depth at which water saturation approaches 1 and the pressure of the oil phase is the same as that of water ( $p_c = 0$ ), while the OWC is defined as the depth at which water saturation approaches 1 with the existence of capillary pressure ( $p_c \neq 0$ ).

- (i) 170 ft above OWC  $\equiv 170 + 41.79$  ft (211.79 ft) above FWL;  $S_w = 0.3$ .
- (ii) At 100 ft above FWL,  $S_w = 0.38$ .
- (iii) Using equation (2.52):

$$\bar{S}_w = \frac{\int_{h_1}^{h_2} S_w dh}{(h_2 - h_1)}$$

But  $\int_{h_1}^{h_2} S_w dh$  defines the area within the limit between  $h_1$  and  $h_2$  (shaded area), as shown in Fig. 2.39. Thus:

$$\int_{h_1}^{h_2} S_w dh = |Area|_{h_1}^{h_2}$$

Hence:

$$\bar{S}_w = \frac{\int_{h_1}^{h_2} S_w dh}{(h_2 - h_1)} = \frac{|Area|_{h_1}^{h_2}}{(h_2 - h_1)}$$

**Table 2.9** Oil–Water Capillary Pressure Data.

Oil–water $p_c$ (psi)	$S_w$
0.00	1.00
2.76	1.00
5.52	1.00
6.64	0.88
7.02	0.81
9.19	0.49
10.60	0.43
19.68	0.32
43.87	0.29

**Table 2.10** Height Above FWL Against  $S_w$ .

Oil–water $p_c$ (psi)	$S_w$	$h_{FWL} = \frac{144p_c}{(p_w - p_o)}$
0.00	1.00	0.00
2.76	1.00	20.90
5.52	1.00	41.80
6.64	0.88	50.35
7.02	0.81	53.17
9.19	0.49	69.62
10.60	0.43	80.34
19.68	0.32	149.14
43.87	0.29	332.48

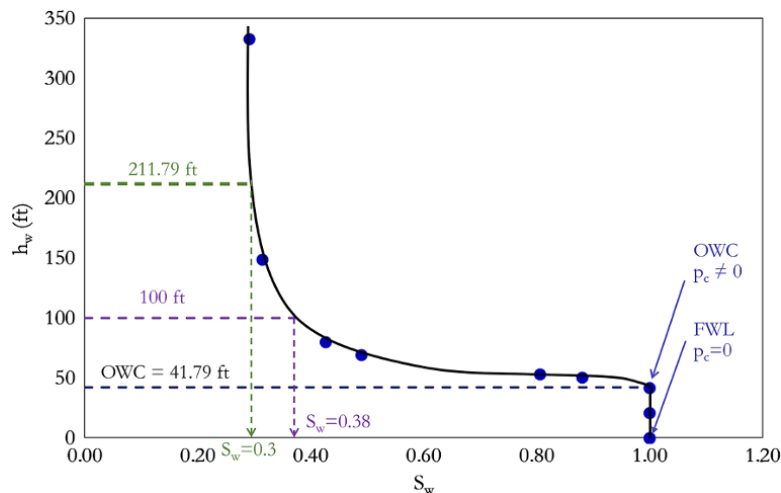


**Figure 2.38** Plot of  $h_w$  against  $S_w$ .



The area within the limit of  $h_1$  and  $h_2$  can be determined by numerical integration methods such as *Trapezoidal Rule*:

$$\int_{h_1}^{h_2} S_w dh = \sum_{j=1}^n \left( \frac{S_{w,j+1} + S_{w,j}}{2} \right) (h_w(S_{w,j+1}) - h_w(S_{w,j})) \tag{2.53}$$

Numerical integration of  $\int_{h_1}^{h_2} S_w dh$  using the trapezoidal rule is shown in Table 2.11.

**Table 2.11** Numerical Integration of  $\int_{h_1}^{h_2} S_w dh$  Using the Trapezoidal Rule.

$S_w$	$h_w$	$-h_w(S_{w,j})$	$S_w \Delta h = \left( \frac{S_{w,j+1} + S_{w,j}}{2} \right) (h_w(S_{w,j+1}) - h_w(S_{w,j}))$
1.00	$h_1 \rightarrow$	41.79	
0.88		50.35	8.05
0.81		53.17	2.38
0.49		69.62	10.69
0.43		80.34	4.93
0.32		149.14	25.80
0.29	$h_2 \rightarrow$	311.79	49.61

Area of region shade =  $\int_{h_1}^{h_2} S_w dh = \sum_{j=1}^n S_w \Delta h = 101.46$

$$\bar{S}_w = \frac{\int_{h_1}^{h_2} S_w dh}{(h_2 - h_1)} = \frac{|Area|_{h_1}^{h_2}}{(h_2 - h_1)} = \frac{101.46}{311.79 - 41.79} = 0.38$$

$$\bar{S}_w = 0.38$$

The area defined by the interval  $h_1$  and  $h_2$  is shown in Fig. 2.39

### 2.5.3. Capillary Pressure Defined as a Function of Radii of Curvature of Interface

$p_c$  can also be defined in terms of the radii of curvature of the interface. A segment of curved surface small enough can be considered a square with arc length of  $a$  (Fig. 2.40). Each of the  $a/2$  on orthogonal planes, which are normal to square (segment) at point A, are subtended by angles  $\theta_1$  and  $\theta_2$  and with radii of  $R_1$  and  $R_2$ , respectively.

From Fig. 2.40:

$$\sin\theta_1 = \frac{a}{2R_1} \text{ and } \sin\theta_2 = \frac{a}{2R_2}$$

At equilibrium:

$$p_c (a \cos\theta)^2 = 2(\sigma a \sin\theta_1) + 2(\sigma a \sin\theta_2)$$

where  $\theta$  is considered very small,  $\cos\theta \approx 1$ . Substituting  $\cos\theta \approx 1$ ,  $\sin\theta_1$ , and  $\sin\theta_2$  into the above equation, the equation becomes:

$$p_c (a \cos(0))^2 = 2 \left( \sigma a \frac{a}{2R_1} \right) + 2 \left( \sigma a \frac{a}{2R_2} \right) \tag{2.54}$$

$$p_c (a)^2 = 2 \left( \sigma a \frac{a}{2R_1} \right) + 2 \left( \sigma a \frac{a}{2R_2} \right)$$

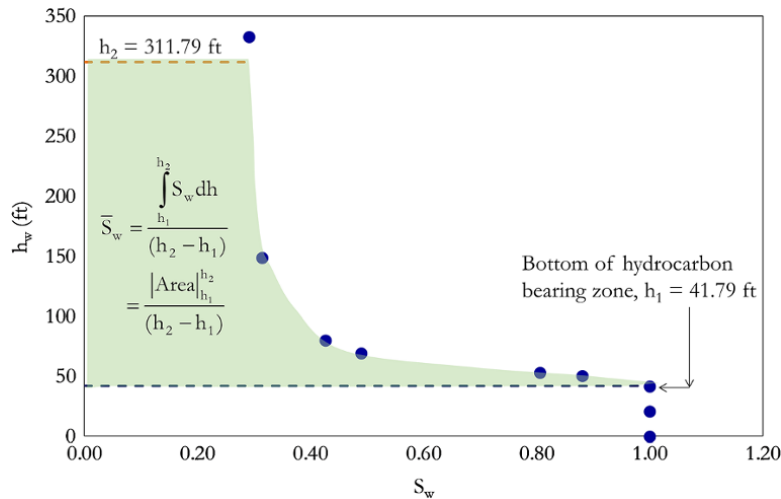


**Figure 2.39** Average water saturation over oil-bearing zone.

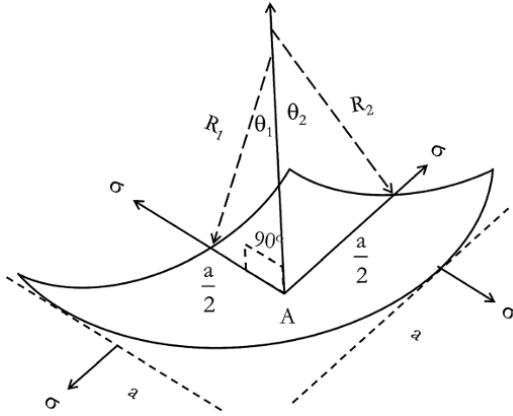


Figure 2.40 Segment of curvature of fluid interface.

$$p_c = \sigma \left( \frac{1}{R_1} + \frac{1}{R_2} \right) \quad (2.55)$$

#### 2.5.4. Experimental Determination of Capillary Pressure

Capillary pressure measurement based on fluid type includes: air–brine; oil–brine; and air–mercury. With known values of interfacial tension, capillary pressure can be converted from one phase to another. The most common experimental setup involves using gas capillary pressure for desaturation a core sample saturated with brine. Mercury may be used for the experiment but requires a different setup and correction to the oil–brine capillary pressure using interfacial tension and wettability. Mercury corrected capillary pressure is generally lower than oil–brine capillary pressure. Some of the experiment setups for capillary pressure measurement include:

- *Porous diaphragm method*: this method measures drainage air–brine capillary pressure. It involves desaturating a core saturated with brine by applying capillary pressure across the core sample and a brine saturated porous plate (Fig. 2.41). This method provides an accurate way of determining  $p_c$  and is considered representative of reservoir conditions, since reservoir fluids can be used for the experiment. This method is slow, taking days to even months. Diaphragm methods are limited by the displacement pressure of porous rock.

- *Mercury injection method*: this method provides a quick way of measuring  $p_c$ . Mercury injection can be carried over a wide range of  $p_c$ . This method involves conversion from mercury–air to reservoir fluid. One disadvantage of the mercury injection method is its destruction of the core sample. Disposal of the core sample contaminated with mercury is another environmental challenge. This method tends to produce low  $S_{wc}$  due to poor fluid–rock interactions.

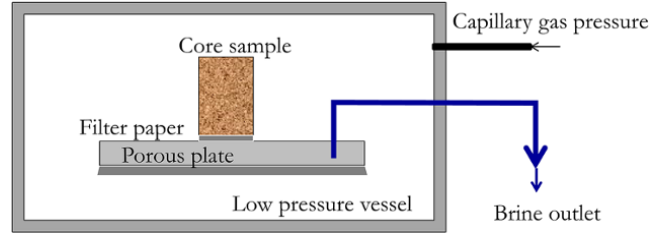


Figure 2.41 Experimental measurement of capillary pressure (porous plate).

- *Centrifuge method*: this method involves using centrifugal force to desaturate core samples and measuring pressure differential across the core sample from centrifugal force, then converting capillary pressure to appropriate reservoir fluid and conditions. This method is a fairly quick method for  $p_c$  measurement compared to the porous plate method, taking hours to weeks. It is a reasonably accurate method.

- *Dynamic method*: this method involves simultaneous injection of two fluid types and recovering of one of the fluid types behind a semipermeable membrane.

**2.5.4.1. Scaling  $p_{c(\text{air-brine})}$  to  $p_{c(\text{oil-brine})}$  Using Interfacial Tension (IFT) and Wettability.** From equation (2.38):

$$p_{c(\text{oil-brine})} = \frac{2(\sigma \cos \theta)_{\text{oil-brine}}}{r} \quad \text{and}$$

$$p_{c(\text{air-brine})} = \frac{2(\sigma \cos \theta)_{\text{air-brine}}}{r}$$

Solving these equations simultaneously by eliminating  $r$ :

$$p_{c(\text{oil-brine})} = p_{c(\text{air-brine})} \times \frac{(\sigma \cos \theta)_{\text{oil-brine}}}{(\sigma \cos \theta)_{\text{air-brine}}}$$

Using contact angle and interfacial tension from Table 2.5, assuming the experiment was carried out under reservoir conditions, and that conversion to oil–brine equivalent is at reservoir conditions.

$$p_{c(\text{oil-brine})} = p_{c(\text{air-brine})} \times \frac{25 \cos 30^\circ}{72 \cos 0^\circ}$$

$$p_{c(\text{oil-brine})} = 0.3093 p_{c(\text{air-brine})} \quad (2.56)$$

**2.5.4.2. Scaling  $p_{c(\text{air-mercury})}$  to  $p_{c(\text{oil-brine})}$  Using IFT and Wettability.** From (2.38):

$$p_{c(\text{oil-brine})} = \frac{2(\sigma \cos \theta)_{\text{oil-brine}}}{r} \quad \text{and}$$

$$p_{c(\text{air-Hg})} = \frac{2(\sigma \cos \theta)_{\text{air-Hg}}}{r}$$

Solving the above equations simultaneously by eliminating  $r$ :

$$P_{c(oil-brine)} = P_{c(air-Hg)} \times \frac{(\sigma \cos\theta)_{oil-brine}}{(\sigma \cos\theta)_{air-Hg}}$$

Using contact angle and interfacial tension from Table 2.5, assuming the experiment was carried out under laboratory conditions, and conversion to oil-brine equivalent is at reservoir conditions.

$$P_{c(oil-brine)} = P_{c(air-Hg)} \times \frac{25 \cos 30^\circ}{480 \cos 130^\circ} \quad (2.57)$$

$$P_{c(oil-brine)} = 0.07017 P_{c(air-Hg)}$$

### 2.5.5. Leverett J-Function

The Leverett J-Function is use for averaging and upscaling capillary pressure curves. It is also useful in converting all capillary pressure data to a universal curve. The Leverett J-Function is defined as:

$$J(S_w) = \frac{P_c}{\sigma \cos\theta} \sqrt{\frac{k}{\phi}} \quad (\text{Leverett, 1941}) \quad (2.58)$$

#### Exercise 2.12 Capillary Pressure Experiment and Leveret J-Function

An air–mercury and air–brine capillary pressure experiment was carried out on core samples taken over a 10 m depth interval along a vertical well.

1. Convert air–mercury capillary pressure for samples 1A, 2A, 3A, and 4A to oil–brine capillary pressure data ( $p_c$  against  $S_w$ ).

2. Convert air–brine capillary pressure for samples 1B, 2B, 3B, and 4B to oil–brine capillary pressure data ( $p_c$  against  $S_w$ ).

3. Using capillary pressure data from air–mercury (Q1.), how many facies can be identified using the Leverett J-function.

4. Compare the oil–brine capillary pressure derived from sample 4A air–mercury (Q1.) with that derived from sample 4B air–brine (Q2.). What are the key difference between results?

Core properties and data from the air–mercury experiments are presented in Table 2.12 and Table 2.13, respectively.

**Table 2.12** Properties of Core Samples 1A, 2A, 3A, and 4A Used for Air–Mercury Capillary Measurements.

	Sample 1A	Sample 2A	Sample 3A	Sample 4A
$k_{Liq}$ (mD)	150	270	960	1400
$\phi$ (fraction)	0.24	0.25	0.26	0.2

**Table 2.13** Air–Mercury Capillary Measurements on Core Samples: 1A, 2A, 3A, and 4A Carried Out Under Laboratory Conditions.

Sample 1A		Sample 2A		Sample 3A		Sample 4A	
$P_{c(air-Hg)}$ (psi)	$S_{Hg}$	$P_{c(air-Hg)}$ (psi)	$S_{Hg}$	$P_{c(air-Hg)}$ (psi)	$S_{Hg}$	$P_{c(air-Hg)}$ (psi)	$S_{Hg}$
8.9	0.00	6.4	0.00	3.5	0.00	4.0	0.00
12	0.01	7.4	0.01	4.5	0.01	5.9	0.07
16	0.06	8.9	0.29	5.5	0.04	6.9	0.28
20	0.23	12	0.28	6.4	0.12	7.9	0.39
24	0.38	16	0.49	7.4	0.24	9.9	0.50
30	0.49	20	0.57	8.9	0.36	18	0.64
55	0.64	24	0.62	12	0.50	22	0.68
100	0.72	30	0.67	16	0.58	26	0.70
150	0.77	55	0.75	20	0.63	42	0.76
200	0.79	99	0.81	24	0.66	75	0.81
350	0.83	150	0.84	30	0.70	170	0.86
750	0.88	200	0.85	53	0.77	250	0.87
1,300	0.90	350	0.87	99	0.83	500	0.90
1,800	0.91	740	0.91	200	0.87	1,000	0.93
2,500	0.93	1,200	0.93	750	0.92	1,500	0.94
7,400	0.95	1,700	0.94	1,800	0.94	3,500	0.95
12,000	0.96	2,500	0.95	2,500	0.95	7,400	0.96
17,000	0.97	4,900	0.96	7,400	0.97	12,000	0.97
25,000	0.98	15,000	0.98	25,000	0.98	17,000	0.98
40,000	0.99	20,000	0.98	40,000	0.99	25,000	0.99
49,000	1.00	40,000	1.00	49,000	1.00	40,000	1.00

Core properties and data from the air–brine experiments are presented in Table 2.14 and Table 2.15, respectively.

**Table 2.14** Properties of Core Samples 1B, 2B, 3B, and 4B Used for Air–Brine Capillary Measurements.

	Sample 1B	Sample 2B	Sample 3B	Sample 4B
$k_{Liq}$ (mD)	290	1050	970	1400
$\phi$ (fraction)	0.24	0.27	0.24	0.27

**Table 2.15** Air–Brine Capillary Measurements on Core Samples: 1B, 2B, 3B, and 4B Carried Out at Reservoir Conditions.

$p_{c(air-brine)}$ (psi)	Sample 1B $S_w$	Sample 2B $S_w$	Sample 3B $S_w$	Sample 4B $S_w$
1	0.70	0.53	0.51	0.48
2	0.49	0.43	0.45	0.38
4	0.35	0.36	0.39	0.29
8	0.27	0.30	0.32	0.24
16	0.30	0.26	0.26	0.22
32	0.19	0.23	0.21	0.20
64	0.14	0.18	0.16	0.17

### Solution Steps.

*Step 1:* convert air–mercury capillary pressure to oil–brine capillary using equation (2.57). Note that the air–mercury capillary pressure was under laboratory conditions for equation (2.57) and also for this problem (solution to Question 1).

*Step 2:* convert air–brine capillary pressure to oil–brine capillary using equation (2.56) (solution to Question 2).

*Step 3:* convert air–mercury  $p_c$  from sample 1A, 2A, 3A, and 4A to  $J(S_w)$  using equation (2.58). Plot  $J(S_w)$  against  $S_w$  and determine the number of groups of  $J(S_w)$  from plot.

*Step 4:* plot oil–brine  $J(S_w)$  against  $S_w$  from sample 4A and sample 4B together (solution to Question 3).  $J(S_w)$  is an appropriate way to compare capillary pressure measurement.

### Solutions.

1. Using equation (2.57):

$$p_{c(oil-brine)} = 0.07017 p_{c(air-Hg)}$$

The calculated  $p_{c(oil-brine)}$  for samples 1A, 2A, 3A, and 4A are shown in Table 2.16 and presented graphically in Fig. 2.42.

2. The calculated  $p_{c(oil-brine)}$  for samples 1B, 2B, 3B, and 4B are shown in Table 2.17 and presented graphically in Fig. 2.43.

3.  $J(S_w)$  were calculated for sample 1A, 2A, 3A and 4A using equation (2.58) and are summarized in Table 2.18 and presented graphically in Fig. 2.44.

The  $J(S_w)$  against  $S_w$  trend for samples 1A, 2A, 3A, and 4A (Fig. 2.44) shows that the plot can be represented by a single trend. Hence, samples 1A, 2A, 3A, and 4A may be assumed to represent one rock type.

4. The differences between air–mercury and air–brine capillary pressure data are shown with annotations in Fig. 2.45.

## 2.5.6. Empirical Relationship for Capillary Pressure

Capillary pressure data may not be available for reservoir water distribution calculation. In the absence of laboratory measured capillary pressure data, empirical models can be used to predict capillary pressure data. *Hawkins et al.* [1993] gave the empirical  $p_c$  relationship as:

$$\text{Log} p_c = \frac{F_g}{\ln(1 - S_w)} + \log p_d \quad (2.59)$$

where

$$p_d = \frac{937.8}{k_a^{0.3406} \phi}$$

and

$$F_g = \frac{\left[ \ln \left( 5.21 k_a^{0.3406} / \phi \right) \right]^2}{2.303}$$

$k_a$  is air permeability (mD),  $p_c$  is mercury capillary pressure (psi),  $p_d$  is mercury displacement pressure,  $S_w$  is water saturation, and  $\phi$  is porosity (%).

## 2.5.7. Saturation Height Function Prediction in Reservoirs

The Leverett  $J$ -function trends identified from different rock types, characterized by *reservoir quality index* (Section 5.2.4.2), can be used to predict water saturation in the entire reservoir model. Equation (2.60), which relates  $S_w$  to  $J(S_w)$ , is used to determine model parameters  $a$ ,  $b$ , and  $S_{wi}$  for each rock type:

$$S_w = aJ^b + S_{wi} \quad (2.60)$$

**Table 2.16** Oil–Brine Capillary Pressure for Samples 1A, 2A, 3A, and 4A.

Sample 1A		Sample 2A		Sample 3A		Sample 4A	
$S_w = 1 - S_{Hg}$	$p_{c(oil-brine)}$ (psi)	$S_w = 1 - S_{Hg}$	$p_{c(oil-brine)}$ (psi)	$S_w = 1 - S_{Hg}$	$p_{c(oil-brine)}$ (psi)	$S_w = 1 - S_{Hg}$	$p_{c(oil-brine)}$ (psi)
1.00	0.62	1.00	0.45	1.00	0.25	1.00	0.28
0.99	0.84	0.99	0.52	0.99	0.32	0.93	0.41
0.94	1.12	0.71	0.62	0.96	0.39	0.72	0.48
0.77	1.40	0.72	0.84	0.88	0.45	0.61	0.55
0.62	1.68	0.51	1.12	0.76	0.52	0.50	0.69
0.51	2.11	0.43	1.40	0.64	0.62	0.36	1.26
0.36	3.86	0.38	1.68	0.50	0.84	0.32	1.54
0.28	7.02	0.33	2.11	0.42	1.12	0.30	1.82
0.23	10.53	0.25	3.86	0.37	1.40	0.24	2.95
0.21	14.03	0.19	6.95	0.34	1.68	0.19	5.26
0.17	24.56	0.16	10.53	0.30	2.11	0.14	11.93
0.12	52.63	0.15	14.03	0.23	3.72	0.13	17.54
0.10	91.22	0.13	24.56	0.17	6.95	0.10	35.09
0.09	126.31	0.09	51.93	0.13	14.03	0.07	70.17
0.07	175.43	0.07	84.20	0.08	52.63	0.06	105.26
0.05	519.26	0.06	119.29	0.06	126.31	0.05	245.60
0.04	842.04	0.05	175.43	0.05	175.43	0.04	519.26
0.03	1,192.89	0.04	343.83	0.03	519.26	0.03	842.04
0.02	1,754.25	0.02	1,052.55	0.02	1,754.25	0.02	1,192.89
0.01	2,806.80	0.02	1,403.40	0.01	2,806.80	0.01	1,754.25
0.00	3,438.33	0.00	2,806.80	0.00	3,438.33	0.00	2,806.80

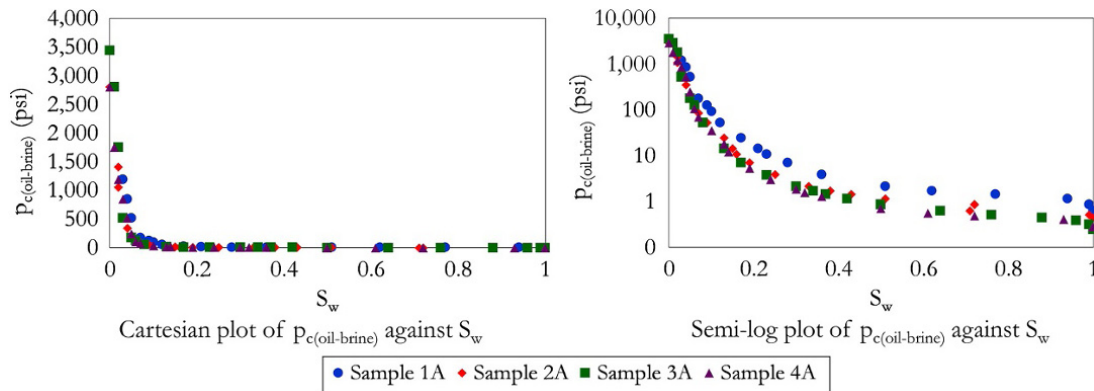


**Figure 2.42** Plot of  $p_{c(oil-brine)}$  against  $S_w$  for samples 1A, 2A, 3A, and 4A.

**Table 2.17** Oil–Brine Capillary Pressure for Samples 1B, 2B, 3B, and 4B.

	Sample 1B	Sample 2B	Sample 3B	Sample 4B
$p_{c(oil-brine)}$ (psi)	$S_w$	$S_w$	$S_w$	$S_w$
0.3039	0.70	0.53	0.51	0.48
0.6078	0.49	0.43	0.45	0.38
1.2156	0.35	0.36	0.39	0.29
2.4312	0.27	0.30	0.32	0.24
4.8624	0.30	0.26	0.26	0.22
9.7248	0.19	0.23	0.21	0.20
19.4496	0.14	0.18	0.16	0.17

$$P_{c(oil-brine)} = 0.3093 P_{c(air-brine)}$$

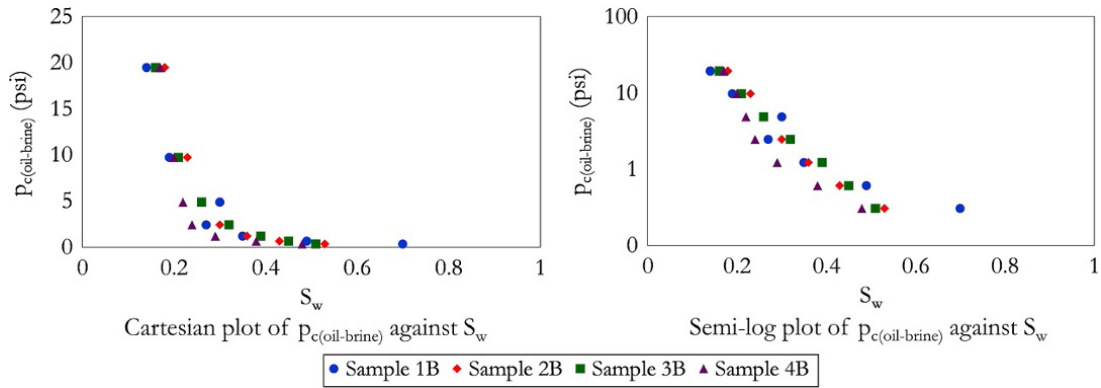


Figure 2.43 Plot of  $p_{c(oil-brine)}$  against  $S_w$  for samples 1B, 2B, 3B, and 4B.

Table 2.18  $J(S_w)$  for Samples 1A, 2A, 3A, and 4A.

Sample 1A		Sample 2A		Sample 3A		Sample 4A	
$S_w = 1 - S_{Hg}$	$J(S_w)$	$S_w = 1 - S_{Hg}$	$J(S_w)$	$S_w = 1 - S_{Hg}$	$J(S_w)$	$S_w = 1 - S_{Hg}$	$J(S_w)$
1.00	0.72	1.00	0.68	1.00	0.69	1.00	1.08
0.99	0.97	0.99	0.79	0.99	0.89	0.93	1.60
0.94	1.30	0.71	0.95	0.96	1.08	0.72	1.87
0.77	1.62	0.72	1.28	0.88	1.26	0.61	2.14
0.62	1.94	0.51	1.70	0.76	1.46	0.50	2.68
0.51	2.43	0.43	2.13	0.64	1.75	0.36	4.88
0.36	4.46	0.38	2.56	0.50	2.36	0.32	5.97
0.28	8.10	0.33	3.20	0.42	3.15	0.30	7.05
0.23	12.15	0.25	5.86	0.37	3.94	0.24	11.39
0.21	16.21	0.19	10.54	0.34	4.73	0.19	20.34
0.17	28.36	0.16	15.98	0.30	5.91	0.14	46.10
0.12	60.77	0.15	21.30	0.23	10.44	0.13	67.79
0.10	105.34	0.13	37.28	0.17	19.50	0.10	135.58
0.09	145.85	0.09	78.82	0.13	39.39	0.07	271.17
0.07	202.57	0.07	127.82	0.08	147.71	0.06	406.75
0.05	599.60	0.06	181.07	0.06	354.50	0.05	949.09
0.04	972.33	0.05	266.28	0.05	492.36	0.04	2,006.65
0.03	1,377.46	0.04	521.91	0.03	1,457.38	0.03	3,254.03
0.02	2,025.68	0.02	1,597.70	0.02	4,923.57	0.02	4,609.88
0.01	3,241.09	0.02	2,130.26	0.01	7,877.71	0.01	6,779.23
0.00	3,970.34	0.00	4,260.53	0.00	9,650.20	0.00	10,846.77

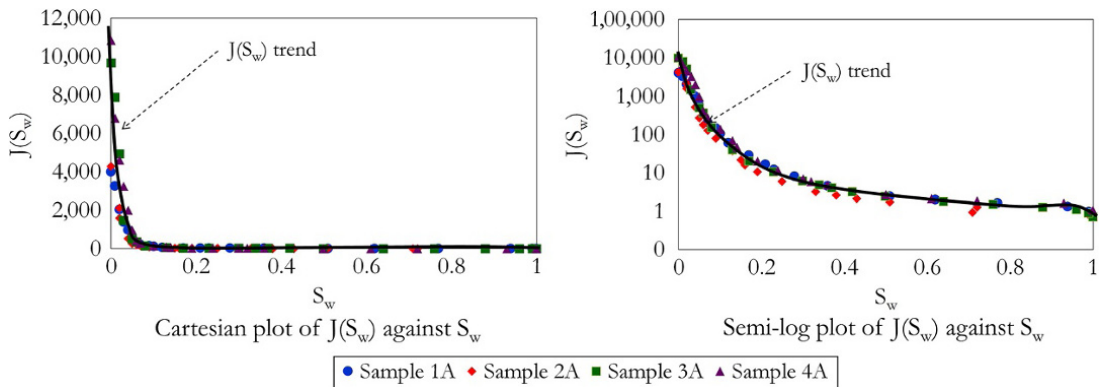


Figure 2.44 Plot of  $J(S_w)$  against  $S_w$  for samples 1A, 2A, 3A, and 4A.

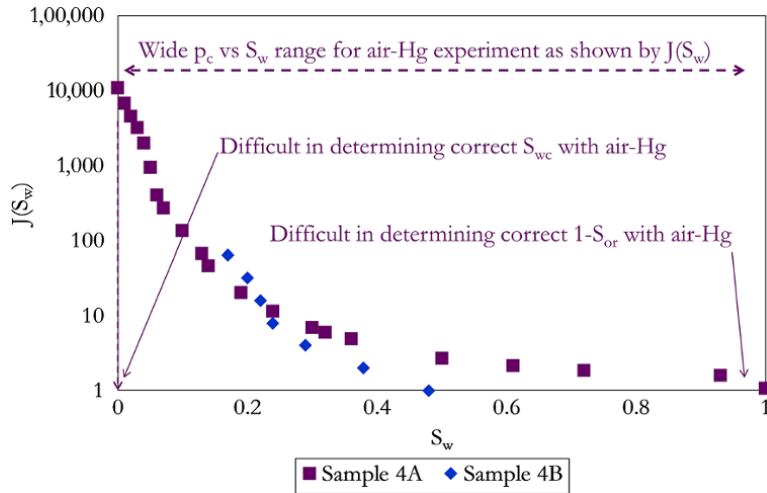


Figure 2.45 Comparison of  $J(S_w)$  from sample 4A and sample 4B.

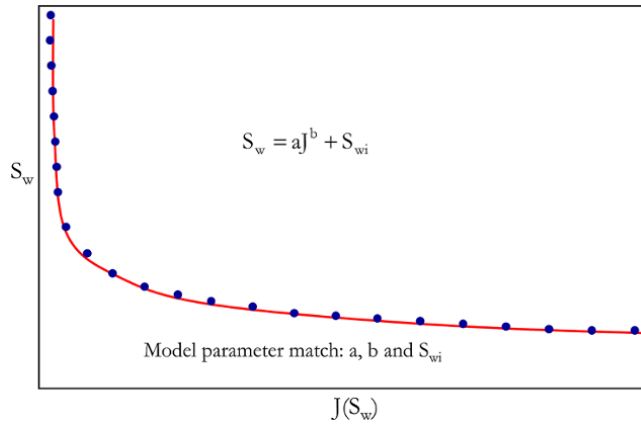


Figure 2.46  $S_w$  against  $J(S_w)$  for specific facie.

Fig. 2.46 shows a schematic of match of  $S_w$  against  $J(S_w)$  with model parameters  $a$ ,  $b$ , and  $S_{wi}$  for a given rock type.

Substituting  $J$  from equation (2.58),  $J(S_w) = \frac{p_c}{\sigma \cos \theta} \sqrt{\frac{k}{\phi}}$ , into equation (2.60):

$$S_w = a \left( \frac{p_c}{\sigma \cos \theta} \sqrt{\frac{k}{\phi}} \right)^b + S_{wi} \quad (2.61)$$

Then substituting  $p_c$  from equation (2.47),  $p_c = \frac{(\rho_w - \rho_{HC})h_w}{144}$ , into equation (2.61):

$$S_w = a \left( \frac{(\rho_w - \rho_{HC})h_w}{144 \sigma \cos \theta} \sqrt{\frac{k}{\phi}} \right)^b + S_{wi} \quad (2.62)$$

Equation (2.62) is a *saturation-height function*, which relates  $S_w$  and height above free water level ( $h_w$ ) for a given facie or rock type defined by model parameters  $a$ ,  $b$ ,  $S_{wi}$ , and  $\sqrt{\frac{k}{\phi}}$ .

## 2.6. RELATIVE PERMEABILITY

The relative permeability of a porous system is a concept used in relating the *absolute permeability* (when total pore volume is fully saturated with a single fluid) to the *effective permeability* (when the same fluid only occupies a fraction of the total pore volume) (Fig. 2.47). Effective permeability can be expressed as:

$$k_e = k \times k_r$$

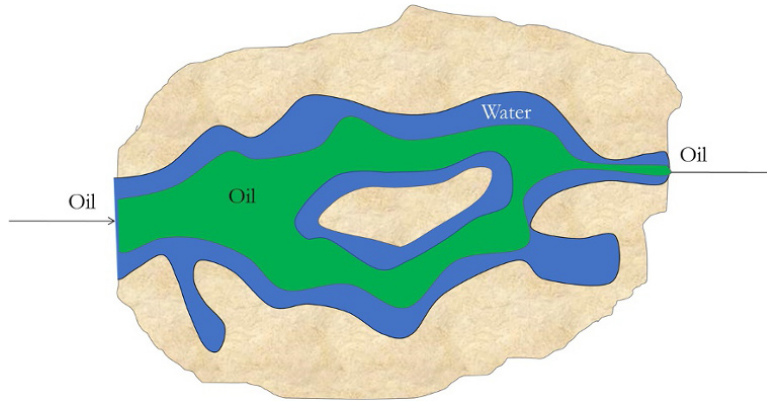


**Figure 2.47** Flow of oil in the presence of water.

Hence,

$$k_r = \frac{k_e}{k} \quad (2.63)$$

where  $k_e$  = effective permeability,  $k$  = absolute permeability, and  $k_r$  = relative permeability.

*Absolute permeability* is a porous media/rock property that is a characteristic of the rock to allow fluid flow through. It refers to the ability of the porous media/rock to conduct a fluid when its saturation is 100% of the pore space. *Effective permeability* is the ability of the porous material to conduct a fluid when its saturation is less than 100% of the pore space.

In water–oil systems, the base relative permeability is often taken as effective permeability to oil ( $k_o$ ) at irreducible water saturation ( $S_{wir}$ ), which is achieved at the end of oil desaturation of a brine saturated core. The general definition of relative permeability is, thus:

$$k_r = \frac{k_e}{k_o(S_{wir})} \quad (2.64)$$

In a water–oil system, the relative permeability of oil is hence defined as:

$$k_{ro} = \frac{k_{eo}}{k_o(S_{wir})} \quad (2.65)$$

and the relative permeability of water is:

$$k_{rw} = \frac{k_{ew}}{k_o(S_{wir})} \quad (2.66)$$

Since relative permeability is measured relative to  $k_o(S_{wir})$ ,  $k_{ro}$  at  $S_{wir}$  will be 1 because  $k_{eo}(S_w = S_{wir}) = k_o(S_{wir})$ .  $k_{rw}$  for all saturation will lie between 0 and 1.

The unsteady-state flooding method is the most common method for determining relative permeability in the laboratory. Steady-state flooding is used for the rate dependent relative permeability experiment.

Detailed analysis of flooding experiments to determine relative permeability model is provided in Chapter 14.2.1.6. Fig. 2.48 is a summary of the steps involved in a unsteady state water flood experiment to determine the oil–water relative permeability model.

In the gas–oil relative permeability model, base relative permeability is also taken as effective permeability to oil ( $k_o$ ) at irreducible water saturation ( $S_{wir}$ ), as such relative permeability of oil is defined as:

$$k_{ro} = \frac{k_{eo}}{k_o(S_{wir})} \quad (2.67)$$

and the relative permeability of gas is:

$$k_{rg} = \frac{k_{eg}}{k_o(S_{wir})} \quad (2.68)$$

Hence,  $k_{ro}$  at  $S_{wir}$  will be 1 while  $k_{rg}$  at  $S_{or}$  will lie between 0 and 1. In the case of the gas–oil relative permeability experiment, values of  $k_{rg}$  at  $S_{or}$  are always close to 1. Because of the dependence of  $S_{wir}$  on desaturating pressure, it is common to present oil–water relative permeability scaled to  $S_{wc}$  (also represented as  $S_{wi}$ ) instead of  $S_{wir}$ . It is, however, not uncommon to see the assumption that  $S_{wir}$  equals  $S_{wc}$ , as  $S_{wir}$  is water at the end of the laboratory drainage process, which may be similar to that at the end of the primary drainage process.

Fig. 2.49 and Fig. 2.50 show relative permeability models for water–oil and gas–oil systems, respectively.

Though during desaturation of the core sample with oil, the core is at  $S_{wir}$  and not  $S_{wc}$ , the relative permeability model can be refined or rescaled to  $S_{wc}$ . Also, in most core flood experiments  $S_w$  may not reach  $S_{wi}$ , hence the need to extrapolate data to  $S_{wir}$ . Porous plate capillary pressure measurement is a reliable approach to determining  $S_{wir}$ . It is advisable that high enough  $p_c$  pressures are applied to core samples to ensure asymptotic value of capillary pressure curves, from where  $S_{wir}$  can be determined.



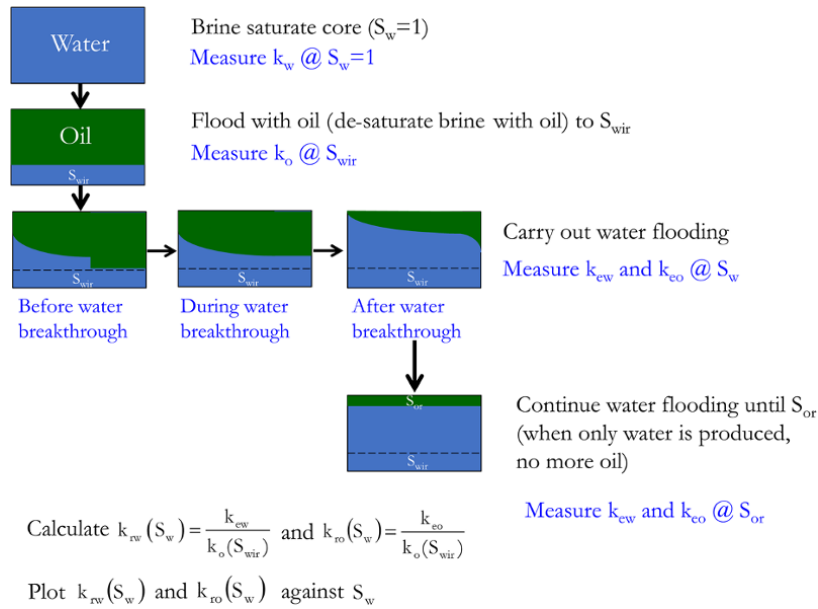


**Figure 2.48** Flow chart for the unsteady-state water flood experiment to determine oil–water relative permeability.

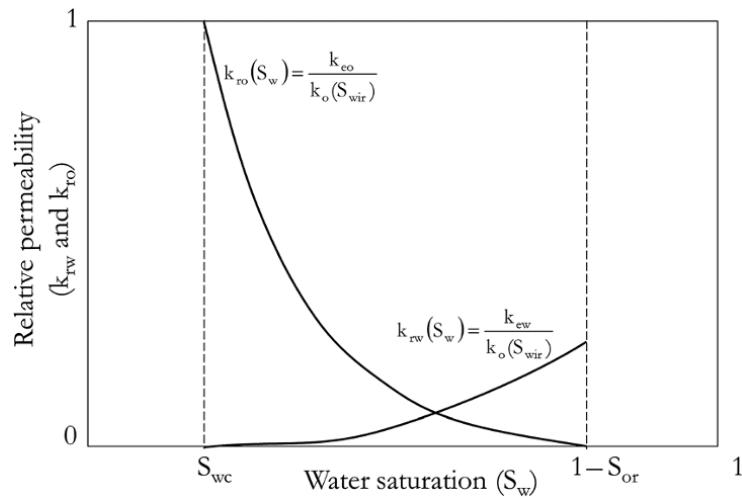


**Figure 2.49** Relative permeability model for the water–oil system.

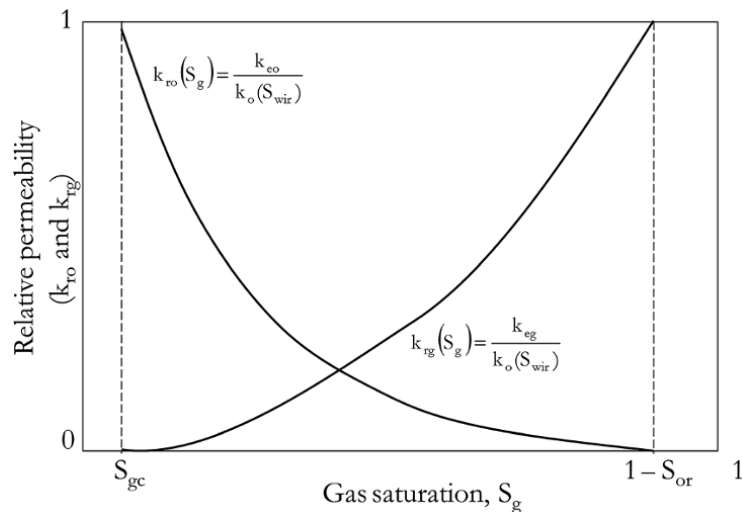


**Figure 2.50** Relative permeability model for the gas–oil system.

Relative permeability depends on rock type and is important in predicting reservoir recovery and performance. It may vary over the life of the field and from one part of the reservoir to another.

### 2.6.1. Relative Permeability Models

Relative permeability can be generally represented by the power law (equation) for three-phase flow:

for the oil phase

$$k_{ro} = k'_{ro} \left( \frac{S_o - S_{or}}{1 - S_{or} - S_{wc} - S_{gc}} \right)^{N_o} \quad (2.69)$$

for the water phase

$$k_{rw} = k'_{rw} \left( \frac{S_w - S_{wir}}{1 - S_{or} - S_{wc} - S_{gc}} \right)^{N_w} \quad (2.70)$$

for the gas phase

$$k_{rg} = k'_{rg} \left( \frac{S_g - S_{gc}}{1 - S_{or} - S_{wc} - S_{gc}} \right)^{N_g} \quad (2.71)$$

Due to difficulty in measuring three-phase relative permeability, they are often estimated from two-phase relative permeability measurements using correlations. Common two-phase relative permeability measurements include, for example water–oil relative permeability; gas–oil relative permeability, and water–gas relative permeability.

*Water–oil relative permeability model*

For the water–oil system

$$S_o = 1 - S_w; S_{gc} = 0;$$

also at  $S_w = S_{wir}$ ,  $k_{eo} = k_{eo}(S_w = S_{wir}) = k_o(S_{wir})$

hence, equation (2.65) becomes:

$$k'_{ro} = \frac{k_{eo}(S_w = S_{wir})}{k_o(S_{wir})} = 1$$

substituting  $S_o$ ,  $S_{gc}$ , and  $k'_{ro}$  from the above into equation (2.69), the relative permeability of oil relative to water can then be expressed as:

$$k_{ro} = \left( \frac{1 - S_w - S_{or}}{1 - S_{wc} - S_{or}} \right)^{N_o} \quad (2.72)$$

Also, substituting  $S_{gc} = 0$  into equation (2.70), the relative permeability of water relative to oil can then be expressed as:

$$k_{rw} = k'_{rw} \left( \frac{S_w - S_{wc}}{1 - S_{or} - S_{wc}} \right)^{N_w} \quad (2.73)$$

*Gas–oil relative permeability model*

for the gas–oil relative system,  $S_o = 1 - S_g - S_{wc}$  and  $k'_{ro} = 1$  and, hence, the relative permeability of oil relative to gas based on equation (2.69) becomes:

$$k_{ro} = \left( \frac{1 - S_g - S_{wc} - S_{or}}{1 - S_{or} - S_{wc} - S_{gc}} \right)^{N_o} \quad (2.74)$$

and based on equation (2.71), the relative permeability of gas relative to oil becomes:

$$k_{rg} = k'_{rg} \left( \frac{S_g - S_{gc}}{1 - S_{or} - S_{wc} - S_{gc}} \right)^{N_g} \quad (2.75)$$

Equations (2.69)–(2.75) are also referred to as modified *Brooks–Corey* relations or simply as *Corey* relations.

**2.6.1.1. Normalizing and Denormalizing Relative Permeability Models.** Different rock sample within the same reservoir/well may have different end-point relative permeability and end-point saturation due to varying rock–fluid properties. Also, when similar core samples are desaturated at different pressures they tend to show different  $S_{wir}$ . In order to average, compare or merge more than one relative permeability model, they have to be scaled within the same range. This is called normalizing and involves rescaling the relative permeability of each phase to range from 0 to 1, with corresponding saturation also ranging from 0 to 1.

Table 2.19 and Table 2.20 summarize the equations for normalizing and denormalizing water–oil and gas–oil relative permeability models, respectively.

**Table 2.19** Normalizing and Denormalizing the Water–Oil Relative Permeability Model.

Parameter	Normalizing	Denormalizing
$S_o$	$S_{on} = \left( \frac{1 - S_w - S_{or}}{1 - S_{wc} - S_{or}} \right)$	$S_o = S_{on}(1 - S_{wc} - S_{or}) + S_{or}$
$k_{ro}$	$k_{ron} = \frac{k_{ro}}{k'_{ro}}$	$k_{ro} = k_{ron} \times k'_{ro}$
$S_w$	$S_{wn} = \left( \frac{S_w - S_{wc}}{1 - S_{or} - S_{wc} - S_{gc}} \right)$	$S_w = S_{wn}(1 - S_{or} - S_{wc} - S_{gc}) + S_{wc}$
$k_{rw}$	$k_{rwn} = \frac{k_{rw}}{k'_{rw}}$	$k_{rw} = k_{rwn} \times k'_{rw}$

**Table 2.20** Normalizing and Denormalizing the Gas–Oil Relative Permeability Model.

Parameter	Normalizing	Denormalizing
$S_o$	$S_{on} = \left( \frac{1 - S_g - S_{wc} - S_{or}}{1 - S_{or} - S_{wc} - S_{gc}} \right)$	$S_o = S_{on}(1 - S_{or} - S_{wc} - S_{gc}) + S_{or}$
$k_{ro}$	$k_{ron} = \frac{k_{ro}}{k'_{ro}}$	$k_{ro} = k_{ron} \times k'_{ro}$
$S_g$	$S_{gn} = \left( \frac{S_g - S_{gc}}{1 - S_{or} - S_{wc} - S_{gc}} \right)$	$S_g = S_{gn}(1 - S_{or} - S_{wc} - S_{gc}) + S_{gc}$
$k_{rg}$	$k_{rgn} = \frac{k_{rg}}{k'_{rg}}$	$k_{rg} = k_{rgn} \times k'_{rg}$

### 2.6.1.2. Quality Control; Refining and Extrapolating Relative Permeability Data. Water–oil relative permeability data

Substituting  $S_{on}$  from Table 2.19 into equation (2.72), the relative permeability of oil relative to water phase can be expressed as

$$k_{ro} = S_{on}^{N_o}$$

therefore,

$$\log(k_{ro}) = N_o \log(S_{on}) \quad (2.76)$$

Hence,

$$N_o = \frac{\log(k_{ro})}{\log(S_{on})} \quad (2.77)$$

From equation (2.76),  $\log(k_{ro})$  against  $S_{on}$  on the log–log scale would yield a straight line for correct values of  $S_{wc}$  and  $S_{or}$ , and a slope corresponding to  $N_o$ .

Also from equation (2.77),  $\frac{\log(k_{ro})}{\log(S_{on})}$  against  $S_{on}$  plot would yield a straight line with a slope of zero and  $y$ -intercept equal to  $N_o$ .

Similarly, for the relative permeability of water relative to the oil phase, substituting  $S_{wn}$  from Table 2.19 into equation (2.73):

$$k_{rw} = k'_{rw} S_{wn}^{N_w}$$

Therefore,

$$\log(k_{rw}) = \log(k'_{rw}) + N_w \log(S_{wn}) \quad (2.78)$$

Hence,

$$N_w = \frac{\log(k_{rw}) - \log(k'_{rw})}{\log(S_{wn})} \quad (2.79)$$

From equation (2.78), plotting  $\log(k_{rw})$  against  $\log(S_{wn})$  would give an extrapolated value  $k_{rw}$  at  $S_{wn} = 1$  (which is  $S_w = 1 - S_{or}$ ) and a slope of  $N_w$  for correct values of  $S_{wc}$  and  $S_{or}$ .

**Table 2.21** Range of Values for Corey Parameters for the Water–Oil Relative Permeability Model.

Wettability	$N_o$	$N_w$	$k'_{rw}$	$S_{or}$
Water-wet	2–3	4–6	0.1–0.4	>0.3
Mixed Wettability	3–5	2–4	0.5–0.9	0.1–0.15
Strong oil-wet	6–8	1.5–3	0.8–1.0	<0.1

Also from equation (2.79),  $\frac{\log(k_{rw}) - \log(k'_{rw})}{\log(S_{wn})}$  against

$S_{wn}$  would yield a straight line with slope of zero and  $y$ -intercept of  $N_w$ .  $S_{or}$  in the  $k_{ro}$  and  $k_{rw}$  model should be the same. Table 2.21 gives range of values for water–oil relative permeability parameters.

### Factors that affect water–oil relative permeability measurement

Refinement of relative permeability data is very important due to factors that affect the accurate relative permeability measurement at a laboratory scale.

*Unstable flood:* this could be due to insufficient  $p_c$ , mixed wettability or fluid fingering through the core sample during experiment. An unstable flood front can cause high  $k_{rw}$  prediction. This problem can be mitigated by flooding at a low rate or using longer core samples.

*Capillary end effect:* this is caused by discontinuity in  $p_c$  when fluid flows across two media of different permeability (Fig. 2.51). This discontinuity causes retention of the wetting phase at the outlet of the core sample during water flood experiments (Fig. 2.51). It can cause relatively low values of  $k_{ro}$  and  $k_{rw}$  to be obtained from the experiment. Capillary end effect can be minimized by using long core sample and high velocity flood. Placing another core or permeable material at the core outflow to ensure effective capillary contact can be used to minimize capillary end effect (Fig. 2.52).

### Gas–oil relative permeability data

Similar to water–oil relative permeability, substituting  $S_{on}$  from Table 2.20 into equation (2.74)

$$k_{ro} = S_{on}^{N_o}$$

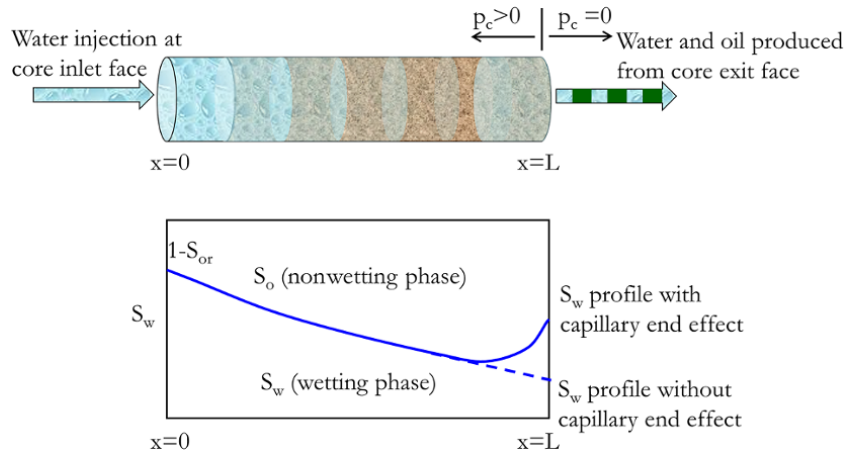


**Figure 2.51** Capillary pressure discontinuity causing capillary end effect.

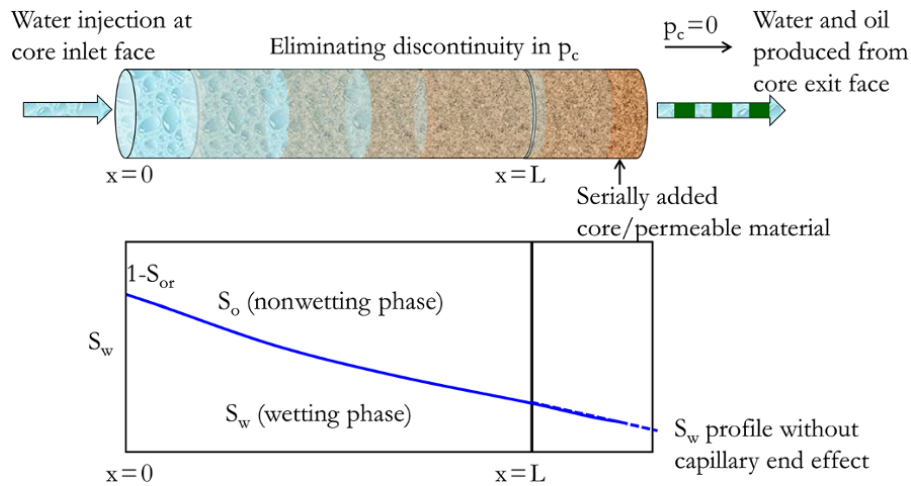


**Figure 2.52** Minimizing capillary end effect by adding core sample or permeable material at core outflow.

Hence,

$$\log(k_{ro}) = N_o \log(S_{on}) \Rightarrow N_o = \frac{\log(k_{ro})}{\log(S_{on})}$$

From the above,  $S_{or}$  and  $N_o$  that match  $\log(k_{ro})$  against  $S_{on}$  and  $\frac{\log(k_{ro})}{\log(S_{on})}$  against the  $S_{on}$  plot will be determined.

Similarly, for relative permeability of gas relative to oil

$$k_{rg} = k'_{rg} S_{gn}^{N_g}$$

$$\log(k_{rg}) = \log(k'_{rg}) + N_g \log(S_{gn})$$

Hence,

$$N_g = \frac{\log(k_{rg}) - \log(k'_{rg})}{\log(S_{gn})}$$

**Table 2.22** Range of Values for Corey Parameters for the Gas–Oil Relative Permeability Model.

Wettability	$N_o$	$N_g$	$k'_{rg}$	$S_{or}$
Oil is strongly wetting in presence of gas	4–7	1.3–2.5	$\approx 1$	$\approx 0$

From the above, plot  $\log(k_{rg})$  against  $\log(S_{gn})$  would give an extrapolated value of  $k'_{rg}$  at  $S_{gn} = 1$  (which is  $S_g = 1 - S_{or} - S_{wc}$ ) and the slope of  $N_g$  for correct values of  $S_{wc}$ ,  $S_{or}$ ,  $S_{gc}$ .

Also  $\frac{\log(k_{rg}) - \log(k'_{rg})}{\log(S_{gn})}$  against  $S_{gn}$  would yield a

straight line with slope of zero and y-intercept that is equal to  $N_g$ .  $S_{or}$  in the  $k_{ro}$  and  $k_{rg}$  model should be the same. Table 2.22 shows the range of values for gas–oil relative permeability parameters.

*Factors that affect gas–oil relative permeability measurement*

Gas fingering has been identified as the most important challenge associated with gas flooding and is caused by high flood rate. The quality check on gas–oil relative permeability is often not as challenging as on water–oil due to the strong wetting of oil in the presence of gas, with true  $S_{or} \approx 0$  and  $k'_{rg} \approx 1$ .

**Exercise 2.13** Refining Water–Oil Relative Permeability Data

An unsteady-state water flood experiment was carried out on a core sample to determine the water–oil relative permeability model that represents the core sample (Table 2.23).

Core details: permeability = 350 mD; porosity = 20%.

**Table 2.23** Relative Permeability for Exercise 2.13.

$S_w$	$k_{ro}$	$k_{rw}$
0.090	1.000	0.000
0.200	0.601	3.00E–04
0.250	0.463	9.00E–04
0.280	0.386	2.00E–03
0.300	0.345	2.80E–03
0.330	0.287	4.30E–03
0.340	0.260	5.00E–03
0.370	0.210	8.60E–03
0.390	0.179	1.26E–02
0.400	0.162	1.48E–02
0.430	0.110	2.34E–02
0.470	0.056	4.20E–02
0.500	0.023	5.97E–02
0.530	0.011	8.70E–02
0.550	1.1E–04	1.05E–01

An imbibition capillary pressure experiment carried out on the same sample gave  $S_{or} = 0.31$  and  $S_{wc} = 0.09$ .

Determine Corey parameters ( $S_{or}$ ,  $N_o$ ,  $k_{rw}$ , and  $N_w$ ) that best describe the water–oil relative permeability data.

Generate a refined relative permeability curve based on calculated Corey parameters and compare with experimental determined relative permeability curve.

**Solutions Steps.**

*Step 1:* normalize  $S_o$  using known values of  $S_{or}$  and  $S_{wc}$  or a guess value (if not given) for initial value prior to refinement (Table 2.24).

*Step 2:* plot both  $k_{ro}$  against  $S_{on}$  and  $\frac{\log(k_{ro})}{\log(S_{on})}$  against  $S_{on}$  on log-log scale (Fig. 2.53).

**Table 2.24**  $k_{ro}$  and  $N_o$  Against  $S_{on}$ .

$S_w$ (given)	$k_{ro}$ (given)	$S_{on}$ (using $S_{or} = 0.31$ )	$N_o = \log(k_{ro})/\log(S_{on})$	$k_{ro\_match}$ (using calculated $N_o$ of 2.5)
0.090	1.000	1.000		1.000
0.200	0.601	0.817	2.514	0.603
0.250	0.463	0.733	2.483	0.461
0.280	0.386	0.683	2.500	0.386
0.300	0.345	0.650	2.470	0.341
0.330	0.287	0.600	2.444	0.279
0.340	0.260	0.583	2.499	0.260
0.370	0.210	0.533	2.483	0.208
0.390	0.179	0.500	2.482	0.177
0.400	0.162	0.483	2.503	0.162
0.430	0.110	0.433	2.639	0.124
0.470	0.056	0.367	2.873	0.081
0.500	0.023	0.317	3.280	0.056
0.530	0.011	0.267	3.412	0.037
0.550	1.1E–04	0.233	6.263	0.026

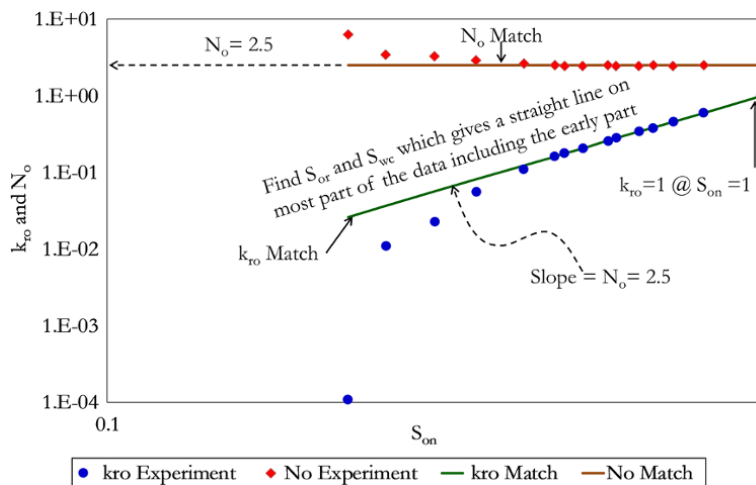


**Figure 2.53** Log-log plot of  $k_{ro}$  and  $N_o$  against  $S_{on}$ .

Step 3: verify that  $S_{or}$  and  $S_{wc}$  give a straight-line for  $k_{ro}$  against  $S_{on}$  on log-log scale (Fig. 2.53). If  $S_{or}$  and  $S_{wc}$  given do not give a straight-line for  $k_{ro}$  against  $S_{on}$ , they can be determined iteratively or using regression match.

Step 4: from  $\frac{\log(k_{ro})}{\log(S_{on})}$  against  $S_{on}$ , determine  $N_o$ , which is y-axis intercept of straight line with slope zero that match reliable parts of the  $\frac{\log(k_{ro})}{\log(S_{on})}$  series (Fig. 2.53).

Step 5: normalize  $S_w$  using given or calculated  $S_{or}$  and  $S_{wc}$  from step 3 (Table 2.25).

Step 6: plot  $k_{rw}$  against  $S_{wn}$  and  $\frac{\log(k_{rw}) - \log(k'_{rw})}{\log(S_{wn})}$  against  $S_{wn}$  on log-log plot (Fig. 2.54).

Step 7: confirm that the final values of  $S_{or}$  and  $S_{wc}$  from step 3 yield a straight line for  $k_{rw}$  against  $S_{wn}$  on a log-log scale (Fig. 2.54).

Step 8: find  $k'_{rw}$  by extrapolating  $k_{rw}$  against  $S_{wn}$  plot to  $S_{wn} = 1$  (Fig. 2.54).

Step 9: from  $\frac{\log(k_{rw}) - \log(k'_{rw})}{\log(S_{wn})}$  against  $S_{wn}$ , determine  $N_w$  which is the y-axis intercept of a straight line with slope zero that matches reliable part of the  $\frac{\log(k_{rw}) - \log(k'_{rw})}{\log(S_{wn})}$  series (Fig. 2.54).

Step 10: with determined  $N_o$ ,  $N_w$ ,  $k'_{rw}$ ,  $S_{or}$ , and  $S_{wc}$ , create a refined  $k_{rw}$  and  $k_{ro}$  using equation (2.72) and equation (2.73) between  $S_w = S_{wc}$  and  $S_w = 1 - S_{or}$ . Refined  $k_{ro}$  and  $k_{rw}$  are summarized in Table 2.26.

Step 11: display the refined relative permeability on a cartesian plot (Fig. 2.55) and semi-log plot (Fig. 2.56), and compare with the original laboratory relative permeability.

**Table 2.25**  $k_{rw}$  and  $N_w$  Against  $S_{wn}$ .

$S_w$ (given)	$k_{rw}$ (given)	$S_{wn}$ (using $S_{wc} = 0.09$ )	$N_w = [\log(k_{rw}) - \log(k'_{rw})] / \log(S_{wn})$	$k_{rw\_match}$ (using calculated $N_w$ of 5 and $k'_{rw}$ of 0.4)
0.090	0.000	0.000		0.00E+00
0.200	3.00E-04	0.183	4.241	8.28E-05
0.250	9.00E-04	0.267	4.613	5.39E-04
0.280	2.00E-03	0.317	4.608	1.27E-03
0.300	2.80E-03	0.350	4.726	2.10E-03
0.330	4.30E-03	0.400	4.947	4.10E-03
0.340	5.00E-03	0.417	5.005	5.02E-03
0.370	8.60E-03	0.467	5.038	8.85E-03
0.390	1.26E-02	0.500	4.989	1.25E-02
0.400	1.48E-02	0.517	4.993	1.47E-02
0.430	2.34E-02	0.567	4.998	2.34E-02
0.470	4.20E-02	0.633	4.934	4.08E-02
0.500	5.97E-02	0.683	4.995	5.96E-02
0.530	8.70E-02	0.733	4.919	8.48E-02
0.550	1.05E-01	0.767	5.034	1.06E-01

**Exercise 2.14** Refining Gas–Oil Relative Permeability Data

An unsteady-state gas flood experiment was carried out on a core sample to determine gas–oil relative permeability models that represent the core sample (Table 2.27).

Core details: permeability = 200 mD; porosity = 13%.

Imbibition capillary pressure carried out on the same sample gave  $S_{or} = 0.0$  and  $S_{wc} = 0.145$ .

Determine Corey parameters ( $S_{or}$ ,  $S_{gc}$ ,  $N_o$ ,  $k'_{rg}$ , and  $N_g$ ) that best describe the gas–oil relative permeability data.

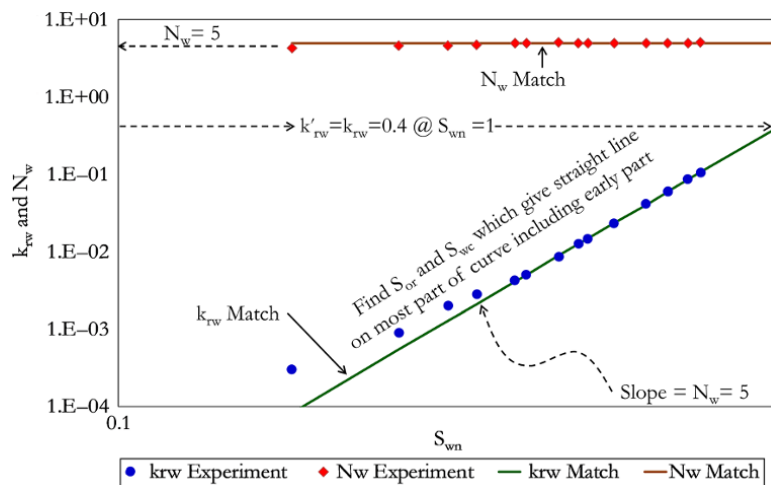


**Figure 2.54** Log-log plot of  $k_{rw}$  and  $N_w$  against  $S_{wn}$ .

**Table 2.26** Refined  $k_{ro}$  and  $k_{rw}$  Data.

	$S_w$	$k_{ro}$	$k_{rw}$
$S_{wc} \rightarrow$	0.090	1	0.000
	0.15	0.768433	4E-06
	0.20	0.602715	8.28E-05
	0.25	0.460525	0.000539
	0.30	0.34063	0.002101
	0.35	0.241724	0.006112
	0.40	0.162412	0.014727
	0.45	0.101193	0.031104
	0.50	0.056429	0.059597
	0.55	0.026299	0.105948
	0.60	0.008714	0.177482
	0.65	0.001148	0.283298
	$1 - S_{or} \rightarrow$	0.67	0.000203
0.68		3.59E-05	0.367759
0.69		8.23E-41	0.400000

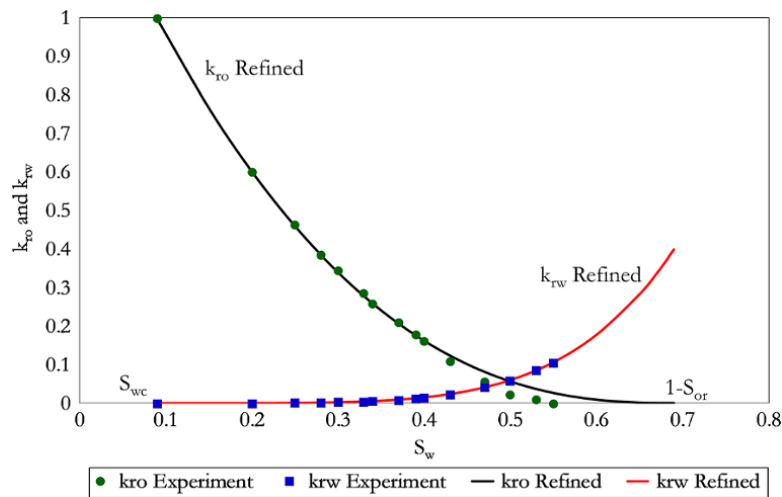


**Figure 2.55** Cartesian plot comparison of refined and experiment  $k_{rw}$  and  $k_{ro}$ .

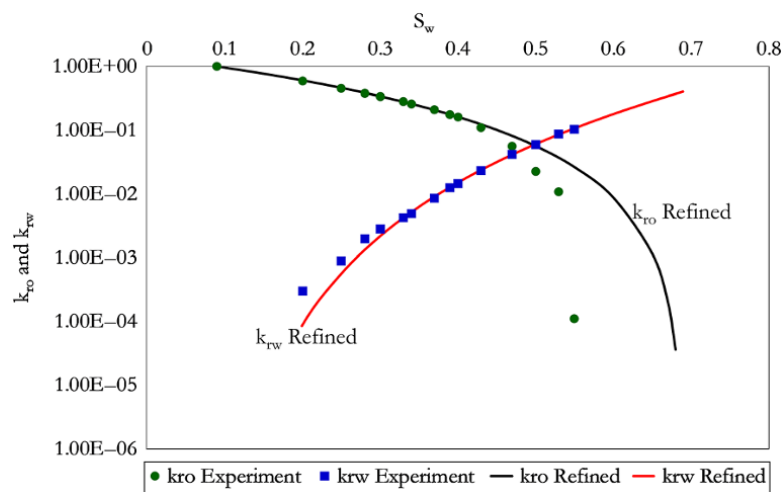


**Figure 2.56** Semi-log plot comparison of refined and experiment  $k_{rw}$  and  $k_{ro}$ .

Generate a refined relative permeability curve based on calculated Corey parameters and compare with experimental determined relative permeability curve.

Calculation of  $k_{ro}$  and  $N_o$  against  $S_{on}$  is summarized in Table 2.28 and a plot of  $k_{ro}$  and  $N_o$  against  $S_{on}$  shown in Fig. 2.57.

Calculation of  $k_{rg}$  and  $N_g$  against  $S_{gn}$  is summarized in Table 2.29 and the plot of  $k_{rg}$  and  $N_g$  against  $S_{gn}$  is shown in Fig. 2.58.

Calculated refined  $k_{rg}$  and  $k_{ro}$  are summarized in Table 2.30. The refined relative permeability Cartesian

plot and semi-log plot are shown in Fig. 2.59 and Fig. 2.60, respectively.

**Note:**  $k_{rg}$  can be plotted against  $S_g$  or against  $S_{wc} + S_g$ .

**Exercise 2.15** Comparing Relative Permeability Data

Water flood experiments were carried out on two core samples, from similar depth intervals from well 1 and well 2 (Fig. 2.61). Core samples 1 and 2 were desaturated at a different pressure differential, hence  $S_{wir}$  are different. Relative permeability was measured relative to  $k_o(S_{wir})$ .

Relative permeability data and model parameters for core samples 1 and 2 are provided in Tables 2.31–2.34.

Refined relative permeability for core sample 1 is shown in Table 2.31 and Corey parameters for core sample 1 are shown in Table 2.32. Refined relative permeability for core sample 2 is shown in Table 2.33 and Corey parameters for core sample 2 are shown in Table 2.34.

1. Compare the relative permeabilities from core 1 and core 2. Can they be considered to be fundamentally the same relative permeability model?

2. Assign the correct relative permeability model to reservoir regions in the reservoir model shown in Fig. 2.61.

Fig. 2.62 is a graphical presentation of the relative permeability models for core1 and core 2.

3. Rescale relative permeability model to  $S_{wc}$  (instead of  $S_{wir}$  from experiment),  $S_{or}$  and  $k_{ro}$  (provided in Tables 2.32 and 2.34); and true  $S_{or}$  (Fig. 2.61).

**Table 2.27** Laboratory Relative Permeability for Exercise 2.14.

$S_{liq}$	$k_{rg}$	$k_{ro}$
1.000	0.000	1.000
0.809	0.036	0.264
0.790	0.046	0.226
0.749	0.067	0.149
0.725	0.084	0.125
0.710	0.091	0.111
0.698	0.100	0.098
0.687	0.116	0.090
0.655	0.133	0.060
0.579	0.215	0.027
0.569	0.220	0.024
0.558	0.230	0.021
0.549	0.245	0.019
0.544	0.254	0.017
0.499	0.320	0.010
0.470	0.330	0.007

$S_{liq}$  is liquid saturation and defined as  $S_o + S_{wc}$

**Table 2.28**  $k_{ro}$  and  $N_o$  Against  $S_{on}$ .

$S_{liq}$ (given)	$k_{ro}$ (given)	$S_o = S_{liq} - S_{wc}$	$S_{wc} + S_g = 1 - S_o$	$S_g = (S_{wc} + S_g) - S_{wc}$	$S_{on}$ (using $S_{or} = 0$ and $S_{wc} = 0.145$ )	$N_o = \log(k_{ro}) / \log(S_{on})$	$k_{ro\_match}$ (using calculated $N_o$ of 5.3)
1.000	1.000	0.855	0.145	0.000	1.000		1.000
0.809	0.264	0.664	0.336	0.191	0.777	5.27	0.262
0.790	0.226	0.645	0.355	0.210	0.754	5.28	0.225
0.749	0.149	0.604	0.396	0.251	0.706	5.48	0.159
0.725	0.125	0.580	0.420	0.275	0.678	5.36	0.128
0.710	0.111	0.565	0.435	0.290	0.661	5.31	0.111
0.698	0.098	0.553	0.447	0.302	0.647	5.33	0.099
0.687	0.090	0.542	0.458	0.313	0.634	5.28	0.089
0.655	0.060	0.510	0.490	0.345	0.596	5.45	0.065
0.579	0.027	0.434	0.566	0.421	0.508	5.33	0.027
0.569	0.024	0.424	0.576	0.431	0.496	5.30	0.024
0.558	0.021	0.413	0.587	0.442	0.483	5.31	0.021
0.549	0.019	0.404	0.596	0.451	0.473	5.29	0.019
0.544	0.017	0.399	0.601	0.456	0.467	5.35	0.018
0.499	0.010	0.354	0.646	0.501	0.414	5.22	0.009
0.470	0.007	0.325	0.675	0.530	0.380	5.13	0.006



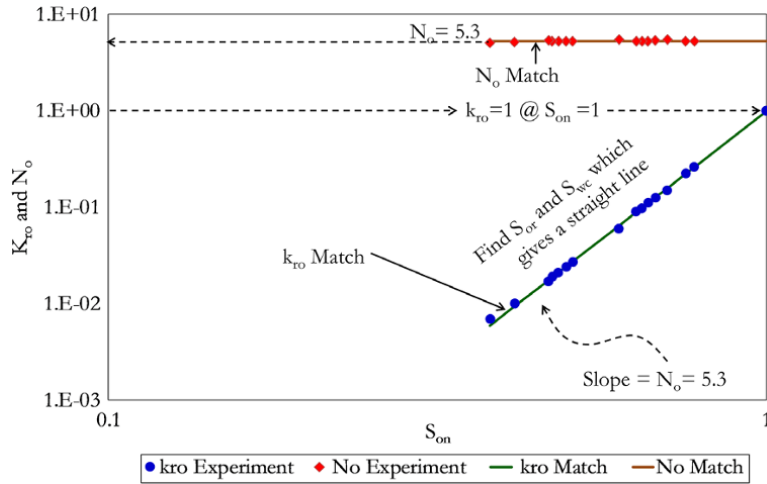


Figure 2.57 Log-log plot of  $k_{ro}$  and  $N_o$  against  $S_{on}$ .

Table 2.29  $k_{rg}$  and  $N_g$  Against  $S_{gn}$ .

$S_g = (S_{wc} + S_g) - S_{wc}$	$k_{rg}$ (given)	$S_{gn}$ (using $S_{gc} = 0, S_{or} = 0, S_{wc} = 0.145$ )	$N_g = [\log(k_{rg}) - \log(k'_{rg})] / \log(S_{gn})$	$k_{rg\_match}$ (using calculated $k'_{rg}$ of 1 and $N_g$ of 2.2)
0.000	0.000	0		0.000
0.191	0.036	0.22	2.22	0.037
0.210	0.046	0.25	2.20	0.046
0.251	0.067	0.29	2.21	0.067
0.275	0.084	0.32	2.18	0.082
0.290	0.091	0.34	2.22	0.093
0.302	0.100	0.35	2.21	0.101
0.313	0.116	0.37	2.14	0.110
0.345	0.133	0.40	2.22	0.136
0.421	0.215	0.49	2.17	0.210
0.431	0.220	0.50	2.21	0.222
0.442	0.230	0.52	2.23	0.234
0.451	0.245	0.53	2.20	0.245
0.456	0.254	0.53	2.18	0.251
0.501	0.320	0.59	2.13	0.309
0.530	0.330	0.62	2.32	0.349

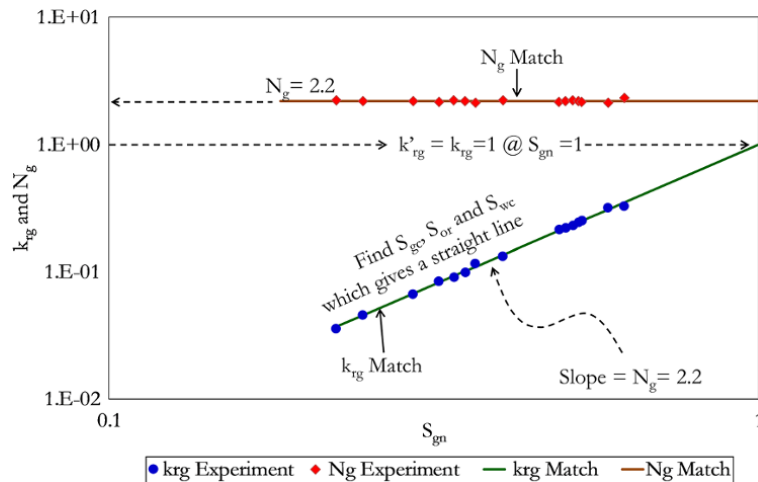


Figure 2.58 Log-log plot of  $k_{rg}$  and  $N_g$  against  $S_{gn}$ .

**Table 2.30** Refined  $k_{rg}$  and  $k_{ro}$  Data.

	$S_g$	$S_{wc} + S_g$	$k_{rg}$	$k_{ro}$
$S_{gc}$	0	0.145	0	1.00000
	0.015	0.16	0.000137	0.910458
	0.02	0.165	0.000258	0.882100
	0.05	0.195	0.001938	0.726604
	0.08	0.225	0.005451	0.594126
	0.11	0.255	0.010983	0.481956
	0.14	0.285	0.018671	0.387616
	0.17	0.315	0.02862	0.308844
	0.20	0.345	0.04092	0.243589
	0.23	0.375	0.055651	0.189996
	0.26	0.405	0.072881	0.146393
	0.29	0.435	0.092672	0.111285
	0.32	0.465	0.115081	0.08334
	0.35	0.495	0.14016	0.06138
	0.38	0.525	0.167957	0.044367
0.41	0.555	0.198518	0.031397	
0.50	0.645	0.307191	0.00948	
0.60	0.745	0.458783	0.001642	
0.70	0.845	0.644006	0.000117	
$1-S_{wc}-S_{or}-S_{gc} \rightarrow$	0.855	1	1	4.08E-88

**Solution Steps.**

*Step 1:* normalize relative permeability models separately, as shown in Table 2.35 for core sample 1 and Table 2.36 for core sample 2.

*Step 2:* compare relative permeability plot by overlaying normalized relative permeability data of core sample 1 and core sample 2 on the Cartesian and semi-log plot, as shown in Fig. 2.63 and Fig. 2.64 respectively.

*Step 3:* decide if the relative permeability model is the same. Also, examine rock type functions that are generally dependent on  $k$  and  $\phi$ . *Reservoir quality index*

(RQI) is defined as  $\left[0.0314\sqrt{\frac{k}{\phi}}\right]$  (Section 5.2.4.2, equation 5.124) and is a common function that is often used to group rock types. Relative permeability is dependent on pore throat size and rock type:

$$\left(0.0314\sqrt{\frac{k}{\phi}}\right)_{\text{Region 1}} = 0.0314\sqrt{\frac{250}{0.23}} = 1.04$$

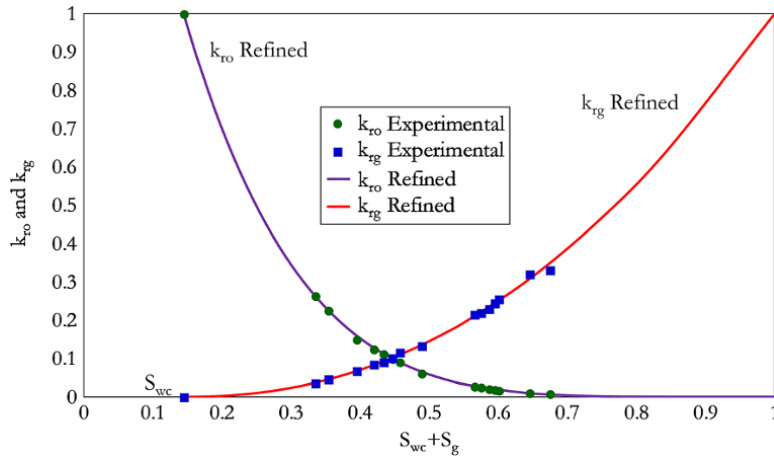


**Figure 2.59** Cartesian plot comparison of refined and experimental  $k_{rg}$  and  $k_{ro}$ .

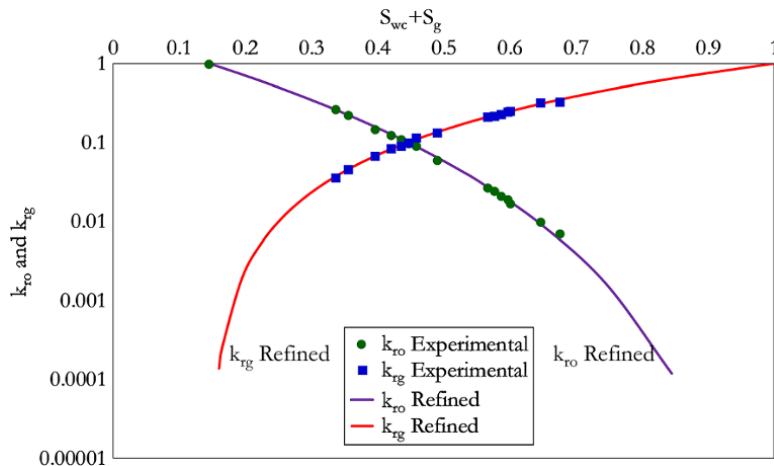


**Figure 2.60** Semi-log plot comparison of refined and experimental  $k_{rg}$  and  $k_{ro}$ .

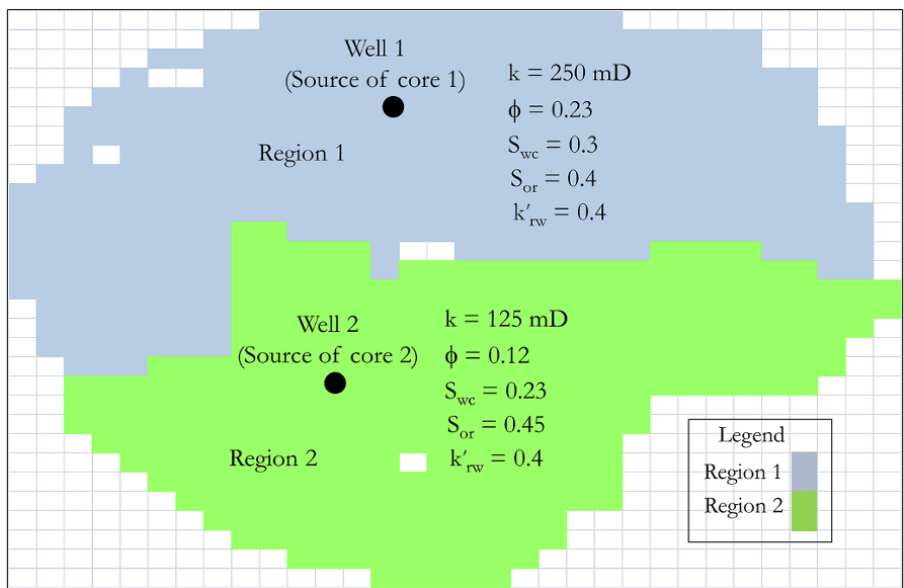


Figure 2.61 Reservoir model showing well location and key regional properties.

Table 2.31 Refined Relative Permeability for Core Sample 1.

$S_w$	$k_{ro}$	$k_{rw}$
0.20	1.000	0.00E+00
0.25	0.810	6.32E-06
0.30	0.640	1.43E-04
0.35	0.490	8.87E-04
0.40	0.360	3.24E-03
0.45	0.250	8.84E-03
0.50	0.160	2.01E-02
0.55	0.090	4.02E-02
0.60	0.040	7.33E-02
0.65	0.010	1.24E-01
0.70	0.000	2.00E-01

Table 2.32 Corey Parameters for Core Sample 1.

$S_{or}$	$k_{ro}$ at $S_{wir}$	$N_o$	$S_{wc}$	$k_{rw}$ at $S_{oc}$	$N_w$
0.3	1	2	0.2	0.2	4.5

$$\left(0.0314 \sqrt{\frac{k}{\phi}}\right)_{\text{Region 2}} = 0.0314 \sqrt{\frac{125}{0.12}} = 1.01$$

Core sample 1 and 2 may be considered to be from the same rock type and relative permeability considered fundamentally the same.

Step 4: denormalize the relative permeability with  $S_{wc}$ ,  $S_{or}$ , and  $k'_{rw}$  from each region. Values of  $S_{wc}$ ,  $S_{or}$ , and

Table 2.33 Refined Relative Permeability for Core Sample 2.

$S_w$	$k_{ro}$	$k_{rw}$
0.150	1.000	0.00E+00
0.200	0.810	9.49E-06
0.225	0.723	5.88E-05
0.250	0.640	2.15E-04
0.275	0.563	5.86E-04
0.300	0.490	1.33E-03
0.325	0.423	2.66E-03
0.350	0.360	4.86E-03
0.375	0.303	8.25E-03
0.400	0.250	1.33E-02
0.425	0.203	2.04E-02
0.450	0.160	3.01E-02
0.475	0.123	4.32E-02
0.500	0.090	6.03E-02
0.525	0.062	8.22E-02
0.550	0.040	1.10E-01
0.575	0.022	1.44E-01
0.600	0.010	1.87E-01
0.650	0.000	3.00E-01

Table 2.34 Corey Parameters for Core Sample 2.

$S_{or}$	$k_{ro}$ at $S_{wir}$	$N_o$	$S_{wc}$	$k_{rw}$ at $S_{oc}$	$N_w$
0.35	1	2	0.15	0.3	4.5

$k'_{rw}$  are shown in Fig. 2.61. Table 2.37 for denormalized relative permeability with region 1 properties and in Table 2.38 for denormalized relative permeability with region 2 properties.

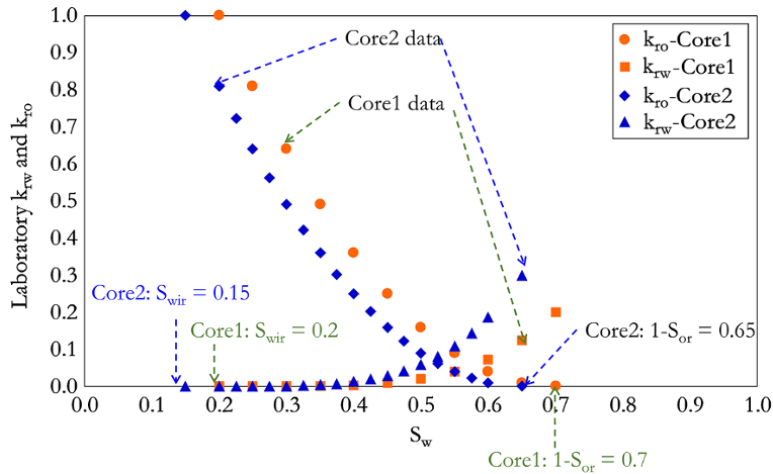


**Figure 2.62** Relative permeability models for core samples 1 and 2.

**Table 2.35** Normalized Relative Permeability for Core Sample 1.

$S_{wn}$	$k_{ron}$	$k_{rwn}$
0.00	1.00	0.00E+00
0.10	0.81	3.16E-05
0.20	0.64	7.16E-04
0.30	0.49	4.44E-03
0.40	0.36	1.62E-02
0.50	0.25	4.42E-02
0.60	0.16	1.00E-01
0.70	0.09	2.01E-01
0.80	0.04	3.66E-01
0.90	0.01	6.22E-01
1.00	0.00	1.00E+00

**Table 2.36** Normalized Relative Permeability for Core Sample 2.

$S_{wn}$	$k_{ron}$	$k_{rwn}$
0.00	1.00	0.00E+00
0.10	0.81	3.16E-05
0.15	0.72	1.96E-04
0.20	0.64	7.16E-04
0.25	0.56	1.95E-03
0.30	0.49	4.44E-03
0.35	0.42	8.88E-03
0.40	0.36	1.62E-02
0.45	0.30	2.75E-02
0.50	0.25	4.42E-02
0.55	0.20	6.79E-02
0.60	0.16	1.00E-01
0.65	0.12	1.44E-01
0.70	0.09	2.01E-01
0.75	0.06	2.74E-01
0.80	0.04	3.66E-01
0.85	0.02	4.81E-01
1.00	0.00	1.00E+00

### 2.6.2. Three-phase Relative Permeability

Three-phase relative permeability depends on saturation of all phases (oil, water, and gas) and is often derived from two-phase relative permeability models because it is experimentally difficult to set up three-phase relative permeability experiments. Some of the three-phase derivation methods from two-phase relative permeability include: *Stone I model* [Stone, 1970]; *Stone II model* [Stone, 1973]; and *saturated-weighted interpolation* [Baker, 1988; Martin, 2000].

#### *Stone I model*

The Stone I model assumes that water and gas impair flow of oil; hence, this impairment is computed from the two-phase relative permeabilities. The Stone I concept is that water and gas relative permeabilities are functions only of their own saturations. Impairment

of oil flow in the presence of water and gas can be expressed as [Stone, 1970]:

$$k_{ro} = \frac{S_{oe} k_{ro}(S_w) k_{ro}(S_g)}{k_{ro}(S_{wc})(1-S_{we})(1-S_{ge})} \quad (2.80)$$

where

$$S_{oe} = \frac{S_o - S_{om}}{1 - S_{wc} - S_{om}} \text{ and } S_{om} = \lambda S_{orw} + (1 - \lambda) S_{org}$$

$$S_{we} = \frac{S_w - S_{wc}}{1 - S_{wc} - S_{om}} \text{ and } \lambda = 1 - \frac{S_g}{1 - S_{wc} - S_{org}}$$

$$S_{ge} = \frac{S_g}{1 - S_{wc} - S_{om}}$$

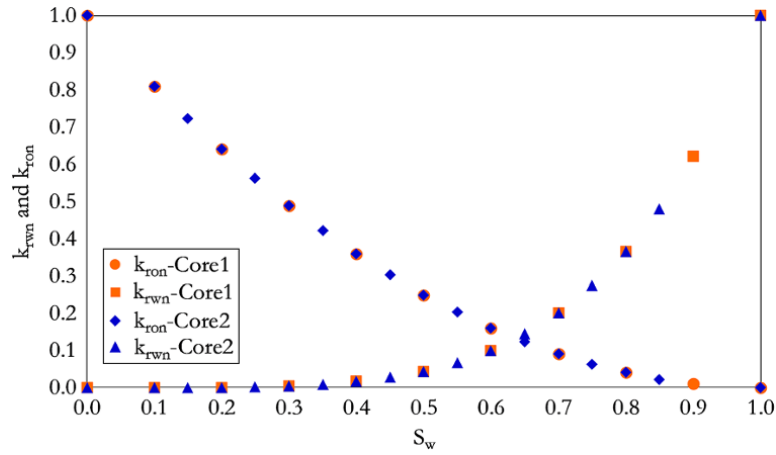


Figure 2.63 Combined normalized relative permeability from Core 1 and Core 2 on Cartesian scale.

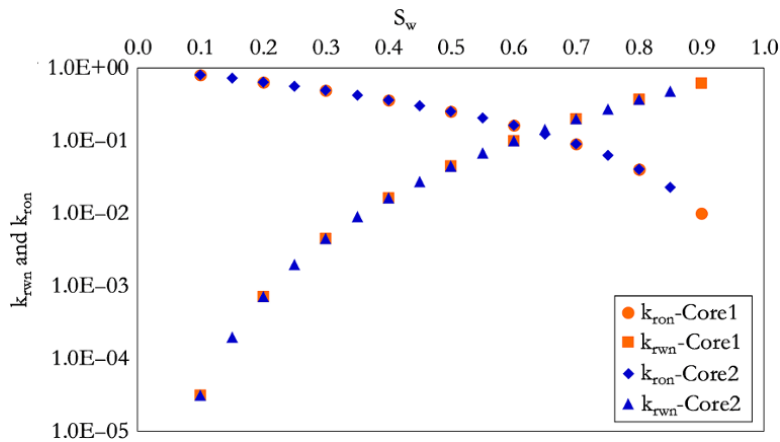


Figure 2.64 Combined normalized relative permeability from Core 1 and Core 2 on semi-log scale.

Table 2.37 Denormalized Relative Permeability with Region 1 Properties.

$S_w = S_{wn} \times (1 - S_{wc} - S_{or}) + S_{wc}$	$k_{ro} = 1 \times k_{ron}$	$k_{rw} = k_{rwn} \times k'_{rwn}$
0.30	1.00	0.00E+00
0.33	0.81	1.26E-05
0.36	0.64	2.86E-04
0.39	0.49	1.77E-03
0.42	0.36	6.48E-03
0.45	0.25	1.77E-02
0.48	0.16	4.02E-02
0.51	0.09	8.04E-02
0.54	0.04	1.47E-01
0.57	0.01	2.49E-01
0.60	0.00	4.00E-01

Table 2.38 Denormalized Relative Permeability with Region 2 Properties.

$S_w = S_{wn} \times (1 - S_{wc} - S_{or}) + S_{wc}$	$k_{ro} = 1 \times k_{ron}$	$k_{rw} = k_{rwn} \times k'_{rwn}$
0.23	1.00	0.00E+00
0.26	0.81	1.26E-05
0.28	0.72	7.84E-05
0.29	0.64	2.86E-04
0.31	0.56	7.81E-04
0.33	0.49	1.77E-03
0.34	0.42	3.55E-03
0.36	0.36	6.48E-03
0.37	0.30	1.10E-02
0.39	0.25	1.77E-02
0.41	0.20	2.71E-02
0.42	0.16	4.02E-02
0.44	0.12	5.76E-02
0.45	0.09	8.04E-02
0.47	0.06	1.10E-01
0.49	0.04	1.47E-01
0.50	0.02	1.93E-01
0.55	0.00	4.00E-01

- $S_{orw}$  = residual oil saturation from the oil-water relative permeability model
- $S_{org}$  = residual oil saturation from the gas-oil relative permeability model
- $S_{om}$  = minimum oil saturation

*Stone II Model*

This three-phase relative permeability model is based on the assumption of segregated phase flow and expressed as [Stone, 1973]:

$$k_{ro} = k_{row}(S_{wc}) \left( \left( \frac{k_{row}}{k_{row}(S_{wc})} + k_{rwo} \right) \left( \frac{k_{rog}}{k_{ro}(S_{wc})} + k_{rgo} \right) - k_{rwo} - k_{rgo} \right), (Stone, 1973) \tag{2.81}$$

where

- $k_{row}$  = oil relative permeability in the two-phase oil-water relative permeability model
- $k_{rog}$  = oil relative permeability in the two-phase gas-oil relative permeability model
- $k_{rwo}$  = water relative permeability in the two-phase oil-water relative permeability model
- $k_{rgo}$  = gas relative permeability in the two-phase gas-oil relative permeability model

The Stone II model as shown above does not require a residual oil saturation to be defined.

*Saturated-weighted interpolation*

This is based on saturation-weighted interpolation between the two-phase values to find the three-phase oil relative permeability and can be expressed as [Baker, 1988]:

$$k_{ro} = \frac{k_{ro}(S_w)(S_w - S_{wc}) + k_{ro}(S_g)(S_g - S_{gr})}{(S_w - S_{wc}) + (S_g - S_{gr})} \tag{2.82}$$

where

- $S_{gr}$  = residual gas saturation

**Exercise 2.16** Three-Phase Relative Permeability Calculation

Given the two-phase relative permeability models below, determine and present a plot of three-phase relative permeability on a ternary diagram using any of the three-phase relative permeability models.

Two-phase water–oil relative permeability

$$k_{rw}(S_w) = 0.3 \left( \frac{S_w - 0.17}{1 - 0.17 - 0.1} \right)^5 \text{ and } k_{ro}(S_w) = 1 \left( \frac{S_w - 0.1}{1 - 0.17 - 0.1} \right)^{2.5}$$

Two-phase gas–oil relative permeability

$$k_{rg}(S_g) = 0.3 \left( \frac{S_g}{1 - 0.47} \right)^{2.1} \text{ and } k_{ro}(S_g) = 1 \left( \frac{S_g - 0.47}{1 - 0.47} \right)^{3.2}$$

**Solution Steps.**

*Step 1:* make a table of  $S_w$ ,  $S_g$ , and  $S_o$  with  $S_w$  starting from  $S_{wc}$  (0.17) while ensuring  $S_w + S_g + S_o = 1$  (Table 2.39).

*Step 2:* compute three-phase  $k_{ro}$  with any of the methods (Stone II model was used for this exercise) as shown in Table 2.39.

*Step 3:* plot  $k_{ro}$  against  $S_w$ ,  $S_g$ , and  $S_o$  on a ternary diagram (Fig. 2.65). The ternary plot and diagram are discussed in Chapter 14.3.1.1.

**Table 2.39**  $k_{ro\_three\_phase}$  Determination Using the Stone II Method.

$S_w$	$S_g$	$S_o$	$k_{ro\_three\_phase}$
0.170	0.000	0.830	1.000
0.316	0.000	0.684	0.572
0.462	0.000	0.538	0.279
0.608	0.000	0.392	0.101
0.754	0.000	0.246	0.018
0.900	0.000	0.100	0.000
0.170	0.106	0.724	0.490
0.316	0.106	0.578	0.276
0.462	0.106	0.432	0.128
0.608	0.106	0.286	0.029
0.170	0.212	0.618	0.195
0.316	0.212	0.472	0.093
0.462	0.212	0.326	0.020
0.170	0.318	0.512	0.053
0.170	0.424	0.406	0.006

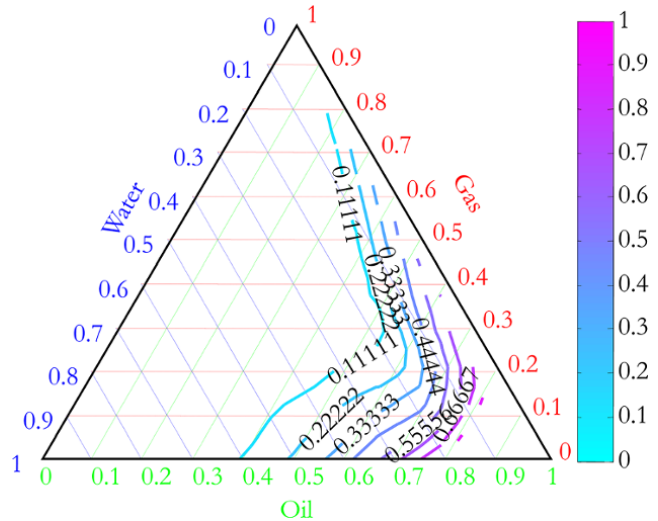


**Figure 2.65** Three-phase relative permeability represented on a ternary diagram.

**Solution.**

Using equation (2.81),  $k_{ro\_three\_phase}$  was determined. Plot  $k_{ro}$  against  $S_w$ ,  $S_g$ , and  $S_o$  as shown in Fig. 2.65.

**REFERENCES**

- Amott, E., 1959. Observations relating to the wettability of porous rock. *Petroleum Transactions, AIME*, **216**, 156–162.
- Anderson, W., 1986. Wettability literature survey – Part 1: rock/oil/brine interactions and the effects of core handling on wettability. *Journal of Petroleum Technology*, **38**(10), 1125–1144.
- Anderson, W., 1986. Wettability literature survey – Part 2: wettability measurement. *Journal of Petroleum Technology*, **38**(11), 1246–1262.
- Baker, L.E., 1988. Three-Phase Relative Permeability Correlations. *Proceedings of the SPE/DOE Symposium on Enhanced Oil Recovery*, Tulsa, SPE 17369.
- Craig, F., 1971. *The Reservoir Engineering Aspects of Waterflooding*, Monograph Series, SPE. Society of Petroleum Engineers, AIME, Volume 3, pp. 12–44.
- Dong, J., Hsu, J.-Y., Wu, W.-J., et al., 2010. Stress-dependence of the permeability and porosity of sandstone and shale from TCDP Hole-A. *International Journal of Rock Mechanics and Mining Sciences*, **47**(7), 1141–1157.
- Hawkins, J., Luffel, D., and Harris, T., 1993. Capillary pressure model predicts distance to gas/water, oil/water contact. *Oil and Gas Journal*, **91**(3), 39–43.
- Hubbert, M., 1956. Darcy's Law and the field equation of the flow of underground fluids. *Transactions AIME*, **207**, 222–239.
- Martin, J., 2000. An empirical model for three-phase relative permeability. *SPE Journal*, **5**(04), 435–445.
- Stone, H.L., 1970. Probability model for estimating three-phase relative permeability. *Journal of Petroleum Technology*, **22**(02), 214–218.
- Stone, H.L., 1973. Estimation of three-phase relative permeability and residual oil data. *Journal of Canadian Petroleum Technology*, **12**(04), 53–61.
- American Petroleum Institute, 1960. *API Recommended Practice for Core-Analysis Procedure*, Dallas, TX: American Petroleum Institute, Division of Production.
- Amyx, J.M., Bass, D.M., and Whiting, R., 1960. *Petroleum Reservoir Engineering-Physical Properties*. New York: McGraw-Hill Book Co.
- Batycky, J., McCaffery, F., Hodgins, P., and Fisher, D., 1981. Interpreting Relative Permeability and Wettability From Unsteady-State Displacement Measurements. *SPEJ*, pp. 296–308.
- Brooks, R. and Corey, A., 1964. Hydraulic properties of porous media. *Hydrology Papers*, Colorado State University, Fort Collins, CO, Volume 3, pp. 22–27.
- Chilingar, G., Buryakovskiy, L., Eremenko, N., and Gorfunkel, M., 2005. *Geology and Geochemistry of Oil and Gas*. 1st edn. Oxford: Elsevier Inc.
- Corey, A., 1954. The interrelation between gas and oil relative permeabilities. *Producers Monthly*, **19**, 38–41.
- Edmister, W.C., 1958. Applied hydrocarbon thermodynamic, Part 4: Compressibility. *Petroleum Refiner*, **37**, 173–179.
- Geertsma, J., 1974. Estimating the coefficient of inertial resistance in fluid flow through porous media. *Society of Petroleum Engineers Journal*, **14**(5), 445–450.
- Hassler, G. and Brunner, E., 1945. Measurement of capillary pressures in small core samples. *Transactions of the AIME*, **160**(1), 114–123.
- Hyne, N., 2012. *Nontechnical Guide to Petroleum Geology, Exploration, Drilling and Production*. 3 edn. Tulsa, OK: Penn-Well Corp.
- Klinkenberg, L.J., 1941. The permeability of porous media to liquids and gases. *American Petroleum Institute Drilling and Production Practice*, pp. 200–213.
- Leverett, M., 1941. Capillary behavior in porous solids. *AIME*, **142**(1), 152–169.
- Manager, G., 1966. *Method-Dependent Values of Bulk, Grain, and Pore Volume as Related to Observed Porosity*, Washington, DC: U.S. Government Printing Office.
- Owens, W. and Archer, D., 1971. The effect of rock wettability on oil-water relative permeability relationships. *Journal of Petroleum Technology*, **23**(07), 873–878.
- Sharma, M. and Wunderlich, R., 1987. The alteration of rock properties due to interactions with drilling fluid components. *Journal of Petroleum Science and Engineering*, **1**(2), 127–143.
- Stiles, J. and Hutfilz, J., 1992. The use of routine and special core analysis in characterizing Brent Group Reservoirs, U.K. North Sea. *Journal of Petroleum Technology*, **44**(06), 704–713.

**BIBLIOGRAPHY**

American Petroleum Institute, 1956. *API Recommended Practice for Determining Permeability of Porous Media*, API RP 27, Dallas, TX: American Petroleum Institute.

# 3

## Reservoir Fluid Properties

Petroleum reservoir fluids mainly consist of 50–97% complex mixtures of *hydrocarbon*, 6–10% *heteroatom* compounds, less than 1% metallic constituents, and water, which can be from interstitial reservoir water or from an aquifer. Hydrocarbons are organic compounds consisting entirely of carbon and hydrogen. Heteroatom compounds, on the other hand, are organic compounds that comprise carbon, hydrogen, and heteroatoms (atoms that are not carbon or hydrogen), which include nitrogen, sulfur, and oxygen. Metallic constituents that have been found in petroleum reservoir fluids include copper, nickel, vanadium, and iron.

Natural occurring hydrocarbons are alkanes (paraffin), aromatics (benzene and its derivatives), and cycloalkanes (naphthenes). Alkenes and alkynes rarely occur naturally but are products of cracking during crude oil refining.

*Petroleum products* are a complex mixture of hydrocarbons derived from crude oil refining processes and *petrochemical*, which are petroleum chemical products derived from petroleum through chemical process. Fig. 3.1 is a summary of the classification of petroleum and petroleum product constituents. As the number of carbon atoms in a petroleum product increases, the complexity of the mixture also increases due to the increased number of possible combinations of atoms present in the mixture. Gasoline with 10 carbon atoms has 75 possible combination of molecules in its mixture, while a mixture with 20 carbon atoms would have 366,319 possible combination of molecules. Fig. 3.2 is a summary of important petroleum products and their range of carbon numbers and boiling points.

### 3.1. PHASE BEHAVIOR OF PETROLEUM HYDROCARBONS

Phase behavior of petroleum hydrocarbons, a multi-component mixture, can be described by a pressure–temperature (P–T) phase diagram (envelope) (Fig. 3.3). The P–T phase diagram is characterized by a *bubble point curve* in the liquid region and a *dew point curve* in the vapor phase region. The point where the bubble point curve and dew point curve meet is the *critical point*, which defines the pressure and temperature conditions where the intensive properties of the vapor and liquid phases are identical. Between the bubble point curve and dew point curve is the two-phase region, which describes the fraction of liquid and vapor in equilibrium for different temperatures and pressures. The bubble point pressure is the pressure at a given temperature below which gas begins to evolve from the hydrocarbon liquid mixture and the dew point temperature is the temperature at a given pressure below which liquid begins to form from the hydrocarbon vapor mixture.

The shape of the phase envelope is dependent on the composition of the hydrocarbon mixture.

The maximum pressure above which a two-phase liquid–vapor can exist in equilibrium is called the *cricondenbar* and the maximum temperature at which a two-phase liquid–vapor can exist in equilibrium is called the *cricondentherm*.

One useful application of the P–T phase diagram is the characterization of hydrocarbon fluid type.



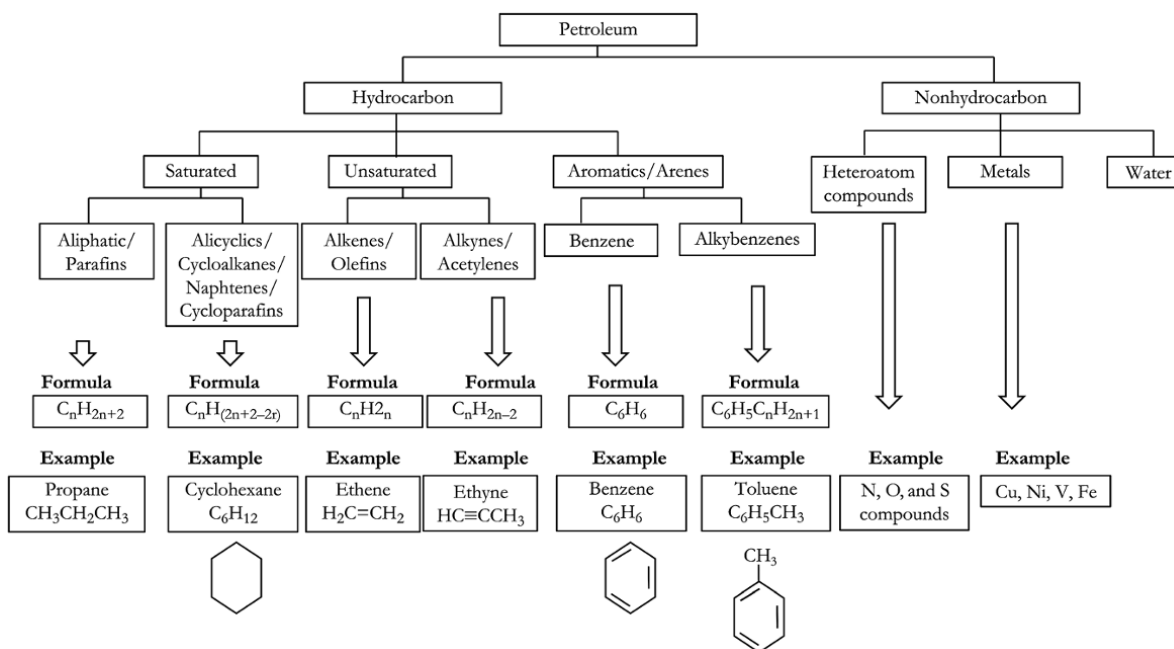


Figure 3.1 Summary of petroleum and petroleum product constituents.

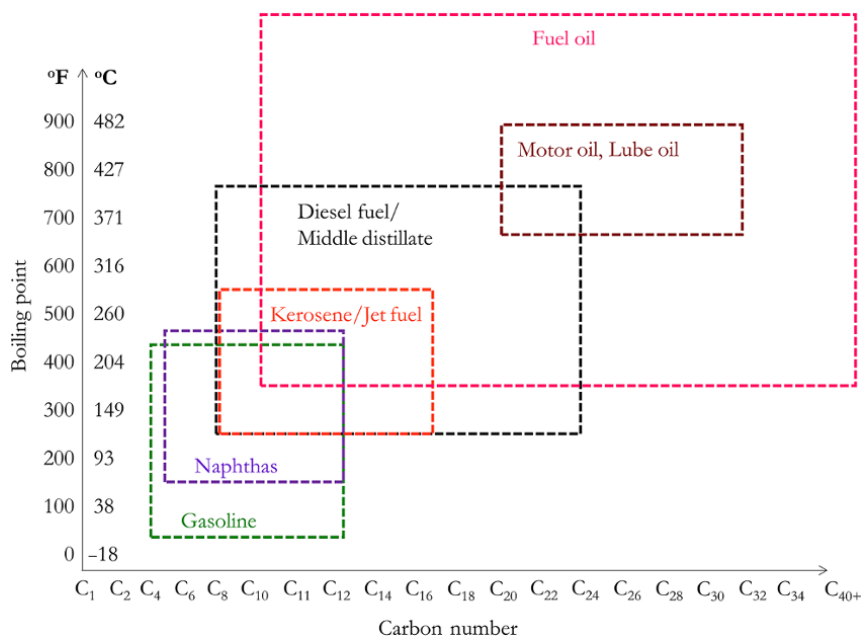
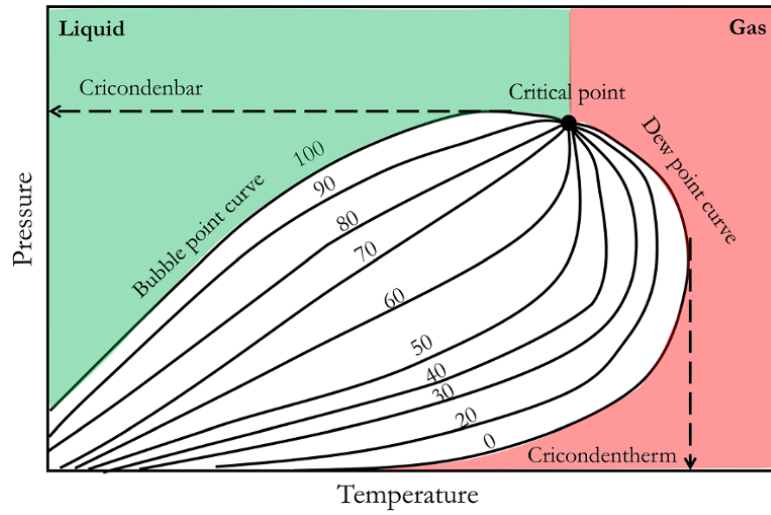


Figure 3.2 Carbon number and boiling point range for key petroleum products.

### 3.1.1. Black Oil (Low Shrinkage Oil)

Black oil, also called *low-shrinkage oil*, is characterized by a relatively high percentage of long, heavy, nonvolatile molecules. Black oil lies within the liquid region of the phase envelope at initial reservoir conditions and are far from the critical point compared with volatile oils.

Consider the isothermal reservoir depletion along A (initial reservoir condition) to A' in Fig. 3.4. At  $A_{\text{sat}}$ , bubble point pressure (100% liquid) is reached and gas begins to come out of the liquid hydrocarbon. Further depletion below  $A_{\text{sat}}$  gives rise to two-phase liquid-vapor in equilibrium, as some of the constituents form vapor and, hence, the liquid fraction reduces (shrinks). Fig. 3.5



**Figure 3.3** P-T phase diagram for petroleum hydrocarbon mixtures at constant composition.

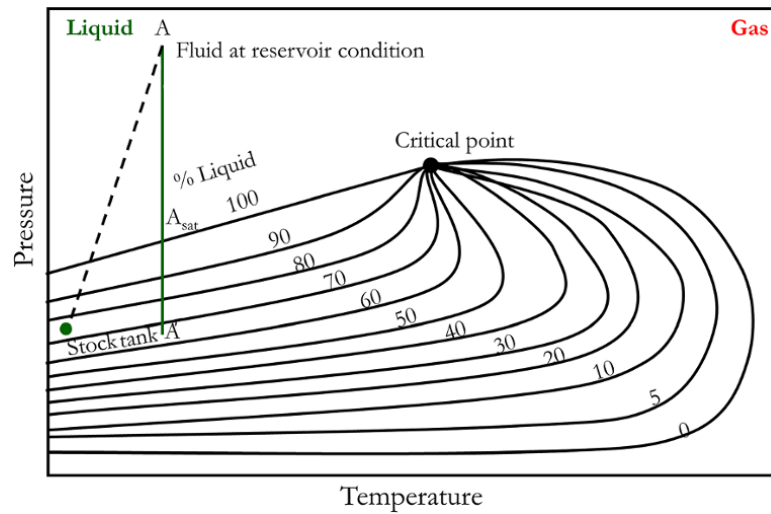


**Figure 3.4** P-T phase envelope for black oil at constant composition.

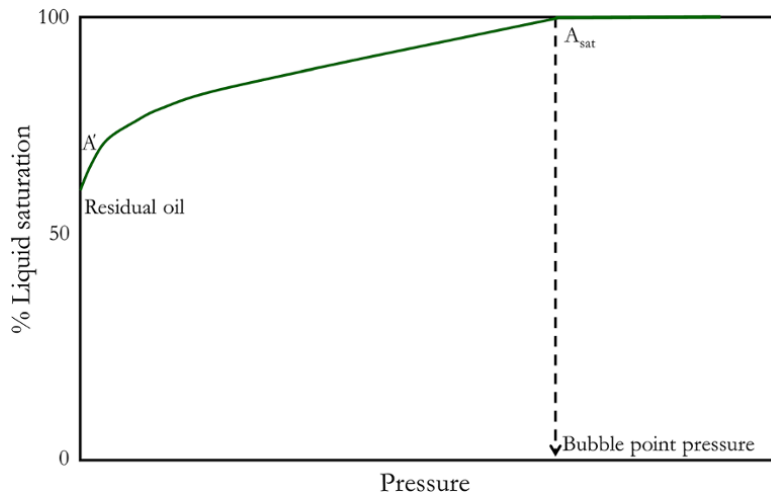


**Figure 3.5** Liquid saturation profile for black oil.

shows a typical liquid saturation change with pressure for a black oil hydrocarbon during isothermal reservoir depletion.

Black oils, though usually black in color, can also have a greenish or brownish color. They have an initial producing gas-oil ratio of 2000 scf/bbl or less with API gravity ( $^{\circ}$ API) below 40 and formation volume factor less than 2 bbl/stb.

### 3.1.2. Volatile Oil (High Shrinkage Oil)

Volatile crude oils are also called *high-shrinkage oils*. They contain relatively few heavy hydrocarbon molecules and more intermediate hydrocarbon molecules compared to black oil. They are also liquid at initial reservoir conditions. Equilibrium two-phase lines (*tie lines*) in volatile crude oils are closer to one another near the bubble point

and more widely spaced at lower pressures than in black oils. Hence, volatile oils produce more gas than black oil for the same pressure drop below the bubble point (Fig. 3.6). They are also characterized by high liquid shrinkage immediately below the bubble point (Fig. 3.7).

Fig. 3.7 shows the liquid saturation profile for isothermal reservoir depletion from the typical volatile oil P-T phase envelope along path A to A' through  $A_{sat}$  (Fig. 3.6).

Volatile oil colors can be brown, orange, or green. They have an initial producing gas-oil ratio between 2000 and 3300 scf/bbl with  $^{\circ}$ API of 40-60. They have a formation volume factor of at least 2 bbl/stb.

### 3.1.3. Retrograde Gas (Gas Condensate)

Retrograde gas (gas condensate) lies within the gas region of the phase envelope (Fig. 3.8). It is gas originally

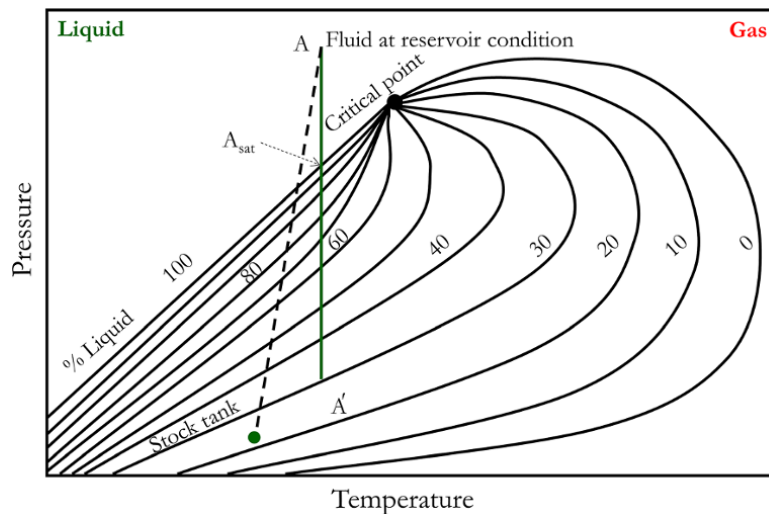


Figure 3.6 P-T phase envelope for volatile oil at constant composition.

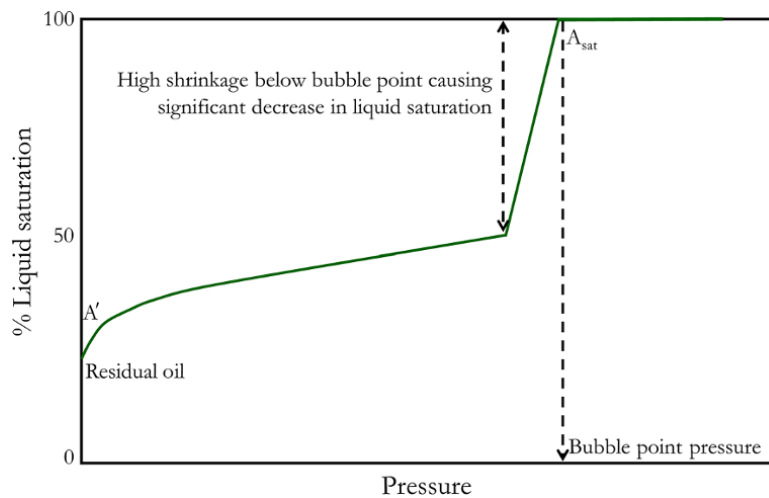
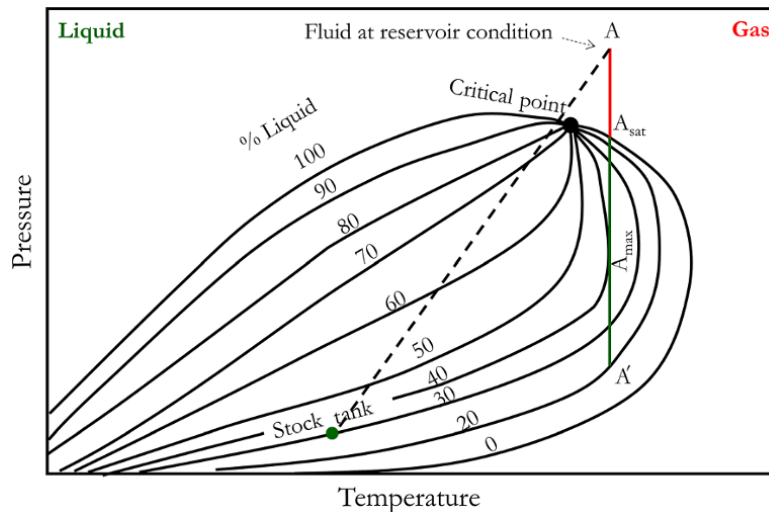
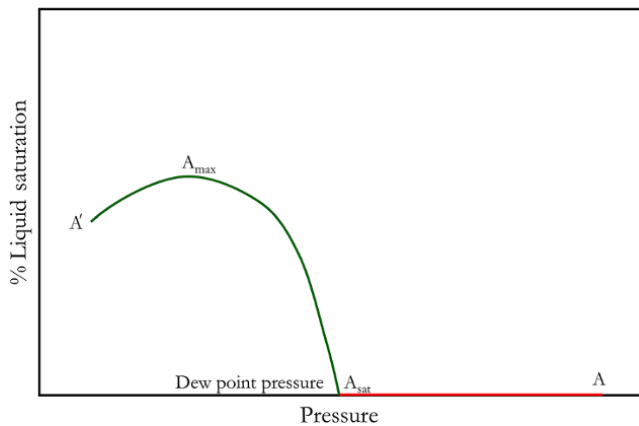


Figure 3.7 Liquid saturation profile for volatile oil.



**Figure 3.8** P-T phase envelope for retrograde gas at constant composition.



**Figure 3.9** Liquid saturation (condensate dropout) profile for retrograde gas.

at initial reservoir condition (point A) with a reservoir temperature between the critical point and cricondentherm on the phase envelope. As the reservoir undergoes isothermal depletion to the dew point ( $A_{sat}$ ) liquid begins to form (*condensate dropout*). Condensate dropout increases until maximum liquid dropout ( $A_{max}$ ). Further depletion to point A' leads to a reduction in condensate saturation, as seen by the depletion line crossing the same tie line twice (before and after  $A_{max}$ ). A plot of liquid saturation (condensate dropout) from Fig. 3.8 along A to A' through  $A_{sat}$  is shown in Fig. 3.9.

Retrograde gas initial gas–oil ratio is 3300 scf/bbl or higher, with °API of 40–60. Gas condensate fluids are generally categorized as lean, medium, and rich, with condensate gas ratios (CGR) of 10–50; 50–125 and greater than 125 stb/MMScf, respectively.

### 3.1.4. Wet Gas

This occurs entirely as gas in the reservoir, even during production. However, it produces liquid condensate at the surface (Fig. 3.10).

Wet gas often has an initial producing gas–oil ratio of 50,000 scf/bbl or higher. °API can be up to 70.

### 3.1.5. Dry Gas

This fluid type is gas at reservoir and surface conditions. It contains mainly methane. Dry gas does not produce condensate either in the reservoir or on the surface (Fig. 3.11).

## 3.2. NATURAL GAS PROPERTIES

Natural gases are gaseous hydrocarbon mixtures consisting of methane ( $CH_4$ ) as their primary constituents, which can be at least 80% in most cases, followed by ethane ( $C_2H_6$ ). Other constituents include propane ( $C_3H_8$ ), butane ( $C_4H_{10}$ ), and pentane ( $C_5H_{12}$ ). Impurities, which are also in gaseous form, include nitrogen, hydrogen, carbon dioxide, hydrogen sulfide, and helium.

The physical properties of a natural gas depends on its constituents. The physical properties of the gas are important in understanding the best way to develop reservoirs; surface facility design; pricing, and end usage.

### 3.2.1. Ideal Gas Behavior

Ideal gas law is the simplest *Equation of State* (EOS) that shows the relationship between pressure, volume, and temperature (PVT) for a perfect gas. The ideal gas

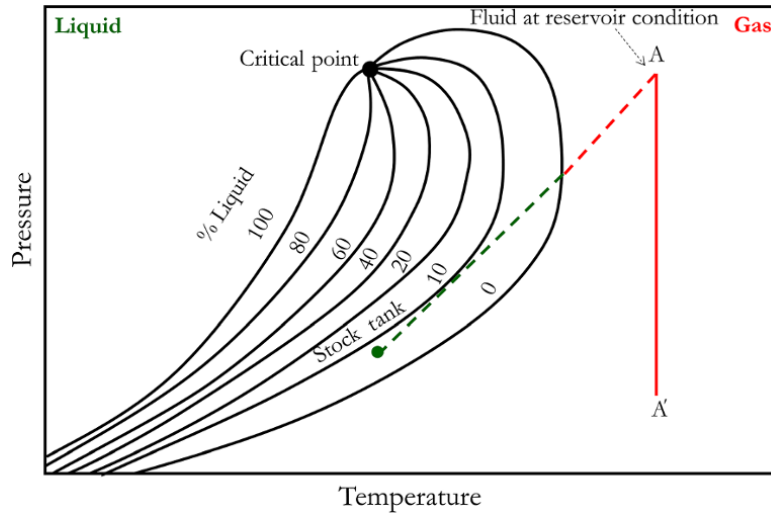


Figure 3.10 P-T phase envelope for wet gas at constant composition.

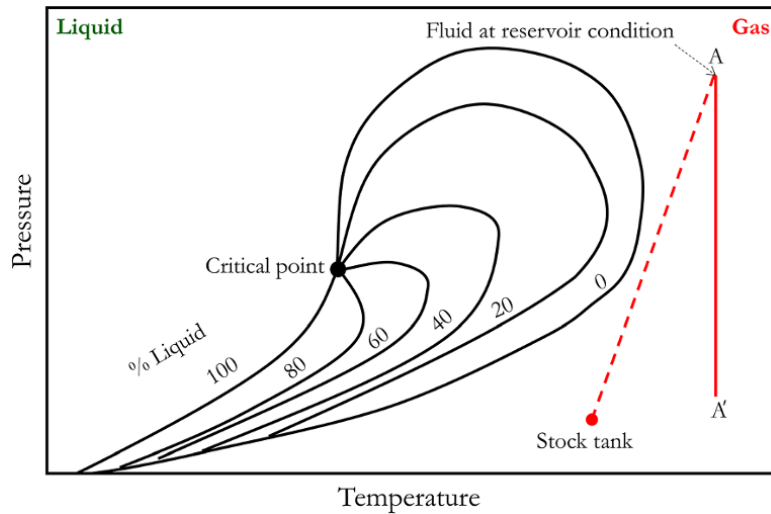


Figure 3.11 P-T phase envelope for dry gas at constant composition.

law is based on the assumption that gas molecules do not interact except when they collide and, when they collide, collision is perfectly elastic. The ideal gas law can be expressed as:

$$pV = nRT \tag{3.1}$$

In oil field units,  $p$  = pressure (psia);  $V$  = volume ( $\text{ft}^3$ );  $T$  = absolute temperature ( $^\circ\text{R}$ );  $n$  = number of moles of gas (lb-mole),  $R$  = universal gas constant =  $10.730 \text{ psia ft}^3/\text{lb-mole } ^\circ\text{R}$

The number of moles can also be expressed as:

$$n = \frac{m}{MW} \tag{3.2}$$

where  $m$  = weight of gas (lb) and  $MW$  = molecular weight (lb/lb-mole).

Using equations (3.1) and (3.2), gas density for an ideal gas can be expressed as:

$$\rho_g = \frac{m}{V} = \frac{pMW}{RT} \tag{3.3}$$

where  $\rho_g$  = gas density and specific volume expressed as:

$$v_g = \frac{V}{m} = \frac{RT}{pMW} = \frac{1}{\rho_g} \tag{3.4}$$

where  $v_g$  = specific volume.

Also, gas specific gravity can be expressed as:

$$\gamma_g = \frac{\rho_g}{\rho_{\text{air}}} = \frac{\frac{pMW_g}{RT}}{\frac{pMW_{\text{air}}}{RT}} = \frac{MW}{MW_{\text{air}}} = \frac{MW}{28.96} \tag{3.5}$$

where  $\gamma_g$  = specific gravity.

For a mixture of hydrocarbon that obeys ideal gas law, the number of moles can be expressed as:

$$n = \frac{m}{MW_a} \quad (3.6)$$

where  $MW_a$  is apparent molecular weight for the gas mixture. *Apparent (average) molecular weight* is the mole fraction weighted molecular weight of the constituent hydrocarbon mixture and expressed as:

$$MW_a = \sum_{i=1}^N y_i \times MW_i \quad (3.7)$$

where  $i$  is the hydrocarbon constituents and  $y_i$  is mole fraction of a particular component and defined as:

$$y_i = \frac{n_i}{n} = \frac{n_i}{\sum_{i=1}^N n_i} \quad (3.8)$$

where volumetric and mass averages are required, or fluid properties are defined on mass or volume basis; weight fractions and volume fractions should be used respectively for averaging in ideal gas mixtures.

The weight fraction of particular component,  $i$ , is defined as:

$$w_i = \frac{m_i}{m} = \frac{m_i}{\sum_{i=1}^N m_i}$$

and the volume fraction of particular component as:

$$v_i = \frac{V_i}{V} = \frac{V_i}{\sum_{i=1}^N V_i}$$

### 3.2.2. Real Gas Behavior

The compressibility factor, also called the compressibility  $Z$ -factor or  $Z$ -factor, is introduced into the ideal gas equation to correct the deviation of ideal gas volume prediction from the real volume determined experimentally. The compressibility factor is, therefore, defined as the ratio of the molar volume of a gas to the molar volume of an ideal gas at the same temperature and pressure.

Hence, the real gas equation can be defined as:

$$pV = ZnRT \quad (3.9)$$

where

$$Z = \frac{V_{\text{actual}}}{V_{\text{ideal}}} \quad (3.10)$$

$Z$ -factor determination requires the critical properties of hydrocarbon mixtures. Kay's rules for determination

of pseudocritical properties of hydrocarbon mixtures is a common approach for determining the pseudocritical properties of hydrocarbon mixture.

Pseudocritical temperature for a hydrocarbon mixture is defined as:

$$T_{pc} = \sum_{i=1}^N y_i \times T_{ci} \quad (3.11)$$

Pseudocritical pressure for a hydrocarbon mixture is defined as:

$$P_{pc} = \sum_{i=1}^N y_i \times P_{ci} \quad (3.12)$$

Pseudocritical density for a hydrocarbon mixture is defined as:

$$\rho_{pc} = \sum_{i=1}^N y_i \times \rho_{ci} \quad (3.13)$$

From the pseudocritical properties, pseudo-reduced properties can then be determined and used to determine the  $Z$ -factor, which can be used for fluid property calculations.

Pseudo-reduced temperature is then expressed as:

$$T_{pr} = \frac{T}{T_{pc}} \quad (3.14)$$

and pseudo-reduced pressure expressed as:

$$p_{pr} = \frac{p}{P_{pc}} \quad (3.15)$$

The pseudocritical properties of a hydrocarbon mixture are not the actual critical properties of the mixture, but it defines the critical property values that would satisfy  $Z$ -factor determination using the principle of corresponding states (PCS). The distinctive relationship between the compressibility factor ( $Z$ ) and the reduced temperature ( $T_r$ ) and reduced pressure ( $p_r$ ) is known as the *two-parameter principle of corresponding states*. This principle states that all fluids compared at the same reduced temperature and reduced pressure will have approximately the same compressibility factor.

**3.2.2.1. Isothermal Compressibility for Real Gas.** Isothermal compressibility is defined as:

$$c_g = -\frac{1}{V} \left( \frac{\partial V}{\partial P} \right)_T \quad (3.16)$$

where

$$V = \frac{ZnRT}{p}$$

Taking the derivative of V with respect to to p:

$$\left(\frac{\partial V}{\partial p}\right)_T = nRT \left[ \frac{1}{p} \left(\frac{\partial Z}{\partial p}\right) - \frac{Z}{p^2} \right]$$

Substituting  $\left(\frac{\partial V}{\partial p}\right)_T$  into equation (3.16) gives

$$c_g = \frac{1}{p} - \frac{1}{Z} \left(\frac{\partial Z}{\partial p}\right) \tag{3.17}$$

Equation (3.17) shows that Z is a function of pressure at a given temperature. Also, from equation (3.17),  $c_g$  can be determined at any pressure.

For an ideal gas,  $Z = 1$  and equation (3.17) becomes:

$$c_g = \frac{1}{p} \tag{3.18}$$

**3.2.2.2. Gas Formation Volume Factor.** Gas formation volume factor is the ratio of gas measured at reservoir conditions to the volume at standard conditions and is expressed as:

$$B_g = \frac{V_{p,T}}{V_{sc}} \tag{3.19}$$

where  $B_g$  = gas formation volume factor (ft<sup>3</sup>/scf),  $V_{p,T}$  = volume of gas at p and T, and  $V_{sc}$  = volume of gas at standard condition.

$$B_g = \frac{ZnRT}{p} \bigg/ \frac{Z_{sc}nRT_{sc}}{p_{sc}} = \frac{p_{sc} ZT}{T_{sc} p}$$

In terms of Z-factor,  $B_g$  can be expressed in consistent units as:

$$B_g = \frac{p_{sc} ZT}{T_{sc} p} \tag{3.20}$$

where  $Z_{sc}$  = Z-factor at standard conditions, which equals 1;  $p_{sc}$  = pressure at standard conditions, which equals 14.7 psia; and  $T_{sc}$  = temperature at standard conditions, which equals 60 °F;

Depending on the unit, gas formation volume factor can be expressed as:

$$B_g = 0.02827 \frac{ZT}{p} \text{ (ft}^3\text{/scf)} \tag{3.21}$$

and

$$B_g = 0.005035 \frac{ZT}{p} \text{ (bbl/scf)} \tag{3.22}$$

The reciprocal of gas formation volume factor ( $B_g$ ) is called the *gas expansion factor* ( $E_g$ ) and is expressed in terms of Z-factor as:

$$E_g = 35.37 \frac{p}{ZT} \text{ (scf/ft}^3\text{)} \tag{3.23}$$

and

$$E_g = 198.6 \frac{p}{ZT} \text{ (scf/bbl)} \tag{3.24}$$

Equations (3.20)–(3.22) shows that  $B_g$  can be determined from Z as function of p data at a given temperature.

**3.2.2.3. Z-factor Calculation Methods.** Methods for calculating the Z-factor include:

(i) Laboratory experiments. Experimental determination of fluid properties including the Z-factor is discussed in section 3.6.

(ii) Principle of corresponding state (PCS) compressibility factor charts. Standing and Katz’s compressibility factor chart is a common compressibility factor chart for determining the Z-factor.

The steps shown in Fig. 3.12 illustrate how the Z-factor can be determined using Standing and Katz’s compressibility factor chart (Fig. 3.13).

(iii) Empirical equations. *Hall and Yarborough* (1973) presented an implicit correlation for Standing and Katz compressibility factors. Their formula is expressed as:

$$Z = \frac{A_1 p_{pr}}{y} \tag{3.25}$$

where y is pseudo-reduced density and a solution of equation:

$$A_1 p_{pr} + \frac{y + y^2 + y^3 - y^4}{(1 - y)^3} - A_2 y^2 + A_3 y^{A_4} = 0 \tag{3.26}$$

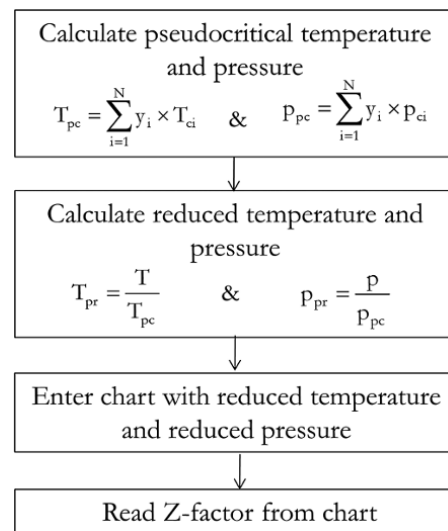


**Figure 3.12** Flow chart for Z-factor determination using Z-factor charts.

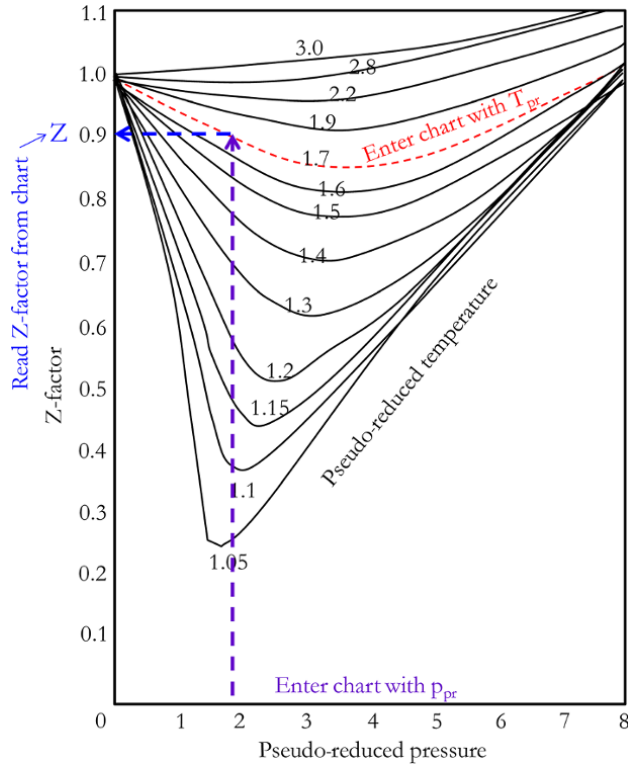


**Figure 3.13** Standing and Katz's compressibility factor chart [Standing, M. & Katz, D., 1942. *Density of Natural Gases*. American Institute of Mining and Metallurgical Engineers Inc., SPE-942140-G, Volume 142, pp. 140–149].

where  $A_1 = 0.06125te^{-1.2(1-t)^2}$ ,  $A_2 = 14.76t - 9.7t^2 + 4.58t^3$ ,  $A_3 = 90.7t - 242.2t^2 + 42.4t^3$ ,  $A_4 = 2.18 + 2.82t$ , and  $t = \frac{1}{T_{pr}}$

The *Hall and Yarborough* (1973) method for computing Z-factor is iterative and not computationally efficient for coding. An explicit solution to Hall and Yarborough's equation [Kareem *et al.*, 2015] is expressed as:

$$Z = \frac{Dp_{pr}(1 + y + y^2 - y^3)}{(Dp_{pr} + Ey^2 - Fy^G)(1 - y)^3} \quad (3.27)$$

where

$$y = \frac{Dp_{pr}}{\left(\frac{1 + A^2}{C} - \frac{A^2B}{C^3}\right)}$$

$$t = \frac{1}{T_{pr}}$$

$$A = a_1te^{a_2(1-t)^2}p_{pr}$$

$$B = a_3t + a_4t^2 + a_5t^6p_{pr}^6$$

**Table 3.1** Constants for Explicit Z-Factor Calculation [Kareem *et al.*, 2015]. Reprinted by permission from Springer.

$a_1$	0.317842	$a_{11}$	-1.966847
$a_2$	0.382216	$a_{12}$	21.0581
$a_3$	-7.76835	$a_{13}$	-27.0246
$a_4$	14.29053	$a_{14}$	16.23
$a_5$	0.000002	$a_{15}$	207.783
$a_6$	-0.00469	$a_{16}$	-488.161
$a_7$	0.096254	$a_{17}$	176.29
$a_8$	0.16672	$a_{18}$	1.88453
$a_9$	0.96691	$a_{19}$	3.05921
$a_{10}$	0.063069		

$$C = a_9 + a_8tp_{pr}t + a_7t^2p_{pr}^2 + a_6t^3p_{pr}^3$$

$$D = a_{10}te^{a_{11}(1-t)^2}p_{pr}$$

$$E = a_{12}t + a_{13}t^2 + a_{14}t^3$$

$$F = a_{15}t + a_{16}t^2 + a_{17}t^3$$

$$G = a_{18} + a_{19}t$$

Constants in the explicit Z formula by Kareem *et al.* are defined in Table 3.1.

(iv) 4 Equation of state (EOS). Determining the Z-factor using EOS is discussed in detail in Chapter 4.

### 3.2.3. Equation of State for Predicting Real Gas Behavior

Molecules of real gases have finite size and exert attractive forces on each other. These attractive forces cause a reduction in pressure that is proportional to the square of the concentration of the molecules or atoms. Several EOS have been published that attempt to capture behavior of real gases. The Earliest being van der Waals equation of state (1873) expressed as:

$$p = \frac{RT}{v-b} - \frac{a}{v^2} \quad (3.28)$$

More accurate EOSs that can predict not only gas properties but also liquid properties have been published. Important EOS for hydrocarbon phase behavior include:

- The Redlich–Kwong equation of state [Redlich and Kwong, 1949] expressed as:

$$p = \frac{RT}{(v-b)} - \frac{a}{v(v+b)T^{0.5}} \quad (3.29)$$

- The Soave–Redlich–Kwong equation of state [Soave, 1972] expressed as:

$$p = \frac{RT}{v-b} - \frac{a(T)}{v(v+b)} \quad (3.30)$$



**Table 3.2** Critical Properties of Some Hydrocarbons.

Hydrocarbon	MW	Critical temperature, $T_c$		Critical pressure, $p_c$	
		$^{\circ}\text{R}$	K	psia	Mpa
$C_1$	16.043	343	191	666	4.6
$C_2$	30.07	550	305	707	4.88
$C_3$	44.097	666	370	617	4.25
$i\text{-}C_4$	58.124	734	408	528	3.65
$n\text{-}C_4$	58.124	765	425	551	3.8
$i\text{-}C_5$	72.151	829	460	491	3.39
$n\text{-}C_5$	72.151	845	470	489	3.37
$n\text{-}C_6$	86.178	913	507	437	3.01
$n\text{-}C_7$	100.205	972	540	397	2.74
$n\text{-}C_8$	114.232	1024	569	361	2.49
$n\text{-}C_9$	128.259	1070	595	332	2.29
$n\text{-}C_{10}$	142.286	1112	618	305	2.1

• The Peng Robinson equation of state [Peng and Robinson, 1976] expressed as:

$$p = \frac{RT}{v-b} - \frac{a(T)}{v(v+b) + b(v-b)} \quad (3.31)$$

where specific volume = volume/number of moles:

$$v = \frac{V}{n}$$

Equations (3.28)–(3.31) are example of *two-parameter EOS*, where characteristic parameters  $a$  and  $b$  are determined experimentally or derived from other component properties of the fluid. Component properties used in calculating  $a$  and  $b$  are published elsewhere in the literature. Equations (3.28)–(3.31), when expressed in standard form, are cubic polynomials with  $V$  having a power of three. Hence, they are called *cubic equations of states*.

The following steps describe the determination of characteristic parameters  $a$  and  $b$  for van der Waals EOS.

Making  $p$  the subject of the formula in equation (3.28):

$$p = \frac{RT}{v-b} - \frac{a}{v^2}$$

At critical conditions

$$\left(\frac{\partial p}{\partial v}\right)_{p_c, T_c} = -\frac{RT}{(v-b)^2} + \frac{2a}{v^3} = 0$$

$$\left(\frac{\partial^2 p}{\partial v^2}\right)_{p_c, T_c} = \frac{2RT}{(v-b)^3} + \frac{6a}{v^4} = 0$$

Solving  $\left(\frac{\partial p}{\partial v}\right)_{p_c, T_c} = \left(\frac{\partial^2 p}{\partial v^2}\right)_{p_c, T_c} = 0$  will yield:

$$a = 3p_c v_c^2 = \frac{27R^2 T_c^2}{64 p_c}$$

**Table 3.3** Universal Gas Constant for Different Units of Pressure, Volume, and Temperature.

$p$	$V$	$T$	$R$
kPa	$\text{m}^3$	K	$8.314(\text{kPa})(\text{M}^3)/(\text{kmol})(\text{K})$
MPa	$\text{m}^3$	K	$0.00831(\text{MPa})(\text{m}^3)/(\text{kmol})(\text{K})$
bar	$\text{m}^3$	K	$0.08314(\text{bar})(\text{m}^3)/(\text{kmol})(\text{K})$
psi	$\text{ft}^3$	$^{\circ}\text{R}$	$10.73(\text{psi})(\text{ft}^3)/(\text{lb-mol})(\text{R})$
$\text{lb/ft}^2$	$\text{ft}^3$	$^{\circ}\text{R}$	$1545(\text{psf})(\text{ft}^3)/(\text{lb-mol})(\text{R})$

$p$  = absolute pressure;  $V$  = volume;  $n$  = number of moles of gas of volume;  $R$  = universal gas constant;  $T$  = absolute temperature.

$$a = \frac{27R^2 T_c^2}{64 p_c} \quad (3.32)$$

and

$$b = \frac{v_c}{3} = \frac{RT_c}{8p_c}$$

$$b = \frac{RT_c}{8p_c} \quad (3.33)$$

$a$  and  $b$  are functions of the critical properties of a fluid.

Critical properties of some hydrocarbons are listed in Table 3.2.

The universal gas constant for different units of pressure, volume, and temperature for the petroleum fluid properties calculation is listed in Table 3.3.

### Exercise 3.1 Gas Volume Calculations

Calculate the volume occupied by 4 lbmol of natural gas with the composition shown in Table 3.4 using (i) the ideal gas equation, (ii) compressibility factor charts, and (iii) van der Waals equation of state, given that  $p = 1454.9$  psia and  $T = 123^{\circ}\text{F}$  ( $+459.67 = 582.67^{\circ}\text{R}$ ).

**Table 3.4** Gas Composition for Exercise 3.1.

Component	Mole fraction
methane (C <sub>1</sub> )	0.83
ethane (C <sub>2</sub> )	0.08
propane (C <sub>3</sub> )	0.03
<i>n</i> -Butane (C <sub>4</sub> )	0.06

**Table 3.5** Composition and Critical Properties of Components.

Component	y <sub>i</sub>	T <sub>ci</sub> (°R)	p <sub>ci</sub> (psi)
methane (C <sub>1</sub> )	0.83	343.2	666.0
ethane (C <sub>2</sub> )	0.08	551.8	707.0
propane (C <sub>3</sub> )	0.03	660.0	617.0
<i>n</i> -Butane (C <sub>4</sub> )	0.06	765.0	528.0

### Solutions.

#### Using the ideal gas equation

Using equation (3.1) and making V the subject of the formula:

$$V = \frac{nRT}{p}$$

$$V = \frac{4 \times 10.73 \times 582.67}{1454.9} = 17.19 \text{ ft}^3$$

$$V = 17.2 \text{ ft}^3$$

#### Using real gas (compressibility chart)

Use the steps in Fig. 3.12.

The composition and critical properties of components are shown in Table 3.5.

#### Determining pseudocritical properties.

Using equations (3.11) and (3.12) with the table above:

$$T_{pc} (\text{°R}) = \sum y_i T_{ci} = 394.7$$

$$p_{pc} (\text{psi}) = \sum y_i p_{ci} = 659.53$$

Using equations (3.14) and (3.15):

$$T_{pr} = \frac{T}{T_{pc}} = 1.47624$$

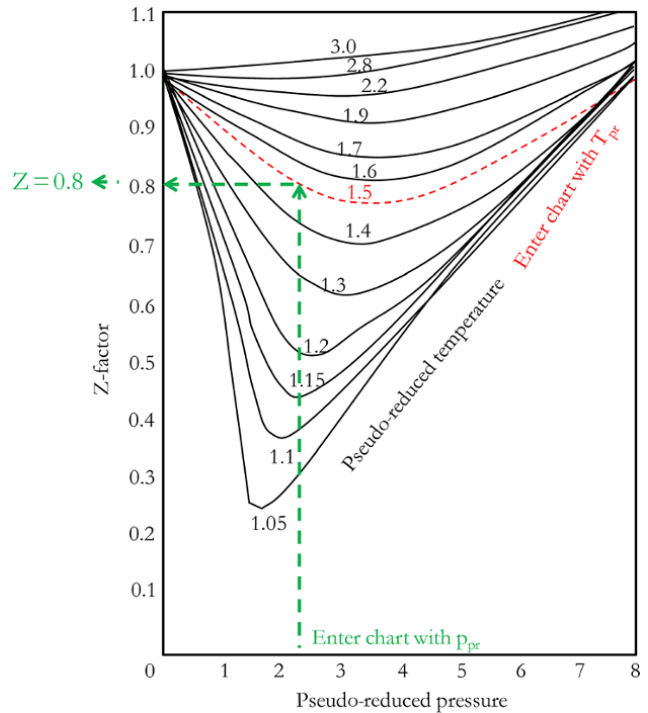
$$p_{pr} = \frac{p}{p_{pc}} = 2.20596$$

Using Fig. 3.13, the Z-factor is determined. Fig. 3.14 shows the Z-factor determination from the reduced temperature and pressure.

$$Z = 0.8$$

Then calculate V using equation (3.9) by making V the subject of the formula:

$$V = \frac{ZnRT}{p}$$


**Figure 3.14** Z-factor determination from reduced temperature and pressure.

$$V = \frac{0.8 \times 4 \times 10.73 \times 582.67}{1454.9} = 13.23 \text{ ft}^3$$

$$V = 13.75 \text{ ft}^3$$

#### Using van der Waals equation

Determine a and b from equations (3.32) and (3.33), respectively, and replace critical temperature and pressure with pseudocritical temperature and pressure, respectively.

$$a = \frac{27R^2 T_{pc}^2}{64 p_{pc}} = \frac{27 \times 10.37^2 \times 394.7^2}{64 \times 659.53} = 11473.157$$

$$b = \frac{RT_{pc}}{8p_{pc}} = \frac{10.73 \times 394.7}{8 \times 659.53} = 0.80268$$

Expanding equation (3.28) in the form:

$$v^3 - \left( b + \frac{RT}{p} \right) v^2 + \frac{a}{p} v - \frac{ab}{p} = 0$$

Iterative techniques, such as goal seek in Microsoft Excel, trial and error or *Cardano's method*, discussed in Chapter 4, can be used.

#### By trial and error

Using v from the ideal gas equation as the starting value:

$$v = \frac{V}{n} = \frac{17.19 \text{ ft}^3}{4 \text{ lbmol}} = 4.2975 \text{ ft}^3/\text{lbmol}$$

Trying  $v = 4.3 \text{ ft}^3/\text{lbmol}$

$$4.3^3 - \left(0.802679749 + \frac{10 \times 582.67}{1454.9}\right) \times 4.3^2 + \frac{11473.15688}{1454.9} \times 4.3 - \frac{11473.15688 \times 0.802679749}{1454.9} = 12.79$$

v = 4.3 ft<sup>3</sup>/lbmol is too large.  
Trying v = 3.1 ft<sup>3</sup>/lbmol

$$3.1^3 - \left(0.802679749 + \frac{10 \times 582.67}{1454.9}\right) \times 3.1^2 + \frac{11473.15688}{1454.9} \times 3.1 - \frac{11473.15688 \times 0.802679749}{1454.9} = -1.1$$

v = 3.1 ft<sup>3</sup>/lbmol is too small.  
Trying v = 3.3 ft<sup>3</sup>/lbmol

$$3.3^3 - \left(0.802679749 + \frac{10 \times 582.67}{1454.9}\right) \times 3.3^2 + \frac{11473.15688}{1454.9} \times 3.3 - \frac{11473.15688 \times 0.802679749}{1454.9} \approx 0$$

Therefore v = 3.3 ft<sup>3</sup>/lbmol

but  $v = \frac{V}{n}$

hence

$$V = v \times n = 3.3 \times 4$$

$$V = 13.27 \text{ ft}^3$$

**Exercise 3.2 Gas Volume Calculation Comparison**

Compare volumes computed using the ideal gas equation, PCS compressibility chart, and van der Waals equation of state for pressure from 1400 to 14.7 psia.

**Solution.**

Create a table of pressure and volume for the three different methods using the steps in Exercise 3.1 with pressure values from 1400 to 14.7 psia (Table 3.6).

Plot volume against pressure, as shown in Fig. 3.15.

Another way to represent Fig. 3.15 is to present the plot as deviation from a reference volumetric calculation method. In this case, using van der Waals EOS as reference method. Fig. 3.16 shows the %-volume deviation of the ideal gas calculation and PCS from van der Waals EOS.

**Table 3.6** Calculated Volumes Using the Ideal Gas Equation, PCS Chart, and van der Waals Equation.

P	volume (ft <sup>3</sup> )		
	Ideal gas	PCS Z chart	van der Waals
1,400	17.86	14.29	13.77
1,000	25.01	21.26	20.74
800	31.26	27.35	26.98
400	62.52	59.39	58.29
200	125.04	121.91	120.86
100	250.08	247.58	245.93
14.7	1,701.24	1,701.24	1,697.10

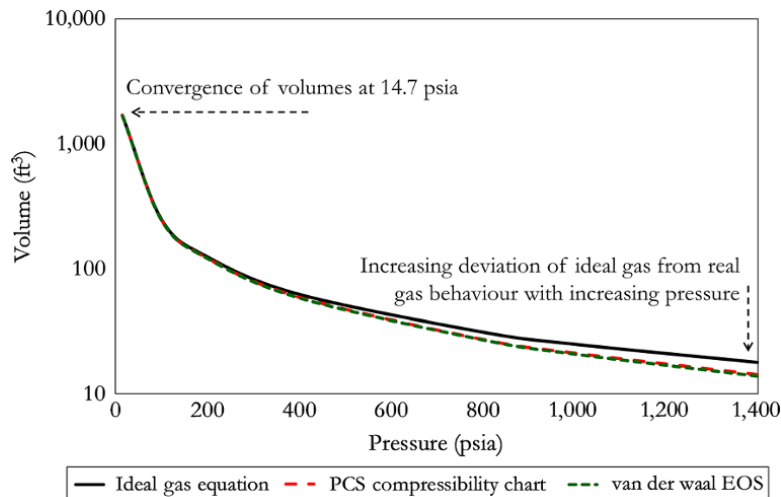


**Figure 3.15** Pressure volume profile for the ideal gas equation, PCS compressibility chart and van der Waals equation.

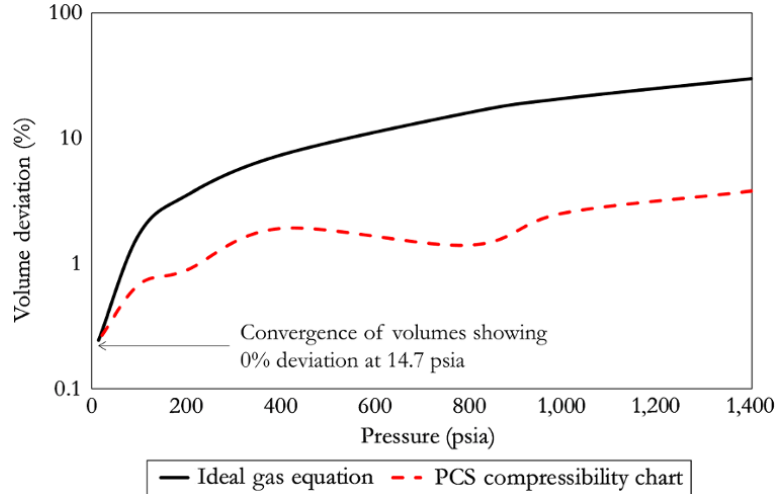


**Figure 3.16** Percentage volume deviation from van der Waals EOS using the ideal gas equation and PCS compressibility chart.

**3.2.3.1. Gas Viscosity Prediction.** There are various gas viscosity models. *Dean and Stiel* (1958) is a common one; it is expressed as:

$$\mu_g = \mu_1 + \frac{10.8(10^{-5}) [\exp(1.439\rho_r) - \exp(-1.111\rho_r^{1.888})]}{\xi_m} \quad (3.34)$$

where

$$\mu_1 = 34(10^{-5}) \frac{(T_{pr})^{8/9}}{\xi_m} \text{ for } T_{pr} \leq 1.5$$

$$\mu_1 = \frac{166.8(10^{-5}) (0.1338T_{pr} - 0.0932)^{5/9}}{\xi_m} \text{ for } T_{pr} \geq 1.5$$

$$\xi_m = 5.4402 \frac{(T_{pc})^{1/6}}{(MW_a)^{0.5} (p_{pc})^{2/3}}$$

$\mu_g$  = gas viscosity (cp) at reservoir temperature and pressure,  $\mu_1$  = gas viscosity (cp) at atmospheric temperature and pressure,  $\rho_r$  = reduced gas density,  $T_{pc}$  and  $p_{pc}$  are pseudocritical temperature and pressure, respectively, while  $T_{pr}$  is pseudo-reduced temperature.

### 3.3. CRUDE OIL PROPERTIES

The physical properties of crude oils depend on their constituents. Physical properties of crude oil are important in understanding the best way to develop reservoirs, surface facility design, transportation, pricing, refining, and end usage. Some of the important physical properties of crudes oil are outlined here.

#### *Density, Specific Gravity and API Gravity*

Density is defined as the mass of a unit volume of a substance at a given pressure and temperature, while the specific gravity of crude oil is defined as the ratio of density of a crude sample to that of water, both at measured at 60 °F and 1 atm.

A more common way of presenting crude oil density is as API gravity, which represents an inverse of specific gravity scaled so that minimum API corresponds to water, with a value of 10. API gravity is expressed as:

$$^\circ\text{API} = \frac{141.5}{\text{SG}} - 131.5 \quad (3.35)$$

API gravity is designed such that most petroleum fluids lie between 10 and 70 °API.

API gravity provides a basis for crude oil classification where:

black oil has API gravity less than 40 °API;

volatile oil has API gravity greater than 40 °API

Though not common to describe hydrocarbon gas by its API value, typical values are:

gas condensate has API gravity greater than 40 °API;

wet gas can have API gravity as high as 70 °API

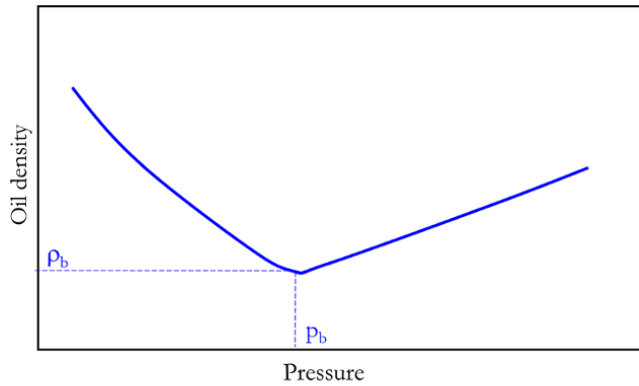
A more delineated classification that is common amongst traders is:

light crude oil is defined as crude oil with API gravity higher than 31.1 °API;

medium crude oil is defined as having an API gravity between 22.3 and 31.1 °API;

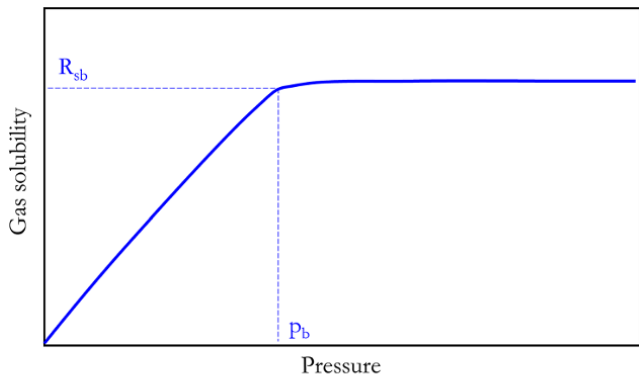
heavy crude oil is defined as having an API gravity between 10 and 22.3 °API;

extra heavy oil, which include bitumen and tar sand, is defined with API gravity below 10.0 °API.



$\rho_b$  is oil density at bubble point pressure,  $p_b$ .

**Figure 3.17** Isothermal change in oil density with pressure.



$R_{sb}$  is oil gas solubility at bubble point pressure,  $p_b$ .

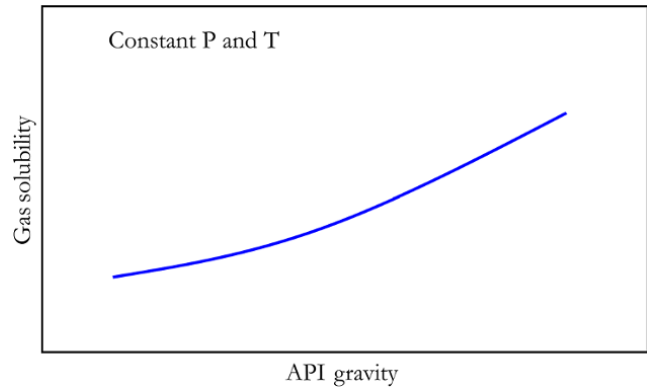
**Figure 3.18** Isothermal change in gas solubility with pressure.

Fig. 3.17 shows the decrease in oil density with isothermal pressure decrease above the bubble point pressure, with minimum density at the bubble point pressure due to the volumetric expansion of fluid. Below the bubble point pressure, a decrease in pressure leads to an increase in density due to continuous loss of light hydrocarbon components.

*Gas Solubility (Solution Gas Ratio) ( $R_s$ )*

This is the amount of gas (in standard cubic feet) that will dissolve in one standard barrel of crude oil at a certain pressure and temperature.  $R_s$  is a function of temperature, pressure, oil gravity, and gas gravity. Fig. 3.18 shows isothermal change in  $R_s$  with pressure.

Typical values of gas solubility for different petroleum hydrocarbon have been discussed in section 3.1, At constant pressure and temperature,  $R_s$  will increase with API gravity (Fig. 3.19).



**Figure 3.19** Gas solubility variation with °API.

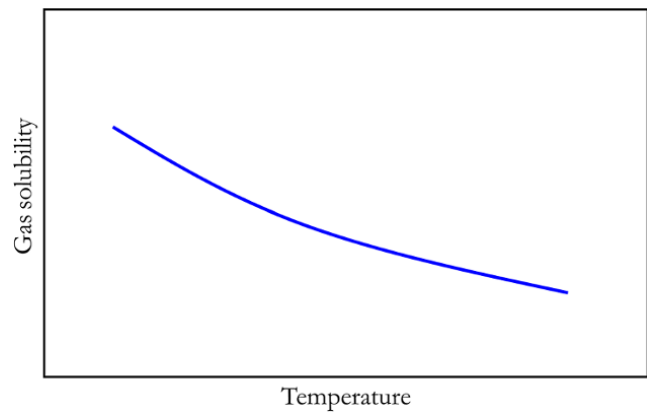


**Figure 3.20** Gas solubility variation with temperature.

Gas solubility of crude oil at a given pressure decreases with increases in temperature, as shown in Fig. 3.20.

*Oil Formation Volume Factor ( $B_o$ )*

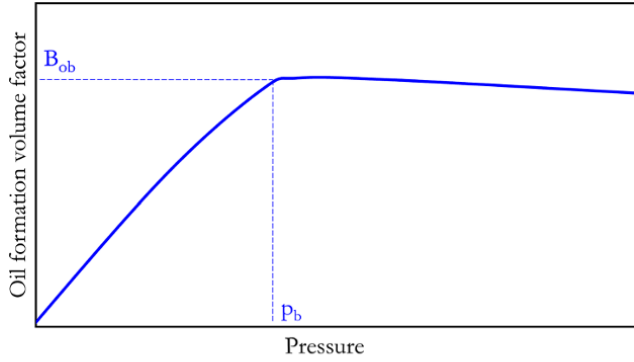
This is the ratio of the volume of oil (including solution gas) at reservoir pressure and temperature to the volume of oil at standard conditions.

$$B_o = \frac{V_{p,T}}{V_{sc}} \tag{3.36}$$

where  $B_o$  = oil formation volume factor (bbl/stb),  $V_{p,T}$  = volume of gas at  $p$  and  $T$ , and  $V_{sc}$  = volume of gas at standard conditions.

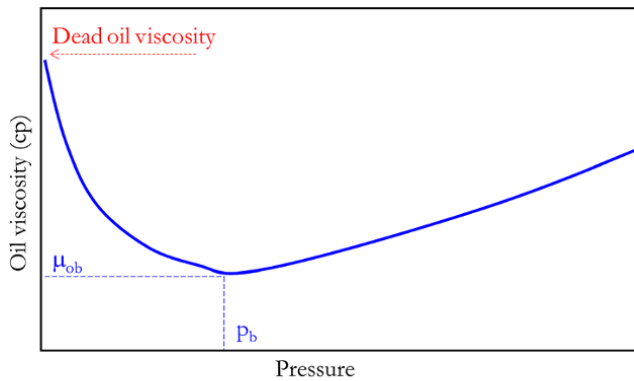
The oil formation volume factor is always greater than or equal to 1.

Fig. 3.21 shows the increase in  $B_o$  with the decrease in pressure under isothermal conditions above the bubble point pressure, with maximum  $B_o$  at the bubble point pressure due to the volumetric expansion of the fluid. Below the bubble point pressure, a decrease in pressure leads to a decrease in  $B_o$  due to loss of light hydrocarbon components until  $B_o = 1$  at atmospheric pressure.



$B_{ob}$  is oil formation volume factor at bubble point pressure,  $p_b$ .

**Figure 3.21** Isothermal change in oil formation volume factor with pressure.



$\mu_{ob}$  is oil viscosity at bubble point pressure,  $p_b$ .

**Figure 3.22** Isothermal change in oil viscosity with pressure.

#### Oil Viscosity ( $\mu_o$ )

In an isothermal depletion process, oil viscosity decreases with decreasing pressure due to the volumetric expansion of oil, until it reaches a minimum value at the bubble point pressure (Fig. 3.22). Reducing the pressure below the bubble point leads to a net increase in oil viscosity due to liberation of light hydrocarbon components until dead oil viscosity is reached at atmospheric pressure.

### 3.3.1. Crude Oil Property Correlations

Most crude oil properties can be predicted using correlation or EOS (Chapter 4). A wide range of correlations have been published in the literature for predicting crude oil properties; some are discussed here.

#### 3.3.1.1. Standing Correlation [Standing, 1947]. Gas: Oil Ratio (GOR):

$$R_s = \gamma_g \left( \frac{p}{18 \times 10^{\gamma_g}} \right)^{1.204} \quad (3.37)$$

where  $\gamma_g = 0.00091(T) - 0.0125(\gamma_{API})$ ,  $R_s$  = solution GOR (scf/stb),  $p$  = pressure (psia), and  $\gamma_g$  = gas gravity (air = 1.0);  $\gamma_{API}$  = oil gravity ( $^{\circ}$ API) and  $T$  = temperature of interest ( $^{\circ}$ F).

*Bubble Point Pressure:*

$$p_b = 18 \left( \frac{R_{sb}}{\gamma_g} \right)^{0.83} 10^{\gamma_g} \quad (3.38)$$

where  $\gamma_g$  = gas mole fraction =  $0.00091(T_R) - 0.0125(\gamma_{API})$ ,  $R_{sb}$  = solution GOR at  $p_b$  (scf/stb),  $p_b$  = bubble point pressure (psia), and  $\gamma_g$  = gas gravity (air = 1.0);  $\gamma_{API}$  = oil gravity ( $^{\circ}$ API) and  $T_R$  = reservoir temperature ( $^{\circ}$ F).

*Oil Formation Volume Factor ( $B_o$ ):*

$$B_o = 0.972 + 0.000147F^{1.175} \quad (3.39)$$

where  $F = R_s(\gamma_g/\gamma_o)^{0.5} + 1.25(T)$  and  $B_o$  = oil FVF (bbl/stb);  $R_s$  = solution GOR (scf/stb),  $\gamma_g$  = gas gravity (air = 1.0),  $\gamma_o$  = oil specific gravity, and  $T$  = temperature of interest ( $^{\circ}$ F).

*Oil Density:*

$$\rho_o = \gamma_g \left( \frac{350\gamma_o + 0.0764\gamma_g R_s}{5.6115B_o} \right)^{1.204} \quad (3.40)$$

where  $\rho_o$  = oil density (lbm/ft<sup>3</sup>),  $B_o$  = oil FVF (bbl/stb),  $R_s$  = solution GOR (scf/stb),  $\gamma_g$  = gas gravity (air = 1.0),  $\gamma_o$  = oil specific gravity, and  $T$  = temperature of interest ( $^{\circ}$ F).

#### 3.3.1.2. Vasquez-Beggs Correlations [Vasquez and Beggs, 1980]. Gas: Oil Ratio (GOR):

$$R_s = C_1 \gamma_g p^{C_2} \exp \left( \frac{C_3 \gamma_{API}}{T + 460} \right) \quad (3.41)$$

where  $R_s$  = solution GOR at  $p$  and  $T$  (scf/stb),  $p$  = pressure (psia),  $\gamma_g$  = gas gravity (air = 1.0),  $\gamma_{API}$  = stock tank oil gravity ( $^{\circ}$ API), and  $T$  = temperature of interest ( $^{\circ}$ F).

Vasquez and Beggs constants for GOR and bubble point pressure calculations are presented in Table 3.7.

*Bubble Point Pressure:*

$$p_b = \left\{ \frac{R_{sb}}{C_1 \gamma_g \exp \left[ \frac{C_3 \gamma_{API}}{T_R + 460} \right]} \right\}^{1/C_2} \quad (3.42)$$

**Table 3.7** Vasquez and Beggs Constants for GOR and Bubble Point Pressure Calculations.

	$^{\circ}$ API $\leq$ 30	$^{\circ}$ API $>$ 30
$C_1$	0.0362	0.0178
$C_2$	1.0937	1.187
$C_3$	25.724	23.93

where  $R_{sb}$  = solution GOR at  $p_b$  (scf/stb),  $p_b$  = bubble point pressure (psia),  $\gamma_g$  = gas gravity (air = 1.0),  $\gamma_{API}$  = oil gravity ( $^{\circ}$ API), and  $T_R$  = reservoir temperature ( $^{\circ}$ F).

*Oil Formation Volume Factor ( $B_o$ ):*

$$B_o = 1 + C_1 R_s + C_2 (T - 60) \left( \frac{\gamma_{API}}{\gamma_{gc}} \right) + C_3 R_s (T - 60) \left( \frac{\gamma_{API}}{\gamma_{gc}} \right) \quad (3.43)$$

where  $B_o$  = oil FVF at  $p$  and  $T$  (bbl/stb),  $R_s$  = solution GOR at  $P, T$  (scf/stb),  $\gamma_{gc}$  = gas gravity, corrected (air = 1.0),  $\gamma_{API}$  = stock tank oil gravity ( $^{\circ}$ API),  $T$  = temperature of interest ( $^{\circ}$ F), and  $p$  = pressure of interest (psia)

Vasquez and Beggs constants for formation volume factor calculations are presented in Table 3.8.

*Oil Density:*

$$\rho_o = \gamma_g \left( \frac{350\gamma_o + 0.0764\gamma_g R_s}{5.6115B_o} \right)^{1.204} \quad (3.44)$$

where  $\rho_o$  = oil density (lbm/ft<sup>3</sup>),  $B_o$  = oil FVF (bbl/stb),  $R_s$  = solution GOR (scf/stb),  $\gamma_g$  = gas gravity (air = 1.0),  $\gamma_o$  = oil specific gravity, and  $T$  = temperature of interest ( $^{\circ}$ F)

*Oil Compressibility:*

$$c_o = \frac{5R_s + 17.2T - 1180\gamma_g + 12.61\gamma_{API} - 1433}{p \times 10^5} \quad (3.45)$$

where  $c_o$  = oil isothermal compressibility (psi<sup>-1</sup>),  $R_s$  = solution GOR at  $p, T$  (scf/stb),  $\gamma_{gc}$  = gas gravity, corrected (air = 1.0),  $\gamma_{API}$  = stock tank oil gravity ( $^{\circ}$ API),  $T$  = temperature of interest ( $^{\circ}$ F), and  $p$  = pressure of interest (psia).

*Oil Viscosity:*

$$\mu_o = \mu_{ob} \left( \frac{p}{p_b} \right)^m \quad (3.46)$$

where  $\mu_o$  = oil viscosity at  $p > p_b$ ,  $\mu_{ob}$  = oil viscosity at  $p_b$ ,  $p_b$  = bubble point pressure (psia),  $p$  = pressure of interest (psia), and  $m = C_1 p^{C_2} \exp(C_3 + C_4 p)$ ;  $C_1 = 2.6$ ,  $C_2 = 1.187$ ,  $C_3 = -11.513$  and  $C_4 = -8.98 \times 10^{-5}$ .

Viscosity at the bubble can be determined using:

$$\mu_{ob} = (10)^a (\mu_{od})^b \quad (3.47)$$

where  $\mu_{ob}$  = oil viscosity (cp) at  $p = p_b$ ,  $\mu_{od}$  = dead oil viscosity (cp) at  $p = 14.7$  and  $T = T_r$ ,  $p_b$  = bubble point pressure (psia), and  $p$  = pressure of interest (psia).

$$a = R_s [2.2(10^{-7}) R_s - 7.4(10^{-4})]$$

$$b = \frac{0.68}{10^c} + \frac{0.25}{10^d} + \frac{0.062}{10^e}$$

$$c = 8.62(10^{-5}) R_s$$

$$d = 1.1(10^{-3}) R_s$$

$$e = 3.74(10^{-3}) R_s$$

*Gas Specific Gravity:*

Where gas specific gravity if required for some of the empirical correlation calculations discussed can be determined using:

$$\frac{P_b \gamma_g}{T_R} = 8.26 y_g^{3.56} + 1.95 \text{ for } y_g > 0.6 \quad (3.48)$$

$$\frac{P_b \gamma_g}{T_R} = 0.679 \exp(2.786 y_g) - 0.323 \text{ for } y_g \leq 0.6 \quad (3.49)$$

where

$$y_g = \frac{R_{sb}/379.3}{R_{sb}/379.3 + 350\gamma_o/M_o}$$

$$\gamma_o = \frac{141.5}{131.5 + \gamma_{API}}$$

$M_o$  = molecular weight of stock tank oil;  $\gamma_o$  is the oil specific gravity and  $\gamma_{API}$  is oil API gravity

### Exercise 3.3 Crude Oil Spreadsheet Calculator

Create a crude oil spreadsheet calculator using Standing and Vasquez-Beggs correlations to determine the following fluid properties: gas-oil ratio, bubble point pressure, oil formation volume factor, oil density, oil isothermal compressibility and oil viscosity.

Determine these fluid properties for a crude oil at a pressure of 3000 psia and temperature of 30  $^{\circ}$ F given the following measured properties: oil API gravity = 40  $^{\circ}$ API, solution gas/oil ratio at  $p_b = 2,345$  scf/bbl, oil viscosity at  $p_b = 0.7$  cp, bubble point pressure = 3,000 psi, and reservoir temperature = 300  $^{\circ}$ F.

### Solution.

The solution to Exercise 3.3 is summarized in Table 3.9.

Table 3.10 gives a summary of the properties of petroleum fluid types. API is the most important property to characterize oil and CGR is the most important property to characterize gas condensate. Values of properties described as typical (initial GOR and  $B_o$ ) are values expected in most cases and may be violated in uncommon cases.

**Table 3.8** Vasquez and Beggs Constants for Formation Volume Factor Calculations.

	$^{\circ}$ API $\leq 30$	$^{\circ}$ API $> 30$
$C_1$	4.677E-04	4.670E-04
$C_2$	1.751E-05	1.100E-05
$C_3$	-1.811E-08	1.337E-09

**Table 3.9** Solution to Exercise 3.3.

Input		Derived properties (which can also be inputs)		Final result	
T = 300 °F, p = 3,000 psi		T = 300 °F, p = 3,000 psi		T = 30 °F, p = 3,000 psi Correlation	
°API	40	$\gamma_o$	0.825	Standing	Vasquez-Beggs
$R_{si}$ at p (scf/bbl)	2,345	$\gamma_g$	0.623	$R_s$ (scf/bbl)	1,092.7 1,048.13
$\mu_o$ (cp)	0.7	$\rho_o$ (lb/ft <sup>3</sup> )	51.508	$p_{bub}$ (psi)	9,960.1 10,608.86
$p_{bub}$ (psi)	3,000	$\rho_g$ (lb/ft <sup>3</sup> )	0.050	$B_o$ (bbl/stb)	1.46 1.47
		$\mu_{od}$ (cp)	7.357	$\rho_o$ (lb/ft <sup>3</sup> )	41.66 41.15
		$M_o$	230	$c_o$ (psi <sup>-1</sup> )	— 3.53E-05
		$\gamma_g$	0.831	$\mu_o$ (cp)	0.88 0.91

**Table 3.10** Summary of Petroleum Fluid Type Characterization.

Petroleum fluid type		API	Typical initial GOR ( $R_{si}$ ) (scf/bbl)	CGR (used for condensate) (stb/MMscf)	Typical formation vol. factor (bbl/stb)	Color
Oil	Black oil					
	Light crude	31.1 < API < 40	900 < $R_{si}$ ≤ 2,000		1.5 < $B_o$ < 2	Usually black.
	Medium crude	22.3 < API ≤ 31.1	200 < $R_{si}$ ≤ 900		1.1 < $B_o$ ≤ 1.5	Can also be
	Heavy crude	10 < API ≤ 22.3	≤ 200		1.0 < $B_o$ ≤ 1.1	greenish or
	Extra heavy crude (bitumen and tar sand)	< 10	≈ 0		≈ 1	brownish
	Volatile oil	40 ≤ API ≤ 60	2,000 < $R_{si}$ < 3,300		≥ 2	Brown, orange, or green
Gas	Retrograde Gas					
	Lean gas condensate	40 ≤ API ≤ 60	≥ 3,300	10 ≤ CGR ≤ 50		
	Medium condensate			50 < CGR ≤ 125		
	Rich condensate			> 125		
	Wet gas	Can be as high as 70		< 10		
	Dry gas	No liquid	Tends to infinity (since no liquid)	≈ 0		

### 3.3.2. Liquid Viscosity Model

The Lohrenz–Bray–Clark (LBC) viscosity model [Lohrenz *et al.*, 1964] is the most widely used viscosity model in petroleum engineering due to consistency, flexibility, and ease of implementation. It is very important to tune the LBC model prior to use considering that, like most viscosity models, it does not accurately predict liquid viscosity without calibration with experimental data. LBC viscosity model is expressed as:

$$[(\eta - \eta^*)\xi + 10^{-4}]^{1/4} = a_1 + a_2\rho_r + a_3\rho_r^2 + a_4\rho_r^3 + a_5\rho_r^4 \quad (3.50)$$

where  $a_1 = 0.10230$ ,  $a_2 = 0.023364$ ,  $a_3 = 0.05833$ ,  $a_4 = -0.040758$ , and  $a_5 = 0.0093324$ ;  $\eta^*$  corresponds to the dilute gas viscosity and given as:

$$\eta^* = \frac{\sum_{i=1}^n x_i \eta_i^* \sqrt{MW_i}}{\sum_{i=1}^n x_i \sqrt{MW_i}} \quad (3.51)$$

The individual component viscosities are expressed as:

$$\eta_i^* = 34 \times 10^{-5} \frac{1}{\xi_i} T_{ri}^{0.94} \text{ for } T_{ri} < 1.5$$

$$\eta_i^* = 17.78 \times 10^{-5} \frac{1}{\xi_i} (4.5T_{ri} - 1.67)^{5/8} \text{ for } T_{ri} > 1.5$$

$\xi$  is a component viscosity reducing parameter. For a mixture of components, viscosity reducing parameter defined as:

$$\xi = \left[ \sum_{i=1}^N z_i T_{ci} \right]^{1/6} \left[ \sum_{i=1}^N z_i MW_i \right]^{-1/2} \left[ \sum_{i=1}^N z_i P_{ci} \right]^{-2/3} \quad (3.52)$$

and the reduced density defined as:

$$\rho_r = \frac{\rho}{\rho_c}$$



Critical density ( $\rho_c$ ) is defined as:

$$\rho_c = \frac{1}{V_c} = \left( \sum_{\substack{i=1 \\ i \neq C7+}}^N z_i V_{ci} + z_{C7+} V_{cC7+} \right)^{-1} \quad (3.53)$$

### 3.3.3. Interfacial Tension

Gas–oil interfacial tension can be calculated either based on composition, pseudocompositional or empirical methods. For a mixture of hydrocarbons, *Weinaug and Katz* (1943) proposed a compositional approach for interfacial tension:

$$\sigma = \left( \sum_{i=1}^N P_i \left( x_i \frac{\rho_l}{MW_l} - y_i \frac{\rho_g}{MW_g} \right) \right)^4 \quad (3.54)$$

$MW_l$  and  $MW_g$  are the molecular weight of the gas and liquid at equilibrium;  $x_i$  and  $y_i$  are the liquid and gas mole fractions, respectively;  $P_i$  is a component parachor, which is a characteristic of pure components and determined experimentally; and  $\rho$  is density, with subscript l and g representing liquid and gas phase, respectively.

## 3.4. VAPOR LIQUID EQUILIBRIUM (VLE)

VLE calculations are important in compositional reservoir simulation and the design of surface separation facilities. The equilibrium constant,  $K_i$ , is defined as the ratio of the mole fraction of the component in the gas phase to the mole fraction of the component in the liquid phase and is defined as:

$$K_i = \frac{y_i}{x_i} = \frac{p_{vi}}{p} \quad (3.55)$$

where  $y_i$  = mole fraction of component in gas phase,  $x_i$  = mole fraction in liquid phase,  $p_{vi}$  = vapor pressure of the component, and  $p$  = saturation pressure.

### 3.4.1. Flash Calculations

The primary objective of flash calculations is to determine the fraction of fluid sample that will exist in equilibrium as vapor and liquid phase at a given temperature and pressure; and the composition of the vapor and liquid phase in equilibrium. Flash calculations are useful for processes such as separation of liquid vapor phase in equilibrium.

Considering a mixture of hydrocarbon, with original constituent mole fraction of  $z_i$ , with vapor and liquid at equilibrium at a given temperature and pressure, as illustrated in Fig. 3.23.

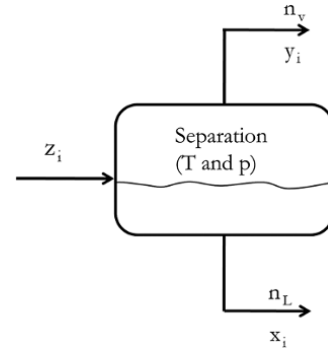


**Figure 3.23** Separation of liquid and vapor phase in equilibrium.

$n_v$  = mole fraction of vapor in equilibrium (gas phase fraction);  $n_L$  = mole fraction of liquid in equilibrium (liquid phase fraction);  $x_i$  = mole fraction of component  $i$  in liquid phase;  $y_i$  = mole fraction of component  $i$  in vapor phase; and  $z_i$  = mole fraction of component  $i$  in original hydrocarbon mixture

Since all mole fractions will add up to 1

$$\sum_{i=1}^n z_i = 1$$

$$\sum_{i=1}^n x_i = 1$$

$$\sum_{i=1}^n y_i = 1$$

Phase fractions will add up to 1 (phase material balance):

$$n_L + n_V = 1 \quad (3.56)$$

The material balance of individual component  $i$ :

$$x_i n_L + y_i n_V = z_i \quad (3.57)$$

Substituting  $y_i$  from equation (3.55) into the material balance equation (3.57) and solving for  $x_i$ :

$$y_i = K_i x_i \quad \text{and} \quad x_i n_L + y_i n_V = z_i$$

$\Rightarrow$

$$x_i n_L + (K_i x_i) n_V = z_i$$

$$x_i (n_L + K_i n_V) = z_i$$

Making  $x_i$  the subject of the formula

$$x_i = \frac{z_i}{(n_L + K_i n_V)} \quad (3.58)$$

Since the mole fraction of the liquid equals 1, then:

$$\sum_{i=1}^n x_i = \sum_{i=1}^n \frac{z_i}{(n_L + K_i n_V)} = 1 \quad (3.59)$$

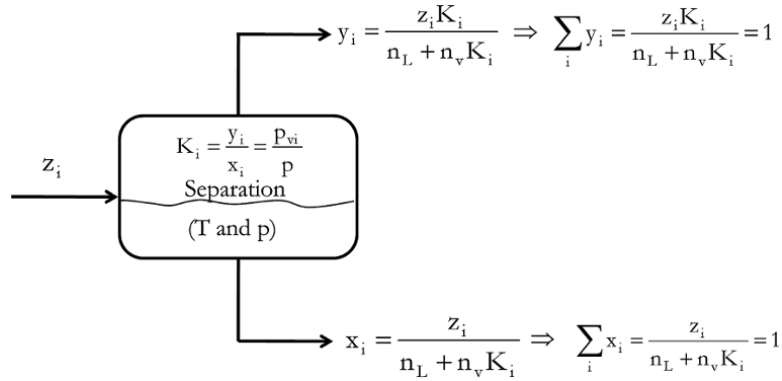


**Figure 3.24** Summary of VLE calculation.

Substituting  $x_i$  from equation (3.55) into the material balance equation (3.57) and solving for  $y_i$ :

$$x_i = \frac{y_i}{K_i} \text{ and } x_i n_L + y_i n_V = z_i$$

Hence:

$$\left(\frac{y_i}{K_i}\right) n_L + y_i n_V = z_i$$

$$y_i (n_L + n_V K_i) = z_i K_i$$

Making  $y_i$  the subject of the formula:

$$y_i = \frac{z_i K_i}{(n_L + n_V K_i)} \quad (3.60)$$

Since the mole fraction of vapor equals 1:

$$\sum_{i=1}^n y_i = \sum_{i=1}^n \frac{z_i K_i}{(n_L + n_V K_i)} = 1 \quad (3.61)$$

The equilibrium phase calculation for a hydrocarbon mixture can be summarized as in Fig. 3.24.

### 3.4.2. K Value Calculations

K value calculations can be based on empirical correlations, the Antoine equation or EOS.

#### 3.4.2.1. Empirical Correlations for VLE Calculations.

Several relationships exist for calculating the equilibrium ratio for VLE calculations. Some include Wilson's correlation [Wilson, 1968], the Whitson and Torp correlation [Whitson and Torp, 1983], the Standing's correlation [Standing, 1979], and the convergence pressure method [Hadden, 1953].

Wilson's correlation [Wilson, 1968] is a common method due to its simplicity and flexibility. This correlation gives a reasonable estimate of  $K_i$  at low pressure, up to 500 psia, as is expressed as:

$$K_i = \frac{p_{ci}}{p} \text{Exp} \left[ 5.37(1 + \omega) \left( 1 - \frac{T_{ci}}{T} \right) \right] \quad (3.62)$$

where  $p_{ci}$  = critical pressure of component  $i$  (psi),  $p$  = system pressure (psi),  $T_{ci}$  = critical temperature of component  $i$  ( $^{\circ}\text{R}$ ),  $T$  = system temperature ( $^{\circ}\text{R}$ ), and  $\omega_i$  = acentric factor of component  $i$ .

**3.4.2.2. Antoine Equation for VLE Calculation.** The Antoine equation, derived from the Clausius–Clapeyron equation [Simot, 2005], defines vapor pressure as a function of the temperature of pure substances and expressed as:

$$\log p_i^{\text{sat}} = A_i - \frac{B_i}{T + C_i} \quad (3.63)$$

where  $A$ ,  $B$ , and  $C$  are Antoine equation parameters, which are published in literature.

Based on Raoult's Law which assumes that vapor phase behaves as an ideal gas and liquid behaves as an ideal solution:

$$K_i = \frac{p_i^{\text{sat}}}{p} \quad (3.64)$$

Making  $p_i^{\text{sat}}$  the subject of the formula from equation (3.63) and substituting into equation (3.64):

$$K_i = \frac{10^{\left( A_i - \frac{B_i}{T + C_i} \right)}}{p} \quad (3.65)$$

Since  $K_i$  has been expressed in terms of  $T$  and  $p$ ,  $K_i$  can be used in a similar way as correlations discussed in section 3.4.2.1.  $p_i^{\text{sat}}$  also exists in other expressions similar to the Antoine equation.

#### 3.4.2.3. Equation of States for VLE calculations.

Equilibrium constants can be obtained from EOS using the  $\phi$ - $\phi$  method. This is discussed in Chapter 4.

**Exercise 3.4** VLE Calculation for a Hydrocarbon Mixture

A hydrocarbon mixture with the overall composition given in Table 3.11 is flashed in a separator at 60 psi and temperature of 70 °F. Assuming equilibrium was achieved, determine the mole fraction and composition of each phase. Use Wilson's correlation to calculate the equilibrium constant with component properties in Table 3.12.

**Solution Steps.**

Calculation steps using a spreadsheet.

*Step 1:* calculate  $K_i$  using  $p$ ,  $T$ ,  $p_{ci}$ ,  $T_{ci}$ , and  $\omega$  (see Table 3.13).

*Step 2:* guess value for  $n_v$ . 0.5 is a good guess to start with.

**Table 3.11** Fluid Composition.

Component	Mole fraction
CO <sub>2</sub>	0.220
C <sub>3</sub>	0.220
<i>i</i> -C <sub>4</sub>	0.070
<i>n</i> -C <sub>4</sub>	0.090
<i>i</i> -C <sub>5</sub>	0.180
<i>n</i> -C <sub>5</sub>	0.200
C <sub>6</sub>	0.020

**Table 3.12** Component Properties of Fluid Constituents.

Component	$T_{ci}$ (°R)	$p_{ci}$ (Psi)	$\omega_i$
CO <sub>2</sub>	547.90	1,071.00	0.2250
N <sub>2</sub>	227.60	493.00	0.0400
C <sub>1</sub>	343.37	667.80	0.0104
C <sub>2</sub>	550.09	707.80	0.0986
C <sub>3</sub>	666.01	616.30	0.1524
<i>i</i> -C <sub>4</sub>	734.98	529.10	0.1848
<i>n</i> -C <sub>4</sub>	765.65	550.70	0.2010
<i>i</i> -C <sub>5</sub>	829.10	490.40	0.2223
<i>n</i> -C <sub>5</sub>	845.70	488.60	0.2539
C <sub>6</sub>	913.70	436.90	0.3007
C <sub>7+</sub>	1,290.00	263.00	0.5340

**Table 3.13** Solution to Exercise 3.4, VLE Calculations using Wilson's Correlation.

Component	Mole fraction	T (°R)		p (psia)		$n_v$	$n_l = 1 - n_v$
		529.67	60.0	0.431383	0.568617		
		$T_{ci}$ (°R)	$p_{ci}$ (psia)	$\omega_i$	$K_i$	$y_i$	$x_i$
CO <sub>2</sub>	0.220	547.9	1071	0.2250	14.23346	0.467	0.033
C <sub>3</sub>	0.220	666.01	616.30	0.1524	2.088537	0.313	0.150
<i>i</i> -C <sub>4</sub>	0.070	734.98	529.10	0.1848	0.748755	0.059	0.079
<i>n</i> -C <sub>4</sub>	0.090	765.65	550.70	0.2010	0.518666	0.059	0.114
<i>i</i> -C <sub>5</sub>	0.180	829.10	490.40	0.2223	0.199947	0.055	0.275
<i>n</i> -C <sub>5</sub>	0.200	845.70	488.60	0.2539	0.146557	0.046	0.317
C <sub>6</sub>	0.020	913.70	436.90	0.3007	0.046012	0.002	0.034
	$\Sigma z_i$					$\Sigma y_i$	$\Sigma x_i$
	1.000					1.000	1.000

*Step 3:* calculate  $n_l = 1 - n_v$ .

*Step 4:* calculate  $y_i$  and  $x_i$  using equations (3.58) and (3.60), respectively.

*Step 5:* calculate  $\Sigma x_i$  and  $\Sigma y_i$  using equations (3.59) and (3.61), respectively.

*Step 6:* use goal seek to set the value of  $\Sigma y_i = 1$  by changing the value of  $n_v$ .

$$T = 60 + 459.67 = 519.67^\circ\text{R}$$

**Solution.**

Set up spreadsheet as shown in Table 3.13 with  $K_i$ ,  $y_i$ , and  $x_i$  as formula. Using goal seek set  $\Sigma y_i$  to 1 by changing  $n_v$ .

**3.4.3. Properties of Pseudocomponents**

Pseudocomponents are a range or mixture of constituents characterized by definite properties such as critical temperature ( $T_c$ ), critical pressure ( $p_c$ ), boiling point temperature ( $T_b$ ), molecular weight (MW), and specific gravity (SG) for manageability of number of constituents.

There are published correlations for determining the properties of pseudocomponents. A reliable example is the Riazi–Daubert correlation [Riazi and Daubert, 1987] for predicting  $T_c$ ,  $p_c$ , and  $T_b$  using MW and SG; it is expressed as:

$$\Theta = a(\text{MW})^b \text{SG}^c \exp(d(\text{MW}) + e\text{SG} + f(\text{MW})\text{SG}) \quad (3.66)$$

where  $\Theta$  = the physical properties  $T_c$ ,  $p_c$ , and  $T_b$ , and  $a$ – $f$  are the coefficients in Table 3.14.

The acentric factor can be determined using the Edmister correlation [Edmister, 1958]:

$$\omega = \frac{3(\log(p_c/14.7))}{7(T_c/T_b - 1)} - 1 \quad (3.67)$$

where  $p_c$  is in psia and  $T_c$  and  $T_b$  are in °R

**Exercise 3.5** VLE Calculation for Crude Oil Sample with Pseudocomponents

A crude oil sample with the composition and properties shown in Table 3.15 is flashed in a separator at 500 psia

and temperature of 60 °F. Assuming equilibrium was achieved, determine the mole fraction and composition of each phases. Use Wilson's correlation to calculate all equilibrium constants, the Riazi–Daubert correlation for  $T_c$  and  $p_c$  of pseudocomponents, and the Edmister correlation for  $\omega_i$  of the pseudocomponents.

### Solution Steps.

*Step 1:* determine  $T_{ci}$ ,  $p_{ci}$ , and  $T_b$  of the pseudocomponents using the Riazi–Daubert correlation (equation (3.66)) as shown in Table 3.16.

*Step 2:* determine  $\omega_i$  of the pseudocomponents using the Edmister correlation (equation (3.67)) as shown in Table 3.16.

*Step 3:* follow the steps in Exercise 3.4.

### Solution.

$$T = 60 + 459.67 = 519.67^\circ\text{R}$$

Set up spreadsheet as shown in Table 3.17 with  $K_i$ ,  $y_i$ , and  $x_i$  as formula. Using goal seek set  $\sum y_i$  to 1 by changing  $n_v$ .

## 3.4.4. Saturation Points

**3.4.4.1. Dew Point.** At the dew point, the system (Fig. 3.24) is vapor and equation (3.56) becomes:  $n_v = 1$  and  $n_L = 0$ ; also,  $x_i = 0$  and equation (3.57) becomes:

$$y_i = z_i$$

**Table 3.14** The Riazi–Daubert Correlation Parameters.

$\Theta$	$T_c$ (°R)	$p_c$ (psia)	$T_b$ (°R)
a	544.4	45,203	6.77857
b	0.2998	-0.8063	0.401673
c	1.0555	1.6015	-1.58262
d	-0.00013478	-0.0018078	0.00377409
e	-0.61641	-0.3084	2.984036
f	0	0	-0.00425288

**Table 3.15** Composition and Properties of Oil Sample for Exercise 3.5.

Component	Mole fraction	$T_{ci}$ (°R)	$p_{ci}$ (psia)	$\omega_i$	MW	SG
N <sub>2</sub>	0.0014	226.566	492.022	0.039		
CO <sub>2</sub>	0.0229	547.362	1,072.955	0.239		
C <sub>1</sub>	0.4880	343.152	673.077	0.011		
C <sub>2</sub>	0.0882	549.468	708.347	0.099		
C <sub>3</sub>	0.0663	665.676	617.379	0.153		
<i>i</i> -C <sub>4</sub>	0.0090	734.364	529.056	0.183		
<i>n</i> -C <sub>4</sub>	0.0331	764.964	550.659	0.199		
<i>i</i> -C <sub>5</sub>	0.0119	829.476	483.058	0.227		
<i>n</i> -C <sub>5</sub>	0.0183	845.262	489.524	0.251		
C <sub>6</sub>	0.0257	913.770	439.704	0.299		
C <sub>7:9</sub>	0.1257				106.569	0.7591
C <sub>10:22</sub>	0.0808				173.639	0.8261
C <sub>23+</sub>	0.0288				325	0.9212

Substituting  $n_v$  and  $n_L$  into equation (3.59):

$$\sum_{i=1}^n x_i = \sum_{i=1}^n \frac{z_i}{(n_L + K_i n_v)} = 1$$

$$\sum_{i=1}^n x_i = \sum_{i=1}^n \frac{z_i}{(0 + K_i \times 1)} = 1$$

$$\sum_{i=1}^n \frac{z_i}{K_i} = 1 \quad (3.68)$$

At the dew point, criteria defined by equation (3.68) must be met.

### Exercise 3.6 Dew Point Pressure Calculations for Natural Gas

Determine the dew point pressure of a natural gas reservoir at 80 °F with the composition shown in Table 3.18. Use the component properties provided in Table 3.12.

### Solution.

Set up spreadsheet as shown in Table 3.20 with  $K_i$  and  $\frac{z_i}{K_i}$  as formula. Using goal seek set  $\sum_{i=1}^n \frac{z_i}{K_i} = 1$  by changing  $p$ .

Calculated  $p$  is the dew point pressure at  $T = 80^\circ\text{F} = 80 + 459.67^\circ\text{R} = 539.67^\circ\text{R}$

### Exercise 3.7 Dew Point Pressure Calculations for Gas Condensate

**Table 3.16** Determined Properties of Pseudocomponents.

Pseudo components	$T_{ci}$	$p_{ci}$	$T_{bi}$	$\omega_i$
C <sub>6</sub>	1,018.605	439.792	698.293	0.37896
C <sub>7:9</sub>	1,225.967	294.778	895.984	0.51532
C <sub>10:22</sub>	1,533.643	156.388	1,175.060	0.44217

**Table 3.17** Solution to Exercise 3.5, Flash Calculation for Crude Oil Sample.

Component	Mole fraction	T (°R)	p (psia)	$\omega_i$	$K_i$	$n_v$	$n_l = 1 - n_v$
		519.67	500.00			0.51625	0.48375
		$T_{ci}$ (°R)	$p_{ci}$ (psia)			$y_i$	$x_i$
N <sub>2</sub>	0.0014	226.566	492.022	0.039000	22.892807	0.0026	0.0001
CO <sub>2</sub>	0.0229	547.362	1,072.955	0.239000	1.5053387	0.0274	0.0182
C <sub>1</sub>	0.4880	343.152	673.077	0.011000	8.5110141	0.8515	0.1000
C <sub>2</sub>	0.0882	549.468	708.347	0.099000	1.0099746	0.0886	0.0878
C <sub>3</sub>	0.0663	665.676	617.379	0.153000	0.2168142	0.0241	0.1113
<i>i</i> -C <sub>4</sub>	0.0090	734.364	529.056	0.183000	0.0766855	0.0013	0.0172
<i>n</i> -C <sub>4</sub>	0.0331	764.964	550.659	0.199000	0.052726	0.0034	0.0648
<i>i</i> -C <sub>5</sub>	0.0119	829.476	483.058	0.227000	0.0190144	0.0005	0.0240
<i>n</i> -C <sub>5</sub>	0.0183	845.262	489.524	0.251000	0.01455	0.0005	0.0373
C <sub>6</sub>	0.0257	913.770	439.704	0.299000	0.0044334	0.0002	0.0528
C <sub>7:9</sub>	0.1257	1,018.605	439.792	0.378962	0.0007188	0.0002	0.2597
C <sub>10:22</sub>	0.0808	1,225.967	294.778	0.515316	9.277E-06	0.0000	0.1669
C <sub>23+</sub>	0.0288	1,533.643	156.388	0.442168	8.564E-08	0.0000	0.0594
	$\Sigma z_i$					$\Sigma y_i$	$\Sigma x_i$
	1.0000					1.0000	1.0000

**Table 3.18** Natural Gas Composition for Exercise 3.6.

Component	Mole fraction
C <sub>1</sub>	0.68921
C <sub>2</sub>	0.04595
C <sub>3</sub>	0.02941
<i>i</i> -C <sub>4</sub>	0.19298
<i>n</i> -C <sub>4</sub>	0.01654
<i>i</i> -C <sub>5</sub>	0.01103
<i>n</i> -C <sub>5</sub>	0.01470
C <sub>6</sub>	0.00018

**Table 3.19** Solution to Exercise 3.6, Dew Point Pressure Calculation of Natural Gas.

Component	Mole fraction	T (°R)	$p_{dew}$ (psi)	$\omega_i$	$K_i$	$z_i/K_i$
		539.67	149.32			
		$T_{ci}$ (°R)	$p_{ci}$ (psi)			
C <sub>1</sub>	0.68921	343.37	667.80	0.0104	32.18467	0.021414
C <sub>2</sub>	0.04595	550.09	707.80	0.0986	4.229793	0.010863
C <sub>3</sub>	0.02941	666.01	616.30	0.1524	0.969373	0.030335
<i>i</i> -C <sub>4</sub>	0.19298	734.98	529.10	0.1848	0.354337	0.544621
<i>n</i> -C <sub>4</sub>	0.01654	765.65	550.70	0.2010	0.247708	0.066776
<i>i</i> -C <sub>5</sub>	0.01103	829.10	490.40	0.2223	0.097191	0.113461
<i>n</i> -C <sub>5</sub>	0.01470	845.70	488.60	0.2539	0.071871	0.204577
C <sub>6</sub>	0.00018	913.70	436.90	0.3007	0.023114	0.007952
	$\Sigma z_i$					$\sum_{i=1}^n \frac{z_i}{K_i}$
	1.0000					1

Determine the dew point pressure of a gas condensate fluid at 267 °F with the properties listed in Table 3.20.

**Solution Steps.**

Follow the steps in Exercise 3.6

**Solution.**

Set up spreadsheet as shown in Table 3.21 with  $K_i$  and  $\frac{z_i}{K_i}$  as formula. Using goal seek set  $\sum_{i=1}^n \frac{z_i}{K_i} = 1$  by changing p.

**3.4.4.2. Bubble Point.** At the bubble point, the system (Fig. 3.24) is liquid and equation (3.56) becomes:

$n_L = 1$  and  $n_V = 0$ ; also,  $y_i = 0$  and equation (3.57) becomes:

$$x_i = z_i$$

Substitute  $n_V$  and  $n_L$  into equation (3.61):

$$\sum_{i=1}^n \frac{z_i K_i}{(n_L + n_V K_i)} = 1$$

**Table 3.20** Composition and Properties of Gas Condensate for Exercise 3.7.

Component	Mole fraction	$T_{ci}$ (°R)	$p_{ci}$ (psi)	$\omega_i$
N <sub>2</sub>	0.003	226.566	492.022095	0.039
CO <sub>2</sub>	0.022	547.36	1072.95496	0.239
C <sub>1</sub>	0.706	343.15	673.076782	0.011
C <sub>2</sub>	0.108	549.47	708.347168	0.099
C <sub>3</sub>	0.049	665.68	617.378967	0.153
n-C <sub>4</sub>	0.030	764.96	550.659119	0.199
n-C <sub>5</sub>	0.014	845.26	489.523773	0.251
C <sub>6</sub>	0.009	913.77	439.704346	0.299
C <sub>7+</sub>	0.059	1,119.18	402.676514	0.350

**Table 3.21** Solution to Exercise 3.7, Dew Point Pressure Calculation of Gas Condensate.

Component	Mole fraction	$T$ (°R)	$p_{dew}$ (psia)	$\omega_i$	$K_i$	$z_i/K_i$
		726.67	128.82			
		$T_{ci}$ (°R)	$p_{ci}$ (psia)			
N <sub>2</sub>	0.003	226.566	492.022095	0.039	177.67883	1.91E-05
CO <sub>2</sub>	0.022	547.36	1072.95496	0.239	43.01467	0.000504
C <sub>1</sub>	0.706	343.15	673.076782	0.011	91.725508	0.007701
C <sub>2</sub>	0.108	549.47	708.347168	0.099	23.189299	0.00464
C <sub>3</sub>	0.049	665.68	617.378967	0.153	8.0590801	0.00613
n-C <sub>4</sub>	0.030	764.96	550.659119	0.199	3.044782	0.009919
n-C <sub>5</sub>	0.014	845.26	489.523773	0.251	1.2695939	0.010633
C <sub>6</sub>	0.009	913.77	439.704346	0.299	0.5664659	0.015888
C <sub>7+</sub>	0.059	1,119.18	402.676514	0.350	0.0622509	0.944565
	$\Sigma z_i$					$\sum_{i=1}^n \frac{z_i}{K_i}$
	1.0000					1.0000

$$\sum_{i=1}^n \frac{z_i K_i}{(1 + 0 \times K_i)} = 1$$

$$\sum_{i=1}^n z_i K_i = 1 \quad (3.69)$$

At the bubble point, the criteria defined by equation (3.69) must be met.

**Exercise 3.8** Bubble Point Pressure Calculations

Determine the bubble point pressure of a hydrocarbon mixture with the composition shown in Table 3.22 at 60 °F. Use the component properties provided in Table 3.15.

**Solution.**

Set up the spreadsheet as shown in Table 3.23 with  $K_i$  and  $\sum_{i=1}^n z_i K_i$  as formula. Using goal seek set  $\sum_{i=1}^n z_i K_i = 1$  by changing p.

Calculated p is the bubble point pressure at  $T = 60$  °F =  $60 + 459.67$  °R =  $519.67$  °R.

**Table 3.22** Hydrocarbon Mixture Composition for Exercise 3.8.

Component	Mole fraction
N <sub>2</sub>	0.001
CO <sub>2</sub>	0.023
C <sub>1</sub>	0.088
C <sub>2</sub>	0.088
C <sub>3</sub>	0.066
i-C <sub>4</sub>	0.009
n-C <sub>4</sub>	0.033
i-C <sub>5</sub>	0.012
n-C <sub>5</sub>	0.018
C <sub>6</sub>	0.026
C <sub>7:9</sub>	0.255
C <sub>10:22</sub>	0.211
C <sub>23+</sub>	0.170

**Table 3.23** Solution to Exercise 3.8, Bubble Point Pressure Calculation Using Wilson's Correlation.

Component	Mole fraction	T (°R)	p (psi)	$\omega_i$	$K_i$	$Z_i'K_i$
		519.6700	456.4168			
		$T_{ci}$ (°R)	$p_{ci}$ (psi)			
N <sub>2</sub>	0.001	226.57	492.02	0.0390	2.5079E+01	2.5079E-02
CO <sub>2</sub>	0.023	547.36	1072.95	0.2390	1.6491E+00	3.7929E-02
C <sub>1</sub>	0.088	343.15	673.08	0.0110	9.3237E+00	8.2049E-01
C <sub>2</sub>	0.088	549.47	708.35	0.0990	1.1064E+00	9.7365E-02
C <sub>3</sub>	0.066	665.68	617.38	0.1530	2.3752E-01	1.5676E-02
<i>i</i> -C <sub>4</sub>	0.009	734.36	529.06	0.1830	8.4008E-02	7.5607E-04
<i>n</i> -C <sub>4</sub>	0.033	764.96	550.66	0.1990	5.7761E-02	1.9061E-03
<i>i</i> -C <sub>5</sub>	0.012	829.48	483.06	0.2270	2.0830E-02	2.4996E-04
<i>n</i> -C <sub>5</sub>	0.018	845.26	489.52	0.2510	1.5939E-02	2.8691E-04
C <sub>6</sub>	0.026	913.77	439.70	0.2990	4.8568E-03	1.2628E-04
C <sub>7:9</sub>	0.255	1,018.61	439.79	0.3790	7.8748E-04	2.0081E-04
C <sub>10:22</sub>	0.211	1,225.97	294.78	0.5153	1.0163E-05	2.1445E-06
C <sub>23+</sub>	0.17	1,533.64	156.39	0.4422	9.3818E-08	1.5949E-08
	$\Sigma z_i$					$\sum_{i=1}^n z_i K_i$
	1					1

### 3.5. RESERVOIR FLUID SAMPLING

Collecting pristine fluid samples from virgin reservoirs is very important in field planning decisions, reserve estimation, design of surface handling facilities, and prediction of potential flow assurance issues. Reservoir fluids can be from the surface (separator) or bottomhole sampling (wireline formation testing).

In formation testing, pressure data, fluid property data, and fluid samples are acquired through probes and or packers. Formation testers have a fluid sampling section with sample bottle(s) to receive reservoir fluids at specific depth.

#### 3.5.1. Bottomhole Sampling

Bottomhole sampling is also called downhole sampling and samples are acquired often through wireline formation test operations. One of the main drawbacks of bottomhole sampling is the risk of contamination of reservoir fluid sample by drilling mud filtrate. Contamination of fluid sample can be a serious issue, especially when oil-based drilling mud is used, due to miscibility between reservoir hydrocarbon and oil-based mud (OBM) filtrate.

Errors associated with bottomhole sampling other than contamination include: risk of two-phase forming due to excessive drawdown or phase segregation; poor tool design has been known to be a potential source of error; and commingling of fluid in a layered reservoir can yield nonrepresentative fluid samples.

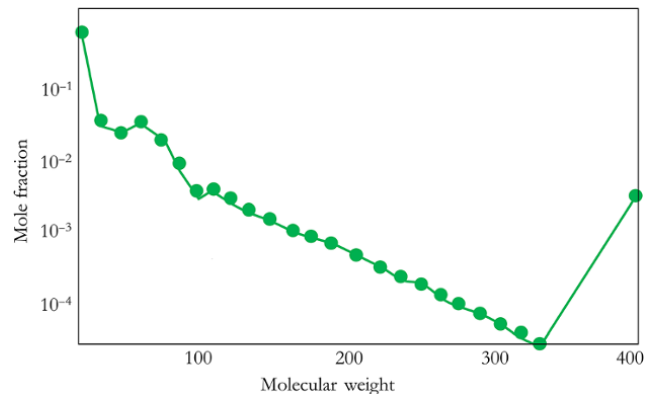


**Figure 3.25** Example of clean component showing semi-log fingerprint.

**3.5.1.1. Fluid Sample Decontamination.** The principle of deriving original composition from an OBM contaminated sample is based on fitting C8 and higher components to a semi-log plot of mole fraction against molecular weight of C8 and higher components. A clean sample will show a straight-line trend on a semi-log plot of mole fraction against molecular weight (fingerprint plot) for C8 and higher components excluding pseudo components (Fig. 3.25). A contaminated sample will show a nonlinear trend on a semi-log plot of mole fraction against molecular weight (fingerprint plot) for C8 and higher components (Fig. 3.26).

Two approaches used for decontaminating OBM contaminated samples are: *skimming* and *subtracting methods*.

The skimming method involves adjusting C8 and higher components of the contaminated sample to fit a semi-log linear trend on fingerprint plot. The semi-log relationship is then used to determine clean sample composition. This approach does not require the composition of the OBM contaminant to be known. The subtraction method involves subtracting a known composition of contaminant to get the composition of the uncontaminated sample using the material balance. A given volume of contaminant is used iteratively until a straight line on the fingerprint plot is achieved with minimum deviation from the semi-log relationship.

Fingerprint plots can be described by the semi-log linear trend for C8 and higher components by:

$$\ln z_i = A + B \times MW \quad (3.70)$$

where A and B are fitting parameters for determining uncontaminated samples.

For both the skimming and subtracting methods, fitting parameters A and B can be adjusted to determine the composition of the decontaminated sample (Fig. 3.27).

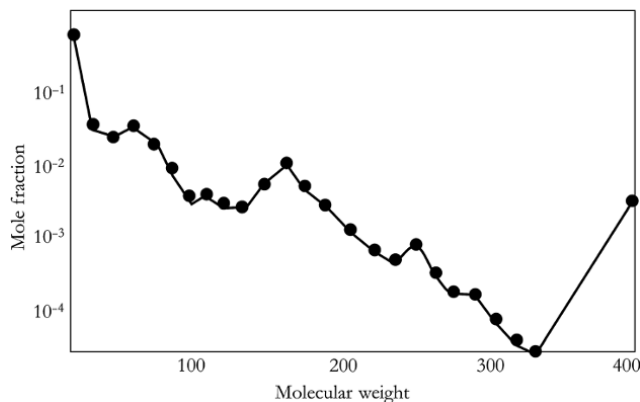


**Figure 3.26** Examples of fluid sample contaminated with oil-based mud filtrate.

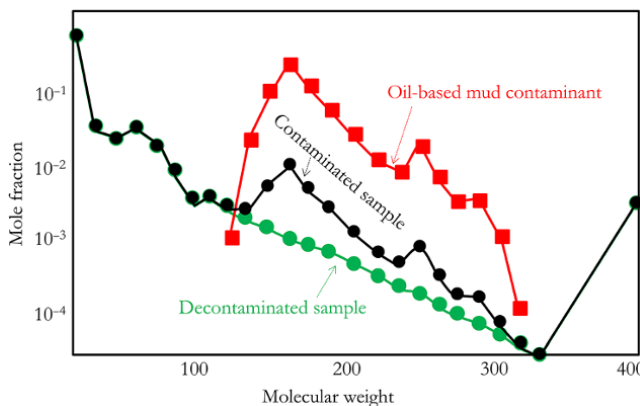


**Figure 3.27** Subtracting contaminant from contaminated fluid sample.

### 3.5.2. Surface Sampling

Surface sampling of reservoir fluids involves taking gas and oil samples from test or production separators. It is an inexpensive method of obtaining reservoir fluid samples. Sampling could be done during drill stem test (DST) or routinely during production. Surface sampling requires the measurement of gas and oil rates to determine the sampling gas-oil-ratio to be used for recombination of the sampled oil and gas to get representative reservoir fluid sample. Separator sampling often involves collecting pressured fluid samples from the separator. However, samples can be further flashed during analysis or measurement, hence measured properties and or composition from a flashed separator sample would represent two-stage separation. Where separator fluid samples are flashed the entire separation stages, which include separator and laboratory flash, should be correctly accounted for during recombination and use for analysis. Fig. 3.28 shows a two-stage separation involving field separator sample flashed in a separator cell in the laboratory.

Errors during surface sampling include gas and oil streams sampled not having been properly equilibrated. Also, gas streams with liquid entrainment or liquids with gas carry-under and liquid oils with emulsions, which is due poor separator design, can affect the quality of sampling.

## 3.6. FLUID EXPERIMENTS

Laboratory fluid experiments, also called PVT experiments, are carried out to provide a description of how important fluid properties vary with temperature, pressure, and composition. Experimental prediction of hydrocarbon fluid properties is important for direct petroleum engineering calculations, such as prediction of reservoir and well performance, design of the surface facility and pipelines, and flow assurance studies. Experimental hydrocarbon fluid properties predictions can also be used to tune black oil correlation or equation of state (EOS) models, which can then be used for various petroleum engineering calculations discussed above. It is important that EOS models can predict laboratory fluid property measurements to minimize uncertainty and errors in petroleum engineering calculations.

### 3.6.1. Gas Laboratory Experiment

**3.6.1.1. Constant Volume Depletion (CVD) Experiment.** This is a very important experiment for gas condensate and volatile oil reservoir fluids. CVD experiments best describe the reservoir depletion process when the condensate is immobile. The test process involves expansion



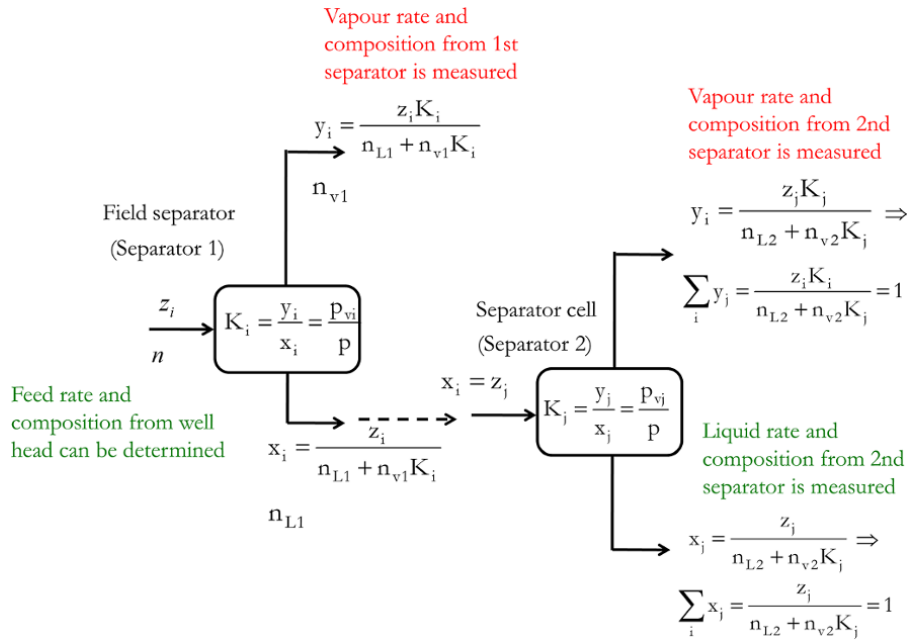


Figure 3.28 Field separator sample flashed in a separator cell in the laboratory.

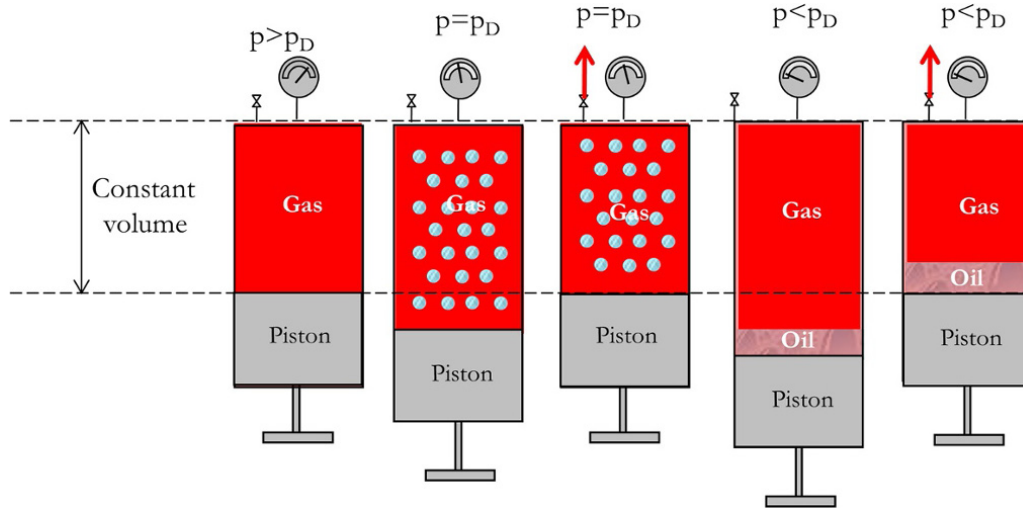


Figure 3.29 Constant volume depletion experiment.

(pressure drop) in a windowed pressure–volume–temperature (PVT) cell followed by expelling excess gas (compression) to keep the volume constant (Fig. 3.29). Windowed PVT cells ensure that observation of phase change and condensate dropout can be monitored. The composition of expelled gas is measured using mostly cryogenic distillation and/or gas chromatographic techniques. Fluid properties are measured at each pressure depletion stage. The liquid dropout profile (Fig. 3.30) is a very important test in the CVD experiment, as it crucial

in predicting well deliverability impairment due to condensate dropout below saturation pressure.

Tables 3.24 and 3.25 show examples of results from a CVD experiment.

Fig. 3.31 shows a *Hoffmann quality plot*, which is a plot of  $\log(KP)$  against a characteristic F function. The resultant plot should yield an approximate straight line where liquid and vapor samples are reasonably in equilibrium at the separation conditions and, as such, minimum error is expected in the composition of the liquid and vapor.

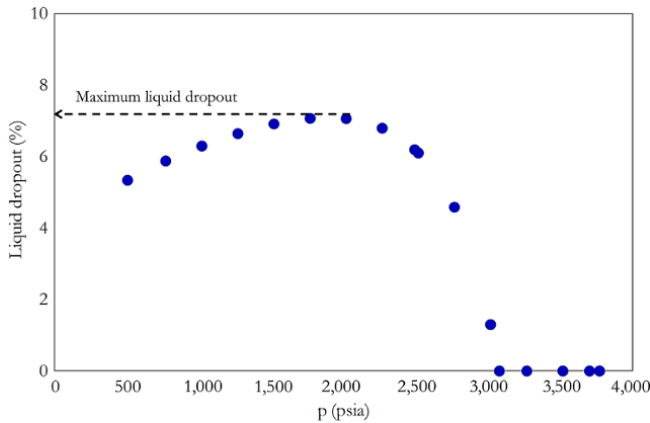


**Figure 3.30** Condensate (liquid) dropout from CVD experiment.

**Table 3.24** Gas Condensate CVD Experiment Result at 267 °F.

Pressure (psia)	Liquid dropout (%)	$\mu_{oil}$ (cp)	$Z_{vapor}$	$\mu_{gas}$ (cp)	$B_{gas}$ (ft <sup>3</sup> /scf)
$p_{initial}$ 3,770.00	0.00		0.856	0.033	0.0047
3,700.20	0.00		0.851	0.032	0.0047
3,515.20	0.00		0.839	0.031	0.0049
3,265.61	0.00		0.825	0.029	0.0052
$p_{sat}$ 3,076.05	0.00	0.09	0.815	0.028	0.0054
3,014.73	1.29	0.09	0.816	0.027	0.0056
2,764.33	4.58	0.10	0.822	0.024	0.0061
2,514.6	6.10	0.12	0.828	0.022	0.0068
2,489.12	6.19	0.12	0.829	0.022	0.0068
2,264.00	6.79	0.14	0.836	0.020	0.0076
2,014.57	7.06	0.16	0.845	0.018	0.0086
1,764.82	7.07	0.18	0.856	0.017	0.0100
1,514.01	6.91	0.22	0.869	0.016	0.0118
1,264.15	6.64	0.25	0.883	0.015	0.0144
1,014.72	6.29	0.30	0.899	0.015	0.0182
764.43	5.87	0.36	0.917	0.014	0.0247
500.13	5.33	0.44	0.939	0.014	0.0386

The Hoffman characterization factor is defined as:

$$F_i = \frac{(\log p_{ci} - \log p_{sc}) \left( \frac{1}{T_{bi}} - \frac{1}{T_{sep}} \right)}{\left( \frac{1}{T_{bi}} - \frac{1}{T_{ci}} \right)} \quad (3.71)$$

where  $T$  is the temperature of interest and corresponds to the temperature at equilibrium separation condition,  $p_{ci}$  = critical pressure of component  $i$  (psia),  $p_{sc}$  = standard pressure (psia),  $T_{ci}$  = critical temperature of component  $i$  (°R),  $T_{bi}$  = normal boiling point temperature of component  $i$  (°R), and  $T_{sep}$  = separator temperature (°R).

Use of the Hoffman characterization factor for fluid modelling quality control is discussed in Chapter 4.

**3.6.1.2. Constant Compositional Expansion Experiment.** This test is common with gas condensate and volatile oil and requires various forms of volumetric measurements. Constant composition expansion (CCE) is also called *constant mass expansion (CME)*, *flash liberation*, *flash vaporization* or *flash expansion*. CCE best describes the reservoir depletion process during pseudo-steady state considering that condensate dropouts and gas are both mobile and the mixture composition can be assumed to be constant. It is common to find the term *flash liberation*, *flash vaporization* or *flash expansion* used when the fluid sample is crude oil instead of gas. However, as shown in section 3.6.2.1, the procedures are the same for both oil or gas.

The procedure for the CCE test involves raising the pressure in a PVT cell above the saturation pressure. This is then followed by decreasing it in stages with pressure and total volume of cell measured (Fig. 3.32).

Saturation pressure corresponds to pressure where there is an abrupt increase in total fluid compressibility due to the formation of a two-phase mixture. The change in total compressibility is more gradual in gas at the dew point than in oil at the bubble point, hence it is more difficult to determine dew point pressure using this approach. Some of the tests that will be typically carried out during CCE at different pressures are shown here.

*Relative Volume*

$$V_{rel} = \frac{V_{total}(T,p)}{V_{sat}} \quad (3.72)$$

*Compressibility*

$$c = -\frac{1}{V} \left( \frac{\partial V}{\partial p} \right)_T \quad (3.73)$$

Compressibility can be expressed also in terms of relative volume

$$c = -\frac{1}{V_{rel}} \left( \frac{\partial V_{rel}}{\partial p} \right)_T \quad (3.74)$$

*Liquid Saturation or Dropout*

$$S_{liq} = 100 \frac{V_{liquid}}{V_{sat}} \quad (3.75)$$

In CCE experiments,  $S_{liq}$  can be defined relative to volume at saturation pressure ( $V_{sat}$ ) or original fluid volume in PVT cell ( $V$ ). In such instance where  $S_{liq}$  is defined relative to original fluid volume,  $S_{liq}$  becomes

$$S_{Liq} = 100 \frac{V_{liquid}}{V} \quad (3.76)$$

**Table 3.25** Gas Condensate CVD Compositional Analysis at 267 °F.

Pressure (psia)	N <sub>2</sub>	CO <sub>2</sub>	C1	C2	C3	nC4	nC5	C6	C7+
p <sub>initial</sub> 3,770.00	0.34	2.17	70.64	10.76	4.94	3.02	1.35	0.90	5.88
3,700.20	0.34	2.17	70.64	10.76	4.94	3.02	1.35	0.90	5.88
3,515.20	0.34	2.17	70.64	10.76	4.94	3.02	1.35	0.90	5.88
3,265.61	0.34	2.17	70.64	10.76	4.94	3.02	1.35	0.90	5.88
p <sub>sat</sub> 3,076.05	0.34	2.17	70.64	10.76	4.94	3.02	1.35	0.90	5.88
3,014.73	0.34	2.17	71.00	10.77	4.92	3.00	1.33	0.88	5.59
2,764.33	0.35	2.19	72.17	10.80	4.88	2.92	1.27	0.82	4.61
2,514.60	0.35	2.20	73.01	10.83	4.85	2.87	1.23	0.78	3.88
2,489.12	0.36	2.20	73.08	10.84	4.85	2.86	1.23	0.77	3.82
2,264.00	0.36	2.21	73.63	10.88	4.84	2.83	1.20	0.74	3.32
2,014.57	0.36	2.22	74.06	10.93	4.84	2.81	1.17	0.72	2.88
1,764.82	0.36	2.24	74.35	10.98	4.86	2.81	1.16	0.70	2.54
1,514.01	0.36	2.25	74.49	11.05	4.90	2.83	1.16	0.69	2.28
1,264.15	0.36	2.26	74.46	11.13	4.95	2.87	1.17	0.69	2.11
1,014.72	0.36	2.27	74.24	11.21	5.04	2.94	1.21	0.71	2.03
764.43	0.35	2.28	73.73	11.30	5.16	3.06	1.28	0.75	2.09
500.13	0.35	2.28	72.63	11.39	5.33	3.29	1.43	0.87	2.44

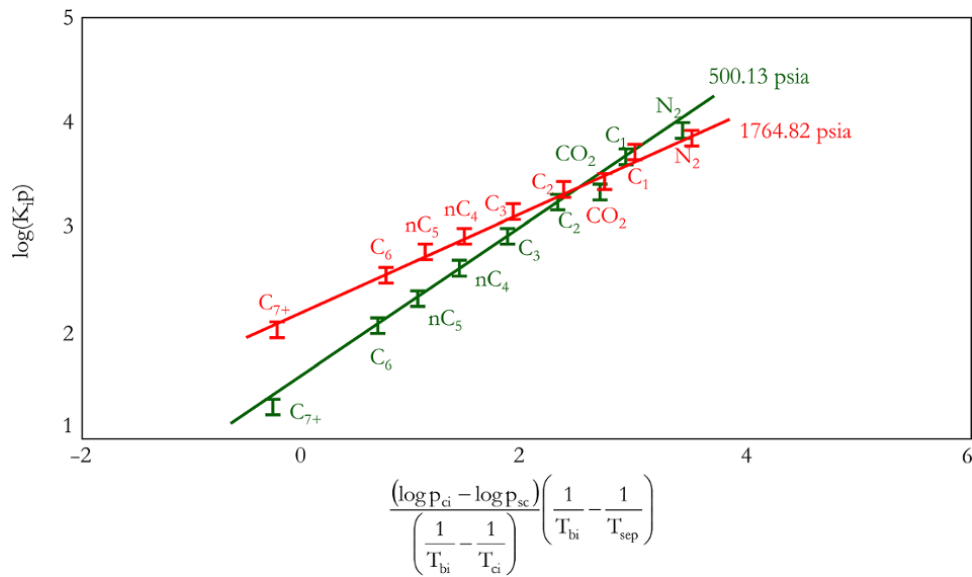


**Figure 3.31** Hoffmann quality plot for measured composition during CVD experiment.

It is, therefore, very important to know how  $S_{liq}$  has been calculated before using for any analysis or calculations

*Coefficient of Thermal Expansion*

$$\beta = -\frac{1}{V} \frac{dV}{dT} \tag{3.77}$$

Laboratory data from CCE tests, especially relative volume, are often smoothed and sometimes evaluated or extrapolated using the Y-function. A plot of Y-function against pressure on a Cartesian scale should yield a

straight line or slightly curved line for relative volume below saturation pressure; it is expressed as:

$$Y = \frac{p_{sat} - p}{p(V_{rel} - 1)} \tag{3.78}$$

Table 3.26 shows examples of results from a CCE experiment.

**Exercise 3.9** Extrapolation of CCE Experiment to Determine  $V_{rel}$

Determine relative volume from the CCE experiment in Table 3.26 at a pressure of 700 psia.

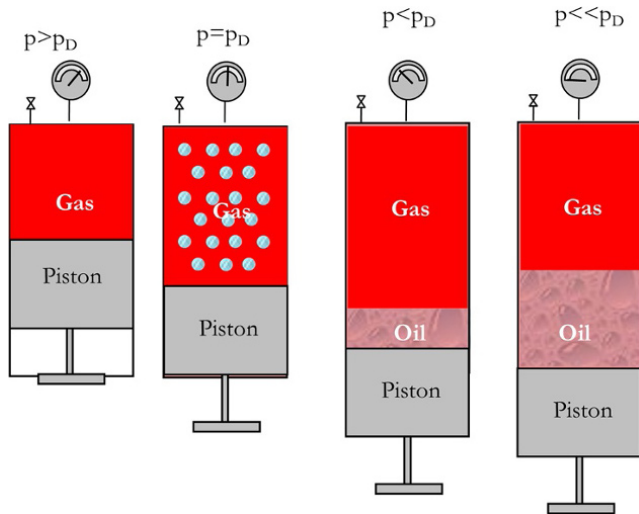


**Figure 3.32** The constant composition expansion experiment.

#### Solution Steps.

*Step 1:* create a table of  $Y$ -function for pressure points below the saturation pressure using equation (3.78) as shown in Table 3.27.

*Step 2:* plot  $Y$ -function vs  $p$  and determine the line of best fit in the form of:  $Y = ap + b$  (Fig. 3.33).

*Step 3:* use equation of fit to determine  $Y$  at a pressure of 700 psia.

*Step 4:* using the equation, determine relative volume at 700 psia.

#### Solution.

$Y = 5.5141 \times 10^{-5}p + 0.87409$  from Fig. 3.33.

at 700 psia,  $Y = 5.5141 \times 10^{-5} \times 700 + 0.87409 = 0.91269$

From equation (3.78), making  $V_{rel}$  the subject of the formula and substituting  $p$  and  $Y$ :

$$V_{rel} = \frac{p_{sat} - p}{pY} + 1$$

$$V_{rel} = \frac{3076.05 - 700}{700 \times 0.91269} + 1 = 3.7191$$

$$V_{rel} \text{ at 700 psia} = 3.7191$$

### 3.6.2. Oil Laboratory Experiment

**3.6.2.1. Flash Liberation Experiment.** This is similar to the CCE discussed in section 3.6.1.2. It is also called *flash vaporization* or *flash expansion* when the fluid sample is crude oil instead of gas. During the flash liberation experiment, the entire system composition remains unchanged, hence making it a CCE or CME. A flash liberation experiment represents the reservoir depleting below the bubble point pressure when critical gas saturation has not been reached (gas is immobile). The hydrocarbon vapor liquid separation process in a separator is best described by the flash liberation experiment. Bubble point pressure and isothermal fluid compressibility are very important results from a flash liberation experiment.

The experiment begins with the pressure in PVT cell being raised above the bubble point pressure and

**Table 3.26** Gas Condensate CCE Experiment Results at 267 °F.

Pressure (psia)	Liquid dropout ( $p_{sat}$ Vol) (%)	$\rho_{gas}$ (gm/cc)	$\mu_{gas}$ (cp)	$Z_{vapor}$	Relative volume	$\rho_{oil}$ (g/cc)	$\mu_{oil}$ (cp)	$Z_{liquid}$
3,770.00	0	0.272532	0.0328	0.8559	0.8571			
3,629.29	0	0.265259	0.0318	0.8465	0.8806			
3,488.57	0	0.257684	0.0308	0.8376	0.9065			
3,347.86	0	0.249792	0.0299	0.8292	0.9351			
3,207.14	0	0.241567	0.0289	0.8214	0.9670			
$p_{sat}$ 3,076.05	0	0.233591	0.0279	0.8148	1.0000			
3,066.43	0.22	0.232261	0.0278	0.8150	1.0030	0.47486	0.0840	0.6959
2,925.71	2.77	0.214045	0.0259	0.8180	1.0496	0.49602	0.0922	0.6743
2,785.00	4.45	0.197668	0.0243	0.8212	1.1017	0.51417	0.1007	0.6523
2,644.29	5.61	0.182661	0.0229	0.8246	1.1600	0.53012	0.1098	0.6297
2,503.57	6.44	0.168728	0.0216	0.8285	1.2258	0.54439	0.1194	0.6064
2,362.86	7.04	0.155669	0.0206	0.8328	1.3003	0.55734	0.1298	0.5824
2,222.14	7.47	0.143341	0.0196	0.8375	1.3854	0.56922	0.1410	0.5576
2,081.43	7.76	0.131639	0.0188	0.8427	1.4832	0.58025	0.1532	0.5319
1,940.71	7.96	0.120482	0.0180	0.8484	1.5965	0.59057	0.1665	0.5054
1,800.00	8.08	0.109808	0.0173	0.8547	1.7290	0.60032	0.1811	0.4779

NB: Relative volume =  $\frac{V_{total(T,P)}}{V_{sat}}$ ,  $Y$ -function =  $\frac{p_{sat} - p}{p(V_{rel} - 1)}$ , and percentage liquid dropout =  $100 \frac{V_{liquid}}{V_{sat}}$

**Table 3.27** Y-Function at Pressure Points Below Saturation Pressure.

Pressure below bubble point (pia)	Y-function
3,066.43	1.04226
2,925.71	1.03517
2,785.00	1.0278
2,644.29	1.02031
2,503.57	1.01274
2,362.86	1.00497
2,222.14	0.99708
2,081.43	0.98902
1,940.71	0.98081
1,800.00	0.97244

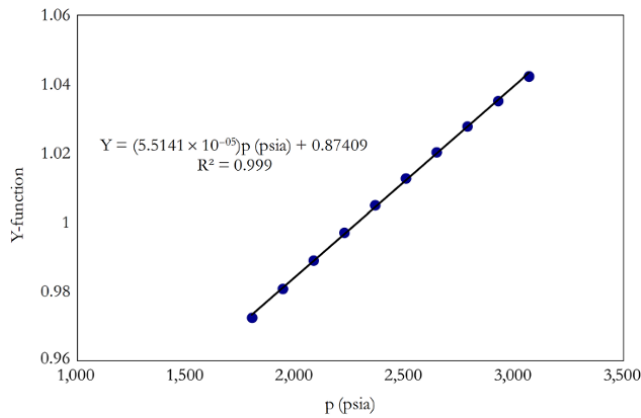


**Figure 3.33** Plot of Y-function against pressure showing line of best of fit and equation.

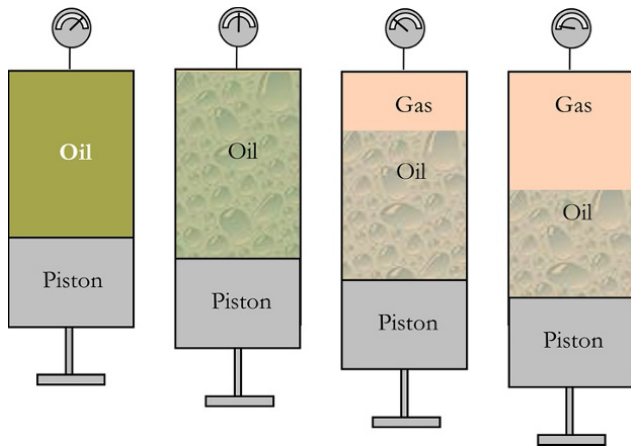


**Figure 3.34** Flash liberation experiment.

decreased in stages, with the pressure and total volume in the cell being measured (Fig. 3.34).

The procedure follows the same method discussed for CCE in section 3.6.1.2. The bubble point corresponds

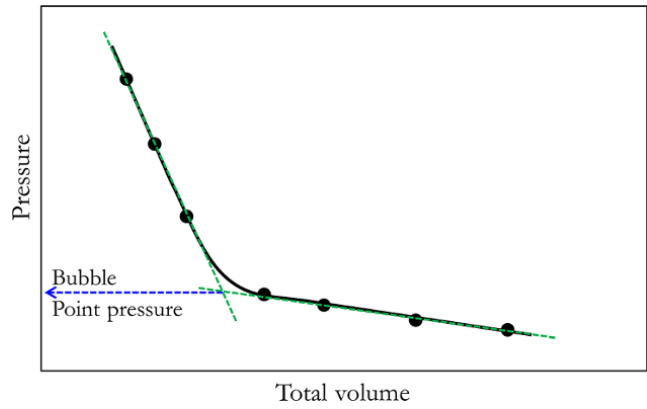


**Figure 3.35** Flash liberation determination of bubble point pressure.

to the point where there is sharp increase in total fluid compressibility, which is due to gas evolution. This can be determined where there is abrupt increase in pressure change with total volume (Fig. 3.35), as discussed for the CCE experiment (section 3.6.1.2).

When the bubble point pressure is reached, liberation of gas makes the compressibility of the total system increase significantly, while below the bubble point the rate of change of pressure with volume in the PVT cell decreases, hence giving an indication of bubble point pressure.

Even in an opaque PVT cell, bubble point pressure can be determined using pressure against total volume or relative volume. In volatile oil, it can be difficult to determine the bubble point pressure using this method, as change in compressibility is subtle and not abrupt, as shown in a plot of pressure against relative volume for the volatile oil flash liberation experiment from Table 3.28 (Fig. 3.36).

**3.6.2.2. Differential Liberation Experiment.** The differential liberation experiment is also called the *differential vaporization experiment* and it best describes a reservoir depleting below the bubble point pressure where critical gas saturation has been reached and gas is mobile. Important properties measured during the differential liberation experiment include  $R_s$ ,  $B_o$ , density of remaining oil, composition of liberated gas, gas compressibility factor, and gas specific gravity.

The experiment involves reducing the pressure of a fluid sample in a PVT cell until saturation pressure is reached; the volume at saturation is then measured. The pressure is subsequently depleted below saturation pressure; the gas produced at each stage is expelled and volume of displaced gas at standard condition is measured (Fig. 3.37).

Fluid properties measured at each pressure depletion stage include specific gravity and volume of remaining

**Table 3.28** Volatile Oil Flash Liberation Experiment Result at 225 °F.

Pressure (psia)	S <sub>liq</sub> (p <sub>sat</sub> vol.) (%)	Relative volume	ρ <sub>o</sub> (g/cc)	μ <sub>o</sub> (cp)	Z <sub>liquid</sub>	ρ <sub>g</sub> (g/cc)	μ <sub>o</sub> (cp)	Z <sub>vapor</sub>
5,014.70	100.00	0.9686	0.5338	0.2016	1.1180			
4,728.99	100.00	0.9756	0.5314	0.1971	1.0619			
4,443.27	100.00	0.9831	0.5290	0.1926	1.0054			
4,157.56	100.00	0.9912	0.5265	0.1881	0.9485			
p <sub>sat</sub> 3,882.59	100.00	0.9995	0.5241	0.1836	0.8932			
3,586.13	94.47	1.0341	0.5431	0.1983	0.8508	0.2093	0.0265	0.8834
3,300.41	89.74	1.0768	0.5609	0.2144	0.8078	0.1917	0.0246	0.8727
3,014.70	85.63	1.1307	0.5773	0.2315	0.7619	0.1743	0.0228	0.8647
2,728.99	81.97	1.1999	0.5927	0.2499	0.7129	0.1570	0.0213	0.8596
2,443.27	78.65	1.2904	0.6071	0.2700	0.6607	0.1398	0.0199	0.8574
2,157.56	75.57	1.4119	0.6209	0.2922	0.6049	0.1226	0.0186	0.8585
1,871.84	72.64	1.5792	0.6343	0.3170	0.5451	0.1056	0.0176	0.8628
1,586.13	69.80	1.8194	0.6473	0.3453	0.4810	0.0888	0.0166	0.8707
1,300.41	66.94	2.1830	0.6605	0.3783	0.4119	0.0723	0.0158	0.8822
1,014.70	63.98	2.7797	0.6741	0.4182	0.3372	0.0561	0.0150	0.8975
5,014.70	100.00	0.9686	0.5338	0.2016	1.1180			

NB: Relative volume =  $\frac{V_{total(T,P)}}{V_{sat}}$  and percentage liquid saturation =  $100 \frac{V_{liquid}}{V_{sat}}$

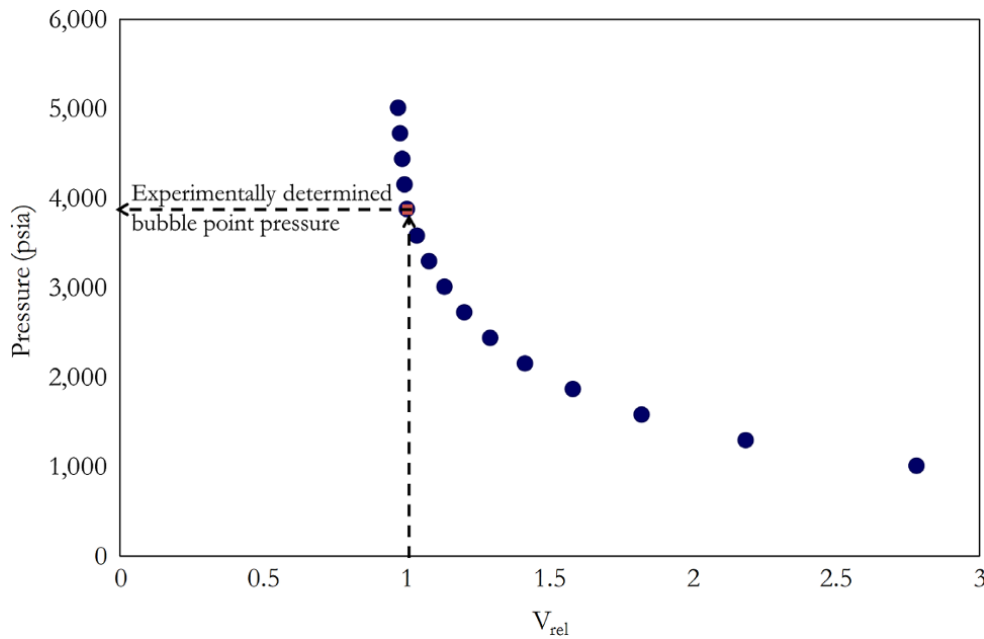


**Figure 3.36** Volatile oil showing subtle change in  $\left(\frac{\partial V_{rel}}{\partial p}\right)_T$  at the bubble point pressure.

oil at stock tank condition. The composition of expelled gas is also collected and measured using, mostly, cryogenic distillation and/or gas chromatographic techniques. Test from differential liberation experiment include:

*Oil Formation Volume Factor*

$$B_o = \frac{V_{oil(T,P)}}{V_{oil(T_{sc}, P_{sc})}} \quad (3.79)$$

*Solution Gas–Oil-Ratio*

$$R_s = \left(\frac{V_{gas(T_{sc}, P_{sc})}}{V_{oil(T_{sc}, P_{sc})}}\right)_{T,P} \quad (3.80)$$

*Gas Formation Volume Factor*

$$B_g = \frac{V_{gas(T,P)}}{V_{gas(T_{sc}, P_{sc})}} \quad (3.81)$$

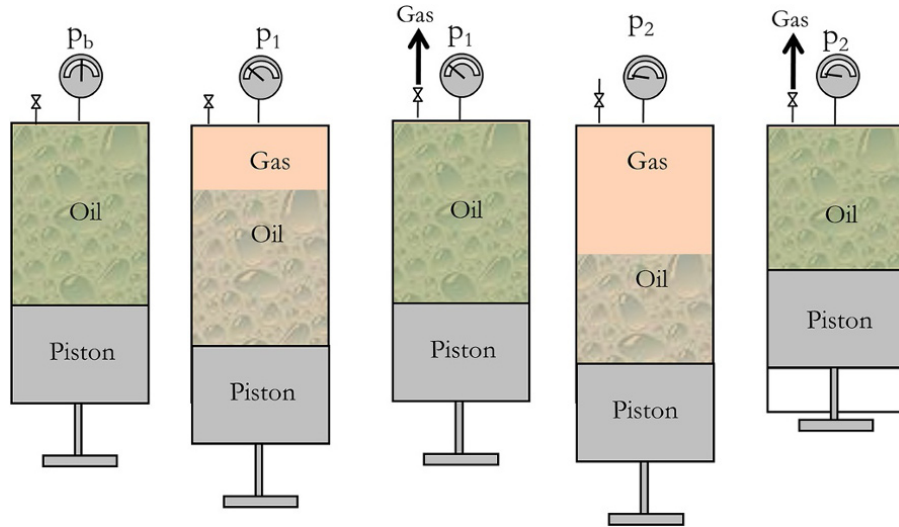


Figure 3.37 The differential liberation experiment.

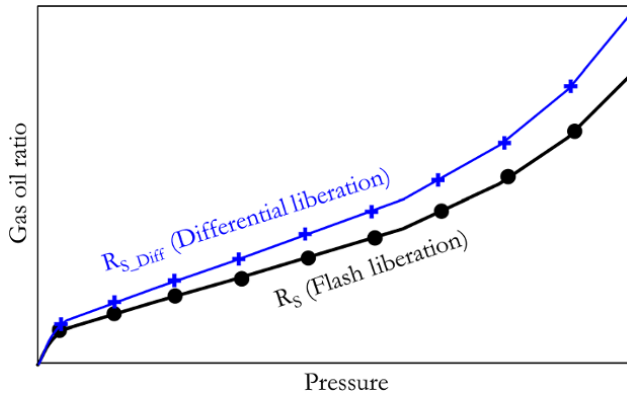


Figure 3.38  $R_s$  from differential liberation test and flash liberation experiment.

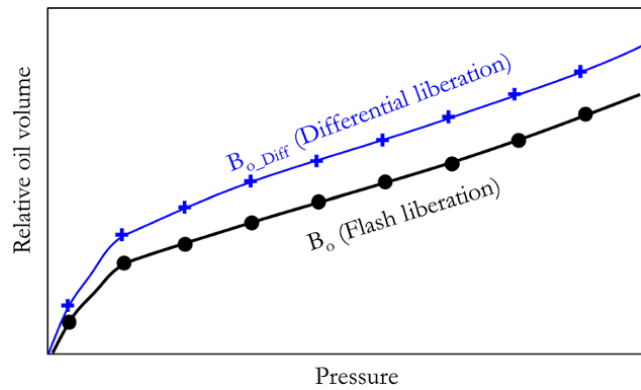


Figure 3.39  $B_o$  from differential liberation test and flash liberation experiment.

Differential liberation and flash liberation have different equilibrium separation pathways, hence properties, of each phase; the cumulative gas recovered at standard conditions and the final volume of equilibrium oil will be different. Though flash liberation often yields smaller oil volumes than differential liberation, this is not true in all cases. In single stage gas–oil separation (flash liberation), more intermediates tend to be expelled with the recovered gas compared to stage separation (differential liberation). In the differential vaporization test, part of the intermediates remains in contact with the oil phase in each stage. Flash liberation test in volatile crude oil will generally yield smaller final equilibrium oil volume than corresponding differential liberation. Fig. 3.38 and Fig. 3.39 show generalized comparison of flash and differential  $R_s$  and  $B_o$ , respectively.

Material balance calculations relate fluid at reservoir condition with that at separator condition, which is closer

to the flash experiment than differential liberation. Using the differential liberation test instead of the separator test can cause errors as high as 25% in hydrocarbon reserve calculations.

Where differential liberation test data are to be used for material balance purposes, they have to be adjusted to equivalent separator conditions.

Oil formation volume ( $B_o$ ) from the flash test, which should be used for material balance, can be determined from differential liberation test using:

$$B_o = B_{o\_Diff} \frac{B_{o\_Bubble}}{B_{o\_Bubble\_Diff}} \quad (3.82)$$

Solution gas–oil ratio ( $R_s$ ) below the bubble point by the flash test can also be derived from the differential liberation test

**Table 3.29** Volatile Oil Differential Liberation Experiment Result at 225°F.

Pressure (psia)	Relative volume	$\rho_o$ (g/cc)	$\mu_o$ (cp)	$B_o$ (rb/stb)	$Z_{liquid}$	$Z_{vapor}$	$\mu_g$ (cp)	$B_g$ (ft <sup>3</sup> /scf)	$R_s$ (scf/stb)
4,999.70	1.0000	0.5307	0.1979	2.2361	1.1117				2,197.80
4,812.70	1.0048	0.5291	0.1950	2.2468	1.0753				2,197.80
4,627.70	1.0098	0.5275	0.1922	2.2580	1.0391				2,197.80
4,417.70	1.0157	0.5257	0.1889	2.2712	0.9977				2,197.80
4,207.70	1.0220	0.5239	0.1856	2.2852	0.9562				2,197.80
3,882.59	1.0324	0.5210	0.1804	2.3085	0.8913	0.8981	0.0285	0.0045	2,197.80
3,856.70	1.0268	0.5229	0.1817	2.2959	0.8879	0.8981	0.0285	0.0045	2,173.39
3,827.70	1.0204	0.5249	0.1832	2.2816	0.8840	0.8967	0.0283	0.0045	2,146.49
3,295.70	0.9213	0.5596	0.2121	2.0602	0.8063	0.8752	0.0245	0.0051	1,723.80
2,806.70	0.8493	0.5872	0.2420	1.8991	0.7258	0.8633	0.0217	0.0060	1,411.70
2,303.70	0.7877	0.6124	0.2772	1.7614	0.6328	0.8596	0.0193	0.0072	1,141.63
1,801.70	0.7344	0.6351	0.3181	1.6423	0.5277	0.8646	0.0174	0.0093	908.34
1,301.70	0.6869	0.6561	0.3667	1.5360	0.4086	0.8788	0.0159	0.0131	701.27
804.70	0.6417	0.6766	0.4273	1.4350	0.2728	0.9020	0.0146	0.0217	509.93
297.70	0.5870	0.7016	0.5236	1.3126	0.1116	0.9377	0.0132	0.0610	298.23
14.70	0.4791	0.7454	0.7649	1.0713	0.0064	0.9880	0.0101	1.3027	0.00

$$R_s = R_{s\_Bubble} - (R_{s\_Bubble\_Diff} - R_{s\_Dif}) \frac{B_{o\_Bubble}}{B_{o\_Bubble\_Diff}} \quad (3.83)$$

where subscript *Diff* represents the differential liberation experiment while subscript *Bubble* represents bubble point condition.

Table 3.29 shows examples of the results from a differential liberation experiment.

### 3.6.3. Enhanced Oil Recovery Experiments

Two important experiments for enhanced oil recovery (EOR) using fluid samples are the *solubility swelling test* and the *miscibility test*. EOR methods are described in Chapter 14.

**3.6.3.1. Solubility Swelling Test.** The solubility swelling test (or swelling test) is a single-contact phase behavior experiment measuring the solubility of injection gas or solvent in a crude oil sample. It is called a swelling test as dissolution of injected gas into a PVT cell with an oil sample causes an increase in the volume of the oil sample. It is important in screening of miscible gas flooding for enhanced oil recovery.

The swelling test would normally involve creating 5–10 mixtures of injected gas and reservoir oil. Some of the samples will be mixed to ensure the fluid has a bubble point while some will be mixed to ensure the fluid has a dew point. CCE experiments are then conducted on each of the samples formed from injected gas and reservoir oil. Results of the CCE experiments, which include saturation pressure and oil relative volumes, are then reported. The viscosity of the mixture of fluids at reservoir temperature

is measured at different pressures. Flash experiments are also carried out on the different mixture samples to determine phase separation and hydrocarbon extraction following gas injection. Another important experiment carried out during the solubility swelling test is the measurement of asphaltene content before and after gas injection, to determine possibilities of asphaltene deposition, as gas injection can affect the stability of crude oil.

**3.6.3.2. Slim-Tube Experiments.** Slim-tube experiments are used for determining *minimum miscibility pressure* (MMP), which is the lowest pressure at a given temperature and composition at which first or multiple contact miscibility can be achieved. Miscibility is achieved when the interfacial tension between the mixed fluids is zero, as such there is no interface.

The setup for determining MMP consist of either a column or coiled steel tub, often about 5–40 ft in length with a diameter of about 0.24–0.34 inches filled with glass beads or sand with known porosity and permeability after packing in the column before commencement of the experiment (Fig. 3.40).

The experiment involves injecting gas of known composition at a rate of about 0.1 cc/min to displace oil, with collection of evolved products from the column. Volume and mass of the evolved gas are measured. Gas flow meters connected to separator gas can be used for measuring the gas flow rate. Residual liquid volume and density are measured at a predetermined frequency, such as hourly or continuously, using an inline densitometer. The pressure in the column/coil can be maintained by an installing a back-pressure regulator (BPR) at the outlet of the column.



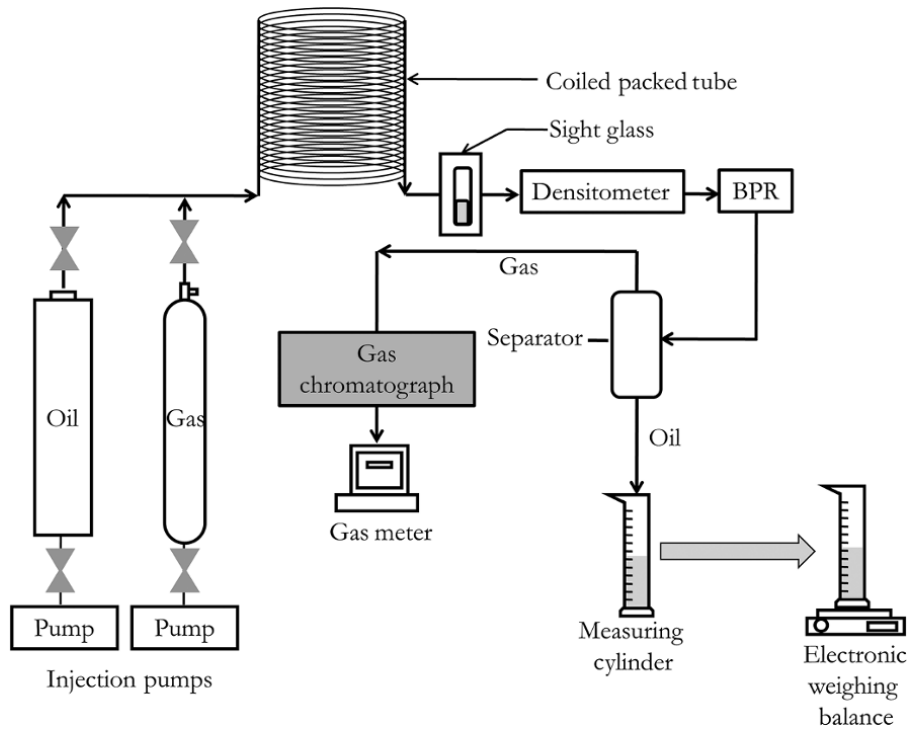


Figure 3.40 Experimental setup for the slim-tube test.

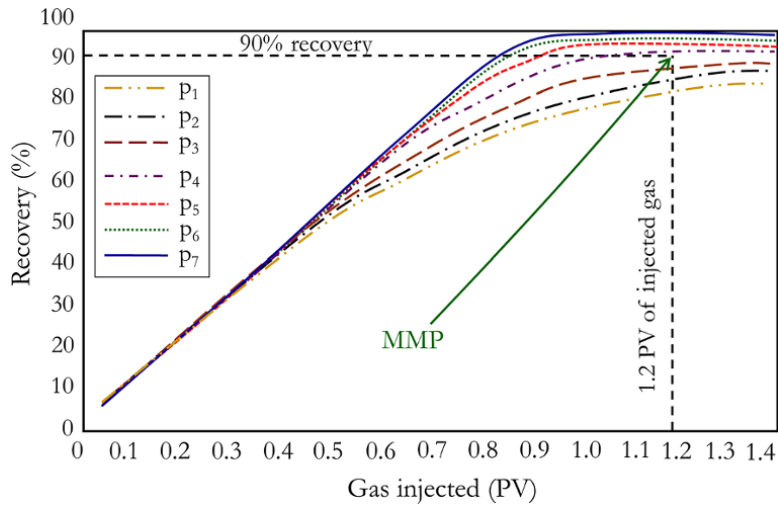


Figure 3.41 Plot of recovery against pore volume (PV) of gas injected.

A PVT cell with window and camera are useful in the experimental setup for visual observations, especially the occurrence of gas breakthrough.

A sharp rise in GOR and reduction in residual liquid density is an indication of gas breakthrough. Gas injection is carried out until 1.2–1.4 pore volume (PV) of gas is

injected into the column or coil, after which the column/coil is blown down and residual oil in the column or coil also collected and weighed.

At pressures above the MMP, injected gas is assumed to be miscible with reservoir fluid. The MMP has different definitions from experiment; however, the most common

and widely accepted definition is the pressure at which the recovery is 90% when 1.2 pore volumes of gas have been injected. The region of the MMP is shown in the plot of recovery against the pore volume of gas injected in Fig. 3.41.

The correct MMP may be difficult to determine from a plot of recovery against pore volume of gas injected in Fig. 3.41, as the test may not have been carried out at the pressure corresponding to the MMP; hence, it may require some form of interpolation. A plot of percentage recovery at 1.2 PV of injected gas against test pressure can be used to determine the MMP from the intersection of the immiscible line and the multiple-contact miscible lines, as shown in Fig. 3.42.

**Exercise 3.10**

1. Describe the following reservoir fluid types: black oil, volatile oil, retrograde gas, wet gas, and dry gas.
2. Draw a typical fluid phase envelope showing regions corresponding to the different fluid types.
3. Why is the fluid phase envelope important to reservoir engineers?
4. Show that the isothermal compressibility of an ideal gas is the reciprocal of pressure.
5. Gas and liquid phase composition was measured from a two-stage separator illustrated in Fig. 3.43. Calculate the composition of the stream from the wellhead.

The solution to q.5 above is summarized in Fig. 3.44.

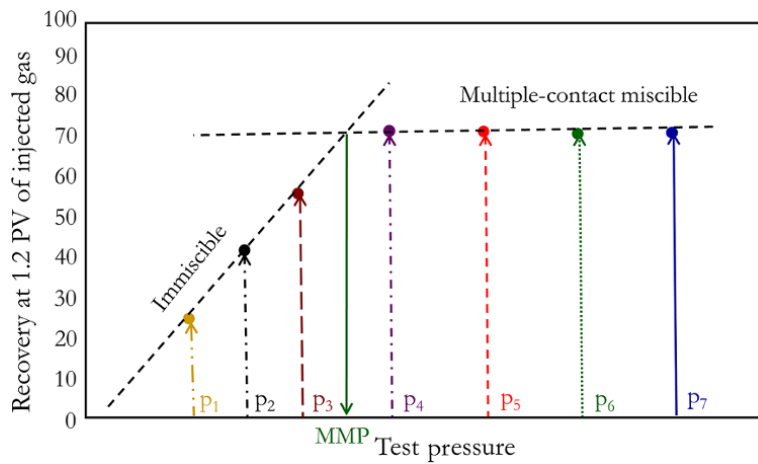


**Figure 3.42** Plot of recovery at 1.2 pore volumes of injected gas against test pressure showing the MMP.

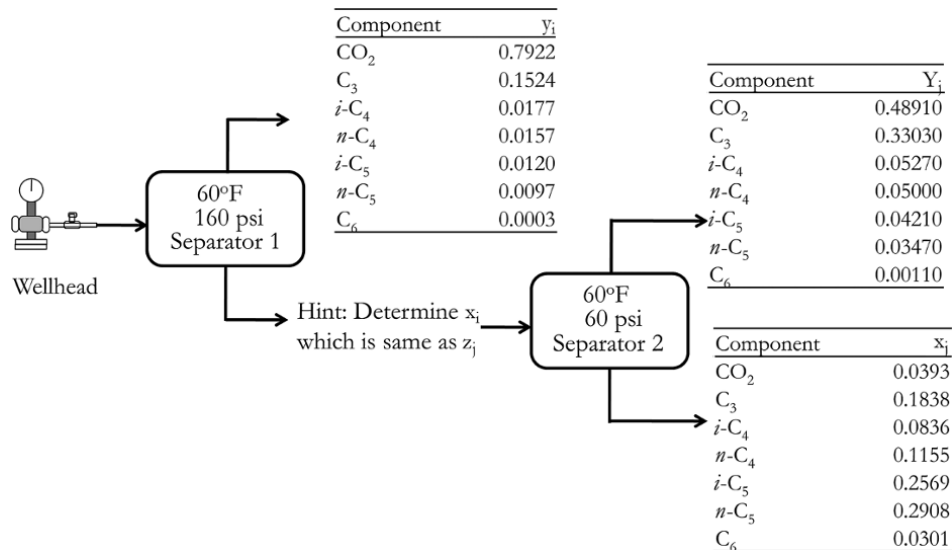


**Figure 3.43** Two-stage separator composition.

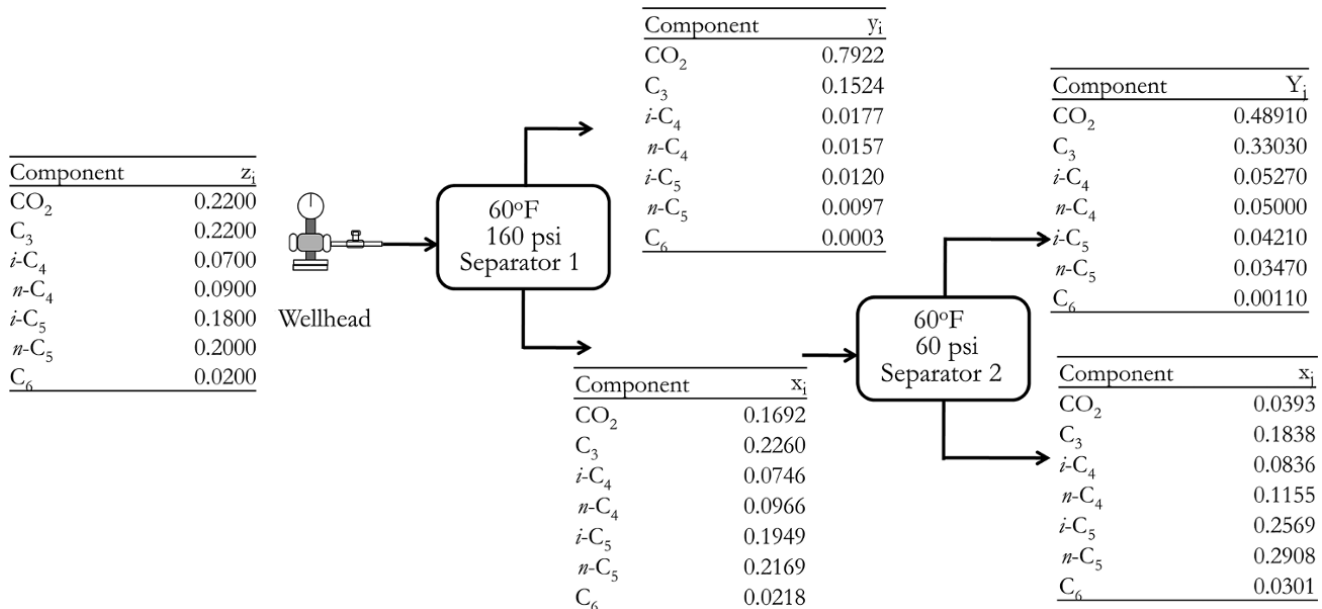


Figure 3.44 Solution to exercise 3.10.

## REFERENCES

- Dean, D. and Stiel, L., 1958. The viscosity of nonpolar gas mixtures at moderate and high pressures. *AIChE Journal*, **4**, 430–436.
- Edmister, W., 1958. Applied hydrocarbon thermodynamics, Part 4: compressibility factors and equations of state. *Petroleum Refinery*, **37**, 173–179.
- Hadden, J.T., 1953. Convergence pressure in hydrocarbon vapor-liquid equilibria. Chemical Engineering Progress Symposium Series, **49**(7), 53.
- Hall, K. and Yarborough, L., 1973. A new equation of state for Z-factor calculations. *Oil & Gas Journal*, **71**(25), 82.
- Kareem, L., Iwalewa, T., and Al-Marhoun, M., 2016. New explicit correlation for the compressibility factor of natural gas: linearized z-factor isotherms. *Journal of Petroleum Exploration and Production Technology*, **6**(3), 481–492.
- Lohrenz, J., Bray, B., and Clark, C., 1964. Calculating viscosities of reservoir fluids from their compositions. *Journal of Petroleum Technology*, **16**(10), 1171–1176.
- Peng, D.Y. and Robinson, D.B., 1976. A new two-constant equation of state. *Industrial & Engineering Chemistry Fundamentals*, **15**, 59–64.
- Redlich, O. and Kwong, J.N.S., 1949. On the thermodynamics of solutions: V. An equation of state: fugacities of gaseous solutions. *Chemistry Review*, **44**, 233–244.
- Riazi, M.R. and Daubert, T.E., 1987. Characterizing parameters for petroleum fractions. *Industrial & Engineering Chemistry Research*, **26**(24), 755–759.
- Sinnot, R., 2005. *Chemical Engineering Design, Coulson & Richardson's Chemical Engineering*. Elsevier Butterworth-Heinemann.
- Soave, G., 1972. Equilibrium constants from a modified Redlich-Kwong equation of state. *Chemical Engineering Science*, **27**, 1197–1203.
- Standing, M., 1947. A pressure-volume-temperature correlation for mixtures of California oil and gases. *Drilling and Production Practice, API*.
- Standing, M.B., 1979. A set of equations for computing equilibrium ratios of a crude oil/natural gas system at pressures below 1,000 psia. *Journal of Petroleum Technology*, **31**(09), 1193–1195.
- Standing, M. and Katz, D., 1942. Density of natural gases. *American Institute of Mining and Metallurgical Engineers Inc, SPE-942140-G*, **142**, 140–149.
- Vasquez, M. and H.D. Beggs, 1980. Correlations for fluid physical property prediction. *Journal of Petroleum Technology*, **32**(6), 968–970.
- Weinaug, C. and Katz, D., 1943. Surface tensions of methane-propane mixtures. *Industrial and Engineering Chemistry*, **35**(2), 239–246.
- Whitson, C.H. and Torp, S.B., 1983. Evaluating constant volume depletion data. *Journal of Petroleum Technology*, **35**(03), 610–620.
- Wilson, G., 1968. A modified Redlich-Kwong equation of state applicable to general physical data calculations. *65th AIChE National meeting*, Paper No. 15C.

## BIBLIOGRAPHY

- Ahmed, T., 1989. *Hydrocarbon Phase Behavior, Contributions in Petroleum Geology & Engineering*. Gulf Publishing Company.
- American Petroleum Institute (API), 2003. *Recommended Practice for Sampling Petroleum Reservoir Fluids*, Washington, DC: API.
- Archer, J. and Wall, C., 1999. *Petroleum Engineering Principles and Practice*. Dordrecht/Boston: Kluwer Academic Publishers Group.

- Brooks, B., 1955. *The Chemistry of Petroleum Hydrocarbons*. Reinhold.
- Coats, K., 1980. An equation of state compositional model. *Society of Petroleum Engineers Journal*, **20**(5), 363–376.
- Coats, K. and Smart, G., 1986. Application of a regression-based EOS PVT program to laboratory data. *SPE Reservoir Engineering*, **1**(3), 277–299.
- Hoffmann, A.E., Crump, J.S., and Hocott, C., 1953. Equilibrium constants for a gas-condensate system. *Transactions of the AIME*, **198**, 1–10.
- Kwak, T.Y., Benmekki, E., and Ransoori, C.A., 1986. van der Waals mixing rules for cubic equations of state, applications for supercritical fluid extraction modeling and phase equilibrium calculations. *Chemical Engineering Science*, **41**(5), 1303–1309.
- Martin, J., 1983. PVT Analysis of a new cubic-perturbed, hard-sphere equation of state. *AIChE Journal*, **29**(3), 369–372.
- McCain Jr., W. and Alexander, R., 1992. Sampling gas-condensate wells. *SPE Reservoir Engineering*, **7**(3), 358–362.
- Moses, P., 1986. Engineering applications of phase behavior of crude oil and condensate. *Journal of Petroleum Technology*, **38**, 715–723.
- Muller, E. and A-Fuentes, C., 1989. General expressions for multi-component fugacity coefficients and residual properties from cubic equation of state. *Latin American Applied Research*, **19**, 99–109.
- Whitson, C. and Brulé, M.R., 2000. *Phase Behavior*, SPE Monograph Series, Vol. 20, Richardson, TX: Society of Petroleum Engineers.

# 4

## Equations of States

As discussed in Chapter 3, important Equation of State (EOS) models for predicting hydrocarbon phase properties are the: *Redlich–Kwong Equation of State* [Redlich and Kwong, 1949], shown in equation (4.1); *Soave–Redlich–Kwong Equation of State* [Soave, 1972], shown in equation (4.2); and the *Peng Robinson Equation of State* [Peng and Robinson, 1976], shown in equation (4.3). These EOS models can be generally represented in the form that describes the pressure of a system as a difference between repulsive and attractive pressure terms:  $p = p_{\text{repulsive}} - p_{\text{attractive}}$ .

$$p = \frac{RT}{(v-b)} - \frac{a}{v(v+b)T^{0.5}} \quad (4.1)$$

$$p = \frac{RT}{v-b} - \frac{a(T)}{v(v+b)} \quad (4.2)$$

$$p = \frac{RT}{v-b} - \frac{a(T)}{v(v+b) + b(v-b)} \quad (4.3)$$

where specific volume = volume/number of moles:

$$v = \frac{V}{n}$$

Consistent units for parameters in EOS calculations were summarized in Table 3.3.

EOS models defined by equations (4.1)–(4.3) are termed two-parameter equations of state; they depend on two characteristic parameters,  $a$  and  $b$ , determined experimentally or derived from other fluid component properties. Two-parameter equations of state were originally formulated to deal with the limitation of the ideal gas equation and, subsequently, extended to calculate state properties of liquid hydrocarbons.

### 4.1. GENERALIZED REPRESENTATION OF EOS MODELS

Martin [1979] showed that all cubic equations of state can be expressed in terms of the compressibility factor ( $Z$ ):

$$Z^3 + E_2 Z^2 + E_1 Z + E_0 = 0 \quad (4.4)$$

where

$$E_2 = (m_1 + m_2 - 1)B - 1$$

$$E_1 = A - (2(m_1 + m_2) - 1)B^2 - (m_1 + m_2)B$$

$$E_0 = -(AB + m_1 m_2 B^2 (B + 1))$$

where  $m_1$  and  $m_2$  depend on the EOS model as summarized in Table 4.1 and  $Z$  is defined as:

$$Z = \frac{pV}{RT} \quad (4.5)$$

For a single component:

$$A = \frac{a(T)p}{(RT)^2} \quad (4.6)$$

$$B = \frac{bP}{RT} \quad (4.7)$$

Parameters  $a(T)$ ,  $b$ ,  $m_1$ ,  $m_2$ ,  $E_2$ ,  $E_1$ , and  $E_0$  depend on the EOS model and are defined in Table 4.1.

$a(T)$  can be expressed generally as:

$$a(T) = \Omega_A \frac{R^2 T_c^2}{P_c} \alpha(T) \quad (4.8)$$

and  $b$  as:

$$b = \Omega_B \frac{RT_c}{P_c} \quad (4.9)$$

where  $\Omega_A$ ,  $\Omega_B$ , and  $\alpha(T)$  depend on the EOS model and are shown in Table 4.2.

**Table 4.1** Parameters  $a(T)$ ,  $b$ ,  $m_1$ ,  $m_2$ ,  $E_2$ ,  $E_1$ , and  $E_0$  for Different EOS Models [Adapted from Martin, 1979; Coats, 1980].

EOS	$m_1$	$m_2$	$E_2$	$E_1$	$E_0$	$a(T)$	$b$
Redlich–Kwong (RK)	0	1	-1	$A - B - B^2$	-AB	$\Omega_A \frac{R^2 T_c^2}{P_c} \alpha(T)$	$\Omega_B \frac{RT_c}{P_c}$
Soave–Redlich–Kwong (SRK)	0	1	-1	$A - B - B^2$	-AB	$\Omega_A \frac{R^2 T_c^2}{P_c} \alpha(T)$	$\Omega_B \frac{RT_c}{P_c}$
Peng Robinson (PR)	$1 + \sqrt{2}$	$1 - \sqrt{2}$	$-1 + B$	$A - 2B - 3B^2$	$-AB + B^2 + B^3$	$\Omega_A \frac{R^2 T_c^2}{P_c} \alpha(T)$	$\Omega_B \frac{RT_c}{P_c}$

**Table 4.2** Parameters  $\Omega_A$ ,  $\Omega_B$ , and  $\alpha(T)$  for Different EOS Models [Adapted from Martin, 1979; Coats, 1980].

EOS	$\Omega_A$	$\Omega_B$	$\alpha(T)$
Redlich–Kwong (RK)	0.42748	0.08664	$T^{-0.5}$
Soave–Redlich–Kwong (SRK)	0.42748	0.08664	$[1 + (0.48 + 1.574\omega - 0.176\omega^2)(1 - T_r^{0.5})]^2$
Peng Robinson (PR)	0.45724	0.07779	$[1 + (0.3746 + 1.5423\omega - 0.2699\omega^2)(1 - T_r^{0.5})]^2$ for $\omega < 0.49$ $[1 + (0.3746 + 1.485030\omega - 0.164423\omega^2 + 0.01666\omega^3)(1 - T_r^{0.5})]^2$ for $\omega > 0.49$

The original Redlich–Kwong (RK) EOS expressed in equation (4.1) is:

$$p = \frac{RT}{(v-b)} - \frac{a}{v(v+b)T^{0.5}}$$

Then redefined as:

$$p = \frac{RT}{(v-b)} - \frac{a(T)}{v(v+b)} \quad (4.10)$$

where  $a(T) = \frac{a}{T^{0.5}}$  to conform with the generalized EOS defined in equation (4.4).

As such,  $\alpha(T)$  in equation (4.8) for the RK EOS is  $\frac{1}{T^{0.5}}$ , as shown in Table 4.2.

For pure substances, from equation (4.6):

$$A = \frac{a(T) p}{(RT)^2}$$

Also from Table 4.1,  $a(T) = \Omega_A \frac{R^2 T_c^2}{P_c} \alpha(T)$ , and substituting into expression for A above:

$$A = \Omega_A \frac{(p/p_c)}{(RT/RT_c)^2} \alpha(T)$$

$$A = \Omega_A \frac{P_r}{T_r^2} \alpha(T) \quad (4.11)$$

From equation (4.7):

$$B = \frac{bP}{RT}$$

Also from Table 4.1,  $b = \Omega_B \frac{RT_c}{P_c}$ , and substituting into expression for B above:

$$B = \Omega_B \frac{(p/p_c)}{(RT/RT_c)}$$

$$B = \Omega_B \frac{P_r}{T_r} \quad (4.12)$$

The Peng Robinson (PR) EOS (equation (4.3)), has become the most popular EOS for petroleum hydrocarbons systems in the petroleum industry. Predictive capabilities of the PR-EOS and the SRK-EOS are close. However, the PR-EOS has been shown to have better predictive capabilities for near critical hydrocarbons such volatile oil and gas condensates.

Characteristic parameters in the RK, SRK, and PR equations of state are: parameter a, which is dependent on critical properties and the acentric factor, and parameter b, which is dependent on critical properties only.

## 4.2. EOS MODELS FOR MULTICOMPONENTS

Cubic EOS models, including PR, were originally formulated for pure substances. However, they have been modified to suit mixtures. In order to use cubic EOS for mixtures, some form of average mixture properties will have to be used in the EOS models.

### 4.2.1. Simple Mixing Rule

The simplest approach for extending EOS models to hydrocarbon mixtures is using the *simple mixing rule*, which involves using mole fraction weighted-averages of EOS parameters. Using the simple mixing rule, parameter a can be defined as:

$$a = \sum_i^N x_i a_i \quad (4.13)$$

where  $a_i$  is defined in Table 4.1 for each component  $i$ .

Also, using the simple mixing rule, parameter  $b$  will be defined as:

$$b = \sum_i^N x_i b_i \quad (4.14)$$

where  $b_i$  is defined in Table 4.1 for each component  $i$ .

From equation (4.6):

$$A = \frac{a(T) p}{(RT)^2}$$

and substituting  $a$  from equation (4.13) into the expression for  $A$  above:

$$A = \frac{p}{(RT)^2} \sum_i^N x_i a_i(T)$$

Also from Table 4.1:

$$a_i(T) = \Omega_A \frac{R^2 T_{ci}^2}{P_{ci}} \alpha_i(T)$$

Therefore:

$$\begin{aligned} A &= \frac{p}{(RT)^2} \sum_i^N x_i \left( \Omega_A \frac{R^2 T_{ci}^2}{P_{ci}} \alpha_i(T) \right) \\ A &= \Omega_A \frac{p}{T^2} \sum_i^N \left( x_i \frac{T_{ci}^2}{P_{ci}} \alpha_i(T) \right) \\ A &= \Omega_A \sum_i^N \left( x_i \frac{P_{ri}}{T_{ri}^2} \alpha_i(T) \right) \end{aligned} \quad (4.15)$$

Also from equation (4.7),

$$B = \frac{bP}{RT}$$

substituting  $b$  from equation (4.14) into the expression for  $B$ :

$$B = \frac{p}{RT} \sum_i^N x_i b_i$$

from Table 4.1:

$$b_i = \Omega_B \frac{RT_{ci}}{P_{ci}}$$

Therefore:

$$\begin{aligned} B &= \frac{p}{RT} \sum_i^N x_i \Omega_B \frac{RT_{ci}}{P_{ci}} \\ B &= \Omega_B \frac{p}{T} \sum_i^N x_i \frac{T_{ci}}{P_{ci}} \\ B &= \Omega_B \sum_i^N x_i \frac{P_{ri}}{T_{ri}} \end{aligned} \quad (4.16)$$

The simple mixing rule approach, although straightforward, is not commonly used because it does not account for the molecular interactions of constituent species and can lead to poor prediction of fluid properties.

#### 4.2.2. van der Waals Mixing Rule

A more robust approach for extending EOS models to hydrocarbon mixtures is using the *van der Waals (VDW) mixing rule* to determine parameters  $a$  and  $b$  for hydrocarbon mixtures. This approach is dependent on the composition and molecular interactions of constituent species. EOS parameters using the VDW mixing rule are given as:

$$a = \sum_i^N \sum_j^N x_i x_j a_{ij} \quad (4.17)$$

where

$$a_{ij} = (a_i a_j)^{0.5} (1 - k_{ij}) \quad (4.18)$$

$a_i$  and  $a_j$  represent the  $a(T)$  functions for component  $i$  and  $j$  respectively.

Also:

$$b = \sum_i^N \sum_j^N x_i x_j b_{ij} \quad (4.19)$$

where

$$b_{ij} = \frac{1}{2} (b_i + b_j) (1 - l_{ij}) \quad (4.20)$$

$b_i$  and  $b_j$  represent  $b$  for components  $i$  and  $j$  respectively as defined by Table 4.1.

The VDW mixing approach introduces  $k_{ij}$  (equation (4.18)) and  $l_{ij}$  (equation (4.20)), which relate to the molecular interaction between dissimilar molecules.  $k_{ij}$  and  $l_{ij}$  are the binary interaction parameters/coefficients obtained by fitting EOS model predictions to measured fluid experiments or from empirical relationships.

$l_{ij}$  is often set to zero and the expression for  $b$  in equation (4.19) becomes the mole fraction weighted-average of constituent  $b$ , as shown in equation (4.21):

$$b = \sum_i^N x_i b_i \quad (4.21)$$

Hence, using the van der Waal mixing rule for multicomponents:

$$A = \sum_{j=1}^n \sum_{k=1}^n (x_j x_k A_{jk}) \quad (4.22)$$

where

$$A_{jk} = (1 - k_{jk}) (A_j A_k)^{0.5}$$

and

$$A_j = \Omega_A \frac{p_{ij}}{T_{ij}^2} \alpha_j(T)$$

Also:

$$B = \sum_{j=1}^n x_j B_j \quad (4.23)$$

where

$$B_j = \Omega_B \frac{p_{ij}}{T_{ij}}$$

#### 4.2.3. EOS Model Parameters

*Binary interaction coefficients* ( $k_{ij}$ ) represent a flexible way of modeling EOS predictions to match measured experimental data.

$\Omega_A$  and  $\Omega_B$  are coefficients of  $a(T)$  and  $b$ , which by default are 0.45724 and 0.0778, respectively, for PR-EOS (Table 4.2). However, in EOS modeling software packages, this may be allowed to vary so as to add more flexibility to the EOS modeling predictions when matching experimental data. Allowing  $\Omega_A$  and  $\Omega_B$  to change is a way of changing  $a(T)$  and  $b$  while ensuring that properties such as  $T_c$  and  $p_c$  for pure components do not change in EOS models when matching models to experimental data.

*Acentric (a-centric) factors* are a means of defining the nonsphericity (centricity) of molecules in models. Acentric factor is useful in the description of matter and serves as parameter which can be used in the equation of state to improve match of predicted pressure–volume–temperature (PVT) relationships. *Pitzer* [1955] proposed an acentric factor as:

$$\omega = -\log_{10} \left( \frac{p^{\text{sat}}}{p_c} \right)_{\tau/T_c=0.7} - 1 \quad (4.24)$$

where  $p^{\text{sat}}$  is saturation pressure

**4.2.3.1. Volume Shift EOS Parameter.** The concept of *volume shift* in EOS modeling evolved from inherent limitations of the two-parameter EOS models to predict liquid volumes (and hence liquid densities). Introduction of a third parameter,  $c$  (*volume shift*), solves the difficulty of matching density predicted EOS to measured density. The factor is a systematic “shift” (reduction or increase) in molar volume to force the EOS to match laboratory data. Corrected molar volume ( $v_{\text{corrected}}$ ) due to volume shift is expressed as:

$$v_{\text{corrected}} = v - c \quad (4.25)$$

**Table 4.3** Shift Parameter for Calculating Volume Shift [Adapted from *Jhaveri and Youngren, 1988*].

Component	$S_E$	Component	$S_E$
C <sub>1</sub>	-0.154	<i>n</i> -C <sub>4</sub>	-0.06413
C <sub>2</sub>	-0.1002	<i>i</i> -C <sub>5</sub>	-0.0435
C <sub>3</sub>	-0.08501	<i>n</i> -C <sub>5</sub>	-0.04183
<i>i</i> -C <sub>4</sub>	-0.07935	C <sub>6</sub>	-0.01478

**Table 4.4**  $\psi$  and  $\chi$  for Calculating Shift Parameter [Adapted from *Jhaveri and Youngren, 1988*].

Hydrocarbon type	$\psi$	$\chi$
Paraffins	2.258	0.1823
Naphthenes	3.004	0.2324
Aromatics	2.526	0.2008

$c$  for hydrocarbon mixture is mole fraction weighted-average:

$$c = \sum_{i=1}^N x_i c_i \quad (4.26)$$

where  $c_i = S_{Ei} b_i$  [*Jhaveri and Youngren, 1988*].

The *shift parameter*,  $S_E$ , is defined in Table 4.3.

A more convenient way of determining shift parameter ( $S_{Ei}$ ) is using the correlation defined in equation (4.27):

$$S_{Ei} = 1 - \frac{\psi}{MW^\chi} \quad (4.27)$$

[*Jhaveri and Youngren, 1988*]

where  $MW$  is molecular weight.  $\psi$  and  $\chi$  are parameters defined in Table 4.4.

EOS with parameters  $a$ ,  $b$ , and  $c$  are called three-parameter equation of states. Volume shift affects the  $Z$ -factor and properties derived from the  $Z$ -factor, some of which include: density, GOR, formation volume factor, and relative volume.

#### 4.2.4. Solution of Cubic EOS

Cardano's method [*Kalman, 1987*] of solving cubic equations can be used to solve the generalized EOS in equation (4.4).

$$Z^3 + E_2 Z^2 + E_1 Z + E_0 = 0$$

Defining

$$Q = \frac{(3E_1 - E_2^2)}{9}$$

$$R = \frac{(9E_2 E_1 - 27E_0 - 2E_2^3)}{54}$$



and discriminant

$$D = Q^3 + R^2$$

If  $D > 0$ , the equation has only one root:

$$Z_1 = \sqrt[3]{(R + \sqrt{D})} + \sqrt[3]{(R - \sqrt{D})} - \frac{E_2}{3}$$

If  $D < 0$ , the equation has three real roots:

$$Z_1 = 2\sqrt{-Q} \cos\left(\frac{\theta}{3}\right) - \frac{E_2}{3}; Z_2 = 2\sqrt{-Q} \cos\left[\left(\frac{\theta}{3}\right) + 120^\circ\right] - \frac{E_2}{3} \text{ and } Z_3 = 2\sqrt{-Q} \cos\left[\left(\frac{\theta}{3}\right) + 240^\circ\right] - \frac{E_2}{3}$$

$$\text{where } \cos^{-1}\left(\frac{R}{\sqrt{-Q^3}}\right)$$

If  $D = 0$ , the equation has three real roots, at least two of them equal:

$$Z_1 = 2\sqrt[3]{R} - \frac{E_2}{3}; Z_2 = Z_3 = -\sqrt[3]{R} - \frac{E_2}{3}$$

The largest and smallest value of  $Z$  from the cubic equation are the  $Z$ -factors for vapor and liquid, respectively. The calculated  $Z$  is then used for predicting fluid properties as shown in the next section.

#### 4.2.5. Fluid Property Prediction using EOS

##### Fluid Density

Hydrocarbon fluid density ( $\rho_{HC}$ ) can be determined using:

$$\rho_{HC} = \frac{1}{v} \sum_{i=1}^N MW_i z_i$$

where  $v$  is specific volume,  $z_i$  is hydrocarbon mole fraction for component  $i$ , and  $MW_i$  the molecular weight of component  $i$ . Expressing  $v$  in terms of  $Z$  from equation (4.5) ( $v = \frac{ZRT}{p}$ ) and substituting into the above equation:

$$\rho_{HC} = \frac{p}{Z_{HC}RT} \sum_{i=1}^N MW_i z_i \quad (4.28)$$

$Z_{HC}$  is the  $Z$ -factor for the hydrocarbon mixture.

Liquid hydrocarbon density ( $\rho_{liq}$ ) is, hence:

$$\rho_{liq} = \frac{1}{v_{liq}} \sum_{i=1}^N MW_i x_i$$

where subscript  $liq$  is for liquid phase and  $x_i$  is the mole fraction of component  $i$  in the liquid phase. Expressing  $v$  in terms of  $Z$  from equation (4.5) ( $v = \frac{ZRT}{p}$ ) and substituting into the above equation:

$$\rho_{liq} = \frac{p}{Z_{liq}RT} \sum_{i=1}^N MW_i x_i \quad (4.29)$$

Vapor hydrocarbon density ( $\rho_{vap}$ ) is:

$$\rho_{vap} = \frac{1}{v_{vap}} \sum_{i=1}^N MW_i y_i$$

Expressing  $v$  in terms of  $Z$  from equation (4.5) ( $v = \frac{ZRT}{p}$ ) and substituting into the above equation:

$$\rho_{vap} = \frac{p}{Z_{vap}RT} \sum_{i=1}^N MW_i y_i \quad (4.30)$$

where subscript  $vap$  is for vapor phase and  $y_i$  is the mole fraction of component  $i$  in the vapor phase.

##### Gas Specific Gravity

Gas specific gravity ( $S_g$ ) can be defined as:

$$S_g = \frac{MW_{vap}}{MW_{air}} = \frac{MW_{vap}}{28.96} = \frac{\sum_{i=1}^N MW_i y_i}{28.96} \quad (4.31)$$

##### Gas Formation Volume Factor

Gas formation volume factor ( $B_g$ ) can be expressed as:

$$B_g = \frac{v_{vap}}{v_{sc}} = Z_{vap} \left(\frac{T}{T_{sc}}\right) \left(\frac{p_{sc}}{p}\right) = Z_{vap} \left(\frac{T}{519.67}\right) \left(\frac{14.7}{p}\right) = 0.028287 Z_{vap} \left(\frac{T}{p}\right)$$

$$B_g = 0.028287 Z_{vap} \left(\frac{T}{p}\right) \quad (4.32)$$

##### Oil Formation Volume Factor

Oil formation volume factor ( $B_o$ ) can be expressed as:

$$B_o = \frac{V_{oil}(T, p)}{V_{sc}} = \frac{Z_{Liq} nRT}{p} \bigg/ \frac{Z_{sc} nRT_{sc}}{p_{sc}} = \frac{0.028287 Z_{Liq} T}{Z_{sc} p}$$

where  $V_{oil}(T, p)$  is the volume at reservoir temperature and pressure and  $V_{sc}$  is the volume at standard condition.

$$B_o = \frac{0.028287 Z_{Liq} T}{Z_{sc} p} \quad (4.33)$$

The subscript  $sc$  represents standard condition where  $p_{sc} = 14.7$  psia and  $T_{sc} = 60^\circ F = 519.67^\circ R$  in engineering oil field (EOF) units.

##### Relative Volume

The relative volume of oil ( $V_{rel}$ ) is expressed as:

$$V_{rel} = \frac{V_{oil}(T, p)}{V_{sat}} = \frac{Z_{Liq} nRT}{p} \bigg/ \frac{Z_{sat} nRT_{sat}}{p_{sat}} = \frac{Z_{Liq} T p_{sat}}{Z_{sat} T_{sat} p} \quad (4.34)$$

where  $V_{sat}$  is the volume of liquid hydrocarbon at saturation pressure and the subscript  $sat$  in the equation represents saturation condition.

#### 4.2.6. Matching and Tuning EOS Models

Relative error of match for a given test A can be expressed as:

$$\epsilon_i = \frac{A_i - A(x_i : a)}{A_i} \quad (4.35)$$

The sum of the square of relative errors can then be expressed as:

$$\epsilon^2 = \sum_{i=1}^n \left( \frac{A_i - A(x_i : a)}{A_i} \right)^2 \quad (4.36)$$

$A_i$  is a measured property and  $A(x_i : a)$  is the EOS model estimated property.

Hence, minimizing the sum of square of relative errors,  $\epsilon^2$ , which is the objective function, yields a parameter vector of tuning parameters a.

For multiple test A, B, C etc. the weighted sum of the square of relative errors can be expressed as:

$$\begin{aligned} \epsilon^2 = & w_a \sum_{i=1}^n \left( \frac{A_i - A(x_i : a)}{A_i} \right)^2 + w_b \sum_{j=1}^n \left( \frac{B_j - B(z_j : a)}{B_j} \right)^2 \\ & + w_c \sum_{k=1}^n \left( \frac{C_k - C(z_k : a)}{C_k} \right)^2 + \dots \end{aligned} \quad (4.37)$$

where  $A_i, B_j, C_k, \dots$  = measured properties with data point  $i, j, k, \dots$ , a is a vector of the tuning parameter,  $\epsilon^2$  is the objective function to be minimized,  $w_m$  ( $m = a, b, c, \dots$ ) is a weighting factor for test a, b, c, ...

Hence, minimizing the weighted sum of the square of relative errors,  $\epsilon^2$ , which is the objective function, yields the parameter vector of tuning parameters a for multiple test A, B, C, ...

### 4.3. PRACTICAL STEPS IN TUNING EOS MODEL

The following are important steps for tuning EOS models.

*Step 1:* checking that measured fluid properties are consistent and make physical sense.

For example, an oil sample with a high  $B_o$  (for example, a value greater than 2 bbl/stb), which suggests it is a volatile oil, is not expected to have a low initial producing GOR (for example 500 scf/stb). Also, a fluid with high initial GOR, for example 3,300 scf/bbl, which suggests the fluid is a volatile oil or condensate, is not expected to have

an API gravity as low as 22°, which represents a heavy oil except in a nonequilibrium oil and gas sample. Nonequilibrium gas in contact with oil exists in a very few reservoirs found around the world.

*Step 2:* checking that fluid composition is not contaminated.

Fluid contamination is one of the challenges associated with oil-based mud because of filtrate miscibility with formation hydrocarbon fluids during drilling. Where samples are contaminated, the appropriate fluid decontamination algorithm (Chapter 3.5.1.1) should be used to derive a representative fluid sample for EOS modeling.

*Step 3:* matching EOS with all or components up to highest molecular weight components possible as a quality check to ensure that untuned and ungrouped components from laboratory measurements can reasonably be predicted by the chosen EOS model.

This quality control (QC) step helps to determine accuracy of measured composition for a given laboratory experiment. This step also helps in selecting EOS that would be most suitable for predicting fluid sample properties before and after the sample component grouping/lumping.

*Step 4:* grouping components based on end use.

The grouping of some components to pseudocomponents will depend on the end use of the fluid model. If the fluid model is for surface facility design, components can be left as original measured components with their original compositions. Surface facility modeling software can easily handle a large number of components. In reservoir simulation, it is common to group components to reduce the number components to a number that will yield acceptable simulation run time. Table 4.5 shows an example of component grouping for gas condensate simulation where the objective is to predict gas and condensate recovery, while Table 4.6 shows grouping for an integrated production modeling of reservoir and surface facility, where composition of produced fluid is for production planning of a gas-to-liquid (GTL) plant.

*Step 5:* regression parameter must make physical sense.

For fluid sample define by only pure components (without pseudocomponents), theoretically EOS should match the laboratory without the need to tune EOS. However, this does not happen due to limitations of the EOS models. This leads to the need to change parameters that would enable EOS models to match laboratory predictions. For pure components,  $T_c, p_c, \omega, k_{ij}$ , and  $S_{Ei}$  in the EOS should not be changed, considering that these are inherent component properties of pure constituents and

**Table 4.5** Example of Grouping for Gas Condensate Dropout and Recovery Simulation.

N <sub>2</sub>	CO <sub>2</sub>	C <sub>1</sub>	C <sub>2</sub>	C <sub>3</sub>	i-C <sub>4</sub>	n-C <sub>4</sub>	i-C <sub>5</sub>	n-C <sub>5</sub>	C <sub>6</sub>	C <sub>7+</sub>
----------------	-----------------	----------------	----------------	----------------	------------------	------------------	------------------	------------------	----------------	-----------------

**Table 4.6** Example of Grouping for GTL Production Planning.

N <sub>2</sub>	CO <sub>2</sub>	C <sub>1</sub>	C <sub>2</sub>	C <sub>3</sub>	<i>i</i> -C <sub>4</sub>	<i>n</i> -C <sub>4</sub>	<i>i</i> -C <sub>5</sub>	<i>n</i> -C <sub>5</sub>	C <sub>6</sub>	C <sub>7</sub> –C <sub>9</sub>	C <sub>10</sub> –C <sub>22</sub>	C <sub>23+</sub>
----------------	-----------------	----------------	----------------	----------------	--------------------------	--------------------------	--------------------------	--------------------------	----------------	--------------------------------	----------------------------------	------------------

would not make physical sense to change them. Also, considering that some of these component properties are used for the prediction of non-EOS predictions such as viscosity, changing them in an EOS model may yield erroneous non-EOS property predictions. In a pure component system, the only properties that can be regressed on are  $\Omega_a$  and  $\Omega_b$ . Options that can be considered when changing  $\Omega_a$  and  $\Omega_b$  are: changing  $\Omega_a$ ,  $\Omega_b$  of nonhydrocarbon components only or a global change in  $\Omega_a$  and  $\Omega_b$  such that all constituents have the same values. This makes sense, as what is changing effectively is  $a_i$  and  $b_i$  in the EOS equation while keeping inherent component properties such as  $T_c$ ,  $p_c$ ,  $\omega$ ,  $k_{ij}$  unchanged.

For fluid samples with pseudocomponents, which are transformed components without component library properties, all component properties such as  $T_c$ ,  $p_c$ ,  $\omega$ ,  $k_{ij}$ ,  $S_{Ei}$  can be changed. Considering that a binary interaction coefficient between heavy hydrocarbon molecules is always insignificant, then a binary interaction coefficient that may be considered for regression is that between heavy-end pseudocomponents and light-end molecules. This approach has shown to improve EOS model match with laboratory experiments. Where changing component properties of pseudocomponents violates monotonicity of predicted properties, molecular weight (MW) and specific gravity (SG) of pseudo-components can be considered for regression within reasonable ranges. Other properties that can be considered when there is violation of monotonicity of properties include  $\Omega_a$  and  $\Omega_b$  of pseudocomponents. Problems with regression on  $\Omega_a$  and/or  $\Omega_b$  is when reservoir models with a different  $\Omega_a$  and  $\Omega_b$  are integrated with surface facility models where  $\Omega_a$  and  $\Omega_b$  do not normally change, inconsistencies in property calculation from reservoir to surface facility can occur.

*Step 6:* checking that EOS models match all tests in all fluid experiments within acceptable limits.

Important hydrocarbon fluid experiments useful for tuning EOS models are discussed in Chapter 3. A generally acceptable match is 5% deviation between EOS predicted value and measured value at any given data point. However, important experiments to focus on during tuning would also depend on fluid type and fluid model end use. For example, in gas condensate EOS models, the *liquid dropout test* in the *constant volume depletion* (CVD) experiments is important because condensate dropout during a CVD experiment best describes the near wellbore dynamics of gas condensate systems below dew point.

Matching compressibility factor ( $Z$ ) with minimum error is also important in all EOS modeling, as most fluid properties are derived from the  $Z$ -factor (section 4.2.5).

For volatile oil and gas condensate systems, where liquid recovery at the surface is important in defining the value of the hydrocarbon, matching separator test reasonably is important. Important fluid experiments that can be used to tune EOS models were discussed in Chapter 3.6.

Deviation of 10% may be acceptable in the separator test considering the field separator test result may vary from separator to separator as vapor–liquid equilibrium in field separators depends on separator design.

A viscosity test should be included in a regression match except when significant error in viscosity measurement is suspected. Though viscosity is not an EOS prediction property, viscosity models use component properties such as  $T_c$  and  $p_c$ , which are also key tuning parameters in EOS models.

*Step 7:* checking that all component properties, including those of pseudocomponents, make physical sense.

Property trends are an important quality check for an EOS model. Critical temperature of hydrocarbon molecules should increase with increasing MW and carbon number; critical pressure should decrease with increasing MW and carbon number; acentric factor should increase with increasing MW and carbon number; boiling point should increase with MW and carbon number. These quality checks are important, especially when different fluid samples will be mixed in a reservoir or surface facilities. If component property trends are not consistent and make physical sense, EOS property predictions after fluid mixing will be wrong.

*Step 8:* checking fluid quality plots.

The *Hoffmann quality plot* [Hoffmann *et al.*, 1953] is an important quality plot. It is based on a plot of  $\log(Kp)$  against a characteristic  $F$  function (equation (4.38)), yielding an approximate straight line where liquid and vapor samples are reasonably in equilibrium at the separator conditions (Fig. 4.1). When liquid and vapor are in equilibrium, minimum error is expected in the composition of liquid and vapor. This technique, although originally for quality control (QC) of separator sampled data, has been extended to check for consistency in component properties after grouping components and regression to ensure properties, especially those of pseudocomponents, are consistent.

The Hoffman characterization factor is defined as:

$$F_i = \frac{(\log p_{ci} - \log p_{sc}) \left( \frac{1}{T_{bi}} - \frac{1}{T_{sep}} \right)}{\left( \frac{1}{T_{bi}} - \frac{1}{T_{ci}} \right)} \quad (4.38)$$

where  $T$  is the temperature of interest and corresponds to the separator temperature for QC of separator sampling;  $K$  is an equilibrium constant;  $p_{ci}$  is the critical pressure of

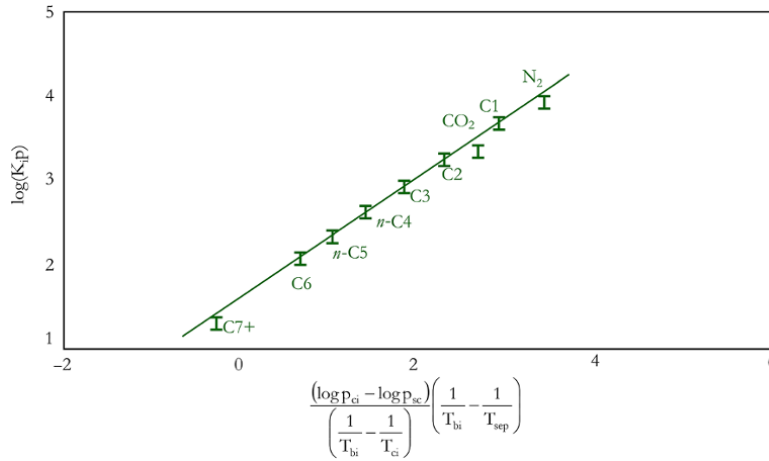


Figure 4.1 Example of Hoffmann quality plot for a gas condensate fluid.

component *i* (psia);  $p_{sc}$  is standard pressure (psia);  $T_{ci}$  is the critical temperature of component *i* in °R;  $T_{bi}$  is the normal boiling point temperature of component *i* in °R; and  $T_{sep}$  is the separator temperature in °R.

4.3.1. Challenges in Tuning EOS Models

Tuning experiments for near a critical fluid such as gas condensate and volatile oil sometimes may create challenges that include absence of a critical point or distortion of the bubble point curve at low temperature and pressure. Distortion of the bubble point curve at low temperature and pressure may not be a problem if the model is not used within temperature range where distortion occurs.

Exercise 4.1 Equation of State (EOS) Calculations for Liquid and Gas Phase

Given a gas condensate composition as shown in Table 4.7 and properties of components as shown in Table 4.8, determine the molar volume of liquid and vapor at 1200 psia and 70 °F using the Peng–Robison equation of state.

Solution.

Step 1: create a table of binary interaction coefficient ( $k_{ij}$ ) as shown in Table 4.9. Binary interaction coefficients are available in literature as tables or correlations.

Step 2: create a table of  $A_{jk}$  (Table 4.10) using

$$A_j = \Omega_A \frac{p_{ij}}{T_{ij}^2} \alpha_j(T) \text{ and } A_{jk} = (1 - k_{jk})(A_j A_k)^{0.5}$$

Step 3: create a table of  $x_j x_k$  (Table 4.11).

Step 4: create a table of  $x_j x_k A_{jk}$  (Table 4.12).

Table 4.7 Fluid Composition for Exercise 4.1.

Component	Mole fraction
N <sub>2</sub>	0.003
CO <sub>2</sub>	0.022
C <sub>1</sub>	0.706
C <sub>2</sub>	0.108
C <sub>3</sub>	0.049
n-C <sub>4</sub>	0.030
n-C <sub>5</sub>	0.014
C <sub>6</sub>	0.009
C <sub>7+</sub>	0.059

Table 4.8 Component Properties of Fluid for Exercise 4.1.

Component	$T_{ci}$ (°R)	$p_{ci}$ (psi)	$\omega_i$
CO <sub>2</sub>	547.90	1,071.00	0.2250
N <sub>2</sub>	227.60	493.00	0.0400
C <sub>1</sub>	343.37	667.80	0.0104
C <sub>2</sub>	550.09	707.80	0.0986
C <sub>3</sub>	666.01	616.30	0.1524
i-C <sub>4</sub>	734.98	529.10	0.1848
n-C <sub>4</sub>	765.65	550.70	0.2010
i-C <sub>5</sub>	829.10	490.40	0.2223
n-C <sub>5</sub>	845.70	488.60	0.2539
C <sub>6</sub>	913.70	436.90	0.3007
C <sub>7+</sub>	1,290.00	263.00	0.5340

Sum all element in Table 4.12 ( $x_j x_k A_{jk}$ ) to get A. A = 0.38.

Step 5: determine B (Table 4.13):

$$B_j = \Omega_B \frac{p_{rj}}{T_{rj}} \text{ and } B = \sum_{j=1}^n x_j B_j$$

$$B = 0.056759819$$

Step 6: determine the coefficient in the generalized EOS equation, equation (4.4):

**Table 4.9** Binary Interaction Coefficient ( $k_{ij}$ ).

	k-N <sub>2</sub>	k-CO <sub>2</sub>	k-C <sub>1</sub>	k-C <sub>2</sub>	k-C <sub>3</sub>	k-n-C <sub>4</sub>	k-n-C <sub>5</sub>	k-C <sub>6</sub>	k-C <sub>7+</sub>
k-N <sub>2</sub>	0								
k-CO <sub>2</sub>	0.1241	0							
k-C <sub>1</sub>	0.14	0.0078	0						
k-C <sub>2</sub>	0.1333	0.0033	0	0					
k-C <sub>3</sub>	0.14	0.0111	0.004	0.017	0				
k-n-C <sub>4</sub>	0.14	0.012	0.002	0.017	0	0			
k-n-C <sub>5</sub>	0.1496	0.0267	0.024	0.0174	0	0	0		
k-C <sub>6</sub>	0.1592	0.0414	0.046	0.0178	0	0	0	0	
k-C <sub>7+</sub>	0.1688	0.0561	0.068	0.0182	0	0	0	0	0

**Table 4.10** Calculated  $A_{jk}$ .

	A-N <sub>2</sub>	A-CO <sub>2</sub>	A-C <sub>1</sub>	A-C <sub>2</sub>	A-C <sub>3</sub>	A-n-C <sub>4</sub>	A-n-C <sub>5</sub>	A-C <sub>6</sub>	A-C <sub>7+</sub>
A-N <sub>2</sub>	0.604682	0.390496	0.496416	0.254978	0.168555	0.124479	0.097625	0.079785	0.033245
A-CO <sub>2</sub>	0.604682	0.425624	0.485928	0.547881	0.392659	0.274354	0.242965	0.219647	0.141783
A-C <sub>1</sub>	0.496416	0.471178	0.436848	0.496416	0.355774	0.289264	0.248583	0.220142	0.199015
A-C <sub>2</sub>	0.254978	0.340317	0.314503	0.355774	0.254978	0.207311	0.178156	0.157773	0.142631
A-C <sub>3</sub>	0.168555	0.274557	0.253706	0.288106	0.203787	0.168555	0.14485	0.128278	0.115967
A-n-C <sub>4</sub>	0.124479	0.235945	0.217828	0.248086	0.175127	0.14485	0.124479	0.110237	0.099658
A-n-C <sub>5</sub>	0.097625	0.206617	0.190036	0.214859	0.155027	0.128278	0.110237	0.097625	0.088256
A-C <sub>6</sub>	0.079785	0.184679	0.169203	0.18986	0.140092	0.115967	0.099658	0.088256	0.079785
A-C <sub>7+</sub>	0.033245	0.11785	0.107546	0.119729	0.090393	0.074857	0.064329	0.056969	0.051502

Numbers in grids with dotted lines represent matrix of  $A_{jk} = (1 - k_{jk})(A_j A_k)^{0.5}$

**Table 4.11** Calculated  $x_j x_k$ .

	x-N <sub>2</sub>	x-CO <sub>2</sub>	x-C <sub>1</sub>	x-C <sub>2</sub>	x-C <sub>3</sub>	x-n-C <sub>4</sub>	x-n-C <sub>5</sub>	x-C <sub>6</sub>	x-C <sub>7+</sub>
	0.003	0.022	0.706	0.108	0.049	0.03	0.014	0.009	0.059
x-N <sub>2</sub>	0.003	0.00001	0.00007	0.00212	0.00032	0.00015	0.00009	0.00004	0.000177
x-CO <sub>2</sub>	0.022	0.00007	0.00048	0.01553	0.00238	0.00108	0.00066	0.00031	0.000198
x-C <sub>1</sub>	0.706	0.00212	0.01553	0.49844	0.07625	0.03459	0.02118	0.00988	0.006354
x-C <sub>2</sub>	0.108	0.00032	0.00238	0.07625	0.01166	0.00529	0.00324	0.00151	0.000972
x-C <sub>3</sub>	0.049	0.00015	0.00108	0.03459	0.00529	0.00240	0.00147	0.00090	0.000441
x-n-C <sub>4</sub>	0.03	0.00009	0.00066	0.02118	0.00324	0.00147	0.00090	0.00042	0.00027
x-n-C <sub>5</sub>	0.014	0.00004	0.00031	0.00988	0.00151	0.00069	0.00042	0.00020	0.000126
x-C <sub>6</sub>	0.009	0.00003	0.00020	0.00635	0.00097	0.00044	0.00027	0.00013	0.000081
x-C <sub>7+</sub>	0.059	0.00018	0.00130	0.04165	0.00637	0.00289	0.00177	0.00083	0.000531

**Table 4.12** Calculated  $x_j x_k A_{jk}$ .

0.00001	0.00003	0.00116	0.00013	0.00005	0.00002	0.00001	0.00001	0.00001	0.00003
0.00003	0.00019	0.00684	0.00075	0.00028	0.00015	0.00006	0.00003	0.00003	0.00015
0.00100	0.00679	0.24743	0.02713	0.01001	0.00526	0.00218	0.00126	0.00126	0.00535
0.00011	0.00075	0.02713	0.00297	0.00110	0.00058	0.00024	0.00014	0.00014	0.00059
0.00004	0.00027	0.00997	0.00108	0.00040	0.00021	0.00009	0.00005	0.00005	0.00022
0.00002	0.00014	0.00525	0.00057	0.00021	0.00011	0.00005	0.00003	0.00003	0.00011
0.00001	0.00006	0.00212	0.00023	0.00009	0.00005	0.00002	0.00001	0.00001	0.00005
0.00000	0.00003	0.00121	0.00014	0.00005	0.00003	0.00001	0.00001	0.00001	0.00003
0.00002	0.00014	0.00499	0.00058	0.00022	0.00011	0.00005	0.00003	0.00003	0.00012

**Table 4.13** Calculated  $x_j B_j$ .

	$B_j$	$x_j B_j$
B-N <sub>2</sub>	0.074384	0.000223
B-CO <sub>2</sub>	0.067126	0.001477
B-C <sub>1</sub>	0.066786	0.047151
B-C <sub>2</sub>	0.044186	0.004772
B-C <sub>3</sub>	0.031777	0.001557
B-n-C <sub>4</sub>	0.0247	0.000741
B- n-C <sub>5</sub>	0.01984	0.000278
B-C <sub>6</sub>	0.01642	0.000148
B-C <sub>7+</sub>	0.007001	0.000413
	$B = \sum_{j=1}^n x_j B_j =$	0.05676

$$Z^3 + E_2 Z^2 + E_1 Z + E_0 = 0$$

where  $E_2$ ,  $E_1$ , and  $E_0$  are defined for PR in Table 4.1 as:  $E_2 = -0.943240181$ ,  $E_1 = 0.2559416$ , and  $E_0 = -0.0181146$ .

*Step 7:* use Cardano's method described in section 4.2.4 to solve for  $Z$  values.

$$Q = -0.013541915, R = -9.68518E-05, \text{ and}$$

$$D = -2.47398E-06.$$

$$\theta = 1.632294385.$$

$$Z_1 = 0.5135, Z_2 = 0.1105, \text{ and } Z_3 = 0.3192.$$

The largest and smallest value of  $Z$  from the cubic equation are the  $Z$ -factor for vapor ( $Z_v$ ) and liquid ( $Z_l$ ), respectively:

$$Z_v = 0.5135 \text{ and } Z_l = 0.1105.$$

*Step 8:* determine  $v$  using equation (4.5):  $Z = \frac{pv}{RT}$

$v_v = 2.4 \text{ ft}^3/\text{lbmol}$  and  $v_l = 0.52 \text{ ft}^3/\text{lbmol}$ , where subscripts  $v$  and  $l$  represent the vapor and liquid phase, respectively.

#### 4.4. EQUATION OF STATES FOR VAPOR-LIQUID EQUILIBRIUM CALCULATIONS

Fugacity ( $f$ ), a very important parameter for phase equilibrium calculation in real gases, is "adjusted pressure" that ensures that the ideal chemical potential equation, equation (4.39), holds for true gases.

$$\mu(p, T)_{ideal} = \mu(T, p_0) + RT \ln \left( \frac{p}{p_0} \right) \quad (4.39)$$

This "adjusted pressure" gives correct (real) values of the chemical potential of a real gas by replacing pressure ( $p$ ) with fugacity ( $f$ ) in equation (4.39) to become equation (4.40).

$$\mu(p, T)_{real} = \mu(T, p_0) + RT \ln \left( \frac{f}{p_0} \right) \quad (4.40)$$

where

$p_0$  is the reference pressure,  $\mu(p, T)_{ideal}$  is the ideal chemical potential at temperature  $T$  and pressure  $p$ ,  $\mu(p, T)_{real}$  is

the real chemical potential at temperature  $T$  and pressure  $p$ , and  $\mu(p_0, T)$  is the chemical potential at temperature  $T$  and reference pressure  $p_0$ .

The chemical potential of a specie  $i$  ( $\mu_i$ ) is a measure of change in free energy ( $G$ ) per unit change in the number of species  $i$  while other species remain constant under *isothermal* (constant temperature,  $T$ ) and *isobaric* (constant pressure,  $p$ ) conditions.

$$\mu_i = \left( \frac{\partial G}{\partial N_i} \right)_{T, P, N_{j \neq i}} \quad (4.41)$$

where  $G$  is Gibbs free energy, which is a measure of the amount of energy available to do work in an isothermal and isobaric thermodynamic system, and  $N_i$  is the number of particles (or number of moles) of species  $i$ .

Fugacity has a unit of pressure, as it is "adjusted pressure" that would fit chemical potential equation for a real gas (equation (4.40)). The relationship between measured pressure ( $p$ ) and fugacity ( $f$ ) can, thus, be defined as:

$$f = \phi p \quad (4.42)$$

where  $\phi$  is the fugacity coefficient, which is a form of "correction factor" that adjusts the actual measured pressure to ensure the real chemical potential of a real gas can be calculated.

At low pressure ( $p \rightarrow 0$ ), gas tends to ideal behavior and, hence,  $f \rightarrow p$  and  $\phi \rightarrow 1$ .

From the chemical potential equation for real and ideal gas, and the ideal and real gas equation of state, fugacity can be expressed as a function of pressure ( $p$ ) and compressibility factor ( $Z$ ) in the form:

$$\ln \left( \frac{f}{p} \right) = \ln \phi = \int_0^p \left( \frac{Z-1}{p} \right) p \quad (4.43)$$

Equation (4.43), when combined with the generalized EOS described in equation (4.4), can be used for determining the fugacity coefficient of pure components as shown below:

$$\ln(\phi_i) = (Z-1) \frac{B_i}{B} - \ln(Z-B) + \frac{A}{(m_1 - m_2)B} \left( \frac{2 \sum_j^N x_j A_{ij}}{A} - \frac{B_i}{B} \right) \ln \left( \frac{Z + m_2 B}{Z + m_1 B} \right) \quad (4.44)$$

Hence, for RK and SRK, where  $m_1 = 0$  and  $m_2 = 1$ , the fugacity coefficient is expressed as:

$$\ln(\phi_i) = (Z-1) \frac{B_i}{B} - \ln(Z-B) - \frac{A}{B} \left( \frac{2 \sum_j^N x_j A_{ij}}{A} - \frac{B_i}{B} \right) \ln \left( \frac{Z+B}{Z} \right) \quad (4.45)$$

Therefore, the fugacity coefficient for the vapor phase using RK and SRK is:

$$\ln(\phi_{vi}) = (Z_v - 1) \frac{B_{vi}}{B_v} - \ln(Z_v - B_v) - \frac{A_v}{B_v} \left( \frac{2 \sum_j^N y_j A_{ij}}{A_v} - \frac{B_{vi}}{B_v} \right) \ln \left( \frac{Z_v + B_v}{Z_v} \right) \quad (4.46)$$

and for the liquid phase is:

$$\ln(\phi_{li}) = (Z_l - 1) \frac{B_{li}}{B_l} - \ln(Z_l - B_l) - \frac{A_l}{B_l} \left( \frac{2 \sum_j^N x_j A_{ij}}{A_l} - \frac{B_{li}}{B_l} \right) \ln \left( \frac{Z_l + B_l}{Z_l} \right) \quad (4.47)$$

For PR where  $m_1 = 1 + \sqrt{2}$  and  $m_2 = 1 + \sqrt{2}$ , the fugacity expression, equation (4.44), becomes:

$$\ln(\phi_i) = (Z - 1) \frac{B_i}{B} - \ln(Z - B) + \frac{A}{2\sqrt{2}B} \left( \frac{2 \sum_j^N x_j A_{ij}}{A} - \frac{B_i}{B} \right) \ln \left( \frac{Z + (1 - \sqrt{2})B}{Z + (1 + \sqrt{2})B} \right) \quad (4.48)$$

Therefore, the fugacity coefficient for the vapor phase using PR is:

$$\ln(\phi_{vi}) = (Z_v - 1) \frac{B_{vi}}{B_v} - \ln(Z_v - B_v) + \frac{A_v}{2\sqrt{2}B_v} \left( \frac{2 \sum_j^N y_j A_{ij}}{A_v} - \frac{B_{vi}}{B_v} \right) \ln \left( \frac{Z_v + (1 - \sqrt{2})B_v}{Z_v + (1 + \sqrt{2})B_v} \right) \quad (4.49)$$

and for the liquid phase is:

$$\ln(\phi_{li}) = (Z_l - 1) \frac{B_{li}}{B_l} - \ln(Z_l - B_l) + \frac{A_l}{2\sqrt{2}B_l} \left( \frac{2 \sum_j^N x_j A_{ij}}{A_l} - \frac{B_{li}}{B_l} \right) \ln \left( \frac{Z_l + (1 - \sqrt{2})B_l}{Z_l + (1 + \sqrt{2})B_l} \right) \quad (4.50)$$

$Z_v$  and  $Z_l$  are the vapor and liquid compressibility factors, respectively.

From equation (4.42), the fugacity of component  $i$  in the vapor phase can be defined as:

$$f_i^V = y_i p \phi_{vi} \quad (4.51)$$

and the fugacity of component  $i$  in the liquid phase defined as:

$$f_i^L = x_i p \phi_{li} \quad (4.52)$$

where  $f_i^V$  is the fugacity of component  $i$  in the vapor phase, and  $f_i^L$  is the fugacity of component  $i$  in the liquid phase.

At phase equilibrium, the fugacity of component  $i$  in the liquid and vapor phases must be equal:

$$f_i^L = f_i^V \quad (4.53)$$

Hence, from equations (4.51) and (4.52) with the condition defined in equation (4.53):

$$y_i p \phi_{vi} = x_i p \phi_{li}$$

$$\frac{y_i}{x_i} = \frac{\phi_{li}}{\phi_{vi}}$$

Substituting  $K_i = \frac{y_i}{x_i}$  from equation (3.55) into the above, the equilibrium constants can then be determined as follows:

$$K_i = \frac{\phi_{li}}{\phi_{vi}} \quad (4.54)$$

Equation (4.54) therefore satisfies the condition for phase equilibrium where  $\phi_{vi}$  is the fugacity coefficient of component  $i$  in the vapor phase and  $\phi_{li}$  is the fugacity coefficient of component  $i$  in the liquid phase.

#### 4.4.1. Steps in Carrying Out VLE Calculations using EOS

Vapor liquid equilibrium (VLE) calculations using EOS is iterative and can be summarized using the steps shown in Fig. 4.2.

*Step 1:* determine an initial  $K$  value for each component ( $K_{i,\text{start}}$ ) from any correlation, such as Wilson's correlation (equation 3.62 in Section 3.4.2.1), at given temperature ( $T$ ) and pressure ( $p$ ).

*Step 2:* perform flash calculations with the initial  $K$  values to determine starting values of  $n_b$  and  $x_i$  for the liquid phase and  $n_v$  and  $y_i$  for the vapor phase using equations (3.58)–(3.61) as shown in Exercises 3.4 and 3.5.

*Step 3:* using the EOS described in equation (4.4) determine  $Z_l$  and  $Z_v$  using composition  $x_i$  for the liquid phase and  $y_i$  for the vapor phase. Exercise 4.1 shows the calculation of the  $Z$ -factor.

*Step 4:* using EOS-VLE calculation models (equations (4.45)–(4.50)), determine the fugacity coefficient of the liquid ( $\phi_{li}$ ) and vapor ( $\phi_{vi}$ ) using initial liquid and vapor fractions ( $x_i$  and  $y_i$  respectively) from flash

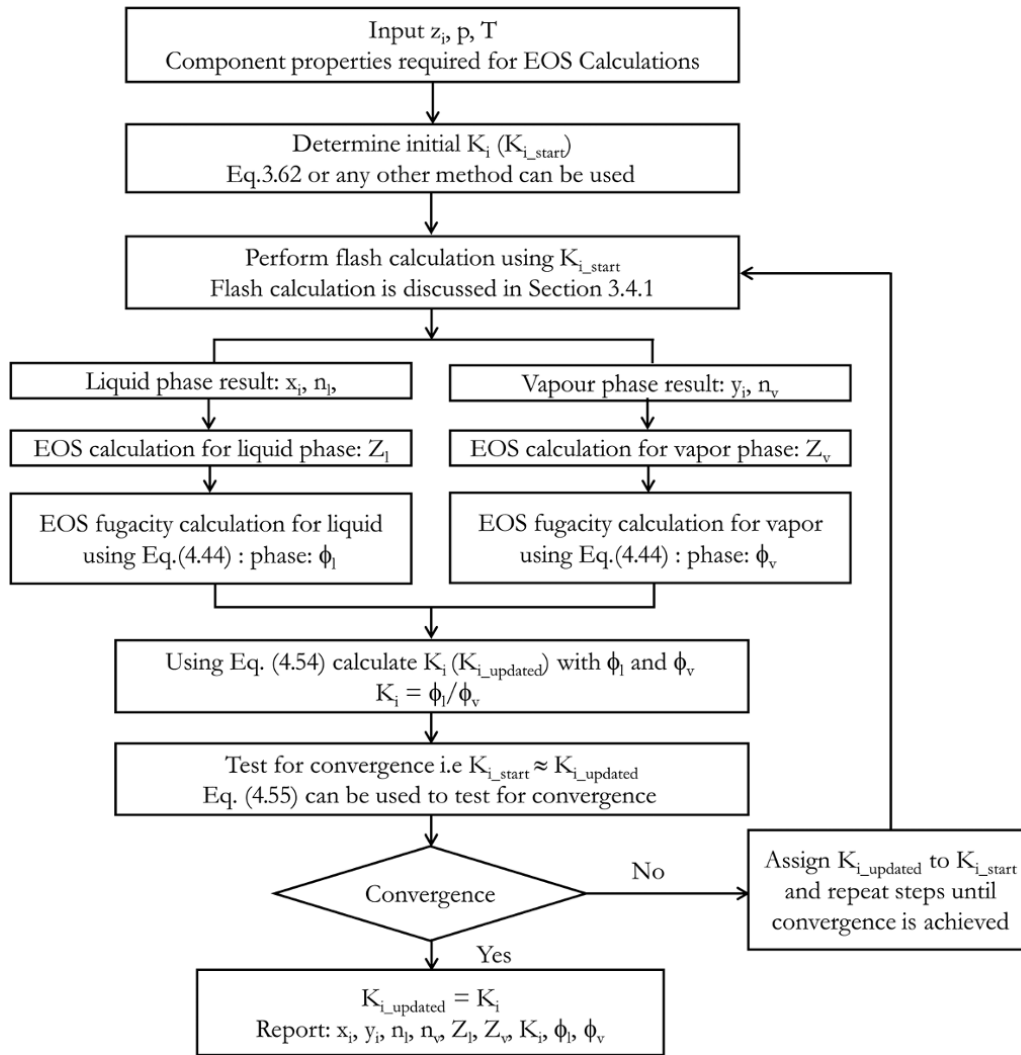


Figure 4.2 Flow chart for VLE calculations using EOS.

calculations (from Step 2) and initial liquid and vapor Z-factors ( $Z_L$  and  $Z_V$  respectively) from EOS calculations (from Step 3).

Step 5: determine updated  $K_i$  ( $K_{i,updated}$ ) value using the ratio of fugacity coefficient defined in equation (4.54), which is  $K_i = \frac{\phi_{li}}{\phi_{vi}}$ .

Step 6: check that there is convergence in  $K_i$  solution, i.e.  $K_{i-start} \approx K_{i,updated}$ . This can be tested using:

$$\sum_{i=1}^n \epsilon^2 = \sum_{i=1}^n \left( \frac{K_{i-start} - K_{i,updated}}{K_{i-start}} \right)^2 \leq 1 \times 10^{-5} \quad (4.55)$$

$\epsilon^2 \leq 1 \times 10^{-5}$  is a reasonable value for convergence for  $K_i$  determination. Where the value of  $K_i$  does not converge, the entire process in Section 4.4.1. is repeated starting with an updated  $K_i$  value ( $K_{i,updated}$ ) as the starting  $K_i$  ( $K_{i-start}$ ) value for the flash calculation in step 2.

#### 4.4.2. Saturation Points Calculation using the EOS-VLE Method

The workflow described in Fig. 4.2 shows that for a given input –  $z_i$ ,  $T$ , and  $p$  – the output –  $x_i$ ,  $y_i$ ,  $n_l$ ,  $n_v$ , and  $K_i$  – can be calculated. The entire workflow in Fig. 4.2 can be set up as a *parameterized function* using various approaches, including VBA *call function* in Excel with input as  $z_i$ ,  $T$ , and  $p$  and output as  $x_i$ ,  $y_i$ ,  $n_l$ ,  $n_v$ , and  $K_i$ . With the call function setup, at a given temperature ( $T$ ) and fluid composition ( $z_i$ ), pressure ( $p$ ) can be varied iteratively to meet criteria defined by equation (3.68)

$\left( \sum_i \frac{z_i}{K_i} = 1 \right)$  for dew point pressure calculation and criteria defined by equation (3.69)  $\left( \sum_i (z_i K_i) = 1 \right)$  for bubble point pressure calculation.



Variation of pressure at a given temperature to determine dew point pressure and bubble point pressure are demonstrated in Exercise 3.7 and Exercise 3.8, respectively, using Wilson's correlation [Wilson, 1968], a parameterized function that relates  $K_i$  to  $T$ ,  $p$  explicitly and a material balance that relates  $K_i$  to  $z_i$ ,  $x_i$ , and  $y_i$  through equations (3.59) and (3.61).

#### Exercise 4.2 VLE Calculation Using EOS Models

A gas condensate sample with the composition and properties shown in Table 4.14 is flashed in a first stage separator at 1200 psia and temperature of 70 °F. Assuming equilibrium was achieved, determine the mole fraction and composition of each phase using the fugacity coefficient derived from the Peng Robinson EOS.

#### Solution.

Using the steps in Fig. 4.2, the solution is summarized in Table 4.15.

**Table 4.14** Composition and Properties of Gas Condensate for Exercise 4.3.

Component	Mole fraction	$T_{ci}$ (°R)	$p_{ci}$ (psi)	$\omega_i$
N <sub>2</sub>	0.003	226.57	492.02	0.039
CO <sub>2</sub>	0.022	547.36	1,072.96	0.239
C <sub>1</sub>	0.706	343.15	673.08	0.011
C <sub>2</sub>	0.108	549.47	708.35	0.099
C <sub>3</sub>	0.049	665.68	617.38	0.153
<i>n</i> -C <sub>4</sub>	0.030	764.96	550.66	0.199
<i>n</i> -C <sub>5</sub>	0.014	845.26	489.52	0.251
C <sub>6</sub>	0.009	913.77	439.70	0.299
C <sub>7+</sub>	0.059	1,119.18	402.68	0.350

**Table 4.15** Use of Fugacity Defined by PR for VLE Calculation.

Component	Mole fraction	Wilson's initial calculation			Final calculation following iteration		
		$K_i$	$n_v$	$n_l = 1 - n_v$	$K_i$	$n_v$	$n_l = 1 - n_v$
			0.737	0.263		0.782	0.218
		$y_i$	$x_i$		$y_i$	$x_i$	
N <sub>2</sub>	0.003	9.93E+00	3.93E-03	3.96E-04	5.90E+00	4.15E-03	7.03E-04
CO <sub>2</sub>	0.022	7.12E-01	1.99E-02	2.79E-02	1.00E+00	2.17E-02	2.16E-02
C <sub>1</sub>	0.706	3.75E+00	8.75E-01	2.33E-01	2.82E+00	8.22E-01	2.91E-01
C <sub>2</sub>	0.108	4.70E-01	8.32E-02	1.77E-01	7.58E-01	1.01E-01	1.33E-01
C <sub>3</sub>	0.049	1.04E-01	1.50E-02	1.44E-01	3.18E-01	3.37E-02	1.06E-01
<i>n</i> -C <sub>4</sub>	0.030	2.59E-02	2.75E-03	1.06E-01	1.36E-01	1.27E-02	9.30E-02
<i>n</i> -C <sub>5</sub>	0.014	7.33E-03	3.82E-04	5.21E-02	6.10E-02	3.10E-03	5.08E-02
C <sub>6</sub>	0.009	2.30E-03	7.81E-05	3.39E-02	2.83E-02	1.06E-03	3.74E-02
C <sub>7+</sub>	0.059	1.60E-06	3.59E-07	2.24E-01	2.76E-03	7.35E-04	2.67E-01
	$\Sigma z_i$		$\Sigma x_i$	$\Sigma y_i$		$\Sigma y_i$	$\Sigma x_i$
	1.000		1.00	1.00		1.00	1.00

## 4.5. COMPOSITIONAL GRADING

Due to the pressure and temperature gradient in a reservoir, hydrocarbon properties may vary with depth. Even over geological time some reservoirs may not attain compositional homogeneity, as molecular diffusion is a very slow process. The formation and saturation pressure profile in a reservoir with a gas-oil contact where the vapor (gas) and liquid (oil) phases are in equilibrium is shown in Fig. 4.3.

At the GOC, for the gas and oil fluid column to be in pressure equilibrium, gas and oil formation pressure must be equal. Also, the formation pressure must be equal to the saturation pressure at the GOC for the vapor and liquid to be in phase equilibrium (Fig. 4.3).

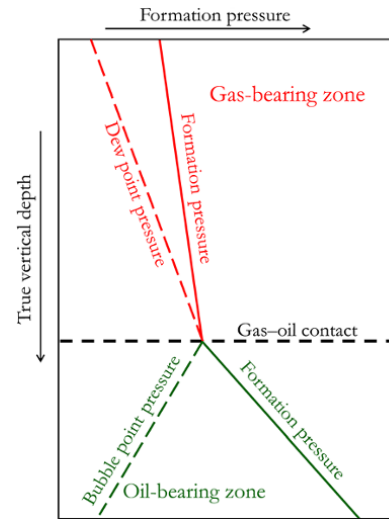


**Figure 4.3** Formation pressure profile in a formation with gas and oil in equilibrium.

The effect of compositional grading may not be obvious from the formation pressure log (formation pressure–depth plot) where the change in fluid composition with depth is subtle. However, where the composition gradient is severe and significantly impacts density, a formation pressure log may show continuously increasing pressure gradient with depth (Fig. 4.4).

Gas-oil contact in reservoir with compositional grading can have a transition from gas to oil occurring at *saturated gas-oil contact* (Fig. 4. 4a). An uncommon transition from gas to oil without a saturated gas-oil contact also exist. In

this fluid system, which has been observed in some near critical fluid, an undersaturated critical fluid mixture creates a smooth and continuous transition from gas to oil (Fig. 4. 4b). This undersaturated critical fluid mixture at the gas-oil transition interface is at formation temperature which is equal to critical temperature. The critical pressure of the fluid mixture at the gas-oil transition, which is the maximum saturation pressure along the entire fluid column, is considered the saturation pressure at the gas-oil contact. This critical pressure of the fluid mixture which defines the transition between gas and oil column is lower

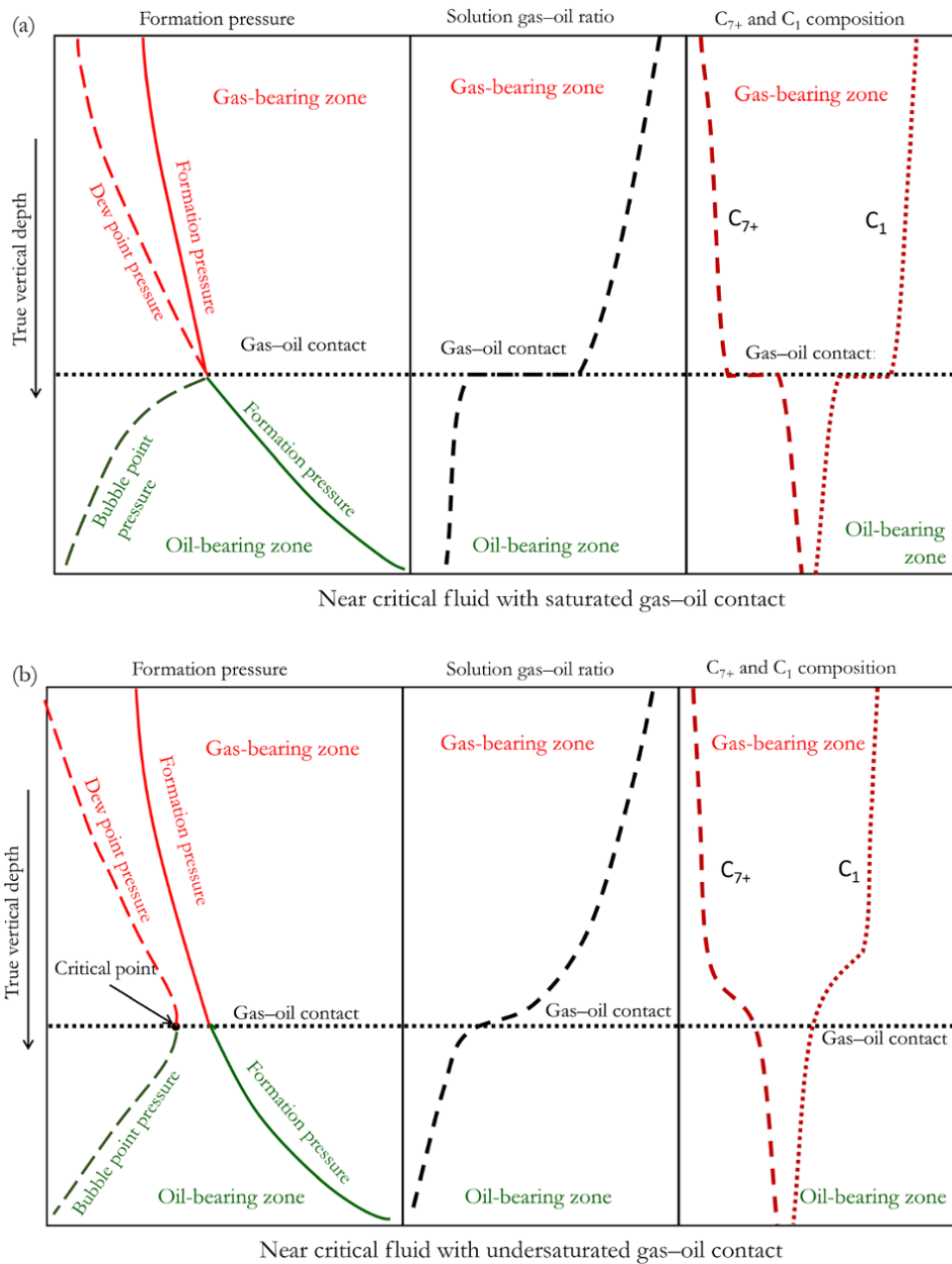


Figure 4.4 Saturated and Undersaturated GOC in Fluid with Compositional Grading.

than the formation pressure at that depth, and hence this depth is also called *undersaturated gas-oil contact* (Fig. 4.4b)

#### Exercise 4.3 Determining Gas–Oil Contact from Fluid Properties

A Wireline formation tester was used to sample gas and oil zones in a reservoir with both gas and oil present. The composition of gas sample is given in Table 4.16 and the composition of the oil sample is given in Table 4.17.

1. Using PR-EOS, determine the saturation pressure of the gas and oil columns given that the average reservoir temperature is 190 °F.

2. Is the gas column in equilibrium with the oil column?

3. Given that the formation pressure in the gas zone can be described by:  $p_{\text{gas}}(\text{psia}) = 0.11 z_{\text{gas}} + 3001$ , determine the gas–oil contact.  $Z_{\text{gas}}$  is true vertical depth subsea in ft within the gas zone.

#### Solution Steps.

*Step 1:* using the steps outlined in Section 4.4.2, determine the dew point pressure ( $p_{\text{dew}}$ ) at 190 °F for the gas sample and the bubble point pressure ( $p_{\text{bubble}}$ ) at 190 °F for the oil sample.

*Step 2:* if  $p_{\text{bubble}} = p_{\text{dew}}$ , then the gas and oil are most likely to be in equilibrium. However, if  $p_{\text{bubble}} \neq$

$p_{\text{dew}}$  then the gas and oil columns are not in equilibrium.

*Step 3:* to determine the GOC, substitute  $p_{\text{bubble}}$  or  $p_{\text{dew}}$  into the formation pressure equation and the corresponding depth gives the GOC.

#### Solutions.

1. Using the steps outlined in Section 4.4.2,  $p_{\text{bubble}}$  and  $p_{\text{dew}}$  were determined as:  $p_{\text{bubble}} = p_{\text{dew}} = 3,300$  psia.

2. Since  $p_{\text{bubble}} = p_{\text{dew}}$ , the gas and oil columns can be assumed to be in pressure equilibrium.

3.  $p_{\text{gas}} = 0.11 z_{\text{gas}} + 3,001$

$$Z_{\text{gas}} = \frac{(p_{\text{gas}} - 3,001)}{0.11}$$

at the GOC

$$z_{\text{gas}} = \text{GOC} = \frac{(p_{\text{sat}} - 3,001)}{0.11}$$

$$z_{\text{gas}} = \text{GOC} = \frac{(3,300 - 3,001)}{0.11} = 2,718.18 \text{ ft}$$

GOC = 2,718.18 ft

An EOS software can be used for the above exercise, whereby it is easy to generate a phase envelope and to also check graphically if  $p_{\text{dew}}$  and  $p_{\text{bubble}}$  are equal as shown in Fig. 4.5.

**Table 4.16** Composition of Gas Sample for Exercise 4.3.

Components	Mol %	MW	SG
N <sub>2</sub>	0.000		
CO <sub>2</sub>	0.687		
H <sub>2</sub> S	0.035		
C <sub>1</sub>	72.138		
C <sub>2</sub>	13.309		
C <sub>3</sub>	6.327		
n-C <sub>4</sub>	2.822		
n-C <sub>5</sub>	1.434		
C <sub>6</sub>	0.971		
C <sub>7+</sub>	2.276	193	0.836

**Table 4.17** Composition of Oil Sample for Exercise 4.3.

Components	Mol %	MW	SG
N <sub>2</sub>	0.000		
CO <sub>2</sub>	0.691		
H <sub>2</sub> S	0.042		
C <sub>1</sub>	53.221		
C <sub>2</sub>	13.639		
C <sub>3</sub>	8.084		
n-C <sub>4</sub>	4.476		
n-C <sub>5</sub>	2.770		
C <sub>6</sub>	2.243		
C <sub>7+</sub>	14.835	193	0.836

#### Exercise 4.4 Sample Recombination

The reservoir in Exercise 4.3 was tested as part of a drill stem test (DST) program with the entire 90 ft formation tested. The interval tested produced reservoir hydrocarbon fluid with a dew point pressure of 3,826.32 psia at 190 °F.

1. Determine the fraction of the gas-bearing zone and the oil-bearing zone contributing to the produced fluid during the DST, assuming that the Parrine–Martin [Perrine, 1956; Martin, 1959] assumption of uniform distribution of all phases in the reservoir during testing is considered valid. Parrine–Martin assumptions in multi-phase well testing are discussed in Chapter 8.9.1.

2. What would a good recommendation be if oil production is the objective of field development?

Note: It is more accurate to use EOS instead of the Wilson correlation, as the Wilson correlation is accurate only at pressures up to 500 psia.

#### Solution.

1. Combining equations (3.56) and (3.57) to eliminate  $n_L$ :

$$z_i = n_v y_i + (1 - n_v) x_i \quad (4.56)$$

Vary  $n_v$  (vapor fraction) starting from  $n_v = 0.5$  in equation (4.56) to get a fluid mixture ( $z_i$ ) with saturation

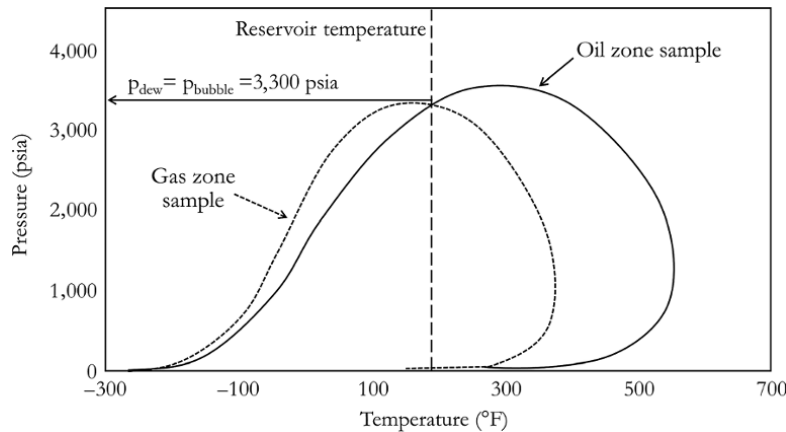


Figure 4.5 Phase envelope of oil and gas sample showing common saturation pressure.

Table 4.18 Representative Produced Fluid from the Recombination of 0.7 of Gas and 0.3 of Oil.

Components	Mol %	MW	SG
N <sub>2</sub>	0.000		
CO <sub>2</sub>	0.688		
H <sub>2</sub> S	0.037		
C <sub>1</sub>	66.463		
C <sub>2</sub>	13.408		
C <sub>3</sub>	6.854		
n-C <sub>4</sub>	3.318		
n-C <sub>5</sub>	1.835		
C <sub>6</sub>	1.353		
C <sub>7+</sub>	6.044	193	0.836

pressure of 3,826.32 psia through an iterative process using the setup described in section 4.4.2 by varying  $n_v$  for given  $p_{dew}$  in this case.

Only one of  $n_v$  or  $n_l$  need to be varied considering that  $n_v = 1 - n_l$  or  $n_l = 1 - n_v$ .

0.7 of gas and 0.3 of oil will give  $z_i$  (Table 4.18) with  $p_{dew}$  of 3,826.32 psia.

2. With significant vapor fraction ( $n_v = 0.7$ ) from the DST and considering oil production for field development, the production interval should be kept further away from the gas zone to minimize gas production.

## REFERENCES

- Coats, K., 1980. An equation of state compositional model. *Society of Petroleum Engineers Journal*, **20**(5), 363–376.
- Hoffmann, A. E., Crump, J. S. and Hocott, C., 1953. Equilibrium constants for a gas-condensate system. *Transactions of the AIME*, **198**, 1–10.
- Jhaveri, B. and Youngren, G., 1988. Three-parameter modification of the Peng-Robinson equation of state to improve volumetric predictions. *SPE Reservoir Engineering*, **3**, 3.

## BIBLIOGRAPHY

- Kalman, D., 1987. *Uncommon Mathematical Excursions: Polynomials and Related Realms*. The American Mathematical Society, Dolciani Mathematical Expositions #35.
- Martin, J., 1959. Simplified equations of flow in gas drive reservoirs and the theoretical foundation of multiphase pressure buildup analyses. *Transactions of the AIME*, **216**, 321–323.
- Martin, J., 1979. Cubic equation of state – Which?. *Industrial & Engineering Chemistry Fundamentals*, **18**(2), 81–97.
- Peng, D.Y. and Robinson, D.B., 1976. A new two-constant equation of state. *Industrial & Engineering Chemistry Fundamentals*, **15**, 59–64.
- Perrine, R., 1956. Analysis of pressure build-up curves. *API Drilling and Production Practice*, 482–509.
- Pitzer, K., 1955. The volumetric and thermodynamic properties of fluids. I. Theoretical basis and virial coefficients. *Journal of the American Chemical Society*, **77**(13), 3427–3433.
- Redlich, O. and Kwong, J.N.S., 1949. On the thermodynamics of solutions: V. An equation of state: fugacities of gaseous solutions. *Chemistry Review*, **44**, 233–244.
- Soave, G., 1972. Equilibrium constants from a modified Redlich-Kwong equation of state. *Chemical Engineering Science*, **27**, 1197–1203.
- Standing, M. and Katz, D., 1942. Density of natural gases. *American Institute of Mining and Metallurgical Engineers Inc, SPE-942140-G*, **142**, 140–149.
- Wilson, G., 1968. A modified Redlich-Kwong equation of state applicable to general physical data calculations. *65th AIChE National meeting*, Paper No. 15C.

- Ahmed, T., 1989. *Hydrocarbon Phase Behavior, Contributions in Petroleum Geology & Engineering*. Gulf Publishing Company.
- American Petroleum Institute (API), 2003. *Recommended Practice for Sampling Petroleum Reservoir Fluids*, Washington, DC: API.
- Archer, J. and Wall, C., 1999. *Petroleum Engineering Principles and Practice*. Dordrecht/Boston: Kluwer Academic Publishers Group.

- Brooks, B., 1955. *The Chemistry of Petroleum Hydrocarbons*. Reinhold.
- Coats, K. and Smart, G., 1986. Application of a regression-based EOS PVT program to laboratory data. *SPE Reservoir Engineering*, **1**(3), 277–299.
- Hall, K. and Yarborough, L., 1973. A new equation of state for Z-factor calculations. *Oil & Gas Journal*, **71**(25), 82.
- Hoier, L., Cheng, N. and Whitson, C.H., 2004. *Miscible Gas Injection in Undersaturated Gas-Oil Systems*, Paper SPE 90379 presentation at the SPE Annual Technical Conference and Exhibition, Houston, U.S.A., September 26–29.
- Kareem, L., Iwalewa, T. and Al-Marhoun, M., 2016. New explicit correlation for the compressibility factor of natural gas: linearized Z-factor isotherms. *Journal of Petroleum Exploration and Production Technology*, **6**(3), 481–492.
- Kwak, T.Y., Benmekki, E., and Ransoori, C.A., 1986. van der Waals mixing rules for cubic equations of state, applications for supercritical fluid extraction modeling and phase equilibrium calculations. *Chemical Engineering Science*, **41**(5), 1303–1309.
- Martin, J., 1983. PVT Analysis of a new cubic-perturbed, hard-sphere equation of state. *AIChE Journal*, **29**(3), 369–372.
- McCain Jr., W. and Alexander, R., 1992. Sampling gas-condensate wells. *SPE Reservoir Engineering*, p. 358–362.
- Moses, P., 1986. Engineering applications of phase behavior of crude oil and condensate. *Journal of Petroleum Technology*, **38**, 715–723.
- Muller, E. and A-Fuentes, C., 1989. General expressions for multicomponent fugacity coefficients and residual properties from cubic equation of state. *Latin American Applied Research*, **19**, 99–109.
- Pitzer, K.S., Lippmann, D.Z., Curl Jr., R.F., *et al.*, 1955. The volumetric and thermodynamic properties of fluids. II. Compressibility factor, vapor pressure and entropy of vaporization. *Journal of the American Chemical Society*, **77**(13), 3433–3440.
- Whitson, C. and Belery, P., 1994. *Compositional Gradients in Petroleum Reservoirs*, Paper SPE 2800 presented at the University of Tulsa Petroleum Engineering Symposium, Tulsa, Oklahoma, U.S.A., August 29–31.
- Whitson, C. and Brulé, M.R., 2000. *Phase Behavior*, SPE Monograph Series, Vol. 20, Richardson, TX: Society of Petroleum Engineers.

## 5

### Formation Evaluation

Formation evaluation involves determination of the petrophysical properties of formation using wireline logs. Determined petrophysical properties from formation evaluation is important for qualitative and quantitative reservoir characterization.

Detailed interpretation of well logs is considered to fall within the domain of petrophysics; however, all disciplines involved in the reservoir management team are expected to have some level of understanding of well logs, either for qualitative or quantitative formation characterization. For petroleum engineers, basic qualitative and quantitative interpretation of well logs is very important.

For geology and geophysics, well logs are an important information source for: depth of formation tops; understanding of facies and lithology; hydrocarbon accumulations; petrophysical properties such as porosity, water distribution, and fluid contact for geological and simulation models; and important input for creating synthetic seismic sections.

For drilling and completion engineering, well logs are used for: calculating hole volume required for cementing operation; determining keyseat (channel or groove cut in the side of the hole) and severe doglegs; determining the best location to set a Whipstock; determining completion interval for hydrocarbon production; and determining production or test packer interval.

For reservoir and production engineering, well logs provides information on: reservoir pay zone; vertical and horizontal property distribution using single and/or multiples wells; providing key input parameters for in-place hydrocarbon volume calculations; well completion optimization; well deliverability prediction; formation and well test analysis; reservoir development options; understanding reservoir compartmentalization

for reservoir development strategies; predicting chances of gas and water production.

#### 5.1. FORMATION EVALUATION

The response of logging tools in a reservoir depends generally on lithology (rock type) and fluid in the formation, which could be one or more of gas, oil, and water (fresh or saline). Lithology generally describes the gross characteristics of a rock and relates to mineral content, texture, grain size, and color. Typical lithologies include: sandstone (or sand), limestone, dolomite, clay, shale, chert, diatomite, anhydrite, gypsum, halite, and tuff [Chilingar *et al.*, 2005].

Interpretation of logs acquired along the well can be used for: reservoir fluid description; lithological description; matching logs and depth correlation; lithology description; identification of permeable and nonpermeable regions of the reservoir; movable hydrocarbon; reservoir zonation (dividing reservoir into different fluid zones); porosity calculation within a zone of interest; and calculating hydrocarbon saturation within a zone of interest near and away from the wellbore.

Formation evaluation provides a very important input in defining lithofacies, which are mappable subdivisions of a stratigraphic entity that can be characterized by facies or lithology. *Facies* means the total characteristic of a rock or sediment unit that reflects its origin and environment of deposition, and allows it to be differentiated from another rock unit around it. Attributes that can be used to define facies include: lithology (lithological facies); deposition (depositional facies); biotic (biofacies); and diagenesis (diagenetic facies).

A key objective of petrophysical data and their interpretation is to identify and quantify hydrocarbon resources in the subsurface and evaluate the rock and fluid properties. As shown in equation. (1.8)–(1.13) in Chapter 1, all reservoir properties except area and fluid properties can be derived from petrophysical evaluation of well logs.

For reservoir engineering purposes, petrophysical properties that affect hydrocarbon fluid storage (porosity) in a reservoir and the flow of hydrocarbon (permeability) are very important. Formation evaluation is also useful for determining fluid contacts, reservoir rock saturation, porosity, permeability, and lithology.

The use of openhole logs for formation characterization involves the integration of information and data from mud logs, which include drill cutting and side wall cores, vertical seismic profiles, formation test data, geological information, geophysical data, well test data, and interpretation results and any other form of formation characterization data or analysis.

**5.1.1. Well Deviation Survey Calculation**

During logging, depth is measured along the well path from the derrick. This depth is called *measured depth (driller depth or logging depth)*, which is originally measured from *derrick floor*, or *drill floor elevation (DFE)* or *rotary kelly bushing (RKB)*. The measured depth from the kelly bushing (KB) can be converted to measured depth referenced from *mean sea level (MSL)* by subtracting elevation of KB from mean sea level. Such depth is termed as measured depth MSL (MD MSL).

The different depth definitions are summarized in Fig. 5.1.

*True vertical depth (TVD)*, which is vertical displacement of the well in the vertical axis from a reference, is a useful depth in reservoir characterization and subsurface mapping of properties. Many reservoir characterization methods, including formation pressure log analysis

(FPLA) and reservoir simulation, are always carried out in true vertical depth and referenced from a mean sea level datum. When true vertical depth is referenced from KB, it is termed *true vertical depth kelly bushing (TVDKB)* or *true vertical depth DFE (TVDDFE)* and when referenced from mean seal level, it is termed *true vertical depth mean sea level (TVD MSL)* or *true vertical depth subsea (TVDSS)*.

The objective of a well deviation survey in log analysis and formation testing is defining the relationship between measure depth (MD) and true vertical depth (TVD). Well deviation surveys are also used to determine downhole location relative to a surface reference during directional drilling and other well operations.

In order to calculate well deviation survey and coordinates the following inputs are required: inclination; azimuth; MD; and a reference coordinate (usually coordinates of wellhead). Accelerometer measurements ( $G_x, G_y, G_z$ ) and magnetometer measurements ( $B_x, B_y, B_z$ ) are used in determining hole inclination, magnetic azimuth, and tool orientation.

Tool inclination (I) from accelerometer reading is expressed as:

$$I = \cos^{-1} \left( \frac{G_z}{\sqrt{G_x^2 + G_y^2 + G_z^2}} \right) \text{ or} \tag{5.1}$$

$$I = \sin^{-1} \left( \frac{\sqrt{G_x^2 + G_y^2}}{\sqrt{G_x^2 + G_y^2 + G_z^2}} \right)$$

Magnetic azimuth (A) from accelerometer and magnetometer measurement is expressed as:

$$A = \tan^{-1} \left( \frac{(G_x B_y - G_y B_x) \sqrt{G_x^2 + G_y^2 + G_z^2}}{B_z (G_x^2 + G_y^2) - G_z (G_x B_x - G_y B_y)} \right) \tag{5.2}$$

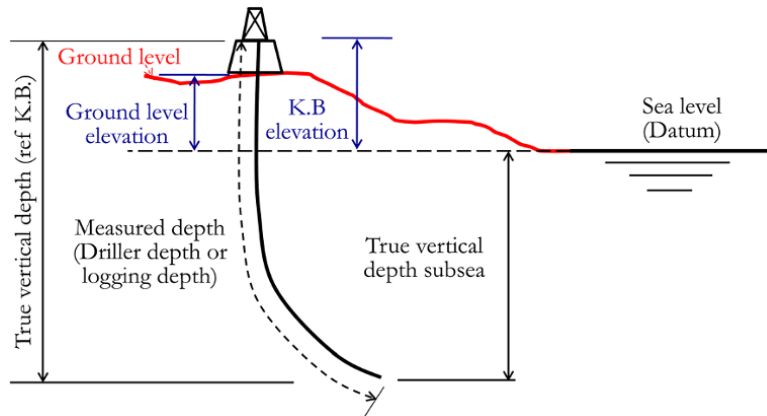


**Figure 5.1** Depth measurement in well logging.

The direction which the tool is pointing, *tool face*, is determined from the  $x$  and  $y$  components of the accelerometer measurements as:

$$\text{Tool Face} = \tan^{-1} \left( \frac{G_x}{G_y} \right) \quad (5.3)$$

#### 5.1.1.1. Methods for Calculating Deviation Survey.

The most common methods for calculating deviation survey include the: *average method*; *balanced tangential method*; *minimum curvature method*; *tangential method*; *radius of curvature*; and the *tangential method*. The radius of curvature and minimum curvature methods are the most accurate of the methods, while the tangential method is the least accurate. Given the coordinates of a survey station described by coordinates  $X(\text{ft})$ ,  $Y(\text{ft})$ , and  $Z(\text{ft})$ , for a survey station at  $X_1$  (ft) (positive towards the east);  $Y_1$  (ft) (positive towards the north);  $Z_1$  (ft) (TVD, positive downwards), the coordinates of an adjacent survey station ( $X_2$ ,  $Y_2$ , and  $Z_2$ ) will be:

$$X_2 = X_1 + \Delta\text{East}; Y_2 = Y_1 + \Delta\text{North} \text{ and } Z_2 = Z_1 + \Delta\text{Vert} \quad (5.4)$$

where  $\Delta\text{East}$  is the adjacent survey station in the east,  $\Delta\text{North}$  is in the northing, and  $\Delta\text{Vert}$  is in vertical direction. The methods listed here describe how  $\Delta\text{East}$ ,  $\Delta\text{North}$ , and  $\Delta\text{Vert}$  are calculated.

##### Average Method

This method uses the average of  $I_1$  and  $I_2$  ( $I$  at stations 1 and 2, respectively) as an inclination, the average of  $A_1$  and  $A_2$  ( $A$  at stations 1 and 2, respectively) as a direction, and assumes the entire survey interval ( $\Delta\text{MD}$ ) to be tangent to the average angle.

$$\Delta\text{North} = \Delta\text{MD} \times \sin \left( \frac{I_1 + I_2}{2} \right) \times \cos \left( \frac{A_1 + A_2}{2} \right) \quad (5.5)$$

$$\Delta\text{East} = \Delta\text{MD} \times \sin \left( \frac{I_1 + I_2}{2} \right) \times \sin \left( \frac{A_1 + A_2}{2} \right) \quad (5.6)$$

$$\Delta\text{Vert} = \Delta\text{MD} \times \cos \left( \frac{I_1 + I_2}{2} \right) \quad (5.7)$$

##### Balanced Tangential Method

This method treats half the measured distance ( $\text{DMD}/2$ ) as being tangent to  $I_1$  and  $A_1$  and the remainder of the measured distance ( $\text{DMD}/2$ ) as being tangent to  $I_2$  and  $A_2$ .

$$\Delta\text{North} = \frac{\Delta\text{MD}}{2} [\sin(I_1) \times \cos(A_1) + \sin(I_2) \times \cos(A_2)] \quad (5.8)$$

$$\Delta\text{East} = \frac{\Delta\text{MD}}{2} [\sin(I_1) \times \sin(A_1) + \sin(I_2) \times \sin(A_2)] \quad (5.9)$$

$$\Delta\text{Vert} = \frac{\Delta\text{MD}}{2} [\cos(I_1) + \cos(I_2)] \quad (5.10)$$

##### Minimum Curvature Method

This method smoothens the two straight-line segments of the balanced tangential method using the ratio factor RF.

$$\text{RF} = \left( \frac{2}{\text{DL}} \right) \tan \left( \frac{\text{DL}}{2} \right) \quad (5.11)$$

$\text{DL} = \beta$  and must be in radians

To avoid a singularity in the straight hole, it is necessary either to set  $\text{RF} = 1$  when  $\text{DL}$  is less than some fixed angle  $\theta$ , or to use the following truncated series expansion when  $\text{DL}$  is less than some fixed  $\theta$  and fixed angle  $\phi$ :

$$\text{RF} = 1 + \frac{\text{DL}^2}{12} + \frac{\text{DL}^4}{120} + \frac{17\text{DL}^6}{20160} \quad (5.12)$$

If the fixed values obey  $\theta < 0.01^\circ$  and  $\phi < 13^\circ$ , the resultant error will be less than 1 part in  $10^9$ .

The dogleg angle,  $\beta$ , is given by:

$$\cos(\beta) = \cos(I_2 - I_1) - \sin(I_1) \times \sin(I_2) (1 - \cos(A_2 - A_1)) \quad (5.13)$$

Hence, for the minimum curvature method:

$$\Delta\text{North} = \frac{\Delta\text{MD}}{2} [\sin(I_1) \times \cos(A_1) + \sin(I_2) \times \cos(A_2)] \times \text{RF} \quad (5.14)$$

$$\Delta\text{Vert} = \frac{\Delta\text{MD}}{2} [\cos(I_1) + \cos(I_2)] \times \text{RF} \quad (5.15)$$

$$\Delta\text{East} = \frac{\Delta\text{MD}}{2} [\sin(I_1) \times \sin(A_1) + \sin(I_2) \times \sin(A_2)] \times \text{RF} \quad (5.16)$$

##### Radius of Curvature Method

This is based on the assumption that the well path is an arc when viewed from the vertical and horizontal planes.

$$\Delta\text{North} = \frac{\Delta\text{MD} [\cos(I_1) - \cos(I_2)] [\sin(A_2) - \sin(A_1)]}{(I_2 - I_1)(A_2 - A_1)} \left( \frac{180}{\pi} \right)^2 \quad (5.17)$$

$$\Delta\text{East} = \frac{\Delta\text{MD} [\cos(I_1) - \cos(I_2)] [\cos A_1 - \cos A_2]}{(I_2 - I_1)(A_2 - A_1)} \left( \frac{180}{\pi} \right)^2 \quad (5.18)$$



$$\Delta V_{\text{vert}} = \frac{\Delta MD [\sin(I_2) - \sin(I_1)]}{(I_2 - I_1)} \left(\frac{180}{\pi}\right)^2 \quad (5.19)$$

If angles are kept in radians,  $180 = \pi$ , equations (5.17)–(5.19) can be expressed as:

$$\Delta N_{\text{orth}} = \frac{\Delta MD [\cos(I_1) - \cos(I_2)] [\sin(A_2) - \sin(A_1)]}{(I_2 - I_1)(A_2 - A_1)} \quad (5.20)$$

$$\Delta E_{\text{ast}} = \frac{\Delta MD [\cos(I_1) - \cos(I_2)] [\cos A_1 - \cos A_2]}{(I_2 - I_1)(A_2 - A_1)} \quad (5.21)$$

$$\Delta V_{\text{ert}} = \frac{\Delta MD [\sin(I_2) - \sin(I_1)]}{(I_2 - I_1)} \quad (5.22)$$

*Tangential Method*

This approach describes the well path as a straight line that is defined by the inclination and azimuth.

$$\Delta N_{\text{orth}} = \Delta MD \sin(I_2) \cos(A_2) \quad (5.23)$$

$$\Delta E_{\text{ast}} = \Delta MD \sin(I_2) \sin(A_2) \quad (5.24)$$

$$\Delta V_{\text{ert}} = \Delta MD \cos(I_2) \quad (5.25)$$

**5.1.2. Well Log Measurement**

Well log acquisition involves measuring and recording properties of formation using tools lowered into the well at varying depths or at a fixed depth at varying times in the case of formation testing.

Openhole log acquisition can be achieved through *logging while drilling* (LWD), where acquisition of logs is through a sensor attached to the drilling string. Though LWD has become increasingly common, not all measurements that can be carried out through wireline logging (WL) are available through LWD. In WL, acquisition of logs is carried out after the drilling operation using a tool/sensor attached to electrical cables (wireline) for *wireline logging* (WL) or *coil tubing* for *coil tubing logging* (CTL). In a situation where the well is highly deviated; horizontal wells, and wells with complex architecture where logging tools cannot travel along well path via gravity, logging tools are pushed along the well path using drill pipes with tools attached to the end of the drill pipes with electrical cables through the drill pipes in a process called *tough logging condition* (TLC).

Fig. 5.2 illustrates openhole logging from a truck-mounted surface acquisition unit.

The principle of measurement of different logging tools varies, as does their depth of investigation and vertical resolution in formation. Fig. 5.3 shows the depth of investigation and vertical resolution of some common well logging tools.

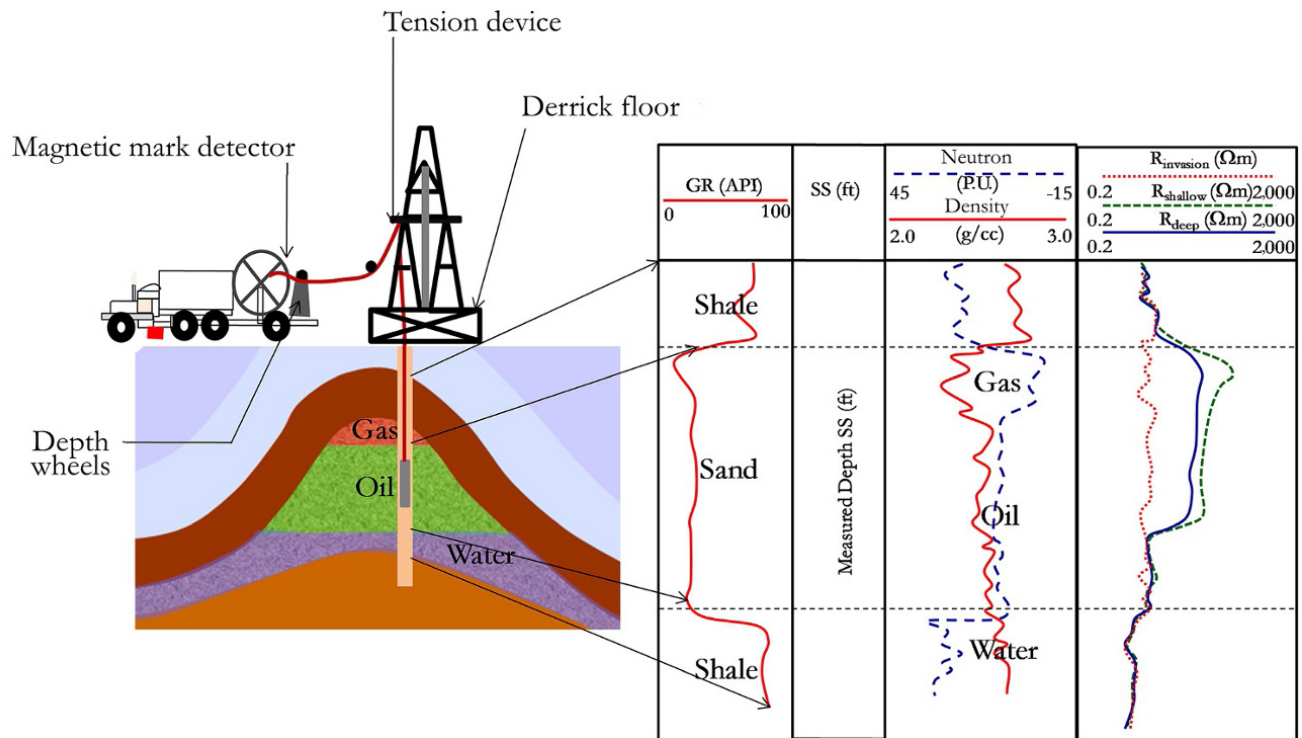


Figure 5.2 Openhole logging from a truck-mounted surface acquisition unit.

Measured logs are displayed on tracks with properties scaled on the horizontal axis above the track and depth recorded vertically increasing downwards. Fig. 5.4 shows an example of track for recording openhole logs.

### 5.1.3. Caliper Log

A caliper log, which is acquired with a *caliper logging tool*, is a measure of wellbore size. It gives an indication

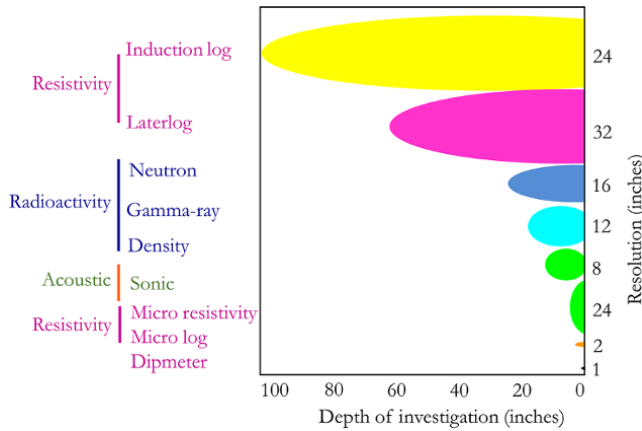


Figure 5.3 Typical resolution of some well logging tools.

of well washouts, cave-ins or shale swelling. Fig. 5.5 shows an example of a caliper logging tool and Fig. 5.6 shows an example of a caliper log.

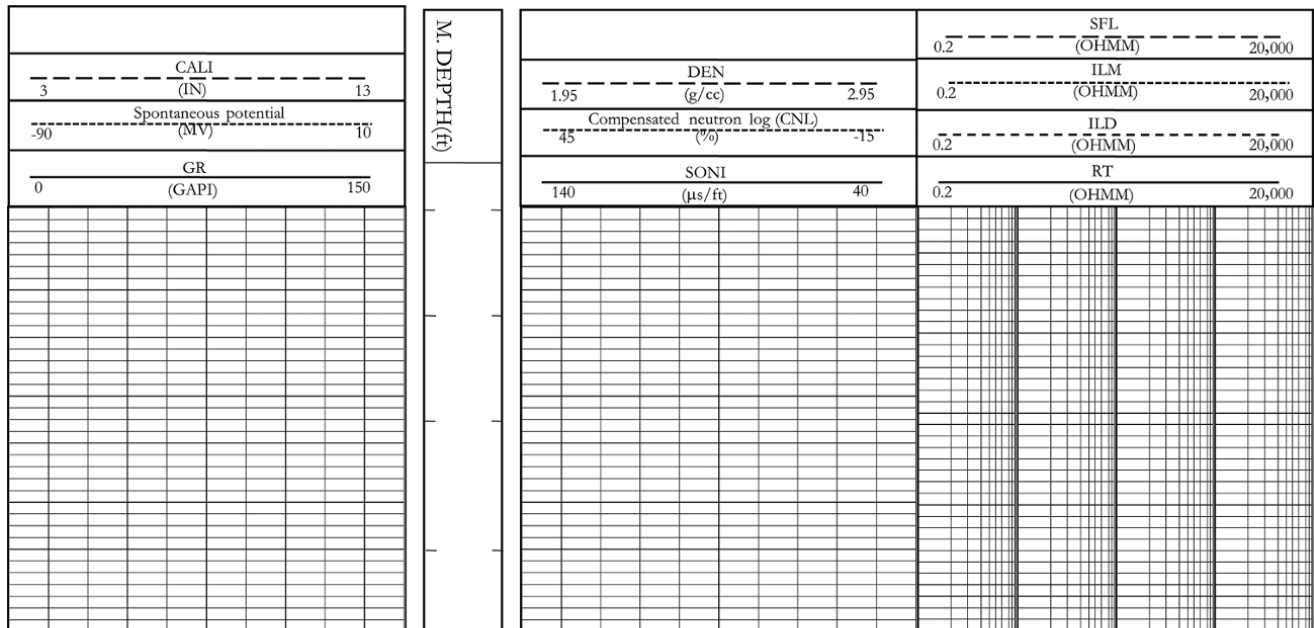
Caliper logs also provide supporting information for lithological characterization, as washouts are expected in shaly formations and stable hole size is expected in consolidated sandstone formations.

### 5.1.4. Gamma Ray (GR) Log

A gamma ray (GR) log is a measurement of the natural gamma radiation of the formation. Shale consists of  $^{40}\text{K}$ ,  $^{238}\text{U}$ , and  $^{232}\text{Th}$ , which emits gamma radiation. A gamma ray log therefore gives indication of the amount of shale in a given lithology, hence distinguishing between shale and nonshales. GR logs are scaled in GAPI units. Fig. 5.7 shows a schematic of gamma ray logging.

Gamma ray logs can be used for determining the shale content in a given formation using the linear relationship between  $V_{sh}$  and  $GR_{zone}$ , as shown in equation (5.26):

$$V_{sh}(\text{fraction}) = \frac{GR_{zone} - GR_{clean}}{GR_{shale} - GR_{clean}} \quad (5.26)$$



Calliper log  
 Spontaneous potential  
 Gamma ray log  
 Density log  
 Neutron log  
 Sonic log  
 Shallow resistivity log  
 Medium resistivity log  
 Deep resistivity log

Figure 5.4 Example of tracks for openhole logs.

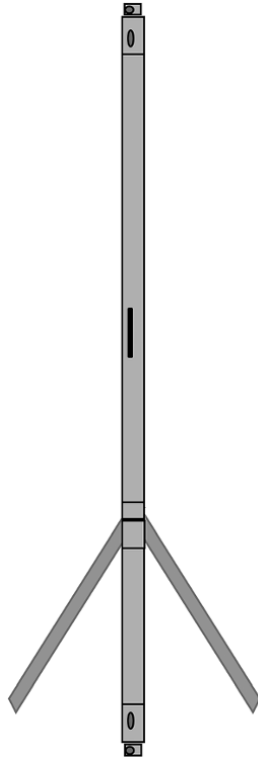


Figure 5.5 Caliper logging tool.

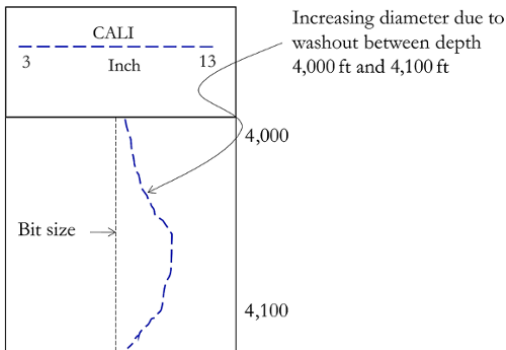


Figure 5.6 Caliper log showing hole size.

Equation (5.26) is also called the *gamma ray index* ( $I_{GR}$ ). Hence, the gamma ray index is defined as:

$$I_{GR} = \frac{GR_{zone} - GR_{clean}}{GR_{shale} - GR_{clean}} \quad (5.27)$$

Fig. 5.8 shows an example of GR log response to shale-sand lithology with high GR response corresponding to shale and low GR response corresponding to sand.

Considering Zone B in Fig. 5.8, with average GR response of 50 GAPI, the shale content ( $V_{sh}$ ) for Zone B, based on Gamma Ray Index (linear interpolation of GR), is therefore:

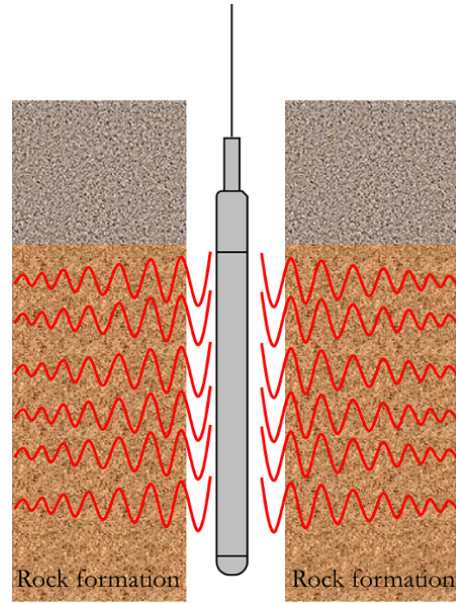


Figure 5.7 Gamma ray logging.

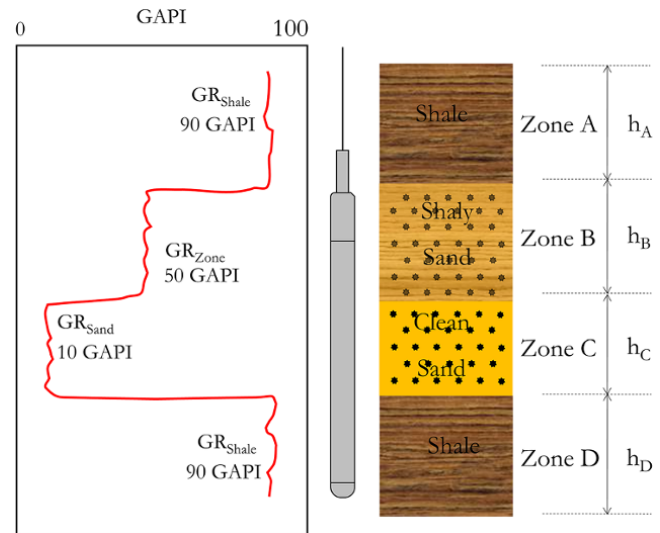


Figure 5.8 Gamma ray log and lithology.

$$V_{sh}(\text{fraction}) = \frac{GR_{zone} - GR_{clean}}{GR_{shale} - GR_{clean}}$$

$$V_{sh}(\text{fraction}) = \frac{50 - 10}{90 - 10} = 0.5$$

Other  $V_{sh}$  methods published [Asquith and Krygowski, 2004; Cannon, 2016] are summarized in Table 5.1.

Gamma ray logs are an important input in calculating net-to-gross ratio (NTG or N/G). NTG defines the ratio

**Table 5.1**  $V_{sh}$  Calculation Methods.

Method	Formula	Formulation and comments
Linear (Gamma Ray Index)	$V_{sh} = I_{GR}$	(5.28) Based on linear relationship between shale volume and GR response.
Larionov [1969] for tertiary (unconsolidated) rock	$V_{sh} = 0.083 (2^{3.7I_{GR}} - 1)$	(5.29) Based on empirical correlation. Linear relationship (5.27) overestimates $V_{sh}$ for tertiary (unconsolidated) rocks.
Larionov [1969] for pre-tertiary (older and consolidated) rock	$V_{sh} = 0.33 (2^{2I_{GR}} - 1)$	(5.30) Based on empirical correlation. Linear relationship (5.27) overestimates $V_{sh}$ pre-tertiary (consolidate) rocks
Stieber [1970]	$V_{sh} = \frac{0.5I_{GR}}{(1.5 - I_{GR})}$	(5.31) Calibration to Gulf coast log.
Clavier <i>et al.</i> [1971]	$V_{sh} = 1.7 - (3.38 - (I_{GR} + 0.7)^2)^{\frac{1}{2}}$	(5.32) Compromise between Larionov Tertiary and old rock model

$I_{GR}$  is defined in equation (5.27)

**Table 5.2** Acquired Openhole Logs for Exercise 5.1.

MD (KB) (ft)	SP (mV)	GR (GAPI)	LLD ( $\Omega$ -m)	MD (KB) (ft)	SP (mV)	GR (GAPI)	LLD ( $\Omega$ -m)
6,200	-81.69	61.01	2.16	6,325	-54.62	107.73	1.55
6,205	-78.28	77.61	1.70	6,330	-45.48	109.43	1.39
6,210	-71.75	90.41	1.46	6,335	-42.71	108.00	1.36
6,215	-59.25	102.64	1.45	6,340	-43.14	105.03	1.79
6,220	-48.85	109.53	1.44	6,345	-48.20	104.32	1.65
6,225	-44.41	111.86	1.42	6,350	-56.10	105.09	1.49
6,230	-44.41	111.86	1.38	6,355	-61.14	105.85	1.43
6,235	-44.08	112.36	1.33	6,360	-53.40	105.80	1.46
6,240	-43.28	113.14	1.19	6,365	-61.00	108.22	1.41
6,245	-42.10	113.14	1.00	6,370	-61.91	100.40	1.31
6,250	-40.08	110.01	0.91	6,375	-60.34	97.88	1.25
6,255	-38.05	97.88	0.87	6,380	-58.78	97.88	1.25
6,260	-36.03	97.88	0.82	6,385	-52.29	100.79	1.25
6,265	-36.07	97.88	0.78	6,390	-41.67	100.53	1.13
6,270	-37.55	100.68	0.77	6,395	-57.99	90.55	0.88
6,275	-39.03	102.97	0.76	6,400	-81.86	63.07	0.73
6,280	-40.50	102.97	0.76	6,405	-85.57	59.61	0.64
6,285	-45.51	90.55	1.02	6,410	-86.00	57.95	0.55
6,290	-52.41	68.00	3.48	6,415	-87.00	58.12	0.67
6,295	-68.40	69.40	9.08	6,420	-83.31	60.00	0.99
6,300	-75.86	69.41	14.57	6,425	-71.29	71.52	1.16
6,305	-75.39	70.00	4.56	6,430	-67.75	83.05	1.21
6,310	-49.57	107.83	2.16	6,435	-64.20	94.22	1.25
6,315	-56.01	109.19	1.90	6,440	-63.05	103.43	1.24
6,320	-55.46	108.30	1.65	6,445	-63.05	101.35	1.22

of net reservoir interval to gross thickness. The NTG for the entire interval covered by the GR log in Fig. 5.8 is therefore:

$$NTG = \frac{h_B + h_C}{h_A + h_B + h_C + h_D}$$

**Exercise 5.1** Sensitivity on  $V_{sh}$  Calculation

Given the openhole logs in Table 5.2 determine  $V_{sh}$  using the five methods listed in Table 5.1.

**Solution.**

$GR_{Clean}$  and  $GR_{Shale}$  is determined as shown in Fig. 5.9.

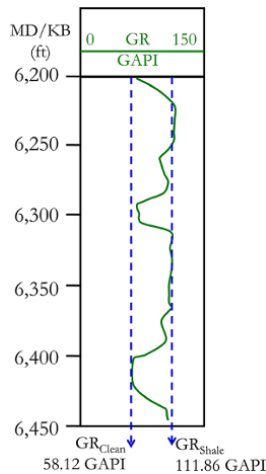


Figure 5.9 GR log showing GR<sub>Clean</sub> and GR<sub>Shale</sub>.

$I_{GR}$  is calculated using equation (5.27) and shown in Table 5.3.

$V_{sh}$  for each method listed in Table 5.1 depends only on  $I_{GR}$  (first column of Table 5.3).

A comparison of each  $V_{sh}$  from the different methods used is displayed in Fig. 5.10.

Comparison of different  $V_{sh}$  calculations showing deviation from linearity is shown in Fig. 5.11.

The gamma ray signal measured during logging, which is also called *natural gamma ray* or *standard gamma ray log*, consists of the sum of contributing signals from thorium (Th), uranium (U), and potassium (K) as shown in equation (5.33):

$$GR(GAPI) = R_{Th}[Th(ppm)] + R_U[U(ppm)] + R_K[K(wt\%)] \quad (5.33)$$

where  $R_{Th}$ ,  $R_U$ , and  $R_K$  are the contributing ratios of thorium, uranium, and potassium, respectively, for weighting contribution of each signal. Thorium and uranium are in ppm while potassium is in weight-%.

The gamma ray log, which is also called *natural gamma ray* or *standard gamma ray log*, should not be used in radioactive sands, which can give the response expected of a shale formation, thereby leading to wrong lithological characterization (Fig. 5.12). Figure 5.12 shows further that following spectral decomposition of the GR, potassium and thorium did not respond to the radioactive sand unlike uranium, which showed a positive response. The gamma ray log corrected for the effect of uranium, which can be present in both clean and shaly formations, should be used in radioactive sands.

Table 5.3  $V_{sh}$  Calculation Using Different Methods.

$I_{GR}$ equation (5.28)	Larinov (Tertiary) equation (5.29)	Larinov (Pre-tertiary) equation (5.30)	Steiber equation (5.31)	Clavier equation (5.32)
0.05	0.01	0.03	0.02	0.02
0.36	0.13	0.22	0.16	0.20
0.60	0.30	0.43	0.33	0.40
0.83	0.61	0.71	0.62	0.68
0.96	0.88	0.91	0.88	0.90
1.00	1.00	0.99	1.00	1.00
1.00	1.00	0.99	1.00	1.00
1.00	1.00	0.99	1.00	1.00
1.00	1.00	0.99	1.00	1.00
0.97	0.90	0.93	0.90	0.92
0.74	0.47	0.59	0.49	0.56
0.74	0.47	0.59	0.49	0.56
0.74	0.47	0.59	0.49	0.56
0.79	0.55	0.66	0.56	0.63
0.83	0.62	0.72	0.63	0.69
0.83	0.62	0.72	0.63	0.69
0.60	0.31	0.43	0.34	0.40
0.18	0.05	0.10	0.07	0.09
0.21	0.06	0.11	0.08	0.10
0.21	0.06	0.11	0.08	0.10
0.22	0.06	0.12	0.09	0.11
0.92	0.81	0.86	0.80	0.84
0.95	0.87	0.90	0.86	0.89
0.93	0.83	0.87	0.82	0.86
0.92	0.80	0.86	0.80	0.84
0.95	0.88	0.91	0.88	0.90
0.93	0.81	0.86	0.81	0.85
0.87	0.70	0.78	0.70	0.75
0.86	0.67	0.76	0.67	0.73
0.87	0.70	0.78	0.70	0.75
0.89	0.73	0.80	0.73	0.77
0.89	0.72	0.80	0.72	0.77
0.93	0.82	0.87	0.82	0.85
0.79	0.54	0.65	0.55	0.62
0.74	0.47	0.59	0.49	0.56
0.74	0.47	0.59	0.49	0.56
0.79	0.55	0.66	0.56	0.63
0.79	0.55	0.66	0.56	0.62
0.60	0.31	0.43	0.34	0.40
0.09	0.02	0.04	0.03	0.04
0.03	0.01	0.01	0.01	0.01
0.00	0.00	0.00	0.00	0.00
0.00	0.00	0.00	0.00	0.00
0.03	0.01	0.02	0.01	0.01
0.25	0.07	0.14	0.10	0.13
0.46	0.19	0.30	0.22	0.28
0.67	0.38	0.51	0.41	0.48
0.84	0.64	0.73	0.64	0.70
0.80	0.57	0.68	0.58	0.64

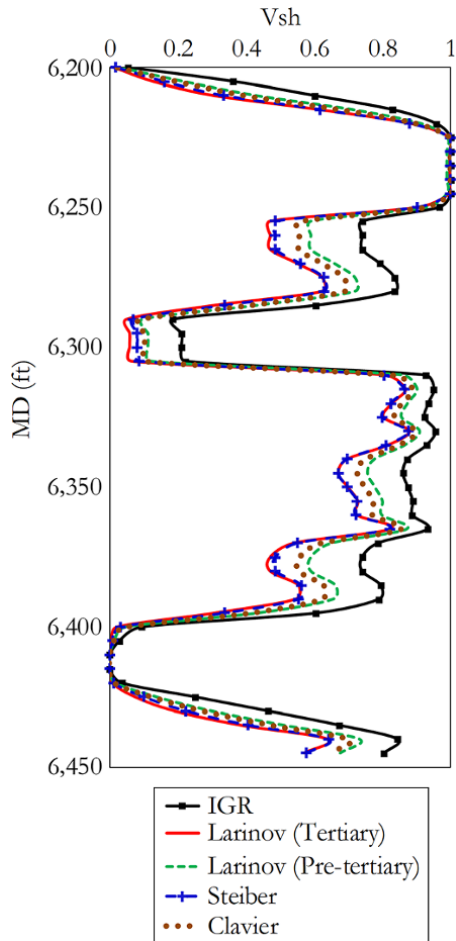


Figure 5.10 Comparison of  $V_{sh}$  by different methods.

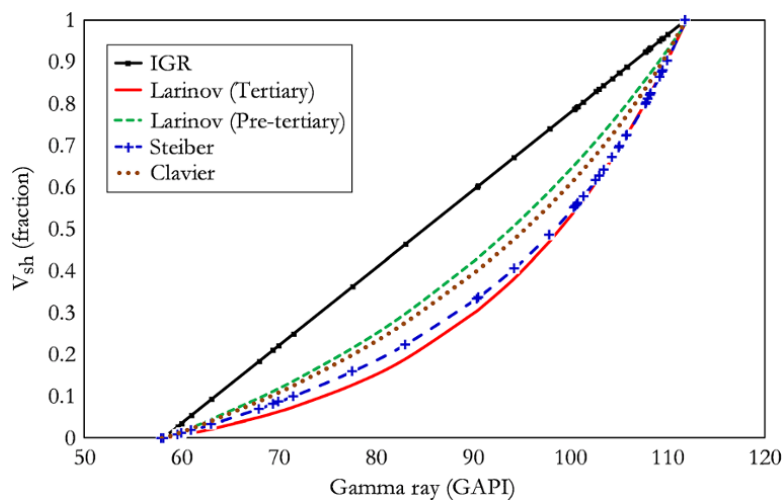


Figure 5.11 Comparison of different  $V_{sh}$  showing deviation from linearity.

The sum of the potassium-40 and thorium radiation (SGR minus uranium contribution) is called *computed gamma ray response (CGR)* or *uranium free gamma ray*.

Spectral gamma ray constituents are useful for formation characterization often by using the ratio of the constituent signal.

The Th/U ratio has been observed to vary from one environmental deposition to another. They have been observed to be highest in sediments deposited in continental oxidizing environments and lowest in marine reducing environments. High U/K in shale characterizes potential hydrocarbon source rock and Th/K is important in defining clay types.

**5.1.4.1. Limitation of Gamma Ray for Formation Characterization.** Potassium chloride (KCl) mud due to presence of potassium (K) results in high GR (standard gamma ray) and SGR (spectrometry gamma ray) leading to the wrong CGR. Barite mud results in a reduced GR and SGR.

When both GR and CGR are provided, both logs should be compared to check for the presence of radioactive sands. Also, it is good practice to compare the calculation using GR with that using CGR for consistency.

### 5.1.5. Spontaneous Potential (SP) Log

The spontaneous potential log (SP) is a measure of the spontaneous potential difference (sometimes called self-potential) between a moving electrode in the wellbore and a surface electrode (Fig. 5.13). The deflection of the SP is due to electrical current flow arising from *electrochemical* and *electrokinetic* potentials in the

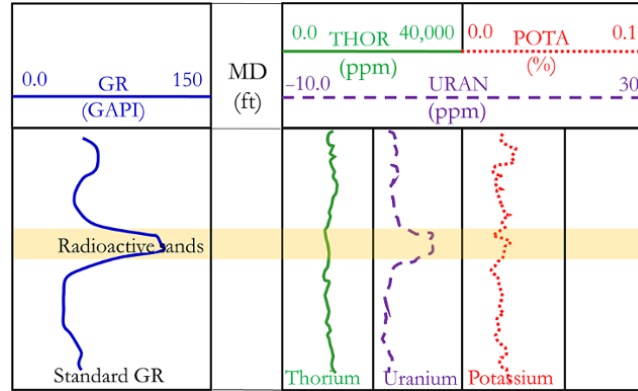


Figure 5.12 Standard gamma ray log with spectral decomposition.

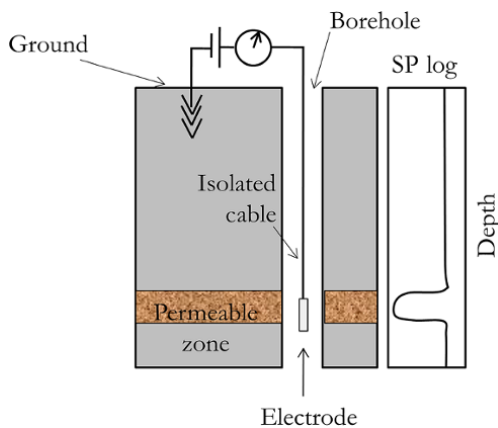


Figure 5.13 Measurement and tool arrangement for SP log.

formation. The electrochemical component of the SP response is made up of *membrane potential*, due to migration of  $\text{Na}^+$  (when  $R_w < R_m$ ) through selective shale membrane causing a flow of current, and the *liquid-junction potential*, which is due to movement of predominantly  $\text{Cl}^-$  ions that are smaller and more mobile than  $\text{Na}^+$  and, hence, generate current in opposite direction of flow to  $\text{Cl}^-$  ions. The electrokinetic component is due to the flow of electrolyte through permeable formation. Although the electrochemical component of SP is small, it can become significant when there is a large pressure differential that ensures a significant flow of electrolyte. The *static spontaneous potential* (SSP) of a formation, which is the sum of the electrokinetic, membrane and liquid junction potential can be expressed as:

$$SSP = E_k + E_m + E_j \quad (5.34)$$

SP deflection is to the left (negative) when the formation water salinity is higher than the salinity of the mud filtrate, which is often the case; however, deflection is to the right (positive) when formation salinity is less than salinity of

the mud. The recorded SP log approaches the SSP in thick permeable formations.

Spontaneous potential can be used for identification of permeable beds, formation water resistivity ( $R_w$ ) calculation in the absence of resistivity log, and log correlation and identification of shaliness of a formation. SP for calculation of  $V_{sh}$  should be considered only when GR is not available or in radioactive sand where CGR (uranium free gamma ray) is not available.

SP logs for formation evaluation have some limitations; these include: not being able to be acquired in cased holes; alteration of SP current when high resistive formations are present between shale and a permeable formation; SP base line shift along the SP track due to a difference in salinity when the formation is separated by shale; not being able to be acquire in conductive mud or when there is no contrast in resistivity between mud filtrate resistivity ( $R_{mf}$ ) and formation water resistivity ( $R_w$ ). SP logs are seriously affected by external power sources and cable lines.

Shale content using SP log is calculated in similar approach to GR.  $V_{sh}$  using SP log can be calculated using:

$$V_{sh}(\text{fraction}) = \frac{SP_{\text{zone}} - SP_{\text{clean}}}{SP_{\text{shale}} - SP_{\text{clean}}} = \frac{SSP - PSP}{SSP} = \left(1 - \frac{PSP}{SSP}\right) \quad (5.35)$$

In the SP log shown in Fig. 5.14, the shale content ( $V_{sh}$ ) of the zone of interest can be calculated using equation (5.35).

$$V_{sh} = \frac{SP_{\text{zone}} - SP_{\text{clean}}}{SP_{\text{shale}} - SP_{\text{clean}}} = \frac{SSP - PSP}{SSP} = \left(1 - \frac{PSP}{SSP}\right)$$

Where

$$SP_{\text{clean}} \equiv SP_{\text{sand}}$$

$$V_{sh} = \left(1 - \frac{PSP}{SSP}\right) = 1 - \frac{PSP}{SSP} = 1 - \frac{52.3}{72.7} = 0.28$$

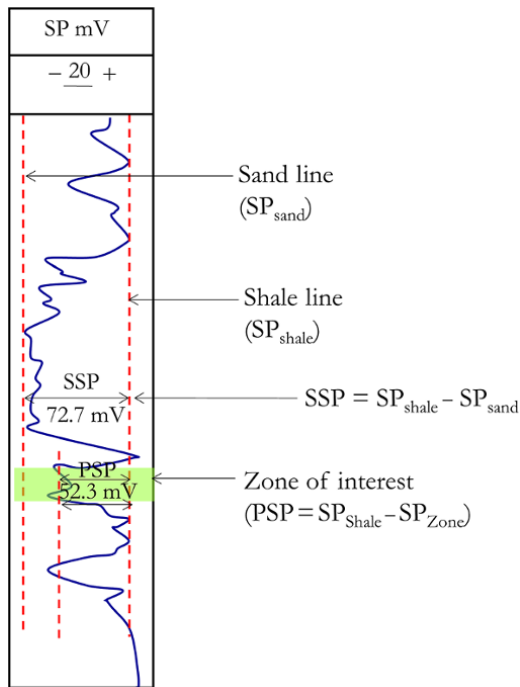


**Figure 5.14** SP log showing sand line, shale line, and SP of the zone of interest.

**Exercise 5.2** Calculation of Shale Content Using SP and GR Logs

Determine the shale content in the formation between the interval of 6,290 and 6,305 ft (Fig. 5.15) for a well drilled with mud with filtrate resistivity greater than formation water resistivity ( $R_w < R_{mf}$ ) using GR and SP log separately given the acquired openhole well logs in Table 5.2.

**Solution Steps.**

*Step 1:* determine  $GR_{Sand}$  and  $GR_{Shale}$  required for  $V_{sh}$  calculation using the GR log as shown in Fig. 5.8 and  $SP_{Sand}$  and  $SP_{Shale}$  for  $V_{sh}$  determination using the SP log as shown in Fig. 5.14.

*Step 2:* mark out the depth interval (zone) where  $V_{sh}$  is to be calculated. Determine  $GR_{Zone}$  for  $V_{sh}$  determination using the GR log as shown in Fig. 5.8 and  $SP_{Zone}$  for  $V_{sh}$  determination using the SP log as shown in Fig. 5.14.

Fig. 5.16 shows determination of  $GR_{Clean}$ ,  $GR_{Shale}$ , and  $GR_{Zone}$  for GR and  $SP_{Sand}$ ,  $SP_{Shale}$ , and  $SP_{Zone}$  for SP.

*Step 3:* determine  $V_{sh}$  using equation (5.26) for GR log and equation (5.35) for SP log.

**Solution.**

From equation (5.26)

$$V_{sh}(\text{fraction}) = \frac{GR_{zone} - GR_{clean}}{GR_{shale} - GR_{clean}} = \frac{69.41 - 58.12}{111.86 - 58.12} = 0.21$$

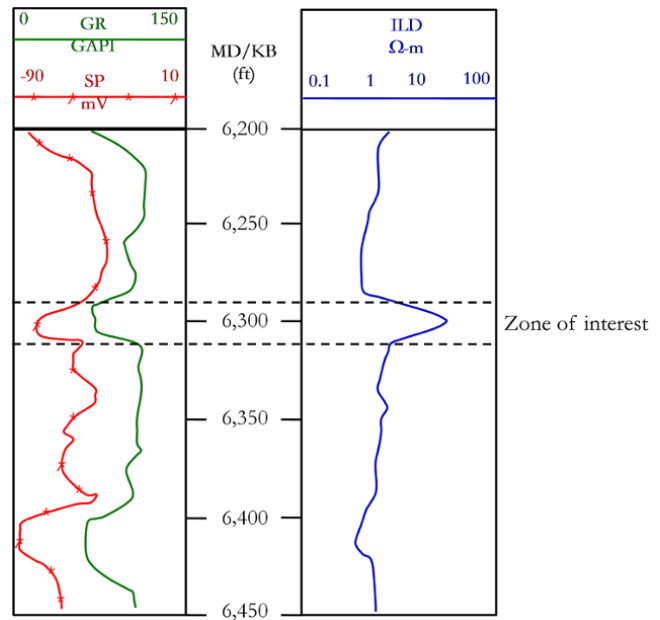


**Figure 5.15** Well log showing GR, SP, ILD, and zone of interest.

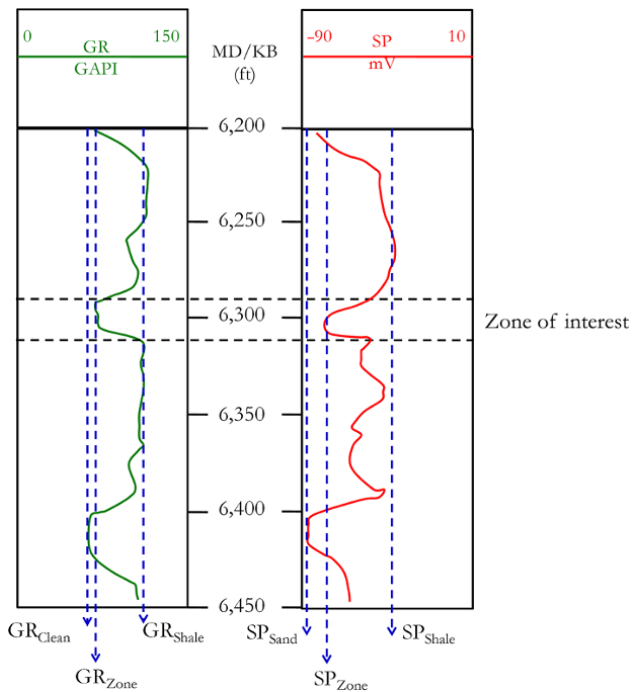


**Figure 5.16**  $GR_{Clean}$ ,  $GR_{Shale}$ , and  $GR_{Zone}$  for GR and  $SP_{Sand}$ ,  $SP_{Shale}$ , and  $SP_{Zone}$  for SP.

$V_{sh}$  based on GR is 0.21.  
From equation (5.35)

$$V_{sh} = \frac{SP_{zone} - SP_{clean}}{SP_{shale} - SP_{clean}} = \frac{-75 - (-86)}{-36.5 - (-86)} = 0.22$$

$V_{sh}$  based on SP is 0.22.



**5.1.5.1. SP Log for  $R_w$  Determination.** SP can be used to calculate  $R_w$ . This method, though widely used, may not yield an accurate  $R_w$ , as SP logs are easily affected by environmental factors. For use of SP for  $R_w$  calculation, it is expected that SP remains constant over considerable thickness and  $R_{mf}$  constant over the same interval of clean sand.

The steps for using SP log for  $R_w$  calculation are summarized here.

*Step 1:* convert mud resistivity ( $R_m$ ) and filtrate resistivity ( $R_{mf}$ ) from measurement temperature ( $T_m$ ) to that at formation temperature ( $T_f$ ).

Formation temperature if not given can be calculated using the temperature gradient, which can be derived if the temperature of another formation in the same area is known:

$$G_T = \left( \frac{T_{f@D} - T_s}{D} \right) \times 100 \quad (5.36)$$

where  $G_T$  is geothermal gradient in  $^{\circ}\text{F}/100$  ft,  $T_{f@D}$  is the known formation temperature in  $^{\circ}\text{F}$ , at depth  $D$  in ft, and  $T_s$  is the mean surface temperature in  $^{\circ}\text{F}$ .

$G_T$  calculated with equation (5.36) can then be used to determine the temperature of formation at another depth. Where formation temperature at any depth in the given area is not known to derive  $G_T$ , values of regional  $G_T$  published from the literature can be used. As such, the temperature of formation of interest as a function of depth can be expressed as:

$$T_f = T_s + \left[ G_T \frac{Z}{100} \right] \quad (5.37)$$

where  $T_f$  is the reservoir/formation temperature of interest in  $^{\circ}\text{F}$  and  $Z$ , the depth of interest in ft, is usually taken to be mid-formation.

Temperature correction for resistivity  $R_1$  at  $T_1$  to  $R_2$  at  $T_2$  is:

$$R_2 = R_1 \left\{ \frac{(T_1 + 6.77)}{(T_2 + 6.77)} \right\} \quad (5.38)$$

Hence, for  $R_m$  and  $R_{mf}$  at  $T_f$ , respectively:

$$R_{mf@T_f} = R_{mf}(T_f) = R_{mf}(T_m) \left\{ \frac{(T_m + 6.77)}{(T_f + 6.77)} \right\} \quad (5.39)$$

$$R_{m@T_f} = R_m(T_f) = R_m(T_m) \left\{ \frac{(T_m + 6.77)}{(T_f + 6.77)} \right\} \quad (5.40)$$

where  $T$  is in  $^{\circ}\text{F}$ .

*Step 2:* calculate the *resistivity ratio* (RI):

$$RI = \frac{R_i}{R_m(T_f)} \quad (5.41)$$

where  $R_i$  is the resistivity of the invaded zone.

*Step 3:* determine the SP correction factor (CP) for formations less than 50 ft. Where the formation is 50 ft and above, correction of SP is not required.

$$CF = \frac{\left[ 4 \left( \frac{R_i}{R_m(T_f)} + 2 \right) \right]^{\frac{1}{3.65}} - 1.5}{h - \left[ \frac{\left( \frac{R_i}{R_m(T_f)} + 11 \right)}{0.65} \right]^{\frac{1}{6.05}} - 0.1} + 0.95 \quad (5.42)$$

*Step 4:* determine SP ( $SSP_{U_{\text{corrected}}}$ ), which is the difference between  $SP_{\text{Shale}}$  and  $SP_{\text{Clean}}$  over a clean sand interval. Then calculate corrected SSP using:

$$SSP = CF \times SP \quad (5.43)$$

where CP is the correction factor determined in equation (5.42) and

$$SP = SP_{\text{Clean}} - SP_{\text{Shale}} \quad (5.44)$$

*Step 5:* calculate  $R_{mfe}$  from  $R_{mf}$  at  $T_f$ :

$$R_{mfe} = 0.85 \times R_{mf}(T_f) \text{ for } R_{mf}(T_f) > 0.2 \quad (5.45)$$

and

$$R_{mfe} = \left[ \frac{[146R_{mf}(T_f) - 5]}{[337R_{mf}(T_f) + 77]} \right], \text{ for } R_{mf}(T_f) \leq 0.2 \quad (5.46)$$

*Step 6:* determine  $R_{we}$  using:

$$R_{we} = R_{mfe} 10^{\frac{SSP}{(61 + 0.133 \times T_f)}} \quad (5.47)$$

*Step 7:* calculate  $R_w$  from  $R_{we}$ :

$$R_w(T_f) = - (0.58 - 10^{0.69R_{we} - 0.24}) \text{ for } R_{we} > 0.12 \quad (5.48)$$

and

$$R_w(T_f) = \left[ \frac{77R_{we} + 5}{146 - 337R_{we}} \right] \text{ for } R_{we} \leq 0.12 \quad (5.49)$$

where  $R_w$  is the formation water resistivity,  $R_w(T_f)$  is formation water resistivity at the formation temperature,  $R_{we}$  is equivalent formation water resistivity and calculated from SSP (difference between shale baseline and clean sand line) with correction for formation thickness where required as shown in equation (5.47),  $R_{mf}$  is the resistivity of the mud filtrate at formation temperature, and  $R_{mfeq}$  is the equivalent resistivity of the mud filtrate.

The steps for using the SP log for  $R_w$  calculation are summarized in Fig. 5.17.

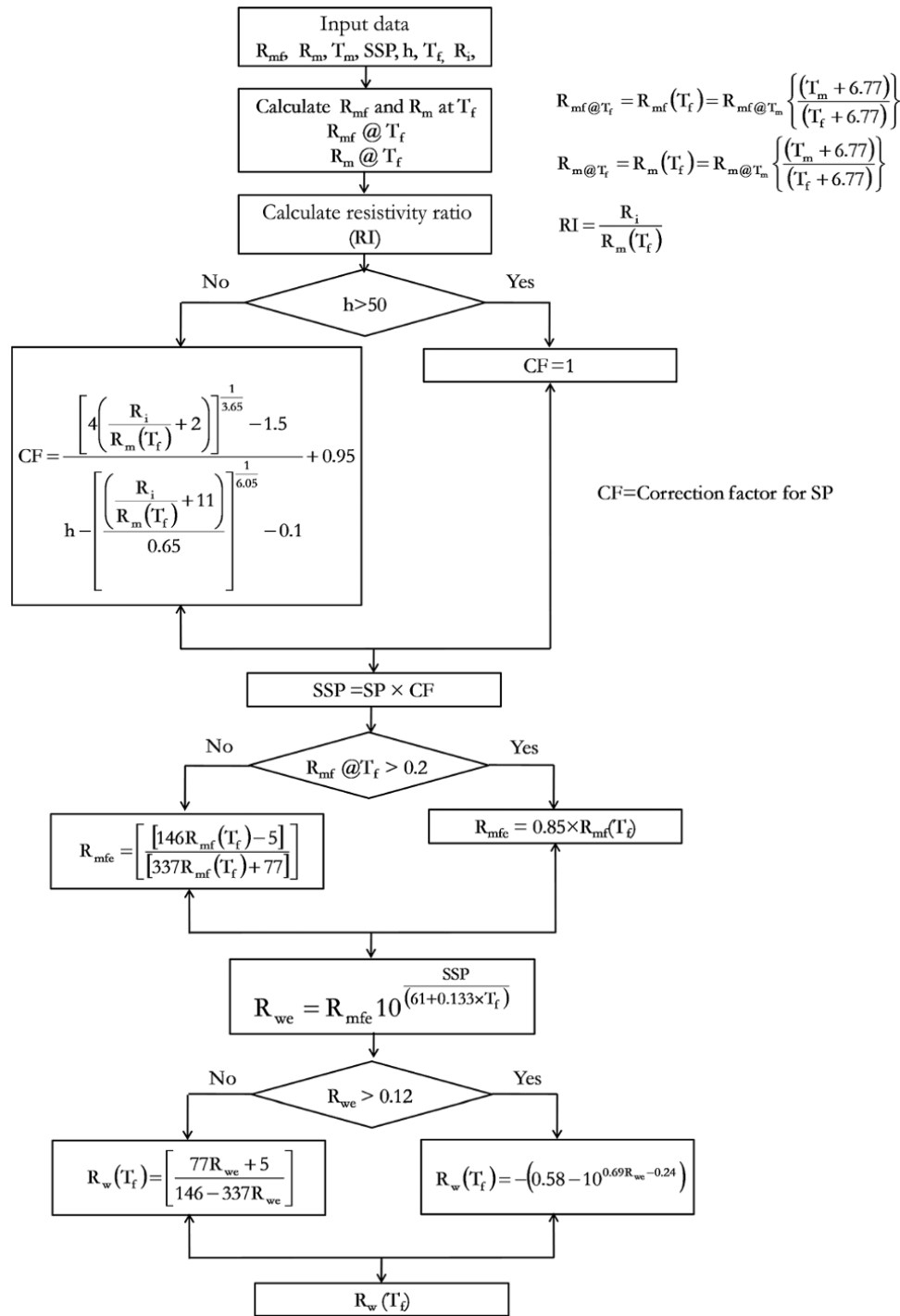


Figure 5.17 Flow chart for  $R_w$  calculation from the SP log.

**Exercise 5.3** Calculate  $R_w$  Using SP Logs

Given the openhole log from a vertical well in Table 5.4 for a well with a total measured depth of 8,400 ft, a bottomhole temperature at total depth recorded as 259.8°F, and a mean surface temperature of the area is 75°F:

Determine  $R_w$  given: mud filtrate resistivity ( $R_{mf}$ ) = 1.2Ω-m at a measured temperature of 55°F and mud

resistivity ( $R_m$ ) of 1.6 Ω-m at a measured temperature of 55°F and resistivity of invaded zone is 11.8 Ω-m.

**Solution.**

Identify the thick bed of porous clean sand a shown in Fig. 5.18.

Following the steps described above

**Table 5.4** Openhole Log for Exercise 5.3.

Depth (ft)	Caliper (in)	SP (mV)	Gamma (GAPI)	ILD ( $\Omega$ -m)	Focused resistivity ( $\Omega$ -m)	Density porosity	Neutron porosity
8,200.00	8.64	-88.00	74.33	1.06	2.56	21.25	25.93
8,203.00	9.09	-53.04	82.86	0.93	0.95	18.44	25.84
8,206.00	9.02	-48.81	71.08	0.82	2.58	12.53	36.88
8,209.00	8.95	-53.99	72.45	0.63	2.24	13.52	34.13
8,212.00	8.68	-67.08	67.77	0.44	1.08	20.05	33.91
8,215.00	8.79	-68.42	62.95	0.47	1.09	21.61	39.27
8,218.00	9.20	-55.35	75.47	0.52	0.99	23.26	39.26
8,221.00	8.88	-56.38	65.97	0.57	1.14	14.88	32.22
8,224.00	8.81	-55.59	69.06	0.64	1.63	12.87	31.91
8,227.00	9.03	-57.81	71.92	0.69	1.39	23.24	36.74
8,230.00	10.31	-45.22	79.73	0.68	1.07	20.52	36.88
8,233.00	11.14	-32.70	82.99	0.67	0.59	23.53	49.38
8,236.00	10.74	-29.93	88.38	0.68	0.64	24.86	50.72
8,239.00	10.51	-27.58	85.00	0.74	0.76	25.20	47.47
8,242.00	9.12	-27.65	90.00	1.03	1.20	24.15	42.16
8,245.00	9.58	-27.73	86.00	0.90	1.41	24.35	45.06
8,248.00	9.96	-27.80	92.42	0.69	1.12	25.53	49.90
8,251.00	11.49	-27.88	96.80	0.59	0.82	33.02	50.10
8,254.00	10.47	-28.83	98.27	0.68	0.82	26.27	51.41
8,257.00	10.08	-29.99	100.54	0.84	0.93	20.26	39.46
8,260.00	9.55	-43.74	88.98	1.04	1.08	16.56	41.60
8,263.00	8.51	-64.64	59.05	1.31	1.82	21.09	31.45
8,266.00	8.36	-86.98	49.05	1.68	3.26	23.31	27.44
8,269.00	8.35	-99.06	45.08	2.48	5.43	26.71	20.84
8,272.00	8.33	-104.22	45.90	5.32	11.78	33.10	15.29
8,275.00	8.29	-107.46	48.06	12.50	27.07	37.13	14.90
8,278.00	8.25	-106.84	55.47	23.15	28.81	37.44	15.69
8,281.00	8.24	-106.23	55.50	29.97	30.54	37.81	15.94
8,284.00	8.24	-105.93	51.55	36.00	35.32	38.57	16.35
8,287.00	8.23	-106.01	51.68	25.40	22.99	39.29	16.76
8,290.00	8.23	-106.08	52.37	21.14	23.93	38.75	16.91
8,293.00	8.22	-106.16	54.55	7.53	7.34	38.35	15.64
8,296.00	8.22	-106.18	58.40	2.51	3.97	28.51	30.76
8,299.00	8.18	-102.49	60.92	2.16	3.00	25.93	38.17
8,302.00	8.15	-98.79	58.18	1.67	2.92	27.20	29.43
8,305.00	8.11	-100.11	58.64	0.80	2.79	24.89	32.58
8,308.00	8.16	-108.38	59.55	0.90	1.15	25.97	25.87
8,311.00	8.20	-107.08	60.46	0.38	1.21	26.76	29.37
8,314.00	8.25	-105.78	62.60	0.34	1.09	25.96	30.22
8,317.00	8.30	-103.81	65.28	0.35	1.02	24.73	30.54
8,320.00	8.35	-99.36	72.75	0.39	1.35	22.95	30.56
8,323.00	8.45	-90.58	74.67	0.45	1.02	25.41	30.58
8,326.00	8.63	-81.31	76.59	0.52	1.10	22.52	34.84
8,329.00	9.02	-57.58	94.13	0.60	1.04	20.89	41.79
8,332.00	9.17	-43.76	87.55	0.65	1.27	26.11	39.85
8,335.00	9.26	-31.95	83.80	0.70	1.85	16.72	33.71
8,338.00	9.50	-28.07	93.63	0.67	0.95	19.65	43.85
8,341.00	9.38	-28.15	91.14	0.63	0.78	24.19	45.63
8,344.00	9.11	-39.64	83.46	0.57	0.78	22.63	45.83
8,347.00	8.84	-74.68	60.22	0.51	1.00	24.26	39.31
8,350.00	8.57	-80.53	63.52	0.43	1.32	23.74	29.99
8,353.00	8.65	-44.72	74.21	0.43	0.76	24.21	36.42
8,356.00	9.03	-40.85	91.17	0.58	0.91	27.04	41.20

**Table 5.4** (Continued)

Depth (ft)	Caliper (in)	SP (mV)	Gamma (GAPI)	ILD ( $\Omega$ -m)	Focused resistivity ( $\Omega$ -m)	Density porosity	Neutron porosity
8,359.00	8.79	-52.99	82.36	0.71	1.06	20.08	32.14
8,362.00	8.55	-82.03	54.65	0.34	1.17	23.01	35.61
8,365.00	8.53	-99.74	55.40	0.26	1.27	24.35	30.14
8,368.00	8.52	-109.68	56.15	0.27	1.32	25.54	28.75
8,371.00	8.52	-108.11	56.90	0.28	1.23	24.69	29.15
8,374.00	8.81	-108.18	60.21	0.34	1.14	27.00	29.43
8,377.00	9.16	-84.75	64.40	0.41	1.69	26.03	29.23
8,380.00	9.50	-50.37	72.73	0.63	1.65	25.31	33.06
8,383.00	9.95	-31.17	86.51	0.70	1.50	23.31	43.55
8,386.00	9.47	-27.35	90.93	0.74	1.34	27.72	50.87
8,389.00	9.33	-25.39	95.34	0.75	1.19	26.41	46.36
8,392.00	9.66	-25.46	95.23	0.76	1.03	24.56	45.11
8,395.00	9.88	-25.54	94.42	0.75	1.01	22.67	43.61
8,398.00	9.87	-29.01	85.05	0.75	1.64	21.00	39.09
8,400.00	9.87	-33.01	76.46	0.72	1.78	20.00	32.91

Neutron and density porosity are in percentage

Step 1: from equation (5.36):

$$G_T = \left( \frac{T_{f@D} - T_s}{D} \right) \times 100$$

$$G_T = \left( \frac{259.8 - 75}{8400} \right) \times 100 = 2.2^\circ\text{F}/100\text{ft}$$

The formation temperature of a thick continuous bed with a fairly constant SP reading (Fig. 5.18) is determined using equation (5.37):

$$T_f = T_s + \left[ G_T \frac{Z}{100} \right]$$

where  $Z$  is the middle of the formation of interest, which will give arithmetic mean temperature of formations:

$$Z = \frac{Z_{\text{Top}} + Z_{\text{Base}}}{2} = \frac{8272 + 8314}{2} = 8293 \text{ ft}$$

Hence:

$$T_f = T_s + \left[ G_T \frac{Z}{100} \right] = 75 + \left[ 2.2 \frac{8293}{100} \right] = 257.45^\circ\text{F}$$

Using equations (5.39) and (5.40) to determine  $R_{mf}(T_f)$  and,  $R_m(T_f)$  respectively:

$$\begin{aligned} R_{mf}(T_f) &= R_{mf}(T_m) \left\{ \frac{(T_m + 6.77)}{(T_f + 6.77)} \right\} \\ &= 1.2 \left\{ \frac{(55 + 6.77)}{(257.45 + 6.77)} \right\} = 0.281 \Omega\text{-m} \end{aligned}$$

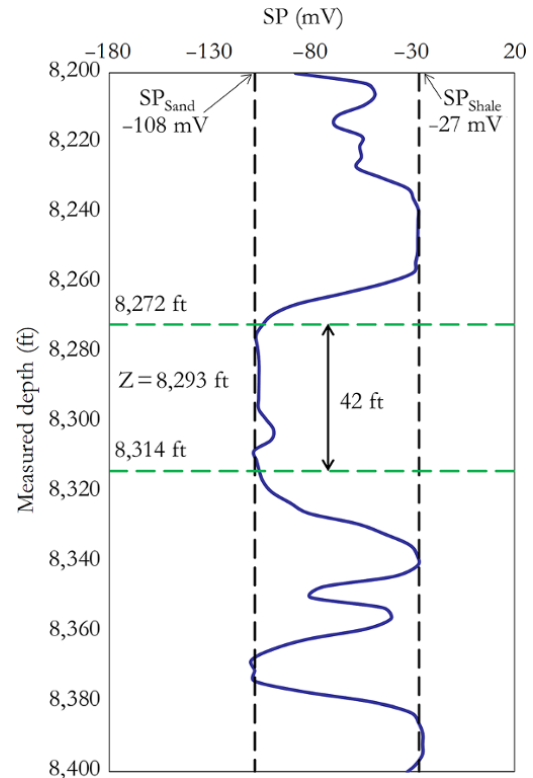


**Figure 5.18** SP log with key parameters required for calculations.

$$\begin{aligned} R_m(T_f) &= R_m(T_m) \left\{ \frac{(T_m + 6.77)}{(T_f + 6.77)} \right\} \\ &= 1.6 \left\{ \frac{(55 + 6.77)}{(257.45 + 6.77)} \right\} = 0.374 \Omega\text{-m} \end{aligned}$$

Step 2: calculate the resistivity ratio (RI) using equation (5.41) which is required for calculating the correction factor (CF) when h is less than 50 ft.

$$RI = \frac{R_i}{R_m(T_f)} = \frac{11.5}{0.374} = 30.744 \text{ ft}$$

Step 3: determine the SP correction factor (CF) using equation (5.42), as the formation thickness of interest (h) is less than 50 ft. Using equation (5.42):

$$CF = \frac{\left[4\left(\frac{R_i}{R_m(T_f)} + 2\right)\right]^{\frac{1}{3.65}} - 1.5}{h - \left[\frac{\left(\frac{R_i}{R_m(T_f)} + 11\right)}{0.65}\right]^{\frac{1}{6.05}} - 0.1} + 0.95$$

$$= CF = \frac{[4(30.744 + 2)]^{\frac{1}{3.65}} - 1.5}{42 - \left[\frac{(30.744 + 11)}{0.65}\right]^{\frac{1}{6.05}} - 0.1} + 0.95 = 1.01$$

Step 4: determine the uncorrected SP ( $SSP_{Uncorrected}$ ) over the clean sand interval. Then calculate corrected SSP using equation (5.43), where the SP is determined from equation (5.44) and values read from the SP log shown in Fig. 5.18 as:

$$SP = SP_{Clean} - SP_{Shale}$$

$$SP = -108 - (-27) = -81 \text{ mV}$$

Using equation (5.43):

$$SSP = CF \times SP$$

$$SSP = CF \times SP = 1.01 \times (-81) = -81.81 \text{ mV}$$

Step 5: calculate  $R_{mfe}$  from  $R_{mf}$  at  $T_f$ .

Since  $R_{mf}(T_f) = 0.281 \Omega\text{-m}$  and is greater than 0.2, using equation (5.45):

$$R_{mfe} = 0.85 \times R_{mf}(T_f)$$

$$R_{mfe} = 0.85 \times 0.281 = 0.239 \Omega\text{-m}$$

Step 6: determine  $R_{we}$  using equation (5.47):

$$R_{we} = R_{mfe} 10^{\frac{SSP}{(61 + 0.133 \times T_f)}} = 0.239 10^{\frac{-81.81}{(61 + 0.133 \times 237.45)}} = 0.033 \Omega\text{-m}$$

Step 7: calculate  $R_w$  from  $R_{we}$ .

Since  $R_{we}$  is less than 0.12, using equation (5.49):

$$R_w(T_f) = \left[\frac{77R_{we} + 5}{146 - 337R_{we}}\right] = \left[\frac{77 \times 0.033 + 5}{146 - 337 \times 0.033}\right] = 0.056 \Omega\text{-m}$$

$$R_w(T_f) = 0.056 \Omega\text{-m}$$

where  $R_w(T_f)$  is formation water resistivity at formation temperature.

**Exercise 5.4**  $V_{sh}$  Calculation Using SP and GR Logs

Using openhole well log data from a well with mud filtrate salinity lower than formation water salinity ( $R_w < R_{mf}$ ) in Table 5.4, determine  $V_{sh}$  content along the well using SP and GR logs.

**Solution.**

Following the same steps as in Exercise 5.2.

Fig. 5.19 shows the determination of parameters from GR and SP logs required for  $V_{sh}$ .

Using equations (5.26) and (5.35) to determine gamma ray  $V_{sh}$  ( $V_{sh\_GR}$ ) and SP  $V_{sh}$  ( $V_{sh\_SP}$ ), respectively.

For  $V_{sh\_GR}$ , equation (5.26) was used,  $V_{sh\_GR} = \frac{GR_{zone} - GR_{clean}}{GR_{shale} - GR_{clean}}$

For  $V_{sh\_SP}$  equation (5.35) was used,  $V_{sh\_SP} = \frac{SP_{zone} - SP_{clean}}{SP_{shale} - SP_{clean}}$

Table 5.5 summarizes the  $V_{sh\_GR}$  and  $V_{sh\_SP}$  calculations.

Fig. 5.20 shows a comparison of  $V_{sh}$  using GR and SP logs.

GR should always be considered in preference to SP log for  $V_{sh}$  calculation except in radioactive sands because SP

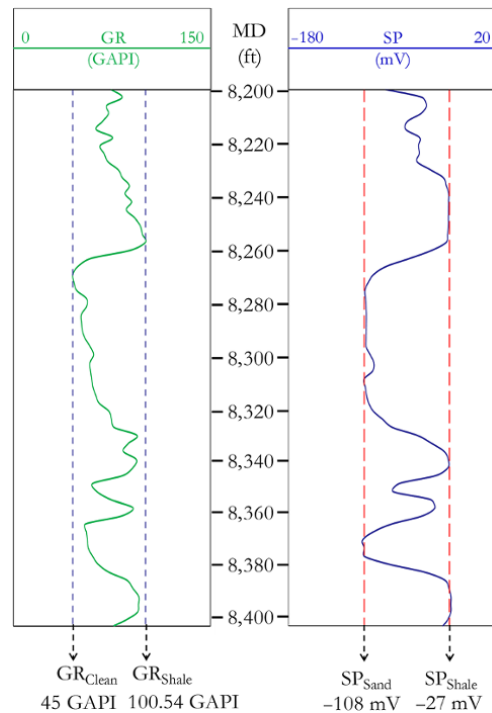


Figure 5.19 Parameters from GR and SP log required for  $V_{sh}$ .

**Table 5.5**  $V_{sh\_GR}$  and  $V_{sh\_SP}$  Calculation Table.

MD (ft)	$V_{sh\_GR}$ using equation (5.26))	$V_{sh\_SP}$ using equation (5.35)	MD (ft)	$V_{sh\_GR}$ using equation (5.26)	$V_{sh\_SP}$ using equation (5.35)
8,200.00	0.53	0.25	8,302.00	0.24	0.11
8,203.00	0.68	0.68	8,305.00	0.24	0.10
8,206.00	0.47	0.73	8,308.00	0.26	0.00
8,209.00	0.49	0.67	8,311.00	0.28	0.01
8,212.00	0.41	0.51	8,314.00	0.32	0.03
8,215.00	0.32	0.49	8,317.00	0.36	0.05
8,218.00	0.55	0.65	8,320.00	0.50	0.11
8,221.00	0.38	0.64	8,323.00	0.53	0.22
8,224.00	0.43	0.65	8,326.00	0.57	0.33
8,227.00	0.48	0.62	8,329.00	0.88	0.62
8,230.00	0.62	0.78	8,332.00	0.77	0.79
8,233.00	0.68	0.93	8,335.00	0.70	0.94
8,236.00	0.78	0.96	8,338.00	0.88	0.99
8,239.00	0.72	0.99	8,341.00	0.83	0.99
8,242.00	0.81	0.99	8,344.00	0.69	0.84
8,245.00	0.74	0.99	8,347.00	0.27	0.41
8,248.00	0.85	0.99	8,350.00	0.33	0.34
8,251.00	0.93	0.99	8,353.00	0.53	0.78
8,254.00	0.96	0.98	8,356.00	0.83	0.83
8,257.00	1.00	0.96	8,359.00	0.67	0.68
8,260.00	0.79	0.79	8,362.00	0.17	0.32
8,263.00	0.25	0.54	8,365.00	0.19	0.10
8,266.00	0.07	0.26	8,368.00	0.20	0.00
8,269.00	0.00	0.11	8,371.00	0.21	0.00
8,272.00	0.01	0.05	8,374.00	0.27	0.00
8,275.00	0.05	0.01	8,377.00	0.35	0.29
8,278.00	0.19	0.01	8,380.00	0.50	0.71
8,281.00	0.19	0.02	8,383.00	0.75	0.95
8,284.00	0.12	0.03	8,386.00	0.83	1.00
8,287.00	0.12	0.02	8,389.00	0.91	1.00
8,290.00	0.13	0.02	8,392.00	0.90	1.00
8,293.00	0.17	0.02	8,395.00	0.89	1.00
8,296.00	0.24	0.02	8,398.00	0.72	0.98
8,299.00	0.29	0.07	8,400.00	0.57	0.93

logs can be influenced by environmental factors, as already discussed section 5.1.5.

### 5.1.6. Density Log

The density log is used in determining formation density and to estimate formation porosity. Together with other logs like the Neutron, the lithology and formation fluid type can also be determined.

The density logging tool (Fig. 5.21) is an active tool with measurement based on the *Compton effect* (scattering of gamma radiation) when the formation is bombarded with a radioactive source. When gamma rays collide with atomic particles, they experience loss of energy that is characterized as *Compton scattering* (which occurs in the energy range of 75 keV to 10 MeV) and *photoelectric absorption* (which occurs at an energy level less than

75 keV). The scattered gamma ray count reaching the detector is related to the average electron density and to the bulk density of the formation volume investigated by the tool. The density tool can distinguish between oil and gas in the pore space by virtue of their different densities. Typical depth of investigation of the density logging tool rarely exceeds 6 in and decreases with increasing density.

The density log, which is a response to the number of electrons per unit volume of the formation rock, depends on the density of matrix, formation porosity, and density of pore filled fluid. Formation bulk density ( $\rho_b$ ) follows a linear bulk mixing law, hence:

$$\rho_b = \phi_D \rho_f + (1 - \phi_D) \rho_{ma} \quad (5.50)$$

where  $\phi_D$  is the porosity from the density log,  $\rho_{ma}$  is matrix density,  $\rho_b$  is formation bulk density (value read

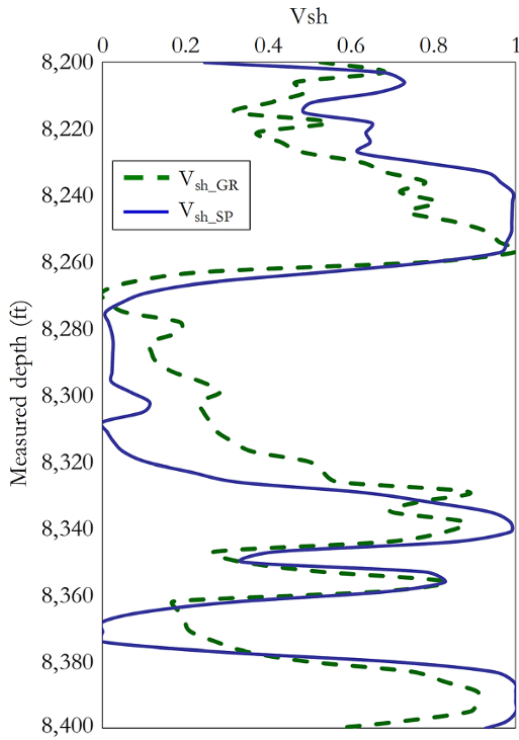


Figure 5.20 Comparison of  $V_{sh}$  using GR and SP logs.

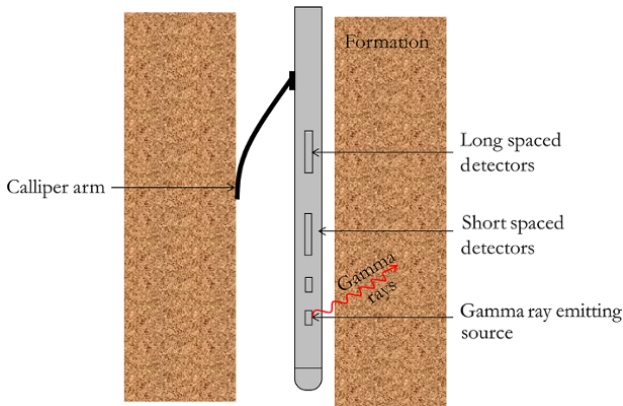


Figure 5.21 Density logging tool.

directly from log), and  $\rho_f$  is the density of the fluid saturating the formation within the radius of the investigation of tool.

Making  $\phi_D$  in equation (5.50) the subject of the formula:

$$\phi_D = \frac{\rho_{ma} - \rho_b}{\rho_{ma} - \rho_f} \quad (5.51)$$

Fig. 5.22 show the density log for a clean matrix of sandstone, limestone, and dolomite; the bulk density decreases due to the effect of the pore spaces (porosity) in each lithology.

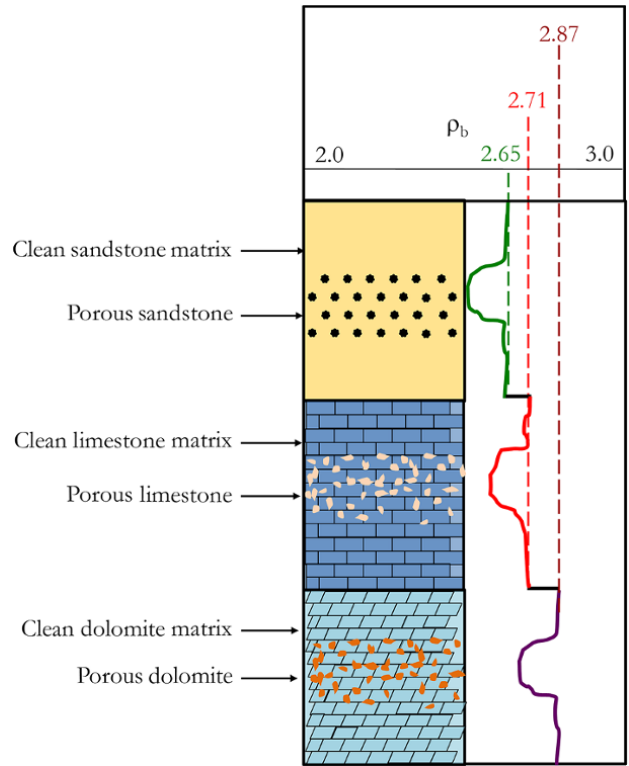


Figure 5.22 Density of a clean matrix and the effect of porosity on the bulk density of the formation.

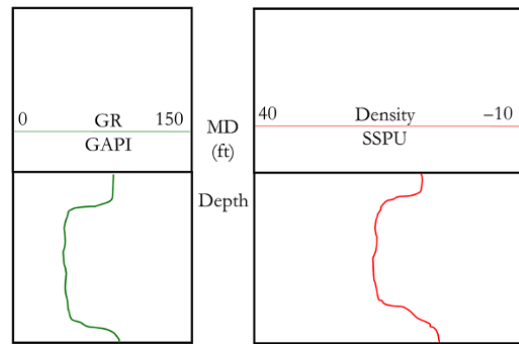


Figure 5.23 Density log as density porosity with sandstone in porosity unit.

Figure 5.22 has the density log presented as bulk density. Another way of presenting the density log is as the *density porosity log* (Fig. 5.23), which is based on using porosity derived from the linear relationship between bulk density ( $\rho_b$ ) and porosity, as shown in equation (5.50) for a known matrix.

Due to the shallow depth of investigation of the density tool, the zone measured by density is often mud filtrate pore filled. Hence, the fluid density required to convert  $\rho_b$  to density porosity is typically between 1 and 1.2.

The unit for  $\rho_b$  is g/cc and density porosity is in porosity units (pu). When a sandstone matrix density is used for calculating density porosity, it is called the *sandstone porosity unit* (SSPU or SPU); when a limestone matrix density is used for density porosity calculations, the porosity unit is the *limestone porosity unit* (LPU). Sandstone porosity will give the correct porosity only in sandstone while the limestone porosity unit will give the correct porosity in the limestone region. Another approach for presenting the density porosity is using the varying lithology of the formation at different depths. Hence, density porosity at each depth is calculated with the correct matrix density when known.

The density log can be used to determine mechanical properties of formation when combined with a sonic log; lithology characterization when combined with neutron logs; acoustic properties of the formation when combined with a sonic log; identification of the presence of gas in a formation when combine with a neutron log; identification of formation mineral when combined with *photoelectric factor* (PEF) log and neutron log. Density logging tools and logs requires that matrix type be known in order for it to be used for porosity calculation:

The density log can be affected by the rugosity of the hole and logs may require some form of correction for rugose holes; the presence of residual hydrocarbons can lead to lower calculated porosity. Density porosity can also be affected by fluid type, so corrections need to be made to estimate density porosity in a gas-bearing zone.

Porosity calculated using equation (5.51) is the total porosity, which includes the reservoir pore space occupied by fluid bound in shales. For an effective porosity ( $\phi_e$ ) calculation, wetted shale volume ( $V_{sh\_w}$ ) and shale density ( $\rho_{sh}$ ) is required:

$$\rho_b = \phi_e \rho_f + (1 - \phi_e - V_{sh\_w}) \rho_{ma} + V_{sh\_w} \rho_{sh} \quad (5.52)$$

For equations (5.50) and (5.52), if lithology is known, grain density can be taken from a known source. Matrix and fluid density are summarized in Table 5.6.

**Table 5.6** Matrix and Fluid Density.

Lithology/ Fluid	Matrix density (g/cm <sup>3</sup> )	Fluid density (g/cm <sup>3</sup> )
Sandstone	2.65	
Limestone	2.71	
Dolomite	2.87	
Anhydrite	2.98	
Halite	2.04	
Coal	~1.2	
Barite	4.09	
Gas		0.20
Oil		~0.85
Water		1.0–1.2

From equation (5.52),  $\phi_e$  can be made the subject of the formula:

$$\phi_e = \frac{\rho_{ma} - \rho_b}{\rho_{ma} - \rho_f} - V_{sh\_w} \left( \frac{\rho_{ma} - \rho_{sh}}{\rho_{ma} - \rho_f} \right) \quad (5.53)$$

Substituting  $\phi_t = \frac{\rho_{ma} - \rho_b}{\rho_{ma} - \rho_f}$  and  $\phi_{tsh} = \frac{\rho_{ma} - \rho_{sh}}{\rho_{ma} - \rho_f}$  into equation (5.53):

$$\phi_e = \phi_t - V_{sh\_w} \phi_{tsh} \quad (5.54)$$

With  $S_{wb} \phi_t = V_{sh\_w} \phi_{tsh}$ ,

Substituting  $S_{wb} \phi_t = V_{sh\_w} \phi_{tsh}$  into equation (5.54)

$$\phi_e = \phi_t (1 - S_{wb}) \quad (5.55)$$

Where  $V_{sh\_w}$  is wetted shale fraction,  $S_{wb}$  is bond water saturation,  $\phi_{tsh}$  is porosity of wetted shale, and  $\phi_t$  is total porosity.

Effective porosity would generally mean total porosity excluding ineffective pores spaces. What is considered ineffective pore space varies. For petroleum engineering and simulation of hydrocarbon recovery, ineffective pore space is unconnected pore spaces that do not contribute to flow. Hence, for reservoir engineering purposes, effective porosity is fraction of pore space that is connected and contributes to flow and recovery of reservoir fluids or simply total porosity less isolated porosity. In some laboratory core measurement, effective porosity maybe defined as total porosity less fraction of clay-bound water. In well log analysis, effective porosity is total porosity less the fraction of clay-bound water or fraction of shale ( $V_{sh}$ ).

**5.1.6.1. Photoelectric (PE) Absorption Log.** This is a log of photoelectric absorption of the formation that is represented as *photoelectric absorption factor* ( $P_e$  or PEF). Photoelectric absorption is a response from low energy gamma rays, which are characterized by photoelectric absorption from gamma rays emitted by the density logging tool. They are related to atomic number and are useful for lithological characterization.  $P_e$  logs give a direct indication of lithology and are independent of porosity. Values for each lithology shown in Table 5.7.  $P_e$  is often combined with density and neutron logs to enhance the capability for lithology identification. The photoelectric absorption factor ( $P_e$ ) has units in barns/electrons.

$P_e$  in (barns/electron) does not follow a volume weighted averaging (linear mixing law) and, hence, is converted to  $U$  in barns/cm<sup>3</sup>, which follows linear bulk mixing law and always preferable.

$$U_{log} = \sum_i^n U_i V_i \quad (5.56)$$



**Table 5.7**  $P_e$  Value of Minerals in Barns/Electron ( $P_e$ ) and Barns/cm<sup>3</sup> (U).

Mineral	Formula	$P_e$ (barns/electron)	U (barns/cm <sup>3</sup> )
Quartz	SiO <sub>2</sub>	1.8	4.8
Calcite	CaCO <sub>3</sub>	5.1	13.8
Dolomite	CaCO <sub>3</sub> · MgCO <sub>3</sub>	3.1	9
Kaolinite	Al <sub>2</sub> Si <sub>2</sub> O <sub>5</sub> (OH) <sub>4</sub>	1.8	4.4
Illite		3.5	8.7
Chloride		6.3	17
Fresh Water		0.36	0.4
Brine (120 kppm NaCl)		0.81	0.96
Oil	(CH <sub>2</sub> ) <sub>n</sub>	0.12	0.12
Barrite	BaSO <sub>4</sub>	266.8	1070
Gypsum	CaSO <sub>4</sub> ·2H <sub>2</sub> O	3.4	9.37
Methane	CH <sub>4</sub>	0.095	0.119
Coal		0.18	
Shale		3.42	
Pyrite	FeS <sub>2</sub>	19.97	82.1

where U is a transform of photoelectric factor in barns/cm<sup>3</sup> using electron number density ( $\rho_e$ ) weighted  $P_e$  (in barns/electron) and expressed as:

$$U_i = P_{ei}\rho_{ei} \quad (5.57)$$

where  $P_{ei}$  is  $P_e$  (barns/e) for each constituent,  $\rho_{ei}$  is  $\rho_e$  the electron number density for each constituent,  $U_{log}$  is the tool response photoelectric effect in barns/cm<sup>3</sup>, and  $V_i$  is the volume of a particular constituent

### 5.1.7. Neutron Log

Neutron logs are the response from nuclear bombardment of a formation by fast moving neutrons from a neutron chemical source or minitron (Fig. 5.24). These neutrons are slowed and then captured, primarily by hydrogen atoms in the formation. The slowed neutrons deflected back to the tool are counted by detectors. The neutron logging tool has a radioactive source that emits high energy neutrons, which enter the formation colliding with the nuclei of atoms on their path. Collision with nuclei makes them lose energy, hence slowing down and following law of conservation of momentum. Successive collisions of neutrons with atoms leads to neutrons at a low energy level called *thermal level*. The presence of a hydrogen nucleus, which is of a similar mass to a neutron, increases the probability of high energy loss from bombarding neutrons to slow them down to a thermal energy level.

Neutron logs are used mainly for delineation of porous formations and determination of porosity in open and cased holes. A neutron log responds primarily to the

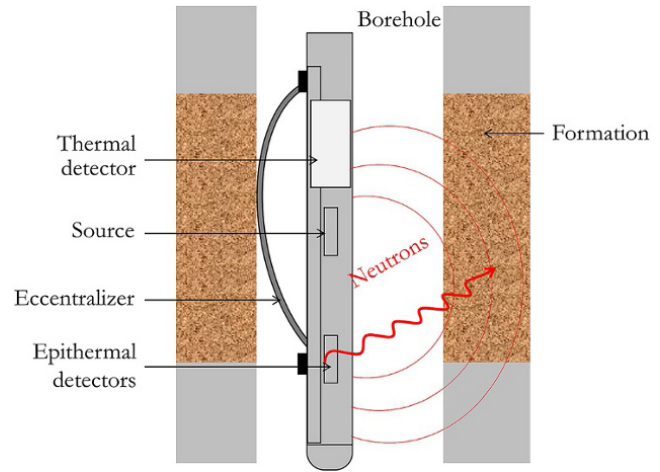


**Figure 5.24** Neutron logging tool.

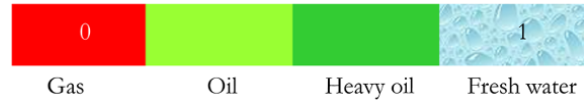


**Figure 5.25** Hydrogen index of different fluid types.

amount of hydrogen in the formation characterized as the *hydrogen index* (HI). The hydrogen index is directly related to porosity, with fresh water having hydrogen index of 1, gas having a very small hydrogen index, in oil the hydrogen index varies between that of water and gas (Fig. 5.25). Hence, in clean formations with pores filled with water or oil, the neutron log reflects the amount of liquid filled porosity.

Neutron porosity log due to high depth of investigation, and measurement dependent on formation fluid, can be used for detecting gas zones where present. Gas zone identification though often carried out using neutron log and density, can also be done using the comparison of the neutron log with other porosity logs or core porosity. Neutron logs when combined with density and *photoelectric factor* (PEF) logs can be used for identification of formation mineral.

Porosity calculation using the neutron log as shown in equation (5.58) requires knowing the matrix type.

$$\phi_N = \phi_e I_{H\_pf} + (1 - \phi_e - V_{sh})\phi_{app\_ma} + V_{sh}\phi_{app\_sh} \quad (5.58)$$

where  $I_{H\_pf}$  is the hydrogen index of the pore fluid,  $\phi_e$  is the effective porosity,  $V_{sh}$  the volume of shale,  $\phi_{app\_ma}$  is the apparent matrix porosity measured by neutron log in lithology, and  $\phi_{app\_sh}$  is apparent  $V_{shale}$  porosity measured by neutron log in lithology.

The presence of bond water in shale causes apparent increased neutron porosity compared with density porosity. Other factors that can affect neutron log readings include the presence of neutron absorbers, which aid the slowness of bombarding neutrons, causing an increased neutron porosity reading, and the presence of residual hydrocarbon, which can cause slightly lower porosity. Due to a neutron's unique response to shale, with bond water, a neutron log can be used for  $V_{sh}$  calculation in formations without gas using:

$$V_{sh} = \frac{(\phi_N - \phi_D)}{(\phi_{Nsh} - \phi_{Dsh})} \quad (5.59)$$

where  $\phi_N$  is neutron porosity,  $\phi_D$  is density porosity,  $\phi_{Nsh}$  is neutron porosity in shale, and  $\phi_{Dsh}$  is density porosity in shale.

Neutron logs require a borehole size correction, which is done automatically during logging. Other corrections that maybe carried out to neutron logs include: mudcake correction; formation salinity correction; mud weight correction; pressure and temperature correction; stand-off correction, fluid type correction, and shaliness correction. The neutron log is reported in the unit of porosity. It is calibrated to give the correct porosity for the matrix used for calibration.

Considering that the neutron log has deeper depth of investigation than the density log, neutron porosity can be expressed as saturated weighted average properties in a flushed zone with saturation of  $S_{xo}$  and an uninvaded zone with saturation of  $(1 - S_{xo})$ . Hence, neutron porosity expressed in terms of HI and  $S_{xo}$  is:

$$\phi_N = \phi(HI_{mf}S_{xo} + HI_{HC}(1 - S_{xo})) \quad (5.60)$$

HI for oil ( $HI_{Oil}$ ) = 1.003 and for water ( $HI_{Water}$ ) = 1.0

Hence, for water or oil-based mud,  $HI_{Oil} \approx HI_{Water}$  and equation (5.60) becomes:

$$\phi_N = \phi \quad (5.61)$$

For a neutron logging tool calibrated with limestone, in 100% water (which is theoretically a formation of 100% saturated with water) the tool would read an HI of 1 and, hence, a porosity of 1. When in a pure limestone block of 0% porosity, the tool will read HI of 0, as a limestone block has no hydrogen atoms and this corresponds to zero porosity. With this limit of porosity from 0 to 100%, the unit of the neutron log is thus set to the limestone porosity unit (LPU). In this case, since the tool has been calibrated in limestone, the tool will yield correct porosity in a limestone region but not in another lithology. In other lithologies, correction for effect of the matrix may be required. This correction is often ignored, as correction is minimal.

### 5.1.8. Combined Neutron–Density Log

A combination of neutron and density has proved to be very useful for lithology identification, identification of the presence of gas, and more accurate porosity calculation compared to using only one of the logs.

Fig. 5.26 shows typical neutron–density log response in different lithologies with the neutron log presented in *limestone porosity units* (LPU).

Where there is no gas present in a formation, the combination of neutron porosity and density porosity can be used to calculate  $V_{sh}$  based on the linear scaling relationship equation (5.62) as shaly sands are expected to show higher neutron porosity values than density porosity values.

$$V_{sh}(\text{neut, dens}) = \frac{\phi_{\text{neutron}} - \phi_{\text{density}}}{\phi_{\text{neutronshale}} - \phi_{\text{densityshale}}} \quad (5.62)$$

The combination of neutron and density porosity is powerful in gas detection. Separation of neutron log from density log, with density porosity greater than neutron porosity (*gas crossover*) is an indication of presence of gas in the formation (Fig. 5.27).

**5.1.8.1. Neutron–Density Compatible Scale.** As shown in Fig. 5.27, density porosity (derived from bulk density) and neutron porosity would overlay in a matrix with pore space filled with water (precisely fresh water). It is also desirable when bulk density ( $\rho_b$ ), instead of density porosity ( $\phi_D$ ) is plotted against neutron porosity ( $\phi_N$ ) to ensure

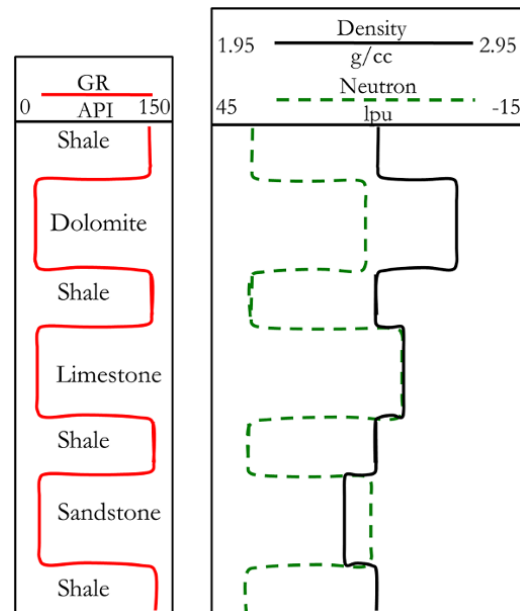


Figure 5.26 Neutron-porosity log in different lithologies.

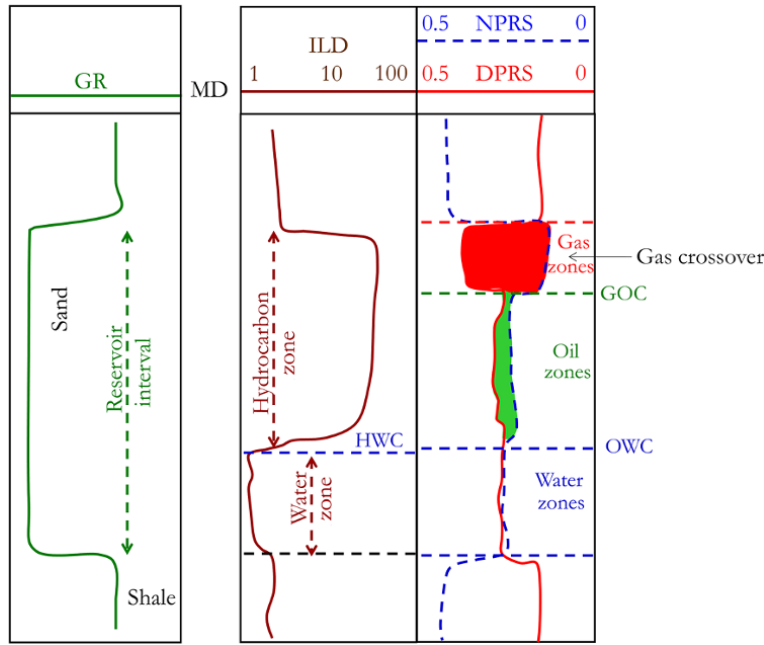


Figure 5.27 Neutron–density porosity log showing gas crossover effect.

that in matrix calibrated with pore space filled with fresh-water, bulk density log will visually overlay neutron porosity for a given scale of neutron porosity. This type of scale section is called *compatible scale*.

*Sandstone Compatible Scale*

For any given value of  $\phi_N$  in pure quartz with pores filled with fresh water:

$$\phi_N = \phi_D; \rho_f = 1 \text{ (density of fresh water);}$$

$$\rho_{ma} = 2.65 \text{ (from Table 5.6)}$$

Substituting the above into the bulk density expression from equation (5.50):

$$\rho_b = \phi_D \rho_f + (1 - \phi_D) \rho_{ma}$$

$$\rho_b = \phi_N + (1 - \phi_N) 2.65$$

$$\rho_b = 2.65 - 1.65 \phi_N \tag{5.63}$$

Hence, for  $\phi_N$  scaled between 0.45 and -0.15 in sandstone porosity unit (SPU), in order for  $\rho_b$  to overlay  $\phi_N$ ,  $\rho_b$  must be scaled to honor equation (5.63).

Hence, the lower and upper limits of  $\rho_b$  will be:

$$\rho_{b\_lower} = 2.65 - 1.65(-0.15) \approx 2.9$$

$$\rho_{b\_upper} = 2.65 - 1.65(0.45) \approx 1.9$$

The *sandstone compatible scale* for neutron porosity and bulk density is shown in Fig. 5.28:

*Limestone Compatible Scale*

For any given value of  $\phi_N$  in pure calcite with pores filled with fresh water:

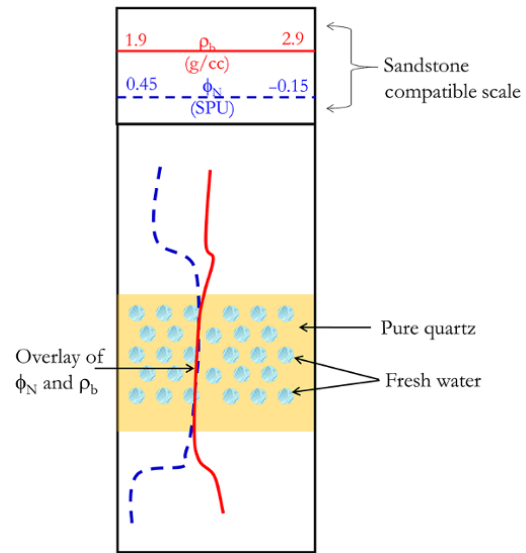


Figure 5.28 Illustration of sandstone compatible scale.

$$\phi_N = \phi_D; \rho_f = 1 \text{ (density of fresh water);}$$

$$\rho_{ma} = 2.7 \text{ (from Table 5.6)}$$

Substituting the above into the bulk density expression from equation (5.50):

$$\rho_b = \phi_D \rho_f + (1 - \phi_D) \rho_{ma}$$

$$\rho_b = \phi_N + (1 - \phi_N) 2.7$$

$$\rho_b = 2.71 - 1.71 \phi_N \tag{5.64}$$

Hence, for  $\phi_N$  scaled between 0.45 and -0.15 in limestone porosity unit (LPU), in order for  $\rho_b$  to overlay  $\phi_N$ ,  $\rho_b$  must be scaled to honor equation (5.63).

Hence, the lower and upper limits of  $\rho_b$  will be:

$$\rho_{b\_lower} = 2.7 - 1.7(-0.15) \approx 2.95$$

$$\rho_{b\_upper} = 2.7 - 1.7(0.45) \approx 1.95$$

The limestone compatible scale for neutron porosity and bulk density is shown in Fig. 5.29.

Compatible scales are important as crucial features such as gas effect can be missed due to setting the scales wrongly.

**5.1.8.2. True Porosity Calculation from Neutron-Density Logs.** There are two approaches common for determining true porosity from combined neutron and density logs: (i) averaging of neutron and density porosity from logs (ii) use of neutron-density cross-plots.

*True Porosity from Neutron and Density Porosity Average*

Where the zone is water or oil, the true porosity from neutron and density porosity can be expressed as:

$$\phi = \frac{\phi_D + \phi_N}{2} \tag{5.65}$$

and where the zone is gas true porosity from neutron and density porosity can be expressed as:

$$\phi = \frac{2\phi_D + \phi_N}{3} \tag{5.66}$$

Equation (5.66) is weighted to skew the average towards  $\phi_D$  for the gas zone since  $\phi_N$  is always overestimated in the gas zone as discussed in section 5.1.8 (under gas crossover effect).

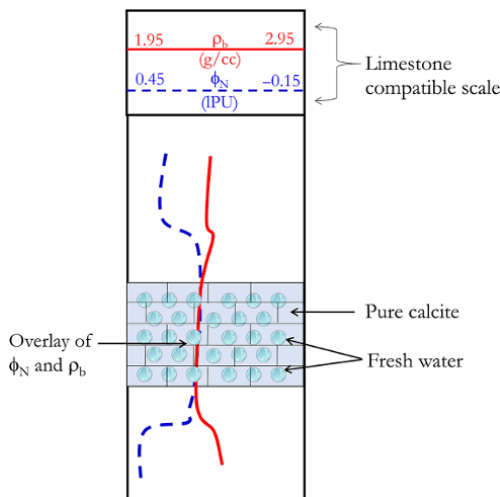


Figure 5.29 Illustration of limestone compatible scale.

Another form of averaging the neutron and density porosity is the use of *root mean square (RMS)*, which is the square root of the arithmetic mean of the squares of the values and expressed as:

$$\phi = \sqrt{\frac{\phi_D^2 + \phi_N^2}{2}} \tag{5.67}$$

*True Porosity from Neutron and Density Cross-Plots*

Cross-plots are used in formation evaluation to calculate properties base on two or more data with graphs and lithology identification. The use of cross-plots for porosity calculation involves the use of a density-neutron cross-plot from a database or log analysis chart book.

For example, for a given limestone neutron porosity of 25% with lithology defined as dolomitic limestone with bulk density of 2.45 g/cc. The true porosity from a neutron-density cross-plot is determined by identifying the coordinate corresponding to given density and neutron porosity as shown in Fig. 5.30.

Reading true porosity as values on one of the lines (ribs) joining lithologies that defines the zone of interest (dolomitic limestone in this case). In this case the coordinate  $\rho_b = 2.45$  g/cc and  $25\% = \phi_N$  lies on the 23% line joining limestone with dolomite. Also, the fraction of length from the limestone and dolomite lithology gives the fraction of limestone and dolomite. In this case, the coordinate lies in the middle of the 23% line joining limestone and dolomite. Hence formation can be described as equal fractions of limestone and dolomite.

Effective porosity can be determined in similar way to the approach in equation (5.55). Due to the difficulty of determining  $S_{wb}$  which depends on porosity of wetted shale and wetted shale fraction, a more practical form of equation (5.55) is:

$$\phi_e = \phi_t(1 - V_{sh}) \tag{5.68}$$

where effective porosity,  $\phi_e$  can also be denoted as  $\phi_{eff}$

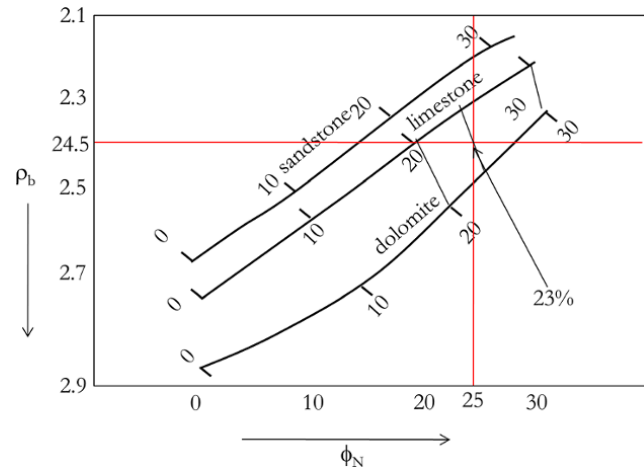


Figure 5.30 Neutron-density cross-plot.

**Exercise 5.5**  $V_{sh}$  Calculation using Neutron Logs

Well log data acquired from an openhole wellbore with  $R_w < R_{mf}$  is given in Table 5.8 and displayed graphically in Fig. 5.31. Drill cutting shows the main lithology to be sand and shale.

1. Determine zones of interest.
2. Determine  $V_{sh}$  using GR and neutron–density logs.
3. Determine the fluid occupying zone of interest using the neutron–density porosity log only.

**Solution.**

1. The zone of interest is defined by low gamma ray response (Fig. 5.32), as sandstone and limestone would generally have low gamma ray response except in radioactive sand. Sand typically has a PEF reading between 1.8 and 2.7 barns/electron (Table 5.7).

A high gamma ray log reading and high neutron porosity (due to bound water) are characteristic of shale. Also, a PEF log reading around 3.4 barns/electron based on Table 5.7 gives an indication of shale.

2. The values of  $GR_{Clean}$  and  $GR_{Shale}$  for  $V_{sh}$  calculated using GR log and  $\phi_{N\_shale}$  and  $\phi_{D\_Shale}$  for neutron–density log are shown in Fig. 5.32.

$$\text{Using equation (5.26), } V_{sh}(GR) = \frac{GR_{zone} - GR_{clean}}{GR_{shale} - GR_{clean}}$$

$$\text{and equation (5.59), } V_{sh}(N-D) = \frac{(\phi_N - \phi_D)}{(\phi_{Nsh} - \phi_{Dsh})}$$

Table 5.9 summarizes  $V_{sh}(GR)$  and  $V_{sh}(N-D)$  calculations and results.

Fig. 5.33 shows a comparison of  $V_{sh}$  using GR and N–D logs.

3. The neutron–density porosity plot shows close values of  $\phi_N - \phi_D$ , suggesting liquid (oil or water). No gas effect (separation of  $\phi_N - \phi_D$ ) was observed. The deep resistivity log, discussed in section 5.1.10, can distinguish between formation water (if not fresh water) and hydrocarbon (oil or gas).

**5.1.9. Sonic Log**

The sonic log measures the travel interval time ( $\Delta t$ ) of *compressional sound wave* (P-wave) travelling through the formation of interest along the axis of the wellbore. The interval transit time is dependent on lithology and porosity. Sonic logs are also called *sonic travel time logs* or *slowness logs*.

**Table 5.8** Well Log Data for Exercise 5.5

MD (ft)	GR (GAPI)	CAL (in)	PEF (barns/e)	Deep resistivity ( $\Omega$ -m)	NPRS	DPRS	MD (ft)	GR (GAPI)	CAL (in)	PEF (barns/e)	Deep resistivity ( $\Omega$ -m)	NPRS	DPRS
11,400	142.54	6.44	3.06	6.04	0.35	0.17	11,504	45.40	6.49	2.44	62.06	0.29	0.28
11,404	146.31	6.38	3.11	5.98	0.36	0.16	11,508	49.17	6.40	2.41	58.81	0.30	0.29
11,408	145.54	6.35	3.11	5.63	0.37	0.17	11,512	52.07	6.32	2.39	47.05	0.30	0.28
11,412	142.00	6.43	3.12	6.01	0.37	0.18	11,516	50.83	6.27	2.39	51.17	0.30	0.27
11,416	146.09	6.44	3.12	6.16	0.37	0.19	11,520	50.53	6.24	2.39	55.28	0.30	0.26
11,420	135.46	6.48	3.13	6.19	0.38	0.19	11,524	50.74	6.33	2.37	58.73	0.30	0.27
11,424	142.65	6.63	3.13	6.22	0.40	0.18	11,528	52.20	6.43	2.36	59.03	0.31	0.29
11,428	148.44	6.78	3.13	6.25	0.39	0.19	11,532	57.41	6.37	2.36	59.32	0.31	0.30
11,432	142.75	6.94	3.22	6.28	0.38	0.19	11,536	55.40	6.41	2.37	63.21	0.30	0.28
11,436	142.71	7.09	3.19	6.31	0.38	0.18	11,540	53.55	6.54	2.40	69.56	0.29	0.29
11,440	146.43	6.98	3.19	6.34	0.38	0.17	11,544	52.50	6.61	2.47	65.70	0.31	0.29
11,444	150.77	6.89	3.14	6.52	0.38	0.19	11,548	60.06	6.65	2.56	52.91	0.31	0.28
11,448	154.87	6.89	3.07	6.80	0.38	0.20	11,552	106.04	6.60	2.70	24.21	0.30	0.27
11,452	156.13	6.82	3.01	7.07	0.38	0.19	11,556	119.53	6.53	2.74	15.52	0.29	0.23
11,456	120.79	6.73	2.87	9.55	0.35	0.17	11,560	125.07	6.31	2.77	15.78	0.30	0.20
11,460	86.75	6.59	2.70	22.13	0.31	0.19	11,564	131.89	6.34	2.79	15.05	0.31	0.17
11,464	82.66	6.72	2.60	19.44	0.30	0.19	11,568	135.44	6.42	2.74	14.48	0.31	0.15
11,468	66.22	6.89	2.48	25.30	0.29	0.24	11,572	130.19	6.37	2.65	13.99	0.30	0.14
11,472	43.87	6.80	2.41	42.43	0.28	0.26	11,576	120.51	6.32	2.60	15.77	0.29	0.14
11,476	45.18	6.59	2.48	49.49	0.27	0.27	11,580	112.26	6.27	2.58	19.27	0.26	0.14
11,480	45.31	6.80	2.48	55.62	0.28	0.28	11,584	88.55	6.23	2.55	25.66	0.25	0.15
11,484	44.04	6.89	2.49	60.98	0.28	0.29	11,588	71.64	6.31	2.59	30.61	0.26	0.17
11,488	47.26	6.41	2.49	62.29	0.29	0.27	11,592	65.03	6.33	2.64	33.58	0.27	0.20
11,492	45.44	6.36	2.41	62.84	0.28	0.25	11,596	58.87	6.31	2.49	40.35	0.29	0.24
11,496	47.54	6.38	2.40	64.75	0.28	0.25	11,600	61.00	6.16	2.48	42.09	0.30	0.26
11,500	49.18	6.52	2.46	66.35	0.28	0.27							

NPRS = sandstone neutron porosity; DPRS = sandstone density porosity

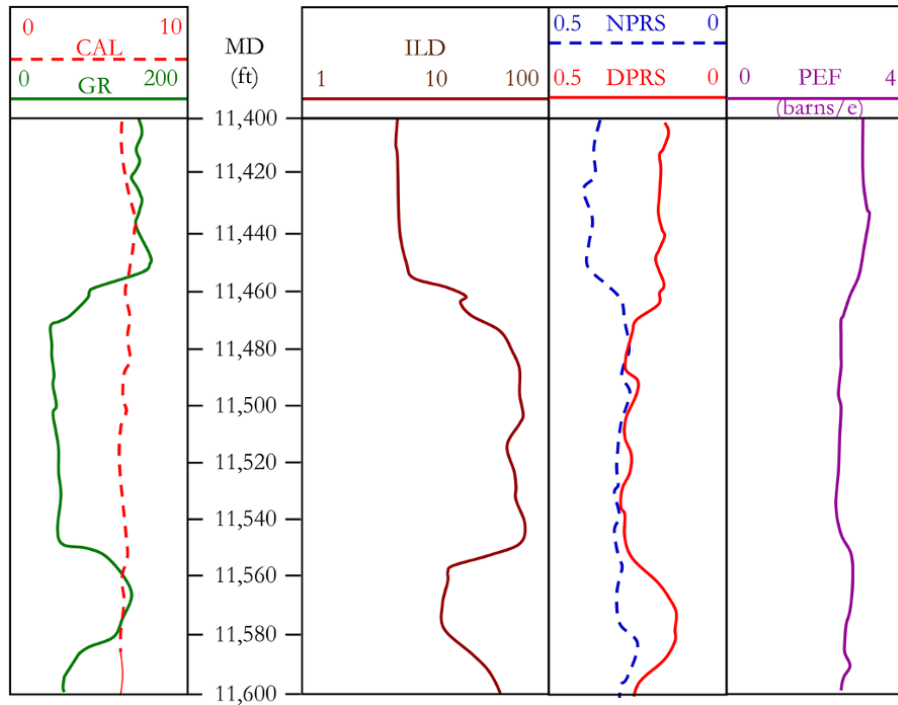


Figure 5.31 Well log plot for Exercise 5.5.

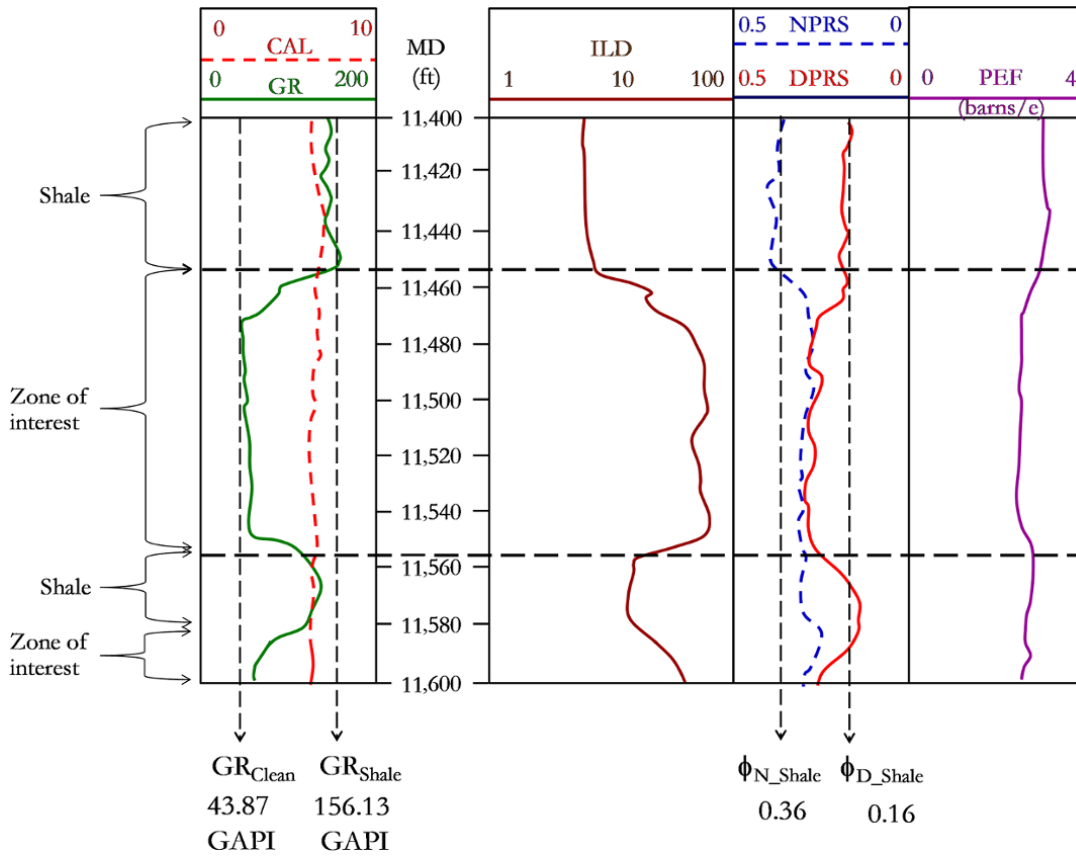
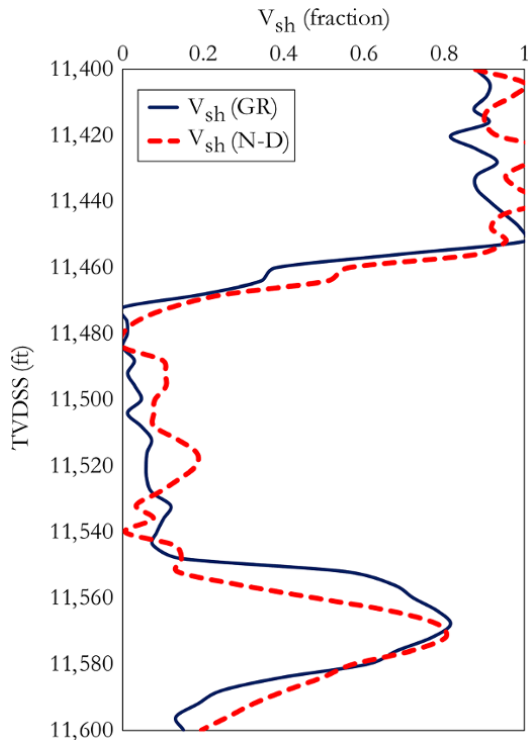


Figure 5.32  $GR_{Clean}$ ,  $GR_{Shale}$ ,  $\phi_{N\_shale}$ ,  $\phi_{D\_Shale}$ ,  $V_{sh}$  calculations.

**Table 5.9**  $V_{sh}$  Calculation Using Equations (5.26) and (5.59).

Depth (ft)	$V_{sh}(GR)$	$V_{sh}(N\_D)$	Depth (ft)	$V_{sh}(GR)$	$V_{sh}(N\_D)$	Depth (ft)	$V_{sh}(GR)$	$V_{sh}(N\_D)$
11,400	0.88	0.88	11,468	0.20	0.26	11,536	0.10	0.08
11,404	0.91	1.00	11,472	0.00	0.12	11,540	0.09	0.01
11,408	0.91	0.97	11,476	0.01	0.04	11,544	0.08	0.13
11,412	0.87	0.91	11,480	0.01	0.00	11,548	0.14	0.15
11,416	0.91	0.90	11,484	0.00	0.00	11,552	0.55	0.14
11,420	0.82	0.93	11,488	0.03	0.10	11,556	0.67	0.29
11,424	0.88	1.07	11,492	0.01	0.11	11,560	0.72	0.48
11,428	0.93	1.01	11,496	0.03	0.11	11,564	0.78	0.67
11,432	0.88	0.95	11,500	0.05	0.08	11,568	0.82	0.79
11,436	0.88	0.99	11,504	0.01	0.08	11,572	0.77	0.80
11,440	0.91	1.04	11,508	0.05	0.08	11,576	0.68	0.72
11,444	0.95	0.95	11,512	0.07	0.14	11,580	0.61	0.57
11,448	0.99	0.92	11,516	0.06	0.18	11,584	0.40	0.50
11,452	1.00	0.95	11,520	0.06	0.18	11,588	0.25	0.41
11,456	0.69	0.88	11,524	0.06	0.14	11,592	0.19	0.33
11,460	0.38	0.56	11,528	0.07	0.09	11,596	0.13	0.26
11,464	0.35	0.51	11,532	0.12	0.03	11,600	0.15	0.20



**Figure 5.33** Comparison of  $V_{sh}$  using GR and N-D logs.

When an elastic wave (sound) is sent from the transmitter of the sonic logging tool, the pulse generated travels through the formation and the time it takes to reach the receiver is measured. Different types of waves can be measured by the receiver and, due to their different velocities, they arrive at different times.

The different waves in order of their arrival at the transmitter are: (i) pressure (or compressional or

longitudinal) wave, also called a P-wave; (ii) transverse (or share) wave, also called an S-wave, which is characterized by a higher amplitude than the P-wave; (iii) Rayleigh waves; (iv) Stoneley waves; and (v) mud waves.

The velocity of P-waves ( $V_p$ ) can be related to bulk modulus ( $K$ ), shear modulus ( $\mu$ ), and the density of the solid material ( $\rho$ ) using:

$$V_p = \sqrt{\frac{K + \frac{3}{4}\mu}{\rho}} \quad (5.69)$$

And share wave velocity defined as:

$$V_p = \sqrt{\frac{\mu}{\rho}} \quad (5.70)$$

From the relationship between the velocity of P-waves and the bulk modulus, the elastic properties in homogeneous isotropic materials can be derived as a two-parameter relationship [Schlumberger, 1989] as shown in equations (5.71)–(5.75):

$$\begin{aligned} \lambda &= K - \frac{2}{3}\mu = \frac{2\mu\nu}{1-2\nu} = \frac{\mu(E-2\mu)}{3\mu-E} = \frac{3K\nu}{1+\nu} = \frac{E\nu}{(1+\nu)(1-2\nu)} \\ &= \frac{3K(3K-E)}{9K-E} \end{aligned} \quad (5.71)$$

$$\mu = \frac{3}{2}(K-\lambda) = \frac{\lambda(1-2\nu)}{2\nu} = \frac{E}{2(1+\nu)} = \frac{3K(1-2\nu)}{2(1+\nu)} = \frac{2KE}{9K-E} \quad (5.72)$$

$$\nu = \frac{\lambda}{2(\lambda+\mu)} = \frac{\lambda}{(3K-\lambda)} = \frac{E}{2\mu} - 1 = \frac{3K-2\mu}{2(3K+\mu)} = \frac{3K-E}{6K} \quad (5.73)$$

$$E = \frac{\lambda(1+\nu)(1-2\nu)}{\nu} = \frac{\mu(3\lambda+2\mu)}{\lambda+\mu} = \frac{9K(K-\lambda)}{3K-\lambda} = 2\mu(1+\nu)$$

$$= 3K(1-2\nu) = \frac{9K\mu}{3K+\mu} \tag{5.74}$$

$$K = \frac{\lambda(1+\nu)}{3\nu} = \lambda + \frac{2}{3}\mu = \frac{\mu E}{3(3\mu-E)} = \frac{2\mu(1+\nu)}{3(1-2\nu)} = \frac{E}{3(1-2\nu)} \tag{5.75}$$

where  $\lambda$  is Lamé's first constant,  $\mu$  is shear modulus,  $\nu$  is Poisson's ratio,  $E$  is Young's modulus, and  $K$  is bulk modulus.

The *borehole-compensate* (BHC) sonic tool, though not the most advanced sonic tool, is often considered the industry standard for sonic log measurement. It has the advantages of not affected by mud; tilt, and path. Fig. 5.34 shows the configuration of the BHC sonic tool with two transmitters and four receivers. The BHC sonic tool compensates for the effect of tool misalignment.

From Fig. 5.34, slowness is defined as:

$$\Delta t = \frac{(y-z) + (b-d)}{2L} = \frac{(TT1 - TT3) + (TT4 - TT2)}{2L} \tag{5.76}$$

A sonic log can be combined with other porosity logs, such as density and neutron logs, on the same track and can also be presented on a separate track without

combining with other logs. The sonic log is used for determining porosity in an openhole wellbore.

*Wyllie Time-Average Porosity Method*

Measured sonic travel time can be related to formation porosity and matrix travel time:

$$\Delta t = \phi\Delta t_f + (1-\phi)\Delta t_{ma} \tag{5.77}$$

Porosity ( $\phi$ ) can then be determined by making  $\phi$  the subject of the formula:

$$\phi = \left( \frac{\Delta t - \Delta t_{ma}}{\Delta t_f - \Delta t_{ma}} \right) \tag{5.78}$$

where  $\Delta t$  is the measure sonic travel time from the log,  $\Delta t_f$  is the fluid sonic travel time, and  $\Delta t_{ma}$  is the matrix sonic travel time.

Equation (5.78) is known as the *Wyllie time-average* equation.

For porosity calculation using a sonic log interval transit time, matrix and fluid most be known. Table 5.10 is a list of sonic properties for some rock matrix and fluids.

The Wyllie equation is known to overestimate porosity for an unconsolidated formation. Hence, for an unconsolidated formation, the Wyllie equation is modified to include a *compaction factor* and expressed as:

$$\phi = \left( \frac{\Delta t - \Delta t_{ma}}{\Delta t_f - \Delta t_{ma}} \right) \times \frac{1}{C_p} \tag{5.79}$$

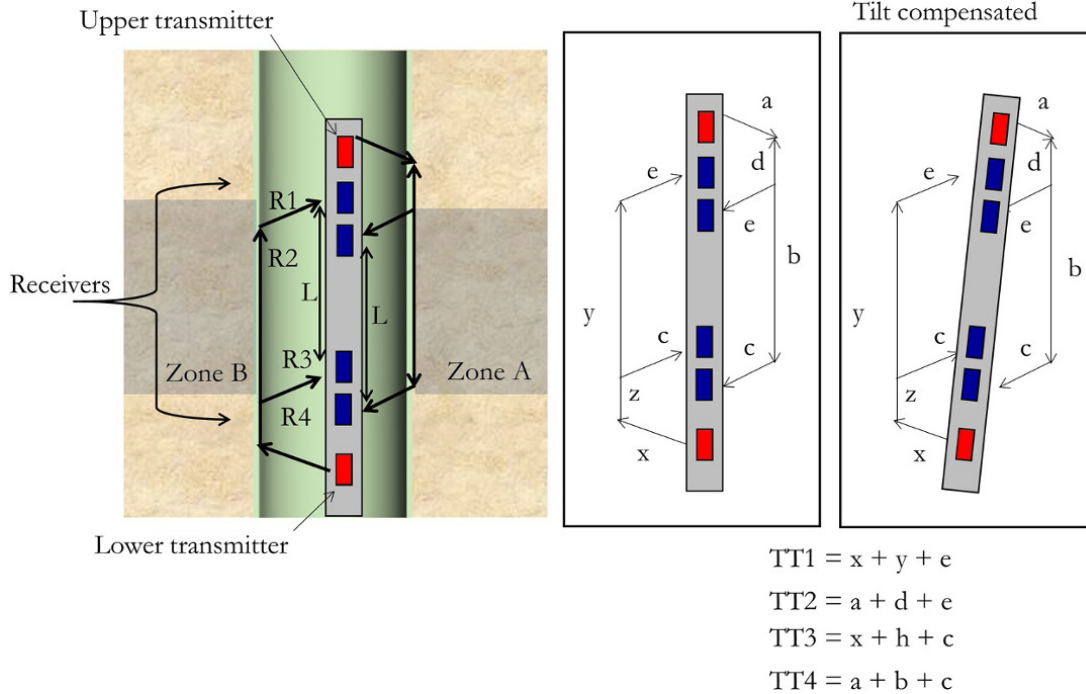


Figure 5.34 The BHC sonic tool with two transmitters and four receivers.



**Table 5.10** Matrix and Fluid Sonic Properties.

Lithology	$V_{ma}(ft/s) \times 10^3$	$V_{ma}(m/s) \times 10^3$	$\Delta t_{ma}(\mu s/ft)$	$\Delta t_{ma}(\mu s/m)$
Sandstone	18.00–19.50	5.50–5.95	55.50–51.00	182.00–167.00
Limestone	21.00–23.00	6.40–7.00	47.60–43.50	156.00–143.00
Dolomite	23.00	7.00	43.50	143.00
Anhydrite	20.00	6.10	50.00	164.00
Salt	15.00	4.58	66.70	219.00
Freshwater mud filtrate	5.28	1.61	189.00	620.00
Saltwater mud filtrate	5.40	1.55	185.00	607.00
Gas	1.08	0.33	920.00	3018.00
Oil	4.35	1.32	230.00	755.00
Iron casing	17.50	5.33	57.00	187.00

where  $C_p$ , which is the compaction factor, can be expressed as:

$$C_p = \frac{\Delta t_{sh} \times C}{100}$$

where  $C$  is a constant and often taken as 1 and  $\Delta t_{sh}$  is shale sonic travel time, which is often taken from an adjacent shale formation

Another common method for calculating porosity from a sonic log is the use of *Raymer–Hunt* equation, which gives a high accuracy in porosity calculation and is expressed as:

$$\frac{1}{\Delta t} = \frac{\phi}{\Delta t_f} + \frac{(1-\phi)^2}{\Delta t_{ma}} \quad (5.80)$$

Other than for porosity determination, the sonic log can be used for improving seismic data interpretation, calculating mechanical properties of a formation for well stability prediction, determination of secondary porosity such as reservoir fissures, and assessment of cement and bond quality. When combined with other logs, such as density and neutron logs, a sonic log can be used for lithology identification.

The most common challenge with a sonic log is an abrupt change towards a higher travel time or spiking, which is known as *cycle skipping* and caused by dampening of the first arrival at the far receiver. Cycle skipping (Fig. 5.35) can be caused by logging through an unconsolidated formation, gas-bearing formations or fractured formations. Cycle skipping can also be caused by poor a signal transmitter or receiver and logging too fast.

Signal detection in a sonic log can be reduced due to fracture, the presence of gas, hole rugosity, and large hole size. Electrical or mechanical noise can trigger the detection sensor, hence creating false signal arrival.

**5.1.9.1. Sonic Cross-Plot.** Similar to the neutron–density log, a sonic log can be combined with either neutron or density logs for lithology identification and

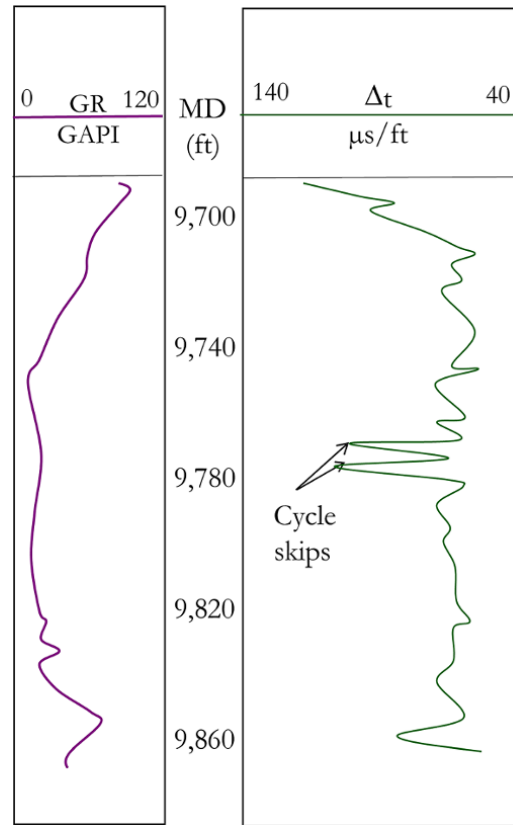


**Figure 5.35** Sonic log showing cycle skipping.

porosity calculation (Fig. 5.36). A cross-plot of sonic porosity against density has poor reservoir rock (sandstone, limestone, dolomite) resolution but is useful for some evaporates.

**5.1.10. Resistivity Log**

The relationship between formation resistivity and water saturation is an important relationship in determining water saturation and, hence, hydrocarbon saturation.

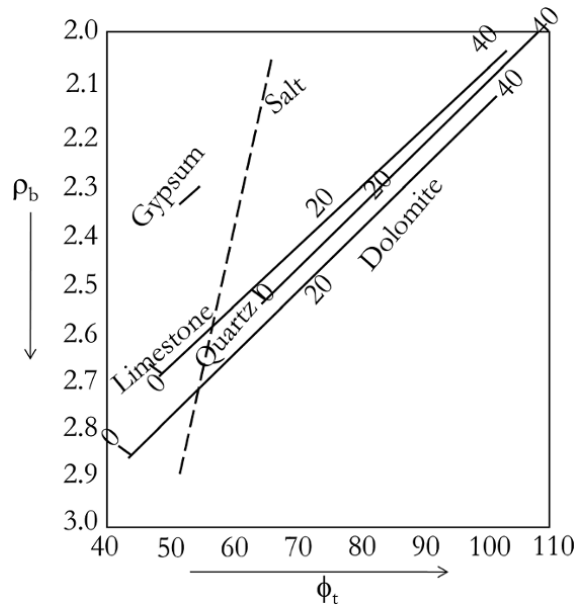


Figure 5.36 Sonic–density cross-plot.

The simplest and most common relationship between true formation resistivity and water saturation is the *Archie equation* [Archie, 1942], which is expressed as:

$$R_t = \frac{FR_w}{S_w^n} \quad (5.81)$$

where

$R_t$  is the true resistivity of formation from electrical logs, induction logs or laterologs,  $F$  is the formation resistivity factor,  $R_w$  is the resistivity of formation water at the formation temperature,  $S_w$  is the water saturation of the uninvaded zone, and  $n$  is a saturation exponent, which varies from 1.8 to 2.5 but is normally equal to 2.0.

$R_w$  is determined from laboratory analysis of the formation water, sampled at the bottom or surface. Where there is no  $R_w$  from a water sample, it can be derived from SP logs. SP logs, however, have the limitation of possibly being affected by environmental factors (section 5.1.5). The Archie equation can be used to determine  $R_w$  from clean water zones. Published regional knowledge and water catalogues are also sources of  $R_w$ .

$F$  can be expressed as:

$$F = \frac{a}{\phi^m} \quad (5.82)$$

where

$a$  is a tortuosity factor from core analysis,  $m$  is a cementation exponent from core analysis, and  $\phi$  is the porosity from core analysis, well log analysis using density, neutron, sonic, resistivity logs or magnetic resonance logs.

By substituting equation (5.82) into equation (5.81),  $R_t$  can be expressed as:

$$R_t = \frac{aR_w}{\phi^m S_w^n} \quad (5.83)$$

Making  $S_w$  the subject of the formula:

$$S_w = \left( \frac{a \times R_w}{\phi^m R_t} \right)^{\frac{1}{n}} \quad (5.84)$$

Values of  $a$ ,  $m$ , and  $n$  are determined from laboratory experiments. Where values are not available, reasonable assumptions that can be used are:

for sand  $a = 0.62$ ,  $m = 2.15$ , and  $n = 2$ ;  
for carbonates  $a = 1$ ,  $m = 2$  and  $n = 2$ .

Resistivity logs are used qualitatively for differentiating between hydrocarbons and water and quantitatively for determining the proportion of water, and therefore hydrocarbon, in the pore spaces.

Qualitative and quantitative analysis of resistivity logs relies on the difference in resistivity of salt water and hydrocarbon. The resistivity log cannot be used to distinguish between gas and oil because neither oil nor gas conduct electricity.

When mud filtrate invades the formation, radial-composite saturation zones (two distinct zones, one flushed the other uninvaded) are formed. The resistivity of the zone invaded by the filtrate depends on the salinity of the drilling fluid along with other parameters (Fig. 5.37).

In fresh water drilling mud where the resistivity of the flushed zone is higher than the uninvaded zone, which contains hydrocarbon and salty formation water, the resistivity of the flushed zone ( $R_{xo}$ ) would be higher than that of the uninvaded zone ( $R_t$ ) with a resistivity profile, as shown in Fig. 5.37a. On the other hand, in saltwater drilling mud having lower resistivity compared with the formation bearing hydrocarbon and saltwater,  $R_{xo}$  will be lower than  $R_t$ , as shown in Fig. 5.37b.

Resistivity logs are important logs when combined with SP logs (another electrical log) and can be useful for lithology and fluid characterization. Fig. 5.38 shows the response of the formation to SP and resistivity logs.

**5.1.10.1. Resistivity Logging Tools.** Formation resistivity logs are generally displayed with a minimum of three resistivity measurements with different depths of investigation (Fig. 5.39). This ensures that the effect of the flushed zone can be removed from the deep resistivity reading for correct determination of true formation resistivity ( $R_t$ ).

Resistivity logging tools can broadly be classified as laterolog or induction tools. Laterolog operates on the principle of measurement of potential difference at

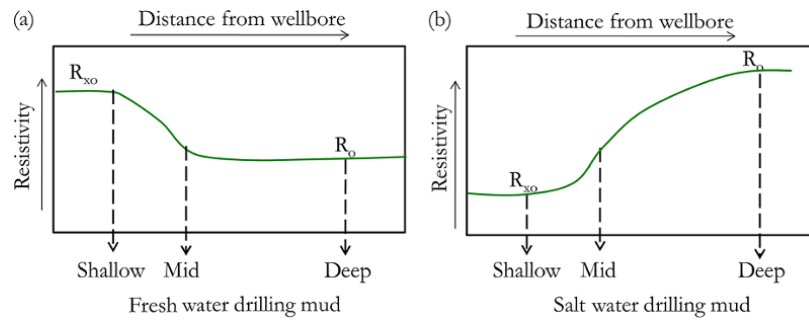


Figure 5.37 Effect of drilling mud type on resistivity profile.

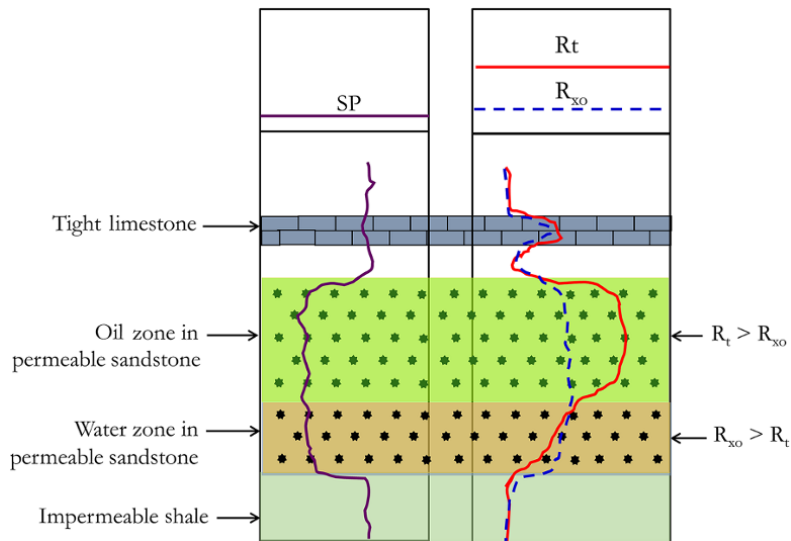


Figure 5.38 SP and resistivity log responses.

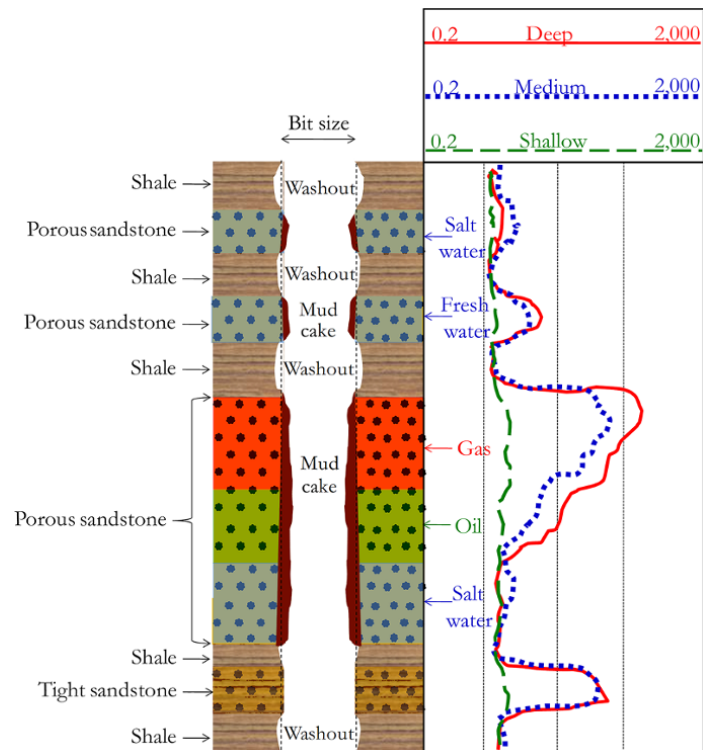


Figure 5.39 Resistivity log response in shale and sandstone with reservoir fluids.

different points on the tool due to current flow initiated into the formation from the tool. Induction tools, on the other hand, measure the intensity of induced current in the formation by coils and magnets. The intensity of the current measured on a receiver coil is then related to the conductivity and, hence, resistivity of the formation.

**5.1.10.2. Microresistivity Devices.** Microresistivity devices, which have pad contacts to ensure shallow depth of investigation, are used for measuring resistivity of flushed zones ( $R_{xo}$ ) that is in close proximity in depth from borehole. Microresistivity logs are required for calculating the resistivity of the uninvaded zone ( $R_t$ ) from deep resistivity measurements; estimation of  $S_{xo}$ , and calculation of movable oil.

The microresistivity pad makes contact with borehole to ensure that the effect of hole rugosity is minimal in readings. Microresistivity readings depend on resistivity of the mud cake and readings can be significantly affected by thick mud cake due to the shallow depth of investigation. Microresistivity readings incorporate corrections for hole size and mud cake. Microresistivity devices are generally not used for oil-based mud.

Microlaterolog (MLL), proximity log (PL), and microspherically focused log (MSFL) are pad-type focused electrode logs for measuring the resistivity in the flushed zone ( $R_{xo}$ ).

From equation (5.84):

$$S_w = \left( \frac{a \times R_w}{\phi^m R_t} \right)^{\frac{1}{n}}$$

For a flushed zone with water saturation of  $S_{xo}$ ,  $R_t = R_{xo}$  and  $R_w = R_{mf}$  and, hence:

$$S_{xo} = \left( \frac{a \times R_{mf}}{\phi^m R_{xo}} \right)^{\frac{1}{n}} \quad (5.85)$$

#### Microlog (ML)

The microlog, is a pad-type microresistivity log. Microlog resistivity measurement is used mainly for determining permeable intervals by detecting mud cake. Detection of mud cake is an indication of a permeable interval, as formation of mud cake requires a permeable formation. A microlog is one of the most convincing indications of a permeable formation. The curves from the microlog are the *normal* curve (ML) and *inverse* curve (MIV) (Fig. 5.40). The degree of separation of ML from MIV ( $ML > MIV$ ) is an indication of a permeable formation, with a sand formation showing separation and shale showing little or no separation. The microlog is always combined with a microcaliper log (for revealing borehole rugosity), as large holes in a shaly formation can give rise

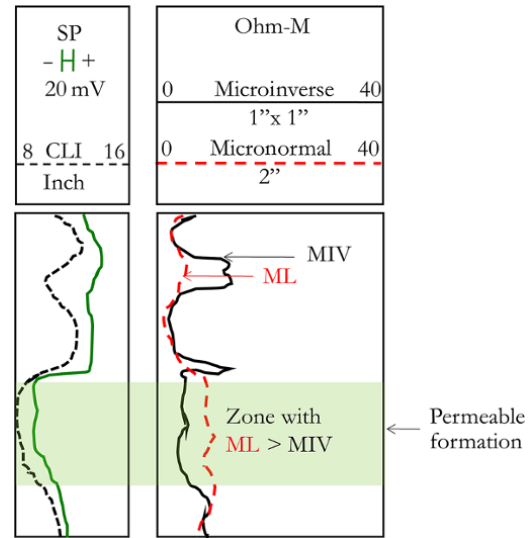


**Figure 5.40** Positive separation of a microlog ( $ML > MIV$ ) indicating permeable formation.

to false positive separation, which might wrongly suggest a permeable formation.

**5.1.10.3. Laterolog Resistivity.** Laterolog tools focus current flow laterally into the formation and voltage is measured at different points. The laterolog measures the true resistivity of the formation ( $R_t$ ) for a borehole filled with saltwater muds. The tool delivers a current from electrodes; this forces the current into the formation. Surveying electrodes with the same polarity as focusing electrodes are placed above and below the surveying electrodes, which ensure that the current is focused. The laterolog can be affected by invasion.

When the filtrate is salt water,  $R_{mf} \approx R_w$ , and the effect of invasion on the laterolog is minimal. However, if the filtrate is freshwater, where  $R_{mf} > 3R_w$ , invasion can significantly affect the laterolog and, hence, the laterolog should not be used under freshwater filtrate conditions.

Laterologs require corrections for hole size, mud resistivity, bed thickness, and tool string length.

#### Dual Laterolog

The dual laterolog measures deep ( $R_t$ ) and a shallow ( $R_i$ ) formation resistivity ( $R_{LLD}$  and  $R_{LLS}$  respectively) (Fig. 5.41 and Fig. 5.42). The dual laterolog works in high resistivity formations and low resistivity muds. It has excellent bed resolution and definition.

**5.1.10.4. Induction Resistivity.** Induction logs were originally designed for resistivity measurement in wells drilled with oil-based muds. They are also used in wells

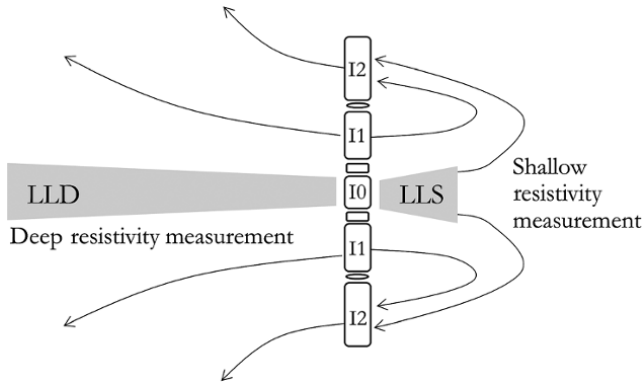


Figure 5.41 Dual laterolog operating principle.

drilled with high salinity water-based muds; they work in wells drilled with fresh water-based muds and air-filled boreholes.

Induction tools have electromagnetic coils that create magnetic fields which induce the flow of a current into the formation; this sequentially induces a secondary magnetic field and current which flows in a receiver coils (Fig. 5.43). The loop current received is proportional to the conductivity of the formation.

The principle of inducing a magnetic field is the main principle that allows the measurement of current in the formation without a direct circuit connection with the formation. This phenomenon of inducing a magnetic field is also the basis on which induction tools can be used in

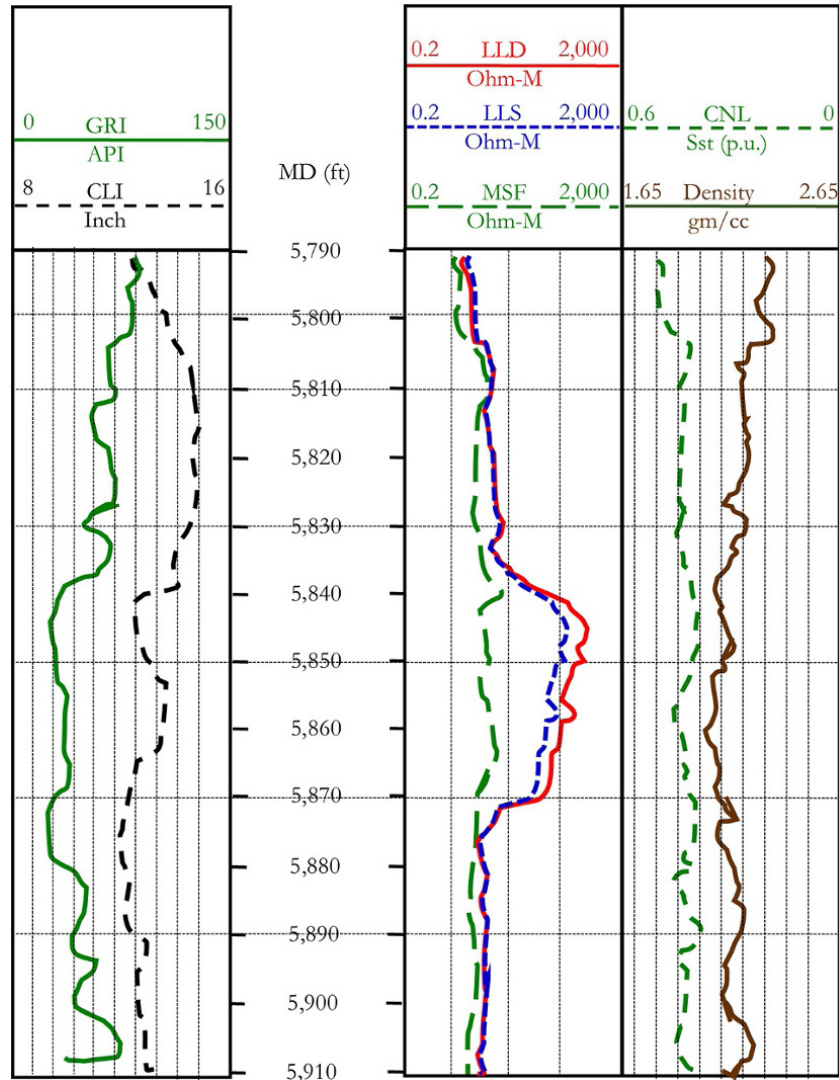


Figure 5.42 Laterolog (middle track) showing LLD, LLS, and MSF.

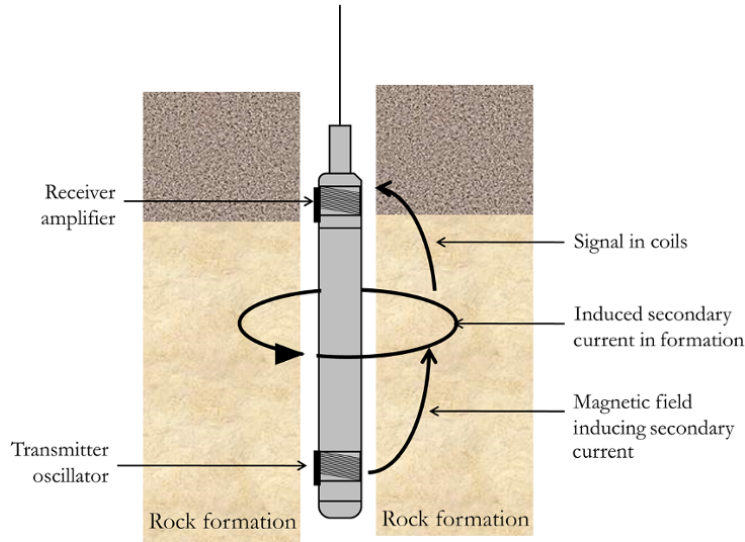


Figure 5.43 Operating principle of the induction logging tool.

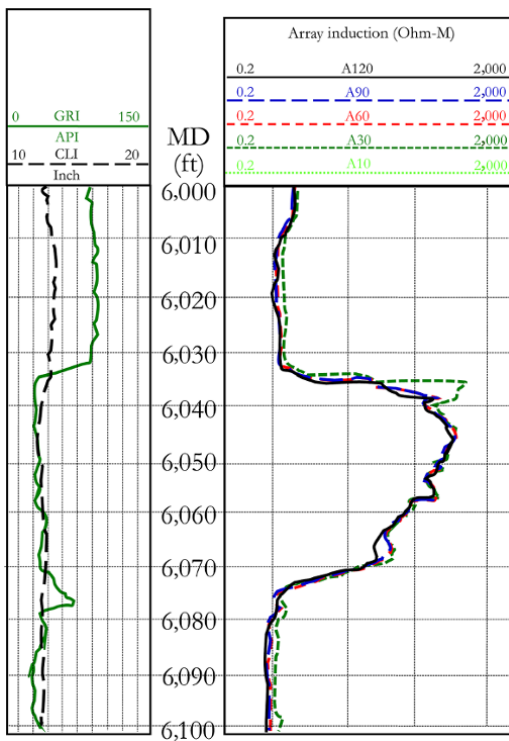


Figure 5.44 Example of induction resistivity logs.

nonconductive mud. Due to an array of different transmitters and receivers, measurements are focused for different depth of investigation and vertical resolutions) Fig. 5.44).

Resistivity measurement from induction tool can be affected by a skin effect, which is when current is pushed out from the original loop due to highly conductive formations, thereby resulting in reduced signal and increased apparent resistivity. A direct coupling effect and the shoulder bed effect are factors that may affect induction resistivity measurement. However, these factors are managed through corrections using signal processing techniques such as deconvolution.

**5.1.10.5.  $S_w$  Calculation from Resistivity Log.** Fluid saturation is very important in calculating the amount of water and hydrocarbon in a formation. This is key in various reservoir characterization and calculation processes, which include well testing, formation testing, in-place hydrocarbon volume calculations, and reservoir performance prediction.

$S_w$  calculation from resistivity logs is based on the dependence of  $R_t$  on porosity and the salinity of water formation, as shown in the Archie equation. Most  $S_w$  calculation methods are either based on rearrangement of, or modification to, the Archie equation to accommodate the limitations of the Archie equation for certain formations.

The simplest method for calculating water saturation derived from the Archie equation is the *ratio method*. This approach is based on the assumption that the formation is made of two distinct zones (flushed and uninvaded) of equal formation factor and, hence, independent of porosity.

By dividing  $S_w$  from equation (5.84) by  $S_{xo}$  from equation (5.85):

$$\frac{S_w}{S_{xo}} = \left( \frac{a \times R_w}{\phi^m R_t} \right)^{\frac{1}{n}} / \left( \frac{a \times R_{mf}}{\phi^m R_{xo}} \right)^{\frac{1}{n}}$$

$$\frac{S_w}{S_{xo}} = \left( \frac{R_w R_{xo}}{R_t R_{mf}} \right)^{\frac{1}{n}} \quad (5.86)$$

$\frac{S_w}{S_{xo}}$  is termed the *index of oil movability* (IOM). The value of 1 would imply  $S_w = S_{xo}$  meaning no hydrocarbon has been moved by invasion of filtrate. It is desirable to have lower values, which are an indication of hydrocarbon movability. Values of 0.7 or less would indicate the presence of movable hydrocarbons.

Another important relationship between  $S_w$  and  $S_{xo}$  is *movable hydrocarbon* (MH) defined as:

$$MH = S_{xo} - S_w \quad (5.87)$$

**5.1.10.6.  $R_w$  Calculation from Resistivity Logs.** The *Pickett plot* is a graphical solution to the Archie equation for determining formation water resistivity [Pickett, 1973]. A plot of true formation resistivity against porosity on a-logarithmic scale will produce linear arrangements of the data where the Archie equation is valid. From equation (5.84):

$$S_w = \left( \frac{a \times R_w}{\phi^m R_t} \right)^{\frac{1}{n}}$$

$$\log(S_w) = \log \left( \frac{a R_w}{\phi^m R_t} \right)^{\frac{1}{n}}$$

$$\log(S_w) = \frac{1}{n} \log \left( \frac{a R_w}{\phi^m R_t} \right)$$

$$n \log(S_w) = \log(a R_w) - m \log(\phi) - \log(R_t)$$

$$\log(\phi) = \frac{1}{m} \log(a R_w) - \frac{n}{m} \log(S_w) - \frac{1}{m} \log(R_t) \quad (5.88)$$

Hence, a plot of  $\log(\phi)$  against  $\log(R_t)$  for defined values of  $S_w$  will give a family of straight lines with a slope of  $-\frac{1}{m}$  (Fig. 5.45).

When  $S_w = 1$  and  $\phi = 1$ , equation (5.88) reduces to:

$$0 = \frac{1}{m} \log(a R_w) - \frac{1}{m} \log(R_t)$$

$$\log(R_t) = \log(a R_w)$$

$$R_t = a R_w$$

Thus, on the plot of  $\log(\phi)$  vs  $\log(R_t)$ , values of  $R_t$  read at  $S_w = 1$  and  $\phi = 1$  will give  $(a R_w)$  when a good trend is observed in the clean water zone (Fig. 5.45).  $R_w$  is then determined when  $(a)$  is known or assumed.

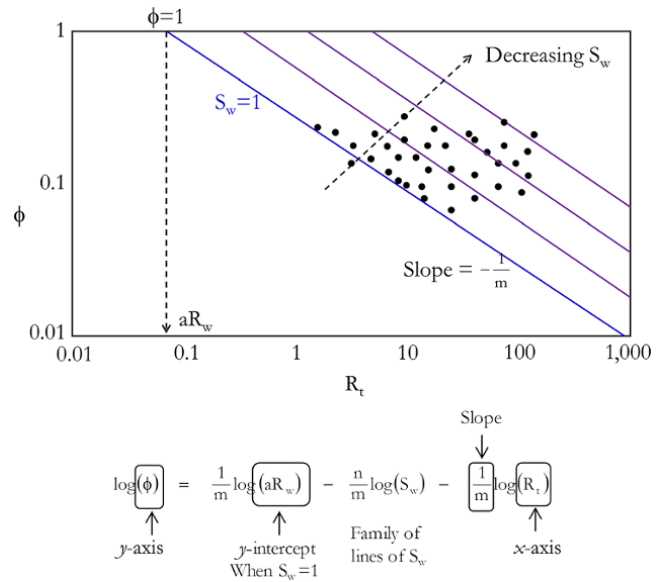


Figure 5.45 A Pickett plot.

**Exercise 5.6**  $R_w$  Calculation using a Pickett Plot

Using a Pickett plot, determine  $R_w$  for the data used in Exercise 5.3 (Table 5.4) given the tortuosity factor,  $a$ , as 0.6 and effective porosity defined as:  $\phi_{eff} = \phi_T(1 - V_{sh})$ , where  $V_{sh}$  is shale fraction.

**Solution Steps.**

What is required for the  $R_w$  calculation using a Pickett plot is a deep resistivity reading and the effective porosity in the water zone ( $S_w = 1$ ). The steps for calculating  $R_w$  using Pickett plot can be summarized as:

*Step 1:* determine total porosity ( $\phi_t$ ) using an appropriate equation. In this instance, since we are interested in the water zone, equation (5.65) is sufficient.

*Step 2:* determine effective porosity using  $\phi_{eff} = \phi_t(1 - V_{sh})$ .

*Step 3:* plot log of effective porosity against log of  $R_w$  on a Cartesian scale or (actual values of effective porosity against  $R_w$  on a log-log scale) for  $S_w = 1$  (water zone).

*Step 4:* the value of  $R_t$  at  $S_w = 1$  (water zone) for  $\phi_{eff} = 1$  will give  $a R_w$  on the straightline trend seen on the Pickett plot.

*Step 5:* calculate  $R_w$  from  $a R_w$  with a known value of  $a$ .

**Solution.**

Table 5.11 summarizes the calculations for Exercise 5.6. Pickett plots in Cartesian and log-log scales are shown in Fig. 5.46 and Fig. 5.47, respectively.

From either Fig. 5.46 and Fig. 5.47,  $a R_w = 0.0103 \Omega\text{-m}$ . Given  $a = 0.6$ :

$$R_w = \frac{a R_w}{a}$$

**Table 5.11** Summary of Calculations for Exercise 5.6.

Depth (ft)	ILD (Ω-m)	ϕ <sub>D</sub> (%)	ϕ <sub>N</sub> (%)	V <sub>sh</sub> (5.26)(5.32)	ϕ <sub>T</sub> (5.65) (fraction)	ϕ <sub>eff</sub> (fraction)	log(R <sub>t</sub> )	log(ϕ <sub>eff</sub> )
8,365	0.26	24.35	30.14	0.186	0.272	0.222	-0.585	-0.654
8,368	0.27	25.54	28.75	0.200	0.271	0.217	-0.569	-0.663
8,371	0.28	24.69	29.15	0.213	0.269	0.212	-0.553	-0.674
8,374	0.34	27	29.43	0.273	0.282	0.205	-0.469	-0.688
8,377	0.41	26.03	29.23	0.348	0.276	0.180	-0.387	-0.745
8,380	0.63	25.31	33.06	0.499	0.292	0.146	-0.201	-0.835

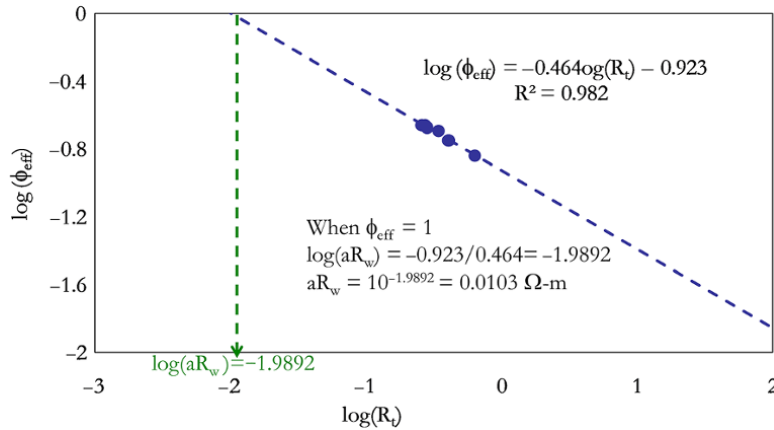


**Figure 5.46** Cartesian Pickett plot using log of ϕ<sub>eff</sub> against log of R<sub>w</sub>.

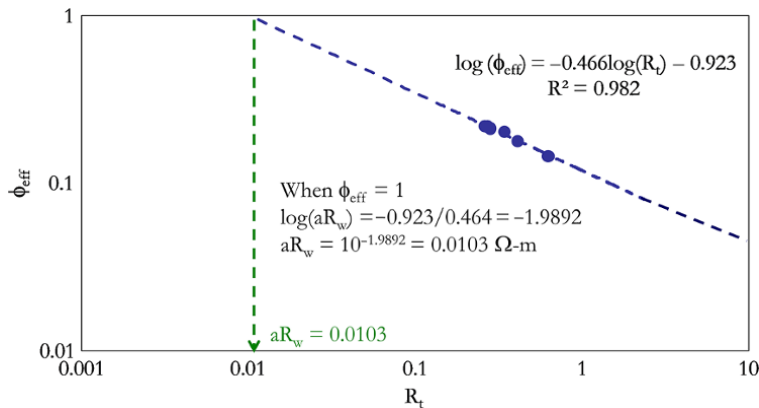


**Figure 5.47** Log-log Pickett plot using ϕ<sub>eff</sub> against R<sub>w</sub>.

$$R_w = \frac{0.0103}{0.6} = 0.017\Omega\text{-m}$$

$$R_w = 0.017 \Omega\text{-m}$$

A comparison of  $R_w$  determined from the SP log (Exercise 5.3) and Pickett plot shows significant differences. SP logs are generally affected by many factors and, where possible, measured  $R_w$  should always be preferable, and where a visible trend is observed on a Pickett plot then it can be considered. However, the use of a Pickett plot or ratio method requires that the underlying

water zone has the same  $R_w$  as the reservoir to be analyzed.

**5.1.10.7. Shaly  $S_w$  Calculation Models.** Shale distribution in a reservoir create challenges in log interpretation as it affects porosity and resistivity measurements. Shale distribution in a reservoir can be general be described as *laminar*, where the shale exists as thin layers between reservoir sand, *structural*, where clay is distributed within the



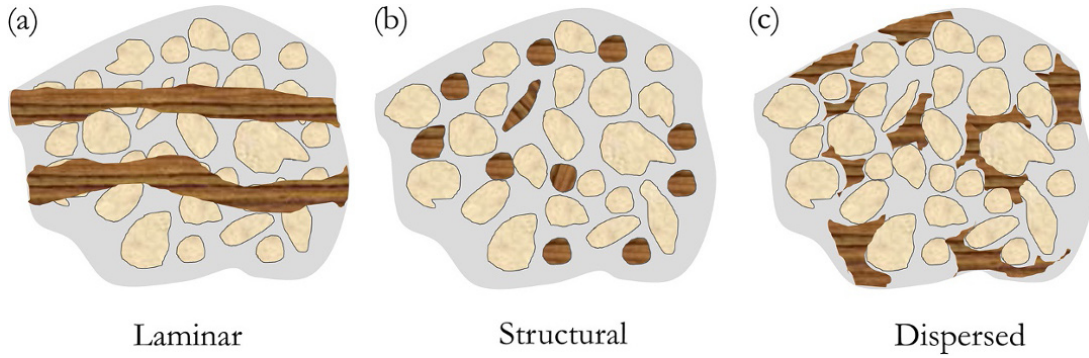


Figure 5.48 Shale distribution in reservoirs.

reservoir rock matrix and hence becomes part of the rock, and *dispersed*, where the clay occupies open space between the grains of clastic matrix (Fig. 5.48).

The Archie equation is only applicable to clean sand and overpredicts  $S_w$  in shaly sand or shaly formations because it ignores the conductivity of shale due to ion movement when laden with water. Different models have been published to improve prediction of  $S_w$  in shaly formations.

*Total Shale Model*

The Total Shale Model [Schlumberger, 1989] works for many shale formations independent of the distribution of the shale and is expressed as:

$$\frac{1}{R_t} = \frac{\phi^2 S_w^2}{aR_w(1-V_{sh})} + \frac{V_{sh}}{R_{sh}} \quad (5.89)$$

$R_{sh}$  is the resistivity of adjacent shale beds and  $V_{sh}$  is the shale volume fraction.

*Laminar Clay Model*

This is based on the concept of the effective resistivity of parallel resistors. The effective resistivity of parallel layers of sand and shale can be defined as:

$$\frac{1}{R_t} = \frac{V_{sh}}{R_{sh}} + \frac{V_{sd}}{R_{sd}} \quad (5.90)$$

With  $V_{sd} = 1 - V_{sh}$

$$\frac{1}{R_t} = \frac{V_{sh}}{R_{sh}} + \frac{1-V_{sh}}{R_{sd}} \quad (5.91)$$

Where  $R_{sd}$  is the resistivity of clean sand and defined using the Archie equation (equation (5.83)):

$$R_{sd} = \frac{aR_w}{\phi_{sd}^m S_{wsd}^n}$$

The subscript *sd* represents sand properties. Hence, equation (5.91) becomes:

$$\frac{1}{R_t} = \frac{V_{sh}}{R_{sh}} + \frac{\phi_{sd}^m S_{wsd}^n (1-V_{sh})}{aR_w} \quad (5.92)$$

Making  $S_w$  the subject of the formula:

$$S_w = S_{wsd} = \left[ \frac{aR_w}{\phi_{sd}^m (1-V_{sh})} \left( \frac{1}{R_t} - \frac{V_{sh}}{R_{sh}} \right) \right]^{\frac{1}{n}} \quad (5.93)$$

Values of  $\phi_{sd}$  can be estimated from adjacent thick clean sand.

*Simandoux and Modified Simandoux Equation*

This gives good  $S_w$  prediction in dispersed shaly sand formation. Equation (5.91) can also be expressed in relation to  $F$ . As such, from equation (5.81):

$$R_t = \frac{FR_w}{S_w^n}$$

and

$$R_{sd} = \frac{FR_w}{S_{wsd}^n}$$

Substituting  $R_{sd}$  into equation (5.91):

$$\frac{1}{R_t} = \frac{V_{sh}}{R_{sh}} + \frac{1-V_{sh}}{R_{sd}}$$

Hence:

$$\frac{1}{R_t} = \frac{V_{sh}}{R_{sh}} + \frac{S_{wsd}^n}{FR_w} (1-V_{sh}) \quad (5.94)$$

Simadoux [1963] presented an equation similar to that above in the form:

$$\frac{1}{R_t} = \epsilon \frac{V_{sh}}{R_{sh}} + \frac{S_w^n}{FR_w} \quad (5.95)$$

where  $\epsilon = 1$  when  $S_w = 1$  and  $\epsilon < 1$  when  $S_w < 1$ .

Making  $S_w$  the subject of the formula in equation (5.95):

$$S_w = \left[ FR_w \left( \frac{1}{R_t} - \epsilon \frac{V_{sh}}{R_{sh}} \right) \right]^{\frac{1}{n}} \quad (5.96)$$

Equation (5.96) is called the Simandoux equation [Simandoux, 1963] or original Simandoux equation. Bardon and Pied [1969] presented equation (5.95) with  $\varepsilon = S_w$  and hence becoming:

$$\frac{1}{R_t} = S_w \frac{V_{sh}}{R_{sh}} + \frac{S_w^2}{FR_w} \quad (5.97)$$

with

$F = \frac{a}{\phi^m}$  from equation (5.82), equation (5.97) becomes:

$$\frac{1}{R_t} = S_w \frac{V_{sh}}{R_{sh}} + \frac{\phi^m S_w^2}{aR_w}$$

which is a quadratic equation with solution:

$$S_w = \frac{-\frac{V_{sh}}{R_{sh}} \pm \sqrt{\left(\frac{V_{sh}}{R_{sh}}\right)^2 + 4\frac{\phi^m}{aR_w R_t}}}{2\frac{\phi^m}{aR_w}} \quad (5.98)$$

Equation (5.98) is often called the *modified Simandoux equation* though some authors still call it the Simandoux equation.

#### Indonesia Equation

This was empirically derived using water-bearing shaly sand. Though the model was based on field data from Indonesia [Poupon and Leveaux, 1971], it can be applied to any shaly sand reservoir and expressed as.

$$S_w = \left[ \left( \left( \frac{V_{sh}^2 - V_{sh}}{R_{sh}} \right)^{\frac{1}{2}} + \left( \frac{\phi_e^m}{aR_w} \right)^{\frac{1}{2}} \right)^2 R_t \right]^{-\frac{1}{n}} \quad (5.99)$$

The Indonesian model can easily be used when there are limited or no measured electrical properties of the core sample in the laboratory.

#### Waxman–Smits Method

This is an empirical relationship developed for dispersed clay. It defines the relationship between electrical resistivity of water saturated shaly sand to the water resistivity and cation-exchange capacity per unit pore volume [Waxman and Smits, 1968]. The model predicts saturation of total porosity and the solution is iterative as the equation is nonlinear. The Waxman–Smits equation is expressed as:

$$S_{wt}^{n*} = \frac{R_w}{R_t \phi^{m*} \left( 1 + R_w B \frac{Q_v}{S_{wt}} \right)} \quad (5.100)$$

where  $S_{wt}$  is the saturation of the total porosity,  $B$  is a constant that is dependent on temperature, and  $Q_v$  is the

cation exchange capacity per unit pore volume in meq/unit pore volume in cc and defined as:

$$B = \frac{(-1.28 + 0.25 \times T - 0.000409 \times T^2)}{(1 + (0.04 \times T - 0.27) R_w^{1.23})} \quad (5.101)$$

$T$  is the temperature in °C.

The relationship between  $Q_v$  and CEC is:

$$Q_v = \frac{CEC \times \rho}{100 \times \phi} \quad (5.102)$$

CEC is cation exchange capacity in meq/100g of clay  
*Dual Water Model*

A dual water model is based on the assumption that the exchange cations contribute to the conductivity of clay-bound water that is separated from the bulk water [Clavier *et al.*, 1984]. The dual water model is similar to the Waxman–Smits method and the saturation calculated is the saturation of total porosity and expressed as:

$$S_{wt}^{n*} = \frac{R_{wf}}{R_t \phi^{m*} \left( 1 + \frac{R_{wf} S_{wb}}{S_{wt}} \left( \frac{1}{R_{wb}} - \frac{1}{R_{wf}} \right) \right)} \quad (5.103)$$

where

$$S_{wb} = 1 - \frac{\phi_e}{\phi_t}$$

$R_{wb}$  is the resistivity of the bound water in the shale and defined as:

$$R_{wb} = R_{t\_sh} \phi_t^m$$

$R_{wf}$  is the resistivity of free formation water in the clean zone and defined as:

$$R_{wf} = R_{t\_clean} \phi_t^m$$

where  $R_{t\_sh}$  is the true resistivity of the shale formation and  $R_{t\_clean}$  is the true resistivity of the clean zone formation.

Hence, for the clean zone  $R_{wf}$  can be varied to get  $S_w = 1$  in the clean water leg.

The saturation of effective saturation is then determined using:

$$S_{we} = \frac{S_{wt} - S_{wb}}{1 - S_{wb}}$$

This method requires the neutron–density log for a good estimate of  $\phi_t$  and is best obtained from a neutron–density cross-plot.

Table 5.12 summarizes the the models for calculating  $S_w$  from resistivity log.

**Table 5.12** Models for Calculating  $S_w$  from the Resistivity Log.

Model Name	Model	Concept and application	Limitation
Archie	$S_w = \left( \frac{a \times R_w}{\phi^m R_t} \right)^{\frac{1}{n}}$	Clean sand. Ignores conductivity of shale due to ion movement when laden with water.	Archie should only be used in clean sandstone. Using Archie for shaly formation would overestimate $S_w$ and may yield $S_w$ greater than 1.
Ratio method	$S_w = S_{xo} \left( \frac{R_w R_{xo}}{R_t R_{mf}} \right)^{\frac{1}{n}}$	This approach is based on the assumption that the formation is made of two distinct zones (flushed and uninvaded) of equal formation factor and, hence, independent of porosity.	
Laminar clay model	$S_w = S_{wsd} = \left[ \frac{a R_w}{\phi_{sd}^m (1 - V_{sh})} \left( \frac{1}{R_t} - \frac{V_{sh}}{R_{sh}} \right) \right]^{\frac{1}{n}}$	Concept that conductive materials saturated with conducting fluid can be modeled as resistors in parallel [Wyllie and Southwick, 1954].	
Simandoux	$S_w = \left[ F R_w \left( \frac{1}{R_t} - e \frac{V_{sh}}{R_{sh}} \right) \right]^{\frac{1}{n}}$	Dispersed shaly sand. Better with saline water.	
Modified Simandoux	$S_w = \frac{-\frac{V_{sh}}{R_{sh}} \pm \sqrt{\left( \frac{V_{sh}}{R_{sh}} \right)^2 + 4 \frac{\phi^m}{a R_w R_t}}}{2 \frac{\phi^m}{a R_w}}$		
Indonesian (Poupon–Leveaux)	$S_w = \left[ \left( \left( \frac{V_{sh}^2 - V_{sh}}{R_{sh}} \right)^{\frac{1}{2}} + \left( \frac{\phi_e^m}{a R_w} \right)^{\frac{1}{2}} \right)^2 R_t \right]^{-\frac{1}{n}}$	Dispersed shaly sand. Based on field observation and developed for better evaluation of the fresh water formations. Empirically modeled using water-bearing shaly sand.	Though model is based on field data from Indonesia, it can be applied on any shaly sand reservoir.
Waxman–Smits	$S_{wt}^{n^*} = \frac{R_w}{R_t \phi^{m^*} \left( 1 + R_w B \frac{Q_w}{S_{wt}} \right)}$ where $B = \frac{(-1.28 + 0.25 \times T - 0.000409 \times T^2)}{(1 + (0.04 \times T - 0.27) R_w^{1.23})}$	Dispersed shaly sand. An empirical relationship	Requires laboratory data input and solution of $S_w$ is iterative.
Dual water model	$S_{wt}^{n^*} = \frac{R_{wf}}{R_t \phi^{m^*} \left( 1 + \frac{R_{wf} S_{wb}}{S_w} \left( \frac{1}{R_{wb}} - \frac{1}{R_{wf}} \right) \right)}$	Assumes that the exchange cations contribute to the conductivity of clay-bound water that is separated from the bulk water.	

**Exercise 5.7** Openhole Log Interpretation

Given the resized log-data in Table 5.13, determine the following:

1. Possible/probable lithology.
2. Zone of interest (permeable zone).
3. The fluid in the permeable zone.
4.  $S_w$  as a continuous log using the Archie, Waxman–Smits and Indonesian equations.

Available resistivity log measurements are: microspherically focused (MSFL) with a depth of investigation (DOI) of 4 in, which can be considered to measure the

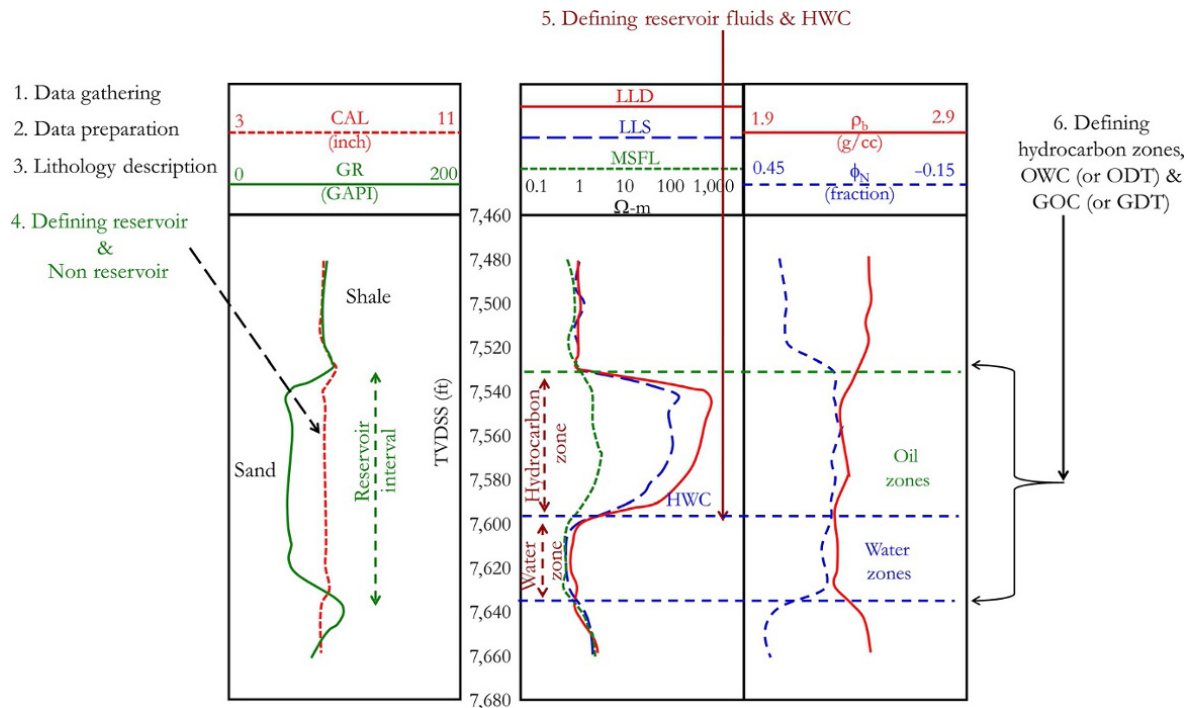
resistivity of the flushed zone; shallow laterolog (LLS) with DOI of 14 in, which can be considered to measure the resistivity of the shallow zone; and deep laterolog (LLD) with a DOI of 45 in, which can be considered to measure the resistivity of the uninvaded zone.

$R_w$  at the formation temperature ( $R_w(T_f)$ ) is 0.057  $\Omega$ -m.

The Archie model parameters determined from advanced core analysis are:  $a = 0.65$ ;  $m = 2$ , and  $n = 2$ . Waxman–Smits model parameter are  $m^* = 2.02$  and  $n^* = 2.05$ . The resistivity of the shale at formation temperature ( $R_{sh}(T_f)$ ) is 1.519  $\Omega$ -m.

**Table 5.13** Log Data for Exercise 5.7.

Depth (ft)	CAL (in)	GR (GAPI)	MSFL ( $\Omega$ -m)	LLS ( $\Omega$ -m)	LLD ( $\Omega$ -m)	$\phi_N$ (fraction)	$\rho_b$ (g/cc)
7,480	6.48	84.375	0.694	1.063	1.007	0.359	2.465
7,490	6.45	83.006	0.871	0.952	1.019	0.350	2.463
7,500	6.38	82.031	0.874	1.181	1.091	0.341	2.472
7,510	6.26	81.434	0.811	0.954	0.989	0.344	2.447
7,520	6.47	83.461	0.681	0.991	1.005	0.328	2.458
7,530	7.22	88.608	1.165	1.200	1.200	0.223	2.421
7,540	6.45	52.028	1.777	54.862	193.442	0.213	2.370
7,550	6.51	52.292	1.800	41.090	192.646	0.210	2.338
7,560	6.55	54.123	1.924	48.241	160.007	0.197	2.344
7,570	6.55	53.571	2.592	45.080	125.405	0.219	2.355
7,580	6.55	51.602	2.050	23.845	67.279	0.215	2.364
7,590	6.55	49.932	1.412	9.291	22.295	0.221	2.323
7,600	6.62	51.022	0.670	1.045	1.146	0.224	2.306
7,610	6.62	52.983	0.579	0.611	0.774	0.244	2.327
7,620	6.59	53.529	0.616	0.661	0.772	0.240	2.323
7,630	6.79	80.767	0.547	0.733	0.907	0.245	2.311
7,640	6.30	101.435	1.151	1.202	1.020	0.369	2.408
7,650	6.22	84.699	1.794	1.641	1.699	0.401	2.457
7,660	6.17	70.312	2.031	1.782	2.261	0.385	2.474

**Figure 5.49** Steps 1–6 for Exercise 5.7.**Solution.**

Calculation steps 1 to 6 are illustrated in Fig. 5.49.

*Step 1:* the calculations of petrophysical properties are summarized in Table 5.14.

A graphical comparison of all the  $S_w$  calculations within the interval of interest is shown in Fig. 5.50.

**5.2. PERMEABILITY LOGS**

Measured permeability well logs can be created from continuous measurements of formation test permeability, stressed core permeability, stress-corrected core permeability, and average interval permeability from well tests (Fig. 5.51).

**Table 5.14** Summary of Calculations for Exercise 5.7.

Depth (ft)	$V_{sh}$	$\phi_D$	Total porosity ( $\phi_T$ )	$\phi_{eff}$	$S_w$ (Archie)	$S_w$ (Waxman–Smits)	$S_w$ (Indonesia)
equation →	(5.26)	(5.51)	(5.65)	(5.68)	(5.84)	(5.100)	(5.99)
7,480	0.67	0.11	0.24	0.08	0.81	0.81	0.97
7,490	0.64	0.11	0.23	0.08	0.82	0.82	0.96
7,500	0.62	0.11	0.22	0.08	0.82	0.82	0.93
7,510	0.61	0.12	0.23	0.09	0.83	0.83	0.96
7,520	0.65	0.12	0.22	0.08	0.86	0.87	0.99
7,530	0.75	0.14	0.18	0.05	0.97	1.00	1.00
7,540	0.04	0.17	0.19	0.18	0.07	0.04	0.07
7,550	0.05	0.19	0.20	0.19	0.07	0.03	0.07
7,560	0.08	0.19	0.19	0.18	0.08	0.03	0.08
7,570	0.07	0.18	0.20	0.18	0.09	0.04	0.09
7,580	0.03	0.17	0.19	0.19	0.12	0.06	0.12
7,590	0.00	0.20	0.21	0.21	0.19	0.13	0.19
7,600	0.02	0.21	0.22	0.21	0.83	0.84	0.84
7,610	0.06	0.20	0.22	0.21	1.00	1.03	1.01
7,620	0.07	0.20	0.22	0.20	1.00	1.03	1.02
7,630	0.60	0.21	0.23	0.09	0.90	0.91	1.01
7,640	1.00	0.15	0.26	0.00	0.74	0.73	1.22
7,650	0.68	0.12	0.26	0.08	0.57	0.53	0.72
7,660	0.40	0.11	0.25	0.15	0.52	0.47	0.57

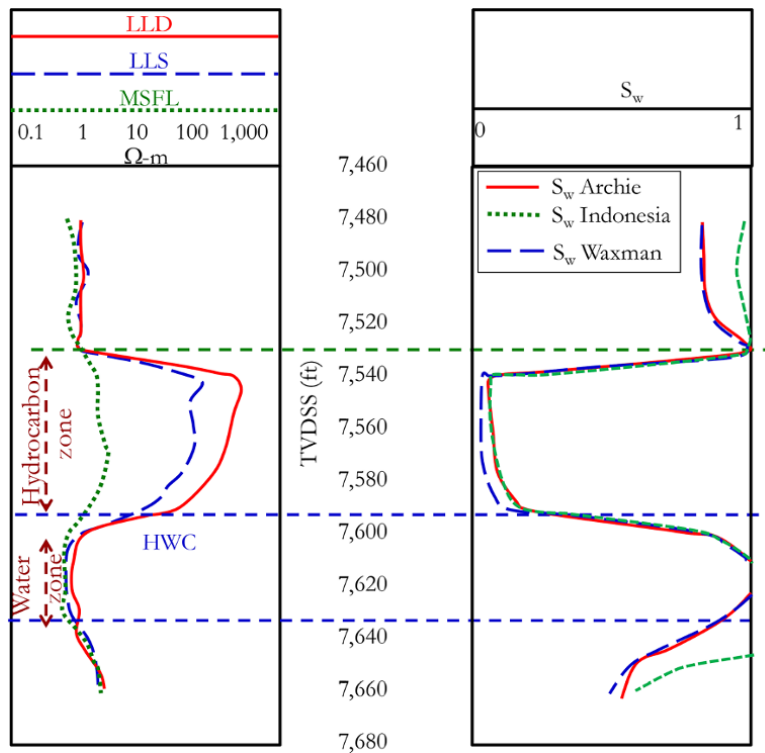


**Figure 5.50** Comparison of  $S_w$  calculations scaled from 0 to 1

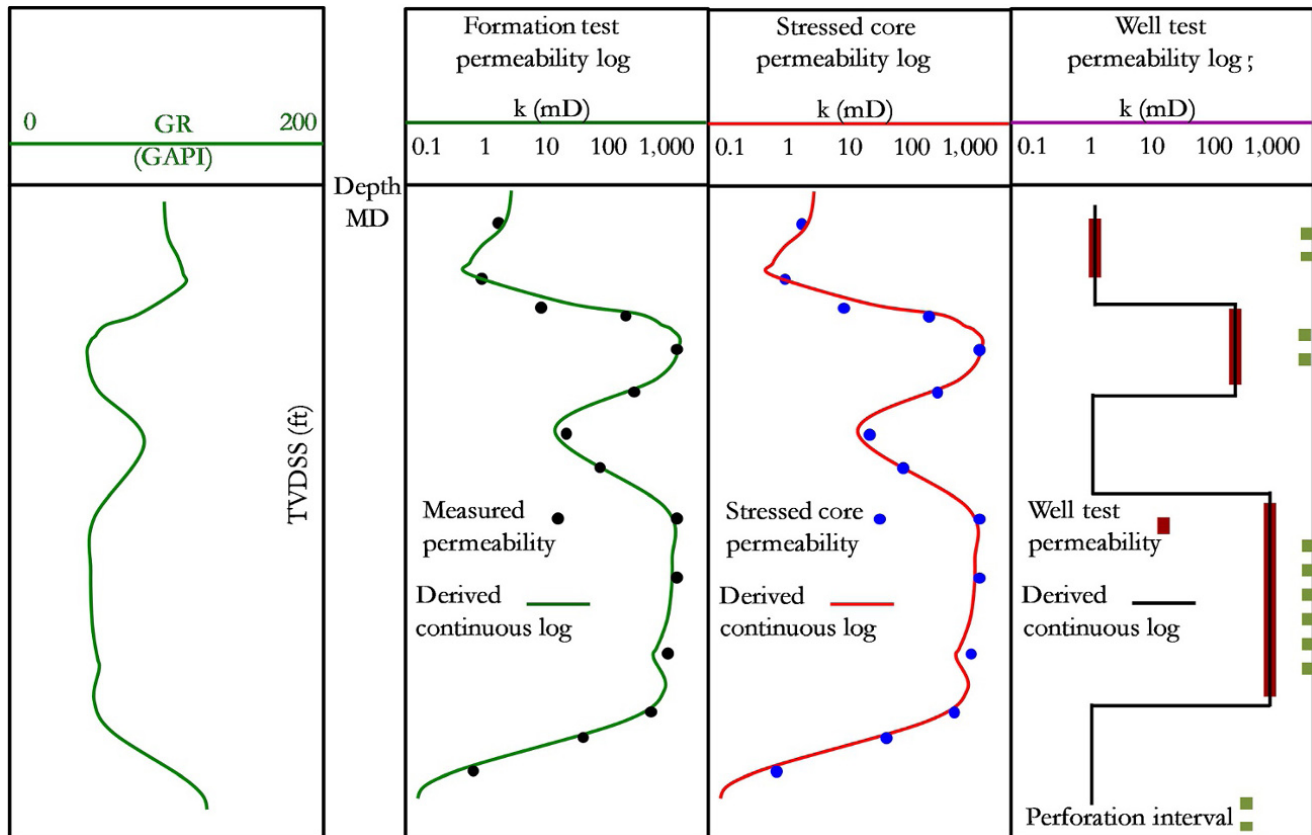


Figure 5.51 Permeability well logs from different permeability measurements.

### 5.2.1. Permeability Logs from Formation Test

This is based on methods that include: pretest-mobility, flow rate analysis (FRA), and pressure transient analysis (PTA). These methods are discussed in Chapters 6 and 8. Permeabilities from formation testing are for discrete stations (depths). However, by matching these discrete formation test permeabilities with appropriate permeability prediction models, a continuous permeability log can be derived.

### 5.2.2. Permeability Logs from Core Data

Details of permeability determination from core samples were discussed in Chapter 2.2. Cores from selected intervals are analyzed and discrete permeabilities at different depths are determined. Continuous permeability logs can then be derived by matching permeability prediction models with measured core permeabilities at discrete depths. Important information that would ensure that the model is matched to the correct data is knowing if core permeability is absolute or effective and also to know if core permeabilities were measured under stressed conditions corresponding to reservoir pressure.

### 5.2.3. Permeability Logs from Well Test Permeability

Well test analysis gives average permeabilities over test intervals, and does not give discrete permeabilities per depth (Fig. 5.51). However, continuous permeability logs can be derived by matching permeability models with average permeabilities over test intervals (Fig. 5.51). Well test interpretation is discussed in detail in Chapter 8.

### 5.2.4. Permeability Log Estimation from other Properties

Continuous formation permeability measurements along a well are often not available for operational and cost reasons. A more practical approach for creating permeability well logs is to derive continuous permeability from a combination of other log properties, such as porosity, water saturation, and nuclear magnetic resonance.

The concept of permeability log prediction is based on relationships that show the dependence of permeability ( $k$ ) on porosity ( $\phi$ ) and other properties. The most fundamental relationship between  $k$  and  $\phi$  is the Kozeny–Carman (KC) equation developed by *Kozeny* [1927] and modified by *Carman* [1937]. For uniformly sized spheres

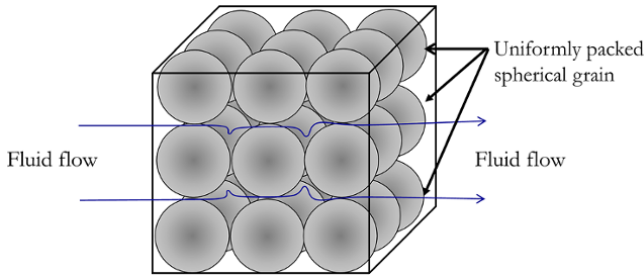


Figure 5.52 Uniform size, uniformly packed spherical grains.

with uniform packing (Fig. 5.52), the Kozeny–Carman equation can be expressed as:

$$k = \frac{\phi^3}{(1-\phi^2)} \left( \frac{1}{5 S_{gv}^2} \right) \quad (5.104)$$

where  $S_{gv}$  = surface area of grains exposed to the fluid per unit volume of solid material.

Though reservoir grains are nonuniform in size and are irregular in shape, equation (5.104) shows that porosity alone is not sufficient to predict permeability; also permeability is inversely proportional to exposed surface area. This is a very important relationship that forms the basis of predicting permeability from porosity.

Equation (5.104) can be modified to account for the effect of irregular shaped grains and nonuniform size distribution (Fig. 5.53) by introducing a *shape factor* ( $F_s$ ) and *tortuosity* ( $\tau$ ).

The modified Kozeny–Carman equation (MKC) for irregular shaped grains with nonuniform packing can be expressed as:

$$k = \frac{\phi^3}{(1-\phi^2)} \left( \frac{1}{F_s \tau S_{gv}^2} \right) \quad (5.105)$$

where  $\tau$  is the *tortuosity* and  $F_s$  is the *shape factor*. There are laboratory techniques that can be used to determine  $F_s$ ,  $\tau$ , and  $S_{gv}$ . However, these methods are laborious and expensive. A more useful approach is to correlate  $\frac{1}{F_s \tau S_{gv}^2}$  with properties that can easily be determined/measured.

**5.2.4.1. Permeability Log Prediction Based on Correlating  $\frac{1}{F_s \tau S_{gv}^2}$  with  $S_{wir}$ .** The most common prop-

erty that has been used to correlate  $\frac{1}{F_s \tau S_{gv}^2}$  is the irreducible water saturation in the formation. Since irreducible water adheres primarily to the grain surface and depends

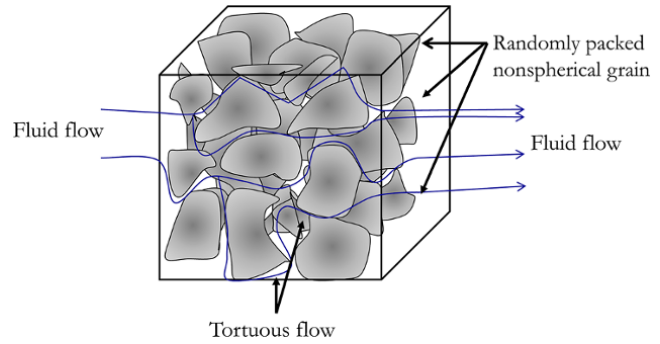


Figure 5.53 Nonuniform size, randomly packed irregular shaped grains.

on grain size,  $S_{wir}$  can be correlated with  $\frac{1}{F_s \tau S_{gv}^2}$ . Some of the published empirical permeability prediction model based on correlation of  $\frac{1}{F_s \tau S_{gv}^2}$  with  $S_{wir}$  include:

*Tixier [1949]*

$$k^{\frac{1}{2}} = 250 \frac{\phi^3}{S_{wir}} \quad (5.106)$$

*Timur [1968]*

$$k = 0.136 \frac{\phi^{4.4}}{S_{wir}^2} \quad (5.107)$$

*Coates and Denoo [1981]*

$$k^{\frac{1}{2}} = 100 \frac{\phi^2(1-S_{wir})}{S_{wir}} \quad (5.108)$$

*Wyllie and Rose [1950]*

$$k = \left( \frac{C\phi^3}{S_{wir}} \right)^2 \quad (5.109)$$

where  $C = 79$  and  $250$  for gas and medium gravity crude, respectively. A generalize form of correlating  $\frac{1}{F_s \tau S_{gv}^2}$  with  $S_{wir}$  is expressed below as a *power law* model:

$$k = a \frac{\phi^b}{S_{wir}^c} \quad (5.110)$$

Equation (5.110), which is a generalized form of equations (5.106)–(5.109), is important since for any given formation or facie, parameters  $a$ ,  $b$ , and  $c$  can be determined by calibrating the permeability model to measured permeability, such as stressed core permeability or formation test permeability.

Error of match, which is the difference between actual measured permeability and model predicted permeability, for each sample point can be expressed as:

$$\epsilon_j = k_j - k(a, b, c) \quad (5.111)$$

where  $k_j$  is the measured permeability under stressed condition or from the formation test at any given depth.

The sum of the square of the errors can thus be expressed as:

$$\epsilon^2 = \sum_{j=1}^n (\epsilon_j)^2 = \sum_{j=1}^n (k_j - k(a, b, c))^2 \quad (5.112)$$

minimizing the sum of square of errors,  $\epsilon^2$ , which is the objective function, yields parameters  $a$ ,  $b$ , and  $c$  that describe the *power law* model for the formation.

*Initial Connate Water Saturation ( $S_{wi}$ ) and Irreducible Water Saturation ( $S_{wir}$ )*

$S_{wir}$ , which is required for permeability estimation in equation (5.110), can be determined from core experiments by using oil or gas flow to displace water under differential pressure or through centrifugal force to irreducible water saturation.  $S_{wir}$  determined from this method depends on the final drive pressure or centrifugal speed. Since  $S_{wir}$  from core experiments is dependent on displacement pressure, it may not be equal to the initial connate water saturation ( $S_{wi}$ ) in the reservoir determined from resistivity logs. Due to inconsistencies in  $S_{wir}$  from core experiments, it is more practical to use  $S_{wir}$  derived from the well log. In the reservoir hydrocarbon zone, initial connate water saturation can be considered equal to the irreducible water saturation, which is not producible ( $S_{wi} = S_{wir}$ ). In the transition zone, some of the connate water can be produced and initial water saturation in the transition zone is greater than irreducible water saturation ( $S_{wi} > S_{wir}$ ). In the water zone, water saturation is 1 ( $S_w = 1$ ) and greater than  $S_{wir}$ . (Fig. 5.54).

Since  $S_{wi}$ , the initial water saturation calculated from the resistivity log at the initial reservoir condition, in the hydrocarbon zone is  $S_{wir}$ ,  $S_{wi}$  can be used in equations

(5.106)–(5.110) directly in the hydrocarbon zones. However, in the transition and water zones,  $S_{wir}$  has to be calculated and  $S_{wi}$  determined from electrical logs cannot be used directly in permeability prediction models (equations (5.106)–(5.110)).

*Calculation of  $S_{wir}$  from  $S_{wi}$  in the Transition and Water Zones*

Buckles [1965] showed the relationship between  $S_{wir}$  and porosity ( $\phi$ ) as:

$$\phi S_{wir} = C_{Bkl} \quad (5.113)$$

where  $C_{Bkl}$  is *Buckles constant* and equal to the *bulk volume of irreducible water (BVI)*.

Making porosity the subject of the formula:

$$\phi = \frac{C_{Bkl}}{S_{wir}} \quad (5.114)$$

The plot of porosity against  $S_{wir}$  will give an exponential relationship with a family of curves characterizing rock of different grain size (Fig. 5.55).  $S_{wir}$  and porosity for the Buckles plot can be taken from core analysis or from log analysis in a hydrocarbon bearing zone where  $S_{wi} = S_{wir}$ .

Typical values of  $C_{Bkl}$  are:

Sandstones: 0.02–0.1.

Intergranular carbonates: 0.01–0.06.

Vuggy carbonates 0.005–0.06.

Expressing equation (5.114) in terms of log terms:

$$\log \phi = \log C_{Bkl} - \log S_{wir} \quad (5.115)$$

Fig. 5.56 shows the Buckles plot on a log-log scale.

When  $S_{wir} = 1$ , from equation (5.115):

$$\log \phi = \log C_{Bkl}$$

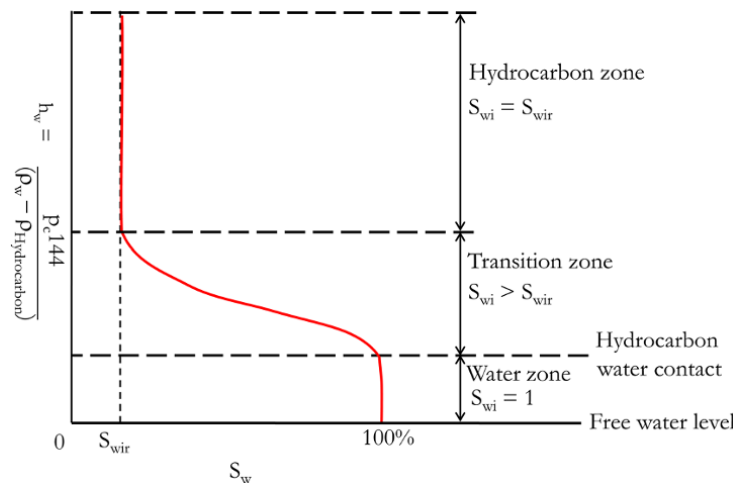


Figure 5.54 Initial connate water saturation and irreducible water saturation in a reservoir.



Hence, when a trend for a given rock type is extrapolated to  $S_{wir} = 1$ , the value of  $\phi$  read, corresponds to  $C_{Bkl}$ . From determined  $C_{Bkl}$  for a given rock type,  $S_{wir}$  can be determined in the transition or water zones using equation (5.113)

$$S_{wir} = \frac{C_{Bkl}}{\phi} \tag{5.116}$$

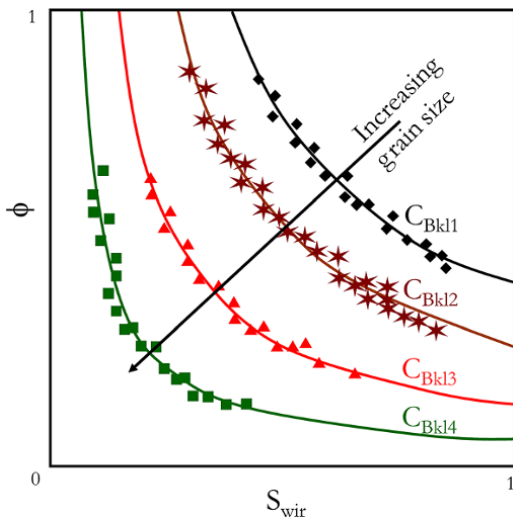


Figure 5.55 Buckles plot on a Cartesian scale.

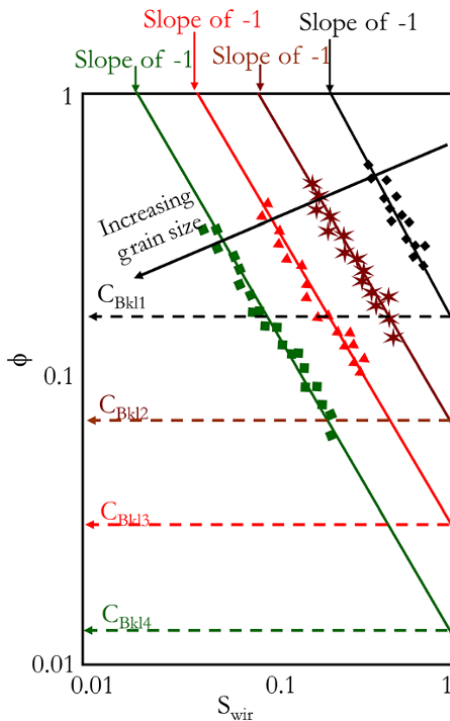


Figure 5.56 Buckles plot on a log-log scale.

$S_{wir}$  calculated for the transition and water zones can then be used to calculate permeability in those zones using equations (5.110) and (5.112). Predicting permeability in the water zone is important, especially where the reservoir deliverability is dependent on aquifer response.

$C_{Bkl}$ , which is equal to BVI, can be determined from nuclear magnetic resonance log (section 5.2.4.4).

**Exercise 5.8** Power Law Permeability Log Prediction Using Simple Regression

Porosity from well log analysis, initial water saturation from well log analysis, and permeability from core analysis are summarized in Table 5.15. Determine permeability power law model parameters (a, b, and c) and create a permeability log over the depth of 10,050–10,145 ft which has an average reservoir pressure of 2340 psia.

Table 5.16 shows the porosity and initial connate water saturation well logs.

**Solution Steps.**

Step 1: set up permeability model prediction with porosity and  $S_{wir}$  and initial guess values of a, b, and c.

Step 2: create an objective function using equation (5.112) and minimize the function to get correct values of a, b, and c.

**Solution.**

Table 5.17 summarizes the solution for the well log permeability prediction for Exercise 5.8.

Minimize function  $\sum_{j=1}^n (\epsilon_j)^2 = \sum_{j=1}^n (k_j - k(a, b, c))^2$  by changing a, b, and c.

From regression, a = 4300; b = 2.92 and c = 2.

Hence, using equation (5.110), the power law permeability model that described the formation is:

$$4300 \frac{\phi^{2.92}}{S_{wir}^2} \tag{5.117}$$

**Table 5.15** Porosity, Irreducible Water Saturation, and Permeability.

Sample number	Depth (ft)	Confining pressure (psia)	$S_{wir} = S_{wi}$ (from well log)	Klinkenberg permeability k (mD)
1	10,056	2340	0.05	0.8
2	10,073	2340	0.18	544
3	10,087	2340	0.23	612
4	10,109	2340	0.11	60
5	10,125	2340	0.03	0.2
6	10,143	2340	0.34	2,350

The calculated permeability well log prediction over the depth 10,050–10,145 ft is summarized in Table 5.18.

A graphical depiction of predicted and measured core permeability over the depth 10,050–10,145 ft is shown in Fig. 5.57.

Using simple regression only, as done in Exercise 5.8, for a large data set can be difficult when determining the permeability power model parameters a, b, and c due to the non-unique solution (that is, more than one possible combination of a, b, and c can match the data).

A practical workflow to determine permeability model parameters a, b, and c is discussed here.

From equation (5.110)

$$k = a \frac{\phi^b}{S_{wir}^c}$$

Hence

$$\log k = \log a + b \log \phi - c \log S_{wir} \quad (5.118)$$

**Table 5.16** Porosity and Initial Connate Water Saturation Well Logs.

Depth (ft)	$\phi$	$S_{wi}$
10,050	0.22	0.33
10,055	0.03	0.90
10,060	0.10	0.35
10,065	0.12	0.29
10,070	0.15	0.22
10,075	0.23	0.36
10,080	0.32	0.21
10,085	0.34	0.26
10,090	0.32	0.19
10,095	0.34	0.31
10,100	0.36	0.40
10,105	0.31	0.28
10,110	0.41	0.36
10,115	0.32	0.27
10,120	0.28	0.37
10,125	0.10	0.35
10,130	0.07	0.88
10,135	0.09	0.87
10,140	0.21	0.43
10,145	0.31	0.45

*Calculating Parameter a*

When  $S_{wir} = 1$ , and  $\phi = 1$ , equation (5.118) reduces to:

$$\log k = \log a + b \log(1) - c \log(1)$$

and

$$\log k = \log a$$

Hence, on a plot of  $\log(k)$  against  $\log(\phi)$ , for  $S_{wir} = 1$  trend, the value of k at  $\phi = 1$  will give the value of model parameter a.  $S_{wir} = 1$  will correspond to shale or a shaly formation with bound water.

*Calculating Parameter b*

From equation (5.118), a plot of k against  $\phi$  on a log-log scale will yield a family of trends for different  $S_{wir}$  whose slopes equal b.

*Calculating Parameter c*

From equation (5.118) when  $S_{wir} = 1$

$$\log k(S_{wir} = 1) = \log a + b \log \phi(S_{wir} = 1) \quad (5.119)$$

Solving equations (5.118) and (5.119) simultaneously by subtracting equation (5.118) from equation (5.119) and making c the subject of the formula:

$$c = \frac{\log \frac{k(S_{wir} = 1)}{k} - b \log \frac{\phi(S_{wir} = 1)}{\phi}}{\log S_{wir}} \quad (5.120)$$

Hence, for a given k,  $\phi$ , and  $S_{wir}$  with a value on a clearly defined trend where  $S_{wir} \neq 1$ , equation (5.120) can be used to determine value of parameter c. It is preferable to use k and  $\phi$  from the k- $\phi$  trend corresponding to the lowest  $S_{wir}$  for calculating parameter c in equation (5.120).

With initial values of a, b, and c determined, forward simulation of k is then carried out and regression using equation (5.112) may then be used to refine the match to get improved values of the a, b, and c parameters.

An integrated workflow for creating a permeability well log model that involves model diagnosis and initial value determination, forward simulation, and refining the

**Table 5.17** Solution for the Well Log Permeability Prediction for Exercise 5.8.

Sample number	Depth (ft)	Stress (psia)	$\phi$	$S_{wir}$	k (mD)	$k_i(a, b, c)$ (mD) using equation (5.110)	$\epsilon^2$ using equation (5.112)
1	10,056	2340	0.05	0.89	0.8	0.86	0.003887
2	10,073	2340	0.18	0.23	544	543.76	0.056856
3	10,087	2340	0.23	0.31	612	612.34	0.113424
4	10,109	2340	0.11	0.33	60	62.71	7.320966
5	10,125	2340	0.03	0.78	0.2	0.25	0.002769
6	10,143	2340	0.34	0.28	2,350	2,350.02	0.000258

**Table 5.18** Predicted Permeability Well Log Using Equation (5.117).

Depth (ft) from Table 5.16	$\phi$ from Table 5.16	$S_{wir}=S_{wi}$ from Table 5.16	$k_{predicted}$ (mD) using equation (5.117)
10,050	0.22	0.33	475
10,055	0.03	0.90	0
10,060	0.10	0.35	42
10,065	0.12	0.29	105
10,070	0.15	0.22	349
10,075	0.23	0.36	454
10,080	0.32	0.21	3,500
10,085	0.34	0.26	2,725
10,090	0.32	0.19	4,276
10,095	0.34	0.31	1,917
10,100	0.36	0.40	1,361
10,105	0.31	0.28	1,794
10,110	0.41	0.36	2,456
10,115	0.32	0.27	2,117
10,120	0.28	0.37	763
10,125	0.10	0.35	42
10,130	0.07	0.88	2
10,135	0.09	0.87	5
10,140	0.21	0.43	244
10,145	0.31	0.45	695

match using total least square regression is summarized in Fig. 5.58.

**Exercise 5.9** Power Law Permeability Log Prediction Using Integrated Workflow

Stressed core permeability and porosity data from core analysis are summarized in Table 5.19.

Determine the permeability well log model using the power law model and create the permeability log over a depth of 10,358–10,753 ft, which is above transition zone.

**Solution Steps.**

Since the interval of interest is above the transition zone, the assumption of  $S_{wir} = S_{wi}$  is valid.

Following the steps summarized in Fig. 5.58.:

*Step 1:* plot  $k$  against  $\phi$  on a log-log scale with the  $S_{wir}$  value as a data label on plot.

*Step 2:* from the  $k$ - $\phi$  trend, with  $S_{wir}=1$ , determine parameter  $a$ , which is the value of  $k$  when  $\phi = 1$ .

*Step 3:* from the  $k$ - $\phi$  trend, with  $S_{wir} = 1$ , determine parameter  $b$ , which is the slope of trend.

*Step 4:* from any  $k$  and  $\phi$  on trend with  $S_{wir} \neq 1$  determine parameter  $c$  using equation (5.120).

*Step 5:* simulate  $k$  with determined parameter  $a$ ,  $b$ , and using equation (5.110).

*Step 6:* use regression to refine the match and improve values of  $a$ ,  $b$ , and  $c$ .

**Solution.**

The cross-plot of  $k$  against  $\phi$  showing values of  $S_{wir}$  is shown in Fig. 5.59.

The graphical determination of  $a$  and  $b$  is summarized in Fig. 5.60.

Calculation of parameter  $c$  is summarized in Fig. 5.61.

Substitute any value of  $k$  and  $\phi$  at  $S_{wir} = 0.1$  (the lowest saturation with good trend) (Fig. 5.61) with  $a$  and  $b$  into equation (5.120).

Using a value of  $k = 0.003$  mD and  $\phi = 0.04$  (Fig. 5.61) and substituting into equation (5.120) to calculate parameter  $c$ :

$$c = \frac{\log \frac{k(S_{wir} = 1)}{k} - b \log \frac{\phi(S_{wir} = 1)}{\phi}}{\log S_{wir}}$$

$$c = \frac{\log \frac{0.31}{0.003} - 5.87 \log \frac{0.13}{0.04}}{0.1} = 2.0$$

$a = 4200$ ,  $b = 5.87$ , and  $c = 2.0$

Forward simulation to examine the match of the model's prediction with core permeability on a diagnostic plot (Fig. 5.62) and permeability-depth log (Fig. 5.63) is carried out.

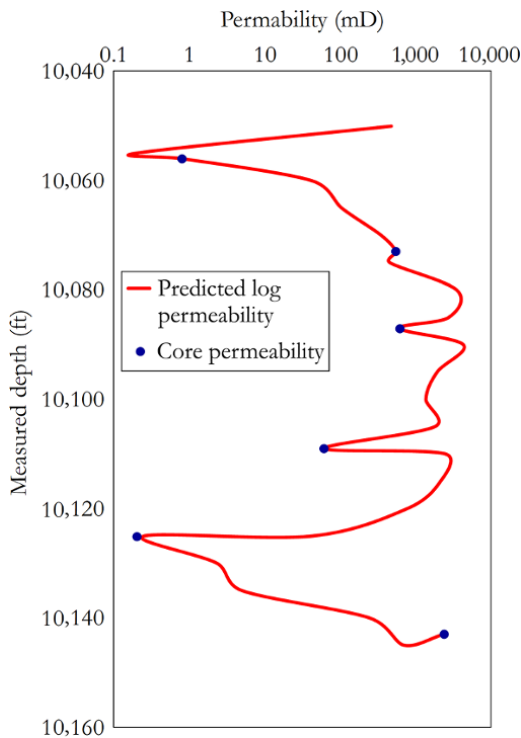


**Figure 5.57** Permeability log prediction with match to measured core permeability.

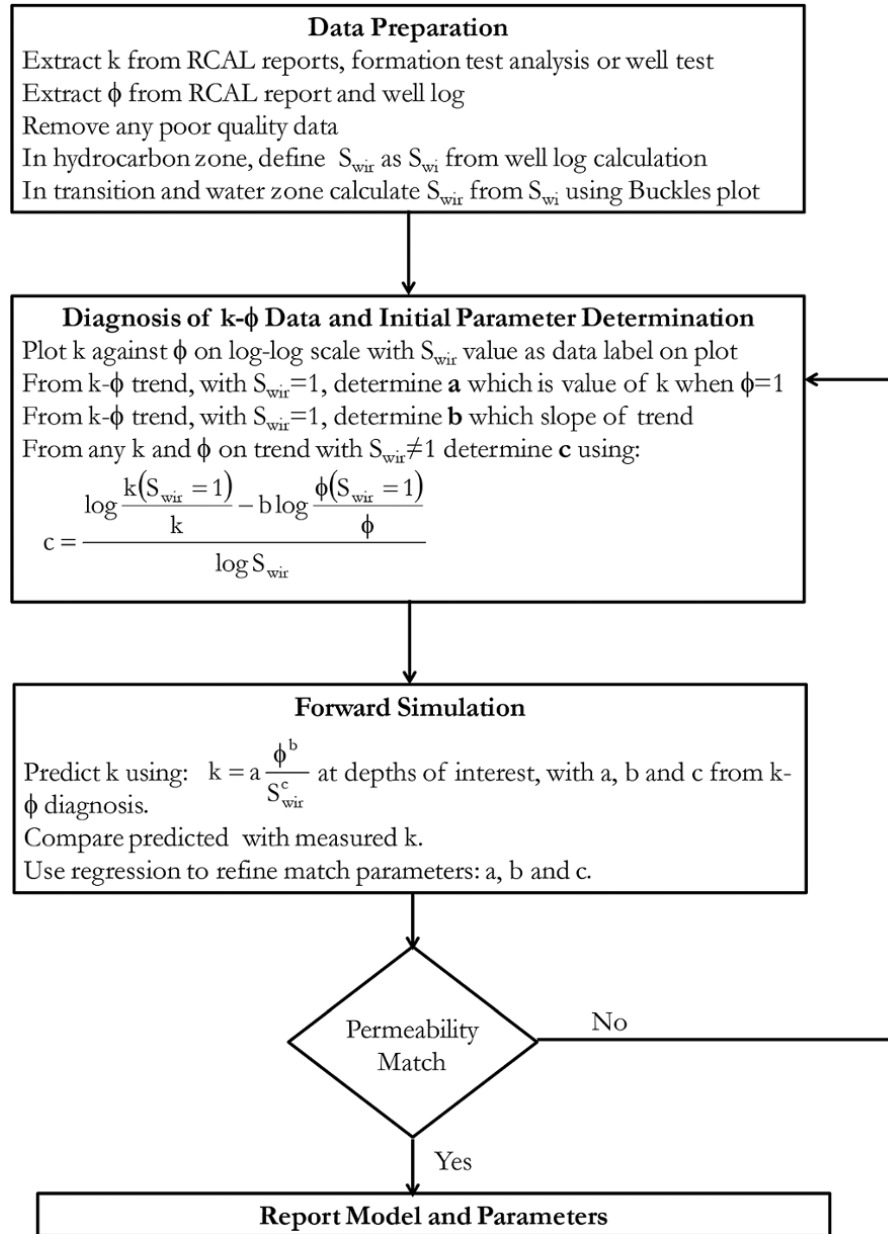


Figure 5.58 Workflow for calculating parameters for the power law permeability model.

Permeability log prediction using power law model parameters from diagnosis ( $a = 4,200$ ,  $b = 5.87$ , and  $c = 2.0$ ) gives a good match when compared with measured permeability (Fig. 5.63) and, therefore, there is no need for regression to improve the match and refine parameters  $a$ ,  $b$ , and  $c$ .

Hence, the final permeability power law model from equation (5.110) and calculated model parameters is:

$$k = 4200 \frac{\phi^{5.87}}{S_{wir}^2}$$

#### 5.2.4.2. Permeability Log Prediction Based on Correlating $\frac{1}{F_s \tau S_{gv}^2}$ with Flow Zone Indicator. Amaefule et al.

[1993] rearranged the MCK equation (equation (5.105)) as:

$$\sqrt{\frac{k}{\phi}} = \left( \frac{\phi}{1-\phi} \right) \left( \frac{1}{\sqrt{F_s \tau S_{gv}}} \right) \text{ in consistent unit} \quad (5.121)$$

In *engineering oil field* (EOF) units:

$$0.0314 \sqrt{\frac{k}{\phi}} = \left( \frac{\phi}{1-\phi} \right) \left( \frac{1}{\sqrt{F_s \tau S_{gv}}} \right) \quad (5.122)$$

**Table 5.19** Permeability, Porosity, and Connate Water from Core Analysis and Well Log.

Depth (ft)	k (mD) from core	$\phi$ from well log	$S_{wi}$ from well log
10,358.0	0.003	0.04	0.10
10,375.9	0.009	0.06	0.20
10,418.7	0.523	0.14	0.30
10,434.6	0.187	0.11	0.25
10,453.5	0.168	0.10	0.20
10,473.4	0.015	0.06	0.15
10,494.3	0.186	0.10	0.19
10,515.2	3.06	0.13	0.10
10,554.0	18.57	0.24	0.24
10,575.9	7.68	0.22	0.29
10,597.8	0.184	0.08	0.10
10,613.7	0.042	0.08	0.21
10,635.6	0.107	0.11	0.33
10,655.5	0.341	0.13	0.30
10,672.4	0.680	0.20	0.74
10,694.3	15.028	0.31	0.56
10,712.2	5.18	0.28	0.71
10,733.1	0.276	0.19	1.00
10,753.0	0.031	0.13	1.00

where  $k$  = permeability (mD), and  $\phi$  = porosity (volume fraction).

Equation (5.122) can be expressed further as:

$$RQI = \phi_z FZI \text{ in EOF unit} \quad (5.123)$$

where

$$RQI = 0.0314 \sqrt{\frac{k}{\phi}} \quad (5.124)$$

RQI is the reservoir quality index in  $\mu\text{m}$  and relates to the mean pore throat size of the formation rock.

$$\phi_z = \left( \frac{\phi}{1-\phi} \right) \quad (5.125)$$

$\phi_z$  is pore-to-grain volume ratio and

$$FZI = \frac{1}{\sqrt{F_s \tau S_{gv}}} \quad (5.126)$$

where FZI is the *flow zone indicator* in  $\mu\text{m}$ . FZI defines *hydraulic flow units* (HU or HFU), which are dependent on mineralogy and texture but independent of lithofacies. Zones with the same FZI do not necessarily mean they have the same geological unit or facies.

From equation (5.123).

$$\log RQI = \log \phi_z + \log FZI \quad (5.127)$$

From equation (5.127), a plot of  $\log RQI$  against  $\log \phi_z$  for samples in a reservoir with different FZI is expected to



**Figure 5.59** Cross-plot of  $k$  against  $\phi$  showing values of  $S_{wir}$ .

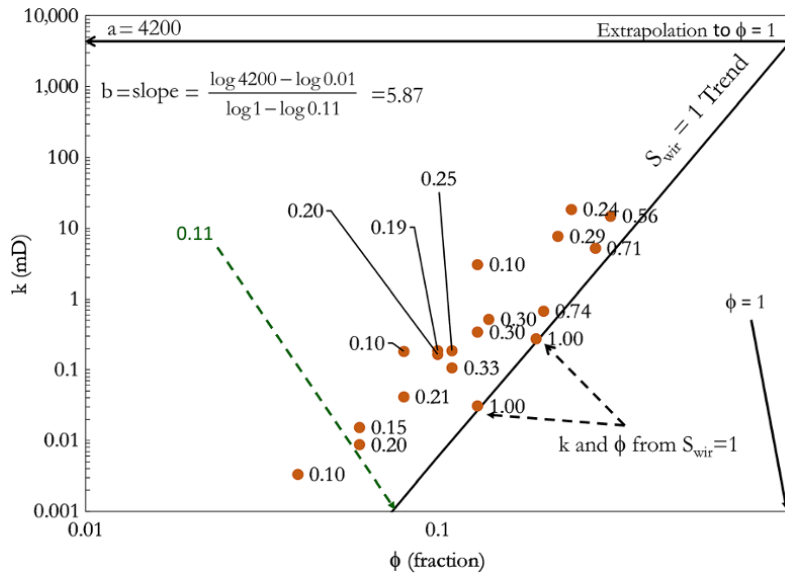


Figure 5.60 Calculating a and b from k- $\phi$  plot

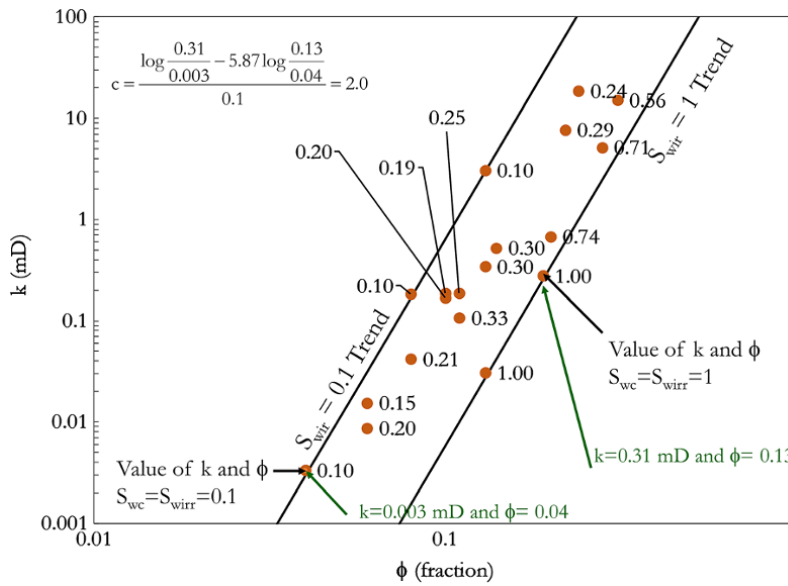


Figure 5.61 Using  $k$  and  $\phi$  at  $S_{wir} \neq 1$  for calculation of parameter  $c$ .

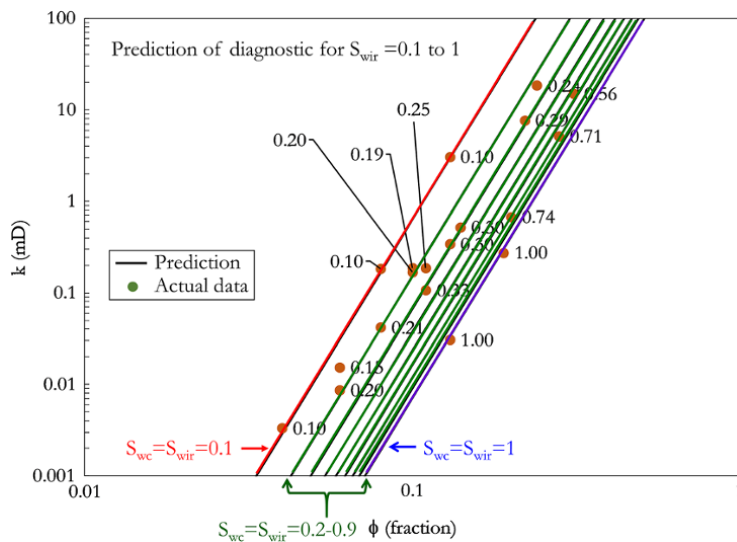
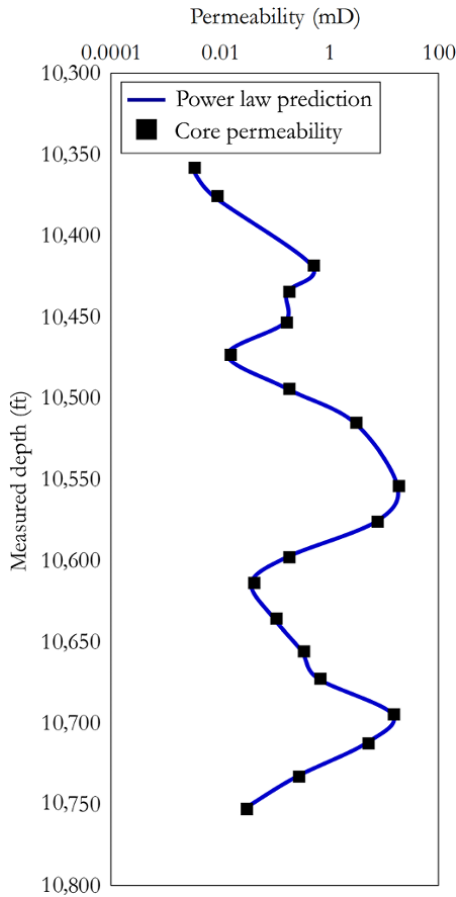


Figure 5.62 Simulation of permeability on a diagnostic plot of  $k$  against  $\phi$ .



**Figure 5.63** Simulation of a permeability well log for Exercise 5.9.

yield a family of straightline trends with a slope of 1, with each trend defining a HU with characteristic value of FZI.

The intercept of each trend of the plot logRQI against log  $\phi_z$  at  $\phi_z = 1$  would give value of FZI on the logRQI axis for each HU (Fig. 5.64). This can also be shown by substituting  $\phi_z = 1$  into equation (5.127) as:

$$\log RQI = \log(1) + \log FZI$$

$$\log RQI = \log FZI$$

$$RQI = FZI$$

Hence, when core samples are considered representative of different hydraulic flow units in reservoir, a plot of log-RQI against log  $\phi_z$  may be used to determine FZI.

From equation (5.123)

$$RQI = \phi_z FZI$$

$$\text{Substituting } RQI = 0.0314 \sqrt{\frac{k}{\phi}} \text{ and } \phi_z = \left( \frac{\phi}{1-\phi} \right)$$

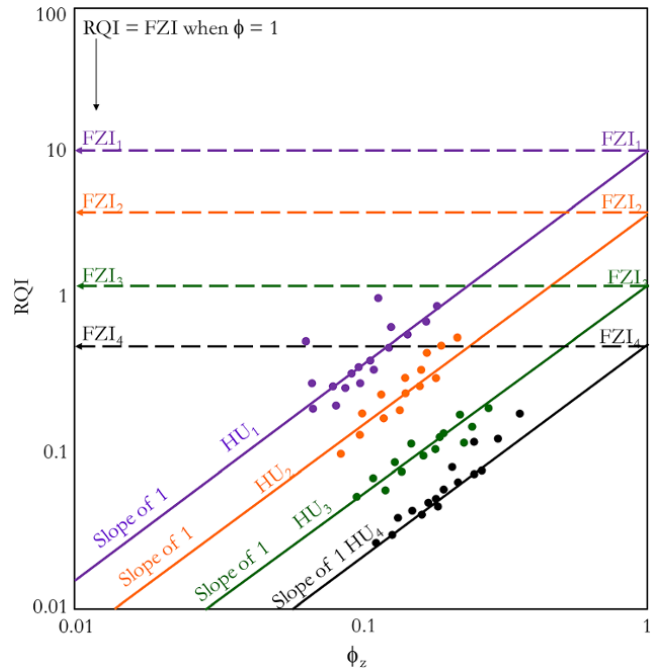


**Figure 5.64** FZI determination from RQI against  $\phi_z$  plot.

$$0.0314 \sqrt{\frac{k}{\phi}} = \left( \frac{\phi}{1-\phi} \right) FZI$$

Making k the subject of the formula:

$$k = 1014.24 \frac{\phi^3}{(1-\phi)^2} FZI^2 \quad (5.128)$$

Determined FZI from diagnosis (Fig. 5.64) is then used in equation (5.128) to predict permeability for depth where permeability has been measured, to check that FZI for each HU can predict measured permeability with an acceptable level of accuracy. This is a very important validation step and ensures that the FZI determined can predict permeability. Regression can be used to improved FZI values where the match between predicted and measured permeability needs to be improved.

The challenges of using FZI for permeability prediction include (i) obvious delineation of HU from the RQI–FZI plot may not exist and (ii) it can be difficult to correlate FZI to other attributes for permeability prediction away from well, as FZI does not directly relate to facies.

A practical workflow for a permeability well log prediction model using the FZI approach is summarized in Fig. 5.65.

**Exercise 5.10** FZI Permeability Log Prediction

Using the same data as in Exercise 5.9, create a permeability well log prediction model using the FZI method and predict permeability over 10,358 to 10,753 ft.

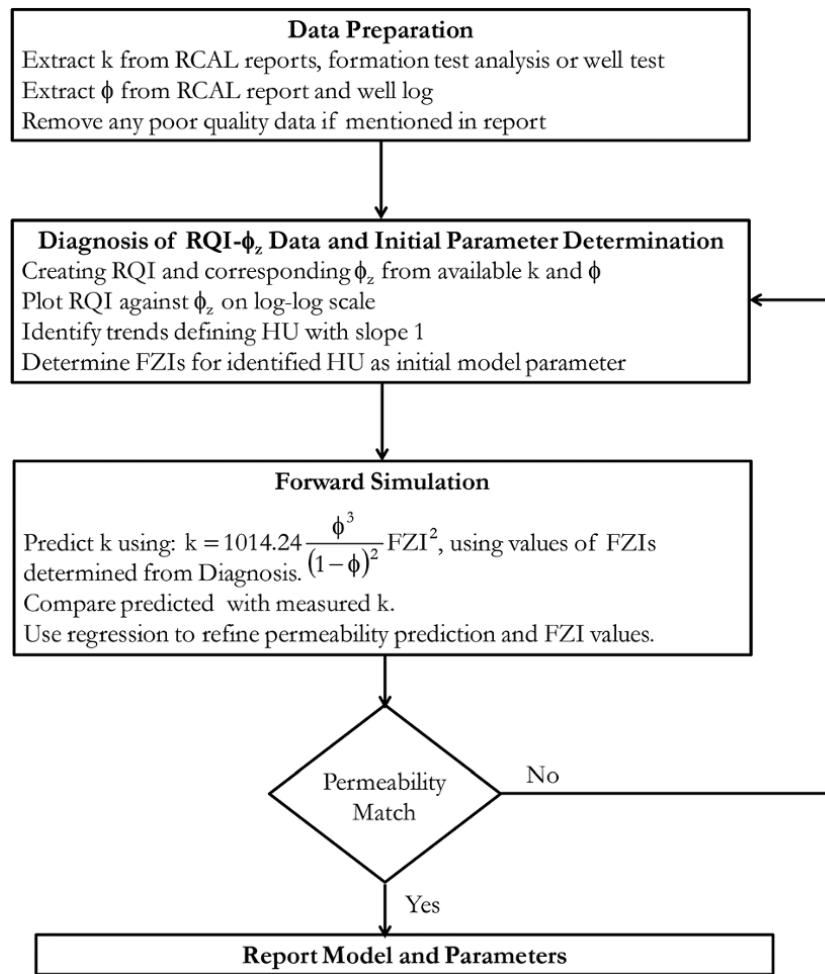


Figure 5.65 Workflow for permeability well log prediction using the FZI approach.

### Solution Steps.

Step 1: determine RQI using equation (5.124) and  $\phi_z$  using equation (5.125).

Step 2: plot RQI against  $\phi_z$  on a log-log scale.

Step 3: identify trends with slope 1 defining HU.

Step 4: determine FZIs for identified HU as the initial model parameter.

Step 5: Predict k using equation (5.128) and improve match by regression if necessary.

### Solution.

Calculation of RQI and  $\phi_z$  are summarized in Table 5.20.

Identification of HU and graphical determination of FZI are shown in Fig. 5.66.

FZI permeability prediction using equation (5.126) is summarized in Table 5.21

Comparison of predicted k (from Table 5.21) and measured k (Table 5.20) is shown graphically in Fig. 5.67.

The match in Fig. 5.67 can be improved by minimizing the sum of the square of the errors between core permeability and model permeability expressed as:

$$\epsilon^2 = \sum_{j=1}^n (\epsilon_j)^2 = \sum_{j=1}^n (k_j - k(FZI_i))^2 \quad (5.129)$$

Minimizing the sum of the square of the errors,  $\epsilon^2$ , which is the objective function, yields a refined value of FZI<sub>i</sub> where i = 1–6 for this exercise.

Table 5.22 shows the FZI permeability calculation after regression.

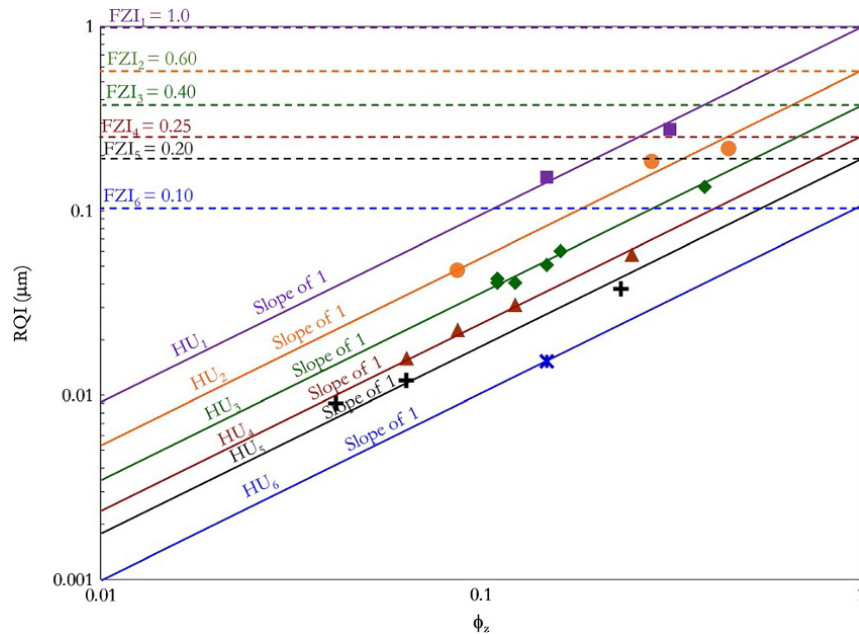
Final regression shows that HU 5 and 4 have the same FZI. This is an indication that HU 5 and 4 can be grouped as one single flow unit.

Fig. 5.68 shows the improved permeability prediction match for Exercise 5.10.



**Table 5.20** Calculation of RQI and  $\phi_z$ .

Depth (ft)	k (mD)	$\phi$	$S_{wir}$	RQI	$\phi_z$
From Table 5.19	Table 5.19	Table 5.19	Table 5.19	Using equation (5.124)	Using equation (5.125)
10,358.0	0.003	0.04	0.10	0.009	0.042
10,375.9	0.009	0.06	0.20	0.012	0.064
10,418.7	0.523	0.14	0.30	0.061	0.163
10,434.6	0.187	0.11	0.25	0.041	0.124
10,453.5	0.168	0.1	0.20	0.041	0.111
10,473.4	0.015	0.06	0.15	0.016	0.064
10,494.3	0.186	0.1	0.19	0.043	0.111
10,515.2	3.06	0.13	0.10	0.153	0.149
10,554.0	18.57	0.24	0.24	0.276	0.316
10,575.9	7.68	0.22	0.29	0.186	0.282
10,597.8	0.184	0.08	0.10	0.048	0.087
10,613.7	0.042	0.08	0.21	0.023	0.087
10,635.6	0.107	0.11	0.33	0.031	0.124
10,655.5	0.341	0.13	0.30	0.051	0.149
10,672.4	0.68	0.2	0.74	0.058	0.250
10,694.3	15.028	0.31	0.56	0.219	0.449
10,712.2	5.18	0.28	0.71	0.135	0.389
10,733.1	0.276	0.19	1.00	0.038	0.235
10,753.0	0.031	0.13	1.00	0.015	0.149



**Figure 5.66** Graphical determination of FZI from core samples.

**5.2.4.3. Permeability Log Prediction Based on Correlating  $\frac{1}{F_s \tau S_{gv}^2}$  with Mineral Content.** Herron [1987]

showed that the MCK equation (equation (5.105)) can be expressed in terms of mineralogical abundances as:

$$k = A_f \frac{\phi^3}{(1-\phi^2)} \exp\left(\sum B_i M_i\right) \quad (5.130)$$

where  $\frac{1}{F_s \tau S_{gv}^2}$  from equation (5.105) is equal to  $A_f \exp\left(\sum B_i M_i\right)$  in equation (5.130).

$A_f$  is defined as:

$$A_f = 4.9 + 2F_{max}$$

where  $F_{max}$  is the maximum feldspar content in the formation of interest,  $M_i$  is the molecular weight of a fraction

**Table 5.21** FZI Permeability Calculation.

Depth (ft)	HU Number Fig. 5.66	FZI From Fig. 5.66	k (mD) using equation (5.126)
10,358.0	5	0.1	0.001
10,375.9	5	0.1	0.002
10,418.7	3	0.4	0.602
10,434.6	3	0.4	0.273
10,453.5	3	0.4	0.200
10,473.4	4	0.1	0.002
10,494.3	3	0.4	0.200
10,515.2	1	1.0	2.944
10,554.0	1	1.0	24.274
10,575.9	2	0.6	6.390
10,597.8	2	0.6	0.221
10,613.7	4	0.1	0.006
10,635.6	4	0.1	0.017
10,655.5	3	0.4	0.471
10,672.4	4	0.1	0.127
10,694.3	2	0.6	22.847
10,712.2	3	0.4	6.872
10,733.1	5	0.1	0.106
10,753.0	6	0.1	0.029

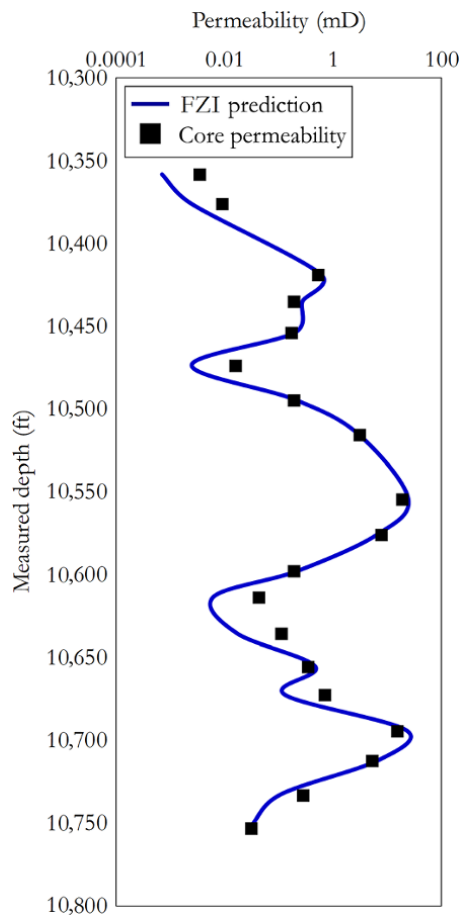


**Figure 5.67** Simulation of permeability as well log for Exercise 5.10.

**Table 5.22** FZI Permeability Calculation after Regression.

Depth (ft)	HU number Fig. 5.66	FZI after regression	k (mD) after regression
10,358.0	5	0.2	0.003
10,375.9	5	0.2	0.010
10,418.7	3	0.4	0.602
10,434.6	3	0.4	0.273
10,453.5	3	0.4	0.200
10,473.4	4	0.2	0.010
10,494.3	3	0.4	0.200
10,515.2	1	1.0	2.944
10,554.0	1	1.0	24.274
10,575.9	2	0.6	6.390
10,597.8	2	0.6	0.221
10,613.7	4	0.2	0.025
10,635.6	4	0.2	0.068
10,655.5	3	0.4	0.471
10,672.4	4	0.2	0.507
10,694.3	2	0.6	22.847
10,712.2	3	0.4	6.872
10,733.1	5	0.2	0.424
10,753.0	6	0.1	0.029

of constituent mineral in rock sample, and  $B_i$  is a constant that characterizes different minerals.

In this approach an estimate of mineral composition is required to compute permeability. Mineral content can be measured using nuclear spectrometry. The mineral content has an effect on grain size texture and the morphology of the grains.

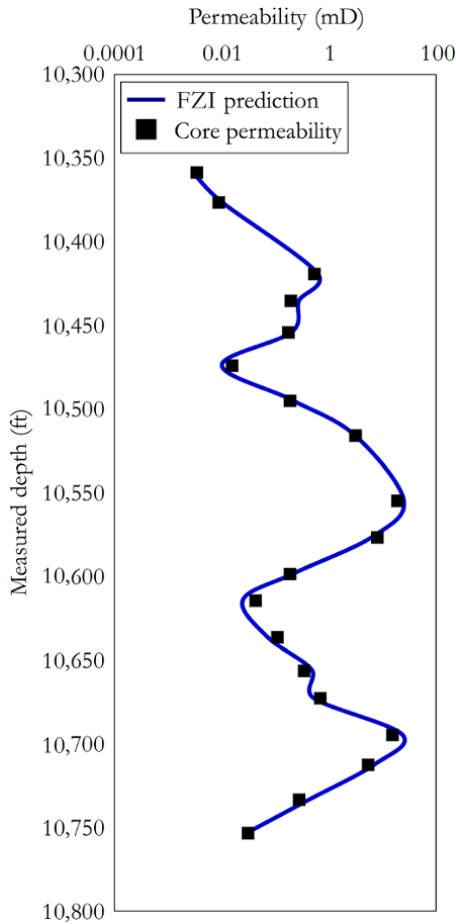


Figure 5.68 Improved permeability prediction match for Exercise 5.10.

**5.2.4.4. Permeability Log Prediction Based on Correlating  $\frac{1}{F_s \tau S_{gv}^2}$  with Nuclear Magnetic Resonance Log.**

The principle of NMR for logging is based on the release of waves due to the reorientation of protons under the influence of a magnetic field. A primary measurement derived from a *nuclear magnetic resonance* (NMR) log is the *free fluid index* (FFI), which relates to the amount of movable fluid in the formation pores spaces and is expressed as:

$$FFI = \phi(1 - S_{wir}) \tag{5.131}$$

Making  $S_{wir}$  in equation (5.131) the subject of the formula:

$$S_{wir} = 1 - \frac{FFI}{\phi} \tag{5.132}$$

NMR logs are also used in determining the *bulk volume of irreducible water* (BVI), which equals  $C_{Bkl}$  in section 5.2.4.1 and expressed as:

$$BVI = \phi S_{wir} \tag{5.133}$$

One approach of correlating  $\frac{1}{F_s \tau S_{gv}^2}$  with NML is by substituting  $S_{wir}$  in equation (5.132) into any of the empirical permeability relationships in equations (5.106)–(5.110) that depend on  $S_{wir}$ .

Considering the coats permeability model in equation (5.108):

$$k^{\frac{1}{2}} = 100 \frac{\phi^2(1 - S_{wir})}{S_{wir}}$$

substituting  $\frac{FFI}{\phi} = (1 - S_{wir})$ , from equation (5.131) into above coats permeability model:

$$k^{\frac{1}{2}} = 100 \frac{\phi^2 FFI}{\phi S_{wir}} \tag{5.134}$$

Substituting BVI from equation (5.133) into equation (5.134):

$$k^{\frac{1}{2}} = 100 \frac{\phi^2 FFI}{BVI}$$

$$k = \left[ (10\phi)^2 \left( \frac{FFI}{BVI} \right) \right]^2 \tag{5.135}$$

Equation (5.135) is expressed in a general form by substituting  $C = \frac{1}{10}$ :

$$k = \left[ \left( \frac{\phi}{C} \right)^2 \left( \frac{FFI}{BVI} \right) \right]^2 \tag{5.136}$$

C in equation (5.136) is used to calibrate the model prediction to known permeability such as that from a stressed core sample.

Another permeability prediction based on the NMR log is the *Schlumberger model*, expressed as:

$$k = C \times T_{2gm}^2 \times \phi^4 \tag{5.137}$$

where  $T_{2gm}$  is the geometric mean of the  $T_2$  distribution and C is a constant used in calibrating the model and varies from formation to formation. It is very important to calibrate NMR permeability to other known permeability such as permeability from stressed core analysis.

Other than permeability prediction, NMR logs can be used for identification of movable and immovable fluid in a formation, porosity determination independent of formation lithology, and identification of pore size distribution.

**5.3. SUMMARY OF FORMATION EVALUATION**

Quantitative and qualitative use of openhole logs are summarized in Table 5.23.

Fig. 5.69 summarizes the steps for analysis of well logs for reservoir characterization.

**Table 5.23** Summary of Characteristics of Openhole Logs with Qualitative and Quantitative Use.

Well log	Characteristic	Inference/Qualitative use	Quantitative use	Validation logs
GR	Measurement of the natural gamma radiation from formation.	Low reading: nonshale (Sandstone limestone or other minerals.) High reading: shale except in radioactive sands.	Calculating $V_{sh}$ GR is often preferred to SP for $V_{sh}$ calculation except in radioactive sands. In radioactive sand, <i>computed gamma ray</i> response (CGR) should be used in preference to SP as SP is often affected by environmental factors. GR is also important in computing NTG.	Checking resistivity logs to discriminate between sandstone and limestone. Using neutron-density (N-D) logs to validate presence of shale.
SP	Deflection in porous media with salinity contrast between mud and formation water.	Deflection in permeable formation (reservoir rock) and no deflection in nonpermeable formation (nonreservoir rock).	Calculating $V_{sh}$ and NTG in absence of GR. Should be considered for $V_{sh}$ in radioactive sand only in absence of CGR as SP more affected by environmental factors than GR.	Checking resistivity logs to discriminate between sandstone and limestone. Using N-D to validate presence of shale.
Density/ Neutron	Density log is measured bulk formation density and used for estimating formation porosity. Neutron log responds primarily to the amount of hydrogen in the formation (Hydrogen Index), which directly relates to porosity.	Low density with density log on left of neutron log is a characteristic of sandstone reservoir. Significantly higher apparent $\phi_D$ than apparent $\phi_N$ (gas crossover effect) can be caused by presence of gas. Presence of gas increases the apparent density porosity but decreases the apparent neutron porosity hereby causing a gas crossover.	Calculation of: $\phi$ and $V_{sh}$ .	Confirm sandstone with low GR reading.  Check for rugose hole condition which can create gas effect. Check that correct matrix for calibration is used. Measuring porosity in formation with tool calibrated with another matrix can create false gas effect.
Density/ Neutron		When density lies to right of neutron, with significant separation, shale is suspected. Shale effect is opposite to gas effect. Dolomite give similar response with high density. High density reading which is very close to neutron reading would suggest Limestone. This is an important characteristic of limestone.		Confirm shale with high GR reading. Confirm dolomite with low GR reading.  Check for low GR which characterizes limestone.

(continued overleaf)

**Table 5.23** (Continued)

Well log	Characteristic	Inference/Qualitative use	Quantitative use	Validation logs
Resistivity	Measures total resistivity of formation with fluid within pore spaces. Minimum of three resistivity measurements with different depths of investigation: shallow, mid and deep resistivity logs is recommended. Resistivity with measurements at varying depth of investigation is also common.	Separation of deep and shallow resistivity curves suggests presence of a permeable formation. Overlay of deep and shallow resistivity suggest impermeable zone such as shale. Higher deep resistivity reading compared with shallow is an indication of hydrocarbon bearing zone for saline water-based mud. High shallow, mid and deep resistivity with reading closely pack would suggest limestone. High resistivity (low electrical conductivity) is characteristic of carbonate. Closely crammed resistivity indicates low filtrate invasion Low resistivity characterizes water zone (salt water formation) since formation water has high conductivity (low resistivity). Sandstone with dispersed clay, which is conductive due to conductive bond water, can show characteristic of low resistivity (Low Resistivity Pay). Thinly laminated shales can cause low resistivity too.	Calculation of: $S_w$ $S_{xo}$ $IOM = \frac{S_w}{S_{xo}}$ $MH = S_{xo} - S_w$	GR should be examined to confirm sandstone. GR should be examined to confirm shale. N–D should be examined to determine if HC is gas (when gas effect is observed) or not  GR should be examined for low GR to confirm limestone. N–D should be examined for characteristic of limestone discussed under neutron-density log.  GR can reveal laminate shale lithology to check if low resistivity is due to shale.

Well log interpretation steps shown in the flow chart (Fig. 5.69) can be summarized with the illustration shown in Fig. 5.70.

It is very important to ensure that final quantitative and qualitative well log interpretation results are consistent with geological core descriptions, core analysis, and other information gathered from the formation.

#### **Exercise 5.11** Qualitative Formation Description from Well Log

Sketch the possible formation and fluid type that best describe the well log in Exercise 5.5.

#### **Solution.**

Note that no hydrocarbon–water contact (HWC) was observed but, rather an oil-down-to (ODT).

Also, the log showed reduced GR after shale, indicating a good reservoir at the base of the log with the presence of hydrocarbon beneath the shale, as shown in Fig. 5.71.

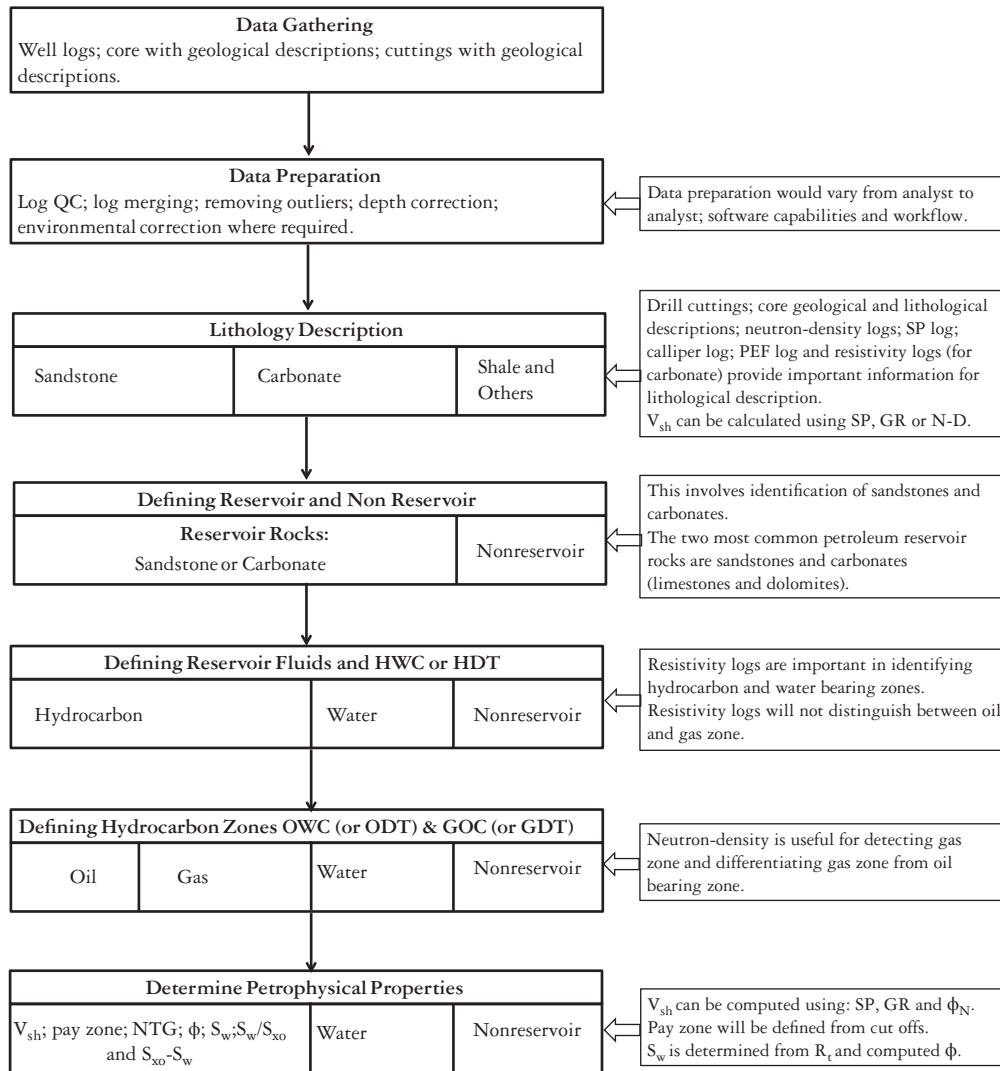


Figure 5.69 Steps for analysis of well logs for reservoir characterization.

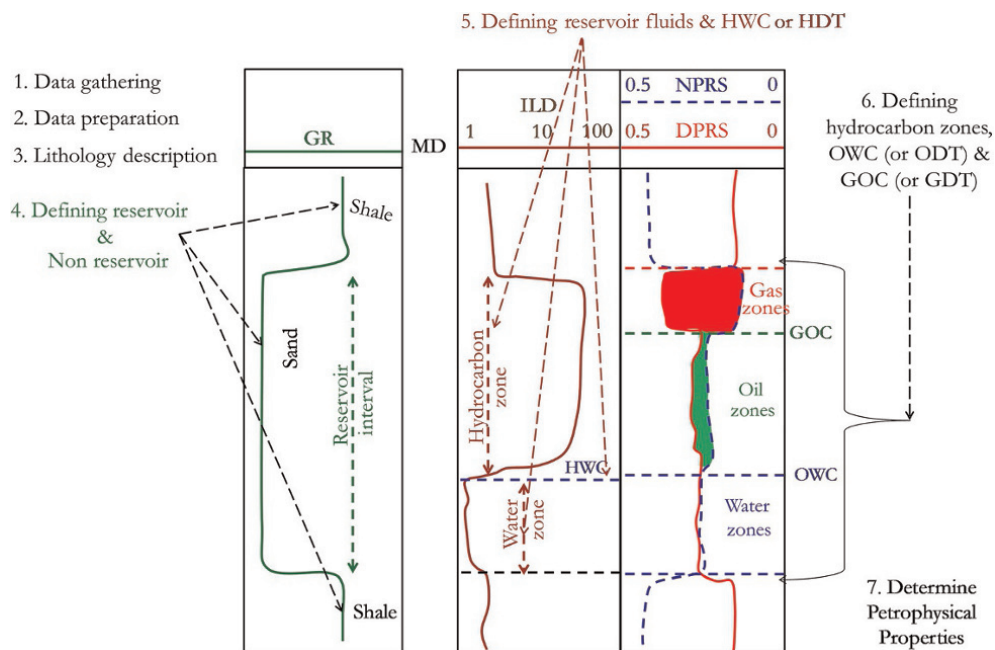


Figure 5.70 Illustration showing steps for well logs analysis.

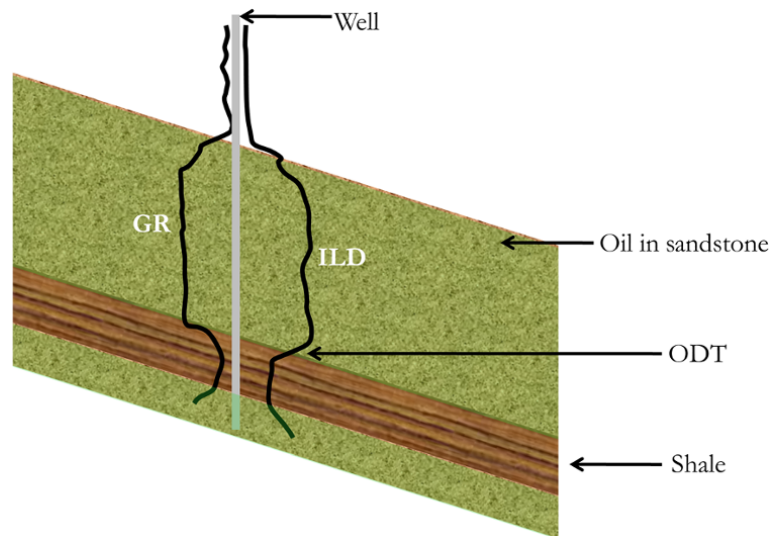


Figure 5.71 Sketch of possible formation for logs in Exercise 5.11.

## REFERENCES

- Amaefule, J.O., Altunbay, M., Tiab, D. *et al.*, 1993. *Enhanced Reservoir Description: Using core and log data to identify hydraulic (flow) units and predict permeability in Uncored Intervals/Wells*. SPE Annual Technical Conference and Exhibition, 3–6 October, Houston, TX.
- Archie, G., 1942. The electrical resistivity log as an aid in determining some reservoir characteristics. *Transactions of the AIME*, **146**(1), 54–62.
- Asquith, G. and Krygowski, D., 2004. *Basic Well Log Analysis*. American Association of Petroleum Geologists.
- Bardon, C. and Pied, B., 1969. *Formation Water Saturation In Shaly Sands*. SPWLA 10th Annual Logging Symposium, 25–28 May, Houston, TX.
- Buckles, R., 1965. Correlating and averaging connate water saturation data. *Journal of Canadian Petroleum Technology*, **9**(1), 42–52.
- Cannon, S., 2016. *Petrophysics: A Practical Guide*. 1st edn. Wiley Blackwell.
- Carman, P., 1937. Fluid flow through granular beds. *Transaction of the Institute of Chemical Engineers*, **15**, 150–166.
- Chilingar, G., Buryakovsky, L., Eremenko, N., and Gorfunkel, M., 2005. *Geology and Geochemistry of Oil and Gas, Developments in Petroleum Science 52*. 1st edn. Elsevier B.V.
- Clavier, C., Hoyle, W., and Meunier, D., 1971. Quantitative interpretation of thermal neutron decay time logs: Part I. Fundamentals and techniques, *Journal of Petroleum Technology*, **23**(6), 743–755.
- Clavier, C., Coates, G., and Dumanoir, J., 1984. Theoretical and experimental bases for the dual-water model for interpretation of shaly sands. *Society of Petroleum Engineers Journal*, **24**(02), 153–168.
- Coates, G. and Denoo, S., 1981. The producibility answer product. *Schlumberger Technical Review*, **29**(2), 55–144.
- Eremenko, N.A. and Ul'yanov, A.V., 1960. Oil and gas-bearing sequences of the world, their features and distribution. Regional and structural problems of petroleum geology. *Proceedings of the XXI International Geological Congress*, 19–21.
- Herron, M., 1987. Estimating the intrinsic permeability of clastic sediments from geochemical data. SPWLA 28th Annual Logging Symposium, 29 June–2 July, London.
- Kozeny, J., 1927. Ueber kapillare Leitung des Wassers im Boden (Concerning capillary conduction of water in the soil). *Wien*, **136**(2a), 271–306.
- Larionov, V.V., 1969. *Radiometriya skvazhin [Radiometry of boreholes]*. Moscow: Nedra.
- Pickett, G.R., 1973. *Pattern recognition as a means of formation evaluation*. Houston, TX, Society of Petrophysicists and Well-Log Analysts (SPWLA).
- Poupon, A. and Leveaux, J., 1971. Evaluation of water saturations in shaly formations. *The Log Analyst*, **12**(4), 1–2.
- Schlumberger, 1989. *Log Interpretation Principles/Applications*. Houston, TX: Schlumberger.
- Simandoux, P., 1963. Dielectric Measurements in Porous Media and Application to Shaly Formation. *Revue de l'Institut Francais du Petrole* (Translated text in *SPWLA Reprint Volume Shaly Sand*, July 1982), Supplementary Issue, 193–215.
- Stieber, S.J., 1970. *Pulsed Neutron Capture Log Evaluation – Louisiana Gulf Coast*. SPE 45th Annual Fall meeting, Houston, TX.
- Timur, A., 1968. An investigation of permeability, porosity, & residual water saturation relationships for sandstone reservoirs. *The Log Analyst*, **9**(4), 8–17.
- Tixier, M., 1949. Evaluation of permeability from electric log resistivity gradient. *Oil and Gas Journal*, **2**, 113–123.
- Waxman, M. and Thomas, E., 1974. Electrical conductivities in shaly sands – I. The relation between hydrocarbon saturation and resistivity index; II. The Temperature coefficient of electrical conductivity. *Journal of Petroleum Technology*, **26**(2), 213–225.

- Wyllie, M. and Rose, W., 1950. Some theoretical considerations related to the quantitative evaluation of the physical characteristics of reservoir rock from electrical log data. *Journal of Petroleum Technology*, **2**(4), 105–118.
- Wyllie, M.R.J. and Southwick, P.F., 1954. An experimental investigation of the S.P. and resistivity phenomena in dirty sands. *Journal of Petroleum Technology*, **6**(2), 44–57.

### BIBLIOGRAPHY

- Anderson, W.G., 1987. Wettability literature survey Part 5: The effects of wettability on relative permeability. *Journal of Petroleum Technology*, **39**(11), 1453–1468.
- Bassiouni, Z., 1994. *Theory, Measurement and Interpretation of Well Logs*. SPE Textbook Series Vol. 4. Richardson, TX: Society of Petroleum Engineers.
- Carman, P., 1938. Fundamental principles of industrial filtration (A critical review of present knowledge). *Transaction of the Institute of Chemical Engineers*, **16**, 168–188.
- Coates, G., 1973. *A New Approach To Improved Log-Derived Permeability*. Lafayette, LA, SPWLA.
- Radcliffe, D., 1986. *An Analysis of the Validity of Permeability Derived from the RFT*. M.Eng. Thesis, Heriot-Watt University, Edinburgh.
- Waxman, M. and Smits, L., 1968. Electrical conductivities in oil-bearing shaly sands. *Society of Petroleum Engineers Journal*, **8**(2), 107–122.



# 6

## Formation Testing

Formation test(ing) involves measurement of pressure and fluid properties, with *formation testers*, at different stations (depths) where each station involves a flow of fluid from the formation over a given elapsed time. Formation tests are different from other openhole logs as data acquisition involves: stopping the formation tester at a specific station; setting the tool; initiating and controlling flow from the formation over an elapsed time while taking pressure measurements; unsetting the tool after measurement; then moving to another station to repeat the measurements.

Formation testers, a type of wireline tool, have become increasingly important as environmental considerations play a crucial role in petroleum exploration activities. Formation testing can sometimes be an alternative to the conventional well testing in characterizing formation at exploration and appraisal stages. *Wireline formation tests* (WFT) are cheaper than *drill stem tests* (DST) from an acquisition standpoint and can have lower environmental impact. Table 6.1 shows a comparison of formation testing and conventional well testing for formation characterization.

In recent times, formation testers have evolved from formation pressure measurement and sampling to more complex testing applications, which include: *in situ* fluid composition; fluid properties such as saturation point, fluid density, fluid viscosity, fluid compressibility, asphaltene onset, cloud point, and other complex PVT properties; relative permeability using neural network algorithms; and stress testing (stress magnitude) [Desbrandes and Gualdron, 1988; Dong and Hegeman, 2003; Wu et al., 2006; Raghuraman et al., 2007].

The main objectives of modern (modular) formation testing include: determining formation pressure at the reservoir zone of interest; creating pressure profiles and

gradients over an interval of interest; identifying zones in hydraulic communication or compartmentalized zones; determining fluid type and fluid contacts; estimating formation permeability and mobility; formation fluid sampling; and downhole determination of fluid properties and composition.

A properly designed and executed formation test job will provide valuable information for reservoir modelling, well completion strategy, infill drilling, optimization of drilling mud, and detection of movement of fluid contact.

Formation testing is sometimes confronted with challenges such as insufficient gauge resolution to record interpretable pressure in high permeability [Whittle et al., 2003] and problems such as supercharging in low permeability formation.

### 6.1. FORMATION TESTERS

Fig. 6.1 shows a schematic of a single probe wireline formation tester (probe module).

In formation testing, flow from the formation through an aperture can be initiated using a *pretest chamber* (*test chamber*) or *pumpout module*. The pretest chamber (Fig. 6.2) has a piston whose movement initiates flow from the formation through flow aperture(s) and flowlines into the chamber, thus creating a *pressure drawdown*. When the piston stops moving following initial drawdown, the pressure in the formation builds up to final formation pressure. During the displacement of the chamber piston, the volume of fluid withdrawn from the formation is measured by displaced volume in the chamber

Instantaneous rate flow of fluid withdrawal from the formation into the pretest chamber can be expressed as:

**Table 6.1** Comparison of Formation Testing and Well Testing.

Formation testing	Well testing
Saves time.	Time consuming.
Less expensive than well testing.	Expensive.
Shallow depth of investigation	Deep radius of investigation.
Environmentally friendly due to small produced reservoir fluid.	Difficult to create containment of large volume of reservoir fluid produced.
Difficult estimating actual skin due to damage when setting tool.	Most appropriate way to estimate well skin.
Insufficient gauge resolution can be a problem in high permeability.	Gauge resolution is rarely a problem.
Mud filtrate invasion can affect result in low permeability formation.	Clean-up can reduce effect of filtrate invasion.

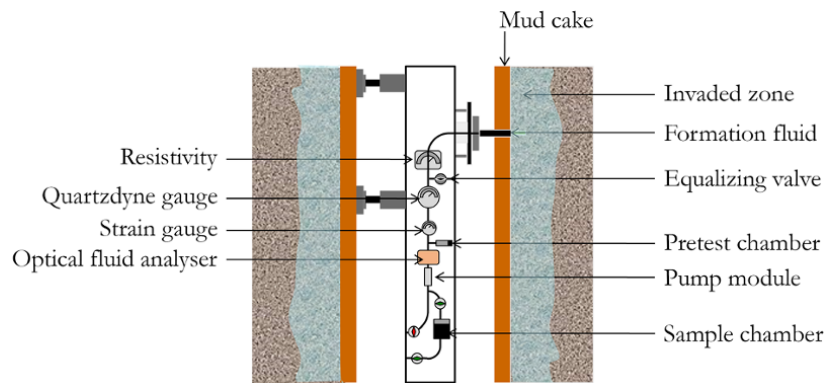


**Figure 6.1** Configuration of simple wireline formation tester.

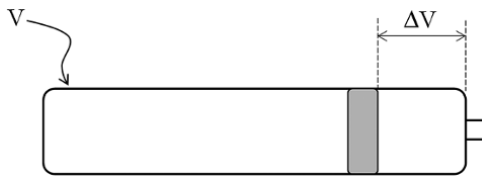


**Figure 6.2** Change of volume in pretest chamber.

$$q(t) = \frac{\Delta V}{\Delta t} \tag{6.1}$$

For withdrawal into the chamber of volume,  $V$ , which is filled over an elapsed time,  $t$ , the average rate of withdrawal during the entire process is expressed as:

$$q_{Avg} = \frac{V}{t} \tag{6.2}$$

Pretest chamber volumes in wireline formation testers can be fixed or variable with volumes in the range 20–100 cm<sup>3</sup> for wireline formation testers. A volume in the range 10–20 cm<sup>3</sup> is often sufficient if tool storage effect is small. In cases where tool storage effect is high, either due to tool volume or high fluid compressibility, a higher

pretest volume chamber is often required to ensure that formation response is measured by the tool in a reasonable time.

During wireline formation testing for acquisition of pressure data, the measurement of fluid property or fluid sampling, flow from the formation into the tool's flow-lines and chamber is through apertures (probes and or packers). The need for proper seals to isolate apertures hydraulically from the surrounding fluid, which may interfere with pressure or fluid property measurement, is vital. Single probes (snorkel) are the most common flow apertures in formation testing. In situations where the well or reservoir is characterized by fracture/fissures, low permeability, thin or laminated zones, the use of a single-probe configuration becomes inappropriate because of the difficulty in achieving hydraulic communication with the tool and hydraulic isolation from wellbore fluid. In instances where a single-probe configuration cannot achieve a hydraulic seal, an oval pad or dual packers become suitable alternatives [Zefzaf and Fattah, 2006].

The different flow apertures in wireline formation testers are illustrated in Fig. 6.3.

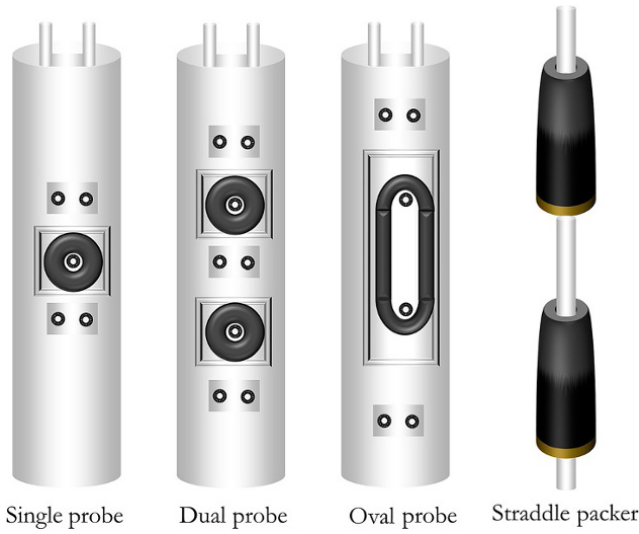


Figure 6.3 Different flow apertures in wireline formation testers.

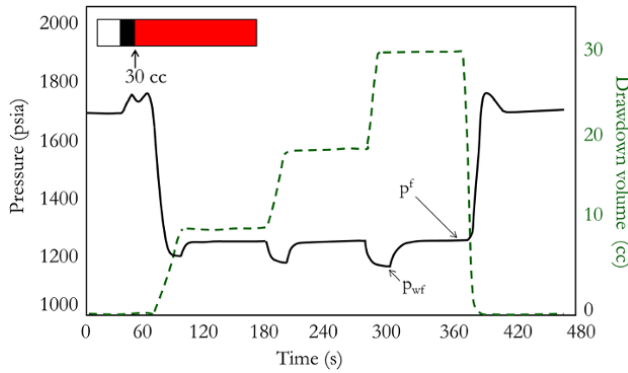


Figure 6.4 Pressure and cumulative volume profile during formation testing.

Fig. 6.4 shows an example of a pressure and cumulative fluid profile from a formation using a single probe flow aperture with a pretest chamber for volume withdrawal. The test shows increasing volume during pretest (drawdown) and constant volume when the piston stops moving (buildup).

A simple derivative of displaced volume with respect to time is sufficient to determine the flow rate of fluid into the pretest chamber from the formation, as shown in Fig. 6.5.

### 6.1.1. Flowline (Tool) Storage Effect (FLSE)

Flowline storage effect is similar to the well test storage effect discussed in Chapter 8.4.3.3. Flowline storage effect (FLSE) is the “dead volume” in the tool adding storage capacity during pretest (drawdown) and buildup (Fig. 6.6).

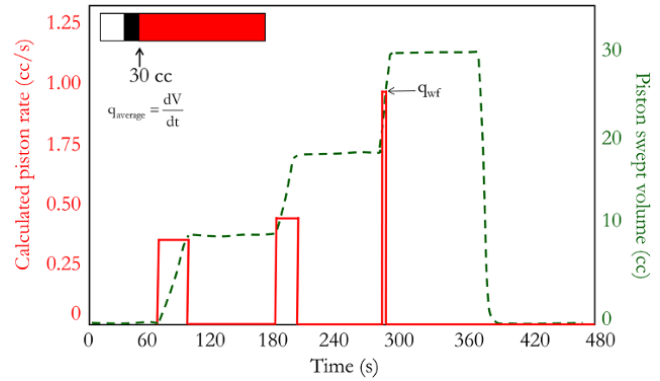


Figure 6.5 Pretest rate calculation from cumulative volume swept by piston.

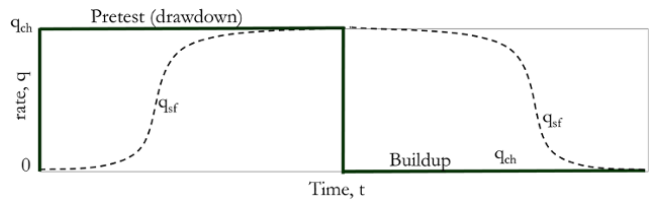


Figure 6.6 Flowline storage effect during drawdown and buildup.

During a FLSE dominated flow regime, the rate of change of piston volume in the tool is actually a volumetric expansion of fluid in the flowlines (tool) during the start of pretest drawdown and volumetric compression during buildup (Fig. 6.6). The relationship between sand-face rate ( $q_{sf}$ ) and pretest chamber test rate ( $q_{ch}$ ) is expressed as:

$$q_{sf} = q_{ch} - C_{sys} V_{tool} \left. \frac{\partial p_p}{\partial t} \right|_{r=r_w} \quad (6.3)$$

Equation (6.3) can be further express as:

$$q_{sf} = q_{ch} - C_{sys} V_{tool} \frac{dp_p}{dt} \quad (6.4)$$

Since  $C_{sys} = C_{sys} V_{tool}$  substituting  $C_{sys}$  into Equation (6.4):

$$q_{sf} = q_{ch} - C_{sys} \frac{dp_p}{dt}$$

which can also be expressed as:

$$q_{ch} - q_{sf} = C_{sys} \frac{dp_p}{dt}$$

During pretest drawdown in storage dominated flow, as shown in Fig. 6.6,  $q_{ch} >> q_{sf}$

Hence, the above equation reduces to:

$$q_{ch} = C_{sys} \frac{dp_p}{dt}$$

In engineering oil field (EOF) units this becomes:

$$q_{ch} = 24C \frac{dp_p}{dt}$$

During a FLSE dominated flow regime, the pretest drawdown and buildup pressure signal can be related to elapsed time in EOF units as:

$$\Delta p_p = \frac{q\Delta t}{24C} \quad (6.5)$$

where: the rate,  $q$ , is the same as  $q_{ch}$ , which is the rate measured in the pretest chamber (bbl/d);  $q_{sf}$  is the rate at the sandface (bbl/d);  $C_{sys}$  is the flowline storage coefficient (bbl/psi);  $p_p$  is the measured probe pressure by gauge (psi); and  $t$  is time (hr).

Therefore, a plot of  $\Delta p_p$  against  $\Delta t$  on a Cartesian scale will yield a straight line with a slope =  $q/24C$  (in EOF units) when FLSE dominates the pressure response.

Equation (6.5) can be expressed in logarithmic terms as:

$$\log \Delta p_p = \log \Delta t + \log \left( \frac{q}{24 \times C_{sys}} \right) \quad (6.6)$$

Therefore, a plot of  $\Delta p_p$  against  $\Delta t$  on a log-log scale will yield a straight line of slope 1 (unit slope) when FLSE dominates pressure transient response. This behavior is an important characteristic of FLSE.

## 6.2. ANALYSIS OF WIRELINE FORMATION TEST DATA

The analysis that can be carried out with any wireline formation tester depends on the tool sections/modules configured together. In order to analyze any pressure data for permeability, the pressure with the corresponding rate measurement must be acquired. In formation testing, flow rate is either derived from the cumulative volume measured by the pretest chamber or measured from continuous flow with a pump (module pump). Also, flow aperture in the formation tester configuration determines the kind of analysis that can be carried out.

For flow through a probe aperture, analysis includes *steady state pretest analysis*, *flow rate analysis*, and *pressure transient analysis*.

For flow through dual packers, analysis that can be carried out is *pressure transient analysis* using a *limited entry* (partial penetration) well test interpretation model (Chapter 8.4.3.6 and 8.5.1.7). For flow through an active probe or packer with observation probe (probe-probe or probe-packer configuration), data can be used for *vertical interference testing* (Chapter 8.11.1).

### 6.2.1. Single Probe/Snorkel Module/Probe Module

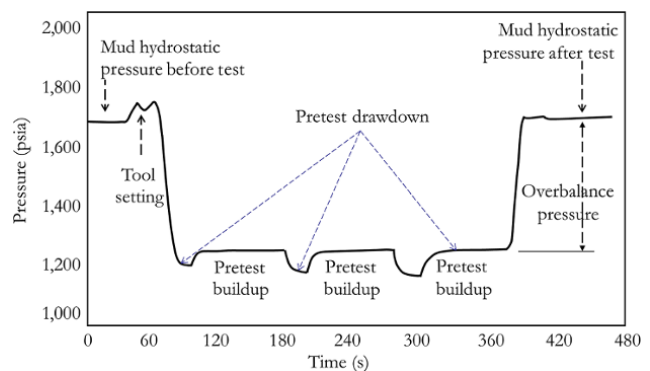
A single probe module can be a stand-alone tool or modular, with other tool sections for measuring other properties connected to it. For the probe module, fluid flow from formation can be initiated either by pump (for pumpout drawdown) or by pretest chamber (for pretest drawdown). Pretest chambers are generally sufficient for moderate permeability formations and pumpout (or pump-piston) is considered for a moderate to very high permeability range. The typical permeability range may be defined as: very low when less than 0.1 mD; low when in the range 0.1–5 mD; moderate when in the range –100 mD; high when in the range 100– 500 mD; and very high when greater than 500 mD.

During acquisition of formation pressure at multiple stations, each test (sequence of pretest and buildup) consists of more than one pretest and buildup (Fig. 6.7). A sequence of three pretests followed by buildup is always a good practice to check for consistency and repeatability in formation pressure (final stabilized buildup pressure) measurement.

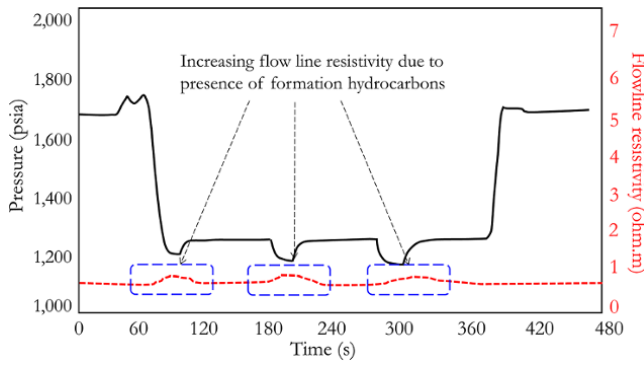
The behavior of the pressure history (pressure against time) is a very important qualitative characteristic of the formation and is also useful for quality control of data during acquisition.

Fig. 6.8 shows probe module data for a test in a formation well drilled with water-based mud (WBM).

Fig. 6.8 shows increased fluid resistivity during the test due to flow of hydrocarbon from the formation. Most formation testers are equipped with a resistivity tool as part of a stand-alone probe section or as separate module for fluid property measurement. On the other hand, when drilling fluid is oil-based mud (OBM), a change in fluid resistivity is not expected as there is no difference between formation resistivity and filtrate resistivity, as shown in Fig. 6.9.



**Figure 6.7** Pressure profile from a probe module with rate controlled by pretest chamber.



**Figure 6.8** Probe resistivity response from a well drilled with WBM.

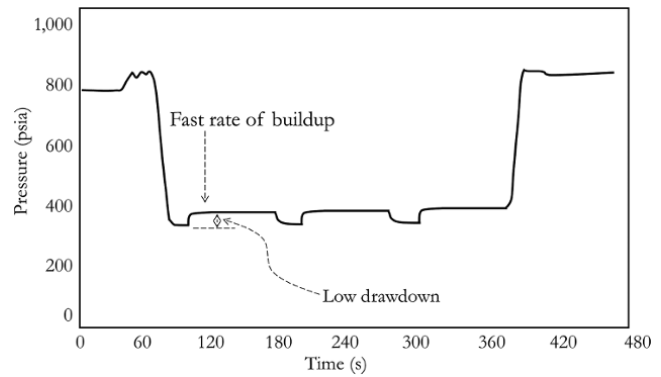


**Figure 6.11** Pressure response in a high permeability formation.

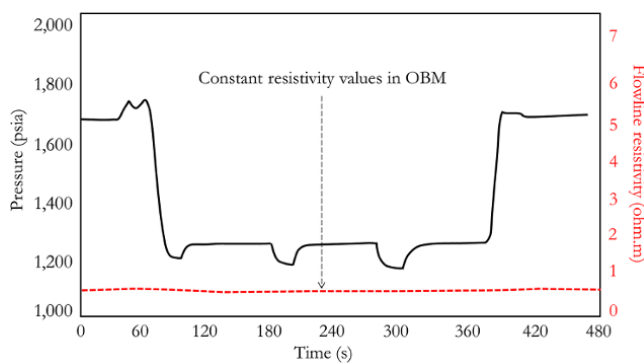


**Figure 6.9** Probe resistivity response from a well drilled with OBM.

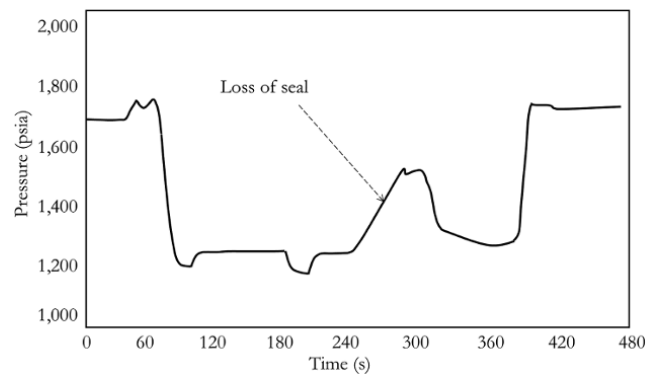


**Figure 6.12** Abrupt pressure increase due to loss of seal.

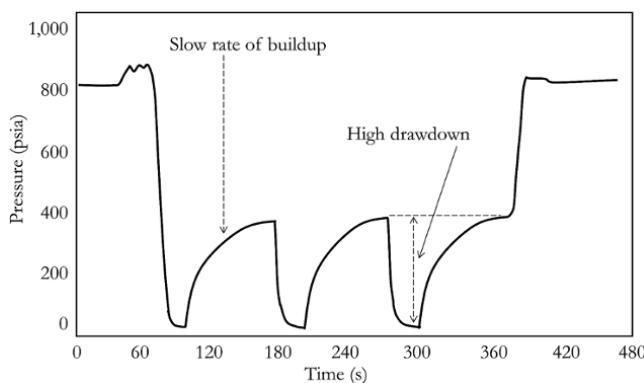


**Figure 6.10** Pressure response in a tight permeability test or dry test.

A very important response during formation testing is shown in Fig. 6.10, which characterizes a very tight formation or a dry test (impermeable formation).

A very tight formation will show very high drawdown pressure, with drawdown pressure dropping very low and for an impermeable formation dropping as low as

14.7 psia or even lower. The buildup following pretest also will show a very slow rate of buildup for low permeability formation.

A high permeability formation, on the other hand, will show a lower pressure drawdown and high rate of buildup, as shown in Fig. 6.11.

A loss of seal during a test would create hydraulic communication between the tool's gauge and the mud in the borehole, thereby creating an abrupt increase in pressure, as the mud has a higher pressure than the formation giving an overbalanced condition. This abrupt increase in pressure is illustrated in Fig. 6.12.

Mud filtrate invasion due to hydrostatic mud pressure can alter the pressure measurement around the wellbore, especially in a tight formation where there is poor sealing of mud cake, thereby giving higher formation fluid pressure than in the unaffected part of the reservoir, a phenomenon referred to as *supercharging*. The effect of supercharging is shown in Fig. 6.13.

### 6.2.2. Spherical Flow Equation for a Probe

The point source solution for spherical flow [Moran and Finklea, 1962] at a wellbore can be written as:

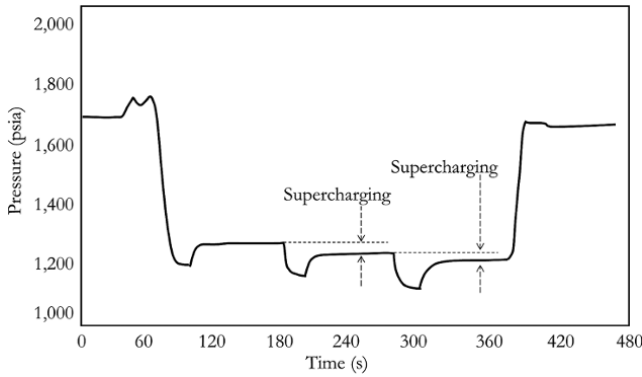


Figure 6.13 Supercharging.

$$p_D = \operatorname{erfc}\left(\frac{1}{2\sqrt{t_D}}\right) \quad (6.7)$$

where

$$p_D = \frac{(p_i - p(t))}{\frac{q\mu}{4\pi k r_p}}$$

$$t_D = \frac{kt}{\phi\mu c_t r_p^2}$$

$$r_D = \frac{r}{r_p}$$

Including the skin effect (S), equation (6.7) becomes:

$$p_D = \operatorname{erfc}\left(\frac{1}{2\sqrt{t_D}}\right) + S_e + S_d \quad (6.8)$$

where the skin effect can be expressed as the sum of the skin effect due to anisotropy ( $S_e$ ) and that due to damage ( $S_d$ ):

$$S = S_e + S_d \quad (6.9)$$

The combined effect of storage and skin effect can be included into equation (6.7) using the *Van Everdingen and Hurst* [1949] approach discussed in Chapter 8.5.1.6:

$$\bar{P}_{FL-S}(s, S, C_D) = \frac{s\bar{P}_D(s) + S}{s[1 + C_D s(s\bar{P}_D(s) + S)]} \quad (6.10)$$

where  $\bar{P}_D(s)$  is the Laplace transform of  $P_D(t_D)$  without skin and  $C_D$ . While  $\bar{P}_{FL-S}(s, S, C_D)$  is the Laplace transform of  $P_D(t_D, S, C_D)$ , which is  $P_D$  with skin and  $C_D$ , where:

$$C_D = \frac{0.89}{\phi c_t r_w r_p^2} C$$

But  $C = c_{fluid} V_{tool}$  and, hence, the above becomes:

$$C_D = \frac{0.89}{\phi c_t r_w r_p^2} c_{fluid} V_{tool} \quad (6.11)$$

For  $p_D = \operatorname{erfc}\left(\frac{1}{2\sqrt{t_D}}\right) + S$ ,

the Laplace transform of  $p_D$ ,  $\bar{P}_D(s)$  can be expressed as:

$$\bar{P}_D(s) = \frac{1}{s} \exp(-\sqrt{s}) \quad (6.12)$$

With  $\bar{P}_D(s)$  defined in equation (6.12) and  $\bar{P}_{FL-S}(s, S, C_D)$  defined in equation (6.10), numerical Laplace inversion (Chapter 8.5.1.3) can be used to determine  $P_D(t_D, S, C_D)$ .

### 6.2.3. Formation Pressure

This is the *static fluid pore pressure* (also called *pore pressure*), denoted as  $p^f$  and determined from direct measurement of the final stable buildup pressure after a pretest drawdown. Hence,  $p^f$  is also called *final stable buildup pressure*. When formation pressures are collected at multiple stations (*multiple station formation testing*), a *formation pressure log* is created. Formation pressure logs can be analyzed to give an indication of reservoir communication, reservoir fluid type, zone, and contact.

More than one buildup, often three, are taken at a given station to check for repeatability and ensure accurate  $p^f$  determination. Where the three-buildup test does not show repeatability, often due to the supercharging effect, such a test should be discarded and not used for formation pressure log analysis.

### 6.2.4. Formation Mobility and Permeability Calculation

At each station with a probe module or stand-alone probe type formation tester, three analyses can be carried out to determine mobility ( $\frac{k}{\mu}$ ) and, thus, permeability ( $k$ ) if the viscosity of the fluid produced from the formation is known. These analyses include: (i) steady state pretest analysis; (ii) flow rate analysis (FRA), and (iii) pressure transient analysis.

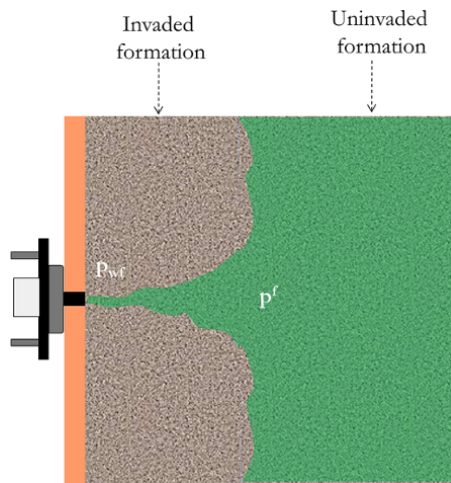
The estimation of permeability from mobility requires prior knowledge of the fluid viscosity of the pumped fluid, which is often difficult to estimate considering the effect of mud filtrate invasion, which may dominate the fluid mixture for the pretest chamber displaced formation fluid.

Table 6.2 is a summary of results that can be determined from each of the various method probe module formation tester.

**6.2.4.1. Steady State Pretest Analysis.** During pretest drawdown, the formation can be described as a composite formation system with an invaded zone and an uninvaded zone. Production is mainly from the invaded zone, which is small compared to the uninvaded zone, which creates a constant pressure boundary system (Fig. 6.14). The pretest drawdown flow can, therefore, be described as steady

**Table 6.2** Results from Formation Test Probe Module.

		Methods		
		Steady state	FRA	Pressure transient
Calculated Properties	Pressure	From final stable pressure from buildup following pretest.	Intercept of FRA plot on vertical (pressure) axis.	Regression match with workflow described in Chapter 8.10.
	Mobility	Equation (6.13). Method requires a geometric factor	From slope of FRA plot (Fig. 6.18). Method requires geometric factor	From radial flow stabilization on derivative or slope of superposition function. When radial flow does not manifest, spherical mobility can be determined. Method is described in Chapter 8.10.
	Skin effect	Skin cannot be determined.	Skin cannot be determined.	Skin can be determined but not reliable.

**Figure 6.14** Flow through probe aperture.

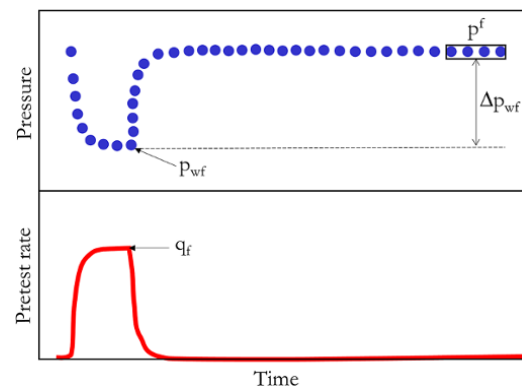
state response similar to well producing from a reservoir with a strong aquifer support (Chapter 8.5.1.12).

Using the steady state approach [Stewart and Wittmann, 1979], radial formation mobility can be calculated using:

$$\frac{k_r}{\mu} = \frac{221.82786 q_f}{G_0 r_p \Delta p_{wf}} \text{ in engineering oil field (EOF) units} \quad (6.13)$$

where  $q_f$  is the final stable rate during pretest in bbl/d, as shown in Fig. 6.15;  $p_{wf}$  is the final stable flowing pretest pressure in psia, as shown in Fig. 6.15;  $r_p$  is the probe radius in ft;  $\Delta p_{wf}$  is the difference between the final stable buildup pressure ( $p^f$ ) and final flowing pretest pressure ( $p_{wf}$ ), as illustrated in Fig. 6.15.

$$\Delta p_{wf} = p^f - p_{wf} \quad (6.14)$$

**Figure 6.15** Parameters for the pretest steady state calculation.

$G_0$  is a geometric factor that helps to correct for deviation from spherical flow due to the permeability anisotropy effect and orientation of wellbore relative to the probe. This varies from tool to tool and is often supplied by the services company.  $G_0$  is a function of  $\frac{k_v}{k_r}$  and  $\frac{r_p}{r_w}$ .

Mobility calculations can be carried out on more than one sequence of pretest and buildup in a test. Hence, for a test of three pretest and buildup, three mobilities of approximately equal values can be calculated for a valid test.

### Exercise 6.1 Mobility Calculation Using the Steady State Method

Determine formation mobility using the steady state method given the formation and tool properties in Table 6.3; formation pressure with cumulative volume swept by the pretest chamber is in Table 6.4.

**Table 6.3** Formation and Tool Properties.

Formation porosity (fraction)	0.25
Layer temperature (°F)	120
Total formation compressibility (psi <sup>-1</sup> )	3.5E-5
Probe internal diameter (in)	0.3
Tool internal volume (bbl)	0.002202
Geometric factor (G <sub>0</sub> )	4.67

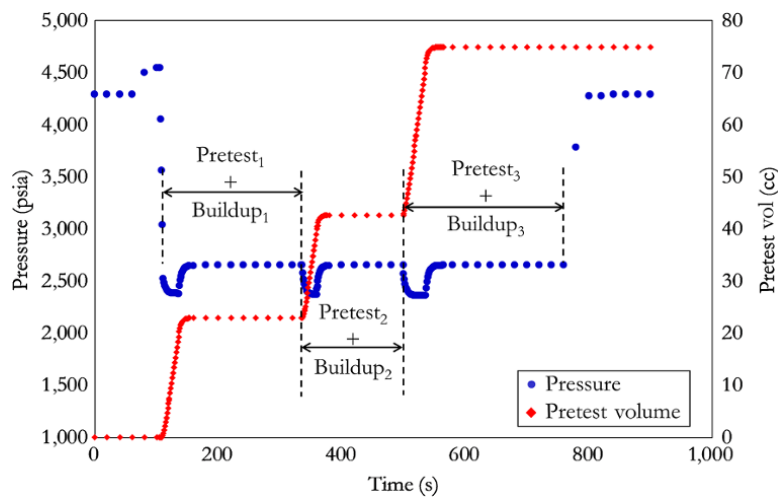
**Table 6.4** Probe Pressure and Sweat Volume History.

Time (s)	Pressure (psi)	Vol (cc)	Time (s)	Pressure (psi)	Vol (cc)	Time (s)	Pressure (psi)	Vol (cc)
0.00	4,289.93	0.00	131.61	2,380.31	16.29	335.79	2,649.97	22.92
20.00	4,289.92	0.00	132.84	2,380.08	17.28	337.02	2,573.24	23.20
40.00	4,289.88	0.00	134.07	2,379.91	18.28	338.25	2,517.53	23.70
60.00	4,289.87	0.00	135.30	2,379.78	19.27	339.48	2,477.04	24.34
80.00	4,498.82	0.00	136.53	2,379.67	20.26	340.00	2,464.58	24.65
100.00	4,540.86	0.00	137.76	2,453.11	20.98	340.71	2,447.57	25.09
104.55	4,541.06	0.00	138.99	2,506.41	21.51	341.94	2,426.12	25.92
105.78	4,540.38	0.00	140.00	2,538.19	21.82	343.17	2,410.48	26.80
107.01	4,048.97	0.00	140.22	2,545.16	21.89	344.40	2,399.07	27.73
108.24	3,557.55	0.00	141.45	2,573.34	22.16	345.63	2,390.73	28.69
109.47	3,039.99	0.28	142.68	2,593.86	22.37	346.86	2,384.64	29.67
110.70	2,522.42	0.75	143.91	2,608.81	22.51	348.09	2,380.18	30.66
111.93	2,483.81	1.37	145.14	2,619.71	22.62	349.32	2,376.91	31.67
113.16	2,455.72	2.09	146.37	2,627.67	22.70	350.55	2,374.50	32.69
114.39	2,435.26	2.88	147.60	2,633.49	22.75	351.78	2,372.73	33.71
115.62	2,420.34	3.73	148.83	2,637.74	22.80	353.01	2,371.43	34.73
116.85	2,409.46	4.62	150.06	2,640.86	22.83	354.24	2,370.46	35.76
118.08	2,401.52	5.54	151.29	2,643.14	22.85	355.47	2,369.74	36.80
119.31	2,395.70	6.48	152.52	2,644.82	22.87	356.70	2,369.20	37.83
120.00	2,393.31	7.01	160.00	2,648.82	22.91	357.93	2,368.80	38.86
120.54	2,391.45	7.43	180.00	2,649.77	22.91	359.16	2,368.49	39.90
121.77	2,388.33	8.40	200.00	2,649.87	22.92	360.00	2,420.72	40.41
123.00	2,386.04	9.37	220.00	2,649.91	22.92	360.39	2,444.99	40.65
124.23	2,384.35	10.35	240.00	2,649.93	22.92	361.62	2,500.52	41.20
125.46	2,383.10	11.33	260.00	2,649.95	22.92	362.85	2,540.87	41.59
126.69	2,382.18	12.32	280.00	2,649.95	22.92	364.08	2,570.23	41.88
127.92	2,381.50	13.31	300.00	2,649.96	22.92	365.31	2,591.60	42.09
129.15	2,380.98	14.30	320.00	2,649.97	22.92	366.54	2,607.17	42.24
130.38	2,380.60	15.29	334.56	2,649.97	22.92	367.77	2,618.52	42.36
369.00	2,626.81	42.44	520.00	2,360.60	57.79	553.50	2,645.52	74.85
370.23	2,632.86	42.50	520.29	2,360.47	58.04	554.73	2,646.53	74.86
371.46	2,637.28	42.54	521.52	2,360.05	59.11	555.96	2,647.28	74.86
372.69	2,640.52	42.57	522.75	2,359.74	60.18	557.19	2,647.84	74.87
373.92	2,642.90	42.60	523.98	2,359.50	61.24	558.42	2,648.26	74.87
375.15	2,644.65	42.61	525.21	2,359.32	62.31	559.65	2,648.57	74.88
380.00	2,648.07	42.65	526.44	2,359.17	63.39	560.00	2,648.64	74.88
400.00	2,649.74	42.66	527.67	2,359.06	64.46	560.88	2,648.81	74.88
420.00	2,649.85	42.66	528.90	2,358.97	65.52	562.11	2,648.99	74.88
440.00	2,649.90	42.66	530.13	2,358.90	66.60	563.34	2,649.13	74.88
460.00	2,649.92	42.66	531.36	2,358.84	67.67	564.57	2,649.24	74.88
480.00	2,649.93	42.66	532.59	2,358.79	68.74	580.00	2,649.68	74.89
499.38	2,649.94	42.66	533.82	2,358.74	69.81	600.00	2,649.80	74.89
500.61	2,570.83	42.96	535.05	2,358.71	70.88	620.00	2,649.85	74.89
501.84	2,513.40	43.47	536.28	2,358.68	71.95	640.00	2,649.88	74.89
503.07	2,471.65	44.13	537.51	2,431.99	72.75	660.00	2,649.90	74.89
504.30	2,441.27	44.90	538.74	2,490.97	73.33	680.00	2,649.91	74.89
505.53	2,419.15	45.76	539.97	2,533.84	73.75	700.00	2,649.92	74.89



**Table 6.4** (Continued)

Time (s)	Pressure (psi)	Vol (cc)	Time (s)	Pressure (psi)	Vol (cc)	Time (s)	Pressure (psi)	Vol (cc)
506.76	2,403.02	46.67	540.00	2,534.65	73.76	720.00	2,649.93	74.89
507.99	2,391.26	47.63	541.20	2,565.03	74.06	740.00	2,649.93	74.89
509.22	2,382.67	48.61	542.43	2,587.74	74.28	760.00	2,649.94	74.89
510.45	2,376.38	49.62	543.66	2,604.28	74.44	780.00	3,779.20	74.89
511.68	2,371.79	50.65	544.89	2,616.35	74.56	800.00	4,276.61	74.89
512.91	2,368.41	51.69	546.12	2,625.16	74.65	820.00	4,277.17	74.89
514.14	2,365.93	52.74	547.35	2,631.60	74.71	840.00	4,288.62	74.89
515.37	2,364.11	53.79	548.58	2,636.31	74.76	860.00	4,288.60	74.89
516.60	2,362.76	54.85	549.81	2,639.76	74.79	880.00	4,288.63	74.89
517.83	2,361.77	55.91	551.04	2,642.29	74.81	900.00	4,288.58	74.89
519.06	2,361.02	56.97	552.27	2,644.15	74.83			

**Figure 6.16** Pressure–volume history showing pretest and buildup sequence.**Solution Steps.**

*Step 1:* calculate the instantaneous rate flow of fluid withdrawal from the formation into the pretest chamber ( $q(t)$ ) using equation (6.1):  $q(t) = \frac{\Delta V}{\Delta t}$ .

*Step 2:* determine  $p_{wf}$ ,  $q_{wf}$ , and  $p^f$  from the subsequent buildup from the pressure–rate history.

*Step 3:* calculate  $\Delta p_{wf}$  by subtracting  $p_{wf}$  from  $p^f$  as shown in equation (6.14):  $\Delta p_{wf} = p^f - p_{wf}$ .

*Step 4:* calculate  $\frac{k}{\mu}$  using equation (6.13).

**Solution.**

Fig. 6.16 is the pressure–volume history for Exercise 6.1 showing the start and end of the combined pretest and subsequent buildup ( $\text{Pretest}_i + \text{Buildup}_i$ ).

Table 6.5 is calculation of instantaneous flow rate of fluid withdrawal from the formation into the pretest chamber. Rate was then converted to bbl/d for calculation in engineering oil field (EOF) units.

Fig. 6.17 shows the pressure–rate history for Exercise 6.1 showing  $p_{wf}$ ,  $p^f$ , and  $q_f$ .

From the determined  $p_{wf}$ ,  $p^f$  and  $q_f$  (Fig. 6.17), mobility is calculated as shown in Table 6.6.

**6.2.4.2. Formation Rate Analysis (FRA).** This is a technique for analysis of probe type formation tester pressure data. The approach is based on the material balance and storage effect of the tool flowline. The FRA method, apart for determining mobility, can be used for quality control purposes by site engineers during formation test data acquisition [Kasap *et al.*, 1999].

Using the material balance relationship where the rate of accumulation in the formation tester is the difference between the rate of withdrawal from the formation and the rate of withdrawal from the tool into the pretest chamber (pretest rate):

$$q_{\text{accum}} = q_{\text{form}} - q_{\text{tool}} \quad (6.15)$$

**Table 6.5** Rate Calculation from Cumulative Pretest Volume.

Time (s)	Rate (cc/s)	Rate (bbl/d)	Time (s)	Rate (cc/s)	Rate (bbl/d)	Time (s)	Rate (cc/s)	Rate (bbl/d)
0.00	0.00E+00	0.00E+00	126.69	8.02E-01	4.36E-01	200.00	4.76E-05	2.59E-05
20.00	0.00E+00	0.00E+00	127.92	8.04E-01	4.37E-01	220.00	1.98E-05	1.08E-05
40.00	0.00E+00	0.00E+00	129.15	8.06E-01	4.38E-01	240.00	1.07E-05	5.79E-06
60.00	0.00E+00	0.00E+00	130.38	8.07E-01	4.38E-01	260.00	6.87E-06	3.74E-06
80.00	0.00E+00	0.00E+00	131.61	8.07E-01	4.39E-01	280.00	3.48E-06	1.89E-06
100.00	0.00E+00	0.00E+00	132.84	8.08E-01	4.39E-01	300.00	3.48E-06	1.89E-06
104.55	0.00E+00	0.00E+00	134.07	8.08E-01	4.39E-01	320.00	3.48E-06	1.89E-06
105.78	0.00E+00	0.00E+00	135.30	8.09E-01	4.39E-01	334.56	1.71E-06	9.32E-07
107.01	0.00E+00	0.00E+00	136.53	8.09E-01	4.40E-01	335.79	0.00E+00	0.00E+00
108.24	0.00E+00	0.00E+00	137.76	5.86E-01	3.18E-01	337.02	2.33E-01	1.26E-01
109.47	2.26E-01	1.23E-01	138.99	4.25E-01	2.31E-01	338.25	4.00E-01	2.18E-01
110.70	3.86E-01	2.10E-01	140.00	3.09E-01	1.68E-01	339.48	5.22E-01	2.84E-01
111.93	5.01E-01	2.73E-01	140.22	3.09E-01	1.68E-01	340.00	6.10E-01	3.31E-01
113.16	5.85E-01	3.18E-01	141.45	2.25E-01	1.22E-01	340.71	6.10E-01	3.31E-01
114.39	6.46E-01	3.51E-01	142.68	1.64E-01	8.90E-02	341.94	6.74E-01	3.66E-01
115.62	6.91E-01	3.75E-01	143.91	1.19E-01	6.48E-02	343.17	7.20E-01	3.91E-01
116.85	7.23E-01	3.93E-01	145.14	8.70E-02	4.73E-02	344.40	7.54E-01	4.10E-01
118.08	7.46E-01	4.06E-01	146.37	6.35E-02	3.45E-02	345.63	7.79E-01	4.23E-01
119.31	7.63E-01	4.15E-01	147.60	4.64E-02	2.52E-02	346.86	7.96E-01	4.33E-01
120.00	7.76E-01	4.22E-01	148.83	3.39E-02	1.84E-02	348.09	8.09E-01	4.40E-01
120.54	7.76E-01	4.22E-01	150.06	2.49E-02	1.35E-02	349.32	8.19E-01	4.45E-01
121.77	7.85E-01	4.26E-01	151.29	1.82E-02	9.91E-03	350.55	8.26E-01	4.49E-01
123.00	7.91E-01	4.30E-01	152.52	1.34E-02	7.28E-03	351.78	8.31E-01	4.52E-01
124.23	7.96E-01	4.33E-01	160.00	5.25E-03	2.85E-03	353.01	8.35E-01	4.54E-01
125.46	8.00E-01	4.35E-01	180.00	4.68E-04	2.54E-04	354.24	8.37E-01	4.55E-01

Time (s)	Rate (cc/s)	Rate (bbl/d)	Time (s)	Rate (cc/s)	Rate (bbl/d)	Time (s)	Rate (cc/s)	Rate (bbl/d)	Time (s)	Rate (cc/s)	Rate (bbl/d)
355.47	8.39E-01	4.56E-01	500.61	2.40E-01	1.30E-01	530.13	8.71E-01	4.73E-01	559.65	2.50E-03	1.36E-03
356.70	8.41E-01	4.57E-01	501.84	4.13E-01	2.24E-01	531.36	8.71E-01	4.73E-01	560.00	1.89E-03	1.03E-03
357.93	8.42E-01	4.57E-01	503.07	5.38E-01	2.92E-01	532.59	8.71E-01	4.73E-01	560.88	1.89E-03	1.03E-03
359.16	8.43E-01	4.58E-01	504.30	6.29E-01	3.42E-01	533.82	8.71E-01	4.73E-01	562.11	1.44E-03	7.82E-04
360.00	6.10E-01	3.32E-01	505.53	6.95E-01	3.78E-01	535.05	8.71E-01	4.73E-01	563.34	1.11E-03	6.01E-04
360.39	6.10E-01	3.32E-01	506.76	7.43E-01	4.04E-01	536.28	8.71E-01	4.73E-01	564.57	8.59E-04	4.67E-04
361.62	4.43E-01	2.41E-01	507.99	7.77E-01	4.22E-01	537.51	6.48E-01	3.52E-01	580.00	2.79E-04	1.52E-04
362.85	3.22E-01	1.75E-01	509.22	8.03E-01	4.36E-01	538.74	4.71E-01	2.56E-01	600.00	5.87E-05	3.19E-05
364.08	2.34E-01	1.27E-01	510.45	8.21E-01	4.46E-01	539.97	3.42E-01	1.86E-01	620.00	2.57E-05	1.40E-05
365.31	1.71E-01	9.27E-02	511.68	8.35E-01	4.54E-01	540.00	2.49E-01	1.35E-01	640.00	1.43E-05	7.75E-06
366.54	1.24E-01	6.75E-02	512.91	8.44E-01	4.59E-01	541.20	2.49E-01	1.35E-01	660.00	9.02E-06	4.90E-06
367.77	9.06E-02	4.92E-02	514.14	8.51E-01	4.63E-01	542.43	1.81E-01	9.85E-02	680.00	6.96E-06	3.78E-06
369.00	6.61E-02	3.59E-02	515.37	8.57E-01	4.66E-01	543.66	1.32E-01	7.18E-02	700.00	3.94E-06	2.14E-06
370.23	4.83E-02	2.62E-02	516.60	8.60E-01	4.68E-01	544.89	9.63E-02	5.23E-02	720.00	3.48E-06	1.89E-06
371.46	3.53E-02	1.92E-02	517.83	8.63E-01	4.69E-01	546.12	7.03E-02	3.82E-02	740.00	3.48E-06	1.89E-06
372.69	2.59E-02	1.41E-02	519.06	8.65E-01	4.70E-01	547.35	5.14E-02	2.79E-02	760.00	3.48E-06	1.89E-06
373.92	1.90E-02	1.03E-02	520.00	8.67E-01	4.71E-01	548.58	3.76E-02	2.04E-02	780.00	3.48E-06	1.89E-06
375.15	1.39E-02	7.57E-03	520.29	8.67E-01	4.71E-01	549.81	2.75E-02	1.50E-02	800.00	1.25E-06	6.80E-07
380.00	6.93E-03	3.77E-03	521.52	8.68E-01	4.72E-01	551.04	2.02E-02	1.10E-02	820.00	0.00E+00	0.00E+00
400.00	8.21E-04	4.46E-04	522.75	8.69E-01	4.72E-01	552.27	1.49E-02	8.07E-03	840.00	0.00E+00	0.00E+00
420.00	5.43E-05	2.95E-05	523.98	8.69E-01	4.72E-01	553.50	1.09E-02	5.95E-03	860.00	0.00E+00	0.00E+00
440.00	2.08E-05	1.13E-05	525.21	8.70E-01	4.73E-01	554.73	8.09E-03	4.39E-03	880.00	0.00E+00	0.00E+00
460.00	1.11E-05	6.05E-06	526.44	8.70E-01	4.73E-01	555.96	5.99E-03	3.26E-03	900.00	0.00E+00	0.00E+00
480.00	6.96E-06	3.78E-06	527.67	8.70E-01	4.73E-01	557.19	4.46E-03	2.42E-03			
499.38	3.87E-06	2.10E-06	528.90	8.70E-01	4.73E-01	558.42	3.33E-03	1.81E-03			

Rate in cc/s was calculated using equation (6.1), then converted to bbl/d

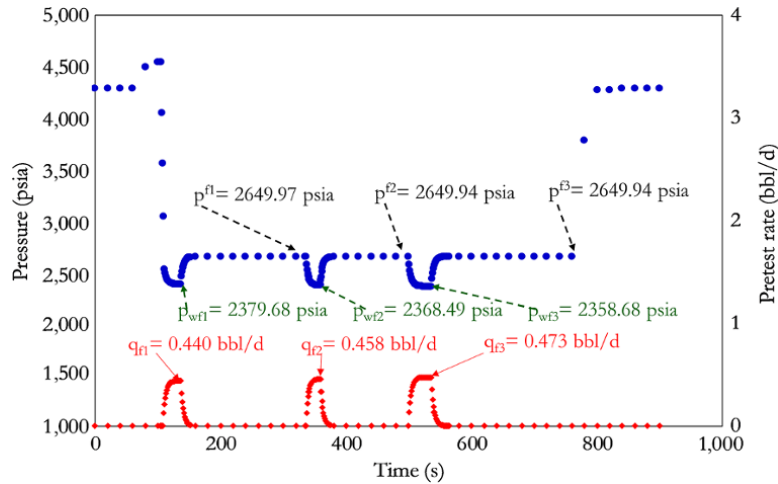


Figure 6.17 Pressure–rate history for Exercise 6.1.

Table 6.6 Mobility Calculation for Exercise 6.1.

$t(p_{wf})$ (s)	$p_{wf}$ (psia)	$q_f$ (bbl/d)	$p^f$ (psia)	$\Delta p_{wf}$ (psi) using equation (6.14)	$\frac{k_r}{\mu}$ (mD/cp) using equation (6.13)
136.53	2,379.68	0.440	2,649.97	270.29	6.18
359.16	2,368.49	0.458	2,649.94	281.45	6.18
536.28	2,358.68	0.473	2,649.94	291.26	6.18

where  $q_{accum}$  is the rate of accumulation in the formation tester,  $q_{form}$  is the rate of withdrawal from the formation, and  $q_{tool}$  is the rate of withdrawal from the tool into the pretest chamber (pretest rate).

$$q_{accum} = c_{sys} V_{tool} \frac{dp(t)}{dt} \tag{6.16}$$

and

$$q_{form} = [p^f - p(t)] \left( \frac{k_r G_0 r_p}{221.828 \mu} \right) \tag{6.17}$$

Substituting equations (6.16) and (6.17) into equation (6.15) gives:

$$c_{sys} V_{tool} \frac{dp(t)}{dt} = [p^f - p(t)] \left( \frac{k_r G_0 r_p}{221.828 \mu} \right) - q_{tool}$$

where  $G_0$  is a geometric factor.

Making  $p(t)$  the subject of the formula:

$$p(t) = p^f - c_{sys} V_{tool} \frac{dp(t)}{dt} \left( \frac{221.828 \mu}{k_r G_0 r_p} \right) + q_{tool} \left( \frac{221.828 \mu}{k_r G_0 r_p} \right) \tag{6.18}$$

in engineering oil field (EOF) units.

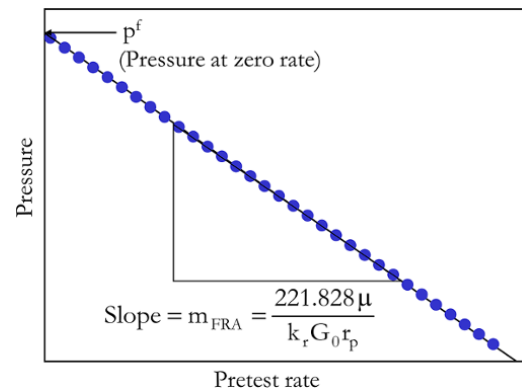


Figure 6.18 Flow rate analysis plot.

A combined plot of  $p(t)$  against  $q_{tool}$  from pretest (drawdown) and buildup should yield a straight line for a valid test with a slope that is equal to  $\frac{221.828 \mu}{k_r G_0 r_p}$  and extrapolation of the straight line to  $p^f$  on the vertical axis. Hence, when pressure ( $p(t)$ ) during pretest (drawdown) and buildup is plotted against  $q_{tool}$ , the plot will yield a straight line as shown in Fig. 6.18.

From equation (6.18) and Fig. 6.18:

$$\text{Slope} = m_{FRA} = \frac{221.828 \mu}{k_r G_0 r_p}$$

Hence,

$$\frac{k_r}{\mu} = \frac{221.828}{m_{FRA} G_0 r_p} \text{—in engineering oil field (EOF) units} \tag{6.19}$$

FRA analysis can be carried out using a single pretest and subsequent buildup or by combining multiple pretests and their corresponding subsequent buildups.

**Exercise 6.2** Mobility Calculation Using Flow Rate Analysis Method

Using data provided in Exercise 6.1, calculate mobility using the *flow rate analysis* method for (i) separate pretest combined with subsequent buildup and (ii) combining entire pretest and subsequent buildups (pressure–rate history).

**Solution Steps.**

*Step 1:* using separate pretest combined with subsequent buildup, select all pressures in a given Pretest<sub>i</sub> + Buildup<sub>i</sub> (as defined in Fig. 6.16) and plot against q(t).

*Step 2:* using combination of entire pretest and buildup data, select all pressures in all Pretest<sub>i</sub> + Buildup<sub>i</sub> and plot against q(t).

**Solution.**

The FRA plot for pretest<sub>1</sub> + buildup<sub>1</sub> is shown Fig. 6.19; the FRA plot for pretest<sub>2</sub> + buildup<sub>2</sub> is shown Fig. 6.20; the FRA plot for pretest<sub>3</sub> + buildup<sub>3</sub> is shown Fig. 6.21; and the FRA plot for all pretest and buildup is shown Fig. 6.22.

From Fig. 6.19–Fig. 6.22 the slope and extrapolation of plot to  $p^f$  is determined from a line fit equation in the form  $y = mx + C$  where  $m$  is the slope and  $C$  is the intercept on

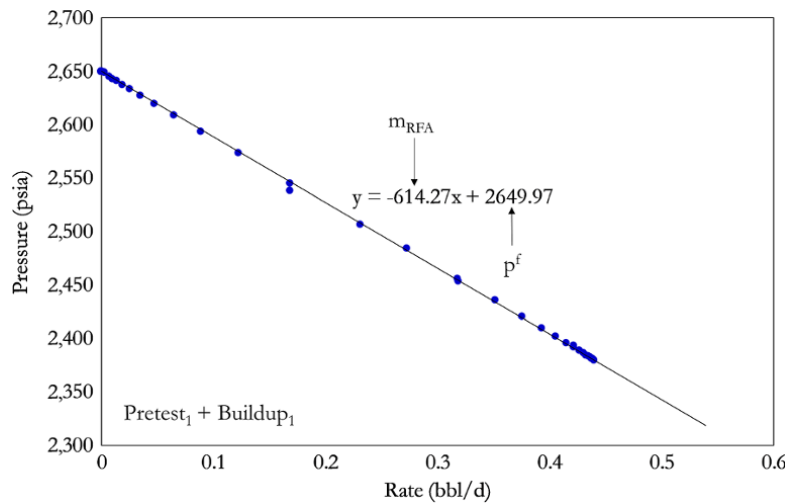


**Figure 6.19** FRA plot for pretest<sub>1</sub> + buildup<sub>1</sub>.

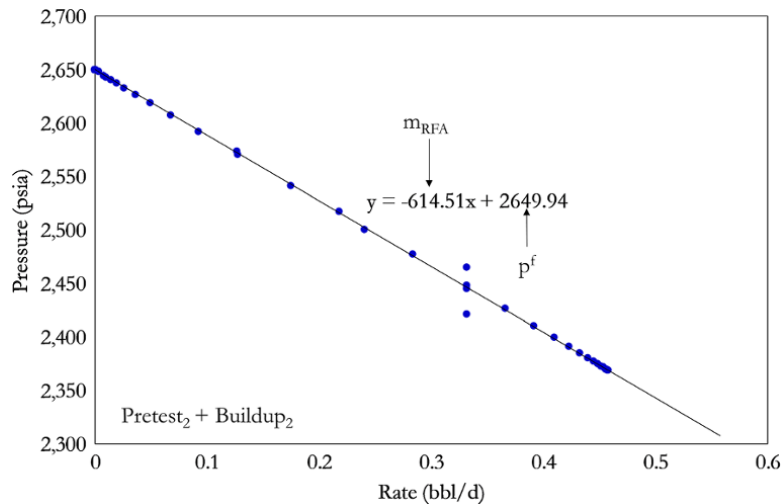


**Figure 6.20** FRA plot for pretest<sub>2</sub> + buildup<sub>2</sub>.

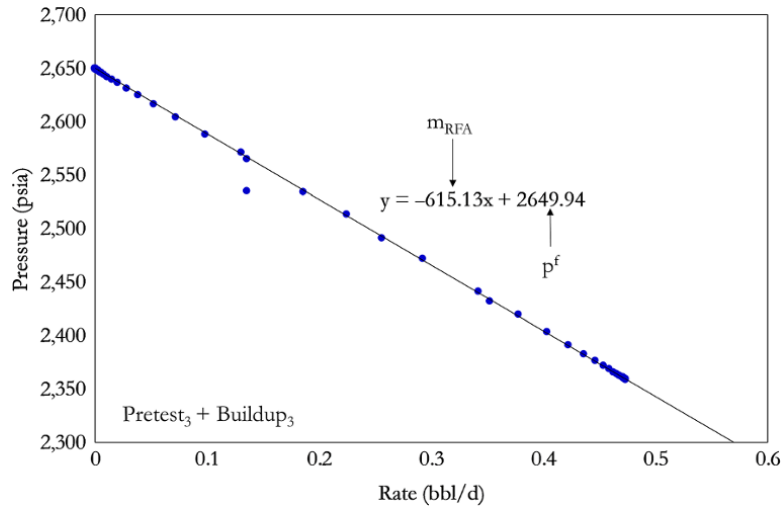


Figure 6.21 FRA plot for pretest<sub>3</sub> + buildup<sub>3</sub>.

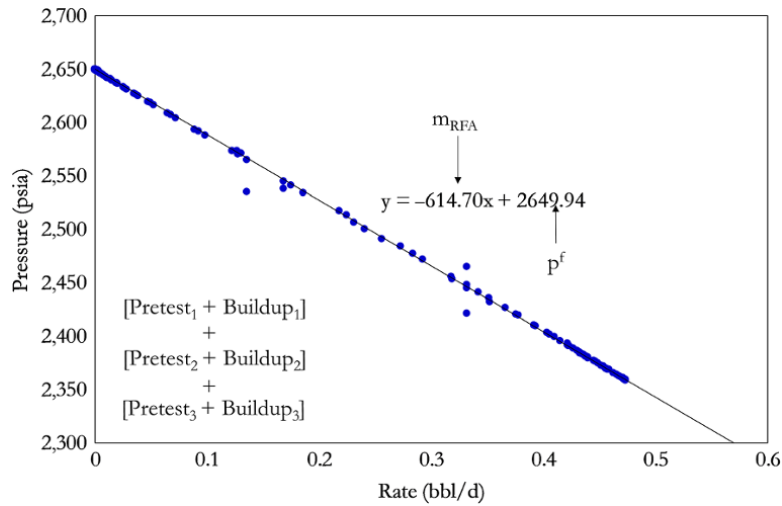


Figure 6.22 FRA plot for all pretest and buildup.

the y-axis. The summary for the FRA analysis for Exercise 6.2 is shown in Table 6.7.

**6.2.4.3. Pressure Transient Analysis.** Pressure and rate history from the probe module can be analyzed like conventional well test data described in Chapter 8.10.

**6.2.5. Upscaling WFT Permeability**

Permeability determined from formation testing is localized and represents permeability at a given station (depth). In order to get an average permeability that represents a given formation interval, continuous

permeability can be upscaled. During upscaling, formation test permeability, formation or reservoir can be divided into several layers for averaging. Hence, the average permeability-thickness product ( $\bar{k}h$ ) due to the contribution of individual layers ( $h_i$ ) can be expressed as:

$$\bar{k}h = \sum_{i=1}^n k_{xyi}h_i \tag{6.20}$$

Vertical permeability relates to spherical ( $k_{xyz}$ ) and horizontal permeability ( $k_{xy}$ ) as shown:

$$k_z = \frac{k_{xyz}^3}{k_{xy}^2} \tag{6.21}$$

**Table 6.7** FRA analysis for Exercise 6.2.

Test	$m_{FRA}$ (Fig. 6.19– Fig. 6.22)	$p^f$ (Fig. 6.19– Fig. 6.22)	$k_r/u$ using equation (6.19)
Pretest <sub>1</sub> + Buildup <sub>1</sub>	614.27	2,649.97	6.19
Pretest <sub>2</sub> + Buildup <sub>2</sub>	614.51	2,649.94	6.18
Pretest <sub>3</sub> + Buildup <sub>3</sub>	615.13	2,649.94	6.18
All Pretest and Buildup	614.70	2,649.94	6.18

Making  $k_{xy}$  the subject of the formula:

$$k_{xy} = \sqrt{\frac{k_{xyz}^3}{k_z}}$$

$$k_{xy} = \sqrt{\frac{k_{xyz}}{k_z}} k_{xyz} \quad (6.22)$$

Substituting  $k_{xy}$  in equation (6.22) into equation (6.20):

$$\bar{k}h = \sum_{i=1}^n \left( \sqrt{\frac{k_{xyzi}}{k_{zi}}} k_{xyzi} \right) h_i \quad (6.23)$$

### 6.2.6. Mud Hydrostatic Pressure

Though mud hydrostatic pressure is still reported in most formation testing jobs, it does not have much use. In the past, mud hydrostatic pressure was used for quality assessment of the pressure gauge. Mud hydrostatic pressure is tested at regular depths down the wellbore. Then, with known mud weight calculated, mud hydrostatic pressure before and after the test is compared with the tool reading, hence giving confidence in tool reading. Due to the improved accuracy and precision of pressure gauges, this test is not necessary. Mud hydrostatic pressure in psia is expressed as:

$$p_{Mud} = Z \times 0.052 \times \rho_{Mud} \quad (6.24)$$

where  $Z$  is the vertical depth in ft and  $\rho_{Mud}$  is the mud weight in lb/gal

Fig. 6.23 shows mud hydrostatic pressure before and after the test for Exercise 6.1.

### 6.2.7. Straddle/Dual Packer Module

In situations where the single-probe configuration fails, oval pad or dual packers become a useful alternative, for

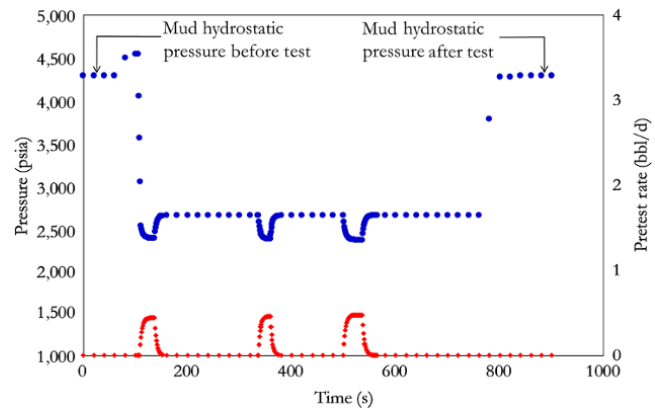


**Figure 6.23** Mud hydrostatic pressure before and after test for Exercise 6.1.

example in fissured reservoirs and fracture wells. When running WFT tools, both the bottom of the top packer and the top of bottom packer are reported. For well test analysis, the mid packer or mid reservoir is often used as the test reference depth. Other referenced depths can also be used, especially when more than one well is compared or when data are integrated in a dynamic model. A schematic of a *straddle/dual packer* is shown in Fig. 6.24.

Rate is controlled in straddle/dual packer test with a pump in the *pump module*, which can be attached to the tool configuration as a separate module. Transient well test analysis methods with a limited entry (partial penetration) interpretation model are the most rigorous approach for mobility and, hence permeability determination (Chapter 8.4.3.6 and 8.5.1.7). The straddle packer yields the following results: initial formation/reservoir pressure, permeability (or mobility), and skin effect.

An example of pressure–rate history from a straddle packer test is shown in Fig. 6.25.

### 6.2.8. Probe–Probe or Probe–Packer Configuration

Other tool configurations in formation testing where pressure and rate are acquired for formation characterization include the probe–probe configuration and probe–packer configuration, which is used for vertical interference testing and is discussed in Chapter 8.11.1.

Probe–probe or probe–packer configurations are primarily for the *vertical interference test* (VIT), which is used for qualitative and quantitative characterization of vertical communication across zones. The concept of VIT is similar to that of the *horizontal interference test*

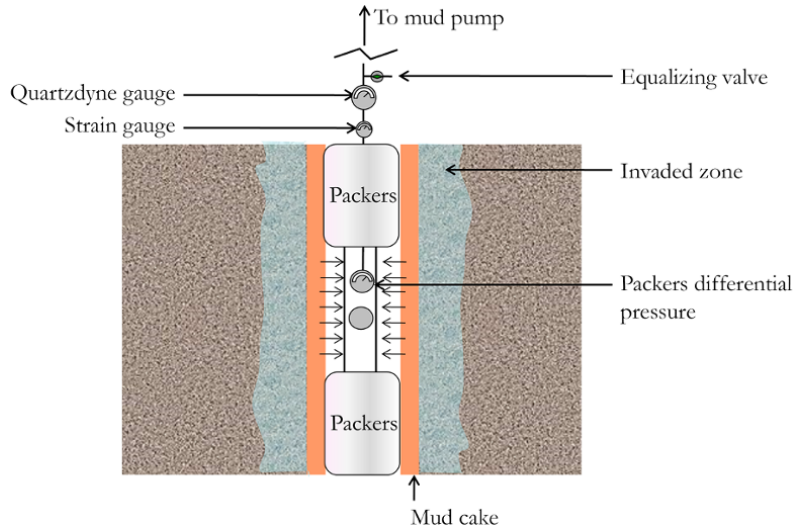


Figure 6.24 Straddle/dual packer module.

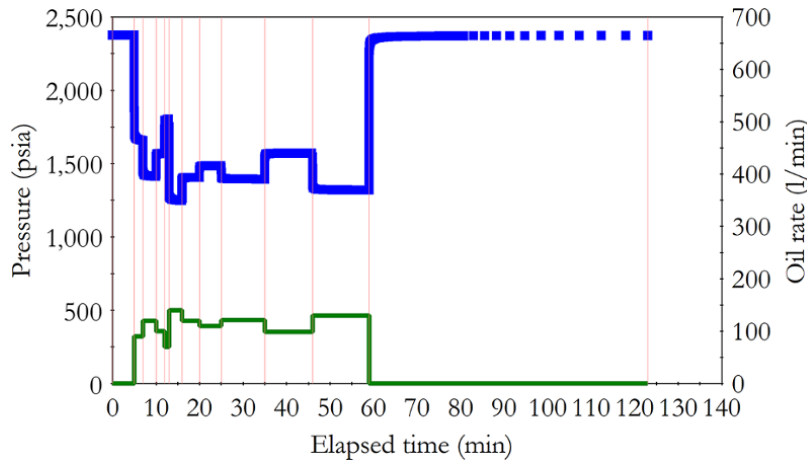


Figure 6.25 Example of pressure–rate history from a straddle packer test.

(HIT), which is used for testing lateral communication between wells. VIT involves a source (active probe or packer) that initiates and controls flow from the formation and sink (probe) where pressure is observed.

The vertical interference test can be used in determining vertical hydraulic communication, average vertical reservoir permeability, lateral continuity of shales, and reservoir layering behavior. Vertical reservoir property variation can provide useful information on the best way to develop and produce a layered reservoir, where the effect of differential depletion can significantly affect reservoir deliverability.

Fig. 6.26 shows a probe–probe configuration for VIT while Fig. 6.27 shows a probe–packer configuration for VIT.

Analysis of vertical inference test data is explained in Chapter 8.11.1.

### 6.2.9. Fluid Sampling and Property Measurement

Modern (modular) formation testers have capabilities not only to sample formation fluid but to also measure fluid properties and composition in real time.

**6.2.9.1. Fluid Sampling.** Collecting representative reservoir fluid samples from the formation is very important in development planning, estimating reserves, designing surface handling facilities, and predicting potential flow assurance issues. Wireline formation testers are equipped with measurement sensors that improve the quality of



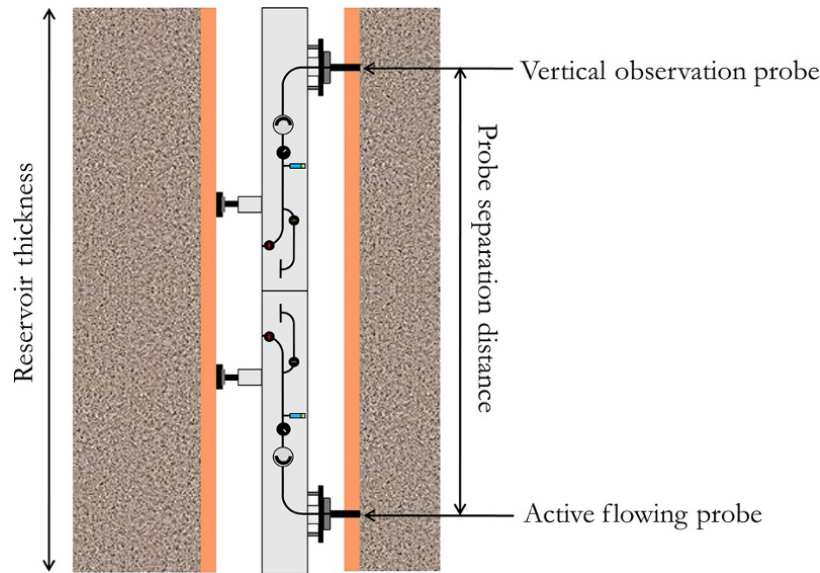


Figure 6.26 Active probe with observation probe for VIT.

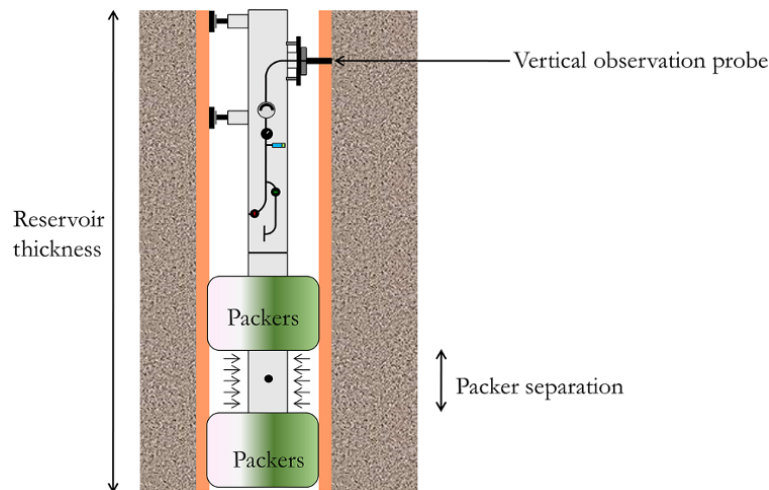


Figure 6.27 Active packer with observation probe for VIT.

sampled fluid during the test. Modular formation testers are equipped with fluid property measurement sensors and analyzers to enhance the quality of the fluid sampled from the formation.

Samples retrieved from the formation invaded by oil-base mud filtrate (predominantly diesel) can be severely contaminated due to the miscibility of the filtrate and reservoir hydrocarbon. Contaminated samples need to be decontaminated before they are used in any fluid analysis (Chapter 3.5.1.1). An illustration of the sample chamber of a wireline formation tester is shown in Fig. 6.28.

The sample module in formation testers can be a *single sample chamber*, which holds one sample cylinder bottle,

or a *multiple sample chamber*, which can hold more than one sample bottle (Fig. 6.29).

In a multiple sample chamber configuration, fluid samples obtained downhole from different stations are placed into different bottles with unique identification numbers (ID). A fluid sample must have the following information: charge pressure; charge fluid; sample pressure; sample bottle numbers/identifiers; number of sample bottles; station depth; sample temperature; and any other information and observations during sampling.

Contamination during formation fluid sampling can be minimized by monitoring fluid sample contamination levels before diverting the flow into the sample bottles.

Methane content measurement in a flowing fluid using optical spectroscopy during testing is a useful approach for contamination monitoring if there is a significant amount of methane contained in the reservoir hydrocarbon compared to the oil-base mud filtrate [Dong and Hegeman, 2003].

Measurement of increasing fluid coloration by NIR (near infrared) analyzers (with darker color indicating formation oil) is another useful qualitative approach for contamination monitoring during pumping [Mullins and Schroer, 2000]. For light oils and gas condensates, the use of coloration becomes a challenge due to little or no color contrast between oil and filtrate [Dong and Hegeman, 2003]. More than one method is often used for contamination monitoring to ensure consistency and improve accuracy in estimating clean-up time. Good practices to

ensure taking a representative fluid sample include minimizing contamination through fluid analyzers such as optical spectroscopy and prevention of phase change, which can be done through control of the pressure drawdown/pump-out rate.

**6.2.9.2. Fluid Property Measurement. Viscosity**

Viscosity is a shear measurement whose measurement must be under shear conditions. Different type of viscometers can be design for formation testers in the fluid property measurement module.

*Vibrational viscometers* are based on the principle that the higher the viscosity, the larger the damping imposed on the resonator, which be determine by: power input to achieve constant vibration amplitude, decay time of vibration or frequency of vibration. This method often involves calibrating equipment within a specific viscosity range.

*Rotational viscometers* are based on generating shear and measuring rotation generated using a spindle in a container. Viscosity of a fluid can be defined as:

$$\mu = \frac{\tau}{\gamma} \tag{6.25}$$

where

$$\tau = \frac{T}{2\pi R_s^2 L} \text{ and } \gamma = \frac{2\omega R_c^2 R_s^2}{x^2(R_c^2 - R_s^2)}$$

$\mu$  is dynamic viscosity ( $\text{Pa s}^{-1}$ ),  $\tau$  is shear stress ( $\text{N cm}^{-2}$ ),  $\gamma$  is shear rate ( $\text{s}^{-1}$ ),  $T$  is torque ( $\text{N m}^{-1}$ ),  $L$  is effective spindle length (m),  $R_s$  is spindle radius (m),  $R_c$  is container radius (m),  $\omega$  is rotational speed ( $\text{rad s}^{-1}$ ),

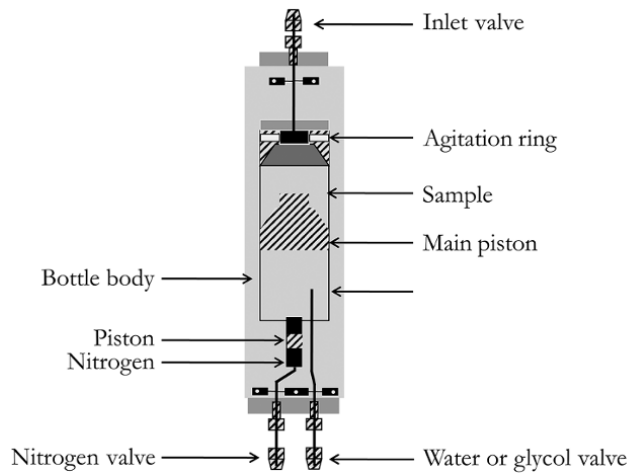


**Figure 6.28** Sample chamber of a wireline formation tester.

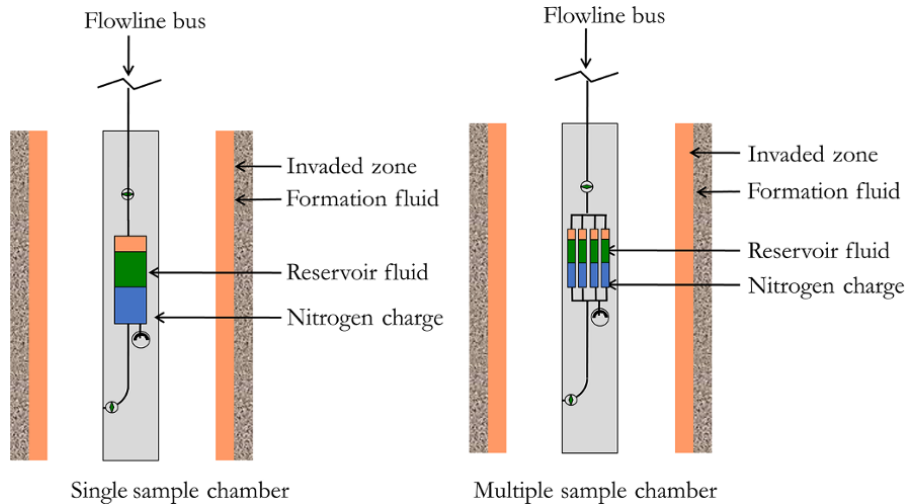


**Figure 6.29** Single and multiple sample chambers.

and  $x$  is radial location where the shear rate is being calculated.

*Fluid Density*

Fluid density can be measured using fluid mechanical principles such as the *Coriolis effect*. This is based on the relationship between the fluid density flowing through a *Coriolis tube* and the resonance frequency. The density of a liquid ( $\rho$ ) based on the Coriolis effect is given by:

$$\rho = \frac{1}{V} \left[ \left( \frac{K_s}{4\pi^2 f^2} \right) - m_t \right] \tag{6.26}$$

where  $\rho$  is fluid density,  $V$  is the internal volume of the resonance tube,  $m_t$  is tube mass,  $K_s$  is the spring constant of the tube, and  $f$  is the resonance frequency of the tube

Fluid density can also be measured using the principle of *Compton scattering*. This is based on the relationship between fluid count rate measurement (at a detector) and bulk fluid density. Gamma rays generated by  $^{137}\text{Cs}$  (cesium) or  $^{241}\text{Am}$  (americium) as source are transmitted through a flow line to a detector that measures the count rate, which relates to bulk fluid density.

*Resistivity*

The resistivity of a fluid gives an indication of the fluid either flowing through the tool section or fluid been sampled (Fig. 6.8 and Fig. 6.9). Fluid resistivity measuring devices involve configurations of electrodes forming a *Wenner array*. The resistivity array is an internal cylindrical array open at the source of fluid flow and completely shielded from the outside borehole fluid, so that only fluid resistivity is measured.

*Dielectric Property*

Dielectric measurement of fluid can be achieved by measuring current between the outer and inner coaxial cylinders for a given stable potential difference. With the properties of the coaxial cylinders known, the amount of electrical energy stored in the fluid and, hence, the dielectric property of the flowing fluid can be deduced. Dielectric properties can also be used for differentiating fluid type. When combined with resistivity data they can give good indication of fluid type.

**6.2.10. Downhole Fluid Analysis**

Wireline formation testing in recent time has been extended to wider applications that include downhole fluid analysis. Some of the properties that can be determined using downhole fluid analysis such as *optical spectroscopy* include: *in situ* determination of fluid composition and properties that relate to composition, such as the GOR,  $\text{CO}_2$ ,  $\text{H}_2\text{S}$ , and Hg contents; asphaltene onset; and other complex PVT properties.

The primary measurement of downhole fluid analysis is by spectroscopy, which involves the use of the absorption,

emission, or scattering of electromagnetic radiation by atoms, molecules or ions, to study physical processes. Optical spectroscopy can also be used for contamination monitoring, especially in wells drilled with oil-based mud.

On-site composition from optical spectroscopy can provide information on fluid type, which is useful for making an early judgement on facility type required to develop the field and appropriate existing facilities for tieback.

Compositional gradient (Fig. 6.30) from optical spectroscopy has been used to show the effect of fluid gradient and verify lateral reservoir compartmentalization [Mullins and Schroer, 2000].

**6.2.11. Formation Pressure Log (Multistation Formation Testing)**

Formation pressure logs are acquired from formation testing at multiple stations, which involves acquisition of formation pressure at different depths (stations), as shown in Fig. 6.31.

Formation pressure logs can be used for barrier detection and vertical compartmentalization of zones. The no-flow barrier due to shale in Fig. 6.31 does not

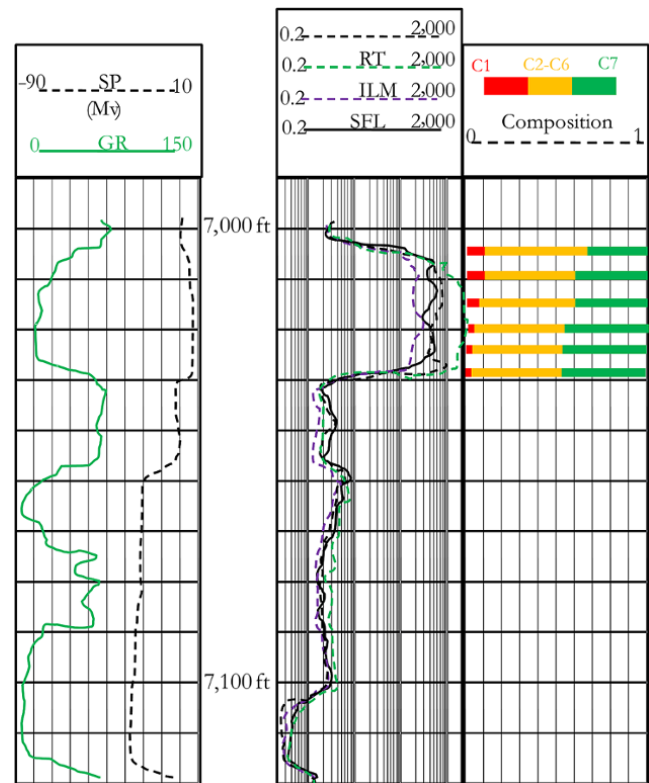


**Figure 6.30** Example of fluid composition from optical fluid analysis.

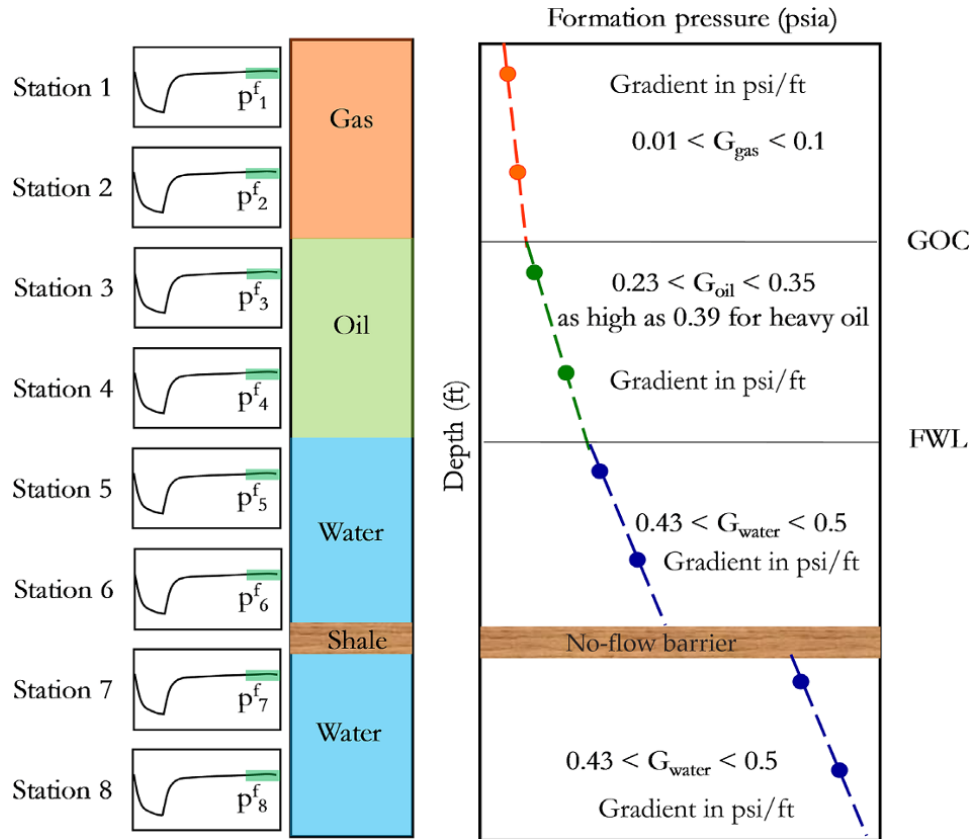


Figure 6.31 Formation pressure log acquisition and analysis.

allow the pressure regime in the separate zones to equilibrate. Formation pressure logs can be used for determination of reservoir fluid type based on the calculated fluid gradient, as shown in Fig. 6.31. The typical range of fluid gradient for different fluid types is discussed in Chapter 1.5.1 and shown in Fig. 6.31. Also, as shown in Fig. 6.31, formation pressure logs can be used to determine reservoir fluid contacts.

Collection of  $p^f$  at different stations (depths), using a dual packer configuration, can be used for pressure gradient and fluid contact analysis. If producing oil in a reservoir with a water zone is of interest, it is advisable that the shallowest point in the packer interval be used for fluid contact analysis to reduce the possibility of completing the well in the water zone.

Therefore, the depth of *buildup final stable* pressure test can be defined as the bottom of the top packer, especially for fluid oil–water contact analysis. Defining the depth of the test as the bottom of the top packer can, however, increase the possibilities of completing well in the gas zone, if a gas zone exists when the interest is producing oil.

**6.2.11.1. Factors Affecting Formation Testing.** Mud filtrate invasion due to hydrostatic mud pressure creates an invaded zone (Fig. 6.32) and also alters the formation pressure around the wellbore. The effect of mud filtrate invasion is more pronounced in a tight formation (low permeability) where there is poor sealing of the mud cake.

*Effect of Mud Filtrate Invasion on Sampling*

Prior to sampling during formation testing, fluid flow from the formation is monitored until contamination due to filtrate invasion reaches acceptable limit. The complication arising from mud filtrate in a fluid sample depends on the type of drilling mud, which can be either oil-based or water-based. In the case of water-based mud, it is easy to separate water from sampled hydrocarbon as both fluids are immiscible. However, in wells drilled with oil-based mud, where the filtrate is miscible with formation hydrocarbon fluid, contamination monitoring can be more challenging. The permeability of the formation also plays a crucial role on invasion of mud filtrate and, hence, sampling. Severe invasion is more pronounced in

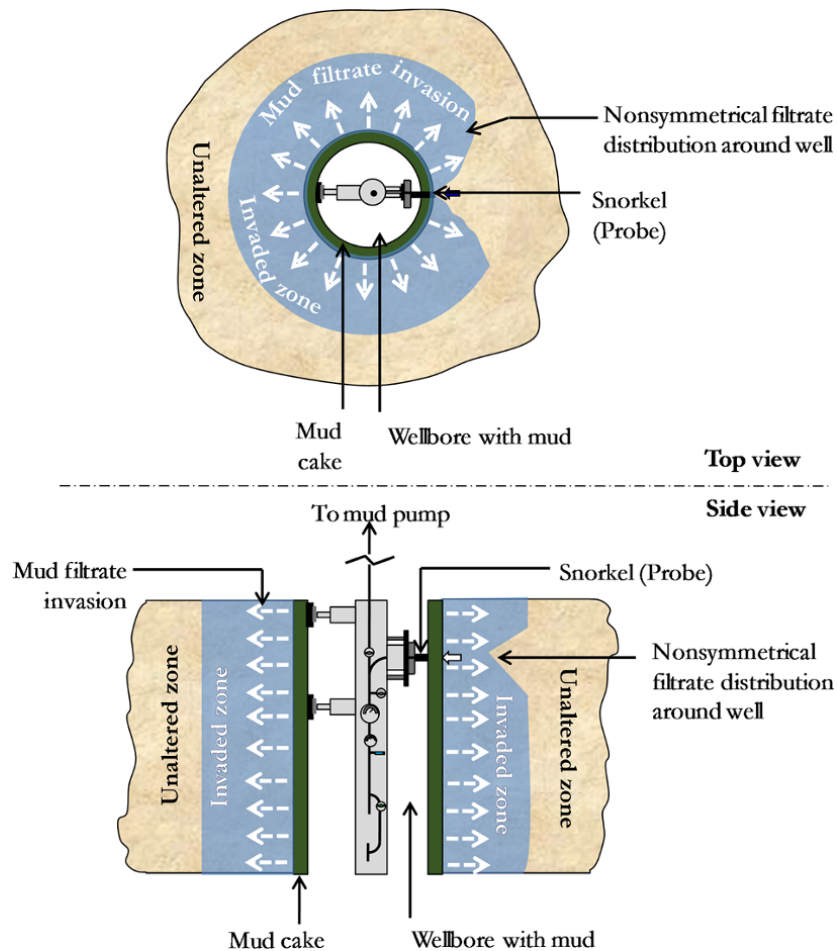


Figure 6.32 Filtrate invasion in formations.

a tight formation (low permeability), where there is poor sealing of the mud cake. Fig. 6.32 shows a schematic of filtrate invasion around the wellbore.

The difference in density between filtrate and formation hydrocarbon can cause the downward vertical movement of filtrate with time after invasion. Gravity causes the filtrate to sink to the bottom of an impermeable zone. This is called the *slumping effect* (Fig. 6.33). Sampling at the top of an impermeable barrier can lead to a long clean-up time or poor sampling. It is always good practice to sample below a nonpermeable zone.

Mud filtrate invasion can also alter the wettability of the formation, thus affecting capillary pressure of the formation. The pressure measured by the formation tester is different from the actual formation pressure by the amount of the capillary pressure [Elshahawi *et al.*, 2000]. The effect of capillary pressure on formation test formation pressure log analysis may reflect in the difference between the calculated free water level from formation testing

(WFT) and the actual FWL (FWL). The difference between calculated free water level and actual free water level due to the effect of capillary pressure effect is summarized using Fig. 6.34 and Fig. 6.35.

## 6.2.12. Analysis of Formation Pressure Log

A robust workflow for analysis of the formation pressure log is summarized in Fig. 6.36. A very important validation during formation pressure log analysis is to always ensure that formation pressure log interpretation is consistent with available well log interpretation and other information where relevant.

**6.2.12.1. Formation Pressure Data Preparation and QC.** Quality control of formation pressure will generally include identification of outlier data and excluding them from analysis. Supercharged formation pressure should

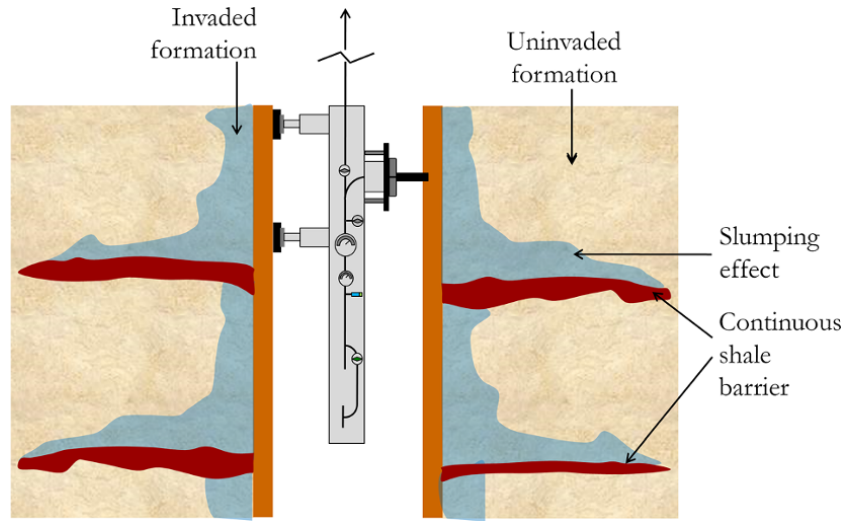


Figure 6.33 Increased filtrate saturation due to impermeable barriers.

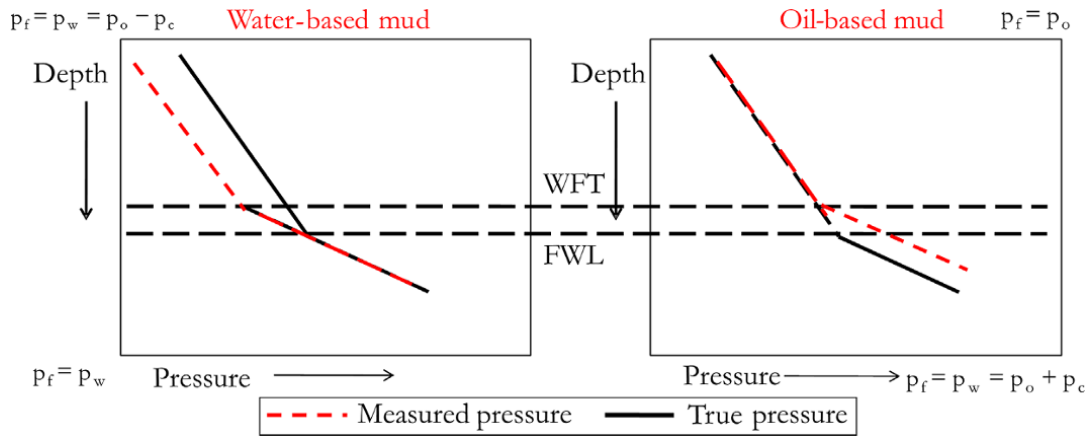


Figure 6.34 Effect of capillary pressure on a water-wet reservoir [Elshahawi et al., 2000].

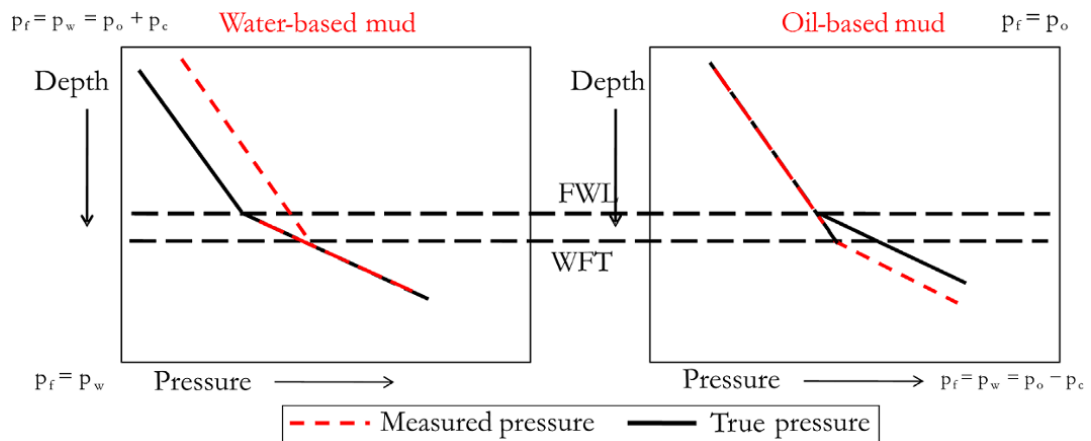


Figure 6.35 Effect of capillary pressure on an oil-wet reservoir [Elshahawi et al., 2000].

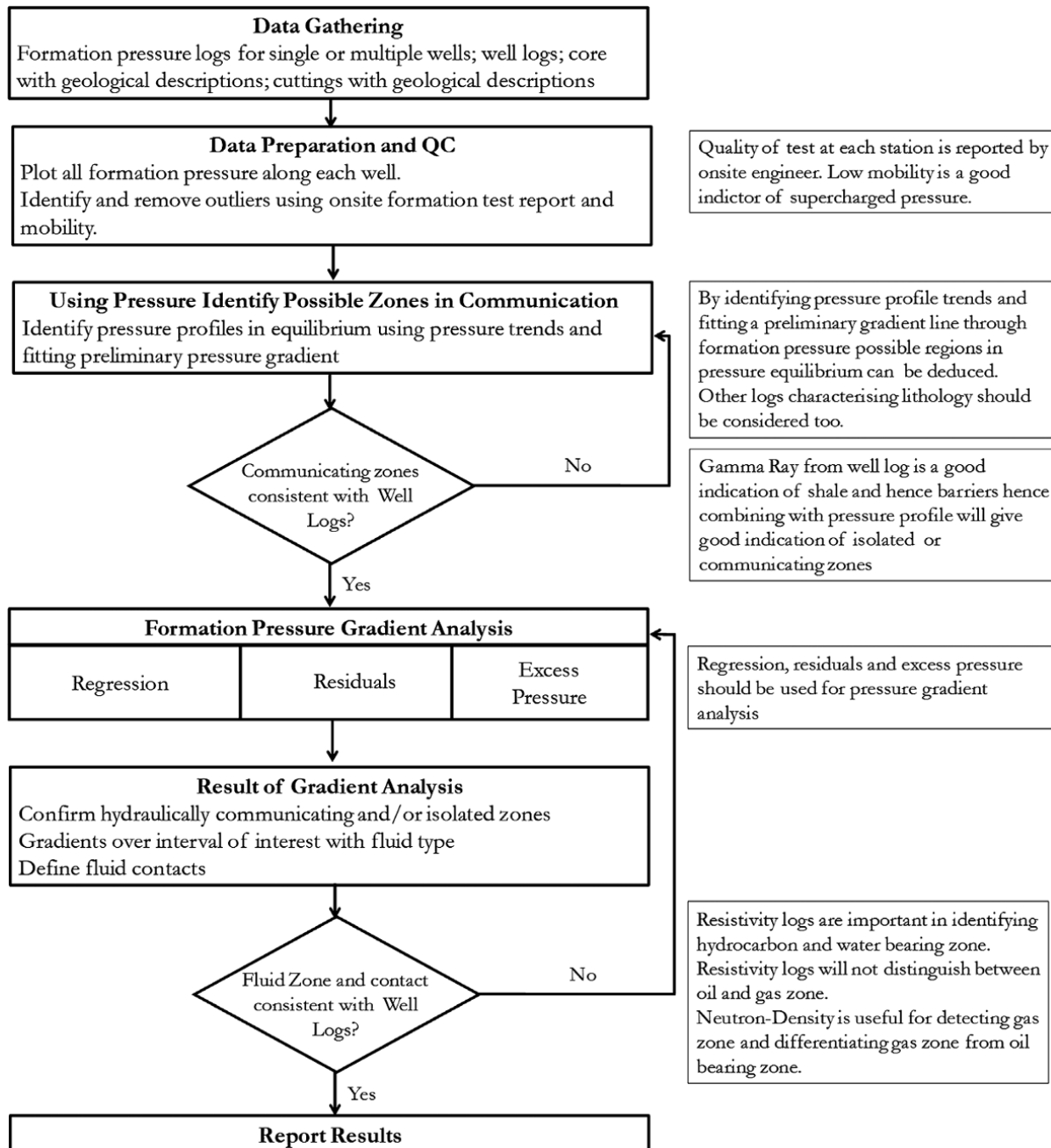


Figure 6.36 Workflow for analysis of formation pressure log.

be identified and removed prior to analysis. Also, low mobility values are an indication of potentially supercharged formation pressure, as low permeability (and hence mobility) is the formation most prone to supercharging.

**6.2.12.2. Formation Pressure Gradient Analysis.** It is always advisable to combine more than one statistical/

mathematical technique to determine fluid gradient line. Different techniques have their strengths and by combining more than one technique diagnosis, analysis, and accuracy of results are improved.

*Simple Linear Regression for Gradient Analysis*

*Simple linear regression* is a statistical method that derives the relationship between an independent (also called predictor or explanatory) variable and a dependent

(also called response or outcome) variable. In formation pressure log analysis, TVDSS is considered an independent variable while pressure is the dependent variable. Formation pressure prediction at a point in the formation can be expressed as:

$$p = G_{\text{fluid}}Z_j + C_{\text{fluid}} \quad (6.27)$$

The predicted formation pressure in equation (6.27) can be represented as a function of the independent variable  $Z_j$  (depth at each station) and model match parameters  $G_{\text{fluid}}$  and  $C_{\text{fluid}}$ :

$$p(Z_j, G_{\text{fluid}}, C_{\text{fluid}})$$

The error of match, which is the difference between actual pressure and predicted pressure for each station, can be expressed as:

$$\epsilon_j = p_j - p(Z_j, G_{\text{fluid}}, C_{\text{fluid}}) \quad (6.28)$$

where  $p_j$  is the measured formation pressure at each depth  $Z_j$ .

The sum of the square of the errors can be then expressed as:

$$\epsilon^2 = \sum_{j=1}^n (\epsilon_j)^2 = \sum_{j=1}^n \left( p_j - p(Z_j, G_{\text{fluid}}, C_{\text{fluid}}) \right)^2 \quad (6.29)$$

Minimizing the sum of the square of errors,  $\epsilon^2$ , which is the objective function, yields  $G_{\text{fluid}}$  and  $C_{\text{fluid}}$  that characterize the formation.

The quotient of variances,  $r^2$ , defines the degree of fit of the measured data to regression model prediction and can be expressed as.

$$r^2 = \frac{\sum_{j=1}^n \left( \bar{p}_j - p(Z_j, G_{\text{fluid}}, C_{\text{fluid}}) \right)^2}{\sum_{j=1}^n \left( p_j - p(Z_j, G_{\text{fluid}}, C_{\text{fluid}}) \right)^2} \quad (6.30)$$

The closer the value of  $r^2$  is to 1, the more acceptable the regression fit model is. However, there are instances when  $r^2$  is close to one and the regression fit model is not correct.

#### Residual Plots

The residual value of a given data point is the difference between the actual value and the model predicted value from simple regression. A perfect match will have a residual of zero for all data points. An acceptable regression match would have residuals distributed vertically around zero value. When residuals do not distribute evenly or randomly vertically but show a clear trend

and/or residual values higher than the acceptable level expected from prediction, there is a need to refine the regression fit. Residuals are useful when the difference in density (and hence fluid gradient) between oil and water is close and determining the contact between such fluid interface is difficult. An example is the case of heavy oil with oil–water contact.

Visual inspection and analysis of the residuals and corresponding plot remain the most valuable method for deciding the need for refinement or accepting a regression fit in formation pressure log analysis. Acceptable values for residuals with pressure as the independent variable and depth as the dependent variable are in the range of  $\pm 2$ , while values above  $\pm 5$  should be refined.

#### Exercise 6.3 Use of Residuals to Refine Regression Fit

Using the formation pressure log data in Table 6.8, determine the fluid gradient and contact(s). Residuals can be used to refine the regression fit where necessary.

#### Discussion on Exercise 6.3.

Fig. 6.37 shows a profile of the formation pressure log.

#### Notes

Without a systematic workflow, it can be misleading to just fit a line through data as shown in Fig. 6.38. In this case, fitting one gradient line through the entire data with  $R^2 = 0.991$  seems to make sense. However, the interpretation is wrong.

#### Solution Steps.

Use the steps in Fig. 6.36 where the necessary information is available.

#### Solution.

Identify and remove poor quality data and outliers as shown in Fig. 6.39.

Outliers identified in Fig. 6.39 will be excluded in formation log analysis and only the good data will be carried forward for analysis. Residuals of good data were determined; they are shown in Fig. 6.40.

The residual plot can be used to refine data to fit two sets of regression as shown in Fig. 6.41.

Examine the residuals of each of the two regression sets (Fig. 6.42).

From Fig. 6.42, formation pressure data in Table 6.8 can be described by two straight-line regression fit, as shown in Fig. 6.43.

An oil gradient with a value of 0.36 psi/ft and water with a gradient of 0.43 psi/ft based on regression line fit can be identified.

FWL is determined by simultaneously solving the pressure equation for oil and water:



**Table 6.8** Formation Pressure Log Data for Exercise 6.3.

Station No.	Zone	Depth (ft) (MDKB*)	Depth (ft) (TVDKB*)	Depth (ft) (TVDSS*)	Hydrocarbon pressure before (psia)	Formation pressure (psia)	Hydrocarbon pressure after (psia)	Pretest mobility (mD/cp)	Comments
1	Mosh	7,616.00	7,616.00	7,543.00	3899.47	3,463.10	3,898.10	1.37	Supercharged
2	Mosh	7,623.00	7,623.00	7,550.00	3,902.46	3,465.10	3,901.73	0.73	Very low mobility, supercharged
3	Mosh	7,628.50	7,628.50	7,555.50	3,905.27	3,465.68	3,904.58	245	Good
4	Mosh	7,635.90	7,635.90	7,562.90	3,909.36	3,468.3,4	3,908.41	107	Good
5	Mosh	7,643.10	7,643.10	7,570.10	3,912.27	3,470.94	3,912.14	98	Good
6	Mosh	7,643.50	7,643.50	7,570.50	3,912.52	3,471.08	3,912.35	214	Good
7	Mosh	7,650.65	7,650.65	7,577.65	3,916.55	3,473.65	3,916.05	434	Good
8	Mosh	7,653.70	7,653.70	7,580.70	3,919.10	3,474.7,5	3,917.63	192	Good
9	Mosh	7,661.00	7,661.00	7,588.00	3,922.02	3,476.10	3,921.41	1.9	Stabilized pressure not reached
10	Mosh	7,670.00	7,670.00	7,597.00	3,926.73		3,926.07		Loss of seal, invalid test
11	Mosh	7,688.13	7,688.13	7,615.13	3,936.81	3,487.51	3,935.46	324	Good
12	Mosh	7,692.23	7,692.23	7,619.23	3,938.32	3,489.27	3,937.59	129	Good
13	Mosh	7,696.00	7,696.00	7,623.00	3,940.08	3,492.60	3,939.54	4	Supercharged
14	Mosh	7,703.50	7,703.50	7,630.50	3,943.65	3,494.12	3,943.43	155	Good

\* MDKB = measured depth relative to kelly bushing; TVDKB = true vertical depth relative to kelly bushing; TVDSS = true vertical depth subsea (Detailed explanation of these various depth is discussed in Section 5.1.1 Well Deviation Survey Calculation).

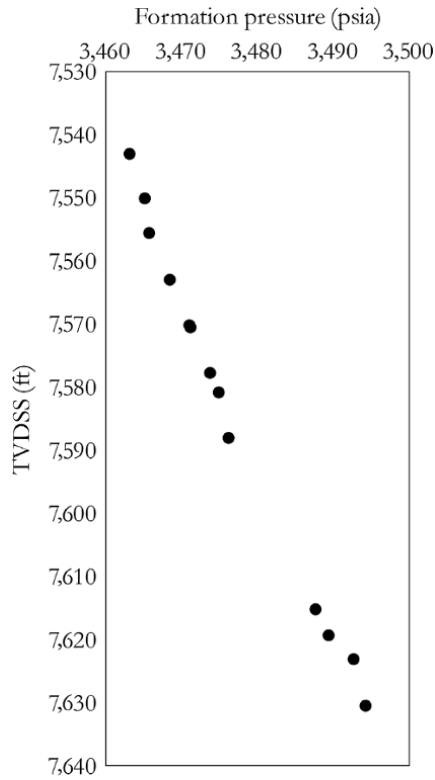


Figure 6.37 Formation pressure log for Exercise 6.3.

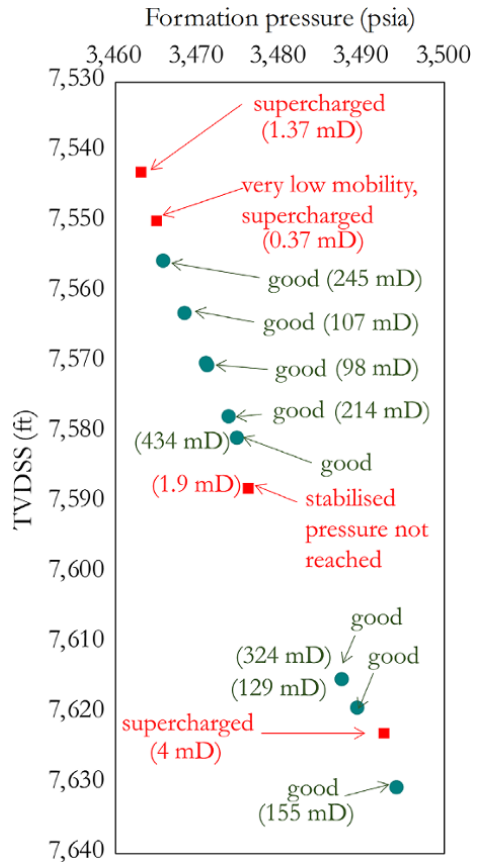


Figure 6.39 Identification of poor quality data and outliers.

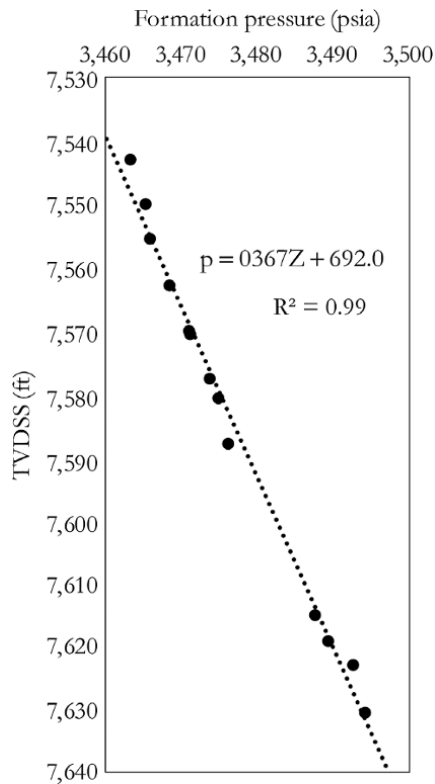


Figure 6.38 Incorrect interpretation of Exercise 6.3.

$$p_{oil} = 0.36Z + 745.7 = p_{water} = 0.43Z + 213$$

$$0.36Z + 745.7 = 0.43Z + 213$$

solving for Z, which is the FWL:

$$Z = FWL = 7,610\text{ft}$$

**6.2.12.3. Excess Pressure.** Excess pressure is the difference between measured pressure and the regression model predicted pressure [Brown, 2003]. The concept of excess pressure is useful in determining contact between the fluid zones with small difference in gradient such as between heavy oil and water.

The steps in the use of excess pressure to detect fluid contact are:

1. Choosing base data, such as the water zone, to create a gradient equation that will be defined as a regression model.
2. Using the regression model, predict pressure for all depths.
3. Finding the excess pressure, which is the difference between the measured pressure and the regression model predicted pressure.

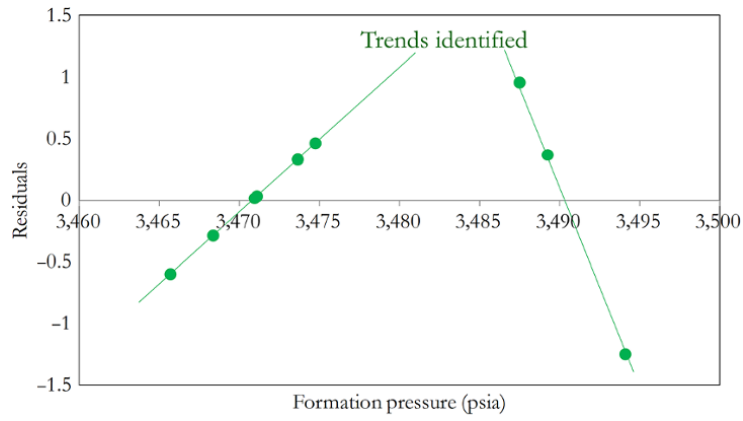


Figure 6.40 Formation pressure residual plot.

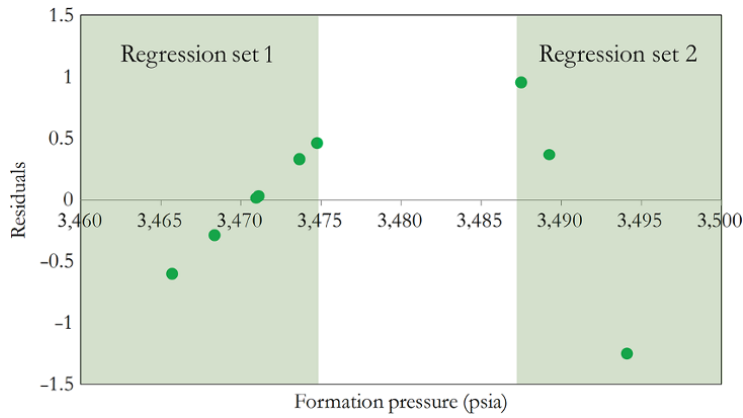


Figure 6.41 Use of residuals to refine formation pressure into two regression lines of fit.

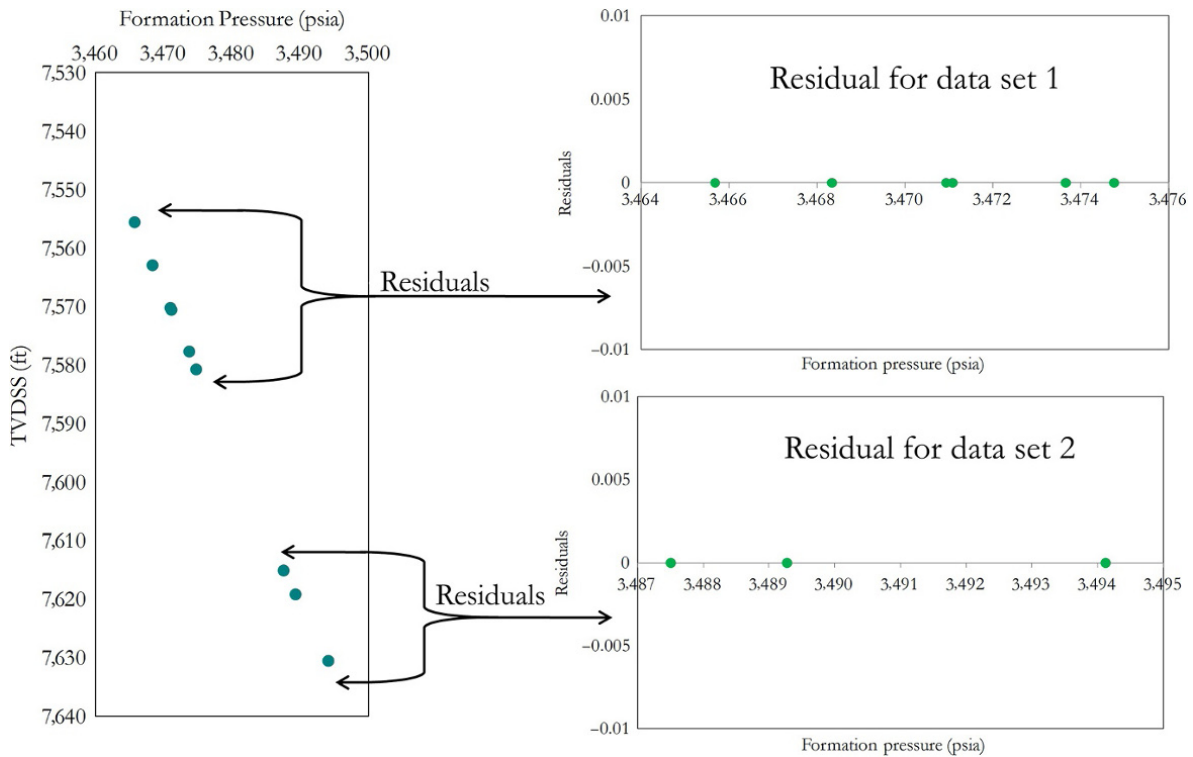


Figure 6.42 Residual plot for data set 1 and 2 showing very low values.

4. Plotting excess pressure with depth and using line fit to determine contact.

**Exercise 6.4** Use of Excess Pressure to Determine Fluid Contact

Use excess pressure to determine the FWL in Exercise 6.3.

More than one set of data can be considered to define the base prediction model.

**Solution.**

Use the deepest station or last two stations to develop a straight-line regression with the water gradient. Where regression model is not based on water, excess pressure will show a trend deviating from the excess pressure of water.

Using the straight-line equation, the water formation pressure equation through the deepest station with valid formation pressure (7,630.50 ft TVDSS) is:

$$p = 0.43Z + 213 \tag{6.31}$$

The calculation of excess pressure for Exercise 6.4 using the water gradient equation is summarized in Table 6.9.

A plot of excess pressure log (excess pressure against TVDSS) is shown in Fig. 6.44.

**Exercise 6.5** Fluid Contact Comparison from Formation Pressure Log and Openhole Log

Compare the fluid contact observed in Exercise 6.4 and the fluid contact from water saturation determined from the resistivity log in Exercise 5.7.

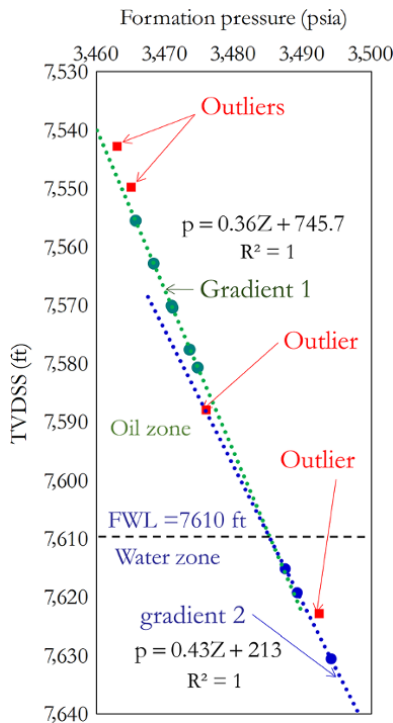


**Figure 6.43** Fluid gradient and contact for Exercise 6.3.

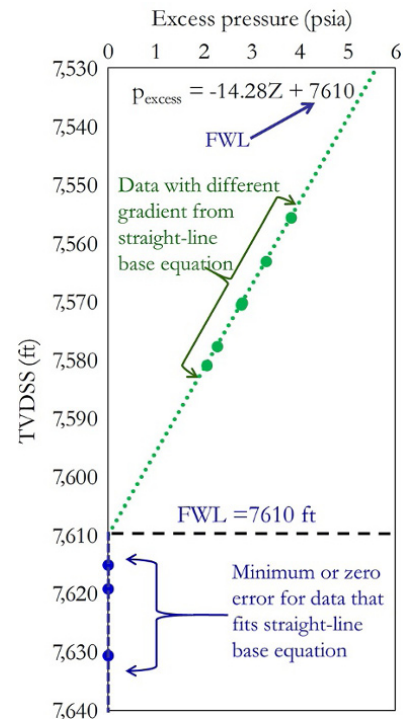


**Figure 6.44** FWL determination using excess pressure plot.

**Table 6.9** Calculation of Excess Pressure for Exercise 6.4 Using the Water Gradient Equation.

Depth (ft) (TVDSS) (good data from Table 6.8)	$p_{\text{measured}}$ (psia) (good data from Table 6.8)	$p_{\text{predicted}}$ (psia) (using equation (6.31))	$\Delta p_{\text{excess}} =$ $p_{\text{measured}} - p_{\text{predicted}}$
7,555.50	3,465.68	3,461.865	3.815
7,562.90	3,468.34	3,465.047	3.297
7,570.10	3,470.94	3,468.143	2.793
7,570.50	3,471.08	3,468.315	2.765
7,577.65	3,473.65	3,471.39	2.2645
7,580.70	3,474.75	3,472.701	2.051
7,615.13	3,87.51	3,487.506	0
7,619.23	3,489.27	3,489.269	0
7,630.50	3,494.12	3,494.115	0

$\Delta p_{\text{excess}}$  is excess pressure;  $p_{\text{measured}}$  is measured formation pressure;  $p_{\text{predicted}}$  is water gradient predicted pressure

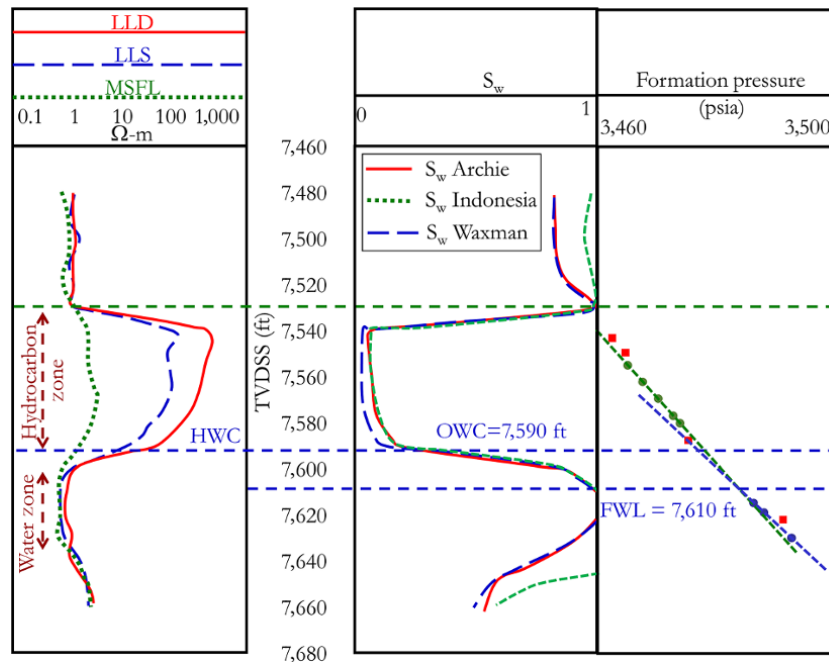


Figure 6.45 OWC from  $S_w$  log and FWL from formation pressure log analysis.

### Solution.

The OWC from  $S_w$  log and the FWL from formation pressure log analysis are shown in Fig. 6.45.

The OWC seen in the openhole log is at 7,590 ft and that from the formation pressure log interpretation is at 7,610 ft. The contact seen in the formation pressure is actually a free water level (FWL) below which water saturation is 100%. Though it is quite common to take the FWL from the formation pressure gradient analysis as the OWC but in correct terms it is actually the free water level.

### REFERENCES

- Brown, A., 2003. Improved interpretation of wireline pressure data. *AAPG Bulletin*, **87**(2), pp. 295–311.
- Desbrandes, R. & Gualdrón, A., 1988. In-Situ Rock Wettability Determination using Wireline Formation Tester Data. *The Log Analyst*, **29**(04), p. 244–252.
- Dong, C. & Hegeman, P., 2003. Advances in Downhole Contamination Monitoring and GOR Measurement of Formation Fluid Samples. *SPWLA 44th Annual Logging Symposium*, 22–25 June, Galveston, Texas.
- Elshahawi, H., Samir, M. & Fathy, K., 2000. Correcting for Wettability and Capillary Pressure Effects on Formation Tester Measurements. *SPWLA 41st Annual Logging Symposium*, 4–7 June, Dallas, Texas.
- Kasap, E., Huang, K., Shwe, T. & Georgi, D., 1999. Formation-Rate-Analysis Technique: Combined Drawdown and Buildup Analysis for Wireline Formation Test Data. *SPE Reservoir Evaluation & Engineering*, **2**(3).
- Moran, J. & Finklea, E., 1962. Theoretical Analysis of Pressure Phenomena of the Wireline Formation Tester. *JPT*, **14**(08).

- Mullins, O. & Schroer, J., 2000. Real-Time Determination of Filtrate Contamination During Openhole Wireline Sampling by Optical Spectroscopy. *Dallas, Texas, SPE Annual Technical Conference and Exhibition*, 1–4 October.
- Raghuraman, B. et al., June 2007. Real Time Downhole pH Measurement Using Optical Spectroscopy. *SPE Reservoir Eval. & Eng.*, **10**(03), pp. 302–311.
- Stewart, G. & Wittmann, M., 1979. *Interpretation of The Pressure Response Of The Repeat Formation Tester*. Las Vegas, Nevada, SPE.
- Whittle, T., Lee, J. & Gringarten, A. C., 2003. Will Wireline Formation Tests Replace Well Test?. *Denver, Colorado, SPE Annual Technical Conference and Exhibition*, 5–8 October.
- Wu, J., Lee, J. & Meister, M., 2006. *A New Invasion Model for Supercharging Estimation*. Veracruz, Mexico, *SPWLA 47th Annual Logging Symposium*, 4–7 June.
- Zefzaf, T. & Fattah, M., 2006. Formation Testing and Sampling Using an Oval Pad in Al Hamd Field, Egypt. *San Antonio, SPE Annual Technical Conference and Exhibition*, 24–27 September.

### BIBLIOGRAPHY

- Agarwal, R., Al-Hussainy, R., and Ramey, H., 1970. An investigation of wellbore storage and skin effect in unsteady liquid flow – I. Analytical treatment. *SPE Journal*, **10**(3), 279–290.
- Akram, A., Halford, F., and Fitzpatrick, A., 1999. A model to predict wireline formation tester sample contamination. *SPE Reservoir Evaluation and Engineering*, **2**(6), 499–505.
- Alpak, F., Elshahawi, H., Hashem, M., and Mullins, O., 2006. *Compositional Modeling of Oil-Based Mud-Filtrate Clean-Up During Wireline Formation Tester Sampling*. Paper SPE 100393, *SPE Annual Technical Conference and Exhibition*, 24–27 September, San Antonio, TX.

- Anderson, W.G., 1987. Wettability literature survey part 5: the effects of wettability on relative permeability. *Journal of Petroleum Technology*, **39**(11), 1453–1468.
- Beardell, M., 1986. *Capillary Pressure Effects on Wireline Formation Tester Surveys*. Edinburgh: Heriot-Watt University.
- Bourdarot, G., 1998. *Well Testing: Interpretation Methods*. Technip et Institut français du pétrole.
- Cañas, J.A., Freitas, E., Andrews, A.B., et al., 2007. *New Downhole Fluid Analysis (DFA) Technologies Supporting Improved Reservoir Management*. Paper SPE 108097, SPE Latin American and Caribbean Petroleum Engineering Conference, 15–18 April, Buenos Aires, Argentina.
- Carnegie, A.J.G., 2007. *Understanding the Pressure Gradient Improves Production from Oil/Water Transition Carbonate Zones*. 48th Annual Logging Symposium, 3–6 June, Austin, TX.
- Carlsaw, H. and Jaeger, J., 1947. *Conduction of Heat in Solids*. London: OUP.
- Chang, Y., Hammond, P.S., and Pop, J., 2008. When should we worry about supercharging in formation-pressure-while-drilling measurements. *SPE Reservoir Evaluation & Engineering*, **11**(1), 165–174.
- Chatas, A.T., 1966. Unsteady spherical flow in petroleum reservoirs. *Journal of the Society of Petroleum Engineers*, **6**(2), 102–114.
- Chin, W. and Proett, M., 2005. *Formation Tester Immiscible and Miscible Flow Modelling for Job Planning Applications*. SPWLA 46th Annual Logging Symposium, 26–29 June New Orleans, LA.
- Dussan, E.B. and Sharma, Y., 1992. Analysis of the pressure response of a single probe formation tester. *SPE Formation Evaluation*, **7**, 151–156.
- Ehlig-Economides, C. and Ayoub, J., 1986. Vertical interference testing across a low-permeability zone. *SPE Formation Evaluation*, **1**, 497–510.
- Eremenko, N.A. and Ul'yanov, A.V., 1960. Oil and gas-bearing sequences of the world, their features and distribution. Regional and structural problems of petroleum geology. *Proceedings of the XXI International Geological Congress*, pp. 19–21.
- Falong, H., Lizhi, X., and Yuanzhong, Z., 2005. *The Minimum Testing Time Determination For Wireline Formation Tester Applying To Low Porosity/Low Permeability Formation*. SPWLA 46th Annual Logging Symposium, 26–29 June, New Orleans, LA.
- Gok, I., Onur, M., Hegeman, P., and Kuchuk, F., 2003. *Effect of an Invaded Zone on Pressure Transient Data from Multi-probe and Packer-Probe Wireline Formation Testers in Single and Multilayer Systems*. SPE Annual Technical Conference and Exhibition, 5–8 October, Denver, CO.
- Hammond, P., 1991. One- and two-phase flow during fluid sampling by wireline tool. *Transport in Porous Media*, **6**, 299–330.
- Kuchuk, F., Ramakrishnan, T., and Dave, Y., 1994. *Interpretation of Wireline Formation Tester Packer and Probe Pressures*. SPE Annual Technical Conference and Exhibition, 25–28 September, New Orleans, LA.
- Mullins, O., 2008. *The Physics of Reservoir Fluids: Discovery Through Downhole Fluid Analysis*. Schlumberger.
- Mullins, O., Cribbs, W.E., Beck, G.F., et al., K., 2001. *Downhole Determination of GOR on Single-Phase Fluids by Optical Spectroscopy*. SPWLA 42nd Annual Logging Symposium, 17–20 June, Houston, TX.
- Pham, T. Al-afaleg, N., Kelder, O., et al., 2005. *Field example of capillary pressure effects on wireline formation tester measurements and OWC estimation in a mixed-wettability oil reservoir*. SPE Middle East Oil and Gas Show and Conference, 12–15 March, Bahrain.
- Radcliffe, D., 1986. An Analysis of the Validity of Permeability Derived from the RFT. M.Eng. Thesis, Heriot-Watt University, Edinburgh.
- Sanni, M., Aluko, O.A., John-Nwoso, E., et al., 2015. *Simulation of Formation Test for Reservoir Characterisation*. EUR-OPEC 2015, 1–4 June, Madrid, Spain.
- Schlumberger, 2008. InSitu Fluid Analyzer – Quantitative fluid measurements at reservoir conditions, in real time. Schlumberger.
- Sparks, D., Smith, R., Massoud-Ansari, S., and Najafi, N., 2004. *Coriolis Mass Flow, Density and Temperature Sensing with a Single Vacuum Sealed Membrane Chip*. Ypsilanti, MI: Integrated Sensing Systems Inc..
- Stewart, G., 2010. *Well Test Design and Analysis*. Tulsa, OK: Pennwell.
- Van Evardingen, A. and Hurst, W., 1949. The application of the Laplace transformation to flow problems in reservoirs. *Journal of Petroleum Technology*, **1**, 305–324.
- Viswanath, D.S., Ghosh, T.K., Prasad, H.L., et al., 2007. *Viscosity of Liquids: Theory, Estimation, Experiment, and Data*. Springer.

# 7

## Fluid Flow in Reservoirs

Equations governing the flow of fluid in reservoirs are very important in various petroleum engineering calculations, which include well test analysis (Chapter 8), reservoir deliverability prediction (Chapters 9 and 12), and well production diagnosis and optimization (Chapter 10).

The transient flow of fluid in petroleum reservoirs is governed by a combination of:

*Darcy's law* (Chapter 2), which defines the flow of fluid through porous media under steady state conditions.

*Continuity equation* (conservation of mass equation), which ensures that mass is conserved when fluid is flowing through porous media, as porous media have fluid storage capacity during fluid flow.

*Equation of State* (PVT relationship), which describes the dependence of flowing fluid properties on pressure change.

The combination of Darcy's law, continuity equation, and equation of state forms the *diffusivity equation* (diffusion equation). The diffusivity equation is a differential equation that governs the transient flow of fluid through a porous medium. Factors that affects the transient flow of fluid in a reservoir include the: condition of the source of flow (well and wellbore); reservoir property; extent of the reservoir; type of reservoir boundary; and fluid type.

### 7.1. DIFFUSIVITY EQUATION

The diffusivity equation describes variation of pressure with time and position in the reservoir. When a vertical well is opened to the flow of reservoir fluid, due to the pressure difference between the reservoir and the wellhead, fluid flows from the reservoir radially into the wellbore and to the surface (Fig. 7.1). Fig. 7.2 shows the

pressure profile in a reservoir when a well is flowing;  $r_w$  is the wellbore radius and  $p_i$  is the initial reservoir pressure.

Equations required for formulation of the diffusivity equation for slightly compressible fluid are:

Darcy's law, which has been described in Chapter 2.2.2 and 2.2.5, and expressed for radial flow as:

$$u = -\frac{k \partial p}{\mu \partial r} \quad (7.1)$$

Continuity equation, which is also called mass conservation equation, and is expressed as:

$$-\frac{\partial(r\rho u)}{\partial r} = r \frac{\partial(\rho\phi)}{\partial t} \quad (7.2)$$

Equations of states for oil and the formation, which are expressed respectively as:

$$c_o = \frac{1}{\rho} \frac{\partial \rho}{\partial p} \quad (7.3)$$

and

$$c_f = \frac{1}{\phi} \frac{\partial \phi}{\partial p} \quad (7.4)$$

where  $c_f$  is formation compressibility,  $c_o$  is compressibility of a slightly compressible fluid like oil,  $\phi$  is porosity, and  $\rho$  is fluid density.

Substituting equation (7.1) into the left-hand side (LHS) of equation (7.2), the continuity equation:

$$-\frac{\partial(r\rho u)}{\partial r} = -\frac{k}{\mu} \frac{\partial}{\partial r} \left( -r\rho \frac{\partial p}{\partial r} \right) = \frac{k}{\mu} \frac{\partial}{\partial r} \left( \frac{\partial \rho}{\partial r} r \frac{\partial p}{\partial r} + \rho \frac{\partial}{\partial r} \left( -r \frac{\partial p}{\partial r} \right) \right) \quad (7.5)$$

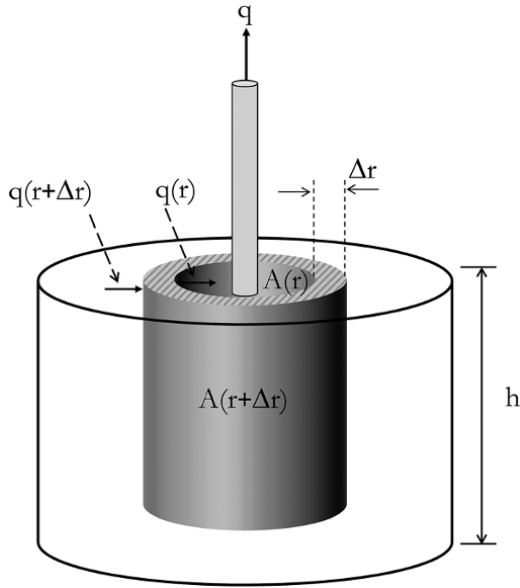


Figure 7.1 Radial flow in a reservoir.

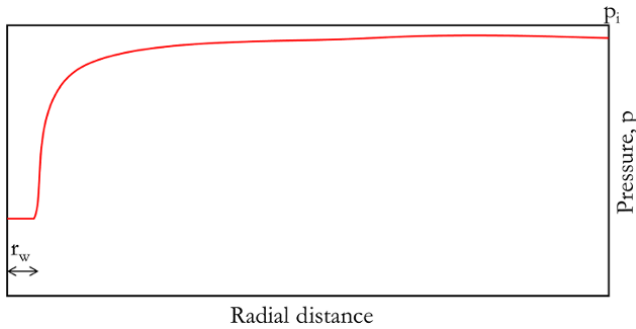


Figure 7.2 Pressure profile in reservoir with a flowing well.

Expressing  $\frac{\partial \rho}{\partial r}$  in the form:

$$\frac{\partial \rho}{\partial r} = \frac{1}{\rho} \frac{\partial \rho}{\partial p} \frac{\partial p}{\partial r} \tag{7.6}$$

From equation (7.3):

$$c_o = \frac{1}{\rho} \frac{\partial \rho}{\partial p}$$

Substituting  $\frac{1}{\rho} \frac{\partial \rho}{\partial p}$  with  $c_o$  into equation (7.6);

$$\frac{\partial \rho}{\partial r} = c_o \rho \frac{\partial p}{\partial r}$$

Substituting  $\frac{\partial \rho}{\partial r}$  into equation (7.5):

$$-\frac{\partial(r\rho u)}{\partial r} = \frac{k}{\mu} \frac{\partial}{\partial r} \left( c_o \rho r \left( \frac{\partial p}{\partial r} \right)^2 + \rho \frac{\partial}{\partial r} \left( r \frac{\partial p}{\partial r} \right) \right) \tag{7.7}$$

For small pressure gradient and fluid compressibility, the terms in bracket above satisfies condition:

$$c_o \rho r \left( \frac{\partial p}{\partial r} \right)^2 \ll \rho \frac{\partial}{\partial r} \left( r \frac{\partial p}{\partial r} \right)$$

Hence, equation (7.7) becomes:

$$-\frac{\partial(r\rho u)}{\partial r} = \frac{k}{\mu} \frac{\partial}{\partial r} \left( 0 + \rho \frac{\partial}{\partial r} \left( r \frac{\partial p}{\partial r} \right) \right) \tag{7.8}$$

The LHS of the continuity equation is thus expressed as:

$$-\frac{\partial(r\rho u)}{\partial r} = \frac{k}{\mu} \rho \frac{\partial}{\partial r} \left( r \frac{\partial p}{\partial r} \right) \tag{7.9}$$

Also, expanding the right-hand side (RHS) of the continuity equation (equation (7.2)):

$$r \frac{\partial(\rho\phi)}{\partial t} = r \left( \rho \frac{\partial \phi}{\partial t} + \phi \frac{\partial \rho}{\partial t} \right)$$

Expressing this further as,

$$r \frac{\partial(\rho\phi)}{\partial t} = r \left( \rho \frac{1}{\phi} \frac{\partial \phi}{\partial p} \phi \frac{\partial p}{\partial t} + \phi \frac{1}{\rho} \frac{\partial \rho}{\partial p} \rho \frac{\partial p}{\partial t} \right)$$

Substituting equations (7.3) and (7.4) into the above:

$$r \frac{\partial(\rho\phi)}{\partial t} = r \left( \rho c_f \phi \frac{\partial p}{\partial t} + \phi c_o \rho \frac{\partial p}{\partial t} \right)$$

$$r \frac{\partial(\rho\phi)}{\partial t} = r \left( (c_f + c_o) \phi \rho \frac{\partial p}{\partial t} \right)$$

The RHS of the continuity equation becomes:

$$r \frac{\partial(\rho\phi)}{\partial t} = r \left( c_t \phi \rho \frac{\partial p}{\partial t} \right) \tag{7.10}$$

where  $c_t$  is the total compressibility and is defined as:  $c_t = c_f + c_o$ .

Equating the LHS to the RHS of the continuity equation, from equation (7.9) and equation (7.10), respectively:

$$\frac{k}{\mu} \rho \frac{\partial}{\partial r} \left( r \frac{\partial p}{\partial r} \right) = r c_t \phi \rho \frac{\partial p}{\partial t}$$

Rearranging above equation:

$$\frac{1}{r} \frac{\partial}{\partial r} \left( r \frac{\partial p}{\partial r} \right) = \frac{\phi \mu c_t}{k} \frac{\partial p}{\partial t} \tag{7.11}$$

Equation (7.11) is the diffusivity equation for a slightly compressible fluid and is applicable to oil reservoirs. Equation (7.11) is a linear equation in terms of pressure (p) with the highest power of the p term being one (1). The linearity of the diffusivity equation makes superposition of solutions in time (well producing/injecting at different starting times) and superposition of solutions in space (well producing/injecting at different locations)



possible for reservoir systems with the same initial reservoir pressure. For a slightly compressible fluid, *hydraulic diffusivity*  $\left(\frac{k}{\phi\mu c_t}\right)$  is independent of pressure. Where *hydraulic diffusivity*  $\left(\frac{k}{\phi\mu c_t}\right)$  is dependent on pressure, equation (7.11) becomes unsuitable, as the diffusivity equation that describes pressure variation in this situation becomes nonlinear in terms of the pressure (p) term. Where the diffusivity equation is nonlinear, the appropriate pseudopressure transforms should be used to linearize the diffusivity equation, as in the case of compressible fluid (gas), multiphase flow, and unconsolidated rock.

Total formation compressibility when the reservoir pore space is occupied by oil, water, and gas is defined as:

$$c_t = c_f + S_o c_o + S_w c_w + S_g c_g \quad (7.12)$$

where:  $c_f$  is the formation compressibility;  $c_o$ ,  $c_w$ , and  $c_g$  are the compressibility for oil, water, and gas, respectively;  $S_o$ ,  $S_w$ , and  $S_g$  are the saturation of oil, water, and gas, respectively, occupying formation pore space.

### Exercise 7.1 Diffusivity Equation Derivation

Derive radial flow diffusivity equation for:

- (i) Single phase, slightly compressible fluid in a homogeneous reservoir.
- (ii) Single phase, ideal gas in a homogeneous reservoir.
- (iii) Single phase, real gas in a homogeneous reservoir.
- (iv) Single phase, incompressible fluid in a homogeneous reservoir.

#### Solution.

(i) For a single-phase, slightly compressible fluid in a homogeneous reservoir

See equation (7.11).

(ii) For a single-phase, ideal gas in a homogeneous reservoir

Using equations (7.1) and (7.2)

$$\text{Darcy's law: } u = -\frac{k}{\mu} \frac{\partial p}{\partial r}$$

and

continuity equation (mass conservation equation):

$$-\frac{\partial(r\rho u)}{\partial r} = r \frac{\partial(\rho\phi)}{\partial t}$$

Defining EOS for areal gas using equation (3.9):

$$pV = ZnRT$$

Making V the subject of the formula:

$$V = \frac{ZnRT}{p} \quad (7.13)$$

Also, the density of gas can be expressed as:

$$\rho = \frac{m}{V} \quad (7.14)$$

where m is mass and V is volume.

Substituting V in equation (7.13) into expression for density in equation (7.14):

$$\rho = \frac{m}{nRTZ}$$

But  $MW = \frac{m}{n}$ , hence the density expression above becomes:

$$\rho = \frac{MW}{RTZ} p \quad (7.15)$$

where MW is molecular weight.

Starting from the continuity equation:

$$-\frac{\partial(r\rho u)}{\partial r} = r \frac{\partial(\rho\phi)}{\partial t}$$

Substituting equations (7.1) and (7.15) into the above:

$$\frac{\partial}{\partial r} \left( \frac{MW}{RT} \frac{pr}{\mu Z} \frac{\partial p}{\partial r} \right) = \frac{r}{k} \frac{MW}{RT} \frac{\partial}{\partial t} \left( \phi \frac{p}{Z} \right) \quad (7.16)$$

$$\frac{\partial}{\partial r} \left( \frac{MW}{RT} \frac{pr}{\mu Z} \frac{\partial p}{\partial r} \right) = \frac{r}{k} \frac{MW}{RT} \left( \frac{\partial \phi}{\partial t} \frac{p}{Z} + \phi \frac{\partial}{\partial t} \left( \frac{p}{Z} \right) \right)$$

$$\frac{\partial}{\partial r} \left( \frac{MW}{RT} \frac{pr}{\mu Z} \frac{\partial p}{\partial r} \right) = \frac{r}{k} \frac{MW}{RT} \phi \left( \frac{1}{\phi} \frac{\partial \phi}{\partial t} \left( \frac{p}{Z} \right) + \frac{\partial}{\partial t} \left( \frac{p}{Z} \right) \right) \quad (7.17)$$

The  $\frac{\partial}{\partial t} \left( \frac{p}{Z} \right)$  term in equation (7.17) can be expressed as:

$$\frac{\partial}{\partial t} \left( \frac{p}{Z} \right) = \left( \frac{\partial p}{\partial t} \frac{1}{Z} - \frac{p}{Z^2} \frac{\partial Z}{\partial t} \right)$$

$$\frac{\partial}{\partial t} \left( \frac{p}{Z} \right) = \frac{\partial p}{\partial t} \left( \frac{1}{Z} - \frac{p}{Z^2} \frac{\partial Z}{\partial t} \frac{1}{\partial p} \right)$$

$$\frac{\partial}{\partial t} \left( \frac{p}{Z} \right) = \frac{\partial p}{\partial t} \left( \frac{1}{Z} - \frac{p}{Z^2} \frac{\partial Z}{\partial p} \right)$$

$$\frac{\partial}{\partial t} \left( \frac{p}{Z} \right) = \frac{\partial p}{\partial t} \left( \frac{p}{Z} \right) \left( \frac{1}{p} - \frac{1}{Z} \frac{\partial Z}{\partial p} \right)$$

Substituting  $c_g = \frac{1}{p} - \frac{1}{Z} \frac{\partial Z}{\partial p}$  from equation (3.17) into the above equation:

$$\frac{\partial}{\partial t} \left( \frac{p}{Z} \right) = \frac{\partial p}{\partial t} \left( \frac{p}{Z} \right) c_g$$

Substituting  $\frac{\partial}{\partial t} \left( \frac{p}{Z} \right)$  from the above into equation (7.17):

$$\frac{MW}{RT} \frac{\partial}{\partial r} \left( \frac{pr}{\mu Z} \frac{\partial p}{\partial r} \right) = \frac{r}{k} \frac{MW}{RT} \phi \left( \frac{1}{\phi} \frac{\partial \phi}{\partial t} \left( \frac{p}{Z} \right) + \frac{\partial p}{\partial t} \left( \frac{p}{Z} \right) c_g \right)$$

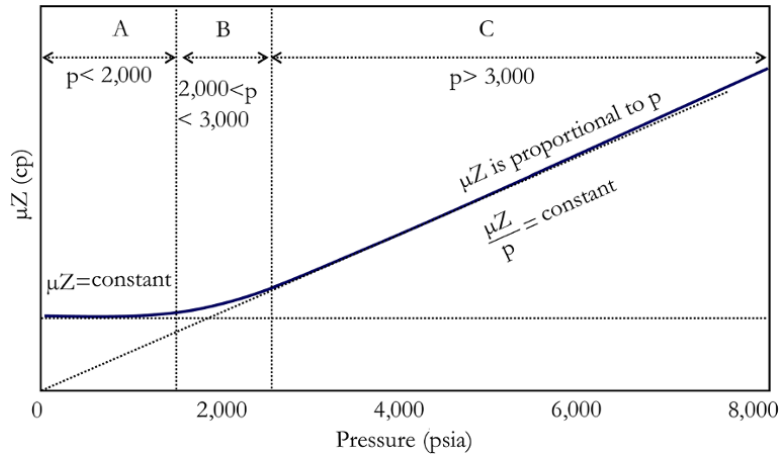


Figure 7.3 Dependence of  $\mu Z$  on pressure.

$$\begin{aligned} \frac{\partial}{\partial r} \left( \frac{pr}{\mu Z} \frac{\partial p}{\partial r} \right) &= \frac{r}{k} \phi \frac{\partial p}{\partial t} \left( \frac{p}{Z} \right) \left( \frac{1}{\phi} \frac{\partial \phi}{\partial t} \frac{\partial t}{\partial p} + c_g \right) \\ \frac{\partial}{\partial r} \left( \frac{pr}{\mu Z} \frac{\partial p}{\partial r} \right) &= \frac{r}{k} \phi \frac{\partial p}{\partial t} \left( \frac{p}{Z} \right) \left( \frac{1}{\phi} \frac{\partial \phi}{\partial p} + c_g \right) \\ \frac{\partial}{\partial r} \left( \frac{pr}{\mu Z} \frac{\partial p}{\partial r} \right) &= \frac{r}{k} \phi \frac{\partial p}{\partial t} \left( \frac{p}{Z} \right) (c_f + c_g) \\ \frac{\partial}{\partial r} \left( \frac{pr}{\mu Z} \frac{\partial p}{\partial r} \right) &= \frac{r}{k} \phi \frac{\partial p}{\partial t} \left( \frac{p}{Z} \right) c_t \\ \frac{\partial}{\partial r} \left( r \frac{p}{\mu Z} \frac{\partial p}{\partial r} \right) &= r \frac{\phi \mu c_t}{k} \frac{p}{\mu Z} \frac{\partial p}{\partial t} \end{aligned} \quad (7.18)$$

$\mu Z$  can be considered constant up to 2,000 psia (Fig. 7.3).

Thus, equation (7.18) becomes:

$$\frac{\partial}{\partial r} \left( r p \frac{\partial p}{\partial r} \right) = r \frac{\phi \mu c_t}{k} p \frac{\partial p}{\partial t}$$

Substituting  $p \frac{\partial p}{\partial r} = \frac{1}{2} \frac{\partial p^2}{\partial r}$  into the above equation to become:

$$\frac{\partial}{\partial r} \left( r \frac{\partial p^2}{\partial r} \right) = r \frac{\phi \mu c_t}{k} \frac{\partial p^2}{\partial t} \quad (7.19)$$

Equation (7.19) defines diffusivity for single-phase ideal gas in a homogeneous reservoir with a small gradient everywhere within the reservoir and is valid for pressure up to 2,000 psia.

(iii) For single-phase, real gas in homogeneous reservoir

Defining transform (pseudopressure) to linearize the nonlinear expression equation (7.17).

$$m(p) = 2 \int_{p_0}^p \frac{p}{\mu(p)Z(p)} dp \quad (7.20)$$

where  $p_0$  is any low reference pressure.

From equation (7.20):

$$\frac{\partial m(p)}{\partial p} = \frac{2p}{\mu Z}$$

also

$$\frac{\partial m(p)}{\partial r} = \frac{\partial m(p)}{\partial p} \frac{\partial p}{\partial r} = \frac{2p}{\mu Z} \frac{\partial p}{\partial r}$$

Making  $\frac{\partial p}{\partial r}$  the subject of the formula:

$$\frac{\partial p}{\partial r} = \frac{\mu Z}{2p} \frac{\partial m(p)}{\partial r} \quad (7.21)$$

and

$$\frac{\partial m(p)}{\partial t} = \frac{2p}{\mu Z} \frac{\partial p}{\partial t}$$

Making  $\frac{\partial p}{\partial t}$  the subject of the formula:

$$\frac{\partial p}{\partial t} = \frac{\mu Z}{2p} \frac{\partial m(p)}{\partial t} \quad (7.22)$$

Substituting  $\frac{\partial p}{\partial r}$  and  $\frac{\partial p}{\partial t}$  in terms of  $m(p)$  from equations (7.21) and (7.22), respectively, into equation (7.18):

$$\frac{\partial}{\partial r} \left( r \frac{p}{\mu Z} \frac{\partial p}{\partial r} \right) = r \frac{\phi \mu c_t}{k} \frac{p}{\mu Z} \frac{\partial p}{\partial t}$$

$$\frac{\partial}{\partial r} \left( r \frac{p}{\mu Z} \frac{\mu Z}{2p} \frac{\partial m(p)}{\partial r} \right) = r \frac{\phi \mu c_t}{k} \frac{p}{\mu Z} \frac{\mu Z}{2p} \frac{\partial m(p)}{\partial t}$$

$$\frac{1}{r} \frac{\partial}{\partial r} \left( r \frac{\partial m(p)}{\partial r} \right) = \frac{\phi \mu c_t}{k} \frac{\partial m(p)}{\partial t} \quad (7.23)$$

Equation (7.23) defines the radial diffusivity equation for a single-phase real gas in a homogeneous reservoir and is valid at all pressures. The importance of equation (7.23) is that it retains the form similar to equation (7.11). Gas flow in porous media can be described in a similar way to oil, however, in terms of pseudopressure ( $m(p)$ ).

(iv) For a single-phase, incompressible fluid in a homogeneous reservoir

Incompressible fluid means density and volume is constant, hence equations (7.2)–(7.4) vanish and the only relevant equation is Darcy's law.

Hence:

$$\begin{aligned} u &= -\frac{k \partial p}{\mu \partial r} \\ \frac{q}{2\pi r h} &= -\frac{k \partial p}{\mu \partial r} \\ \frac{q}{2\pi h} \frac{\partial r}{r} &= -\frac{k}{\mu} \partial p \end{aligned}$$

Integrating the radial distance between the defined external reservoir radial distance  $r_e$  with external reservoir pressure  $p_e$  and the wellbore radius  $r_w$  with flowing bottomhole pressure  $p_{wf}$ :

$$\begin{aligned} \frac{q}{2\pi h} \int_{r_w}^{r_e} \frac{\partial r}{r} &= -\frac{k}{\mu} \int_{p_{wf}}^{p_e} \partial p \\ \frac{q}{2\pi h} \ln \left( \frac{r_e}{r_w} \right) &= -\frac{k}{\mu} (p_e - p_{wf}) \\ \frac{q}{2\pi h r} &= \frac{k (p_e - p_{wf})}{r \mu \ln \left( \frac{r_w}{r_e} \right)} \\ u &= \frac{k (p_e - p_{wf})}{r \mu \ln \left( \frac{r_w}{r_e} \right)} \end{aligned} \quad (7.24)$$

The diffusivity equation for a single-phase, incompressible fluid in a homogeneous reservoir is, in fact, Darcy's law.

### 7.1.1. Diffusivity Equation for Gas

The diffusivity equation for gas flow has been derived in Exercise 7.1 (Qii) and (Qiii). These are the radial diffusivity equation for isothermal single-phase ideal gas flow in a homogeneous reservoir (equation (7.19)) and isothermal single-phase real gas flow in a homogeneous reservoir (equation (7.23)).

Ideal gas behavior with constant  $\mu Z$  is valid for pressure up to 2,000 psia (Fig. 7.3). Hence, when reservoir pressure

is less than 2,000, the pseudopressure integral (equation (7.20)) becomes:

$$m(p) = 2 \int_{p_0}^p \frac{p}{\mu(p)Z(p)} dp = \frac{2}{\mu Z} \int_{p_0}^p p dp = \frac{p^2 - p_0^2}{\mu Z} \quad (7.25)$$

However, above 2,000 psia, the ideal gas assumption is not valid and gas pseudopressure defined by equation (7.20) should be used without the ideal gas law assumption with constant  $\mu Z$ .

Also, when pressure is above 3,000 psia,  $\frac{\mu Z}{p}$  becomes constant (Fig. 7.3) and the pseudopressure integral becomes:

$$m(p) = 2 \int_{p_0}^p \frac{p}{\mu(p)Z(p)} dp = \frac{2p}{\mu Z} \int_{p_0}^p dp = \frac{(p - p_0)p_i}{\mu Z} \quad (7.26)$$

From Fig. 7.3:

*Region A:* when  $p < 2,000$  psia,  $\mu Z = \text{constant}$  and the simplified pseudopressure integral given by equation (7.25) can be used.

*Region B:* when  $2,000 < p < 3,000$  psia there is no approximation and equation (7.20) should be used without simplification.

*Region C:* when  $p > 3,000$  psia,  $\frac{\mu Z}{p} = \text{constant}$  and the simplified pseudopressure integral given by equation (7.26) can be used.

where  $\mu$  and  $Z$  are available as a function of pressure, equation (7.20) should always be used as it is valid for all pressure ranges for single-phase gas flow.

### 7.1.2. Normalized Pseudopressure

*Normalized pseudopressure* is a more convenient way of presenting pseudopressure because the unit of pseudopressure is  $\text{psi}^2/\text{cp}$  and the scale can be in the order of magnitude of  $10^6$  in unit of  $\text{psi}/\text{cp}$ . The pseudopressure integral equation (7.20) can be multiplied by  $\frac{\mu Z}{2p}$  at average reservoir pressure or initial reservoir pressure to convert the unit to  $\text{psi}$  and scale pseudopressure to the pressure range. Hence, the normalized pseudopressure is defined as:

$$m_n(p) = \left( \frac{\mu Z}{2p} \right)_{p_i} \int_{p_0}^p \frac{2p}{\mu(p)Z(p)} dp \quad (7.27)$$

or

$$m_n(p) = \left( \frac{\mu Z}{2p} \right)_p \int_{p_0}^p \frac{2p}{\mu(p)Z(p)} dp \quad (7.28)$$

where  $p_i$  is initial reservoir pressure and  $\bar{p}$  is average reservoir pressure.

For a compressible fluid, diffusivity or flow equation can be solved by substituting  $m_n(p)$  directly into the appropriate equation for a slightly compressible fluid then solving the equation

If equation (7.27) is used for the reservoir parameter calculation, the fluid property corresponding to initial reservoir pressure must be used. However, if equation (7.28) is used for the reservoir parameter calculation, the fluid property corresponding to average reservoir pressure must be used.

## 7.2. SOLUTION OF DIFFUSIVITY EQUATION

Diffusivity equations derived for different fluid types are differential equations. The diffusivity equation can be solved for three boundary conditions described as: initial condition, which is pressure at the beginning of test; inner boundary condition, which is flow rate at the well; and outer boundary condition, which is pressure at the reservoir boundaries.

Pressure response in a reservoir can be described as transient (unsteady state) when pressure change with time due to flow is a function of location and time in the reservoir. This is characteristic of a reservoir when pressure change has not diffused to full reservoir boundaries and is defined as:

$$\frac{\partial p}{\partial t} = f(r, t) \quad (7.29)$$

Pseudosteady or semi-steady describes the situation where pressure change with time is constant. This is characteristic of a depleting reservoir and occurs when diffusing pressure change reaches full no-flow reservoir boundaries. Pseudosteady state response is expressed as:

$$\frac{\partial p}{\partial t} = \text{Constant} \quad (7.30)$$

The steady state condition describes the situation where pressure change with time is zero. The measured flowing well bottomhole pressure against time will show a zero slope during a steady state flow regime. A steady state flowing pressure response occurs when the diffusing pressure change reaches a constant pressure boundary (strong aquifer or gas cap). Steady state response is expressed as:

$$\frac{\partial p}{\partial t} = 0 \quad (7.31)$$

### 7.2.1. Mathematical Methods for Solving the Diffusivity Equation

Laplace transforms have been a useful way of solving the diffusivity equation for specific flow regimes or entire flow regimes (interpretation models). Solution in the

Laplace domain can then be inverted analytically or numerically using the *Stehfest numerical Laplace inversion* [Stehfest, 1970]. The *Den Iseger algorithm* [Iseger, 2006] is becoming another popular numerical Laplace inversion technique that has proved to be powerful. The numerical Laplace inversion is the backbone of solving simple and complex well test models. Other methods for solving the diffusivity equation include: use of *Green's function*; *Boltzmann transformation*, and *Henkel transforms*.

**7.2.1.1. Radial Flow Equation.** For a reservoir with homogeneous behavior, pressure diffusion is described by equation (7.11):

$$\frac{1}{r} \frac{\partial}{\partial r} \left( r \frac{\partial p}{\partial r} \right) = \frac{\phi \mu c_t}{k} \frac{\partial p}{\partial t}$$

Defining the *diffusivity constant* (also called hydraulic diffusivity),  $\eta$ , as:

$$\eta = \frac{k}{\phi \mu c_t}$$

Using Boltzmann's transformation:

$$s = \frac{r^2}{4\eta t} = \frac{\phi \mu c_t r^2}{4kt}$$

Taking the partial derivative of  $s$  with respect to  $t$ :

$$\frac{\partial s}{\partial t} = -\frac{\phi \mu c_t r^2}{4kt^2} = -\frac{1}{t} s \quad (7.32)$$

and  $s$  with respect to  $r$ :

$$\frac{\partial s}{\partial r} = \frac{\phi \mu c_t r}{2kt} = \frac{2}{r} s \quad (7.33)$$

Expressing the diffusivity equation in terms of  $s$ :

$$\frac{1}{r} \frac{\partial}{\partial s} \left( r \frac{\partial p}{\partial s} \frac{\partial s}{\partial r} \right) \frac{\partial s}{\partial r} = \frac{\phi \mu c_t}{k} \frac{\partial p}{\partial s} \frac{\partial s}{\partial t}$$

Substituting equations (7.32) and (7.33) into the above:

$$\frac{1}{r} \frac{\partial}{\partial s} \left( r \frac{\partial p}{\partial s} \frac{2}{r} s \right) \frac{2}{r} s = -\frac{\phi \mu c_t}{k} \frac{\partial p}{\partial s} \frac{1}{t}$$

$$2 \frac{s}{r^2} \frac{\partial}{\partial s} \left( 2s \frac{\partial p}{\partial s} \right) = -\frac{\phi \mu c_t r^2}{4kt} \frac{\partial p}{\partial s} \frac{4}{r^2 s}$$

$$2 \frac{s}{r^2} \frac{\partial}{\partial s} \left( 2s \frac{\partial p}{\partial s} \right) = -s \frac{\partial p}{\partial s} \frac{4}{r^2 s}$$

$$\frac{2s}{r^2} \frac{\partial}{\partial s} \left( 2s \frac{\partial p}{\partial s} \right) = -\frac{4s^2}{r^2} \frac{\partial p}{\partial s}$$

$$\frac{\partial}{\partial s} \left( s \frac{\partial p}{\partial s} \right) = -s \frac{\partial p}{\partial s}$$

Using  $\frac{dp}{ds} = p'$ , the above equation becomes:

$$p' + s \frac{dp'}{ds} = -sp'$$

$$\frac{dp'}{p'} = -\frac{(s+1)}{s} ds$$

$$\frac{dp'}{p'} = -\left(\frac{1}{s} + 1\right) ds$$

$$\ln p' = -\ln s - s + A$$

$$\ln p' = -\ln s + \ln(e^{-s}) + \ln(e^A)$$

$$p' = e^A \frac{e^{-s}}{s}$$

Defining  $B = e^A$ :

$$p' = B \frac{e^{-s}}{s}$$

Using the inner boundary condition to determine the constant of integration  $B$ :

$$u = \frac{q}{A} = \frac{k \partial p}{\mu \partial r}$$

$$\lim_{r \rightarrow 0} \frac{\partial p}{\partial r} = \frac{q\mu}{2\pi r k h}$$

$$\lim_{r \rightarrow 0} r \frac{\partial p}{\partial r} = \frac{q\mu}{2\pi k h} = r \frac{dp}{ds} \frac{\partial s}{\partial r}$$

From equation (7.33),  $r \frac{\partial s}{\partial r} = 2$ , hence the above equation becomes:

$$\frac{q\mu}{2\pi k h} = 2s \frac{dp}{ds}$$

$$\frac{q\mu}{4\pi k h} = s \frac{dp}{ds}$$

But  $p' = \frac{dp}{ds} = B \frac{e^{-s}}{s}$  hence:

$$s \frac{dp}{ds} = B e^{-s}$$

Therefore:

$$\frac{q\mu}{4\pi k h} = B e^{-s}$$

As  $r \rightarrow 0$ ,  $s \rightarrow 0$ :

$$B = \frac{q\mu}{4\pi k h}$$

Hence:

$$p' = \frac{q\mu}{4\pi k h} \frac{e^{-s}}{s} \quad (7.34)$$

Integrating the LHS of equation (7.34) between  $p_i$  (initial pressure) and  $p$  at time  $t$  and the RHS of equation (7.34) between the limits of  $t=0$  ( $s \rightarrow \infty$ ) and  $t$  ( $s = x$ ):

$$\int_{p_i}^p dp = \frac{q\mu}{4\pi k h} \int_{\infty}^x \frac{e^{-s}}{s} ds$$

$$p(r, t) = p_i - \frac{q\mu}{4\pi k h} \int_{x = \frac{\phi \mu c_t r^2}{4kt}}^{\infty} \frac{e^{-s}}{s} ds \quad (7.35)$$

$\int_{\infty}^x \frac{e^{-s}}{s} ds$  is an exponential integral is denoted as  $E_i(x)$

If  $x < 0.01$ :

$$E_i(x) \approx -\ln(\gamma x)$$

where  $\gamma = 1.781$ .

Equation (7.35) at wellbore ( $r = r_w$ ) becomes:

$$p(r, t) = p_{wf} = p_i + \frac{q\mu}{4\pi k h} \ln \frac{\gamma \phi \mu c_t r_w^2}{4kt}$$

$$p_{wf} = p_i - \frac{q\mu}{4\pi k h} \ln \frac{4kt}{\gamma \phi \mu c_t r_w^2}$$

Adding the skin effect (well condition for damage or stimulation):

$$p_{wf} = p_i - \frac{q\mu}{4\pi k h} \ln \left( \frac{4kt}{\gamma \phi \mu c_t r_w^2} + 2S \right) \quad (7.36)$$

In engineering oil field (EOF) units equation (7.36) becomes:

$$p_i - p_{wf} = 162.6 \frac{qB\mu}{kh} \left( \log t + \log \frac{k}{\phi \mu c_t r_w^2} - 3.23 + 0.87S \right) \quad (7.37)$$

In EOF units,  $k$  is permeability in mD, length is in ft,  $\mu$  is viscosity in cp,  $p$  is pressure in psia,  $q$  is rate in stb/d,  $B$  is the formation volume factor in bbl/stb,  $c_t$  is total compressibility in  $\text{psi}^{-1}$ , and  $\phi$  is porosity in fraction.

Equation (7.37) shows that a plot of  $p_{wf}$  against  $\log t$  will show a straight line within the period where radial homogeneous dominates the flow in the reservoir. The slope of the straightline section, which corresponds to radial homogeneous flow,  $m_{RF}$ , is:

$$m_{RF} = 162.6 \frac{qB\mu}{kh} \quad (7.38)$$

### 7.3. BOUNDARY CONDITIONS DURING PRESSURE DIFFUSION IN RESERVOIRS

The pressure variations at the well can be used to determine reservoir properties within the zone of diffusing pressure change. At the beginning of the test the pressure measured at the well reflects the reservoir properties in

the vicinity of the well. As the compressible zone diffuses further into the reservoir, reservoir behavior dominates measured pressure at the well. As reservoir boundaries manifest later, measured bottomhole pressure is dominated by boundary characteristics. The effects of the well–reservoir–boundary system on measured bottomhole pressure are generally grouped as *near wellbore effects* (which occur at early time), *reservoir behavior* (which occurs at mid-time), and *boundary effect* (which occur at late time). Properties that characterizes each of these regimes can be calculated separately using *specialized straight-line* analysis or together using *well test interpretation model* (Chapter 8.5). A practical workflow for well test analysis is to determine well, reservoir, and boundary parameters using a combination of straight-line (*specialized straight-line*) methods, derivative, and overall pressure history match (Chapter 8). Table 7.1 shows important factors that affect early time (near wellbore storage), middle time (reservoir behavior), and late times (boundary effect).

**7.3.1. Near Wellbore Effects**

Early time bottomhole pressure response is dominated by wellbore storage (combined effect of wellbore volume and fluid compressibility), skin, well stimulation, effect of well orientation, and architecture. Near wellbore effects that can be characterized using pressure transient analysis are summarized in the first column of Table 7.1.

**7.3.1.1. Wellbore Storage (WBS) Effect.** During a WBS dominated flow regime, measured rate at the surface is

due to volumetric expansion of the fluid in the wellbore during drawdown (well flowing) and due to volumetric compression during buildup (well shut-in) (Fig. 7.4) and can be expressed as:

$$q_{sf} = q_{wh} - c_w V_w \left. \frac{\partial p_w}{\partial t} \right|_{r=r_w} \tag{7.39}$$

where  $q_{sf}$  is sandface rate,  $q_{wh}$  is the measured rate at the wellhead,  $p_w$  is the measured bottomhole pressure that can be flowing ( $p_{wf}$ ) or shut-in ( $p_{ws}$ ),  $c_w$  is compressibility of fluid in the wellbore,  $V_w$  is wellbore volume, and  $t$  is time.

Equation (7.39) can express as:

$$q_{sf} = q_{wh} - c_w V_w \frac{dp_w}{dt} \tag{7.40}$$

but

$$C = c_w V_w \tag{7.41}$$

where  $C$  is the wellbore storage coefficient and  $c_w$  is compressibility of fluid in the wellbore.

Substituting  $C = c_w V_w$  from equation (7.41) into equation (7.40):

$$q_{sf} = q_{wh} - C \frac{dp_w}{dt}$$

expressed further as:

$$q_{wh} - q_{sf} = C \frac{dp_w}{dt}$$

During drawdown in storage dominated flow, as shown in Fig. 7.4,  $q_{wh} > q_{sf}$ .

**Table 7.1** Transient Flow Regime Characterization.

Near wellbore effects (at early times)	Reservoir behavior (at middle times)	Boundary effects (at late times)
Wellbore storage	Homogeneous	Constant pressure
Skin	Heterogeneous: double porosity;	No-flow
Fractures: low and high conductivity fractures	double permeability; composite	Leaky
Partial penetration (limited entry)	(linear and radial); multilayered	Boundary distance
Well orientation: vertical, inclined or horizontal	reservoirs.	Boundary geometry

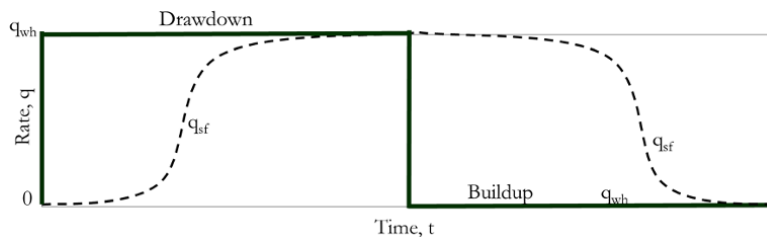


**Figure 7.4** Wellbore storage effect during drawdown and buildup.

Hence, the above equation reduces to:

$$q_{wh} = C \frac{dp_w}{dt}$$

In EOF units this becomes:

$$q_{wh} = 24C \frac{dp_w}{dt}$$

During WBS dominated flow regime, the drawdown and buildup pressure signal can be related to elapsed time in EOF units as:

$$\Delta p_w = \frac{qB\Delta t}{24C} \tag{7.42}$$

where the rate,  $q$ , is the same as  $q_{wh}$ , which is the rate measured at well head for surface controlled rate.

For a well with loading liquid,

$$C = c_w V_w = \left( -\frac{\Delta V_w}{V_w} \frac{1}{\Delta p} \right) V_w = -\frac{\Delta V_w}{\Delta p} = \frac{V_u h_f}{\rho g h_f} = \frac{V_u}{\rho g}$$

where  $V_w$  is wellbore volume,  $\Delta V_w$  is the change in volume of liquid in the well due to the change in liquid level,  $\Delta p$  is the change in hydrostatic pressure due to liquid loading, and  $h_f$  is the height of liquid loaded in the well

The wellbore storage coefficient for a well with the liquid level in EOF units from the above equation is, therefore:

$$C = 144 \frac{V_u}{\rho \left( \frac{g}{g_c} \right)} \tag{7.43}$$

where  $V_u$  is the volume of the well per unit length (bbl/ft) and  $\rho$  is fluid density (lb/ft<sup>3</sup>).

Equation (7.42) is called the specialized straight-line equation for a well test dominated by WBS and can be expressed as:

$$\Delta p = \frac{qB\Delta t}{24C}$$

A plot of  $\Delta p$  against  $\Delta t$  during WBS dominated flow for either drawdown or build will yield a straight line through the intercept 0,0 on the  $x$ - and  $y$ -axes with a slope of  $m_{WBS}$ , which is then used to determine the wellbore storage coefficient ( $C$ ) as shown in equation:

$$C = \frac{qB}{24m_{WBS}} \text{ bbl/psi} \tag{7.44}$$

**Exercise 7.2** Wellbore Storage Effect Calculation using Well Volume and Fluid Property

A vertical well was tested using a drill string of 5-inch ID in a 100-ft hydrocarbon column normally pressured reservoir with a water gradient of 0.44 psi/ft. Determine the wellbore storage coefficient for a:

- (i) reservoir with 40 °API oil and oil–water contact (OWC) at 5,000 ft;
- (ii) reservoir with 40 °API oil and OWC at 15,000 ft;
- (iii) reservoir with 0.1 psi/ft gas gradient with gas–water contact (GWC) at 5,000 ft;
- (iv) reservoir with 0.1 psi/ft gas gradient and GWC at 15,000 ft.

Oil properties are:  $R_s = 2345$  scf/stb and  $\gamma_g = 0.623$  at reservoir temperature of (T) of 300 °F

Use equation (3.45) for the oil compressibility calculation and the ideal gas compressibility equation (equation (3.18)) for gas.

**Solution Steps.**

- Step 1:* determine volume per unit length for the well.
- Step 2:* determine the formation pressure equation using fluid gradient or API.
- Step 3:* determine fluid compressibility at agiven pressure using equation (3.45) shown here for oil compressibility:

$$c_o = \frac{5R_s + 17.2T - 1180\gamma_g + 12.61\gamma_{API} - 1433}{p \times 10^5}$$

and equation (3.18) for gas:

$$c_g = \frac{1}{p}$$

where  $p$  is formation pressure and can be taken at the middle of the formation, which can be calculated from the depth of hydrocarbon water contact (HWC) using:

$$h_{mid} = z_{HWC} - \frac{h}{2} \tag{7.45}$$

where  $h_{mid}$  is the depth of the middle of the formation,  $h$  is formation thickness, and  $z_{HWC}$  is the depth of hydrocarbon water contact.

- Step 4:* determine the wellbore storage coefficient ( $C$ ) using the relationship between the compressibility of fluid in the wellbore ( $c_w$ ) and the volume of the wellbore ( $V_w$ ), which is equation (7.41):  $C = c_w V_w$

**Solution.**

$$r = 5/2 \text{ in} = 0.20833 \text{ ft.}$$

$$\text{Volume per unit length, } V_u:$$

$$V_u = \pi r^2 = \pi(0.20833)^2 = 0.13635 \text{ ft}^2$$

*Oil gradient calculation*

Using equation (3.35):

$$API^\circ = \frac{141.5}{SG} - 131.5$$

$$SG = \frac{141.5}{API^\circ + 131.5}$$

$$SG = \frac{141.5}{40 + 131.5} = 0.8251$$

Oil gradient ( $G_{oil}$ ) is hence:

$$G_{oil} = SG_{oil} \times 0.433 \text{ psi/ft} \quad (7.46)$$

where  $SG_{oil}$  is the specific gravity of oil and 0.433 is the pressure gradient for freshwater in psi/ft:

$$G_{oil} = 0.8251 \times 0.433 = 0.357 \text{ psi/ft}$$

Hence, oil with 40 °API has a gradient of 0.357 psi/ft  
*Formation pressure calculation*

Formation pressure in the water zone from equation (1.1) is:

$$p_{water} = G_{water}z_{water} + C_{water}$$

where  $C_{water} = 14.7$  psia for a normally pressured aquifer.

Formation pressure in the hydrocarbon zone from equations (1.2) and (1.3) is:

$$p_{HC} = G_{HC}z_{HC} + C_{HC} \quad (7.47)$$

At the hydrocarbon water contact (HWC),  $p_{HC} = p_{water}$ .

Using the water gradient equation, the pressure at the HWC ( $p_{HWC}$ ) can thus be determined:

$$p_{HWC} = p_{HC} = p_{water} = G_{water}z_{HWC} + C_{water}$$

$$p_{HWC} = 0.44z_{HWC} + 14.7 \quad (7.48)$$

The constant of the gradient equation for fluid hydrocarbon ( $C_{HC}$ ) can be determined by substituting  $p_{HC} = p_{HWC}$  and  $z_{HC} = z_{HWC}$  into equation (7.47) and making  $C_{HC}$  the subject of the formula.

$$C_{HC} = p_{HWC} - G_{HC}z_{HWC} \quad (7.49)$$

Note:  $p_{HC} = p_{HWC}$  at  $z_{HC} = z_{HWC}$  as the hydrocarbon and water zones are in pressure equilibrium at the hydrocarbon–water contact (HWC), as discussed in Chapter 1.5.1.

With  $C_{HC}$  determined, using equation (7.49), the hydrocarbon formation pressure can be determined at any depth of interest using equation (7.47).

Table 7.2 summarizes the solution to Exercise 7.2.

NB: the wellbore storage coefficient (storage effect) for oil for surface shut-in is about 0.01 bbl/psi, for gas it is about 0.05 bbl/psi, and well loading with liquid is about 0.05 bbl/psi. In order to reduce storage effect, downhole shut-in is recommended. The wellbore storage coefficient can be reduced to as low as 0.0001 bbl/psi for an oil well with downhole shut-in.

**Exercise 7.3** Wellbore Storage Effect Calculation from Pressure–Rate Data

Using the drawdown pressure–rate data provided in Table 7.3, determine the wellbore storage coefficient, given:  $q_{oil} = 150$  stb/d;  $r_w = 0.33$  ft;  $\phi = 0.2$ ;  $h = 50$  ft;  $B_o = 1.5$  rb/stb;  $\mu_{oil} = 0.5$  cp; and  $c_t = 5 \text{ E-5 psi}^{-1}$ .

**Solution Steps.**

- Step 1:* determine the drawdown pressure  $\Delta p$  signal ( $p_{wf}(0) - p_{wf}(t)$ ) and elapsed time  $\Delta t$  ( $t - t_0$ ) for the data points provided.
- Step 2:* plot  $\Delta p$  against  $\Delta t$  on a Cartesian scale.
- Step 3:* inspect the early part of  $\Delta p$  against  $\Delta t$  to determine the start and end of WBS, which will be characterized by a straight line.
- Step 4:* fit the early part of the data characterizing WBS with a straight line through the intercept 0,0 on the  $x$ - and  $y$ -axes.
- Step 5:* determine the slope of  $m_{WBS}$ .

**Table 7.2** Solution to Exercise 7.2.

	Ex 7.2 (i)	Ex 7.2 (ii)	Ex 7.2 (iii)	Ex 7.2 (iv)
Reservoir fluid	Oil	Oil	Gas	Gas
$z_{HWC}$ (ft)	5,000	15,000	5,000	15,000
$p_{HWC}$ (psia) using equation (7.48)	2,214.7	6,614.7	2,214.7	6,614.7
Hydrocarbon gradient (psi/ft): using equation (7.46) for oil and explicit values given for gas	0.357	0.357	0.1	0.1
Gradient equation constant, $C_{HC}$ (psia) using equation (7.49)	429.7	1,259.7	1,714.7	5,114.7
$p_{HC}$ at mid-reservoir (psia) using equation (7.47) with mid-reservoir defined by equation (7.45)	2,196.85	6,596.85	2,209.7	6,609.7
HC compressibility, $c_{HC}$ ( $\text{psi}^{-1}$ ), using equation (3.45) for oil and equation (3.18) for gas	6.93E–05	2.31E–05	4.53E–04	1.51E–04
Well length up to reservoir top, $h_{top}$ (ft) at [ $h_{top} = z_{HWC} - 100$ ]	4,900	14,900	4,900	14,900
Volume of wellbore ( $V_{well}$ ) [ $V_{well} (\text{ft}^3) = V_u \times h_{top}$ ]	668.13	2,031.67	668.13	2,031.67
Converting wellbore volume from $\text{ft}^3$ to bbl: $V_{well}$ (bbl)	119	361.86	119.00	361.86
C (wellbore storage coefficient) = $c_{HC} \times V_{well}$ (bbl/psi)	0.01	0.01	0.054	0.055



**Table 7.3** Pressure–Rate History for Exercise 7.3.

Time (hr)	Rate (stb/D)	Pressure (psia)	Time (hr)	Rate (stb/D)	Pressure (psia)	Time (hr)	Rate (stb/D)	Pressure (psia)	Time (hr)	Rate (stb/D)	Pressure (psia)
0.0000	150	5,000.00	1.1514	150	4,628.36	1,000.0010	0	4,405.47	1,001.1514	0	4,776.48
0.0013	150	4,999.17	1.5264	150	4,581.77	1,000.0013	0	4,405.67	1,001.5264	0	4,823.06
0.0018	150	4,998.90	2.0236	150	4,541.90	1,000.0018	0	4,405.94	1,002.0236	0	4,862.92
0.0023	150	4,998.55	2.6827	150	4,510.82	1,000.0023	0	4,406.30	1,002.6827	0	4,894.00
0.0031	150	4,998.07	3.5565	150	4,488.78	1,000.0031	0	4,406.77	1,003.5565	0	4,916.03
0.0041	150	4,997.45	4.7149	150	4,474.38	1,000.0041	0	4,407.40	1,004.7149	0	4,930.42
0.0054	150	4,996.62	6.2506	150	4,465.31	1,000.0054	0	4,408.22	1,006.2506	0	4,939.46
0.0072	150	4,995.53	8.2864	150	4,459.36	1,000.0072	0	4,409.32	1,008.2864	0	4,945.40
0.0095	150	4,994.08	10.9854	150	4,454.94	1,000.0095	0	4,410.76	1,010.9854	0	4,949.78
0.0126	150	4,992.17	14.5635	150	4,451.21	1,000.0126	0	4,412.67	1,014.5635	0	4,953.48
0.0168	150	4,989.65	19.3070	150	4,447.77	1,000.0168	0	4,415.19	1,019.3070	0	4,956.87
0.0222	150	4,986.34	25.5955	150	4,444.48	1,000.0222	0	4,418.51	1,025.5955	0	4,960.09
0.0295	150	4,981.98	33.9322	150	4,441.28	1,000.0295	0	4,422.86	1,033.9322	0	4,963.21
0.0391	150	4,976.28	44.9843	150	4,438.14	1,000.0391	0	4,428.57	1,044.9843	0	4,966.24
0.0518	150	4,968.84	59.6362	150	4,435.03	1,000.0518	0	4,436.01	1,059.6362	0	4,969.19
0.0687	150	4,959.18	79.0604	150	4,431.96	1,000.0687	0	4,445.67	1,079.0604	0	4,972.07
0.0910	150	4,946.72	104.8113	150	4,428.91	1,000.0910	0	4,458.12	1,104.8113	0	4,974.88
0.1207	150	4,930.79	138.9496	150	4,425.88	1,000.1207	0	4,474.05	1,138.9496	0	4,977.59
0.1600	150	4,910.65	184.2070	150	4,422.85	1,000.1600	0	4,494.19	1,184.2070	0	4,980.20
0.2121	150	4,885.55	244.2053	150	4,419.84	1,000.2121	0	4519.29	1,244.2053	0	4,982.69
0.2812	150	4,854.85	323.7458	150	4,416.83	1,000.2812	0	4549.99	1,323.7458	0	4,985.04
0.3728	150	4,818.20	429.1934	150	4,413.83	1,000.3728	0	4586.64	1,429.1934	0	4,987.23
0.4942	150	4,775.78	568.9866	150	4,410.83	1,000.4942	0	4629.06	1,568.9866	0	4,989.23
0.6551	150	4,728.54	754.3120	150	4,407.84	1,000.6551	0	4676.30	1,754.3120	0	4,991.05
0.8685	150	4,678.43	1,000.0000	150	4,404.84	1,000.8685	0	4726.40	2,000.0000	0	4,992.65

Step 6: calculate the wellbore storage coefficient (C) using equation (7.44).

**Solution.**

Table 7.4 shows the values of Δt and Δp with Δt = t – t<sub>0</sub> and Δp = p<sub>wf</sub>(0) – p<sub>wf</sub>(t).

t is the time corresponding to a given flowing bottom-hole pressure p (or p<sub>wf</sub>(t)) and t<sub>0</sub> is the beginning of the flow period with the corresponding initial bottomhole flowing pressure (p<sub>wf</sub>(0)).

The specialized straight-line plot for the WBS is shown in Fig. 7.5.

From the slope of the specialized straight-line plot of WBS (Fig. 7.5), the wellbore storage coefficient is calculated using equation (7.44):

$$C = \frac{qB}{24m_{WBS}}$$

$$C = \frac{qB}{24m_{WBS}} = \frac{150 \times 1.5}{24 \times 614.62} = 0.015$$

C = 0.015 bbl/psi

**7.3.1.2. Skin Effect.** Skin factor (S) is a dimensionless parameter that characterizes well conditions. Damaged

**Table 7.4** Elapsed Time and Drawdown Pressure.

Δt (hr) = t <sub>i</sub> – 0	Δp (psi) = 5000 – p
0	0
0.0013	0.83
0.0018	1.10
0.0023	1.45
0.0031	1.93
0.0041	2.55
0.0054	3.38
0.0072	4.47
0.0095	5.92
0.0126	7.83
0.0168	10.35
0.0222	13.66
0.0295	18.02
0.0391	23.72
0.0518	31.16
0.0687	40.82
0.0910	53.28
0.1207	69.21
0.1600	89.35
...	...

wells have more flow restrictions at the reservoir–wellbore interface than undamaged wells, hence there is a greater pressure drop. Damaged wells are characterized by a positive skin (S > 0). Stimulated wells have improved flow

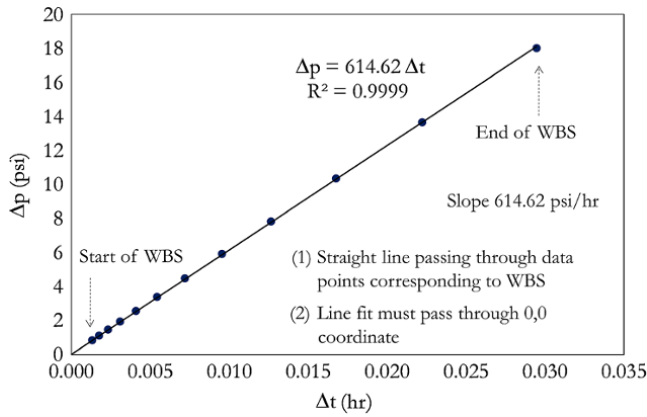


Figure 7.5 Specialized straight-line plot for WBS.

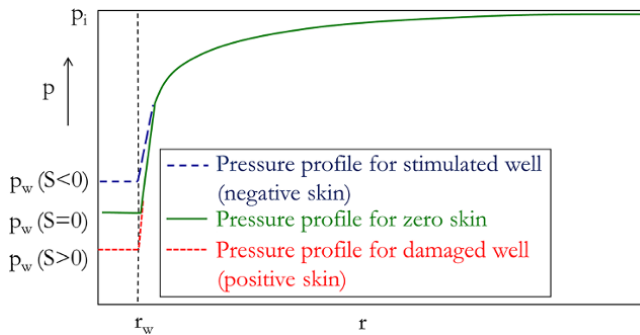


Figure 7.6 Skin effect and pressure drop near wellbore.

conditions at the reservoir wellbore–interface and pressure drop is less compared to unstimulated wells, as shown in Fig. 7.6. Stimulated wells are characterized by a negative skin ( $S < 0$ ). A zero skin represents a wellbore condition with the same properties as the reservoir (undamaged and unstimulated).

Skin effect can be related to additional pressure drop around the wellbore due to the presence of the skin and expressed as:

$$S = \frac{kh}{141.2qB\mu} \Delta p_{skin} \tag{7.50}$$

$\Delta p_{skin}$  is the additional pressure drop in the vicinity around the wellbore due to the presence of the skin.

In the case where a damaged or stimulated wellbore can be described as a circular zone around the wellbore, then additional pressure can be expressed as:

$$\Delta p_{skin} = p_{w,S} - p_{w,S=0} = \frac{141.2qB\mu}{k_s h} \ln \frac{r_s}{r_w} - \frac{141.2qB\mu}{kh} \ln \frac{r_s}{r_w} \tag{7.51}$$

where  $p_{w,s}$  is bottomhole pressure with skin and  $p_{w,s=0}$  is bottomhole pressure without skin,  $k_s$  is the permeability of the altered zone (damaged or stimulated) near the well bore,  $k$  is reservoir permeability,  $h$  is reservoir thickness,  $r_s$

is the radial distance of the damaged or stimulated zone away from the well,  $r_w$  is wellbore radius,  $B$  is the formation volume factor of fluid, and  $q$  is the production or test rate

Substituting  $\Delta p_{skin}$  from equation (7.50) into equation (7.51):

$$S = \left( \frac{k}{k_s} - 1 \right) \ln \frac{r_s}{r_w} \tag{7.52}$$

From equation (7.52), when the altered zone around the wellbore is damaged  $k_s < k$  and the calculated  $S$  will be positive; when the altered zone around the wellbore is stimulated  $k_s > k$  and the calculated  $S$  will be negative; and when the wellbore region is unaltered  $k_s = k$  and the calculated  $S$  will be zero.

The permeability of the altered zone (damaged or stimulated) can be expressed from equation (7.52) as:

$$k_s = \frac{k}{\left( 1 + \frac{S}{\ln \frac{r_s}{r_w}} \right)} \tag{7.53}$$

Also, equation (7.52) can be expressed in terms of the radius of the altered zone as:

$$r_s = r_w e^{\frac{S}{(k/k_s - 1)}} \tag{7.54}$$

*Equivalent wellbore radius* is an important concept in well testing that will be used in describing different wellbore conditions and defined as  $r_s$  when  $k_s \rightarrow \infty$ , which is the well condition with no pressure loss. Hence, from equation (7.54), equivalent wellbore radius becomes:

$$r_{we} = r_w e^{-S} \tag{7.55}$$

**Exercise 7.4** Skin Effect Calculation Based on Fluid Loss

A reservoir with a wellbore of radius of 0.35 ft and depth of filtrate invasion of 3.05 ft was determined using openhole resistivity logs. Assume a radial saturation distribution of filtrate around the well with discontinuity at the filtrate–oil interface in the reservoir (Fig. 7.7). Special core analysis of a core sample, considered representative of the reservoir, showed 65% reduction in permeability due to the effect of filtrate invasion.

Calculate the skin effect due to the drilling operation (mechanical skin).

**Solution Steps.**

Step 1: determine  $r_s$ , which is  $r_s = d_i + r_w$ .

Step 2: determine  $\frac{k}{k_s}$  using percentage  $k$  reduction.

Step 3: calculate  $S$  using equation (7.54).

**Solution.**

$$r_s = d_i + r_w$$

$$r_s = 3.05 + 0.35 = 3.4 \text{ ft}$$

For 65% reduction in permeability near wellbore:

$$k_s = k \left( 1 - \frac{65}{100} \right) = 0.35k$$

Therefore:

$$\frac{k}{k_s} = \frac{k}{0.35k} = \frac{1}{0.35}$$

Substituting values of  $r_s$  and  $\frac{k}{k_s}$  into equation (7.52):

$$S = \left( \frac{1}{0.35} - 1 \right) \ln \frac{3.4}{0.35} = 4.2$$

$$S = 4.2$$

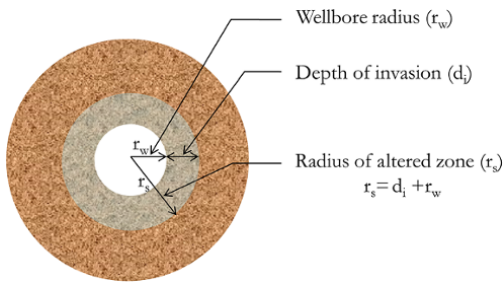


**Figure 7.7** Near wellbore region for effective skin calculation.

The total skin effect is the net effect due to a contribution of factors that reduce pressure drop near the wellbore (stimulation and/or flow enhancement) and those that increase pressure drop near the wellbore (damage and/or flow impairments). Since individual skin components that make up total skin can either be positive or negative, total skin, too, can either be positive or negative.

A positive skin effect is due to well completion, formation damage (mechanical skin), non-Darcy flow, and limited entry. A negative skin effect is due to well stimulation treatments (e.g. acidizing or hydraulic fracture), natural reservoir fissures, well deviation, and horizontal wells (under most conditions). Total skin ( $S_{Total}$ ) can, therefore, be defined as:

$$S_{Total} = S_{Mechanical} + S_{Fluid} + S_{completion} + S_{Geology} + S_{Rate\ Dependent} \quad (7.56)$$

Table 7.5 is a summary of the components of the skin in equation (7.56), where S is skin and the subscript defines skin components.

**7.3.1.3. Well Fractures.** Vertical hydraulic fractures (Fig. 7.8) are designed to increase well-reservoir contact. Hydraulic fracturing is a common approach for improving the productivity of oil and gas producing from damaged wells or wells producing from low-permeability reservoirs.

Hydraulic fracturing involves pumping high-pressure fluid with propping agents into the formation to exceed the rock strength and open a fracture in the rock. The propping agents are designed to prevent the fracture from

**Table 7.5** Summary of Skin Effect Type.

Skin type	Definition	Typical/Limits of values
Mechanical	Due to actual damage or well stimulation.	Minimum of -2 for acidizing (acidizing rarely reduces skin below zero). Can be as high as 20 in a severely damaged well due to significant filtrate loss.
Fluid	Due to gas bank in volatile oil reservoirs below bubble point pressure; gas condensate in gas wells below bubble point pressure; presence of kill fluid around wellbore region etc.	+2-20
Completion	Due to well-reservoir interaction, such as: limited entry effect; inclined well effect; horizontal well and fracture.	Minimum of -6 in massive hydraulic infinite-conductivity fracture. As high as 100 for poor gravel pack. High as 600 for limited entry with low penetration ratio.
Geological effect	Due to the geological characteristic of formation, such as natural fissure in reservoirs; reservoir anisotropy.	-4 to 0 for well intersecting natural fissures.
Rate dependent skin	Due to turbulence, common with gas phase flow.	5-25

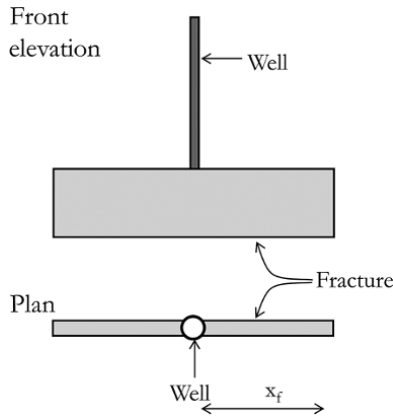


Figure 7.8 Front and plan view of vertical hydraulic fracture.

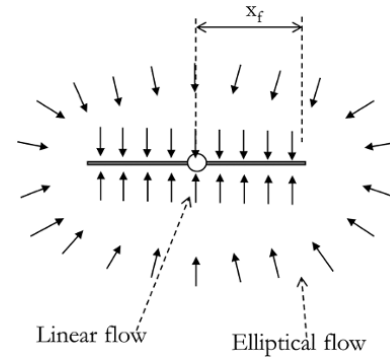


Figure 7.9 Flow behavior around an infinite conductivity fracture.

closing. Fracture height is dependent on the strength of the cap and base rock, hence it is often difficult to control fracture height.

Vertical hydraulic fractures can generally be described either as an *infinite conductivity fracture* (high conductivity fracture) or a *finite conductivity fracture* (low conductivity fracture).

In a infinite conductivity fracture (high conductivity fracture), the width of the fracture is small relative to fracture length. Hence, the fracture behave like a “pipe” with infinite permeability, hence there is no pressure within the fracture.

In a finite conductivity fracture (low conductivity fracture), the fracture has significant width relative to fracture length. Finite conductivity fractures have finite permeability and are characterized by pressure drop.

*Infinite Conductivity Fracture (ICF)*

ICF is characterized by linear flow, (LF) (Fig. 7.9) after a short-lived storage effect.

The pressure signal (pressure change during drawdown or buildup) during an ICF dominated flow period can be expressed as:

$$\Delta p = 4.06 \frac{qB}{hx_f} \sqrt{\frac{\mu}{\phi c_t k}} \sqrt{\Delta t}, \text{ Gringarten } et al. 1974 \quad (7.57)$$

From equation (7.57), a plot of  $\Delta p$  against  $\Delta t^{1/2}$  will yield a straight line for an ICF dominated flow regime due to linear flow (Fig. 7.10), with a slope  $m_{LF}$  that can be used to calculate fracture half length ( $x_f$ ) using equation (7.58).

$$x_f = 4.06 \frac{qB}{hm_{LF}} \sqrt{\frac{\mu}{\phi c_t k}} \quad (7.58)$$

Equations (7.57) and (7.58) are straight-line characteristic equations for ICF.

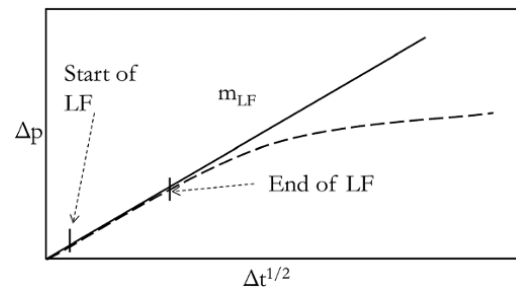


Figure 7.10 Specialized straight-line plot for an infinite conductivity fracture.

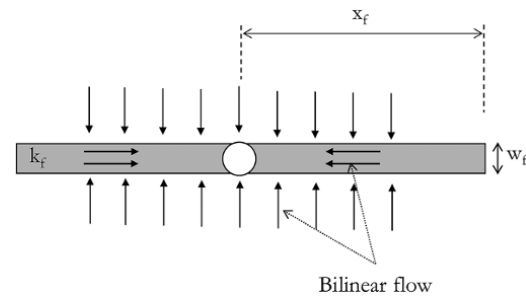


Figure 7.11 Flow behavior around a finite conductivity fracture.

*Finite Conductivity Fracture (FCF)*

A FCF is characterized by bilinear flow, (BLF) (Fig. 7.11) after a short-lived storage effect.

The pressure signal (pressure change during drawdown or buildup) during a FCF dominated flow period can be expressed as [Cinco-Ley and Samaniego 1981]:

$$\Delta p = 44.11 \frac{qB\mu}{h\sqrt{k_f w_f^3} \sqrt{\phi c_t k}} \sqrt{\Delta t} \quad (7.59)$$

From equation (7.59) a plot of  $\Delta p$  against  $\Delta t^{1/4}$  will yield a straight line for a FCF dominated flow regime due to bilinear flow (Fig. 7.12), with slope  $m_{BLF}$ , which can be used to calculate *fracture flow capacity* ( $k_f w_f$ ) using equation (7.60).

$$k_f w_f = 1944.8 \sqrt{\frac{1}{\phi c_t k} \left( \frac{q B \mu}{h m_{BLF}} \right)^2} \quad (7.60)$$

Equations (7.59) and (7.60) are straight-line characteristic equations for a finite conductivity fracture.

**7.3.1.4. Limited Entry (LE).** It is not uncommon to complete a well partially (limited entry) when a fluid zone in a reservoir is not desirable for production (Fig. 7.13).

Flow behavior around a limited entry well is Fig. 7.14.

For instance, when a well penetrates an oil zone with a gas zone at the top and water zone below, with oil as fluid of interest for production, the well will be partially completed in the oil zone as shown in Fig. 7.15a. Also, for a gas reservoir with a water zone, perforation will be partial to keep the perforation away from the water zone (Fig. 7.15b).

Pressure change during limited entry dominated flow regime can be described as:

$$\Delta p = 70.6 \frac{q B \mu}{k_s r_s} - 2452.9 \frac{q B \mu \sqrt{\phi \mu c_t}}{k_s^{3/2} \sqrt{\Delta t}}, \text{ Brons } et al. 1961 \quad (7.61)$$

From equation (7.61), a plot of  $\Delta p$  against  $\Delta t^{-1/2}$  will yield a straight line for a limited entry (LE) dominated flow regime due to *spherical flow* (SPH) behavior (Fig. 7.16), with a slope  $m_{SPH}$  that can be used to calculate *spherical permeability* ( $k_s$ ) using equation (7.62).

$$k_s = \left( 2452.9 q B \mu \frac{\sqrt{\phi \mu c_t}}{m_{SPH}} \right)^{2/3} \quad (7.62)$$

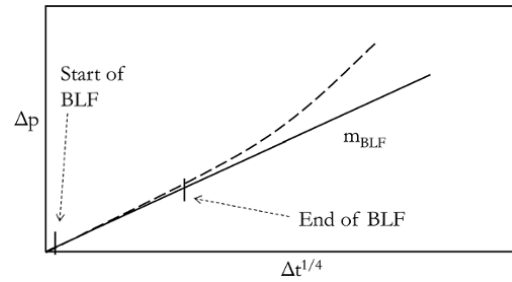


Figure 7.12 Specialized straight-line plot for a finite conductivity fracture.

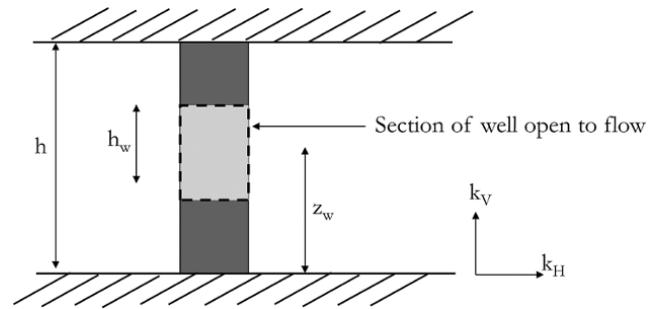


Figure 7.13 Limited entry well schematic.

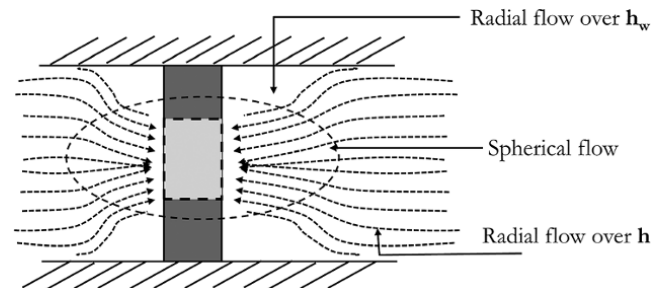


Figure 7.14 Flow behavior around a limited entry well.

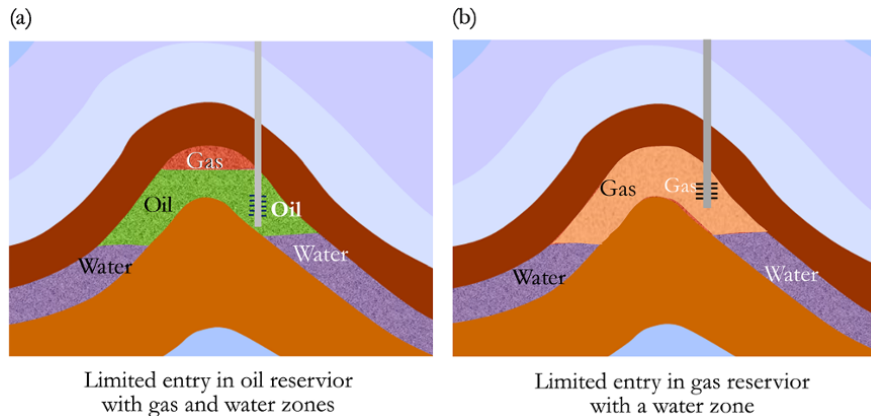


Figure 7.15 Limited entry completions.

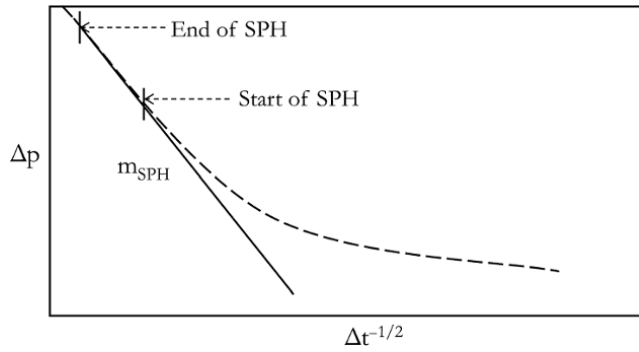


Figure 7.16 Specialized straight-line plot for SPH.

Spherical permeability is defined as:

$$k_s = \sqrt[3]{k_x k_y k_z} \quad (7.63)$$

Where  $k_x = k_y = k_{xy}$ , equation (7.63) becomes:

$$k_s = \sqrt[3]{k_{xy}^2 k_z} \quad (7.64)$$

When radial flow manifest, radial permeability ( $k_r = k_{xy}$ ) can be determined as shown in Exercise 7.5 to Exercise 7.7. Vertical permeability is, hence, determined from equation (7.64):

$$k_z = \frac{k_s^3}{k_{xy}^2} \quad (7.65)$$

Note that  $k_{xy}$  can be represented as  $k_H$  (horizontal permeability) or  $k_r$  (radial permeability in vertical wells). Additionally,  $k_z$  can also be represented as  $k_v$  (vertical permeability). The  $\frac{k_z}{k_{xy}}$  ratio, which is also termed the  $\frac{k_v}{k_H}$  ratio, is often defined as *reservoir permeability anisotropy*.

From equation (7.65), reservoir permeability anisotropy can be expressed in terms of  $k_s$  and  $k_{xy}$ :

$$\frac{k_z}{k_{xy}} = \left(\frac{k_s}{k_{xy}}\right)^3 \quad (7.66)$$

### 7.3.2. Reservoir Behavior

The simplest reservoir behavior has been described in the radial flow equation, equation (7.23), as *homogeneous reservoir behavior*. In well test analysis, a reservoir is said to be homogeneous in behavior when the reservoir can be described by one *transmissibility*, also called *mobility thickness* ( $kh/\mu$ ), and one *storativity* ( $\phi c_r h$ ). This means that, for such reservoirs, measured pressure can be simulated with one transmissibility and one storativity value. In well test analysis, a reservoir is said to be heterogeneous when the reservoir cannot be described by single values of mobility and storativity.

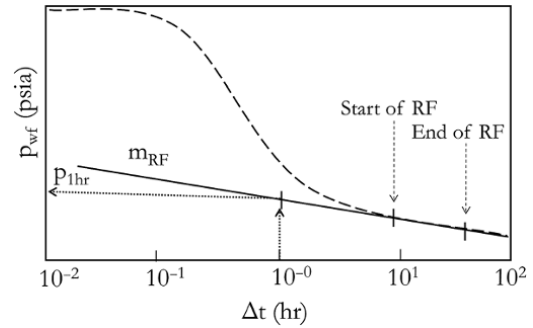


Figure 7.17 Specialized straight-line plot for drawdown radial flow.

#### 7.3.2.1. Homogeneous Behavior.

##### Drawdown Test and Analysis

During drawdown (well open to flow) in a homogeneously behaving reservoir, when reservoir response dominates flow behavior the flowing bottomhole pressure honors equation (7.37) and for an elapsed time of  $\Delta t$  during drawdown:

$$p_i - p_{wf} = 162.6 \frac{qB\mu}{kh} \left( \log \Delta t + \log \frac{k}{\phi \mu c_t r_w^2} - 3.23 + 0.87S \right) \quad (7.67)$$

From equation (7.67), a plot of  $p_{wf}$  against  $\Delta t$  on semi-log scale will yield a straight line for a reservoir behavior dominated flow regime (Fig. 7.17) with a slope of  $m_{RF}$ , which relates to *radial permeability* ( $k_r$ ), as shown in equation (7.68).

$$m_{RF} = 162.6 \frac{qB\mu}{k_r h} \quad (7.68)$$

Radial permeability is hence calculated from  $m_{RF}$ :

$$k_r = \frac{162.6 qB\mu}{m_{RF} h} \quad (7.69)$$

Substituting  $162.6 \frac{qB\mu}{k_r h} = m_{RF}$ , from equation (7.68) into equation (7.67) and solving at  $\Delta t = 1$  h gives the expression for skin (S):

$$S = 1.15 \left( \frac{p_i - p_{1hr}}{m_{RF}} - \log \frac{k}{\phi \mu c_t r_w^2} + 3.23 \right) \quad (7.70)$$

where  $p_{1hr}$  is the value of the bottomhole pressure read on the straight line defined by the slope of  $m_{RF}$ .

#### Exercise 7.5 Radial Permeability and Skin Effect Calculation from Drawdown Data

Using the drawdown pressure–rate data provided in Table 7.3, determine the reservoir radial permeability and wellbore skin effect, given that  $p_i = 5000$  psia. Note  $p_i$  is determined from buildup data.

**Table 7.6**  $p_{wf}$  and  $\Delta t$  Determined from Drawdown Test Data.

$\Delta t = t - t_0$ (hr)	$p_{wf}$ (psia)	$\Delta t = t - t_0$ (hr)	$p_{wf}$ (psia)	$\Delta t = t - t_0$ (hr)	$p_{wf}$ (psia)	$\Delta t = t - t_0$ (hr)	$p_{wf}$ (psia)
0.0000	5,000.00	0.0391	4,976.28	1.5264	4,581.77	59.6362	4,435.03
0.0013	4,999.17	0.0518	4,968.84	2.0236	4,541.90	79.0604	4,431.96
0.0018	4,998.90	0.0687	4,959.18	2.6827	4,510.82	104.8113	4,428.91
0.0023	4,998.55	0.0910	4,946.72	3.5565	4,488.78	138.9496	4,425.88
0.0031	4,998.07	0.1207	4,930.79	4.7149	4,474.38	184.2070	4,422.85
0.0041	4,997.45	0.1600	4,910.65	6.2506	4,465.31	244.2053	4,419.84
0.0054	4,996.62	0.2121	4,885.55	8.2864	4,459.36	323.7458	4,416.83
0.0072	4,995.53	0.2812	4,854.85	10.9854	4,454.94	429.1934	4,413.83
0.0095	4,994.08	0.3728	4,818.20	14.5635	4,451.21	568.9866	4,410.83
0.0126	4,992.17	0.4942	4,775.78	19.3070	4,447.77	754.3120	4,407.84
0.0168	4,989.65	0.6551	4,728.54	25.5955	4,444.48	1,000.0000	4,404.84
0.0222	4,986.34	0.8685	4,678.43	33.9322	4,441.28		
0.0295	4,981.98	1.1514	4,628.36	44.9843	4,438.14		

**Solution Steps.**

- Step 1: determine elapsed time  $\Delta t$  i.e.  $(t - t_0)$  for each drawdown data point (Table 7.6).
- Step 2: plot  $p_{wf}$  against  $\Delta t$  on a semi-log scale with  $p_{wf}$  on the vertical Cartesian axis and  $\Delta t$  on the horizontal log axis.
- Step 3: inspect  $p_{wf}$  against the  $\Delta t$  plot to determine the start and end of *radial flow* (RF), which will be characterized by a straight line.
- Step 4: fit data characterizing RF with a straight line.
- Step 5: determine the slope of RF straight-line ( $m_{RF}$ ) then calculate  $k_r$  using equation (7.69).
- Step 6: determine  $p_{1hr}$  (value of  $p_{wf}$  on straight line at  $\Delta t = 1$  hr) then calculate  $S$  using equation (7.70).

**Solution.**

Plot  $p_{wf}$  against  $\Delta t$ .

$m_{RF}$  in psi/log cycle can be calculated by determining the pressure change over 1 log cycle of elapsed time ( $\Delta t$ ) as shown as shown Fig. 7.18. Also,  $p_{1hr}$  is determined by reading values of  $p_{wf}$  corresponding to 1 hr on a straight line (not on the data) shown Fig. 7.18.

Note parameters given:  $q = q_{oil} = 150$  stb/D;  $r_w = 0.33$  ft;  $\phi = 0.2$ ;  $h = 50$  ft;  $B_o = 1.5$  rb/stb;  $\mu_{oil} = 0.5$  cp;  $c_t = 5 \times 10^{-5}$  psi<sup>-1</sup>.

From equation (7.69):

$$k_r = \frac{162.6qB\mu}{m_{RF}h}$$

$$k_r = \frac{162.6 \times 150 \times 1.5 \times 0.5}{24.68 \times 50}$$

$$= 14.8 \text{ mD}$$

$$k_r = 14.8 \text{ mD}$$

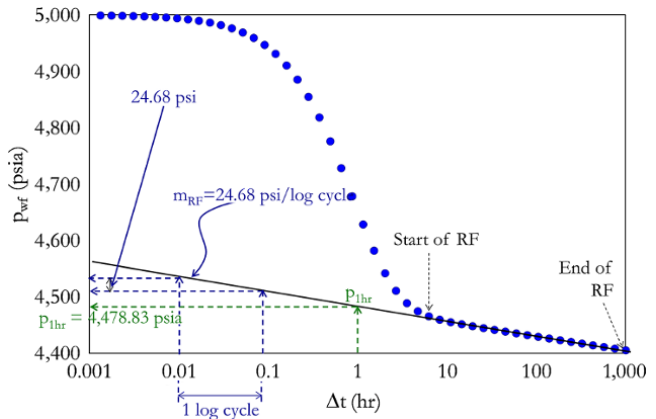


**Figure 7.18** Specialized straight-line plot for drawdown RF showing  $m_{RF}$  and  $p_{1hr}$ .

From equation (7.70):

$$S = 1.15 \left( \frac{p_i - p_{1hr}}{m_{RF}} - \log \frac{k}{\phi \mu c_t r_w^2} + 3.23 \right)$$

$p_i = 5000$  psia,  $p_{1hr} = 4478.83$  psia,  $m_{RF} = 24.68$  psi/log cycle.

Hence:

$$S = 1.15 \left( \frac{5000 - 4478.83}{24.68} - \log \frac{14.8}{0.2 \times 0.5 \times 5 \times 10^{-5} \times 0.33^2} + 3.23 \right)$$

$$= 19.45$$

$S = 19.5$

**Buildup Test and Analysis**

It is more desirable to analyze buildup data for reservoir behavior than drawdown, as zero flow rate during

buildup eliminates pressure fluctuation, which is common during drawdown.

For a well that has produced for  $t_p$  which is then followed by a buildup, pressure at the start of the buildup,  $p_{ws}(\Delta t = 0)$ , is equal to the pressure at the end of drawdown,  $p_{wf}(\Delta t = t_p)$ , i.e.  $p_{ws}(\Delta t = 0) = p_{wf}(t_p)$ .

Using the superposition principle (which is discussed in detail in *Multiple-Rate and Variable-Rate Test*).

$$p_i - p_{ws}(\Delta t) = (p_i - p_{wf}(t_p + \Delta t)) - (p_i - p_{wf}(\Delta t))$$

Using semi-logarithmic expression:

$$p_i - p_{ws}(\Delta t) = \frac{qB\mu}{4\pi kh} \ln \frac{t_p + \Delta t}{\Delta t}$$

In engineering oil field (EOF) units:

$$p_i - p_{ws}(\Delta t) = \frac{162.6qB\mu}{kh} \log \frac{t_p + \Delta t}{\Delta t} \quad (7.71)$$

Equation (7.71) is called the *Horner buildup equation*.

*Skin Calculation from Horner's Method*

From the Horner buildup equation, equation (7.71):

$$p_i - p_{ws}(\Delta t) = \frac{162.6qB\mu}{kh} \log \frac{t_p + \Delta t}{\Delta t}$$

Considering one hour of buildup:

$$p_i - p_{ws}(\Delta t = 1) = \frac{162.6qB\mu}{kh} \log(t_p + 1) \quad (7.72)$$

Also, from the drawdown equation, equation (7.67):

$$p_i - p_{wf}(\Delta t) = 162.6 \frac{qB\mu}{kh} \left( \log \Delta t + \log \frac{k}{\phi\mu c_t r_w^2} - 3.23 + 0.87S \right)$$

The pressure value at end of drawdown equals pressure at the start of buildup:

$$p_i - p_{wf}(\Delta t = t_p) = 162.6 \frac{qB\mu}{kh} \left( \log t_p + \log \frac{k}{\phi\mu c_t r_w^2} - 3.23 + 0.87S \right) \quad (7.73)$$

Solving for S using equations (7.72) and (7.73)

$$S = 1.15$$

$$\left( \frac{p_{ws}(\Delta t = 1) - p_{wf}(\Delta t = t_p)}{m_{RF}} + \log \frac{t_p + 1}{t_p} - \log \frac{k}{\phi\mu c_t r_w^2} + 3.23 \right)$$

where  $m_{RF}$

$$m_{RF} = 162.6 \frac{qB\mu}{k_r h}$$

Defining  $p_{ws}(\Delta t = 1) = p_{1hr}$  and  $p_{wf}(\Delta t = t_p) = p_{wf}(t_p)$ , the skin equation above becomes:

$$S = 1.15 \left( \frac{p_{1hr} - p_{wf}(t_p)}{m_{RF}} + \log \frac{t_p + 1}{t_p} - \log \frac{k}{\phi\mu c_t r_w^2} + 3.23 \right) \quad (7.74)$$

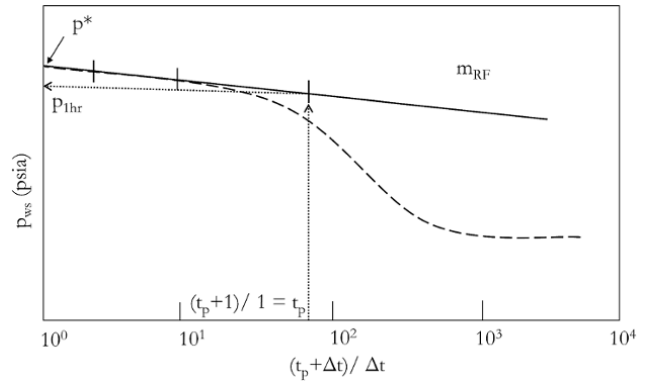


Figure 7.19 Specialized straight-line plot for buildup RF.

From equation (7.71), a plot of  $p_{ws}$  against  $\frac{t_p + \Delta t}{\Delta t}$  on a semi-log scale will yield a straight line for a reservoir behavior dominated flow regime (Fig. 7.19) with a slope of  $m_{RF}$ , which relates to *radial permeability* ( $k_r$ ) as shown in equation (7.75).

$$m_{RF} = 162.6 \frac{qB\mu}{k_r h} \quad (7.75)$$

Radial permeability is thus calculated from  $m_{RF}$  as:

$$k_r = \frac{162.6qB\mu}{m_{RF} h} \quad (7.76)$$

Skin is calculated using equation (7.74).

Another important parameter from buildup data is  $p^*$ ; this cannot be determined from drawdown. When the reservoir is shut-in for a very long time ( $\Delta t \rightarrow \infty$ ) and  $\frac{t_p + \Delta t}{\Delta t} = 1$ . The Horner RF line therefore extrapolates to Horner time of 1 to determine  $p^*$ . When the reservoir is nondepleting,  $p^*$  is equal to initial reservoir pressure. However, for a depleting reservoir  $p^*$  is not equal to initial reservoir pressure.

**Exercise 7.6** Radial Permeability, Skin Effect, and  $p^*$  Calculation from Buildup Data

Using the buildup pressure–rate data provided in Table 7.3, determine  $p^*$ , initial reservoir pressure ( $p_i$ ), reservoir radial permeability, and wellbore skin effect.

**Solution Steps.**

*Step 1:* determine elapsed time  $\Delta t$  i.e.  $(t - t_0)$ , then Horner time  $\left( \frac{t_p + \Delta t}{\Delta t} \right)$  for given test data points during buildup (Table 7.7).



**Table 7.7**  $p_{ws}$  and  $\frac{t_p + \Delta t}{\Delta t}$  Determined from Buildup Test Data.

T (hr)	$\Delta t$ (hr)	$\frac{t_p + \Delta t}{\Delta t}$	$p_{ws}$ (psia)	t (hr)	$\Delta t$ (hr)	$\frac{t_p + \Delta t}{\Delta t}$	$p_{ws}$ (psia)
1,000.0010	0.0010	1,000,001.00	4,405.47	1,001.1514	1.1514	869.51	4,776.48
1,000.0013	0.0013	769,231.77	4,405.67	1,001.5264	1.5264	656.14	4,823.06
1,000.0018	0.0018	555,556.56	4,405.94	1,002.0236	2.0236	495.17	4,862.92
1,000.0023	0.0023	434,783.61	4,406.30	1,002.6827	2.6827	373.76	4,894.00
1,000.0031	0.0031	322,581.65	4,406.77	1,003.5565	3.5565	282.18	4,916.03
1,000.0041	0.0041	243,903.4,4	4,407.40	1,004.7149	4.7149	213.09	4,930.42
1,000.0054	0.0054	185,186.19	4,408.22	1,006.2506	6.2506	160.98	4,939.46
1,000.0072	0.0072	138,889.89	4,409.32	1,008.2864	8.2864	121.68	4,945.40
1,000.0095	0.0095	105,264.16	4,410.76	1,010.9854	10.9854	92.03	4,949.78
1,000.0126	0.0126	79,366.08	4,412.67	1,014.5635	14.5635	69.66	4,953.48
1,000.0168	0.0168	59,524.81	4,415.19	1,019.3070	19.3070	52.79	4,956.87
1,000.0222	0.0222	45,046.05	4,418.51	1,025.5955	25.5955	40.07	4,960.09
1,000.0295	0.0295	33,899.31	4,422.86	1,033.9322	33.9322	30.47	4,963.21
1,000.0391	0.0391	25,576.45	4,428.57	1,044.9843	44.9843	23.23	4,966.24
1,000.0518	0.0518	19,306.02	4,436.01	1,059.6362	59.6362	17.77	4,969.19
1,000.0687	0.0687	14,557.04	4,445.67	1,079.0604	79.0604	13.65	4,972.07
1,000.0910	0.0910	10,990.01	4,458.12	1,104.8113	104.8113	10.54	4,974.88
1,000.1207	0.1207	8,286.00	4,474.05	1,138.9496	138.9496	8.20	4,977.59
1,000.1600	0.1600	6,51.00	4,494.19	1,184.2070	184.2070	6.43	4,980.20
1,000.2121	0.2121	4,715.76	4,519.29	1,244.2053	244.2053	5.09	4,982.69
1,000.2812	0.2812	3,557.19	4,549.99	1,323.7458	323.7458	4.09	4,985.04
1,000.3728	0.3728	2,683.40	4,586.64	1,429.1934	429.1934	3.33	4,987.23
1,000.4942	0.4942	2,024.47	4,629.06	1,568.9866	568.9866	2.76	4,989.23
1,000.6551	0.6551	1,527.48	4,676.30	1,754.3120	754.3120	2.33	4,991.05
1,000.8685	0.8685	1,152.41	4,726.40	2,000.0000	1,000.0000	2.00	4,992.65

Step 2: plot  $p_{ws}$  against  $\frac{t_p + \Delta t}{\Delta t}$  on a semi-log scale with

$p_{ws}$  on the vertical Cartesian axis and  $\frac{t_p + \Delta t}{\Delta t}$  on the horizontal log axis.

Step 3: inspect  $p_{ws}$  against the  $\frac{t_p + \Delta t}{\Delta t}$  plot to determine the start and end of RF, which will be characterized by a straight line.

Step 4: fit data characterizing RF with a straight line and extrapolate line to  $\frac{t_p + \Delta t}{\Delta t} = 1$ , to get  $p^*$ .

Step 5: determine the slope of  $m_{RF}$  then calculate  $k_r$  using equation (7.76).

Step 6: determine  $p_{ws}$  at  $\Delta t = 1$  hr, which corresponds a to Horner time of  $t_p + 1$ .

Step 7: calculate S using equation (7.74).

**Solution.**

Plot  $p_{ws}$  against  $\frac{t_p + \Delta t}{\Delta t}$  with  $t_p = 1,000$  hr.

$m_{RF}$  in the psi/log cycle can be calculated by determining pressure change over 1 log cycle of Horner time  $\left(\frac{t_p + \Delta t}{\Delta t}\right)$  as shown Fig. 7.20. Also,  $p_{1hr}$  is determined

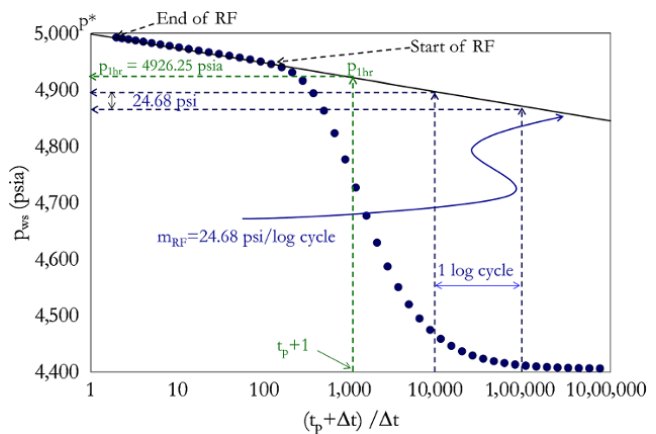


**Figure 7.20** Specialized straight-line (Horner) plot for buildup RF showing  $m_{RF}$ ,  $p^*$ , and  $p_{1hr}$ .

by reading values of  $p_{ws}$  corresponding to  $\Delta t = 1$  hr (which is Horner time of  $t_p + 1$ ) on a straight line (not on the data) as shown Fig. 7.20.  $p^*$  is determined by extrapolating the radial straight line to a Horner time of 1.

$\frac{t_p + \Delta t}{\Delta t}$  is Horner time.

From Fig. 7.20,  $p^* = 5000$  psia,

Initial reservoir pressure  $p_i = p^*$  as pressure response is infinite acting, i.e. radial flow persists until the end of buildup and no boundary effect was observed.

$p_i = 5000$  psia

From equation (7.76):

$$k_r = \frac{162.6qB\mu}{m_{RF}h}$$

$$k_r = \frac{162.6 \times 150 \times 1.5 \times 0.5}{24.68 \times 50} = 14.8 \text{ mD}$$

$k_r = 14.8$  mD

From equation (7.74):

$$S = 1.15 \left( \frac{p_{1hr} - p_{wf}(t_p)}{m_{RF}} + \log \frac{t_p + 1}{t_p} - \log \frac{k}{\phi\mu c_t r_w^2} + 3.23 \right)$$

$p_{wf}(t_p) = 4404.84$  from data (end of drawdown).

$$S = 1.15 \left( \frac{4926.25 - 4404.84}{24.68} + \log \frac{1000 + 1}{1000} - \log \frac{14.8}{0.2 \times 0.5 \times 5 \times 10^{-5} \times 0.33^2} + 3.23 \right) = 19.45$$

$S = 19.5$

Other published straight-line methods for buildup analysis after first drawdown include *Miller Dyes and Hutchinson* (MDH) and *Agarwal* (Agarwal Effective Time). These methods have not been discussed as they do not have any advantage over Horner methods and the superposition principle discussed below.

*Multiple Rate and Variable Rate Test*

The methods discussed so far in this section for analysis of drawdown and buildup tests, are for reservoirs with wells producing at constant rate. Typical well production is characterized by a combination of multiple flowing and shut-in periods or varying production/test rates.

Pressure variations due to changing flow rates are equal to the sum of the pressure drops due to each rate change (superposition principle), as this accounts for the history of the previous rate for any current flow period being analyzed or described.

Defining dimensionless pressure in a consistent unit as:

$$p_D = \frac{2\pi kh}{qB\mu} \Delta p \tag{7.77}$$

The pressure drop due to flow rate  $q$  is hence:

$$p_i - p(t) = \frac{qB\mu}{2\pi kh} p_D \tag{7.78}$$

For two sequential rate changes,  $q_1$  and  $q_2$  (Fig. 7.21), the pressure drop, which is based on superposition in time, is hence given as:

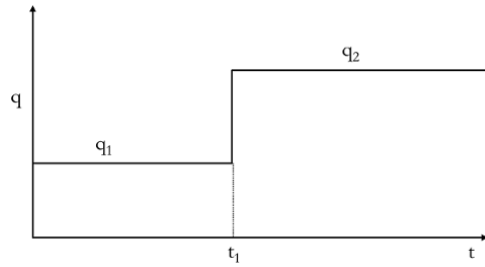


Figure 7.21 Two sequential rate changes.

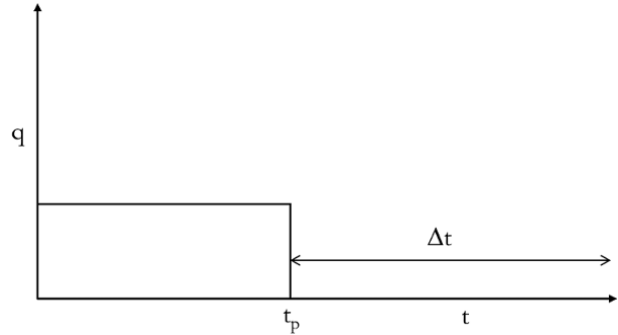


Figure 7.22 Buildup following single drawdown.

$$p_i - p(t) = \frac{q_1 B\mu}{2\pi kh} p_D(t) + \frac{(q_2 - q_1) B\mu}{2\pi kh} p_D(t - t_1) \tag{7.79}$$

For buildup following first drawdown,  $q_2 = 0$  and  $t_1 = t_p$  as shown in Fig. 7.22.

The pressure change during the buildup test is hence given as:

$$p_i - p_{ws}(\Delta t) = \frac{q_1 B\mu}{2\pi kh} (p_D(t_p + \Delta t) - p_D(\Delta t)) \tag{7.80}$$

In EOF units, equation (7.80) becomes:

$$p_i - p_{ws}(\Delta t) = \frac{141.2q_1 B\mu}{kh} (p_D(t_p + \Delta t) - p_D(\Delta t)) \tag{7.81}$$

Equation (7.81) is Horner's equation in dimensionless pressure. Using  $E_i$  approximation in logarithmic terms ( $E_i(x) \approx -\ln(\gamma x)$ , where  $\gamma = 1.781$ , equation (7.81) becomes:

$$p_i - p_{ws}(\Delta t) = \frac{162.6q_1 B\mu}{kh} \log \frac{t_p + \Delta t}{\Delta t} \tag{7.82}$$

*Multiple Rate Testing*

Consider the rate changes shown in Fig. 7.23 with  $q_0 = 0$  and  $t_0 = 0$

Pressure change can be expressed as in similar way to equation (7.79):

$$p_i - p(t) = \frac{B\mu}{2\pi kh} \sum_{i=1}^n (q_i - q_{i-1}) p_D(t - t_{i-1})$$

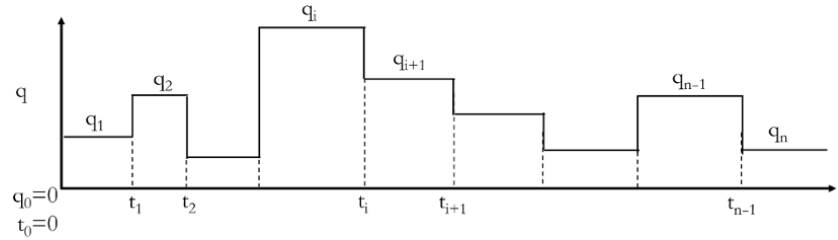


Figure 7.23 Multiple rate test sequence.

At the end of the wellbore storage, with  $E_i$  approximation in logarithm terms, the above equation becomes:

$$p_i - p_{wf}(t) = \frac{B\mu}{2\pi kh} \sum_{i=1}^n (q_i - q_{i-1}) \left( \ln \frac{\eta(t-t_{i-1})}{r_w^2} + 0.81 + 2S \right)$$

where  $\eta = \frac{k}{\phi\mu c_t}$  is the hydraulic diffusivity of a porous medium.

In EOF units:

$$p_i - p_{wf}(t) = 162.6 \frac{B\mu}{kh} \sum_{i=1}^n (q_i - q_{i-1}) \left( \log(t-t_{i-1}) + \log \frac{k}{\phi\mu c_t r_w^2} - 3.23 + 0.87S \right) \quad (7.83)$$

From equation (7.83), the plot of  $p_{wf}(t)$  against  $\sum_{i=1}^n (q_i - q_{i-1}) \log(t-t_{i-1})$  on a Cartesian scale will give a slope of  $162.6 \frac{B\mu}{kh}$  (not  $162.6 \frac{qB\mu}{kh}$ ). The superposition equation, equation (7.83), can be described with respect to a specific rate, such as  $n_{th}$  flow period, hence equation becomes:

$$p_i - p_{wf}(t) = \frac{162.6 q_n B\mu}{kh} \sum_{i=1}^n \frac{(q_i - q_{i-1})}{q_n} \left( \log(t-t_{i-1}) + \log \frac{k}{\phi\mu c_t r_w^2} - 3.23 + 0.87S \right) \quad (7.84)$$

Equation (7.84) can also be defined with respect to the rate difference between the current flow period and the previous flow period:  $(q_{n-1} - q_n)$ . Hence, equation (7.83) becomes:

$$p_i - p_{wf}(t) = \frac{162.6 (q_{n-1} - q_n) B\mu}{kh} \sum_{i=1}^n \frac{(q_i - q_{i-1})}{(q_{n-1} - q_n)} \left( \log(t-t_{i-1}) + \log \frac{k}{\phi\mu c_t r_w^2} - 3.23 + 0.87S \right) \quad (7.85)$$

Therefore, the plot of  $p_{wf}(t)$  against  $\sum_{i=1}^n \frac{(q_i - q_{i-1})}{(q_{n-1} - q_n)} \log(t-t_{i-1})$  on a Cartesian scale will give a slope of  $\frac{162.6 (q_{n-1} - q_n) B\mu}{kh}$ .

$\sum_{i=1}^n \frac{(q_i - q_{i-1})}{(q_{n-1} - q_n)} \log(t-t_{i-1})$  is called the *superposition function* with respect to radial flow or, simply, the *radial flow superposition function*, often denoted as  $f_{radial}(t)$ . In

this book,  $\sum_{i=1}^n \frac{(q_i - q_{i-1})}{(q_{n-1} - q_n)} \log(t-t_{i-1})$  will be termed *log radial flow superposition function* and denoted as  $f_{log\_radial}(t)$ . Another similar radial flow superposition function/transform termed the *ln radial flow superposition function* is discussed in Chapter 8.4.3. The log radial flow superposition function is defined as:

$$f_{log\_radial}(t) = \sum_{i=1}^n \frac{(q_i - q_{i-1})}{(q_{n-1} - q_n)} \log(t-t_{i-1}), \text{ for cartesian plot} \quad (7.86)$$

It may be desirable to plot the superposition plot to look like the classical Horner plot (semi-log plot) shown in Fig. 7.19 and Fig. 7.20. In such instances, a semi-log plot

of  $p_{wf}(t)$  against  $10 \sum_{i=1}^n \frac{(q_i - q_{i-1})}{(q_{n-1} - q_n)} \log(t-t_{i-1})$  will then be used to give a slope of  $\frac{162.6 (q_{n-1} - q_n) B\mu}{kh}$ .

Where the semi-log presentation of superposition function has been used,  $10 \sum_{i=1}^n \frac{(q_i - q_{i-1})}{(q_{n-1} - q_n)} \log(t-t_{i-1})$  is the *radial flow superposition function* and will be denoted as  $f_{antilog\_radial}(t)$ .

$$f_{antilog\_radial}(t) = 10 \sum_{i=1}^n \frac{(q_i - q_{i-1})}{(q_{n-1} - q_n)} \log(t-t_{i-1}), \text{ for semi-log plot} \quad (7.87)$$

If the latter definition of radial flow superposition function (equation (7.87)) is used, the plot must be made on semi-log scale.

In some literature or software applications, the time component in the superposition function is defined with respect to flow period duration ( $\Delta t_i$ ) and elapsed time since the last change in flow rate ( $\Delta t$ ). Hence, the radial flow superposition function becomes:

$$f_{\log\_radial}(t) = \sum_{i=1}^{n-1} \frac{(q_i - q_{i-1})}{(q_{n-1} - q_n)} \log \left( \sum_{j=i}^{n-1} \Delta t_j + \Delta t \right) - \log \Delta t, \text{ for cartesian plot} \quad (7.88)$$

and

$$f_{\text{antilog\_radial}}(t) = 10^{\sum_{i=1}^{n-1} \frac{(q_i - q_{i-1})}{(q_{n-1} - q_n)} \log \left( \sum_{j=i}^{n-1} \Delta t_j + \Delta t \right) - \log \Delta t},$$

for semi-log plot (7.89)

The superposition function can be described with respect to other flow regimes, if those regimes characterize pressure response of interest.

Superposition function with respect to linear flow regime is:

$$f_{\text{linear}}(t) = \sum_{i=1}^n \frac{(q_i - q_{i-1})}{(q_{n-1} - q_n)} \sqrt{t - t_{i-1}} \quad (7.90)$$

Superposition function with respect to bilinear flow regime is:

$$f_{\text{bilinear}}(t) = \sum_{i=1}^n \frac{(q_i - q_{i-1})}{(q_{n-1} - q_n)} \sqrt{t - t_{i-1}} \quad (7.91)$$

Superposition function with respect to spherical flow regime is:

$$f_{\text{bilinear}}(t) = \sum_{i=1}^n \frac{(q_i - q_{i-1})}{(q_{n-1} - q_n)} \frac{1}{\sqrt{t - t_{i-1}}} \quad (7.92)$$

From the radial flow superposition plot (Fig. 7.24), the slopes  $m_{RF}$  and  $p_{1hr}$  can be determined. From the equation relating slope  $m_{RF}$  to radial permeability, equation (7.93), radial permeability can then be calculated using equation (7.94) and skin calculated using equation (7.95).

$$m_{RF} = \frac{162.6(q_{n-1} - q_n)B\mu}{k_r h} \quad (7.93)$$

$$k_r = \frac{162.6(q_{n-1} - q_n)B\mu}{m_{RF} h} \quad (7.94)$$

$$S = 1.15 \left( \frac{p_{1hr} - p_{wf}(t_{n-1})}{m_{RF}} - \log \frac{k}{\phi \mu c_t r_w^2} + 3.23 \right) \quad (7.95)$$

During variable rate or multiple rate tests, the superposition principle should always be used.

Rate simplification methods, which involve replacing multiple-rate with single-rate production data and using

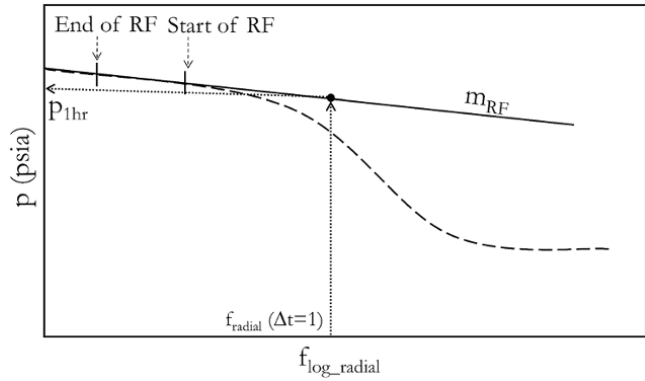


**Figure 7.24** Superposition plot (also called the generalized Horner plot).

equivalent production time as published in some literature, should be avoided.

**Exercise 7.7** Radial Permeability, Skin, and  $p^*$  Calculation using the Superposition Function

Using the superposition principle, determine  $k$ ,  $S$ , and  $p^*$  for the fifth flow period for the data given in Table 7.8 given  $r_w = 0.25$  ft;  $\phi = 0.25$ ;  $h = 100$  ft;  $B_o = 2.1$  rb/stb;  $\mu_{oil} = 1.3$  cp;  $c_t = 4.7E-5$  psi<sup>-1</sup>.

The pressure-rate history for Exercise 7.7 is shown in Fig. 7.25.

From Fig. 7.25, DD represent drawdown and BU represent buildup; the numbers following DD and BU are the flow period numbers, which are in sequence 1–5.

**Solution Steps.**

*Step 1:* create schedule parameter as shown in Table 7.9 and 7.10.

*Step 2:* determine elapsed time  $\Delta t$  for the fifth flow period. See column 2 of Table 7.11.

*Step 3:* determine  $(q_i - q_{i-1}) \log(t - t_{i-1})$  for each of the flow period ( $i = 1$  to 5). See columns 5–9 of Table 7.11.

*Step 4:* determine  $\sum_{i=1}^n (q_i - q_{i-1}) \log(t - t_{i-1})$ . See column 10 of Table 7.11.

*Step 5:* determine  $f_{\log\_radial}(t) = \sum_{i=1}^n \frac{(q_i - q_{i-1})}{(q_{n-1} - q_n)} \log$

$(t - t_{i-1})$  by dividing  $\sum_{i=1}^n (q_i - q_{i-1}) \log(t - t_{i-1})$  by  $(q_{n-1} - q_n)$ . See column 11 of Table 7.11.

NB:

$$\frac{\sum_{i=1}^n (q_i - q_{i-1}) \log(t - t_{i-1})}{(q_{n-1} - q_n)} = \sum_{i=1}^n \frac{(q_i - q_{i-1})}{(q_{n-1} - q_n)} \log(t - t_{i-1})$$

**Table 7.8** Pressure–Rate History for Exercise 7.7.

t (hr)	q (stb/D)	p (psia)	t (hr)	q (stb/D)	p (psia)	t (hr)	q (stb/D)	p (psia)
0.0010	150	4,097.47	100.2812	0	4,158.53	350.0687	100	4,033.48
0.0020	150	4,084.05	100.5690	0	4,175.39	350.13,90	100	4,027.88
0.0041	150	4,069.46	101.1514	0	4,192.20	350.2812	100	4,022.24
0.0083	150	4,054.00	102.3300	0	4,208.89	352.3300	100	4,005.24
0.0168	150	4,037.94	104.7149	0	4,225.31	354.7149	100	3,999.52
0.033,9	150	4,021.49	109.5410	0	4,241.20	359.5410	100	3,993.74
0.0429	150	4,015.96	119.3070	0	4,256.12	369.3070	100	3,987.85
0.0543	150	4,010.40	139.0694	0	4,269.41	389.0694	100	3,981.75
0.0687	150	4,004.82	179.0604	0	4,280.30	429.0604	100	3,975.32
0.13,90	150	3,988.01	200.0000	0	4,283.30	450.0000	100	3,973.07
0.2812	150	3,971.12	200.0010	50	4,215.79	450.0010	0	4,108.09
0.5690	150	3,954.19	200.0021	50	4,211.15	450.0021	0	4,117.36
1.1514	150	3,937.24	200.0043	50	4,206.10	450.0043	0	4,127.47
2.3300	150	3,920.27	200.0384	50	4,189.50	450.0089	0	4,138.18
4.7149	150	3,903.30	200.0797	50	4,183.74	450.0185	0	4,149.30
9.5410	150	3,886.32	200.1653	50	4,177.94	450.0384	0	4,160.68
19.3070	150	3,869.34	200.3429	50	4,172.13	450.0797	0	4,172.21
39.0694	150	3,852.36	201.4758	50	4,160.57	450.1653	0	4,183.81
79.0604	150	3,835.38	206.3510	50	4,149.41	450.3429	0	4,195.46
100.0000	150	3,829.72	213.1749	50	4,144.26	450.7114	0	4,207.12
100.0010	0	4,032.25	227.3306	50	4,139.69	451.4758	0	4,218.75
100.0020	0	4,045.66	256.6961	50	4,135.91	453.0615	0	4,230.31
100.0041	0	4,060.26	317.6134	50	4,132.83	456.3510	0	4,241.72
100.0083	0	4,075.72	350.0000	50	4,131.88	463.1749	0	4,252.82
100.0168	0	4,091.78	350.0010	100	4,064.37	477.3306	0	4,263.37
100.033,9	0	4,108.22	350.0020	100	4,059.90	506.6961	0	4,272.98
100.0687	0	4,124.88	350.0041	100	4,055.03	567.6134	0	4,281.24
100.13,90	0	4,141.67	350.0339	100	4,039.04	600.0000	0	4,283.63

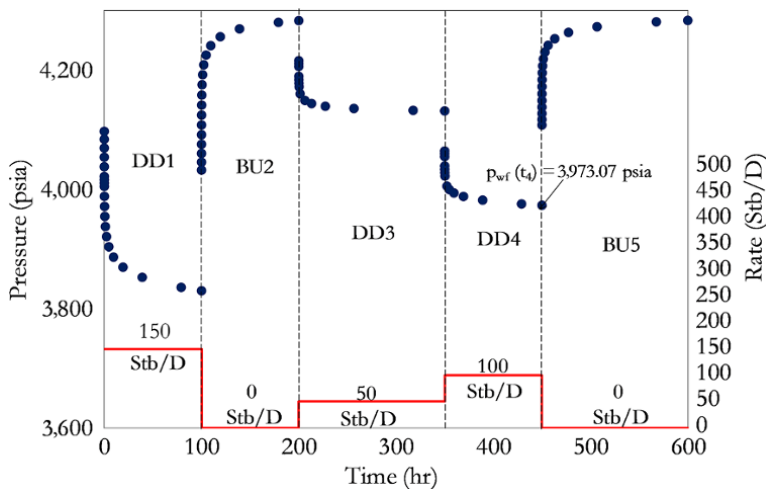


**Figure 7.25** Pressure–rate history for Exercise 7.7

**Table 7.9** Schedule Parameters for the Fifth Flow Period.

n (flow period of interest)	5
q <sub>n</sub> (flow rate of period of interest)	0
q <sub>n-1</sub> (flow rate of previous flow period)	100
q <sub>n-1</sub> - q <sub>n</sub>	100

**Table 7.10** Rate Changes with Elapsed Time for Flow Periods 1–5.

i (Flow period)	t <sub>i</sub> (Elapsed time for i)	q <sub>i</sub> (rate for i)	q <sub>i</sub> - q <sub>i-1</sub>
0	0	0	
1	100	150	150
2	200	0	-150
3	350	50	50
4	450	100	50
5	600	0	-100

**Table 7.11** Radial Flow Superposition Function Calculation Solution to Exercise 7.2.

Col1	Col2	Col3	Col4	Col5	Col6	Col7	Col8	Col9	Col10	Col11
t (hr)	$\Delta t_5$ (hr)	q (Stb/D)	p (psia)	$(q_i - q_{i-1}) \log(t - t_{i-1})$				$\sum_{i=1}^n (q_i - q_{i-1}) \log(t - t_{i-1})$	$f_{\text{radial}}(t) = \sum_{i=1}^n \frac{(q_i - q_{i-1})}{(q_{n-1} - q_n)} \log(t - t_{i-1})$	
				i = 1	i = 2	i = 3	i = 4			
450.0000	0.0000	100	3,973.07	397.98	-381.61	119.90	100.00		236.27	2.36
450.0010	0.0010	0	4,108.09	397.98	-381.61	119.90	100.00	300.00	536.27	5.36
450.0021	0.0021	0	4,117.36	397.98	-381.61	119.90	100.00	268.32	504.59	5.05
450.0043	0.0043	0	4,127.47	397.98	-381.61	119.90	100.00	236.62	472.89	4.73
450.0089	0.0089	0	4,138.18	397.98	-381.61	119.90	100.00	204.93	441.20	4.41
450.0185	0.0185	0	4,149.30	397.98	-381.61	119.90	100.00	173.24	409.51	4.10
450.0384	0.0384	0	4,160.68	397.99	-381.62	119.90	100.01	141.55	377.83	3.78
450.0797	0.0797	0	4,172.21	397.99	-381.63	119.90	100.02	109.86	346.15	3.46
450.1653	0.1653	0	4,183.81	398.01	-381.64	119.91	100.04	78.17	314.48	3.14
450.3429	0.3429	0	4,195.46	398.03	-381.67	119.93	100.07	46.48	282.84	2.83
450.7114	0.7114	0	4,207.12	398.08	-381.74	119.96	100.15	14.79	251.24	2.51
451.0000	1.0000	0		398.13	-381.80	119.98	100.22	0.00	236.53	2.37
451.4758	1.4758	0	4,218.75	398.20	-381.88	120.02	100.32	-16.90	219.75	2.20
453.0615	3.0615	0	4,230.31	398.42	-382.18	120.16	100.65	-48.59	188.47	1.88
456.3510	6.3510	0	4,241.72	398.89	-382.78	120.44	101.34	-80.28	157.61	1.58
463.1749	13.1749	0	4,252.82	399.86	-384.02	121.01	102.69	-111.97	127.57	1.28
477.3306	27.3306	0	4,263.37	401.82	-386.51	122.15	105.25	-143.66	99.05	0.99
506.6961	56.6961	0	4,272.98	405.71	-391.39	124.34	109.75	-175.36	73.05	0.73
567.6134	117.6134	0	4,281.24	413.11	-400.48	128.27	116.88	-207.05	50.73	0.51
600.0000	150.0000	0	4,283.63	416.72	-404.85	130.10	119.90	-217.61	44.27	0.44

Row with  $\Delta t = 1$  was inserted to calculate  $f_{\text{radial}}$  at 1 hr ( $f_{\text{radial}}(\Delta t = 1)$ ) which is 2.37

Step 6: plot  $p$  against  $\sum_{i=1}^n \frac{(q_i - q_{i-1})}{(q_{n-1} - q_n)} \log(t - t_{i-1})$  on a Cartesian scale.

Step 7: inspect the  $p$  against  $\sum_{i=1}^n \frac{(q_i - q_{i-1})}{(q_{n-1} - q_n)} \log(t - t_{i-1})$  plot to determine the start and end of radial flow (RF); this will be characterized by a straight line.

Step 8: fit data characterizing RF with a straight line and extrapolate line to  $\sum_{i=1}^n \frac{(q_i - q_{i-1})}{(q_{n-1} - q_n)} \log(t - t_{i-1}) = 0$  to get  $p^*$ .

Step 9: determine the slope  $m_{RF}$  then calculate  $k_r$  using equation (7.94).

Step 10: determine  $p_{1hr}$ . Using  $\Delta t = 1$  hr determine  $f_{radial}(\Delta t = 1$  hr) then read the pressure on the straight line described by the slope of  $m_{RF}$  to get  $p_{1hr}$ .

Step 11: determine  $p_{wf}(t_{n-1})$ , which is  $p_{wf}(t_4)$ , and calculate  $S$  using equation (7.95).

**Solution.**

See schedule parameters (Table 7.9 and Table 7.10) used for  $f_{radial}$  flow calculations.

See Table 7.11 for calculation of  $f_{radial}$ .

The superposition plot from Table 7.11 is shown in Fig. 7.26.

From equation (7.94):

$$k_r = \frac{162.6(q_{n-1} - q_n)B\mu}{m_{RF}h}$$

$$k_r = \frac{162.6 \times 100 \times 2.1 \times 1.3}{36.98 \times 100}$$

$$k_r = 12 \text{ mD}$$

From equation (7.95):

$$S = 1.15 \left( \frac{p_{1hr} - p_{wf}(t_{n-1})}{m_{RF}} - \log \frac{k}{\phi\mu c_t r_w^2} + 3.23 \right)$$

$p_{wf}(t_{n-1}) = 3973.07$  psia (from Fig. 7.25).

$p_{1hr} = 4212.53$  psia (from Fig. 7.26).

$p_{1hr}$  is the value of  $p$  corresponding to  $f_{radial}(\Delta t = 1)$ .  $f_{radial}(\Delta t = 1) = 2.37$  as shown in Table 7.11.

$$S = 1.15 \left( \frac{4212.53 - 3973.07}{36.98} - \log \frac{12}{0.25 \times 1.3 \times 4.7 \times 10^{-5} \times 0.25^2} + 3.23 \right) = 3.0$$

$S = 3.0$

$p^* = 4,300$  psia (from Fig. 7.26).

Reservoir behavior during well testing is discussed further in Chapter 8.5.1.11.

**7.3.2.2. Double Porosity Behavior.** A double porosity reservoir system describes a reservoir with a fissure and matrix system. Fig. 7.27 shows examples of simplification of fissure–matrix systems. Examples of a reservoir with double porosity include limestone and dolomite with fissures, vugs, and matrix.

The Warren and Root model [Warren and Root, 1963] is one of the most common geometric descriptions of the double porosity system. The model description is based

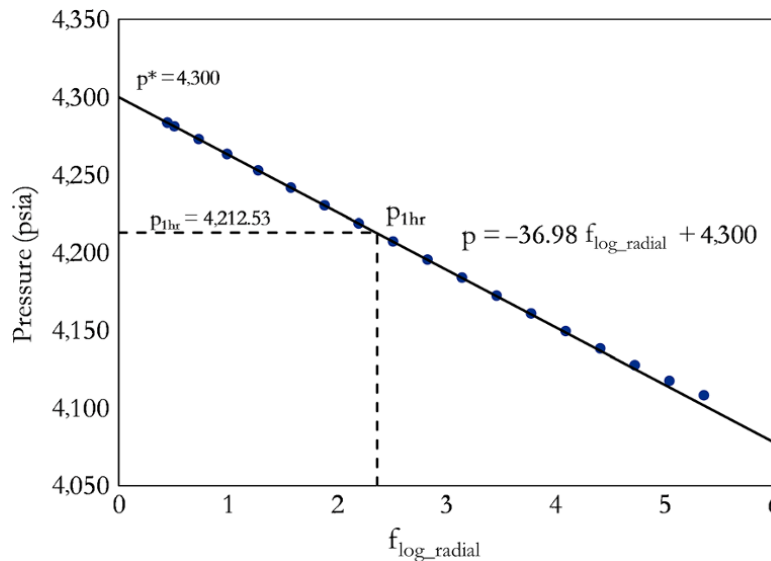
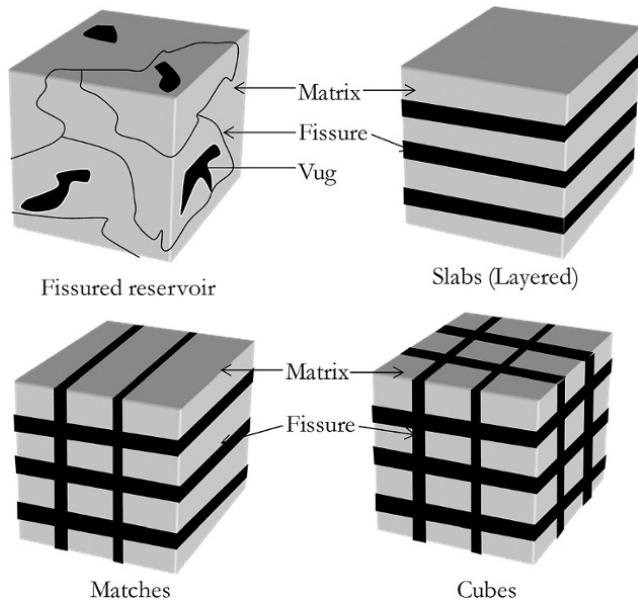


Figure 7.26 Superposition plot for Exercise 7.7.



**Figure 7.27** Geometrical representation of a fissured reservoir by Warren and Root.

on the assumption that matrix blocks are homogeneous and can be described as rectangular parallelepiped shape with faces corresponding to the orthogonal fissure plane. The Warren and Root model assumes the reservoir volume tested is significantly greater than matrix blocks, fluid production from the reservoir into the well is primarily from fissures, and fissure storage capacity is small compared to reservoir storage capacity.

Warren and Root matrix block geometries depend on the number of matrix faces available for matrix-fissure fluid exchange where  $n = 1$  is for slab matrix blocks,  $n = 2$  for match blocks, and  $n = 3$  for cubic matrix blocks.

*Geometry*

The effect of geometry on fluid flow between matrix and fissure is characterized by a *geometric coefficient* expressed as:

$$\alpha = \frac{n(n + 2)}{r_m^2} \tag{7.96}$$

Where  $n$  is the number of matrix planes available for fluid exchange with fissures and  $r_m$  is the matrix block size and expressed as:

$$r_m = n \frac{V_{matrix}}{A_{matrix}} \tag{7.97}$$

$V_{matrix}$  and  $A_{matrix}$  are the volume and area of the matrix, respectively.

*Matrix concentration* ( $V_m$ ) is the volumetric fraction of the matrix in the bulk volume ( $V$ ):

$$V_m = \frac{V_{matrix}}{V} \tag{7.98}$$

*Fissure concentration* ( $V_f$ ) is the volumetric fraction of the fissures in the bulk volume ( $V$ ):

$$V_f = \frac{V_{fissure}}{V} \tag{7.99}$$

$V$  is total volume of block.

$V_{matrix}$  is matrix volume in a block.

$V_{fissure}$  is fissure volume in a block.

$$V_m + V_f = 1 \tag{7.100}$$

Since  $V_f < 0.01\%$ ,  $V_m \approx 1$

*Matrix porosity* ( $\phi_m$ ) is defined as:

$$\phi_m = \frac{\text{Matrix pore volume}}{\text{Matrix volume}} \tag{7.101}$$

*Fissure porosity* ( $\phi_f$ ) is defined as:

$$\phi_f = \frac{\text{Fissure pore volume}}{\text{Fissure volume}} \tag{7.102}$$

Hence, the total porosity of the matrix-fissure system can be expressed as:

$$\phi = \phi_f V_f + \phi_m V_m \tag{7.103}$$

*Storativity Ratio*

This describes the fractional contribution of the fissure to the total storativity of the system and is expressed as:

$$\omega = \frac{(\phi V c_t)_f}{(\phi V c_t)_f + (\phi V c_t)_m} = \frac{(\phi V c_t)_f}{(\phi V c_t)_{f+m}} \tag{7.104}$$

where  $(\phi V c_t)$  is *storativity* with subscript “f” representing the fissure, “m” represents the matrix and “f + m” represents matrix-fissure systems.

Typical values for  $\omega$  are  $0.01 < \omega < 0.1$  for a single phase and  $0.1 < \omega < 0.2$  for multiphase.

*Interporosity Flow Coefficient*

This describes the matrix-fissure exchange capacity and is dependent on the geometry of the matrix block (Fig. 7.27), matrix and fissure permeability. Interporosity flow coefficient ( $\lambda$ ) is expressed as:

$$\lambda = \alpha r_w^2 \frac{k_m}{k_f} \tag{7.105}$$

where  $r_w$  is wellbore radius,  $k_m$  is matrix permeability,  $k_f$  is fissure permeability, and  $\alpha$  is the geometric coefficient defined in equation (7.96).

Typical values of  $\lambda$  lie between  $10^{-3}$  and  $10^{-7}$ .

A double porosity system is characterized with two radial flows (RF) with equal slopes. The first RF corresponds to the mobility/permeability of the fissure and



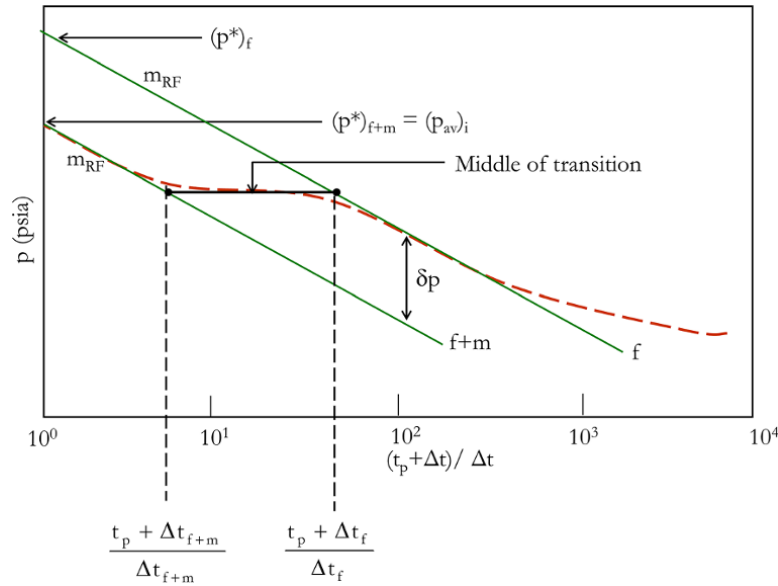


Figure 7.28 Horner plot for a double porosity reservoir.

the second corresponds to the mobility/permeability of the matrix plus fissure. The vertical distance between the two slopes (Fig. 7.28) relates to the *storativity ratio* ( $\omega$ ), equation (7.108), while the time when fissure dominated flow ends or time fissure plus matrix dominated flow begins relates to the *interporosity flow coefficient* ( $\lambda$ ), equation (7.109).

From the RF slope, slope =  $m_{RF} = m_{f+m} = m_f$

$$m_{RF} = 162.6 \frac{qB\mu}{k_f h} \quad (7.106)$$

Fissure permeability is determined using:

$$k_f = k_{f+m} = \frac{162.6qB\mu}{m_{RF} h} \quad (7.107)$$

$\omega$  and  $\lambda$  are determined for buildup analysis using equation (7.108) and equation (7.109), respectively [Bourdet and Gringarten, 1980]:

$$\omega = 10^{-\frac{\delta p}{m_{RF}}} \quad (7.108)$$

$$\begin{aligned} \lambda &= \frac{(\phi V c_t)_f \mu r_w^2 (t_p + \Delta t_f)}{0.000264 \gamma k_f t_p (\Delta t_f)} \\ &= \frac{(\phi V c_t)_{f+m} \mu r_w^2 (t_p + \Delta t_{f+m})}{0.000264 \gamma k_f t_p (\Delta t_{f+m})}, \text{ in EOF units} \end{aligned} \quad (7.109)$$

For drawdown analysis,  $\omega$  is determined using equation (7.108) and  $\lambda$  determined using equation (7.110) [Bourdet and Gringarten, 1980]:

$$\begin{aligned} \lambda &= \frac{(\phi V c_t)_f \mu r_w^2}{0.000264 \gamma k_f (\Delta t_f)} \\ &= \frac{(\phi V c_t)_{f+m} \mu r_w^2}{0.000264 \gamma k_f (\Delta t_{f+m})}, \text{ in EOF units} \end{aligned} \quad (7.110)$$

$\gamma = 1.78$  (the exponential of Euler constant).

Double porosity reservoir behavior during well testing is discussed further in Chapter 8.5.1.11.

### 7.3.3. Boundary Effects

Dimensionless variables make manipulation of pressure transient equations easier, and variables in these equations become independent of the magnitude of physical parameters such as fluid and rock properties; flow rates, etc. For the purpose of boundary characterization during reservoir flow, the following dimensionless variables will be used:

*Dimensionless pressure*

$$P_D = \frac{kh}{141.2qB\mu} \Delta p \quad (7.111)$$

*Dimensionless time*

$$t_D = \frac{0.000264k}{\phi \mu c_t r_w^2} \Delta t \quad (7.112)$$

*Dimensionless wellbore storage*

$$C_D = \frac{0.8936}{\phi c_t h r_w^2} C \quad (7.113)$$

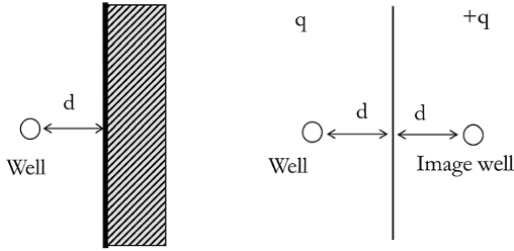


**Figure 7.29** Schematic of well in a reservoir with a single sealing fault represented as an image well.

Dimensionless radial distance

$$r_D = \frac{r}{r_w} \tag{7.114}$$

Variables are in EOF units defined in section 7.2.1.1.

**7.3.3.1. Single Sealing Fault.** One of the most convenient ways of adding the effect of boundaries to pressure transient models is using the concept of image well. Fig. 7.29 shows the schematic of a single well in a reservoir with a single sealing fault. The image well distance on the opposite side of the fault is equal to the actual well distance from the fault. The image well has the same flow rate as the actual well. The principle behind the use of image wells for adding boundaries to the well test model is further discussed in Chapter 8.5.1.12.

The pressure drop measured at the well is a superimposed effect of actual pressure drop at the well and the pressure drop by the image well. This is expressed as:

$$p_D = p(t_D, r_D = 1, S) + p(t_D, 2r_D, 0)$$

and further as:

$$p_D = \frac{1}{2} \left( \ln t_D + 0.81 + 2S - E_i \left( -\frac{(2r_D)^2}{4t_D} \right) \right) \tag{7.115}$$

When the compressible zone has not reached the fault, the  $E_i$  component in equation (7.115) is zero and behavior becomes that of infinite acting reservoir. Hence, equation (7.115) becomes:

$$p_D = \frac{1}{2} (\ln t_D + 0.81 + 2S) \tag{7.116}$$

When the compressible zone reaches the fault, the contribution of the  $E_i$  component in equation (7.115) becomes significant. Using logarithmic approximation of the  $E_i$  function ( $E_i(x) \approx -\ln(\gamma x)$ ), the  $E_i$  term in equation (7.115) can be expressed as:

$$-E_i \left( -\frac{(2r_D)^2}{4t_D} \right) = \ln \frac{t_D}{(2r_D)^2} + 0.81$$

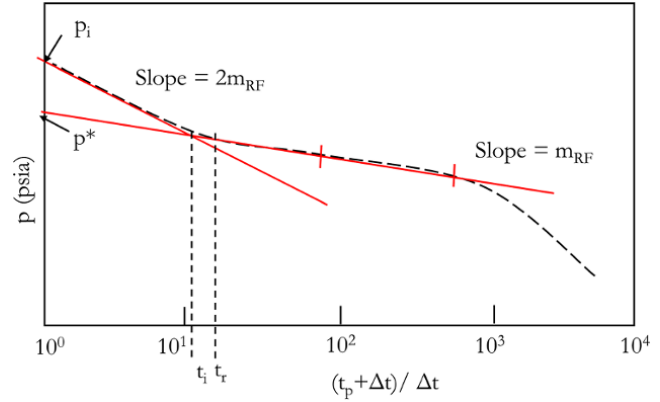


**Figure 7.30** Horner plot for a single sealing fault.

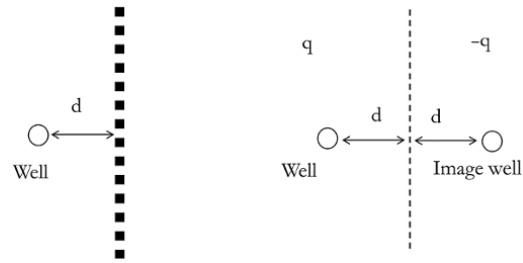


**Figure 7.31** Schematic of well in a reservoir with a constant pressure boundary represented as an image well.

Hence, equation (7.115) becomes:

$$p_D = (\ln t_D + 0.81 + S - \ln(2r_D)) \tag{7.117}$$

A comparison of equation (7.117) with equation (7.116) shows a doubling of the slope by the second RF relative to the first RF. This is illustrated by Fig. 7.30.

Base on the time the compressible zone reaches the fault, the distance of well to the fault can be calculated using equation (7.118) or equation (7.119):

$$d_{\text{fault}} = 0.012 \sqrt{\frac{kt_i}{\phi\mu c_t}} \tag{7.118}$$

or

$$d_{\text{fault}} = 0.032 \sqrt{\frac{kt_r}{\phi\mu c_t}} \tag{7.119}$$

where  $t_i$  and  $t_r$  are defined in Fig. 7.30.

**7.3.3.2. Constant Boundary Pressure.** When pressure change diffuses due to rate change and the compressional zone reaches a gas cap or aquifer laterally, such boundaries are characterized as constant pressure boundaries (Fig. 7.31).

Sealing fault and constant pressure linear boundaries describe two limiting cases of the linear composite system with zero and infinite mobility in the outer reservoir region, respectively.

Image well configuration for a constant pressure boundary is similar to single sealing fault except that the image well is an injection well with the same magnitude of flow rate as the actual well. The principle behind the use of image wells for adding boundaries to the well test model is further discussed in Chapter 8.5.1.12.

Pressure drop measured at the well is a superimposed effect of actual pressure drop at the well and the pressure drop by image well. This can be expressed as:

$$p_D = p(t_D, r_D = 1, S) - p(t_D, 2r_D, 0)$$

and further as:

$$p_D = \frac{1}{2} \left( \ln t_D + 0.81 + 2S + E_i \left( -\frac{(2r_D)^2}{4t_D} \right) \right) \quad (7.120)$$

When the compressible zone reaches a constant pressure boundary, using a logarithmic approximation for the  $E_i$  term ( $E_i(x) \approx -\ln(\gamma x)$ ), equation (7.120) becomes:

$$p_D = (S + 2 \ln(2r_D))$$

Expressing the above in real variables:

$$p_i - p_{wf} = 141.2 \frac{qB\mu}{kh} \left( \ln \frac{d}{r_w} + S \right) \quad (7.121)$$

Equation (7.121) shows that the pressure drop in a constant pressure boundary system can be described by Darcy's law for radial flow, with flow behavior characterized mainly by  $\frac{qB\mu}{kh}$  and skin effect. A Semi-log drawdown plot for a constant pressure boundary is shown in Fig. 7.32.

Equations (7.118) and (7.119) can be used for calculating distance to a constant pressure boundary where  $t_r$  and  $t_i$  are defined in Fig. 7.32.

**7.3.3.3. Wedge Fault.** A sealing wedge fault with an angle of  $\theta$  can be shown to yield a pressure response shown in Fig. 7.33, where the final straight line is characterized by a slope  $\frac{2\pi m_{RF}}{\theta}$ .

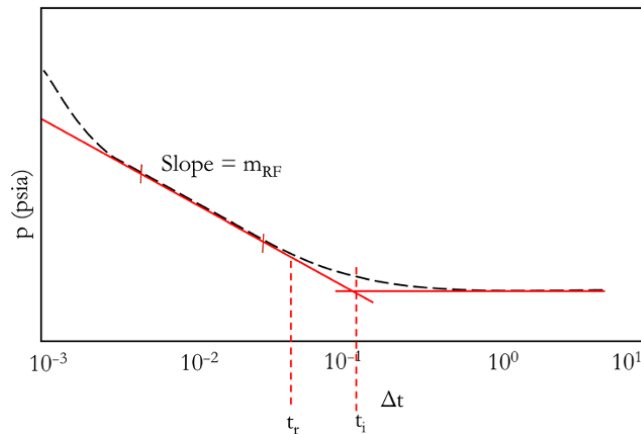


Figure 7.32 Semi-log drawdown plot for a constant pressure boundary.

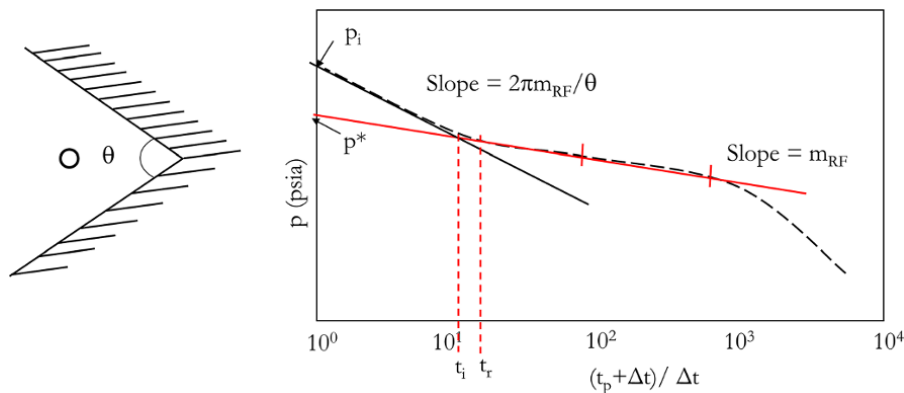


Figure 7.33 Schematic of wedge fault and corresponding Horner plot.



Figure 7.34 Schematics of a closed reservoir boundary system.

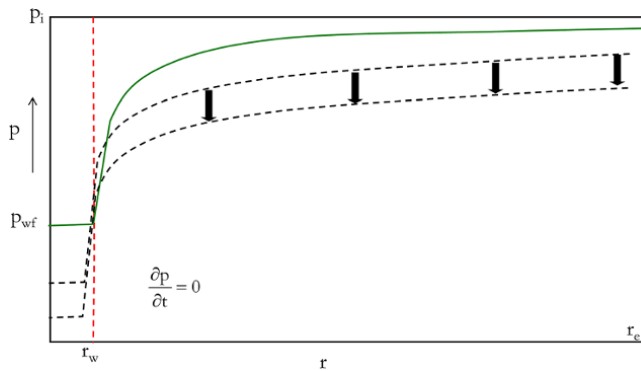


Figure 7.35 Pressure profile showing the constant shape of pressure profile in the reservoir.

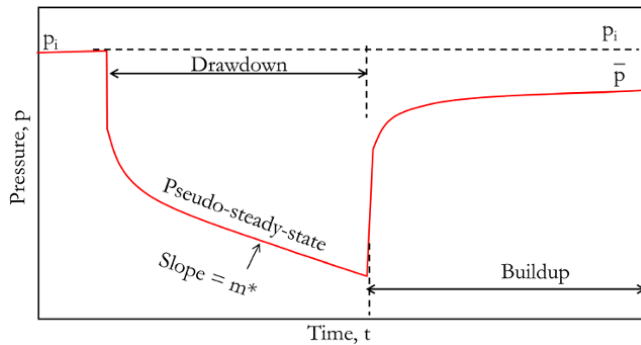


Figure 7.36 Pressure history for a closed reservoir system.

**7.3.3.4. Closed Reservoir.** When the compressible zone due to rate change reaches all the boundaries enclosing the reservoir (Fig. 7.34), the *shape* of the pressure profile with time becomes *constant*, and it simply drops as the reservoir is being depleted (Fig. 7.35).

During drawdown periods, when all boundaries have been reached by the compressible zone, after the infinite acting behavior, the reservoir starts to deplete. The response follows the *pseudo-steady-state* flow behavior, and the well flowing pressure becomes proportional to time (Fig. 7.36). During buildups, after shut-in, the



Figure 7.37 Channel boundaries.

pressure starts to buildup, behaving initially as an infinite acting reservoir, but later stabilizes tending towards the *average reservoir pressure* (Fig. 7.36).

The specialized straight-line equation for the pseudo-steady-state flow regime during drawdown can be expressed as:

$$p_i - p_{wf} = 0.234 \frac{qB}{\phi c_t h A} \Delta t + 162.6 \frac{qB\mu}{kh} \left( \log \frac{A}{r_w^2 C_A} + 0.351 + 0.87S \right) \quad (7.122)$$

where  $A$  is the area in  $ft^2$  and  $C_A$  is a shape factor discussed further in Chapter 9.2.1.

Equation (7.122) shows a linear relationship between  $p_{wf}$  and  $\Delta t$  with a slope of  $m^*$  during pseudo-steady-state flow as shown in Fig. 7.36.

$$m^* = 0.234 \frac{qB}{\phi c_t h A} \quad (7.123)$$

Reservoir pore volume (PV) can be determined from the slope of pseudo-steady state pressure graph using the expression:

$$PV = \phi h A = 0.234 \frac{qB}{c_t m^*} \quad (7.124)$$

**7.3.3.5. Channel Boundaries.** Other common boundary configurations include channel boundaries (Fig. 7.37) and the bounded channel (open rectangle) boundary (Fig. 7.38). Characterization of reservoir boundaries is further discussed in Chapter 8.4.5.



Figure 7.38 Bounded channel (open rectangle) boundary.

## REFERENCES

- Bourdet, D. and Gringarten, A., 1980. *Determination of Fissure Volume and Block Size in Fractured Reservoirs by Type-curve Analysis*. SPE paper 9293, 55th Annual Fall Technical Conference of SPE-AIME, 21–24 September, Dallas, TX.
- Brons, F. and Marting, V., 1961. The effect of restricted fluid entry on well productivity. *Journal of Petroleum Technology*, **13**(12), 172–174.
- Cinco-Ley, H; Samaniego-V, F., 1981. Transient pressure analysis of fractured wells. *Journal of Petroleum Technology*, **33** (09), 1749–1766
- Gringarten, A.C., Ramey, H.J., and Raghavan, R., 1974. Unsteady state pressure distributions created by a well with a single infinite conductivity vertical fracture. *Society of Petroleum Engineers Journal*, **14**(4), 347.
- Iseger, P., 2006. Numerical transform inversion using Gauss quadrature. *Probability in the Engineering and Informational Sciences*, **20**, 1–44.
- Stehfest, H., 1970. Algorithm 368. Numerical inversion of Laplace Transforms. *D-5. Communications of the ACM*, **13**(1), 47–49.
- Warren, J. and Root, P., 1963. The behavior of naturally fractured reservoirs. *Society of Petroleum Engineers Journal*, **3**(3) 245–255.

## BIBLIOGRAPHY

- Agarwal, R., 1979. *Real Gas Pseudo-Time – A New Function for Pressure Buildup Analysis of MHF Gas Wells*. SPE Annual Technical Conference and Exhibition, 23–26 September, Las Vegas, NV.
- Agarwal, R., Al-Hussainy, R., and Ramey, H., 1970. An investigation of wellbore storage and skin effect in unsteady liquid flow: I. Analytical treatment. *Society of Petroleum Engineers Journal*, **10**(3), 279–290.
- Al-Hussainy, R., Ramey Jr., H.J., and Crawford, P.B., 1966. The flow of real gas through porous media. *Journal of Petroleum Technology*, **18**(5), 637–642.
- Archer, J. and Wall, C., 1999. *Petroleum Engineering Principles and Practice*. Dordrecht/Boston: Kluwer Academic Publishers.

- Ayan, C. and Lee, W., 1988. Effects of multiphase flow on interpretation of buildup tests. *SPE Formation Evaluation*, **3**(2), 459–466.
- Bourdarot, G., 1998. *Well Testing: Interpretation Methods*. Technip and Institut francais du petrole.
- Bourgeois, M. and Horne, R., 1993. Well test model recognition with Laplace space. *SPE Formation Evaluation*, **8**(1), 17–25.
- Collins, R., 1991. *Flow of Fluid through Porous Materials*. REC Publishers.
- Earlougher, R.J., 1977. *Advances in Well Test Analysis*. Monograph Series, Issue 5. Dallas, TX: SPE.
- Gringarten, A., 2006. *The Evolution of the State of the Art in Well Test Analysis*. SPE paper 102079, SPE Annual Technical Conference and Exhibition, San Antonio, TX.
- Gringarten, A. and Ramey, H., 1973. The use of source and Green's functions in solving unsteady-flow problems in reservoirs. *Society of Petroleum Engineers Journal*, **13**(5), 285–296.
- Hegeman, P., Halford, D., and Joseph, J., 1991. *Well Test Analysis With Changing Wellbore Storage*. SPE paper 21829, SPE Rocky Mountain Regional/Low Permeability Reservoirs Symposium, 15–17 April, Denver, CO.
- Jones, P., 1956. Reservoir limit tests. *Oil and Gas Journal*, **54**(59), 184.
- Lee, J., 1982. *Well Testing*. Textbook Series Vol 1, Dallas, TX: SPE-AIME.
- Marsily, G., 1986. *Quantitative Hydrology*. Academic Press.
- Matthews, C., Brons, F., and Hazebroek, P., 1954. A method for determination of average pressure in a bounded reservoir. *Transactions of the AIME*, **201**, 182–191.
- Matthews, C. and Russels, D., 1967. *Pressure Build and Flow Tests in Wells*. SPE Monograph Series, Volume 1.
- Muskat, M. and Meres, M., 1963. The flow of heterogeneous fluids through porous media. *Journal of Applied Physics*, **7**, 346–363.
- Tiab, D. and Kumar, A., 1980. Detection and location of two parallel sealing faults around a well. *Journal of Petroleum Technology*, **32**(10), 1701–1708.
- Van Evarlingen, A. and Hurst, W., 1949. The application of the Laplace transformation to flow problems in reservoirs. *Petroleum Transactions AIME*, **1**(12), 305–324.
- van Poolen, H., 1965. Drawdown curves given angle between intersecting faults. *Oil and Gas Journal*, **71**, 71–75.
- Wattenbarger, R. and Ramey Jr, H., 1970. An investigation of wellbore storage and skin effects in unsteady liquid flow: II. Finite difference treatment. *Society of Petroleum Engineers Journal*, **10**(3), 291–296.
- Yaxley, L., 1987. Effect of a partially communicating fault on transient pressure behaviour. *SPE Formation Evaluation*, **2**(4), 590–598.

# 8

## Well Test Analysis

“Well test” is commonly used to describe a *production well test* or *transient well test*. A production well test involves diverting a producing well to a test separator and measuring the steady-state rate with the corresponding wellhead and bottomhole pressures. These kinds of tests are used for well/reservoir monitoring and well rate allocation. The transient well test involves carrying out a sequence of designed well flows (drawdowns) and shut-ins (buildups), and measuring bottomhole pressure and rate. This kind of test is used for wellbore, reservoir, and boundary characterization. Fig. 8.1 shows the schematic of a well test set-up.

Pressure–rate history acquired during well testing (*transient well testing*) (Fig. 8.2), together with fluid properties, well and petrophysical properties, is used for well test analysis to determine wellbore, reservoir, and boundary properties.

When the well is flowing (drawdown), the drawdown pressure signal ( $\Delta p_{DD}$ ) is defined as:

$$\Delta p_{DD} = p_{wf}(\Delta t = 0) - p_{wf}(\Delta t) \quad (8.1)$$

where  $p_{wf}(\Delta t = 0)$  corresponds to the flowing bottomhole pressure at start of the drawdown test and  $p_{wf}(\Delta t)$  corresponds to flowing bottomhole pressure at a given time during the drawdown flow period.

When the well is shut-in (buildup), the buildup pressure signal ( $\Delta p_{BU}$ ) is defined as:

$$\Delta p_{BU} = p_{ws}(\Delta t) - p_{ws}(\Delta t = 0) \quad (8.2)$$

where  $p_{ws}(\Delta t = 0)$  corresponds to the shut-in bottomhole pressure at start of the buildup test (well shut-in) and  $p_{ws}(\Delta t)$  corresponds to shut-in bottomhole pressure at a given time during the buildup flow period. Fig. 8.2 shows the drawdown and buildup pressure signals,  $\Delta p_{DD}$  and  $\Delta p_{BU}$ , with corresponding drawdown and buildup elapsed time, respectively.

Using well test analysis for well and reservoir characterization involves defining a simple model that honors all relevant static and dynamic data acquired. This simple model is called the *Interpretation Model*, which is discussed in detail in Section 8.5.

Well test analysis is also important in well performance prediction. The *inflow performance relationship* (IPR) model, which is used for predicting well production rate for a given flowing pressure ( $p_{wf}$ ), is derived from the well test analysis models.

### 8.1. TYPES OF WELL TEST

A well test generally involves creating a diffusing pressure disturbance by rate change and measuring this pressure disturbance to characterize wellbore, reservoir, and boundaries. The process of achieving a diffusing pressure disturbance by rate change can be created in various ways; these define the type of well test. The different type of well test include:

- *Drawdown (DD) Test*

This is generally used to describe pressure and rate measurement where the well is flowing. When the well is producing at a constant rate, bottomhole pressure decreases and flowing bottomhole pressure ( $p_{wf}$ ) is used for analysis. In practice, it is often difficult to achieve constant rate, hence difficult to analyze drawdown data.

- *Buildup (BU) Test*

Buildup describes the well test conditions when a well is shut-in after a drawdown test. During buildup, after a drawdown, bottomhole pressure increases. The shut-in bottomhole pressure is used for analysis during a buildup test. During buildup, since the rate is zero, there is no pressure fluctuation and the quality of data is often better than drawdown and preferred for analysis.

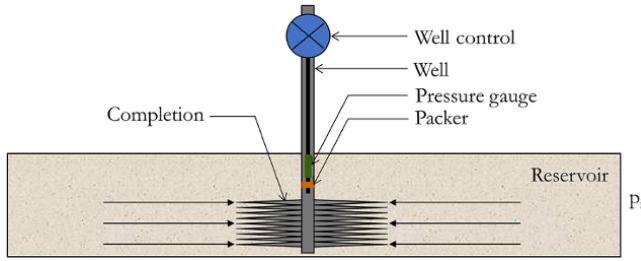


Figure 8.1 Well test setup.

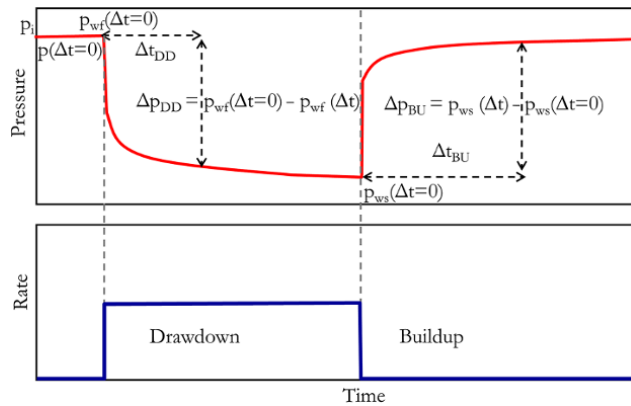


Figure 8.2 Pressure signal for drawdown and buildup test.

• *Injection Test*

This describes a test involving measuring the fluid injection rate through the well into the reservoir at a controlled rate and the corresponding pressure increase due to injection. This kind of test is very important in assessing the well and reservoir capacity to inject fluid.

• *Fall-off Test*

This describes well shut-in following fluid injection into the reservoir. During a fall-off test, bottomhole pressure decreases. A fall-off test follows an injection test.

• *Interference Test*

This type of well test involves producing or injecting fluid from a well, called the *active well*, and monitoring the pressure response from a different well, called the *observation well*, which is at a known distance away from the producing or injecting well. An interference test is carried out to evaluate communication between wells and investigate compartmentalization between different reservoir sections.

• *Slug Test*

A slug test is a test involving increasing bottomhole pressure due to rising liquid level in the well. Slug tests are created due to the inability of the well to produce to the surface, leading to buildup of *slug of liquid* in the

wellbore. During a slug test, the liquid level instead of rate, and corresponding bottomhole pressure (back pressure) due to the slug are measured. A slug test is generally followed by a buildup, which is intentionally initiated by shutting the well or the well shutting (killing) itself when the hydrostatic pressure equals the bottomhole flowing pressure.

• *Impulse Test*

This test is generally used to describe a well test involving drawdown or injection tests over very short periods, often lasting for a few minutes, and followed by a buildup.

• *Formation Testing*

This type of well test involves displacing a small volume of reservoir fluid often through probes (small aperture) placed on the wellbore from the reservoir. When fluid displacement (drawdown or pretest) stops, buildup is initiated. Reservoir fluid is often displaced using *pretest chambers*, which are often 20–100 cc in volume. Formation testing is discussed in detail in Chapters 6 and 8 (8.10).

**8.2. PHILOSOPHY OF WELL TEST ANALYSIS**

Since the dynamic reaction of well bottomhole pressure to rate changes depends on the reservoir and well properties, analysis of the dynamic pressure behavior in response to an appropriately designed sequence of well rate changes can provide properties that characterize wells and reservoirs during testing.

**8.2.1. Well Test Objectives**

Well tests play a crucial role in reservoir evaluation, description, and management. Well tests, especially at the appraisal stage of field development, provide key parameters that can be used to evaluate well and reservoir potential by providing basic reservoir and fluid parameters, including flow capacity, initial reservoir pressure, and fluid samples for PVT analysis.

Well test interpretation techniques can be used for deducing the key reservoir description, which includes: anisotropy, heterogeneity, drainage geometry and boundary conditions. The need to continuously monitor wells and reservoirs is important in reservoir and field management. Analysis of permanent bottomhole gauge pressure can be used to determine/validate hydrocarbon reserves, reservoir drive mechanism, reservoir boundaries/compartmentalization, geological structure, and other information for reservoir management and modeling.

Information that can be obtained from well testing is summarized in Table 8.1.

### 8.2.2. Well Testing at Different Stages of Field Life

During the exploration phase of a field's life, the *drill stem test* remains the most common well test method for proving exploration hypothesis. This kind of testing involves reservoir fluid flowing through the drill stem used for drilling. Also, during appraisal phase of field life, well testing provides an important approach for evaluating the key reservoir properties that define the reservoir and well productivity. Finally, during the development stage of a field's life, continuous bottom-hole measurement with permanent downhole tools such as pressure gauges provides a useful way for monitoring well and reservoir performance over well and field life. The role of well testing at different stages of field life is summarized in Table 8.2.

from a *direct problem*, such as reservoir simulation, where pressure response is predicted using a defined reservoir model and rate input (Fig. 8.4). A well test as an inverse problem may be characterized as nonunique, as more than one interpretation model may yield the same pressure and rate response, unlike forward reservoir simulation where there is only one possible pressure response for a given rate input.

Due to the nonuniqueness of well test interpretation, it is important to ensure that the interpretation model deduced from well test interpretation does not only predict pressure response for the same rate input but is also consistent with all other data acquired and, most importantly, makes sense.

Steps for well test interpretation are summarized in the flow chart shown in Fig. 8.5.

### 8.3. WELL TEST INTERPRETATION METHODOLOGY

Well test analysis is an *inverse problem* that involves determining a *well test interpretation model* using the pressure and rate signal (Fig. 8.3). This is quite different

**Table 8.1** Reservoir and Well Characterization Information from Well Test.

Well description	Reservoir description	Boundaries
Well condition (skin).	Permeability (horizontal and vertical).	Boundary types (no-flow, constant pressure, leaky, etc.).
Productivity index (production potential).	Reservoir heterogeneities (fissures, layering, characteristic change).	Boundary dimensions.
Well geometry.	Pressures (initial and average).	

**Table 8.2** Role of Well Testing at Different Stages of Field Life.

Exploration	Appraisal	Development
Confirmation of exploration hypothesis.	Assessing well productivity.	Monitoring of well conditions during life span of reservoir.
Forecasting initial production profile.	Defining reservoir heterogeneities.	Monitoring reservoir performance and pressure.
Determining nature and rate of produced fluid.	Defining reservoir boundaries.	
Determining initial reservoir pressure.	Determine reservoir drive mechanism.	
Evaluating well and reservoir properties.	Collecting pristine reservoir fluid sample.	

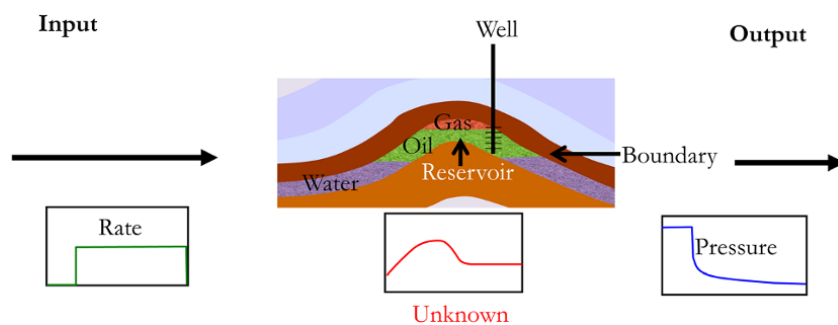


**Figure 8.3** Well test analysis as an inverse problem.



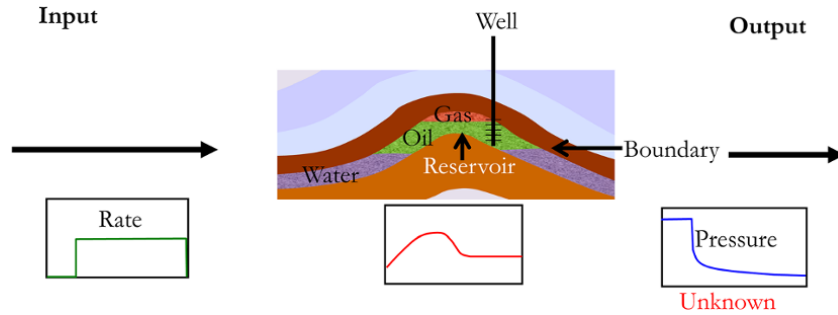


Figure 8.4 Reservoir simulation as a direct problem (Convolution).

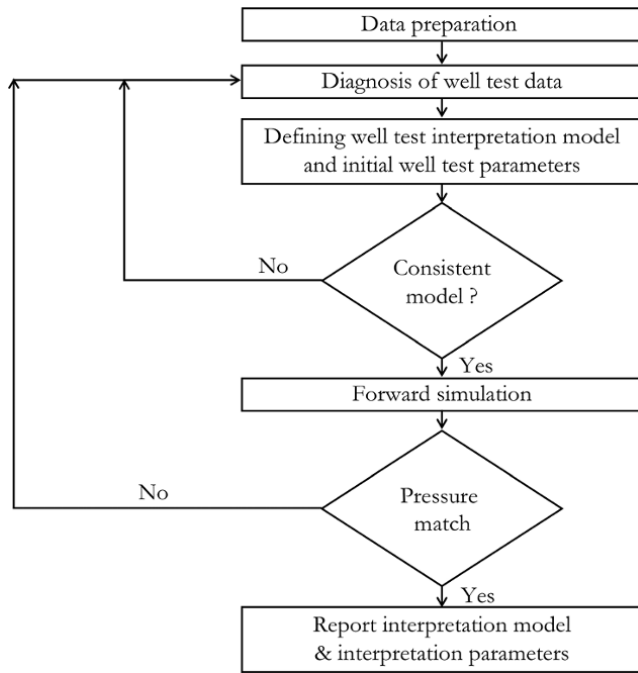


Figure 8.5 Summary of the well test interpretation process.

### 8.4. WELL TEST ANALYSIS APPROACH

The approach recommended for well test analysis is an integrated approach that includes specialized straight-line equations (Chapter 7) combined with well test derivative analysis (Section 8.4.2) for diagnosis and initial parameter calculation then an analytical well test model (Section 8.5.1) for forward simulation and regression to improve calculated well test parameters.

Well test specialized straight-line equations, diagnostic derivatives, and analytical interpretation models are all derived from the diffusivity equation (equation (7.11)),

which describes the variation in pressure change with time and position in the reservoir. Another well test analysis method, which is also derived from the diffusivity equation, is the *pressure-type curve analysis*, which is not common any more.

#### 8.4.1. Pressure-type Curve Analysis

This involves matching data and an applicable interpretation model on a log-log graph to obtain the desired well and reservoir parameters. pressure-types curves are defined in terms of dimensionless. Dimensionless pressure and dimensionless time are directly proportional to pressure change and elapsed time, respectively. Hence, actual pressure drop on a log-log graph varies from the model match by displacement along both the pressure and time axes. Using this displacement, reservoir and well parameters can then be calculated.

**8.4.1.1. Gringarten-type Curve.** The Gringarten-type curve (Fig. 8.6) is for well test analysis in a reservoir with wellbore storage and skin effect. Dimensionless variables in engineering oil field (EOF) units are defined as:

Dimensionless pressure

$$P_D = \frac{kh}{141.2qB\mu} \Delta p \tag{8.3}$$

Dimensionless time

$$\frac{t_D}{C_D} = 0.000295 \frac{kh \Delta t}{\mu C} \tag{8.4}$$

Wellbore storage

$$C_{De}^{2S} = \frac{0.8936}{\phi c_r h r_w^2} C_e^{2S} \tag{8.5}$$

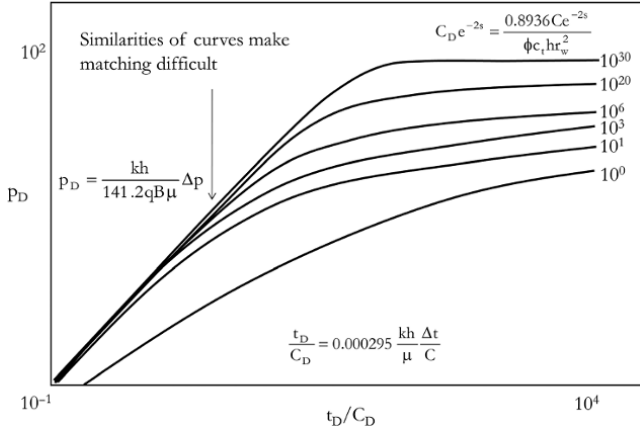


**Figure 8.6** Gringarten-type curves [Adapted from Gringarten, Bourdet, Landel, & Kniazeff, 1979].

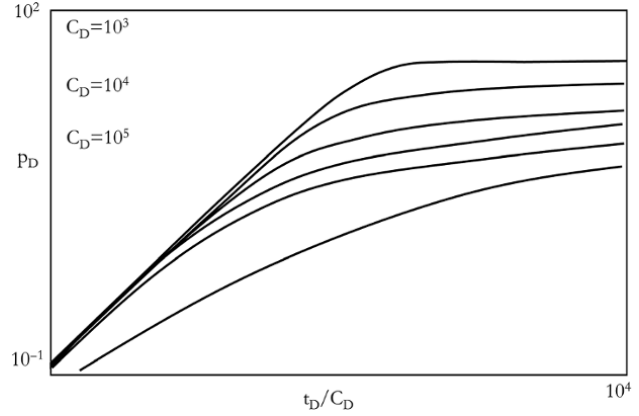


**Figure 8.8** Wellbore storage and skin type curve with  $t_D/C_D$  as an independent variable.

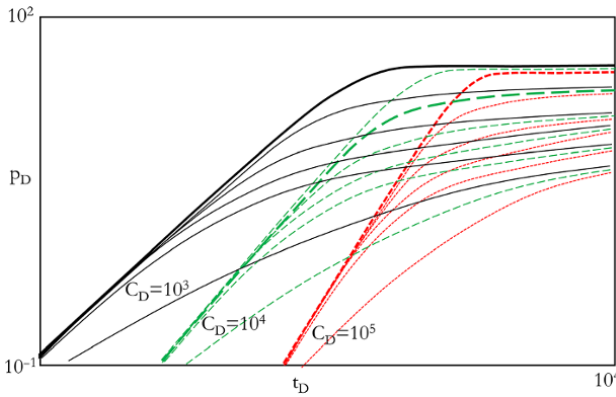


**Figure 8.7** Wellbore storage and skin type curve with  $t_D$  as an independent variable.

The Gringarten-type curve solution in the Laplace domain is expressed as:

$$\bar{p}_{wD}(C_D, s, S) = \frac{1}{s \left\{ s + \frac{1}{2} \frac{1}{\ln \frac{s}{\sqrt{s/C_D} e^{-2s}}} \right\}} \quad (8.6)$$

Defining the independent variable as  $\frac{t_D}{C_D} = 0.000295 \frac{kh \Delta t}{\mu C}$  rather than  $t_D = \frac{0.000264k}{\phi \mu c_t r_w^2} \Delta t$  is important, as shown in Fig. 8.7 and Fig. 8.8. For  $t_D = \frac{0.000264k}{\phi \mu c_t r_w^2} \Delta t$ , multiple curves exist for the same  $C_D$ . However, when the independent variable is defined as  $\frac{t_D}{C_D} = 0.000295 \frac{kh \Delta t}{\mu C}$ ,

$C_D = 10^3, 10^4,$  and  $10^5$  all overlay as a single type curve and reduces to Fig. 8.8.

*Gringarten-type Curves – Interpretation Process*

1. Field data ( $\Delta p$  against  $\Delta t$ ) are plotted on log-log scale on a tracing (see dotted chart in Fig. 8.9).

2. Data are then matched on the curves using steps i to iv:

- (i) pick any convenient point (match point) (Fig. 8.10);
- (ii) read  $\Delta p$  and  $p_D$  corresponding to the match point and calculate  $\frac{p_D}{\Delta p}$  (Fig. 8.10);
- (iii) read  $\Delta t$  and  $\frac{t_D}{C_D}$  corresponding to the match point and calculate  $\frac{t_D}{C_D} / \Delta t$  (Fig. 8.10);
- (iv) read the matching value of  $C_D e^{-2s}$ ;

3. calculate well test parameters in the sequence :

- (i)  $k = \frac{141.2qB\mu}{h} \left( \frac{p_D}{\Delta p} \right)_{@match}$
- (ii)  $C = 0.000295 \frac{kh}{\mu} \left( \frac{\Delta t}{t_D/C_D} \right)_{@match}$
- (iii)  $S = \frac{1}{2} \ln \left( \frac{0.8936C}{\phi c_t h r_w^2 (C_D e^{-2S})_{@match}} \right)$

For a fractured well, skin can be related to *fractured half-length* ( $x_f$ ) using the *equivalent wellbore radius*, equation (7.55):

$$r_{we} = r_w e^{-S} = \frac{x_f}{2}$$

Hence, fracture half-length can be calculated using:

$$x_f = 2r_w e^{-S} \quad (8.7)$$

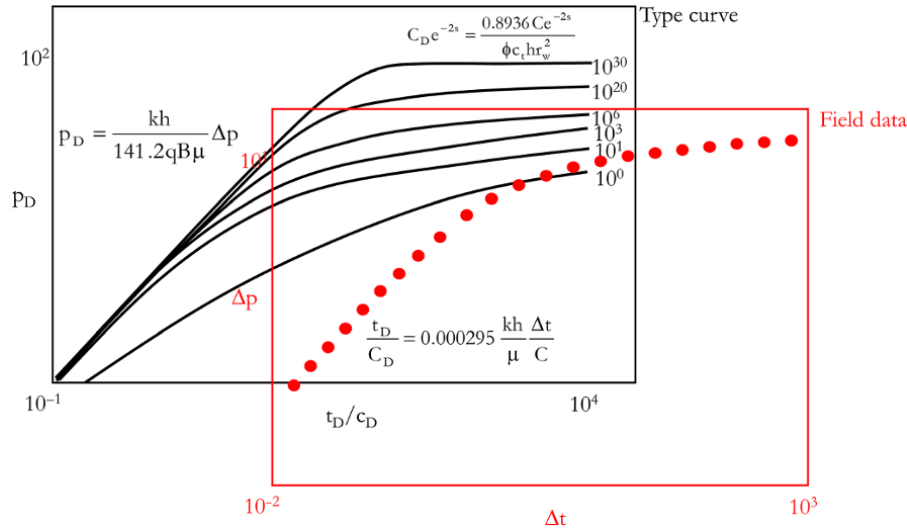


Figure 8.9 Unmatched field data with Gringarten-type curve.

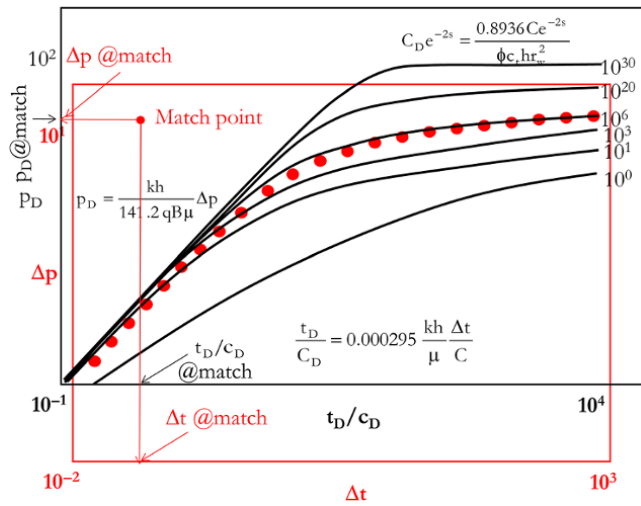


Figure 8.10 Matched field data with a Gringarten-type curve.

**8.4.1.2. Bourdet-type Curves.** Bourdet *et al.* [1983] presented a set of curves that included the pressure derivative plot together with pressure change (Fig. 8.11). The advantage of the derivative is that it accentuates the various flow regimes, thus enhancing the diagnostic capability for the interpreter.

Considering the semi-log straight-line equation for radial flow behavior:

$$p_D = \frac{1}{2} \ln t_D + 0.4045 + S \quad (8.8)$$

Taking the derivative with respect to  $\ln(t_D)$ :

$$\frac{dp_D}{d \ln(t_D)} = 0.5 = \frac{t_D dp_D}{d(t_D)} \quad (8.9)$$

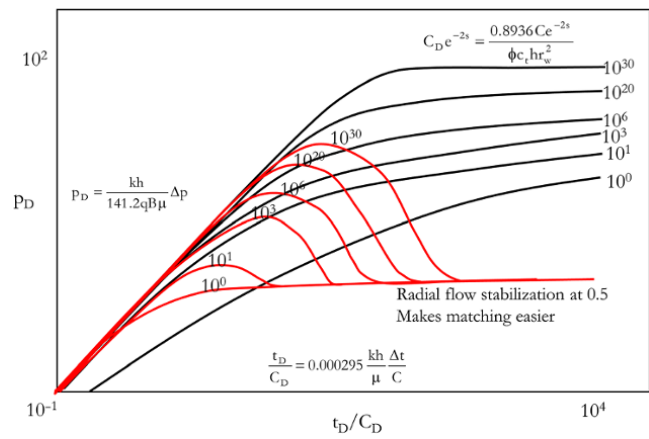


Figure 8.11 Bourdet derivative type curves [Adapted from Bourdet, Whittle, Douglas, & Pirard, 1983].

This means that radial flow stabilization that corresponds to homogeneous reservoir behavior will correspond to a value of 0.5 for the derivative of pressure change in dimensionless variable terms.

Hence, to match field data to the type of curve, the derivatives of the data are placed to match the derivative of a type curve at 0.5 and movement of field data will only be horizontally to match type curve (Fig. 8.12 and Fig. 8.13). This makes matching easier than the Gringarten-type curve.

Well test parameters are then calculated using the same approach described in a Gringarten-type curve using equations (8.3)–(8.5).

Bourdet *et al.* [1983] published the *double porosity type curves* (Fig. 8.14). The dashed line defines  $\frac{\lambda C_D}{\omega(1-\omega)}$  and is used to determine  $\omega$  and  $\lambda$ .

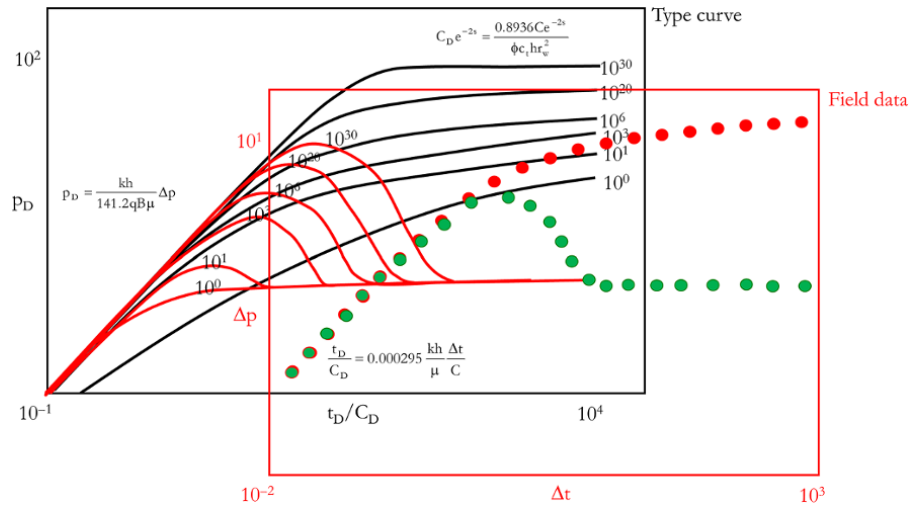


**Figure 8.12** Unmatched field data with a Bourdet-type curve [Adapted from Bourdet, Whittle, Douglas, & Pirard, 1983].

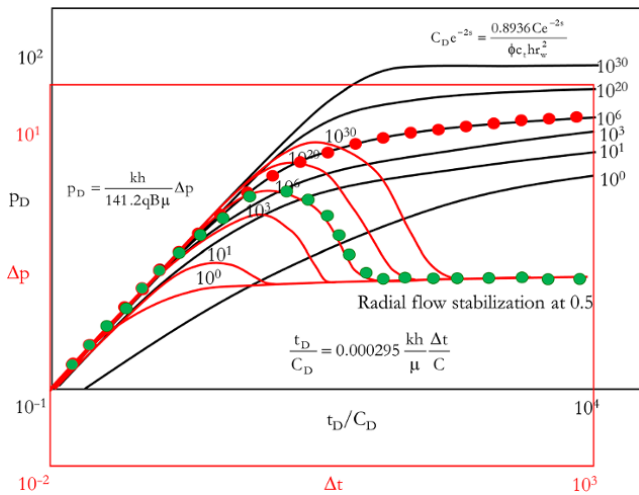


**Figure 8.13** Matched field data with a Bourdet-type curve [Adapted from Bourdet, Whittle, Douglas, & Pirard, 1983].

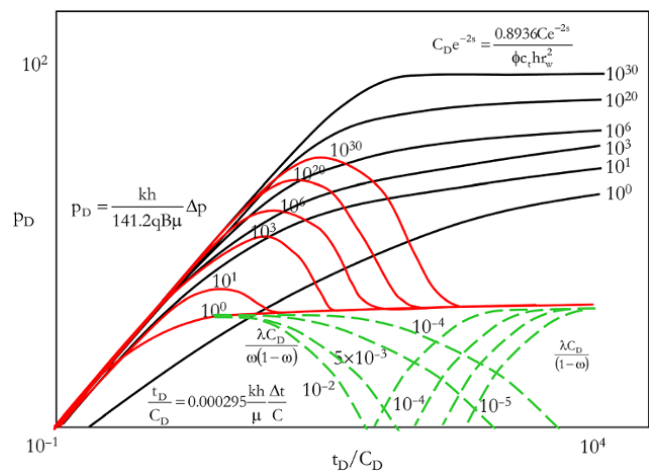


**Figure 8.14** Bourdet double porosity type curve [Adapted from Bourdet, Whittle, Douglas, & Pirard, 1983].

### 8.4.2. Pressure Derivatives

Pressure derivatives have been the most important diagnostic plot in well test analysis. As shown in Fig. 8.15a, the first drawdown semi-log specialized plot (Fig. 7.17 and Fig. 8.15a) shows that radial flow in a homogeneous reservoir is characterized by a straight-line with a slope of  $m_{RF}$ . Therefore, the derivative of pressure change ( $\Delta p$ ) for first drawdown with respect to  $\ln(\Delta t)$  will give a horizontal line with a slope of zero when radial flow is manifest during first drawdown (Fig. 8.15b).

Similarly, buildup following first drawdown is characterized by straight-line with a slope of  $m_{RF}$  during radial flow in an homogeneous reservoir on a Horner plot

(Fig.7.19 and Fig. 8.16a). Hence derivative of pressure change ( $\Delta p$ ) with respect to  $\ln\left(\frac{t_p + \Delta t}{\Delta t}\right)$  will give a horizontal line with a slope of zero when radial flow is manifest during buildup following first drawdown (Fig. 8.16b).

For a varying flow rate (multirate) test, radial flow is characterized by a straight-line with slope  $m_{RF}$  (Fig. 7.24 and Fig. 8.17a) on the superposition plot. Hence, the derivative of  $\Delta p$  with respect to the superposition function ( $f_{radial}$ ) will give a horizontal line with a slope of zero when radial flow is manifest during a multirate test (Fig. 8.17b).

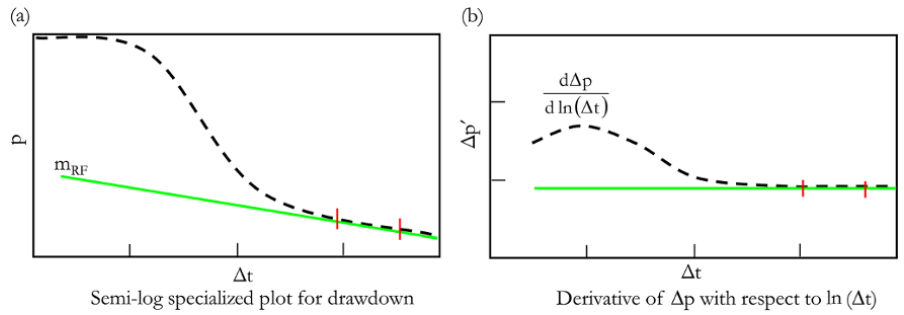


Figure 8.15 Specialized straight-line and derivative plot for drawdown.

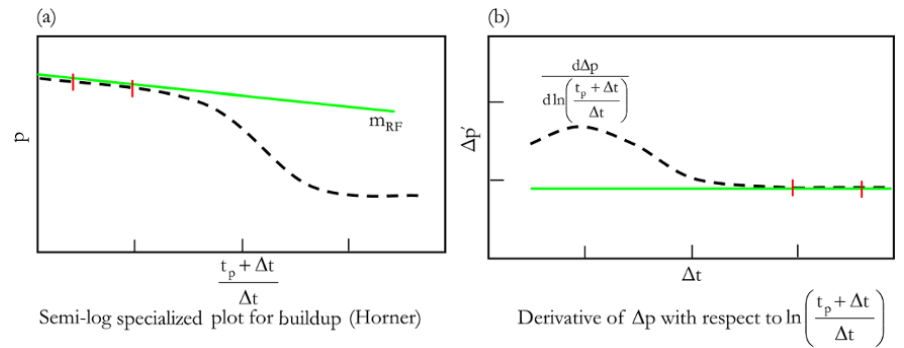


Figure 8.16 Specialized straight-line and derivative plot for buildup.

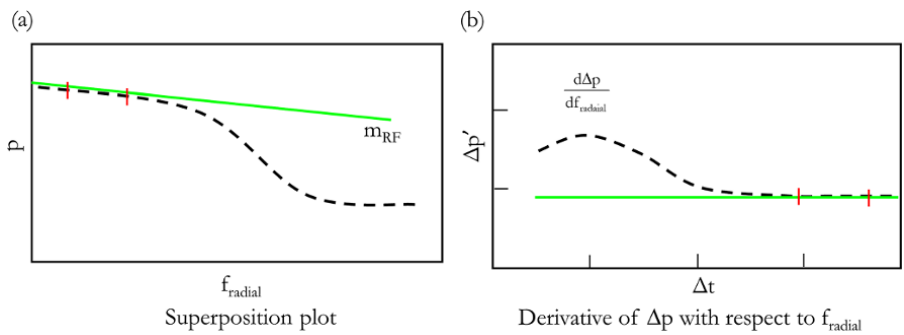


Figure 8.17 Superposition plot and derivative with respect to  $f_{radial}$ .

As shown in Fig. 8.15–Fig. 8.17, the well test log-log derivative is plotted against elapsed time ( $\Delta t$ ).

### 8.4.3. Well Test Derivative Diagnostic Plot

The derivative used in well test analysis is different from the conventional derivative used in classical mathematics/sciences. The well test derivative is defined by a window length ( $L$ ) that introduces smoothing to suppress the effect

of noise associated with pressure measurements [Bourdet *et al.*, 1989].

The derivative at the point of interest,  $j$ , for a given smoothing value,  $L$ , is expressed in equation (8.10), where the parameters used in the equation are defined in Fig. 8.18.  $Y$  corresponds to  $\Delta p$  and  $X$  corresponds to any one of the time transforms, the independent variable for derivative as shown in Fig. 8.15–Fig. 8.17. These time transforms include  $\ln(\Delta t)$ ,  $\ln\left(\frac{t_p + \Delta t}{\Delta t}\right)$ , and  $f_{radial}$ . For a

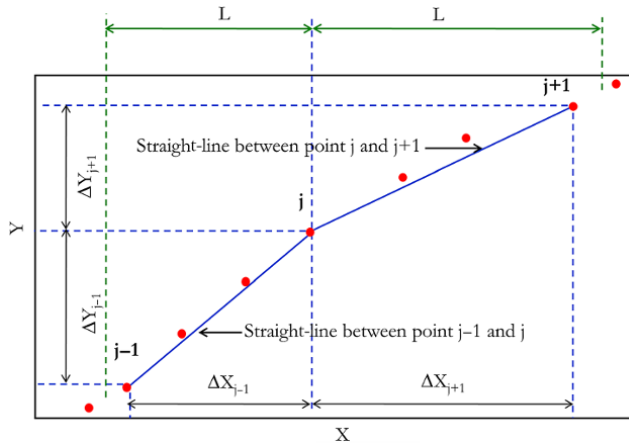


**Figure 8.18** Parameters for well test derivative [Adapted from Bourdet, Ayoub, & Pirard, 1989].

derivative with a window length of  $2L$  with  $j - 1$  and  $j + 1$  being adjacent data points within the limits of  $2L$  close to  $j$  (Fig. 8.18), the derivative at the point of interest  $j$  for a given smoothing value of  $L$  is:

$$\Delta p'_j = \left( \frac{\Delta Y}{\Delta X} \right)_j = \frac{\frac{\Delta Y_{j-1}}{\Delta X_{j-1}} \Delta X_{j+1} + \frac{\Delta Y_{j+1}}{\Delta X_{j+1}} \Delta X_{j-1}}{\Delta X_{j-1} + \Delta X_{j+1}} \quad (8.10)$$

$L$  should be kept as small as possible so as not to suppress important well and/or reservoir features on well test derivative.  $L = 0$  means no derivative smoothing (using consecutive points for derivative calculation) while  $L = 0.5$  (50%) means extreme smoothing.

**8.4.3.1. Radial Flow Behavior on Derivative Diagnostic Plot.** For first drawdown, the derivative is defined with respect to  $\ln(\Delta t)$ :

$$\begin{aligned} \Delta p'_{\text{radial}} &= \frac{d\Delta p}{d\ln(\Delta t)} = \frac{d\Delta p}{d\left(\frac{\log(\Delta t)}{\log e_{10}}\right)} = \frac{d\Delta p(\log e_{10})}{d\log(\Delta t)} \\ &= \frac{0.4342d\Delta p}{d\log(\Delta t)} = 0.4342m_{\text{RF}} \end{aligned} \quad (8.11)$$

Similarly, for the first buildup following a single drawdown, the derivative is defined with respect to  $\ln\left(\frac{t_p + \Delta t}{\Delta t}\right)$ .

$$\begin{aligned} \Delta p'_{\text{radial}} &= \frac{d\Delta p}{d\ln\left(\frac{t_p + \Delta t}{\Delta t}\right)} = \frac{d\Delta p}{d\left(\frac{\log\left(\frac{t_p + \Delta t}{\Delta t}\right)}{\log e_{10}}\right)} \\ &= \frac{0.4342d\Delta p}{d\log\left(\frac{t_p + \Delta t}{\Delta t}\right)} = 0.4342m_{\text{RF}} \end{aligned} \quad (8.12)$$

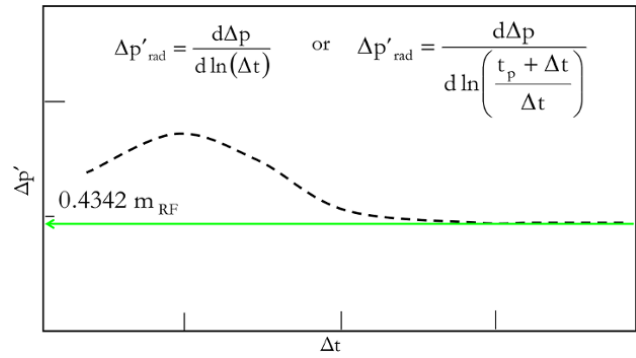


**Figure 8.19** Relationship between derivative with respect to  $\ln(\Delta t)$  or  $\ln\left(\frac{t_p + \Delta t}{\Delta t}\right)$  and  $m_{\text{RF}}$ .

From equations (8.11) and (8.12), the level (value) of radial flow stabilization on the  $y$ -axis of the log-log derivative plot corresponds to  $0.4342$  multiplied by the slope on the specialized drawdown and buildup plot as illustrated in Fig. 8.19. The value of radial flow stabilization from the derivative plot for the derivative with respect to  $\ln(\Delta t)$  or  $\ln\left(\frac{t_p + \Delta t}{\Delta t}\right)$  can be expressed as:

$$\Delta p'_{\text{rad}} = 0.4342m_{\text{RF}} \quad (8.13)$$

Note that the value  $0.4342$ , which is  $\frac{1}{\ln(10)}$  in Fig. 8.19, is due to the fact that the derivative was plotted on a log-log ( $\log_{10}$  by  $\log_{10}$ ) scale but the derivative was taken with respect to time transform defined by a natural log ( $\ln$ ).

For a derivative taken with respect to log radial superposition function ( $f_{\log\_radial}$ ) defined by equation (7.86),  $f_{\log\_radial}(t) = \sum_{i=1}^n \frac{(q_i - q_{i-1})}{(q_{n-1} - q_n)} \log(t - t_{i-1})$ , the value of radial flow stabilization on the derivative ( $\Delta p'_{\text{rad}}$ ) will relate to  $m_{\text{RF}}$  by:

$$\Delta p'_{\text{rad}} = m_{\text{RF}} \quad (8.14)$$

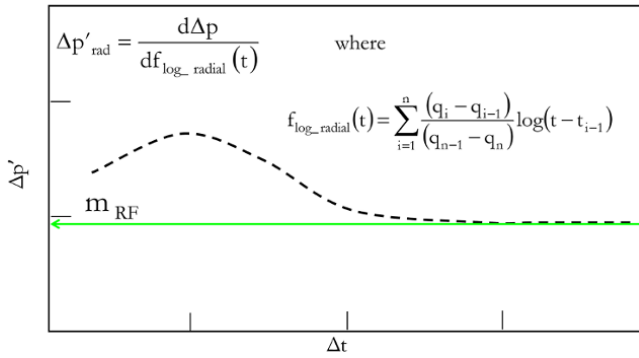
However, if the independent variable for the derivative is defined as:

$$f_{\ln\_radial}(t) = \sum_{i=1}^n \frac{(q_i - q_{i-1})}{(q_{n-1} - q_n)} \ln(t - t_{i-1}) \quad (8.15)$$

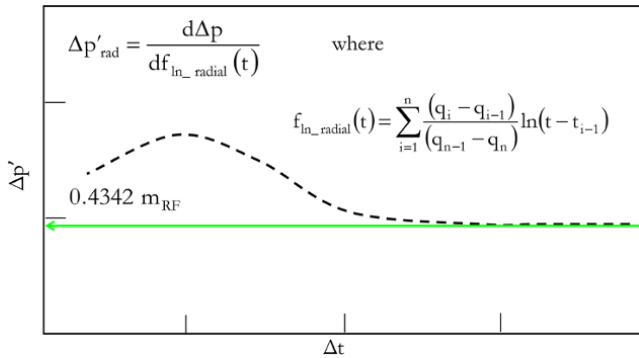
then equation (8.13), which is  $\Delta p'_{\text{rad}} = 0.4342m_{\text{RF}}$ , holds.

Fig. 8.20 and Fig. 8.21 show relationships between  $m_{\text{RF}}$  and  $\Delta p'$  depending on how the independent variable for the derivative is defined.

In order to keep the derivative plot and level of derivative in a variable-rate test consistent with that of the drawdown and buildup test, the variable-rate (multirate) test



**Figure 8.20** Relationship between derivative with respect to  $\sum_{i=1}^n \frac{(q_i - q_{i-1})}{(q_{n-1} - q_n)} \log(t - t_{i-1})$  and  $m_{RF}$ .



**Figure 8.21** Relationship between derivative with respect to  $\sum_{i=1}^n \frac{(q_i - q_{i-1})}{(q_{n-1} - q_n)} \ln(t - t_{i-1})$  and  $m_{RF}$ .

pressure change derivative should be taken with respect to the *ln radial superposition function* ( $f_{ln\_radial}$ ). This ensures the equation (8.13), which is  $\Delta p'_{rad} = 0.4342 m_{RF}$ , holds for the drawdown test, buildup test, flow-after-flow and variable-rate test.

The relationship between  $f_{ln\_radial}$  and  $f_{log\_radial}$  is:

$$\begin{aligned} \sum_{i=1}^n \frac{(q_i - q_{i-1})}{(q_{n-1} - q_n)} \ln(t - t_{i-1}) &= \sum_{i=1}^n \frac{(q_i - q_{i-1})}{(q_{n-1} - q_n)} \frac{\log(t - t_{i-1})}{\log e} \\ &= \frac{1}{0.4342} \sum_{i=1}^n \frac{(q_i - q_{i-1})}{(q_{n-1} - q_n)} \log(t - t_{i-1}) \\ f_{ln\_radial} &= \frac{1}{0.4342} f_{log\_radial} \end{aligned} \quad (8.16)$$

Also for the flow-after-flow or variable-rate test, the relationship between the derivative with respect to  $f_{ln\_radial}$  and the derivative with respect to  $f_{log\_radial}$  is:

$$\begin{aligned} \Delta p'_{radial} &= \frac{d\Delta p}{df_{ln\_radial}} = \frac{d\Delta p}{\frac{df_{log\_radial}}{0.4342}} = 0.4342 \frac{d\Delta p}{df_{log\_radial}} \\ \frac{d\Delta p}{df_{ln\_radial}} &= 0.4342 \frac{d\Delta p}{df_{log\_radial}} \end{aligned} \quad (8.17)$$

**8.4.3.2. Skin Effect on the Derivative Diagnostic Plot.**

Considering a drawdown test. From equation (7.67):

$$p_i - p_{wf} = 162.6 \frac{qB\mu}{kh} \left( \log \Delta t + \log \frac{k}{\phi \mu c_t r_w^2} - 3.23 + 0.87S \right)$$

Considering any data point on radial flow stabilization on derivative plot at elapsed time  $\Delta t_{rad}$ :

$$\begin{aligned} p_i - p_{wf}(\Delta t_{rad}) &= 162.6 \frac{qB\mu}{k_r h} \\ &\left( \log \Delta t_{rad} + \log \frac{k}{\phi \mu c_t r_w^2} - 3.23 + 0.87S \right). \end{aligned}$$

Substituting  $m_{RF} = 162.6 \frac{qB\mu}{k_r h}$  into equation above:

$$\Delta p_{rad} = m_{RF} \left( \log \Delta t_{rad} + \log \frac{k}{\phi \mu c_t r_w^2} - 3.23 + 0.87S \right)$$

and making S the subject of the formula:

$$S = 1.15 \left( \frac{\Delta p_{rad}}{m_{RF}} - \log \frac{k \Delta t_{rad}}{1698.244 \phi \mu c_t r_w^2} \right)$$

Substituting  $m_{RF} = \frac{\Delta p'_{rad}}{0.4342}$  from equation (8.13) into the above, the skin effect for drawdown from the derivative plot is thus:

$$S = 1.15 \left( \frac{0.4342 \Delta p_{rad}}{\Delta p'_{rad}} - \log \frac{k \Delta t_{rad}}{1698.244 \phi \mu c_t r_w^2} \right) \quad (8.18)$$

$$S = 1.15 \left( \frac{p_i - p_{1hr}}{m_{RF}} - \log \frac{k}{\phi \mu c_t r_w^2} + 3.23 \right)$$

From equation (8.18), the magnitude of  $\frac{\Delta p_{rad}}{\Delta p'_{rad}}$  is directly proportional directly to the skin effect S. Hence, the greater the distance between  $\Delta p$  and  $\Delta p'$  the greater the skin effect. A combined plot of  $\Delta p$  and  $\Delta p'$  against elapsed time  $\Delta t$  is generally referred to as *log-log diagnostic plot*. The log-log diagnostic plot in Fig. 8.22 shows how to read  $\Delta p_{rad}$  and  $\Delta p'_{rad}$  at any given  $\Delta t_{rad}$ .

Because the level of radial stabilization depends on rate, for comparison of a log-log diagnostic plot with different rate,  $\Delta p_{rad}$  and  $\Delta p'_{rad}$  should be rate normalized by

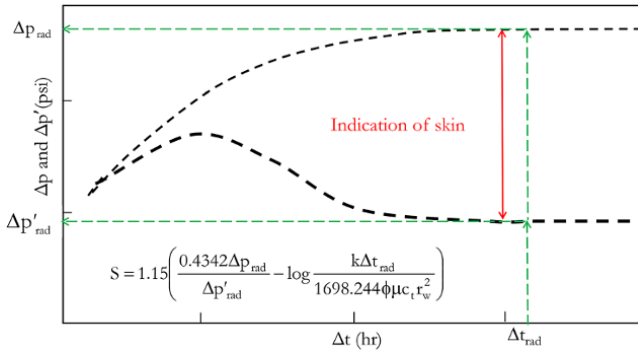


**Figure 8.22** Skin effect calculation using a log-log diagnostic plot.

dividing  $\Delta p_{rad}$  and  $\Delta p'_{rad}$  by rate change ( $q_i - q_{i-1}$ ) to remove the effect of rate on derivative.

Skin effect for buildup analysis from a derivative plot can be derived from equation (7.74):

$$S = 1.15 \left( \frac{p_{1hr} - p_{wf}(t_p)}{m_{RF}} + \log \frac{t_p + 1}{t_p} - \log \frac{k}{\phi \mu c_t r_w^2} + 3.23 \right).$$

The equation above is the same as:

$$S = 1.15 \left( \frac{p_{rad} - p_{rad} + p_{1hr} - p_{wf}(t_p)}{m_{RF}} + \log \frac{t_p + 1}{t_p} - \log \frac{k}{\phi \mu c_t r_w^2} + 3.23 \right).$$

Note that  $p_{rad}$  was added and subtracted.

Where  $p_{rad}$  is any pressure point corresponding to  $t_{rad}$  (any point where radial flow exists), the above equation becomes:

$$S = 1.15 \left( \frac{p_{rad} - p_{wf}(t_p)}{m_{RF}} + \frac{p_{1hr} - p_{rad}}{m_{RF}} + \log \frac{t_p + 1}{t_p} - \log \frac{k}{\phi \mu c_t r_w^2} + 3.23 \right) \quad (8.19)$$

Note that from the Horner plot:

$$\frac{p_{1hr} - p_{rad}}{\log \left( \frac{t_p + \Delta t_{rad}}{\Delta t_{rad}} \right) - \log \left( \frac{t_p + 1}{1} \right)} = m_{RF}$$

Hence:

$$\frac{p_{1hr} - p_{rad}}{m_{RF}} = \log \left( \frac{t_p + \Delta t_{rad}}{\Delta t_{rad}} \right) - \log \left( \frac{t_p + 1}{1} \right)$$

Substituting expression for  $\frac{p_{1hr} - p_{rad}}{m_{RF}}$  above into equation (8.19):

$$S = 1.15 \left( \frac{p_{rad} - p_{wf}(t_p)}{m_{RF}} + \log \left( \frac{t_p + \Delta t_{rad}}{\Delta t_{rad}} \right) - \log \left( \frac{t_p + 1}{1} \right) + \log \frac{t_p + 1}{t_p} - \log \frac{k}{\phi \mu c_t r_w^2} + 3.23 \right)$$

$$S = 1.15 \left( \frac{\Delta p_{rad}}{m_{RF}} + \log \left( \frac{t_p + \Delta t_{rad}}{t_p \Delta t_{rad}} \right) - \log \frac{k}{\phi \mu c_t r_w^2} + 3.23 \right) \quad (8.20)$$

From equation (8.13)  $m_{RF} = \frac{\Delta p'_{rad}}{0.4342}$

Substituting  $m_{RF} = \frac{\Delta p'_{rad}}{0.4342}$  into equation (8.20):

$$S = 1.15 \left( \frac{0.4342 \Delta p_{rad}}{\Delta p'_{rad}} - \log \frac{k t_p \Delta t_{rad}}{1698.244 \phi \mu c_t r_w^2 (t_p + \Delta t_{rad})} \right) \quad (8.21)$$

Also for a buildup test, as shown by equation (8.21), the magnitude of  $\frac{\Delta p_{rad}}{\Delta p'_{rad}}$  is directly proportional directly to the skin effect S.

For flow periods (test) in a multirate test, normalized pressure change and normalized derivative  $\left( \frac{\Delta p}{q_i - q_{i-1}} \right)$  and  $\frac{\Delta p'}{q_i - q_{i-1}}$  respectively) should be used for the log-log diagnostic plot. For such a test, with the derivative taken with respect to  $f_{in\_radial} = \sum_{i=1}^n \frac{(q_i - q_{i-1})}{(q_{n-1} - q_n)} \ln(t - t_{i-1})$ ,  $\Delta p'_{rad} = 0.4342 m_{RF}$  as defined by equation (8.13) is valid. Hence, the skin effect for the multirate test defined in equation (7.95) is:

$$S = 1.15 \left( \frac{p_{1hr} - p_{wf}(t_{n-1})}{m_{RF}} - \log \frac{k}{\phi \mu c_t r_w^2} + 3.23 \right)$$

and becomes:

$$S = 1.15 \left( \frac{p_{rad} - p_{rad} + p_{1hr} - p_{wf}(t_{n-1})}{m_{RF}} - \log \frac{k}{\phi \mu c_t r_w^2} + 3.23 \right)$$

$$S = 1.15 \left( \frac{p_{rad} - p_{wf}(t_{n-1})}{m_{RF}} + \frac{p_{1hr} - p_{rad}}{m_{RF}} - \log \frac{k}{\phi \mu c_t r_w^2} + 3.23 \right) \quad (8.22)$$

Note that, from the superposition function plot:

$$\frac{p_{1hr} - p_{rad}}{f_{log\_radial}(\Delta t_{rad}) - f_{log\_radial}(\Delta t_{1hr})} = m_{RF}$$

Hence:

$$\frac{p_{1hr} - p_{rad}}{m_{RF}} = f_{log\_radial}(\Delta t_{rad}) - f_{log\_radial}(\Delta t_{1hr})$$



Substituting the expression for  $\frac{P_{1hr} - P_{rad}}{m_{RF}}$  above into equation (8.22):

$$S = 1.15 \left( \frac{P_{rad} - P_{wf}(t_{n-1})}{m_{RF}} + f_{log\_radial}(\Delta t_{rad}) - f_{log\_radial}(\Delta t_{1hr}) - \log \frac{k}{\phi \mu c_t r_w^2} + 3.23 \right)$$

$$S = 1.15 \left( \frac{P_{rad} - P_{wf}(t_{n-1})}{m_{RF}} - \log \frac{k}{\phi \mu c_t r_w^2} + [f_{log\_radial}(\Delta t_{rad}) - f_{log\_radial}(\Delta t_{1hr})] + 3.23 \right)$$

$$S = 1.15 \left( \frac{\Delta p_{rad}}{m_{RF}} - \log \frac{k}{\phi \mu c_t r_w^2} + [f_{log\_radial}(\Delta t_{rad}) - f_{log\_radial}(\Delta t_{1hr})] + 3.23 \right)$$

For the superposition principle equation (8.13),  $\Delta p'_{rad} = 0.4342 m_{RF}$  holds:

Hence, for a multirate test, with derivative taken with respect to  $f_{ln\_radial} = \sum_{i=1}^n \frac{(q_i - q_{i-1})}{(q_{n-1} - q_n)} \ln(t - t_{i-1})$ , the skin effect becomes:

$$S = 1.15 \left( \frac{0.4342 \Delta p_{rad}}{\Delta p'_{rad}} - \log \frac{k}{\phi \mu c_t r_w^2} + [f_{log\_radial}(\Delta t_{rad}) - f_{log\_radial}(\Delta t_{1hr})] + 3.23 \right) \tag{8.23}$$

For a multirate test, similar to the drawdown and buildup test, the magnitude of  $\frac{\Delta p_{rad}}{\Delta p'_{rad}}$  is directly proportional directly to the skin effect S.

**8.4.3.3. Wellbore Storage Effect Behavior on the Log-Log Diagnostic Plot.** From the wellbore storage (WBS) equation, equation (7.42):

$$\Delta p = \frac{qB\Delta t}{24C}$$

Taking the derivative with respect to  $\ln(\Delta t)$  for drawdown:

$$\Delta p' = \frac{d\Delta p}{d\ln(\Delta t)} = \frac{d\Delta p}{d\Delta t} \times \frac{d\Delta t}{d\ln(\Delta t)} = \frac{d\Delta p}{d\Delta t} \times \frac{1}{1/\Delta t} = \frac{d\Delta p}{d\Delta t} \times \Delta t$$

Substituting  $\frac{\Delta p}{\Delta t} = \frac{qB}{24C}$  (from the WBS equation) into the equation above:

$$\Delta p' = \frac{qB\Delta t}{24C} \tag{8.24}$$

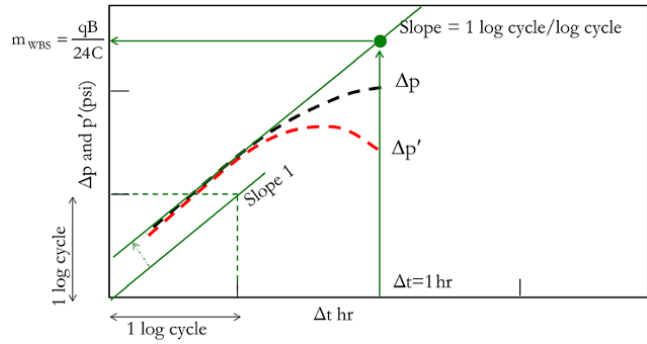


**Figure 8.23** Wellbore storage effect calculation using a log-log diagnostic plot.

Equation (8.24) describes pressure derivative response for WBS and shows that pressure and derivative response have the same characteristic during WBS. Expressing the WBS equation in logarithmic form:

$$\log(\Delta p) = \log(\Delta t) + \log\left(\frac{qB}{24C}\right) \tag{8.25}$$

From equation (8.25), when  $\Delta t = 1$  on a log scale,  $\Delta p = \frac{qB}{24C}$ . Therefore, the value of  $\Delta p$  taken on a slope of 1 at  $\Delta t = 1$  equals  $\frac{qB}{24C}$  which is  $m_{WBS}$ . From  $m_{WBS} = \frac{qB}{24C}$  C can then be determined (Fig. 8.23).

**Exercise 8.1** Using the Well Test Derivative to Calculate C,  $k_r$ , and S

Using the well test derivative method, determine C,  $k_r$ , and S from the buildup flow period data provided in Table 7.3.

**Solution Steps.**

*Step 1:* create a log-log diagnostic plot.

- (i) determine buildup pressure signal,  $\Delta p$ , which is  $p_{ws}(t) - p_{wf}(0)$ , and elapsed time  $\Delta t$ , which is  $t - t_0$ , for the buildup data provided;
- (ii) determine  $\Delta p'$  using equation (8.10);
- (iii) plot  $\Delta p$  against  $\Delta t$  and  $\Delta p'$  against  $\Delta t$  together on the log-log scale Fig. 8.23.

*Step 2:* calculate WBS.

- (i) inspect the early part of  $\Delta p$  against  $\Delta t$  and  $\Delta p'$  against  $\Delta t$  on a log-log plot to determine the start and end of WBS, which will be characterized by a straight-line with a slope of 1 (note on a log-log scale the slope has to be one unlike a specialized Cartesian plot where the slope is  $m_{WBS} = \frac{qB}{24C}$ );
- (ii) at time  $\Delta t = 1$  hr, on the slope of 1 fitted through  $\Delta p$  against  $\Delta t$  and  $\Delta p'$  against  $\Delta t$ , read the value of  $\Delta p$  on the

y-axis. The value corresponds to  $m_{WBS} = \frac{qB}{24C}$  as illustrated in Fig. 8.23;

(iii) using  $m_{WBS} = \frac{qB}{24C}$ , C is then calculated using  $C = \frac{qB}{24m_{WBS}}$ .

Step 3: calculating  $k_r$ .

(i) inspect  $\Delta p'$  against  $\Delta t$  on a log-log scale to determine when the derivative is flat (slope of zero), Fig. 8.19;

(ii) fit a straight line of slope zero through derivative data with slope zero and read the value of  $\Delta p'$  corresponding to slope zero (radial flow stabilization) on the derivative (Fig. 8.19). The read value, which is  $\Delta p'_{rad}$ , equals 0.4342  $m_{RF}$ , where  $m_{RF} = \frac{162.6qB\mu}{k_r h}$ ;

(iii) using  $\Delta p'_{rad} = 0.4342 m_{RF}$  determined from radial flow stabilization,  $k_r$  is then calculated using  $k_r = \frac{162.6qB\mu}{m_{RF}h}$ .

Step 4: calculate S.

$$\Delta p' = \Delta p'_j = \frac{\frac{(\Delta p_j - \Delta p_{j-1})}{\left[ \ln\left(\frac{t_p + \Delta t_j}{\Delta t_j}\right) - \ln\left(\frac{t_p + \Delta t_{j-1}}{\Delta t_{j-1}}\right) \right]} \left[ \ln\left(\frac{t_p + \Delta t_{j+1}}{\Delta t_{j+1}}\right) - \ln\left(\frac{t_p + \Delta t_j}{\Delta t_j}\right) \right] + \frac{(\Delta p_{j+1} - \Delta p_j)}{\left[ \ln\left(\frac{t_p + \Delta t_{j+1}}{\Delta t_{j+1}}\right) - \ln\left(\frac{t_p + \Delta t_j}{\Delta t_j}\right) \right]} \left[ \ln\left(\frac{t_p + \Delta t_j}{\Delta t_j}\right) - \ln\left(\frac{t_p + \Delta t_{j-1}}{\Delta t_{j-1}}\right) \right]}{\left[ \ln\left(\frac{t_p + \Delta t_{j+1}}{\Delta t_{j+1}}\right) - \ln\left(\frac{t_p + \Delta t_{j-1}}{\Delta t_{j-1}}\right) \right]}$$

The derivative calculation is summarized in Table 8.3 and the log-log diagnostic plot shown in Fig 8.24.

**Calculating WBS**

$$m_{WBS} = \frac{qB}{24C} = 625 \text{ psi/hr from Fig. 8.25.}$$

$$C = \frac{qB}{24m_{WBS}} = \frac{150 \times 1.5}{24 \times 625} = 0.015 \text{ bbl/psi}$$

$$C = 0.015 \text{ bbl/psi}$$

**Calculating  $k_r$**

$0.4342 m_{RF} = 10.71 \text{ psi}$  from Fig. 8.26.

Therefore:

$$m_{RF} = \frac{10.71}{0.4342} = 24.67 \text{ psi/log cycle}$$

From equation (7.69):

$$k_r = \frac{162.6qB\mu}{m_{RF}h}$$

$$k_r = \frac{162.6 \times 150 \times 1.5 \times 0.5}{24.67 \times 50} = 14.8 \text{ mD}$$

$$k_r = 14.8 \text{ mD.}$$

(i) pick any elapsed time  $\Delta t_{rad}$  on radial flow stabilization, read the value of  $\Delta p'_{rad}$  and  $\Delta p_{rad}$  on the y-axis, as illustrated in Fig. 8.22;

(ii) determine S using equation (8.21);

$$(iii) S = 1.15 \left( \frac{0.4342 \Delta p_{rad}}{\Delta p'_{rad}} - \log \frac{kt_p \Delta t_{rad}}{1698.244 \phi \mu c_t r_w^2 (t_p + \Delta t_{rad})} \right).$$

**Solution.**

$$t_0 = t_p = 1000 \text{ hr}$$

$$p_0 = p_{ws}(\Delta t = 0) = p_{wf}(t_p) = 4404.845 \text{ psia}$$

Taking the derivative:

$$\Delta p'_j = \left( \frac{\Delta Y}{\Delta X} \right)_j = \frac{\frac{\Delta Y_{j-1}}{\Delta X_{j-1}} \Delta X_{j+1} + \frac{\Delta Y_{j+1}}{\Delta X_{j+1}} \Delta X_{j-1}}{\Delta X_{j-1} + \Delta X_{j+1}}$$

For buildup following the first drawdown, the above equation becomes:

**Calculating S**

From the log-log diagnostic plot (Fig. 8.27):

$\Delta p_{rad} = 570.03 \text{ psi}$  and  $\Delta p'_{rad} = 10.71 \text{ psi}$  at  $\Delta t_{rad} = 105 \text{ hr}$

Substituting  $\Delta p_{rad}$  and  $\Delta p'_{rad}$  into equation (8.18):

$$S = 1.15 \left( \frac{0.4342 \Delta p_{rad}}{\Delta p'_{rad}} - \log \frac{kt_p \Delta t_{rad}}{1698.244 \phi \mu c_t r_w^2 (t_p + \Delta t_{rad})} \right)$$

$$S = 1.15 \left( \frac{0.4342 \times 570.03}{10.71} - \log \frac{14.8 \times 1000 \times 105}{1698.244 \times 0.2 \times 0.5 \times 5 \times 10^{-5} \times 0.33^2 \times (1000 + 105)} \right)$$

$$= 19.467$$

$$S = 19.5.$$

**8.4.3.4. Infinite Conductivity Fracture Behavior on the Diagnostic Plot.** From the ICF equation, equation (7.57):

$$\Delta p = 4.06 \frac{qB}{hx_f} \sqrt{\frac{\mu}{\phi c_t k}} \sqrt{\Delta t}$$

**Table 8.3** Solution to Exercise 8.1.

t (hr)	p (psia)	$\Delta t(\text{hr})=t-t_0$	$(t_p+\Delta t)/\Delta t$	$\Delta p(\text{psi})=p - p_0$	$\Delta p'$ (psi)	t (hr)	p (psia)	$\Delta t(\text{hr})=t-t_0$	$(t_p+\Delta t)/\Delta t$	$\Delta p(\text{psi})=p - p_0$	$\Delta p'$ (psi)
1,000.0010	4,405.47	0.0010	1,000,001.00	0.62	—	1,001.1514	4,776.48	1.1514	869.5117	371.63	171.6025
1,000.0013	4,405.67	0.0013	754,148.81	0.83	0.837	1,001.5264	4,823.06	1.5264	656.1285	418.21	153.5276
1,000.0018	4,405.94	0.0018	568,829.21	1.10	1.110	1,002.0236	4,862.92	2.0236	495.1713	458.07	126.0555
1,000.0023	4,406.30	0.0023	429,185.55	1.45	1.470	1,002.6827	4,894.00	2.6827	373.7593	489.15	94.42601
1,000.0031	4,406.77	0.0031	323,730.36	1.93	1.946	1,003.5565	4,916.03	3.5565	282.1769	511.18	64.79943
1,000.0041	4,407.40	0.0041	244,201.24	2.55	2.576	1,004.7149	4,930.42	4.7149	213.0951	525.57	41.74798
1,000.0054	4,408.22	0.0054	184,196.98	3.38	3.408	1,006.2506	4,939.46	6.2506	160.9859	534.62	26.72772
1,000.0072	4,409.32	0.0072	138,947.78	4.47	4.506	1,008.2864	4,945.40	8.2864	121.6793	540.55	18.44931
1,000.0095	4,410.76	0.0095	104,811.82	5.92	5.952	1,010.9854	4,949.78	10.9854	92.02981	544.94	14.49056
1,000.0126	4,412.67	0.0126	79,058.63	7.83	7.854	1,014.5635	4,953.48	14.5635	69.66488	548.64	12.74449
1,000.0168	4,415.19	0.0168	59,638.40	10.35	10.346	1,019.3070	4,956.87	19.3070	52.79474	552.02	11.95039
1,000.0222	4,418.51	0.0222	44,985.26	13.66	13.601	1,025.5955	4,960.09	25.5955	40.0694	555.25	11.5329
1,000.0295	4,422.86	0.0295	33,932.66	18.02	17.838	1,033.9322	4,963.21	33.9322	30.47052	558.36	11.27472
1,000.0391	4,428.57	0.0391	25,596.74	23.72	23.311	1,044.9843	4,966.24	44.9843	23.22996	561.39	11.09827
1,000.0518	4,436.01	0.0518	19,307.88	31.16	30.328	1,059.6362	4,969.19	59.6362	17.76833	564.35	10.97205
1,000.0687	4,445.67	0.0687	14,564.46	40.82	39.226	1,079.0604	4,972.07	79.0604	13.64855	567.23	10.8799
1,000.0910	4,458.12	0.0910	10,986.39	53.28	50.346	1,104.8113	4,974.88	104.8113	10.54095	570.03	10.81172
1,000.1207	4,474.05	0.1207	8,287.45	69.21	63.974	1,138.9496	4,977.59	138.9496	8.196857	572.74	10.76086
1,000.1600	4,494.19	0.1600	6,251.55	89.35	80.241	1,184.2070	4,980.20	184.2070	6.428675	575.35	10.72266
1,000.2121	4,519.29	0.2121	4,715.87	114.45	98.968	1,244.2053	4,982.69	244.2053	5.094915	577.84	10.69367
1,000.2812	4,549.99	0.2812	3,557.48	145.15	119.458	1,323.7458	4,985.04	323.7458	4.088844	580.19	10.67153
1,000.3728	4,586.64	0.3728	2,683.70	181.79	140.274	1,429.1934	4,987.23	429.1934	3.329952	582.38	10.65449
1,000.4942	4,629.06	0.4942	2,024.59	224.21	159.081	1,568.9866	4,989.23	568.9866	2.757511	584.39	10.64122
1,000.6551	4,676.30	0.6551	1,527.42	271.45	172.740	1,754.3120	4,991.05	754.3120	2.325711	586.20	10.63081
1,000.8685	4,726.40	0.8685	1,152.40	321.56	177.810	2,000.0000	4,992.65	1,000.0000	2.000000	587.80	—

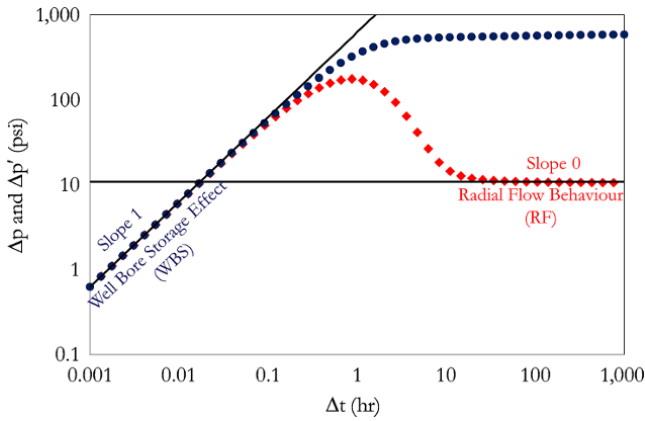


Figure 8.24 Log-log diagnostic plot showing WBS and RF.

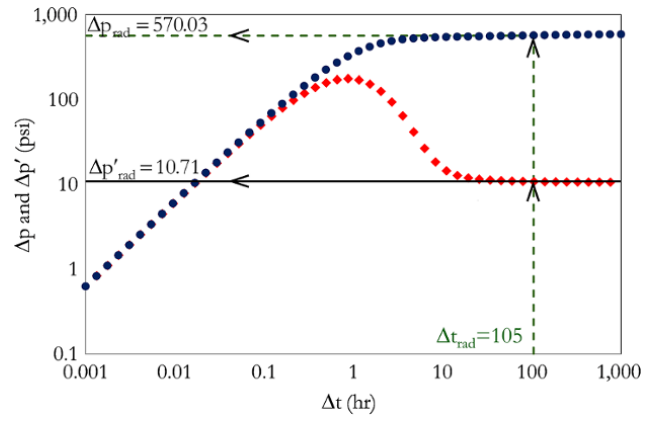


Figure 8.27 Determination of  $\Delta p_{rad}$  and  $\Delta p'_{rad}$  at  $\Delta t_{rad}$  from the log-log diagnostic plot.

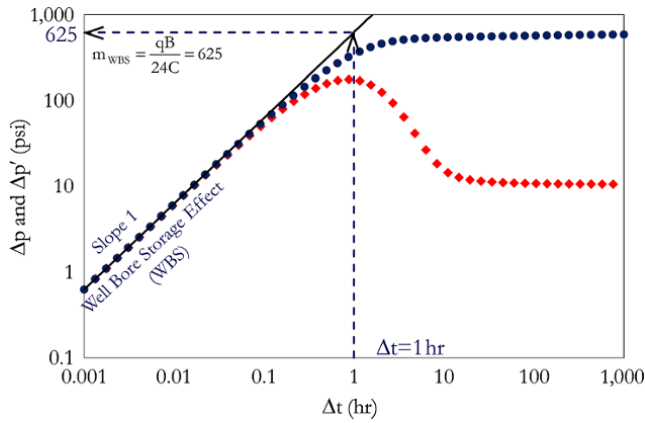


Figure 8.25 Calculation of  $m_{WBS}$  from the log-log diagnostic plot.

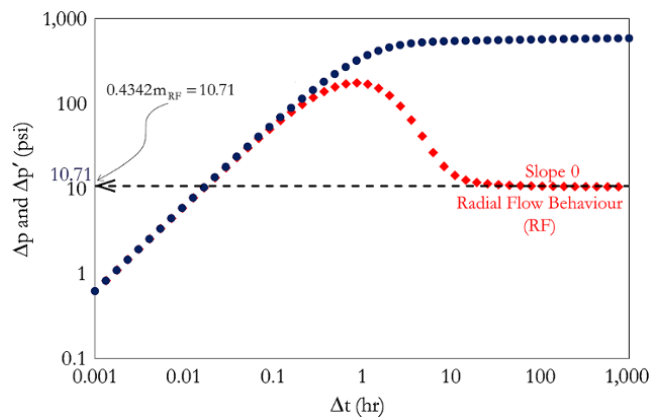


Figure 8.26 Calculation of  $m_{RF}$  from the log-log diagnostic plot.

$$\Delta p' = \frac{d\Delta p}{d\ln(\Delta t)} = \frac{d\Delta p}{d\sqrt{\Delta t}} \times \frac{d\sqrt{\Delta t}}{d\ln(\Delta t)} = \frac{d\Delta p}{d\sqrt{\Delta t}} \times \frac{1/2 \Delta t^{-1/2}}{1/\Delta t} = \frac{d\Delta p}{d\sqrt{\Delta t}} \times 1/2 \Delta t^{1/2} \Rightarrow$$

$$\Delta p' = 2.03 \frac{qB}{hx_f} \sqrt{\frac{\mu}{\phi c_t k}} \sqrt{\Delta t} \quad (8.26)$$

Equation (8.26) describes the pressure derivative response for the infinite conductivity fracture (ICF).

Expressing the ICF equation in logarithm terms:

$$\log \Delta p = \frac{1}{2} \log \Delta t + \log \left( 4.06 \frac{qB}{hx_f} \sqrt{\frac{\mu}{\phi c_t k}} \right) \quad (8.27)$$

Also, expressing the pressure derivative response for the ICF as a logarithm:

$$\log \Delta p' = \frac{1}{2} \log \Delta t + \log \left( 2.03 \frac{qB}{hx_f} \sqrt{\frac{\mu}{\phi c_t k}} \right) \quad (8.28)$$

A plot of  $\Delta p$  against  $\Delta t$  and  $\Delta p'$  against  $\Delta t$  on a log-log scale will both give a slope of one half ( $1/2$ ) as shown by equations (8.27) and (8.28). The level of derivative is half of the pressure (comparing equations (7.57) and (8.26)).

From equation (8.27), when  $\Delta t = 1$  on a log scale,  $\Delta p = 4.06 \frac{qB}{hx_f} \sqrt{\frac{\mu}{\phi c_t k}}$ . Therefore, the value of  $\Delta p$  taken on a slope of  $1/2$  at  $\Delta t = 1$  equals the  $m_{LF}$ , which is

$$4.06 \frac{qB}{hx_f} \sqrt{\frac{\mu}{\phi c_t k}}$$

From

$$m_{LF} = 4.06 \frac{qB}{hx_f} \sqrt{\frac{\mu}{\phi c_t k}} \quad (8.29)$$

$x_f$  can be determined. Fig. 8.28 shows the determination of  $m_{LF}$ .

**8.4.3.5. Finite Conductivity Fracture Behavior on a Diagnostic Plot.** From the finite conductivity fracture (FCF) equation, equation (7.59):

$$\Delta p = 44.11 \frac{qB\mu}{h\sqrt{k_f w_f^4 \phi c_t k}} \sqrt[4]{\Delta t}$$

$$\Delta p' = \frac{d\Delta p}{d \ln(\Delta t)} = \frac{d\Delta p}{d\sqrt[4]{\Delta t}} \times \frac{d\sqrt[4]{\Delta t}}{d \ln(\Delta t)} = \frac{d\Delta p}{d\sqrt[4]{\Delta t}} \times \frac{1/4 \Delta t^{-3/4}}{1/\Delta t} = \frac{d\Delta p}{d\sqrt[4]{\Delta t}} \times 1/4 \Delta t^{1/4} \Rightarrow$$

$$\Delta p' = 11.03 \frac{qB\mu}{h\sqrt{k_f w_f^4 \phi c_t k}} \sqrt[4]{\Delta t} \quad (8.30)$$

Equation (8.30) describes the pressure derivative response for the FCF.

Expressing the FCF equation, equation (7.59), in logarithmic terms:

$$\log \Delta p = \frac{1}{4} \log \Delta t + \log \left( 44.11 \frac{qB\mu}{h\sqrt{k_f w_f^4 \phi c_t k}} \right) \quad (8.31)$$

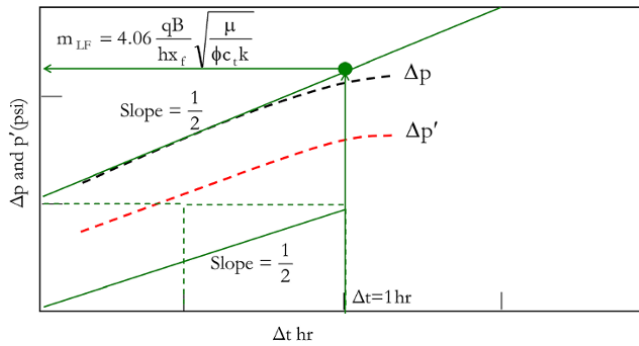


Figure 8.28 ICF calculation using a log-log diagnostic plot.

Also, expressing the pressure derivative response equation, equation (8.30), for the FCF in logarithmic terms:

$$\log \Delta p' = \frac{1}{4} \log \Delta t + \log \left( 11.03 \frac{qB\mu}{h\sqrt{k_f w_f^4 \phi c_t k}} \right) \quad (8.32)$$

A plot of  $\Delta p$  against  $\Delta t$  and  $\Delta p'$  against  $\Delta t$  on a log-log scale will both give a slope of a quarter ( $\frac{1}{4}$ ) (Fig. 8.29).

The level of derivative is one-quarter of the pressure as shown in comparison of equations (7.59) and (8.30).

From equation (8.31), when  $\Delta t = 1$  on a log scale,  $\Delta p = 44.11 \frac{qB\mu}{h\sqrt{k_f w_f^4 \phi c_t k}}$ . Therefore, the value of  $\Delta p$  taken on a slope of one-quarter at  $\Delta t = 1$  equals  $m_{BLF}$ , which is  $44.11 \frac{qB\mu}{h\sqrt{k_f w_f^4 \phi c_t k}}$ .

From equation (8.33):

$$m_{BLF} = 44.11 \frac{qB\mu}{h\sqrt{k_f w_f^4 \phi c_t k}} \quad (8.33)$$

$k_f w_f$  can be then determined using:

$$k_f w_f = 1944.8 \sqrt{\frac{1}{\phi c_t k}} \left( \frac{qB\mu}{h m_{BLF}} \right)^2$$

**8.4.3.6. Limited Entry Behavior on a Diagnostic Plot.** From the limited entry equation, equation (7.61):

$$\Delta p = 70.6 \frac{qB\mu}{k_s r_s} - 2452.9 \frac{qB\mu \sqrt{\phi \mu c_t}}{k_s^{3/2} \sqrt{\Delta t}}$$

From the above equation:

$$\frac{d\Delta p}{d \left( \frac{1}{\sqrt{\Delta t}} \right)} = -2452.9 \frac{qB\mu \sqrt{\phi \mu c_t}}{k_s^{3/2}} \quad (8.34)$$

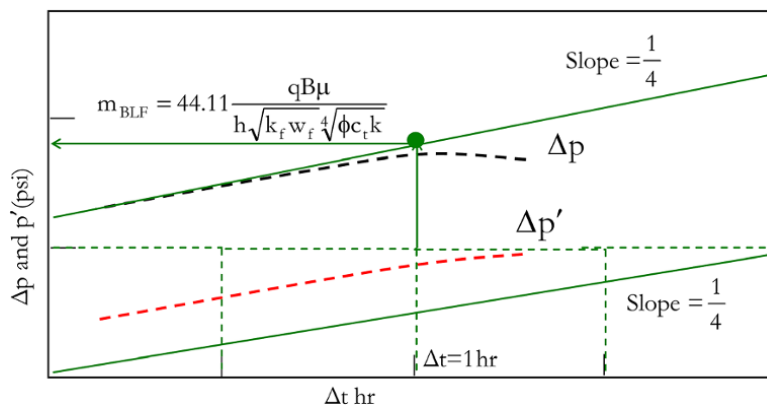


Figure 8.29 FCF calculation using a log-log diagnostic plot.

Taking the derivative of  $\Delta p$  with respect to  $\ln \Delta t$ :

$$\Delta p' = \frac{d\Delta p}{d \ln(\Delta t)} = \frac{d\Delta p}{d\left(\frac{1}{\sqrt{\Delta t}}\right)} \times \frac{d\left(\frac{1}{\sqrt{\Delta t}}\right)}{d \ln(\Delta t)} = \frac{d\Delta p}{d\left(\frac{1}{\sqrt{\Delta t}}\right)} \times \frac{-\frac{1}{2}\Delta t^{-3/2}}{1/\Delta t} = -\frac{1}{2\sqrt{\Delta t}} \frac{d\Delta p}{d\left(\frac{1}{\sqrt{\Delta t}}\right)}$$

Substituting  $\frac{d\Delta p}{d\left(\frac{1}{\sqrt{\Delta t}}\right)}$  from equation (8.34) into the above:

$$\Delta p' = 2452.9 \frac{qB\mu\sqrt{\phi\mu c_t}}{2k_s^{3/2}\sqrt{\Delta t}} \tag{8.35}$$

Expressing equation (8.35) in logarithmic form:

$$\log \Delta p' = -\frac{1}{2} \log \Delta t + \log \left( 1226.4 \frac{qB\mu\sqrt{\phi\mu c_t}}{k_s^{3/2}} \right) \tag{8.36}$$

From equation (8.36), a plot of  $\Delta p'$  against  $\Delta t$  on a log-log scale will give a negative slope of one half  $\left(-\frac{1}{2}\right)$  (Fig. 8.30). From equation (8.36), when  $\Delta t = 1$  on a log scale,  $\Delta p' = 1226.4 \frac{qB\mu\sqrt{\phi\mu c_t}}{k_s^{3/2}}$ . Therefore, the value of  $\Delta p'$  taken on a slope of  $-\frac{1}{2}$  at  $\Delta t = 1$  equals  $\Delta p'_{SPH-1hr}$ , which is  $1226.4 \frac{qB\mu\sqrt{\phi\mu c_t}}{k_s^{3/2}}$ .

From  $\Delta p'_{SPH-1hr} = 1226.4 \frac{qB\mu\sqrt{\phi\mu c_t}}{k_s^{3/2}}$ ,  $k_s$  can then be determined.

$k_s$  is then used in determining  $k_z$  using equation (7.65) with known  $k_{xy}$  ( $k_r$ ). It is important to note that  $k_{xy}$  ( $k_r$ ) is determined from radial flow stabilization, which has already been discussed in Exercise 8.1.

**8.4.3.7. Horizontal Well Behavior on a Diagnostic Plot.**

In an infinite acting homogeneous reservoir, the derivative plot for a horizontal well is generally characterized by three flow regimes (Fig. 8.31): *vertical radial flow* (VRF) in the vertical plane; *linear flow* (LF) regime, which manifests when pressure diffusion reaches the upper and lower reservoir limits; *horizontal radial* (HR) flow regime, which manifests when there is a convergent flow around the well from all reservoir directions. A log-log pressure derivative for a horizontal well in an homogeneous infinite acting reservoir is summarized in Fig. 8.32.

**8.4.4. Reservoir Behavior**

Log-log pressure derivative plots for reservoir behaviors manifest in middle times relative to near wellbore and boundary behavior. Figures 8.33–8.36 summarize log-log derivative plots for different reservoir behaviors. A log-log derivative plot for radial flow behavior is shown in Fig. 8.33; a log-log derivative plot for mobility change behavior is shown in Fig. 8.34; a log-log derivative plot for double porosity behavior is shown in Fig. 8.35; and a log-log derivative plot for storativity change behavior is shown in Fig. 8.36.

**8.4.5. Reservoir Boundary Behavior**

Log-log pressure derivative plots for reservoir boundaries manifest in late times relative to near wellbore and reservoir behavior. Figures 8.37–8.41 summarize log-log derivative plots for different reservoir boundary behaviors. The log-log derivative plot for single no-flow boundary behavior is shown in Fig. 8.37; the log-log derivative plot for channel boundary behavior is shown in Fig. 8.38; the log-log derivative plot for wedge boundary behavior is shown in Fig. 8.39; the log-log derivative plot for constant pressure boundary behavior is shown in

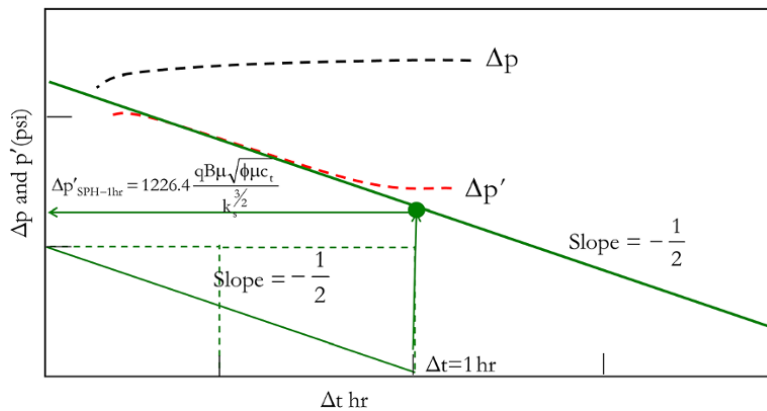


**Figure 8.30** Limited entry well calculation using a log-log diagnostic plot.

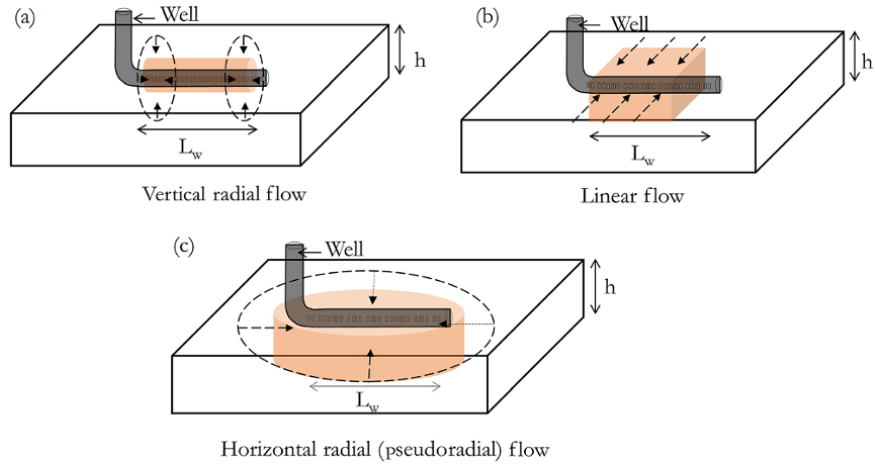


Figure 8.31 Flow regimes around a horizontal well.

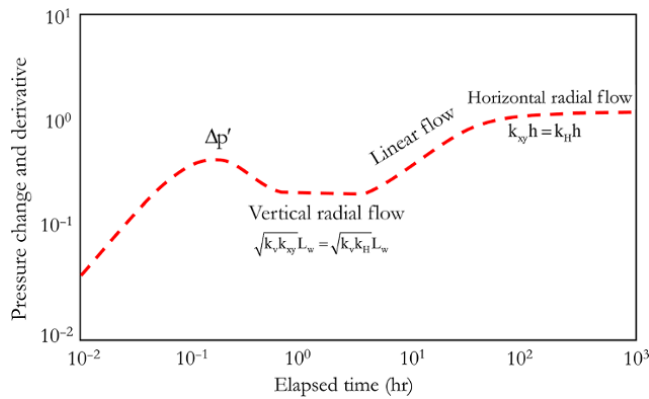


Figure 8.32 Log-log derivative plot showing flow regimes in a horizontal well.

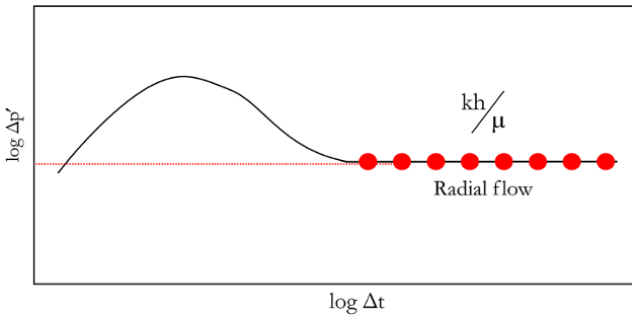


Figure 8.33 Log-log derivative plot for radial flow behavior.

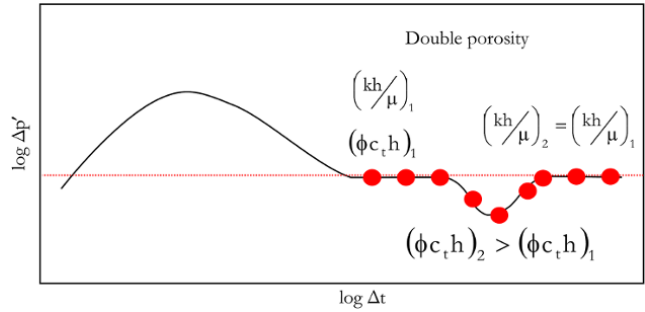


Figure 8.35 Log-log derivative plot for double porosity behavior.

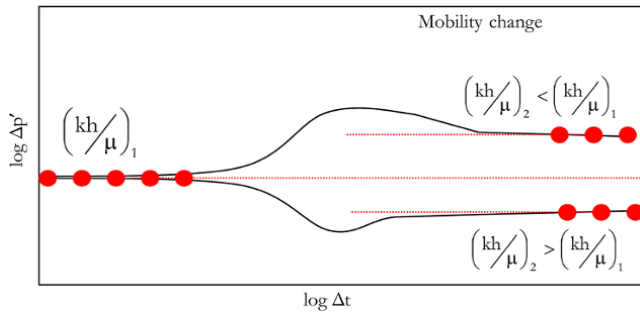


Figure 8.34 Log-log derivative plot for mobility change behavior.

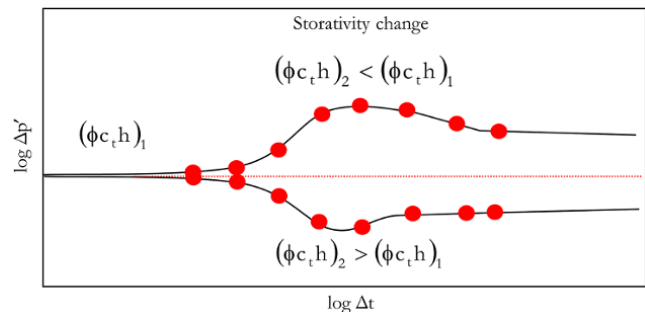


Figure 8.36 Log-log derivative plot for storativity change behavior.

Fig. 8.40; and the log-log derivative plot for closed reservoir boundary behavior is shown in Fig. 8.41.

In the case of a closed reservoir system, drawdown behavior and buildup behavior are different, as shown in Fig. 8.41a and 8.41b.

**8.4.6. Deconvolution**

Deconvolution is an inversion process carried out to reverse the effect of convolution on well test data. Deconvolution extracts a unit drawdown-type curve from rate

and pressure data with duration that is equal to the entire test period.

Consider a well test made up of a drawdown with rate +q followed by a buildup as shown in Fig. 8.42.

The entire pressure and rate response in Fig. 8.42 can be expressed as a convolution of drawdown with rate +q lasting for the total duration,  $T_{total}$  (Fig. 8.43a) and injection profile with rate -q lasting the duration of buildup (Fig. 8.43b).

The deconvolution algorithm discussed in most literature seeks to find a *unit rate drawdown pressure response*

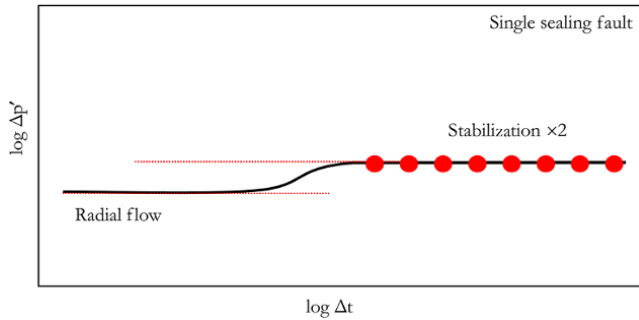


**Figure 8.37** Log-log derivative plot for single no-flow boundary.

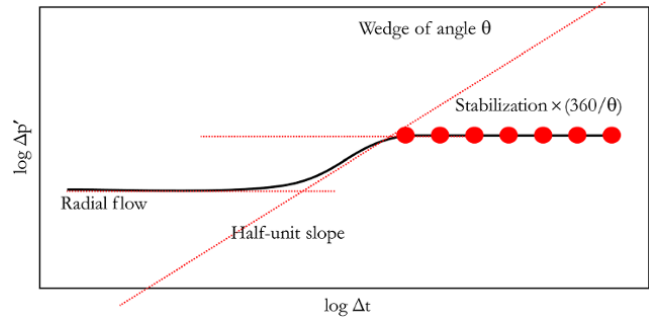


**Figure 8.39** Log-log derivative plot for wedge boundary.

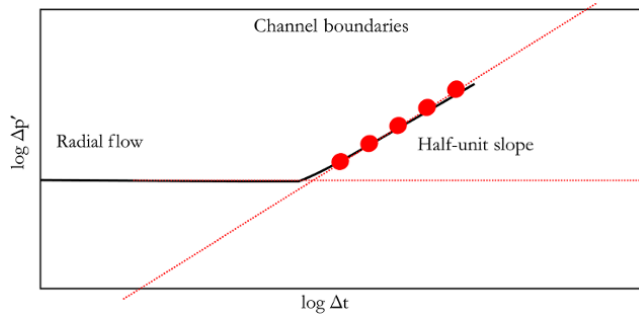


**Figure 8.38** Log-log derivative plot for channel boundary.

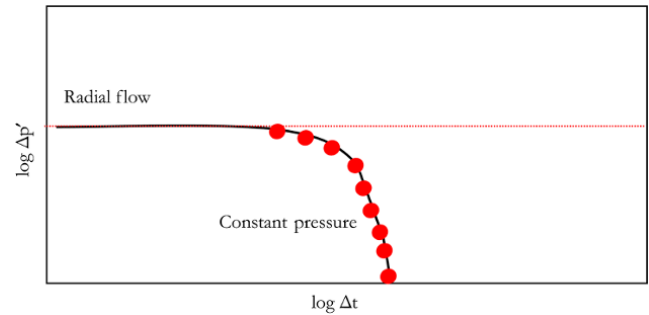


**Figure 8.40** Log-log derivative plot for constant pressure boundary.

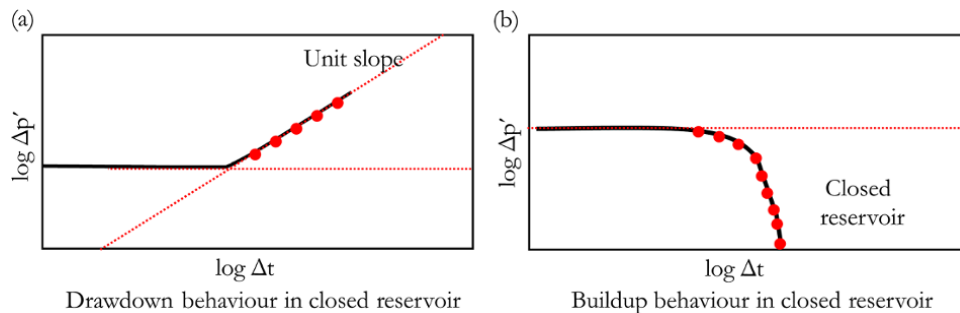


**Figure 8.41** Log-log derivative plot for closed reservoir boundary.



for the duration of the entire test ( $T_{total}$ ), which is similar to Fig. 8.43a but for a unit rate. The deconvolved unit rate pressure drawdown pressure signal is shown in Fig. 8.44.

Since the unit drawdown pressure response from deconvolution has a duration that is equal to the entire test duration ( $T_{total}$ ), analysis of deconvolved pressure will reveal more features in the later times of the derivative plot. Hence improving reservoir and boundary characterization and ensuring better use of pressure data.

Deconvolution in well test analysis seeks to extract a unit rate response ( $p_{DU}$ ) from pressure and rate data.

From the superposition principle discussed under multi-rate test:

$$p_i - p(t) = \frac{B\mu}{2\pi kh} \sum_{i=1}^n (q_i - q_{i-1}) p_D(t - t_{i-1})$$

$$p_i - p(t) = \frac{B\mu}{2\pi kh} \sum_{i=1}^n \frac{(q_i - q_{i-1})}{(t - t_{i-1})} [p_D(t - t_{i-1})](t - t_{i-1})$$

(8.37)

as  $\Delta t_i \rightarrow 0$

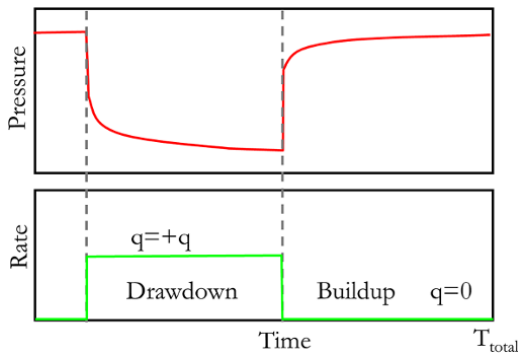
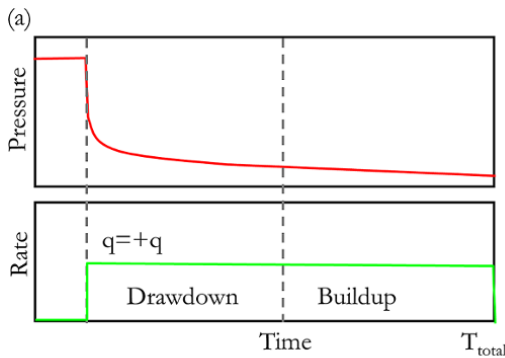
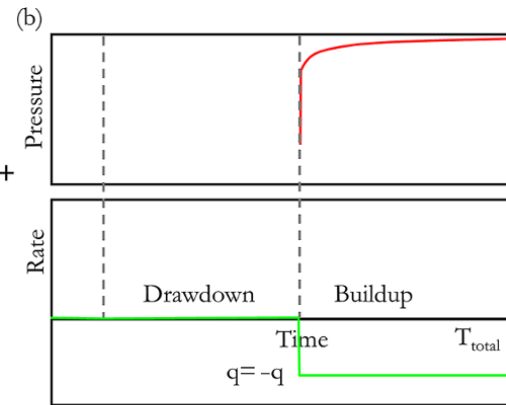


Figure 8.42 Convolved pressure-rate history.



Drawdown signal with  $T_{total}$  duration



Injection signal with buildup duration

Figure 8.43 Deconvolved pressure-rate history.

The above can expressed as:

$$p_i - p(t) = \frac{B\mu}{2\pi kh} \int_0^t q(\tau) \left( \frac{dp_D(t-\tau)}{dt} \right) \quad (8.38)$$

Equation (8.38) shows that the measured well pressure signal satisfies the convolution integral, which is called *Duhamel's principle* or the *superposition principle*. As shown in equation (8.37), the convolution integral equation was derived from the superposition principle. Hence, convolution and superposition are synonyms.

Writing the convolution integral in equation (8.38) with the unit rate response:

$$p_i - p(t) = \frac{B\mu}{2\pi kh} \int_0^t q(\tau) \left( \frac{dp_{DU}(t-\tau)}{dt} \right) \quad (8.39)$$

where  $p_{DU}$  is unit rate pressure response.

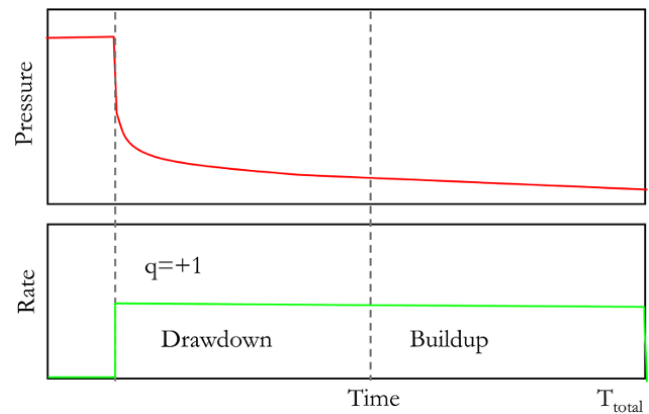


Figure 8.44 Unit drawdown pressure response from deconvolution.

**8.4.6.1. Deconvolution Using Total Least Square Regression.** Deconvolution of well test data can be achieved by total least square (TLS) regression [Von Schroeter et al., 2004]. TLS regression for well test deconvolution can be expressed as:

$$E = W_p^2(E_{\text{measured}} - P_{\text{simulated}})^2 + W_q^2(q_{\text{measured}} - q_{\text{adapted}})^2 + W_c^2 E_{\text{curve}}^2 \tag{8.40}$$

The objective function E is the summation of the square of error on pressure match, rate match, and curvature, where:  $W_p$ ,  $W_q$ , and  $W_c$  are weighting factors for pressure, rate, and curvature control parameter,  $E_{\text{curve}}$ .  $E_{\text{curve}}$  defines the amount of curvature added to the matched derivative during regression.

The steps involved in deconvolution of well test data using TLS regression can be summarized as:

- (i) create an initial guess derivative plot (Fig. 8.45a);
- (ii) superimpose the initial derivative with measured rate history to create simulated pressure response (Fig. 8.45c and Fig. 8.45d);
- (iii) calculate error between measured p and simulated p and between measured q and calculated q (where rate is to be adapted); define curvature using curvature control parameter  $E_{\text{curve}}$ .
- (iv) create summation of all errors for each data point equation (8.40);

(v) minimize sum of square of errors (objective function E) to get final derivative (Fig. 8.45a);

(vi) analyze deconvolved unit rate pressure response using conventional well test methods discussed in Section 8.5.

As shown in Fig. 8.44, deconvolution can, therefore, transform variable rate pressure response to constant rate initial drawdown with a duration equal the total duration of entire test. Deconvolution also yields, directly, the corresponding pressure derivative normalized to a unit rate (Fig. 8.45).

The ability of deconvolution to analyze well test data with variable rates has made it important in analyzing large sets of well test data over long periods of time (a few years to tens of years) from permanent downhole gauges. Such data contain reservoir information at distances away from the well, which can be significantly greater than that obtained from a single flow period [Von Schroeter et al., 2004]. Deconvolution has also proved to be useful for determining more accurate rates, especially for production wells with permanent bottom-hole gauges where rates are determined through well allocation process, and errors can be as high as 20%.

To get reasonable reservoir characterization from deconvolution, minimum noise and outliers are expected in measured data; good estimate of initial reservoir pressure (from RFT or initial DST) is expected, and consistencies in buildup derivatives to be used for regression is important.

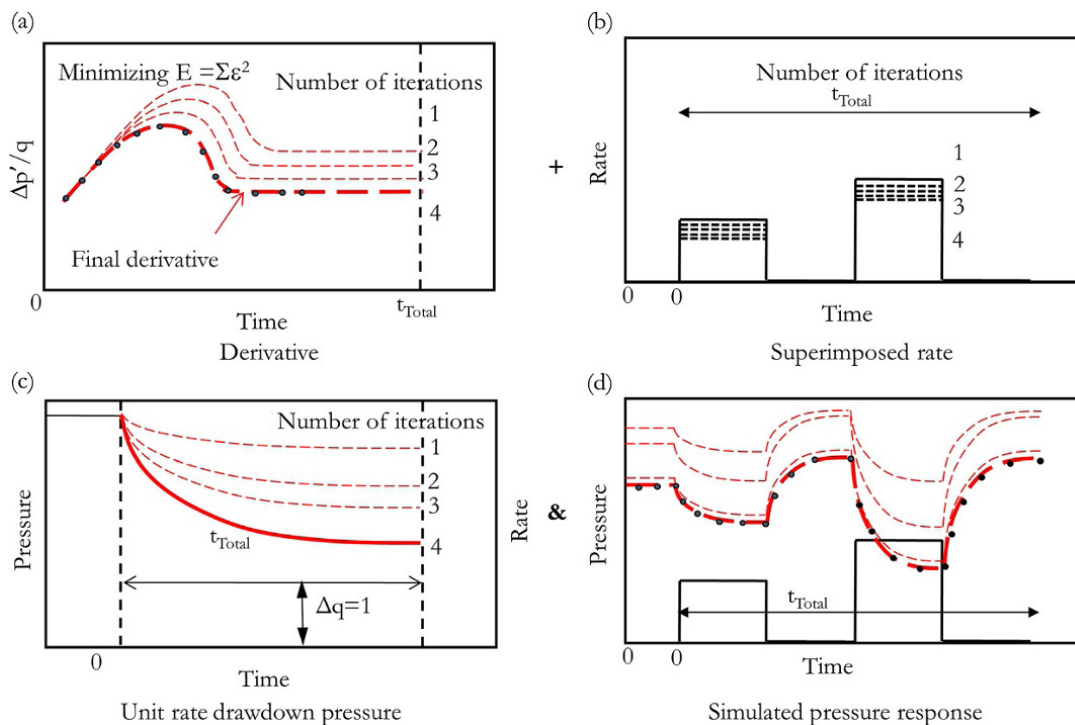


**Figure 8.45** Summary of deconvolution process using TLS regression.

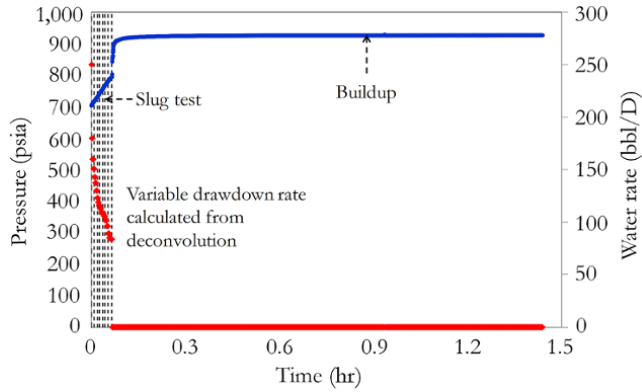


**Figure 8.46** Computed variable drawdown rate using deconvolution.

One important application of deconvolution is in specialized well test analysis, such as *slug testing* and *closed chamber testing*, where variable drawdown rate is calculated using deconvolution, as shown in Fig. 8.46.

Average rate from cumulate oil produced was used as the initial rate. Deconvolution was then used to determine variable rate (adapted rate), which honors pressure response during a slug test. Variable drawdown can also be calculated using:

$$q_{sf} = 24C_s \frac{dp_w}{dt} \quad (8.41)$$

$C_s$  is the storage effect due to the changing fluid level.

**8.4.6.2. Minimum Connected Volume and Reservoir Compartment Volume.** Well test analysis remains the only method for estimating connected pore volume. Minimum connected pore volume gives an estimation of the minimum hydrocarbon region around the well that can be produced.

The minimum connected volume (MCV) is defined as:

$$MCV = (1 - S_w) \phi \pi r_i^2 \text{ in consistent unit}$$

and in EOF unit as:

$$MCV = \frac{0.178108(1 - S_w) \phi \pi r_i^2}{B_{oi}} \quad (8.42)$$

where  $r_i$  is the radius of investigation in feet.

The Lee *et al.* formula shows the relationship between the elapsed test time ( $\Delta t_{test}$ ) and the radius of investigation ( $r_i$ ):

$$r_i = 0.032 \sqrt{\frac{k \Delta t_{test}}{\phi \mu c_t}} \quad (8.43)$$

where  $\Delta t_{test}$  is the total elapsed time of the test without the boundary effect as shown in Fig. 8.47.

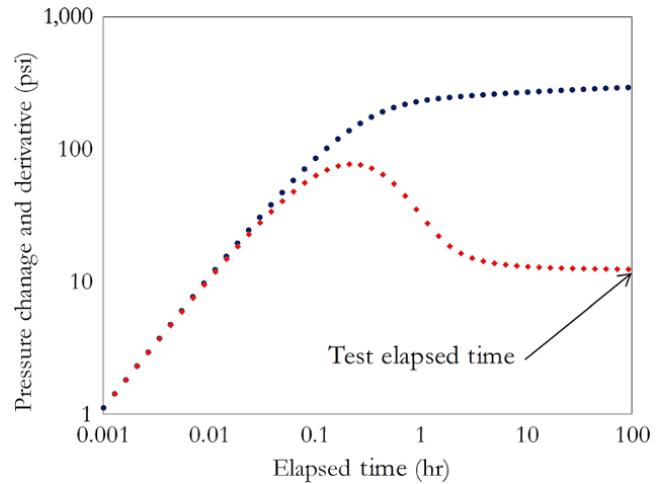


**Figure 8.47** Elapsed time corresponding to radius of investigation.

Where a closed boundary system exists from interpretation, reservoir compartment volume (RCV) is calculated using dimension of the closed reservoir from interpretation. This volume is the actual hydrocarbon in the compartment tested, which is expressed as:

$$RCV = \frac{0.178108(1 - S_w) \phi h A_{Comp}}{B_{oi}} \quad (8.44)$$

where  $A_{Comp}$  is the area of the reservoir compartment with dimensions determined from well test analysis.

Unit rate pressure response from deconvolution has the duration of the entire test duration rather than the duration of one flow period as in conventional well test analysis. Hence, deconvolution of well tests with multiple flow periods will yield a larger MCV compared with using a single flow period. This increase in confirmed MCV is vital in increasing hydrocarbon reserve booking.

## 8.5. INTERPRETATION MODELS

Identifying a *well test interpretation model* that honors all relevant static and dynamic data is an important part of well test analysis. The interpretation model should simulate the entire pressure response with measured rate history and relevant petrophysical parameters as input. Analytical or numerical models can be used for simulating pressure response in well testing. Although well test analysis is mainly based on analytical models, numerical simulation models for well test analysis are becoming popular, especially for complex boundary systems.

### 8.5.1. Analytical Well Test Models

The simplest form of analytical well test interpretation model is the *infinitely acting radial homogeneous reservoir with wellbore storage and skin effect*. Infinite acting means

that during well testing, a boundary effect was not observed. As such, the reservoir behaves as infinite in extent. Hence, if a reservoir is described as *infinitely acting radial homogeneous reservoir with wellbore storage and skin effect*, the pressure response for the entire test can be simulated using the measured rate and well test parameters that describe this model; these are: skin effect (S); wellbore storage constant (C), and radial/horizontal permeability ( $k_r$ ).

**8.5.1.1. Infinitely Acting Radial Homogeneous Reservoir with Wellbore Storage and Skin Model.** From the diffusivity equation, equation (7.11):

$$\frac{1}{r} \frac{\partial}{\partial r} \left( r \frac{\partial p}{\partial r} \right) = \frac{\phi \mu c_t}{k} \frac{\partial p}{\partial t}$$

Defining dimensionless variables for pressure, time, and radial distance in consistent unit:

$$p_D = \frac{2\pi kh}{q\mu} (p_i - p) \quad (8.45)$$

$$t_D = \frac{kt}{\phi \mu c_t r_w^2} \quad (8.46)$$

$$r_D = \frac{r}{r_w} \quad (8.47)$$

In dimensionless variable terms, the diffusivity equation becomes:

$$\frac{1}{r_D} \frac{\partial}{\partial r_D} \left( r_D \frac{\partial p_D}{\partial r_D} \right) = \frac{\partial p_D}{\partial t_D} \quad (8.48)$$

The diffusivity equation can be solved using initial and boundary conditions that describe an infinitely acting radial homogeneous reservoir with wellbore storage and skin effect in the Laplace domain. The derived solution in the Laplace domain will then be inverted to a time domain analytically or numerically.

$p = p(r, t)$  can be represented in a dimensionless variable as:

$$p_D = p_D(r_D, t_D)$$

where the Laplace transform of  $p_D$  is denoted as  $\bar{p}_D$

Applying the Laplace transformation to equation (8.48):

$$\frac{1}{r_D} \frac{\partial}{\partial r_D} \left( r_D \frac{\partial \bar{p}_D}{\partial r_D} \right) = s \bar{p}_D - \bar{p}_D(r_D, t_D = 0) \quad (8.49)$$

The boundary conditions can then be defined.

*Inner Boundary*

A well with wellbore storage is defined by:

$$q_{sf} = q_{wh} - c_w V_w \frac{\partial p_w}{\partial t} \Big|_{r=r_w} \quad (8.50)$$

where, from Darcy's law:

$$q_{sf} = -\frac{k}{\mu} (2\pi rh) \frac{\partial p(r, t)}{\partial r} \Big|_{r=r_w}$$

and  $c_w V_w = C$ .

Substituting  $c_w V_w$  and  $q_{sf}$  into equation (8.50):

$$q_{wh} = -\frac{2\pi kh}{\mu} r \frac{\partial p}{\partial r} + C \frac{\partial p_w}{\partial t} \Big|_{r=r_w}$$

Rearranging this gives:

$$1 = -\frac{2\pi kh}{q_{wh} \mu r_w} \frac{\partial p}{\partial \left( \frac{r}{r_w} \right)} + C \frac{\mu}{2\pi kh \phi \mu c_t r_w^2} \frac{k}{k} \frac{\phi \mu c_t r_w^2}{q_{wh} \mu} \frac{2\pi kh}{k} \frac{\partial p_w}{\partial t} \Big|_{r=r_w}$$

Expressing the above in terms of dimensionless pressure and time:

$$1 = -r_D \frac{\partial p_D}{\partial r_D} + \frac{C}{2\pi \phi c_t h r_w^2} \frac{\partial p_{wD}}{\partial t_D} \Big|_{r_D=1}$$

Substituting  $C_D = \frac{C}{2\pi \phi c_t h r_w^2}$  into the above, this becomes:

$$1 = -r_D \frac{\partial p_D}{\partial r_D} + C_D \frac{\partial p_{wD}}{\partial t_D} \Big|_{r_D=1}$$

Expressing this in the Laplace domain:

$$\frac{1}{s} = s C_D \bar{p}_{wD} - r_D \frac{\partial \bar{p}_D}{\partial r_D} \Big|_{r_D=1} \quad (8.51)$$

*Well with Skin Condition*

$$p_{well} = p - S \frac{q_{sf} \mu}{2\pi kh} \Big|_{r=r_w}$$

Substituting  $q_{sf} = -\frac{k}{\mu} (2\pi rh) \frac{\partial p(r, t)}{\partial r} \Big|_{r=r_w}$  into the above gives:

$$p_{well} = p + Sr \frac{\partial p(r, t)}{\partial r} \Big|_{r=r_w} \quad (8.52)$$

Rearranging this equation:

$$\frac{2\pi kh}{q\mu} (p_i - p_{well}) = \frac{2\pi kh}{q\mu} (p_i - p) - Sr \frac{2\pi kh}{q\mu} \frac{\partial p(r, t)}{\partial r} \Big|_{r=r_w}$$

Expressing the above equation in dimensionless variables:

$$p_{wD}(t_D, S) = p_D(t_D, S=0) - Sr_D \frac{\partial p_D(r_D, t_D)}{\partial r_D} \Big|_{r_D=1}$$

Expressing this in the Laplace domain:

$$\bar{p}_{wD}(s, S) = \bar{p}_D(r_D, s) - Sr_D \frac{\partial \bar{p}_D(r_D, s)}{\partial r_D} \Big|_{r_D=1} \quad (8.53)$$

*Initial Reservoir Condition and Outer Boundary*

Since  $p_D = \frac{2\pi kh}{q\mu}(p_i - p)$ , and the initial reservoir condition is defined as  $p = p_i$ , the initial reservoir condition in dimensionless terms can be defined as:

$$p_D(r_D, t_D = 0) = 0$$

In the Laplace domain:

$$\bar{p}_D(r_D, t_D = 0) = 0 \tag{8.54}$$

where  $\bar{p}_D$  is the Laplace transform of  $p_D$ .

For a radial infinitely acting reservoir  $p = p_i$ , hence:

$$p_D(r_D \rightarrow \infty, t_D) = 0$$

In the Laplace domain:

$$\bar{p}_D(r_D \rightarrow \infty, s) = 0 \tag{8.55}$$

*Homogeneous Reservoir with Wellbore Storage and Skin Effect*

Substitute equation (8.54) into equation (8.49):

$$\frac{1}{r_D} \frac{\partial}{\partial r_D} \left( r_D \frac{\partial \bar{p}_D}{\partial r_D} \right) = s\bar{p}_D \tag{8.56}$$

The general solution of equation (8.56) is:

$$\bar{p}_D(r_D, S) = A I_0(r_D \sqrt{s}) + B K_0(r_D \sqrt{s}) \tag{8.57}$$

Substitute equation (8.55), outer boundary condition, into equation (8.57) and solving to get  $A = 0$ :

$$\bar{p}_D(r_D, S) = B K_0(r_D \sqrt{s}) \tag{8.58}$$

Taking the derivative of  $\bar{p}_D(r_D, S)$  with respect to  $r_D$ :

$$\begin{aligned} \left. \frac{d\bar{p}_D(r_D, S)}{dr_D} \right|_{r_D=1} &= -BK_1(r_D \sqrt{s}) \Big|_{r_D=1} \\ \left. \frac{d\bar{p}_D(r_D, S)}{dr_D} \right|_{r_D=1} &= -BK_1(\sqrt{s}) \end{aligned} \tag{8.59}$$

Substituting equation (8.59) into equation (8.51):

$$\begin{aligned} \frac{1}{s} &= sC_D \bar{p}_{wD} + B\sqrt{s}K_1(\sqrt{s}) \\ sC_D \bar{p}_{wD} + B\sqrt{s}K_1(\sqrt{s}) &= \frac{1}{s} \end{aligned} \tag{8.60}$$

Substituting equations (8.58) and (8.59) into equation (8.53):

$$\bar{p}_{wD} = BK_0(r_D \sqrt{s}) + SB\sqrt{s}K_1(\sqrt{s}) \tag{8.61}$$

The following steps describe solving simultaneously equations (8.60) and (8.61) for  $p_{wD}$  (eliminating B):

From equation (8.61):

$$\bar{p}_{wD} = B(K_0(r_D \sqrt{s}) + S\sqrt{s}K_1(\sqrt{s})) \tag{8.62}$$

Substituting equation (8.62) into equation (8.60):

$$\begin{aligned} sC_D B(K_0(r_D \sqrt{s}) + S\sqrt{s}K_1(\sqrt{s})) + B\sqrt{s}K_1(\sqrt{s}) &= \frac{1}{s} \\ B[sC_D(K_0(r_D \sqrt{s}) + S\sqrt{s}K_1(\sqrt{s})) + \sqrt{s}K_1(\sqrt{s})] &= \frac{1}{s} \end{aligned}$$

Making B the subject of the formula:

$$B = \frac{1}{s[sC_D(K_0(r_D \sqrt{s}) + S\sqrt{s}K_1(\sqrt{s})) + \sqrt{s}K_1(\sqrt{s})]}$$

Substituting B into equation (8.62) [Agarwal et al., 1970]:

$$\begin{aligned} \bar{p}_{wD} &= \frac{K_0(r_D \sqrt{s}) + S\sqrt{s}K_1(\sqrt{s})}{s[sC_D(K_0(r_D \sqrt{s}) + S\sqrt{s}K_1(\sqrt{s})) + \sqrt{s}K_1(\sqrt{s})]} \\ \bar{p}_{wD} &= \frac{\frac{K_0(r_D \sqrt{s})}{\sqrt{s}K_1(\sqrt{s})} + S}{s \left[ 1 + C_D s \left( \frac{K_0(r_D \sqrt{s})}{\sqrt{s}K_1(\sqrt{s})} + S \right) \right]} \\ \bar{p}_{wD}(s, S, C_D, r_D) &= \frac{\frac{K_0(r_D \sqrt{s})}{\sqrt{s}K_1(\sqrt{s})} + S}{s \left[ 1 + C_D s \left( \frac{K_0(r_D \sqrt{s})}{\sqrt{s}K_1(\sqrt{s})} + S \right) \right]} \end{aligned} \tag{8.63}$$

The above describes pressure response in an infinite acting reservoir with WBS and skin effect at a distance of  $r$  from the well with radius of  $r_w$ .

The *fundamental solution for homogeneous reservoir behavior*, which is equation (8.63), without wellbore storage and skin effect can be defined as:

$$\bar{p}_{wD}(s, r_D) = \bar{p}_{wD}(s, S = 0, C_D = 0, r_D)$$

Substituting  $S = 0, C_D = 0$  into equation (8.63) to derive the fundamental equation for a homogeneous reservoir,  $\bar{p}_{wD}(s, r_D)$ :

$$\bar{p}_{wD}(s, r_D) = \frac{1}{s} \frac{K_0(r_D \sqrt{s})}{\sqrt{s}K_1(\sqrt{s})} \tag{8.64}$$

Equation (8.63) can be expressed in terms of  $\bar{p}_{wD}(s, r_D)$ , and hence re-written as:

$$\bar{p}_{wD}(s, S, C_D, r_D) = \frac{s\bar{p}_{wD}(s, r_D) + S}{s[1 + C_D s(s\bar{p}_{wD}(s, r_D) + S)]} \tag{8.65}$$

In EOF units, dimensionless variables are defined as:

$$p_D = \frac{kh}{141.2qB\mu} \Delta p, \text{ for pressure} \tag{8.66}$$

$$t_D = \frac{0.000264k}{\phi\mu c_r r_w^2} \Delta t, \text{ for time} \tag{8.67}$$

$$C_D = \frac{0.8936}{\phi c_t h r_w^2} C, \text{ for wellbore storage} \quad (8.68)$$

$$r_D = \frac{r}{r_w}, \text{ for radial distance} \quad (8.69)$$

Equations (8.63) and (8.64) are in the Laplace domain and can be convert to the  $t_D$  domain using numerical Laplace inversion techniques such as the Stehfest or Den Iseger inversion algorithm.

**8.5.1.2. Constant Terminal Rate (CTR) and Constant Terminal Pressure (CTP) Solutions.** Equation (8.64) is the constant terminal rate (CTR) solution for radial flow in an infinite acting, homogeneous reservoir. This is the pressure drop response for a well producing at constant rate in a homogeneous reservoir from an initial equilibrium state. Another important solution, other than the CTR, is the constant terminal pressure (CTP) solution, which is for a well production rate at constant pressure at a given radius.

*Van Evardingen and Hurst* [1949] showed that for any CTR pressure drop,  $\bar{p}_{wD}(s)$ , there exists a CTP production rate,  $\bar{q}_D(s)$ , with the relationship given as:

$$\bar{q}_D(s) = \frac{1}{s^2 \bar{p}_{wD}(s)} \quad (8.70)$$

where in EOF units,  $q_D = \frac{141.2B\mu}{k_{eff} h \Delta p} q$ .

Also, the relationship between CTR pressure drop,  $\bar{p}_{wD}(s)$  and CTP cumulative production,  $\bar{Q}_D(s)$  is given as:

$$s \bar{p}_{wD}(s) \bar{Q}_D(s) = \frac{1}{s^2}$$

Rearranging this:

$$\bar{Q}_D(s) = \frac{1}{s^3 \bar{p}_{wD}(s)} \quad (8.71)$$

where  $Q_D = \frac{Q}{1.12\phi h c_t r_e^2 \Delta p}$ .

Combining equations (8.70) and (8.71) shows that the relationship between CTP production rate,  $\bar{q}_D(s)$ , and CTP cumulative production,  $\bar{Q}_D(s)$ , can be expressed as:

$$\bar{Q}_D(s) = \frac{\bar{q}_D(s)}{s} \quad (8.72)$$

Laplace solutions for radial flow in homogeneous reservoir for infinite extent, no-flow outer boundary, constant pressure boundary, and prescribed flux boundary are summarized in Table 8.4.

From the different solutions of  $\bar{p}_{wD}(s)$  listed in Table 8.4,  $\bar{q}_D(s)$  and  $\bar{Q}_D(s)$  can be determined using equations (8.70) and (8.71), respectively.

*Fetkovich* [1980] showed that the constant terminal pressure solution in a no-flow boundary reservoir creates an exponential decline rate. The concept of exponential depletion when pseudosteady state has been reached is important for performance prediction and is described in Chapter 13.

**8.5.1.3. Stehfest Numerical Laplace Inversion.** The Stehfest numerical Laplace inversion [*Stehfest*, 1970] remains one of the most widely used numerical Laplace inversion techniques and is expressed as:

$$f_N(t) = \frac{\ln 2}{t} \sum_{i=1}^N V_i F\left(\frac{i \ln 2}{t}\right) \quad (8.73)$$

where  $F$  is the Laplace transform of  $f_N$  and

$$V_i = (-1)^{(N/2)-i} \sum_{k=(i+1/2)}^{\min(i, N/2)} \frac{k^{N+1} (2k)!}{\left(\frac{N}{2} - k\right)! k! (k-1)! (i-k)! (2k-i)!} \quad (8.74)$$

$N$  is an even number and is between 6 and 18;  $i$  is an integer number. For example, for  $N = 6$ , the values of  $i$ ,  $k$ , and  $V_i$  are shown in Table 8.5.

With the table for  $N = 6$ , estimation of  $V_i$  can be left out of the calculation or program code and calculation of  $f_N(t)$  becomes easy to implement. The accuracy of numerical

**Table 8.4** Laplace Solution for Radial Flow in Homogeneous Reservoir for Different Reservoir Boundaries.

Reservoir boundary	Pressure response for constant production rate
Infinite acting	$\bar{p}_{wD}(s, r_D) = \frac{1}{s} \frac{K_0(r_D \sqrt{s})}{\sqrt{s} K_1(\sqrt{s})}$
No-flow outer boundary	$\bar{p}_{wD}(s, r_D) = \frac{1}{s^{3/2}} \frac{K_0(r_D \sqrt{s}) I_1(r_{eD} \sqrt{s}) + K_1(r_{eD} \sqrt{s}) I_0(r_D \sqrt{s})}{[K_1(\sqrt{s}) I_1(r_{eD} \sqrt{s}) - K_1(r_{eD} \sqrt{s}) I_1(\sqrt{s})]}$
Constant pressure boundary	$\bar{p}_{wD}(s, r_D) = \frac{1}{s^{3/2}} \frac{K_0(r_D \sqrt{s}) I_0(r_{eD} \sqrt{s}) - K_0(r_{eD} \sqrt{s}) I_0(r_D \sqrt{s})}{[K_1(\sqrt{s}) I_0(r_{eD} \sqrt{s}) + K_0(r_{eD} \sqrt{s}) I_1(\sqrt{s})]}$
Prescribed flux boundary	$\bar{p}_{wD}(s, r_D) = \frac{1}{s^{3/2}} \frac{K_0(r_D \sqrt{s}) I_1(r_{eD} \sqrt{s}) + K_1(r_{eD} \sqrt{s}) I_0(r_D \sqrt{s})}{[K_1(\sqrt{s}) I_1(r_{eD} \sqrt{s}) - K_1(r_{eD} \sqrt{s}) I_1(\sqrt{s})]} + \frac{\bar{q}_{Dext}(s) \sqrt{s} K_0(r_D \sqrt{s}) I_1(\sqrt{s}) + I_0(r_D \sqrt{s})}{s r_{eD} [K_1(\sqrt{s}) I_1(r_{eD} \sqrt{s}) - I_1(\sqrt{s})]}$

inversion can be improved by using higher values for N. The  $V_i$  table for  $N = 2-14$  is presented in Table 8.6.

Hence,  $p_D$ , the response at time  $t_D$  for an infinitely acting radial homogeneous reservoir with wellbore storage and skin effect, can be expressed as:

$$p_D(C_D, S, t_D, r_D) = \frac{\ln 2}{t_D} \sum_{i=1}^N V_i \bar{p}_D \left( C_D, S, \frac{i \ln 2}{t_D}, r_D \right) \quad (8.75)$$

N between 6 and 18 is sufficient for most well test analysis problems. At high values of N, the numerical approximation of  $V_i$  can lead to noisy inverted pressure response.

**8.5.1.4. Superposition in Time.** Where rate variation occurs during the production/well test, the superposition principle must be applied to obtain the correct  $p_D$  at any given time. Continuous rate change can be simplified by a series of step rate changes as shown in Fig. 8.48.

Dimensionless pressure response for a well with changing rate as shown above can be expressed as:

$$(\Delta p)_D = p_D(\Delta t_1 + \Delta t_2 + \Delta t_3 + \Delta t)_D + p_D(\Delta t_2 + \Delta t_3 + \Delta t)_D + p_D(\Delta t_3 + \Delta t)_D + p_D(\Delta t)_D \quad (8.76)$$

**Table 8.5**  $V_i$  Table for  $N = 6$ .

i	k	$V_i$
1	1	1
2	2	-49
3	2	366
4	3	-858
5	3	810
6	3	-270

**Table 8.6**  $V_i$  for the Stehfest Numerical Laplace Inversion for  $N = 2-14$ .

	$V(i,2)$	$V(i,4)$	$V(i,6)$	$V(i,8)$	$V(i,10)$	$V(i,12)$	$V(i,14)$
$V(1,N)$	2	-2	1	-3.33333E-01	8.33333E-02	-1.66667E-02	2.777777778E-03
$V(2,N)$	-2	26	-49	4.83333E+01	-3.20833E+01	1.60167E+01	-6.402777778E+00
$V(3,N)$	—	-48	366	-9.06000E+02	1.27900E+03	-1.24700E+03	9.240500000E+02
$V(4,N)$	—	24	-858	5.46467E+03	-1.56237E+04	2.75543E+04	-3.459792778E+04
$V(5,N)$	—	—	810	-1.43767E+04	8.42442E+04	-2.63281E+05	5.403211111E+05
$V(6,N)$	—	—	-270	1.87300E+04	-2.36958E+05	1.32414E+06	-4.398346367E+06
$V(7,N)$	—	—	—	-1.19467E+04	3.75912E+05	-3.89171E+06	2.108759178E+07
$V(8,N)$	—	—	—	2.98667E+03	-3.40072E+05	7.05329E+06	-6.394491304E+07
$V(9,N)$	—	—	—	—	1.64063E+05	-8.00534E+06	1.275975796E+08
$V(10,N)$	—	—	—	—	-3.28125E+04	5.55283E+06	-1.701371881E+08
$V(11,N)$	—	—	—	—	—	-2.15551E+06	1.503274670E+08
$V(12,N)$	—	—	—	—	—	3.59251E+05	-8.459216150E+07
$V(13,N)$	—	—	—	—	—	—	2.747888477E+07
$V(14,N)$	—	—	—	—	—	—	-3.925554967E+06

In real variables, in EOF units:

$$p_i - p(t) = \frac{141.2B\mu}{kh} \left[ q_1 p_D(\Delta t_1 + \Delta t_2 + \Delta t_3 + \Delta t)_D + (q_2 - q_1) p_D(\Delta t_2 + \Delta t_3 + \Delta t)_D + (q_3 - q_2) p_D(\Delta t_3 + \Delta t)_D + (q_4 - q_3) p_D(\Delta t)_D \right] \quad (8.77)$$

A generalized expression for pressure with changing rates for n flow periods (variable-rates or sequence of buildup and drawdown) can be expressed as:

$$p_i - p(t) = \frac{141.2B\mu}{kh} \sum_{i=1}^N (q_i - q_{i-1}) p_D \left( \sum_{j=i}^{n-1} \Delta t_j + \Delta t \right)_D \quad (8.78)$$

For a two-rate change (drawdown followed by a buildup) the pressure drop is thus:

$$(\Delta p)_D = p_D(\Delta t_1 + \Delta t)_D + p_D(\Delta t)_D$$

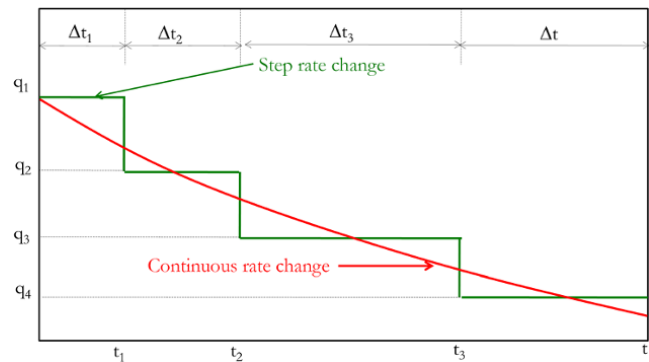


**Figure 8.48** Simplifying continuous rate change with step rate changes.

and in EOF units

$$p_i - p(t) = \frac{141.2B\mu}{kh} [q_1 p_D(\Delta t_1 + \Delta t)_D + (q_2 - q_1) p_D(\Delta t)_D] \quad (8.79)$$

**Exercise 8.2** Numerical Laplace Inversion for Well Test Model

Simulate a well test response for the parameters calculated in Exercise 8.1 ( $C = 0.015$  bbl/psi) and Exercise 7.6 ( $p_i = 5000$  psia,  $k_r = 14.8$  mD, and  $S = 19.5$ ) using an *infinitely acting radial homogeneous reservoir with wellbore storage and skin effect* model. Compare the simulated and actual log-log diagnostic plot of buildup, and compare the simulated and actual superposition plot of buildup. Actual (measured) pressure–rate data are given in Table 7.3.

**Solution Steps.**

*Step 1:* define the equation for pressure at the well ( $r_D = 1$ ) for an infinitely acting radial homogeneous reservoir with wellbore storage and skin effect model using equation (8.63)

$$\bar{p}_{wD}(s, S, C_D) = \frac{\frac{K_0(\sqrt{s})}{\sqrt{s}K_1(\sqrt{s})} + S}{s \left[ 1 + C_D s \left( \frac{K_0(\sqrt{s})}{\sqrt{s}K_1(\sqrt{s})} + S \right) \right]}$$

and using the Stehfest algorithm for inversion from the Laplace domain to the  $t_D$  domain:

$$p_{wD}(C_D, S, t_D) = \frac{\ln 2}{t_D} \sum_{i=1}^N V_i \bar{p}_{wD} \left( C_D, S, \frac{i \ln 2}{t_D} \right) \quad (8.80)$$

The solution of the dimensionless pressure response at a well of an infinitely acting radial homogeneous reservoir with wellbore storage and skin effect model is hence:

$$p_{wD}(C_D, S, t_D) = \frac{\ln 2}{t_D} \sum_{i=1}^N V_i \left[ \frac{\frac{K_0 \left( \sqrt{\frac{i \ln 2}{t_D}} \right)}{\sqrt{\frac{i \ln 2}{t_D}} K_1 \left( \sqrt{\frac{i \ln 2}{t_D}} \right)} + S}{1 + C_D \frac{i \ln 2}{t_D} \left( \frac{K_0 \left( \sqrt{\frac{i \ln 2}{t_D}} \right)}{\sqrt{\frac{i \ln 2}{t_D}} K_1 \left( \sqrt{\frac{i \ln 2}{t_D}} \right)} + S \right)} \right] \quad (8.81)$$

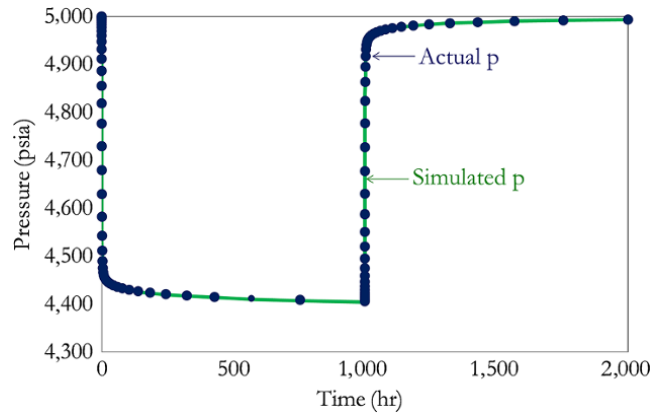


**Figure 8.49** Comparison of simulated and actual pressure history.

*Step 2:* use equation (8.79), which is a specific form of equation (8.78) for a two-rate change, to convolve (superimpose) the pressure signals ( $p_D$ ). Note that in this case  $q_1 = q$  (drawdown) and  $q_2 = 0$  (buildup).

*Step 3:* plot the actual and simulated pressure responses together for comparison (Fig. 8.49).

**Solution.**

*Step 1:* calculation of simulated  $p(t)$ .

Table 8.7 summarizes the calculation of  $p(t)$  for the exercise.

(i) Column 1: time ( $t$ ) taken from actual pressure data.

(ii) Column 2:  $\Delta t_j + \Delta t$ , which is required in equation (8.78). For two-rate changes,  $\Delta t_j + \Delta t = \Delta t_1 + \Delta t$ .

Column 3:  $\Delta t$ , which is required in equation (8.78).

$\Delta t_1 + \Delta t$  is the total elapsed time in the first flow period plus elapsed time in the second flow period, while  $\Delta t$  is the elapsed time during the second flow period.

(iii) Columns 4 and 5:  $(\Delta t_1 + \Delta t)_D$  and  $(\Delta t)_D$  are dimensionless time for  $(\Delta t_1 + \Delta t)$  and  $\Delta t$ , respectively, they are calculated using equation (8.67).

(iv) Columns 6 and 7:  $p_{wD}(\Delta t_1 + \Delta t)_D$  and  $p_{wD}(\Delta t)_D$  are dimensionless pressure for  $(\Delta t_1 + \Delta t)_D$  and  $(\Delta t)_D$ , respectively, they are calculated using equation (8.81) with  $V_i$  from Table 8.5.

(v) Column 8:  $p_i - p(t)$  is calculated using equation (8.79).

(vi) Column 9:  $p(t)$  is calculated using  $p_i - (p_i - p(t))$ .

*Step 2:* create the log-log diagnostic plot for the buildup test using simulated pressure and compare with the log-log diagnostic plot using actual pressure response (Fig. 8.50). Exercise 8.1 shows how to create a log-log diagnostic plot.



**Table 8.7** Simulation of Pressure Response.

	col 1	col 2	col 3	col 4	col 5	col 6	col 7	col 8	col 9
	t (hr)	$\Delta t_1 + \Delta t$ (hr)	$\Delta t$ (hr)	$(\Delta t_1 + \Delta t)_D$	$(\Delta t)_D$	$p_w D$ $(\Delta t_1 + \Delta t)_D$	$p_w D$ $p_w D (\Delta t)_D$	$p_i - p(t)$ (psi)	$p(t)$ (psia)
Start of DD	0.0010	0.0010	0.0000	7.176E+00	0.0000E+00	0.029065	0.000000	0.624	4,999.38
	0.0013	0.0013	0.0000	9.515E+00	0.0000E+00	0.038532	0.000000	0.827	4,999.17
	0.0018	0.0018	0.0000	1.261E+01	0.0000E+00	0.051069	0.000000	1.096	4,998.90
	0.0023	0.0023	0.0000	1.672E+01	0.0000E+00	0.067657	0.000000	1.452	4,998.55
	0.0031	0.0031	0.0000	2.217E+01	0.0000E+00	0.089647	0.000000	1.924	4,998.08
	0.0041	0.0041	0.0000	2.938E+01	0.0000E+00	0.118758	0.000000	2.549	4,997.45
	0.0054	0.0054	0.0000	3.896E+01	0.0000E+00	0.157296	0.000000	3.377	4,996.62
	0.0072	0.0072	0.0000	5.164E+01	0.0000E+00	0.208262	0.000000	4.471	4,995.53
	0.0095	0.0095	0.0000	6.846E+01	0.0000E+00	0.275642	0.000000	5.917	4,994.08
	0.0126	0.0126	0.0000	9.077E+01	0.0000E+00	0.364653	0.000000	7.828	4,992.17
	0.0168	0.0168	0.0000	1.203E+02	0.0000E+00	0.482049	0.000000	10.348	4,989.65
	0.0222	0.0222	0.0000	1.595E+02	0.0000E+00	0.636740	0.000000	13.668	4,986.33
	0.0295	0.0295	0.0000	2.115E+02	0.0000E+00	0.840132	0.000000	18.034	4,981.97
	0.0391	0.0391	0.0000	2.803E+02	0.0000E+00	1.106854	0.000000	23.760	4,976.24
	0.0518	0.0518	0.0000	3.717E+02	0.0000E+00	1.455616	0.000000	31.247	4,968.75
	0.0687	0.0687	0.0000	4.927E+02	0.0000E+00	1.909681	0.000000	40.994	4,959.01
	0.0910	0.0910	0.0000	6.532E+02	0.0000E+00	2.497728	0.000000	53.617	4,946.38
	0.1207	0.1207	0.0000	8.660E+02	0.0000E+00	3.253930	0.000000	69.850	4,930.15
	0.1600	0.1600	0.0000	1.148E+03	0.0000E+00	4.217334	0.000000	90.530	4,909.47
	0.2121	0.2121	0.0000	1.522E+03	0.0000E+00	5.429098	0.000000	116.542	4,883.46
	0.2812	0.2812	0.0000	2.018E+03	0.0000E+00	6.926624	0.000000	148.688	4,851.31
	0.3728	0.3728	0.0000	2.675E+03	0.0000E+00	8.732440	0.000000	187.452	4,812.55
	0.4942	0.4942	0.0000	3.546E+03	0.0000E+00	10.837767	0.000000	232.646	4,767.35
	0.6551	0.6551	0.0000	4.701E+03	0.0000E+00	13.183541	0.000000	283.001	4,717.00
	0.8685	0.8685	0.0000	6.232E+03	0.0000E+00	15.648469	0.000000	335.913	4,664.09
	1.1514	1.1514	0.0000	8.262E+03	0.0000E+00	18.057709	0.000000	387.631	4,612.37
	1.5264	1.5264	0.0000	1.095E+04	0.0000E+00	20.220289	0.000000	434.053	4,565.95
	2.0236	2.0236	0.0000	1.452E+04	0.0000E+00	21.985845	0.000000	471.953	4,528.05
	2.6827	2.6827	0.0000	1.925E+04	0.0000E+00	23.291704	0.000000	499.985	4,500.02
	3.5565	3.5565	0.0000	2.552E+04	0.0000E+00	24.172123	0.000000	518.884	4,481.12
	4.7149	4.7149	0.0000	3.383E+04	0.0000E+00	24.726540	0.000000	530.785	4,469.21
	6.2506	6.2506	0.0000	4.485E+04	0.0000E+00	25.070907	0.000000	538.178	4,461.82
	8.2864	8.2864	0.0000	5.946E+04	0.0000E+00	25.300736	0.000000	543.111	4,456.89
	10.9854	10.9854	0.0000	7.883E+04	0.0000E+00	25.477769	0.000000	546.911	4,453.09
	14.5635	14.5635	0.0000	1.045E+05	0.0000E+00	25.634435	0.000000	550.274	4,449.73
	19.3070	19.3070	0.0000	1.385E+05	0.0000E+00	25.784602	0.000000	553.498	4,446.50
	25.5955	25.5955	0.0000	1.837E+05	0.0000E+00	25.932907	0.000000	556.681	4,443.32
	33.9322	33.9322	0.0000	2.435E+05	0.0000E+00	26.080363	0.000000	559.847	4,440.15
	44.9843	44.9843	0.0000	3.228E+05	0.0000E+00	26.226968	0.000000	562.994	4,437.01
	59.6362	59.6362	0.0000	4.279E+05	0.0000E+00	26.372626	0.000000	566.120	4,433.88
	79.0604	79.0604	0.0000	5.673E+05	0.0000E+00	26.517351	0.000000	569.227	4,430.77
	104.8113	104.8113	0.0000	7.521E+05	0.0000E+00	26.661248	0.000000	572.316	4,427.68
	138.9496	138.9496	0.0000	9.971E+05	0.0000E+00	26.804463	0.000000	575.390	4,424.61
	184.2070	184.2070	0.0000	1.322E+06	0.0000E+00	26.947136	0.000000	578.453	4,421.55
	244.2053	244.2053	0.0000	1.752E+06	0.0000E+00	27.089393	0.000000	581.507	4,418.49
	323.7458	323.7458	0.0000	2.323E+06	0.0000E+00	27.231332	0.000000	584.554	4,415.45
	429.1934	429.1934	0.0000	3.080E+06	0.0000E+00	27.373033	0.000000	587.595	4,412.40
	568.9866	568.9866	0.0000	4.083E+06	0.0000E+00	27.514554	0.000000	590.633	4,409.37
	754.3120	754.3120	0.0000	5.413E+06	0.0000E+00	27.655941	0.000000	593.668	4,406.33
End of DD	1,000.0000	1,000.0000	0.0000	7.176E+06	0.0000E+00	27.797226	0.000000	596.701	4,403.30
=Start of BU	1,000.0010	1,000.0010	0.0010	7.176E+06	7.1758E+00	27.797226	0.029065	596.077	4,403.92
	1,000.0013	1,000.0013	0.0013	7.176E+06	9.5151E+00	27.797226	0.038532	595.874	4,404.13
	1,000.0018	1,000.0018	0.0018	7.176E+06	1.2615E+01	27.797227	0.051069	595.605	4,404.39
	1,000.0023	1,000.0023	0.0023	7.176E+06	1.6720E+01	27.797227	0.067657	595.249	4,404.75
	1,000.0031	1,000.0031	0.0031	7.176E+06	2.2166E+01	27.797227	0.089647	594.777	4,405.22
	1,000.0041	1,000.0041	0.0041	7.176E+06	2.9385E+01	27.797228	0.118758	594.152	4,405.85
	1,000.0054	1,000.0054	0.0054	7.176E+06	3.8957E+01	27.797228	0.157296	593.325	4,406.68
	1,000.0072	1,000.0072	0.0072	7.176E+06	5.1644E+01	27.797229	0.208262	592.231	4,407.77
	1,000.0095	1,000.0095	0.0095	7.176E+06	6.8464E+01	27.797230	0.275642	590.784	4,409.22

**Table 8.7** (Continued)

col 1	col 2	col 3	col 4	col 5	col 6	col 7	col 8	col 9
t (hr)	$\Delta t_1 + \Delta t$ (hr)	$\Delta t$ (hr)	$(\Delta t_1 + \Delta t)_D$	$(\Delta t)_D$	$\frac{p_w D}{(\Delta t_1 + \Delta t)_D}$	$p_{wD}(\Delta t)_D$	$p_i - p(t)$ (psi)	$p(t)$ (psia)
1,000.0126	1,000.0126	0.0126	7.176E+06	9.0766E+01	27.797232	0.364653	588.874	4,411.13
1,000.0168	1,000.0168	0.0168	7.176E+06	1.2032E+02	27.797234	0.482049	586.354	4,413.65
1,000.0222	1,000.0222	0.0222	7.176E+06	1.5952E+02	27.797237	0.636740	583.033	4,416.97
1,000.0295	1,000.0295	0.0295	7.176E+06	2.1148E+02	27.797240	0.840132	578.667	4,421.33
1,000.0391	1,000.0391	0.0391	7.176E+06	2.8035E+02	27.797245	1.106854	572.942	4,427.06
1,000.0518	1,000.0518	0.0518	7.176E+06	3.7167E+02	27.797252	1.455616	565.455	4,434.54
1,000.0687	1,000.0687	0.0687	7.176E+06	4.9272E+02	27.797260	1.909681	555.708	4,444.29
1,000.0910	1,000.0910	0.0910	7.176E+06	6.5321E+02	27.797271	2.497728	543.085	4,456.91
1,000.1207	1,000.1207	0.1207	7.177E+06	8.6596E+02	27.797286	3.253930	526.853	4,473.15
1,000.1600	1,000.1600	0.1600	7.177E+06	1.1480E+03	27.797306	4.217334	506.173	4,493.83
1,000.2121	1,000.2121	0.2121	7.177E+06	1.5219E+03	27.797332	5.429098	480.161	4,519.84
1,000.2812	1,000.2812	0.2812	7.178E+06	2.0177E+03	27.797367	6.926624	448.016	4,551.98
1,000.3728	1,000.3728	0.3728	7.178E+06	2.6748E+03	27.797412	8.732440	409.253	4,590.75
1,000.4942	1,000.4942	0.4942	7.179E+06	3.5461E+03	27.797473	10.837767	364.061	4,635.94
1,000.6551	1,000.6551	0.6551	7.180E+06	4.7010E+03	27.797554	13.183541	313.708	4,686.29
1,000.8685	1,000.8685	0.8685	7.182E+06	6.2322E+03	27.797661	15.648469	260.797	4,739.20
1,001.1514	1,001.1514	1.1514	7.184E+06	8.2621E+03	27.797802	18.057709	209.083	4,790.92
1,001.5264	1,001.5264	1.5264	7.187E+06	1.0953E+04	27.797990	20.220289	162.665	4,837.34
1,002.0236	1,002.0236	2.0236	7.190E+06	1.4521E+04	27.798238	21.985845	124.770	4,875.23
1,002.6827	1,002.6827	2.6827	7.195E+06	1.9250E+04	27.798568	23.291704	96.745	4,903.25
1,003.5565	1,003.5565	3.5565	7.201E+06	2.5520E+04	27.799004	24.172123	77.855	4,922.14
1,004.7149	1,004.7149	4.7149	7.210E+06	3.3833E+04	27.799582	24.726540	65.967	4,934.03
1,006.2506	1,006.2506	6.2506	7.221E+06	4.4852E+04	27.800347	25.070907	58.591	4,941.41
1,008.2864	1,008.2864	8.2864	7.235E+06	5.9461E+04	27.801360	25.300736	53.679	4,946.32
1,010.9854	1,010.9854	10.9854	7.255E+06	7.8829E+04	27.802699	25.477769	49.907	4,950.09
1,014.5635	1,014.5635	14.5635	7.280E+06	1.0450E+05	27.804469	25.634435	46.582	4,953.42
1,019.3070	1,019.3070	19.3070	7.314E+06	1.3854E+05	27.806805	25.784602	43.409	4,956.59
1,025.5955	1,025.5955	25.5955	7.359E+06	1.8367E+05	27.809886	25.932907	40.292	4,959.71
1,033.9322	1,033.9322	33.9322	7.419E+06	2.4349E+05	27.813942	26.080363	37.213	4,962.79
1,044.9843	1,044.9843	44.9843	7.499E+06	3.2280E+05	27.819268	26.226968	34.181	4,965.82
1,059.6362	1,059.6362	59.6362	7.604E+06	4.2794E+05	27.826242	26.372626	31.204	4,968.80
1,079.0604	1,079.0604	79.0604	7.743E+06	5.6732E+05	27.835341	26.517351	28.292	4,971.71
1,104.8113	1,104.8113	104.8113	7.928E+06	7.5210E+05	27.847153	26.661248	25.457	4,974.54
1,138.9496	1,138.9496	138.9496	8.173E+06	9.9707E+05	27.862395	26.804463	22.710	4,977.29
1,184.2070	1,184.2070	184.2070	8.498E+06	1.3218E+06	27.881911	26.947136	20.066	4,979.93
1,244.2053	1,244.2053	244.2053	8.928E+06	1.7524E+06	27.906661	27.089393	17.544	4,982.46
1,323.7458	1,323.7458	323.7458	9.499E+06	2.3231E+06	27.937692	27.231332	15.163	4,984.84
1,429.1934	1,429.1934	429.1934	1.026E+07	3.0798E+06	27.976067	27.373033	12.945	4,987.06
1,568.9866	1,568.9866	568.9866	1.126E+07	4.0829E+06	28.022787	27.514554	10.910	4,989.09
1,754.3120	1,754.3120	754.3120	1.259E+07	5.4128E+06	28.078674	27.655941	9.074	4,990.93
End of BU	2,000.0000	2,000.0000	1,000.0000	1.435E+07	7.1758E+06	28.144277	7.450	4,992.55

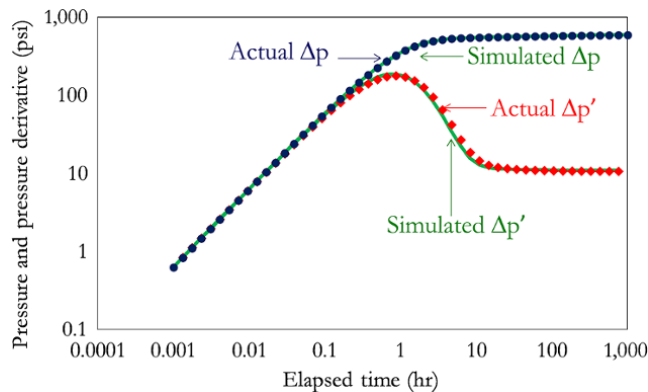


**Figure 8.50** Comparison of simulated and actual log-log diagnostic plot.

Step 3: create the superposition plot for the buildup test using simulated pressure and compare with the superposition plot from the actual pressure response (Fig. 8.51). Since the buildup test considered in this problem is the first following the first drawdown, the superposition plot reduces to the Horner plot. Exercise 7.7 shows how to create the superposition plot and Exercise 7-6 shows how to create the Horner plot.

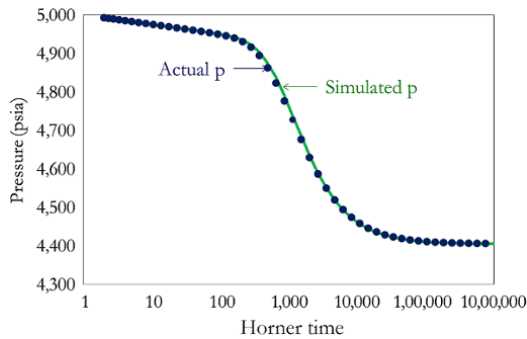


Figure 8.51 Comparison of simulated and actual pressure on Horner plot.

The entire calculation in Exercise 8.2 describes forward simulation in well test analysis. This is a very important verification step to ensure that calculated well test parameters characterizing the well–reservoir system can simulate the entire pressure history. The process of forward simulation is summarized with Fig. 8.52.

**8.5.1.5. Regression and Simulation Match.** In Exercise 8.2, the input parameters simulate pressure, the log-log diagnostic plot, and the Horner (superposition) correctly with minimum error. This may not be true in all cases. Where there is a need to improve the match, regression is used to improve the simulation match. Regression involves defining the square of the normalized error between the measured  $y_j$  and the estimated property  $y(x_j : a)$ , then minimizing the sum of the square of the normalized error:

$$\epsilon^2 = \sum_{j=1}^n \left( \frac{y_j - y(x_j : a)}{y_j} \right)^2 \tag{8.82}$$

where  $y_j$  is the measured property,  $y(x_j : a)$  is an estimated property,  $a$  is the vector of the parameter to be estimated, and  $\epsilon^2$  is the sum of the square of the normalized error, which is the objective function to be minimized.

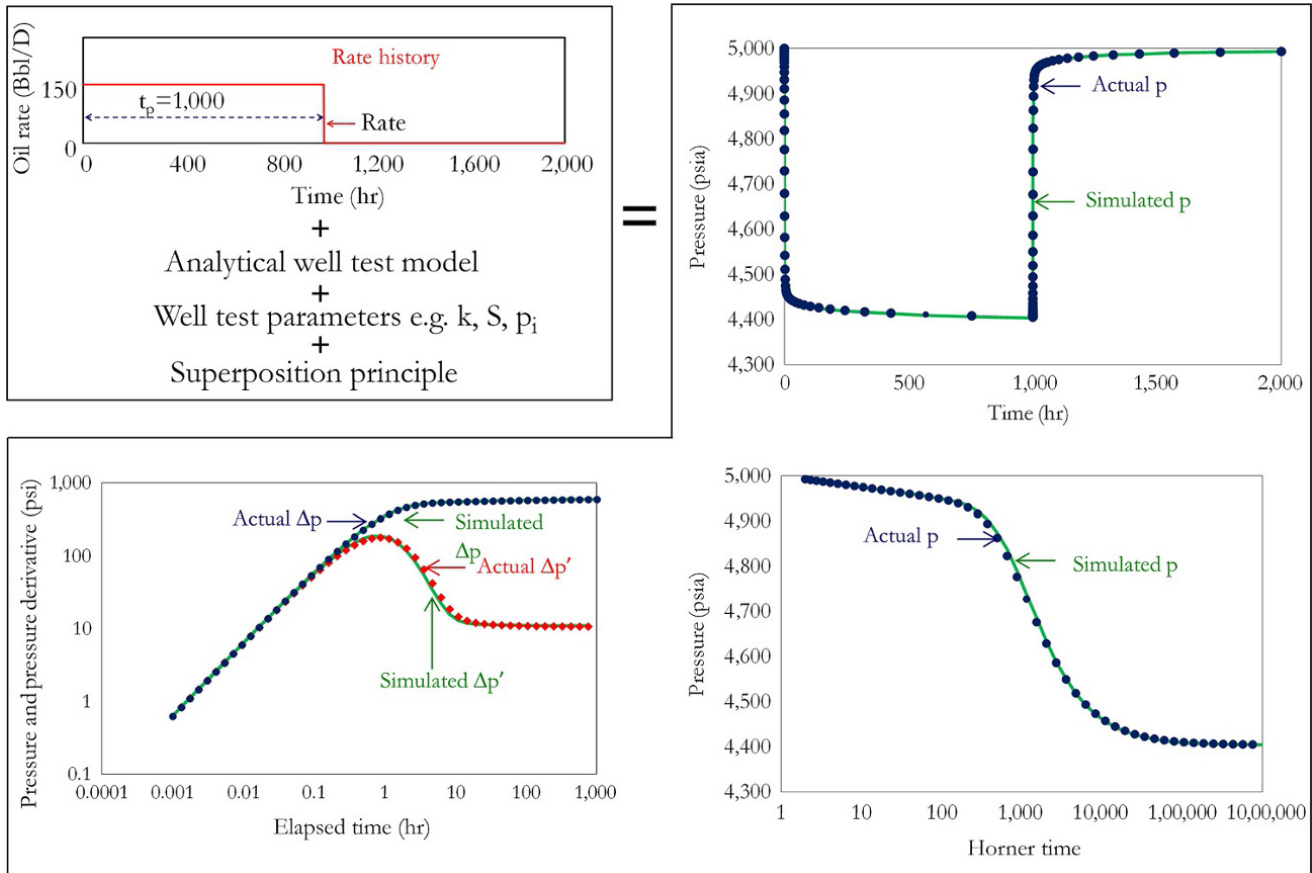


Figure 8.52 Summary of forward simulation for Exercise 8.2.

For a homogeneous reservoir with wellbore storage and skin effect, the objective function to be minimized can be defined as:

$$\epsilon^2 = \sum_{j=1}^n \left( \frac{p_j - p(t_j, C, k, S, p_i)}{p_j} \right)^2 \quad (8.83)$$

where  $p_j$  is the measured pressure,  $p(t_j, C, k, S, p_i)$  is the estimated pressure, and  $(C, k, S, p_i)$  is the model parameter to be estimated.

In a spreadsheet, this can be achieved using the ‘‘Solver’’ option.

**8.5.1.6. Wellbore Storage and Skin Effect.** One convenient way of adding wellbore storage (WBS) and skin effect to any well test interpretation model is to formulate the model without WBS and skin effect (fundamental solution), then add WBS and skin effect in the Laplace domain. Wellbore storage (WBS) and skin effect can be added to any well test analysis model in the Laplace domain by using equation (8.65). Hence, for pressure measured at the wellbore ( $r_D = 1$ ), wellbore storage and skin effect can be added to the fundamental equation using:

$$\bar{p}_D(s, S, C_D) = \frac{s\bar{p}_D(s) + S}{s[1 + C_D s(s\bar{p}_D(s) + S)]} \quad (8.84)$$

[Van Everdingen and Hurst, 1949; Agarwal et al., 1970].

$\bar{p}_D(s)$  is any fundamental solution (model without wellbore storage and skin effect);  $\bar{p}_D(s, S, C_D)$  is the model with wellbore storage and skin effect.

Changing the WBS is often encountered when there is a phase change during well testing. The phenomenon of changing WBS is discussed in Section 8.6.2.2. Changing wellbore storage can be included in any well test analysis model in the Laplace domain using:

$$\bar{p}_D(s, S, C_D, C_{\phi D}, \alpha_D) = \frac{(s\bar{p}_D(s) + S) \left[ 1 + s^2 \times C_D \left( \frac{C_{\phi D}}{s} - \frac{C_{\phi D}}{s + (1/\alpha_D)} \right) \right]}{s[1 + C_D s(s\bar{p}_D(s) + S)]} \quad (8.85)$$

[Fair, 1979; Hegeman et al., 1993]

where

$$C_D = \frac{0.8936}{\phi c_t h r_w^2 C}$$

$$\alpha_D = \frac{0.000264 k_r}{\phi \mu c_t r_w^2} \alpha$$

$$C_{\phi D} = \frac{k_r h}{141.2 q B \mu} C_{\phi}$$

$C_{\phi}$  is the changing-storage pressure parameter

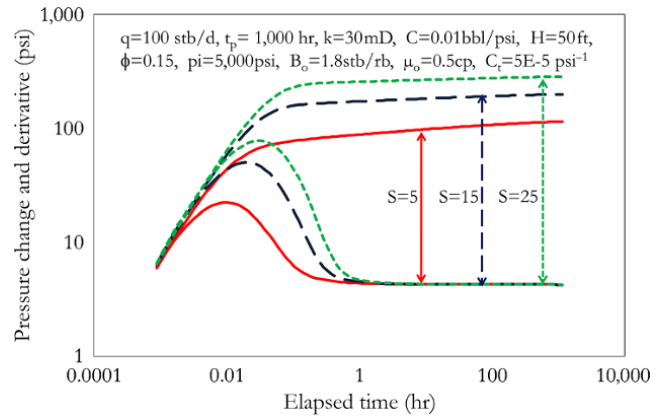


Figure 8.53 Effect of skin effect on well test behavior.

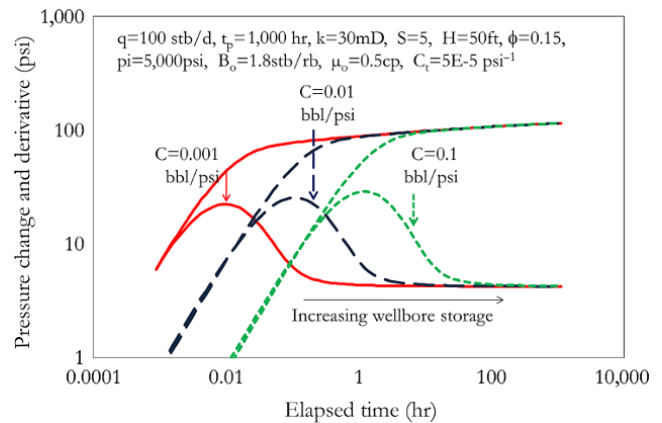


Figure 8.54 Effect of changing WBS on well test behavior.

Fig. 8.53 is the well test simulation showing the effect of skin on the well test diagnostic plot. As the skin effect increases, the distance between the radial flow stabilization line on  $\Delta p'$  and the corresponding  $\Delta p$  increases.

Fig. 8.54 shows the effect on well test behavior of changing the wellbore storage constant ( $C$ ). As  $C$  increases, the early part of reservoir behavior characterizing radial flow stabilization may be masked by storage effect.

**8.5.1.7. Limited Entry Well.** Parameters defining a limited entry (partial penetrating) are shown in Fig. 8.55. Penetration ratio is defined as:

$$b = \frac{h_p}{h} \quad (8.86)$$

where  $h_p$  is completion interval and defined as:

$$h_p = h_2 - h_1 \quad (8.87)$$

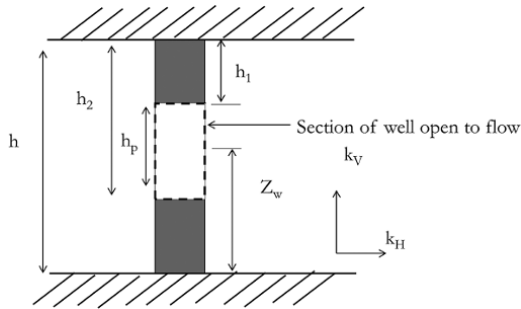


Figure 8.55 Schematic of a limited entry well.

Intervals in Fig. 8.55 are defined in dimensionless variables as:

$$h_{pD} = \frac{h_p}{r_w} \sqrt{\frac{k_r}{k_z}} \quad (8.88)$$

$$h_D = \frac{h}{r_w} \sqrt{\frac{k_r}{k_z}} \quad (8.89)$$

$$h_{1D} = \frac{h_1}{h} \quad (8.90)$$

$$h_{2D} = \frac{h_2}{h} \quad (8.91)$$

and b is also defined as:

$$b = h_{2D} - h_{1D} \quad (8.92)$$

Limited entry creates an additional pressure drop compared to a fully completed well. The effective (apparent) skin due to the combined effect of wellbore damage (mechanical or true skin) and converging flow (completion) skin is expressed as:

$$S_a = \frac{S_w}{b} + S_c \quad (8.93)$$

where

$$S_c = \frac{2}{\pi^2 b^2} \sum_{n=1}^{\infty} \frac{1}{n^2} [\sin(n\pi h_{2D}) - \sin(n\pi h_{1D})]^2 k_0 \left( \frac{n\pi}{h_D} \right), \quad [Stewart, 2010] \quad (8.94)$$

$S_w$  is the mechanical (true) skin, and  $S_c$  is the completion skin due to the limited entry effect.

Where the first radial flow stabilization on the  $\Delta p'$  is evident due to low  $\frac{k_z}{k_r}$ ,  $k_r$  can be calculated, since the first radial flow stabilization line corresponds to  $k_r h_p$ , as shown in Fig. 8.56. It is not uncommon that the first radial flow stabilization line is not obvious and, hence, the second radial flow stabilization, which corresponds to  $k_r h$ ,

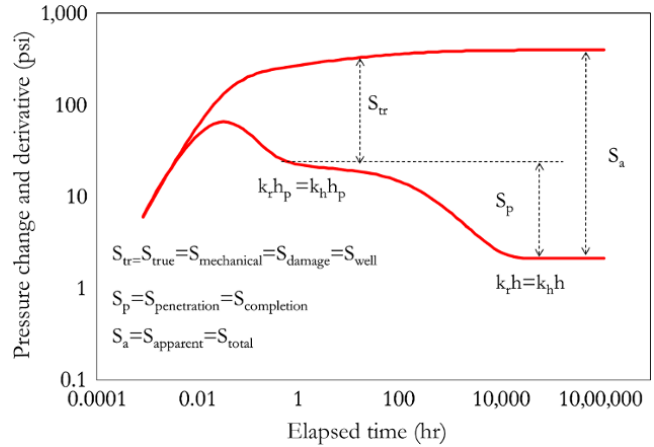


Figure 8.56 Log-log diagnostic plot of a well with limited entry.

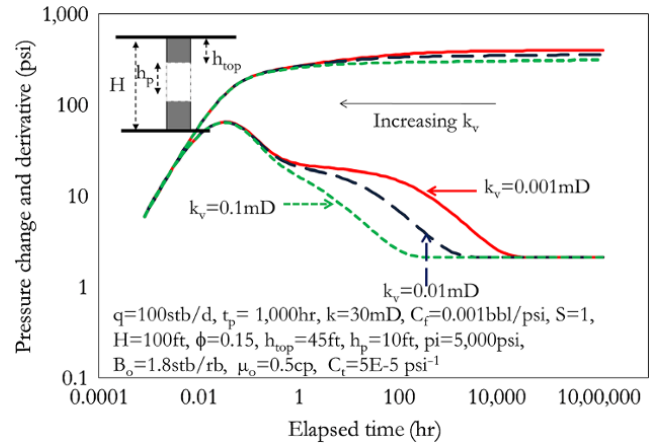


Figure 8.57 Effect of  $\frac{k_z}{k_r}$  on limited entry well test behavior.

is the most reliable feature to determine  $k_r$ . With  $k_r$  determined,  $k_z$  can then be determined using equation (7.65), where  $k_s$  is determined from a spherical flow regime as discussed in Chapter 7 (7.3.1.4) and Section 8.4.3.6.

Fig. 8.57 shows the effect of  $\frac{k_z}{k_r}$  (changing  $k_z$  while  $k_r$  is constant for all cases on the plot) on well test behavior. The smaller the  $\frac{k_z}{k_r}$ , the more accentuated is the first radial flow stabilization on the derivative and the longer it takes for the second radial flow to manifest.

**8.5.1.8. Fractures.** The effect of fractured wells can be captured in interpretation models using effective wellbore radius as described in equation (7.55) and demonstrated with Exercise 8.3. Equation (8.95) shows the relationship between effective wellbore radius ( $r_{we}$ ), wellbore radius ( $r_w$ ), and wellbore skin effect ( $S$ ).

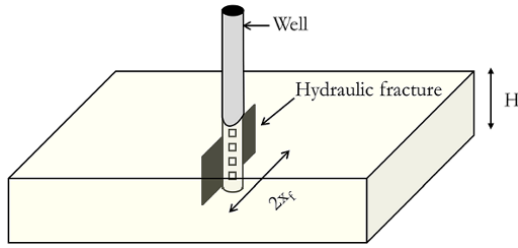


Figure 8.58 Schematic of a vertical hydraulic fracture.

$$r_{we} = r_w e^{-S} \tag{8.95}$$

A schematic of a vertical hydraulic fracture showing fracture length is shown in Fig. 8.58.

*Infinite Conductivity Fracture*

Effective well bore radius determined from equation (8.95) can be related to fracture half-length ( $x_f$ ) using:

$$r_{we} = \frac{x_f}{2} \tag{8.96}$$

Calculation of fracture half-length from skin effect in a fractured well is demonstrated in Exercise 8.3

*Finite Conductivity Fracture*

Finite conductivity fractures can be described with flow capacity ( $k_f w_f$ ). Flow capacity in dimensionless form is called *dimensionless fracture conductivity* or simply *fracture conductivity* and is expressed as [Cinco-Ley et al., 1978]:

$$F_{CD} = k_{fD} w_{fD} = \frac{k_f w_f}{k x_f}, \tag{8.97}$$

As shown above, a low permeability reservoir will tend to have high  $F_{CD}$  except in cases where fracture permeability is low. Fracture conductivity ( $F_{CD}$ ) can be significantly improved by propping fracture to give a large fracture width ( $w_f$ ).  $F_{CD}$  provides an approach for evaluating effectiveness of fracture job carried out using the following  $F_{CD}$  ranges:

- $F_{CD} < 10$  for ineffective treatment.
- $10 < F_{CD} < 50$  for effective treatment.
- $F_{CD} > 50$  for very effective treatment.

As in other fracture models discussed, fracture properties can be related to effective wellbore radius and then skin effect. A *Cinco-Ley type curve* provides the relationship between  $F_{CD}$  and effective wellbore radius (Fig. 8.59).

For  $F_{CD} \leq 0.1$ :

$$r_{we} = 0.28 \left( \frac{k_f w_f}{k} \right) \tag{8.98}$$

Based on the definition of  $F_{CD}$ , when it is greater than 300, fracture can be defined as infinite conductivity.

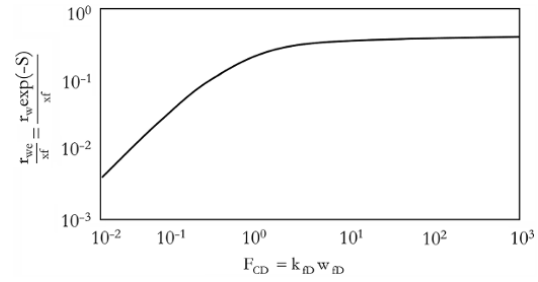


Figure 8.59 Cinco-Ley type curve for finite conductivity [Adapted from Cinco-Ley, Samaniego, & Dominguez, 1978].

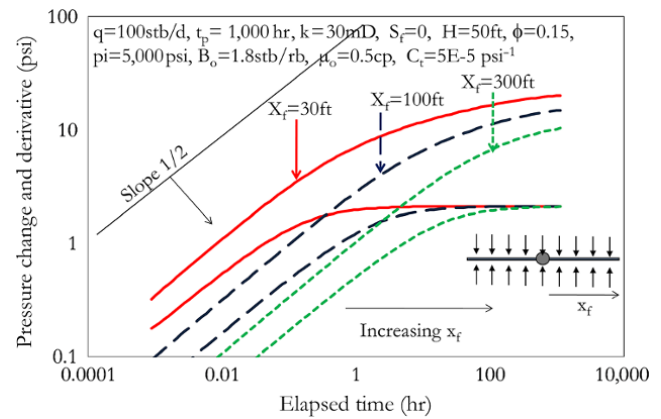


Figure 8.60 Effect of  $x_f$  on ICF well test behavior.

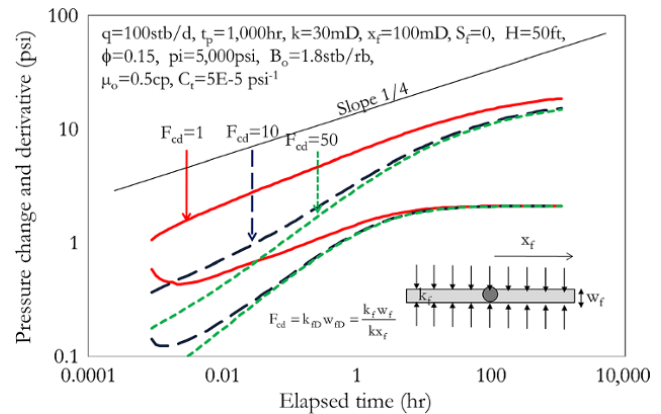


Figure 8.61 Effect of  $F_{CD}$  on FCF well test behavior.

Fig. 8.60 shows the well test simulation of a well with an infinite conductivity fracture with varying  $x_f$ . Increasing  $x_f$  increases the time when the radial flow/reservoir property will manifest.

Fig. 8.61 shows the well test simulation of a well with a finite conductivity fracture with varying  $F_{CD}$ . As  $F_{CD}$  increases the  $1/4$  characteristic behavior of FCF may be less accentuated.

**Exercise 8.3** Use of Effective Wellbore Radius to Define Wellbore Fractures in Interpretation Models

A well test was carried out on a hydraulically fractured well with a wellbore radius of 0.35 ft in a 35 ft net pay reservoir with porosity of 0.23 and  $c_t$  of  $4.7 \text{ E-5 psi}^{-1}$ . Pressure–rate history for the well test is shown in Table 8.8. Oil produced has a viscosity of 0.75 cp at reservoir condition and formation volume factor of 1.2 stb/rb. Reservoir properties estimation from seismic inversion and geostatistical interpolation of properties from other wells suggest a fairly homogeneous reservoir.

1. Identify the start and end of each flow regime.
2. Determine the well test interpretation model.
3. Determine the well test interpretation parameters.
4. Simulate pressure response and compare with actual pressure measured.
5. Refine simulated pressure response using regression where required.

**Solution.**

## 1. Data preparation

This involves examination of the entire pressure–rate history, defining flow periods (drawdown and buildup) (Fig. 8.62), identifying and removing outliers (where they exist).

## 2. Diagnosis of well test

Diagnosis involves examination of the log-log diagnostic plot (log-log pressure change and derivative) to identify flow regimes that help in defining the well test interpretation model. Fig. 8.63 shows the derivative of the buildup test with important flow regimes that characterize well and reservoir behavior. Exercise 8.1 discusses well test derivative calculation and plotting of log-log diagnostic plots for well test analysis.

## 3. Defining the well test interpretation model

From diagnosis, the well-reservoir system is characterized as: infinite conductivity well behavior (linear flow),

**Table 8.8** Well Test Data (Pressure–Rate History) for Exercise 8.3.

Time (hr)	Rate (stb/D)	Pressure (psia)	Time (hr)	Rate (stb/D)	Pressure (psia)	Time (hr)	Rate (stb/D)	Pressure (psia)
0.0006	107	6,731.888	8.0099	107	6,716.558	550.0880	0	6,696.615
0.0007	107	6,731.861	10.6188	107	6,715.247	550.1167	0	6,696.990
0.0010	107	6,731.828	14.0775	107	6,713.891	550.1546	0	6,697.410
0.0013	107	6,731.789	18.6627	107	6,712.495	550.2050	0	6,697.879
0.0017	107	6,731.743	24.7414	107	6,711.064	550.2718	0	6,698.400
0.0023	107	6,731.688	32.7999	107	6,709.603	550.3603	0	6,698.977
0.0030	107	6,731.623	43.4832	107	6,708.115	550.4777	0	6,699.613
0.0040	107	6,731.548	57.6462	107	6,706.605	550.6333	0	6,700.310
0.0052	107	6,731.460	76.4223	107	6,705.076	550.8395	0	6,701.072
0.0070	107	6,731.358	101.3138	107	6,703.532	551.1130	0	6,701.898
0.0092	107	6,731.241	134.3129	107	6,701.974	551.4755	0	6,702.789
0.0122	107	6,731.105	178.0602	107	6,700.406	551.9561	0	6,703.745
0.0162	107	6,730.950	236.0564	107	6,698.830	552.5932	0	6,704.766
0.0215	107	6,730.772	312.9426	107	6,697.246	553.4378	0	6,705.847
0.0285	107	6,730.569	414.8716	107	6,695.657	554.5575	0	6,706.987
0.0378	107	6,730.339	550.0000	107	6,694.063	556.0420	0	6,708.181
0.0501	107	6,730.077	550.0006	0	6,694.175	558.0099	0	6,709.423
0.0664	107	6,729.781	550.0007	0	6,694.203	560.6188	0	6,710.708
0.0880	107	6,729.447	550.0010	0	6,694.235	564.0775	0	6,712.029
0.1167	107	6,729.072	550.0013	0	6,694.274	568.6627	0	6,713.379
0.1546	107	6,728.652	550.0017	0	6,694.321	574.7414	0	6,714.750
0.2050	107	6,728.182	550.0023	0	6,694.375	582.7999	0	6,716.133
0.2718	107	6,727.660	550.0030	0	6,694.440	593.4832	0	6,717.518
0.3603	107	6,727.082	550.0040	0	6,694.515	607.6462	0	6,718.894
0.4777	107	6,726.445	550.0052	0	6,694.603	626.4223	0	6,720.250
0.6333	107	6,725.746	550.0070	0	6,694.705	651.3138	0	6,721.574
0.8395	107	6,724.983	550.0092	0	6,694.823	684.3129	0	6,722.851
1.1130	107	6,724.154	550.0122	0	6,694.958	728.0602	0	6,724.068
1.4755	107	6,723.259	550.0162	0	6,695.113	786.0564	0	6,725.210
1.9561	107	6,722.298	550.0215	0	6,695.291	862.9426	0	6,726.264
2.5932	107	6,721.271	550.0285	0	6,695.494	964.8716	0	6,727.219
3.4378	107	6,720.181	550.0378	0	6,695.724	1,100.0000	0	6,728.068
4.5575	107	6,719.029	550.0501	0	6,695.986			
6.0420	107	6,717.821	550.0664	0	6,696.281			

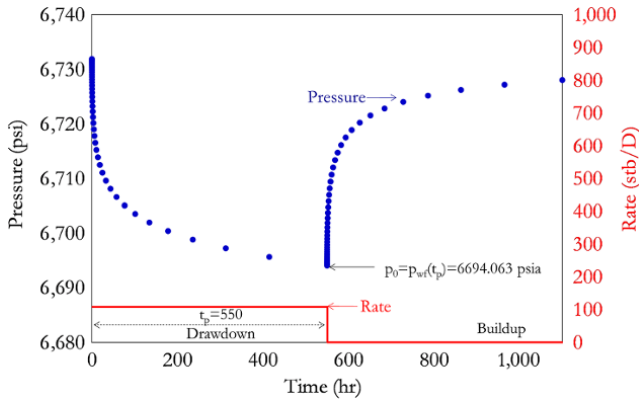


**Figure 8.62** Pressure–rate history showing drawdown and buildup test.

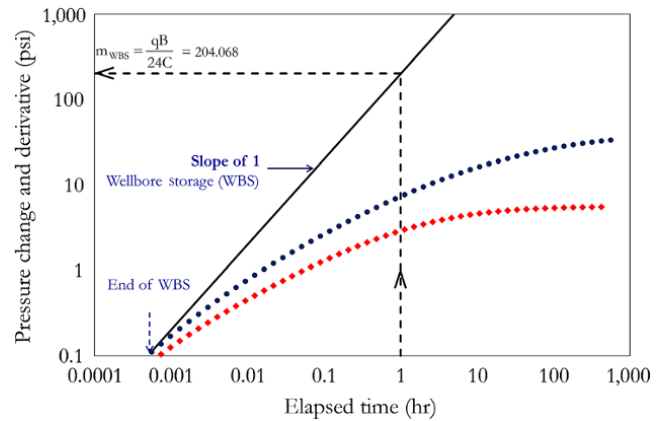


**Figure 8.64**  $m_{WBS}$  calculation from the log-log diagnostic plot.

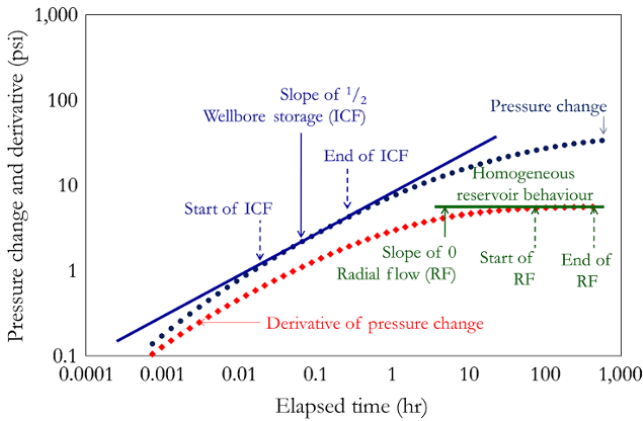


**Figure 8.63** Log-log diagnostic plot for buildup test showing flow regimes.

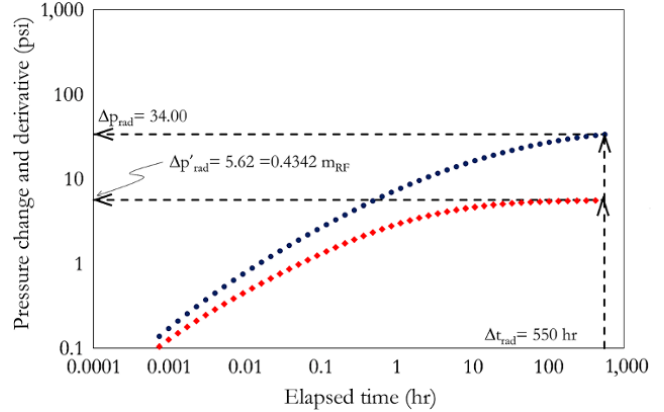


**Figure 8.65** Log-log diagnostic plot with  $\Delta p_{rad}$  and  $\Delta p'_{rad}$  calculation.

reservoir with homogeneous behavior, and infinite acting boundary behavior. This system can thus be described as an *infinite acting homogeneous reservoir with infinite conductivity (high conductivity) well*.

4. Model parameters

*Wellbore Storage Constant Calculation*

The WBS effect may be masked by the fracture behavior as seen in most cases. This does not mean it does not exist. Fitting a WBS slope of 1 through the first point on the diagnostic plot will give a C value larger than actual C value that fit the entire pressure data. However, this value will be refined using regression in forward simulation. From Fig. 8.64:

$$m_{WBS} = \frac{qB}{24C} = 204.068 \text{ psi/hr}$$

Hence,

$$C = \frac{qB}{24m_{WBS}} = \frac{107 \times 1.2}{24 \times 204.068} = 0.0026 \text{ bbl/psi}$$

$$C = 0.026 \text{ bbl/psi.}$$

*Radial Permeability Calculation*

From Fig. 8.65:

$$0.4343 m_{RF} = 5.62 \text{ psi}$$

Therefore:

$$m_{RF} = \frac{5.62}{0.4343} = 12.94 \text{ psi/log cycle}$$

From equation (7.69):

$$k_r = \frac{162.6qB\mu}{m_{RF}h}$$

Given  $q = 107 \text{ stb/D}$ ,  $B = 1.2 \text{ stb/rb}$ , and  $\mu = 0.75 \text{ cp}$ :

$$k_r = \frac{162.6 \times 107 \times 1.2 \times 0.75}{12.94 \times 35} = 34.6 \text{ mD}$$

$$k_r = 34.6 \text{ mD}$$

*Skin Calculation from Radial Flow*

From Fig. 8.65:

$$\Delta p_{rad} = 34.00 \text{ psi and } \Delta p'_{rad} = 5.62 \text{ psi}$$



Substituting  $\Delta p_{rad}$  and  $\Delta p'_{rad}$  into equation (8.21):

$$S = 1.15 \left( \frac{0.4342 \Delta p_{rad}}{\Delta p'_{rad}} - \log \frac{k t_p \Delta t_{rad}}{1698244 \phi \mu c_t r_w^2 (t_p + \Delta t_{rad})} \right)$$

$$S = 1.15 \left( \frac{0.4342 \times 34}{5.62} - \log \frac{34.6 \times 550 \times 550}{1698244 \times 0.23 \times 0.75 \times 4.7 \times 10^{-5} \times 0.35^2 \times (550 + 550)} \right)$$

$$= -4.7$$

$S = -4.7$

*Fracture Half-Length ( $x_f$ ) Calculation*

From Fig. 8.66:

$$m_{LF} = 8.61 \text{ psi/hr}^{-1/2}$$

From equation (8.29):

$$m_{LF} = 4.06 \frac{qB}{hx_f} \sqrt{\frac{\mu}{\phi c_t k}}$$

Substituting values of  $q$ ,  $B$ ,  $h$ ,  $\mu$ ,  $\phi$ ,  $c_t$ , and  $k$ :

$$8.61 = 4.06 \frac{107 \times 1.2}{35 \times x_f} \sqrt{\frac{0.75}{0.23 \times 4.7 \times 10^{-5} \times 34.6}}$$

Making  $x_f$  the subject of the formula:

$$x_f = 77.5 \text{ ft}$$

*Skin Calculation from Fracture Half-Length ( $x_f$ )*

The skin effect can also be calculated from fracture properties.

From equation (8.95):  $r_{we} = r_w e^{-S}$

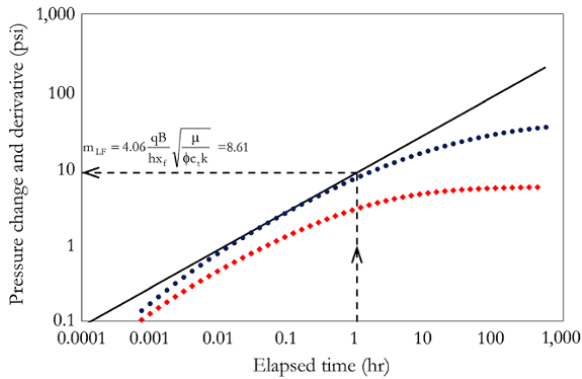


**Figure 8.66**  $m_{LF}$  calculation from the log-log diagnostic plot.

Also from equation (8.96):  $r_{we} = \frac{x_f}{2}$

Substituting  $r_{we} = \frac{x_f}{2}$  from equation (8.96) into equation (8.95):

$$\frac{x_f}{2} = r_w e^{-S}$$

Solving for  $S$ :

$$S = -\ln \left( \frac{x_f}{2r_w} \right) \tag{8.99}$$

Hence:

$$S = -\ln \left( \frac{77.5}{2 \times 0.35} \right)$$

$$S = -4.7.$$

Note the consistency in skin values from radial flow ( $\Delta p_{rad}$  and  $\Delta p'_{rad}$  method) and from fracture half-length method.

*Initial Reservoir Pressure Calculation*

$p^*$  (from radial flow extrapolation on superposition or Horner plot, Fig. 8.67) equals initial reservoir pressure for infinitely acting reservoir system.

Hence,  $p^* = p_i = 6731.92$  psia.

5. Interpretation model consistency check (see Table 8.9)

6. Forward Simulation

From equation (8.63), active well response is defined by:

$$\bar{p}_{wD}(s, S, C_D, r_D) = \frac{\frac{K_0(r_D \sqrt{s}) + S}{\sqrt{s} K_1(\sqrt{s})} + S}{s \left[ 1 + C_D s \left( \frac{K_0(r_D \sqrt{s})}{\sqrt{s} K_1(\sqrt{s})} + S \right) \right]}$$

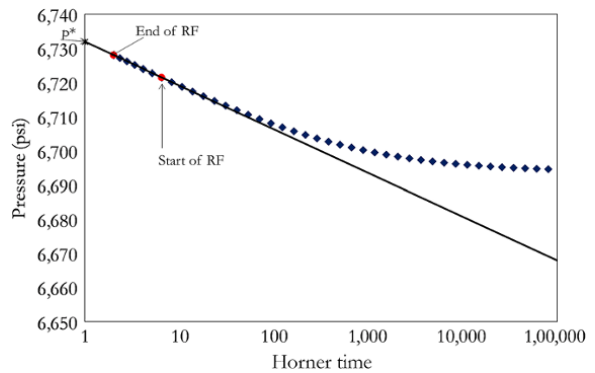


**Figure 8.67** Horner plot with extrapolation of RF line to  $p^*$ .

**Table 8.9** Model Consistency Check.

Near wellbore	Reservoir	Boundaries
Well was mentioned to have been hydraulically fractured. Hence, <i>infinite conductivity fracture</i> is consistent with well engineering information.	Geophysical information supports homogeneous behavior. Flat derivative is a clear indication of homogeneous radial flow behavior. There is no reason to suggest otherwise.	Infinite acting reservoir system suggests no boundary effect was observed. There is no reason to suggest otherwise for now, except structural analysis indicates boundaries within the radius of investigation.

For pressure measured at wellbore,  $r_D = 1$ , hence:

$$\bar{p}_{wD}(s, S, C_D) = \frac{\frac{K_0(\sqrt{s})}{\sqrt{s}K_1(\sqrt{s})} + S}{s \left[ 1 + C_D s \left( \frac{K_0(\sqrt{s})}{\sqrt{s}K_1(\sqrt{s})} + S \right) \right]}$$

Following the steps described Exercise 8.2 with negative skin included in the interpretation model, using the equivalent wellbore radius described in equation (8.95):

$$r_{we} = r_w e^{-S}$$

Substituting values of  $r_w$  and  $S$  into the above equation:

$$r_{we} = 0.35 \times e^{-(-4.7)} = 38.48 \text{ ft}$$

Solution of the forward simulation is shown in Table 8.10 and summarized with plots in Fig. 8.68. The match in Fig. 8.68 can be improved using total least square regression, which can be setup in a spreadsheet as shown in Table 8.11. The regression equation defined in equation (8.82) can be used to improve the match on pressure prediction as shown below:

$$\epsilon_{\text{pressure}}^2 = \sum_{j=1}^n \left( \frac{p_j - p(t_j, C, k, S, p_i)}{p_j} \right)^2$$

Total least regression can also be carried out on the derivative in similar way as carried out on pressure:

$$\epsilon_{\text{derivative}}^2 = \sum_{j=1}^n \left( \frac{\Delta p'_j - \Delta p'(t_j, C, k, S, p_i)}{\Delta p'_j} \right)^2$$

The solution setup for regression on the pressure change derivative is shown in Table 8.12.

The sum of square of normalized error on pressure match from Table 8.11 is:

$$\epsilon_{\text{pressure}}^2 = \sum_{j=1}^n \left( \frac{p_j - p(t_j, C, k, S, p_i)}{p_j} \right)^2 = 5.02E-07$$

While the sum of square of normalized error on pressure change derivative match from Table 8.12 is:

$$\epsilon_{\text{derivative}}^2 = \sum_{j=1}^n \left( \frac{\Delta p'_j - \Delta p'(t_j, C, k, S, p_i)}{\Delta p'_j} \right)^2 = 1.75E-01$$

Derivative match is generally sensitive to changes in parameters and, as such, it is often beneficial to carry out regression on the derivative plot.

The objective function, the sum of normalized square, is set to minimum with  $C$ ,  $k$ ,  $S$ , and  $p_i$  changing. This can be done using *solver* in a spreadsheet.

For software implementation, regression should be made possible on a log-log derivative plot, superposition function plot, and pressure history plot. Updated parameters from regression on any of the plots should automatically update all matches on every plot accordingly.

Fig. 8.69 shows the improved match after regression and Table 8.13 shows initial and refined parameters after regression.

**8.5.1.9. Slant Wells.** Slant wells (Fig. 8.70) increase the well contact with the reservoir, thereby increasing well deliverability. Increasing well-reservoir contact can help in reducing the rate-dependent skin effect, especially in gas wells. Slant wells improve deliverability, thus creating a negative apparent skin effect relative to reservoir behavior.

Apparent skin effect due to a slant well is a combined effect of the true (mechanical) skin effect ( $S_w$ ) and the geometric skin effect ( $S_g$ ) [Cinco-Ley et al., 1975]:

$$S_a = \frac{\cos \psi_w}{\sqrt{\cos^2 \psi_w + \left(\frac{k_z}{k_r}\right) \sin^2 \psi_w}} S_w + S_g \quad (8.100)$$

where geometric skin effect is defined as:

$$S_g = \frac{\cos \psi_w}{\sqrt{\cos^2 \psi_w + \left(\frac{k_z}{k_r}\right) \sin^2 \psi_w}} \left( -\ln \frac{1 + \frac{1}{\sqrt{\cos^2 \psi_w + \left(\frac{k_z}{k_r}\right) \sin^2 \psi_w}}}{2} \right) + \left( \left(\frac{\psi'_w}{41}\right)^{2.06} - \left(\frac{\psi'_w}{56}\right)^{1.865} \right) \log \frac{h}{100r_w} \sqrt{\frac{k_r}{k_v}} \quad (8.101)$$

and

$$\psi'_g = \tan^{-1} \left( \sqrt{\frac{k_z}{k_r} \tan \psi} \right) \quad (8.102)$$

Fig. 8.71 shows the well test simulation of a slant well with varying slant angle ( $\psi$ ). As slant angle increases, skin effect reduces and, at high slant angle, the well test behavior of a slant well tends to horizontal well behavior, as shown in Fig. 8.71.

**8.5.1.10. Horizontal Well.** Horizontal wells can be modeled with one or a combination of no-flow boundary and constant pressure boundaries (Fig. 8.72).

The solution for a horizontal well model in the time domain can be expressed [Kuchuk et al., 1991] as:

$$p_D(t_D) = 2\pi h_D \int_0^{t_D} d\tau G_x(\tau) G_y(\tau) G_z(\tau), \quad (8.103)$$

**Table 8.10** Solution of Forward Simulation for Exercise 8.3.

$(\Delta t_1 + \Delta t)_D$	$(\Delta t)_D$	$p_D(\Delta t_1 + \Delta t)_D$	$p_D(\Delta t)_D$	$p_i - p(t)$ (psi)	$p(t)$ (psia)	$(\Delta t_1 + \Delta t)_D$	$(\Delta t)_D$	$p_D(\Delta t_1 + \Delta t)_D$	$p_D(\Delta t)_D$	$p_i - p(t)$ (psi)	$p(t)$ (psia)
3.43E-04	0.00E+00	0.007064	0.000000	0.079315	6,731.84	3.94E-01	0.00E+00	0.543528	0.000000	6.102940	6,725.82
4.54E-04	0.00E+00	0.008944	0.000000	0.100432	6,731.82	5.23E-01	0.00E+00	0.611212	0.000000	6.862922	6,725.06
6.02E-04	0.00E+00	0.011268	0.000000	0.126524	6,731.79	6.93E-01	0.00E+00	0.684639	0.000000	7.687388	6,724.23
7.98E-04	0.00E+00	0.014118	0.000000	0.158519	6,731.76	9.19E-01	0.00E+00	0.763915	0.000000	8.577523	6,723.34
1.06E-03	0.00E+00	0.017595	0.000000	0.197563	6,731.72	1.22E+00	0.00E+00	0.848983	0.000000	9.532703	6,722.39
1.40E-03	0.00E+00	0.021804	0.000000	0.244820	6,731.68	1.62E+00	0.00E+00	0.939756	0.000000	10.551926	6,721.37
1.86E-03	0.00E+00	0.026864	0.000000	0.301639	6,731.62	2.14E+00	0.00E+00	1.036061	0.000000	11.633277	6,720.29
2.47E-03	0.00E+00	0.032903	0.000000	0.369449	6,731.55	2.84E+00	0.00E+00	1.137656	0.000000	12.774025	6,719.15
3.27E-03	0.00E+00	0.040065	0.000000	0.449868	6,731.47	3.76E+00	0.00E+00	1.244237	0.000000	13.970756	6,717.95
4.33E-03	0.00E+00	0.048506	0.000000	0.544644	6,731.38	4.99E+00	0.00E+00	1.355451	0.000000	15.219504	6,716.70
5.74E-03	0.00E+00	0.058390	0.000000	0.655621	6,731.26	6.61E+00	0.00E+00	1.470907	0.000000	16.515898	6,715.40
7.62E-03	0.00E+00	0.069905	0.000000	0.784924	6,731.14	8.77E+00	0.00E+00	1.590197	0.000000	17.855322	6,714.06
1.01E-02	0.00E+00	0.083250	0.000000	0.934764	6,730.99	1.16E+01	0.00E+00	1.712900	0.000000	19.233079	6,712.69
1.34E-02	0.00E+00	0.098639	0.000000	1.107553	6,730.81	1.54E+01	0.00E+00	1.838605	0.000000	20.644539	6,711.28
1.77E-02	0.00E+00	0.116311	0.000000	1.305989	6,730.61	2.04E+01	0.00E+00	1.966915	0.000000	22.085259	6,709.83
2.35E-02	0.00E+00	0.136519	0.000000	1.532886	6,730.39	2.71E+01	0.00E+00	2.097462	0.000000	23.551087	6,708.37
3.12E-02	0.00E+00	0.159535	0.000000	1.791323	6,730.13	3.59E+01	0.00E+00	2.229906	0.000000	25.038222	6,706.88
4.13E-02	0.00E+00	0.185650	0.000000	2.084550	6,729.84	4.76E+01	0.00E+00	2.363945	0.000000	26.543257	6,705.38
5.48E-02	0.00E+00	0.215170	0.000000	2.416006	6,729.50	6.31E+01	0.00E+00	2.499311	0.000000	28.063192	6,703.86
7.27E-02	0.00E+00	0.248409	0.000000	2.789230	6,729.13	8.37E+01	0.00E+00	2.635771	0.000000	29.595425	6,702.32
9.63E-02	0.00E+00	0.285692	0.000000	3.207853	6,728.71	1.11E+02	0.00E+00	2.773130	0.000000	31.137736	6,700.78
1.28E-01	0.00E+00	0.327339	0.000000	3.675485	6,728.24	1.47E+02	0.00E+00	2.911218	0.000000	32.688246	6,699.23
1.69E-01	0.00E+00	0.373666	0.000000	4.195660	6,727.72	1.95E+02	0.00E+00	3.049898	0.000000	34.245392	6,697.67
2.24E-01	0.00E+00	0.424970	0.000000	4.771716	6,727.15	2.58E+02	0.00E+00	3.189053	0.000000	35.807877	6,696.11
2.98E-01	0.00E+00	0.481517	0.000000	5.406652	6,726.51	3.43E+02	0.00E+00	3.328589	0.000000	37.374640	6,694.55
3.43E+02	3.43E-04	3.328590	0.007064	37.295331	6,694.62	3.43E+02	3.94E-01	3.329159	0.543528	31.278102	6,700.64
3.43E+02	4.54E-04	3.328590	0.008944	37.274216	6,694.65	3.43E+02	5.23E-01	3.329345	0.611212	30.520204	6,701.40
3.43E+02	6.02E-04	3.328590	0.011268	37.248126	6,694.67	3.43E+02	6.93E-01	3.329591	0.684639	29.698499	6,702.22
3.43E+02	7.98E-04	3.328590	0.014118	37.216134	6,694.70	3.44E+02	9.19E-01	3.329916	0.763915	28.812022	6,703.11
3.43E+02	1.06E-03	3.328591	0.017595	37.177094	6,694.74	3.44E+02	1.22E+00	3.330348	0.848983	27.861689	6,704.06
3.43E+02	1.40E-03	3.328591	0.021804	37.129843	6,694.79	3.44E+02	1.62E+00	3.330920	0.939756	26.848884	6,705.07
3.43E+02	1.86E-03	3.328592	0.026864	37.073032	6,694.85	3.45E+02	2.14E+00	3.331676	1.036061	25.776030	6,706.14
3.43E+02	2.47E-03	3.328593	0.032903	37.005231	6,694.91	3.45E+02	2.84E+00	3.332678	1.137656	24.646528	6,707.27
3.43E+02	3.27E-03	3.328594	0.040065	36.924825	6,695.00	3.46E+02	3.76E+00	3.334003	1.244237	23.464670	6,708.46
3.43E+02	4.33E-03	3.328595	0.048506	36.830067	6,695.09	3.48E+02	4.99E+00	3.335753	1.355451	22.235578	6,709.68
3.43E+02	5.74E-03	3.328597	0.058390	36.719112	6,695.20	3.49E+02	6.61E+00	3.338065	1.470907	20.965139	6,710.95
3.43E+02	7.62E-03	3.328600	0.069905	36.589840	6,695.33	3.51E+02	8.77E+00	3.341113	1.590197	19.659938	6,712.26
3.43E+02	1.01E-02	3.328604	0.083250	36.440040	6,695.48	3.54E+02	1.16E+01	3.345125	1.712900	18.327231	6,713.59
3.43E+02	1.34E-02	3.328608	0.098639	36.267304	6,695.65	3.58E+02	1.54E+01	3.350395	1.838605	16.974943	6,714.95
3.43E+02	1.77E-02	3.328615	0.116311	36.068939	6,695.85	3.63E+02	2.04E+01	3.357296	1.966915	15.611716	6,716.31
3.43E+02	2.35E-02	3.328623	0.136519	35.842136	6,696.08	3.70E+02	2.71E+01	3.366301	2.097462	14.246998	6,717.67
3.43E+02	3.12E-02	3.328634	0.159535	35.583824	6,696.34	3.79E+02	3.59E+01	3.377994	2.229906	12.891156	6,719.03
3.43E+02	4.13E-02	3.328649	0.185650	35.290761	6,696.63	3.90E+02	4.76E+01	3.393085	2.363945	11.555568	6,720.36
3.43E+02	5.48E-02	3.328668	0.215170	34.959524	6,696.96	4.06E+02	6.31E+01	3.412413	2.499311	10.252657	6,721.67
3.43E+02	7.27E-02	3.328694	0.248409	34.586589	6,697.33	4.26E+02	8.37E+01	3.436935	2.635771	8.995767	6,722.92
3.43E+02	9.63E-02	3.328728	0.285692	34.168351	6,697.75	4.54E+02	1.11E+02	3.467693	2.773130	7.798811	6,724.12
3.43E+02	1.28E-01	3.328774	0.327339	33.701229	6,698.22	4.90E+02	1.47E+02	3.505750	2.911218	6.675627	6,725.24
3.43E+02	1.69E-01	3.328834	0.373666	33.181728	6,698.74	5.38E+02	1.95E+02	3.552110	3.049898	5.639030	6,726.28
3.43E+02	2.24E-01	3.328914	0.424970	32.606567	6,699.31	6.01E+02	2.58E+02	3.607605	3.189053	4.699662	6,727.22
3.43E+02	2.98E-01	3.329019	0.481517	31.972818	6,699.95	6.85E+02	3.43E+02	3.672793	3.328589	3.864848	6,728.06

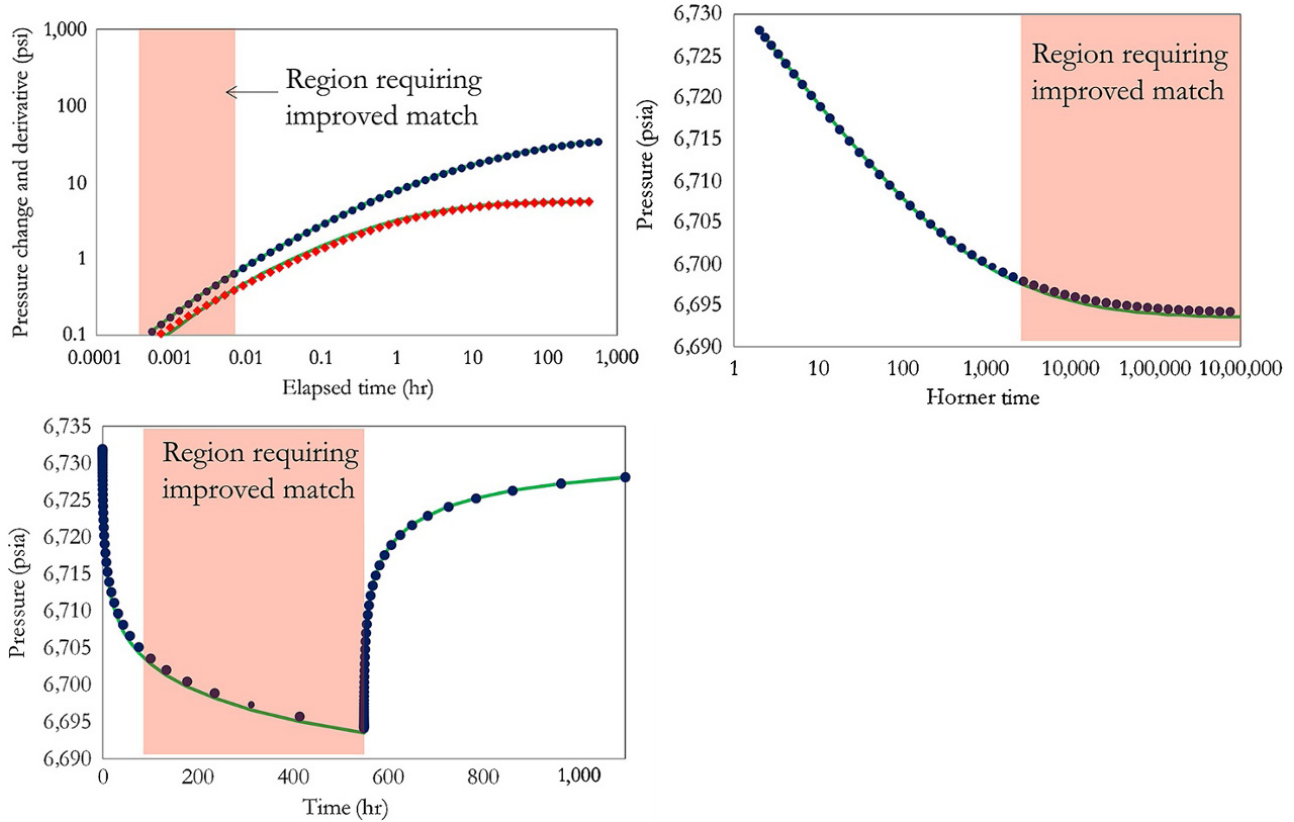


Figure 8.68 Diagnostic, Horner and pressure simulation match with using calculated  $k$ ,  $C$ ,  $S$ , and  $p_i$ .

where

$$G_x(\tau) = \frac{1}{2} \left[ \operatorname{erf} \left( \frac{1}{\sqrt{\tau}} \right) + \frac{\tau}{\pi} \exp \left( -\frac{1}{\tau} - 1 \right) \right]$$

$$G_y(\tau) = \frac{1}{2} \sqrt{\pi \tau}$$

$$G_z(\tau) = \frac{1}{h_D} \left[ 1 + 2 \sum_{n=1}^{\infty} \cos \frac{n\pi z_D}{h_D} \cos \frac{n\pi z_{wD}}{h_D} \exp \frac{-n^2 \pi^2 \tau}{h_D^2} \right]$$

For the no-flow upper boundary and

$$G_z(\tau) = \frac{2}{h_D} \sum_{n=1}^{\infty} \cos \frac{(n-1/2)\pi z_D}{h_D} \cos \frac{(n-1/2)\pi z_{wD}}{h_D} \exp \frac{-(n-1/2)^2 \pi^2 \tau}{h_D^2}$$

for a constant pressure upper boundary.

Equation (8.103) can be converted to the Laplace domain, then mechanical skin effect and wellbore storage can then be added using equation (8.84).

A typical horizontal well in an homogeneous well displays three important features, as shown Fig. 8.32. Each of the flow regime can be described by a straight-line

specialized equation as shown in equations (8.104)–(8.114). These straight-lines can be used to provide initial parameter value, which can then be refined with interpretation model using regression.

*Semi-log Straight Line for Vertical Radial Flow Regime*

When vertical radial flow dominates in a horizontal well, pressure response can be described [Kuchuk, 1995] using:

$$p_i - p_{wf} = \Delta p = \frac{162.6qB\mu}{2\sqrt{k_z k_{xy}} L}$$

$$\left( \log \frac{\sqrt{k_z k_{xy}} \Delta t}{\phi \mu c_t r_w^2} - 3.23 + 0.87S_w - 2 \log \frac{1}{2} \left( \sqrt[4]{\frac{k_z}{k_{xy}}} + \sqrt[4]{\frac{k_{xy}}{k_z}} \right) \right), \tag{8.104}$$

Assuming uniform mechanical skin effect, the total skin factor ( $S_{tv}$ ) for early radial flow analysis can be expressed as the combined effect of wellbore mechanical skin factor,  $S_w$ , and skin effect due to anisotropy,  $S_{ani}$ :

$$S_{tv} = S_w + S_{ani} = S_w - \ln \frac{\left( \sqrt[4]{\frac{k_z}{k_{xy}}} + \sqrt[4]{\frac{k_{xy}}{k_z}} \right)}{2} \tag{8.105}$$

**Table 8.11** Total Least Square Regression on Pressure History for Exercise 8.3.

Time (hr)	Actual p(t) (psia)	Sim p(t) (psia)	Normalized error square	Time (hr)	Actual p(t) (psia)	Sim p(t) (psia)	Normalized error square
0.0006	6,731.89	6,731.84	5.39E-11	550.0006	6,694.18	6,693.51	9.76E-09
0.0007	6,731.86	6,731.82	4.36E-11	550.0007	6,694.20	6,693.54	9.91E-09
0.0010	6,731.83	6,731.79	3.40E-11	550.0010	6,694.24	6,693.56	1.01E-08
0.0013	6,731.79	6,731.76	2.55E-11	550.0013	6,694.27	6,693.60	1.02E-08
0.0017	6,731.74	6,731.71	1.85E-11	550.0017	6,694.32	6,693.64	1.04E-08
0.0023	6,731.69	6,731.66	1.32E-11	550.0023	6,694.38	6,693.69	1.05E-08
0.0030	6,731.62	6,731.60	9.44E-12	550.0030	6,694.44	6,693.75	1.06E-08
0.0040	6,731.55	6,731.53	7.21E-12	550.0040	6,694.52	6,693.82	1.07E-08
0.0052	6,731.46	6,731.44	6.33E-12	550.0052	6,694.60	6,693.91	1.07E-08
0.0070	6,731.36	6,731.34	6.84E-12	550.0070	6,694.71	6,694.01	1.07E-08
0.0092	6,731.24	6,731.22	9.19E-12	550.0092	6,694.82	6,694.13	1.06E-08
0.0122	6,731.11	6,731.08	1.45E-11	550.0122	6,694.96	6,694.27	1.05E-08
0.0162	6,730.95	6,730.92	2.48E-11	550.0162	6,695.11	6,694.44	1.02E-08
0.0215	6,730.77	6,730.73	4.34E-11	550.0215	6,695.29	6,694.62	9.91E-09
0.0285	6,730.57	6,730.51	7.48E-11	550.0285	6,695.49	6,694.84	9.50E-09
0.0378	6,730.34	6,730.26	1.25E-10	550.0378	6,695.72	6,695.09	9.00E-09
0.0501	6,730.08	6,729.98	2.02E-10	550.0501	6,695.99	6,695.37	8.43E-09
0.0664	6,729.78	6,729.66	3.16E-10	550.0664	6,696.28	6,695.69	7.79E-09
0.0880	6,729.45	6,729.30	4.76E-10	550.0880	6,696.62	6,696.05	7.09E-09
0.1167	6,729.07	6,728.89	6.95E-10	550.1167	6,696.99	6,696.46	6.34E-09
0.1546	6,728.65	6,728.44	9.85E-10	550.1546	6,697.41	6,696.91	5.56E-09
0.2050	6,728.18	6,727.93	1.36E-09	550.2050	6,697.88	6,697.42	4.77E-09
0.2718	6,727.66	6,727.37	1.83E-09	550.2718	6,698.40	6,697.98	3.99E-09
0.3603	6,727.08	6,726.75	2.40E-09	550.3603	6,698.98	6,698.60	3.24E-09
0.4777	6,726.45	6,726.07	3.08E-09	550.4777	6,699.61	6,699.28	2.53E-09
0.6333	6,725.75	6,725.33	3.87E-09	550.6333	6,700.31	6,700.02	1.90E-09
0.8395	6,724.98	6,724.52	4.77E-09	550.8395	6,701.07	6,700.83	1.35E-09
1.1130	6,724.15	6,723.64	5.74E-09	551.1130	6,701.90	6,701.70	9.00E-10
1.4755	6,723.26	6,722.71	6.79E-09	551.4755	6,702.79	6,702.63	5.44E-10
1.9561	6,722.30	6,721.70	7.88E-09	551.9561	6,703.75	6,703.63	2.87E-10
2.5932	6,721.27	6,720.63	8.98E-09	552.5932	6,704.77	6,704.69	1.20E-10
3.4378	6,720.18	6,719.51	1.00E-08	553.4378	6,705.85	6,705.81	2.99E-11
4.5575	6,719.03	6,718.32	1.10E-08	554.5575	6,706.99	6,706.98	3.31E-13
6.0420	6,717.82	6,717.09	1.19E-08	556.0420	6,708.18	6,708.21	1.33E-11
8.0099	6,716.56	6,715.80	1.27E-08	558.0099	6,709.42	6,709.47	5.13E-11
10.6188	6,715.25	6,714.47	1.33E-08	560.6188	6,710.71	6,710.77	9.86E-11
14.0775	6,713.89	6,713.10	1.38E-08	564.0775	6,712.03	6,712.11	1.43E-10
18.6627	6,712.49	6,711.70	1.41E-08	568.6627	6,713.38	6,713.47	1.76E-10
24.7414	6,711.06	6,710.26	1.42E-08	574.7414	6,714.75	6,714.84	1.93E-10
32.7999	6,709.60	6,708.80	1.42E-08	582.7999	6,716.13	6,716.23	1.93E-10
43.4832	6,708.11	6,707.32	1.40E-08	593.4832	6,717.52	6,717.61	1.78E-10
57.6462	6,706.60	6,705.82	1.37E-08	607.6462	6,718.89	6,718.98	1.52E-10
76.4223	6,705.08	6,704.30	1.33E-08	626.4223	6,720.25	6,720.32	1.20E-10
101.3138	6,703.53	6,702.77	1.28E-08	651.3138	6,721.57	6,721.64	8.55E-11
134.3129	6,701.97	6,701.23	1.22E-08	684.3129	6,722.85	6,722.90	5.39E-11
178.0602	6,700.41	6,699.68	1.16E-08	728.0602	6,724.07	6,724.10	2.82E-11
236.0564	6,698.83	6,698.13	1.09E-08	786.0564	6,725.21	6,725.23	1.05E-11
312.9426	6,697.25	6,696.57	1.03E-08	862.9426	6,726.26	6,726.27	1.41E-12
414.8716	6,695.66	6,695.00	9.57E-09	964.8716	6,727.22	6,727.21	5.94E-13
550.0000	6,694.06	6,693.43	8.88E-09	1100.0000	6,728.07	6,728.05	0.00E+00

$$e_{\text{pressure}}^2 = 5.02E-07$$

**Table 8.12** Total Least Square Regression on Pressure Change Derivative of Buildup Data for Exercise 8.3.

Time (hr)	Actual $\Delta p'$ (psi)	Sim $\Delta p'$ (psi)	Normalized error square	Time (hr)	Actual $\Delta p'$ (psi)	Sim $\Delta p'$ (psi)	Normalized error square
0.0007	0.11	0.11	2.92E-02	0.8395	2.82	3.21	3.29E-03
0.0010	0.13	0.13	2.12E-02	1.1130	3.05	3.44	2.74E-03
0.0013	0.15	0.16	1.44E-02	1.4755	3.29	3.67	2.24E-03
0.0017	0.18	0.20	8.94E-03	1.9561	3.52	3.88	1.76E-03
0.0023	0.21	0.24	4.83E-03	2.5932	3.75	4.09	1.34E-03
0.0030	0.25	0.28	2.07E-03	3.4378	3.96	4.28	9.82E-04
0.0040	0.29	0.34	5.29E-04	4.5575	4.17	4.46	6.87E-04
0.0052	0.34	0.40	6.07E-06	6.0420	4.37	4.62	4.54E-04
0.0070	0.39	0.46	2.51E-04	8.0099	4.55	4.77	2.78E-04
0.0092	0.45	0.54	1.01E-03	10.6188	4.71	4.90	1.52E-04
0.0122	0.52	0.62	2.04E-03	14.0775	4.86	5.02	6.99E-05
0.0162	0.59	0.72	3.15E-03	18.6627	4.99	5.11	2.26E-05
0.0215	0.67	0.82	4.21E-03	24.7414	5.11	5.20	2.35E-06
0.0285	0.77	0.94	5.12E-03	32.7999	5.20	5.27	1.72E-06
0.0378	0.87	1.07	5.82E-03	43.4832	5.29	5.33	1.44E-05
0.0501	0.99	1.21	6.31E-03	57.6462	5.36	5.38	3.53E-05
0.0664	1.12	1.36	6.58E-03	76.4223	5.42	5.42	6.04E-05
0.0880	1.26	1.52	6.66E-03	101.3138	5.47	5.45	8.69E-05
0.1167	1.41	1.70	6.56E-03	134.3129	5.51	5.48	1.13E-04
0.1546	1.58	1.89	6.32E-03	178.0602	5.55	5.50	1.38E-04
0.2050	1.76	2.09	5.97E-03	236.0564	5.58	5.52	1.60E-04
0.2718	1.95	2.30	5.52E-03	312.9426	5.60	5.54	1.81E-04
0.3603	2.15	2.52	5.00E-03	414.8716	5.62	0.00	1.99E-04
0.4777	2.37	2.75	4.45E-03	550.0000	0.00	0.00	0.00E+00
0.6333	2.59	2.98	3.89E-03				$\epsilon_{\text{derivative}}^2 = 1.75E-01$

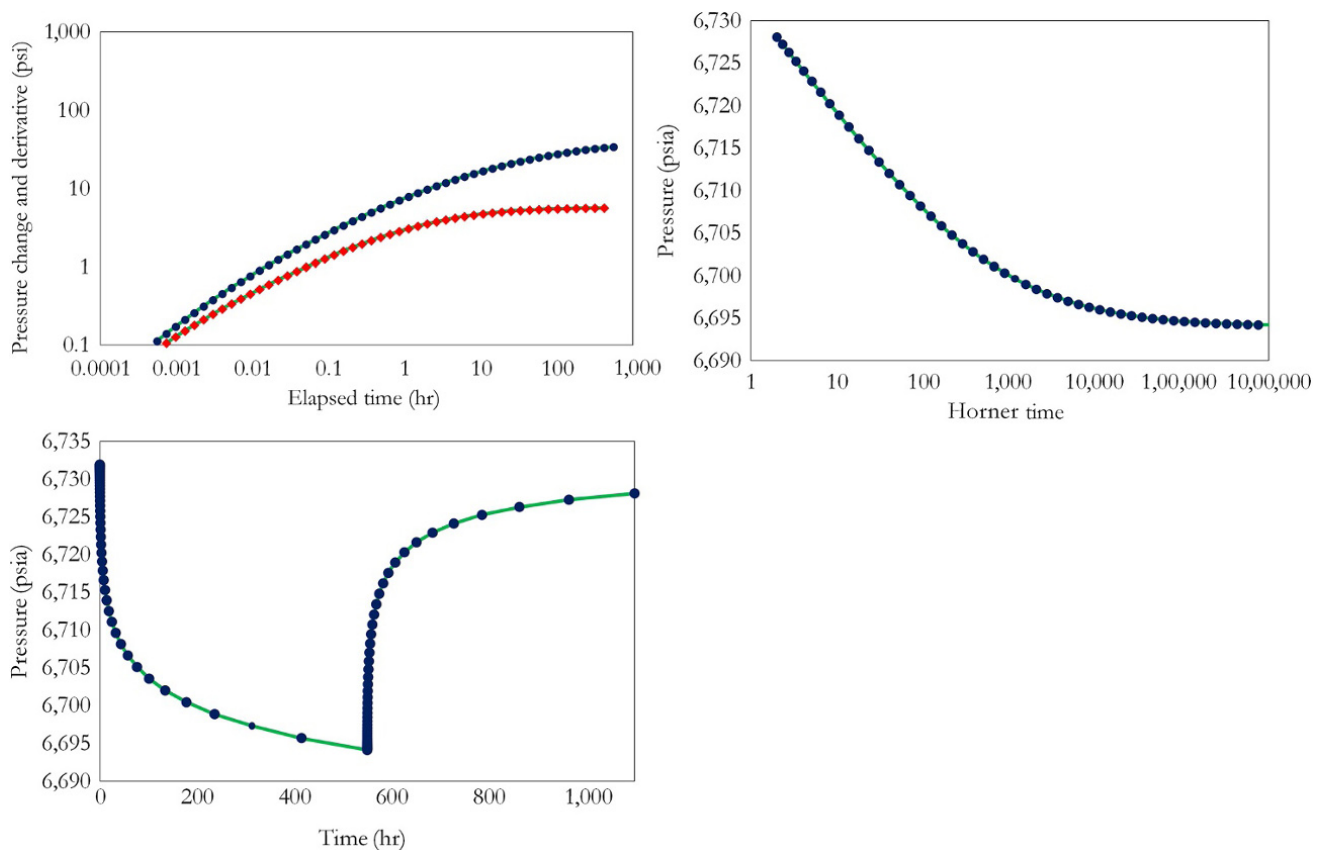


**Figure 8.69** Improved diagnostic, Horner and pressure simulation match.

**Table 8.13** Initial and Final Well Test Parameters Determined from Analysis.

Parameter	Initial	Refined (final)
C (bbl/psi)	0.026	0.015
K (mD)	34.6	34
S	-4.7	-4.8
p <sub>i</sub> (psia)	6,731.9	6,732

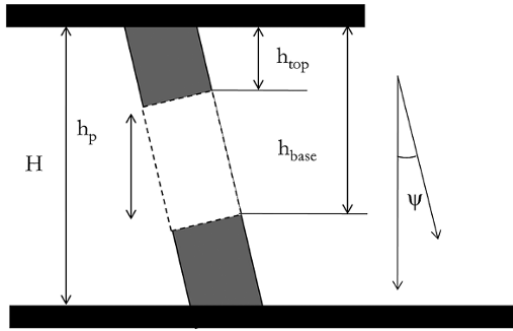


**Figure 8.70** Schematic of a slant well.

*Linear Flow Regime*

During a linear dominated flow regime, pressure response can be described as:

$$p_i - p_{wf} = \Delta p = \frac{8.128qB\mu}{2Lh} \sqrt{\frac{\mu\Delta t}{\phi\mu c_t k_{xy}}} + \frac{141.2qB\mu}{2\sqrt{k_z k_{xy} E}} S_w + \frac{141.2qB\mu}{k_{xy} h} S_z \tag{8.106}$$

This equation shows that  $\Delta p \propto \sqrt{\Delta t}$ . Hence a slope of one half (1/2) on the diagnostic derivative plot is an important characteristic of linear flow in the horizontal well model. This behavior is similar to the ICF derivative signature as shown in Section 8.4.3.4.

During the linear flow regime, the two skin effects,  $S_w$  and  $S_z$ , are additive, where  $S_z$  is the partial penetrating skin effect of the horizontal well located at  $z_w$  in the formation thickness and defined as.

$$S_z = -1.151 \sqrt{\frac{k_{xy} h}{k_z L}} \log \left[ \frac{\pi r_w}{h} \left( 1 + \sqrt{\frac{k_v}{k_{xy}}} \right) \sin \left( \frac{\pi z_w}{h} \right) \right] \tag{8.107}$$

*Pseudoradial Flow Regime*

When a pseudoradial flow regime dominates in a horizontal well, pressure response can be described using:

$$p_i - p_{wf} = \Delta p = \frac{162.6qB\mu}{k_{xy} h} \left( \log \frac{k_{xy} \Delta t}{\phi\mu c_t L^2} - 2.53 \right) + \frac{141.2qB\mu}{2\sqrt{k_z k_{xy} L}} S_w + \frac{141.2qB\mu}{k_{xy} h} S_{zt} \tag{8.108}$$

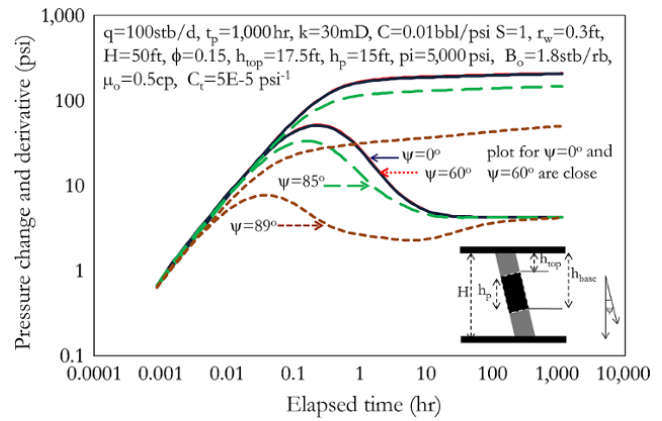


**Figure 8.71** Effect of slant angle on slant well test behavior.

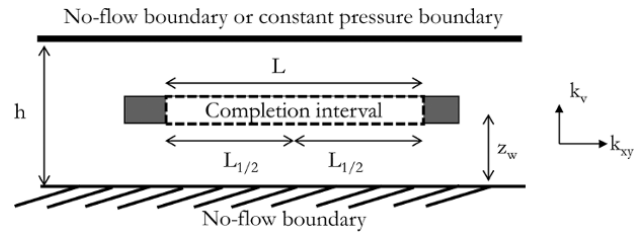


**Figure 8.72** Schematic of a horizontal well.

$S_{zt}$  is defined as:

$$S_{zt} = S_z - 0.5 \frac{k_{xy} h^2}{k_z L^2} \left( \frac{1}{3} - \frac{z_w}{h} + \frac{z_w^2}{h^2} \right) \tag{8.109}$$

Dimensionless parameters in EOF units are defined as:

$$p_D = \frac{k_{xy} h}{141.2qB\mu} \Delta p \tag{8.110}$$

$$t_D = \frac{0.000264k_{xy} \Delta t}{\phi\mu c_t L_{1/2}^2} \tag{8.111}$$

$$h_D = \frac{h}{L_{1/2}} \sqrt{\frac{k_{xy}}{k_z}} \tag{8.112}$$

$$z_{wD} = \frac{z_w}{L_{1/2}} \sqrt{\frac{k_{xy}}{k_z}} \tag{8.113}$$

$$r_{wD} = \left( \frac{r_w}{2L_{1/2}} \right) \left( 1 + \sqrt{\frac{k_{xy}}{k_z}} \right) \tag{8.114}$$

$$k_{xy} \equiv k_H \text{ and } k_z \equiv k_v.$$

Fig. 8.73 shows typical well test behavior of a horizontal with skin components.

From Fig. 8.74, reduction in  $k_z$  for fixed  $k_{xy}$  (reduction in  $\frac{k_z}{k_{xy}}$ ), can cause vertical radial flow regime to be less

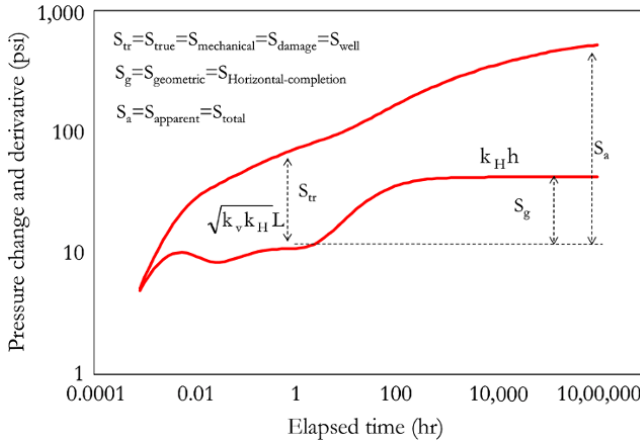


Figure 8.73 Typical well test behavior of a horizontal well with skin components.

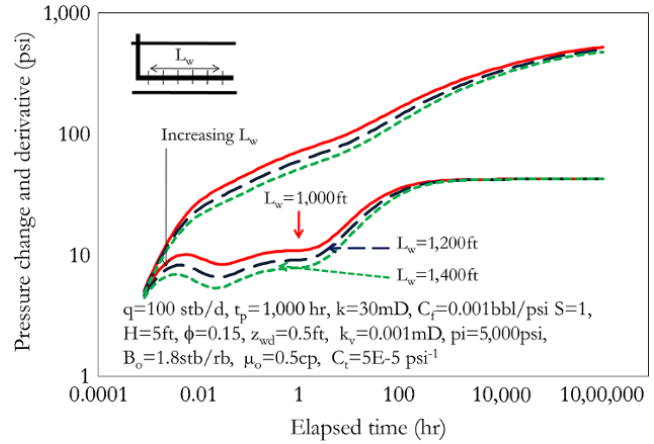


Figure 8.75 Effect of  $L_w$  on horizontal well test behavior.

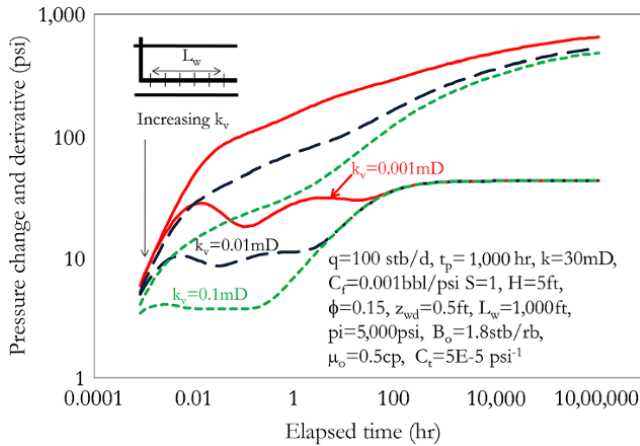


Figure 8.74 Effect of  $\frac{k_z}{k_r}$  on horizontal well test behavior.

accentuated. Also, in Fig. 8.75 reduction in  $L$  reduces the level of the first radial flow stabilization, which corresponds to vertical radial flow.

**8.5.1.11. Reservoir Model. Double Porosity Model**

Double porosity occurrence in reservoir characterization was discussed in Chapter 7 (7.3.2.2) and Section 8.4.4. The interpretation model for an *infinite acting double porosity* (IADP) reservoir with WBS and skin can be determined by replacing “s” with “sf(s)” in the fundamental solution for an *infinite acting radial homogeneous* (IARH) reservoir to obtain the fundamental solution for IADP, and then adding the effect of WBS to get the IADP with WBS and skin.

Starting with the fundamental solution for the IARH model:

$$\bar{p}_{wD}(s) = \frac{1}{s} \frac{K_0(r_D \sqrt{s})}{\sqrt{s} K_1(\sqrt{s})}$$

Replacing  $s$  with  $sf(s)$  in the fundamental solution for IARH (except the  $s$  in the  $\frac{1}{s}$  part of the equation) gives the fundamental solution for IADP:

$$\bar{p}_{wFD}(s) = \frac{1}{s} \frac{K_0(r_D \sqrt{sf(s)})}{\sqrt{sf(s)} K_1(\sqrt{sf(s)})} \quad (8.115)$$

Adding WBS and skin using equation (8.84):

$$\bar{p}_D(s, S, C_D) = \frac{s \bar{p}_{wFD}(s) + S}{s [1 + C_D s (s \bar{p}_{wFD}(s) + S)]}$$

$$\bar{p}_D(s, S, C_D) = \frac{s \frac{1}{s} \frac{K_0(r_D \sqrt{sf(s)})}{\sqrt{sf(s)} K_1(\sqrt{sf(s)})} + S}{s \left[ 1 + C_D s \left( s \frac{1}{s} \frac{K_0(r_D \sqrt{sf(s)})}{\sqrt{sf(s)} K_1(\sqrt{sf(s)})} + S \right) \right]}$$

$$\bar{p}_D(s, S, C_D) = \frac{\frac{K_0(r_D \sqrt{sf(s)})}{\sqrt{sf(s)} K_1(\sqrt{sf(s)})} + S}{s \left[ 1 + C_D s \left( \frac{K_0(r_D \sqrt{sf(s)})}{\sqrt{sf(s)} K_1(\sqrt{sf(s)})} + S \right) \right]}$$

[Bourdet et al., 1984]

(8.116)

where  $f(s)$  is defined for different matrices as shown in Fig. 8.76.

This approach of adding the double porosity effect to an interpretation model can be extended to other fundamental solutions, such as a horizontal well model in a homogeneous reservoir.



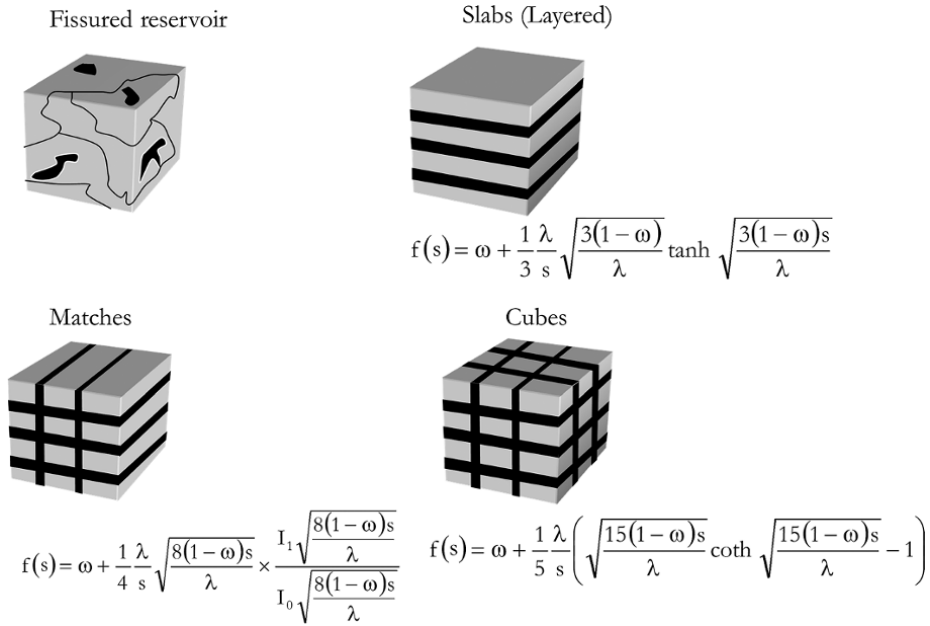


**Figure 8.76** Definition of  $f(s)$  for different matrix models [Adapted from Bourdet and Gringarten, 1980; Stewart, 2010].

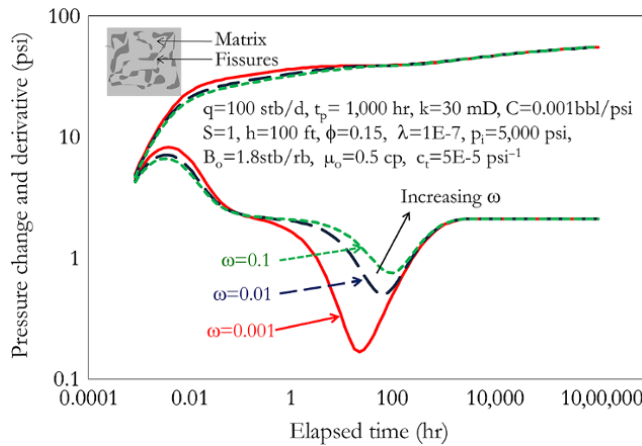


**Figure 8.77** Effect of increasing  $\omega$  characterized by decreasing derivative minimum.

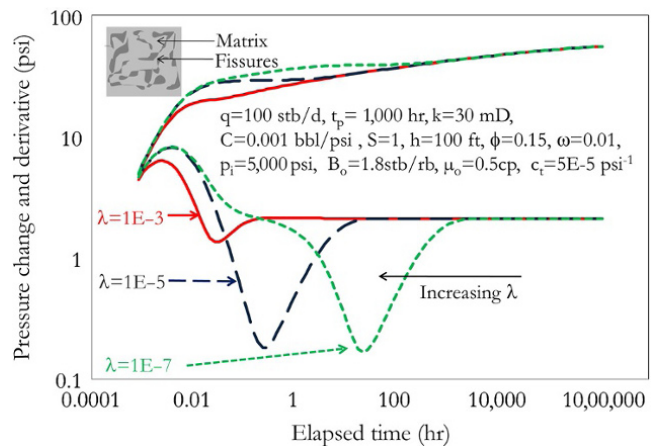


**Figure 8.78** Effect of decreasing  $\lambda$  characterized by increasing displacement of derivative minimum on  $\Delta t$  axis.

The minimum during transition in double porosity is a function of  $\omega$  (storativity ratio) and  $\lambda$  (interporosity flow coefficient). Fig. 8.77 shows that the effect of increasing  $\omega$  is characterized by a reduction in the minimum that characterizes double porosity behavior.

Fig. 8.78 shows that the effect of decreasing  $\lambda$  is characterized by increasing displacement of the minimum on the elapsed time axis.

The minimum in the double porosity model on the pressure change derivative plot can be expressed as [Bourdet, 2002]:

$$p'_D(t_D) = 0.5 \left( 1 + e^{\left( \frac{\lambda t_D}{\omega(1-\omega)} \right)} - e^{\left( \frac{\lambda t_D}{(1-\omega)} \right)} \right) \quad (8.117)$$

This equation provides a convenient way to determine initial regression values for the double porosity model using well test derivative plot.

*Radial Composite Reservoir Model*

A radial composite model describes a reservoir system with a radial change in  $\frac{kh}{\mu}$  and/or  $\phi c_t h$  (Fig. 8.79). This

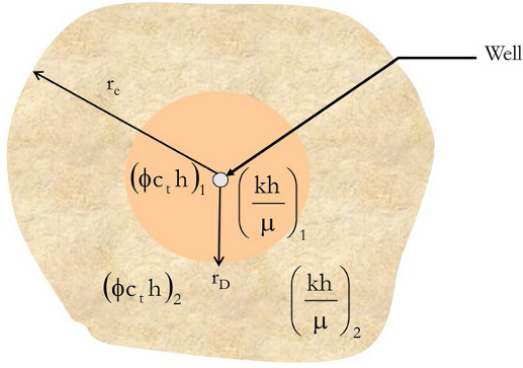


Figure 8.79 Schematic of a radial composite reservoir model.

can be due to a change in reservoir property such as permeability, porosity or reservoir thickness. This can also be due to a change in fluid properties. Common examples where a fluid property change creates a radial composite model include: *condensate banking* in gas condensate producing below the dew point pressure; *gas banking* in a volatile oil reservoir producing below the bubble point pressure; *water banking* after killing a well with water.

Pressure response in a radial composite reservoir can be expressed as [Satman *et al.*, 1980]:

$$\bar{p}_D(s_{D2}, r_D, \eta_{2/1}, \omega) = AI_0(\sqrt{s_{D2}\eta_{2/1}}) + BK_0(\sqrt{s_{D2}\eta_{2/1}}) \quad (8.118)$$

where

$$A = \frac{BB_1}{BB_2}; \quad BB_1 = C_1B_2C_3 - C_1C_2B_3; \quad BB_2 = A_1B_2C_3 - A_3B_1C_2 - A_1B_3C_2 - A_2B_1C_3$$

$$A_1 = \sqrt{s_{D2}\eta_{2/1}}I_1(\sqrt{s_{D2}\eta_{2/1}}); \quad B_1 = \sqrt{s_{D2}\eta_{2/1}}K_1(\sqrt{s_{D2}\eta_{2/1}}); \quad C_1 = \frac{1}{s_{D2}}$$

$$A_2 = I_0(r_{Dd}\sqrt{s_{D2}\eta_{2/1}}); \quad B_2 = K_0(r_{Dd}\sqrt{s_{D2}\eta_{2/1}}); \quad C_2 = -K_0(r_{Dd}\sqrt{s_{D2}});$$

$$A_3 = \sqrt{s_{D2}\eta_{2/1}}I_1(r_{Dd}\sqrt{s_{D2}\eta_{2/1}}); \quad B_3 = -\sqrt{s_{D2}\eta_{2/1}}K_1(r_{Dd}\sqrt{s_{D2}\eta_{2/1}}); \quad C_3 = \sigma\sqrt{s_{D2}}K_1(r_{Dd}\sqrt{s_{D2}});$$

$$C_3 = \omega\sqrt{s_{D2}}K_1(r_{Dd}\sqrt{s_{D2}})$$

and

$$B = \frac{C_1 - AA_1}{B_1}$$

$s_{D2}$  is the Laplace image space variable for dimensionless time  $t_{D2}$

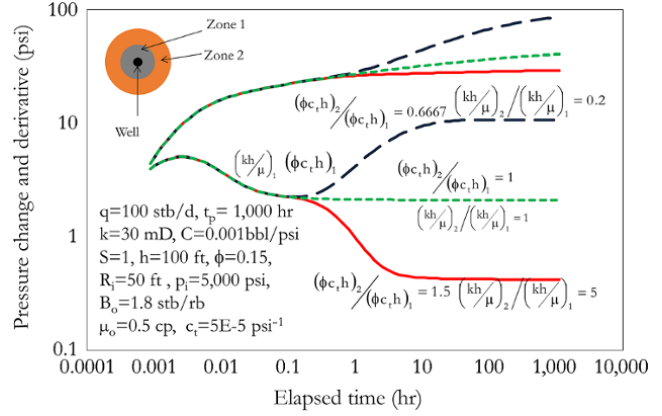


Figure 8.80 Effect of changing mobility ratio on reservoir well test behavior.

Hydraulic diffusivity is defined as:

$$\eta = \frac{k}{\phi\mu c_t}$$

$$\eta_{1/2} = \frac{\frac{k_2}{\phi_2\mu_2c_{t2}}}{\frac{k_1}{\phi_1\mu_1c_{t1}}} = \frac{M}{\omega}$$

where the mobility ratio is defined as:

$$M = \frac{\frac{k_2h_2}{\mu_2}}{\frac{k_1h_1}{\mu_1}}$$

Storativity (Capacity) ratio is defined as:

$$M = \frac{\phi_2c_{t2}h_2}{\phi_1c_{t1}h_1}$$

and the dimensionless radius of mobility discontinuity as:

$$r_{Dd} = \frac{r_d}{r_w}$$

where  $r_d$  is radius of mobility discontinuity.

Dimensionless parameters are defined as:

$$p_D = \frac{k_1h_1}{141.2qB\mu_1}\Delta p;$$

$$t_{D1} = \frac{0.000264k_1}{\phi_1\mu_1c_{t1}r_w^2}\Delta t; \quad \text{and} \quad t_{D2} = \frac{0.000264k_2}{\phi_2\mu_2c_{t2}r_w^2}\Delta t$$

Well test behavior showing the effect of changing mobility and storativity is shown in Fig. 8.80 and Fig. 8.81, respectively.

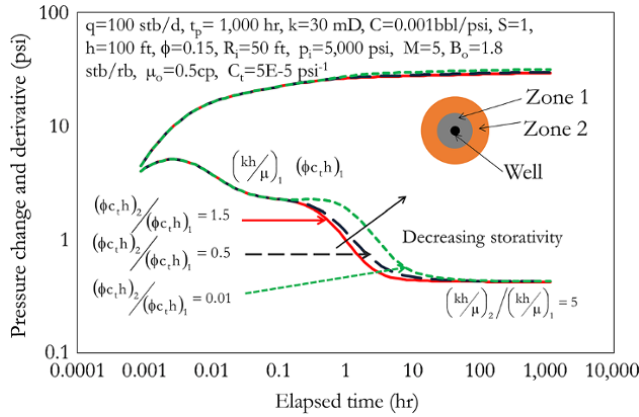


**Figure 8.81** Effect of changing storativity ratio on reservoir well test behavior.

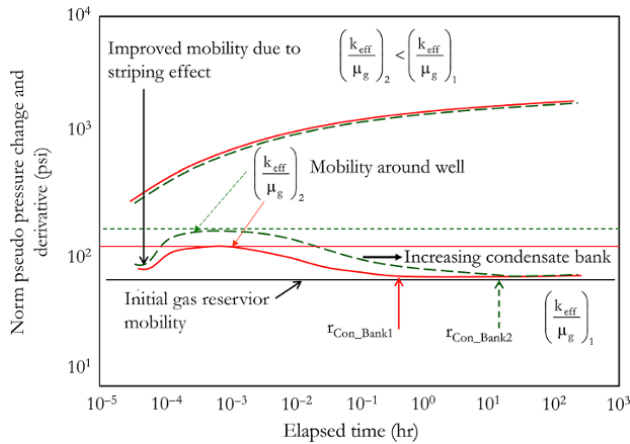


**Figure 8.82** Composite behavior of gas condensate reservoir below the dew point pressure.

*Well Test Analysis in Near Critical Fluids*

When bottomhole pressure falls below the saturation pressure in near critical fluids (gas condensate and volatile oil reservoirs) during testing or production, around the wellbore a *condensate bank* is created in gas condensate reservoirs and a *gas bank* is created in volatile oil reservoirs. The formation of two phases around the wellbore in near critical fluids can be described as a radial composite behavior with a two-phase zone (zone 1) near the wellbore and single-phase zone (zone 2) away from the wellbore. Zone 1 (two-phase region) and zone 2 (single-phase region) are characterized by different mobility and storativity. The log-log pressure derivative plot of the buildup in near critical fluid below the saturation pressure reflects the mobility distribution of the reservoir at the end of the preceding drawdown. Fig. 8.82 shows typical well test behavior in gas condensate below gas dew point pressure and Fig. 8.83 shows well test behavior in volatile oil reservoir below bubble point pressure.

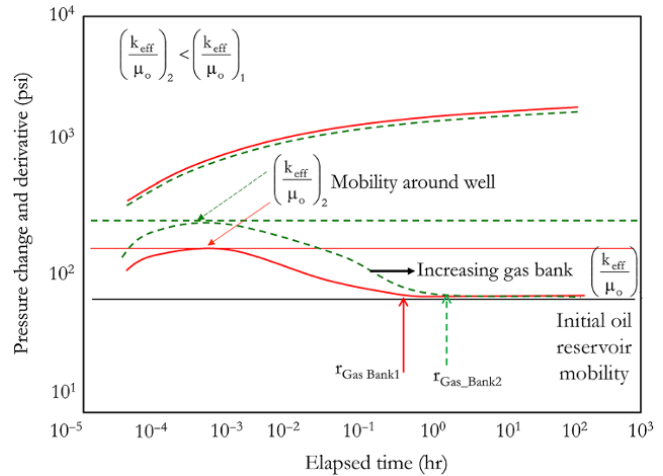


**Figure 8.83** Composite behavior of volatile oil reservoir below the bubble point.

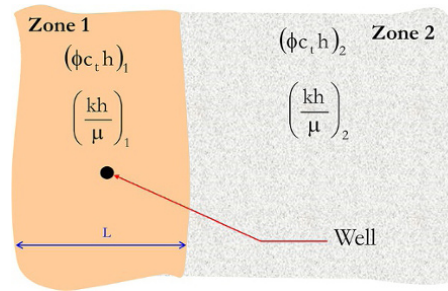


**Figure 8.84** Schematic of a linear composite reservoir model.

*Linear Composite Reservoir*

Composite change in a reservoir due to reservoir rock property is most likely to follow a linear pattern than radial. This change can be due to  $k$ ,  $\phi$ , and  $h$  away from the well.

A schematic of a linear composite reservoir model is shown in Fig. 8.84.

The first region is characterized by homogeneous behavior, after which a second homogeneous behavior follows when the diffusing pressure change reaches the linear interface between the first and second linear composite zones. When the linear composite model is compared with the radial composite model, the property of the first radial flow is that of the region before interface between linear composite zones, while the property of the second radial flow is that the arithmetic averaged properties between the first and the second zones, defined as *apparent mobility-thickness (apparent transmissibility)*.

Apparent mobility-thickness is expressed as:

$$\left(\frac{k_2 h_2}{\mu_2}\right)_{\text{apparent}} = 0.5 \left(\frac{k_1 h_1}{\mu_1} + \frac{k_2 h_2}{\mu_2}\right) = 0.5(1 + M_{2/1}) \left(\frac{k_1 h_1}{\mu_1}\right) \tag{8.119}$$

where  $M_{2/1}$  is the mobility ratio of zone 2 to zone 1 and is defined as:

$$M_{2/1} = \frac{\left(\frac{k_2 h_2}{\mu_2}\right)}{\left(\frac{k_1 h_1}{\mu_1}\right)}$$

where apparent mobility ratio becomes:

$$M_{\text{apparent}^2/1} = \frac{\left(\frac{k_2 h_2}{\mu_2}\right)_{\text{apparent}}}{\left(\frac{k_1 h_1}{\mu_1}\right)} = 0.5(1 + M_{2/1}) \quad (8.120)$$

$L$  is distance of mobility discontinuity:

$$L_D = \frac{L}{r_w}$$

*Multilayered Reservoirs*

Reservoirs may exist as layers of different facies. Deposition of rocks of different properties over geological time results in reservoirs having layers with different properties. Multilayered reservoirs can generally be categorized as *multilayered reservoirs with cross-flow* across layers (layers in hydraulic communication in the reservoir) or *multilayered reservoirs without cross-flow* (layers without hydraulic communication in the reservoir) with the contribution of all layers occurring only through commingled tubing production.

*Ehlig-Economides and Joseph* [1987] presented a rigorous pressure transient solution for multilayered reservoirs with  $n$  layers and  $N$  zones, with formation cross-flow between layers in the same zone (Fig. 8.85).

The solution of wellbore pressure of reservoir with  $n$  layers and  $N$  zones with cross-flow between layers can be expressed as:

$$\bar{p}_{wD} = \frac{1}{\left(C_D s^2 + \frac{1}{\bar{p}_{wD_{C_D=0}}}\right)} \quad (8.121)$$

where  $s$  is the Laplace space variable,  $C_D$  is dimensionless wellbore storage, and  $\bar{p}_{wD_{C_D=0}}$  is the wellbore pressure solution when  $C_D = 0$  expressed as:

$$\bar{p}_{wD_{C_D=0}} = \sum_{k_i=1}^{m_i} A_1^{k_i} \alpha_1^{k_i} \{K_0(\sigma_{k_i}) + b^{k_i} I_0(\sigma_{k_i}) + S_1 \sigma_{k_i} [K_1(\sigma_{k_i}) - b^{k_i} I_1(\sigma_{k_i})]\} \quad (8.122)$$

$A_1^{k_i}$  is the coefficient for the first layer and the  $k$ th root in zone  $i$  is determined numerically from  $n$  equations defined by equations (8.123)–(8.125).

$$\sum_{k_i=1}^{m_i} A_1^{k_i} \left( \alpha_{j-1}^{k_i} \{K_0(\sigma_{k_{i-1}}) + b^{k_i} I_0(\sigma_{k_{i-1}}) + S_{j-1} \sigma_{k_{i-1}} [K_1(\sigma_{k_{i-1}}) - b^{k_i} I_1(\sigma_{k_{i-1}})]\} - \alpha_j^{k_i} \{K_0(\sigma_{k_i}) + b^{k_i} I_0(\sigma_{k_i}) + S_j \sigma_{k_i} [K_1(\sigma_{k_i}) - b^{k_i} I_1(\sigma_{k_i})]\} \right) = 0 \quad (8.123)$$

$$\sum_{k_{i-1}=1}^{m_{i-1}} A_1^{k_{i-1}} \alpha_{j-1}^{k_{i-1}} \{K_0(\sigma_{k_{i-1}}) + b^{k_{i-1}} I_0(\sigma_{k_{i-1}}) + S_{j-1} \sigma_{k_{i-1}} [K_1(\sigma_{k_{i-1}}) - b^{k_{i-1}} I_1(\sigma_{k_{i-1}})]\} - \sum_{k_i=1}^{m_i} A_1^{k_i} \alpha_j^{k_i} \{K_0(\sigma_{k_i}) + b^{k_i} I_0(\sigma_{k_i}) + S_j \sigma_{k_i} [K_1(\sigma_{k_i}) - b^{k_i} I_1(\sigma_{k_i})]\} = 0 \quad (8.124)$$

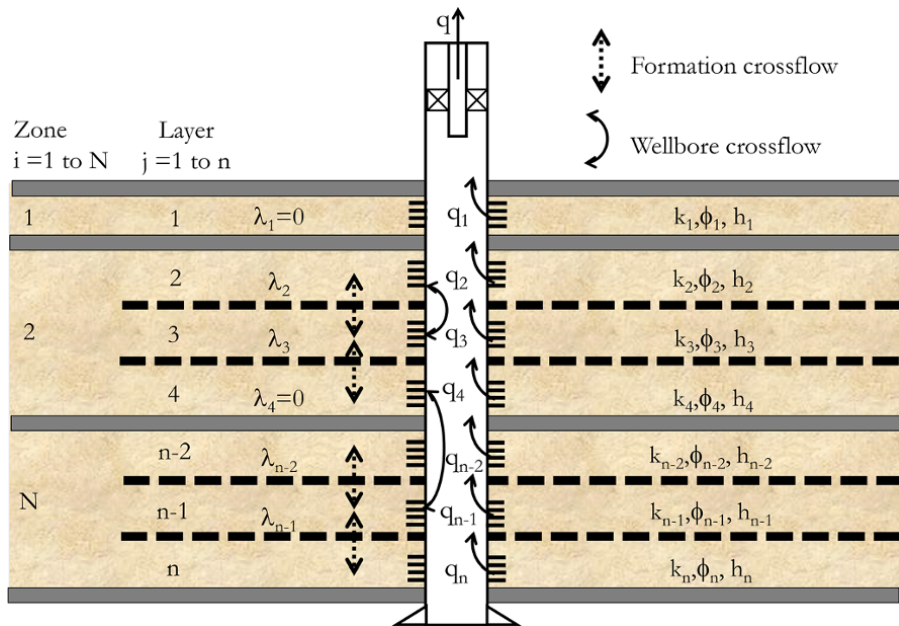


Figure 8.85 Multilayered reservoir with formation cross-flow between layers in the same zone.

$$\sum_{j=1}^n k_j \sum_{k_i=1}^{m_i} A_1^{k_i} \alpha_j^{k_i} \sigma_{k_i} [K_1(\sigma_{k_i}) - b^{k_i} I_1(\sigma_{k_i})] = \frac{1}{S} \quad (8.125)$$

where  $b^{k_i}$  for different outer boundary conditions is defined as:

$$\begin{aligned} b^{k_i} &= 0 && \text{for infinity outer boundary condition} \\ b^{k_i} &= \frac{K_1(\sigma_{k_i} r_{eD})}{I_1(\sigma_{k_i} r_{eD})} && \text{for no-flow outer boundary condition} \\ b^{k_i} &= -\frac{K_0(\sigma_{k_i} r_{eD})}{I_0(\sigma_{k_i} r_{eD})} && \text{for constant pressure outer boundary condition} \end{aligned}$$

$S_j$  is the wellbore skin for layer  $j$ .

$\alpha_j^{k_i}$  is coefficient of  $A_1^{k_i}$  for layer  $j$ , root  $k$  in zone  $i$  in equation (8.126):

$$\bar{p}_{jD} = \sum_{k_i=1}^{m_i} A_j^{k_i} [K_0(\sigma_{k_i} r_{jD}) + b^{k_i} I_0(\sigma_{k_i} r_{jD})] \quad (8.126)$$

Expressing  $A_j^{k_i}$  in equation (8.126) in terms of  $A_1^{k_i}$

$$\begin{aligned} A_2^k &= -\frac{a_{11}}{a_{12}} A_1^k = \alpha_2^k A_1^k \\ A_3^k &= -\frac{1}{a_{23}} (a_{21} A_1^k + a_{22} A_2^k) = \alpha_3^k A_1^k \\ A_n^k &= -\frac{1}{a_{n-1,n}} (a_{n-1,n-2} A_{n-2}^k + a_{n-1,n-1} A_{n-1}^k) = \alpha_n^k A_1^k \end{aligned}$$

Equation (8.126) becomes:

$$\bar{p}_{jD} = \sum_{k_i=1}^{m_i} A_1^{k_i} \alpha_j^{k_i} [K_0(\sigma_{k_i} r_{jD}) + b^{k_i} I_0(\sigma_{k_i} r_{jD})]$$

$\sigma_{k_i}$  is the  $k$ th root in zone  $i$  of the polynomial:

$$\gamma_j = a_{jj} \gamma_{j-1} - (a_{j-1,j})^2 \gamma_{j-2}$$

for  $j = 2 \dots n$  with  $\gamma_0 = 1$  and  $\gamma_1 = a_{11}$ , where

$$a_{jk} = \left\{ \begin{array}{ll} \lambda_{j-1}, & \text{for } k = j-1; j > 1, \\ \kappa_j \sigma^2 - \omega_j s - \lambda_{j-1} - \lambda_j, & \text{for } k = j, \\ \lambda_j, & \text{for } k = j+1; j < n \\ 0, & \text{for } k \neq j-1, j, \text{ or } j+1 \end{array} \right\}$$

Dimensionless variables in consistent units are defined as:

$$p_{jD}(r_{jD}, t_{jD}) = \frac{2\pi(kh)_t}{q_t \mu} (p_i - p_j)$$

$$q_{jD}(t_{jD}) = \frac{q_j}{q} = -\kappa_j \frac{\partial p_{jD}}{\partial r_{jD}}$$

$$t_{jD} = \frac{(kh)_t \Delta t}{(\phi h)_t \mu c_t r_w^2}$$

$$r_{jD} = \frac{r}{r_w}$$

$$r_{eD} = \frac{r_e}{r_w}$$

$$C_D = \frac{C}{2\pi(\phi h)_t c_t r_w^2}$$

$$(kh)_t = \sum_{j=1}^n (kh)_j$$

$$(\phi h)_t = \sum_{j=1}^n (\phi h)_j$$

$$\kappa_j = \frac{(kh)_j}{(kh)_t}$$

$$\omega_j = \frac{(\phi h)_j}{(\phi h)_t}$$

$$\lambda_j = \frac{X_j r_w^2}{kh}$$

where  $X_j$ , the semi-permeability between layers  $j$  and  $j+1$ , is defined by:

$$X_j = \frac{2}{2 \left[ \frac{(\Delta h)_j}{(k_v)_j} \right] + \frac{h_{j+1}}{k_{zj+1}} + \frac{h_j}{k_{zj}}}$$

where :  $X_0 = X_n = 0$ ;  $(\Delta h)_j$  is the thickness of nonperforated zones between layers  $j$  and  $j+1$ ;  $(k_v)_j$  is vertical permeability of nonperforated zones between layers  $j$  and  $j+1$ ;  $k_{zj}$  is the vertical permeability of layer  $j$  nonperforated zones between layers  $j$  and  $j+1$  (if there is no perforated zone between layer  $j$  and  $j+1$ , then  $(\Delta h)_j$  is zero; if there is no formation cross-flow between layers  $j$  and  $j+1$ , then  $X_j = 0$ );  $A_j^{k_i}$  is the coefficient for  $j$ th layer,  $k$ th root in zone  $i$ ;  $m_i$  is number of layers in zone  $i$ ;  $p_i$  is reservoir pressure in layer  $i$ ;  $p_j$  is reservoir pressure in layer  $j$ ;  $p_j^i$  is reservoir pressure in layer  $j$  in zone  $i$ ;  $p_{jD}$  is dimensionless reservoir pressure in layer  $j$ ;  $q$  is surface production rate;  $q_i$  is total flow rate for zone  $i$ ;  $q_j$  is flow rate of layer  $j$ ; and  $q_{jD}$  is dimensionless flow rate of layer  $j$

The radial pressure distribution for each layer is expressed as:

$$\bar{p}_{jD} = (1 - C_D \bar{p}_{wD} S^2) \sum_{k_i=1}^{m_i} A_1^{k_i} \alpha_j^{k_i} [K_0(\sigma_{k_i} r_{jD}) + b^{k_i} I_0(\sigma_{k_i} r_{jD})] \quad (8.127)$$

and flow rate for each layer given as

$$\bar{q}_{jD} = (1 - C_D \bar{p}_{wD} S^2) k_j \sum_{k_i=1}^{m_i} A_1^{k_i} \alpha_j^{k_i} \sigma_{k_i} [K_1(\sigma_{k_i}) - b^{k_i} I_1(\sigma_{k_i})] \quad (8.128)$$

Early time behavior of a cross-flow reservoir system is identical to that of a system without formation cross-flow with commingled tubing production (equation (8.129)).

Solution of wellbore pressure for an n-layered reservoir without formation cross-flow between layers, with commingled tubing production (Fig. 8.86) can be expressed as:

$$\bar{p}_{wD} = \frac{1}{s \left[ C_{DS} + \sum_{j=1}^n \frac{\kappa_j \sigma_j K_1(\sigma_j)}{K_0(\sigma_j) + s_j \sigma_j K_1(\sigma_j)} \right]} \quad (8.129)$$

and flow rate for each layer expressed as:

$$\bar{q}_{jD} = -\kappa_j \frac{\partial \bar{p}_{jD}}{\partial r_{jD}} \Big|_{r_{jD}=1} = \frac{\kappa_j \sigma_j K_1(\sigma_j) \bar{p}_{wD}}{K_0(\sigma_j) + s_j \sigma_j K_1(\sigma_j)} \quad (8.130)$$

where

$$\sigma_j = \sqrt{\frac{\omega_j}{\kappa_j} s}$$

A multilayered reservoir system producing under a pseudosteady state (PSS) condition is described further in Chapter 9 (9.2.12.1 and 9.2.12.2).

The simplest form of layered reservoir system is a two-layered system (Fig. 8.87).

The simplest well test model that can be used to describe behavior of a two-layered reservoir with cross-flow is the *double permeability* well test model with instantaneous pseudosteady state vertical flow between layer 1 and 2, and horizontal fluid flow in each layer. The assumption of a double permeability system includes: both layers are at the same initial pressure and flow between layers

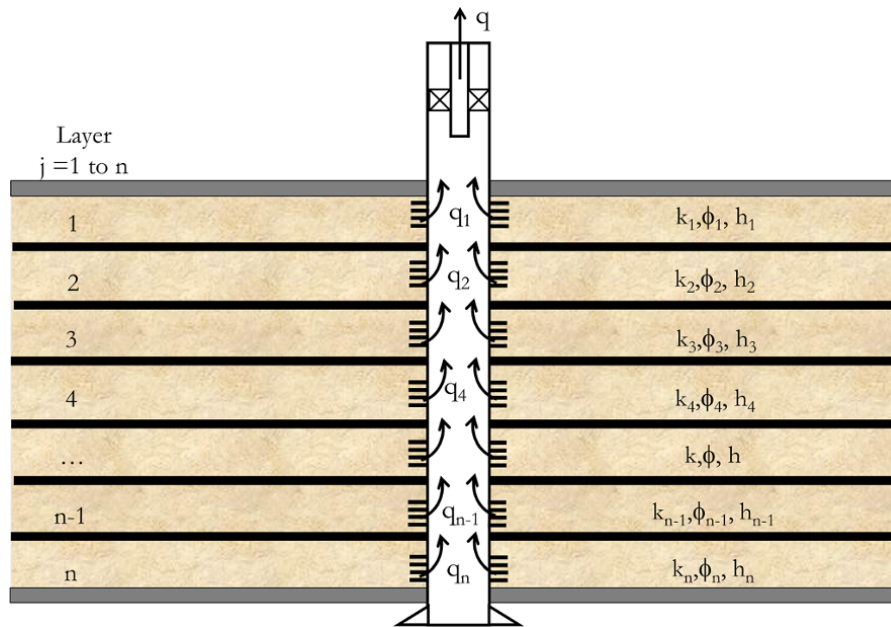


Figure 8.86 Multilayered reservoir without formation cross-flow with commingled tubing production.

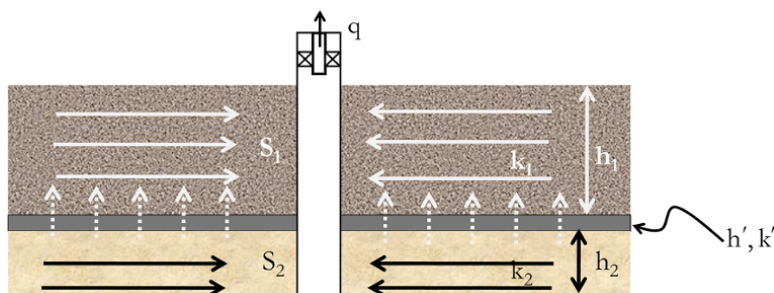


Figure 8.87 A two-layer reservoir model with  $k_1 > k_2$ .

is at pseudosteady state condition. For a double permeability well test model:

Total reservoir kh is defined as:  $kh = k_1h_1 + k_2h_2$

Total reservoir storativity is defined as:  $(\phi c_t h)_{Total} = (\phi c_t h)_1 + (\phi c_t h)_2$

kh contrast, which is similar to the mobility ratio in radial composite model, is defined as:  $\kappa = \frac{k_1h_1}{kh_{Total}} = \frac{k_1h_1}{k_1h_1 + k_2h_2}$

Storage contrast, which is similar to storativity ratio in a vradial composite model, is defined as:  $\omega = \frac{(\phi c_t h)_1}{(\phi c_t h)_{Total}} = \frac{(\phi c_t h)_1}{(\phi c_t h)_1 + (\phi c_t h)_2}$

Reservoir cross-flow, which is described by the *inter-layer cross-flow coefficient*, is defined as [Gao, 1984]:

$$\lambda = \frac{r_w^2}{k_1h_1 + k_2h_2} \frac{2}{2 \frac{h'}{k_z'} + \frac{h_1}{k_{z1}} + \frac{h_2}{k_{z2}}} \quad (8.131)$$

Fig. 8.88 shows the effect of  $\kappa$  on well test behavior in a double permeability model.

When  $k_1h_1 = k_2h_2$  then  $\kappa = \frac{1}{2} = 0.5$ , and model becomes a homogeneous reservoir model.

When  $k_1h_1 \gg k_2h_2$  then  $\kappa = \frac{k_1h_1}{k_1h_1} = 1$ , and model tends to double permeability reservoir model.

More than one reservoir layer *with cross-flows* can be described by typical behavior shown in Fig. 8.89, which shows the effect of increasing skin contrast between

layers. The final stabilization corresponds to  $\sum_{i=1}^n k_i h_i$ , where n is the number of layers.

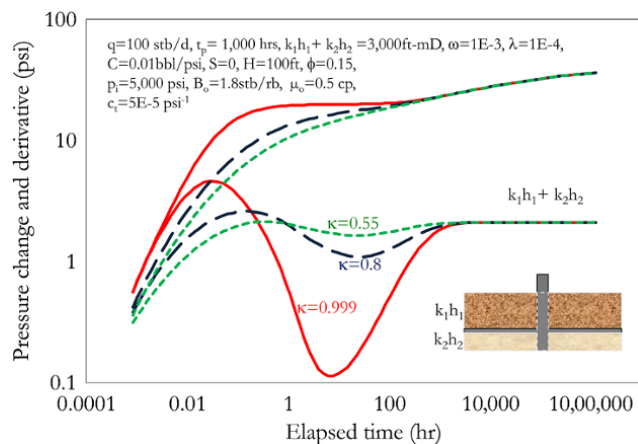


Figure 8.88 Effect of  $\kappa$  on double permeability reservoir model.

Where there is *no cross-flow* between layers, but layered reservoirs are produced through commingled tubing production, with no skin contrast between the well sections in different reservoir layers, final radial stabilization will correspond to  $\sum_{i=1}^n k_i h_i$ . With increasing skin contrast between layers, the most permeable layer will dominate the pressure response if the least permeable ( $k_2$ ) has the highest skin contrast.

Fig. 8.90 shows increasing skin contrast with most permeable having higher skin contrast compared to the least permeable. The least permeable, depending on overall deliverability, will dominate the pressure response. The extreme limit shows the most permeable layer ( $k_1$ ) closed (extremely high skin contrast) with the least permeable ( $k_2$ ) flowing.

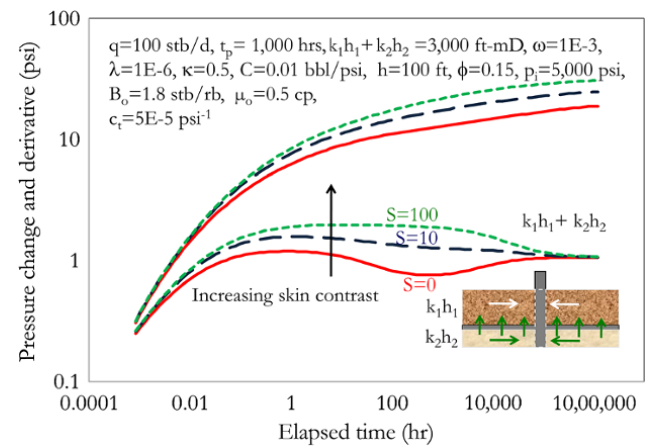


Figure 8.89 Effect of skin contrast in multilayered reservoir with cross-flow.

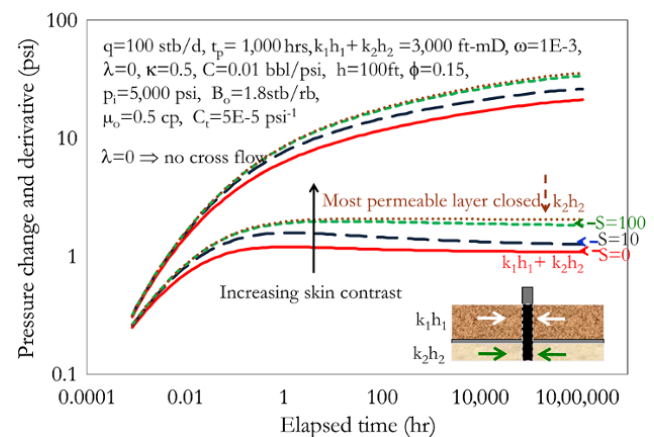


Figure 8.90 Effect of skin contrast in multilayered reservoir without cross-flow with commingled flow.

**8.5.1.12. Boundary Models. Concept of Image Wells**

When two identical wells are producing at the same rate and are separated by a distance 2d, at the midpoint (distance d) the net flux towards either well is zero. Hence, putting an impermeable fault at the midpoint (distance d) will not affect pressure diffusion and fluid flow. However, if wells are producing with equal but opposite production sign (one is a producer and the other is injection), then the pressure drop at the midpoint will be zero; hence, pressure is constant.

The concept of defining reservoir boundaries with image wells is valid as the diffusivity equation satisfies superposition in space. The concept of image wells will be used in conjunction with superposition in time to account for test periods with different flow rates.

Generally, the dimensionless pressure response for an active well with boundaries can be defined as:

$$p_{wD} = p_{wD\_active} + p_{wD\_image} \tag{8.132}$$

where  $p_{wD\_active}$  describes the dimensionless pressure response of a well in an infinite acting reservoir and  $p_{wD\_image}$  describes the dimensionless pressure response of the boundary effect using an appropriate number of image wells.

Also, equation (8.132) can be expressed in the Laplace domain as:

$$\bar{p}_{wD} = \bar{p}_{wD\_active} + \bar{p}_{wD\_image} \tag{8.133}$$

**Single Linear Boundary**

A single linear sealing fault (no-flow boundary) is modelled with two wells of equal rate producing at a distance of 2d apart while a single linear constant pressure boundary is modelled as an injection well with the same magnitude as a producing well placed at a distance of 2d apart, as shown in Fig. 8.91.

For a single linear boundary (sealing or constant boundary),  $p_{wD\_image}$  can be defined as:

$$p_{wD\_image} = \frac{1}{2} \sum_{i=1}^n E_i \left( \frac{(2d_d)^2}{4t_D} \right) \tag{8.134}$$

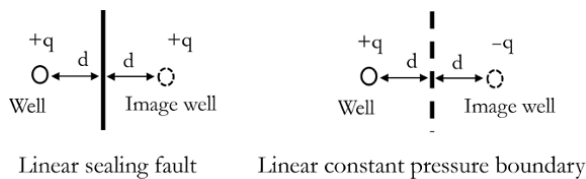


**Figure 8.91** Single linear sealing and constant pressure boundaries.

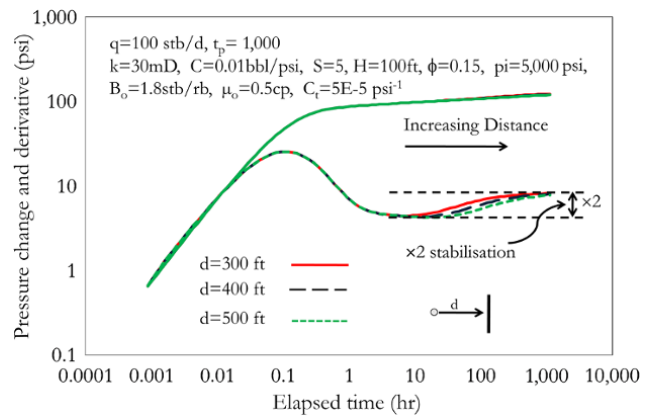
where  $d_D = \frac{d}{r_w}$ .

Fig. 8.92 shows the simulated well test behavior for a radial homogeneous reservoir with a single linear sealing fault. The simulation shows deviation from the radial flow occurring earlier when the fault is closer to well. The final stabilization on the derivative corresponding to single linear sealing fault is double (twice) that of reservoir radial flow stabilization (Fig. 8.92).

A constant pressure boundary is characterized by a derivative tending to zero, as shown in Fig. 8.93. As the constant boundary becomes closer, the deviation from reservoir radial flow manifests sooner.

**Wedge Boundary**

The wedge boundary is characterized by angle  $\theta$  subtended by boundaries that can be mixture of sealing and constant pressure. For a sealing (no-flow) wedge boundary, the level of final stabilization corresponding to the boundary effect is  $\frac{2\pi}{\theta}$  for angle in radians and  $\frac{360}{\theta}$  for angle in degrees.



**Figure 8.92** Effect of single sealing fault distance on well test behavior.

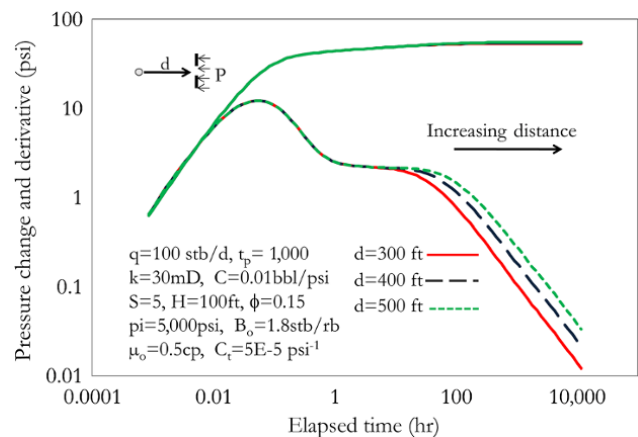


**Figure 8.93** Effect of constant pressure boundary distance on well test behavior.



Considering a well in a reservoir having a wedge boundary configuration with an angle of  $\theta$  and perpendicular distance to the boundary of  $d$ , as shown in Fig. 8.94, the active and image well configuration for such a wedge boundary can be described by Fig. 8.95.

$n$  represents the number of image wells; it is defined by  $n = \left(\frac{360}{\theta} - 1\right)$

From Fig. 8.95, image 1 has distance of  $2d$  from an active well.

The distance from an active well to image well 2 based on Fig. 8.96, using the cosine rule for a triangle, can be shown to be:

$$\begin{aligned} (d_{img\_2})^2 &= L^2 + L^2 - 2LL\cos\theta \\ (d_{img\_2})^2 &= 2L^2 - 2L^2\cos\theta \\ (d_{img\_2})^2 &= 2L^2(1 - \cos\theta) \end{aligned} \tag{8.135}$$

Also from Fig. 8.96,  $L = \frac{d}{\sin\left(\frac{\theta}{2}\right)}$

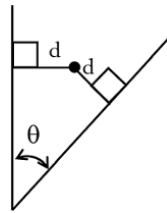


Figure 8.94 Wedge boundary.

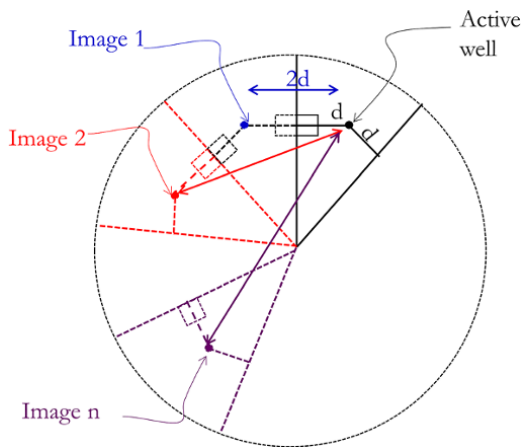


Figure 8.95 Image well pattern for a wedge boundary.

Substituting  $L$  defined above into equation (8.135):

$$(d_{img\_2})^2 = 2 \left( \frac{d}{\sin\left(\frac{\theta}{2}\right)} \right)^2 (1 - \cos 2\theta)$$

The distance from an active well to image well 3 can be shown to be:

$$(d_{img\_3})^2 = 2 \left( \frac{d}{\sin\left(\frac{\theta}{2}\right)} \right)^2 (1 - \cos(3\theta))$$

And for image well  $n$ :

$$\begin{aligned} (d_{img\_n})^2 &= 2 \left( \frac{d}{\sin\left(\frac{\theta}{2}\right)} \right)^2 (1 - \cos(n\theta)) \\ (d_{img\_n})^2 &= 4d^2 \times \frac{2}{4} \left( \frac{1}{\sin\left(\frac{\theta}{2}\right)} \right)^2 (1 - \cos(n\theta)) \end{aligned}$$

Therefore, the distance from an active well to any image well,  $i$ , in a wedge boundary can be defined as:

$$(d_{img\_i})^2 = 4d^2 \times \frac{1}{2} \left( \frac{1}{\sin\left(\frac{\theta}{2}\right)} \right)^2 (1 - \cos(i\theta))$$

This can be further represented as:

$$(d_{img\_i})^2 = 4d^2 a_i \tag{8.136}$$

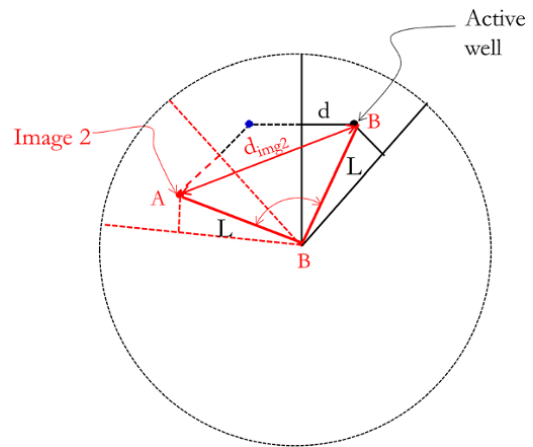


Figure 8.96 Distance of image well number 2 ( $d_{img\_2}$ ) from an active well.

And in dimensionless form as:

$$(d_{img-i})_D^2 = 4d_D^2 a_i \tag{8.137}$$

where

$$a_i = \frac{1}{2} \times \left( \frac{1}{\sin\left(\frac{\theta}{2}\right)} \right)^2 (1 - \cos(i\theta))$$

$$i = 1 \text{ to } \left( \frac{360}{\theta} - 1 \right)$$

Hence,  $p_{wD\_image}$  for a well in a reservoir with a wedge boundary system can be expressed as:

$$p_{wD\_image} = \frac{1}{2} \sum_{i=1}^n E_i \left( a_i \frac{(2d_D)^2}{4t_D} \right)$$

$$p_{wD\_image} = \frac{1}{2} \sum_{i=1}^n E_i \left( a_i \frac{d_D^2}{t_D} \right) \tag{8.138}$$

where  $n$  is the number of images,  $a_i$  is defined in Table 8.14,  $t_D = \frac{0.000264k}{\phi\mu c_t r_w^2} \Delta t$ ,  $d_D = \frac{d}{r_w}$  and  $n = \frac{360}{\theta} - 1$ .

The effect of the sealing wedge angle on well test behavior is shown in Fig. 8.97.

*Semipermeable (Leaky) Fault*

Faults may be nonsealing (leaky) or noncontinuous, as such a fault is permeable to flow (Fig. 8.98). A leaky fault can be described by the pressure equation shown in equation (8.139).

Analytical solution of partially communicating/semi-permeable/leaky fault is expressed as [Yaxley, 1987]:

$$p_D = -\frac{1}{2} E_i \left( -\frac{1}{4t_D} \right) - \frac{1}{2} E_i \left( -\frac{1}{4t_{DL}} \right)$$

$$- \sqrt{\pi\alpha} \int_0^{t_{DL}} \exp(4\alpha^2 u + 4\alpha) \operatorname{erfc} \left( 2\alpha\sqrt{u} - \frac{1}{\sqrt{u}} \right) \frac{du}{\sqrt{u}}$$

(8.139)

where the dimensionless specific transmissibility is defined as:

$$\alpha = \frac{k_f \bar{h}}{k h} \frac{w_f \mu}{L \mu}$$

Dimensionless parameters in EOF units are:

$$t_D = \frac{0.000264k}{\phi\mu c_t r_w^2} \Delta t$$

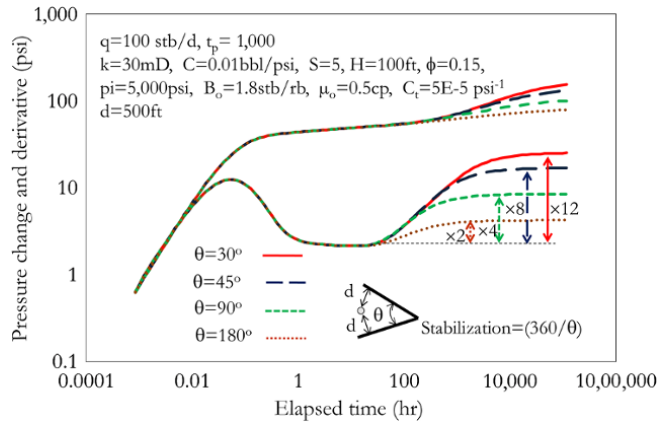


Figure 8.97 Effect of sealing wedge angle on well test behavior.

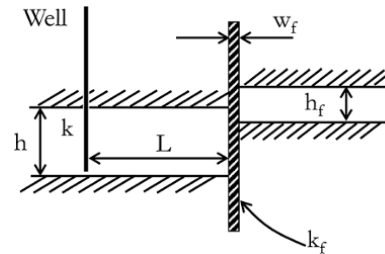


Figure 8.98 Parameters describing a leaky fault.

Table 8.14 Values of  $a_i$  for Different Angles.

$\theta =$	180	120	90	72	60	45	30	
$n = \left( \frac{360}{\theta} - 1 \right) =$	1	2	3	4	5	7	11	
$i$	$a_i$	$a(i,1)$	$a(i,2)$	$a(i,3)$	$a(i,4)$	$a(i,5)$	$a(i,7)$	$a(i,11)$
1	$a(1,n)$	2	2	2	2	2	2	2
2	$a(2,n)$		2	4	5.2361	6	6.8284	7.4641
3	$a(3,n)$			2	5.2361	8	11.6569	14.9282
4	$a(4,n)$				2	6	13.6569	22.3923
5	$a(5,n)$					2	11.6569	27.8564
6	$a(6,n)$						6.8284	29.8564
7	$a(7,n)$						2	27.8564
8	$a(8,n)$						0	22.3923
9	$a(9,n)$							14.9282
10	$a(10,n)$							7.4641
11	$a(11,n)$							2

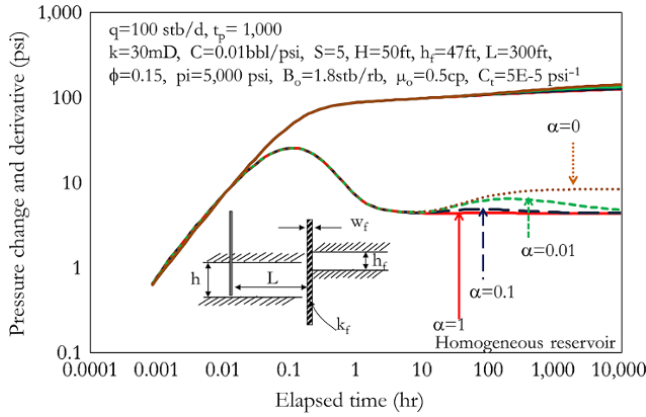


Figure 8.99 Effect of a leaky fault  $\alpha$  on well test behavior.

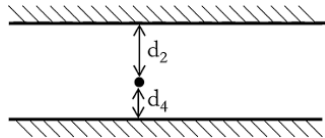


Figure 8.100 Parallel sealing faults.

$$t_{DL} = \frac{0.000264k}{\phi\mu c_i r L^2} \Delta t$$

and  $\bar{h}$  is defined as:

$$\bar{h} = \frac{h + h_f}{2}$$

The effect of a leaky fault on well test behavior is shown in Fig. 8.99.

*Parallel Sealing Faults (Channel Boundary)*

A well in a reservoir with parallel sealing faults (Fig. 8.100) will have active-image well configuration as shown in Fig. 8.101.

Distances of image wells away from an active well, based on Fig. 8.101, can be defined as:

$$\begin{aligned} y_1 &= 2d_4 \\ y_2 &= 2d_2 \\ y_3 &= 2d_4 + 2d_2 \\ y_4 &= 2d_2 + 2d_4 \\ y_5 &= 2d_4 + 2d_2 + 2d_4 \\ y_6 &= 2d_2 + 2d_4 + 2d_2 \\ y_7 &= 2d_4 + 2d_2 + 2d_4 + 2d_2 \\ y_8 &= 2d_2 + 2d_4 + 2d_2 + 2d_4 \\ &\vdots \\ &\infty \end{aligned} \tag{8.140}$$

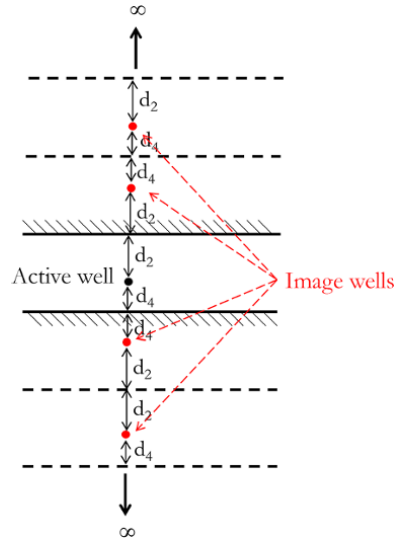


Figure 8.101 Image well pattern for a well with parallel sealing faults.

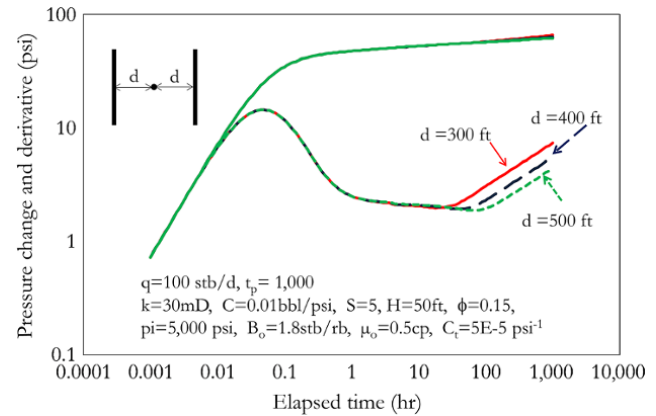


Figure 8.102 Effect of parallel sealing fault distance on well test behavior.

Hence,  $p_{wD\_image}$  is defined as:

$$p_{wD\_image} = \frac{1}{2} \sum_{j=1}^{\infty} E_i \left( \frac{(y_{Dj})^2}{4t_D} \right) \tag{8.141}$$

where:  $t_D = \frac{0.000264k}{\phi\mu c_i r_w^2} \Delta t$ ,  $y_{Di} = \frac{y_i}{r_w}$ , and  $p_D = \frac{kh}{141.2qB\mu} \Delta p$  as defined in equation (8.66)

The effect of parallel sealing fault distance on well test behavior is illustrated by the test simulation shown in Fig. 8.102.

*Open Rectangular Boundary*

A well in a reservoir with an open rectangular boundary with sealing faults (Fig. 8.103), will have an active-image well configuration as shown in Fig. 8.104.

Hence, the dimensionless pressure response for image wells that defines an open rectangular boundary based with sealing faults in Fig. 8.104 is:

$$P_{wD\_image} = \frac{1}{2} \left[ \sum_{j=1}^{\infty} E_i \left( \frac{(y_{Dj})^2}{4t_D} \right) + \sum_{j=1}^{\infty} E_i \left( \frac{(y_{Dj})^2 + (2d_{1D})^2}{4t_D} \right) + E_i \left( \frac{(d_{1D})^2}{t_D} \right) \right] \quad (8.142)$$

where  $y_i$  is defined in equation (8.140) and  $y_{Di} = \frac{y_i}{r_w}$ .

*Rectangular Boundary*

For a closed rectangular boundary system with sealing faults (Fig. 8.105), the image well pattern is described in Fig. 8.106.

From above, the dimensionless pressure response for image wells that defines a closed rectangular boundary with sealing faults is:

$$P_{wD\_image} = \frac{1}{2} \left[ \sum_{i=2}^{\infty} E_i \left( \frac{(x_{Di})^2}{4t_D} \right) + 4 \sum_{j=1}^{\infty} \sum_{i=1}^{\infty} E_i \left( \frac{(y_{Dj})^2 + (x_{Di})^2}{4t_D} \right) \right] \quad (8.143)$$

where  $y_i$  is defined in equation (8.140) and  $y_{Di} = \frac{y_i}{r_w}$ ;  $x_i$  is defined as:

$$\begin{aligned} x_1 &= 0 \\ x_2 &= 2d_1 \\ x_3 &= 2d_3 \\ x_4 &= 2d_1 + 2d_3 \\ x_5 &= 2d_3 + 2d_1 \\ x_6 &= 2d_1 + 2d_3 + 2d_1 \\ x_7 &= 2d_3 + 2d_1 + 2d_3 \\ x_8 &= 2d_1 + 2d_3 + 2d_1 + 2d_3 \\ x_9 &= 2d_3 + 2d_1 + 2d_3 + 2d_1 \\ &\vdots \\ &\infty \end{aligned} \quad (8.144)$$

and  $x_{Di}$  is defined as:

$$x_{Di} = \frac{x_i}{r_w}$$

Larsen [1985], using combination of four-well rectangles, as shown in Fig. 8.107, presented an approach for adding mixed no-flow and constant pressure boundaries to well test interpretation models.

Dimensionless wellbore pressure drop due to a rectangular drainage area of mixed no-flow and constant pressure outer boundaries can be expressed as:

$$P_{wD\_bound} = \frac{1}{2} \sum_{i=1}^{\infty} \alpha E_i \left( \frac{x_i^2 + y_i^2}{4A t_{DA}} \right) \quad (8.145)$$

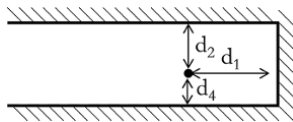


Figure 8.103 Open rectangular boundary with sealing faults.

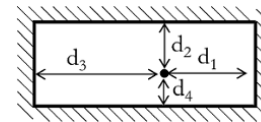


Figure 8.105 Closed rectangular boundary with sealing faults.

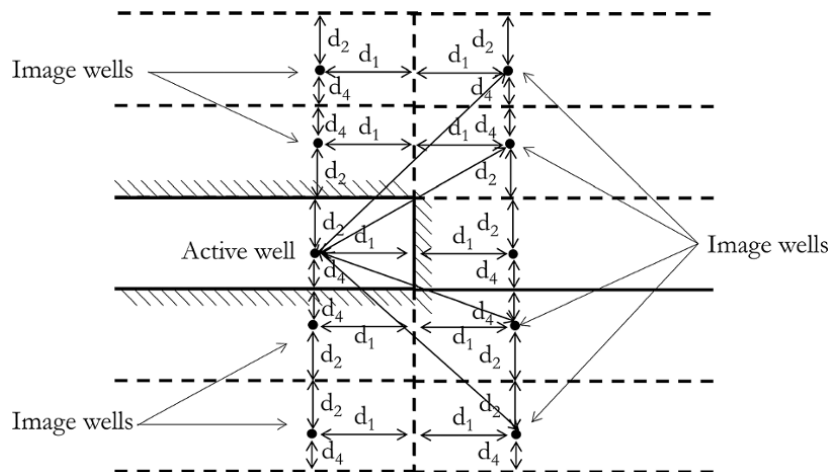


Figure 8.104 Image well pattern for an open rectangular boundary with sealing faults.

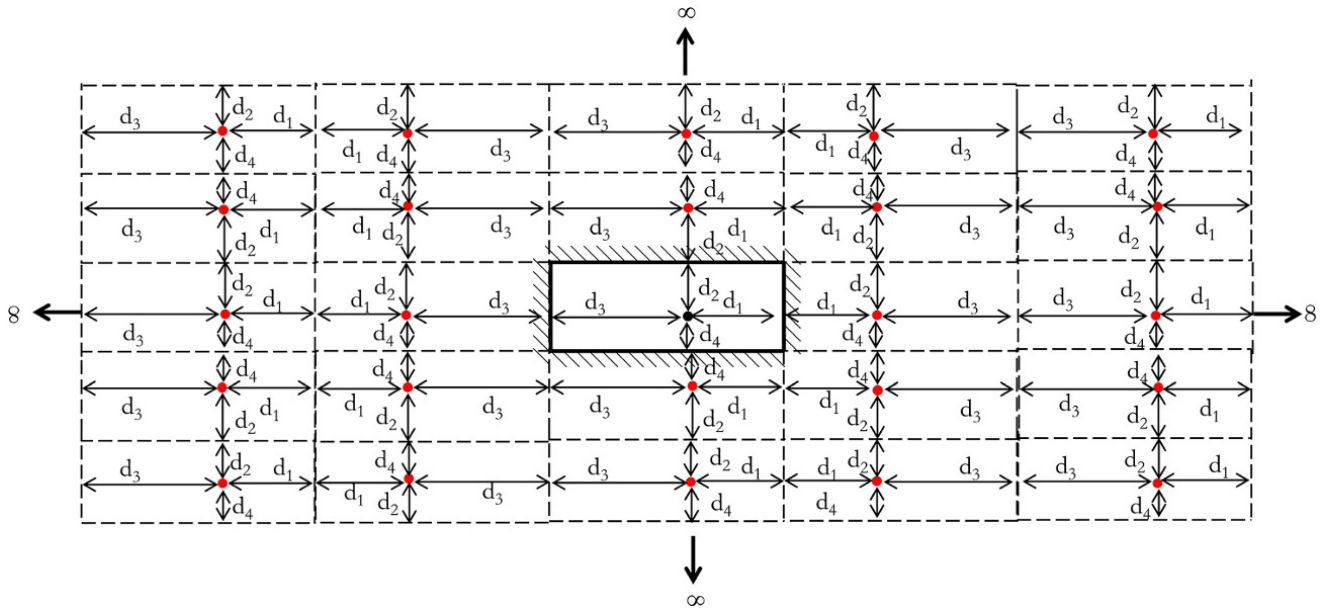


Figure 8.106 Image well pattern for a closed rectangular boundary with sealing faults.

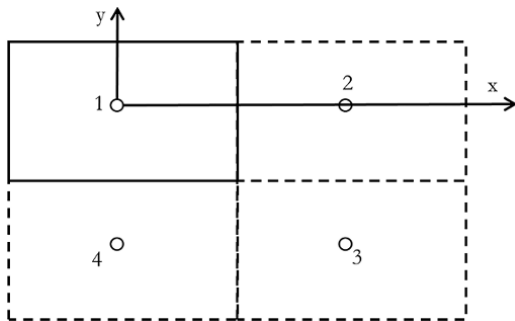


Figure 8.107 Four-well rectangular drainage pattern.

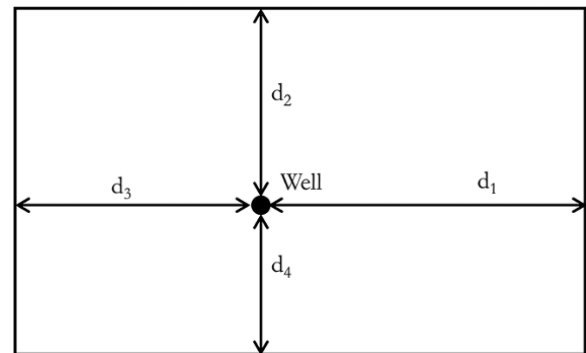


Figure 8.108 Single well in a rectangular boundary.

where  $\alpha = -1$  for an injecting well and  $+1$  for a producing well;  $x_i, y_i$  is the location of the  $i$ th image well for  $i \geq 2$  with well 1 having  $x = 0$  and  $y = 0$ .

The number of columns of four-well rectangles on each side of the  $x$  direction ( $n_c$ ) and number of rows on each side in the  $y$  direction ( $n_r$ ) required to determine the appropriate pressure distribution can be calculated using equations (8.146) and (8.147), respectively.

$$n_c = \text{int} \left( 1 + 4\sqrt{Ft_{DA}} \right) \quad (8.146)$$

$$n_r = \text{int} \left( 1 + 4\sqrt{\frac{t_{DA}}{F}} \right) \quad (8.147)$$

For the single well in a rectangular boundary shown in Fig. 8.108:

$$F = \frac{d_2 + d_4}{d_1 + d_3}$$

$$b = \frac{d_4}{d_2 + d_4}$$

$$a = \frac{d_1}{d_1 + d_3}$$

$$t_{DA} = \frac{0.000264 \text{ kt}}{\phi\mu c_t A} \text{ in EOF units}$$

where  $t_{DA}$  is dimensionless time based on the drainage area and  $A$  is the drainage area defined as:  $A = (d_1 + d_3)(d_2 + d_4)$

The  $x, y$  coordinate of well 1 in the four-well rectangle in the  $j$ th column and  $k$ th row are:

$$x = \frac{-2(n_c + 1 - j)}{\sqrt{F}} \quad (8.148)$$

$$y = \frac{-2(n_r + 1 - k)}{\sqrt{F}} \quad (8.149)$$

where  $j = 1 \dots 2n_c + 1$  and  $k = 1 \dots 2n_r + 1$ .

**Table 8.15** Rectangular Drainage with Mixed No-flow and Constant Pressure Outer Boundaries.





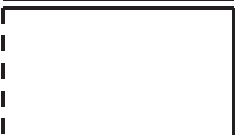
Boundary Types	Well	Well type	$n_c$ and $n_r$ condition
	2 and 4	injector	—
	1 and 3	producer	—
	1 and 3	producer	$n_c+1 - j$ is even
	2 and 4	injector	$n_c+1 - j$ is even
	1 and 3	injector	$n_c+1 - j$ is odd
	2 and 4	producer	$n_c+1 - j$ is odd
	1 and 4	producer	—
	2 and 3	injector	—
	1,2,3 and 4	producer	$(n_c+1 - j)+(n_r+1 - k)$ is even
	1,2,3 and 4	injector	$(n_c+1 - j)+(n_r+1 - k)$ is odd
	1,2,3 and 4	producer	$n_c+1 - j$ is even
	1,2,3 and 4	injector	$n_c+1 - j$ is odd

Table 8.15 shows the characteristics of the four-well rectangles for different boundary conditions; continuous lines indicate a no-flow boundary and dashed lines indicate a constant pressure boundary.

A closed system shows a different well test behavior for drawdown and buildup tests. The buildup well test diagnostic log-log plot is similar to that for a constant pressure boundary while that for drawdown is characterized by a slope of one at late times.

A very good way to differentiate a constant pressure boundary and closed boundary system is to examine drawdown and buildup well test behavior. In a constant pressure boundary system, both buildup and drawdown derivatives will tend to zero on the log-log derivative plot, while in a closed boundary system the drawdown will display increasing derivative with a slope of one or tending to one and buildup will have a log-log pressure change derivative tending to zero.

Well test behavior for drawdown and buildup tests in a closed boundary reservoir (with sealing faults) is shown for a simulated test in Fig. 8.109.

**Exercise 8.4** Complete Well Test Workflow for an Oil Producing Well

A 30-ft net pay oil bearing, clean sandstone with porosity of 0.3 and  $c_t$  of  $5 \times 10^{-5} \text{ psi}^{-1}$  was tested using surface rate control. Well test data are shown in Table 8.16. Separator

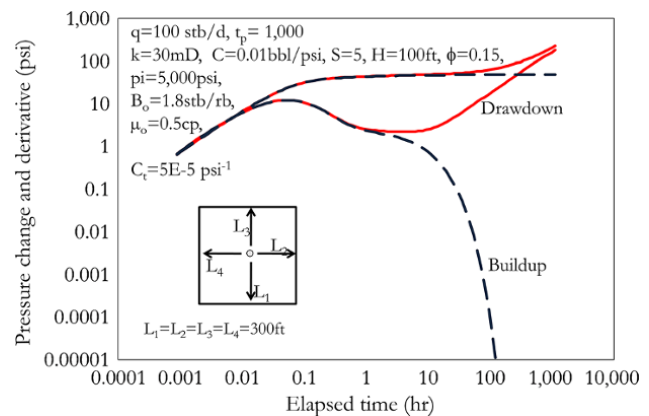


**Figure 8.109** Well test behavior for drawdown and buildup tests in a closed boundary reservoir.

oil and gas samples were recombined to reservoir condition in the laboratory. The viscosity and formation volume factors of the recombined oil sample were measured at reservoir condition as 0.79 cp and 1.23 stb/rb, respectively. The structural map from seismic interpretation indicates a continuous fault away from the well.

1. Identify the start and end of each flow regime.
2. Determine the well test interpretation model.
3. Determine well test interpretation parameters.

**Table 8.16** Pressure-Rate Data for Exercise 8.4.

Time (hr)	Rate (stb/D)	Pressure (psia)	Time (hr)	Rate (stb/D)	Pressure (psia)	Time (hr)	Rate (stb/D)	Pressure (psia)	Time (hr)	Rate (stb/D)	Pressure (psia)
0.00100	135	6,497.11	0.43738	135	6,178.52	150.00100	0	6,057.37	150.43738	0	6,375.89
0.00128	135	6,496.39	0.55782	135	6,165.90	150.00128	0	6,058.08	150.55782	0	6,388.49
0.00163	135	6,495.48	0.71143	135	6,156.33	150.00163	0	6,059.00	150.71143	0	6,398.04
0.00207	135	6,494.33	0.90733	135	6,149.08	150.00207	0	6,060.15	150.90733	0	6,405.26
0.00265	135	6,492.86	1.15718	135	6,143.46	150.00265	0	6,061.61	151.15718	0	6,410.84
0.00337	135	6,491.01	1.47583	135	6,138.90	150.00337	0	6,063.47	151.47583	0	6,415.35
0.00430	135	6,488.66	1.88222	135	6,134.96	150.00430	0	6,065.82	151.88222	0	6,419.22
0.00549	135	6,485.69	2.40052	135	6,131.38	150.00549	0	6,068.79	152.40052	0	6,422.72
0.00700	135	6,481.94	3.06153	135	6,127.98	150.00700	0	6,072.53	153.06153	0	6,426.03
0.00893	135	6,477.24	3.90457	135	6,124.62	150.00893	0	6,077.24	153.90457	0	6,429.26
0.01139	135	6,471.35	4.97976	135	6,121.23	150.01139	0	6,083.12	154.97976	0	6,432.49
0.01452	135	6,464.02	6.35101	135	6,117.73	150.01452	0	6,090.46	156.35101	0	6,435.78
0.01852	135	6,454.93	8.09985	135	6,114.06	150.01852	0	6,099.54	158.09985	0	6,439.19
0.02362	135	6,443.77	10.33027	135	6,110.18	150.02362	0	6,110.71	160.33027	0	6,442.74
0.03012	135	6,430.18	13.17486	135	6,106.07	150.03012	0	6,124.29	163.17486	0	6,446.44
0.03842	135	6,413.87	16.80276	135	6,101.72	150.03842	0	6,140.60	166.80276	0	6,450.27
0.04900	135	6,394.62	21.42965	135	6,097.15	150.04900	0	6,159.85	171.42965	0	6,454.21
0.06249	135	6,372.41	27.33063	135	6,092.35	150.06249	0	6,182.06	177.33063	0	6,458.20
0.07969	135	6,347.50	34.85653	135	6,087.37	150.07969	0	6,206.96	184.85653	0	6,462.21
0.10164	135	6,320.52	44.45480	135	6,082.22	150.10164	0	6,233.94	194.45480	0	6,466.17
0.12963	135	6,292.46	56.69610	135	6,076.92	150.12963	0	6,261.99	206.69610	0	6,470.03
0.16532	135	6,264.61	72.30823	135	6,071.51	150.16532	0	6,289.84	222.30823	0	6,473.72
0.21084	135	6,238.31	92.21939	135	6,066.00	150.21084	0	6,316.13	242.21939	0	6,477.20
0.26890	135	6,214.76	117.61338	135	6,060.41	150.26890	0	6,339.68	267.61338	0	6,480.43
0.34295	135	6,194.74	150.00000	135	6,054.76	150.34295	0	6,359.69	300.00000	0	6,483.36

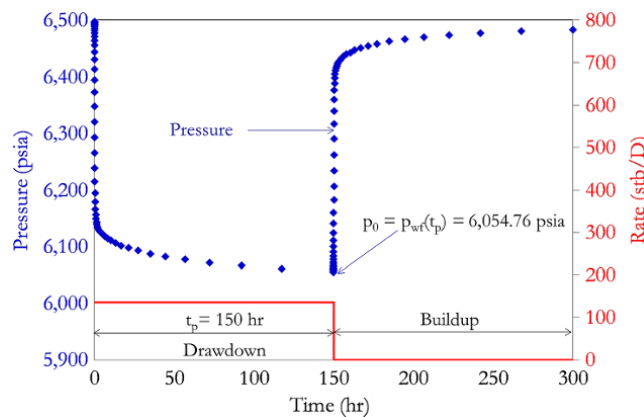


**Figure 8.110** Pressure–rate history showing defined drawdown and buildup tests.

4. Simulate pressure response and compare with actual pressure measured.
5. Refine simulated pressure response using regression where required.

**Solution.**

1. Data preparation

This involves examining the entire pressure–rate history, defining flow periods (drawdown and buildup) and identifying outliers (where they exist) (Fig. 8.110).

2. Diagnosis of well test

Diagnosis involves examining the log-log diagnostic plot (log-log pressure change and derivative) to identify flow regimes that help to define the well test interpretation model. Fig. 8.111 shows the derivative of the buildup test. Exercise 8.1 shows how to calculate the well test derivative and create a log-log diagnostic plot for well test analysis.

3. Defining the well test interpretation model

From the diagnosis, the reservoir–well is characterized by the following flow regime: a well with wellbore storage

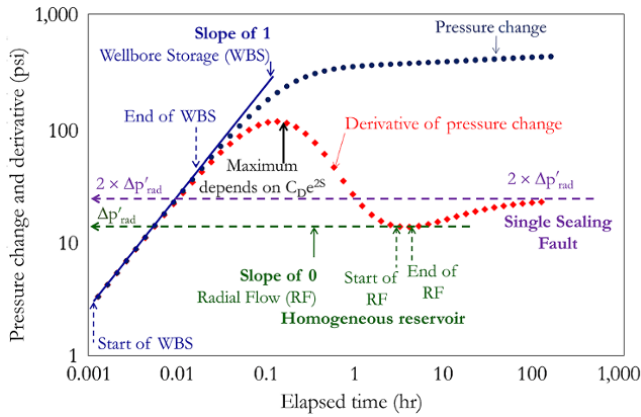


**Figure 8.111** Log-log diagnostic plot for buildup test showing flow regimes.

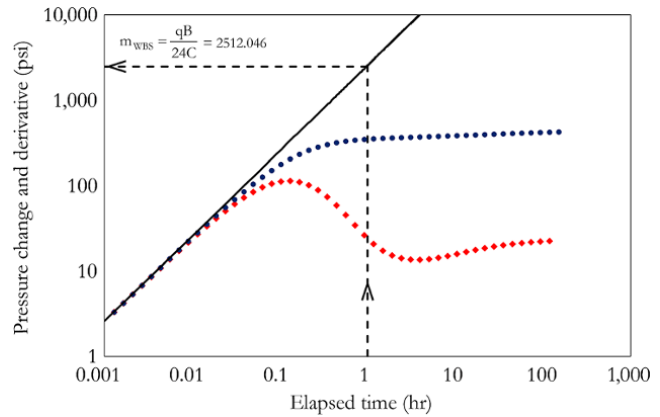


**Figure 8.112**  $m_{WBS}$  Calculation from the log-log diagnostic plot.

**Table 8.17** Parameters Defining Interpretation Model for Exercise 8.4.

Model behavior	Parameters
Wellbore storage effect	Storage effect coefficient, C
Skin effect (wellbore condition)	Skin, S
Homogeneous reservoir property	Reservoir permeability, k
Single-sealing fault	Distance to fault $d_{fault}$

and skin; reservoir with homogeneous behavior and a single-sealing fault boundary. This system can thus be described as a *reservoir with single-sealing fault producing from well with wellbore storage and skin*.

4. Model parameters

For the interpretation model, the parameters shown in Table 8.17 are calculated.

5. Storage effect calculation

Exercise 7.3 (straight-line method) and Exercise 8.1 (derivative method) show the steps for calculating C from pressure data. The derivative method will be used in this exercise.

*Wellbore Storage Constant Calculation*

From Fig. 8.112,  $m_{WBS} = \frac{qB}{24C} = 2512.046 \text{ psi/hr}$ . Hence:

$$C = \frac{qB}{24m_{WBS}} = \frac{135 \times 1.23}{24 \times 2512.046} = 0.00275 \text{ bbl/psi}$$

$$C = 0.00275 \text{ bbl/psi}$$

*Reservoir Permeability Calculation*

From Fig. 8.113  $0.4342m_{RF} = 12.9 \text{ psi}$ .

Therefore:

$$m_{RF} = \frac{12.9}{0.4342} = 29.71 \text{ psi/log cycle}$$

From equation (7.69):

$$k_r = \frac{162.6qB\mu}{m_{RF}h}$$

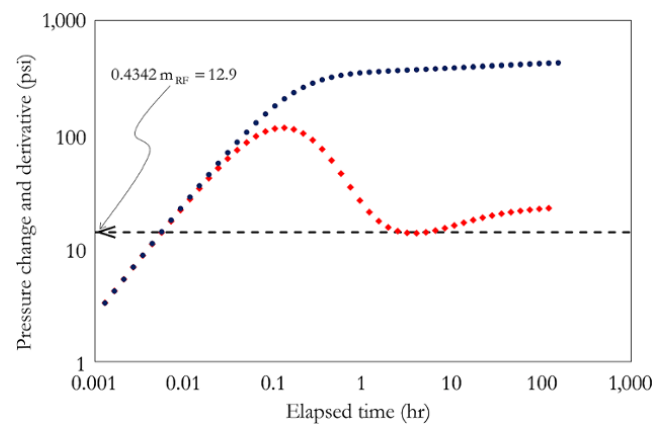


**Figure 8.113**  $m_{RF}$  calculation from the log-log diagnostic plot.

$$k_r = \frac{162.6 \times 135 \times 1.23 \times 0.79}{29.71 \times 30} = 23.93 \text{ mD}$$

$$k_r = 23.93 \text{ mD}$$

*Well Skin Calculation*

From Fig. 8.114,  $\Delta p_{rad} = 372.26 \text{ psi}$  and  $\Delta p'_{rad} = 12.91 \text{ psi}$  at  $\Delta t_{rad} = 3.0615 \text{ hr}$

Substituting  $\Delta p_{rad}$  and  $\Delta p'_{rad}$  into equation (8.21):

$$S = 1.15 \left( \frac{0.4342\Delta p_{rad}}{\Delta p'_{rad}} - \log \frac{kt_p \Delta t_{rad}}{1698.244\phi\mu c_t r_w^2 (t_p + \Delta t_{rad})} \right)$$

$$S = 1.15 \left( \frac{0.4342 \times 372.26}{12.91} - \log \frac{23.93 \times 150 \times 3.0615}{1698.244 \times 0.3 \times 0.79 \times 5 \times 10^{-5} \times 0.3^2 \times (150 + 3.0615)} \right) = 9.11$$

$$S = 9.11$$



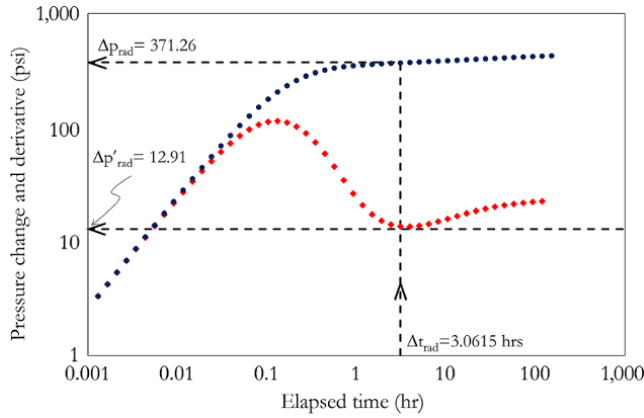


**Figure 8.114**  $\Delta p_{rad}$  and  $\Delta p'_{rad}$  calculation from the log-log diagnostic plot.

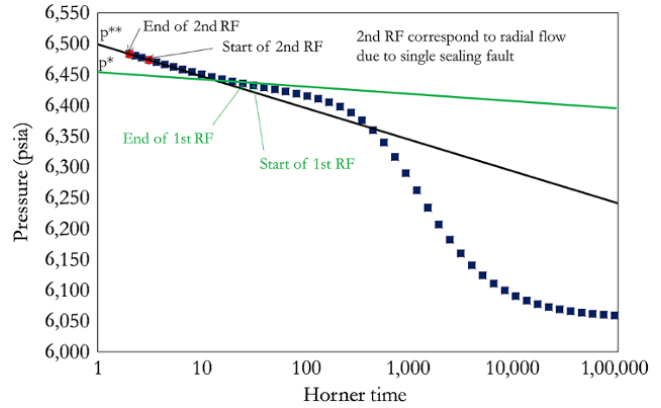


**Figure 8.116**  $p^{**}$  calculation from the Horner plot.

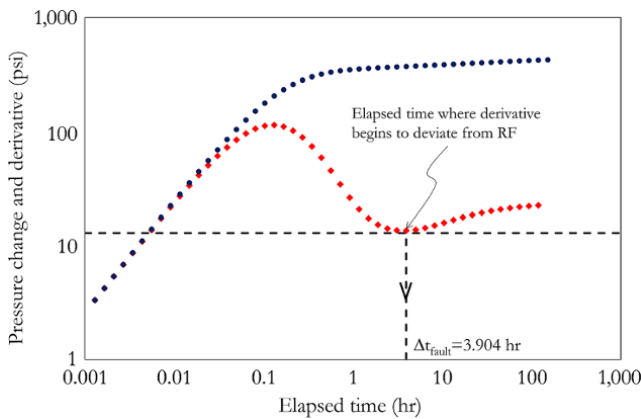


**Figure 8.115**  $\Delta t_{fault}$  calculation from the log-log diagnostic plot.

*Distance to Fault*

Determine the distance to fault using equation (8.43).

$$d_{fault} = 0.032 \sqrt{\frac{k \Delta t_{fault}}{\phi \mu c_t}}$$

where  $\Delta t_{fault}$  corresponds to elapsed time when the derivative begins to deviate from the RF line (Fig. 8.115).

$$d_{fault} = 0.032 \sqrt{\frac{23.93 \times 3.904}{0.3 \times 0.79 \times 5 \times 10^{-5}}} = 89.85 \text{ ft}$$

$$d_{fault} = 89.85 \text{ ft}$$

*Initial Reservoir Pressure Calculation*

$p^*$  (from radial flow extrapolation on superposition) equals the initial reservoir pressure for an infinitely acting

reservoir only. Where there is a fault,  $p^*$  is less than reservoir pressure.  $p^{**}$ , which is the extrapolation of the radial flow corresponding to 2RF (second radial flow) defining the single-sealing fault flow regime, can give a pressure value close to the reservoir pressure.  $p^{**}$  will be used for initial reservoir pressure, which will then be refined using regression match if required (Fig. 8.116).

$$p^{**} \approx p_i = 6,500 \text{ psia}$$

*Model Consistency*

The interpretation model and result must be checked with any other information to ensure that the model and model parameters are consistent (Table 8.18).

Note: if the test duration was short, fault behavior may not be observed on the well test data.

6. Forward simulation

Fig. 8.117 shows the active and image well configuration for the well test pressure response simulation.

From equation (8.63), active well response in the Laplace domain is defined by:

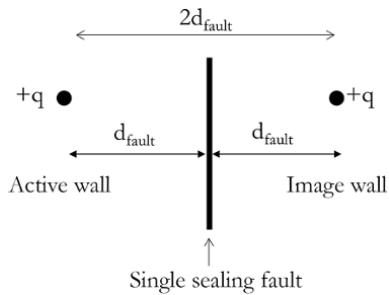
$$\bar{p}_{wD\_active}(s, S, C_D, r_D = 1) = \frac{\frac{K_0(r_D \sqrt{s})}{\sqrt{s} K_1(\sqrt{s})} + S}{s \left[ 1 + C_D s \left( \frac{K_0(r_D \sqrt{s})}{\sqrt{s} K_1(\sqrt{s})} + S \right) \right]}$$

$$\bar{p}_{wD\_active}(s, S, C_D) = \frac{\frac{K_0(\sqrt{s})}{\sqrt{s} K_1(\sqrt{s})} + S}{s \left[ 1 + C_D s \left( \frac{K_0(\sqrt{s})}{\sqrt{s} K_1(\sqrt{s})} + S \right) \right]}$$

From equation (8.63), the pressure response of the image well, which is a distance of  $2d_{fault}$  away from

**Table 8.18** Model Consistency Check.

Near wellbore	Reservoir	Boundaries
No history of well stimulation, hence positive skin expected. Well surface well control was used, hence well storage effect also expected.	Reservoir is described as clean sandstone, hence behavior is most likely to be homogeneous in behavior.	Structure analysis indicated presence of continuous fault, hence the presence of fault in interpretation model is consistent.

**Figure 8.117** Active and image well configuration for forward simulation.

the active well, in the Laplace domain can be defined as:

$$\begin{aligned} \bar{p}_{wD\_image} \left( s, S=0, C_D=0, r_D = \frac{2d_{fault}}{r_w} \right) &= \frac{\frac{K_0(r_D\sqrt{s})}{\sqrt{s}K_1(\sqrt{s})} + S}{s \left[ 1 + C_{DS} \left( \frac{K_0(r_D\sqrt{s})}{\sqrt{s}K_1(\sqrt{s})} + S \right) \right]} = \frac{1}{s} \frac{K_0 \left( \frac{2d_{fault}}{r_w} \sqrt{s} \right)}{\sqrt{s}K_1(\sqrt{s})} \\ \bar{p}_{wD\_image}(s) &= \frac{1}{s} \frac{K_0 \left( \frac{2d_{fault}}{r_w} \sqrt{s} \right)}{\sqrt{s}K_1(\sqrt{s})} \end{aligned}$$

$$\bar{p}_{wD} = \bar{p}_{wD\_active} + \bar{p}_{wD\_image}$$

Pressure simulation using the active and image well with the superposition principle is shown in Table 8.19

The simulation match for Exercise 8.4 is shown in Fig. 8.118.

In this case, since there is a good match between test data and simulated data, there is no need to refine the match with regression.

The final result is the interpretation model and parameters that define this interpretation model, as summarized in Tables 8.20 and 8.21.

## 8.6. UNCERTAINTY ASSOCIATED WITH WELL TEST ANALYSIS RESULT

Like any petroleum engineering calculations, there are also uncertainties associated with well test interpretation. These uncertainties can be due to errors in measurement

of the input data used for well test analysis and the non-uniqueness of the well test interpretation model. The non-uniqueness of the interpretation model is not only peculiar to well testing but to any process where models or parameters are determined through an inversion process. In well testing an inversion process can yield more than one possible solution/model that can predict the pressure response of the reservoir–well system. It is, therefore, not uncommon to have more than one possible interpretation model during well test analysis. However, with other well and reservoir characterization information and a robust well test interpretation process, appropriate interpretation models can often be narrowed to one or two possibilities. The near wellbore behavior (early time behavior) can be verified with workover history, well completion, and well architecture from the well engineering report to ensure that the model selected is consistent with the near wellbore model selected. The reservoir behavior (mid time) can be validated with geological information describing rock type, seismic inversion results that can provide qualitative and quantitative description of the reservoir/field, open hole logs, and production logging test (PLT) that gives information on reservoir layering. Reservoir boundaries (late time) behavior can be validated with structural maps derived from seismic analysis.

### 8.6.1. Confidence of Intervals in Well Test Analysis

*Azi et al.* [2008] suggested that acceptable confidence intervals for well test analysis based on the uncertainty generally associated with well testing and interpretation; these are summarized in Table 8.22.

### 8.6.2. Factors that Affect Well Test Interpretation

Factors that may be from operational, measurement, or analysis aspects can affect well test behavior and, hence, well test analysis results.

**8.6.2.1. Phase Redistribution.** This is a well test phenomenon caused by phase segregation (rise of gas and fall of liquids trapped in a wellbore) after a surface shut-in. Phase redistribution is characterized by a severe “hump” and often discontinuity in the derivative plot and can obscure reservoir response (Fig. 8.119).

**Table 8.19** Pressure Simulation using Active and Image Well with Superposition Principle.

$(\Delta t_1 + \Delta t)_D$	$(\Delta t)_D$	Active well		Image well		$p_i - p(t)$ (psi)	$p(t)$ (psia)
		$p_D(\Delta t_1 + \Delta t)_D$	$p_D(\Delta t)_D$	$p_D(\Delta t_1 + \Delta t)_D$	$p_D(\Delta t)_D$		
5.924	0.000	0.0969251	0.0000	1.00E-90	0.0000	2.50	6,497.50
7.553	0.000	0.123415	0.0000	1.58E-80	0.0000	3.18	6,496.82
9.638	0.000	0.1572225	0.0000	1.83E-71	0.0000	4.06	6,495.94
12.286	0.000	0.1999958	0.0000	1.80E-63	0.0000	5.16	6,494.84
15.674	0.000	0.2544772	0.0000	2.31E-56	0.0000	6.57	6,493.43
19.986	0.000	0.3234152	0.0000	4.42E-50	0.0000	8.34	6,491.66
25.489	0.000	0.4107497	0.0000	1.64E-44	0.0000	10.60	6,489.40
32.509	0.000	0.521143	0.0000	1.42E-39	0.0000	13.45	6,486.55
41.465	0.000	0.6604105	0.0000	3.38E-35	0.0000	17.04	6,482.96
52.880	0.000	0.8354112	0.0000	2.53E-31	0.0000	21.55	6,478.45
67.440	0.000	1.0547365	0.0000	6.90E-28	0.0000	27.21	6,472.79
86.011	0.000	1.3283891	0.0000	7.65E-25	0.0000	34.27	6,465.73
109.699	0.000	1.6679971	0.0000	3.83E-22	0.0000	43.04	6,456.96
139.904	0.000	2.0863343	0.0000	9.48E-20	0.0000	53.83	6,446.17
178.431	0.000	2.5971849	0.0000	1.26E-17	0.0000	67.01	6,432.99
227.561	0.000	3.2134916	0.0000	9.59E-16	0.0000	82.91	6,417.09
290.227	0.000	3.9456898	0.0000	4.48E-14	0.0000	101.80	6,398.20
370.148	0.000	4.7979012	0.0000	1.36E-12	0.0000	123.79	6,376.21
472.069	0.000	5.7639131	0.0000	2.80E-11	0.0000	148.71	6,351.29
602.063	0.000	6.8231211	0.0000	4.11E-10	0.0000	176.04	6,323.96
767.847	0.000	7.9378134	0.0000	4.44E-09	0.0000	204.80	6,295.20
979.290	0.000	9.0553805	0.0000	3.64E-08	0.0000	233.64	6,266.36
1,248.950	0.000	10.115517	0.0000	2.32E-07	0.0000	260.99	6,239.01
1,592.868	0.000	11.062607	0.0000	1.17E-06	0.0000	285.43	6,214.57
2,031.487	0.000	11.858217	0.0000	4.76E-06	0.0000	305.95	6,194.05
2,590.888	0.000	12.489008	0.0000	1.55E-05	0.0000	322.23	6,177.77
3,304.327	0.000	12.966315	0.0000	4.09E-05	0.0000	334.55	6,165.45
4,214.227	0.000	13.318432	0.0000	8.53E-05	0.0000	343.63	6,156.37
5,374.672	0.000	13.579856	0.0000	1.35E-04	0.0000	350.38	6,149.62
6,854.672	0.000	13.782295	0.0000	1.41E-04	0.0000	355.60	6,144.40
8,742.210	0.000	13.949892	0.0000	1.73E-05	0.0000	359.92	6,140.08
11,149.508	0.000	14.098501	0.0000	-2.89E-04	0.0000	363.75	6,136.25
14,219.692	0.000	14.237289	0.0000	-6.60E-04	0.0000	367.32	6,132.68
18,135.305	0.000	14.371004	0.0000	-6.25E-04	0.0000	370.77	6,129.23
23,129.131	0.000	14.501884	0.0000	0.00079	0.0000	374.18	6,125.82
29,498.085	0.000	14.630926	0.0000	0.00507	0.0000	377.62	6,122.38
37,620.829	0.000	14.758589	0.0000	0.01407	0.0000	381.15	6,118.85
47,980.288	0.000	14.885125	0.0000	0.02975	0.0000	384.82	6,115.18
61,192.381	0.000	15.010717	0.0000	0.05385	0.0000	388.68	6,111.32
78,042.626	0.000	15.135522	0.0000	0.08767	0.0000	392.77	6,107.23
99,532.839	0.000	15.259679	0.0000	0.13189	0.0000	397.12	6,102.88
126,940.705	0.000	15.383308	0.0000	0.18662	0.0000	401.72	6,098.28
161,895.741	0.000	15.506516	0.0000	0.25146	0.0000	406.57	6,093.43
206,476.167	0.000	15.629387	0.0000	0.32560	0.0000	411.65	6,088.35
263,332.490	0.000	15.751991	0.0000	0.40805	0.0000	416.95	6,083.05
335,845.062	0.000	15.874386	0.0000	0.49770	0.0000	422.42	6,077.58
428,325.054	0.000	15.996615	0.0000	0.59345	0.0000	428.04	6,071.96
546,270.813	0.000	16.118714	0.0000	0.69430	0.0000	433.79	6,066.21
696,694.708	0.000	16.24071	0.0000	0.79933	0.0000	439.65	6,060.35
888,540.084	0.000	16.362626	0.0000	0.90775	0.0000	445.59	6,054.41
888,546.008	5.924	16.36263	0.0969	0.907754	1.001E-90	443.09	6,056.91
888,547.637	7.553	16.36263	0.1234	0.907755	1.576E-80	442.41	6,057.59
888,549.722	9.638	16.36263	0.1572	0.907756	1.826E-71	441.54	6,058.46
888,552.370	12.286	16.36263	0.2000	0.907757	1.803E-63	440.43	6,059.57

Table 8.19 (Continued)

$(\Delta t_1 + \Delta t)_D$	$(\Delta t)_D$	Active well		Image well		$p_i - p(t)$ (psi)	$p(t)$ (psia)
		$p_D(\Delta t_1 + \Delta t)_D$	$p_D(\Delta t)_D$	$p_D(\Delta t_1 + \Delta t)_D$	$p_D(\Delta t)_D$		
888,555.758	15.674	16.36264	0.2545	0.907759	2.306E-56	439.03	6,060.97
888,560.071	19.986	16.36264	0.3234	0.907761	4.421E-50	437.25	6,062.75
888,565.574	25.489	16.36264	0.4107	0.907764	1.644E-44	435.00	6,065.00
888,572.593	32.509	16.36264	0.5211	0.907767	1.421E-39	432.15	6,067.85
888,581.550	41.465	16.36265	0.6604	0.907772	3.376E-35	428.56	6,071.44
888,592.964	52.880	16.36266	0.8354	0.907778	2.532E-31	424.04	6,075.96
888,607.525	67.440	16.36266	1.0547	0.907785	6.898E-28	418.38	6,081.62
888,626.095	86.011	16.36267	1.3284	0.907795	7.653E-25	411.32	6,088.68
888,649.784	109.699	16.36269	1.6680	0.907807	3.835E-22	402.56	6,097.44
888,679.988	139.904	16.36271	2.0863	0.907822	9.484E-20	391.77	6,108.23
888,718.515	178.431	16.36273	2.5972	0.907842	1.257E-17	378.59	6,121.41
888,767.645	227.561	16.36275	3.2135	0.907867	9.588E-16	362.69	6,137.31
888,830.311	290.227	16.36279	3.9457	0.907898	4.484E-14	343.80	6,156.20
888,910.232	370.148	16.36284	4.7979	0.907939	1.359E-12	321.81	6,178.19
889,012.154	472.069	16.36289	5.7639	0.907991	2.803E-11	296.89	6,203.11
889,142.147	602.063	16.36297	6.8231	0.908057	4.108E-10	269.57	6,230.43
889,307.931	767.847	16.36306	7.9378	0.908141	4.438E-09	240.81	6,259.19
889,519.374	979.290	16.36318	9.0554	0.908249	3.641E-08	211.98	6,288.02
889,789.034	1,248.950	16.36333	10.1155	0.908386	2.324E-07	184.64	6,315.36
890,132.952	1,592.868	16.36352	11.0626	0.908560	1.175E-06	160.21	6,339.79
890,571.571	2,031.487	16.36377	11.8582	0.908783	4.758E-06	139.70	6,360.30
891,130.972	2,590.888	16.36409	12.4890	0.909067	1.554E-05	123.44	6,376.56
891,844.411	3,304.327	16.36449	12.9663	0.909428	4.086E-05	111.14	6,388.86
892,754.312	4,214.227	16.36500	13.3184	0.909889	8.531E-05	102.08	6,397.92
893,914.757	5,374.672	16.36565	13.5799	0.910476	1.354E-04	95.36	6,404.64
895,394.756	6,854.672	16.36648	13.7823	0.911224	1.407E-04	90.18	6,409.82
897,282.294	8,742.210	16.36753	13.9499	0.912177	1.733E-05	85.91	6,414.09
899,689.592	11,149.508	16.36887	14.0985	0.913388	-2.886E-04	82.15	6,417.85
902,759.776	14,219.692	16.37058	14.2373	0.914930	-6.602E-04	78.66	6,421.34
906,675.389	18,135.305	16.37275	14.3710	0.916889	-6.251E-04	75.32	6,424.68
911,669.215	23,129.131	16.37550	14.5019	0.919376	0.00079	72.04	6,427.96
918,038.170	29,498.085	16.37899	14.6309	0.922531	0.00507	68.77	6,431.23
926,160.913	37,620.829	16.38340	14.7586	0.926525	0.01407	65.46	6,434.54
936,520.372	47,980.288	16.38898	14.8851	0.931574	0.02975	62.07	6,437.93
949,732.466	61,192.381	16.39600	15.0107	0.937941	0.05385	58.55	6,441.45
966,582.710	78,042.626	16.40481	15.1355	0.945946	0.08767	54.89	6,445.11
988,072.923	99,532.839	16.41582	15.2597	0.955973	0.13189	51.09	6,448.91
1,015,480.789	126,940.705	16.42953	15.3833	0.968478	0.18663	47.17	6,452.83
1,050,435.826	161,895.741	16.44649	15.5065	0.983987	0.25146	43.15	6,456.85
1,095,016.251	206,476.167	16.46731	15.6294	1.003097	0.32560	39.10	6,460.90
1,151,872.575	263,332.490	16.49266	15.7520	1.026458	0.40805	35.07	6,464.93
1,224,385.146	335,845.062	16.52323	15.8744	1.054757	0.49770	31.11	6,468.89
1,316,865.139	428,325.054	16.55970	15.9966	1.088675	0.59345	27.31	6,472.69
1,434,810.897	546,270.813	16.60265	16.1187	1.128850	0.69430	23.70	6,476.30
1,5852,34.792	696,694.708	16.65256	16.2407	1.175817	0.79933	20.34	6,479.66
1,777,080.169	888,540.084	16.70975	16.3626	1.229960	0.90775	17.27	6,482.73

Calculation of  $(\Delta t_1 + \Delta t)_D$ ,  $(\Delta t)_D$ ,  $p_D(\Delta t_1 + \Delta t)_D$ ,  $p_D(\Delta t)_D$ ,  $p_i - p(t)$ , and  $p(t)$  have been discussed in Exercise 8.2

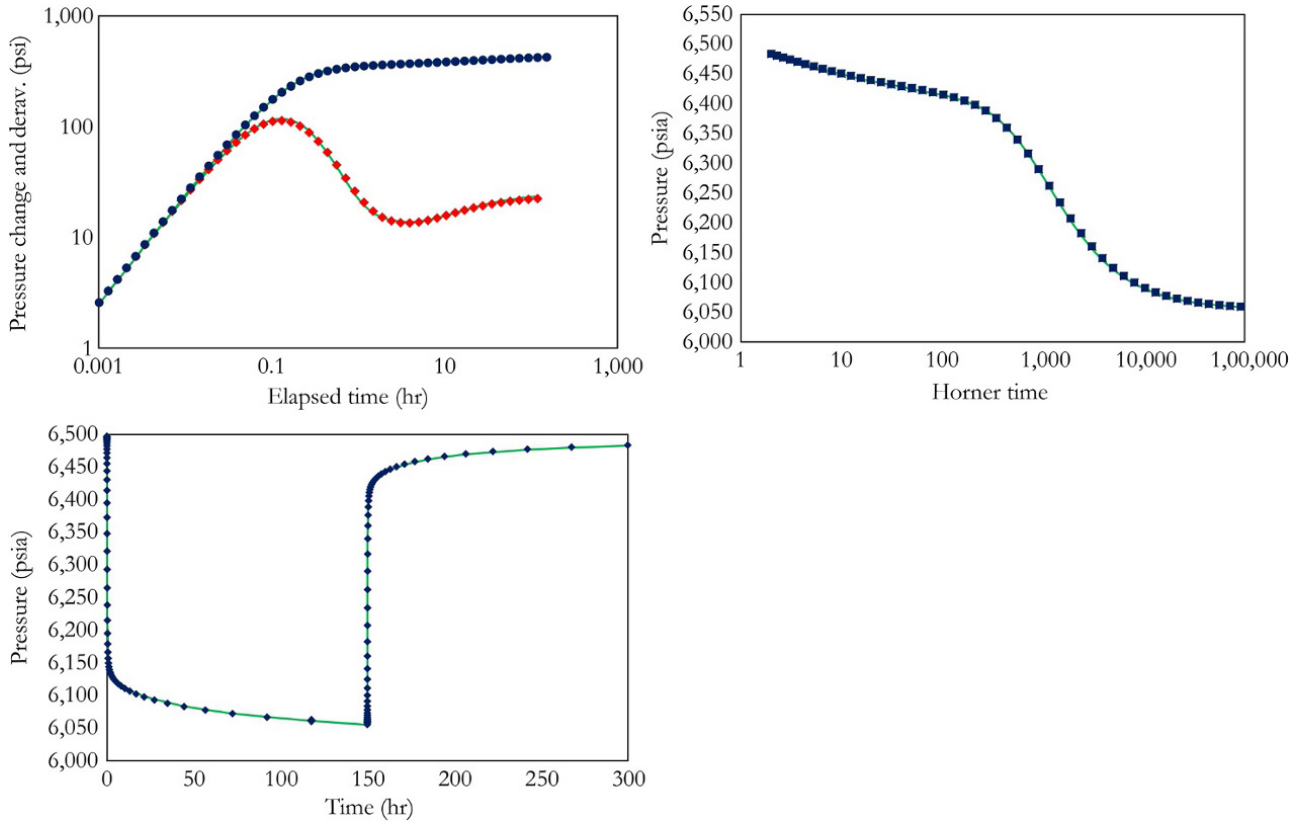


Figure 8.118 Simulation match (simulated in continuous line and test data in dotted line).

Table 8.20 Well Test Interpretation Model for Exercise 8.4.

Model
Well with C and S
Homogeneous reservoir behavior
Single-sealing fault boundary

Table 8.21 Well Test Interpretation Parameters for Exercise 8.4.

Parameters	Values
$p_i$ (psia)	6,500
$d_{\text{fault}}$ (ft)	90
S	9
$k_r$ (mD)	24
C (bbl/psi)	0.003

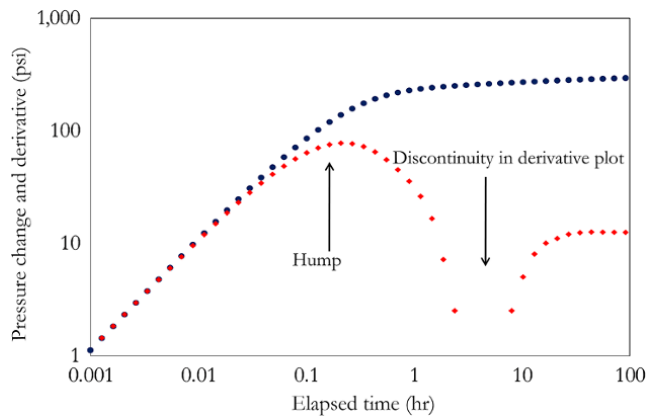
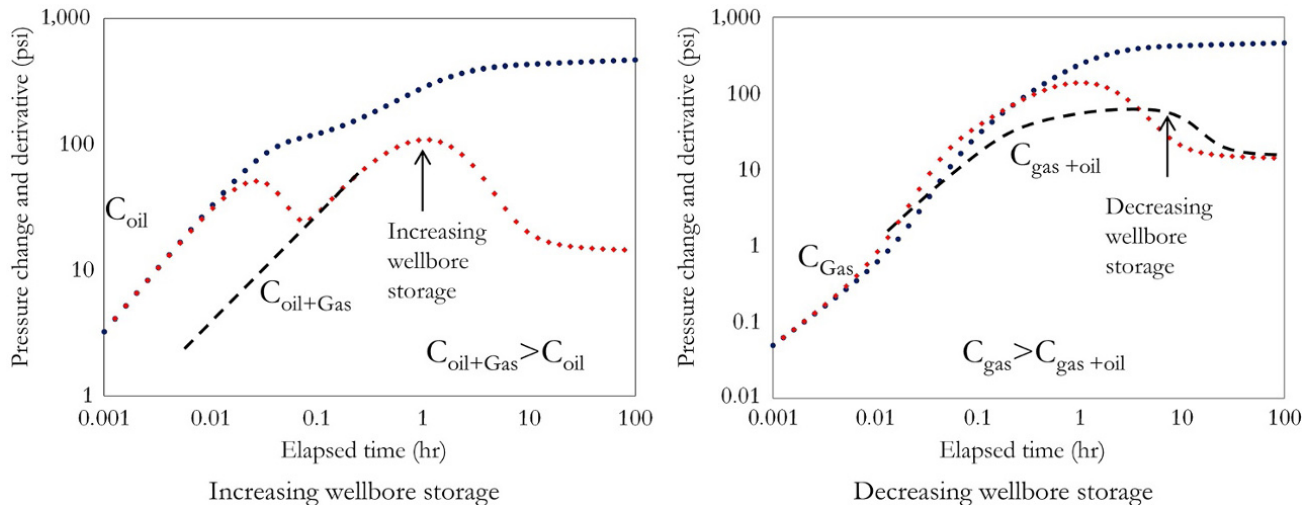


Figure 8.119 Phase redistribution well test behavior.

Table 8.22 Limit of Accuracy Associated with Well Test Analysis.

Parameter	Limit of accuracy
kh	15 %
k	20 %
C	20 %
S	$\pm 0.3$
Distances	25 %



**Figure 8.120** Changing wellbore storage well test behavior.

Operationally, phase redistribution can be reduced by shutting the well close to the top of perforation and eliminated by *downhole shut-in*.

**8.6.2.2. Changing Wellbore Storage.** Phase changes that can occur due to gas evolution from oil or due to condensate formation from gas can create a sudden change in the wellbore storage constant during well testing (Fig. 8.120). Changes in wellbore storage can distort the derivative plot at early times. Operationally, changing wellbore storage can be eliminated by downhole shut-in. During interpretation, the effect of changing wellbore storage can be handled by including the changing wellbore model discussed in Section 8.5.1.6. This helps in improving the match and better characterizing well–reservoir system.

**8.6.2.3. Wrong Rate Recording.** Accurate rate measurement is a challenge in well testing, especially in well test analysis of production test data. Rates may not be measured continuously for a production test even, when there is a permanent bottomhole gauge, due to cost and, hence, rates will be estimated periodically. Well rates in a field producing from multiple wells may be determined by production *back-allocation techniques*, which may not be accurate. Also, during a drill stem test (DST), wrong flow meter calibration, faulty flow meters, and a multiphase effect can affect the accuracy of rate recording. During a DST where GOR is low and a separator is used to separate gas and oil before measurement, error can be significant, especially in heavy oil, where separation of gas and oil may not be efficient. Error rate measurement, especially from a production test, can be as high 20%.

Rate validation is a very important step in well test analysis to ensure that the rate used for analysis is correct. As discussed in Section 8.4.3.1, equation (8.11), log-log derivative plot during reservoir behavior is dependent on  $0.4342 \left( 162.6 \frac{qB\mu}{k_r h} \right)$ . When the derivative is rate normalized, the effect of rate is removed, and radial flow stabilization will correspond to  $0.4342 \left( 162.6 \frac{B\mu}{k_r h} \right)$ . Therefore, for different flow periods from the same test, where the fluid phase in the reservoir has not changed, rate normalized radial flow stabilization corresponding to reservoir behavior should be the same except if the rate is wrong. Fig. 8.121 shows a pressure–rate history with  $-50\%$  rate error measurement in the first flow period (DD1), while Fig. 8.122 shows a comparison of the normalized log-log derivative of BU2 and BU5 from the pressure–rate history.

Deconvolution is an effective method for adapting the rate of production test to obtain a more accurate rate representing the pressure signal measured.

**8.6.2.4. Rate Simplification.** The use of *equivalent production time* is a common rate simplification algorithm in the petroleum industry that should be avoided. This involves using the last rate before buildup and equivalent production time for buildup analysis after a variable-rate test. Equivalent production time is the ratio of the cumulative production divided by the last rate before the buildup of interest. The use of this simplification often leads to erroneous analysis. The full superposition principle should always be used in analysis involving rate variation or flow-after-flow test. As the rate variation

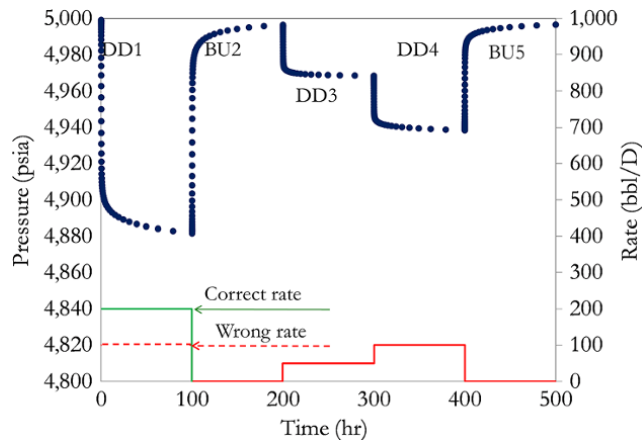


**Figure 8.121** Pressure–rate history with imposed reduced rate by 50% for DD1.

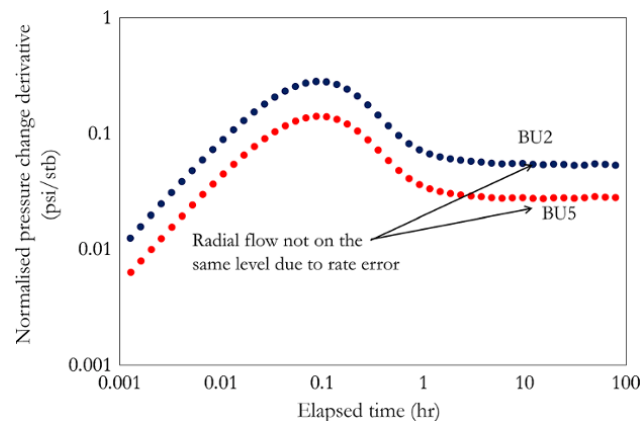


**Figure 8.122** Effect of the wrong rate on normalized log-log derivative pressure.

during a flow-after-flow test increases, error due to rate simplification increases. Also, as the production time duration during a variable-rate test becomes shorter, well test behavior of the buildup response based in a simplified rate becomes distorted on the derivative plot. This distortion can create a false boundary effect, as shown in Fig. 8.123.

**8.6.2.5. Error at Start of Flow Period ( $\Delta p_0$  and  $\Delta t_0$  error).** This error is associated with picking incorrect pressure and time at the start of a drawdown or buildup period ( $p_0$  and  $t_0$ ). Pressure fluctuation at the start of a period can make picking the correct  $p_0$  and  $t_0$  a nontrivial task. Fig. 8.124 shows different cases of  $p_0$  and  $t_0$  for the same test data with Fig. 8.124a showing the correct  $p_0$  and  $t_0$  for the analysis.

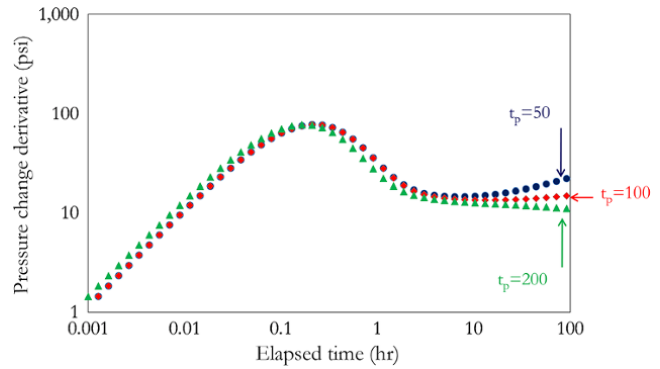


**Figure 8.123** Effect of rate simplification for different production times ( $t_p$ ) on buildup test.

**8.6.2.6. Well Loading.** Well loading occurs in liquid or high liquid rate gas wells, where there is no sufficient velocity to lift the liquid to the surface (Fig. 8.125). Liquid can be water, oil or condensate. When gas velocity is lower than critical (terminal liquid) velocity, the well will load. Well loading creates extra back (hydrostatic) pressure on the formation and may create unstable flow from the reservoir that may eventually kill the well. Operationally, artificial lift or redesigning production tubing can be used to unload wells. During loading, an accurate well rate may not be determined and an average rate based on cumulative production is often provided. Where well test data have been acquired during well loading, deconvolution can be used to determine the correct rate during the loading period of the test/production. Conventional well test analysis will then be carried out using measured pressure and adapted rate from deconvolution.

**8.6.2.7. Derivative End Effect.** A derivative end effect occurs when the derivative at a point becomes closer to the last data point than smoothing window  $L$ . Smoothing becomes impossible and leads to distortion in the shape of the derivative at late time (Fig. 8.126). A “pseudo-right” approach, which involves a fixed derivative, defined between the last point and the first point before the last, such that  $\Delta X > L$ , can be used to correct this effect [Bourdet et al., 1989].

**8.6.2.8. Pressure Gauge Noise.** This is unwanted or less significant pressure measurement caused by interfering signals (mechanical or electrical) that affect pressure signal acquisition or transmission during well testing. Noise can lead to scattering of derivative data points. Fig. 8.127 shows a pressure history with noise of +3.2 psi per  $\log \Delta t$  (+1 psi every 3 points) and Fig. 8.128 shows the effect of noise on log-log derivative. Where there is noise in the pressure history derivative, smoothing may help reduce the effect. However, an appropriate derivative window

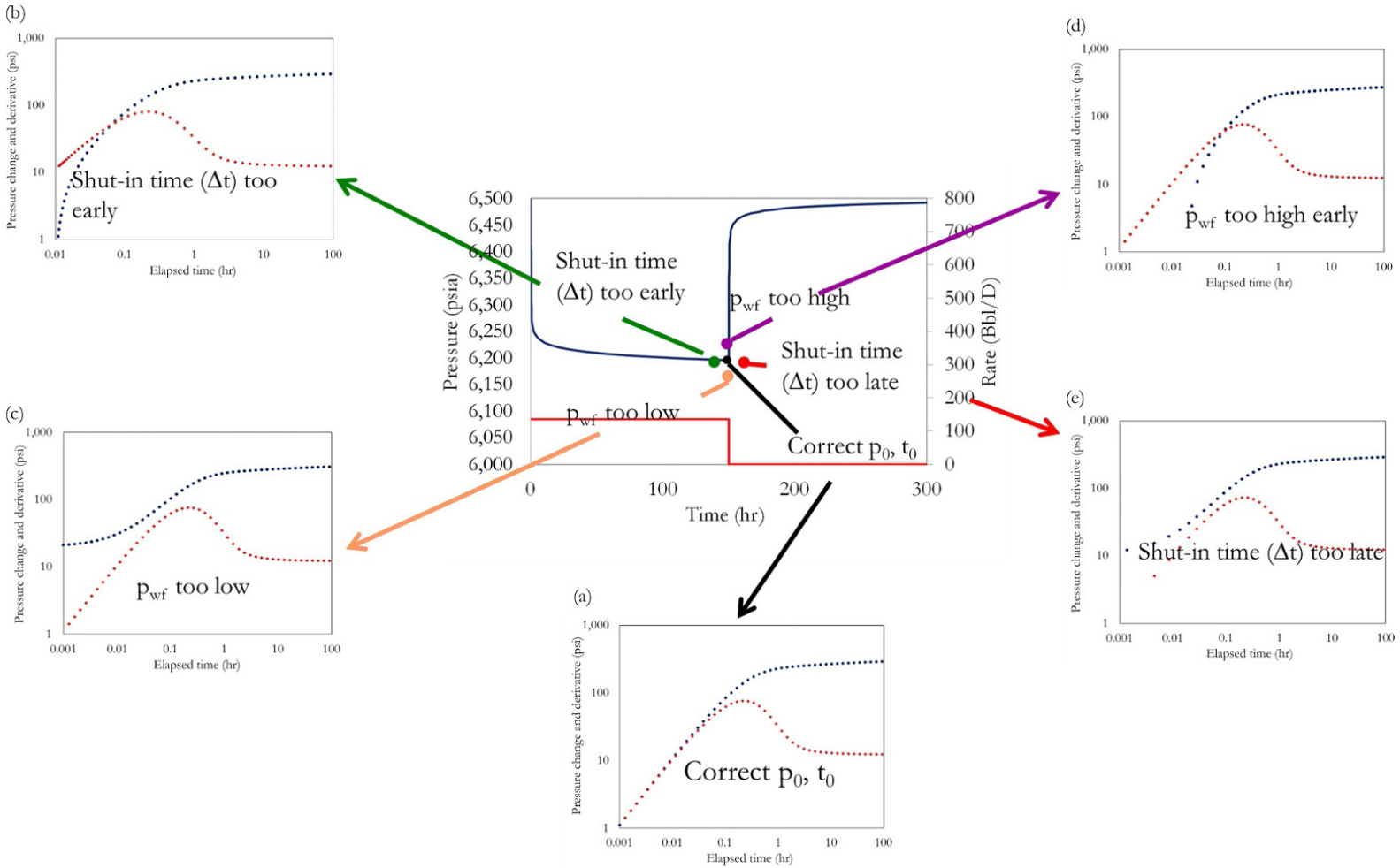


Figure 8.124 Effect of  $p_0$ - $t_0$  on well test behavior.



should be selected to avoid oversmoothing, which can add artefacts to the derivative behavior as discussed in Section 8.6.2.7.

### 8.7. WELL TEST ANALYSIS IN THE GAS RESERVOIR

Well test analysis in gas introduces two important features: nonlinearity of pressure in the diffusivity, discussed in Chapter 7 (7.1), and rate dependent skin effect.

The diffusivity equation for a gas well can be derived by replacing the pressure term (p) with a normalized pseudo-pressure term (m<sub>n</sub>(p)), as discussed in Chapter 7 (7.1.2):

$$\frac{1}{r} \frac{\partial}{\partial r} \left( r \frac{\partial m_n(p)}{\partial r} \right) = \frac{\phi \mu c_t}{k} \frac{\partial m_n(p)}{\partial t} \tag{8.150}$$

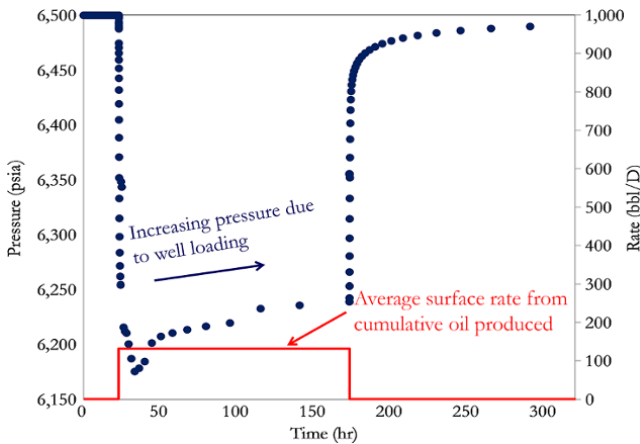


Figure 8.125 Effect of well loading on pressure history.

In dimensionless variables terms:

$$\frac{1}{r_D} \frac{\partial}{\partial r_D} \left( r_D \frac{\partial m_{nD}(p)}{\partial r_D} \right) = \frac{\partial m_{nD}(p)}{\partial t_D} \tag{8.151}$$

Similar to equation (7.67), the radial flow equation for gas can be expressed in terms of normalized pseudopressure as:

$$m_n(p_i) - m_n(p_{wf}) = 162.6 \frac{q_g B_{gi} \mu_i}{k_r h} \left( \log \Delta t + \log \frac{k}{\phi \mu_{gi} c_{ti} r_w^2} - 3.23 + 0.87S' \right) \tag{8.152}$$

where B<sub>gi</sub> is gas formation volume factor in bbl/Mscf and q<sub>g</sub> is gas flow rate in Mscf/D. Hence, q<sub>g</sub>B<sub>gi</sub> has the unit of bbl/D, which is the same as that of qB in a slightly compressible fluid.

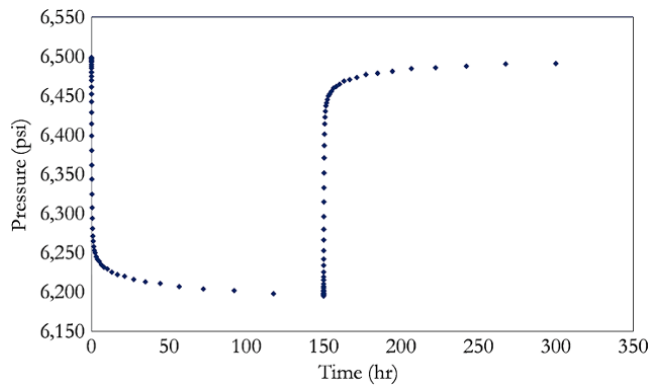


Figure 8.127 Noise of +3.2 psi per logΔt (+1 psi every 3 points).

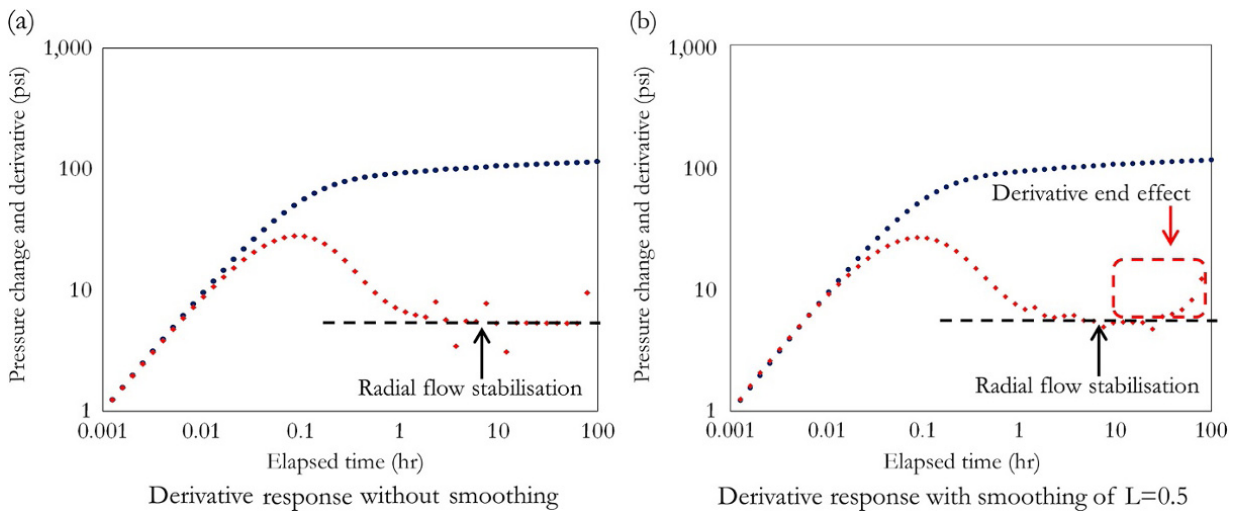
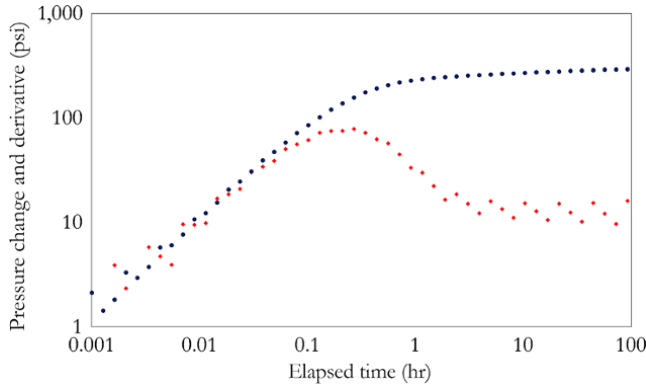


Figure 8.126 Derivative end effect due to smoothing of noisy pressure data.



**Figure 8.128** Scattering of derivative plot due to noise in the pressure data.

From equation (3.20):

$$B_{gi} = \frac{Z_i T_i p_{sc}}{p_i T_{sc}} \text{ (cf/scf)}$$

$$B_{gi} = 0.1781 \frac{Z_i T_i p_{sc}}{p_i T_{sc}} \text{ (bbl/scf)}$$

$$B_{gi} = 0.1781 \times 10^3 \frac{Z_i T_i p_{sc}}{p_i T_{sc}} \text{ (bbl/Mscf)}$$

Substituting  $B_{gi}$  above into equation (8.152):

$$\begin{aligned} m_n(p_i) - m_n(p_{wf}) &= 162.6 \times 0.1781 \\ &\times 10^3 \frac{Z_i T_i p_{sc} q_g \mu_i}{p_i T_{sc} k_r h} \left( \log \Delta t + \log \frac{k}{\phi \mu_{gi} c_{ti} r_w^2} - 3.23 + 0.87S' \right) \\ m_n(p_i) - m_n(p_{wf}) &= 28.95906 \times 10^3 \frac{Z_i T_i p_{sc} q_g \mu_i}{p_i T_{sc} k_r h} \\ &\left( \log \Delta t + \log \frac{k}{\phi \mu_{gi} c_{ti} r_w^2} - 3.23 + 0.87S' \right) \end{aligned} \quad (8.153)$$

Hence,  $m_{RF}$  for gas is expressed as:

$$m_{RF} = 28.95906 \times 10^3 \frac{Z_i T_i p_{sc} q_g \mu_i}{p_i T_{sc} k_r h} \quad (8.154)$$

$S'$  is the apparent skin factor, which is defined as:

$$S' = S_w + D(q_i + q_{i+1}) \quad (8.155)$$

where  $S_w$  is the mechanical skin effect due to actual well damage or stimulation and  $D$  is the non-Darcy skin coefficient in  $1/(\text{Mscf}/D)$

From equation (8.155), a plot of  $S'$  against  $q_i + q_{i+1}$  will give a slope that is equal to  $D$ . Calculation of  $D$  is an important step in well test analysis of gas.

Similar to an oil well, the wellbore storage effect for a gas well is defined as:

$$C = \frac{q_g B_{gi}}{24m_{WBS}} \text{ from Chapter 7 (7.3.1.1) and Exercise 7.3.}$$

But with  $B_{gi}$  defined as:

$$B_{gi} = 0.1781 \times 10^3 \frac{Z_i T_i p_{sc}}{p_i T_{sc}} \text{ (bbl/Mscf)}$$

Hence:

$$C = 0.1781 \times 10^3 \frac{Z_i T_i p_{sc}}{p_i T_{sc}} \frac{q_g}{24m_{WBS}}$$

The wellbore storage coefficient for gas can be expressed as:

$$C = 7.42 \frac{Z_i T_i p_{sc}}{p_i T_{sc}} \frac{q_g}{m_{WBS}} \quad (8.156)$$

### Exercise 8.5 Well Test Analysis in a Gas Reservoir

A DST was carried out in a sandstone reservoir with a gas zone of 45 ft, porosity of 0.2,  $B_{gi} = 0.006 \text{ ft}^3/\text{scf}$ ,  $\mu_i = 0.01 \text{ cp}$ ,  $c_{ti} = 3.7 \text{ E-4}$ ,  $Z_i = 0.89$ , and reservoir temperature of  $234^\circ\text{F}$ . With the data provided in Tables 8.23 and 8.24, carry out a full well test analysis showing: data preparation; diagnosis; initial parameter calculation; model and parameter validation if required; forward simulation; and regression to improve match if required.

#### Solution Steps.

*Step 1.* carry out data preparation

(i) define flow periods;

(ii) create normalized a pseudopressure table between  $p_i$  and  $p_0$  where  $p_0$  is any low pressure not higher than the minimum pressure in the data and convert pressure data to normalized pseudopressure.

*Step 2:* carry out a well test diagnosis, preferably using buildup log-log diagnostic plot.

*Step 3:* define well test interpretation model.

*Step 4:* calculate initial well test parameters

(i) use superposition/Horner to determine  $p_i$ ;

(ii) use the buildup diagnostic plot to determine  $C$  and  $k_r$ ;

(iii) calculate three apparent skin factors for each of the drawdowns using either the straight-line (Exercise 7.5) or derivative (Exercise 8.1) method.

(iv) plot  $S'$  against  $q_i + q_{i+1}$  to determine  $D$  and  $S_w$ .

*Step 5:* check for model consistency if there is any available information.

*Step 6:* carry out forward simulation.

*Step 7:* refine well test parameters with interpretation model using regression (where required).

*Step 8:* report final result.

#### Solution.

*Data Preparation*

Define flow periods (Fig. 8.129).

*Creating a Normalized Pseudopressure Table*

**Table 8.23** Well Test Data for Exercise 8.5.

Time (hs)	Gas rate (Mscf/D)	Pressure (psia)	Time (hr)	Gas rate (Mscf/D)	Pressure (psia)
0.00000	300	2,656.000	100.00312	400	2,612.412
0.00100	300	2,655.508	100.00552	400	2,612.211
0.00177	300	2,655.142	100.00976	400	2,611.875
0.00312	300	2,654.537	100.01724	400	2,611.327
0.00552	300	2,653.558	100.03047	400	2,610.488
0.00976	300	2,651.991	100.05385	400	2,609.301
0.01724	300	2,649.652	100.09518	400	2,607.813
0.03047	300	2,646.376	100.16820	400	2,606.216
0.05385	300	2,642.199	100.29726	400	2,604.805
0.09517	300	2,637.507	100.52536	400	2,603.796
0.16820	300	2,633.025	100.92847	400	2,603.211
0.29726	300	2,629.958	101.64091	400	2,602.916
0.52536	300	2,627.513	102.90001	400	2,602.757
0.92848	300	2,626.189	105.12523	400	2,602.641
1.64091	300	2,625.351	109.05790	400	2,602.523
2.90001	300	2,624.781	116.00817	400	2,602.384
5.12523	300	2,624.292	128.29149	400	2,602.209
9.05790	300	2,623.831	150.00000	400	2,601.980
16.00817	300	2,623.378	150.00101	0	2,602.690
28.29149	300	2,622.930	150.00171	0	2,603.186
50.00000	300	2,622.485	150.00290	0	2,604.008
50.00100	350	2,622.396	150.00493	0	2,605.386
50.00177	350	2,622.329	150.00839	0	2,607.637
50.00312	350	2,622.213	150.01428	0	2,611.229
50.00552	350	2,622.014	150.02432	0	2,616.860
50.00975	350	2,621.683	150.04140	0	2,624.732
50.01724	350	2,621.149	150.07048	0	2,634.429
50.03047	350	2,620.342	150.11995	0	2,642.928
50.05385	350	2,619.224	150.20419	0	2,647.668
50.09517	350	2,617.862	150.34757	0	2,649.444
50.16820	350	2,616.451	150.59161	0	2,650.302
50.29726	350	2,615.251	151.00702	0	2,650.942
50.52536	350	2,614.425	151.71411	0	2,651.529
50.92847	350	2,613.958	152.91771	0	2,652.089
51.64091	350	2,613.717	154.96645	0	2,652.632
52.90001	350	2,613.573	158.45372	0	2,653.157
55.12523	350	2,613.452	164.38966	0	2,653.661
59.05790	350	2,613.320	174.49365	0	2,654.134
66.00817	350	2,613.157	191.69235	0	2,654.566
78.29150	350	2,612.949	220.96745	0	2,654.944
100.00000	350	2,612.684	270.79862	0	2,655.257
100.00100	400	2,612.596	355.61975	0	2,655.499
100.00177	400	2,612.528	500.00000	0	2,655.676

Use the trapezoidal rule to calculate pseudopressure.

$$m(p) = 2 \sum_{j=2}^n \frac{1}{2} \left[ \left( \frac{p}{\mu Z} \right)_{j-1} + \left( \frac{p}{\mu Z} \right)_j \right] (p_j - p_{j-1})$$

$$m(p) = \sum_{j=2}^n \left[ \left( \frac{p}{\mu Z} \right)_{j-1} + \left( \frac{p}{\mu Z} \right)_j \right] (p_j - p_{j-1}) \quad (8.157)$$

Normalized pseudopressure is then calculated using equation (7.27), as fluid properties corresponding to initial reservoir pressure are available. Equation (7.27) defines normalized pseudopressure using initial reservoir fluid properties as discussed in Chapter 7 (7.1.2). Using the trapezoidal rule, normalized pseudopressure can be calculated using:

**Table 8.24** Gas Fluid Properties for Exercise 8.5.

Pressure (psia)	Gas viscosity (cp)	Z	Pressure (psia)	Gas viscosity (cp)	Z
14.700	0.01268	0.99854	1,537.812	0.01545	0.88091
75.624	0.01269	0.99253	1,598.737	0.01560	0.87829
136.549	0.01274	0.98658	1,659.661	0.01575	0.87587
197.473	0.01280	0.98070	1,720.586	0.01590	0.87367
258.398	0.01287	0.97489	1,781.510	0.01604	0.87168
319.322	0.01294	0.96917	1,842.435	0.01619	0.86991
380.247	0.01305	0.96352	1,903.359	0.01634	0.86835
441.171	0.01312	0.95798	1,964.284	0.01649	0.86700
502.096	0.01321	0.95252	2,025.208	0.01665	0.86587
563.020	0.01333	0.94717	2,086.133	0.01685	0.86496
623.945	0.01345	0.94193	2,147.057	0.01704	0.86425
684.869	0.01353	0.93681	2,207.982	0.01724	0.86376
745.794	0.01368	0.93181	2,268.906	0.01743	0.86347
806.718	0.01383	0.92693	2,329.831	0.01763	0.86338
867.643	0.01395	0.92220	2,390.755	0.01782	0.86350
928.567	0.01408	0.91760	2,451.679	0.01802	0.86381
989.492	0.01420	0.91316	2,512.604	0.01821	0.86432
1,050.416	0.01431	0.90887	2,573.529	0.01841	0.86501
1,111.341	0.01444	0.90474	2,634.453	0.01860	0.86588
1,172.265	0.01458	0.90078	2,695.377	0.01880	0.86694
1,233.190	0.01472	0.89700	2,756.302	0.01901	0.86816
1,294.114	0.01486	0.89340	2,817.227	0.01922	0.86956
1,355.039	0.01501	0.88998	2,878.151	0.01943	0.87111
1,415.963	0.01516	0.88676	2,939.075	0.01964	0.87283
1,476.888	0.01530	0.88373	3,000.000	0.01985	0.87469

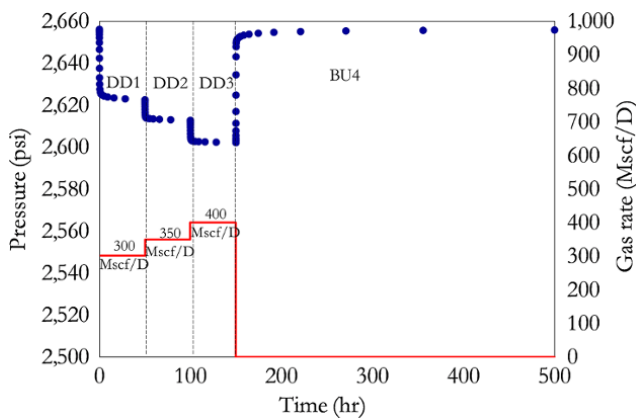


**Figure 8.129** Pressure–rate history with defined flow periods.

$$m_n(p) = \frac{\mu_i Z_i}{2p_i} \sum_{j=2}^n \left[ \left( \frac{p}{\mu Z} \right)_{j-1} + \left( \frac{p}{\mu Z} \right)_j \right] (p_j - p_{j-1}) \tag{8.158}$$

The normalized pseudopressure calculation for Exercise 8.5 is shown in Table 8.25.

*Well Test Diagnosis and Defining the Interpretation Model*

Create a log-log diagnostic plot using the steps discussed in Exercise 8.1. However, in this calculation  $m_n(p)$  will be used instead of pressure. As discussed in Section 8.4.3, the independent variable for the derivative for flow-after-flow or variable rate should be *ln radial superposition function* ( $f_{ln\_radial}$ ) expressed in equation (8.15) and defined as:

$$f_{ln\_radial}(t) = \sum_{i=1}^n \frac{(q_i - q_{i-1})}{(q_{n-1} - q_n)} \ln(t - t_{i-1}).$$

The choice of  $f_{ln\_radial}(t)$  as the independent variable for the derivative ensures radial flow stabilization,  $\Delta p'_{rad}$  equals  $0.4342 m_{RF}$ , which is the same for a derivative for first drawdown taken with respect to  $\ln(\Delta t)$  and the derivative of the first buildup following the first drawdown taken with respect to  $\ln\left(\frac{t_p + \Delta t}{\Delta t}\right)$ .

From the diagnosis, as shown in Fig. 8.130, the reservoir–well system can be described as: an infinitely acting radial homogeneous gas reservoir with wellbore storage and skin.

**Table 8.25** Normalized Pseudopressure Calculation for Exercise 8.5.

p (psia)	μ (cp)	Z	μZ	$\frac{p}{\mu Z}$ (psia/cp)	$\left[ \left( \frac{p}{\mu Z} \right)_{j-1} + \left( \frac{p}{\mu Z} \right)_j \right] (p_j - p_{j-1})$ (psia <sup>2</sup> /cp)	$m(p) = \sum_{j=2}^n \left[ \left( \frac{p}{\mu Z} \right)_{j-1} + \left( \frac{p}{\mu Z} \right)_j \right] (p_j - p_{j-1})$ (psia <sup>2</sup> /cp)	$m_n(p) = m(p) \frac{\mu_i Z_i}{2p_i}$ (psia)
14.700	0.01268	0.99854	0.012662	1.161E+03	0.00E+00	0.00E+00	0.00
139.087	0.01274	0.98633	0.012567	1.107E+04	1.52E+06	1.52E+06	2.55
263.475	0.01288	0.97441	0.012548	2.100E+04	3.99E+06	5.51E+06	9.23
387.862	0.01306	0.96283	0.012574	3.085E+04	6.45E+06	1.20E+07	20.04
512.250	0.01322	0.95162	0.012581	4.071E+04	8.90E+06	2.09E+07	34.95
636.638	0.01346	0.94086	0.012664	5.027E+04	1.13E+07	3.22E+07	53.91
761.025	0.01372	0.93058	0.012767	5.961E+04	1.37E+07	4.58E+07	76.81
885.412	0.01399	0.92084	0.012883	6.873E+04	1.60E+07	6.18E+07	103.56
1,009.800	0.01423	0.91171	0.012977	7.781E+04	1.82E+07	8.00E+07	134.10
1,134.188	0.01449	0.90324	0.013090	8.665E+04	2.05E+07	1.00E+08	168.37
1,258.575	0.01478	0.89548	0.013232	9.511E+04	2.26E+07	1.23E+08	206.25
1,382.963	0.01508	0.88848	0.013394	1.033E+05	2.47E+07	1.48E+08	247.59
1,507.350	0.01538	0.88229	0.013567	1.111E+05	2.67E+07	1.74E+08	292.27
1,631.737	0.01568	0.87695	0.013750	1.187E+05	2.86E+07	2.03E+08	340.15
1,756.125	0.01598	0.87248	0.013943	1.259E+05	3.04E+07	2.33E+08	391.13
1,880.512	0.01628	0.86891	0.014148	1.329E+05	3.22E+07	2.66E+08	445.08
2,004.900	0.01659	0.86622	0.014369	1.395E+05	3.39E+07	3.00E+08	501.86
2,129.287	0.01699	0.86443	0.014682	1.450E+05	3.54E+07	3.35E+08	561.16
2,253.675	0.01738	0.86352	0.015011	1.501E+05	3.67E+07	3.72E+08	622.68
2,378.063	0.01778	0.86346	0.015352	1.549E+05	3.79E+07	4.10E+08	686.25
2,502.450	0.01818	0.86422	0.015709	1.593E+05	3.91E+07	4.49E+08	751.73
2,626.837	0.01858	0.86576	0.016082	1.633E+05	4.01E+07	4.89E+08	818.97
2,751.225	0.01899	0.86805	0.016487	1.669E+05	4.11E+07	5.30E+08	887.79
2,875.613	0.01942	0.87104	0.016917	1.700E+05	4.19E+07	5.72E+08	957.99
3,000.000	0.01985	0.87469	0.017363	1.728E+05	4.26E+07	6.14E+08	1,029.43

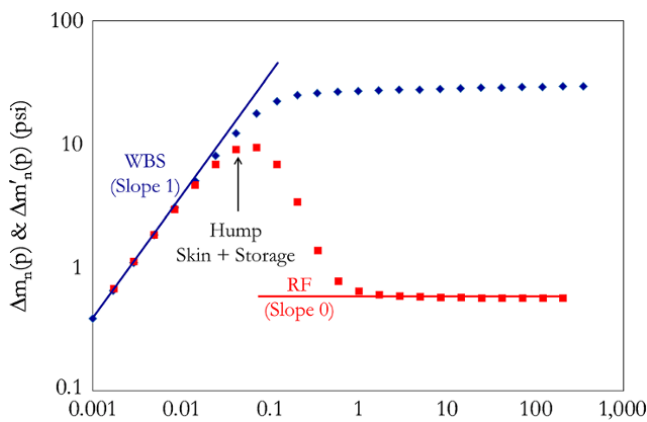


**Figure 8.130** Well test diagnosis showing flow regimes for BU4.

*Calculating Initial Well Test Parameters*

Calculate  $p_i$  from a superposition plot and derivative.

Note that the derivative in the diagnostic plot (Fig. 8.130 and Fig. 8.131a) was taken with respect to  $f_{ln\_radial}$  while the superposition function Fig. 8.131b was plotted against  $f_{log\_radial}$ .

Pick a start and end of the radial flow (any two points on radial flow stabilization on derivative) defined as  $RF_1$  and  $RF_2$  as shown in Fig. 8.131a.

Use the corresponding radial flow points ( $RF_1$  and  $RF_2$ ) from the derivative to fit a straight-line on the superposition function plot (Fig. 8.131b) and extrapolate to  $f_{log\_radial} = 0$  to get  $m_n(p)^*$  on the vertical axis (Fig. 8.131a).

Since the reservoir is infinite acting in behavior:

$$m_n(p)^* = m_n(p)_i = 835.1 \text{ psi}$$

Using the pseudopressure table to convert  $m_n(p)_i$  to  $p_i$ :

$$p_i = 2656 \text{ psia}$$

From Fig. 8.132,  $m_{WBS} = 378.40 \text{ psi/hr}$ .

From equation (8.156),  $C = 7.42 \frac{Z_i T_i p_{sc} q_g}{p_i T_{sc} m_{WBS}}$

Hence

$$C = 7.42 \frac{0.89 \times 694.67 \times 14.7 \times 400}{2656 \times 520.67 \times 378.4} = 0.051 \text{ bbl/psi}$$

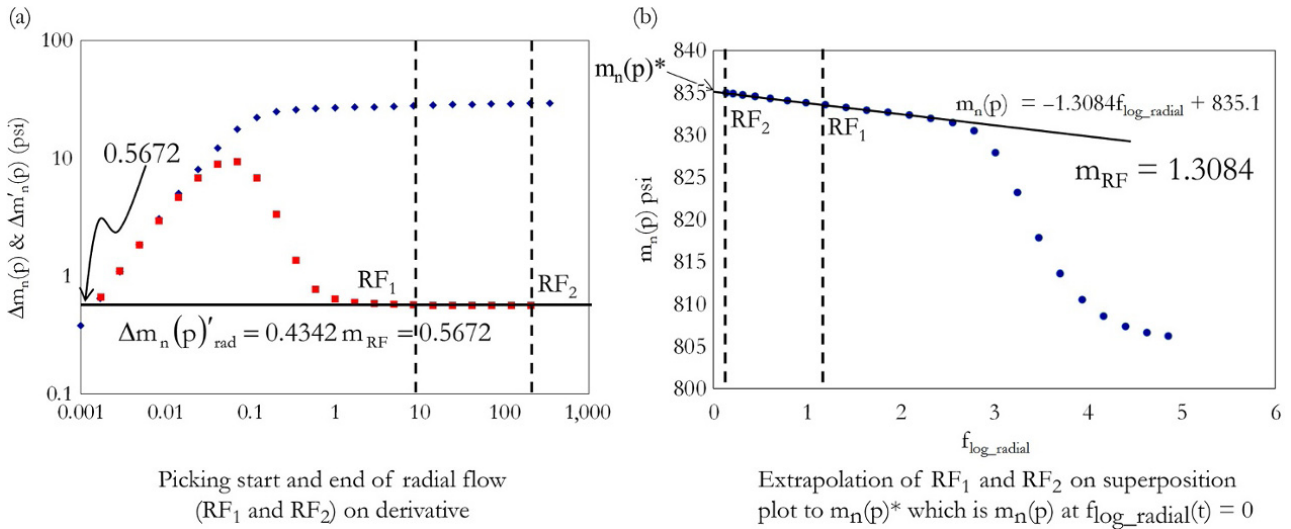


Figure 8.131 Calculation of  $p^*$  using the derivative and superposition function plots for BU4.

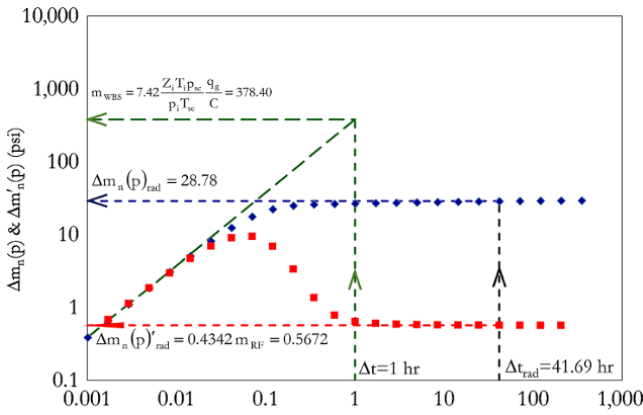


Figure 8.132  $C$ ,  $S'$  and  $k_r$  calculation from the derivative plot.

Also from Fig. 8.132,

$$\Delta m_n(p)'_{rad} = 0.4342 m_{RF} = 0.5672 \text{ psi}$$

$$m_{RF} = \frac{0.5672}{0.4342} = 1.306 \text{ psi/logcycle}$$

Note that  $m_{RF}$  determined from the derivative (1.306 psi/log cycle) is consistent with that from the superposition plot (1.308 psi/log cycle) as shown in Fig. 8.131b.

From equation (8.154)

$$m_{RF} = 28.95906 \times 10^3 \frac{Z_i T_i p_{sc} q_g \mu_i}{p_i T_{sc} k_r h}$$

$$k_r = 28.95906 \times 10^3 \frac{Z_i T_i p_{sc} q_g \mu_i}{p_i T_{sc} m_{RF} h}$$

$$k_r = 28.95906 \times 10^3 \frac{0.89 \times 694.67 \times 14.7400 \times 0.01}{2656 \times 520.67 \times 1.31 \times 45} = 12.9 \text{ mD}$$

$$k_r = 13 \text{ mD}$$

Skin calculation in a gas well is different from that of oil as shown in equations (8.153) and (8.155). Skin calculated from a derivative plot or superposition plot is apparent skin defined by equation (8.155):

$$S' = S_w + D(q_i + q_{i+1})$$

Therefore, at least two skin values from different flow periods are required to determine mechanical skin effect ( $S_w$ ). Also, the calculation gives a non-Darcy skin coefficient,  $D$ . Equation (8.23) is extended for calculating apparent skin effect ( $S'$ ) for a gas well test.

For slightly compressible fluid such as oil, from equation (8.23), the skin effect is:

$$S = 1.15 \left( \frac{0.4342 \Delta p_{rad}}{\Delta p'_{rad}} - \log \frac{k}{\phi \mu c_r r_w^2} + [f_{log\_radial}(\Delta t_{rad}) - f_{log\_radial}(\Delta t_{1hr})] + 3.23 \right)$$

For single-phase gas flow, the apparent skin effect for each flow period is:

$$S' = 1.15 \left( \frac{0.4342 \Delta m_n(p)_{rad}}{\Delta m'_n(p)_{rad}} - \log \frac{k}{\phi \mu c_r r_w^2} + [f_{log\_radial}(\Delta t_{rad}) - f_{log\_radial}(\Delta t_{1hr})] + 3.23 \right) \quad (8.159)$$

where  $f_{log\_radial}(\Delta t_{rad})$  is the value of the superposition function taken at  $\Delta t_{rad}$  hours and  $f_{log\_radial}(\Delta t_{1hr})$  the value of superposition function taken at  $\Delta t = 1$  hr.

Using  $DD1$ ,  $DD2$ ,  $DD3$

When comparing more than one log-log diagnostic plot, rate normalized pressure change and derivative should be used, as discussed in Section 8.4.3.2.

From Fig. 8.133,  $\frac{\Delta m_n(p)_{rad}}{\Delta m'_n(p)_{rad}}$  is determined and substituted into equation (8.159) to determine apparent skin ( $S'$ ). Table 8.26 summarizes the calculation of apparent skin from three drawdown flow periods.

To determine  $S_w$  and  $D$ , plot  $S'$  against  $q_i+q_{i-1}$  (Fig. 8.134).

From Fig. 8.134:

$$D = 0.40 (1/Mscf/D) \text{ and } S_w = 2$$

*Forward Simulation*

$$p_D = \frac{kh}{141.2qB\mu} \Delta p$$

$$B_{gi} = 0.1781 \times 10^3 \frac{Z_i T_i p_{sc}}{p_i T_{sc}} (\text{bbl/Mscf})$$

$$m_n(p)_D = \frac{kh}{141.2qB\mu} \Delta m_n(p)$$

$$m_n(p)_D = \frac{kh}{0.1781 \times 10^3 \times 141.2q\mu} \frac{p_i T_{sc}}{Z_i T_i p_{sc}} \Delta m_n(p)$$

Hence, for normalized pseudopressure,

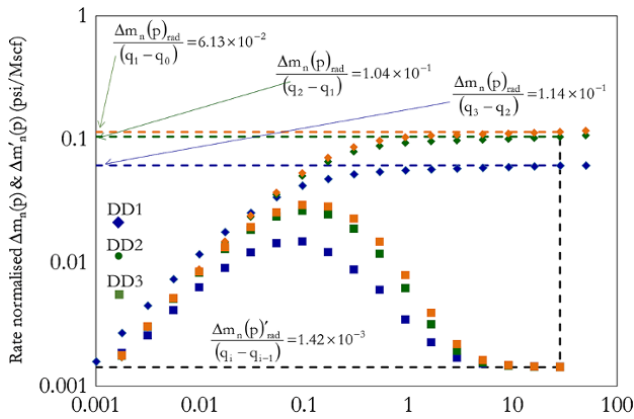


**Figure 8.133** Rate normalized  $\Delta m_n(p)$  and  $\Delta m'_n(p)$ .

$$m_n(p)_D = \frac{kh}{25.14772 \times 10^3 q\mu} \frac{p_i T_{sc}}{Z_i T_i p_{sc}} \Delta m_n(p) \quad (8.160)$$

$$t_D = \frac{0.000264k}{\phi\mu c_i r_w^2 \Delta t, \text{fortime}} \quad (8.161)$$

$$C_D = \frac{0.8936}{\phi c_i h r_w^2 C, \text{forwellbore storage}} \quad (8.162)$$

$$r_D = \frac{r}{r_w}, \text{for radial distance} \quad (8.163)$$

Forward simulation of a well test analytical model is discussed in Exercises 8.2 and 8.4. Forward simulation of a gas well test will be carried out in normalized pseudopressure, with skin effect defined for each flow period using the apparent skin relationship in equation (8.155). Simulated normalized pseudopressure response will then be converted to pressure using pressure against a normalized pseudopressure table (Table 8.25). Forward simulation for Exercise 8.5 is shown in Fig. 8.135:

In this exercise, since there is a good match between test data and simulated data, there is no need to refine the match with regression.

The final results, summarized in Tables 8.27 and 8.28, are the interpretation model and parameters that define this interpretation model.

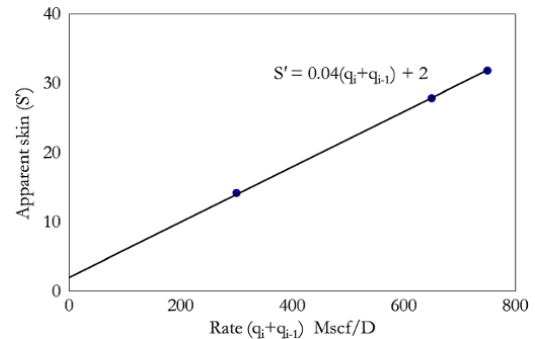


**Figure 8.134** Determination of mechanical skin effect ( $S_w$ ) and non-Darcy coefficient ( $D$ ).

**Table 8.26** Apparent Skin Calculation for Exercise 8.5.

Flow period	q Mscf/D	q <sub>i</sub> +q <sub>i-1</sub> Mscf/D	Δt <sub>rad</sub> hrs	$\frac{\Delta m_n(p)_{rad}}{q_i - q_{i-1}}$ psi/Mscf/D	$\frac{\Delta m'_n(p)_{rad}}{q_i - q_{i-1}}$ psi/Mscf/D	$\frac{0.4342\Delta m_n(p)_{rad}}{\Delta m'_n(p)_{rad}}$	$f_{log\_radial}(\Delta t_{rad})$	$f_{log\_radial}(\Delta t_{1hr})$	S'
DD1	300	300	28.219	6.13E-02	1.42E-03	18.75	1.45	-0.0074	14.16
DD2	350	650	28.219	1.04E-01	1.42E-03	31.76	12.81	10.2380	27.84
DD3	400	750	28.219	1.14E-01	1.42E-03	34.90	15.99	13.7261	31.80

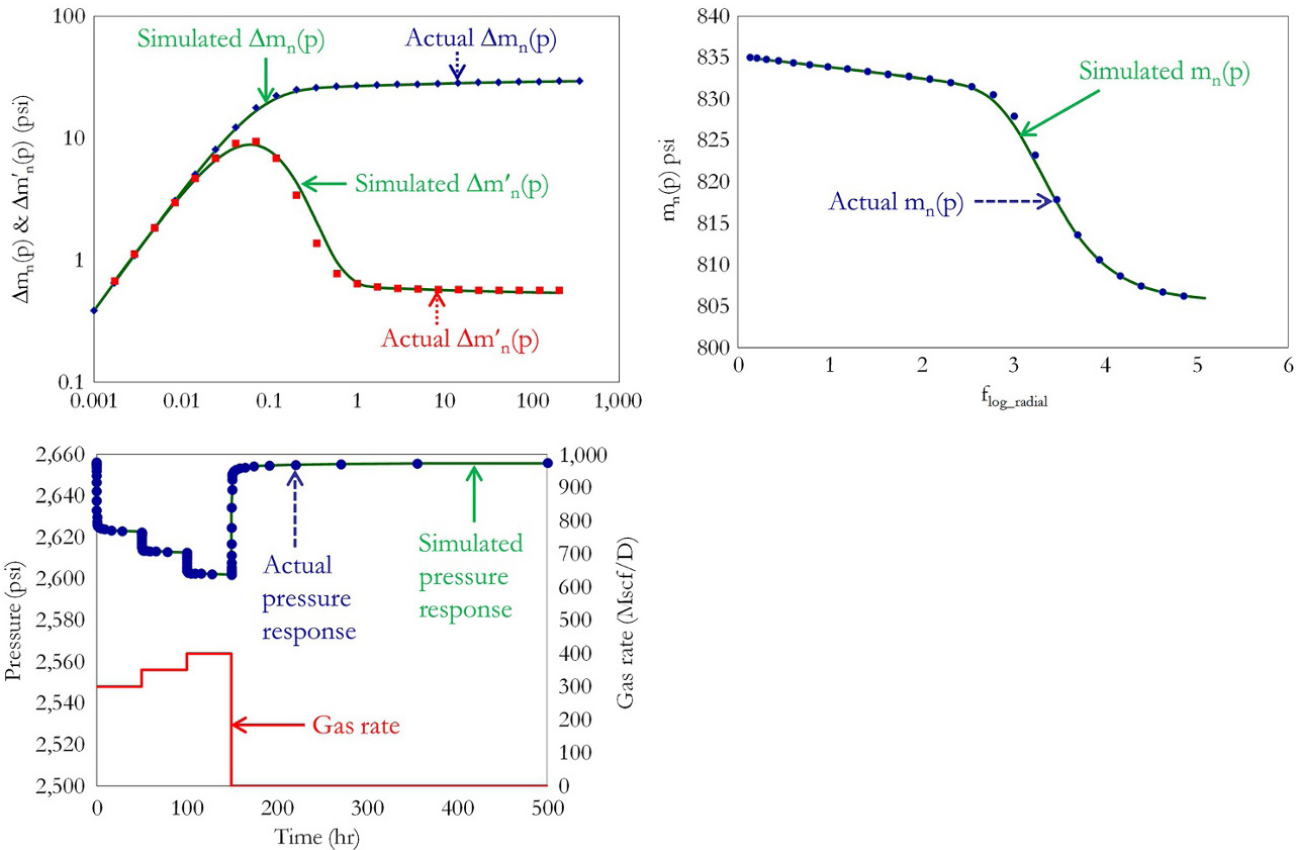


Figure 8.135 Summary of forward simulation for Exercise 8.5.

Table 8.27 Well test interpretation model for Exercise 8.5.

Model
Gas well with C and S
Homogeneous reservoir behavior
Infinite acting

Table 8.28 Well test interpretation parameters for Exercise 8.5.

Parameter	Value
$p_i$	835.1 psia
$k_r$	13 mD
C	0.051 bbl/psi
S	2
D	0.40 D/Mscf

### 8.8. EFFECT OF DEPLETION ON WELL TEST ANALYSIS IN GAS RESERVOIRS

When pseudosteady state has been reached, boundaries and the area defining the reservoir can be determined. The distances to the boundaries depend on  $c_t$ , as show in equations (7.118) and (7.119), and so does the area and in-place volume determined from well test analysis. In oil production, this assumption of constant  $c_t$  is often reasonable for well test analysis. However, in gas reservoirs, this may not be the case. Well test analysis disregards the changing  $c_t$  during pseudosteady state (depletion) and low drawdown pressure in gas production.

In order to ensure that in-place volume determined from well test analysis in a gas reservoir during pseudosteady state is consistent with in-place volume determined

using material balance calculation,  $c_t$  in the well test can be adjusted/corrected to capture the dependence of  $c_t$  on depletion. Two approach that can be used to adjust  $c_t$  in a gas well test analysis to capture the effect of depletion are: *pseudotime transform* and *material balance (p/Z) correction*.

#### 8.8.1. Pseudotime Transform

The pseudotime transform equation (8.164) can be used to deal with changing compressibility ( $c_t$ ), gas viscosity ( $\mu_g$ ) and total porosity ( $c_t$ ) with time and pressure:

$$t_A = \int_{t_0}^t \frac{dt}{\mu(p)c_t(p)} \tag{8.164}$$



Substituting equation (8.164) into the diffusivity equation for gas (equation (7.23)):

$$\frac{1}{r} \frac{\partial}{\partial r} \left( r \frac{\partial m_n(p)}{\partial r} \right) = \frac{\phi \mu c_t}{k} \frac{\partial m_n(p)}{\partial t_A} \quad (8.165)$$

Using the pseudotime approach for well test analysis involves creating a table of pseudotime against time, in a similar way to creating table of pseudopressure against pressure for pseudopressure transform as shown in Exercise 8.5. Generated pseudotime instead of time will then be used for well test analysis.

Pseudotime, like pseudopressure, can be normalized so that normalized pseudotime retains the unit of time like normalized pseudopressure has a unit of pressure in equation 7.28. Normalized pseudotime is thus defined as:

$$t_{An} = \mu_i c_{ti} \int_{t_0}^t \frac{dt}{\mu(p) c_t(p)} \quad (8.166)$$

where

$\mu(p)$  is gas viscosity as a function of pressure ( $p$ ),  $c_t(p)$  is total compressibility as a function of pressure ( $p$ ),  $\mu_i$  is gas viscosity at  $p_i$ , and  $c_{ti}$  is total reservoir compressibility at  $p_i$ .

### 8.8.2. Material Balance Correction

This is also called the  $\frac{p}{Z}$  correction approach for dealing with changing compressibility( $c_t$ ) and viscosity ( $\mu_g$ ) during pseudosteady state gas production. It is based on the principle that depletion of a normally pressured dry gas reservoir will follow a linear trend of  $\frac{p}{Z}$  against cumulative gas produced ( $G_p$ ) (Fig. 8.136). Hence, average reservoir pressure and corresponding compressibility and viscosity can be determined at each time step defined by cumulative gas produced. Compressibility and viscosity for each flow period are replaced by determined values from material balance at calculated average formation pressure.

Average formation pressure is determine using equation (12.62):

$$\bar{p}\bar{Z} = - \frac{p_i G_p(p = \bar{p})}{Z_i G} + \frac{p_i}{Z_i}$$

which can be rearranged as:

$$\bar{p}\bar{Z} = \frac{p_i}{Z_i} \left( \frac{G - G_p(p = \bar{p})}{G} \right) \quad (8.167)$$

where  $G_p$  is cumulative gas produced determined from production/test rate and time of production,  $G$  is initial gas in place,  $p_i$  is initial formation pressure,  $Z_i$  is initial z-compressibility factor,  $\bar{Z}$  is average Z factor at cumulative gas production  $G_p$ , and  $\bar{p}$  is average reservoir pressure at cumulative gas production  $G_p$ .

With  $\bar{p}$  determined at each time step, gas compressibility ( $c_g$ ) can be determined using a fluid property model or

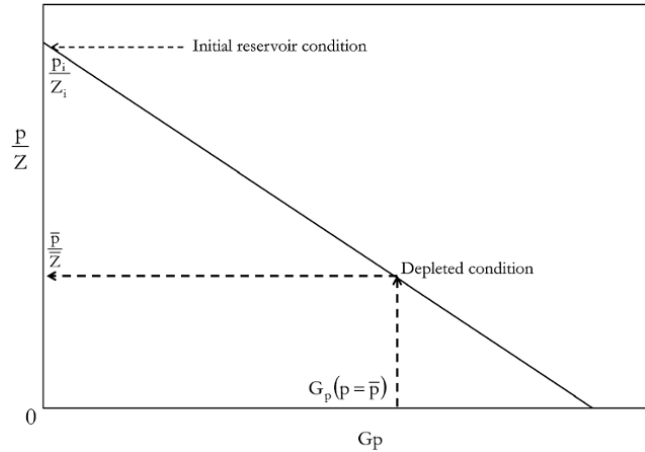


**Figure 8.136**  $p/Z$  plot for correcting the effect of depletion in gas well testing.

the isothermal compressibility of real gas defined in equation 3.17 and expressed as:

$$c_g(p = \bar{p}) = \frac{1}{\bar{p}} - 1\bar{Z} \left( \frac{\partial \bar{Z}}{\partial p} \right)_{\bar{p}} \quad (8.168)$$

Gas viscosity ( $\mu_g$ ) too can be determined at  $\bar{p}$  using appropriate gas viscosity model.

## 8.9. MULTIPHASE WELL TEST ANALYSIS

Multiphase flow when it occurs during well testing affects the relative mobility of the reservoir fluid of preference and, therefore, the well performance. The relative mobility of the reservoir fluid of interest depends on phase viscosity, saturation, and relative permeability.

Well test analysis methods for multiphase fluid flow are either based on the *Perrine–Martin* assumption or *pseudopressure transformations*, which are similar to the concept used in gas well test analysis discussed in Section 8.7. A major challenge with use of the pseudopressure transform approach for well test analysis of oil and gas below saturation pressure is the need for the relative permeability against saturation relationship (relative permeability model) and the pressure against saturation relationship (from constant volume depletion (CVD) fluid experiment), which may not be available. The combination of the relative permeability against saturation relationship and pressure against saturation relationship is to establish a relationship between relative permeability and pressure, which is required in the pseudopressure transform integral.

### 8.9.1. Perrine–Martin Approach

The Perrine-Martin concept [*Perrine, 1956; Martin, 1959*] involves replacing single-phase compressibility, mobility, and rate with the saturation weighted compressibility of all phases, sum of mobility of all phases, and *total*

equivalent rate, respectively, in the well test equation and models. This concept is valid for uniform distribution of all phases and situations with small saturation gradients.

Total equivalent rate (total bottomhole flow rate), which is the sum of the bottomhole flow rate of all phases at bottomhole condition, should be used for the Perrine–Martin approach and is defined as:

$$(qB)_t = q_o B_o + q_w B_w + q_g B_g$$

$q_g B_g$  (gas produced at bottomhole) above can be expressed in terms of surface gas rate  $q_{sc}$  and solution gas-oil-ratio ( $R_s$ ). Hence,  $(qB)_t$  becomes:

$$(qB)_t = q_o B_o + q_w B_w + (q_{sc} - R_s) B_g \quad (8.169)$$

Total mobility determined from well test analysis for multiphase well test analysis using the Perrine–Martine concept is defined as:

$$\left(\frac{k}{\mu}\right)_t = \frac{k_o}{\mu_o} + \frac{k_w}{\mu_w} + \frac{k_g}{\mu_g} \quad (8.170)$$

Saturation weighted compressibility is defined in equation 7.12.

### 8.9.2. Raghavan's Pseudopressure Transformation

Raghavan's pseudopressure transformation [Raghavan, 1976] which is based on Evinger and Muskat's multiphase flow equation [Evinger and Muskat, 1942] for calculating a theoretical productivity factor for oil wells producing by solution gas drive, can be used for well test analysis in oil reservoirs producing below the bubble point pressure. The pressure transformed is then analyzed to obtain the absolute formation permeability. Raghavan's pseudopressure transformation is defined as:

$$m(p) = 2 \int_{p_0}^p \frac{k_{ro}}{\mu_o B_o} dp \quad (8.171)$$

where  $k_{ro}$  is the relative permeability of the oil phase,  $\mu_o$  is the viscosity of the oil phase,  $B_o$  is the oil formation volume factor, and  $p_0$  is any low reference pressure.

This approach requires a relative permeability against saturation relationship (relative permeability model) and a pressure against saturation relationship (from CVD fluid experiment).

### 8.9.3. Jones and Raghavan

The Jones and Raghavan pseudopressure transformation is used for well test analysis in gas condensate reservoirs producing below the dew point pressure. This concept is similar to that of Raghavan's pseudopressure transformation for oil wells producing by solution gas drive. Jones and Raghavan's pseudopressure transformation is expressed as [Jones and Raghavan, 1988]:

$$m(p) = 2 \int_{p_0}^p \left( \rho_o \frac{k_{ro}}{\mu_o} + \rho_g \frac{k_{rg}}{\mu_g} \right) dp \quad (8.172)$$

where  $k_{ro}$  is the relative permeability of the oil phase,  $k_{rg}$  is the relative permeability of the gas phase,  $\rho_o$  is the density of the oil phase,  $\rho_g$  is the density of the gas phase,  $p_0$  is any low reference pressure,  $\mu_o$  is the viscosity of oil phase, and  $\mu_g$  is the viscosity of the gas phase.

This approach, like Raghavan's pseudopressure transformation for oil below saturation pressure, requires a relative permeability against saturation relationship (relative permeability model) and pressure against saturation relationship (from CVD fluid experiment).

## 8.10. WELL TEST ANALYSIS USING FORMATION TEST DATA

Pressure and rate measurements from formation testing (using formation testers) can be used for well test analysis as they satisfy requirements for well test analysis, which are: (i) rate measurement, (ii) rate control, and (iii) pressure measurement. Diagnosis of formation test data for well test analysis will generally yield: flowline storage effect (similar to wellbore storage effect), skin effect, spherical flow behavior (relating to spherical mobility), and radial flow behavior (relating to radial mobility) where it manifests.

Use of wireline formation for pressure transient analysis may create a drawback when a test is completely dominated by a spherical flow regime, with radial flow not manifesting. In situations where this occurs, formation horizontal permeability ( $k_{xy}$ ) becomes indeterminate and only spherical permeability can be determined. In order to increase the chances of having a defined radial flow behavior for radial permeability calculation, a pump (using pump module) can be used for an extended pump-out test to give a significant radius of investigation away from the spherical dominated regime, long enough for radial flow to manifest during buildup analysis following pump-out.

Fig. 8.137 shows the pressure–rate history from Exercise 6.1. A detailed workflow for analysis of well test (pressure transient) data is discussed in Section 8.3. Analysis of final buildup and a match to the entire formation test pressure response is shown in Fig. 8.138.

## 8.11. ANALYSIS OF VERTICAL INTERFERENCE TEST (VIT) FROM FORMATION TESTER

Formation testers can be configured for vertical interference testing (VIT) in probe–probe configuration (Fig. 8.139) or probe–packer configuration (Fig. 8.140).

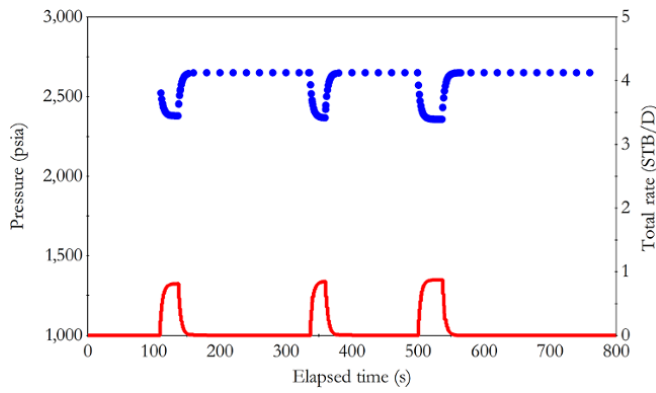


Figure 8.137 Pressure–rate history for Exercise 6.1.

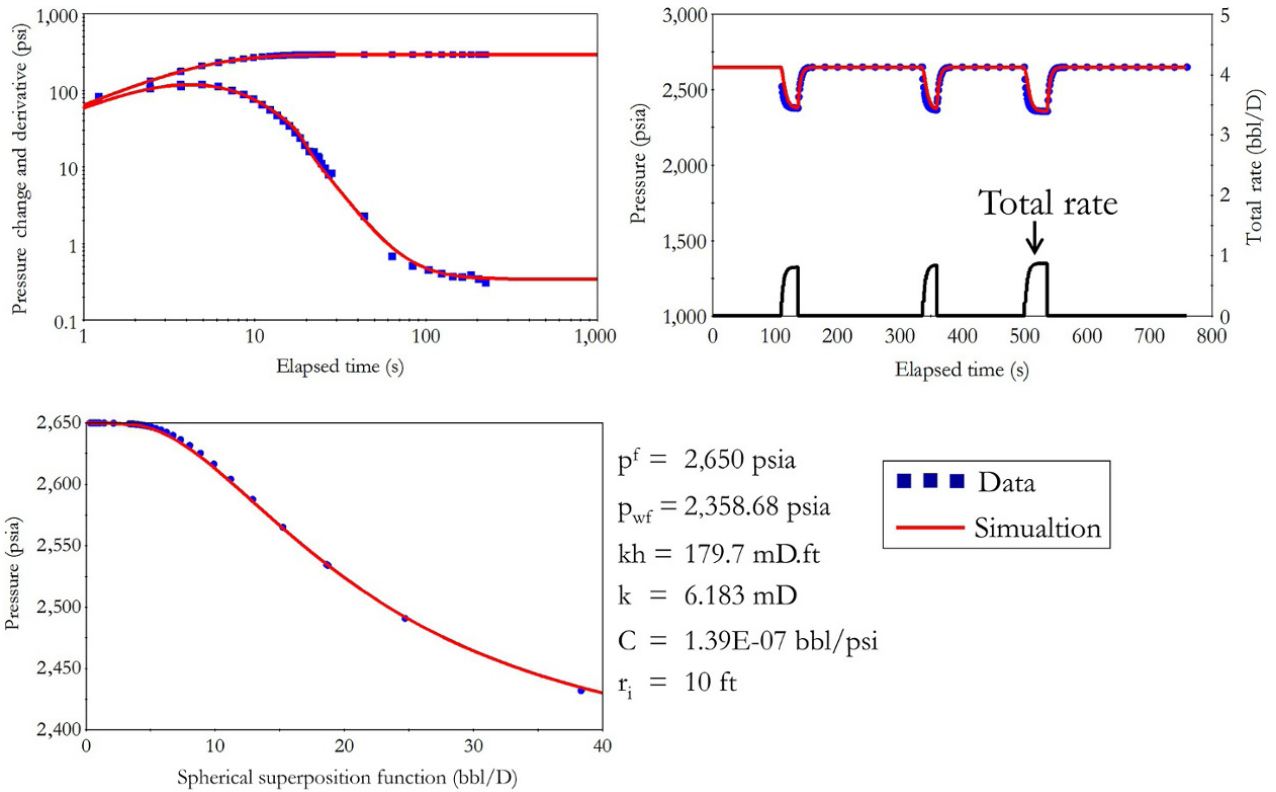


Figure 8.138 Pressure transient analysis of formation probe test from Exercise 6.1.

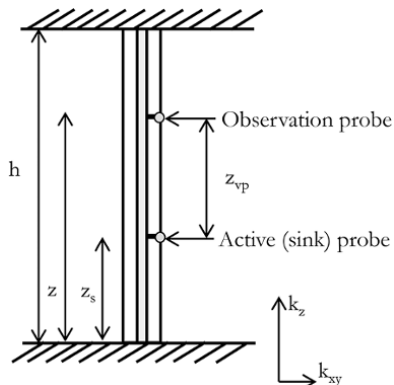


Figure 8.139 Probe–probe configuration for VIT.

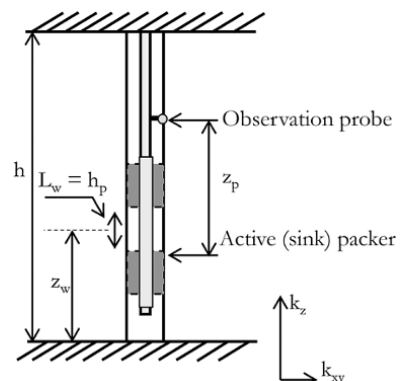
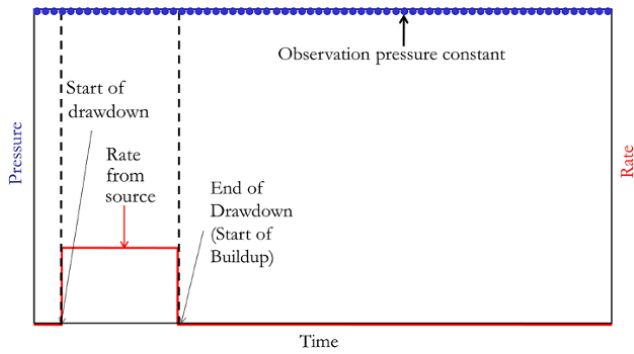
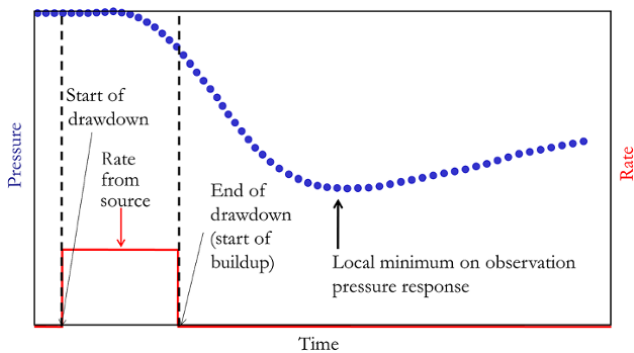


Figure 8.140 Probe–packer configuration for VIT.



**Figure 8.141** Observation probe response for nonarrival of pulse or noncommunicating zones.



**Figure 8.142** Observation probe response for communicating zones.

As mentioned in Chapter 6 (6.2.8), the objectives of carrying out vertical interference testing include: assessing vertical hydraulic communication, average vertical reservoir permeability, lateral continuity of shales, and reservoir layering behavior.

Fig. 8.141 shows a typical response of an observation probe (sink) when diffusing pressure from an active probe or packer (source) has not reached the observation probe or the case when zones with active probe/packer and observation probe are not in hydraulic communication.

Fig. 8.142 shows the response of an observation probe when diffusing pressure from an active probe/packer has reached it and, hence, the zones with active probe/packer and observation probe are in hydraulic communication.

Fig. 8.143 shows a typical well test diagnostic plot of pressure from the observation probe when the active probe/packer and observation probe are in hydraulic communication. The log-log derivative plot has a characteristic “V” shape, which is due to a local minimum in the observation pressure response shown in Fig. 8.142. Although part of the pressure response plot in Fig. 8.142 before the local minimum has a negative derivative, only positive derivative values are displayed on the log-log

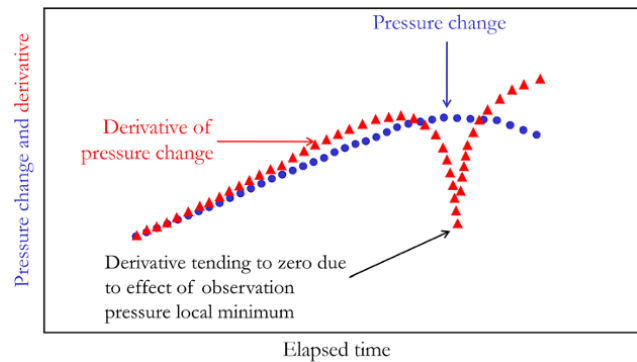


**Figure 8.143** Well test diagnostic plot for observation response in communicating zones.

derivative plot. At local minimum, the pressure derivative will tend to zero as shown in Fig. 8.143.

The elapsed time the local minimum in Fig. 8.142 occurs or elapsed time when “V” was reached from a derivative (Fig. 8.143) is dependent on formation  $\frac{k_z}{k_{xy}}$  for a fixed probe–probe or probe–packer spacing. When  $\frac{k_z}{k_{xy}}$  is low, pressure pulse propagation from the active source travels in an elliptical pattern taking a very long time to reach the observation probe. This is the case for a lot of VIT. Even when probe–probe or probe–packer spacing is reduced, it may take a long time for pressure diffusion from an active source to reach the observation probe. This is the reason why VITs are not as common as other formation testing methods. However, when  $\frac{k_z}{k_{xy}}$  is high, pressure pulse propagation from the active source travels in a spherical or hemispherical pattern, reaching the observation probe much faster than the case with low  $\frac{k_z}{k_{xy}}$ .

Note: In vertical wells,  $x$ – $y$  permeability ( $k_{xy}$ ) can be replaced with radial permeability ( $k_r$ ).

### 8.11.1. Analysis of Vertical Interference Test

Analysis of vertical interference test data involves matching model prediction to measured active and observation pressure response.

For a probe–probe configuration (Fig. 8.139), which is made up of active and observation probes, the active probe response model has been described in Chapter 6 (6.2.1) and Section 8.10, while the observation probe response is described in Sections 8.11.1.1 and 8.11.1.2.

For a probe–packer configuration (Fig. 8.140), which is made up of an active packer (source) and an observation probe, the solution for the active packer is the *limited*

entry (partial penetration) interpretation model described in Section 8.5.1.7, while the observation probe response is described in Section 8.11.1.3.

**8.11.1.1. Observation Probe Without Confinement.**

The pressure response of a vertical observation probe for a probe–probe configuration (Fig. 8.139) when the confining vertical barriers that define the top and bottom for the formation have not been reached by diffusing pressure can be described as *infinite acting confining boundaries* or simply as a formation without confinement. Dimensionless pressure for a vertical observation probe without confinement can be expressed as [Goode and Thambynayagam, 1992]:

$$p_{DOS} = \frac{1}{2\sqrt{\pi}} \int_0^{t_D} \frac{e^{-\left(\frac{z_{vp}^2}{4\beta r_w^2 \left(\frac{k_z}{k_r}\right)}\right)}}{\beta^{1.5}} G_o(\beta) d\beta \quad (8.173)$$

where

$$p_{DOS} = \frac{(p_i - p_{vp(t)}) 4\pi k_r \bar{k}_w}{q\mu} \text{ in consistent units}$$

$p_{vp}$  is the pressure response of the vertical observation probe

$$G_o(\beta) = \frac{8}{\pi^2} \sum_{n=-\infty}^{\infty} \int_0^{\infty} \frac{\beta e^{-\alpha^2 \beta}}{\alpha (J'_n(\alpha)^2 + Y'_n(\alpha)^2)} d\alpha$$

$$t_D = \frac{k_r \Delta t}{\phi \mu c_t r_w^2} \text{ in consistent units}$$

$$\bar{k} = \sqrt{k_r k_z}$$

For computational efficiency, tabulated values of  $G_o(\beta)$ , as shown in Table 8.29, can be used [Stewart, 2012].

**8.11.1.2. Observation Probe With Confinement.** By using a method of images on probe–probe configuration without confinement, an expression for the vertical

**Table 8.29** Values of  $G_o(\beta)$  [Stewart, 2012].

Log10( $\beta$ )	$G_o(\beta)$
-3	1.972
-2	1.913
-1.5	1.858
-1	1.7645
-0.5	1.6272
0	1.4458
0.5	1.2371
1	1.0684
1.5	1.0036
2	0.9939
2.5	0.9963
3	0.9962

observation probe for a probe–probe configuration with confinement (Fig. 8.139) can be derived [Goode and Thambynayagam, 1992]. The use of images for including the effect of boundaries on pressure transient behavior is discussed in Section 8.5.1.12. Equation (8.174) shows the pressure response for the vertical observation probe with top and bottom vertical confining flow barriers.

$$p_{DCO} = \frac{1}{2\sqrt{\pi}} \int_0^{t_D} \sum_{i=-\infty}^{\infty} \left[ \left( \frac{e^{-\gamma_1(i,\beta)}}{\beta^{1.5}} + \frac{e^{-\gamma_2(i,\beta)}}{\beta^{1.5}} \right) G_o(\beta) \right] d\beta \quad (8.174)$$

where

$$p_{DCO} = \frac{(p_i - p_{vp(t)}) 2\pi k_r h}{q\mu} \text{ in consistent units}$$

$$\gamma_1(i,\beta) = \frac{[z - (2hi - z_s)]^2}{4\beta r_w^2 \left(\frac{k_v}{k_r}\right)} \text{ and } \gamma_2(i,\beta) = \frac{[z - (2hi + z_s)]^2}{4\beta r_w^2 \left(\frac{k_v}{k_r}\right)}$$

The relationship between the dimensionless pressure response of a vertical observation probe without confinement ( $p_{DOS}$ ) and dimensionless pressure response of a vertical observation probe with confinement ( $p_{DCO}$ ) is expressed as:

$$p_{DCO} = \frac{(p_i - p_{vp(t)}) 2\pi k_r h}{q\mu} = \frac{h}{2r_w \sqrt{\frac{k_v}{k_r}}} p_{DOS}$$

$$p_{DCO} = \frac{h}{2r_w \sqrt{\frac{k_v}{k_r}}} p_{DOS} \quad (8.175)$$

**8.11.1.3. Observation Probe With Active Packer.**

Fig. 8.140 shows the probe–packer configuration for VIT. The pressure response for the observation probe with packers as source can be expressed by equation (8.176) [Abbaszadeh and Hegeman, 1990]:

$$p_{DO} = \frac{1}{4} \int_0^{t_D} \frac{e^{-\frac{t}{4\tau_D}}}{\tau_D} \left[ 2 + \frac{8h_D}{\pi L_{WD}} \sum_{m=1}^{\infty} \frac{e^{-\frac{t}{4\tau_D}}}{m} \cos(D) \sin(E) \cos(F) \right] d\tau_D \quad (8.176)$$

where dimensionless parameters in consistent units are:

$$p_{DO} = \frac{2\pi k_r (p_i - p_{pf})}{qB\mu}$$

$p_{pf}$  is the pressure response of the observation probe

$$t_D = \frac{k_r \Delta t}{\phi \mu c_t r_w^2}$$

**8.12. WELL TEST DESIGN**

The objective of a well test design is to forecast possible well test response within practical limits in order to increase the probability that a proposed/planned well test job will achieve desired objectives. Well test design may be carried out to determine the time when a specific flow regime that characterizes certain well and reservoir features would manifest, determine the best rate sequence for a proposed well test or understand operational considerations for a proposed well test. Well test design involves forward simulation and analysis of synthetic well test data using a range of well and reservoir parameters that are considered reasonable.

$$D = \frac{m\pi z_D}{h_D}$$

$$E = \frac{m\pi L_{wD}}{2h_D}$$

$$F = \frac{m\pi z_{wD}}{h_D}$$

$$A = \frac{m^2\pi^2\tau_D}{h_D^2}$$

$$z_{wD} = \frac{z_w + \frac{L_w}{2} + z_p}{r_w}$$

$$z_{wD} = \frac{z_w}{r_w} \sqrt{\frac{k_r}{k_z}}; h_D = \frac{h}{r_w} \sqrt{\frac{k_r}{k_z}} \text{ and } L_{wD} = \frac{L_w}{r_w} \sqrt{\frac{k_r}{k_z}}$$

A combination of diagnosis, forward simulation, and regression can be applied to analysis of VIT. The key flow regime that appears during analysis can be used to give initial model parameters. These parameters can then be refined using regression, which has been discussed in Section 8.5.1.5.

Fig. 8.144 shows an example of a VIT analysis showing active and observation response match with a simulated response as a continuous line and actual test data as a dotted line.

**Exercise 8.6 Well Test Design**

A 12 API oil reservoir was hydraulically fractured and propped to improve well deliverability. Well fracture may be considered as finite conductivity. Fig. 8.145 show faults around the reservoir determined from structural analysis using seismic data.

Average reservoir properties are:  $\phi = 0.18$ ,  $k = 800$  mD,  $c_t = 3.5 \text{ E-}5 \text{ psi}^{-1}$ , and  $\mu = 34$  cp.

1. What duration of buildup during testing will be required to characterizes Fault 1.
2. Assuming there is sufficient time for all well test features to manifest, sketch expected drawdown and buildup

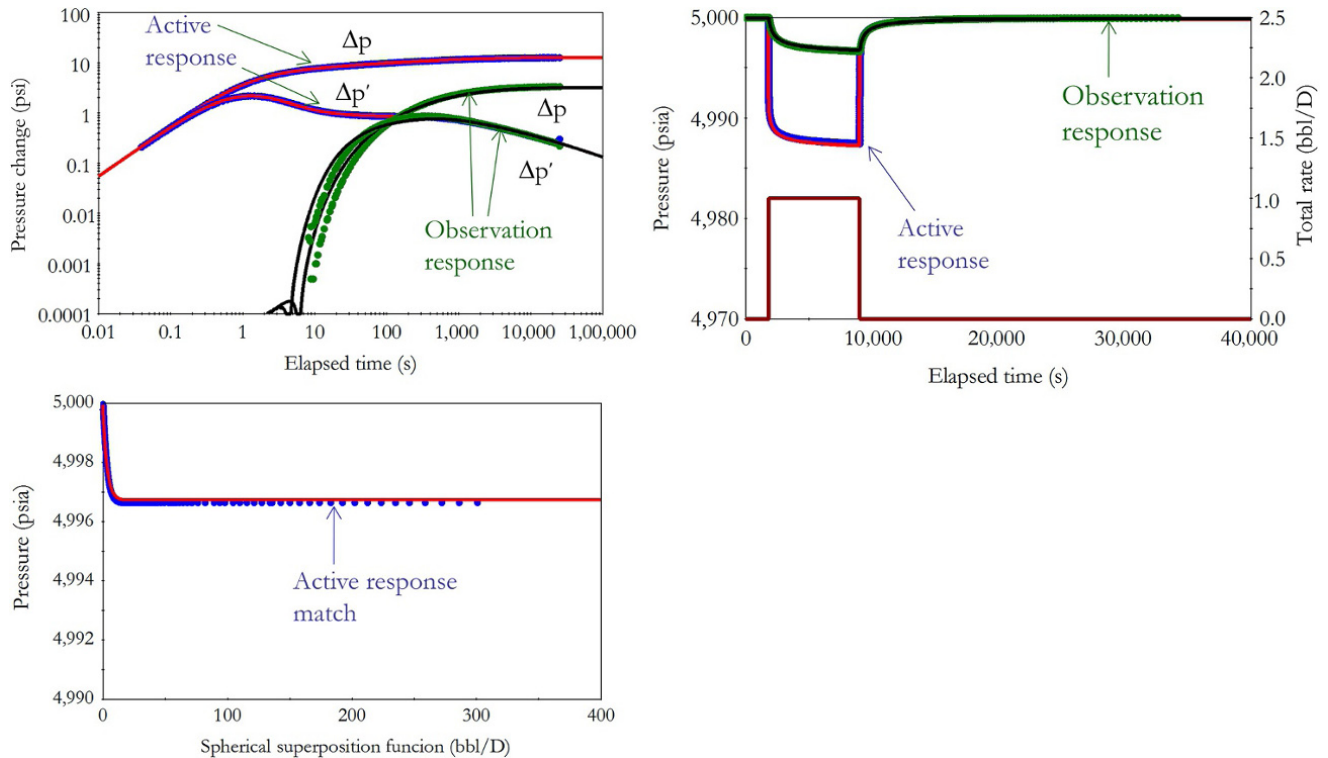


**Figure 8.144** Example of VIT analysis.

log-log pressure derivative response for the well test long enough to test the entire boundaries of the reservoir. All faults and reservoir boundaries are no-flow in nature.

3. What operational or logistic considerations should be made during well test operation in the field.

**Solution.**

1. Using the Lee *et al.* formula in equation (8.43):

$$r_i = 0.032 \sqrt{\frac{k\Delta t_{test}}{\phi\mu c_t}}$$

$$d_{fault} = 0.032 \sqrt{\frac{k\Delta t_{fault}}{\phi\mu c_t}}$$

$$\Delta t_{fault} = \phi\mu c_t \frac{d_{fault}^2}{0.001024k}$$

$$d_{fault} = 200ft$$

$$\Delta t_{fault} = 0.18 \times 34 \times 3.5 \times 10^{-5} \frac{200^2}{0.001024 \times 800} = 10.45hrs$$

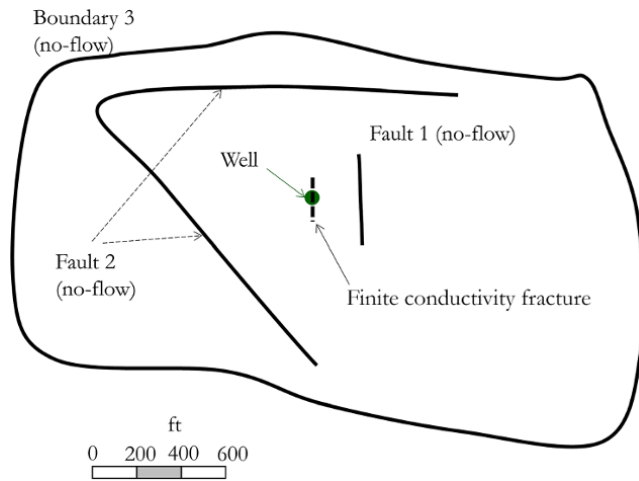


Figure 8.145 Reservoir fault map from seismic interpretation.

Time to detect Fault 1 is about 10.45 hours based on the data supplied.

2. Expected drawdown and buildup log-log derivative response of the well test is shown in Fig. 8.146.

3. A contingency plan for gas lift during testing should be made due to low API (heavy oil). Coil tubing operation can be used for N<sub>2</sub> gas lifting during well testing where required.

**REFERENCES**

Abbaszadeh, M. and Hegeman, P., 1990. Pressure-transient analysis for a slanted well in a reservoir with vertical pressure support. *SPE Formation Evaluation*, 05(03), 277–284.

Agarwal, R., Al-Hussainy, R., and Ramey, H., 1970. An investigation of wellbore storage and skin effect in unsteady liquid flow: I. Analytical treatment. *Society of Petroleum Engineers Journal*, 10(3), 279–290.

Azi, A., Gbo, A., and Gringarten, A., 2008. *Evaluation of Confidence Intervals in Well Test Interpretation Results*. SPE paper 113888, The Europec/EAGE Conference and Exhibition, 9–12 June, Rome, Italy.

Bourdet, D., 2002. *Well Test Analysis: The Use of Advanced Interpretation Models*. Elsevier.

Bourdet, D., Alagoa, A., Ayoub, J., and Pirard, Y., 1984. New Type Curves Aid Analysis of Fissured Zone Well Tests. *World Oil*.

Bourdet, D., Ayoub, J., and Pirard, Y., 1989. Use of pressure derivative in well-test interpretation. *SPE Formation Evaluation*, 4(2), 293–302.

Bourdet, D., Whittle, T., Douglas, A., and Pirard, Y., 1983. A new set of type curves simplifies well test analysis. *World Oil*, 5, 95–106.

Cinco-Ley, H., Miller, F., and Ramey, H., 1975. Unsteady-state pressure distribution created by a directionally drilled well. *Journal of Petroleum Technology*, 27(11), 1392–1402.

Cinco-Ley, H., Samaniego-V., F., and Dominguez, N., 1978. Transient pressure behavior for a well with a finite conductivity vertical fracture. *Society of Petroleum Engineers Journal*, 8(04), 253–264.

Ehlig-Economides, C. and Joseph, J., 1987. A new test for determination of individual layer properties in a multilayered reservoir. *SPE Formation Evaluation*, 2(03), 261–283.

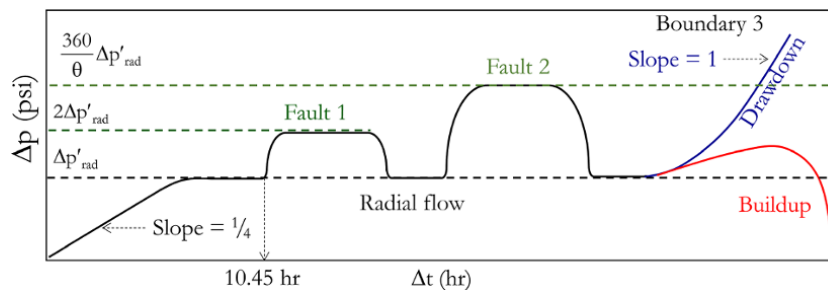


Figure 8.146 Sketch of log-log pressure derivative plot for Exercise 8.6.

- Evinger, H. and Muskat, M., 1942. Calculation of theoretical productivity factor. *Society of Petroleum Engineers, Trans. AIME*, 146(01), 126–139.
- Fair, W., 1979. *Pressure Buildup Analysis With Wellbore Phase Redistribution*. SPE paper 8206, September, Las Vegas, NV.
- Fetkovich, M., 1980. Decline curve analysis using type curves. *Journal of Petroleum Technology*, 32(06), 1–65.
- Gao, C.-T., 1984. Single-phase fluid flow in a stratified porous medium with crossflow. *Society of Petroleum Engineers Journal*, 24(01), 97–106.
- Goode, P. and Thambynayagam, R., 1992. Permeability determination with a multiprobe formation tester. *SPE Formation Evaluation*, 7(04), 297–303.
- Gringarten, A., Bourdet, D., Landel, P., and Kniazeff, V., 1979. *A Comparison between Different Skin and Wellbore Storage Type-Curves for Early-Time Transient Analysis*. SPE paper 8025, 54th Annual Fall Technical Conference of SPE-AIME, 23–26 September, Las Vegas, NV.
- Hegeman, P., Halford, D., and Joseph, J., 1993. Well test analysis with changing wellbore storage. *SPE Formation Evaluation*, 8(03), 201–207.
- Jones, J. and Raghavan, R., 1988. Interpretation of flowing well responses in gas-condensate wells. *Society of Petroleum Engineers Formation Evaluation*, 3(3), 578.
- Kuchuk, F., 1995. Well testing and interpretation for horizontal wells. *Journal of Petroleum Technology*, 47(01), 36–41.
- Kuchuk, F., Goode, P., Wilkinson, D., and Thambynayagam, R., 1991. Pressure transient behaviour of horizontal wells with and without gas cap or aquifer. *Society of Petroleum Engineers Formation Evaluation*, 6(1), 86–94.
- Larsen, L., 1985. A simple approach to pressure distribution in geometric shapes. *Society of Petroleum Engineers Journal*, 25(01), 113–120.
- Martin, J., 1959. Simplified equations of flow in gas drive reservoirs and the theoretical foundation of multiphase pressure buildup analyses. *Trans. AIME*, 216, 321–323.
- Perrine, R., 1956. Analysis of pressure build up curves. *API Drilling and Production Practice*, 482–509.
- Raghavan, R., 1976. Well test analysis: Wells producing by solution gas-drive. *Society of Petroleum Engineers Journal*, 16(4), 196–208.
- Satman, A., Eggenschwiler, M., and Ramey, H., 1980. Interpretation of injection well pressure transient data in thermal oil recovery. SPE paper 8909, California Regional Meeting, 9–11 April, Los Angeles, CA.
- Stehfest, H., 1970. Algorithm 368. Numerical inversion of Laplace Transforms. *D-5. Communications of the ACM*, 13(1), 47–49.
- Stewart, G., 2010. *Well Test Design and Analysis*. Tulsa, OK: Pennwell.
- Stewart, G., 2012. *Wireline Formation Testing and Well Deliverability*. Tulsa, OK: PennWell.
- Van Everdingen, A. and Hurst, W., 1949. The application of the Laplace Transformation to flow problems in reservoirs. *Petroleum Transactions AIME*, 186, 305–324.
- Von Schroeter, T., Hollaender, F., and Gringarten, A., 2004. Deconvolution of well test data as a nonlinear total least-square problem. *Society of Petroleum Engineers Journal*, 9(04), 375–390.
- Yaxley, L., 1987. Effect of a partially communicating fault on transient pressure behaviour. *Society of Petroleum Engineers Formation Evaluation*, 2(04), 590–598.

## BIBLIOGRAPHY

- Agarwal, R., 1979. *Real Gas Pseudo-Time – A New Function for Pressure Buildup Analysis of MHF Gas Wells*. SPE Annual Technical Conference and Exhibition, 23–26 September, Las Vegas, NV.
- Al-Hussainy, R., Ramey Jr., H.J., and Crawford, P.B., 1966. The flow of real gas through porous media. *Journal of Petroleum Technology*, 18(05), 637–642.
- Al-Kahlifa, A., Aziz, K., and Horne, R., 1987. *A New Approach to Multiphase Well Test Analysis*. SPE paper 16743, The 62nd Annual Technical Conference and Exhibition, Sept. 27–30 September, Dallas, TX.
- Archer, J. and Wall, C., 1999. *Petroleum Engineering Principles and Practice*. Dordrecht/Boston: Kluwer Academic Publishers Group.
- Ayan, C. and Lee, W., 1988. Effects of multiphase flow on interpretation of buildup tests. *Society of Petroleum Engineers Formation Evaluation*, 3(2), 459–466.
- Blasingame, T., Johnston, J., and Lee, W., 1989. *Type-Curve Analysis Using the Pressure Integral Method*. SPE paper 18799, SPE California Regional Meeting, Bakersfield, CA.
- Bourdarot, G., 1998. *Well Testing: Interpretation Methods*. Technip and Institut francais du petrole.
- Bourdet, D. and Gringarten, A., 1980. *Determination of Fissure Volume and Block Size in Fractured Reservoirs by Type-curve Analysis*. SPE paper 9293, 55th Annual Fall Technical Conference of SPE-AIME, 21–24 September, Dallas, TX.
- Bourgeois, M. and Horne, R., 1993. Well test model recognition with Laplace space. *Society of Petroleum Engineers Formation Evaluation*, 8(1), 17–25.
- Brons, F. and Marting, V., 1961. The effect of restricted fluid entry on well productivity. *Journal of Petroleum Technology*, 13(12), 172–174.
- Carslaw, H.S. and Jaeger, J., 1947. *Conduction of Heat in Solids*. London: Oxford Science Publications.
- Cinco Ley, H., Samaniego-V., F., and Dominguez-A, N., 1976. *Pressure Transient Analysis of Wells with Finite Conductivity Vertical Fractures in Double Porosity Reservoirs*. SPE Paper 6014, 51st Fall Meeting, SPE of AIME New Orleans, LA.
- Cobenas, R. and Crotti, M., 1999. *Volatile Oil. Determination of Reservoir Fluid Composition from a Non-Representative Fluid Sample*. SPE paper 54005. SPE Latin American and Caribbean Petroleum Engineering Conference, Caracas, Venezuela.
- Collins, R., 1991. *Flow of Fluid through Porous Materials*. REC Publishers.
- Duong, A., 1989. A new set of type curves for well-test interpretation with the pressure/pressure-derivative ratio. *Society of Petroleum Engineers Formation Evaluation*, 4(2), 264–272.
- Earlougher, R.J., 1977. *Advances in Well Test Analysis*. SPE Monograph Series, Society of Petroleum Engineers, Dallas, TX.
- Earlougher Jr., R. and Kersch, K., 1974. Analysis of short-time transient test data by type-curve matching. *Journal of Petroleum Technology*, 26, 793–800.



- Ehlig-Economides, C., 1979. *Well Test Analysis for Wells Produced at a Constant Pressure*. PhD dissertation, Stanford University, Stanford, CA.
- Gringarten, A., 2008. From straight lines to deconvolution: The evolution of the state of the art in well test analysis. *SPE Reservoir Evaluation & Engineering*, 11(01), 41–62.
- Gringarten, A. and Ramey, H., 1973. The use of source and Green's functions in solving unsteady-flow problems in reservoirs. *Society of Petroleum Engineers Journal*, 13(05), 285–296.
- Gringarten, A.C., Bond, D.J., Jackson, M.D., et al., 2000. *A Petroleum Engineering Educational Model Based on the Maureen Field UKCS*. SPE paper 64311, SPE Annual Technical Conference and Exhibition, 1–4 October, Dallas, TX.
- Kniazeff, V. and Naville, S., 1965. Two-phase flow of volatile hydrocarbons. *Society of Petroleum Engineers Journal*, 5(1), 37–44.
- Kuchuck, F., Ramakrishnan, T., and Dave, Y., 1994. *Interpretation of Wireline Formation Tester Packer and Probe Pressures*. SPE Annual Technical Conference and Exhibition, 25–28 September, New Orleans, LA.
- Kuchuk, F., Halford, F., Hafez, H., and Zeybek, M., 2000. *The Use of Vertical Interference Testing to Improve Reservoir Characterization*. Abu Dhabi International Petroleum Exhibition and Conference, 13–15 October, Abu Dhabi, United Arab Emirates.
- Lee, J., 1982. *Well Testing*. Textbook Series, Vol. 1. Dallas, TX: SPE.
- Levitan, M.M., 2005. Practical application of pressure/rate deconvolution to analysis of real well tests. *Society of Petroleum Engineers Reservoir Evaluation & Engineering*, 8, 113–121.
- Levitan, M., Ward, M., Boutaud de la Combe, J., and Wilson, M., 2006. *The Use of Well Testing for Evaluation of Connected Reservoir Volume*. SPE paper 102483, SPE Annual Technical Conference and Exhibition, 24–27 September, San Antonio, TX.
- Marsily, G., 1986. *Quantitative Hydrology*. Academic Press.
- Matthews, C. and Russels, D., 1967. *Pressure Build and Flow Tests in Wells*. SPE Monograph Series Vol. 1, Society of Petroleum Engineers.
- Matthews, C., Brons, F., and Hazebroek, P., 1954. A Method for determination of average pressure in a bounded reservoir. *Trans. AIME*, 201, 182–191.
- McKinley, R., 1971. Wellbore Transmissibility from after flow-dominated pressure buildup data. *Journal of Petroleum Technology*, 23(07), 863–872.
- Merrill Jr., L., Kazemi, H., and Gogarty, W., 1974. Pressure falloff analysis in reservoirs with fluid banks. *Journal of Petroleum Technology*, 26(07), 809–818.
- Muskat, M. and Meres, M., 1963. The flow of heterogeneous fluids through porous media. *Journal of Applied Physics*, 7, 346–363.
- Odeh, A., 1969. Flow test analysis for a well with radial discontinuity. *Journal of Petroleum Technology*, 21(2), 207–210.
- Olarewaju, J., Lee, W., and Lancaster, D., 1991. Type- and decline-curve analysis with composite models. *Society of Petroleum Engineers Formation Evaluation*, 6(1), 79–85.
- Onur, M. and Reynolds, A., 1988. A new approach for constructing derivative type curves for well test analysis. *Society of Petroleum Engineers Formation Evaluation*, 3(1), 197–206.
- Ozkan, E. and Raghavan, R., 2000. A computationally efficient, transient-pressure solution for inclined wells. *SPE Reservoir Evaluation and Engineering*, 3(5), 412–425.
- Peres, A., Onur, M., and Reynolds, A., 1989. *A New General Pressure Analysis Procedure for Slug Tests*. SPE paper 18801, SPE California Regional Meeting, April, Bakersfield, CA.
- Ramey, H.J., Agarwal, R.G., and Martin, I., 1975. Analysis of Slug Test or DST Flow Period Data. *Journal of Canadian Petroleum Technology*, 14(03), 37–42.
- Sanni, M.O. and Gringarten, A.C., 2008. *Well Test Analysis in Volatile Oil Reservoirs*. SPE Annual Technical Conference and Exhibition, 21–24 September, Denver, CO.
- Stewart, G. and Wittmann, M., 1979. *Interpretation of the Pressure Response of the Repeat Formation Tester*. SPE Annual Technical Conference and Exhibition, 23–26 September, Las Vegas, NV.
- Tiab, D. and Kumar, A., 1980. Detection and location of two parallel sealing faults around a well. *Journal of Petroleum Technology*, 32(10), 1701–1708.
- van Poolen, H., 1965. Drawdown curves given angle between intersecting faults. *Oil and Gas Journal*, 63(52), 71–75.
- Warren, J. and Root, P., 1963. The behavior of naturally fractured reservoirs. *Society of Petroleum Engineers Journal*, 3(3), 245–255.
- Wattenbarger, R. and Ramey Jr., H., 1970. An investigation of wellbore storage and skin effects in unsteady liquid flow: II. Finite difference treatment. *Society of Petroleum Engineers Journal*, 10(3), 291–296.

## Reservoir Inflow Performance

Well performance generally relates to production capacity of well at a given well and reservoir condition. Fig. 9.1 shows a well schematic with key features that affect well performance. One common approach for describing the performance/deliverability of a well is the use of a combined plot of *inflow performance relationship* (IPR) and *tubing performance relationship* (TRP).

The *inflow performance relationship* (IPR), also called *well inflow performance relationship*, is defined as the functional relationship between the reservoir fluid production rate into the wellbore ( $q_{in}$ ), reservoir pressure ( $p_r$ ), and the bottomhole flowing pressure ( $p_{wf}$ ). Pressure drop between the reservoir and wellbore ( $\Delta p_{formation}$ ), which is a function of inflow rate ( $q_{in}$ ), can be defined as:

$$\Delta p_{formation}(q_{in}) = p_r - p_{wf}$$

Therefore:

$$p_{wf} = p_r - \Delta p_{formation}(q_{in}) \quad (9.1)$$

The *tubing performance relationship* (TPR) is defined as the functional relationship between the reservoir fluid production rate produced out of well ( $q_{out}$ ), tubing head pressure ( $p_{thp}$ ), and the bottomhole flowing pressure ( $p_{wf}$ ). The pressure drop between the wellbore and well tubing head pressure,  $\Delta p_{tubing}$ , which is a function of outflow rate ( $q_{out}$ ), can be defined as:

$$\Delta p_{tubing}(q_{out}) = p_{wf} - p_{thp}$$

Therefore:

$$p_{wf} = \Delta p_{tubing}(q_{out}) + p_{thp} \quad (9.2)$$

Combined graphical presentation of IPR and TPR is called the *system plot*. The solution of the IPR and TPR at any given node is the *solution point*. Fig. 9.2 shows a system plot with solution point. In well performance analysis, solution may be determined at any point of interest in the production system. Any point of interest where a solution point is determined is called a *node*.

IPR relationships for wells producing under approximately *steady state* (SS) and *pseudosteady state* (PSS) reservoir conditions are important during the life of a fully developed field. SS and PSS conditions have been discussed in detail in Chapter 8.

### 9.1. STEADY-STATE PRESSURE RESPONSE FOR HOMOGENEOUS RESERVOIR

Fig. 9.3 shows a well producing an incompressible fluid with rate  $q$  at steady state, with an injection front of rate  $q$  and external boundary pressure  $p_e$ . Since the rate of fluid injected into the reservoir is equal to the rate of fluid produced, there will be no net accumulation or depletion. Some of the practical instances where a well will flow at SS condition would include: a well producing from a reservoir with a large water aquifer support, creating an influx boundary or a well producing from a reservoir with support from an expanding gas cap.

Fig. 9.4 shows a typical bottomhole pressure in a reservoir at SS conditions.

From Darcy's law, for a fully completed well with radial flow, superficial velocity is defined as:

$$u = -\frac{q}{A} = -\frac{k dp}{\mu dr} \quad (9.3)$$

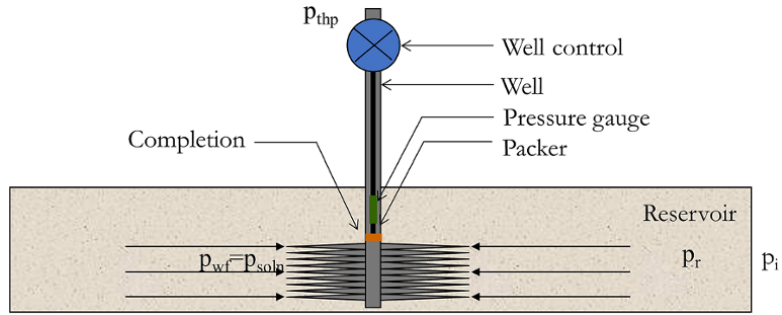


Figure 9.1 Well schematic showing  $p_r$ ,  $p_{wf}$ ,  $p_{thp}$  and  $p_{soln}$ .

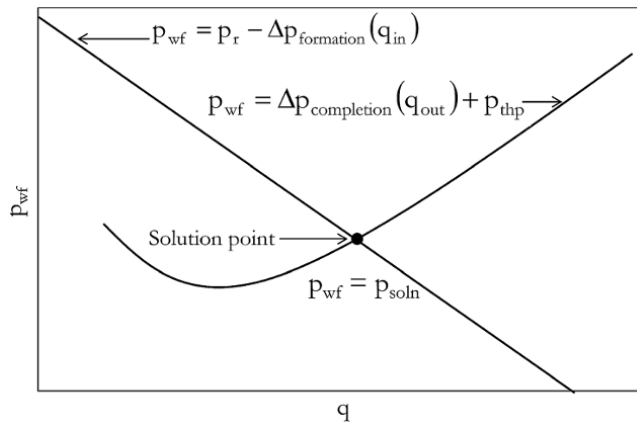


Figure 9.2 System showing solution point.

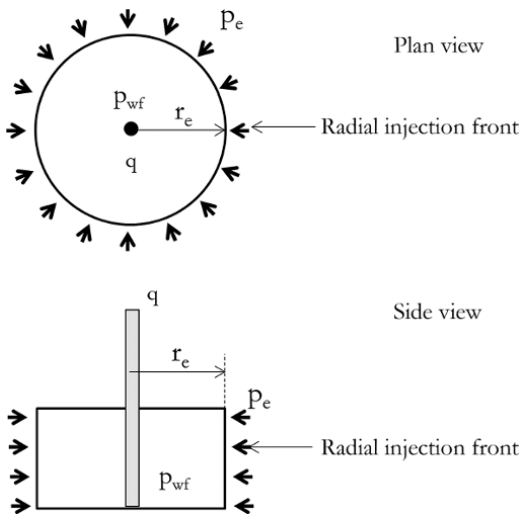


Figure 9.3 Well producing at steady state.

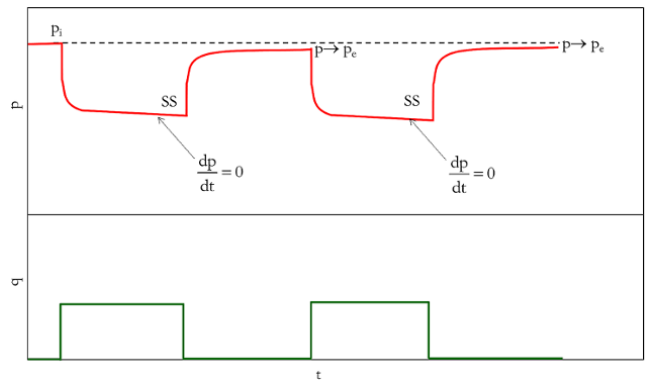


Figure 9.4 Pressure-rate history showing steady state behavior.

where  $q$  is the flow rate,  $k$  is the permeability,  $A$  is the radial flow area,  $\mu$  is the viscosity,  $p$  is the pressure, and  $r$  is the radial distance.

$$-\frac{q}{2\pi rh} = -\frac{k dp}{\mu dr}$$

$$dp = \frac{q\mu}{2\pi kh r} dr$$

$$\int_{p_{wf}}^p dp = \frac{q\mu}{2\pi kh} \int_{r_w}^r \frac{dr}{r}$$

$$p - p_{wf} = \frac{q\mu}{2\pi kh} \ln \frac{r}{r_w} \tag{9.4}$$

Equation (9.4) describes pressure profile at any given radial distance away from the wellbore producing under steady state condition in consistent units. Equation (9.4) in EOF units can be expressed as:

$$p - p_{wf} = \frac{141.2qB\mu}{kh} \ln \frac{r}{r_w} \tag{9.5}$$

where  $q$  = production flow rate (bbl/d),  $B$  = formation volume factor (stb/rb),  $k$  = permeability (mD),  $\mu$  = viscosity (cp),  $p$  = pressure (psia),  $h$  = formation thickness (ft),  $r$  = radial distance away from the well (ft), and  $r_w$  = wellbore radius (ft).

**9.1.1. Pressure Profile for Well Producing at Steady State**

From equation (9.5), the pressure profile ( $p$  against  $r$ ) will depend on  $q$ ,  $B$ ,  $\mu$ ,  $k$ , and  $h$ , hence leading to an unlimited number of profiles depending on how  $q$ ,  $B$ ,  $\mu$ ,  $k$ , and  $h$  are combined. Another way of plotting pressure profile is in dimensionless variables, which are independent of the magnitude of the variables. Dimensionless variables as discussed in Chapter 8 (Well Test Analysis) make well test equation manipulation easier, as variables in pressure equations become independent of the magnitude of the physical parameters such as fluid and rock properties.

Defining dimensionless radial distance using equation (8.47):

$$r_D = \frac{r}{r_w}$$

Defining dimensionless pressure using equation (8.3):

$$p_D = \frac{kh}{141.2qB\mu} \Delta p.$$

From equation (9.5):

$$\Delta p = p - p_{wf} = \frac{141.2qB\mu}{kh} \ln \frac{r}{r_w}$$

Substituting  $\Delta p$  above into the  $p_D$  function from equation (8.3):

$$p_D = \frac{kh}{141.2qB\mu} \frac{141.2qB\mu}{kh} \ln \frac{r}{r_w}$$

Substituting into  $r_D = \frac{r}{r_w}$  above equation

$$p_D = \ln r_D \tag{9.6}$$

As shown in equation (9.6), pressure defined in terms of the  $p_D$  function is independent of the magnitude of reservoir or fluid parameters ( $q$ ,  $k$ ,  $h$ ,  $\mu$ ).

**Exercise 9.1 Pressure Profile in Real and Dimensionless Variables**

Given three wells (Table 9.1) producing under steady state conditions, plot pressure profile for each well as far as 100 ft away from the well in the following forms.

1. Pressure in psia against radial distance from well in feet.
2. Dimensionless pressure and dimensionless radial distance away from well.

$$r_w = 0.35 \text{ ft}; p_{wf} = 2,100 \text{ psia}; B_o = 1.5 \text{ rb/stb}$$

**Solution Steps.**

*Step 1:* create pressure profile plot in real variables.

- (i) create table of values of  $r$  from  $r_w$  to 100 ft (Table 9.2);
- (ii) determine  $p$  using equation (9.5) for every value of  $r$  from above for wells 1 to 4 (Table 9.2);

**Table 9.1** Parameters for Wells in Exercise 9.1.

Parameter	Well 1	Well 2	Well 3	Well 4
$q$ (stb/D)	405	337.5	270	486
$k$ (mD)	150	180	225	125
$h$ (ft)	30	36	45	25
$\mu$ (cp)	1	0.833	0.667	1.22

**Table 9.2** Summary of  $p$  Against  $r$  for Exercise 9.1.

$r$ (ft)	Pressure (psia)			
	Well 1	Well 2	Well 3	Well 4
0.35	2,100.0	2,100.0	2,100.0	2,100.0
0.62	2,110.8	2,105.2	2,102.1	2,122.7
1.08	2,121.6	2,110.4	2,104.3	2,145.5
1.91	2,132.3	2,115.6	2,106.4	2,168.2
3.36	2,143.1	2,120.8	2,108.5	2,190.9
5.92	2,153.9	2,126.0	2,110.6	2,213.6
10.41	2,164.7	2,131.2	2,112.8	2,236.4
18.33	2,175.5	2,136.4	2,114.9	2,259.1
32.27	2,186.2	2,141.6	2,117.0	2,281.8
56.81	2,197.0	2,146.8	2,119.2	2,304.5
100	2,207.8	2,152.0	2,121.3	2,327.3

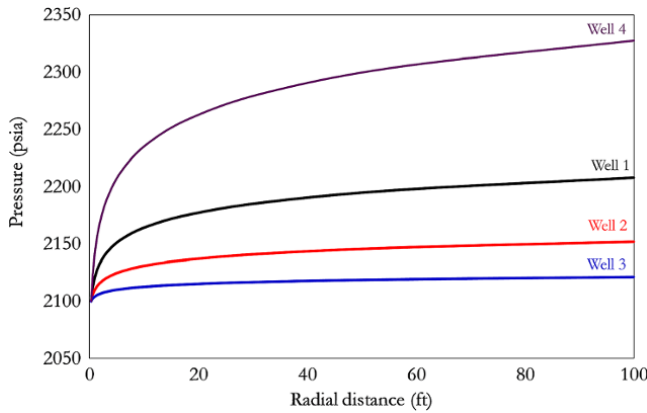


Figure 9.5 Pressure profile in real variables (p against r).

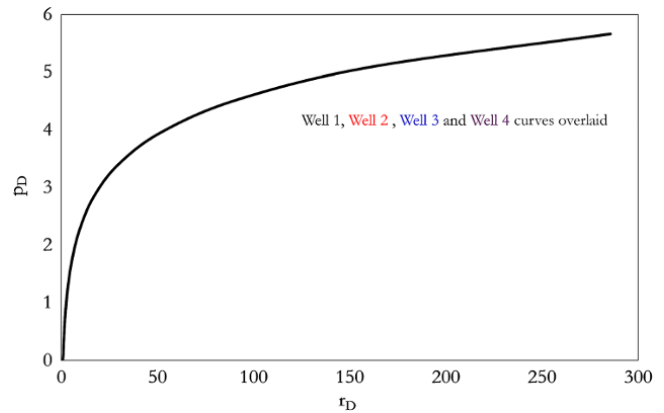


Figure 9.6 Pressure profile in dimensionless variables ( $p_D$  against  $r_D$ ).

Table 9.3 Summary of  $p_D$  Against  $r_D$  for Exercise 9.1.

$r_D$	$p_D$			
	Well 1	Well 2	Well 3	Well 4
1	0.00	0.00	0.00	0.00
1.76	0.57	0.57	0.57	0.57
3.10	1.13	1.13	1.13	1.13
5.45	1.70	1.70	1.70	1.70
9.60	2.26	2.26	2.26	2.26
16.90	2.83	2.83	2.83	2.83
29.75	3.39	3.39	3.39	3.39
52.38	3.96	3.96	3.96	3.96
92.20	4.52	4.52	4.52	4.52
162.31	5.09	5.09	5.09	5.09
285.71	5.65	5.65	5.65	5.65

(iii) plot p against r for wells 1 to 4 (Fig. 9.5).

Step 2: create pressure profile plots in dimensionless variables.

(i) determine  $r_D$  using equation (8.47) where  $r_D = \frac{r}{r_w}$  (Table 9.3);

(ii) calculate  $p_D$  using equation (9.6) for wells 1 to 4 (Table 9.3);

(iii) plot  $p_D$  against  $r_D$  for wells 1 to 4 (Fig. 9.6).

**Solution.**

For this exercise, r can be spaced between  $r_w$  and 100 ft geometrically, arithmetically, or even randomly.

The inflow performance relationship can be derived from the diffusivity equation, which is the basis of well test analysis. Derivation of the diffusivity equation from Darcy’s law, the continuity equation, and equations of state (EOS) were discussed in Chapter 7 (7.1).

From equation (7.11):

$$\frac{1}{r} \frac{\partial}{\partial r} \left( r \frac{\partial p}{\partial r} \right) = \frac{\phi \mu c_i}{k} \frac{\partial p}{\partial t}$$

At steady state:

$$\begin{aligned} \frac{\partial p}{\partial t} &= 0 \Rightarrow \\ \frac{1}{r} \frac{d}{dr} \left( r \frac{dp}{dr} \right) &= 0 \\ \frac{d}{dr} \left( r \frac{dp}{dr} \right) &= 0 \\ \left( r \frac{dp}{dr} \right) &= C \end{aligned} \tag{9.7}$$

At wellbore:

$$\left( r \frac{dp}{dr} \right) \Big|_{r_w} = C \tag{9.8}$$

From Darcy’s law:

$$u_{rad} = -\frac{q}{2\pi r h} = -\frac{k dp}{\mu dr}$$

At wellbore:

$$\begin{aligned} \frac{q}{2\pi r_w h} &= \frac{k dp}{\mu dr} \Big|_{r_w} \\ \left( r_w \frac{q \mu}{2\pi r_w k h} \right) &= r_w \frac{dp}{dr} \Big|_{r_w} \\ \left( \frac{q \mu}{2\pi k h} \right) &= \left( r \frac{dp}{dr} \right) \Big|_{r_w} \\ \left( r \frac{dp}{dr} \right) \Big|_{r_w} &= \left( \frac{q \mu}{2\pi k h} \right) \end{aligned} \tag{9.9}$$

Solving equations (9.8) and (9.9):

$$C = \frac{q \mu}{2\pi k h}$$

Substituting C into equation (9.7):

$$\begin{aligned} \left( r \frac{dp}{dr} \right) &= \\ \left( r \frac{dp}{dr} \right) &= \frac{q\mu}{2\pi kh} \\ \frac{dp}{dr} &= \frac{1}{r} \frac{q\mu}{2\pi kh} \\ dp &= \frac{1}{r} \frac{q\mu}{2\pi kh} dr \\ \int_{p_{wf}}^p dp &= \frac{q\mu}{2\pi kh} \int_{r_w}^r \frac{dr}{r} \\ p - p_{wf} &= \frac{q\mu}{2\pi kh} \ln \frac{r}{r_w} \end{aligned}$$

At a defined external reservoir, radial distance,  $r_e$ , with pressure,  $p_e$ , this solution becomes:

$$p_e - p_{wf} = \frac{q\mu}{2\pi kh} \ln \frac{r_e}{r_w} \quad (\text{boundary conditions: } p = p_e \text{ and } r = r_e)$$

In EOF it becomes:

$$p_e - p_{wf} = \frac{141.2Bq\mu}{kh} \ln \frac{r_e}{r_w} \quad (9.10)$$

As shown in equation (9.10), steady-state IPR is Darcy's law. Hence, steady-state IPR is also called Darcy's IPR.

Including pressure drop due to skin effect defined by *Van Everdingen and Hurst* [1949]:

$$p_e = p_{wf} + \frac{141.2Bq\mu}{kh} \left( \ln \frac{r_e}{r_w} + S \right) \quad (9.11)$$

Equation (9.11) defines the simplest inflow performance relationship.

A more common and useful way of defining an IPR is with respect to average reservoir pressure ( $p_{avg}$ ) rather than to external reservoir boundary pressure ( $p_e$ ). This is because, in well test analysis, for closed systems average reservoir pressure is easily determined. Also, for material balance purposes, where a reservoir is considered as single or multiple tanks, the average reservoir pressure of reservoir/compartments is what is required. Thus, for comparison and easy integration of IPR with material balance, well test analysis, and production optimization, defining IPR with respect to average reservoir pressure is most appropriate.

Average reservoir pressure for a reservoir described by volume elements as shown in Fig. 9.7 can be expressed as:

$$p_{Avg} = \frac{\sum_{j=1}^n p_j \Delta V_j}{\sum_{j=1}^n \Delta V_j} \quad (9.12)$$

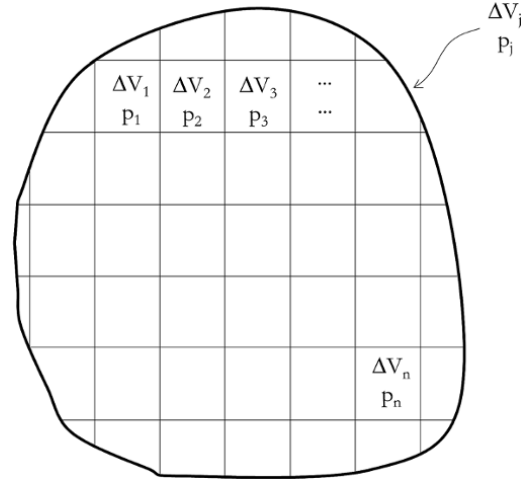


**Figure 9.7** Volume elements,  $\Delta V_j$ , with corresponding pressure,  $p_j$ , for a reservoir.

For reservoir with cylindrical geometry and a well with radial flow, as shown in Fig. 9.3, equation (9.12) becomes:

$$\begin{aligned} p_{Avg} &= \frac{\int_{r_w}^{r_e} p 2\pi r h dr}{\int_{r_w}^{r_e} 2\pi r h dr} \\ p_{Avg} &= \frac{\int_{r_w}^{r_e} p 2\pi r h dr}{\pi (r_e^2 - r_w^2) h} \end{aligned} \quad (9.13)$$

Considering reservoir size is far greater than wellbore radius,  $r_e \gg r_w$ , then  $r_e^2 - r_w^2 \approx r_e^2$  and, hence, equation (9.13) becomes:

$$p_{Avg} = \frac{2}{r_e^2} \int_{r_w}^{r_e} p r dr \quad (9.14)$$

From equation (9.4),  $p = p_{wf} + \frac{q\mu}{2\pi kh} \ln \frac{r}{r_w}$

Substituting  $p$  from equation (9.4) into equation (9.14), equation (9.14) becomes:

$$\begin{aligned} p_{Avg} &= \frac{2}{r_e^2} \int_{r_w}^{r_e} \left( p_{wf} r + r \frac{q\mu}{2\pi kh} \ln \frac{r}{r_w} \right) dr \\ p_{Avg} &= \frac{2}{r_e^2} \left[ \int_{r_w}^{r_e} p_{wf} r dr + \int_{r_w}^{r_e} \left( r \frac{q\mu}{2\pi kh} \ln \frac{r}{r_w} \right) dr \right] \\ p_{Avg} &= \frac{2}{r_e^2} \left[ p_{wf} \frac{(r_e^2 - r_w^2)}{2} + \int_{r_w}^{r_e} \left( r \frac{q\mu}{2\pi kh} \ln \frac{r}{r_w} \right) dr \right] \end{aligned} \quad (9.15)$$

Integration by parts can be used to solve equation (9.15).

The expression in the form  $\int UdV$  can be integrated as follows:  $\int UdV = UV - \int VdU$ .

Evaluating:  $\int_{r_w}^{r_e} \left( r \ln \frac{r}{r_w} \right) dr$ , which is part of equation (9.15), using integration by parts:

$$\begin{aligned} \int_{r_w}^{r_e} \left( r \ln \frac{r}{r_w} \right) dr &= \frac{(r_e^2 - r_w^2)}{2} \ln \frac{r_e}{r_w} - \int_{r_w}^{r_e} \frac{r^2}{2} \frac{1}{r} dr \\ &= \frac{(r_e^2 - r_w^2)}{2} \ln \frac{r_e}{r_w} - \int_{r_w}^{r_e} \frac{r}{2} dr \\ &= \frac{(r_e^2 - r_w^2)}{2} \ln \frac{r_e}{r_w} - \frac{r^2}{4} \Big|_{r_w}^{r_e} \\ &= \frac{(r_e^2 - r_w^2)}{2} \ln \frac{r_e}{r_w} - \frac{(r_e^2 - r_w^2)}{4} \Rightarrow \\ \int_{r_w}^{r_e} \left( r \ln \frac{r}{r_w} \right) dr &= \frac{(r_e^2 - r_w^2)}{2} \ln \frac{r_e}{r_w} - \frac{(r_e^2 - r_w^2)}{4} \end{aligned}$$

Substituting the expression for  $\int_{r_w}^{r_e} \left( r \ln \frac{r}{r_w} \right) dr$  above into equation (9.15):

$$p_{Avg} = \frac{2}{r_e^2} \left[ p_{wf} \frac{(r_e^2 - r_w^2)}{2} + \frac{q\mu}{2\pi kh} \left( \frac{(r_e^2 - r_w^2)}{2} \ln \frac{r_e}{r_w} - \frac{(r_e^2 - r_w^2)}{4} \right) \right]$$

$$p_{Avg} = \frac{2}{r_e^2} \left[ p_{wf} \frac{r_e^2}{2} + \frac{q\mu}{2\pi kh} \left( \frac{r_e^2}{2} \ln \frac{r_e}{r_w} - \frac{r_e^2}{4} \right) \right]$$

$$p_{Avg} = p_{wf} + \frac{q\mu}{2\pi kh} \left( \ln \frac{r_e}{r_w} - \frac{1}{2} \right)$$

Including pressure drop due to skin effect defined by *Van Everdingen and Hurst* [1949]:

$$p_{Avg} = p_{wf} + \frac{q\mu}{2\pi kh} \left( \ln \frac{r_e}{r_w} - \frac{1}{2} + S \right)$$

$$p_{Avg} = p_{wf} + \frac{141.2Bq\mu}{kh} \left( \ln \frac{r_e}{r_w} - \frac{1}{2} + S \right) \quad (9.16)$$

*Difference Between  $p_e$  and  $p_{Avg}$  for SS Conditions*

Equation (9.11) minus equation (9.16):

$$\begin{aligned} p_e - p_{Avg} &= p_{wf} + \frac{141.2Bq\mu}{kh} \left( \ln \frac{r_e}{r_w} + S \right) \\ &\quad - \left( p_{wf} + \frac{141.2Bq\mu}{kh} \left( \ln \frac{r_e}{r_w} - \frac{1}{2} + S \right) \right) \end{aligned}$$

$$p_e - p_{Avg} = \frac{141.2Bq\mu}{2kh}$$

$$p_e - p_{Avg} = 70.6 \frac{Bq\mu}{kh} \text{ in EOF units}$$

### Exercise 9.2 Comparison of $p_e$ and $p_{Avg}$ for Oil Well Producing at Steady State

Consider that well 1 in Exercise 9.1 is producing under steady-state conditions and has a skin effect of 2, and that the reservoir can be described as having an external reservoir radial distance ( $r_e$ ) of approximately 1000 ft. Compare the external reservoir boundary pressure ( $p_e$ ) with the average reservoir pressure ( $p_{Avg}$ ).

#### Solution Steps.

*Step 1:* using equation (9.11) at  $r_e = 1,000$  ft, determine  $p_e$ .

*Step 2:* using equation (9.16), determine  $p_{Avg}$ .

#### Solution.

From equation (9.11), given  $r_e = 1,000$  ft:

$$p_e = p_{wf} + \frac{141.2Bq\mu}{kh} \left( \ln \frac{r_e}{r_w} + S \right)$$

$$p_e = 2,100 + \frac{141.2 \times 1.5 \times 405 \times 1}{150 \times 30} \left( \ln \frac{1,000}{0.35} + 2 \right)$$

$$p_e = 2,289.8 \text{ psia}$$

From equation (9.16):

$$p_{Avg} = p_{wf} + \frac{141.2Bq\mu}{kh} \left( \ln \frac{r_e}{r_w} - \frac{1}{2} + S \right)$$

$$p_{Avg} = 2,100 + \frac{141.2 \times 1.5 \times 405 \times 1}{150 \times 30} \left( \ln \frac{1,000}{0.35} - \frac{1}{2} + 2 \right)$$

$$p_{Avg} = 2,280.28 \text{ psia}$$

Extend the pressure profile in Exercise 9.1 to 1000 ft and show values of  $p_e$  and  $p_{Avg}$  on the pressure profile away from the well to the reservoir extent (Fig. 9.8).

An important plot for reservoir and production engineers is the plot of  $p_{wf}$  against  $q$  ( $q_{surface}$ ). This relationship is the IPR, which is important for well diagnosis,

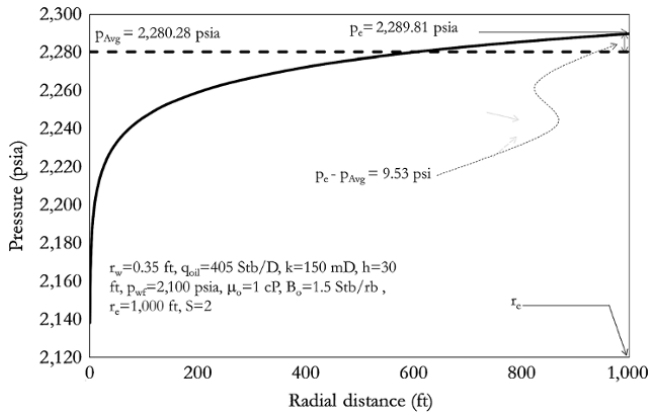


**Figure 9.8** Comparison of  $p_e$  and  $p_{Avg}$  shown on the pressure profile.

performance prediction, and optimization. For a reservoir producing under steady-state conditions, IPR with respect to average reservoir pressures is defined from equation (9.16) as:

$$p_{wf} = p_{Avg} - \frac{141.2Bq\mu}{kh} \left( \ln \frac{r_e}{r_w} - \frac{1}{2} + S \right)$$

The IPR relationship shows the effect of back pressure on the well (which changes sandface pressure  $p_{wf}$ ) and rate of production measured at the surface condition ( $q$ ). This relationship depends on well conditions, reservoir properties, boundary characteristics (size and type), and the flow regime that dominates flow in the reservoir. The reference depth for sandface pressure measurement is often mid-reservoir or mid-perforation. Since pressure gauges are always placed at the top of a perforation or even shallower for very deep wells,  $p_{wf}$  measured by gauges may be less than the sandface pressure. The approach for handling this difference is discussed under nodal solutions in Chapter 11 (11.1).

A plot of  $p_{wf}$  at the sandface against  $q$  for a steady state homogeneous single incompressible fluid condition will yield a straight line with a slope and intercepts that are key characteristic of the reservoir (Fig. 9.9). The inverse of the slope is defined as the *productivity index* (PI); the intercept on the  $p_{wf}$  (vertical) axis is the *average reservoir pressure* ( $p_{Avg}$ ); and the value of production rate on the horizontal axis at minimum pressure of 1 atm (14.7 psia) is the *absolute openhole flow potential* (AOFP or  $q_{max}$ ) (Fig. 9.9).

The PI, which is the fluid flow rate delivered by reservoir to the wellbore per unit pressure drop between the reservoir and bottomhole pressure, is a very important reservoir-wellbore characteristic that gives an indication of the reservoir's capability to deliver fluid to the wellbore. PI can be expressed as:

$$PI = \frac{q}{(p_{Avg} - p_{wf})} \quad (9.17)$$

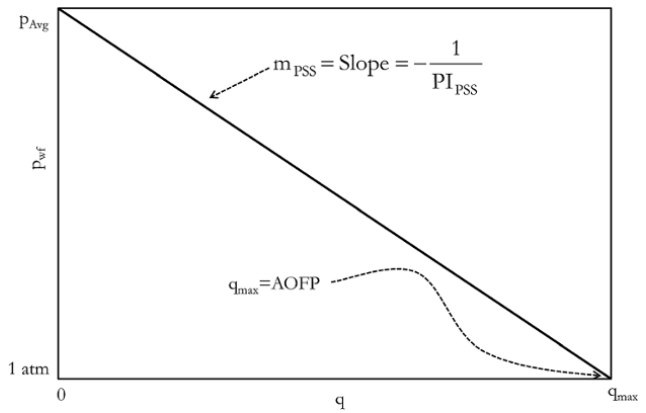


**Figure 9.9** IPR plot for a reservoir-wellbore system producing under steady-state conditions.

In petroleum engineering, the concept of PI is applicable only to single-phase oil wells. For a single-phase, slightly compressible or incompressible fluid, producing under steady-state conditions, PI can be derived from equation (9.16) as:

$$PI_{SS} = \frac{q}{(p_{Avg} - p_{wf})} = \frac{kh}{141.2\mu B \left( \ln \left( \frac{r_e}{r_w} \right) - 0.5 + S \right)} \text{ in EOF} \quad (9.18)$$

AOFP defines the maximum theoretical possible rate that a well can produce at the lowest possible bottomhole pressure.

**Exercise 9.3** IPR for an Oil Well Producing Under Steady-State Conditions

1. Draw an IPR plot for the reservoir system in Exercise 9.2 showing  $p_{Avg}$ ,  $q_{max}$  (AOFP).
2. Determine the PI of the reservoir-wellbore system.

**Solution Steps.**

- Step 1:* determine  $p_{Avg}$  (see Exercise 9.2).  $p_{Avg}$  corresponds to  $p_{wf}$  at rate zero ( $q = 0$ ).
- Step 2:* determine  $q$  at  $p_{wf} = 14.7$  psia using equation (9.16).  $q$  at  $p_{wf} = 14.7$  psia gives AOFP.
- Step 3:* a straight line with coordinates (0 stb/d,  $p_{Avg}$  psia) and (AOFP stb/d, 14.7 psia) defines the SS IPR (Fig. 9.10).
- Step 4:* the PI can be calculated using equation (9.18).

**Solution.**

$p_{Avg} = 2280.28$  psia (calculated in Exercise 9.2).

**AOFP Calculation**

From equation (9.16):

$$p_{Avg} = p_{wf} + \frac{141.2Bq\mu}{kh} \left( \ln \frac{r_e}{r_w} - \frac{1}{2} + S \right)$$



Making  $q$  the subject of the formula:

$$q = \frac{P_{Avg} - P_{wf}}{\frac{141.2B\mu}{kh} \left( \ln \frac{r_e}{r_w} - \frac{1}{2} + S \right)}$$

$q$  at  $p_{wf} = 14.7$  psia defines AOF (  $q_{max}$  ).

Substituting the parameters into the above equation:

$$q_{max} = \frac{2,280.28 - 14.7}{\frac{141.2 \times 1.5 \times 1}{150 \times 30} \left( \ln \frac{1,000}{0.35} - \frac{1}{2} + 2 \right)} = 5,089.63 \text{ stb/D}$$

AOF =  $q_{max} = 5,090 \text{ stb/D}$

**Productivity Index (PI) Calculation**

From equation (9.18):

$$PI_{SS} = \frac{q}{(P_{Avg} - P_{wf})} = \frac{kh}{141.2\mu B \left( \ln \left( \frac{r_e}{r_w} \right) - 0.5 + S \right)}$$

$$PI_{SS} = \frac{kh}{141.2\mu B \left( \ln \left( \frac{r_e}{r_w} \right) - 0.5 + S \right)}$$

$$PI_{SS} = \frac{150 \times 30}{141.2 \times 1 \times 1.5 \left( \ln \left( \frac{1,000}{0.35} \right) - 0.5 + 2 \right)} = 2.246 \text{ stb/D/psi}$$

$PI_{SS} = 2.24 \text{ stb/D/psi}$

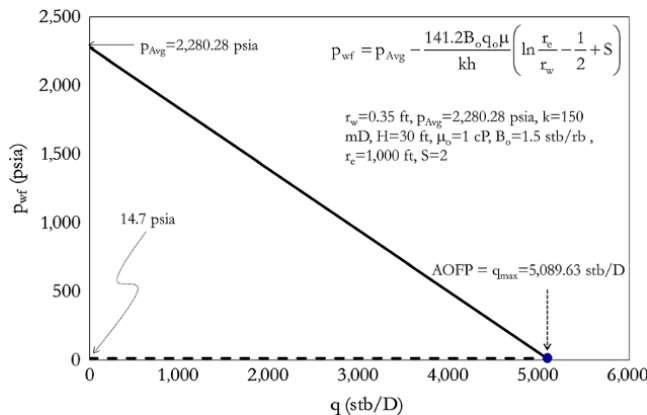


**Figure 9.10** Straight-line relationship between  $p_{wf}$  against  $q$  for steady-state conditions.

**9.2. PSEUDO-STEADY (SEMISTEADY) STATE PRESSURE RESPONSE FOR A HOMOGENEOUS RESERVOIR**

During depletion of a closed reservoir with no-flow boundaries (Fig. 9.11), reservoir fluid is produced by volumetric expansion rather than injection, aquifer, or gas cap support. The pressure response of a well producing under depletion is described as pseudosteady state (PSS) and this condition is very important for reservoir and production management. When a PSS flow regime is reached, the rate of depletion with time becomes constant. The transient period prior to reaching the pseudosteady state condition was discussed in Chapter 8 (Well Test Analysis).

Fig. 9.12 shows the typical bottomhole pressure response for a well producing under PSS conditions.

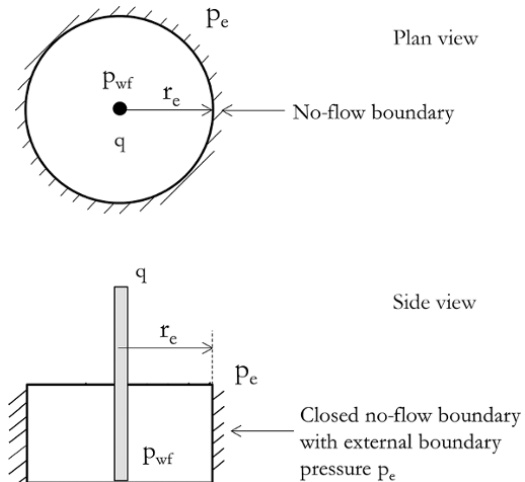


**Figure 9.11** Well producing at pseudosteady state.

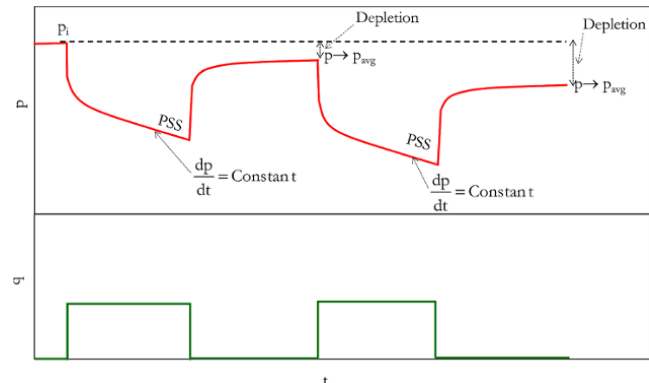


**Figure 9.12** Pressure–rate history showing pseudosteady state behavior.

Depletion by volumetric expansion for a closed boundary system can be expressed as:

$$\Delta V = -c_t V \Delta p$$

where  $c_t$  is total compressibility,  $V$  is reservoir pore volume,  $\Delta p$  is the pressure change from  $p_i$  to  $p_{Avg}$  ( $p_i - p_{Avg}$ ), and  $\Delta V$  is cumulative production, which is the product of constant rate production ( $q$ ) and total flowing time ( $t$ ).

Dividing both sides of the equation above by  $\Delta t$  gives:

$$\frac{\Delta V}{\Delta t} = -c_t V \frac{\Delta p}{\Delta t}$$

PSS is defined by  $r \rightarrow r_e$ , hence:

$$q = -c_t V_{r \rightarrow r_e} \frac{dp}{dt} \quad (9.19)$$

Substituting  $V_{r \rightarrow r_e} = \pi(r_e^2 - r_w^2)h\phi$  into equation (9.19):

$$q = -c_t \pi(r_e^2 - r_w^2)h\phi \frac{dp}{dt} \quad (9.20)$$

Equation (9.20) is an important boundary condition defining PSS and can be rewritten as:

$$\frac{dp}{dt} = -\frac{q}{c_t \pi(r_e^2 - r_w^2)h\phi}$$

Considering that  $r_e^2 \gg r_w^2$ ,  $r_e^2 - r_w^2 \approx r_e^2$ , the above equation can be expressed as:

$$\frac{dp}{dt} = -\frac{q}{c_t \pi r_e^2 h\phi} \quad (9.21)$$

Substituting the expression for  $\frac{dp}{dt}$  in equation (9.21) into the diffusivity equation (equation (7.11)):

$$\frac{1}{r} \frac{\partial}{\partial r} \left( r \frac{\partial p}{\partial r} \right) = \frac{\phi \mu c_t \partial p}{k \partial t}$$

$$\frac{1}{r} \frac{\partial}{\partial r} \left( r \frac{\partial p}{\partial r} \right) = -\frac{\phi \mu c_t}{k} \frac{q_r}{c_t \pi r_e^2 h\phi}$$

$$\frac{1}{r} \frac{\partial}{\partial r} \left( r \frac{\partial p}{\partial r} \right) = -\frac{q_r \mu}{\pi r_e^2 k h}$$

$$\frac{\partial}{\partial r} \left( r \frac{\partial p}{\partial r} \right) = -\frac{q \mu}{\pi r_e^2 k h} r$$

$$r \frac{\partial p}{\partial r} = -\frac{q \mu}{2 \pi r_e^2 k h} r^2 + C$$

$$\frac{\partial p}{\partial r} = -\frac{q \mu}{2 \pi r_e^2 k h} r + \frac{C}{r} \quad (9.22)$$

When  $r = r_e$ , since there is no flux across boundary, the pressure gradient at the boundary is zero:

$$\left. \frac{dp}{dr} \right|_{r=r_e} = 0$$

Therefore, at the boundary, equation (9.22) becomes:

$$0 = -\frac{q \mu}{2 \pi r_e^2 k h} r_e + \frac{C}{r_e}$$

Solving for  $C$ :

$$C = \frac{q \mu}{2 \pi k h}$$

Substituting the value of  $C$  into equation (9.22):

$$\frac{\partial p}{\partial r} = -\frac{q \mu}{2 \pi r_e^2 k h} r + \frac{q \mu}{2 \pi k h r}$$

Integrating between the limits of  $p$  and  $p_{wf}$ ;  $r$  and  $r_w$ :

$$\int_{p_{wf}}^p dp = \int_{r_w}^r \left( -\frac{q \mu}{2 \pi r_e^2 k h} r + \frac{q \mu}{2 \pi k h r} \right) dr$$

$$p - p_{wf} = \frac{q \mu}{2 \pi k h} \int_{r_w}^r \left( \frac{1}{r} - \frac{r}{r_e^2} \right) dr$$

$$p - p_{wf} = \frac{q \mu}{2 \pi k h} \left( \ln \frac{r}{r_w} - \frac{r^2 - r_w^2}{2 r_e^2} \right)$$

Considering that  $r^2 \gg r_w^2 \Rightarrow r^2 - r_w^2 \approx r^2$ , the above expression becomes:

$$p - p_{wf} = \frac{q \mu}{2 \pi k h} \left( \ln \frac{r}{r_w} - \frac{r^2}{2 r_e^2} \right) \quad (9.23)$$

At the reservoir boundary,  $r = r_e$  and  $p = p_e$ , hence:

$$p_e - p_{wf} = \frac{q \mu}{2 \pi k h} \left( \ln \frac{r_e}{r_w} - \frac{r_e^2}{2 r_e^2} \right)$$

Adding the skin effect defined by *Van Everdingen and Hurst* [1949], and making  $p_e$  the subject of the formula:

$$p_e = p_{wf} + \frac{q \mu}{2 \pi k h} \left( \ln \frac{r_e}{r_w} - \frac{1}{2} + S \right) \quad (9.24)$$

Expressing PSS in terms of  $p_{Avg}$  by substituting  $p$  in equation (9.23) into equation (9.14), which is  $p_{Avg} =$

$$\frac{2}{r_e^2} \int_{r_w}^{r_e} p r dr:$$

$$p_{Avg} = \frac{2}{r_e^2} \int_{r_w}^{r_e} \left[ p_{wf} + \frac{q \mu}{2 \pi k h} \left( \ln \frac{r}{r_w} - \frac{r^2}{2 r_e^2} \right) \right] r dr$$

$$p_{Avg} = \frac{2}{r_e^2} \left( \frac{p_{wf} r^2}{2} \Big|_{r_w}^{r_e} + \int_{r_w}^{r_e} \left[ \frac{q \mu}{2 \pi k h} \left( r \ln \frac{r}{r_w} - \frac{r^3}{2 r_e^2} \right) \right] dr \right)$$

Carrying out integration by parts in similar way to equation (9.15):

$$p_{Avg} = \frac{2}{r_e^2} \left( \frac{p_{wf} r_e^2}{2} \Big|_{r_w}^{r_e} + \int_{r_w}^{r_e} \left[ \frac{q\mu}{2\pi kh} \left( r \ln \frac{r}{r_w} - \frac{r^3}{2 r_e^2} \right) \right] dr \right)$$

$$p_{Avg} = \frac{2}{r_e^2} \left( \frac{p_{wf} (r_e^2 - r_w^2)}{2} + \frac{q\mu}{2\pi kh} \left( \left( \frac{r^2}{2} \ln \frac{r}{r_w} - \frac{r^2}{4} \right) \Big|_{r_w}^{r_e} - \frac{r^4}{8 r_e^2} \Big|_{r_w}^{r_e} \right) \right)$$

$$p_{Avg} = \frac{2}{r_e^2} \left( \frac{p_{wf} (r_e^2 - r_w^2)}{2} + \frac{q\mu}{2\pi kh} \left( \left( \frac{r_e^2}{2} \ln \frac{r_e}{r_w} - \frac{(r_e^2 - r_w^2)}{4} - \frac{(r_e^4 - r_w^4)}{8 r_e^2} \right) \right) \right)$$

$$p_{Avg} = \frac{2}{r_e^2} \left( \frac{p_{wf} r_e^2}{2} + \frac{q\mu}{2\pi kh} \left( \frac{r_e^2}{2} \ln \frac{r_e}{r_w} - \frac{r_e^2}{4} - \frac{r_e^4}{8 r_e^2} \right) \right)$$

$$p_{Avg} = \frac{2}{r_e^2} \left( p_{wf} + \frac{q\mu}{2\pi kh} \left( \ln \frac{r_e}{r_w} - \frac{1}{2} - \frac{1}{4} \right) \right)$$

$$p_{Avg} = p_{wf} + \frac{q\mu}{2\pi kh} \left( \ln \frac{r_e}{r_w} - \frac{3}{4} \right)$$

Adding the skin effect defined by *Van Everdingen and Hurst* [1949]:

$$p_{Avg} = p_{wf} + \frac{q\mu}{2\pi kh} \left( \ln \frac{r_e}{r_w} - \frac{3}{4} + S \right)$$

$$p_{Avg} = p_{wf} + \frac{141.2Bq\mu}{kh} \left( \ln \frac{r_e}{r_w} - \frac{3}{4} + S \right) \text{ in EOF units} \tag{9.25}$$

In a similar way to the steady-state condition in Section 9.1, the PI under PSS conditions can be defined as:

$$PI_{PSS} = \frac{q}{(p_{Avg} - p_{wf})} = \frac{kh}{141.2\mu B \left( \ln \left( \frac{r_e}{r_w} \right) - 0.75 + S \right)} \tag{9.26}$$

In a similar way to the steady-state condition in Section 9.1, the difference between  $p_e$  and  $p_{Avg}$  for PSS conditions can be derived by equation (9.24) minus equation (9.25) in consistent units:

$$p_e - p_{Avg} = p_{wf} + \frac{q\mu}{2\pi kh} \left( \ln \frac{r_e}{r_w} - \frac{1}{2} + S \right) - \left( p_{wf} + \frac{q\mu}{2\pi kh} \left( \ln \frac{r_e}{r_w} - \frac{3}{4} + S \right) \right)$$

$$p_e - p_{Avg} = \frac{1}{4} \frac{q\mu}{2\pi kh} = \frac{q\mu}{8\pi kh}$$

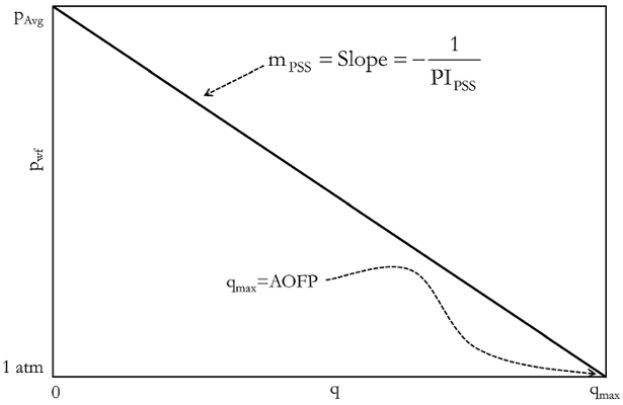


**Figure 9.13** IPR plot for a reservoir–wellbore system producing under PSS conditions.

**Table 9.4** Back Pressure Testing for Exercise 9.4.

$p_{wf}$ (psia)	$q_o$ (stb/D)
2,951.61	30
2,932.38	35
2,901.61	43

In EOF units, this becomes:

$$p_e - p_{Avg} = \frac{141.2Bq\mu}{4 kh}$$

$$p_e - p_{Avg} = 35.3 \frac{Bq\mu}{kh} \text{ in EOF units} \tag{9.27}$$

The IPR plot for a single-phase slightly compressible or incompressible fluid at PSS conditions takes a shape similar to that at steady-state conditions. The plot has the same features but with different values when compared with the SS equivalent (Fig. 9.13).

**Exercise 9.4** Defining the IPR Using PI

A black oil producing with zero water cut above the bubble point pressure from a high permeability reservoir with a closed no-flow boundary system has reached a PSS condition. Stabilized  $p_{wf}$  and corresponding  $q$  measured during back pressure testing are shown in Table 9.4. During the test, reservoir depletion was considered insignificant.

1. Determine the PI of the well–reservoir system; AOFP,  $p_{Avg}$ .
2. If the  $p_{wf}$  is reduced using an artificial lift system to 1,270.85 psia, determine the well flow rate.

**Solution Steps.**

- Step 1: plot  $p_{wf}$  against  $q_o$  (Fig. 9.14).
- Step 2: the negative inverse of slope is the PI.

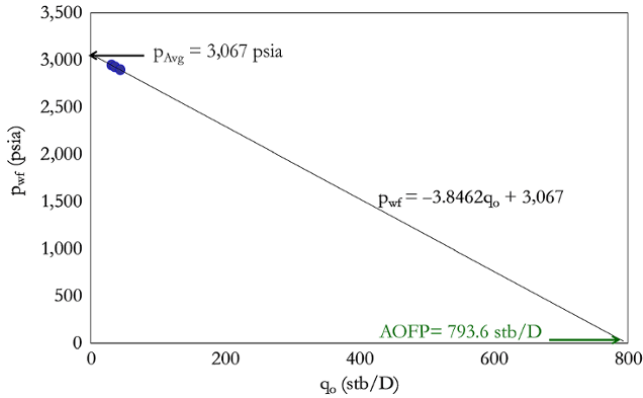


Figure 9.14 IPR for Exercise 9.4.

Step 3:  $q_o$  at  $p_{wf}$  of 14.7 psia is AOF, the intercept of IPR on  $p_{wf}$  axis ( $y$ -axis) is the  $p_{Avg}$ .

Step 4: since the PI has been determined in Q.1, the relationship between  $p_{wf}$  against  $q_o$  is established. Then, with  $p_{wf} = 1,270.85$  psia given,  $q_o$  is determined.

#### Solution.

Calculating the PI

$$PI_{PSS} = -\frac{1}{\text{Slope}}$$

But the slope =  $-3.846$ .

Hence,  $PI_{PSS} = \frac{1}{3.846} = 0.2615$  stb/D/psi.

Determining the IPR Equation

From equation (9.26), the IPR is:

$$PI_{PSS} = \frac{q}{(p_{Avg} - p_{wf})}$$

Substituting  $p_{Avg}$  and  $PI_{PSS}$  into this equation:

$$0.2615 = \frac{q}{(3,067 - p_{wf})}$$

Making  $p_{wf}$  the subject of the formula:

$$\begin{aligned} 3,067 - \frac{q}{0.2615} &= p_{wf} \\ p_{wf} &= 3,067 - 3.846q \end{aligned} \quad (9.28)$$

When  $q_o = 0$ ,  $p_{wf} = p_{Avg}$ .

Substituting  $q_o = 0$  into equation (9.28):

$$\begin{aligned} p_{wf} &= 3,067 - 3.846q \\ p_{Avg} &= 3,067 - 3.846 \times 0 \\ p_{Avg} &= 3,067 \text{ psia} \end{aligned}$$

#### Calculating AOF

$q = q_{max} = \text{AOF}$  when  $p_{wf} = 14.7$  psia.

Substituting  $p_{wf} = 14.7$  into equation (9.28):

$$14.7 = 3067 - 3.846q$$

Making  $q$  the subject of the formula:

$$q = \text{AOF} = 793.6 \text{ stb/D}$$

AOF = 794 stb/D

Calculating Well Flow Rate When  $p_{wf} = 1,270.85$  psia;

Substituting  $p_{wf} = 1,270.85$  psia into equation (9.28):

$$1,270.85 = 3,067 - 3.846q$$

$$q = 467 \text{ stb/D}$$

$q$  at  $p_{wf} = 1,270.85$  psia is 467 stb/D

Where there are limited reservoir and well data for use of analytical IPR models, PI from similar a well–reservoir system maybe the only alternative for back pressure prediction. Where PI has been defined based on analogue, sensitivity analysis should be considered to give a range of possible outcomes.

### 9.2.1. Generalized Pseudosteady State Inflow Equation

PSS IPR described by equation (9.25) was derived for a reservoir with circular geometry; but reservoir boundaries come in various geometries. Noncircular reservoir geometries can be related to circular geometry using *shape correction factors*.

From equation (9.25):

$$p_{Avg} = p_{wf} + \frac{q\mu}{2\pi kh} \left( \ln \frac{r_e}{r_w} - \frac{3}{4} + S \right)$$

$$p_{Avg} = p_{wf} + \frac{q\mu}{2\pi kh} \left( \ln \frac{r_e}{r_w} - \ln \left( e^{\frac{3}{4}} \right) + S \right)$$

$$p_{Avg} = p_{wf} + \frac{q\mu}{2\pi kh} \left( \ln \left( \frac{r_e^2}{r_w^2} \right)^{\frac{1}{2}} - \ln \left( e^{\frac{3}{4}} \right)^{\frac{1}{2}} + S \right)$$

$$p_{Avg} = p_{wf} + \frac{q\mu}{2\pi kh} \left( \ln \left( \frac{r_e^2}{r_w^2 e^{\frac{3}{2}}} \right) + S \right)$$

$$p_{Avg} = p_{wf} + \frac{q\mu}{2\pi kh} \left( \frac{1}{2} \ln \left( \frac{r_e^2}{r_w^2 e^{\frac{3}{2}}} \right) + S \right)$$

$$p_{Avg} = p_{wf} + \frac{q\mu}{2\pi kh} \left( \frac{1}{2} \ln \left( \frac{\pi r_e^2}{\pi r_w^2 e^{\frac{3}{2}}} \right) + S \right)$$

$$p_{Avg} = p_{wf} + \frac{q\mu}{2\pi kh} \left( \frac{1}{2} \ln \left( \frac{4 \pi r_e^2}{4 \pi r_w^2 e^{\frac{3}{2}}} \right) + S \right)$$

$$p_{Avg} = p_{wf} + \frac{q\mu}{2\pi kh} \left( \frac{1}{2} \ln \left( \frac{4A}{4 \pi r_w^2 e^{\frac{3}{2}}} \right) + S \right)$$

$$p_{Avg} = p_{wf} + \frac{q\mu}{2\pi kh} \left( \frac{1}{2} \ln \left( \frac{4A}{56.318566 r_w^2} \right) + S \right)$$

$$p_{Avg} = p_{wf} + \frac{q\mu}{2\pi kh} \left( \frac{1}{2} \ln \left( \frac{4A}{\gamma 31.6206 r_w^2} \right) + S \right)$$

where  $\gamma$  (1.78107) is the exponential of Euler's constant and 31.6206 is the *Dietz shape factor* for circular geometry. A generalized PSS IPR can, therefore, be written as:

$$p_{Avg} = p_{wf} + \frac{q\mu}{2\pi kh} \left( \frac{1}{2} \ln \left( \frac{4A}{\gamma C_A r_w^2} \right) + S \right) \text{ in consistent units}$$

$$p_{Avg} = p_{wf} + \frac{141.2Bq\mu}{kh} \left( \frac{1}{2} \ln \left( \frac{4A}{\gamma C_A r_w^2} \right) + S \right) \text{ in EOF units} \tag{9.29}$$

where  $A$  is the drainage area and  $C_A$  is the Dietz shape factor. Fig. 9.15 shows the Dietz shape factor for different well-reservoir configurations. *Shape factor*,  $C_A$ , is dependent on the drainage shape and well location relative to the reservoir boundaries. Fig. 9.15 also indicates the time for a flowing well in a given reservoir geometry to reach PSS. Since equation (9.29) is for PSS condition, it is very important that PSS is reached before equation (9.29) is used.

$(t_{DA})_{PSS}$  is the dimensionless time for a well producing at constant rate to reach pseudosteady state condition and defined as:

$$(t_{DA})_{PSS} = \frac{k}{\phi\mu c_t A} t_{PSS} \text{ in consistent units and}$$

$$(t_{DA})_{PSS} = \frac{0.000264k}{\phi\mu c_t A} t_{PSS} \text{ in EOF units} \tag{9.30}$$

Analytical methods for calculating shape factors provide a convenient way of defining Dietz shape factors in software development. The Dietz shape factor for an isotropic rectangular reservoir with a vertical well in an arbitrary position can be expressed as:

$$C_A = \frac{16\pi^2 f_1 \sin^2(\pi f_3)}{\gamma \exp(f_4)} = \frac{88.6657 f_1 \sin^2(\pi f_3)}{\exp(f_4)} \text{ (Lu Tiab, 2010)} \tag{9.31}$$

where

$$\gamma = 1.78107, f_1 = \frac{x_e}{y_e}, f_2 = \frac{x_w}{x_e}, f_3 = \frac{y_w}{y_e} \text{ and}$$

$$f_4 = 8\pi f_1 \left( \frac{1}{6} - \frac{f_2}{2} + \frac{f_2^2}{2} \right)$$

Parameters  $x_e, y_e, x_w, y_w$  are defined in Fig. 9.16.

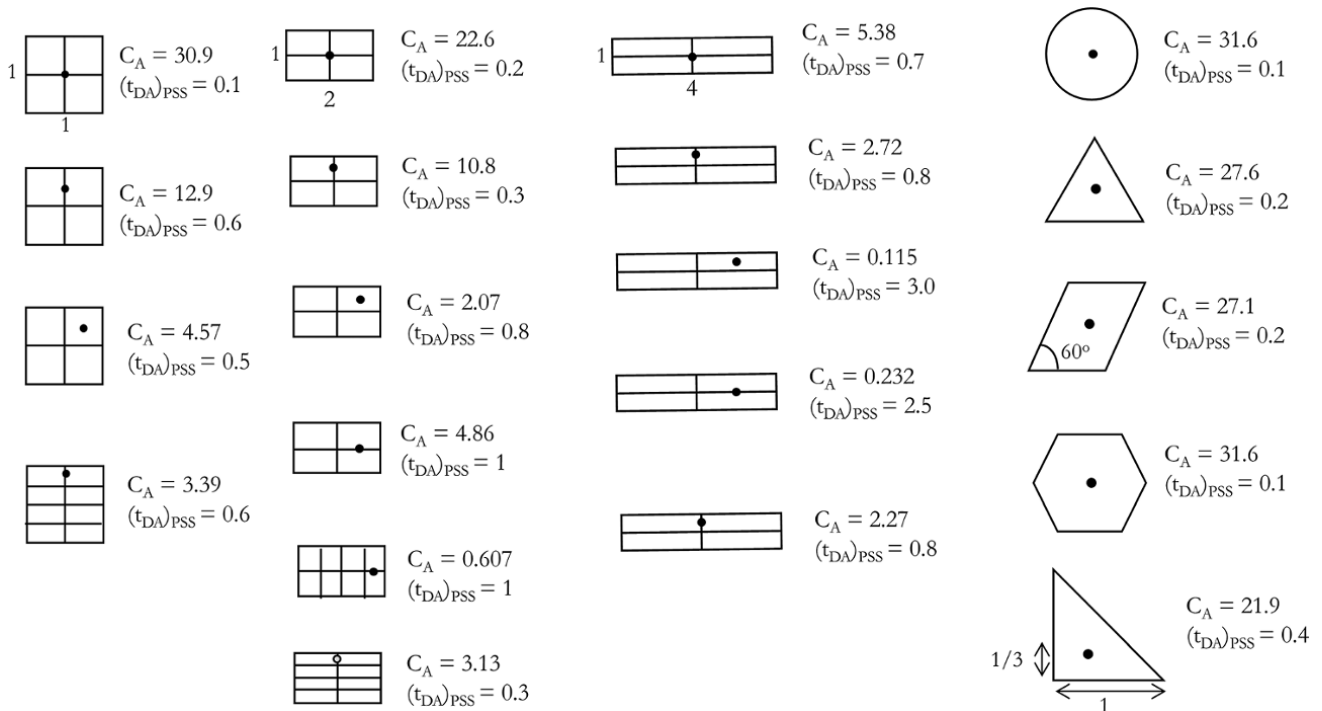


**Figure 9.15** Dietz shape factors ( $C_A$ ) and dimensionless time to reach PSS  $(t_{DA})_{PSS}$  for different reservoir-well geometries [Adapted from Dietz, 1965].

9.2.2. Drainage Area

Drainage area in IPR models can be determined from geological and geophysical analysis, well test analysis or well spacing information. Drainage area can be defined by physical no-flow boundaries, constant pressure boundaries, or a combination of no-flow and constant pressure boundaries. As discussed in Chapter 8 (8.5.1.12), the presence of nearby producing well(s) around a well of interest can create a no-flow boundary effect and the presence of nearby injecting well(s) around a well of interest can create a constant pressure boundary effect.

When enclosing reservoir boundaries have not been reached by diffusing pressure, bottomhole pressure response is characterized by transient behavior. Well test analysis methods described in Chapter 8 must be used for well and reservoir characterization during transient flow.

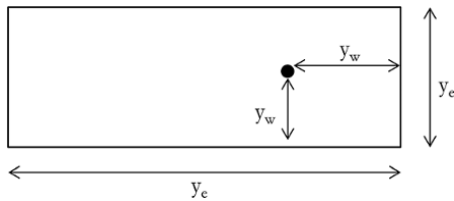


Figure 9.16 Rectangular closed boundary with parameter definition for calculating  $C_A$ .

Exercise 9.5 IPR Calculations for Oil Well Producing Under Pseudosteady State

Table 9.5 shows the sandface bottomhole flowing pressure ( $p_{wf}$ ) and the oil production rate from an oil well with 0.35 ft wellbore radius and skin effect of 2, producing from a 30-ft pay reservoir with permeability of 150 mD, temperature of 135°F, porosity of 0.25, and  $c_t$  of 5 E-5  $\text{psi}^{-1}$ . Oil at reservoir conditions has a  $B_o$  of 1.5 bbl/stb and  $\mu_o$  of 1 cp. The well-reservoir geometry and aspect ratio is best described by Fig. 9.17.

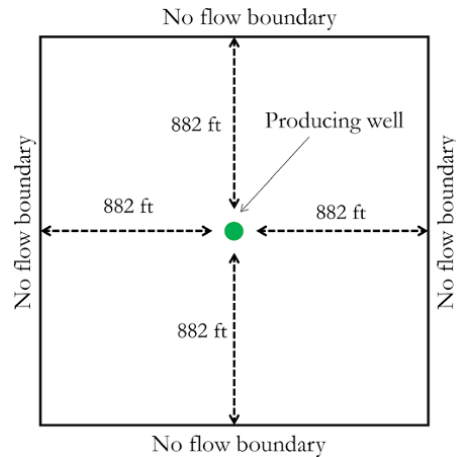


Figure 9.17 Well with boundaries for Exercise 9.5.

Table 9.5 Pressure–Rate History for Exercise 9.5.

Time (hr)	$p_{wf}$ (psia)	Oil Rate (stb/D)	Time (hr)	$p_{wf}$ (psia)	Oil Rate (stb/D)	Time (hr)	$p_{wf}$ (psia)	Oil Rate (stb/D)
0.001	2,289.81	0	139.627	2,267.12	0	1,000.000	2,251.72	0
0.008	2,289.81	0	192.164	2,274.72	0	1,000.001	2,251.23	405
0.063	2,289.81	0	404.000	2,275.57	0	1,000.004	2,249.77	405
0.503	2,289.81	0	404.001	2,275.06	405	1,000.016	2,244.33	405
4.000	2,289.81	0	404.004	2,273.63	405	1,000.061	2,226.42	405
4.001	2,289.31	405	404.015	2,268.32	405	1,000.240	2,184.02	405
4.004	2,287.99	405	404.059	2,250.86	405	1,000.944	2,131.62	405
4.013	2,283.37	405	404.231	2,209.32	405	1,003.716	2,100.60	405
4.049	2,268.72	405	404.900	2,156.94	405	1,014.624	2,084.25	405
4.180	2,232.87	405	407.511	2,125.28	405	1,057.552	2,070.77	405
4.658	2,181.68	405	417.686	2,108.73	405	1,226.500	2,050.00	405
6.410	2,145.72	405	457.354	2,095.15	405	1,226.501	2,050.49	0
12.824	2,127.62	405	612.000	2,075.02	405	1,226.504	2,052.00	0
36.309	2,114.32	405	612.001	2,075.51	0	1,226.516	2,057.76	0
122.300	2,100.02	405	612.004	2,077.08	0	1,226.566	2,077.11	0
122.301	2,100.52	0	612.017	2,083.27	0	1,226.769	2,122.08	0
122.304	2,102.02	0	612.073	2,104.26	0	1,227.590	2,174.25	0
122.316	2,107.74	0	612.305	2,151.94	0	1,230.916	2,203.06	0
122.366	2,126.85	0	613.273	2,203.54	0	1,244.389	2,217.54	0
122.564	2,171.40	0	617.320	2,230.40	0	1,298.960	2,225.36	0
123.366	2,223.60	0	634.226	2,244.14	0	1,520.000	2,227.80	0
126.597	2,252.66	0	704.865	2,250.48	0			

1. Establish if at the end of the first drawdown, PSS condition has been reached.
2. Calculate  $C_A$  using equation (9.31) and compare with published Dietz shape factor (Fig. 9.15).
3. Calculate  $p_{Avg}$  from the 1st, 2nd and 3rd DD (1DD, 3DD and 5DD) using the PSS equation and compare with the stabilized value of 1st, 2nd, and 3rd final value of pressure at the end of each BU.
4. Make IPR for the different flow periods.

**Solution.**

Fig. 9.18 shows the pressure–rate history from Table 9.5. Pressure at the end of each flow period is shown on pressure history.

1. From Fig. 9.15  $(t_{AD})_{PSS} = 0.1$ .  
Also, from equation (9.30):

$$(t_{DA})_{PSS} = \frac{0.000264 \text{ k}}{\phi \mu c_t A} t_{PSS} \text{ in EOF units}$$

Make  $t_{PSS}$  the subject of the formula and substitute given parameters to determine  $t_{PSS}$ :

$$t_{PSS} = (t_{DA})_{PSS} \frac{\phi \mu c_t A}{0.000264 \text{ k}} \quad (9.32)$$

$$A = L^2$$

where L is one of the length of a square boundary.  
From Fig. 9.17,  $L = 2 \times 882 = 1764 \text{ ft}$ .  
Therefore,  $A = 1764^2 = 31,11,696 \text{ ft}^2$ .  
Substituting known parameters into equation (9.30):

$$t_{PSS} = 0.1 \frac{0.25 \times 1 \times 5 \times 10^{-5} \times 31,11,696}{0.000264 \times 150} = 98.22 \text{ hrs}$$

Test duration for the 1DD ( $t_{DD1}$ ) from data given is:

$$t_{DD1} = 118.3 - 4 = 118.3 \text{ hr}$$

Since  $t_{DD1} > t_{PSS}$ , PSS was reached at the end of the 1DD.

2. From equation (9.31):

$$C_A = \frac{16\pi^2 f_1 \sin^2(\pi f_3)}{\gamma \exp(f_4)} = \frac{88.6657 f_1 \sin^2(\pi f_4)}{\exp(f_4)}$$

where  $\gamma = 1.78107$  and the aspect ratios are defined as:

$$f_1 = \frac{x_e}{y_e}, f_2 = \frac{x_w}{x_e}, f_3 = \frac{y_w}{y_e} \text{ and } f_4 = 8\pi f_1 \left( \frac{1}{6} - \frac{f_2}{2} + \frac{f_2^2}{2} \right)$$

Calculating the aspect ratio parameters for the boundary in Fig. 9.17 with parameters from Fig. 9.16:

$$f_1 = \frac{x_e}{y_e} = \frac{2 \times 882}{2 \times 882} = 1$$

$$f_2 = \frac{x_w}{x_e} = \frac{882}{2 \times 882} = \frac{1}{2}$$

$$f_3 = \frac{y_w}{y_e} = \frac{882}{2 \times 882} = \frac{1}{2}$$

$$f_4 = 8 \times \pi \times 1 \times \left( \frac{1}{6} - \frac{1/2}{2} + \frac{(1/2)^2}{2} \right) = 1.047197551$$

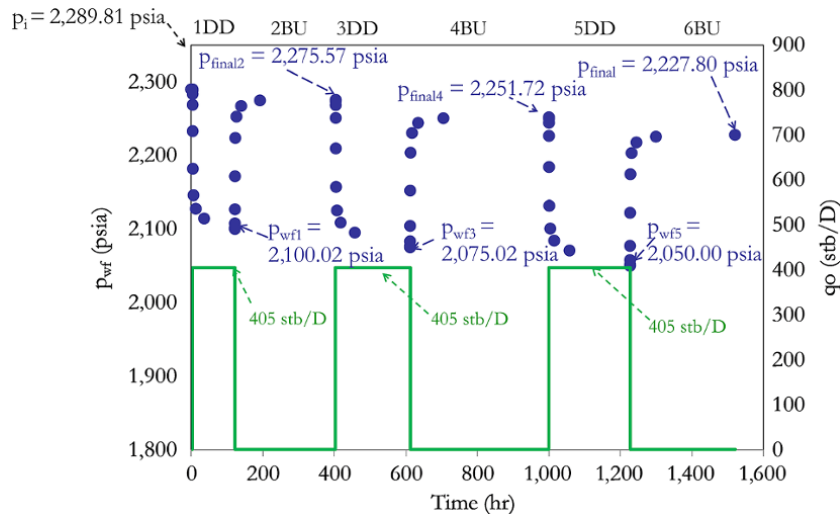


Figure 9.18 Pressure–rate history for Exercise 9.5.

$$C_A = \frac{88.6657(1)\sin^2(\pi(1/2))}{\exp(1.047197551)} = 31.1$$

Comparing  $C_A$  calculated with that from Fig. 9.15, which is 30.9, gives error of about 0.6%.

3. From equation (9.29):

$$p_{Avg} = p_{wf} + \frac{141.2Bq\mu}{kh} \left( \frac{1}{2} \ln \left( \frac{4A}{\gamma C_A r_w^2} \right) + S \right)$$

End of the 1DD,  $p_{wf} = 2,100.02$  psia.

$$p_{Avg1} = p_{wf1} + \frac{141.2Bq\mu}{kh} \left( \frac{1}{2} \ln \left( \frac{4A}{\gamma C_A r_w^2} \right) + S \right)$$

$$p_{Avg1} = 2,100.02 + \frac{141.2 \times 1.5 \times 405 \times 1}{150 \times 30} \left( \frac{1}{2} \ln \left( \frac{4 \times 31,11,696}{1.78107 \times 31.1 \times 0.35^2} \right) + 2 \right) = 2275.60 \text{ psia}$$

End of the 3DD,  $p_{wf} = 2,075.02$  psia.

$$p_{Avg3} = p_{wf3} + \frac{141.2Bq\mu}{kh} \left( \frac{1}{2} \ln \left( \frac{4A}{\gamma C_A r_w^2} \right) + S \right)$$

$$p_{Avg3} = 2,075.02 + \frac{141.2 \times 1.5 \times 405 \times 1}{150 \times 30} \left( \frac{1}{2} \ln \left( \frac{4 \times 31,11,696}{1.78107 \times 31.1 \times 0.35^2} \right) + 2 \right) = 2,250.60 \text{ psia}$$

End of the 5DD,  $p_{wf} = 2,050.00$  psia.

$$p_{Avg5} = p_{wf5} + \frac{141.2Bq\mu}{kh} \left( \frac{1}{2} \ln \left( \frac{4A}{\gamma C_A r_w^2} \right) + S \right)$$

$$p_{Avg5} = 2,050.00 + \frac{141.2 \times 1.5 \times 405 \times 1}{150 \times 30} \left( \frac{1}{2} \ln \left( \frac{4 \times 31,11,696}{1.78107 \times 31.1 \times 0.35^2} \right) + 2 \right) = 2,225.58 \text{ psia}$$

$p_{final}$  for the 2BU, 4BU, and 6BU are shown in Fig. 9.18. Table 9.6 shows the comparison of  $p_{Avg}$  from the 1DD, 3DD and 5DD compared with  $p_{final}$  from the 2BU, 4BU, and 6BU respectively.

**Table 9.6** Comparison of  $p_{Avg}$  and Final Stabilized Buildup Pressure ( $p_{final}$ ) for Exercise 9.5.

$p_{Avg}$ (psia)	$p_{final}$ (psia)	difference (psi)
2,275.60	2,275.57	-0.03
2,250.60	2,251.72	1.12
2,225.58	2,227.80	2.22

Table 9.6 shows that for a well producing at PSS, when the well is shut-in long enough to attain constant and stable pressure,  $p_{wf}$  at the sandface will tend to average reservoir pressure.

**Exercise 9.6** Effect of Depletion on IPR

The pressure profile for an oil well producing from a homogeneous reservoir at PSS is shown in Fig. 9.19.

Given the drainage Area = 31,11,696 ft<sup>2</sup>,  $C_A = 30.9$ ,  $k = 300$  mD,  $S = 0$ ,  $h = 65$  ft,  $r_w = 0.35$  ft,  $\phi = 0.1$ ,  $B_o = 1.7$  bbl/stb,  $\mu_o = 0.5$  cp,  $c_t = 5.5E-5$  psi<sup>-1</sup>.

- Determine  $p_{Avg}$  at the end of each drawdown
- (i) create an IPR plot considering each drawdown as a separate depletion level;  
(ii) create an IPR plot considering all drawdown together as one depletion level;
- (iii) compare all IPR plots in (i) and (ii).
- Compare AOF and PI for each IPR.

**Solution Steps.**

*Step 1:* using equation (9.29) to determine  $p_{Avg}$  for DD1, DD2, and DD3, make three IPR plots (IPR<sub>1</sub>; IPR<sub>2</sub> and IPR<sub>3</sub>).

*Step 2:*

(i) for IPR<sub>1</sub> with coordinate of [ $q = 0$ ,  $p_{Avg1}$ ;  $q_1$ ,  $p_{wf1}$ ], extrapolate to AOF<sub>1</sub> ( $q_{o \max 1}$ ); for IPR<sub>2</sub> with coordinate of [ $q = 0$ ,  $p_{Avg2}$ ;  $q_2$ ,  $p_{wf2}$ ], extrapolate to AOF<sub>2</sub> ( $q_{o \max 2}$ ); for IPR<sub>3</sub> with coordinate of [ $q = 0$ ,  $p_{Avg3}$ ;  $q_3$ ,  $p_{wf3}$ ], extrapolate to AOF<sub>3</sub> ( $q_{o \max 3}$ ).

(ii) Using coordinates:  $q_1$ ,  $p_{wf1}$ ;  $q_2$ ,  $p_{wf2}$  and  $q_3$ ,  $p_{wf3}$ , create IPR<sub>123</sub> then extrapolate to  $p_{Avg123}$  and AOF<sub>123</sub> ( $q_{o \max 123}$ ).

**Solution.**

- As in Exercise 9.5:  
• End of 1DD,  $p_{wf} = 4,323.85$  psia

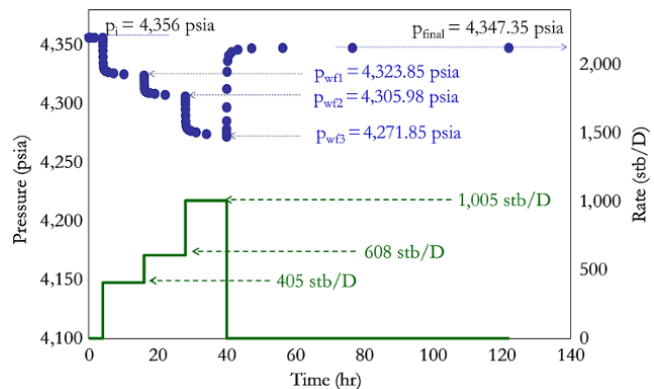


**Figure 9.19** Pressure–rate history for Exercise 9.6.



$$p_{Avg1} = p_{wf1} + \frac{141.2Bq_1\mu}{kh} \left( \frac{1}{2} \ln \left( \frac{4A}{\gamma C_A r_w^2} \right) + S \right)$$

$$p_{Avg1} = 4,323.85 + \frac{141.2 \times 1.7 \times 405 \times 0.5}{300 \times 65} \left( \frac{1}{2} \ln \left( \frac{4 \times 31,11,696}{1.78107 \times 30.9 \times 0.35^2} \right) + 0 \right) = 4,341.83 \text{ psia}$$

• End of 2DD,  $p_{wf} = 4,305.98$  psia

$$p_{Avg2} = p_{wf2} + \frac{141.2Bq_2\mu}{kh} \left( \frac{1}{2} \ln \left( \frac{4A}{\gamma C_A r_w^2} \right) + S \right)$$

$$p_{Avg2} = 4,305.98 + \frac{141.2 \times 1.7 \times 608 \times 0.5}{300 \times 65} \left( \frac{1}{2} \ln \left( \frac{4 \times 31,11,696}{1.78107 \times 30.9 \times 0.35^2} \right) + 0 \right) = 4,332.98 \text{ psia}$$

• End of 3DD,  $p_{wf} = 4,271.85$  psia

$$p_{Avg3} = p_{wf3} + \frac{141.2Bq_3\mu}{kh} \left( \frac{1}{2} \ln \left( \frac{4A}{\gamma C_A r_w^2} \right) + S \right)$$

$$p_{Avg3} = 4,271.85 + \frac{141.2 \times 1.7 \times 1,005 \times 0.5}{300 \times 65} \left( \frac{1}{2} \ln \left( \frac{4 \times 31,11,696}{1.78107 \times 30.9 \times 0.35^2} \right) + 0 \right) = 4,316.48 \text{ psia}$$

2. Calculated IPR data for Exercise 9.6 are shown in Table 9.7

A comparison of IPR plots from the data in Table 9.7 is shown Fig. 9.20.

Calculating AOFP ( $q_o \text{ max}$ ) and PI for each IPR Model

At  $p_{wf} = 14.7$  psia,  $q = q_o \text{ max}$

Also, from Fig. 9.13  $PI_{PSS} = -\frac{1}{\text{Slope}}$

IPR equations are shown in Fig. 9.20.

• AOFP ( $q_o \text{ max}$ ) and PI for IPR<sub>1</sub>:

$$p_{wf1} = -0.0444q + 4,341.83$$

at  $p_{wf1} = 14.7$ ,  $q = \text{AOFP}$

$$14.7 = -0.0444 q_{o \text{ max}} + 4,341.83$$

$$q_{o \text{ max}} = \frac{4,341.83 - 14.7}{0.0444} = 97,052.9 \text{ stb/D}$$

$$PI_{PSS} = \frac{1}{0.0444} = 22.5 \text{ stb/D/psi}$$

• AOFP ( $q_o \text{ max}$ ) and PI for IPR<sub>2</sub>:

$$p_{wf2} = -0.0444q + 4,332.98$$

at  $p_{wf2} = 14.7$ ,  $q = \text{AOFP}$

$$14.7 = -0.0444 q_{o \text{ max}} + 4,332.98$$

$$q_{o \text{ max}} = \frac{4,332.98 - 14.7}{0.0444} = 96,650.45 \text{ stb/D}$$

$$PI_{PSS} = \frac{1}{0.0444} = 22.5 \text{ stb/D/psi}$$

• AOFP ( $q_o \text{ max}$ ) and PI for IPR<sub>3</sub>:

$$p_{wf3} = -0.0444q + 4,316.48$$

at  $p_{wf3} = 14.7$ ,  $q = \text{AOFP}$

$$p_{wf3} = -0.0444 q_{o \text{ max}} + 4,316.48$$

$$q_{o \text{ max}} = \frac{4,316.48 - 14.7}{0.0444} = 95,881.76 \text{ stb/D}$$

$$PI_{PSS} = \frac{1}{0.0444} = 22.5 \text{ stb/D/psi}$$

• AOFP ( $q_o \text{ max}$ ) and PI for IPR<sub>123</sub>:

$$p_{wf123} = -0.0866q + 4,358.79$$

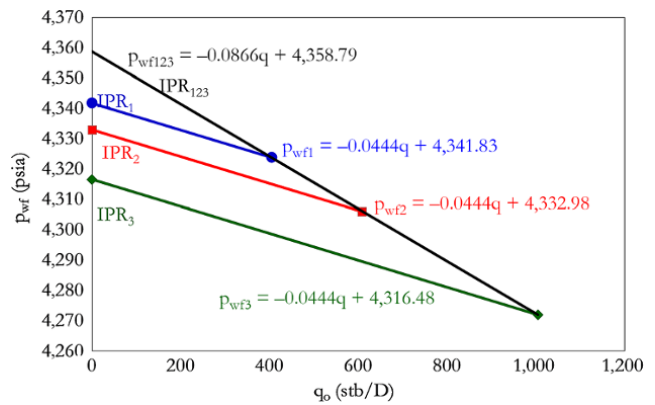
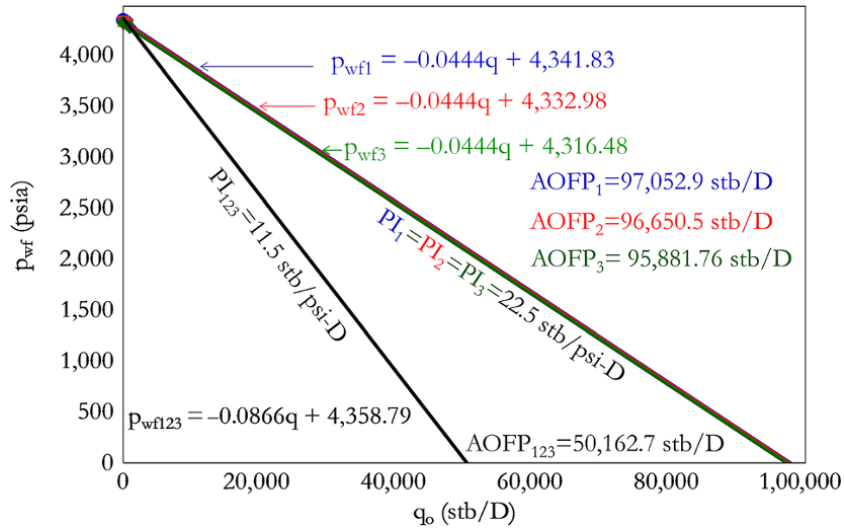


Figure 9.20 Comparison of IPRs showing effect of depletion.

Table 9.7 IPR data for Exercise 9.6.

IPR <sub>1</sub>		IPR <sub>2</sub>		IPR <sub>3</sub>		IPR <sub>123</sub>	
q (stb/D)	p <sub>wf</sub> (psia)	q (stb/D)	p <sub>wf</sub> (psia)	q (stb/D)	p <sub>wf</sub> (psia)	q (stb/D)	p <sub>wf</sub> (psia)
0.0	4,341.83	0.0	4,332.98	0.0	4,316.48	405.0	4,323.85
405.0	4,323.85	608.0	4,305.98	1,005.0	4,271.85	608.0	4,305.98
						1,005.0	4,271.85



**Figure 9.21** Comparison of AOF and PI showing the effect of depletion.

at  $p_{wf123} = 14.7$ ,  $q = \text{AOF}$

$$14.7 = -0.0866q_{\text{omax}} + 4,358.79$$

$$q_{\text{omax}} = \frac{4,358.79 - 14.7}{0.0866} = 50,162.70 \text{ stb/D}$$

$$\text{PI}_{\text{PSS}} = \frac{1}{0.0866} = 11.5 \text{ stb/D/psi}$$

A comparison of AOF and PI for  $\text{IPR}_1$ ,  $\text{IPR}_2$ ,  $\text{IPR}_3$ , and  $\text{IPR}_{123}$  showing the effect of depletion is shown in Fig. 9.21.

Exercise 9.6 shows that there is always some level of depletion that should not be ignored during a multirate test when PSS has been reached. Hence, test data obtained during PSS (depleting) reservoir may not extrapolate to the correct  $p_{\text{Avg}}$  due to the effect of depletion when combined as a single IPR test.

### 9.2.3. Single-Phase Gas IPR

Linearizing the diffusivity equation for different phase conditions has been discussed under gas pseudopressure and two-phase pseudopressure Chapter 7 (7.1.1) and Chapter 8 (8.7).

Replacing pressure with normalized pseudopressure in the generalized IPR equation would yield the equivalent IPR equation for gas.

Starting from equation (9.29):

$$p_{\text{Avg}} = p_{\text{wf}} + \frac{141.2Bq\mu}{kh} \left( \frac{1}{2} \ln \left( \frac{4A}{\gamma C_A r_w^2} \right) + S \right)$$

Replacing pressure with  $m_n(p)$ ; defining  $B_{gi}$  from equation (3.20):

$$B_{gi} = \frac{Z_i T_i p_{\text{sc}}}{p_i T_{\text{sc}}} \text{ (cf/scf)}$$

$$B_{gi} = 0.1781 \frac{Z_i T_i p_{\text{sc}}}{p_i T_{\text{sc}}} \text{ (bbl/scf)}$$

$$B_{gi} = 0.1781 \times 10^3 \frac{Z_i T_i p_{\text{sc}}}{p_i T_{\text{sc}}} \text{ (bbl/Mscf)}$$

Hence:

$$m_n(p_{\text{Avg}}) = m_n(p_{\text{wf}}) + 141.2 \times 0.1781 \times 10^3 \times \frac{Z_i T_i p_{\text{sc}} q_g \mu_i}{p_i T_{\text{sc}} k_g h} \left( \frac{1}{2} \ln \left( \frac{4A}{\gamma C_A r_w^2} \right) + S \right)$$

$$m_n(p_{\text{Avg}}) = m_n(p_{\text{wf}}) + 25.14772 \times 10^3 \frac{Z_i T_i p_{\text{sc}} q_g \mu_i}{p_i T_{\text{sc}} k_g h} \left( \frac{1}{2} \ln \left( \frac{4A}{\gamma C_A r_w^2} \right) + S \right)$$

$$m_n(p_{\text{Avg}}) = m_n(p_{\text{wf}}) + 25.14772 \times 10^3 \frac{Z_i T_i \times 14.7 q_g \mu_i}{p_i \times 520.67 k_g h} \left( \frac{1}{2} \ln \left( \frac{4A}{\gamma C_A r_w^2} \right) + S \right)$$

$$m_n(p_{\text{Avg}}) = m_n(p_{\text{wf}}) + 711 \frac{q_g \mu_i Z_i T_i}{p_i k_g h} \left( \frac{1}{2} \ln \left( \frac{4A}{\gamma C_A r_w^2} \right) + S \right) \text{ in terms of } A \quad (9.33)$$

or

$$m_n(p_{\text{Avg}}) = m_n(p_{\text{wf}}) + 711 \frac{q_g \mu_i Z_i T_i}{p_i k_g h} \left( \ln \frac{r_e}{r_w} - \frac{3}{4} + S \right) \text{ in terms of } r_e \quad (9.34)$$

Note that equation (9.33) when written as pseudopressure ( $m(p)$ ) instead of normalized pseudo-pressure ( $m_n(p)$ ) becomes:

$$m(p_{Avg}) \frac{\mu_i Z_i}{2p_i} = m(p_{wf}) \frac{\mu_i Z_i}{2p_i} + 711 \frac{q_g \mu_i Z_i T_i}{p_i k_g h} \left( \frac{1}{2} \ln \left( \frac{4A}{\gamma C_A r_w^2} \right) + S \right)$$

$$m(p_{Avg}) = m(p_{wf}) + 1422 \frac{q_g T_i}{k_g h} \left( \frac{1}{2} \ln \left( \frac{4A}{\gamma C_A r_w^2} \right) + S \right) \text{ in terms of A} \quad (9.35)$$

Thus, equation (9.34) in terms of  $m(p)$  becomes:

$$m(p_{Avg}) = m(p_{wf}) + 1422 \frac{q_g T_i}{k_g h} \left( \ln \frac{r_e}{r_w} - \frac{3}{4} + S \right) \text{ in terms of } r_e \quad (9.36)$$

For a pressure less than 2000 psia, the pseudopressure integral can be defined by equation 7.25, which is:

$$m(p) = 2 \int_{p_0}^p \frac{p}{\mu(p) Z(p)} dp = \frac{2}{\mu Z} \int_{p_0}^p p dp = \frac{p^2 - p_0^2}{\mu_i Z_i}$$

And, hence, normalized pseudopressure from the above becomes:

$$m_n(p) = \frac{\mu_i Z_i p^2 - p_0^2}{2p_i \mu_i Z_i} = \frac{p^2 - p_0^2}{2p_i}$$

Substituting  $m_n(p)$  above into equation (9.29):

$$\frac{p_{Avg}^2 - p_0^2}{2p_i} = \frac{p_{wf}^2 - p_0^2}{2p_i} + 25.14772 \times 10^3 \frac{Z_i T_i p_{sc} q_g \mu_i}{p_i T_{sc} k_g h} \left( \frac{1}{2} \ln \left( \frac{4A}{\gamma C_A r_w^2} \right) + S \right)$$

$$p_{Avg}^2 = p_{wf}^2 + 50.29544 \times 10^3 \frac{Z_i T_i p_{sc} q_g \mu_i}{T_{sc} k_g h} \left( \frac{1}{2} \ln \left( \frac{4A}{\gamma C_A r_w^2} \right) + S \right)$$

$$p_{Avg}^2 = p_{wf}^2 + 50.29544 \times 10^3 \frac{Z_i T_i \times 14.7 q_g \mu_i}{520.67 k_g h}$$

$$p_{Avg}^2 = p_{wf}^2 + \frac{1422 q_g \mu_i Z_i T_i}{k_g h} \left( \frac{1}{2} \ln \left( \frac{4A}{\gamma C_A r_w^2} \right) + S \right) \text{ in terms of A} \quad (9.37)$$

or

$$p_{Avg}^2 = p_{wf}^2 + \frac{1422 q_g \mu_i Z_i T_i}{k_g h} \left( \ln \frac{r_e}{r_w} - \frac{3}{4} + S \right) \text{ in terms of } r_e \quad (9.38)$$

#### 9.2.4. Two-Phase Flow IPR

IPR for multiphase flow can be defined by the use of the pseudopressure integrals discussed in Section 8.9. *Evinger and Muskat* [1942] described the steady-state flow equation for oil phase production by solution gas drive as:

$$q_o = \frac{7.08 kh}{\ln \left( \frac{r_e}{r_w} \right)} \int_{p_{wf}}^{p_c} \left( \frac{k_{ro}}{B_o \mu_o} \right) dp \quad (9.39)$$

From equation (9.39), the pseudopressure integral for oil wells producing below the bubble point pressure can then be deduced as:

$$m(p) = 2 \int_{p_0}^p \frac{k_{ro}}{\mu_o B_o} dp \text{ Raghavan (1976)} \quad (9.40)$$

where  $k_{ro}$  is the relative permeability of oil phase,  $\mu_o$  is the viscosity of oil phase,  $B_o$  is oil formation volume factor, and  $p_0$  is any low reference pressure.

*Jones and Raghavan* [1988] also proposed a pseudopressure integral interpretation of flowing well response in gas condensate wells as:

$$m(p) = 2 \int_{p_0}^p \left( \rho_o \frac{k_{ro}}{\mu_o} + \rho_g \frac{k_{rg}}{\mu_g} \right) dp \quad (9.41)$$

where  $k_{ro}$  is the relative permeability of the oil phase,  $k_{rg}$  is the relative permeability of the gas phase,  $\rho_o$  is the density of the oil phase,  $\rho_g$  is the density of the gas phase,  $p_0$  is any low reference pressure,  $\mu_o$  is the viscosity of the oil phase, and  $\mu_g$  is the viscosity of the gas phase.

A major challenge with the use of the pseudopressure transform approach for IPR for oil and gas below saturation pressure is the need for the relative permeability against saturation relationship (relative permeability model) and pressure against saturation relationship (from constant volume depletion (CVD) fluid experiment), which may not be available.

#### 9.2.5. Rate Dependent Skin Effect

A rate dependent skin effect, also called *skin due to turbulence*, often occurs in high velocity gas wells and may also occur in oil/liquid wells. Reducing rate dependent skin effect involves increasing the area of fluid flow into the wellbore, consequently creating a decrease in fluid velocity into the wellbore. Reduction of rate dependent

skin effect can be achieved by: increasing perforation density; increasing completion interval; well stimulation; and using horizontal wells instead of vertical wells.

### 9.2.5.1. Rate Dependent Skin Effect in Gas Wells.

Equations (9.34), (9.36), and (9.38) can be rewritten by defining  $S$  (total skin) as the sum of the mechanical skin (skin due to damage) and rate dependent skin effect (skin due to turbulence) as:

$$m_n(p_{Avg}) = m_n(p_{wf}) + 711 \frac{q_g \mu_i Z_i T_i}{p_i k_g h} \left( \ln \frac{r_e}{r_w} - \frac{3}{4} + S_w + Dq_g \right) \quad (9.42)$$

$$m(p_{Avg}) = m(p_{wf}) + 1,422 \frac{q_g T_i}{k_g h} \left( \ln \frac{r_e}{r_w} - \frac{3}{4} + S_w + Dq_g \right) \quad (9.43)$$

$$p_{Avg}^2 = p_{wf}^2 + \frac{1,422 q_g \mu_i Z_i T_i}{k_g h} \left( \ln \frac{r_e}{r_w} - \frac{3}{4} + S_w + Dq_g \right) \quad (9.44)$$

$Dq_g$  (skin due to turbulence) or  $D$  (turbulence factor) can be significant.

Aronofsky and Jenkins [1954], from the Forchheimer flow equation, derived the solution of stabilized gas flow in porous media. Hence, equation (9.42) maybe called the *Forchheimer IPR*, equation (9.43) called *Forchheimer IPR in terms of normalized pseudo pressure*, and equation (9.44) is the *Forchheimer IPR in terms of p-squared*.

Equation (9.42) can be rearranged as:

$$\frac{m_n(p_{Avg}) - m_n(p_{wf})}{q_g} = 711 \frac{\mu_i Z_i T_i}{p_i k_g h} \left( \ln \frac{r_e}{r_w} - \frac{3}{4} + S_w + Dq_g \right)$$

$$\frac{m_n(p_{Avg}) - m_n(p_{wf})}{q_g} = 711 \frac{\mu_i Z_i T_i}{p_i k_g h} \left( \ln \frac{r_e}{r_w} - \frac{3}{4} + S_w \right) + 711 \frac{\mu_i Z_i T_i}{p_i k_g h} Dq_g$$

$$\frac{m_n(p_{Avg}) - m_n(p_{wf})}{q_g} = a_g + b_g q_g \quad (9.45)$$

$$\text{where } a_g = 711 \frac{\mu_i Z_i T_i}{p_i k_g h} \left( \ln \frac{r_e}{r_w} - \frac{3}{4} + S_w \right) \text{ and } b_g = 711$$

$$\frac{\mu_i Z_i T_i}{p_i k_g h} D$$

Equation (9.43) can be rearranged as:

$$\frac{m(p_{Avg}) - m(p_{wf})}{q_g} = 1,422 \frac{T_i}{k_g h} \left( \ln \frac{r_e}{r_w} - \frac{3}{4} + S_w \right) + 1,422 \frac{T_i}{k_g h} Dq_g$$

$$\frac{m(p_{Avg}) - m(p_{wf})}{q_g} = a_g + b_g q_g \quad (9.46)$$

$$\text{where } a_g = 1,422 \frac{T_i}{k_g h} \left( \ln \frac{r_e}{r_w} - \frac{3}{4} + S_w \right) \text{ and } b_g = 1,422$$

$$\frac{T_i}{k_g h} D$$

Equation (9.44) can also be rearranged as:

$$p_{Avg}^2 - p_{wf}^2 = \frac{1,422 \mu_i Z_i T_i}{k_g h} \left( \ln \frac{r_e}{r_w} - \frac{3}{4} + S_w + Dq_g \right)$$

$$p_{Avg}^2 - p_{wf}^2 = \frac{1,422 \mu_i Z_i T_i}{k_g h} \left( \ln \frac{r_e}{r_w} - \frac{3}{4} + S_w \right) + \frac{1,422 \mu_i Z_i T_i}{k_g h} Dq_g$$

$$p_{Avg}^2 - p_{wf}^2 = a_g + b_g q_g \quad (9.47)$$

$$\text{where } a_g = \frac{1,422 \mu_i Z_i T_i}{k_g h} \left( \ln \frac{r_e}{r_w} - \frac{3}{4} + S_w \right) \text{ and } b_g =$$

$$\frac{1,422 \mu_i Z_i T_i}{k_g h} D$$

Hence, plotting the right-hand side of equation (9.45) or (9.46) against  $q_g$  for any range of  $p_{wf}$  values or plotting the right-hand side of equation (9.47) against  $q_g$  for  $p_{wf} < 2000$  psia, will yield a straight-line with a slope equal to the value of  $b_g$ , which is different for equations (9.45), (9.46), and (9.47), from which  $D$  is determined.

**9.2.5.2. Rate Dependent Skin Effect in Oil Wells.**  $Dq_o$  (skin due to turbulence) or  $D$  (turbulence factor) for oil can also be estimated in a similar way to that of gas wells. Considering equation (9.25), which is valid for the flow of oil/liquid:

$$p_{Avg} = p_{wf} + \frac{141.2 B_o q_o \mu_o}{k_o h} \left( \ln \frac{r_e}{r_w} - \frac{3}{4} + S \right)$$

Defining  $S$  (total skin) as the sum of the mechanical skin (skin due to damage) and rate dependent skin effect (skin due to turbulence):

$$p_{Avg} - p_{wf} = \frac{141.2 B_o q_o \mu_o}{k_o h} \left( \ln \frac{r_e}{r_w} - \frac{3}{4} + S_w + Dq_o \right)$$

$$\frac{p_{Avg} - p_{wf}}{q_o} = \frac{141.2 B_o \mu_o}{k_o h} \left( \ln \frac{r_e}{r_w} - \frac{3}{4} + S_w + Dq_o \right)$$

$$\frac{P_{Avg} - P_{wf}}{q_o} = \frac{141.2B_o\mu_o}{k_o h} \left( \ln \frac{r_e}{r_w} - \frac{3}{4} + S_w \right) + \frac{141.2B_o\mu_o}{k_o h} D q_o$$

$$\frac{P_{Avg} - P_{wf}}{q_o} = a_o + b_o q_o \tag{9.48}$$

where  $a_o = \frac{141.2B_o\mu_o}{k_o h} \left( \ln \frac{r_e}{r_w} - \frac{3}{4} + S_w \right)$  and  $b_o =$

$$\frac{141.2B_o\mu_o D}{k_o h}$$

Thus, plotting  $\frac{P_{Avg} - P_{wf}}{q_o}$  against  $q_o$  will yield a straight line with a slope equal to the value of  $b_o$ , from which  $D$  can be estimated.

Equations (9.45), (9.46), and (9.47) are referred to as *Jones IPR for gas* in terms of normalized pseudopressure, pseudopressure, and p-squared, respectively. Equation (9.48) is referred to as *Jones IPR for oil*.

**Exercise 9.7** Exercise on Rate Dependent Skin Effect for Gas

A gas well with a 0.354-ft wellbore radius and producing from a 1.251 mD reservoir at temperature of 150°F with 45 ft pay, 0.3 porosity, and  $c_t$  of 0.0003256  $\text{psi}^{-1}$  was tested at PSS condition. The reservoir can be described as having a circular geometry with  $r_e$  of 118 ft. During testing the reservoir had an average reservoir pressure of 2799 psia.

Determine the turbulence factor ( $D$ ) and mechanical skin (skin due to damage) using:

- (i) IPR defined in terms of  $p^2$ ;
- (ii) IPR defined in terms of  $m_n(p)$ .

Table 9.8 shows the fluid properties of the gas while Table 9.9 is the pressure–rate history of the test.

**Table 9.8** Fluid Properties for Exercise 9.7.

Pressure (psia)	Gas viscosity (cp)	Z	Pressure (psia)	Gas viscosity (cp)	Z
14.7	0.0120	0.998	1,610	0.0154	0.830
115	0.0120	0.985	1,725	0.0158	0.823
230	0.0121	0.970	1,840	0.0163	0.817
345	0.0123	0.956	1,955	0.0168	0.813
460	0.0125	0.942	2,070	0.0173	0.809
575	0.0126	0.928	2,185	0.0178	0.807
690	0.0128	0.914	2,300	0.0183	0.805
805	0.0131	0.901	2,415	0.0189	0.805
920	0.0133	0.889	2,530	0.0194	0.805
1,035	0.0136	0.877	2,645	0.0200	0.807
1,150	0.0139	0.866	2,760	0.0205	0.810
1,265	0.0143	0.856	$p_i = 2,798$	0.0207	0.811
1,380	0.0146	0.846	2,875	0.0211	0.813
1,495	0.0150	0.838	2,900	0.0212	0.814

**Solution.**

From pressure–rate history data, PSS  $q_g$  and the corresponding  $p_{wf}$  are determined as shown in Fig. 9.22.

1. In terms of  $p^2$ :

Using  $p_{wf}$  and  $q_g$  from Fig. 9.22, a table of  $\frac{p_{Avg}^2 - p_{wf}^2}{q_g}$  against  $q_g$  is created as shown in Table 9.10.

From a plot of  $\frac{p_{Avg}^2 - p_{wf}^2}{q_g}$  against  $q_g$  (Fig. 9.23), the slope and intercept with the y-axis are determined.

$$\text{slope} = b_g = \frac{1,422\mu_i Z_i T_i}{k_g h} D$$

$$138.31 = \frac{1,422\mu_i Z_i T_i}{k_g h} D$$

Making  $D$  the subject of the formula:

$$\frac{1,422\mu_i Z_i T_i}{k_g h} D = 138.31$$

$$D = 138.31 \frac{k_g h}{1,422\mu_i Z_i T_i}$$

$$D = 138.31 \frac{1.251 \times 45}{1,422 \times 0.0207 \times 0.811 \times 610}$$

$$D = 0.53 D/Mscf$$

$$\text{Vertical y-axis intercept} = a_g = \frac{1,422\mu_i Z_i T_i}{k_g h} \left( \ln \frac{r_e}{r_w} - \frac{3}{4} + S_w \right)$$

$$\frac{1,422\mu_i Z_i T_i}{k_g h} \left( \ln \frac{r_e}{r_w} - \frac{3}{4} + S_w \right) = 2,303.57$$

**Table 9.9** Pressure–Rate History During Test.

Time (hr)	Gas rate (Mscf/D)	Pressure (psia)	Time (hr)	Gas rate (Mscf/D)	Pressure (psia)	Time (hr)	Gas rate (Mscf/D)	Pressure (psia)	Time (hr)	Gas rate (Mscf/D)	Pressure (psia)
0.0000	0	2,799	3.0730	27.5	2,774.259	15.0003	37.5	2,759.118	21.1624	42.5	2,737.775
0.0001	0	2,799	3.1624	27.5	2,771.751	15.0006	37.5	2,759.06	21.3615	42.5	2,737.112
0.0003	0	2,799	3.3615	27.5	2,770.783	15.0013	37.5	2,758.93	21.8044	42.5	2,736.894
0.0006	0	2,799	3.8044	27.5	2,770.194	15.0030	37.5	2,758.637	22.7903	42.5	2,736.713
0.0013	0	2,799	4.7903	27.5	2,769.671	15.0066	37.5	2,757.969	24.9844	42.5	2,736.454
0.0030	0	2,799	6.9844	27.5	2,769.161	15.0147	37.5	2,756.508	27.0000	42.5	2,736.261
0.0066	0	2,799	9.0000	27.5	2,768.898	15.0328	37.5	2,753.957	27.0003	0	2,736.663
0.0147	0	2,799	9.0001	32.5	2,768.876	15.0730	37.5	2,751.202	27.0006	0	2,737.158
0.0328	0	2,799	9.0003	32.5	2,768.851	15.1624	37.5	2,749.629	27.0013	0	2,738.265
0.0730	0	2,799	9.0006	32.5	2,768.792	15.3615	37.5	2,749.111	27.0030	0	2,740.728
0.1624	0	2,799	9.0013	32.5	2,768.663	15.8044	37.5	2,748.92	27.0066	0	2,746.034
0.3615	0	2,799	9.0030	32.5	2,768.369	16.7903	37.5	2,748.745	27.0147	0	2,756.222
0.8044	0	2,799	9.0066	32.5	2,767.702	18.9844	37.5	2,748.494	27.0328	0	2,771.113
1.7903	0	2,799	9.0147	32.5	2,766.281	21.0000	37.5	2,748.311	27.0730	0	2,784.847
3.0000	0	2,799	9.0328	32.5	2,763.936	21.0001	42.5	2,748.289	27.1624	0	2,792.056
3.0001	27.5	2,798.884	9.0730	32.5	2,761.612	21.0003	42.5	2,748.263	27.3615	0	2,794.528
3.0003	27.5	2,798.741	9.1624	32.5	2,760.387	21.0006	42.5	2,748.205	27.8044	0	2,795.549
3.0006	27.5	2,798.422	9.3615	32.5	2,759.984	21.0013	42.5	2,748.076	28.7903	0	2,796.285
3.0013	27.5	2,797.709	9.8044	32.5	2,759.803	21.0030	42.5	2,747.783	30.9844	0	2,796.893
3.0030	27.5	2,796.135	10.7903	32.5	2,759.615	21.0066	42.5	2,747.114	35.8674	0	2,797.331
3.0066	27.5	2,792.849	12.9844	32.5	2,759.35	21.0147	42.5	2,745.627	41.6199	0	2,797.509
3.0147	27.5	2,787.047	15.0000	32.5	2,759.165	21.0328	42.5	2,742.903	46.7348	0	2,797.593
3.0328	27.5	2,779.777	15.0001	37.5	2,759.144	21.0730	42.5	2,739.731	51.0000	0	2,797.643

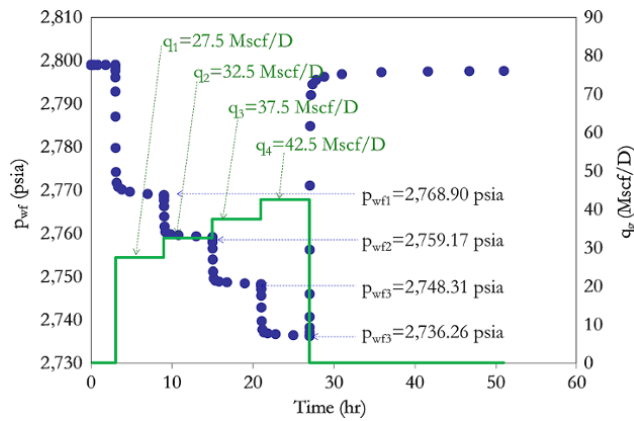


**Figure 9.22** Pressure–rate history showing  $p_{wf}$  and  $q_g$  at PSS for Exercise 9.7.

**Table 9.10**  $\frac{p_{Avg}^2 - p_{wf}^2}{q_g}$  against  $q_g$

$q$ (Mscf/D)	$p_{wf}$ (psia)	$\frac{p_{Avg}^2 - p_{wf}^2}{q_g}$ (psi <sup>2</sup> D/Mscf)
27.50	2,768.90	6,094.78
32.50	2,759.17	6,812.55
37.50	2,748.31	7,498.40
42.50	2,736.26	8,171.25

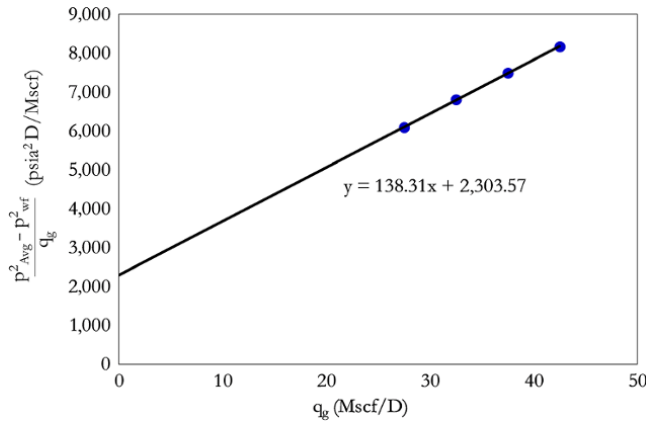


**Figure 9.23** Plot of  $\frac{P_{Avg}^2 - P_{wf}^2}{q_g}$  against  $q_g$  for rate dependent skin effect calculations.

$$S_w = 2,303.57 \frac{k_g h}{1,422 \mu_i Z_i T_i} - \ln \frac{r_e}{r_w} + \frac{3}{4}$$

$$S_w = 2,303.57 \frac{1.251 \times 45}{1,422 \times 0.0207 \times 0.811 \times 610} - \ln \frac{118}{0.354} + \frac{3}{4}$$

$$S_w = 3.9$$

Hence, mechanical skin = 3.9

2. Using trapezoidal rule to calculate pseudopressure (equation (8.157)):

$$m(p) = 2 \sum_{j=2}^n \frac{1}{2} \left[ \left( \frac{p}{\mu Z} \right)_{j-1} + \left( \frac{p}{\mu Z} \right)_j \right] (p_j - p_{j-1})$$

$$m(p) = \sum_{j=2}^n \left[ \left( \frac{p}{\mu Z} \right)_{j-1} + \left( \frac{p}{\mu Z} \right)_j \right] (p_j - p_{j-1})$$

Then, normalizing pseudopressure using equation (8.158):

$$m_n(p) = \frac{\mu_i Z_i}{2 p_i} \sum_{j=2}^n \left[ \left( \frac{p}{\mu Z} \right)_{j-1} + \left( \frac{p}{\mu Z} \right)_j \right] (p_j - p_{j-1})$$

The pseudopressure calculation is summarized in Table 9.11.

Values of  $m_n(p_{Avg})$  and the four  $m_n(p_{wf})$  at PSS are determined using the relationship between pressure and normalized pseudopressure in Table 9.11 by interpolation.

Using  $m_n(p_{wf})$  calculated above and  $q_g$  provided, a table of  $\frac{m_n(p_{Avg}) - m_n(p_{wf})}{q_g}$  against  $q_g$  is created, as shown in Table 9.12:

$m_n(p_{Avg}) = 1,717.336$  psia from the pseudopressure table given  $p_{Avg} = 2,799$  psia.

From a plot of  $\frac{m_n(p_{Avg}) - m_n(p_{wf})}{q_g}$  against  $q_g$  (Fig. 9.24), the slope and intercept with the  $y$ -axis are determined.

where  $a_g = 711 \frac{\mu_i Z_i T_i}{p_i k_g h} \left( \ln \frac{r_e}{r_w} - \frac{3}{4} + S_w \right)$  and  $b_g = 711 \frac{\mu_i Z_i T_i}{p_i k_g h} D$

$$\text{slope} = b_g = 711 \frac{\mu_i Z_i T_i}{p_i k_g h} D$$

$$0.0251 = 711 \frac{\mu_i Z_i T_i}{p_i k_g h} D$$

Making  $D$  the subject of the formula:

$$711 \frac{\mu_i Z_i T_i}{p_i k_g h} D = 0.0251$$

$$D = 0.0251 \frac{p_i k_g h}{711 \mu_i Z_i T_i}$$

$$D = 0.0251 \frac{2,799 \times 1.251 \times 45}{711 \times 0.0207 \times 0.811 \times 610}$$

$$D = 0.54 D / \text{Mscf}$$

Vertically  $y$ -axis intercept = 0.4056 =  $a_g$

$$= 711 \frac{\mu_i Z_i T_i}{p_i k_g h} \left( \ln \frac{r_e}{r_w} - \frac{3}{4} + S_w \right)$$

$$0.4056 = 711 \frac{\mu_i Z_i T_i}{p_i k_g h} \left( \ln \frac{r_e}{r_w} - \frac{3}{4} + S_w \right)$$

$$S_w = 0.4056 \frac{p_i k_g h}{711 \mu_i Z_i T_i} - \ln \frac{r_e}{r_w} + \frac{3}{4}$$

$$S_w = 0.4056 \frac{2,799 \times 1.251 \times 45}{711 \times 0.0207 \times 0.811 \times 610} - \ln \frac{118}{0.354} + \frac{3}{4}$$

$$S_w = 0.4056 \frac{2,799 \times 1.251 \times 45}{711 \times 0.0207 \times 0.811 \times 610} - \ln \frac{118}{0.354} + \frac{3}{4}$$

$$S_w = 3.8$$

The turbulence factor ( $D$ ) = 0.54 D/Mscf and mechanical skin ( $S_w$ ) = 3.8.

**Table 9.11** Pseudopressure Table.

col.1	col.2	col.3	col.4	col.5	col.6	col.7
p (psia)	$\mu$ (cp)	Z	$\frac{p}{\mu Z}$ (psia/cp)	$\left[ \left( \frac{p}{\mu Z} \right)_{j-1} + \left( \frac{p}{\mu Z} \right)_j \right]$	$m(p) = \sum_{j=2}^n \left[ \left( \frac{p}{\mu Z} \right)_{j-1} + \left( \frac{p}{\mu Z} \right)_j \right]$	$m_n(p) = m(p) \frac{\mu_i Z_i}{2p_i}$ (psia)
				$(p_j - p_{j-1})$ (psia <sup>2</sup> /cp)	$(p_j - p_{j-1})$ (psia <sup>2</sup> /cp)	
14.7	0.012	0.998	1.2E+03	0.0E+00	0.00E+00	0.00
115	0.012	0.985	9.7E+03	1.1E+06	1.10E+06	3.29
230	0.012	0.970	2.0E+04	3.4E+06	4.46E+06	13.37
345	0.012	0.956	2.9E+04	5.6E+06	1.01E+07	30.24
460	0.012	0.942	3.9E+04	7.9E+06	1.80E+07	53.91
575	0.013	0.928	4.9E+04	1.0E+07	2.81E+07	84.37
690	0.013	0.914	5.9E+04	1.2E+07	4.05E+07	121.55
805	0.013	0.901	6.8E+04	1.5E+07	5.51E+07	165.37
920	0.013	0.889	7.8E+04	1.7E+07	7.19E+07	215.69
1,035	0.014	0.877	8.7E+04	1.9E+07	9.08E+07	272.34
1,150	0.014	0.866	9.5E+04	2.1E+07	1.12E+08	335.11
1,265	0.014	0.856	1.0E+05	2.3E+07	1.35E+08	403.77
1,380	0.015	0.846	1.1E+05	2.5E+07	1.59E+08	478.02
1,495	0.015	0.838	1.2E+05	2.7E+07	1.86E+08	557.57
1,610	0.015	0.830	1.3E+05	2.8E+07	2.14E+08	642.07
1,725	0.016	0.823	1.3E+05	3.0E+07	2.44E+08	731.18
1,840	0.016	0.817	1.4E+05	3.1E+07	2.75E+08	824.50
1,955	0.017	0.813	1.4E+05	3.2E+07	3.07E+08	921.66
2,070	0.017	0.809	1.5E+05	3.4E+07	3.41E+08	1,022.28
2,185	0.018	0.807	1.5E+05	3.5E+07	3.75E+08	1,125.97
2,300	0.018	0.805	1.6E+05	3.5E+07	4.11E+08	1,232.37
2,415	0.019	0.805	1.6E+05	3.6E+07	4.47E+08	1,341.13
2,530	0.019	0.805	1.6E+05	3.7E+07	4.84E+08	1,451.92
2,645	0.020	0.807	1.6E+05	3.8E+07	5.21E+08	1,564.44
2,760	0.021	0.810	1.7E+05	3.8E+07	5.59E+08	1,678.40
2,798	0.021	0.811	1.7E+05	1.3E+07	5.72E+08	1,716.33
2,875	0.021	0.813	1.7E+05	2.6E+07	5.98E+08	1,793.57
2,900	0.021	0.814	1.7E+05	8.4E+06	6.06E+08	1,818.74

**Table 9.12**  $\frac{m_n(p_{Avg}) - m_n(p_{wf})}{q_g}$  against  $q_g$ .

q (Mscf/D)	$p_{wf}$ (psia)	$m_n(p_{wf})$ (psi)	$\frac{m_n(p_{Avg}) - m_n(p_{wf})}{q_g}$ (psi-D/Mscf)
27.50	2,768.90	1,687.279	1.09298
32.50	2,759.17	1,677.569	1.22361
37.50	2,748.31	1,666.812	1.34730
42.50	2,736.26	1,654.871	1.46976

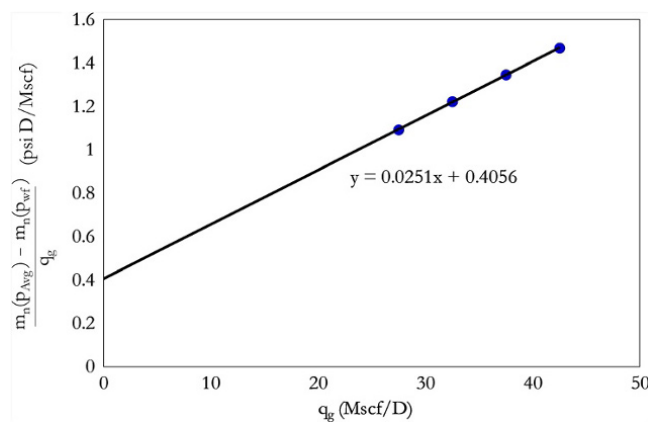


**Figure 9.24** Plot of  $\frac{m(p_{Avg}) - m(p_{wf})}{q_g}$  against  $q_g$  for rate dependent skin effect calculations.



**Exercise 9.8** IPR Calculations for Gas Well Producing Under PSS

1. Create an IPR plot for the well–reservoir system in Exercise 9.7 using IPR in terms of  $m_n(p)$  and  $p^2$  with  $p_{Avg}$  of 2799 psia, mechanical skin of 20, and turbulence factor (D) of 0.54 D/Scf.
2. Determine the maximum gas the reservoir can produce using  $m_n(p)$  and  $p^2$  IPR models.
3. For a stabilized gas production rate ( $q_g$ ) of 100 Mscf/D, determined PSS  $p_{wf}$  using the  $m_n(p)$  and  $p^2$  IPR models and compare results.

**Solution.**

Table 9.13 summarizes the solution to Exercise 9.8.

The range of values of  $q_g$  is selected in any desired spacing. Values can be linear, geometric or with no particular sequence.

$p_{wf}$  is then calculated for given values of  $q_g$ .

$q_g$  values here are defined in no particular sequence but rather values that cover  $p_{Avg}$  to 14.7 psia.

Iteration or simple goal seek in a spreadsheet was used to find  $q_{g\ max}$  ( $q_g$  at  $p_{wf} = 14.7$  psia).

Q1: the plots of IPR based on  $p^2$  and  $m_n(p)$  are shown together in Fig. 9.25.

Q2: the maximum rate ( $q_{g\ max}$ ) is AOFD.

From Table 9.13 and Fig. 9.25:

AOFD = 214.74 Mscf/D using the  $p^2$  IPR equation.

AOFD = 229.78 Mscf/D using the  $m_n(p)$  IPR equation.

Q3:  $p_{wf}$  at 100 Mscf/D.

At 100 Mscf/D, gas rates during PSS production, from Table 9.13 and Fig. 9.25 is:

$p_{wf} = 2,406.07$  psia using the  $p^2$  IPR equation.

$p_{wf} = 2,393.87$  psia using the  $m_n(p)$  IPR equation.

**9.2.6. c and n Back Pressure IPR for Gas**

From gas IPR, equation (9.44):

$$p_{Avg}^2 = p_{wf}^2 + \frac{1,422q_g\mu_i Z_i T_i}{k_g h} \left( \ln \frac{r_e}{r_w} - \frac{3}{4} + S_w + Dq_g \right)$$

Considering the case of where skin due to turbulence is absent, the above reduces to:

$$p_{Avg}^2 = p_{wf}^2 + \frac{1,422q_g\mu_i Z_i T_i}{k_g h} \left( \ln \frac{r_e}{r_w} - 0.75 + S_w \right)$$

Making  $q_g$  the subject of the formula:

$$q_g = \frac{1}{\frac{1,422\mu_i Z_i T_i}{k_g h} \left( \ln \frac{r_e}{r_w} - 0.75 + S_w \right)} (p_{wf}^2 - p_{Avg}^2) \quad (9.49)$$

Equation (9.49) can be expressed as:

$$q_g = C(p_{wf}^2 - p_{Avg}^2) \quad (9.50)$$

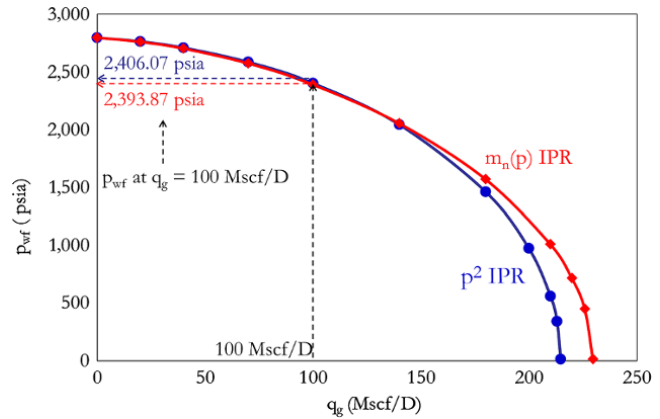


**Figure 9.25** IPR using  $p^2$  and  $m_n(p)$  equations for Exercise 9.8.

**Table 9.13** Summary of the solution to Exercise 9.8.

p <sup>2</sup> IPR Calculations			m <sub>n</sub> (p) IPR Calculations		
q <sub>g</sub> (Mscf/D)	p <sub>wf</sub> (psia) Calculated using equation (9.44)	q <sub>g</sub> (Mscf/D)	m <sub>n</sub> (p <sub>wf</sub> ) (psia) Calculated using equation (9.42)	p <sub>wf</sub> (psia) Using m <sub>n</sub> (p) vs p table	
0.00	2,799.00	0.00	1,717.34	2,799.00	
20.00	2,765.66	20.00	1,681.40	2,763.01	
40.00	2,711.38	40.00	1,623.81	2,704.91	
70.00	2,587.68	70.00	1,496.84	2,575.91	
<b>100.00</b>	<b>2,406.07</b>	<b>100.00</b>	<b>1,321.15</b>	<b>2,393.87</b>	
140.00	2,046.65	140.00	1,011.14	2,057.27	
180.00	1,463.34	180.00	614.54	1,572.53	
200.00	974.69	210.00	260.26	1,010.47	
210.00	558.97	220.00	131.34	715.68	
213.00	340.18	226.00	51.39	447.77	
<b>214.74</b>	<b>14.70</b>	<b>229.78</b>	<b>0.00</b>	<b>14.70</b>	

where

$$C = \frac{1}{\frac{1,422\mu_i Z_i T_i}{k_g h} \left( \ln \frac{r_c}{r_w} - 0.75 + S_w \right)}$$

$C$  is defined as the well *performance constant*. In equation (9.50),  $C$  has been assumed constant because the relationship does not include skin due to turbulence. If effect of skin due to turbulence is included, then  $C$  will be a function of  $q_g$ . Also, as discussed in Chapter 7 (7.1.1) and Section 9.2.3, gas flow equation in terms of  $p^2$  is only valid for  $p < 2,000$  psia. To account for the effect of turbulence and deviation of ideal flow (where  $p^2$  is not applicable), equation (9.50) can be by rewritten as:

$$q_{sc} = C \left( p_{wf}^2 - p_{Avg}^2 \right)^n \quad (9.51)$$

$n$  is close to one for laminar flowing gas (as  $p$  is less than 2,000 psia under such condition).

Equation (9.51) is called the *conventional back pressure equation for gas*; or *C and n equation*. When equation (9.51) is applied to oil wells below saturation pressure, it is called the *Fetkovich equation* (equation (9.55)).

### 9.2.7. Empirical and Semi-Empirical IPR Models

Empirical and semi-empirical IPR models often provide reliable ways of creating IPRs when there are limited reservoir, well or other well test properties. They are also useful in multiphase flow, where formulation of IPR from the fundamental equations can be difficult due to the effect of saturation on the mobility of the different phases. With limited model parameters, empirical IPR models have been shown to provide a good match with field result.

**9.2.7.1. Vogel IPR.** The IPR defined in equations (9.17), (9.25), and (9.29) are all for a single-phase incompressible fluid; this is only applicable to oil wells and not valid when oil and gas flow in the reservoir. *Vogel* [1968], following observation of IPR for several solution-gas drive reservoirs, proposed a general IPR for oil wells below the bubble point pressure as:

$$\frac{q_o}{q_{o \max}} = 1 - 0.2 \left( \frac{p_{wf}}{p_{Avg}} \right) - 0.8 \left( \frac{p_{wf}}{p_{Avg}} \right)^2 \quad \text{for } p_{Avg} < p_{bub} \quad (9.52)$$

Equation (9.52) is presented as dimensionless form with normalized rate ( $q_o/q_{\max}$ ) as the dependent variable and normalized stabilized bottomhole pressure ( $p_{wf}/p_{Avg}$ ) as an independent variable.

Plotting the IPR relationship in normalized/dimensionless form as shown in equation (9.52) ensures that the

dependent and independent variables have a maximum of 1 on both the  $x$ - and  $y$ -axis. This form of presenting IPR is useful for easy comparison of data from different fields and for comparison of different IPR models.

The  $\left( \frac{p_{wf}}{p_{Avg}} \right)^2$  term in equation (9.52) can be seen to represent a two-phase effect that will, therefore, reduce to  $\left( \frac{p_{wf}}{p_{Avg}} \right)$  for a single-phase fluid. Hence, for a single-phase oil (above bubble point pressure), equation (9.52) becomes:

$$\frac{q_o}{q_{o \max}} = 1 - 0.2 \left( \frac{p_{wf}}{p_{Avg}} \right) - 0.8 \left( \frac{p_{wf}}{p_{Avg}} \right)$$

$$\frac{q_o}{q_{o \max}} = 1 - \left( \frac{p_{wf}}{p_{Avg}} \right)$$

which when arranged becomes:

$$q_o = \frac{q_{o \max}}{p_{Avg}} \left( p_{Avg} - p_{wf} \right)$$

$$q_o = PI \left( p_{Avg} - p_{wf} \right)$$

$$PI = \frac{q_o}{\left( p_{Avg} - p_{wf} \right)} \quad (9.53)$$

Equation (9.53) is the same as equation (9.17), which is the IPR for a single-phase oil.

For a test that covers  $p_{wf}$  above and below the bubble point, a combination of Darcy's flow (defined by PI) for a test above the bubble point pressure and Vogel (for two-phase oil and gas) should be used. This approach or model is called *composite Vogel IPR* and is expressed as:

$$\frac{q_o}{q_{o \max}} = 1 - \left( \frac{p_{wf}}{p_{Avg}} \right) \quad \text{when } p_{wf} > p_b$$

$$\frac{q_o}{q_{o \max}} = 1 - 0.2 \left( \frac{p_{wf}}{p_{Avg}} \right) - 0.8 \left( \frac{p_{wf}}{p_{Avg}} \right)^2 \quad \text{when } p_{wf} < p_b \quad (9.54)$$

**9.2.7.2. Fetkovich Method.** Though equation (9.51) was derived for gas, *Fetkovich* [1973] showed it is applicable to two-phase oil and gas. The IPR for highly undersaturated to saturated initial reservoir pressure and partially depleted oil under pseudosteady state conditions can be thus be described as:

$$q_o = C \left( p_{Avg}^2 - p_{wf}^2 \right)^n \quad (9.55)$$

where  $0.5 < n < 1.0$ .

This empirical relationship was deduced from isochronal and flow-after-flow tests (multipoint back pressure testing) for oil wells producing from reservoirs having a wide range of permeabilities.

In summary, equations (9.51) and (9.55) can be applied to gas and two-phase oil and gas wells. One easy way to solve for C and n in equation (9.55) is to transform equation to the form:

$$\log(q_o) = \log(C) + n \log(p_{Avg}^2 - p_{wf}^2)$$

and make a plot of  $\log(q_o)$  against  $\log(p_{Avg}^2 - p_{wf}^2)$ , from which the slope and intercept on the vertical (y-axis) give n and log C, respectively. Another approach is to use total least square regression to fit more than one test point to equation (9.55) with C and n as regression variables. For tests which include the conditions where  $p_{wf} > p_b$  and  $p_{wf} < p_b$ , Fetkovich presented a generalized equation that should be used:

$$q_o = C(p_{Avg}^2 - p_{wf}^2) + PI(p_{Avg} - p_b) \tag{9.56}$$

The Fetkovich IPR also gives a reasonable prediction for gas condensate systems. The Fetkovich equation, like Vogel, was developed for oil wells and when used for oil wells with water, total liquid rate is what is predicted, and oil rate is then determined from the water cut (WCT). Hence, the Fetkovich IPR does not account for the reduced deliverability of liquid rate (oil and water) due to the contrast in mobility between water and oil. Additional reduction in deliverability of liquid rate due to the contrast in mobility between oil and water can be considered insignificant at pseudosteady state condition.

**Exercise 9.9** Vogel IPR for Solution-Gas Oil Well

A multirate test was carried out on a well producing under solution gas drive from a reservoir with an average reservoir pressure of 2,078 psia; the test data are shown in Table 9.14.

1. Determine AOFP using Vogel IPR with test point 1.
2. Determine  $q_o$  for  $p_{wf}$  of 650 psia.
3. Make a Vogel IPR plot.

**Solution.**

1. From test point 1,  $q_o = 17$  stb/D and  $p_{wf} = 1,890$  psia.

**Table 9.14** Multirate Test for Exercise 9.9.

Test number	q (stb/D)Q	p <sub>wf</sub> (psia)
0	0	2,078
1	17	1,890
2	33	1,700
3	47	1,522
4	59	1,345

Calculating  $\frac{p_{wf}}{p_{Avg}}$ :

$$\frac{p_{wf}}{p_{Avg}} = \frac{1,890}{2,078} = 0.90953$$

Substitute these into equation (9.52) to determine  $\frac{q_o}{q_{o\ max}}$ :

$$\frac{q_o}{q_{o\ max}} = 1 - 0.2(0.90953) - 0.8(0.90953)^2 = 0.156300804$$

and calculate  $q_{o\ max}$ :

$$q_{o\ max} = \frac{q_o}{0.156300804}$$

Substituting  $q_o = 17$  stb/D into the above:

$$q_{o\ max} = \frac{17}{0.156300804} = 108.76\text{stb/D.}$$

2. Substituting  $p_{Avg}$  and  $q_{o\ max}$  into equation (9.52), the Vogel IPR for this reservoir is thus derived:

$$q_o = q_{o\ max} \left[ 1 - 0.2 \left( \frac{p_{wf}}{p_{Avg}} \right) - 0.8 \left( \frac{p_{wf}}{p_{Avg}} \right)^2 \right]$$

$$q_o = 108.76 \left[ 1 - 0.2 \left( \frac{p_{wf}}{2,078} \right) - 0.8 \left( \frac{p_{wf}}{2,078} \right)^2 \right] \tag{9.57}$$

For  $p_{wf} = 650$  psia, substituting this into equation (9.57):

$$q_o = 108.76 \left[ 1 - 0.2 \left( \frac{650}{2,078} \right) - 0.8 \left( \frac{650}{2,078} \right)^2 \right] = 93.44\text{stb/D}$$

$q_o$  ( $p_{wf} = 650$  psia) = 93.44 stb/D.

3. Using equation (9.52), a table of  $q_o$  against  $p_{wf}$  for value of  $p_{Avg} < p_{wf} < 14.7$  psia is generated (Table 9.15).

Plot of  $p_{wf}$  against  $q_o$  is shown in Fig. 9.26:

**Table 9.15**  $p_{wf}$  Against  $q_o$  Using the Vogel Equation for Exercise 9.9.

p <sub>wf</sub> (psia)	q <sub>o</sub> (stb/D)
2,078	0
1,890	17.00
1,700	32.73
1,522	46.15
1,345	58.23
1,010	77.63
650	93.44
350	102.63
14.7	108.60

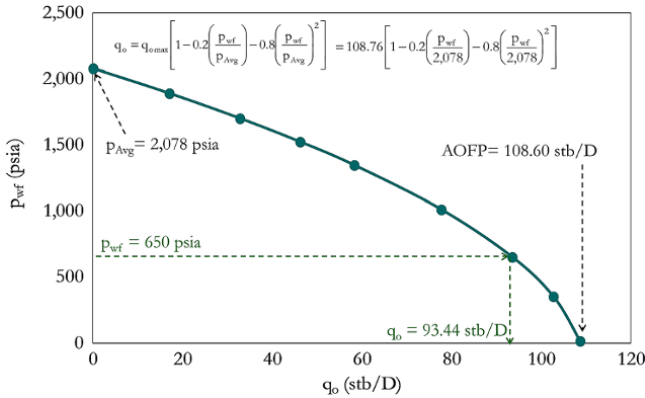


Figure 9.26 Vogel IPR for Exercise 9.9.

Table 9.16  $\log(p_{Avg}^2 - p_{wf}^2)$  and  $\log(q_o)$  for C and n Determination.

$q_o$ (stb/D)	$p_{wf}$ (psia)	$p_{Avg}^2 - p_{wf}^2$ (psia <sup>2</sup> )	$\log(p_{Avg}^2 - p_{wf}^2)$	$\log(q_o)$
0	2,078	0		
17	1,890	745,984	5.8727	1.230
33	1,700	1,428,084	6.1548	1.5185
47	1,522	2,001,600	6.3014	1.6721
59	1,345	2,509,059	6.3995	1.7709

**Exercise 9.10** Fetkovich IPR for Solution-Gas Oil Well  
Using the data in Exercise 9.9:

1. Determine C and n that will fit the entire test points.
2. Determine AOF (q<sub>o max</sub>).
3. Determine q<sub>o</sub> for p<sub>wf</sub> of 650 psia.
4. Make the Fetkovich IPR plot.

**Solutions.**

1. *Determining C and n*

One easy way to solve for C and n in equation (9.55) is to transform the equation to the form:

$$\log(q_o) = \log(C) + n \log(p_{Avg}^2 - p_{wf}^2)$$

and make a plot of  $\log(q_o)$  against,  $\log(p_{Avg}^2 - p_{wf}^2)$  from which the slope and intercept on the vertical (y-axis) give n and  $\log C$ , respectively. A table of  $\log(p_{Avg}^2 - p_{wf}^2)$  and  $\log(q_o)$  for C and n determination is shown in Table 9.16.

The plot of  $\log(q_o)$  against  $\log(p_{Avg}^2 - p_{wf}^2)$  is shown in Fig. 9.27.

From the plot and equation, the intercept on the vertical axis (y-axis) is -4.8043.

Hence,  $\log(C) = -4.8043$

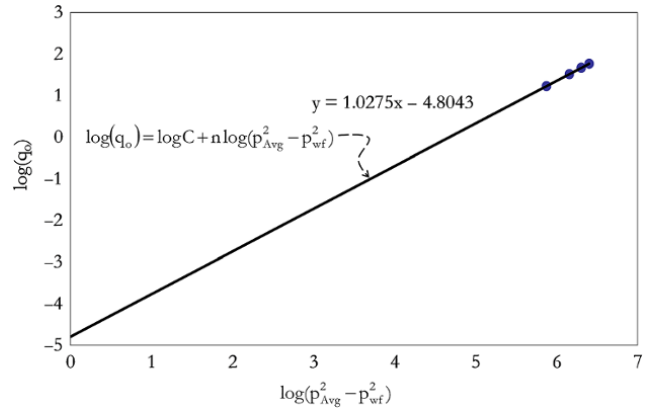


Figure 9.27 Plot of  $\log(q_o)$  against  $\log(p_{Avg}^2 - p_{wf}^2)$  for C and n determination.

Table 9.17  $p_{wf}$  against  $q_o$  using the Fetkovich equation for Exercise 9.10.

$p_{wf}$ (psia)	$q_o$ (stb/D)
2,078	0
1,890	16.99
1,700	33.10
1,522	46.83
1,345	59.07
1,010	78.23
680	91.86
350	100.19
14.7	103.19

$C = 10^{-4.8043}$  thus  $C = 1.56941E-05$

The slope of the graph = 1.027

Therefore,  $C = 1.57E-05$  and  $n = 1.03$

Substituting  $p_{Avg}$ , C, and n into equation (9.55), the Fetkovich IPR for this reservoir is thus derived as:

$$q_o = 1.56941 \times 10^{-5} (43,18,084 - p_{wf}^2)^{1.027} \tag{9.58}$$

2. *Determining q<sub>o max</sub>*

Substituting  $p_{wf} = 14.7$  psia into the IPR equation for the reservoir, equation (9.58)@

$$q_{o \max} = 1.56941 \times 10^{-5} (43,18,084 - 14.7^2)^{1.027} = 103.19 \text{ stb/D}$$

$$q_{o \max} = 103.2 \text{ stb/D}$$

3. *Determining q<sub>o</sub> at p<sub>wf</sub> of 650 psia*

Substituting  $p_{wf} = 650$  psia into equation (9.58):

$$q_o = 1.56941 \times 10^{-5} (43,18,084 - 650^2)^{1.027} = 92.83 \text{ stb/D}$$

$$q_o = 93 \text{ stb/D}$$

4. Using equation (9.58), generate a table of  $q_o$  against  $p_{wf}$  for values of  $p_{Avg} < p_{wf} < 14.7$  psia (Table 9.17).

The plot of  $p_{wf}$  against  $q_o$  is shown in Fig. 9.28.

**Exercise 9.11** Comparison of the Vogel and Fetkovich IPRs

Compare the Vogel and Fetkovich IPRs from Exercise 9.9 and Exercise 9.10 in real and dimensionless variables.

**Solution.**

Table 9.15 and Table 9.17 have  $p_{wf}$  and  $q$  for the Vogel and Fetkovich IPRs, respectively.

$\frac{p_{wf}}{p_{Avg}}$  and  $\frac{q_o}{q_{o\ max}}$  calculated for the Vogel and Fetkovich IPRs are shown in Table 9.18.

Plots of  $p_{wf}$  against  $q_o$  for the Vogel and Fetkovich IPR models are shown in Fig. 9.29.

Plots of  $\frac{p_{wf}}{p_{Avg}}$  against  $\frac{q_o}{q_{o\ max}}$  for the Vogel and Fetkovich IPR models are shown in Fig. 9.30.

**9.2.8. Effect of Changing Skin on IPR Model**

The generalized PSS IPR model shown in equation (9.25) has skin explicitly defined. However, an empirical

IPR model like Vogel and Fetkovich does not have skin explicitly defined. One approach for adding skin effect to an empirical model is using the concept of *flow efficiency*, which is also called *completion factor* or *condition ratio* and defined as:

$$FE = \frac{PI(S \neq 0)}{PI(S = 0)} \tag{9.59}$$

From equation (9.29), the PI under PSS condition is defined as:

$$PI_{PSS} = \frac{q}{p_{Avg} - p_{wf}} = \frac{1}{\frac{141.2B\mu}{kh} \left( \frac{1}{2} \ln \left( \frac{4A}{\gamma C_A r_w^2} \right) + S \right)}$$

Hence:

$$PI_{PSS}(S \neq 0) = \frac{q}{p_{Avg} - p_{wf}} = \frac{1}{\frac{141.2B\mu}{kh} \left( \frac{1}{2} \ln \left( \frac{4A}{\gamma C_A r_w^2} \right) + S \right)} \tag{9.60}$$

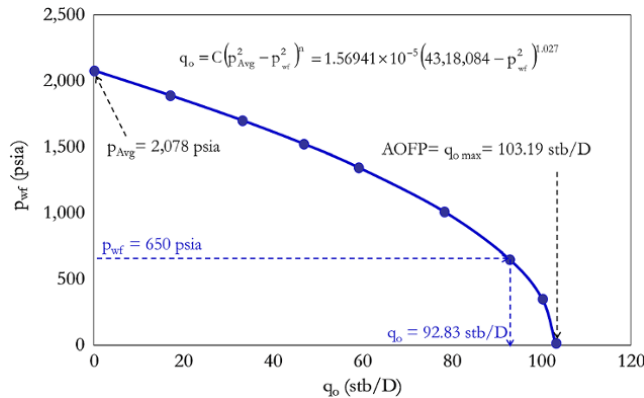


**Figure 9.28** Fetkovich IPR for Exercise 9.10.

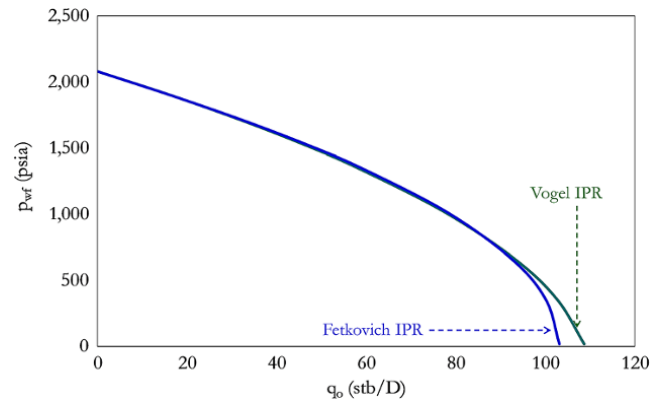


**Figure 9.29** Comparison of the Vogel and Fetkovich IPRs in real variables.

**Table 9.18** Vogel and Fetkovich IPR Model Comparison.

Vogel IPR				Fetkovich			
$p_{wf}$ (psia)	$q_o$ (stb/D)	$\frac{p_{wf}}{p_{Avg}}$	$\frac{q_o}{q_{o\ max}}$	$p_{wf}$ (psia)	$q_o$ (stb/D)	$\frac{p_{wf}}{p_{Avg}}$	$\frac{q_o}{q_{o\ max}}$
From Table 9.15				from Table 9.17			
2,078	0.00	1.00	0.00	2,078	0.00	1.00	0.00
1,890	17.00	0.91	0.16	1,890	16.99	0.91	0.16
1,700	32.73	0.82	0.30	1,700	33.10	0.82	0.32
1,522	46.15	0.73	0.42	1,522	46.83	0.73	0.45
1,345	58.23	0.65	0.54	1,345	59.07	0.65	0.57
1,010	77.63	0.49	0.71	1,010	78.23	0.49	0.76
650	93.44	0.31	0.86	650	92.83	0.31	0.90
350	102.63	0.17	0.94	350	100.19	0.17	0.97
14.7	108.60	0.01	1.00	14.7	103.19	0.01	1.00
$p_{Avg} = 2,078 \quad q_{o\ max} = 108.6 \text{ stb/D}$				$p_{Avg} = 2,078 \quad q_{o\ max} = 103.2 \text{ stb/D}$			

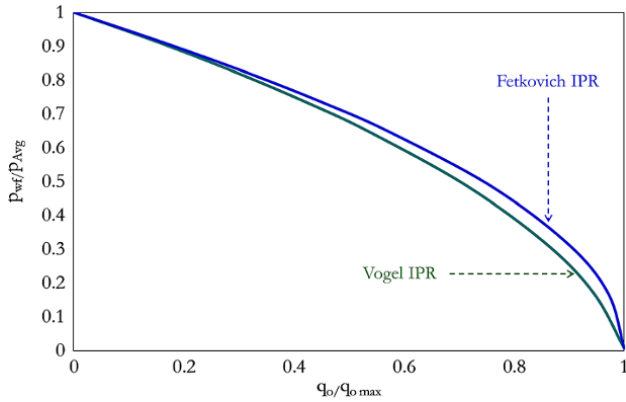


**Figure 9.30** Comparison of the Vogel and Fetkovich IPRs in normalized variables.

and

$$PI_{PSS}(S=0) = \frac{q}{p_{Avg} - p_{wf}} = \frac{1}{\frac{141.2B\mu}{kh} \left( \frac{1}{2} \ln \left( \frac{4A}{\gamma C_A r_w^2} \right) \right)} \tag{9.61}$$

Substituting equations (9.60) and (9.61) into equation (9.59),  $FE_{PSS}$  becomes:

$$FE_{PSS} = \frac{PI(S \neq 0)}{PI(S=0)} = \frac{\frac{1}{2} \ln \left( \frac{4A}{\gamma C_A r_w^2} \right)}{\left( \frac{1}{2} \ln \left( \frac{4A}{\gamma C_A r_w^2} \right) + S \right)} = \frac{p_{Avg} - p_{wf}(S=0)}{p_{Avg} - p_{wf}(S \neq 0)} \tag{9.62}$$

In terms of  $r_e$  (instead of  $A$ ),  $FE_{PSS}$  is expressed as:

$$FE_{PSS} = \frac{PI(S \neq 0)}{PI(S=0)} = \frac{\left( \ln \frac{r_e}{r_w} - \frac{3}{4} \right)}{\left( \ln \frac{r_e}{r_w} - \frac{3}{4} + S \right)} = \frac{p_{Avg} - p_{wf}(S=0)}{p_{Avg} - p_{wf}(S \neq 0)} \tag{9.63}$$

The skin effect can be determined from well test analysis described in Chapter 8.

From equation (9.63):

$$p_{wf}(S=0) = p_{Avg} - FE_{PSS} (p_{Avg} - p_{wf}(S=0)) \tag{9.64}$$

$$p_{wf}(S \neq 0) = p_{Avg} - \frac{p_{Avg} - p_{wf}(S=0)}{FE_{PSS}} \tag{9.65}$$

**Exercise 9.12** Effect of Skin on IPR

The skin effect for the well in Exercise 9.9 obtained from the well test analysis is 4. Carry out a sensitivity analysis of skin effect on IPR using  $S = -3, 0,$  and  $4,$  given that  $r_e = 1,121$  ft and  $r_w = 0.35$  ft.

**Table 9.19**  $p_{wf}(S=0)$  Calculation for Different  $q$ .

Test number	$q$ (stb/D)	$p_{wf}(S=4),$ (psia)	$p_{wf}(S=0)$ (psia) using equation (9.66)
0	0	2,078	2,078.00
1	17	1,890	1,956.42
2	33	1,700	1,833.55
3	47	1,522	1,718.44
4	59	1,345	1,603.97

**Solution Steps.**

*Step 1:* calculate  $FE_{PSS}$  for the original condition by substituting  $r_e, r_w,$  and  $S$  into equation (9.63).

*Step 2:* using equation (9.64), determine  $p_{wf}(S=0)$  for the the same rates as original well conditions. Extend  $q$  to  $q_o$  ( $p_{wf} = 14.7$ )

*Step 3:* using equation (9.65), determine  $p_{wf}(S=-3); p_{wf}(S=4)$  and  $p_{wf}(S=20)$ . Note that  $p_{wf}(S=0)$  has been calculated in Step 2 and  $p_{wf}(S=4)$  is in the original data. Extend  $q$  to  $q_{o,max}$  for all the IPRs.

**Solution.**

1. From equation (9.63),  $FE_{PSS}$  for the original data is given as:

$$FE_{PSS} = \frac{\left( \ln \frac{r_e}{r_w} - \frac{3}{4} \right)}{\left( \ln \frac{r_e}{r_w} - \frac{3}{4} + S \right)}$$

Substituting  $r_e, r_w,$  and  $S$ :

$$FE_{PSS}(S=4) = \frac{\left( \ln \frac{1,121}{0.35} - \frac{3}{4} \right)}{\left( \ln \frac{1,121}{0.35} - \frac{3}{4} + 4 \right)} = 0.6467$$

2. Using equation (9.64) to determine  $p_{wf}(S=0)$ :

$$p_{wf}(S=0) = p_{Avg} - FE_{PSS} (p_{Avg} - p_{wf}(S \neq 0))$$

$$p_{wf}(S=0) = p_{Avg} - FE_{PSS}(S=4) (p_{Avg} - p_{wf}(S=4))$$

Note that for original data  $S = 4$ .

Substituting  $p_{Avg}$  and calculated  $FE_{PSS}(S=4)$ :

$$p_{wf}(S=0) = 2,078 - 0.6467(2,078 - p_{wf}(S=4)) \tag{9.66}$$

The results of determining  $p_{wf}(S=0)$  from  $p_{wf}(S=4)$  for every test number using equation (9.66) are shown in Table 9.19.

Determine  $q_{o \max} (S = 0)$  using the Vogel equation, equation (9.52), and extend Table 9.19 to 14.7 psia.

Any of the test points can be used or all (in regression mode) but for consistency with Exercise 9.9, test point 1 will be used.

$$\frac{q_o(S=0)}{q_{o \max}(S=0)} = 1 - 0.2 \left( \frac{p_{wf}(S=0)}{p_{Avg}} \right) - 0.8 \left( \frac{p_{wf}(S=0)}{p_{Avg}} \right)^2 \tag{9.67}$$

$$q_{o \max}(S=0) = \frac{q_o(S=0)}{1 - 0.2 \left( \frac{p_{wf}(S=0)}{p_{Avg}} \right) - 0.8 \left( \frac{p_{wf}(S=0)}{p_{Avg}} \right)^2}$$

Substituting  $q_o (S = 0)$  and  $p_{wf} (S = 0)$  corresponding to test point 1 from equation (9.20):

$$q_{o \max}(S=0) = \frac{17}{1 - 0.2 \left( \frac{1,956.42}{2,078} \right) - 0.8 \left( \frac{1,956.42}{2,078} \right)^2} = 165.73 \text{ stb/D}$$

Calculate  $q_o$  between  $p_{wf}$  of 14.7 and 1,603.97 psia using equation (9.67). Points should be spaced to ensure a smooth curve. Spacing of data points can be linear, geometric, or not follow any sequence.

From equation (9.67):

$$\frac{q_o(S=0)}{q_{o \max}(S=0)} = 1 - 0.2 \left( \frac{p_{wf}(S=0)}{p_{Avg}} \right) - 0.8 \left( \frac{p_{wf}(S=0)}{p_{Avg}} \right)^2$$

Substituting  $q_{o \max} (S = 0)$  and  $p_{Avg}$  into the above:

$$\frac{q_o(S=0)}{165.73} = 1 - 0.2 \left( \frac{p_{wf}(S=0)}{2,078} \right) - 0.8 \left( \frac{p_{wf}(S=0)}{2,078} \right)^2 \tag{9.68}$$

Equation (9.68) shows the relationship between  $q_o (S = 0)$  and  $p_{wf} (S = 0)$ , and calculation of  $p_{wf} (S = 0)$  extended to 14.7 psia is summarized in (Table 9.20).

3. Determine  $p_{wf} (S = -3)$ ;  $p_{wf} (S = 4)$ :

$$p_{wf}(S \neq 0) = p_{Avg} - \frac{p_{Avg} - p_{wf}(S=0)}{FE_{PSS}}$$

$$p_{wf}(S = -3) = 2,078 - \frac{2,078 - p_{wf}(S=0)}{FE_{PSS}(S = -3)}$$

where  $FE_{PSS}(S = -3) = \frac{\left( \ln \frac{1,121}{0.35} - \frac{3}{4} \right)}{\left( \ln \frac{1,121}{0.35} - \frac{3}{4} - 3 \right)} = 1.6942$

**Table 9.20**  $q$  Against  $p_{wf} (S = 0)$

Test number	$q$ (stb/D)	$p_{wf} (S = 0)$ (psia)
0 (from Table 9.19)	0.00	2,078.00
1 (from Table 9.19)	17.00	1,956.42
2 (from Table 9.19)2	33.00	1,833.55
3 (from Table 9.19)	47.00	1,718.44
4 (from Table 9.19)	59.00	1,603.97
Calculated using equation (9.68)	83.22	1,400.00
Calculated using equation (9.68)	118.30	1,010.00
Calculated using equation (9.68)	142.39	650.00
Calculated using equation (9.68)	156.39	350.00
Calculated using equation (9.68)	165.49	14.70

**Table 9.21** Calculation of  $p_{wf} (S = -3)$  from equation (9.69).

Test number	$q$ (stb/D)	$p_{wf} (S = 0)$ (psia)	$p_{wf} (S = -3)$ (psia) using equation (9.69)
0	0.00	2,078.00	2,078.00
1	17.00	1,956.42	2,006.24
2	33.00	1,833.55	1,933.71
3	47.00	1,718.44	1,865.76
4	59.00	1,603.97	1,798.20

Hence:

$$p_{wf}(S = -3) = 2,078 - \frac{2,078 - p_{wf}(S=0)}{1.6942} \tag{9.69}$$

The calculation of  $p_{wf} (S = -3)$  from equation (9.69) is summarized in Table 9.21.

Determining  $q_{o \max} (S = -3)$ :

$$q_{o \max}(S = -3) = \frac{q_o(S = -3)}{1 - 0.2 \left( \frac{p_{wf}(S = -3)}{p_{Avg}} \right) - 0.8 \left( \frac{p_{wf}(S = -3)}{p_{Avg}} \right)^2}$$

$$q_{o \max}(S = -3) = \frac{17}{1 - 0.2 \left( \frac{2,006.24}{2,078} \right) - 0.8 \left( \frac{2,006.24}{2,078} \right)^2} = 277.74 \text{ stb/D}$$

Using  $q_{o \max}$  calculated and the Vogel IPR, equation (9.52), extend the data to 14.7 psia with more data points between 14.7 to 1,798.20 psia. Exercise 9.9 explains the use of the Vogel equation for matching and predicting IPR.

From equation (9.52):

$$\frac{q_o(S = -3)}{q_{o \max}(S = -3)} = 1 - 0.2 \left( \frac{p_{wf}(S = -3)}{p_{Avg}} \right) - 0.8 \left( \frac{p_{wf}(S = -3)}{p_{Avg}} \right)^2 \tag{9.70}$$

**Table 9.22** Calculation of  $p_{wf}(S = -3)$  extended to 14.7 psia.

Test number	q	$p_{wf}(S = -3)$
0 (from Table 9.21)	0.00	2,078.00
1 (from Table 9.21)	17.00	2,006.24
2 (from Table 9.21)	33.00	1,933.71
3 (from Table 9.21)	47.00	1,865.76
4 (from Table 9.21)	59.00	1,798.20
Calculated using equation (9.71)	139.46	1,400.00
Calculated using equation (9.71)	198.25	1,010.00
Calculated using equation (9.71)	238.62	650.00
Calculated using equation (9.71)	262.08	350.00
Calculated using equation (9.71)	277.33	14.70

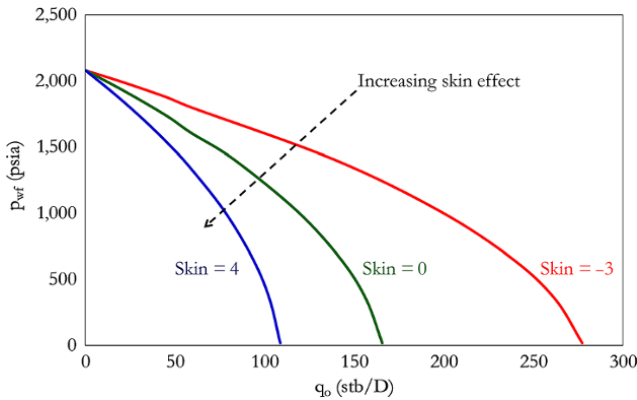


**Figure 9.31** Effect of skin on IPR.

Substituting  $q_{o \max}(S = -3)$  and  $p_{Avg}$  in equation (9.70):

$$\frac{q_o(S = 0)}{165.73} = 1 - 0.2 \left( \frac{p_{wf}(S = 0)}{2,078} \right) - 0.8 \left( \frac{p_{wf}(S = 0)}{2,078} \right)^2$$

$$\frac{q_o(S = -3)}{277.74} = 1 - 0.2 \left( \frac{p_{wf}(S = -3)}{2,078} \right) - 0.8 \left( \frac{p_{wf}(S = -3)}{2,078} \right)^2 \tag{9.71}$$

Equation (9.71) shows the relationship between  $q_o$  ( $S = -3$ ) and  $p_{wf}(S = -3)$

Calculation of  $p_{wf}(S = -3)$  extended to 14.7 psia is summarized in Table 9.22.

Plot IPR ( $S = -3$ ), IPR ( $S = 0$ ), and IPR ( $S = 4$ ) together for comparison and to show graphically the effect of skin on IPR (Fig. 9.31).

**9.2.9. Effect of Changing the Water Cut on the IPR Model**

The IPR prediction for multiphase oil–water can be handled by defining IPR using the total liquid rate.

Water cut (WCT) can be expressed as:

$$WCT = \frac{q_w}{q_L} \tag{9.72}$$

where  $q_w$  is the volumetric test or production rate of water and  $q_L$  is the volumetric test or production rate of liquid.

Making  $q_L$  the subject of the formula:

$$1 - WCT = 1 - \frac{q_w}{q_L}$$

$$(1 - WCT) = 1 - \frac{q_w}{q_L} = \frac{q_L - q_w}{q_L} = \frac{q_o}{q_L}$$

$$q_L = \frac{q_o}{(1 - WCT)} \tag{9.73}$$

From equation 9.73, the oil rate as a function of WCT ( $q_o(WCT)$ ) can be expressed as:

$$q_o(WCT) = q_L(1 - WCT) \tag{9.74}$$

Substituting  $q_L$  from equation (9.73) into any of the IPR equations for a liquid will give an IPR equation with  $q_o$  and WCT as variables. This approach assumes that deliverability of total liquid is independent of contrast in mobility of oil and water.

For a given  $p_{wf}$  and  $q_L$  with a change in WCT from  $WCT_1$  to  $WCT_2$  and a corresponding change in  $q_o$  from  $q_{o1}$  to  $q_{o2}$ , equation (9.73) can then be expressed as:

$$q_L = \frac{q_{o1}}{(1 - WCT_1)} = \frac{q_{o2}}{(1 - WCT_2)} \tag{9.75}$$

Hence, from equation (9.75), making  $q_{o2}$  the subject of the formula:

$$q_{o2} = q_{o1} \frac{(1 - WCT_2)}{(1 - WCT_1)}$$

$$q_o(WCT_2) = q_o(WCT_1) \frac{(1 - WCT_2)}{(1 - WCT_1)} \tag{9.76}$$

**Exercise 9.13** Effect of WCT on IPR

The WCT for the well in Exercise 9.9 is 0.2. Carry out a sensitivity analysis on WCT on IPR using WCT = 0, 0.2, 0.4, and 0.6 given that the deliverability of total liquid is independent of the contrast in mobility of oil and water.  $r_e = 1,121$  ft and  $r_w = 0.35$  ft.

**Solution Steps.**

*Step 1:* the oil rate in Table 9.15 is the assigned oil rate for a WCT of 0.2 ( $q_o(WCT = 0.2)$ ).

*Step 2:* using equation (9.74), calculate  $q_o$  for different WCT.



**Solution.**

Calculation of total liquid flow rate from the base case, at WCT = 0.2, for every data point from Table 9.15 is shown in Table 9.23.

The calculations of  $q_o$  (WCT) for WCT = 0, 0.4, and 0.6 using  $q_L$  from Table 9.23 are summarized in Table 9.24.

Note that original data has WCT = 0.2 and there is no need to repeat the calculation for WCT = 0.2.

From Table 9.24, the plot of  $p_{wf}$  against  $q_o$  for different WCT shows graphically the effect of WCT on IPR (Fig. 9.32).

The limitation of this method is in not accounting for additional reduction in oil deliverability due to contrast in mobility of separate phases. This is, however, not a problem, as reduction in oil deliverability due to the contrast in mobility of water and oil is insignificant [Brown and Beggs, 1977].

**9.2.10. Effect of Changing Condensate Gas Ratio (CGR) on Gas IPR Mode**

One approach for handling the effect of condensate on gas IPR is converting condensate produced from gas to equivalent gas in reservoir condition and adding it to the measured gas rate to get a recombined gas rate. Recombined gas and condensate rate can be expressed as:

$$q_t = q_g \left( 1 + \frac{V_{eq}CGR}{10^6} \right) \tag{9.77}$$

where  $q_t$  is recombined gas with vaporized condensate,  $q_g$  is measured gas rate, and  $V_{eq}$  is the vapor equivalent of the stock tank liquid (scf/stb).

$V_{eq}$  can be calculated using  $V_{eq}$  for a two-stage separation defined by Gold et al. [1989] as:

$$V_{eq} = 635.53 + 0.36182 p_{sep}^{1.0544} \gamma_g^{5.0831} API^{1.5812} T_{sep}^{-0.79130} \text{ (scf/stb)} \tag{9.78}$$

Where CGR is stock tank condensate gas ratio (stb/MMscf),  $\gamma_g$  is specific gravity of separator gas,  $p_{sep}$  is separator pressure (psia),  $T_{sep}$  is separator temperature (°F), and API is oil API gravity.

This concept of recombined gas and condensate rate is also applied to calculating the specific gravity of recombined gas and condensate to get a reservoir equivalent [Gold et al., 1989]:

$$\gamma_t = \frac{\frac{10^6 \gamma_g}{CGR} + 4,602 \gamma_o + q_{pa}}{\frac{10^6}{CGR} + V_{eq}} \tag{9.79}$$

**Table 9.23** Total Liquid Flow Rate from  $q_o$  (WCT = 0.2).

$p_{wf}$ (psia) From (Table 9.23)	$q_o$ (WCT = 0.2)	$q_L = \frac{q_o}{(1 - WCT)}$
	(stb/D) From (Table 9.23)	(stb/D) Using equation (9.73)
2,078	0	0.00
1,890	17.00	21.25
1,700	32.73	40.92
1,522	46.15	57.69
1,345	58.23	72.79
1,010	77.63	97.04
650	93.44	116.80
350	102.63	128.28
14.7	108.60	135.75

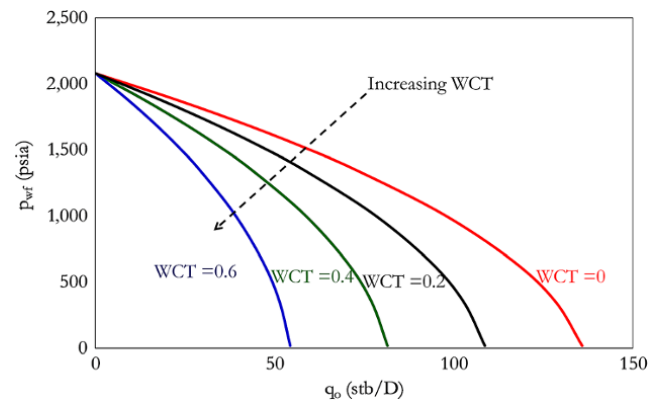


**Figure 9.32** Effect of WCT on oil IPR.

**Table 9.24** Oil Rate Calculation at WCT = 0, 0.4, and 0.6 for a Given  $p_{wf}$ .

$p_{wf}$ (psia)	$q_o$ (WCT = 0.2)	$q_L$ (stb/D)	$q_o$ (WCT = 0.0), (stb/D)	$q_o$ (WCT = 0.4), (stb/D)	$q_o$ (WCT = 0.6), (stb/D)
	from Table 9.23	from Table 9.23	using equation (9.74)	using equation (9.74)	using equation (9.74)
2,078	0	0.00	0.00	0.00	0.00
1,890	17.00	21.25	21.25	12.75	8.50
1,700	32.73	40.92	40.92	24.55	16.37
1,522	46.15	57.69	57.69	34.61	23.08
1,345	58.23	72.79	72.79	43.67	29.11
1,010	77.63	97.04	97.04	58.22	38.82
650	93.44	116.80	116.80	70.08	46.72
350	102.63	128.28	128.28	76.97	51.31
14.7	108.60	135.75	135.75	81.45	54.30

$q_{pa}$  is the additional gas production (vapor evolved at stock tank) in scf/stb for a two-stage separation. It was defined by Gold et al. [1989] as:

$$q_{pa} = 1.4599 \left( p_{sep} - 14.65 \right)^{1.3394} \gamma_g^{7.0943} API^{1.1436} T^{-0.93446} \tag{9.80}$$

$\gamma_o$  is the specific gravity of oil and  $T$  is the temperature ( $^{\circ}F$ ). All parameters are in EOF units.

**Exercise 9.14** Effect of CGR on IPR

Create an IPR plot for the reservoir in Exercise 9.7 given that CGR = 0 at  $p_{Avg} = 2,799$ ; CGR = 50 at  $p_{Avg} = 2,510$ , and CGR = 125 at  $p_{Avg} = 2,007$ .

Note that the case of CGR = 0 at  $p_{Avg} = 2,799$  has been calculated in Exercise 9.8 (shown under  $m_n(p)$  IPR calculations in Table 9.13).

**Solution Steps.**

*Step 1:* using a range of  $q_t$  from 0 to  $q_{t,max}$  ( $q_t$  at  $p_{wf} = 14.7$  psia), calculate  $p_{wf}$  for the case of  $p_{Avg} = 2,799$  psia,  $p_{Avg} = 2,510$  psia, and  $p_{Avg} = 2,007$  psia, respectively, using equation (9.42). In this approach,  $m_n(p_{wf})$  is what is determined from equation (9.42) and  $p_{wf}$  is then determined from the normalized pseudopressure table ( $m_n(p_{wf})$  against  $p_{wf}$ ).

*Step 2:* for the range of  $q_t$  in Q1, determine  $q_g$  for CGR = 0 (calculated in Exercise 9.8), CGR = 50 and 125 Stb/MMScf using equation (9.77).

*Step 3:* create a table of  $p_{wf}$  in Q1 and corresponding  $q_g$  in Q2 for CGR = 0, CGR = 50, and 125 stb/MMscf.

*Step 4:* plot  $p_{wf}$  against  $q_g$  for CGR = 0, CGR = 50, and 125 stb/MMscf

**Solution.**

From equation (9.78):

$$V_{eq} = 635.53 + 0.36182 p_{sep}^{1.0544} \gamma_g^{5.0831} API^{1.5812} T_{sep}^{-0.79130}$$

$$V_{eq} = 635.53 + 0.36182 \times 90.2^{1.0544} \times 0.6^{5.0831} 47^{1.5812} 70^{-0.79130}$$

682.9845672 scf/stb

Substituting into equation (9.77):

$$q_g = q_t / \left( 1 + \frac{V_{eq} CGR}{10^6} \right)$$

The relationship between  $q_g$  and CGR for this exercise can hence be expressed as:

$$q_g = q_t / \left( 1 + \frac{682.98 \times CGR}{10^6} \right) \tag{9.81}$$

The  $p_{wf}$  calculations at CGR = 0, 50, and 125 Mscf/D for Exercise 9.14 are summarized in Table 9.25.

A plot of  $p_{wf}$  against  $q_g$  for CGR = 0, CGR = 50, and 125 stb/MMscf with different  $p_{Avg}$  is shown in Fig. 9.33.

A similar concept can be applied to three-phase flow, where a *total equivalent rate* can be used for deliverability

**Table 9.25**  $p_{wf}$  Calculation at CGR = 0, 50, and 125 Mscf/D for Exercise 9.14.

CGR = 0 stb/MMScf and $p_{Avg} = 2,799$ psia		CGR = 50 stb/MMScf and $p_{Avg} = 2,510$ psia			CGR = 125 stb/MMscf and $p_{Avg} = 2,007$ psia		
$q_g$ (CGR = 0) = $q_t$ (Mscf/D)	$p_{wf}$ (psia) using approach in Exercise 9.8	$q_g$ (CGR = 0) = $q_t$ (Mscf/D)	$p_{wf}$ (psia) using approach in Exercise 9.8	$q_g$ (CGR = 50) (Mscf/D) using equation (9.81)	$q_g$ (CGR = 0) = $q_t$ (Mscf/D)	$p_{wf}$ (psia) using approach in Exercise 9.8	$q_g$ (CGR = 125) (Mscf/D) using equation (9.81)
0	2799	0	2,510	0	0	2,007	0
20	2,763.01	20	2,468.40	19.34	20	1,949.53	18.43
40	2,704.91	40	2,401.49	38.68	40	1,854.47	36.85
70	2,575.91	70	2,250.71	67.69	70	1,632.68	64.49
100	2,393.87	100	2,034.09	96.70	100	1,281.83	92.13
140	2,057.27	140	1,613.97	135.38	110	1,118.41	101.35
180	1,572.53	150	1,474.86	145.05	115	1,023.47	105.95
210	1,010.47	160	1,315.05	154.72	120	915.13	110.56
220	715.68	170	1,126.90	164.39	125	787.15	115.17
226	447.77	180	890.73	174.06	130	628.59	119.77
<b>229.78</b>	<b>14.70</b>	<b>195.92</b>	<b>14.70</b>	<b>189.45</b>	<b>138.56</b>	<b>14.70</b>	<b>127.66</b>
<b>(<math>q_t</math> (<math>p_{wf} = 14.7</math>))</b>		<b>(<math>q_t</math> (<math>p_{wf} = 14.7</math>))</b>			<b>(<math>q_t</math> (<math>p_{wf} = 14.7</math>))</b>		

Note: the last rate point in Table 9.25 can be determined using a spreadsheet goal seek to determine  $q_t$  for  $p_{wf} = 14.7$  in equation setup

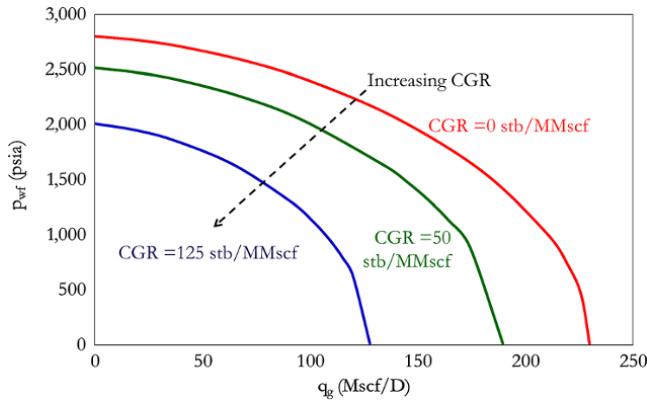


Figure 9.33 Effect of CGR on gas IPR.

calculations and IPR plotted for the dominant fluid phase.

Total equivalent rate in rb/d is defined by equation (8.169) in Chapter 8.as:

$$(qB)_t = q_o B_o + q_w B_w + (q_{sc} - R_s) B_g$$

9.2.11. Horizontal Wells-IPR

Horizontal wells can be used to improve reservoir deliverability. Well test analysis features and benefits of horizontal wells have been discussed in Chapter 8 (8.4.3.7). By combining appropriate boundary conditions using techniques of image wells as discussed in Chapter 8 (8.5.1.12), IPR for SS and PSS conditions can be derived. Other reliable simple approaches for SS and PSS IPR models are discussed here.

9.2.11.1. Steady State IPR Horizontal Well Model.

Drainage area around a horizontal well producing at SS conditions can generally be defined as *Spherocylindrical* or *ellipsoidal* (Fig. 9.34). One of the most common SS horizontal well IPR model is Joshi IPR model (Joshi, 1988) which accounts for vertical-to-horizontal permeability anisotropy, a key parameter that controls horizontal well deliverability. Joshi’s model assumes an elliptical constant pressure drainage whose dimension depends on the well length.

Joshi [1988] presented a well deliverability equation for a horizontal well producing under steady state conditions (constant pressure drainage) as:

$$PI_{SS} = \frac{q}{(p_{Avg} - p_{wf})} = \frac{7.08 \times 10^{-3} k_{xy} h}{\mu_o B_o \left[ \ln \left( \frac{a + \sqrt{a^2 - (L_w/2)^2}}{(L_w/2)} \right) + \frac{\beta^2 h}{L_w} \ln \left( \frac{h}{2r_w} \right) \right]} \tag{9.82}$$

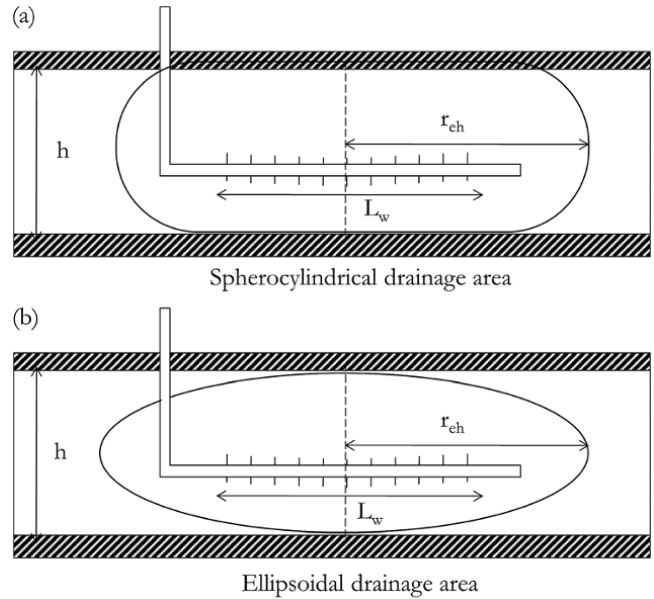


Figure 9.34 Horizontal well drainage area.

where a is one-half the major axis of a drainage ellipse in a horizontal plane and is defined as:

$$a = \frac{L_w}{2} \left( 0.5 + \sqrt{0.25 + \left( \frac{2r_{eh}}{L_w} \right)^4} \right)^{0.5}$$

$$\beta = \sqrt{\frac{k_{xy}}{k_z}}$$

r<sub>eh</sub> is the drainage radius (ft) defined as:

$$r_{eh} = \sqrt{\frac{A}{\pi}}$$

where k<sub>xy</sub> is the horizontal permeability in the x–y direction, also denoted as k<sub>h</sub>, and k<sub>z</sub> is the vertical permeability, also denoted as k<sub>v</sub>.

For an isotropic reservoir, k<sub>z</sub> = k<sub>xy</sub> (k<sub>v</sub> = k<sub>h</sub>) and, hence, β = 1. Equation (9.82) for an isotropic reservoir thus reduces to:

$$PI_{SS} = \frac{q}{(p_{Avg} - p_{wf})} = \frac{7.08 \times 10^{-3} k_{xy} h}{\mu_o B_o \left[ \ln \left( \frac{a + \sqrt{a^2 - (L_w/2)^2}}{(L_w/2)} \right) + \frac{h}{L_w} \ln \left( \frac{h}{2r_w} \right) \right]} \tag{9.83}$$

**Exercise 9.15** Horizontal Well Producing at Steady State Conditions

A horizontal well with an open wellbore radius of 0.35 ft, mechanical skin of 5, and effective length of 1,789 ft is completed in a 45-ft pay anisotropic reservoir with a drainage area of 190 acres,  $k_h$  of 40 mD,  $\frac{k_z}{k_{xy}}$  of 0.012, and  $p_{Avg}$  of 1,909 psia, produces oil with  $\mu_o = 0.75$  cp and  $B_o = 1.56$  stb/rb.

1. Determine SS productivity of the well and IPR equation for this well.
2. Carry out a sensitivity analysis on IPR model for  $k_z/k_{xy}$  of 0.001, 0.012, 0.1, and 1.
3. Carry out a sensitive analysis on the IPR model for  $h = 10, 20, 45,$  and  $60$  ft.
4. Carry out a sensitivity analysis on the IPM model for  $L_w = 1,000, 1,500, 1,789,$  and  $2,000$  ft.

**Solution.**

1.  $A = 190 \text{ Acres} = 43,560 \times 190 \text{ ft}^2 = 82,76,400 \text{ ft}^2$ .

Calculating  $r_{eh}$ :

$$r_{eh} = \sqrt{\frac{A}{\pi}} = \sqrt{\frac{82,76,400}{\pi}} = 1,623.10 \text{ ft}$$

Calculating  $a$ :

$$a = \frac{L_w}{2} \left( 0.5 + \sqrt{0.25 + \left( \frac{2r_{eh}}{L_w} \right)^4} \right)^{0.5}$$

$$= \frac{1,789}{2} \left( 0.5 + \sqrt{0.25 + \left( \frac{2 \times 1,623.10}{1,789} \right)^4} \right)^{0.5} = 1,750.64 \text{ ft}$$

Calculating  $\beta$ :

$$\beta = \sqrt{\frac{k_{xy}}{k_z}} = \sqrt{\frac{1}{\frac{k_z}{k_{xy}}}} = \sqrt{\frac{1}{0.012}} = 9.129$$

Calculating  $PI_{SS}$  using equation (9.83):

$$PI_{SS} = \frac{q}{(1,909 - p_{wf})}$$

$$= \frac{7.08 \times 10^{-3} \times 40 \times 45}{0.75 \times 1.56 \left[ \ln \left( \frac{1,750.64 + \sqrt{1,750.64^2 - (1,789/2)^2}}{(1,789/2)} \right) + \frac{9,921^2 \times 45}{1,789} \ln \left( \frac{45}{2 \times 0.35} \right) \right]}$$

$$= 0.725$$

The IPR equation for the horizontal well producing at steady state conditions is hence:

$$\frac{q}{(1,909 - p_{wf})} = 0.725$$

**Table 9.26** IPR Data for Exercise 9.15.

$p_{wf}$ (psia)	$q_o$ (stb/D)
1,909	0
14.7	1,373.83

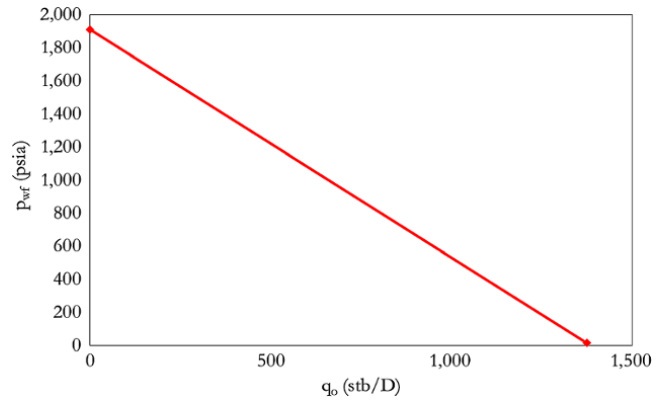


**Figure 9.35** IPR plot for Exercise 9.15.

The above equation is linear, hence two points are sufficient to make an IPR plot.

An IPR table from the above equation is shown in Table 9.26 and a plot is shown in Fig. 9.35.

2. Repeat the IPR calculation for  $\frac{k_z}{k_{xy}} = 0.001, 0.012, 0.1,$  and  $1$  (Table 9.27).

The IPR sensitivity to  $\frac{k_z}{k_{xy}}$  is shown in Fig. 9.36.

3. Repeat the IPR calculation for  $h = 10, 20, 45,$  and  $60$  ft (Table 9.28).

The IPR sensitivity plot to  $h$  is shown Fig. 9.37.

4. Repeat the IPR calculation for  $L_w = 1,000, 1,500, 1,789,$  and  $2,000$  ft (Table 9.29).

The IPR sensitivity plot to  $L_w$  is shown Fig. 9.38.

**9.2.11.2. Pseudosteady State IPR Horizontal Well Model.**

PSS has been discussed as an important condition for production engineers. One of the most robust PSS IPR models for horizontal wells is the Economides horizontal well IPR [Economides et al., 1996]. The model captures the effect of anisotropy, early and late time behavior of horizontal wells, and well-reservoir orientation and configuration.

The Economides PSS IPR model for a horizontal well is expressed as:

$$PI_{PSS} = \frac{q}{(p_{Avg} - p_{wf})} = \frac{\bar{k}x_e}{887.22B\mu \left( p_D + \frac{x_e}{2\pi L_w} \sum S \right)} \tag{9.84}$$

**Table 9.27** IPR Sensitivity to  $\frac{k_z}{k_{xy}}$ .

$\frac{k_z}{k_{xy}} = 0.001$		$\frac{k_z}{k_{xy}} = 0.012$		$\frac{k_z}{k_{xy}} = 0.1$		$\frac{k_z}{k_{xy}} = 1$	
$p_{wf}$ (psia)	$q_o$ (stb/D)	$p_{wf}$ (psia)	$q_o$ (stb/D)	$p_{wf}$ (psia)	$q_o$ (stb/D)	$p_{wf}$ (psia)	$q_o$ (stb/D)
1,909	0	1,909	0	1,909	0	1,909	0
14.7	185.86	14.7	1,373.83	14.7	2,811.43	14.7	3,225.69

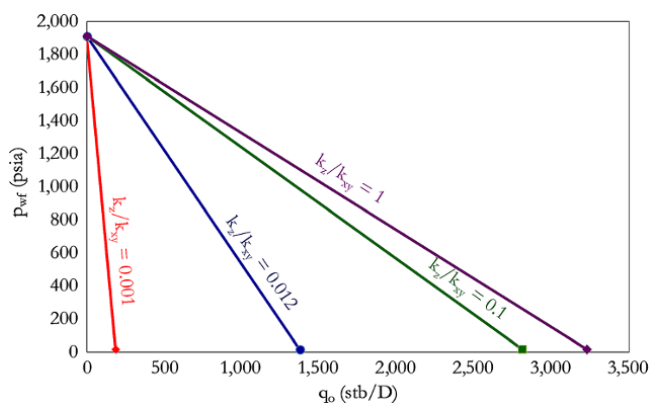


**Figure 9.36** IPR sensitivity to  $\frac{k_z}{k_{xy}}$ .

**Table 9.28** IPR Sensitivity to  $h$

$h$ (ft) = 10		$h$ (ft) = 20		$h$ (ft) = 45		$h$ (ft) = 60	
$p_{wf}$ (psia)	$q_o$ (stb/D)	$p_{wf}$ (psia)	$q_o$ (stb/D)	$p_{wf}$ (psia)	$q_o$ (stb/D)	$p_{wf}$ (psia)	$q_o$ (stb/D)
1,909	0	1,909	0	1,909	0	1,909	0
14.7	608.88	14.7	974.02	14.7	1,373.83	14.7	1,468.68

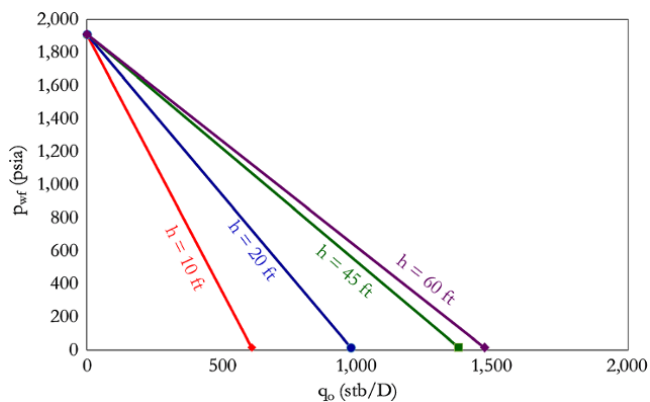


**Figure 9.37** IPR sensitivity to  $h$ .

**Table 9.29** IPR Sensitivity to  $L_w$

$L_w$ (ft) = 1,000		$L_w$ (ft) = 1,500		$L_w$ (ft) = 1,789		$L_w$ (ft) = 2,000	
$p_{wf}$ (psia)	$q_o$ (stb/D)	$p_{wf}$ (psia)	$q_o$ (stb/D)	$p_{wf}$ (psia)	$q_o$ (stb/D)	$p_{wf}$ (psia)	$q_o$ (stb/D)
1,909	0	1,909	0	1,909	0	1,909	0
14.7	917.71	14.7	1,222.72	14.7	1,373.83	14.7	1,475.05

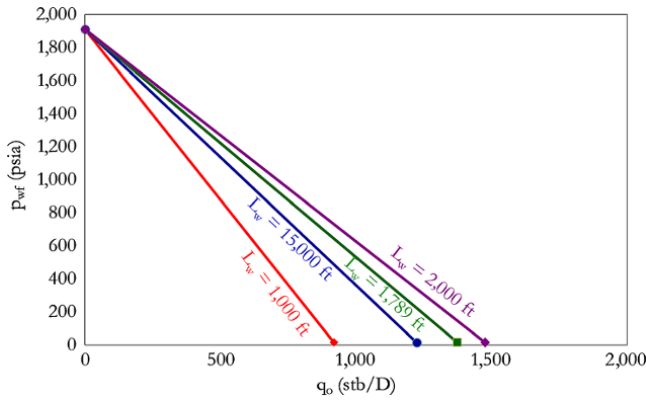


Figure 9.38 IPR sensitivity to  $L_w$ .

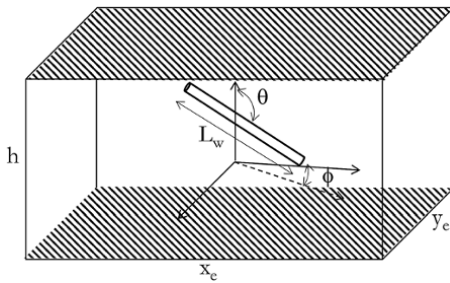


Figure 9.39 Horizontal well with coordinates and IPR parameters [Adapted from Economides, Brad and Frick, 1996].

A horizontal well with coordinates and IPR parameters is defined in Fig. 9.39.

where

$$p_D = \frac{x'_e C_H}{4\pi h} + \frac{x'_e}{2\pi L'_w} S_c \tag{9.85}$$

$C_H$  is defined in Fig. 9.40 for different aspect ratios.

where the skin effect  $S_c$  is:

$$S_c = \ln\left(\frac{h}{2\pi r'_w}\right) - \frac{h}{6 L'_w + S_e} \tag{9.86}$$

and  $S_e$  defined as:

$$S_e = \frac{h}{L'_w} \left( \frac{2z_w}{h} - \frac{1}{2} \left( \frac{2z_w}{h} \right)^2 - \frac{1}{2} \right) - \ln\left(\sin\left(\frac{\pi z_w}{h}\right)\right) \tag{9.87}$$

$z_w$  is the distance of the well from the middle of the reservoir.

$L'_w$  and  $r'_w$  are well length and wellbore radius transformations to account for the effect of anisotropy and non-centricity of the well in the reservoir and are defined as:

$$L'_w = L_w \alpha^{-1/3} \beta$$

and

$$r'_w = r_w \frac{\alpha^{2/3}}{2} \left( \frac{1}{\beta} + 1 \right)$$

where

$$\alpha = \sqrt{\frac{(k_x k_y)^{1/2}}{k_z}}$$

and

$$\beta = \left( \sqrt{\frac{k_y}{k_x}} \cos^2 \phi + \sqrt{\frac{k_x}{k_y}} \sin^2 \phi \right)^{1/2}$$

where  $k_x$ ,  $k_y$ , and  $k_z$  are permeability in the  $x$ ,  $y$ , and  $z$  directions respectively.

Also, for an anisotropic reservoir, the transforms of reservoir dimension defined below should be used:

$$x' = x \frac{\sqrt{k_y k_z}}{\bar{k}} \tag{9.88}$$

$$y' = y \frac{\sqrt{k_x k_z}}{\bar{k}} \tag{9.89}$$

$$z' = z \frac{\sqrt{k_x k_y}}{\bar{k}} \tag{9.90}$$

and  $\bar{k}$  is defined as:

$$\bar{k} = \sqrt[3]{k_x k_y k_z}$$

for an isotropic reservoir  $\bar{k} = k_x = k_y = k_z = k$ ; hence,  $\alpha$  and  $\beta$  become 1 reducing equation (9.84) to:

$$PI_{PSS} = \frac{q}{(p_{Avg} - p_{wf})} = \frac{k x_e}{887.22 B \mu \left( p_D + \frac{x_e}{2\pi L_w} \sum s \right)} \tag{9.91}$$

**Exercise 9.16** Horizontal Well Producing at Pseudosteady State Condition

Repeat Exercise 9.15 with a no-flow drainage boundary rather than a constant pressure boundary. Assume that the ratio of no-flow boundaries reservoir length to width ratio ( $x/y$ ) is the same as the elliptical major to minor axis ratio in Exercise 9.16 (i.e.,  $x/y = a/b$ )

Calculate the pseudosteady state productivity index for this well-reservoir system.

**Solution.**

Calculating  $\bar{k}$

$$k_z = \frac{k_z}{k_{xy}} k_{xy}$$

$$k_z = 0.012 \times 40 \text{mD} = 0.48 \text{mD}$$

Also,  $k_{xy} = k_x = k_y$  (no permeability anisotropy in the  $x$ - $y$  direction). Hence:

$$\bar{k} = \sqrt[3]{k_x k_y k_z} = \sqrt[3]{40 \times 40 \times 0.48} = 9.158 \text{mD}$$

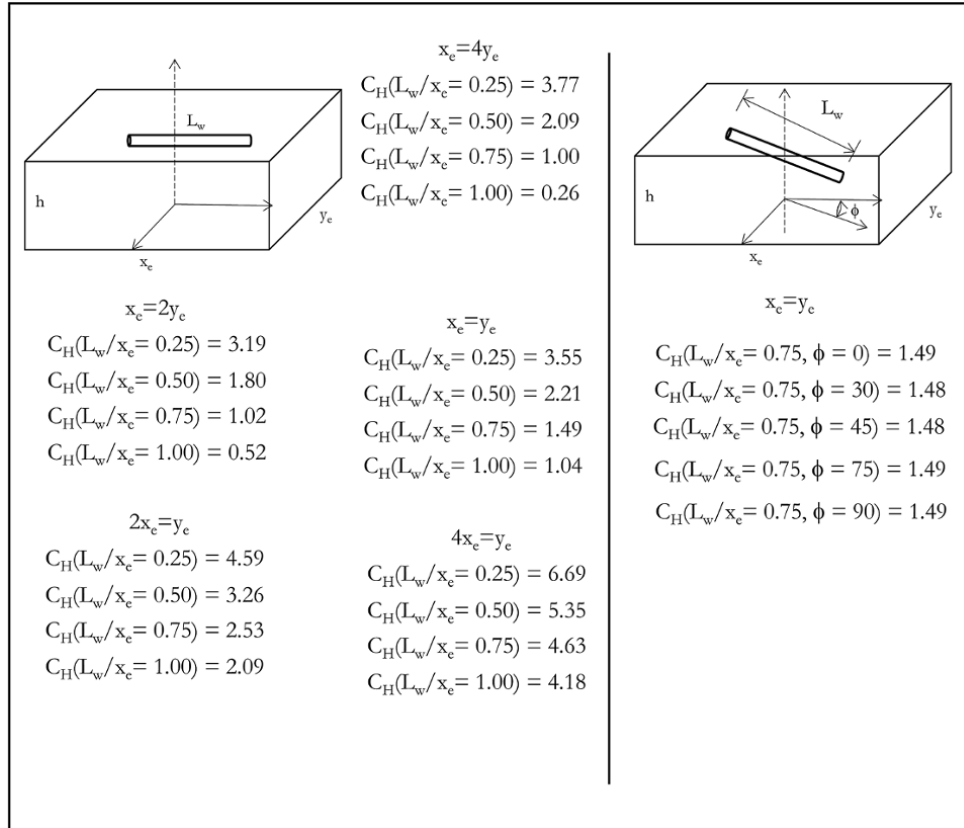


Figure 9.40 Horizontal well shape factor [Adapted from Economides, Brad and Frick, 1996].

Calculating the reservoir dimension for the case of  $x/y = alb$

Area of an ellipse:

$$A = \pi ab$$

where

$$a = \frac{L}{2} + b \text{ hence } b = a - \frac{L}{2}$$

Hence:

$$A = \pi ab = \pi a \left( a - \frac{L}{2} \right)$$

Rearranging the above equation:

$$a^2 - a \frac{L}{2} - \frac{A}{\pi} = 0$$

Solving this for a (using the generalized solution for quadratic equations):

$$a = \frac{\frac{L}{2} + \sqrt{\left(\frac{L}{2}\right)^2 + \frac{4A}{\pi}}}{2}$$

$$= \frac{1,789}{2} + \sqrt{\left(\frac{1,789}{2}\right)^2 + \frac{4 \times 82,76,400}{\pi}}$$

Solving for b:

$$b = a - \frac{L}{2} = 2,130.89 - \frac{1,789}{2} = 1,236.35 \text{ ft}$$

$$\frac{a}{b} = \frac{2,130.89}{1,236.35} = 1.7235$$

The reservoir considered in this exercise has  $\frac{a}{b} =$

$\frac{x_e}{y_e}$ . Hence:

$$\frac{a}{b} = \frac{x_e}{y_e} = 1.7235$$

$$y_e = \frac{x_e}{1.7235} = 1.7235$$

Area of rectangular reservoir:

$$A = 82,76,400 \text{ ft}^2 \text{ (same as elliptical drainage area)}$$

$$A = x_e y_e$$

Substituting  $y_e$  into the above and solving for  $x_e$ :

$$82,76,400 = x_e \frac{x_e}{1.7235}$$

$$x_e = 3,776.82 \text{ ft}$$

Solving for  $y_e$ :

$$y_e = \frac{x_e}{1.7235}$$

$$y_e = \frac{3,776.82}{1.7235}$$

$$y_e = 2,191.36 \text{ ft}$$

Transforming  $x_e$  and  $y_e$  for the effect of anisotropy:

$$x'_e = x_e \frac{\sqrt{k_y k_z}}{k} = 3,776.82 \frac{\sqrt{40 \times 0.48}}{9.158} = 1,807.13 \text{ ft}$$

$$y'_e = y_e \frac{\sqrt{k_x k_z}}{k} = 2,191.36 \frac{\sqrt{40 \times 0.48}}{9.158} = 1,048.52 \text{ ft}$$

Calculating  $\alpha$  and  $\beta$

$$\alpha = \sqrt{\frac{(k_x k_y)^{\frac{1}{2}}}{k_z}} = \sqrt{\frac{(40 \times 40)^{\frac{1}{2}}}{0.48}} = 9.1287$$

and

$$\beta = \left( \sqrt{\frac{k_y}{k_x}} \cos^2 \phi + \sqrt{\frac{k_x}{k_y}} \sin^2 \phi \right)^{1/2} = 1$$

Calculating  $L'_w$  and  $r'_w$

$$L'_w = L_w \alpha^{-1/3} \beta = 1,789 \times 9.1287^{-1/3} \times 1 = 856.00 \text{ ft}$$

$$r'_w = r_w \frac{\alpha^{2/3}}{2} \left( \frac{1}{\beta} + 1 \right) = 0.35 \frac{9.1287^{2/3}}{2} \left( \frac{1}{1} + 1 \right) = 1.5288 \text{ ft}$$

Calculating  $S_c$

From equation (9.87):

$$S_e = \frac{h}{L'_w} \left( \frac{2z_w}{h} - \frac{1}{2} \left( \frac{2z_w}{h} \right)^2 - \frac{1}{2} \right) - \ln \left( \sin \left( \frac{\pi z_w}{h} \right) \right)$$

$$S_e = \frac{45}{856} \left( \frac{2 \times 22.5}{45} - \frac{1}{2} \left( \frac{2 \times 22.5}{45} \right)^2 - \frac{1}{2} \right) - \ln \left( \sin \left( \frac{\pi \times 22.5}{45} \right) \right) = 0$$

From equation (9.86):

$$S_c = \ln \left( \frac{h}{2\pi r'_w} \right) - \frac{h}{6 L'_w} + S_e$$

$$= \ln \left( \frac{45}{2\pi \times 1.5288} \right) - \frac{45}{6 \times 856} + 0 = 1.5356$$

Determining  $C_H$

$$\frac{x'_e}{y'_e} = \frac{1,807.13}{1,048.52} = 1.72 \approx 2$$

Hence,  $x'_e \approx 2y'_e$

Also:

$$\frac{L'_w}{x'_e} = \frac{856.00}{1,807.13} = 0.47368 \approx 0.5$$

From Fig. 9.40, using  $x'_e = 2y'_e$  and  $\frac{L'_w}{x'_e} = 0.5$  (a more refine value could be determined by interpolating for values in Fig. 9.40):

$$C_H = 1.8$$

Calculating  $p_D$

From equation (9.85):

$$p_D = \frac{x'_e C_H}{4\pi h} + \frac{x'_e}{2\pi L'_w} S_c$$

Substituting into the above equation to determine  $p_D$ :

$$p_D = \frac{1,807.13 \times 1.8}{4\pi \times 45} + \frac{1,807.13}{2\pi \times 856.00} 1.5356 = 6.26823$$

Calculating  $PI_{PSS}$

From equation (9.84):

$$PI_{PSS} = \frac{q}{(p_{Avg} - p_{wf})} = \frac{\bar{k} x_e}{887.22 B \mu \left( p_D + \frac{x_e}{2\pi L'_w} \sum s \right)}$$

Making a substitution and solving for  $PI_{PSS}$ :

$$PI_{PSS} = \frac{9.158 \times 1,807.13}{887.22 \times 1.56 \times 0.75 \left( 6.26823 + \frac{1,807.13}{2\pi \times 856.00} 5 \right)}$$

$$= 1.65 \text{ stb/D/psi}$$

## 9.2.12. Multilayered Reservoir

Multilayered reservoirs have been discussed in Chapter 8 (8.5.1.11) and can generally be categorized as *multilayered reservoirs with cross-flow* across layers (layers in hydraulic communication) or *multilayered reservoirs without cross-flow*, where the contribution of all layers is through commingle tubing production (layers without hydraulic communication).



**9.2.12.1. Multilayered Reservoir with Cross-flow.**

During PSS production in multilayered reservoirs with cross-flow, overall deliverability of the reservoir is controlled by the arithmetic average of the all layers and, therefore, IPR can be described with an arithmetic average of contributing layers. When separate layers of a multilayered reservoir with cross-flow are fully completed, the effect of communication between layers does not affect reservoir deliverability, as the effect of partial penetration (limited entry) relative to all layers is absent.

However, when only some of the layers are completed and some layers contribute to production through cross-flow, the effect of the communicating barrier will reflect in the calculated average vertical permeability ( $k_v$ ). Where cross-flow barriers are tight and/or extensive into the reservoir, effective  $k_v$  values will be low.

**9.2.12.2. Multilayered Reservoir without Cross-flow.**

Comingled production in multilayered reservoirs without cross-flow is different, as the layers are not in hydraulic communication. Significant pressure difference between layers without cross-flow may exist, unlike multilayered reservoirs with cross-flow, where layers are in hydraulic equilibrium during PSS production. The absence of continued equilibration between each layer with different deliverability can cause one layer creating a back-pressure effect on another layer through production tubing communication. This back pressure by one layer on another can have a significant effect on the overall deliverability of all layers producing together through the same production conduit. In multilayered reservoir without cross-flow, one layer may dominate the reservoir deliverability due to difference in one or more of  $k$ ,  $h$ ,  $S$ , and  $p_{Avg}$ , thereby causing depletion of one layer in preference to others (*differential reservoir depletion*).

The overall deliverability of a multilayer reservoir with comingled production can be represented as the sum of the productivity of each layer:

$$PI_{PSS,t} = \sum_{i=1}^N PI_{PSS,j} = \frac{q_{surface,t}}{(p_{Avg} - p_{wf})} \quad (9.92)$$

where the productivity index of each layer ( $j$ ) for single-phase, slightly compressible or incompressible fluid is defined by equation (9.29):

$$PI_{PSS,j} = \frac{q_{surface,j}}{(p_{Avg,j} - p_{wf})} = \frac{k_j h_j}{141.2 \mu_j B_j \left( \frac{1}{2} \ln \left( \frac{4A_j}{\gamma C_{A,j} r_{w,j}^2} \right) + S_j \right)} \quad (9.93)$$

From equation (9.92):

$$PI_{PSS,t} = \frac{q_{surface,t}}{(p_{Avg} - p_{wf})}$$

making  $p_{wf}$  subject of formula:

$$p_{wf} = p_{Avg} - \frac{q_{surface,t}}{PI_{PSS,t}} \quad (9.94)$$

where

$$q_{surface,t} = \sum_{i=1}^N q_{surface,j} \quad (9.95)$$

$q_{surface}$  is the surface well production rate and  $PI_{PSS}$  is the productivity index for pseudosteady state production.

The subscripts "t" and "j" represent total and layer properties, respectively.

$p_{Avg}$  is the average pressure for comingled production and is defined as the PI weighted average of all producing layers:

$$p_{Avg} = \frac{\sum_{i=1}^N PI_{PSS,j} p_{Avg,j}}{\sum_{i=1}^N PI_{PSS,j}} \quad (9.96)$$

Substituting equations (9.96) and (9.95) into equation (9.94):

$$p_{wf} = p_{Avg} - \frac{\sum_{i=1}^N q_{surface,j}}{PI_{PSS,t}}$$

$$p_{wf} = \frac{\sum_{i=1}^N PI_{PSS,j} p_{Avg,j}}{\sum_{i=1}^N PI_{PSS,j}} - \frac{\sum_{i=1}^N q_{surface,j}}{\sum_{i=1}^N PI_{PSS,j}} \quad (9.97)$$

where  $PI_{PSS,j}$  is already defined in equation (9.93).

**Exercise 9.17** IPR for Comingled Multilayered Reservoir without Cross-flow

A reservoir consisting of three layers without hydraulic communication in the reservoir has the layer properties shown in Table 9.30.

1. Create the IPR plot for each layer.
2. Create the IPR for comingled production of all layers.

**Solution.**

1. For individual layers

Using equation (9.93), two points are sufficient to create the IPR plot, as the fluid is single-phase oil. The first point is  $p_{Avg}$ , corresponding to  $p_{wf}$  at  $q_o = 0$  stb/D, and the second point for the IPR plot is determined by calculating AOFD for  $p_{wf} = 14.7$  psia (Table 9.31).

2. IPR relationship for commingled production of the three layers

Table 9.32 shows the calculation for  $\sum_{i=1}^N PI_{PSS,j}$  and

$$\sum_{i=1}^N PI_{PSS,j} p_{Avg,j}$$

The values of  $\sum_{i=1}^N PI_{PSS,j}$  and  $\sum_{i=1}^N PI_{PSS,j} p_{Avg,j}$  are substituted into equation (9.96) to determine  $p_{Avg}$ .

$$p_{Avg} = \frac{\sum_{i=1}^N PI_{PSS,j} p_{Avg,j}}{\sum_{i=1}^N PI_{PSS,j}}$$

$$p_{Avg} = \frac{7,924.349}{2.821} = 2,808.72 \text{ psia}$$

**Table 9.30** Layer Properties for Exercise 9.17.

Parameter	Layer 1	Layer 2	Layer 3
k (mD)	100	27	50
h (ft)	11	90	53
$p_{avg}$	3,451	2,998	2,502
S	10	12	5
A (acres)	40	60	50
$C_A$	27	30	22
$r_w$ (ft)	0.35	0.35	0.35
$B_o$ (bbl/stb)	1.5	1.33	1.23
$\mu_o$ (cp)	0.65	0.8	0.83

**Table 9.31**  $p_{wf}$  and corresponding  $q_o$  Over 14.7 and  $p_{Avg}$  for Each Layer.

Layer 1		Layer 2		Layer 3	
$p_{wf}$ (psia)	$q_o$ (stb/D)	$p_{wf}$ (psia)	$q_o$ (stb/D)	$p_{wf}$ (psia)	$q_o$ (stb/D)
3,451	0	2,998	0	2,502	0
14.7	1,615.86	14.7	2,520.82	14.7	3,746.191

**Table 9.32**  $\sum_{i=1}^N PI_{PSS,j}$ ;  $\sum_{i=1}^N PI_{PSS,j} p_{Avg,j}$  Calculations.

Layer	$A_j$ (ft <sup>2</sup> )	$PI_{PSS,j}$ (stb/D/psi)	$PI_{PSS,j} \times p_{Avg,j}$ (stb/D)
Layer 1	1,742,400	0.470	1,622.774
Layer 2	2,613,600	0.845	2,533.243
Layer 3	2,178,000	1.506	3,768.331
		$\sum_{i=1}^N PI_{PSS,j} = 2.821$	$\sum_{i=1}^N PI_{PSS,j} p_{Avg,j} = 7,924.349$

The IPR for all three layers produced through commingled tubing production, using equation (9.97), is hence defined as:

$$p_{wf} = 2,808.72 - \frac{\sum_{i=1}^N q_{surface,j}}{2.821}$$

$$p_{wf} = 2,808.72 - \frac{q_{surface,t}}{2.821}$$

The above IPR is used to create data to plot IPR. Similar to the IPR calculation for individual layers in Q1, two data points are sufficient to make an IPR plot for a single-phase oil (Table 9.33).

Using data points from Tables 9.31 and 9.33, the IPR plot is created (Fig. 9.41).

**9.2.13. Horizontal Well Intersecting Multiple Compartments**

Similar to multilayered reservoirs, the IPR of a horizontal well intersecting multiple compartments with different compartment permeabilities ( $k_1, k_2, \dots, k_N$ ), different effective well lengths within each compartment ( $L_{1\_eff}, L_{2\_eff}, \dots, L_{N\_eff}$ ) and different initial reservoir compartment pressures ( $p_{i_1}, p_{i_2}, \dots, p_{i_N}$ ) can be

**Table 9.33**  $p_{wf}$  and Corresponding  $q_o$  Over 14.7 and  $p_{Avg}$  for Combined Layer.

$p_{wf}$ (psia)	$q_o = q_{surface,t}$ (stb/D)
2,808.72	0
14.7	7,881.93

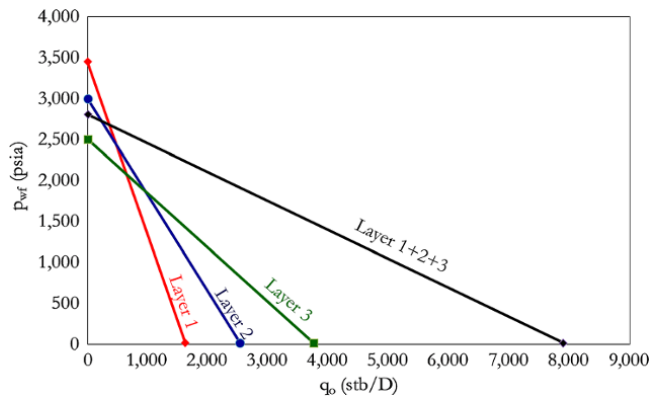


**Figure 9.41** IPR for each layer and for all layers in commingled production.

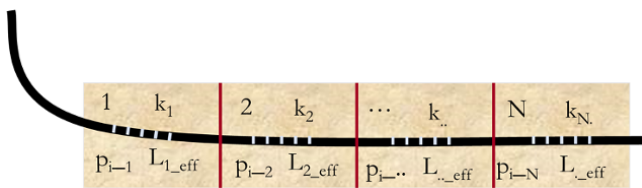


**Figure 9.42** Horizontal well intersecting multiple compartments.

represented by the summation of the PI of all compartments intersected by the well. The PI of a horizontal well intersecting multiple compartments ( $PI_{PSS\_Hz\_Concept}$ ) can be expressed by equation (9.98):

$$PI_{PSS\_Hz\_Comprt} = \sum_{i=1}^N PI_{PSS,j} \quad (9.98)$$

Fig. 9.42 shows the schematic of a horizontal well intersecting multiple compartments.

## REFERENCES

- Aronofsky, J. and Jenkins, R., 1954. A simplified analysis of unsteady radial gas flow. *Journal of Petroleum Technology*, **6**(7), 23–28.
- Brown, K. and Beggs, H., 1977. *The Technology of Artificial Lift Methods*, Vol. 1. Tulsa OK: PennWell Publishing.
- Dietz, D., 1965. Determination of average reservoir pressure from build-up surveys. *Journal of Petroleum Technology*, **17** (8), 955–959.
- Economides, M., Brad, C., and Frick, T., 1996. Well configuration in anisotropic reservoirs. *SPE Formation Evaluation*, **11** (4), 257–262.
- Evinger, H. and Muskat, M., 1942. Calculation of theoretical productivity factor. *Society of Petroleum Engineers, Transactions of the AIME*, **146**(1), 126–139.
- Fetkovich, M., 1973. *The Isochronal Testing of Oil Wells*. Fall Meeting of the Society of Petroleum Engineers of AIME, Las Vegas, NV.

- Gold, D., McCain, W.J., and Jennings, J., 1989. An improved method for the determination of the reservoir-gas gravity for retrograde. *Journal of Petroleum Technology*, **41**(7), 747–752.
- Jones, J. and Raghavan, R., 1988. Interpretation of flowing well responses in gas-condensate wells. *SPE Formation Evaluation*, **3**(3), 578–594.
- Joshi, S., 1988. Augmentation of well productivity with slant and horizontal wells. *Journal of Petroleum Technology*, **40** (6), 729–739.
- Van Everdingen, A. and Hurst, W., 1949. The application of the laplace transformation to flow problems in reservoirs. *Petroleum Transactions AIME*, **1**(12), 305–324.
- Vogel, J.V., 1968. Inflow performance relationship for solution-gas drive wells. *Journal of Petroleum Technology*, **248**, 88–92.

## BIBLIOGRAPHY

- Al-Hussainy, R., Ramey Jr., H.J., and Crawford, P.B., 1966. The flow of real gas through porous media. *Journal of Petroleum Technology*, **18**(05), 637–642.
- Bellarby, J., 2009. *Well Completion Design*, 1st edn. Elsevier.
- Besson, J., 1990. *Performance of Slanted and Horizontal Wells on an Anisotropic Medium*. European Petroleum Conference, 21–24 October, The Hague, Netherlands.
- Brown, K., 1980. *The Technology of Artificial Lift Methods*, Vol. 2a. Tulsa, OK: PennWell Publishing.
- Gilbert, W., 1954. Flowing and gas-lift well performance. In *Drilling and Production Practice*, American Petroleum Institute, pp. 126–157.
- Golan, M. and Whitson, C., 1986. *Well Performance*, 2nd edn. Englewood Cliffs, NJ: Prentice Hall.
- Greene, W., 1983. Analyzing the performance of gas wells. *SPE, Journal of Petroleum Technology*, **35**(7), 1378–1384.
- Guo, B., Lyons, W., and Ghalambor, A., 2007. *Petroleum Production Engineering, A computer-Assisted Approach*. Elsevier Science & Technology Books.
- Jones, L., Blount, E., and Glaze, O.H., 1976. *Use of Short Term Multiple Rate Tests to Predict Performance of Wells Having Turbulence*. SPE paper 6133, SPE 51st Annual Fall Meeting, New Orleans, LA.
- Lu, J. and Tiab, D., 2010. Pseudo-steady-state productivity formula for a partially penetrating vertical well in a box-shaped reservoir. *Mathematical Problems in Engineering*, Volume 2010, Article ID 907206.
- Mach, J., Proano, E., and Brown, K., 1979. *A Nodal Approach For Applying Systems Analysis To The Flowing And Artificial Lift Oil Or Gas Well*. SPE paper 802, Society of Petroleum Engineers.
- Serghides, T., 1984. Estimate friction factor accurately. *Chemical Engineering Journal*, **91**(5), 63–64.
- Stewart, G., 2011. *Wireline Formation Testing and Well Deliverability*. Tulsa, OK: PennWell Corporation.
- Turner, R.G., Hubbard, M.G., and Dukler, A.E., 1969. Analysis and prediction of minimum flow rate for the continuous removal of liquids from gas wells. *Journal of Petroleum Technology*, **21**(11), 1475–1482.
- Van der Waals, J. and Platteeuw, J., 1959. Clathrate solutions. *Advances in Chemical Physics*, **2**, 1–57.

# 10

## Well Production System

Petroleum production engineering belongs to the part of the reservoir management process relating to a broad range of activities required to achieve set production objectives. Production objectives can be maximizing production rate, ultimate recovery by producing wells, and revenue or profitability.

### 10.1. CONCEPT OF PETROLEUM PRODUCTION ENGINEERING

The overall production capability of a production system depends on pressure loss across the entire production system from the reservoir to surface production facilities (Fig. 10.1). A production engineer is generally involved in analysis, management, and design of production systems. Components of a production system would generally include one or more of the following: reservoir, wellbore, production conduit, wellhead, Christmas tree and flow lines.

In some firms the entire *surface production facilities* fall within the domain of production engineering but, in most cases, it is in a separate department, such as *operations, surface facilities* or *process engineering*.

Production engineering tasks broadly include:

- Achieving optimum production system performance.
- Diagnosis of production problems.
- Identifying how best to harness energy in the production system.
- Identifying potential problems in the production system.
- Recommending solutions to production problems.
- Planning and managing remedial and workover operations and resources.

### 10.2. PRODUCTION WELL

Production wells provide a means of producing and controlling reservoir fluids from the reservoir to the surface safely. Fig. 10.2 shows an example of a well with its key components. A well consists of the *downhole equipment/components* and *surface equipment/components*.

#### 10.2.1. Well Downhole Equipment

**10.2.1.1. Casings.** Though casing strings run from the surface to downhole, they are generally considered part of the downhole equipment, as most of the casing is downhole. Casing strings must be selected such that the drill string can fit comfortably through the casing. Casings are permanently cemented into the hole with a continuous and unbroken cement sheath that runs to the surface.

The *conductor casing* is the casing string usually set first, particularly on land wells, to protect the hole from caving in unconsolidated formations. They can also serve as protection against shallow gas. Conductor casings have a diameter of 16–48 inches for offshore wells and 16 inches for onshore wells. They are also called the *conductor pipe* or *drive pipe*.

The *surface casing* is the first casing string to be run during drilling. It runs from the surface attached to the wellhead. The primary function of the surface casing is to protect near surface groundwater from contamination by deeper salt water zones. Surface casings are important for environmental and legal reasons. They are run as part of regulatory requirements in oil and gas operations. Surface casing alone may be the only required casing for shallow and stable wells. Surface casings have diameter of about  $8\frac{5}{8}$ –20 inches.

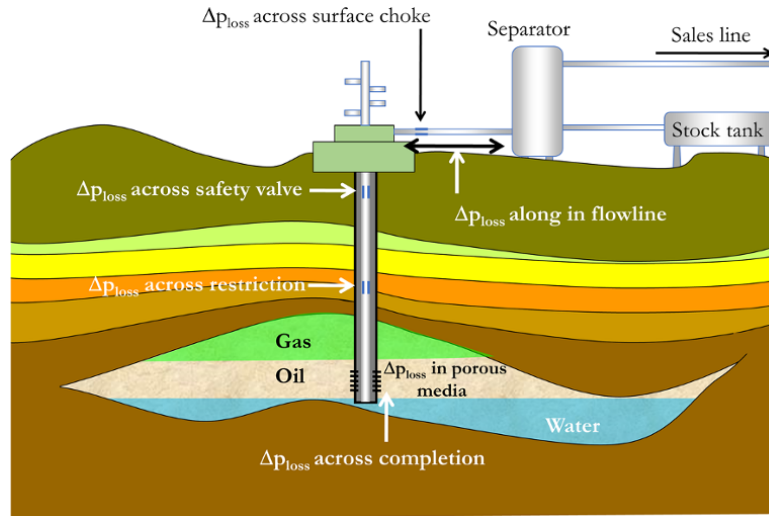


Figure 10.1 Production system.

The *intermediate casing* is run and cemented to support the hole against caving of weak or abnormally high-pressured formations. It is run after the *surface casing* and before the *production casing*. Intermediate casings have a diameter of about  $7\frac{5}{8}$ – $13\frac{3}{8}$  inches.

The *production casing* is run when there is the potential of the well becoming a production well. It is set across the reservoir interval, hence isolating production zones and containing formation pressure. Cement sheath behind the production casing ensures that different zones can be isolated and operated separately. Production casing also supports installation of important downhole completions.

Installing the production casing involves driving the casing to the bottom of the hole. Cement is then pumped through the annulus between the casing and the hole to set the production casing permanently. Production casings have diameter of about  $4\frac{1}{2}$ – $9\frac{5}{8}$  inches.

All casings protect the well from gumbo/sticky mud, which can interfere with drilling operations, due to swelling of shale when water is absorbed.

**10.2.1.2. Production Tubing.** The production tubing serves as the primary path for oil and/or gas to flow to the surface. Production tubing strings are smaller in diameter than the *production casing*. They are about 4 inches or less in diameter and are removable, unlike casings which are permanently fixed.

**10.2.1.3. Production Packer.** Production packers are expandable seals set at a depth just above the producing interval and between the production casing and production tubing string to form a seal between the outside of the tubing and the inside of the production casing. Production packers isolates the producing interval from the

casing annulus or from different producing zones along the wellbore.

**10.2.1.4. Well Perforations.** Perforation are holes made through the production casing or *liner* (a casing string that does not extend to the top of the wellbore with diameter of about  $4\frac{1}{2}$ – $9\frac{5}{8}$  inches), cement, and formation behind the production casing to provide a path for the reservoir fluid to enter the wellbore. Since the production casing is cemented within the pay zone, perforations through the casing and cement sheath and beyond a damaged formation zone must be made for fluid to flow from reservoir to wellbore.

Well perforations, which can be overbalanced (higher wellbore pressure than the formation pressure) or underbalanced (lower wellbore pressure than the formation pressure), are made using *perforation guns* with shaped-charge explosives (Fig. 10.3). When shaped charges are detonated (*shaped charge* or *jet perforator* perforation type), a high velocity jet of fluidized metal travelling at about 25,000 ft/s and a pressure of 15,000,000 psi is created; this displaces the casing and cement along its path and makes a tunnel into the formation with depth of 2–20 inches (5–50 cm). The perforated depth depends on the casing material, design of shaped charge, and formation properties. In deep reservoirs with high effective formation stress, penetration depth maybe reduced compared to shallow formation.

Detonating of charges in perforation guns can be through electrical, mechanical or pressure signals.

Fig. 10.4 shows a perforating gun with shaped charges. Perforations generally have holes of about 0.2–1 inch (0.5–2.5 cm) in diameter. Large perforation holes, for easy gravel packing, can be achieved using large shaped

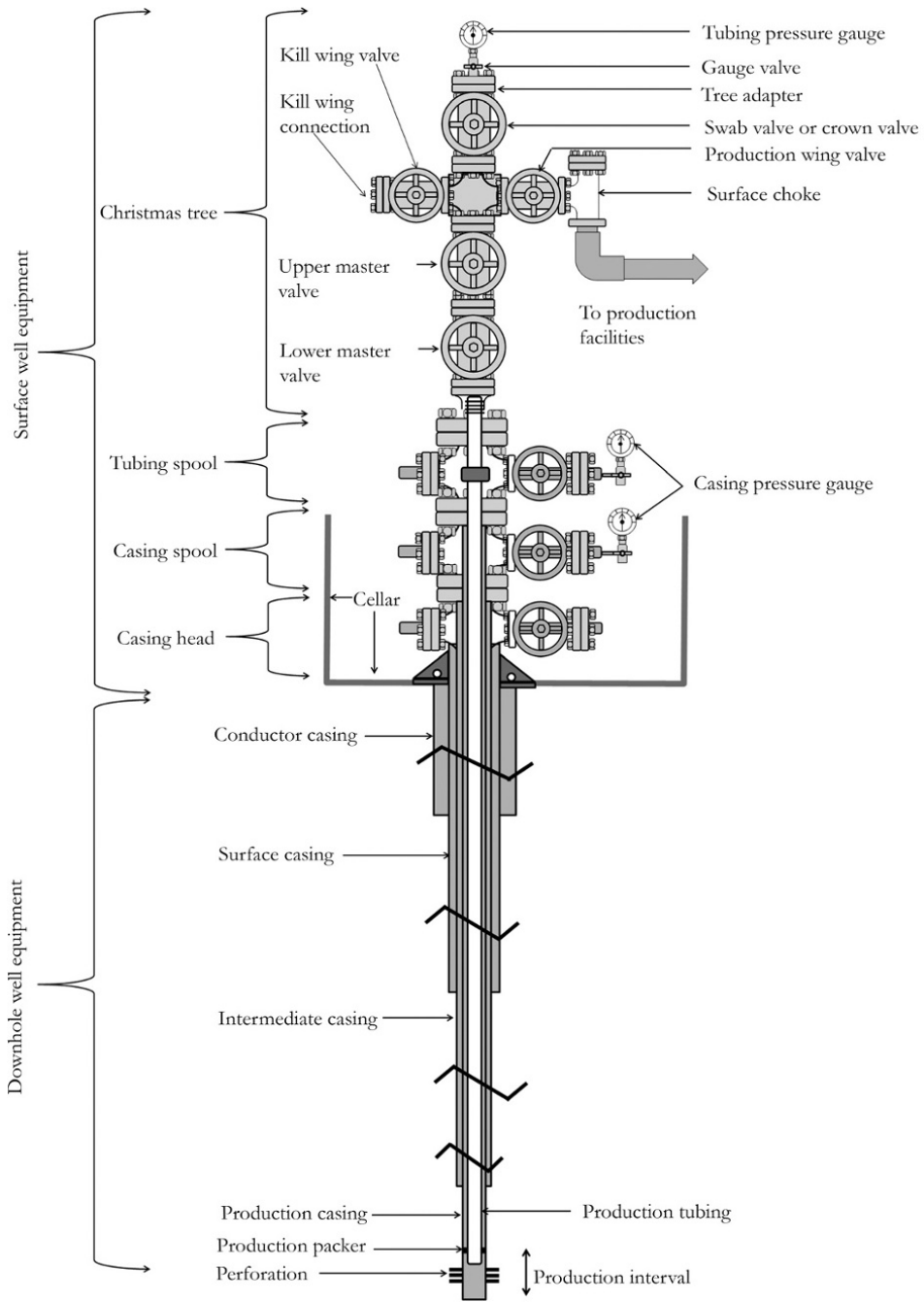


**Figure 10.2** A well with accessories.

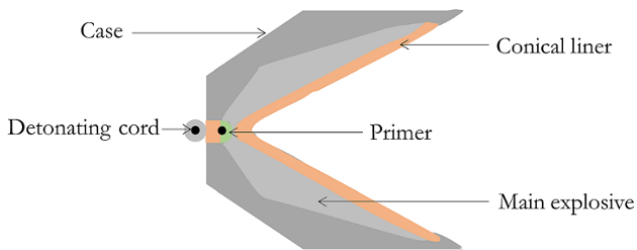


**Figure 10.3** A shaped charge.

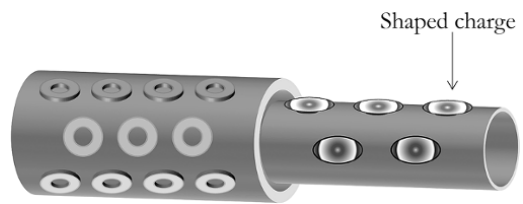


**Figure 10.4** A perforation gun with shaped charge.

charges. Deep perforations may also be preferred when trying to get behind a deep damaged zone. Hence, having a smaller and focused shaped charge becomes a desirable choice. Hole size also plays a role in charge selection. A large shaped charge can be run in large holes with a 6–7<sup>1</sup>/<sub>4</sub> inch diameter carrier while small charge will be on a small carrier, such as 1<sup>11</sup>/<sub>16</sub> inch diameter carrier. Small charges have less explosive force than larger charges during perforation. It is important that gun clearance is as small as possible to achieve deep penetration where required.

Fig. 10.5 shows a schematic of a perforation.

When small guns are run through the tubing (*through tubing guns*) for perforation of large diameter casing, to minimize clearance, the gun is set as zero-degree phasing (position alongside of casing rather than centralized) so as to create one line of deep perforation (Fig. 10.6). Zero-phasing of the gun can cause reduced flow area (limited entry along wellbore surface), subsequently causing a high skin completion skin effect in the well.

Other perforation phase angles that may be considered include: 60°, 90°, 120°, and 180° (Fig. 10.7), which will increase shot density but reduced hole diameter and penetration depth.

Cased hole perforation can be carried out in various ways which include using a:

- *Convention casing perforating gun*, which is run into the well before the completion is run (Fig. 10.8a).
- *Through-tubing perforating gun*, which is run into the well through tubing after completion has been run (Fig. 10.8b). Tubing perforation is an important technique in underbalanced perforation where the well must

be ready with tubing, packers, and the *Christmas tree* required to control flow and pressure. Underbalanced perforation is generally considered good practice where operationally possible, as this method minimizes perforation damage in the wellbore.

- *Tubing conveyed perforating gun*, which involves running the gun at the bottom of the tubing string (Fig. 10.8c). Tubing conveyance of the perforating gun can be used to push guns in highly deviated wells not easily accessible by wireline deployed guns.

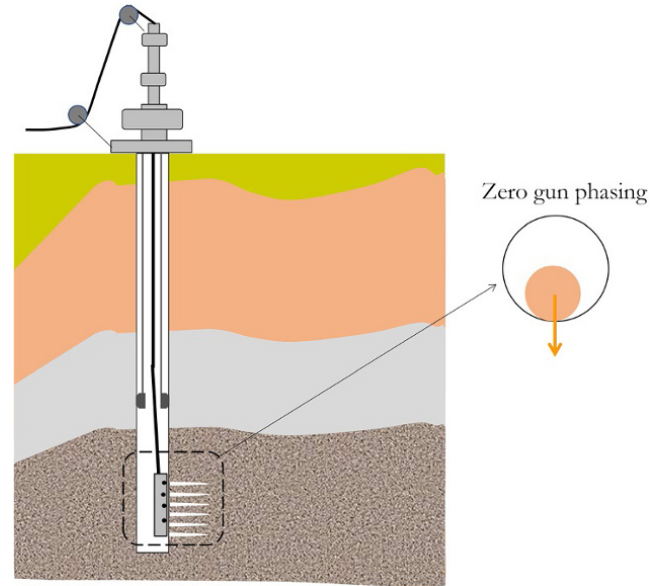


Figure 10.6 Zero gun phasing.

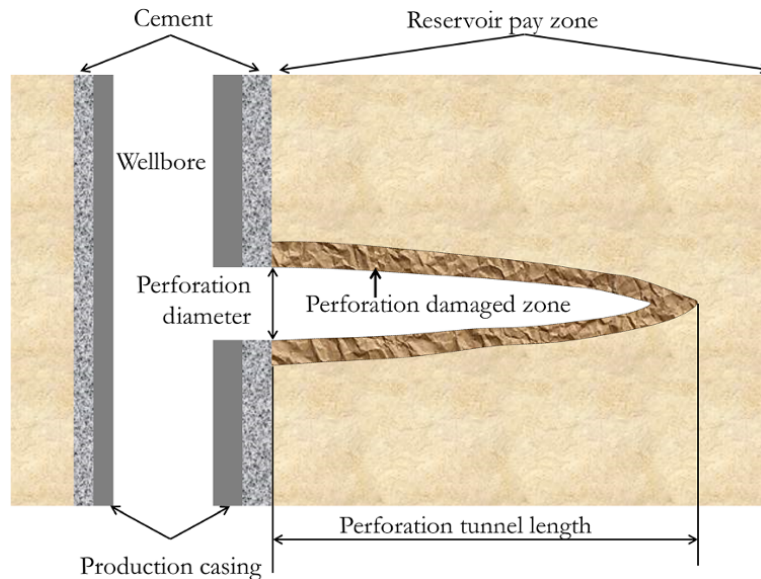


Figure 10.5 Schematic of a perforation.

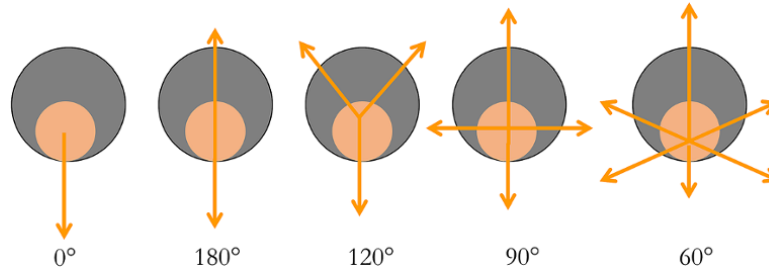


Figure 10.7 Gun phasing.

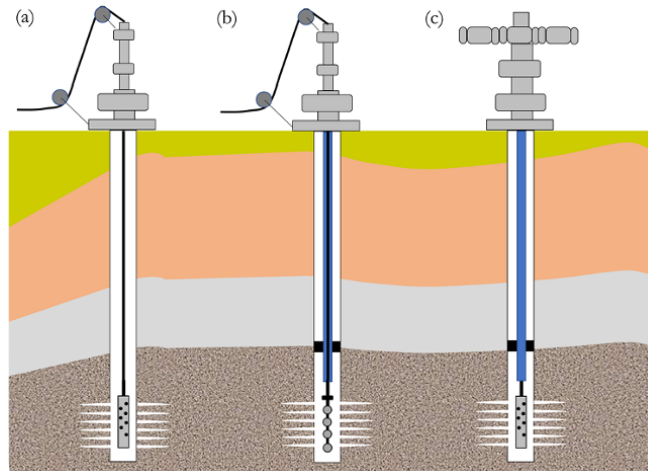


Figure 10.8 Ways of carrying out cased hole perforation: (a) conventional casing perforation; (b) through-tubing perforation; (c) tubing conveyed perforation.

Perforation characterizations based on their energy source include: *shaped charge* or *jet perforator*, which is the most common and has already been discussed in this section; *abrasive perforation*, which involves the use of abrasive-laden fluid flow to drill through casing cement and formation; *water jet perforation*, which involves use of water at pressure as high 20,000 psi to cut through casing and tunnel into the reservoir formation; *bullet gun perforation*, which is based on bullet projectiles from a perforating gun penetrating casing, cement, and formation.

### 10.2.2. Well Surface Equipment

Well surface equipment can generally be grouped as *wellhead* and *Christmas tree*. A wellhead system consist of spools, valves, and adapters that serve as the termination point of casing and tubing strings. The wellhead provides pressure control, access, and seal for tubing/casing bore and annuli at the surface. The ability to control pressure ensures drilling and well completion activities can be carried out as safely as possible. The wellhead is equipped

with facilities for installing casing hangers, production tubing hanger, and the Christmas tree.

The Christmas tree is an assembly of valves, spools, pressure gauges, chokes, and fittings connected to the wellhead to control and divert fluid from and into the well. The Christmas tree sits on the tubing head, which is part of the wellhead.

**10.2.2.1. Wellhead.** Some of the functions of the wellhead include: means of suspending tubing and casing; hydraulic isolation of different casings at the surface; injection access and pressure monitoring in casing/tubing annuli; and attaching a blowout preventer during drilling operations. Accessories/components that form the wellhead include:

- *Casing pressure gauges* that measure and monitor casing annuli pressure. It is important to measure and monitor pressure in all accessible annuli and ensure pressure is maintained within minimum and maximum acceptable operational limits. Where excessive casing pressure in wells persistently rebuilds after bleed-down (*sustained casing pressure*), the integrity of the well can be compromised. *Sustained casing pressure* may be caused by



migration of gas into annuli from a high pressured formation through a leaking cement sheath, leaking tubing connections and accessories, and leaking wellhead seals. When the pressure of trapped gas in the annuli increases due to increased temperature from flowing reservoir fluid in the tubing rather than fluid flow from the formation, the pressure should not increase considerably after bleeding. If, after bleeding, pressure still builds up, proper diagnosis and intervention should be carried out to prevent compromising well integrity.

- *Casing valves* are valves that provide access to the annulus of nonproducing casing strings.

- *The tubing head spool* is equipment attached to the topmost casing head or smallest casing string; it serves the functions of suspending the tubing and sealing the annular space between the tubing and casing.

- *The casing head spool* is equipment attached to a casing head with the functions of suspending and sealing a secondary casing string.

- *Cellar* is a dug-out area around the wellhead providing a cavity in which the casing spool and casing head reside. Cellars have depths that would ensure that the master valve, routinely used, is easily accessible from ground level. The cellar also provides a cavity for the lower part of the blow out preventer (BOP) stack, thus reducing the rig height necessary to clear the BOP stack on the top.

**10.2.2.2. Christmas Trees.** The Christmas tree is also equipped with facilities required for safe access for well intervention operations using slickline, wireline, or coiled tubing. Accessories/components of the Christmas tree include:

- *Tubing pressure gauge*, which is used for measuring and monitoring flowing tubing head pressure during production.

- *Swab valve* or *crown valve*, which is the uppermost valve on a Christmas tree, above the flowline outlet, which provides access to the wellbore from the top of the Christmas tree.

- *Production wing valve*, which is a wing valve used for controlling and isolating production. The production wing valve provides the flow path for the reservoir to the production facilities.

- *Kill wing valve*, which is fitted on the opposite side of the production wing valve and provides access for fluid injection for treatment or well-control purposes.

- *Wellhead choke*, which is a device for controlling the surface pressure and production rate from a well by changing the back pressure imposed on the well. Chokes are selected to ensure critical flow, a condition under which flow rate is a function of upstream pressure and does not depend on downstream pressure. Chokes may be fixed or adjustable in their opening. A variable flow choke valve

is typically a very large needle valve. Its opening is graduated and adjustable in 64ths of an inch ( $1/64$ ) increments called *beans*.

- A *fixed choke* has fixed hole size often called a *bean*. A bean is a replaceable short flow tube/insert made of hardened steel with precise diameter hole. They are graduated in 64ths of an inch with typical values of 8–20 (in 64ths) for wells with low to moderate gas rates and setting greater than 20 for liquid and high gas rate wells. A 48-choke or 48-bean choke diameter would be 48/64 in (3/4 in).

- *Upper master valve*, which lies in the flow path of the fluid from the reservoir. It is often actuated hydraulically and used routinely to control the flow of fluid from the wellbore.

- *Lower master valve*, which also lies in the flow path of fluid from the reservoir and serves as a backup for the master valve and is normally operated manually.

Christmas trees, mounted on wellheads, in offshore developments can be on the surface production deck (*dry tree system/completion*) where they are readily accessible for operations and maintenance. Although the surface dry tree system/completion increases the load on the production deck, it provides easy access to the well for intervention. In deep water development, where platform installation is expensive and production is through floating facilities, a *subsea tree* can be mounted on a *subsea wellhead* on the sea bed (*wet tree system/completion*). In wet tree completion, more than one subsea tree can be connected to a *subsea manifold* through *jumper*s. Comingled fluid at the manifold can then be sent to a *subsea boosting pump station* to provide energy for the produced fluid to flow through the *pipeline end termination* (PLET), flow lines, and, finally, through risers to the production deck of a floating facility.

### 10.3. WELL COMPLETION

After careful interpretation of well data (core, logs, well test, etc.), a decision must be made whether to set the production casing and complete the well or to plug and abandon it. The decision to abandon a well will be made when the well is not capable of producing oil or gas in commercial quantities. Sometimes, wells plugged and abandoned in the past may be re-entered and opened if the price of oil or gas has become more favorable.

Well completion involves a series of activities to prepare the oil well or gas well such that the well flows in a controlled manner. Important parts of well completion include: installing casings; installing tubing; connecting the wellbore with the pay zone; sand control using screens and gravel packing; and equipping the well to allow control of fluid flow.

Many factors affect selection of well completion type, ranging from production philosophy, economics, optimizing production, and regulatory constraints.

**10.3.1. Lower Completion**

*Lower completion* refers to the well completion configuration below the packer, along the production or injection zone.

**10.3.1.1. Openhole Completion.** Openhole completion involves keeping the zone of interest, within the producing formation interval, without casing or liners. In this type of completion, the production casing is set above the zone of interests (Fig. 10.9).

**10.3.1.2. Liner Completions.** A liner, which can be *slotted liner*, *screen liner* or *perforated liner*, is a casing type that does not extend to the top of the wellbore surface (Fig. 10.10). The production casing is often set above the producing zone, and an uncemented slotted or screen liner assembly is installed across the pay zone. Slotted or screen liner assembly are types of *openhole sand control* methods.

Screen liners can be installed as *stand-alone screens* or with *openhole gravel pack* where sand gravel packing is placed in annulus between the openhole and the screen (Fig. 10.11).

In the case of *perforated liner completion*, a liner assembly is installed across the pay zone and cemented in place. The liner is then perforated selectively for production (Fig. 10.12).

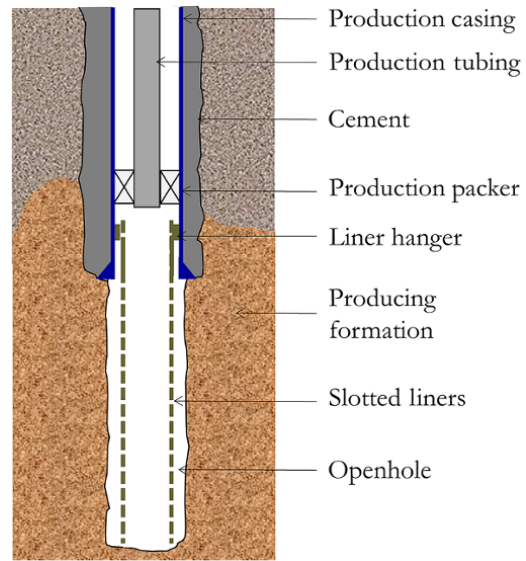


**Figure 10.10** Slotted liner completion.

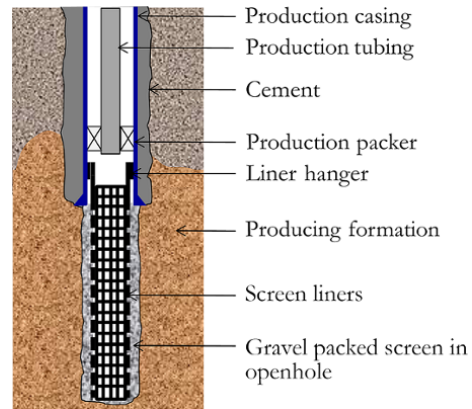


**Figure 10.11** Screen liners with openhole gravel pack.

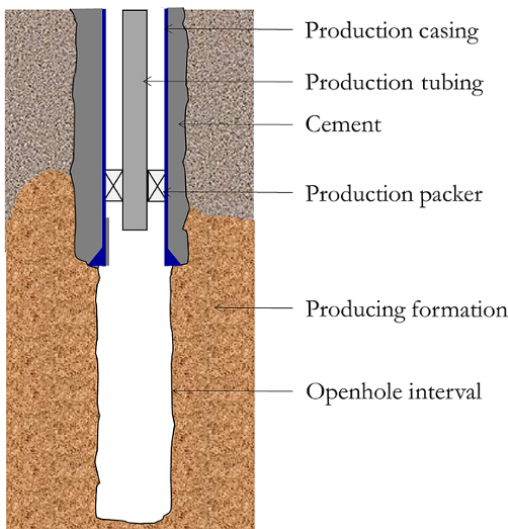


**Figure 10.9** Openhole completion.

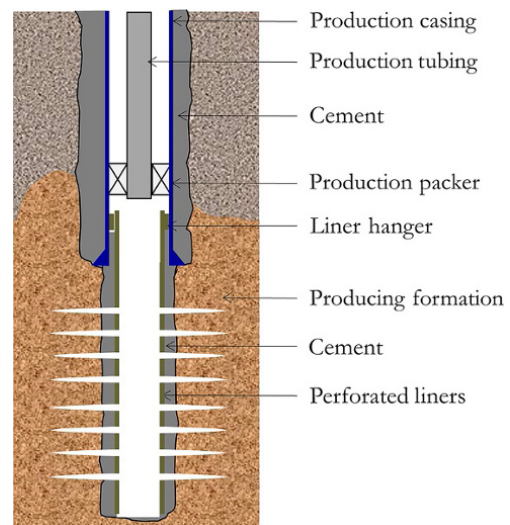


**Figure 10.12** Perforated liner completion.

**10.3.1.3. Perforated Casing Completions.** In perforated casing completion, the production casing is cemented through the producing zone and the zone of interest within the pay section is selectively perforated (Fig. 10.13).

**10.3.1.4. Tubingless or Reduced Diameter Completions.** In tubingless or reduced diameter completions, production tubing or reduced casing diameter is cemented through the producing zone, and the zone of interest within the pay section is perforated along the reduced casing diameter or production tubing for production (Fig. 10.14).

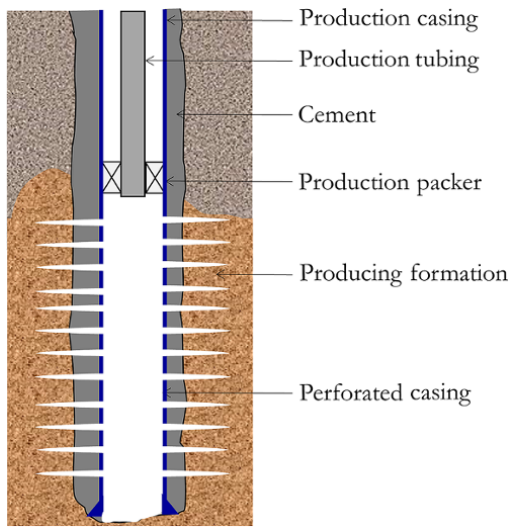


Figure 10.13 Perforated casing completion.

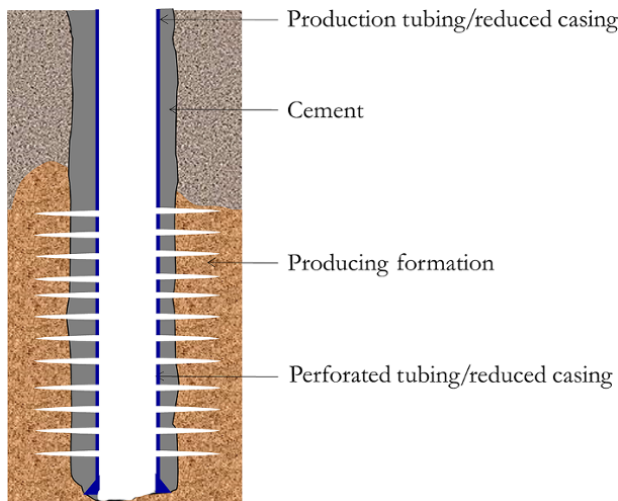


Figure 10.14 Tubingless or reduced diameter completions.

**10.3.1.5. Perforation Skin Effect.** The effectiveness of a well perforation or stimulation can be quantified using the skin effect.

Chapter 8 (8.5.1) discusses how different well conditions can be related to skin affect and typical values of skin effect. The most reliable way to determine the effectiveness of any well perforation is to acquire well test data at a controlled and measured rate then analyze the acquired data as discussed in Chapter 8. It is important to be able to predict effectiveness of perforation prior to a well test or when a well test is not possible. One of the most common and robust methods for predicting effectiveness of perforation, other than the use of well testing, is a method proposed by Karakas and Tariq [1991]. This method enables calculation of perforation skin and total skin (effect of perforation and wellbore damage) for the case where the perforation tunnels are within the damaged zone and when perforation tunnels are beyond the damaged zone. A good well perforation should have perforation tunnels beyond the damaged zone.

*Perforation Within Damaged Zone*

The combined skin effect due to well damage and perforation is important, as this controls the deliverability of the well rather than perforation alone. When a perforation tunnel is within the damaged zone, the combined skin effect due to perforation and wellbore damage is expressed as [Karakas and Tariq, 1991]:

$$s_{dp} = \left(\frac{k}{k_d} - 1\right) \ln\left(\frac{r_d}{r_w}\right) + \left(\frac{k}{k_d}\right) (s_p + s_\chi) \quad (10.1)$$

where the perforation skin is expressed as:

$$s_p = s_h + s_{wb} + s_v + s_c \quad (10.2)$$

where  $s_\chi$  is a correction for boundary effect and can be ignored,  $s_h$  is the skin effect due to phase effect (horizontal flow),  $s_{wb}$  is the skin effect due to wellbore effect (dominant in zero-degree phasing), and  $s_v$  is the skin effect due to vertical flow convergence like partial penetration effect at different perforation.

The different skin effect component in equation (10.2) are defined as:

- Phase (Horizontal) Skin Effect

$$s_h = \ln\left(\frac{r_w}{r_e(\theta)}\right) \quad (10.3)$$

$r_e(\theta)$  is effective wellbore radius as function of phase angle ( $\theta$ ) and perforation tunnel length and defined as:

$$r_e(\theta) = \begin{cases} 0.25l_p & \theta = 0 \\ \alpha(l_p + r_w) & \theta \neq 0 \end{cases} \quad (10.4)$$

where  $\alpha$ , which is a function of  $\theta$ , is defined in Table 10.1 and  $l_p$  is the perforation length (in).

• *Wellbore Skin Effect*

$$s_{wb} = C_1 \exp(C_2 r_{wD}) \quad (10.5)$$

$C_1$  and  $C_2$ , which are functions of  $\theta$ , are defined in Table 10.1 and  $r_{wD}$  is the dimensionless well radius defined as:

$$r_{wD} = \frac{r_w}{(l_p + r_w)} \quad (10.6)$$

$r_w$  is the openhole wellbore radius (in).

• *Vertical Convergence Skin Effect*

This effect is like partial penetration at different perforation and defined as:

$$s_v = 10^a h_D^{b-1} r_{pD}^b \quad (10.7)$$

where

$$a = a_1 \log_{10}(r_{pD}) + a_2$$

$$b = b_1 r_{pD} + b_2$$

$a_1$ ,  $a_2$ ,  $b_1$ , and  $b_2$  as functions of  $\theta$  are defined in Table 10.1;  $h_D$  is the dimensionless perforation height expressed as:

$$h_D = \frac{h_p}{l_p} \sqrt{\frac{k_{xy}}{k_z}} \quad (10.8)$$

and  $r_{pD}$  is the dimensionless perforation radius expressed as:

$$r_{pD} = \frac{r_p}{2h_p} \left( 1 + \sqrt{\frac{k_z}{k_{xy}}} \right) \quad (10.9)$$

$h_p$  is perforation spacing

$$h_p = \frac{12}{SPF} \text{ (in)}$$

SPF is the perforation density in shot per foot.

• *Crushed Zone Skin Effect*

$$s_c = \frac{h_p}{l_p} \left( \frac{k}{k_c} - 1 \right) \ln \left( \frac{r_c}{r_p} \right) \quad (10.10)$$

$\theta$  is the phasing angle between perforation tunnel (degrees),  $l_p$  is the perforation length (in),  $r_p$  is the

perforation radius assuming constant perforation hole size (in),  $r_c$  is the radius of the crushed zone around perforation,  $k_c$  is the crushed zone permeability in mD,  $r_d$  is the radius of damaged zone around wellbore, and  $k$  is the formation permeability mD.

$\frac{k_z}{k_{xy}}$  is the ratio of the vertical to horizontal permeability (permeability anisotropy).

A schematic of well perforation with well perforation parameters is shown in Fig. 10.15.

*Perforation Beyond Damaged Zone*

The combined skin effect due to well damage and perforation when perforation tunnels are beyond the damaged zone is expressed as [Karakas and Tariq, 1991]:

$$s_{dp} = s'_h + s'_{wb} + s'_v + s'_c \quad (10.11)$$

The different skin effect components in equation (10.11) are defined as:

• *Phase (Horizontal) Skin Effect*

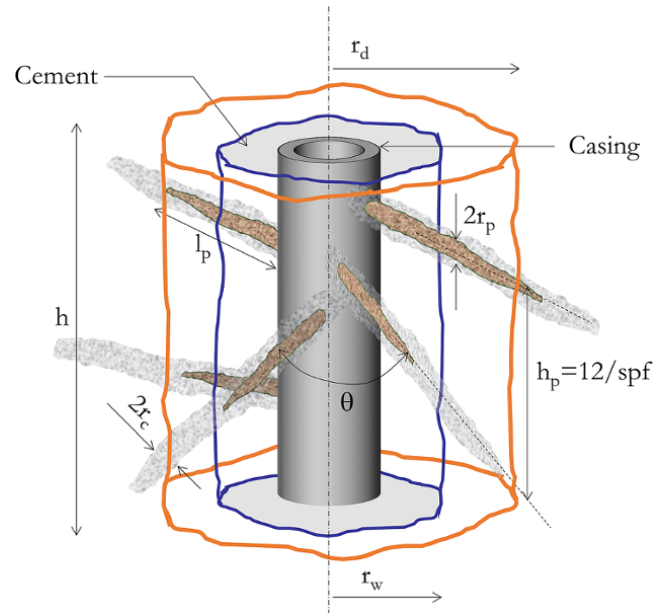


**Figure 10.15** Schematic of well perforation with well perforation parameters.

**Table 10.1** Karakas and Tariq Perforation Model Parameters [Adapted from Karakas and Tariq, 1991].

Perforation phasing (°)	$\alpha(\theta)$	$C_1$	$C_2$	$a_1$	$a_2$	$b_1$	$b_2$
0 (360)	NA	$1.6 \times 10.1$	2.675	-2.091	0.0453	5.313	1.8672
180	0.500	$2.6 \times 10.2$	4.532	-2.025	0.0943	0.0373	1.8115
120	0.648	$6.6 \times 10.3$	5.320	-2.018	0.0634	1.6163	1.7770
90	0.726	$1.9 \times 10.3$	6.155	-1.905	0.1038	1.5674	1.6935
60	0.813	$3.0 \times 10.4$	7.509	-1.898	0.1023	1.3654	1.6490
45	0.860	$4.6 \times 10.5$	8.791	-1.788	0.2398	1.1915	1.6392

$$s'_h = \ln\left(\frac{r_w}{r'_e(\theta)}\right) \quad (10.12)$$

where

$$r'_e(\theta) = \begin{cases} 0.25l'_p & \theta = 0 \\ \alpha(l'_p + r'_w) & \theta \neq 0 \end{cases} \quad (10.13)$$

where

$l'_p$  and  $r'_w$  are transforms of the perforation length and wellbore radius for the case with perforation beyond the damaged zone and defined as:

$$l'_p = l_p - \left(1 - \frac{k_d}{k}\right) l_d$$

$$r'_w = r_w + \left(1 - \frac{k_d}{k}\right) l_d$$

$l_d$  is the depth of the damaged zone expressed as:

$$l_d = r_D - r_w$$

- Wellbore Skin Effect

$$s'_{wb} = C_1 \exp(C_2 r'_{wD}) \quad (10.14)$$

where

$$r'_{wD} = \frac{r'_w}{(l'_p + r'_w)}$$

- Vertical Convergence Skin Effect

$$s'_v = 10^a h_D'^{b-1} r_{pD}^b \quad (10.15)$$

where

$$h'_D = \frac{h_p}{l'_p} \sqrt{\frac{k_{xy}}{k_z}}$$

- Crushed Zone Skin Effect

$$s'_c = \frac{h_p}{l'_p} \left(\frac{k}{k_c} - 1\right) \ln\left(\frac{r_c}{r_p}\right) \quad (10.16)$$

**Exercise 10.1** Total Skin Effect in a Perforated Well

Determine the total skin effect for a 2 SPF perforated well with borehole radius of 0.354 ft and radius of damaged zone around wellbore due to filtrate invasion of 6 in. Perforation tunnels have an average radius of 0.25 in, length of about 10 in, crushed zone radius of 0.75 in, and perforation phasing of 60°. The formation can be considered as having  $\frac{k_z}{k_{xy}} = 0.5$ ,  $\frac{k_c}{k} = 0.6$ , and  $\frac{k_d}{k} = 0.55$ .

**Solution.**

Since the perforation is beyond the damaged zone, equation (10.11) is used:

$$r_w = 0.354 \text{ ft} = 0.354 \times 12 \text{ in} = 4.248 \text{ in}$$

$$h_p = \frac{12}{\text{SPF}} \text{ in} = 6 \text{ in}$$

$$r_p = 0.25 \text{ in}$$

$$l_p = 10 \text{ in}$$

$$r_d = 6 \text{ in}$$

$$r_c = 0.75 \text{ in}$$

Calculating  $l_d$ :

$$l_d = r_D - r_w = l_d = 6 - 4.248 = 1.752 \text{ in}$$

Calculating  $l'_p$  and  $r'_w$ :

$$l'_p = l_p - \left(1 - \frac{k_d}{k}\right) l_d = l'_p = 10 - (1 - 0.55) \times 1.752 = 9.2116$$

$$r'_w = r_w + \left(1 - \frac{k_d}{k}\right) l_d = r'_w = 4.248 + (1 - 0.55) \times 1.752 = 5.0364$$

Calculating  $r'_{wD}$ :

$$r'_{wD} = \frac{r'_w}{(l'_p + r'_w)} = r'_{wD} = \frac{5.0364}{(9.2116 + 5.0364)} = 0.35348$$

Calculating  $r'_e(\theta)$ :

From equation (10.13)

$\alpha = 0.81$  for 60° phase from Table 10.1

$$r'_e(\theta) = \alpha(l'_p + r'_w) = r'_e(\theta) = 0.831(9.2116 + 5.0364) = 11.583624$$

Calculating  $s'_h$ :

From equation (10.12)

$$s'_h = \ln\left(\frac{r_w}{r'_e(\theta)}\right) = \ln\left(\frac{4.248}{11.583624}\right) = -1.003$$

Calculating  $s'_{wb}$ :

$C_1 = 3.00E-04$  and  $C_2 = 7.509$  for 60° phase from Table 10.1

From equation (10.14):

$$s'_{wb} = C_1 \exp(C_2 r'_{wD}) = 3 \times 10^{-4} \exp(7.509 \times 0.3535) = 0.0043$$

Calculating  $s'_v$ :

$$h'_D = \frac{h_p}{l'_p} \sqrt{\frac{k_{xy}}{k_z}} = \frac{6}{9.2116} \sqrt{\frac{1}{0.5}} = 1.3027$$

$$r_{pD} = \frac{r_p}{2h_p} \left(1 + \sqrt{\frac{k_z}{k_{xy}}}\right) = \frac{0.25}{2 \times 6} (1 + \sqrt{0.5}) = 0.03125$$

$$a_1 = -1.898; a_2 = 0.1023$$

$$a = a_1 \log_{10}(r_{pD}) + a_2 = -1.898 \times \log_{10}(0.03125) + 0.1023 = 2.959074659$$

$$b_1 = 1.3654 \text{ and } b_2 = 1.649$$

$$b = b_1 r_{pD} + b_2$$

$$b = 1.3654 \times 0.03125 + 1.649 = 1.69166875$$

From equation (10.15):

$$s'_v = 10^a h_D^{b-1} r_{pD}^b$$

$$= 10^{2.959075} 1.3027^{1.69167-1} 0.03125^{1.69167} = 3.107$$

Calculating  $s'_c$ :

From equation (10.16)

$$s'_c = \frac{h_p}{l_p} \left( \frac{k}{k_c} - 1 \right) \ln \left( \frac{r_c}{r_p} \right) = \frac{6}{9.2116} \left( \frac{1}{0.6} - 1 \right) \ln \left( \frac{0.75}{0.25} \right) = 0.477$$

Calculating  $s_{dp}$ :

From equation (10.11)

$$s_{dp} = s'_h + s'_{wb} + s'_v + s'_c = -1.003 + 0.0043 + 3.107 + 0.477$$

$$s_{dp} = 2.58$$

**Exercise 10.2** Perforation Total Skin Effect Sensitivity

Using the parameters in Exercise 10.2 as the base case:

1. Carry out total skin effect sensitivity analysis to perforation length, with perforation length between 6 and 20 in.
2. Carry out total skin effect sensitivity analysis to perforation density (SPF), using SPF between 1 and 12.

**Solution.**

1. Repeat the calculation in Exercise 10.2 by changing values of  $l_p$  within a range of 6 and 20 in (Table 10.2) and plot  $s_{dp}$  against  $l_p$  (Fig. 10.16).
2. Repeat the calculation in Exercise 10.2 by changing the values of SPF to within the range of 1 and 12 in (Table 10.3) and plot  $s_{dp}$  against SPF (Fig. 10.17).

**10.3.2. Tubing Completion**

Tubing completion defines the configuration of production tubing to develop the production zone. Fig. 10.18 is

**Table 10.2** Total Skin Effect for Different Perforation Lengths.

$l_p$ (in)	$s_{dp}$
6	4.79
8	3.44
10	2.58
12	1.97
14	1.51
16	1.13
18	0.82
20	0.56

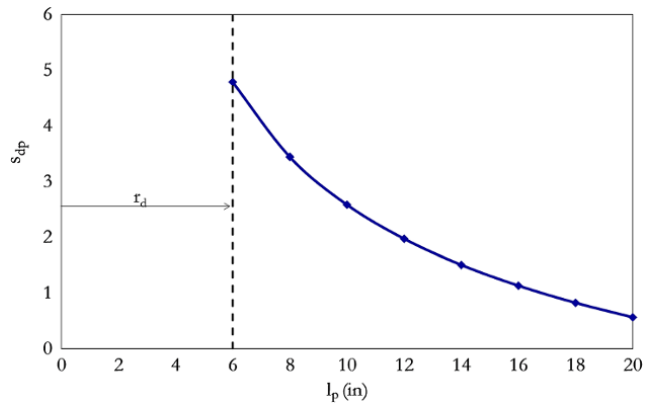


**Figure 10.16** Total skin effect sensitivity analysis to perforation length.

**Table 10.3** Total Skin Effect for Different SPF.

SPF	$h_p$ (in)	$s_{dp}$
1	12	6.15
2	6	2.58
3	4	1.34
4	3	0.69
5	2.4	0.30
6	2	0.04
8	1.5	-0.29
10	1.2	-0.48
12	1	-0.61

an example of a tubing completion showing the important components.

**10.3.2.1. Single String Sequential Completions.** This is the simplest way of completing the well. This configuration involves a single producing zone using single tubing (Fig. 10.19).

**10.3.2.2. Single String Commingled Completions.** This kind of tubing completion involves producing multiple reservoir zones through a single tubing string

(Fig. 10.20). Multiple reservoir zones for commingled completion must be assessed to ensure that overall deliverability of multiple zones is greater than individual zones and that the potential effect of cross-flow from the multiple zones does not affect well deliverability.

**10.3.2.3. Single String Selective Zone Completion.**

This kind of tubing completion allows selective production, injection, testing, stimulation, and isolation of various zones.

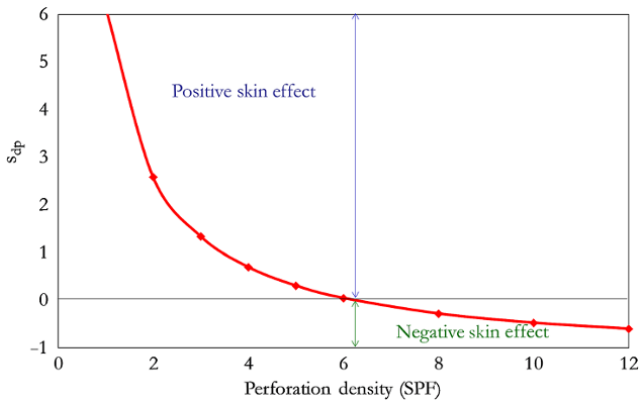


**Figure 10.17** Total skin effect sensitivity analysis to perforation density (SPF).

Selectivity after completion is accomplished by opening and closing sliding sleeves between the packers.

**10.3.2.4. Dual Completion.** This is a variant of *multiple completion* that involves producing two or more zones simultaneously through two production conduits, which

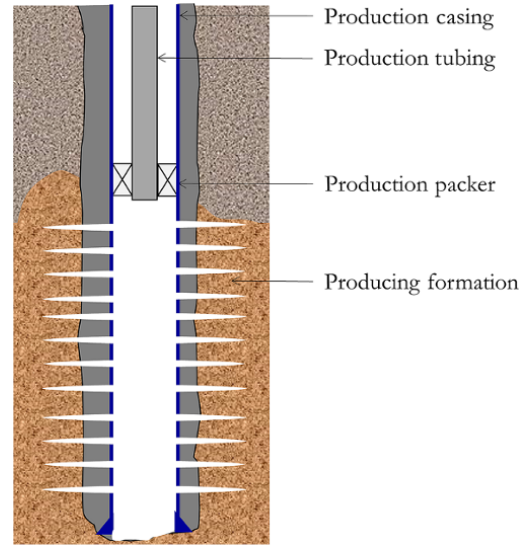


**Figure 10.19** Single string sequential completions.

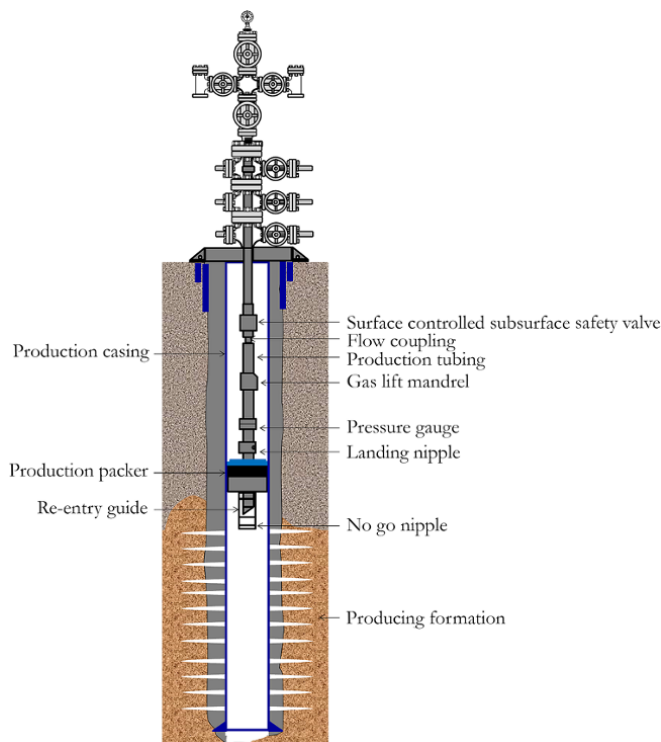


**Figure 10.18** Tubing completion.

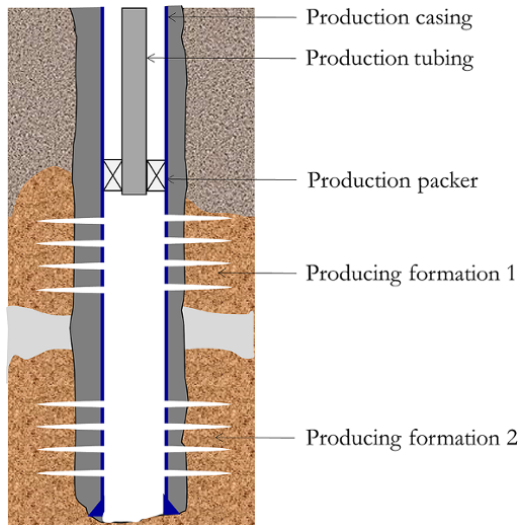


**Figure 10.20** Single string commingled completions.

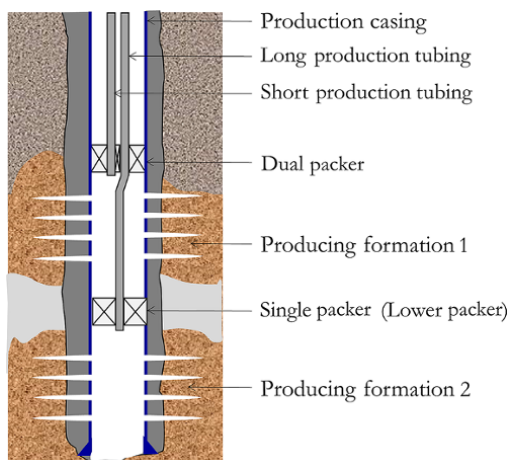


**Figure 10.21** Dual completion using two production tubing strings.

can be two tubing strings (Fig. 10.21) or one tubing and one tubing–casing annulus. Producing multiple zones through two production conduits ensures that flow from multiple zones can be controlled. Dual completion can also help in eliminating the back-pressure effect from one formation on the other, which can lead to severe reduction in overall deliverability in situations where there is productivity contrast between layers.

Another variant of multiple completion is *triple completion*, where three production conduits are used to produce three or more producing zones.

**10.3.2.5. Horizontal Well Completion.** Horizontal wells can be used to produce single or multiple

compartments. Fig. 10.22 shows an example of a horizontal well completion used for producing multiple horizontal compartments. The sliding sleeves can be used to isolate producing zones for production optimization.

**10.3.2.6. Multilateral Well Completion.** This may be considered as variant of horizontal well completion with multiple lateral branches drilled from a single hole (Fig. 10.23). These multiple branches are used to isolate and produce reservoir fluid from different vertical and horizontal sections through a combination of packers and sleeves. Multilateral well completions have been used to improve productivity from closely spaced producing zones.

### 10.3.3. Well Stimulation Treatment

Damage near to the wellbore region due to fluid invasion and fine migration can reduce the deliverability of a well and reservoir. Low permeability in the reservoir can also be the source of reduced well and reservoir deliverability. In situations where fluid cannot flow easily into the well due to wellbore damage or low reservoir permeability, *well stimulation* (improving permeability within as specific region around the wellbore or reducing the *skin effect*) may help in improving deliverability. In low permeability or vugular formation, the objective of well stimulation is to improve pore space interconnectivity as deep into the formation from the wellbore as possible. In damaged wells, the objective will be dissolution, to remove or bypass impediments created by damage. Common well stimulation techniques include: acidizing, propped hydraulic fracturing, and frac packing.

**10.3.3.1. Acidizing.** This involves pumping acid down the well, through the production conduit and perforation to contact a formation that is composed of rocks that can be dissolved by acid, thereby creating a flow path in the rock matrix for fluid flow. Formation damage around the wellbore caused by filtrate invasion can be a good candidate for acidizing. Acid can be injected at bottomhole pressure, below *formation integrity pressure*. As such, the acid only acts by dissolving rock matrix or fine blocking pore throats (*matrix acidizing*). Acid can also be injection at a bottomhole pressure greater than formation integrity pressure, not to only dissolve matrix minerals but to also induce fractures (*acid fracturing*). A high volume of acid pumped at high pressure during acid fracturing will create flow channels on the surface of the fracture, subsequently improving well deliverability considerably, even when fractures close during flow back or formation depletion. Acids commonly used for acidizing include:



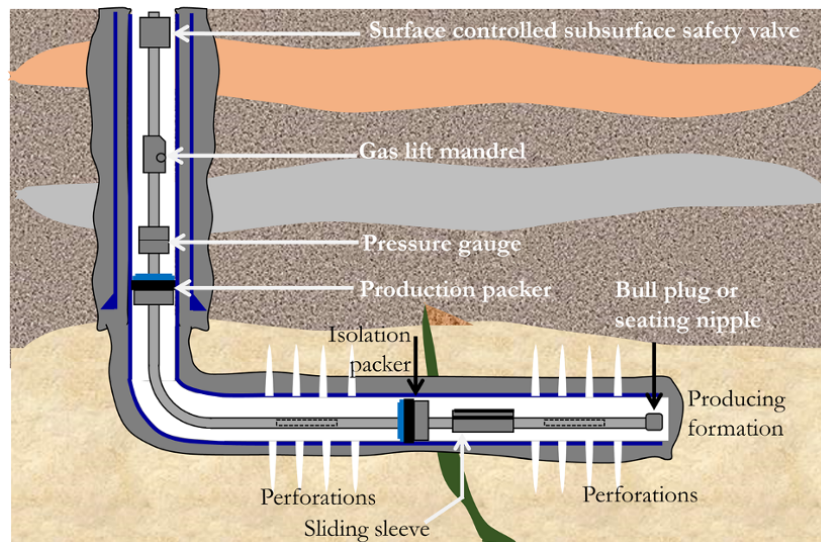


Figure 10.22 Horizontal well completion for producing two compartments.

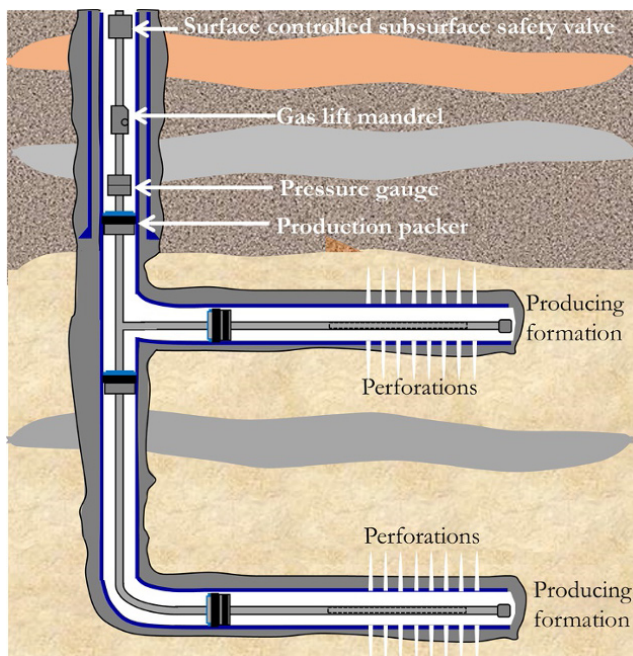


Figure 10.23 Multilateral well completion.

- *Hydrochloric acid (HCl)*, which is most widely used in a concentration of about 15% (typical range 7.5–28%). HCl will dissolve calcium carbonate ( $\text{CaCO}_3$ ), dolomite ( $\text{CaMg}(\text{CO}_3)_2$ ), siderite ( $\text{FeCO}_3$ ), and iron oxide ( $\text{Fe}_2\text{O}_3$ ).

- *Mud acid*, which is a mixture of HCl and HF (hydrofluoric acid) in concentrations of 12% and 3%, respectively, can be used to dissolve clay minerals, silicates, feldspars, and quartz. Mud acid dissolves formation minerals and other components of drilling mud.

- *Organic acids*, such as acetic and formic acids, are also used for well stimulation. Though they have lower reaction rates than HCl and mud acid, in high temperature wells and wells with high corrosion rates they are preferable to minimize tubing corrosion rates.

- *Carboxylic acid*, such as EDTA (ethylenediaminetetraacetic acid), can be used to dissolve carbonates and sulfates. Carboxylic acids are also used for scale removal.

**10.3.3.2. Propped Hydraulic Fracturing.** The process involves injection of fluid at high rate with enough pressure to cause mechanical failure of the formation. To prevent closure of the fracture, they are propped open using proppants of sand or aluminum pellets; these are mixed with the fracturing fluid. When the fracturing fluid flows back into the wellbore, the proppants are held back within the fractures due to pressure reduction during flow-back, hence keeping the fracture opened. Propped fractures increase the flow area around the wellbore, hereby increasing well deliverability.

**10.3.3.3. Frac Packing.** This process involves concurrent hydraulic fracturing and filling of the gravel pack in a casing–screen annulus. The fracturing is achieved using high viscous fluid pumped at a pressure greater than the formation fracturing pressure to induce hydraulic fracture. Frac packing combines well deliverability improvement (through hydraulic fractures) and sand control (through the gravel pack).

## 10.4. TUBING PERFORMANCE RELATIONSHIP (TPR)

Tubings generally serve as the primary conduit for oil and gas production and play a significant role in overall deliverability of the production system. TPRs are mathematical models and correlations that define the relationship between reservoir fluid produced out of a well ( $q_{out}$ ), tubing head pressure ( $p_{thp}$ ), and the bottomhole flowing pressure ( $p_{wf}$ ). TPRs are calculated from the flowing tubing pressure gradient.

### 10.4.1. Flowing Tubing Pressure Gradient

The pressure loss required to deliver reservoir fluid to the surface at a given rate can be determined from the *total flowing fluid gradient* of the fluid flowing through the tubing. Total flowing fluid gradient in well tubing comprises the *hydrostatic pressure gradient*, *frictional pressure gradient*, and *acceleration pressure gradient*. The total gradient of fluid flowing through tubing at steady state  $\left(\frac{dp}{dL}\right)$  can be expressed as:

$$\frac{dp}{dL} = \left(\frac{dp}{dL}\right)_{\text{Hydrostatic}} + \left(\frac{dp}{dL}\right)_{\text{friction}} + \left(\frac{dp}{dL}\right)_{\text{acceleration}} \quad (10.17)$$

#### *Hydrostatic (Elevation) Pressure Gradient Loss*

This is the pressure gradient due to the change in potential/elevation and is a function of fluid density and well orientation. Hydrostatic pressure gradient can be expressed as:

$$\left(\frac{dp}{dL}\right)_{\text{Hydrostatic}} = \left(\frac{g}{g_c}\right) \rho \sin\theta \quad (10.18)$$

where  $\theta$  is the angle of inclination of the tubing – which is considered positive for vertical upward flow and negative for downward flow; hydrostatic gradient loss is zero for horizontal flow –  $\rho$  is the density of the fluid;  $g$  is the acceleration due to gravity; and  $g_c$  is the gravitational constant

#### *Frictional Pressure Gradient Loss*

This a function of fluid density and flowing conditions of the fluid. It can be expressed as:

$$\left(\frac{dp}{dL}\right)_{\text{friction}} = \frac{f \rho v^2}{2g_c d} \quad (10.19)$$

where  $v$  is the velocity of the fluid flowing through tubing,  $f$  is the friction factor,  $d$  is the internal diameter of the tubing.

This component is characterized by pressure loss in the direction of flow regardless of flow direction.

#### *Acceleration Pressure (Kinetic Energy) Gradient Loss*

This is pressure loss associated with a steady state pattern of natural convection and always negligible for TPR calculation. It is expressed as:

$$\left(\frac{dp}{dL}\right)_{\text{acceleration}} = \rho \frac{v dv}{g_c (dL)} \quad (10.20)$$

Substituting equations (10.18), (10.19), and (10.20) into equation (10.17):

$$\begin{aligned} \frac{dp}{dL} &= \left(\frac{g}{g_c}\right) \rho \sin\theta + \frac{f \rho v^2}{2g_c d} + \rho \frac{v dv}{g_c (dL)} \text{ in consistent units} \\ 144 \frac{dp}{dL} &= \left(\frac{g}{g_c}\right) \rho \sin\theta + \frac{f \rho v^2}{2g_c d} + \rho \frac{v dv}{g_c (dL)} \text{ in EOF units} \end{aligned} \quad (10.21)$$

Equation (10.21) can be applied easily and directly for single-phase fluid flow. However, for petroleum engineering, the interest is multiphase flow, which is a typical characteristic of reservoir fluids. For multiphase fluid flow, some of the variables in equation (10.21) must be modified to handle multiphase fluid properties under a wide range of flow conditions.

### 10.4.2. Multiphase Flowing Tubing Pressure Gradient

For multiphase fluid flow, equation (10.21) can be redefined as:

$$\begin{aligned} 144 \frac{dp}{dL} &= \left(\frac{g}{g_c}\right) \rho_m \sin\theta + \frac{f_m \rho_m v_m^2}{2g_c d} \\ &+ \rho_m \frac{v_m (dv_m)}{g_c (dL)} \text{ in EOF units} \end{aligned} \quad (10.22)$$

where the subscript “m” in equation (10.22) defines mixture property. The primary difference between TPR models is the handling of the mixture properties. The handling of mixture properties in different TPR models can be based on assumption of homogeneous flow condition (homogeneous flow TPR models) or separated flow conditions (separated flow TPR models).

*Homogeneous Flow TPR (HFTPR)* models treat multiphase fluid as a homogeneous mixture and ignore the effect of liquid holdup (slip). Though HFTPR are easy to solve, especially in a spreadsheet, they are less accurate than *separated flow TPR* models.

*Separated Flow TPR (SFTPR)* models, on the other hand, are more accurate than the homogeneous flow models, though more difficult to implement, as some of the parameters required for calculating mixture properties are published as charts. For software implementation and coding, some of the graphical relationships required for TPR calculation can be converted to numerical tables, implicit or explicit mathematical relationship.

SFTPR models are more common, as they are considered more realistic, as the effects of liquid holdup (slip) and flow regime are considered.

**10.4.2.1. Concept of Slip and Holdup.** Given  $q_g$  and  $q_l$  as the volumetric flow rate of gas and liquid, respectively, through tubing. The actual velocity of each phase will be given as:

$$v_g = \frac{q_g}{A_g} \quad (10.23)$$

and

$$v_l = \frac{q_l}{A_l} \quad (10.24)$$

where  $v_g$  and  $v_l$  are the actual velocity of gas and liquid, respectively,  $A_g$  and  $A_l$  are the area occupied by the gas and liquid phases, respectively. The difference between the actual velocity of gas phase and liquid phases is called the *slip velocity* (S); it is expressed as:

$$S = v_g - v_l \quad (10.25)$$

The phase superficial velocity, on the other hand, is the velocity of any phase assuming the phase under consideration occupies the entire area of flow. Gas and oil superficial velocities for tubing flow can be expressed, respectively, as:

$$v_{sg} = \frac{q_g}{A} \quad (10.26)$$

and

$$v_{sl} = \frac{q_l}{A} \quad (10.27)$$

where  $A$  is the total area of tubing.

The velocity of the mixture can be expressed as the sum of the superficial velocities of the liquid and gas:

$$v_m = v_{sl} + v_{sg} \quad (10.28)$$

where  $v_{sl}$  and  $v_{sg}$  are the superficial velocities of the liquid and gas, respectively.

Holdup is defined as a section of the tubing occupied by a given phase of the fluid. Hence, liquid holdup can be expressed as:

$$H_l = \frac{A_l}{A} = \frac{v_{sl}}{v_l} \quad (10.29)$$

and gas holdup expressed as:

$$H_g = \frac{A_g}{A} = \frac{v_{sg}}{v_g} \quad (10.30)$$

The relationship between  $H_l$  and  $H_g$  is shown in equation (10.31).

$$H_g = 1 - H_l \quad (10.31)$$

**10.4.2.2. Mixture Properties.** TPR calculation for multiphase fluid flow requires the evaluation of mixture properties.

*Liquid Mixture Properties*

Liquid density ( $\rho_l$ ) is expressed as:

$$\rho_l = \rho_o f_o + \rho_w f_w \quad (10.32)$$

where  $\rho_o$  and  $\rho_w$  are the density of oil and water, respectively, and  $f_o$  and  $f_w$  are the volumetric fraction of oil and water, respectively:

$$f_o = \frac{q_o B_o}{q_o B_o + q_w B_w} = \frac{1}{1 + \text{WOR} \left( \frac{B_w}{B_o} \right)} \quad (10.33)$$

where  $q_o$  and  $q_w$  are the surface oil and water rates, respectively,  $B_o$  and  $B_w$  are the formation volume factor of oil and water rates, respectively, and WOR is the water: oil ratio.

In a similar way, liquid viscosity ( $\mu_l$ ) can be calculated as:

$$\mu_l = \mu_o f_o + \mu_w f_w \quad (10.34)$$

where  $\mu$  is viscosity with subscripts “o” and “w” representing oil and water, respectively.

Liquid surface tension ( $\sigma_l$ ) defined as:

$$\sigma_l = \sigma_o f_o + \sigma_w f_w \quad (10.35)$$

where  $\sigma$  is the surface tension and subscripts “o” and “w” represent oil and water.

*Two-Phase Mixture Properties*

Different TPR models use different definitions of two-phase mixture properties, some which include:

- Two-phase density

Two-phase mixture density can be defined based on *fluid holdup* (H). This is called *slip two-phase density mixture* and expressed as:

$$\begin{aligned} \rho_m &= \rho_l H_l + \rho_g H_g \\ \rho_m &= \rho_l H_l + \rho_g (1 - H_l) \end{aligned} \quad (10.36)$$

where  $H_l$  and  $H_g$  are liquid and gas holdup

Some TPR models use two-phase mixture density based on *no slip holdup* ( $\lambda$ ). This is called *no slip two-phase density mixture* and expressed as:

$$\begin{aligned} \rho_n &= \rho_l \lambda_l + \rho_g \lambda_g \\ \rho_n &= \rho_l \lambda_l + \rho_g (1 - \lambda_l) \end{aligned} \quad (10.37)$$

Another two-phase mixture density used in some TPR calculations, based on the combination of holdup (H) and non slip holdup ( $\lambda$ ) is defined as:

$$\rho_k = \frac{\rho_L \lambda_L^2}{H_1} + \frac{\rho_g \lambda_g^2}{H_g}$$

which is further expressed as:

$$\rho_k = \frac{\rho_l \lambda_1^2}{H_1} + \frac{\rho_g (1 - \lambda_1)^2}{1 - H_1} \tag{10.38}$$

No-slip liquid holdup ( $\lambda_1$ ) is defined as the ratio of liquid in tubing segment to volume of pipe segment if gas and liquid were to travel at the same velocity (no slip condition).

Two-phase mixture density may or may not require multiphase flow regimes (Section 10.4.3) depending on the model used.

• Two-phase viscosity

In a similar approach to two-phase density, a two-phase viscosity mixture required for multiphase TPR calculation can be defined based on  $H_1$  or  $\lambda_1$  for different TPR models.

$$\mu_m = \mu_l H_1 + \mu_g (1 - H_1) \tag{10.39}$$

$$\mu_n = \mu_l \lambda_1 + \mu_g (1 - \lambda_1) \tag{10.40}$$

$$\mu_k = \mu_l^{H_1} + \mu_g^{(1-H_1)} \tag{10.41}$$

The frictional pressure gradient loss in equation (10.19) has an important parameter called the *friction factor*, ( $f$ ), which is determined from the *Moody friction factor chart* [Moody, 1944] shown in Fig. 10.24.

The Moody friction factor chart shows the relationship between the friction factor ( $f$ ) and the Reynolds number ( $N_{Re}$ ). It is the graphical solution of the Colebrook–White equation [Colebrook and White, 1937], which is an implicit expression for  $f$ :

$$\frac{1}{\sqrt{f}} = -2 \log \left( \frac{\epsilon}{3.7 d} + \frac{2.51}{N_{Re} \sqrt{f}} \right) \tag{10.42}$$

where  $\frac{\epsilon}{d}$  is the relative roughness (which is dimensionless),  $f$  is the friction factor (which is dimensionless),  $\epsilon$  is absolute roughness and has a dimension of length,  $d$  is tubing internal diameter with the same unit as  $\epsilon$ . For coding and application development, it is more convenient to define the friction factor ( $f$ ) as an explicit expression in terms of  $f$ .

Many accurate explicit mathematical expressions for friction factor have been published. *Serghide* [1984] proposed an explicit expression for  $f$  as:

$$f = \left( A - \frac{(B-A)^2}{C-2B+A} \right)^{-2} \tag{10.43}$$

where

$$A = -2 \log \left( \frac{\epsilon/d}{3.7} + \frac{12}{N_{Re}} \right)$$

$$B = -2 \log \left( \frac{\epsilon/d}{3.7} + \frac{2.51A}{N_{Re}} \right)$$

$$C = -2 \log \left( \frac{\epsilon/d}{3.7} + \frac{2.51B}{N_{Re}} \right)$$

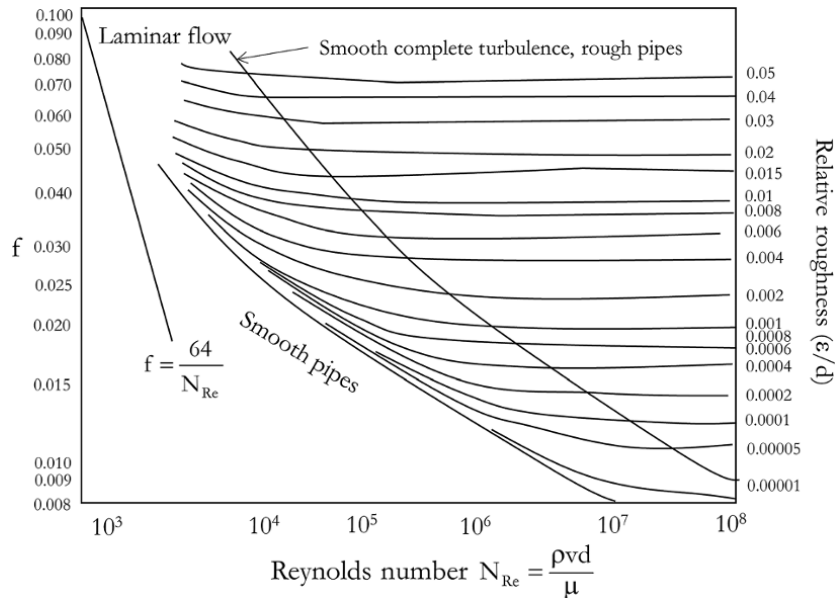


Figure 10.24 Moody friction factor chart [Adapted from Moody, 1944].

The friction factor for multiphase flow required for mixture properties is implemented in different ways for different TPR models. Determination of the friction factor for a two-phase mixture ( $f_m$ ) may require flow regimes/patterns depending on the model.

### 10.4.3. Multiphase Flow Regimes

The geometrical distribution and patterns of different phases during fluid flow through tubing (flow regime) are important in multiphase TPR calculations as they affect calculation of mixture properties. Different names may be used to describe observed flow patterns created by multiphase fluid flow. The most common definition of flow regime for vertical two-phase flow include:

*Bubble/dispersed flow*: when multiphase flow is characterized by this flow regime, the gas phase is present as small bubbles with different sizes and velocities. This flow regime manifests when the liquid flow rate is high enough to break up the gas into bubbles but, however, is not high enough to cause the bubbles to thoroughly mix within the liquid phase. In this flow regime, the wall is predominantly in contact with liquid phase (Fig. 10.25).

*Slug Flow*: this flow regime has gas velocity greater than liquid velocity and is characterized by coalescing of the gas phase with bubble diameter almost the size of tubing. The liquid still exists as a continuous phase and both gas and liquid phases contribute significantly to pressure drop (Fig. 10.25).

*Transition flow*: this flow regime is often characterized by transition changes from continuous liquid phase to continuous gas phase. In this flow regime, liquid may be entrained in the continuous gas phase with irregular characteristics. The gas phase contribution

to pressure gradient is more dominant than that of liquid phase (Fig. 10.25).

*Annular/mist flow*: This flow regime is characterized by the existence of the liquid phase as film on the tubing wall while the gas phase exists as a continuous phase. This flow regime also has liquid entrainment as mist (Fig. 10.25).

### 10.4.4. Flowing Tubing Pressure Gradient Calculation

Calculation of the total flowing fluid gradient can be demonstrated with the Hagedorn and Brown model [Hagedorn and Brown, 1965].

**10.4.4.1. Total Flowing Pressure Gradient using Hagedorn and Brown Model.** Liquid holdup is determined from the calculated ratio of liquid holdup to secondary correlation factor  $\left(\frac{H_l}{\psi}\right)$  and secondary correlation factor ( $\psi$ ) using:

$$H_l = \left(\frac{H_l}{\psi}\right) \psi \quad (10.44)$$

$\frac{H_l}{\psi}$  is determined from the holdup correlation factor chart,

which relates  $\frac{H_l}{\psi}$  with  $\frac{N_{lv}}{N_{gv}^{0.575}} \left(\frac{p}{p_0}\right)^{0.1} \left(\frac{CN_l}{N_d}\right)$  (Fig. 10.26).

where  $N_{lv}$  is the liquid velocity number and is defined as:

$$N_{lv} = 1.938 v_{sl} \sqrt[4]{\frac{\rho_l}{\sigma_l}} \quad (10.45)$$

$N_{gv}$  is the gas velocity number and is defined as

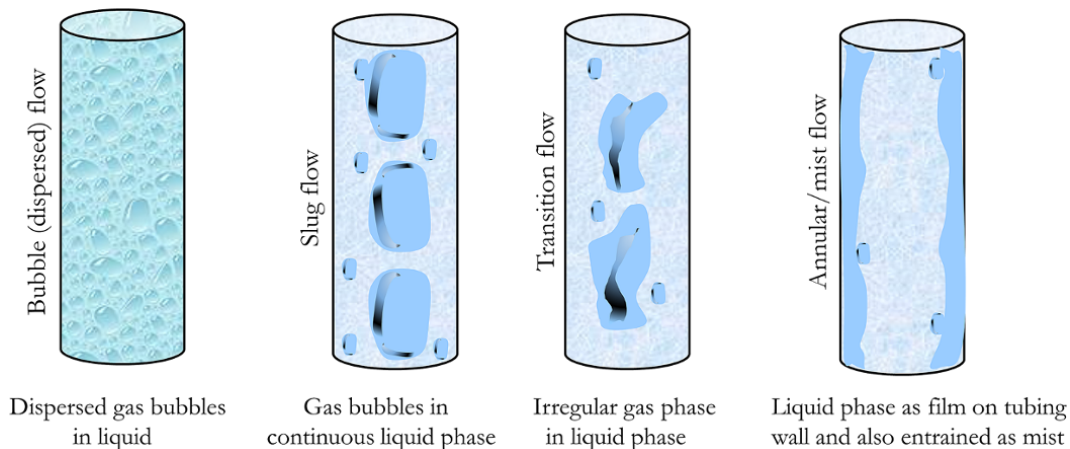


Figure 10.25 Multiphase flow regimes in vertical tubing.

$$N_{gv} = 1.938 v_{sg} \sqrt[4]{\frac{\rho_l}{\sigma_1}} \quad (10.46)$$

$N_d$  is the pipe diameter number and is defined as:

$$N_d = 120.872 d \sqrt[4]{\frac{\rho_l}{\sigma_1}} \quad (10.47)$$

where  $v_{sl}$  is in ft/s,  $v_{sg}$  is in ft/s,  $\rho_l$  is in lbm/ft<sup>3</sup>,  $\sigma_1$  is in dynes/cm,  $\mu_l$  is in cp,  $d$  is in ft,  $p$  is the pressure in psia, and  $p_0$  is a base pressure taken as 14.7 psia.

$CN_l$  is determined from the viscosity number coefficient correlation chart, which is a graphical relationship between  $CN_l$  and  $N_l$  (Fig. 10.27).

where  $CN_l$  is the liquid viscosity number coefficient and  $N_l$  is the liquid viscosity number defined as:

$$N_l = 0.15726 \mu_l \sqrt[4]{\frac{1}{\rho_l \sigma_1^3}} \quad (10.48)$$

The secondary correction factor ( $\psi$ ) is determined from the secondary correlation factor correlation chart (Fig. 10.28).

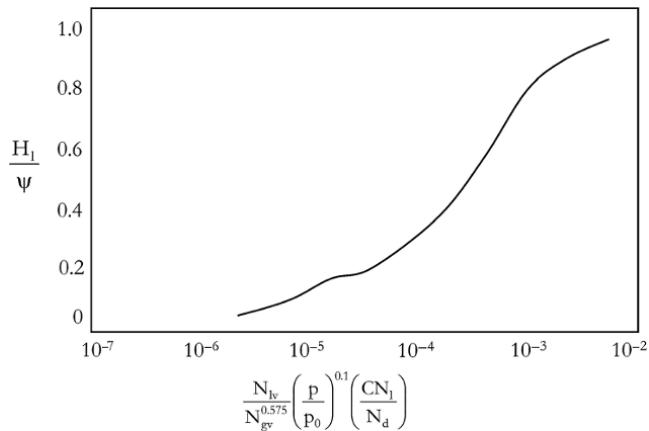


Figure 10.26 Holdup correlation factor chart.

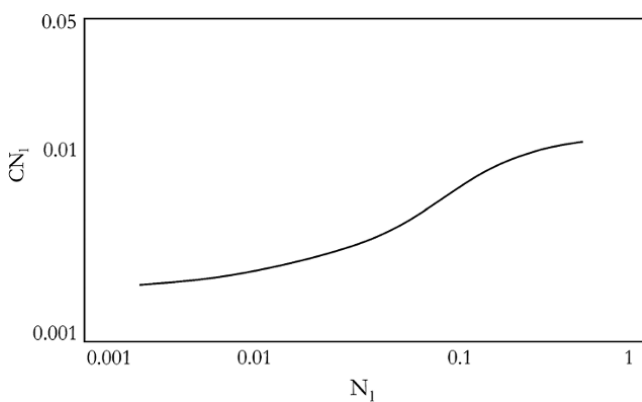


Figure 10.27 Viscosity number coefficient correlation chart.

With  $\frac{H_1}{\psi}$  and  $\psi$  determined, liquid holdup ( $H_l$ ) can then be determined using equation (10.44):

$$H_l = \left(\frac{H_1}{\psi}\right) \psi$$

Expressing Graphical Correlations as Equations. For easy calculation and software development, the graphical relationships in Figures 10.26–10.28 are best described as equations. The holdup correlation factor chart (Fig. 10.26) was fitted to a polynomial of order six by regression (Fig. 10.29).

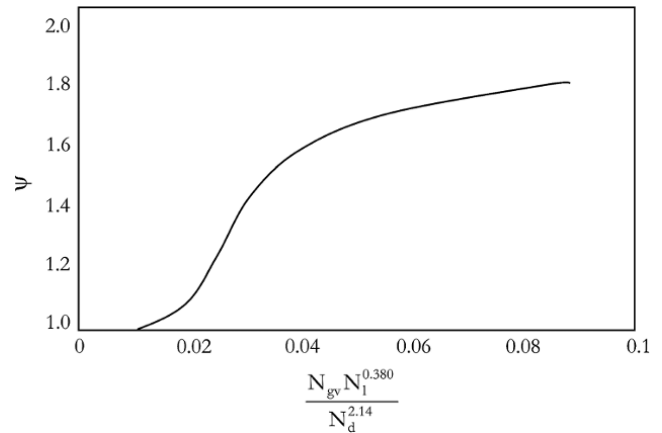


Figure 10.28 Secondary correction factor correlation chart.

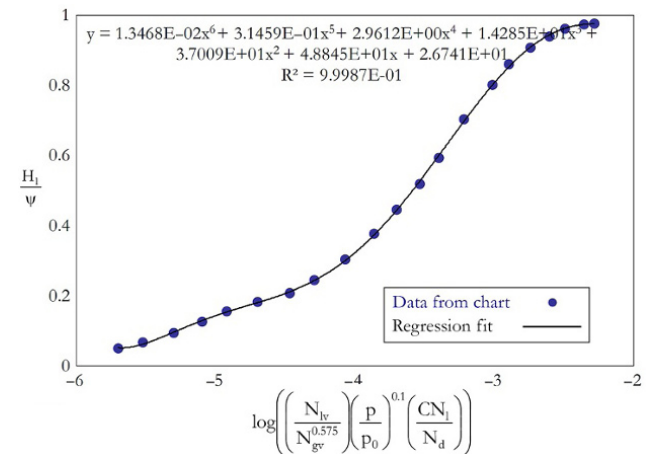


Figure 10.29 Regression fit of  $\frac{H_1}{\psi}$  against  $\log\left(\left(\frac{N_{lv}}{N_{gv}^{0.575}}\right)\left(\frac{p}{p_0}\right)^{0.1}\left(\frac{CN_l}{N_d}\right)\right)$  to polynomial of order six.

$\frac{H_l}{\psi}$  can thus be expressed as:

$$\frac{H_l}{\psi} = 0.013468x^6 + 0.31459x^5 + 2.9612x^4 + 14.285x^3 + 37.009x^2 + 48.845612x + 26.741 \tag{10.49}$$

where

$$x = \log\left(\frac{N_{lv}}{N_{gv}^{0.575}} \left(\frac{p}{p_0}\right)^{0.1} \left(\frac{CN_l}{N_d}\right)\right)$$

$\log(CN_l)$  in Fig. 10.27 was fitted to polynomial of order six with  $\log(N_l)$  as an independent variable, as shown in Fig. 10.30.

$CN_l$  can thus be expressed as:

$$\log(CN_l) = 0.43139x^6 + 2.5715x^5 + 5.7247x^4 + 5.6987x^3 + 2.3310x^2 + 0.47185x - 1.5310 \tag{10.50}$$

where  $x = \log(N_l)$ .

Also, the secondary correction factor chart (Fig. 10.28) was fitted to a polynomial of order seven, as shown in Fig. 10.31.

Hence,  $\psi$  can be expressed as:

$$\psi = 3.63060 \times 10^9 x^7 - 1.15391 \times 10^9 x^6 + 1.40528 \times 10^8 x^5 - 7.89376 \times 10^6 x^4 + 1.74738 \times 10^5 x^3 + 6.61551 \times 10^2 x^2 - 5.04069 \times 10^1 x + 1.33508 \tag{10.51}$$

where

$$x = \frac{N_{gv} N_l^{0.380}}{N_d^{2.14}}$$

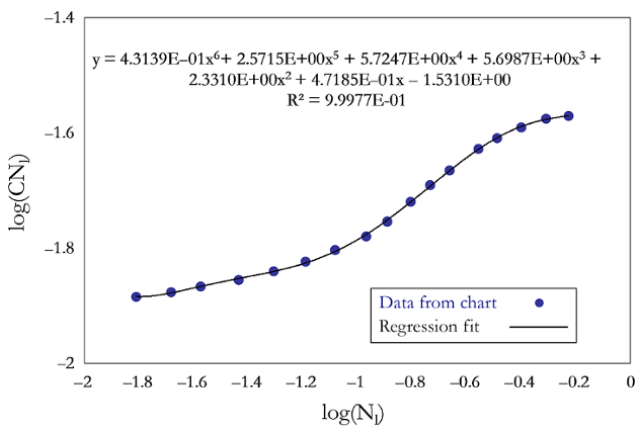


**Figure 10.30** Regression fit of  $\log(CN_l)$  against  $\log(N_l)$  to polynomial of order six.

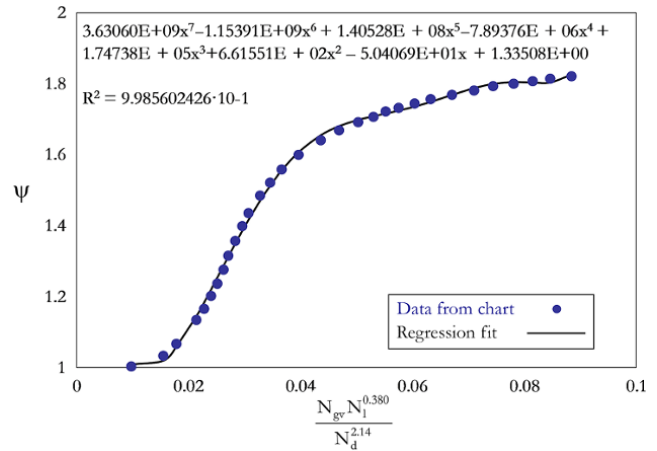


**Figure 10.31** Regression fit of  $\psi$  against  $\frac{N_{gv} N_l^{0.380}}{N_d^{2.14}}$  to polynomial of order seven.

The hydrostatic pressure gradient loss in EOF units is thus calculated as:

$$144 \left(\frac{dp}{dL}\right)_{\text{Hydrostatic}} = \frac{g}{g_c} (\rho_l H_l + \rho_g (1 - H_l)) \tag{10.52}$$

and the friction pressure gradient loss is calculated as:

$$144 \left(\frac{dp}{dL}\right)_{\text{friction}} = \frac{f_m \rho_m v_m^2}{2g_c d} \tag{10.53}$$

In terms of mass flow rate the expression is:

$$144 \left(\frac{dp}{dL}\right)_{\text{friction}} = \frac{f_m W^2}{2.9652 \times 10^{11} \rho_g d^5} \tag{10.54}$$

where  $\rho_g$  is the density based on liquid holdup  $\text{lbm/ft}^3$ ,  $w$  is total mass flow rate  $\text{lbm/d}$ , and  $f_m$  is the two-phase friction factor.

The two-phase friction factor is determined from the Moody diagram (Fig. 10.24) or the explicit expression given in equation (10.43), using the two-phase Reynolds number which is expressed as:

$$N_{\text{Rem}} = \frac{\rho_n v_m d}{\mu_s} \tag{10.55}$$

From equation (10.28):

$$v_m = v_{sl} + v_{sg}$$

From equation (10.41):

$$\mu_s = \mu_l^{H_l} + \mu_g^{H_g}$$

The two-phase Reynolds number can thus be expressed as:

$$N_{\text{Rem}} = \frac{\rho_n (v_{sl} + v_{sg}) d}{(\mu_l^{H_l} + \mu_g^{H_g})} \tag{10.56}$$

Equation (10.55) can be expressed in EOF units as:

$$N_{Rem} = \frac{1488 \rho_n v_m d}{\mu_s} \quad (10.57)$$

and, hence, equation (10.56) in EOF units becomes:

$$N_{Rem} = \frac{1488 \rho_n (v_{sl} + v_{sg}) d}{(\mu_l^{H_l} + \mu_g^{H_g})} \quad (10.58)$$

The acceleration pressure gradient component, though negligible, can be determined from equation (10.20) as:

$$\left(\frac{dp}{dL}\right)_{\text{acceleration}} = \frac{\rho_s \Delta v_m^2}{2g_c \Delta L} \quad (10.59)$$

where  $\Delta v_m^2 = v_m^2(p_1, T_1) - v_m^2(p_2, T_2)$ .

### Exercise 10.3 TPR Calculation using the Hagedorn and Brown Method

A well with tubing length (from wellhead to top of perforation) of 7,890 ft, tubing internal diameter of 3.5 inches, and absolute roughness ( $\epsilon$ ) of 0.0006 inches is producing at a liquid flow rate of 730 stb/D, GLR of 1,300 scf/bbl, and water cut of 10%. The well has a flowing tubing wellhead pressure of 720 psia and flowing tubing wellhead temperature of 90 °F. The oil produced has an API of 30°, viscosity of 5 cp, and oil interfacial tension of 25 dynes/cm. Gas produced has a specific gravity of 0.6. Formation water produced has a specific gravity of 1.05, viscosity of 0.79 cp, and interfacial tension of 55 dynes/cm. The fluid produced from the reservoir has a flowing bottomhole temperature of 180 °F.

1. Determine flowing pressure and gradient along the well, from wellhead to top of perforation.

2. Create the TPR plot ( $p_{wf}$  against  $q_l$ ) at the top perforation for liquid rates between 100 and 800 stb/D.

#### Solution Steps.

Depth along the well is divided into a convenient number of segments for which the pressure gradient will be calculated.

The gradient of the  $n$ th segment  $\left(\left(\frac{dp}{dL}\right)_n\right)$  is a function depth ( $L_n$ ) and pressure at that depth ( $p_n$ ); it is defined as:

$$\left(\frac{dp}{dL}\right)_n = \frac{dp}{dL}(L_n, p_n) \quad (10.60)$$

The pressure at any point is calculated using:

$$p_n = \left(\frac{dp}{dL}\right)_{n-1} \times (L_n - L_{n-1}) + p_{n-1} \quad (10.61)$$

The pressure of the first segment is determined using:

$$p_1 = \left(\frac{dp}{dL}\right)_0 \times (L_1 - L_0) + p_{wh} \quad (10.62)$$

where  $p_{wh}$  is the tubing wellhead pressure.

#### Solution.

1. Table 10.4 shows calculated pressure and pressure gradient along the well at a liquid rate of 730 stb/D while Fig. 10.32 shows a graphical presentation of pressure profile along well tubing at the same liquid rate.

2. The calculation above is repeated for liquid rates between 100 and 800 stb/D and the corresponding bottomhole pressure ( $p_{wf}$ ) at top perforation is recorded against the liquid rate (Table 10.5). This relationship between  $p_{wf}$  against  $q_l$  is the TPR of the system at the top perforation node (Fig. 10.33).

Appendix 10A is a simple VBA code with the spreadsheet setup shown in Fig. 10.34 for calculating the pressure gradient and pressure profile along well tubing.

Tubing performance can change during the life of a well. Water loading when reservoir pressure reduces, and water cut increases, can cause a reduction in tubing performance. Selecting tubing with the appropriate internal diameter that can handle potential well loading is important during well engineering design. For a well with loading problems, tubing performance may be improved by using tubing with a smaller internal diameter. Other methods of dealing with water loading are discussed under artificial lift systems in Chapter 11 (11.4).

**Table 10.4** Pressure and Pressure Gradient at a Liquid Rate of 730 stb/D.

Depth (ft)	p (psia)	dp/dl
0.00	720.00	—
415.26	859.88	0.3369
830.53	997.29	0.3309
1,245.79	1,134.53	0.3305
1,661.05	1,272.66	0.3326
2,076.32	1,412.10	0.3358
2,491.58	1,552.93	0.3391
2,906.84	1,695.01	0.3421
3,322.11	1,838.08	0.3445
3,737.37	1,981.82	0.3461
4,152.63	2,125.88	0.3469
4,567.89	2,269.90	0.3468
4,983.16	2,413.60	0.3460
5,398.42	2,556.75	0.3447
5,813.68	2,699.35	0.3434
6,228.95	2,841.65	0.3427
6,644.21	2,984.51	0.3440
7,059.47	3,129.79	0.3499
7,474.74	3,281.61	0.3656
7,890.00	3,449.83	0.4051



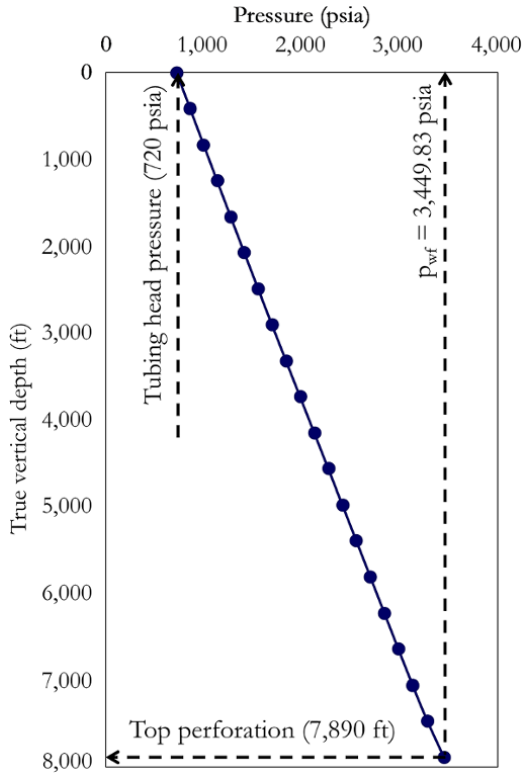


Figure 10.32 Pressure profile along well tubing at a liquid rate of 730 stb/D.

Table 10.5 TPR at the Top Perforation for Exercise 10.3.

$q_l$ (stb/D)	$p_{wrf}$ (psia)
100	2,434.04
400	2,912.89
600	3,202.05
730	3,449.83
800	3,641.55

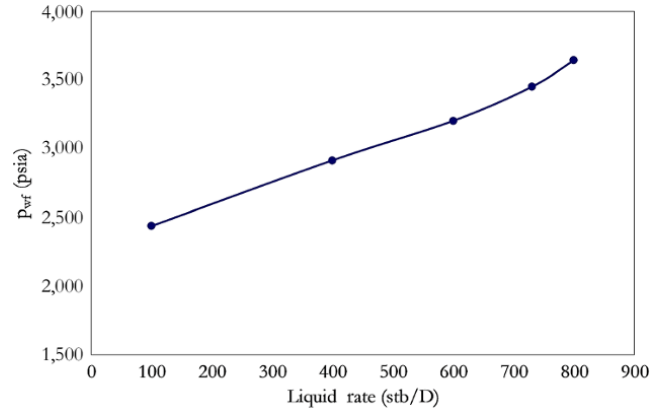


Figure 10.33 Graphical TPR at the top perforation for Exercise 10.3.

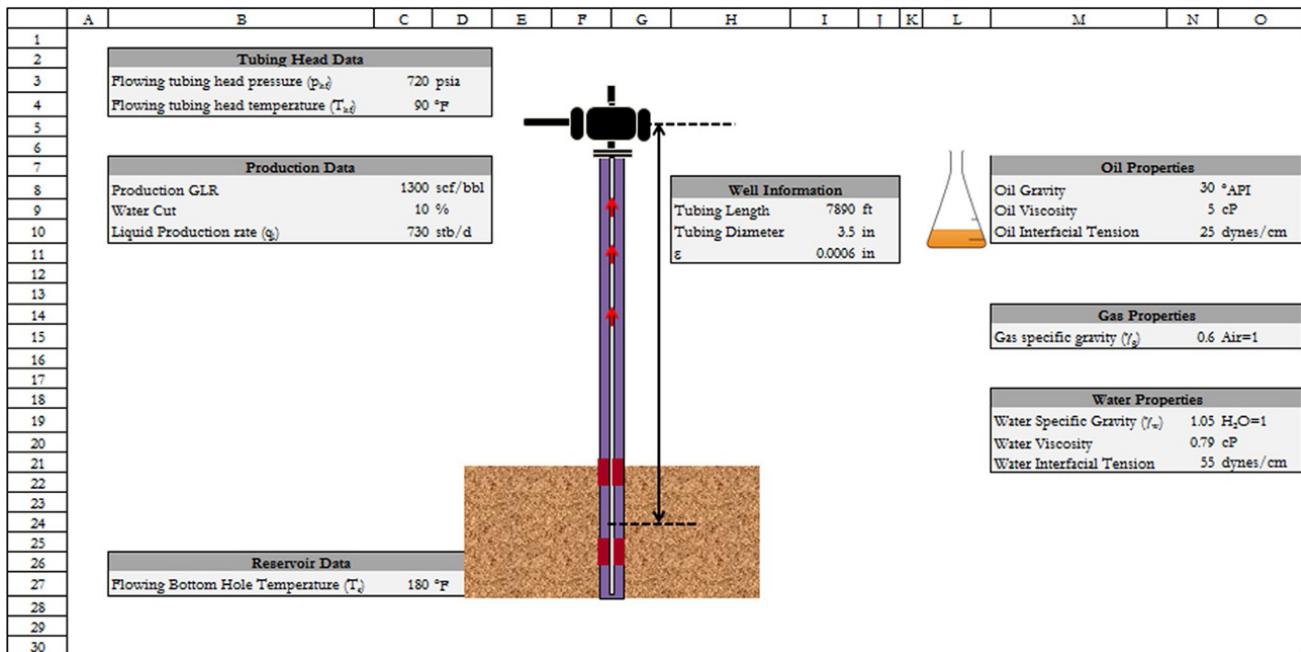


Figure 10.34 Spreadsheet setup for Exercise 10.3.

**Table 10.6** Important Published TPR Models.

TPR model	Field/laboratory setup	Fluid used	Model development and applicability
<i>Fancher Brown</i> [1963]	8,000 ft experimental field setup using 2-in. ID tubing.	Gas, water	Extended correlation of <i>Poettmann and Carpenter</i> [1952] to better predict pressure losses at low flow rates and high GLR. No-slip correlation. Good for diagnosis since model gives the minimum possible gravity pressure loss.
<i>Griffith and Wallis</i> [1961]	Laboratory experiment with narrow pipes/tube.	Gas, water	Gave good results in slug flow region. Slug flow model has been used by other models to improve predictions. Adopted by Hagedorn and Brown (modified Hagedorn and Brown) and others to determine bubble–slug flow boundary.
<i>Duns and Ros</i> [1963]	Laboratory experiment and field experiment (1 <sup>1</sup> / <sub>4</sub> –3 <sup>1</sup> / <sub>8</sub> in. ID).	Oil, gas, water	Gave good prediction for all flow regimes. Best for mist flow regime. Comprehensive work including flow regime map and derivation of holdup correlations.
<i>Hagedorn and Brown</i> [1965]	1,500 ft with 1, 1 <sup>1</sup> / <sub>4</sub> , and 1 <sup>1</sup> / <sub>2</sub> in. ID tube for experimental setup using wide range of viscosity.	Oil, gas, water	Correlation was developed to handle effect of fluid viscosity over wide range. Good correlations for slug flow. Forms basis for many tubing correlations.
<i>Orkiszewski</i> [1967]	Field experiment over wide range of pipe ID.	Oil, gas, water	Extended work by Griffith and Wallis to developed general correlation which handles all multiphase flow regime.
<i>Beggs and Brill</i> [1973]	Laboratory experiment using 1–1 <sup>1</sup> / <sub>2</sub> in. tubing.	Gas, water	Correlation was derived for horizontal flow and then modified for deviated wells. Serves as generalized correlation for prediction pressure drop for all multiphase flow regime at different angle of inclination. Good for pipelines but may over predicts for wells.

**10.4.4.2. TPR Models.** Many TPR models have been formulated using laboratory and field experimental observations. Since formulation of most of the TPR involves developing empirical relationships from experiments, it is important to compare various TPR model predictions to test data, which can be measured pressure profile or single pressure data in the well, for a quality check of the test data and TPR model selection.

Important published TPR models are summarized in Table 10.6.

## REFERENCES

- Beggs, D. and Brill, J.P., 1973. A study of two-phase flow in inclined pipes. *Journal of Petroleum Technology*, **25**(05), 607–617.
- Colebrook, C. and White, C., 1937. Experiments with fluid friction in pipes roughened. *Proceedings of the Royal Society of London, Mathematical and Physical Sciences*, **161**(906), 367–381.
- Duns, H. and Ross, N., 1963. Vertical flow of gas and liquid mixtures in wells. *6th World Pet, Germany*.
- Fancher, G. and Brown, K., 1963. Prediction of pressure gradients for multiphase flow in tubing. *Society of Petroleum Engineers Journal*, **3**(01), 59–69.
- Griffith, P. and Wallis, G., 1961. Two-phase slug flow. *Journal of Heat Transfer*, **83**(3), 307–318.
- Hagedorn, A. and Brown, K., 1965. Experimental study of pressure gradients occurring during continuous two-phase flow in small-diameter vertical conduits. *Journal of Petroleum Technology*, **17**(04), 475–484.
- Karakas, M. and Tariq, S., 1991. Semi analytical productivity models for perforated completions. *SPE Production Engineering*, **6**(1), 73–82.
- Moody, L., 1944. Friction factor for pipe flow. *Transactions of the ASME*, **66**(8), 671–684.
- Orkiszewski, J., 1967. Predicting two-phase pressure drops in vertical pipe. *Journal of Petroleum Technology*, **19**(06), 829–838.
- Poettman, F. and Carpenter, P., 1952. The multiphase flow of gas, oil, and water through vertical flow strings with application to the design of gas-lift installations. In *Drilling and Production Practice*, New York: American Petroleum Institute.
- Serghides, T., 1984. Estimate friction factor accurately. *Chemical Engineering Journal*, **91**(5), 63–64.
- Gilbert, W., 1954. Flowing and *Gas-lift well Performance*. In *Drilling and Production Practice*, American Petroleum Institute, pp. 126–157.
- Golan, M. and Whitson, C., 1986. *Well Performance*, 2nd edn. Englewood Cliffs, NJ: Prentice Hall.
- Greene, W., 1983. Analyzing the performance of gas wells. *Journal of Petroleum Technology*, **35**(07), 1378–1384.
- Guo, B., Lyons, W., and Ghalambor, A., 2007. *Petroleum Production Engineering, A computer-Assisted Approach*. Elsevier Science & Technology Books.
- Jones, L., Blount, E., and Glaze, O.H., 1976. *Use of Short Term Multiple Rate Tests to Predict Performance of Wells Having Turbulence*. SPE paper 6133, SPE 51st Annual Fall Meeting, New Orleans, LA.
- Mach, J., Proano, E., and Brown, K., 1979. *A Nodal Approach for Applying Systems Analysis to the Flowing and Artificial Lift Oil or Gas Well*. TX: Society of Petroleum Engineers.
- Stewart, G., 2011. *Wireline Formation Testing and Well Deliverability*. Tulsa, OK: PennWell Corporation.
- Turner, R.G., Hubbard, M.G., and Dukler, A.E., 1969. Analysis and prediction of minimum flow rate for the continuous removal of liquids from gas wells. *Journal of Petroleum Technology*, **21**(11), 1475–1482.

## APPENDIX 10 A: VBA SOLUTION FOR EXERCISE 10.3

"Define input parameters as public variables

Public Dia As Double  
 Public Liquid As Double  
 Public WCT As Double  
 Public GLR As Double  
 Public SG As Double  
 Public Ts As Double  
 Public Ps As Double  
 Public Tres As Double  
 Public Lw As Double  
 Public VisW As Double  
 Public VisO As Double  
 Public DenW As Double  
 Public API As Double  
 Public InterfW As Double  
 Public InterfO As Double  
 Public ConstE As Double

Function Assign()

" Assigning values to parameters from cells  
 Dia = Worksheets("VLP").Cells(10, "I").Value  
 Liquid = Worksheets("VLP").Cells(10, "C").Value  
 WCT = Worksheets("VLP").Cells(9, "C").Value  
 GLR = Worksheets("VLP").Cells(8, "C").Value  
 SG = Worksheets("VLP").Cells(15, "N").Value  
 Ts = Worksheets("VLP").Cells(4, "C").Value

## BIBLIOGRAPHY

- American Petroleum Institute, 1991. *API Recommended Practice 14E (RP 14E), Recommended Practice for Design and Installation of Offshore Production Platform Piping Systems*. Washington, DC: American Petroleum Institute.
- Bellarby, J., 2009. *Well Completion Design*. 1st edn. Elsevier.
- Brown, K., 1980. *The Technology of Artificial Lift Methods*, Vol. 2a. Tulsa, OK: PennWell Publishing.
- Brown, K. and Beggs, H., 1977. *The Technology of Artificial Lift Methods*, Vol. 1. Tulsa, OK: PennWell Publishing.

```

Ps = Worksheets("VLP").Cells(3, "C").Value
Tres = Worksheets("VLP").Cells(27, "C").Value
Lw = Worksheets("VLP").Cells(9, "I").Value
VisW = Worksheets("VLP").Cells(20, "N").Value
VisO = Worksheets("VLP").Cells(9, "N").Value
DenW = Worksheets("VLP").Cells(19, "N").Value
API = Worksheets("VLP").Cells(8, "N").Value
InterfW = Worksheets("VLP").Cells(21, "N").Value
InterfO = Worksheets("VLP").Cells(10, "N").Value
ConstE = Worksheets("VLP").Cells(13, "I").Value
End Function

Function Area()
Assign
"Area of flow in ft2
Area = 3.14159265358979 * ((Dia / 12) ^ 2 / 4)
End Function

Function SGOil()
"Specific gravity of oil
SGOil = 141.5 / (131.5 + API)
End Function

Function GasRate()
"Gas rate from GLR and liquid rate in scf/D
GasRate = GLR * Liquid
End Function

Function WaterRate()
"Water rate from Liquid rate in stb/D
WaterRate = (WCT / 100) * Liquid
End Function

Function SGLiquid()
"Specific gravity of liquid
SGLiquid = ((Liquid - WaterRate()) * SGOil() +
  WaterRate() * DenW) / Liquid

End Function

Function MassFlow()
"mass flow rate in lb/Day
MassFlow = SGLiquid() * 62.4 * Liquid * 5.615 +
  0.0765 * SG * GasRate()
End Function

Function NoSDensity()
"No slip density in lb/f3
NoSDensity = (SGLiquid() * 62.4 * Liquid *
  5.615 + 0.0765 * SG * GasRate()) /
  (Liquid * 5.615 + GasRate())
End Function

Function LiquidVisc()
" Liquid viscosity in cp
LiquidVisc = (((Liquid - WaterRate()) * VisO
  + WaterRate() * VisW)) / Liquid
End Function

Function TempDepth(depth)
"Temperature at different depth in oF
" Linear relationship between wellhead temperature and
  bottomhole flowing temperature was used

```

```

TempDepth = Ts + ((Tres - Ts) / Lw) * depth
End Function

Function TCritical()
"Critical temperature in oR
TCritical = 168 + 325 * SG - 12.5 * SG ^ 2
End Function

Function PCritical()
"Critical pressure in psia
PCritical = 677 + 15 * SG - 37.5 * SG ^ 2
End Function

Function PReduced(P)
"Reduced pressure
PReduced = P / PCritical()
End Function

Function TReduced(depth)
" Reduced temperature
TReduced = (TempDepth(depth) + 460) / TCritical()
End Function

Function BaseVisc(depth)
" Base Viscosity calculation in unit cp
BaseVisc = (1.709 / 100000 - 2.062 / 1000000 * SG)
  * TempDepth(depth) + 8.188 / 1000 - 6.15 / 1000
End Function

Function GasViscTP(depth, P)
" Gas Viscosity as function of depth
  (which already has Temperature) and
  pressure in cp
a0 = -2.462
a1 = 2.97
a2 = -0.2862
a3 = 0.008054
a4 = 2.808
a5 = -3.498
a6 = 0.3603
a7 = -0.01044
a8 = -0.7933
a9 = 1.396
a10 = -0.1491
a11 = 0.00441
a12 = 0.08393
a13 = -0.1864
a14 = 0.02033
a15 = -0.0006095

Tr = TReduced(depth)
pr = PReduced(P)
GasVisc1 = BaseVisc(depth)

LnFunc = a0 + a1 * pr + a2 * pr ^ 2 + a3 * pr ^ 3 + Tr *
  (a4 + a5 * pr + a6 * pr ^ 2 + a7 * pr ^ 3) + (Tr ^ 2)
  * (a8 + a9 * pr + a10 * pr ^ 2 + a11 * pr ^ 3) + (Tr ^ 3)
  * (a12 + a13 * pr + a14 * pr ^ 2 + a15 * pr ^ 3)
GasViscTP = ((Exp(LnFunc)) / Tr) * GasVisc1
End Function

```

```

Function ZFact(depth, P)
" Z Factor calculation
a1 = 0.317842
a2 = 0.382216
a3 = -7.76835
a4 = 14.29053
a5 = 0.000002
a6 = -0.00469
a7 = 0.096254
a8 = 0.16672
a9 = 0.96691
a10 = 0.063069
a11 = -1.966847
a12 = 21.0581
a13 = -27.0246
a14 = 16.23
a15 = 207.783
a16 = -488.161
a17 = 176.29
a18 = 1.88453
a19 = 3.05921
Tr = TReduced(depth)
pr = PReduced(P)

T = 1 / Tr
a = a1 * T * (Exp(a2 * (1 - T) ^ 2)) * pr
b = a3 * T + a4 * T ^ 2 + a5 * T ^ 6 * pr ^ 6
C = a9 + a8 * T * pr + a7 * T ^ 2 * pr ^ 2 + a6 * T ^ 3
  * pr ^ 3
D = a10 * T * (Exp(a11 * (1 - T) ^ 2)) * pr
E = a12 * T + a13 * T ^ 2 + a14 * T ^ 3
F = a15 * T + a16 * T ^ 2 + a17 * T ^ 3
G = a18 + a19 * T

Y = D * pr / (((1 + a ^ 2) / C) - (a ^ 2 * b / C ^ 3))
ZFact = D * pr * (1 + Y + Y ^ 2 - Y ^ 3) / ((D * pr + E
  * Y ^ 2 - F * Y ^ G) * (1 - Y) ^ 3)
End Function

Function LiqSlipVel()
" Superficial Liquid Velocity at different depth in ft/s
LiqSlipVel = Liquid * 5.615 / 86400 / Area()
End Function

Function GasSlipVel(depth, P)
" Superficial Gas Veleocity at different depth in ft/s
GasSlipVel = 1 / (Area()) * GasRate() * ZFact
  (depth, P) * (460 + TempDepth(depth)) / (460 + 60)
  * (14.7 / P) / 86400
End Function

Function MixVel(depth, P)
" Mixture velocity in ft/s
MixVel = GasSlipVel(depth, P) + LiqSlipVel()
End Function

```

```

Function fFactor(depth, P)
" friction factor calculation
interf = (WaterRate() * InterfW + (Liquid - WaterRate
  ()) * InterfO) / Liquid
Nvl = 1.938 * LiqSlipVel() * (62.4 * SGLiquid() / interf)
  ^ 0.25
NVG = 1.938 * GasSlipVel(depth, P) * (62.4 * SGLi-
  quid() / interf) ^ 0.25
NL = 0.15726 * LiquidVisc() * (1 / (62.4 * SGLiquid() *
  interf ^ 3)) ^ 0.25
Nd = 120.872 * (Dia / 12) * (62.4 * SGLiquid() / interf)
  ^ 0.5
CNL = 10 ^ (0.431387 * WorksheetFunction.Log(NL)
  ^ 6 + 2.571506 * WorksheetFunction.Log(NL)
  ^ 5 + 5.724715 * WorksheetFunction.Log(NL) ^ 4 +
  5.698695 * WorksheetFunction.Log(NL)
  ^ 3 + 2.330958 * WorksheetFunction.Log(NL) ^ 2 +
  0.471851 * WorksheetFunction.Log(NL) - 1.531007)
Ratio2 = Nvl * NL ^ 0.38 / Nd ^ 2.14
phi = 3630597237# * Ratio2 ^ 7 - 1153914461 * Ratio2
  ^ 6 + 140528442.1 * Ratio2 ^ 5 - 7893763.864 *
  Ratio2 ^ 4 + 174738.158 * Ratio2 ^ 3 + 661.551 *
  Ratio2 ^ 2 - 50.407 * Ratio2 + 1.335
Ratio1 = Nvl * (P ^ 0.1) * CNL / ((NVG ^ 0.575) * (14.7
  ^ 0.1) * (Nd))
LogRatio1 = WorksheetFunction.Log(Ratio1)
HLphiRatio = 0.013468 * LogRatio1 ^ 6 + 0.31459 *
  LogRatio1 ^ 5 + 2.9612 * LogRatio1 ^ 4 + 14.285 *
  LogRatio1 ^ 3 + 37.009 * LogRatio1 ^ 2 + 48.845 *
  LogRatio1 + 26.741

HL = HLphiRatio * phi
ReNum = 1488 * NoSDensity() * MixVel(depth, P) *
  (Dia / 12) / (LiquidVisc() ^ HL + GasViscTP(depth,
  P) ^ (1 - HL))
a = -2 * WorksheetFunction.Log(ConstE / (3.7 * Dia))
  + (12 / ReNum)
b = -2 * WorksheetFunction.Log(ConstE / (3.7 * Dia))
  + (2.51 * a / ReNum)
C = -2 * WorksheetFunction.Log(ConstE / (3.7 * Dia))
  + (2.51 * b / ReNum)

fFactor = (a - (((b - a) ^ 2) / (C - 2 * b + a))) ^ (-2)
End Function

Function Gradient(depth, P)
" Total fluid gradient calculation
interf = (WaterRate() * InterfW + (Liquid - WaterRate
  ()) * InterfO) / Liquid
Nvl = 1.938 * LiqSlipVel() * (62.4 * SGLiquid() / interf)
  ^ 0.25
NVG = 1.938 * GasSlipVel(depth, P) * (62.4 * SGLi-
  quid() / interf) ^ 0.25
NL = 0.15726 * LiquidVisc() * (1 / (62.4 * SGLiquid() *
  interf ^ 3)) ^ 0.25

```

```

Nd = 120.872 * (Dia / 12) * (62.4 * SGLiquid() / interf)
  ^ 0.5
CNL = 10 ^ (0.431387 * WorksheetFunction.Log(NL)
  ^ 6 + 2.571506 * WorksheetFunction.Log(NL)
  ^ 5 + 5.724715 * WorksheetFunction.Log(NL) ^ 4 +
  5.698695 * WorksheetFunction.Log(NL)
  ^ 3 + 2.330958 * WorksheetFunction.Log(NL) ^ 2 +
  0.471851 * WorksheetFunction.Log(NL) - 1.531007)
Ratio2 = Nvl * NL ^ 0.38 / Nd ^ 2.14
phi = 3630597237# * Ratio2 ^ 7 - 1153914461 * Ratio2
  ^ 6 + 140528442.1 * Ratio2 ^ 5 - 7893763.864 *
  Ratio2 ^ 4 + 174738.158 * Ratio2 ^ 3 + 661.551 *
  Ratio2 ^ 2 - 50.407 * Ratio2 + 1.335
Ratio1 = Nvl * (P ^ 0.1) * CNL / ((NVG ^ 0.575) * (14.7
  ^ 0.1) * (Nd))
LogRatio1 = WorksheetFunction.Log(Ratio1)

```

```

HLphiRatio = 0.013468 * LogRatio1 ^ 6 + 0.31459 *
  LogRatio1 ^ 5 + 2.9612 * LogRatio1 ^ 4 + 14.285 *
  LogRatio1 ^ 3 + 37.009 * LogRatio1 ^ 2 + 48.845 *
  LogRatio1 + 26.741
HL = HLphiRatio * phi
GasDen = 28.97 * SG * P / (ZFact(depth, P) * 10.73 *
  (460 + TempDepth(depth)))
DenAverage = HL * SGLiquid() * 62.4 + (1 - HL) *
  GasDen
GradientHydro = (1 / 144) * DenAverage
GradientFriction = (1 / 144) * fFactor(depth, P) *
  (DenAverage * MixVel(depth, P) ^ 2 / (2 * Dia / 12))
Gradient = GradientHydro + GradientFriction
End Function

```

## Production System Analysis

The production system plot (Fig. 11.1) is an important model for production system analysis. It allows the combination of *inflow performance relationship* (IPR) (equation (9.1)) and *tubing performance relationship* (TPR) (equation (9-2)) for production prediction; diagnosis, and optimization. The concept of system analysis allows the production system to be broken down into various segments (nodes) and each segment analyzed. This concept satisfies continuity (existence of specific pressure and rate associated with that segment/point). Since each node can be described as having an inflow and outflow, a combined solution of IPR ( $p_{wf}$  against  $q_{in}$ ) and TRP ( $p_{wf}$  against  $q_{out}$ ) will give production rate and corresponding flowing pressure at that node in the production system. Important nodes in a production system includes the wellhead, tubing completion equipment, pressure gauge/sensor, and perforations, which can be at the sandface or in the wellbore.

Well deliverability is important in various instances. During well testing the rate produced is limited by the test string/tubing size. It is, therefore, important to be able to predict the capacity of a well during production, when the well is most likely to be developed using a production tubing size different from that used during testing. It is also very important to be able to predict what the well can produce at different back pressures due to changes in choke settings or when well is tied to an existing facility.

During planning for well test operations, a system plot analysis it very important to asses if a well can deliver stable reservoir fluids to the surface. Where the well cannot produce to the surface or unstable flow is anticipated from the well deliverability assessment, it is very important to make contingency plan for provision of artificial lift systems.

During the life of a well or field, wellbore and reservoir conditions undergo changes that often have significant impact on well deliverability. Ability to predict, assess, and diagnose well deliverability during the entire life of a well or field is very import for managing hydrocarbon assets.

By varying either reservoir properties (from the IPR) and or tubing properties (from the TPR) different system solution can be achieved (Fig. 11.2). Predicting different possible system solutions is key for well sensitivity analysis and well production optimization. Well optimization involves determining system solutions that satisfies a set of defined objectives. Important objectives could be maximizing rate, profit, and recovery per well or entire field.

Decline in production of reservoir fluids can be due to reservoir or well problems. Some of the causes of production decline include: increase in water cut (coning, aquifer influx, water injection breakthrough), increase in wellhead pressure (higher flow line back pressure, facilities constraints), decrease in reservoir pressure (natural depletion, lack of support, high offtake), and well damage and scaling.

### 11.1. PRODUCTION SYSTEM ANALYSIS AT DIFFERENT NODES

Consider a reservoir with an average reservoir pressure ( $p_{Avg}$ ) measured at mid-reservoir, with the gauge placed at depth  $\Delta z_{Gauge}$  shallower than mid-reservoir (Fig. 11.3). The externally mounted gauge in a mandrel, which is in hydraulic communication with the tubing through the tubing wall, measures the tubing pressure.

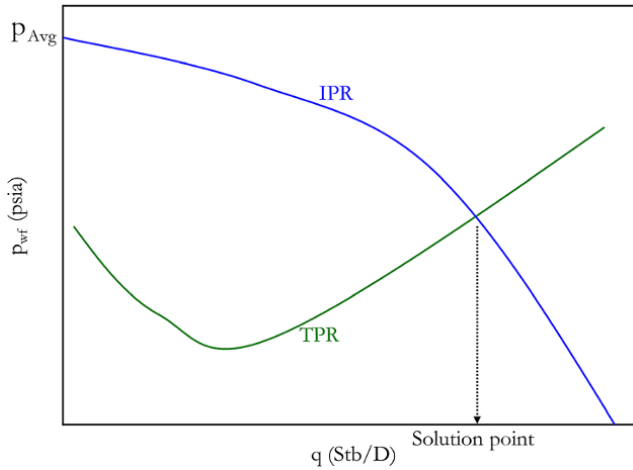


Figure 11.1 Production system plot showing a solution point.

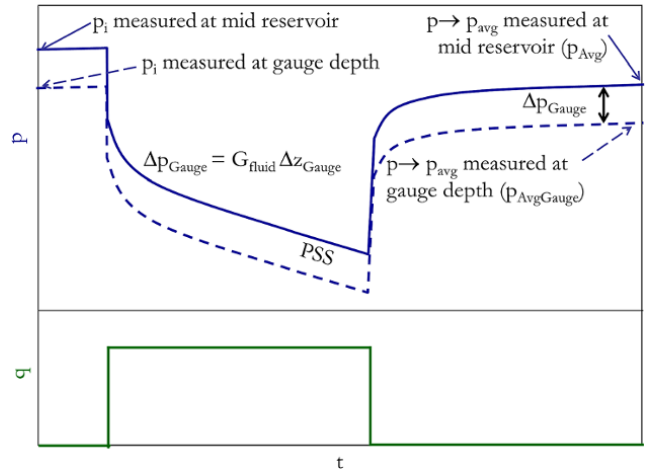


Figure 11.4 Difference in mid-reservoir and gauge pressure profile.

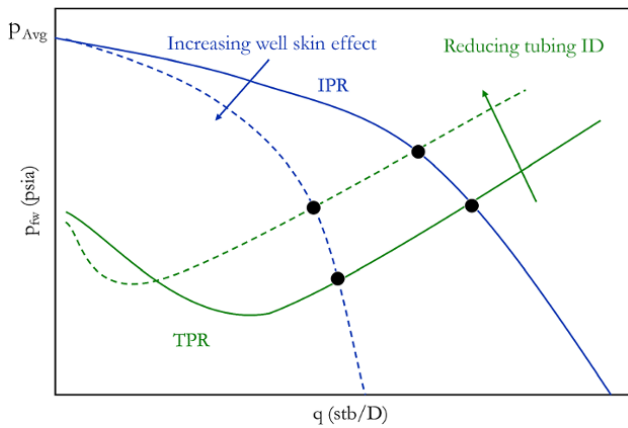


Figure 11.2 System solutions with changing tubing ID and wellbore skin effect.

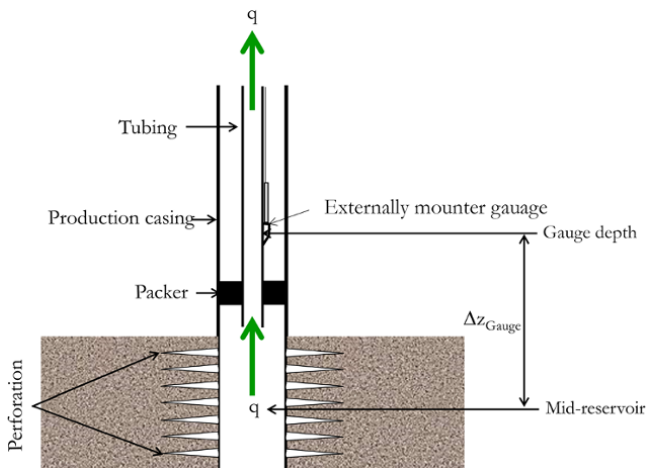


Figure 11.3 Well with gauge placed at a shallower depth than mid-reservoir.

The difference between pressure profile at mid-reservoir and gauge at shallower depth is shown in Fig. 11.4.

As shown in Fig. 11.4, a gauge placed at a shallower depth than the reservoir sandface would measure initial, flowing, shut-in, and average reservoir pressure lower than that at the reservoir sandface. If a well producing at a pseudosteady state is shut long enough to achieve constant and stable pressure, the well will attain average reservoir pressure (Exercise 9.5). The difference between the pressure measured at the mid-reservoir sandface and that at gauge depth shallower than mid-reservoir is called the *gauge pressure correction* relative to mid-reservoir and is expressed as:

$$\Delta p_{\text{Gauge}} = G_{\text{fluid}} (\Delta z_{\text{Gauge}}) \quad (11.1)$$

where  $G_{\text{fluid}}$  is the flowing gradient in the wellbore when the well is flowing and the static gradient in the wellbore when the well is shut-in, and  $\Delta z_{\text{Gauge}}$  is the elevation of the gauge above mid-reservoir.

Pressure correction could be relative to datum levels other than the mid-reservoir. Hence, the pressure difference or shift due to difference in vertical depth is broadly defined as *datum pressure correction*.

Fig. 11.5 shows an example of a system solution plot at mid-reservoir and gauge-depth nodes, where the gauge is placed shallower than mid-reservoir.

Fig. 11.5 shows that for steady state flow of fluids through tubing, both IPR and VLP would shift by the pressure correction defined by equation (11.1) but still retain the same solution. It is not uncommon to see the mistake of IPR being defined at mid-reservoir and TRP defined at gauge depth. In deep wells, gauges are often placed at a depth that is significantly shallower than the



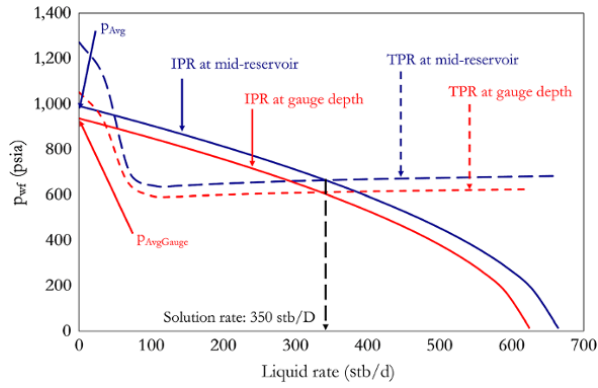


**Figure 11.5** System solution at mid-reservoir and gauge depth for steady state flow in well tubing.

top of the reservoir and, therefore, if the IPR and TPR from different reference points are combined, the system solution will be incorrect.

### 11.1.1. Design of Well Production System

The steps involved in building a well production system plot are summarized in Fig. 11.6. Where an existing production system to be modelled has an artificial lift system, the effect of the artificial lift system must be captured in the tubing performance relationship. Specification and design of artificial lift systems is discussed in Section 11.4.

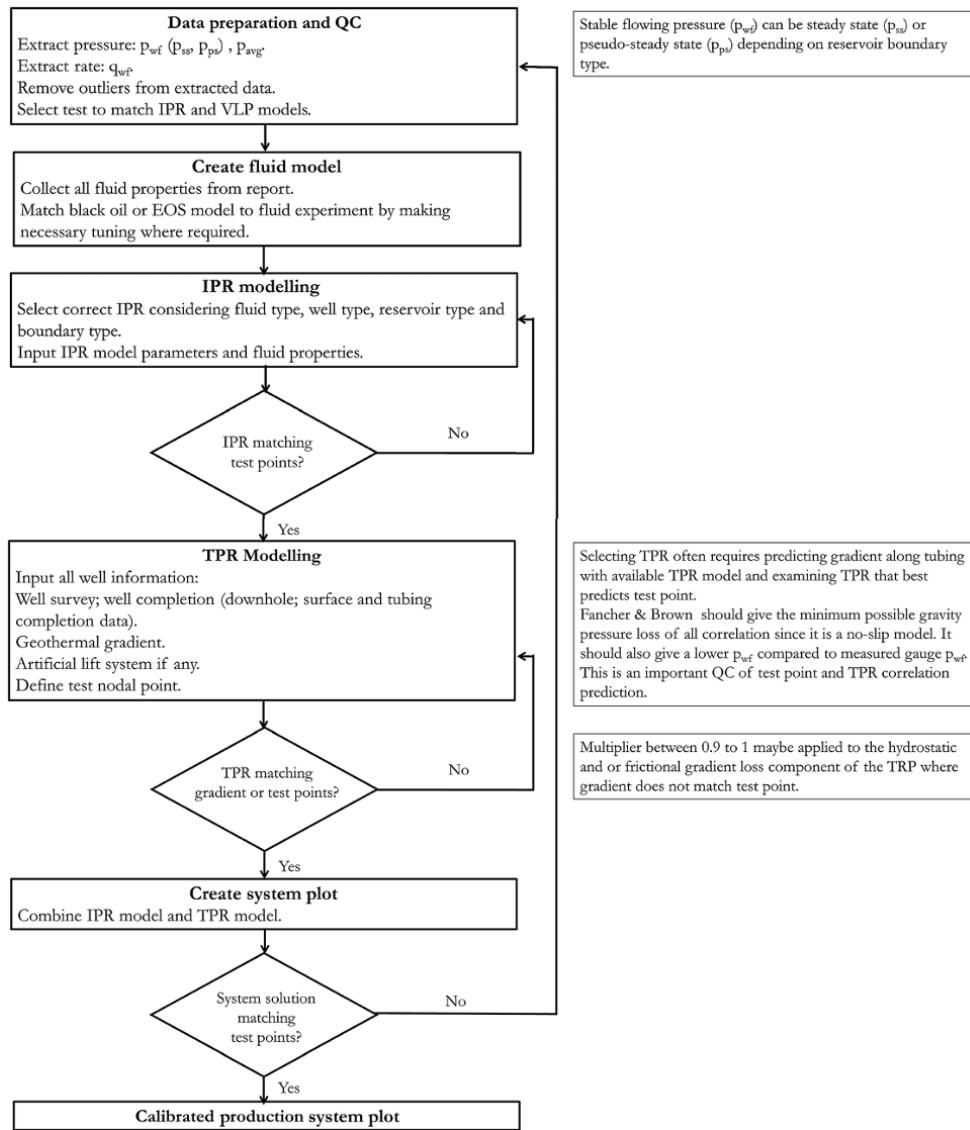


**Figure 11.6** Steps in designing a well production system.

## 11.2. TURNER VELOCITY

In low productivity gas–liquid wells, when the energy of flowing gas is not sufficient to lift liquid (water and or condensate) in the wellbore to the surface, loading of the well that may eventually kill the well can occur. Installation of tubing with small ID (less than 3 inches) or artificial lift methods are ways of dealing with liquid loading, as discussed in Section 11.4.

For liquid to flow to the well surface during production of a multiphase gas–liquid fluid without loading, the *Turner velocity* (drop terminal velocity) must be exceeded. The Turner velocity (also called the *Turner critical velocity*) defines the minimum velocity that must be exceeded to prevent liquid loading in a gas–liquid fluid flow in a well.

Turner critical velocity (drop terminal velocity) is defined as:

$$v_t = 1.593 \frac{\sigma^{\frac{1}{4}} (\rho_l - \rho_g)^{\frac{1}{4}}}{\rho_g^{\frac{1}{2}}} \text{ In EOF unit} \quad (11.2)$$

where  $\sigma$  is the surface tension (dynes/cm) and  $\rho$  is density (lbm/ft<sup>3</sup>).

There have been other publications after Turner's original work with essential differences being the changes in the coefficient in equation (11.2).

Gas density in equation (11.2) can be expressed as a function of pressure ( $p$ ) and compressibility factor ( $Z$ ) from equation (3.3):

$$\rho_g = \frac{m}{V} = \frac{pMW}{RT}$$

It is most common to think of gas flow in terms of rate rather than velocity, hence volumetric gas rate corresponding to the critical velocity is thus computed from critical velocity as:

$$q_g = \frac{3.067 p v_t A}{TZ} \text{ in MMscf/D} \quad (11.3)$$

where  $A$  is the area in ft<sup>2</sup>,  $p$  is the pressure in psia,  $v_t$  is the terminal velocity in ft/s,  $T$  is the temperature in °R, and  $Z$  is the gas compressibility  $Z$ -factor.

As shown in equation (11.3), increasing tubing diameter increases the velocity of the stream. Rearranging equation (11.3) and making internal tubing diameter the subject of the formula would define the maximum tubing size required to handle the liquid loading.

Given the internal cross-sectional area of tubing as:

$$A = \frac{\pi d^2}{4} \quad (11.4)$$

$d$  is inner tubing diameter.

Substituting  $A$  from equation (11.4) into equation (11.3) and making  $d$  the subject of the formula gives:

$$d = d_c = \sqrt{\frac{59.94 q_g TZ}{p v_c}} \quad (11.5)$$

where  $d_c$  is the critical tubing ID in inches.

## 11.3. EROSION VELOCITY

Erosion during production involves gradual wearing away of tubing and piping materials through abrasion. This leads to the thinning of tubing/piping and, eventually, mechanical failure and/or leakage of the tubing/piping. It is very important in production engineering to determine the maximum velocity/rate that will minimize erosion. API-14 [API, 1991] defines *erosion velocity* as:

$$v_e = \frac{C}{\sqrt{\rho}} \quad (11.6)$$

where  $v_e$  is the erosion velocity in ft/s,  $\rho$  is the density of flowing fluid through tubing/piping in lb/ft<sup>3</sup>,  $C$  is an empirical constant,  $v_e$  is a limiting velocity for producing a well to prevent erosion. API-14 (1991) suggests that for solid-free fluids, values of  $C = 100$  can be used for continuous service and  $C = 125$  for intermittent services. For solid-free fluids where corrosion is not anticipated or is controlled by inhibition or corrosion resistant alloys, values of 150–200 may be used for continuous service and values of 250 for intermittent service.

It is important to ensure that production rate or designed rate is not higher than the rate corresponding to the erosion velocity.

## 11.4. ARTIFICIAL LIFT METHODS

Artificial lift methods are techniques that are available to assist the flow of oil to the surface. In some cases, they are essential to the initial economic development of a hydrocarbon reservoir, whilst in other cases they are implemented later in the life of the field to maintain production at economic levels.

Artificial lift is necessary where the reservoir pressure is insufficient to lift fluids to the surface or produce at an economic rate. The principles of artificial lift involve reducing the bottomhole pressure to enable the reservoir to deliver the desirable amount of reservoir fluid. Design of an artificial lift system requires selecting the most appropriate artificial lift method and calculating the

parameters of the selected system to achieve the desired reservoir fluid production rate.

**11.4.1. Operating Principles of Artificial Lift Methods**

The basic operating principles of common artificial lift methods are summarized in Table 11.1.

**11.4.2. Selection and Design of Artificial Lift Systems for Productivity Enhancement**

Figures 11.11–11.16 show summaries of the operating conditions of different artificial lift systems. Operating conditions are one of the many factors to be considered when choosing an artificial lift system.

**Table 11.1** Basic Operating Principle of Artificial Lift Techniques.

Artificial lift method	Principle
Rod pump (Fig. 11.7).	Displacement of fluid due to vertical movement of rod, thereby reducing hydrostatic head and reducing bottomhole pressure.
Progressing cavity pump (PCP) (Fig. 11.8).	Displacement of fluid through rotational movement of a helical screw driven by a motor or sucker rod.
Hydraulic piston	Type of hydraulic pump systems that uses power fluid (usually light oil or water) that is injected from the surface to operate a downhole fluid engine and drives a piston to pump formation fluid and spent power fluid to the surface.
Electrical submersible pump (ESP) (see Section 11.4.3)	Displacement of fluid through rotational speed created by a motor-driven downhole centrifugal pump with power source at the surface.
Hydraulic jet	Type of hydraulic pump without moving parts. Power fluid, which is injected into a small-diameter nozzle in the pump body, mixes with formation fluid and is channeled through an expanding-diameter diffuser that increases the pressure of the mixture high enough to boost fluid flow to the surface.
Plunger lift (Fig. 11.9).	This involves the use of a free piston (plunger) that travels up and down in the well’s tubing string to clear slugs of liquid in the tubing, thereby reducing bottomhole flowing pressure. The plunger is controlled by a surface electronic controller and motor valve.
Gas lift (Fig. 11.10).	Injection of high-pressure gas from the surface into tubing through one or more subsurface valves to reduce the density of the fluid, which reduces the flowing fluid gradient and, finally, bottomhole flowing pressure. This reduction in bottomhole flowing pressure leads to a boost in production.

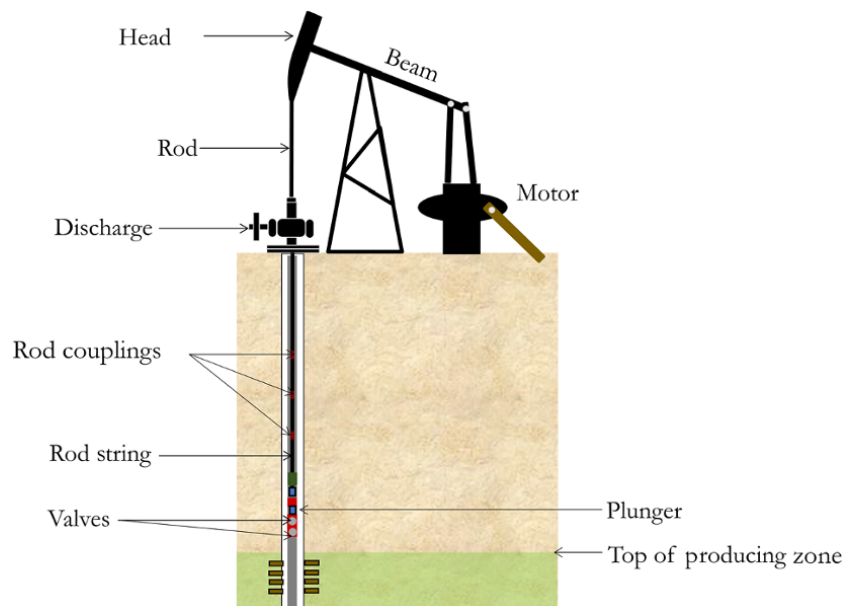


**Figure 11.7** Rod pump (sucker rod pump) system.

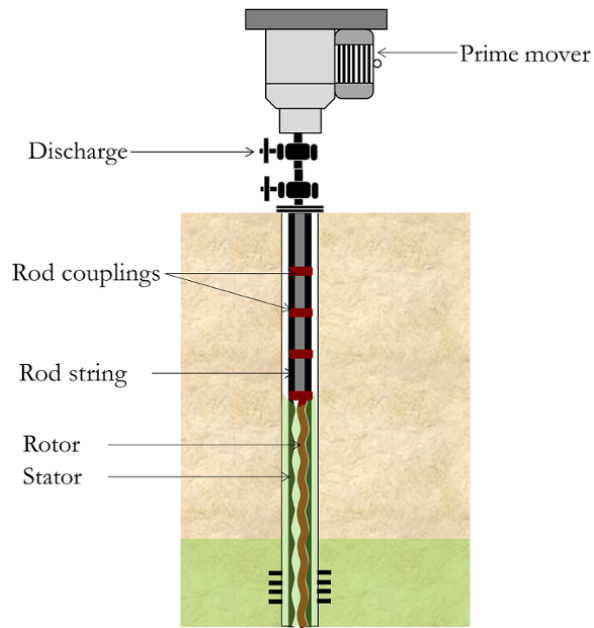


Figure 11.8 Progressing cavity pump (PCP).

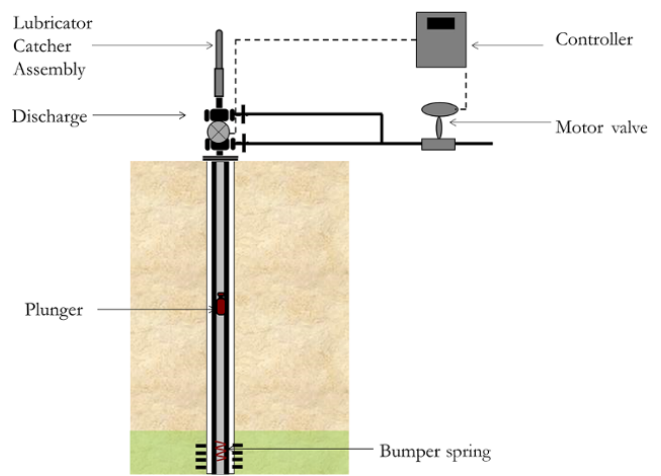


Figure 11.9 Plunger lift system.

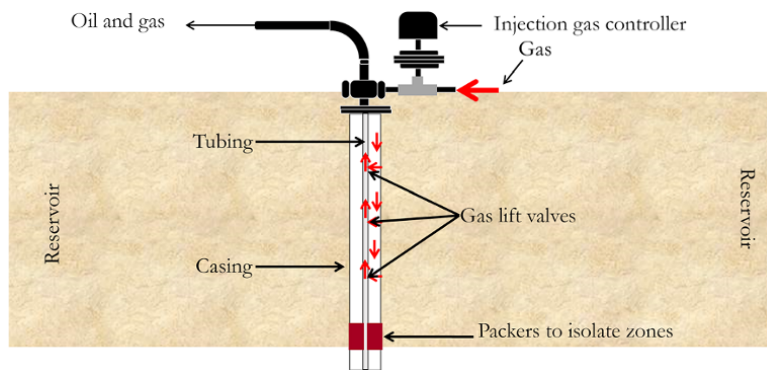


Figure 11.10 Gas lift system.

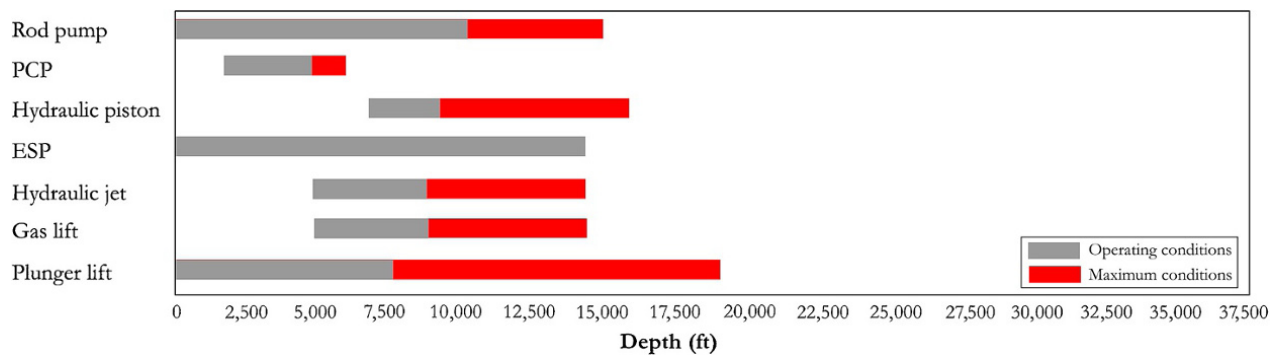


Figure 11.11 Operating depth range for different artificial lift methods.

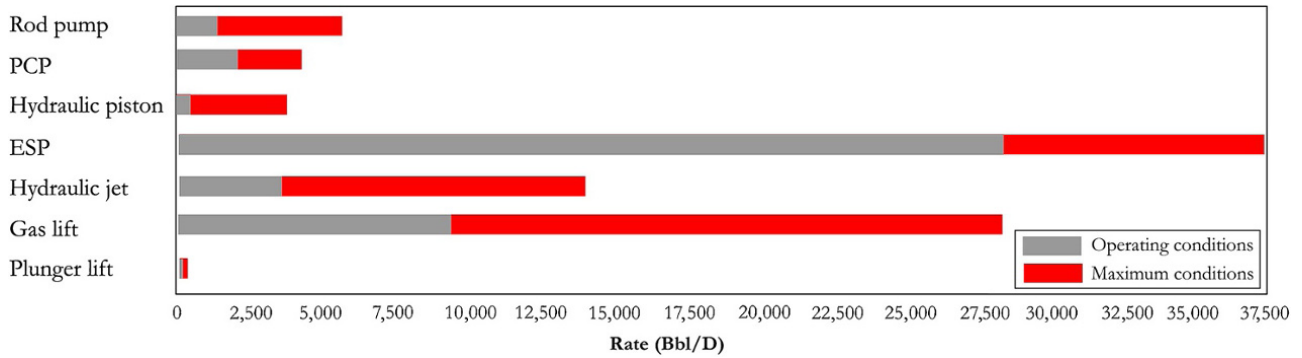


Figure 11.12 Operating rate range for different artificial lift methods.

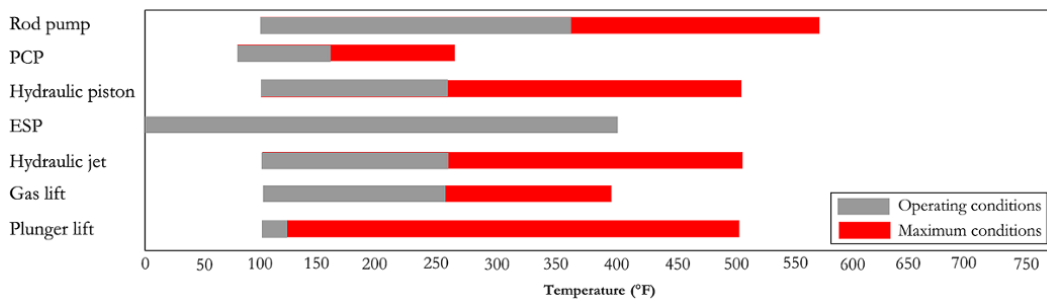


Figure 11.13 Operating temperature range for different artificial lift methods.

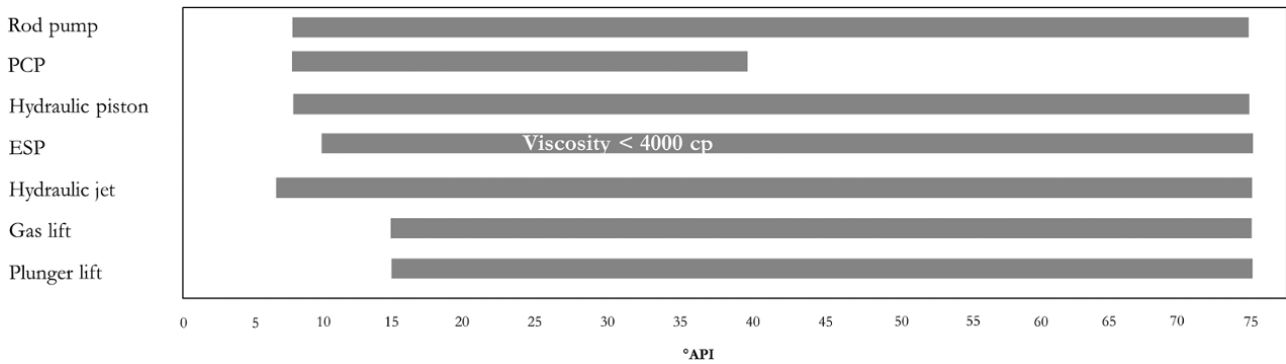


Figure 11.14 Operating fluid API° range for different artificial lift methods.



Figure 11.15 Solid handling capability for different artificial lift methods.

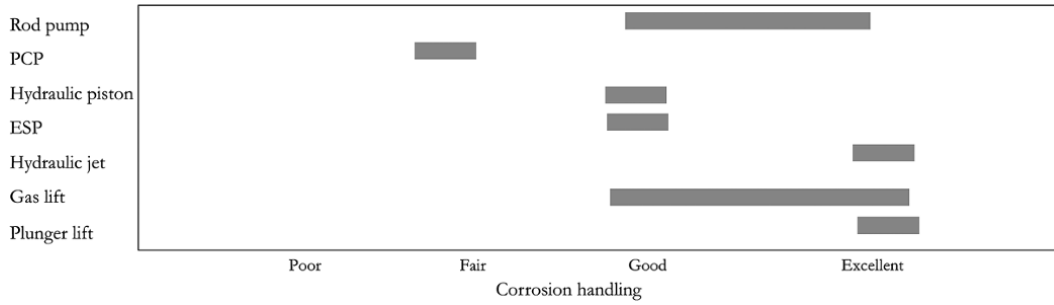


Figure 11.16 Corrosion handling capability for different artificial lift methods.

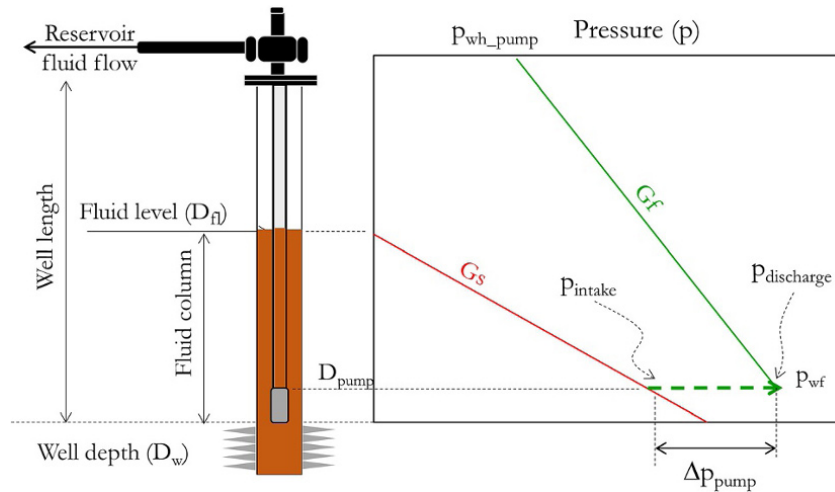


Figure 11.17 Electrical submersible pump in a well.

Fig. 11.11 defines operating depth range. Fig. 11.12 defines operating rate range. Fig. 11.13 defines operating temperature range. Fig. 11.14 defines operating fluid API° range. Fig. 11.15 defines solid handling capability. Fig. 11.16 defines corrosion handling capability for different artificial lift methods.

### 11.4.3. Electrical Submersible Pump (ESP)

When a well is loaded with liquid, an electrical submersible pump (ESP) can be used to displace the fluid column to the surface, making the liquid hydrostatic pressure at the bottom of the well lower than the well bottomhole flowing pressure, and hence making fluid flow into the well.

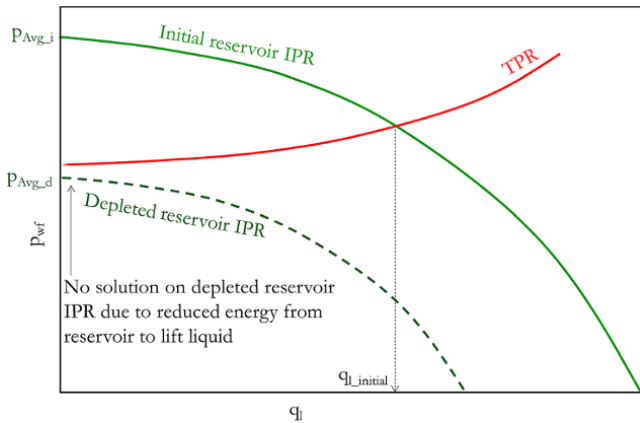
**11.4.3.1. Design and Optimization of an ESP.** As shown in Fig. 11.17, the well is loaded with liquid to level  $D_{fl}$ , exerting hydrostatic pressure on the reservoir sandface that is equal to the bottomhole flowing pressure. Hence, not making the fluid flow from reservoir into the well. To achieve a flowing gradient ( $G_f$ ) sufficient to

flow from the well to the surface, an ESP can be installed to add a pressure difference of  $\Delta p_{pump}$ , which is equal to the difference between the pump discharge and pump intake (Fig. 11.17). When  $\Delta p_{pump}$  is added to tubing at the depth  $D_{pump}$ , fluid will be discharged to the surface at a rate  $q_{design}$  with a flowing tubing gradient  $G_f$  and a wellhead pressure  $p_{wh\_pump}$ .

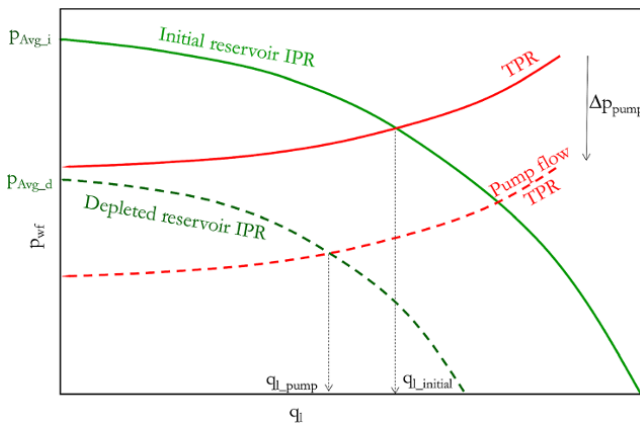
When the energy in a reservoir is not enough or the reservoir pressure has declined to level where it cannot unload a well liquid, build-up of liquid in the well will occur and, eventually, the well may die. The inability of the well to deliver to the surface is characterized by the IPR not intersecting TPR curve on the production system plot (Fig. 11.18).

Fig. 11.18 shows a well producing from a reservoir with an average initial reservoir pressure of  $p_{Avg\_i}$  and producing at  $q_{l\_initial}$ . When the average reservoir pressure depletes to  $p_{Avg\_d}$ , the well cannot produce to the surface, as shown by the depleted reservoir IPR not intersecting with the TPR.

When an ESP is installed, energy is added to the fluid in the system, thereby creating a reduced pressure gradient in



**Figure 11.18** Production system solution for initial and depleted reservoir conditions.



**Figure 11.19** System solution for depleted reservoir condition with ESP.

the tubing and thus allowing fluid to flow from the reservoir and then to the surface, as illustrated by the intersection of the depleted reservoir IPR and reduced pump flow TPR (Fig 11.9).

Evaluating the performance of an ESP and selecting the correct ESP to produce the desired additional pressure ( $\Delta p_{pump}$ ) and discharge pressure at designed liquid rate is important. It is also crucial that selected pumps run optimally during their lifetime. Pumps are described by their performance curve. An example of a pump performance curve is shown in Fig. 11.20.

The energy of centrifugal pumps (including ESP) are often described in terms of *head*, with the unit of length rather than pressure because pressure from a pump is dependent on fluid specific gravity but head is independent of specific gravity. The relationship between pressure and head is expressed as:

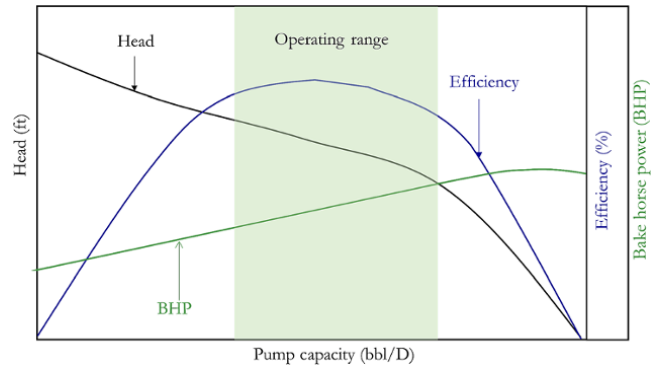


**Figure 11.20** Pump performance curve at a particular frequency.

$$H(\text{ft}) = \frac{p(\text{psig})}{0.43 \times \text{specific gravity}} \quad (11.7)$$

The performance curve in Fig. 11.20 shows that a higher head causes the pump to deliver less flow. The performance curve also shows the power curve. The power curve shows a fairly linear relationship between power and pump flow capacity, and indicates that higher power is required to deliver higher flow rate. The performance curves also show ESP efficiency over a range of pump flow rate capacity. The efficiency of an ESP increases with pump capacity rate initially then diminishes. The *best efficiency of the pump* (BEP) corresponds to the pump capacity rate that gives highest pump efficiency. It is important to operate the pump as close to BEP as possible, to minimize the cost of running the pumps and ensuring longevity of pumps. The pump head curve can be displayed at different frequencies, as shown in Fig. 11.21.

The total dynamic (pump) head ( $H_{TD}$ ) required to deliver the desired flow rate is the sum of net vertical lift ( $H_L$ ), frictional head loss in tubing ( $H_f$ ), and wellhead pressure head ( $H_{wh}$ ):

$$H_{TD} = H_L + H_f + H_{wh} \quad (11.8)$$

#### 11.4.4. Gas Lift

Gas lift generally involves aerating the production tubing column by injecting gas through a surface choke or valve, down the tubing-casing annulus, then through gas lift valves located on mandrels. Gas lift valves control the flow of injected gas from the tubing-casing annulus into the production tubing. Availability of gas is an important factor when considering a gas lift as the artificial lift for a single well or multiple wells in a field.

A gas lift can be *intermittent*, where high pressure gas is injected into tubing to instantaneously displace slugs of liquid in a cyclic approach. In this kind of approach, high

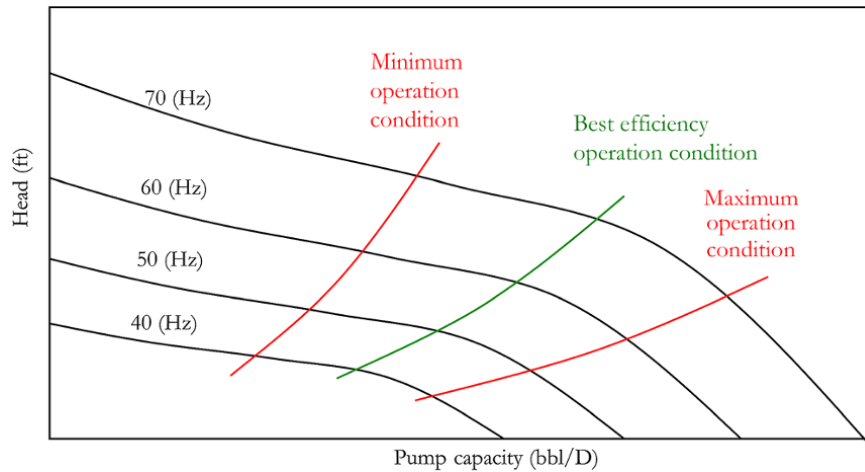


**Figure 11.21** Pump head curve for an ESP with variable frequency drive.

pressure is required during lifting slugs of loaded liquid in the wellbore to the surface. In an intermittent gas lift, handling of gas production at the surface can be challenging due to the cyclical nature of gas injection into the tubing.

A *continuous gas lift*, which is more common, involves the continuous injection of gas to augment the formation gas.

A gas lift can be designed in many ways with different assumptions. However, the fundamental concept is the same – gas is injected to reduce the pressure gradient of the fluid in the production tubing. A common gas lift design approach is that based on API 11v6 [API, 1999].

With sufficient gas volume and operating injection pressure at the surface, a gas lift provides an easily adaptable artificial lift option in terms of depth of injection and well deliverability. A gas lift is operationally challenging for offshore facilities due to limited availability of space for the compressor. A gas lift is also not suitable for high viscosity fluids.

The gas lift valve is a critical part of the gas lift system. Its primary function is aerating wells using gas supplied. *Conventional gas lift valves* have the gas lift mandrel and reverse check valve as part of the production tubing and, hence, require pulling out of the tubing when replacement of gas lift valve is required. *Wireline-retrievable gas lift valves*, which have become common, have the advantage of been able to be installed without killing the well or pulling out production tubing.

A gas lift system can have single or multiple valves depending on available gas volume and surface operating injection-gas pressure. Multiple gas lift valves make it possible to operate gas lift operations at a greater depth than a single gas lift valve. *Unloading valves* are gas lift valves above the *operating valve* and are used mainly at the start

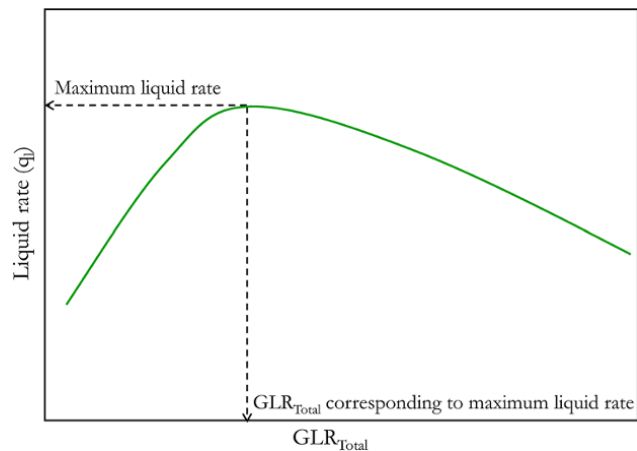


**Figure 11.22** Liquid rate sensitivity to total gas liquid ratio.

of production to *kick-off* or *unload* a well by reducing the density of the liquid above the operating valve, which is often the deepest valve.

**11.4.4.1. Design of a Gas Lift System.** The design of a gas lift system will generally involve:

- (i) Determination of the depth of unloading and operating gas lift valves.
- (ii) Determination of the operating condition of the valves.
- (iii) Determination of the test-rack opening pressure of gas lift valves.

Liquid rate ( $q_l$ ) sensitivity to total gas–liquid ration ( $GLR_{Total}$ ) (Fig. 11.22) can be used to determine maximum or optimum total gas–liquid ratio and, hence, design volumetric rate of injection gas. The relationship between the amount of injected gas (additional gas) required to



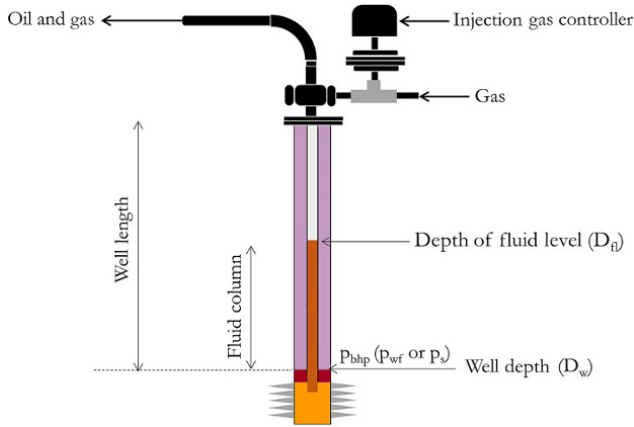


Figure 11.23 Well loaded with liquid.

achieve the desired liquid (or oil rate) and  $GLR_{Total}$  can be expressed as:

$$GLR_{Total} = \frac{GLR_{initial} q_l + q_{g\_inj}}{q_l} \quad (11.9)$$

where  $q_{g\_inj}$  is the designed injected gas and  $GLR_{initial}$  is the initial gas–liquid ratio before gas injection.

Equation (11.9) shows that increasing  $q_{g\_inj}$  increases  $GLR_{Total}$ .

Increasing the gas injection rate ( $q_{g\_inj}$ ), causing an increase in  $GLR_{Total}$ , will reduce fluid mixture density and increase velocity. Reduction in mixture density reduces the hydrostatic pressure gradient (equation (10.18)), while increasing velocity increases the frictional pressure gradient loss (equation (10.19)). Since the total flowing fluid gradient (equation (10.17)) is primarily the sum of hydrostatic pressure gradient and frictional pressure gradient, the effect of increasing gas injection rate ( $q_{g\_inj}$ ), and hence increasing  $GLR_{Total}$ , would be the reduction in hydrostatic pressure gradient and increase in frictional pressure gradient loss. With increasing  $q_{g\_inj}$  causing increasing liquid rate ( $q_l$ ), as shown in Fig. 11.22, a threshold is reached where friction pressure gradient increase is greater than hydrostatic pressure gradient reduction. At this point, called the *gradient reversal point*, the total pressure gradient increases and  $q_l$  reduces with further increases in  $q_{g\_inj}$  (or  $GLR_{Total}$ ).

With the target liquid rate and total gas liquid ratio determined, the production flowing pressure gradient along the well tubing is calculated using methods such as that in Chapter 10 (10.4.4). With known tubing gradient, flowing pressure at any depth in the well under gas lift condition can be determined.

Fig. 11.23 shows a well considered for gas lift with liquid loaded depth  $D_{fl}$ .

The pressure profiles with depth along tubing with loaded liquid and casing with injection gas for the well

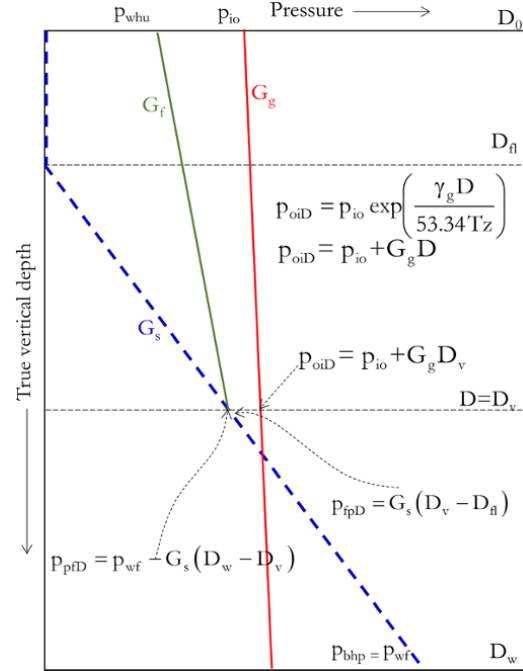


Figure 11.24 Pressure profiles with depth along tubing and casing.

in Fig. 11.23 are shown in Fig. 11.24. The operating injection pressure increases with depth from surface operating injection pressure.

Since the cross-sectional area of the tubing-casing annulus is significantly larger than the cross-sectional area of the gas lift valve, the gas velocity in the annulus is essentially close to zero; hence, the operating injection-gas pressure at any depth can be determined from the static gas pressure (static injection-gas pressure traverse). The operating injection-gas pressure at any depth in the casing can, therefore, be expressed as:

$$p_{oiD} = p_{io} \exp\left(\frac{\gamma_g D}{53.34 TZ}\right) \quad (11.10)$$

where  $p_{io}$  is the surface operating injection-gas pressure (psia),  $\gamma_g$  is the specific gas gravity (relative to air = 1),  $D$  is the true vertical depth (ft),  $T$  is the average gas temperature ( $^{\circ}R$ ), and  $Z$  is the average gas compressibility factor, which is dependent on pressure ( $p$ ) and temperature ( $T$ ).

Using equation (11.10) to calculate  $p_{oiD}$  is iterative, as  $Z$  is a function of  $p_{oiD}$ .

Equation (11.10) can, however, be expressed in terms of injection-gas gradient as:

$$p_{oiD} = p_{io} + G_{gas} D \quad (11.11)$$

where  $G_{gas}$  is the gas gradient.

The level of static fluid can be within the well or at the well surface. The level of liquid in a loaded well can be determined using:

$$D_{fl} = D_w - \frac{P_{bhp}}{G_s} \quad (11.12)$$

where  $D_{fl}$  is fluid level in the well,  $p_{bhp}$  is bottomhole pressure, and  $G_s$  is static fluid gradient of fluid in the well.

**11.4.4.2. Deepest Valve Installation.** A set pressure difference between the operating injection-gas pressure ( $p_{ioD}$ ) and flowing production pressure ( $p_{pFD}$ ) at the maximum valve depth can be used to locate maximum valve depth ( $D = D_{v\_max}$ ). This difference in pressure ( $p_D = p_{ioD} - p_{pFD}$ ) is usually between 100 and 200 psi at maximum valve depth.

From Fig. 11.24,  $p_{pFD}$  at maximum valve depth ( $p_{pFDv\_max}$ ) can be expressed as:

$$p_{pFDv\_max} = p_{oi} + G_g D_{v\_max} - p_D \quad (11.13)$$

where  $p_D$  is the difference between  $p_{ioD}$  and  $p_{pFD}$  at maximum valve depth, and  $D_{v\_max}$  is the maximum valve depth.

Also from Fig. 11.24:

$$G_s = \frac{(p_{wf} - p_{pFDv\_max})}{(D_w - D_{v\_max})} \quad (11.14)$$

Making  $p_{pFDv\_max}$  the subject of formula in equation (11.14)

$$p_{pFDv\_max} = p_{wf} - G_s(D_w - D_{v\_max})$$

Substituting  $p_{pFDv\_max}$  from the above into equation (11.13)

$$p_{wf} - G_s(D_w - D_{v\_max}) = p_{oi} + G_g D_{v\_max} - p_D$$

$$G_s D_{v\_max} - G_g D_{v\_max} = p_{oi} - p_D - p_{wf} + G_s D_w$$

$$D_{v\_max} = \frac{p_{oi} - p_D - p_{wf} + G_s D_w}{(G_s - G_g)}$$

Hence the maximum valve depth can be expressed as:

$$D_{v\_max} = \frac{p_{oi} - p_D - p_{wf} + G_s D_w}{(G_s - G_g)} \quad (11.15)$$

**11.4.4.3. Well Flowing Gradient.** The tubing performance relationship (TPR) with total gas-oil relationship defined to account for the supplemented gas lift supply can be used to define the flowing fluid gradient in the well. However, since the tubing pressure from wellhead to reservoir (top to bottom) should be the same as from reservoir to wellhead (bottom to top) in a gas lift design,

the well flowing gradient between  $D_v$  and  $D_0$  can be expressed as:

$$G_f = \frac{P_{pFD} - P_{whu}}{D_v} \quad (11.16)$$

Determining  $p_{pFD}$  from Fig. 11.24 using  $G_s$ ,  $D_v$ , and  $D_{fl}$ :

$$p_{pFD} = G_s(D_v - D_{fl}) \quad (11.17)$$

Substituting  $p_{pFD}$  from equation (11.17) into equation (11.16):

$$G_f = \frac{G_s(D_v - D_{fl}) - p_{whu}}{D_v} \quad (11.18)$$

where  $p_{whu}$  is the unloading wellhead pressure.

**11.4.4.4. Calculating Depth of Unloading Gas Lift Valves.** When gas injected through the first valve displaces fluid from the top section of the tubing, pressure in the annulus decreases. As injected gas flows through the second valve, injection pressure reduces, leading to closure of the first valve. This sequence of opening of lower valves continues until the deepest gas lift valve opens.

The opening and closing of a gas lift can be controlled primarily by injection-gas pressure (injection-pressure operated valves) or production fluid pressure (production-pressure operated valves).

The first unloading valve is the maximum depth that will allow U-tubing of load fluid at the depth and expressed as:

$$D_1 = \frac{(p_{ko} - \Delta p_a - p_{whu})}{G_s} \quad (11.19)$$

where  $D_1$  is the depth of the top gas lift valve from the wellhead,  $p_{ko}$  is the surface kick-off injection pressure or available surface operating injection pressure,  $p_{whu}$  is the surface wellhead unloading tubing pressure,  $G_s$  is the static-load fluid gradient (psi/ft), and  $\Delta p_a$  is the assigned valve spacing pressure differential at valve depth.

The concept of gas lift design discussed in this book is based on API 11v6 [API, 1999]. This approach is established on the basis that all gas lift valves having the same port size and system have a constant decreasing injection-gas pressure for successive lower gas lift valves. The pressure decrease in subsequent lower gas lift valves is based on the specifications of the gas lift valve. The pressure decrease is always defined to reduce the likelihood of the upper valves remaining open during lifting from lower valves.

The depth of the second gas lift valve is calculated on the basis of the assigned valve spacing pressure differential at valve depth ( $\Delta p_a$ ) (Fig. 11.25) and the minimum decrease in surface operating injection-gas pressure

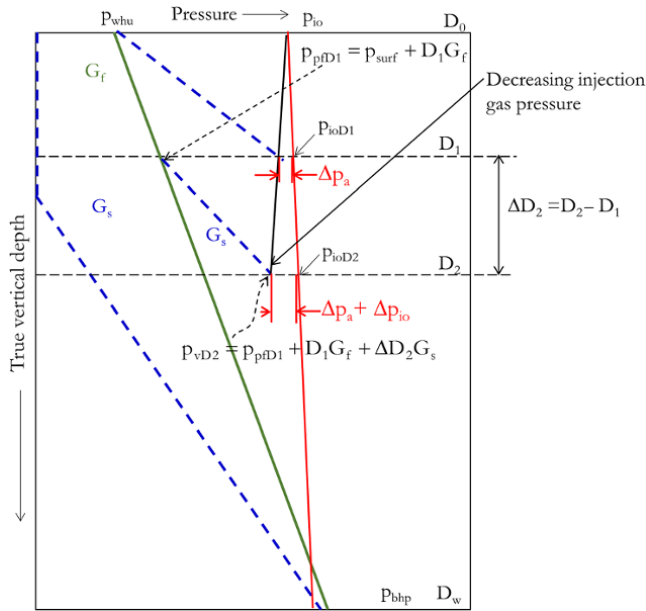


**Figure 11.25** Calculating the depth of the second unloading gas lift valve.

between valves ( $\Delta p_{io}$ ), and is assigned based on gas lift valve specifications:

$$p_{whu} + G_f D_1 + G_s (D_2 - D_1) = p_{ioD2} - \Delta p_a - \Delta p_{io} \quad (11.20)$$

From Fig. 11.25, the operating gas injection pressure at  $D_2$  is:

$$p_{ioD2} = p_{io} + G_g D_2 \quad (11.21)$$

Substituting  $p_{ioD2}$  in equation (11.21) into equation (11.20):

$$p_{whu} + G_f D_1 + G_s (D_2 - D_1) = p_{io} + G_g D_2 - \Delta p_a - \Delta p_{io}$$

Making  $D_2$  the subject of the formula:

$$p_{whu} + G_f D_1 + G_s D_2 - G_s D_1 = p_{io} + G_g D_2 - \Delta p_a - \Delta p_{io}$$

$$G_s D_2 - G_g D_2 = p_{io} - \Delta p_a - \Delta p_{io} + G_s D_1 - G_f D_1 - p_{whu}$$

$$D_2 (G_s - G_g) = p_{io} - \Delta p_a - \Delta p_{io} + G_s D_1 - G_f D_1 - p_{whu}$$

$$D_2 = \frac{p_{io} - \Delta p_a - \Delta p_{io} + D_1 (G_s - G_f) - p_{whu}}{(G_s - G_g)} \quad (11.22)$$

Subsequently deeper valves are determined with decreasing injection-gas pressure by  $\Delta p_{io}$ . The depth of the third gas lift valve is hence determined as:

$$D_3 = \frac{p_{io} - \Delta p_a - 2\Delta p_{io} + D_2 (G_s - G_f) - p_{whu}}{(G_s - G_g)} \quad (11.23)$$

Calculation of the depth of the third valve from the top is shown graphically in Fig. 11.26.

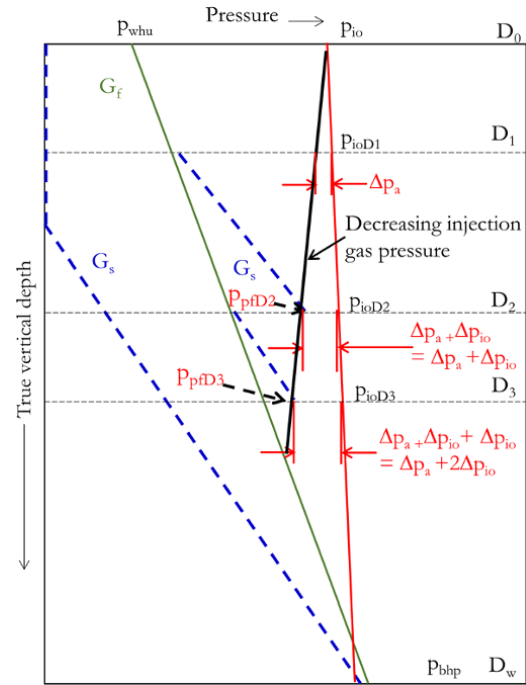


**Figure 11.26** Calculating the depth of the third valve from the top.

The depth of the fourth valve is determined in similar way to the third using:

$$D_4 = \frac{p_{io} - \Delta p_a - 3\Delta p_{io} + D_3 (G_s - G_f) - p_{whu}}{(G_s - G_g)} \quad (11.24)$$

The depth of the  $n$ th valve ( $D_n$ ) is hence calculated as:

$$D_n = \frac{p_{io} - \Delta p_a - (n-1)\Delta p_{io} + D_{n-1} (G_s - G_f) - p_{whu}}{(G_s - G_g)} \quad (11.25)$$

When  $p_{ioD}$  is significantly higher than the production flowing pressure ( $p_{wf}$ ), an additional production-pressure effect for the top gas lift valve ( $\Delta p_{pe}$ ) is also included in the pressure decrease for successive valves (Fig. 11.27).  $\Delta p_{pe}$  represents the decrease in operating injection-gas pressure for each succeeding lower gas lift valve without  $\Delta p_{io}$ .

The pressure difference due to the production effect for the top valve ( $\Delta p_{ppe1}$ ) can be determined using:

$$\Delta p_{ppe1} = (p_{pflmax} - p_{pflmin}) F \quad (11.26)$$

where  $F$  is the production-pressure factor, and  $p_{pflmax}$  and  $p_{pflmin}$  are defined in Fig. 11.27.

#### 11.4.4.5. Valve Unloading and Operating Temperature.

Assuming a linear temperature gradient between the wellhead ( $D_0$ ) – with a temperature of  $T_{whu}$  – and the

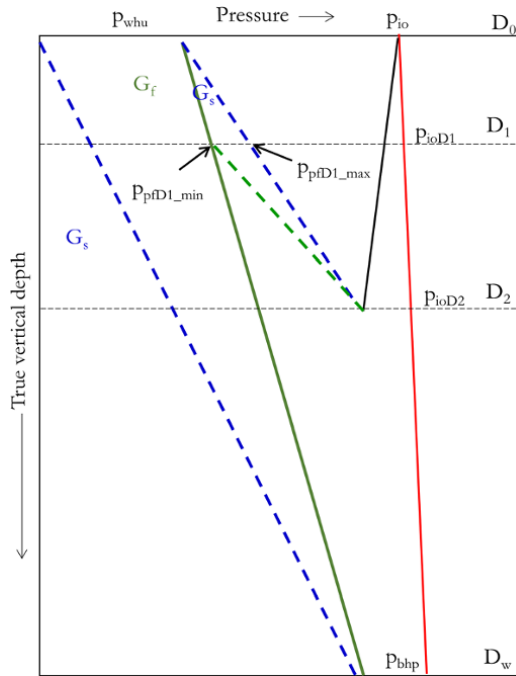


**Figure 11.27** Production effect pressure drop when  $p_{ioD}$  is significantly higher than  $p_{wf}$ .

bottom of the well ( $D_w$ ) – with a temperature of  $T_w$  – the temperature of the unloading and operating valves at depth  $D$  can be expressed as:

$$T_{uvD} = T_{whu} + D \frac{(T_w - T_{whu})}{D_w} \quad (11.27)$$

where  $T_w$  is the bottomhole temperature,  $T_{whu}$  is the unloading wellhead temperature, and  $D_w$  is the depth of the bottom of the tubing.

The temperature gradient is used to determine the temperature of the unloading and operating valves at different depths.

**11.4.4.6. Gas Lift Valve and Chokes.** The size of the choke or valves in a gas lift system plays a critical role in the performance of the gas lift valve system. A high volumetric flow of gas may not flow through a choke or valve of limited size.

The volumetric flow of gas through valves and choke under noncritical flow conditions can be expressed as:

$$q_{gsc} = \frac{155.5C_d(A)p_1 \sqrt{2(g)\left(\frac{k}{k-1}\right) \left[ (F_{du})^{\frac{2}{k}} - (F_{du})^{\frac{k+1}{k}} \right]}}{\sqrt{\gamma_g(T_1)}} \quad (11.28)$$

where  $q_{gsc}$  is the gas flow rate at standard conditions (Mscf/D),  $C_d$  is the discharge coefficient,  $A$  is the area

of the opening (inches),  $p_1$  is the upstream pressure (psia),  $p_2$  is the downstream pressure (psia),  $g$  is acceleration due to gravity ( $ft/s^2$ ),  $k$  is the ratio of specific heat,  $T_1$  is the upstream temperature ( $^{\circ}R$ ), and  $F_{du}$  is the ratio of downstream pressure to upstream pressure defined as:

$$F_{du} = F_{cf} \text{ if } F_{du} < F_{cf}$$

and

$$F_{du} = \frac{p_2}{p_1} \geq F_{cf}$$

where  $F_{cf}$  is the critical flow pressure ratio defined as:

$$\left( \frac{2}{k+1} \right)^{\left( \frac{k}{k-1} \right)}$$

**11.4.4.7. Gas Lift Valve Closing Pressure.** The closing force of a gas lift valve can either be by *charged bellows*, which exert force over an effective bellows areas, or spring force or both. Hence, a pressure greater than the back pressure exerted by the charged bellows or spring must be overcome for the valve to open. The most widely used gas lift valve is the *unbalanced single-element bellows-charged gas lift valve*, which consists of a bellows and dome assembly. Nitrogen is the most commonly used charge gas for gas-lift valves due to its physical properties at various temperatures and pressures, the available supply of nitrogen all over the world, and the affordability and noncorrosive nature of nitrogen.

Initial injection-gas opening pressure for injection-pressure operated (IPO) gas lift valves ( $p_o$ ) can be calculated based on the balance of forces between the opening and closing of the gas lift valves:

Opening Forces = Closing Forces

$$p_o(A_b - A_v) + p_t A_v = p_{bt} A_b + S_t(A_b - A_v)$$

$$p_o(A_b - A_v) = p_{bt} A_b + S_t(A_b - A_v) - p_t A_v$$

$$p_o = \frac{p_{bt}}{\left( \frac{A_b - A_v}{A_b} \right)} + S_t - p_t \left( \frac{A_v}{A_b - A_v} \right)$$

$$p_o = \frac{p_{bt}}{1 - \left( \frac{A_v}{A_b} \right)} - p_t \left( \frac{\frac{A_v}{A_b}}{1 - \frac{A_v}{A_b}} \right) \quad (11.29)$$

and the closing pressure of a gas lift valve can be expressed as:

$$p_{vc} = \left( 1 - \frac{A_v}{A_b} \right) \left( \frac{p_{bt}}{1 - \frac{A_v}{A_b}} \right) \quad (11.30)$$

where  $p_{bt}$  is the pressure in the bellows at operating temperature (psig),  $A_b$  is the area of the bellow ( $\text{in}^2$ ),  $p_o$  is the opening pressure of the gas lift valve with tubing effect (psig),  $A_v$  is the area of valve port ( $\text{in}^2$ ), and  $S_t$  is the effective spring tension (psig).

From equation (11.30), if the closing force of the gas lift valve is by *charged bellows* only,  $S_t$  becomes zero and the valve will close at the pressure exerted by the bellows at operating temperature ( $p_{bt}$ ).

Since it is unrealistic to set each gas lift valve at its well operating temperature, the test-rack opening or closing pressure is set at a standard base temperature. Bellows are charged at a standard condition of  $40^\circ\text{F}$ . The relationship between  $p_{bt}$  and  $p_b$  is expressed as:

$$p_{bt} = p_b \times \frac{Z_T (460 + T_v)}{Z_{60^\circ\text{F}} 520} \quad (11.31)$$

where  $p_b$  is the pressure in the bellows at  $60^\circ\text{F}$  (psig),  $T_v$  is the valve unloading or operating temperature ( $^\circ\text{F}$ ),  $Z_T$  is the compressibility of the gas in the bellows at valve unloading or operating temperature  $T$  ( $^\circ\text{F}$ ), and  $Z_{60^\circ\text{F}}$  is the compressibility of the gas in the bellows at  $60^\circ\text{F}$ .

### Exercise 11.1 Continuous Gas Lift Design

A well with  $3\frac{1}{2}$ -inch tubing and a depth of 7,990 ft is producing from a  $40^\circ\text{API}$  reservoir with bottomhole temperature (BHT) of  $220^\circ\text{F}$ . The well is loaded with fluid at 0.43 psi/ft static gradient. It is desired to produce 1,305 stb/d of oil with a tubing head pressure (THP) of 60 psia, wellhead temperature (WHT) of  $100^\circ\text{F}$  and reservoir IPR of  $p_{wf}(\text{psia}) = -0.04q_o + 2,048.2$ . Design a continuous gas lift system given an available surface injection-gas pressure of 860 psia with casing injection gradient of 0.02 psi/ft, given an assigned valve spacing pressure differential at valve depth ( $\Delta p_a$ ) of 50 psia and minimum decrease in surface operating injection gas pressure between valves ( $\Delta p_{io}$ ) of 15 psia. The deepest valve can be determined with a 200 psia difference between  $p_{ioD}$  (operating injection-gas pressure) and  $p_{pFD}$  (flowing production pressure) at the maximum valve depth (i.e.  $p_D = 200$  psia).

#### Solution Steps.

*Step 1:* depth of unloading gas lift valves:

(i) Determine  $p_{wf}$  for the target rate using the IPR equation given.

(ii) Determine the fluid level in the well using equation (11.12).

(iii) Determine the deepest gas lift valve using equation (11.15).

(iv) Determine the flowing tubing gradient using equation (11.18).

(v) Calculate the depth of the first gas lift valve using equation (11.19), the depth of the second using equation (11.22), the depth of the third using equation (11.23), the

depth of the fourth using equation (11.24), and of the others using the generalized equation for the  $n$ th valve defined by equation (11.25). The depth of the valves can also be solved graphically.

*Step 2:* determine the unloading and operating valve temperatures using equation (11.27):

#### Solution.

$p_{wf}$  for the target rate of 1,305 stb/d of oil:

$$p_{wf} = -0.04q_o + 2,048.2$$

$$p_{wf} = -0.04 \times 1,305 + 2,048.2 = 1,966 \text{ psia}$$

Fluid level ( $D_{fl}$ ) using equation (11.12):

$$D_{fl} = D_w - \frac{p_{bhp}}{G_s}$$

where  $p_{bhp} = p_{wf}$

$$D_{fl} = 7,990 - \frac{1,996}{0.43} = 3,348.14 \text{ ft}$$

The deepest gas lift valve using equation (11.15):

$$D_{v\_max} = \frac{p_{oi} - p_D - p_{wf} + G_s D_w}{(G_s - G_g)}$$

$$D_{v\_max} = \frac{860 - 200 - 1,996 + 0.43 \times 7,990}{(0.43 - 0.02)} = 5,121.22 \text{ ft}$$

Calculating flowing tubing gradient using equation (11.18):

$$G_f = \frac{G_s(D_v - D_{fl}) - p_{whu}}{D_v}$$

$$G_f = \frac{0.43(5,121.22 - 3,348.14) - 60}{5,121.22} = 0.1371 = 0.14 \text{ psi/ft}$$

The depth of the first unloading gas lift valve using equation (11.19):

$$D_1 = \frac{(p_{ko} - \Delta p_a - p_{whu})}{G_s}$$

Available kick-off pressure ( $p_{ko}$ ) is the operating injection pressure at the surface ( $p_{oi}$ ):

$$D_1 = \frac{(860 - 50 - 60)}{0.43} = 1,744.186 \text{ ft}$$

The depth of the second unloading gas lift valve using equation (11.22),  $D_2$ :

$$D_3 = \frac{p_{io} - \Delta p_a - 2\Delta p_{io} + D_2(G_s - G_f) - p_{whu}}{(G_s - G_g)}$$

$$D_2 = \frac{860 - 50 - 15 + 1,744.186(0.43 - 0.1371) - 60}{(0.43 - 0.02)}$$

$$= 3,038.46 \text{ ft}$$

The depth of the third unloading gas lift valve using equation (11.23),  $D_3$ :

$$D_3 = \frac{p_{io} - 2\Delta p_{io} + D_2(G_s - G_f) - p_{whu}}{(G_s - G_g)}$$

$$D_3 = \frac{860 - 50 - 2 \times 15 + 3,038.46(0.43 - 0.1371) - 60}{(0.43 - 0.02)}$$

$$= 3,926.30 \text{ ft}$$

The depth of the fourth unloading gas lift valve using equation (11.24),  $D_4$ :

$$D_4 = \frac{p_{io} - \Delta p_a - 3\Delta p_{io} + D_3(G_s - G_f) - p_{whu}}{(G_s - G_g)}$$

$$D_4 = \frac{860 - 50 - 3 \times 15 + 3,926.30(0.43 - 0.1371) - 60}{(0.43 - 0.02)}$$

$$= 4,523.85 \text{ ft}$$

The depth of the fifth unloading gas lift valve using equation (11.25),  $D_5$ :

$$D_5 = \frac{p_{io} - \Delta p_a - 4\Delta p_{io} + D_4(G_s - G_f) - p_{whu}}{(G_s - G_g)}$$

$$D_5 = \frac{860 - 50 - 4 \times 15 + 4,523.85(0.43 - 0.1371) - 60}{(0.43 - 0.02)}$$

$$= 4917.07 \text{ ft}$$

The depth of the sixth unloading gas lift valve using equation (11.25),  $D_6$ :

$$D_6 = \frac{p_{io} - \Delta p_a - 5\Delta p_{io} + D_5(G_s - G_f) - p_{whu}}{(G_s - G_g)}$$

$$D_6 = \frac{860 - 50 - 5 \times 15 + 4914.07(0.43 - 0.1371) - 60}{(0.43 - 0.02)}$$

$$= 5156.19 \text{ ft}$$

$D_6$  is deeper than calculated maximum gas lift valve, which is  $D_{v\_max} = 5121.22$  ft

Hence,  $D_6$  placed at  $D_{v\_max}$  will be the deepest gas lift valve, which would be at 5121.22 ft

Calculating unloading and operating valve temperatures using equation (11.27):

At  $D_1$ :

$$T_{uvD} = T_{whu} + D_1 \frac{(T_w - T_{whu})}{D_w}$$

$$T_{uvD} = 100 + 1,744.19 \frac{(220 - 100)}{7,990} = 126.20^\circ \text{F}$$

**Table 11.2** Depth of the Gas Lift Valves and Unloading Temperatures.

n (Valve number)	Gas lift valve depth (ft)	Valve temperature ( $^\circ\text{F}$ )
1	1,744.19	126.20
2	3,038.46	145.63
3	3,926.30	158.97
4	4,523.85	167.94
5	4,914.07	173.80
6	5,121.22	176.91

At  $D_2$ :

$$T_{uvD_2} = T_{whu} + D_2 \frac{(T_w - T_{whu})}{D_w}$$

$$T_{uvD_2} = 100 + 3,038.46 \frac{(220 - 100)}{7,990} = 145.63^\circ \text{F}$$

The unloading temperature of the valves at  $D_3$ ,  $D_4$ , and  $D_5$ , and the operating temperature at  $D_6$ , are calculated with a similar approach. Table 11.2 shows a summary of the gas lift valve depths and unloading /operating temperatures.

Fig. 11.28 shows a graphical representation of the depth of the gas lift valves and unloading temperatures.

Opening and closing valve pressure can then be determined using equations (11.29) and (11.30).

## 11.5. FLOW ASSURANCE

Flow assurance involves identification, prediction, and mitigation of risk to flow of reservoir fluid through the wellbore, flow lines, and facilities.

Physicochemical changes to produced fluids may occur due to changes in temperature and pressure as they flow from the reservoir through the wellbore, flow lines, and facilities. These physicochemical changes can result in complex formation and deposition of substances, which can increase the risk to the flow of reservoir fluids. Physicochemical changes associated with depositions and blockage of wellbore, flow lines, and surface facilities include: gas hydrate formation, wax deposition, scale formation and deposition, and paraffin/asphaltene deposition.

### 11.5.1. Gas Hydrates

Gas Hydrates (also known as Clathrate hydrates) are meta-stable ice-like solid compounds that are formed from mixtures of water and suitably sized gas molecules at temperatures greater than that of pure ice. Gas hydrates

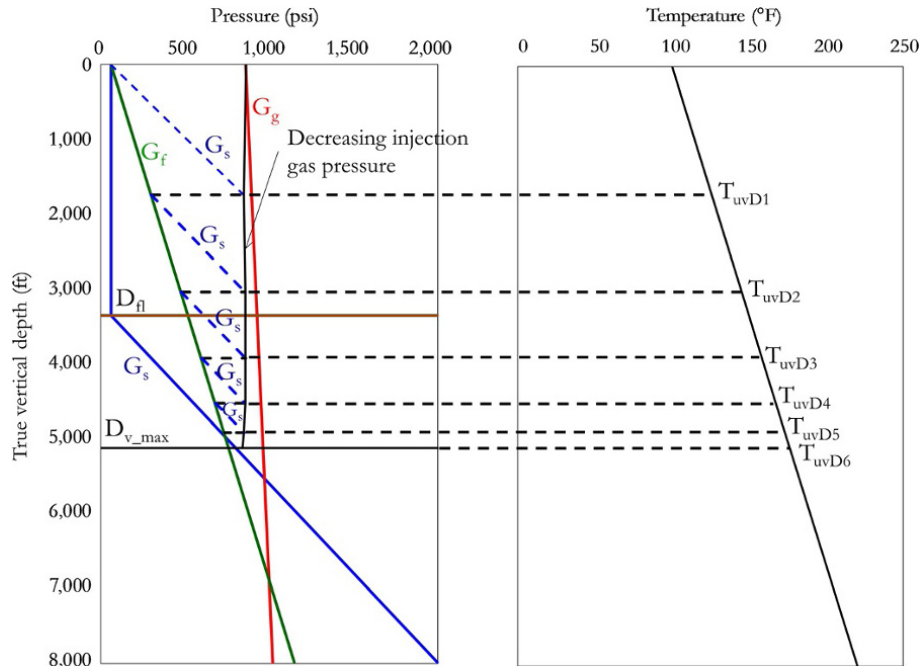


**Figure 11.28** Graphical representation of the continuous gas lift design for Exercise 11.1.

are generally considered as compounds because they have a fixed composition. However, bonding in hydrates is not due to covalent bonding but rather weak van der Waals attraction forces.

When water (host molecule) hydrogen bonds (attractive interaction between polar molecules), lattice structures are created with several interstitial cavities occupied by gas molecules (guest). When the minimum number of cavities required to form a stable crystalline solid is filled, hydrates are formed. This can occur even at temperatures far above freezing point of water [Bradley, 1987]. Hydrate crystal structures can be characterized by *lattice parameters or constants*  $a$ ,  $b$ , and  $c$ , which are physical dimensions of a unit cell in a crystal lattice in units of angstroms ( $\text{\AA}$ ).

**11.5.1.1. Types of Hydrates.** Water forms three types of hydrates – types I, II and H – where hydrate types I and II are most common. Both type I and II can exist as small and large cavities. The size distribution of the cavities within a hydrate and their numbers determines the hydrate type and amount of gas (guest) molecules that can be held by the water molecule (host). There is a minimum of cavities that must be filled for a stable hydrate to be formed.

The unit cell of Type I is a  $12 \text{\AA}$  cube and consists of 46 water molecules forming small and large cages. Carbon dioxide ( $\text{CO}_2$ ) and methane ( $\text{CH}_4$ ) are typical guests in type I hydrates, forming carbon dioxide clathrate and methane clathrate, respectively.

The unit cell of type II is a  $17.3 \text{\AA}$  cube and consists of 136 water molecules forming small and large cages. Oxygen ( $\text{O}_2$ ) and nitrogen ( $\text{N}_2$ ) are considered the gases responsible for the formation of type II hydrates.

The unit cell of Type H is a hexagonal lattice with parameters  $a = 12.26 \text{\AA}$  and  $c = 10.17 \text{\AA}$ , and consists of 34 water molecules, forming two small and one large cage. Large cavities in type H hydrates allows the structure to accommodate larger molecules such as butane, with help from gases to fill and support the remaining cavities [Udachin et al., 1997; Ripmeester et al., 1987].

**11.5.1.2. Hydrate Formation.** Hydrate formation can be due to a decrease in temperature or increase in pressure in flow lines and facilities with natural gas and water. Also, sudden expansion of fluid with natural gas and water through constrictions such as chokes, orifices, and back-pressure regulators can cause hydrate formation [Bradley, 1987].

Hydrates can cause serious flow assurance problems in subsea flow lines and risers in offshore fields. Hydrate blockage in production systems can be removed by direct injection of hydrate inhibitors, such as methanol, where the blockage is close to the injection point. Where the blockage is inaccessible from the injection point, coil tubing can be used to access the blockage location then methanol pumped through to dissociate the hydrate. Coiled tubing can reach lengths as far as 14,000 ft or more for remediation operations. Other options for hydrate

blockage remediation include heating, depressurization, and mechanical removal using coil tubing or pigging in a partial blockage. The use of heating, though fast and effective, can create safety problems, such as flow line rupture due to the release of trapped gas within the hydrate plug at high pressure.

**11.5.1.3. Hydrate Prediction. Hydrate Condition Correlation Chart**

Katz [1945] presented a chart that relates hydrate formation pressure as a function of temperature for sweet gas of varying gas gravity (Fig. 11.29). The limitation of this method is its inability to handle sour gas (gas with H<sub>2</sub>S). Similar charts for the same purpose by various authors have been published.

*Vapor-Solid Equilibrium Method*

This approach involves treating hydrate formation as a vapor-solid equilibrium relationship where phase distribution is determined by a phase equilibrium constant similar to that in the vapor-liquid equilibrium situation in Chapter 3 (3.4.4.1). The approach involves using charts or empirical correlations to predict equilibrium constants (K values), which are then used to calculate hydrate formation conditions in an approach similar to that of dew point calculation in Chapter 3 (3.4.4.1).

$$K_{i,v-s} = \frac{y_i}{x_i} \tag{11.32}$$

where  $K_{i,v-s}$  is the vapor-solid equilibrium values of component I,  $y_i$  is the mole fraction of component i in

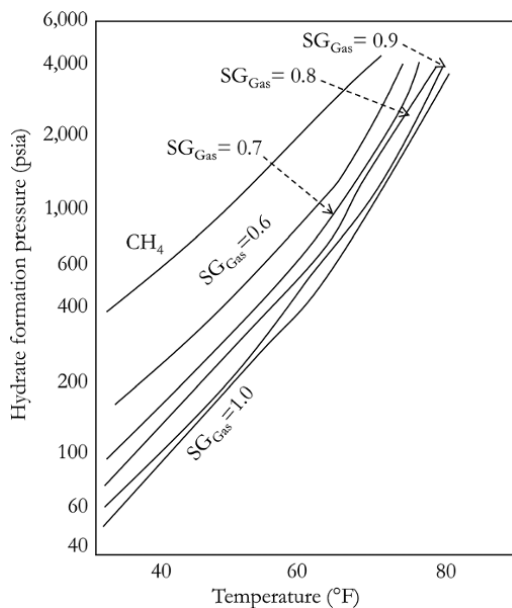


**Figure 11.29** Hydrate formation conditions in natural gas [Adapted from Katz, 1945].

the vapor phase, and  $x_i$  is the mole fraction of component i in the solid phase.

The criteria for solid formation are thus defined in a similar way to dew point condition discussed in Chapter 3 (3.4.4.1) which is:

$$\sum_{i=1}^n \frac{y_i}{K_{i,v-s}} = 1 \tag{11.33}$$

*Van der Waals and Platteeuw Hydrate Model*

This model relates the chemical potential of water in hydrate to the number of cavities of a particular type per water molecule in the basic lattice, and the probability that the cavity of the given hydrate type is occupied by a gas molecule of a given type [Van der Waals and Platteeuw, 1959]:

$$\mu_{wH} = \mu_{wMT} + RT \sum_i n_{ci} \ln \left( 1 - \sum_i y_{ji} \right) \tag{11.34}$$

where

$$y_{ji} = \frac{C_{ji}f_j}{1 + \sum_k C_{ki}f_k}$$

the Langmuir adsorption theory for

determining  $y_{ji}$  [Bradley, 1987].

$\mu_{wH}$  is the chemical potential of water in filled hydrate,  $\mu_{wMT}$  is the chemical potential of water in empty hydrate,  $n_{ci}$  is the number of cavities of type i per water molecule in the basic lattice,  $y_{ji}$  is the fractional occupancy of type i cavity by type j molecule (which is the probability that cavity of type i is occupied by a gas molecule of type j),  $C_{ji}$  is the Langmuir constant for molecule j in cavity of type I,  $f_j$  and  $f_k$  are fugacity of j and k in the gas phase.

**Exercise 11.2 Hydrate Envelope**

Hydrate formation can be described as a vapor-solid equilibrium relationship. For a hydrocarbon without hydrogen sulfide (H<sub>2</sub>S) and at a temperature above 32°F, Poettmann et al. [1989] described an equation that can be used to calculate the vapor-solid equilibrium constant of a constituent, except for carbon dioxide (CO<sub>2</sub>) for type II hydrate expressed as:

$$\ln(K) = A + B \times SG + CT + \frac{D}{P} + \frac{E}{P^2} + F \left( \frac{P}{1,000} \right)^2 + \frac{G}{SG} + H \left( \frac{P}{1,000} \right)^3 + I \times SG \times P + J \ln(P) + LP + M/T \tag{11.35}$$

The parameters for the K values are defined in Table 11.3.

Generate a type II hydrate formation envelope for an operating pressure between 100 and 1,000 psia given the



**Table 11.3** Constants for Vapor–Solid Equilibrium K Values for Different Gas Constituents [Adapted from *Poettmann, Sloan, Mann & McClure, 1989*].

Component	A	B	C	D	E	F	G	H	I	J	L	M
C <sub>1</sub>	-3.8862	-2.6891	0.016296	1.098	555.2	-0.01637	-0.25993	0.00089	1.3690E-04	-0.33731	0	0
C <sub>2</sub>	-48.4314	0.4489	0.116384	155.33	-985.5	0.18459	-1.32568	-0.03029	-2.6145E-04	-1.48522	0	0
C <sub>3</sub>	-46.0752	0.4199	0.120725	-135.638	0	-0.30192	-1.4989	0.01152	3.7850E-05	-2.70863	0.0020863	0
n-C <sub>4</sub>	-48.23	0.0354	0.107702	351.28	-19,245	0.25439	-1.9692	-0.05415	3.0153E-04	-0.82554	0	0
i-C <sub>4</sub>	-54.626	0.1238	0.115242	338.11	-18,643	0.24466	-1.889	-0.05132	2.2811E-04	-0.87306	0	0
N <sub>2</sub>	9.5205	-2.2112	0	-11.86	1,765.3	-0.02781	0.08466	0.00759	-2.50E-04	-0.29777	0	-2,494.9

gas specific gravity (SG) as 0.67 and composition shown in Table 11.4.

**Solution Steps.**

*Step 1:* set  $\sum y_i/k_{i,v-s}$  to 1 by changing temperature (T) and keeping pressure (p) constant (operating pressure condition). Calculated temperature (T) is hydrate formation temperature in °R at given operating pressure (p).

*Step 2:* convert temperature from °R to °F.

*Step 3:* repeat calculation for different values of pressure (p).

*Step 4:* generate table of pressure (p) against temperature (T). The plot of calculated pressure against temperature is the type II hydrate formation envelope.

**Solution.**

The goal seek solution of hydrate formation temperature at 100 psia is shown in Table 11.5.

The hydrate formation envelope for Exercise 11.2 was created by repeating hydrate formation temperature determination at different pressures (Fig. 11.30).

**Table 11.4** Composition of Natural Gas.

Component	Mole fraction
C <sub>1</sub>	0.548
C <sub>2</sub>	0.160
C <sub>3</sub>	0.121
n-C <sub>4</sub>	0.089
i-C <sub>4</sub>	0.081
N <sub>2</sub>	0.001

**Table 11.5** Goal Seek Solution of Hydrate Formation Temperature at 100 psia.

Component	mol fraction (y <sub>i</sub> )	K <sub>i,v-s</sub>	y <sub>i</sub> /K <sub>i,v-s</sub>
C <sub>1</sub>	0.548	1.9578	0.280
C <sub>2</sub>	0.160	25.4277	0.006
C <sub>3</sub>	0.121	0.4887	0.248
n-C <sub>4</sub>	0.089	2.7935	0.032
i-C <sub>4</sub>	0.081	0.1865	0.434
N <sub>2</sub>	0.001	6.6342	0.000
			$\sum y_i/K_{i,v-s} = 1.000$

SG = 0.67  
 P = 100 psia  
 T = 504.758°R  
 T = 44.758°F

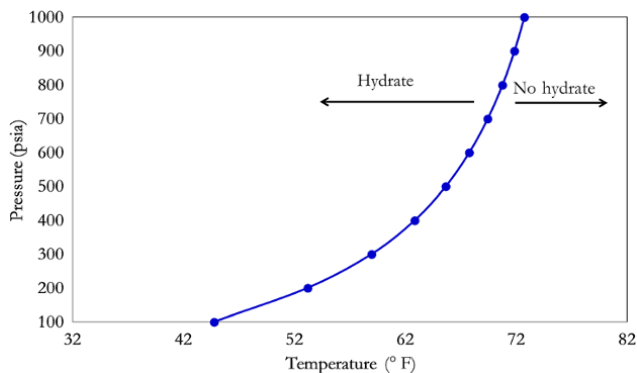


**Figure 11.30** Hydrate formation envelope for Exercise 11.2.

**11.5.1.4. Hydrate Prevention and Inhibitors.** Ways of preventing hydrate formation include: keeping the production stream temperature above the hydrate formation temperature for a given pressure or reducing the pressure below the hydrate formation pressure for a given temperature; drying the gas stream, hence reducing the dew point of water vapor in the gas flow below the operating temperature; and use of hydrate inhibitors such as ethylene glycol (EG), diethylene glycol (DEG), triethylene glycol (TEG), glycols, and methanol.

The most common inhibitor is EG, also called monoethylene glycol (MEG), due to its effectiveness compared with other glycols, lower cost, lower solubility with liquid hydrocarbons, and lower viscosity. Although methanol is the most effective hydrate inhibitor amongst alcohols and glycols (highest temperature shift or hydrate suppression per unit weight), it is not as commonly used as MEG due to safety issues. Also, recovery of methanol by distillation is not as easy and cheap compared with other inhibitors like MEG. Glycols and methanol are generally referred to as *thermodynamic inhibitors* and prevent hydrate formation by suppressing the hydrate formation temperature.

Ammonia has been considered as an hydrate inhibitor as it is more than twice as effective as methanol. However, ammonia can create another problem – blockage due to the reaction of ammonia with carbon dioxide to form carbonate, bicarbonate, and carbamate.

Relying on conservation of heat from produced reservoir fluid to keep the system above the hydrate formation temperature may only be viable during steady state production. In conditions such as low production rates, long subsea flow lines and risers, startups and shutdown, the temperature of the system and fluid in flow lines can fall below the hydrate formation region. During startup, hydrate prevention can be achieved through electrical heating of flow lines or hot dead oil circulation, use of hydrate inhibitors, or fast startup to overtake hydrate formation. During shutdown, hydrate prevention can be

achieved through the use of inhibitors, blowing down of subsea systems to pressures outside hydrate formation region, use of hot dead oil or hydrate inhibitors. For export pipelines, hydrate prevention can be achieved through removal of water from production fluid before transporting for export. For gas production, the use of heat conservation from reservoir fluid is more challenging and, hence, continuous injection of hydrate inhibitors is common for hydrate mitigating in gas production.

The Hammerschmidt equation [Hammerschmidt, 1939] is a common empirical relationship used in determining the required concentration of an inhibitor, in an aqueous solution, for suppressing the hydrate formation temperature by a given amount ( $\Delta T$ ); it is expressed as:

$$\Delta T = \frac{K_H X_I}{MW(1 - X_I)} \quad (11.36)$$

where  $X_I$  is the weight fraction of inhibitor required to prevent hydrate formation,  $K_H$  is the inhibitor K-value,  $\Delta T$  is the reduction in hydrate formation temperature due to addition of the inhibitor ( $^{\circ}F$ ), and MW is the molecular weight of the inhibitor.

Equation (11.36) can be rearranged to make the weight fraction of inhibitor required to suppress hydrate by  $\Delta T$  the subject of the formula:

$$X_I = \frac{\Delta TMW}{K_H + \Delta TMW} \quad (11.37)$$

Values for  $K_H$ , which are dependent on the inhibitors, are shown in Table 11.6.

At very high concentrations, the reduction in hydrate formation temperature ( $\Delta T$ ) using the Hammerschmidt becomes less accurate. For methanol above 25-wt% and glycols above 70-wt%, the Nielsen–Bucklin equation [Nielsen and Bucklin, 1983] yields a more accurate relationship between inhibitor concentration and reduction in hydrate formation temperature. It is expressed as:

$$\Delta T = -129.6 \ln(x_w) \quad (11.38)$$

where  $x_w$  in the Nielsen–Bucklin equation is the mole fraction of water.

With a calculated  $X_I$  using equation (11.37) or (11.38), the mass flow rate of water ( $m_w$ ) in the flow line or

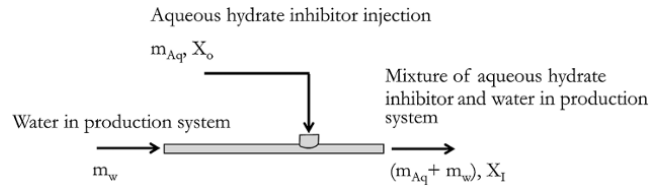


Figure 11.31 Hydrate inhibitor mass balance during injection.

production system required to bring aqueous hydrate inhibitor of mass flow rate of  $m_{Aq}$  and concentration  $X_o$  wt/wt to  $X_I$  can be determined from the mass balance as illustrated in Fig. 11.31.

From Fig. 11.31:

$$X_I = \frac{m_{Aq} X_o}{m_{Aq} + m_w} \quad (11.39)$$

Making  $m_{Aq}$  the subject of the formula in equation (11.39):

$$m_{Aq} = \frac{m_w X_I}{X_o - X_I} \quad (11.40)$$

Equation (11.40) defines the relationship between the mass flow rate of aqueous hydrate inhibitor and mass flow rate of water in the production system.

**Exercise 11.3 Hydrate Suppression**

1. Assess risk for hydrate formation in a flow line on a seabed at 8.8°C (47.84°F) with expected flowing pressure of 700 psia during well startup for the fluid sample in Exercise 11.2.
2. Determine the relationship between volumetric water production rate and volumetric flow rate of 80-wt% MEG required to prevent hydrate formation given the properties of MEG in Table 11.6.

The density of water and MEG at stock tank condition are 1,000 and 1,115 kg/m<sup>3</sup>, respectively.

3. Determine the amount of 80-wt% MEG in stb/d required to suppress hydrate for 500 stb/d of water in flow line.

**Solution.**

1. Hydrate formation temperature at 700 psia is 69.4°F (20.8°C) and operating condition (47.84°F, 700 psia) is on the hydrate part of envelope. Hence, there is risk of hydrate formation (Fig. 11.32).
2. Calculating temperature shift required to suppress hydrate formation:

$$\Delta T = T_{hydrate} - T_{operation}$$

$$\Delta T = 69.4 - 47.8 = 21.6^{\circ}F$$

**Table 11.6**  $K_H$  values for Different Inhibitors [Adapted from Hammerschmidt, 1939].

Inhibitor	Molecular weight	$K_H$ value
Methanol	32	2,335
Mono ethylene glycol	62.07	2,700
Diethylene glycol	106.12	4,000
Triethylene glycol	150.17	5,400

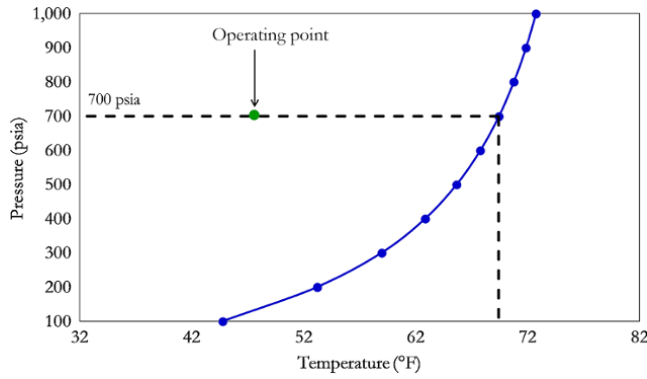


**Figure 11.32** Hydrate formation temperature for  $p_{wf}$  of 700 psia (Exercise 11.3).

Calculating mass concentration of MEG required to suppress hydrate for given conditions equation (11.37):

$$X_I = \frac{\Delta TMW}{K_H + \Delta TMW}$$

$$X_I = \frac{21.6 \times 62.07}{2700 + 21.6 \times 62.07} = 0.3318$$

$$X_I = 0.3318 \text{ wt/wt}$$

Substituting  $X_I$  and  $X_o$  into equation (11.40):

$$m_{Aq} = \frac{m_w 0.3318}{0.8 - 0.3318}$$

$$m_{Aq} = 0.7087 m_w \tag{11.41}$$

Substituting  $m_{Aq} = q_{Aq} \rho_{Aq}$  and  $m_w = q_w \rho_w$  into equation (11.41), where  $q_{Aq}$  and  $q_w$  are the volumetric flow rates of aqueous hydrate inhibitor and water, respectively, at a given condition, and  $\rho_{Aq}$  and  $\rho_w$  are the density of aqueous hydrate inhibitor and water, respectively, at a given condition:

$$q_{Aq} \rho_{Aq} = 0.7087 q_w \rho_w$$

Making  $q_{Aq}$  the subject of the formula

$$q_{Aq} = 0.7087 q_w \frac{\rho_w}{\rho_{Aq}} \tag{11.42}$$

density of aqueous hydrate inhibitor can be determined using equation (11.43):

$$\rho_{Aq} = \frac{1}{\frac{X_I}{\rho_I} + \frac{(1-X_I)}{\rho_w}} \tag{11.43}$$

where  $\rho_I$  is the density of the hydrate inhibitor (100% hydrate inhibitor).

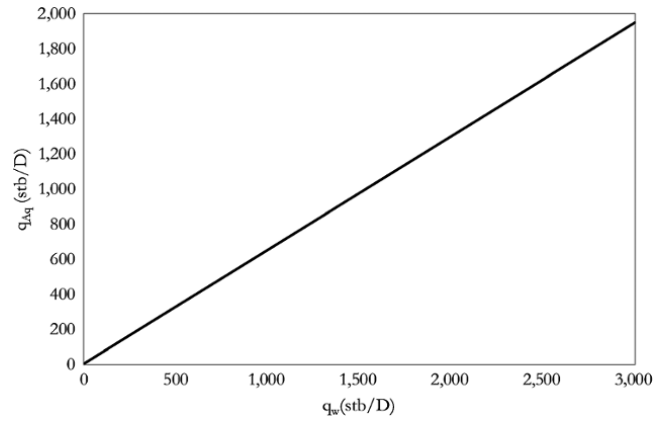


**Figure 11.33** MEG injection rate required as a function of water production rate for Exercise 11.3.

Substituting  $X_I$ ,  $\rho_I$ , and  $\rho_w$  into equation (11.43):

$$\rho_{Aq} = \frac{1}{\frac{0.8}{1115} + \frac{(1-0.8)}{1,000}} = 1089.93 \text{ kg/m}^3$$

$$\rho_{Aq} = 1089.93 \text{ kg/m}^3$$

Substituting  $\rho_{Aq}$  calculated and  $\rho_w$  given into equation (11.42):

$$q_{Aq} = 0.7087 q_w \frac{1,000}{1,089.93}$$

$$q_{Aq} = 0.649 q_w \tag{11.44}$$

where  $q_{Aq}$  and  $q_w$  are stock tank volumetric flow rates in consistent units.

Equation (11.44) can be displayed graphically by making a plot of  $q_{Aq}$  against  $q_w$ , as shown in Fig. 11.33.

As shown in Fig. 11.33, the amount of thermodynamic hydrate inhibitors, such as glycols, increases with an increase in the amount of water in the production stream. The volume and concentration of hydrate inhibitor required to suppress hydrate can become high in production streams with a high water rate.

3. For 500 stb/d of water in a flow line, the aqueous MEG injection rate can be determined by substituting  $q_w = 500$  stb/d into equation (11.44):

$$q_{Aq} = 0.649 q_w$$

$$q_{Aq} = 0.649 \times 500 = 324.5 \text{ stb/d}$$

**11.5.1.5. Low Dosage Hydrate Inhibitors (LDHIs).** LDHIs, which are either *kinetic hydrate inhibitors* (KHIs) or *anti-agglomerants* (AAs), can be used for

hydrate inhibition in low doses and, as such, low injection rates compared with thermodynamic inhibitors (glycols and methanol). The concentration of LDHIs are typically between 0.1 and 1.0-wt%, compared with thermodynamic inhibitors which are required in concentrations higher than 50-wt%. KHIs act by lowering the rate of hydrate formation, thereby inhibiting hydrate formation over a given period of time. Anti-agglomerants work by limiting any hydrate formed to sizes that are submillimeter in size, thereby hydrate formed is dispersed into the oil or condensate. Anti-agglomerants need liquid hydrocarbon (condensate or oil) to enable dispersion of hydrate.

### 11.5.2. Wax

The wax present in petroleum crudes consists primarily of *paraffin hydrocarbons* (C<sub>18</sub>–C<sub>36</sub>), known as *paraffin wax*, and *naphthenic hydrocarbons* (C<sub>30</sub>–C<sub>60</sub>). Paraffin waxes have semicrystalline characteristics and inclined to precipitate from crude oils at and below the thermodynamic cloud point (the equilibrium solid–liquid temperature). Naphthenic hydrocarbons are similar to paraffins in that they are saturated and, therefore, stable.

Asphaltenes, which can be deposited as solid like paraffin wax, are often categorized separately from wax because they are aromatic and not paraffinic. They are, however, sometimes grouped as part of wax deposition, as they are residual oil components that often coprecipitate with the paraffin waxes.

Wax prevention can be achieved by heating using electrical heaters; dispersants or crystal modifiers. Remediation of wax deposition can be achieved by mechanical removal using pigging, hot water or hot water with surfactant, and aromatic solvents.

**11.5.2.1. Wax Deposition Prediction.** The Pedersen wax model [Pedersen *et al.*, 1991] assumes that paraffins and naphthalenes can precipitate as a solid solution. To use the solid precipitation model, the paraffin, naphthalene, and aromatic (PNA) fractions for each carbon number are needed. Measured PNA constituents can be used directly or, where unknown, they can be generated from correlations that splits components heavier than C<sub>6</sub> into their paraffinic (P), naphthalenic (N), and aromatic (A) constituents.

The Pedersen wax model involves manipulation of liquid fugacity to solve for solid (wax) phase using the equation of state models and expressed as:

$$f_i^S(p, T) = f_i^L(p, T) \times \exp \left[ \frac{\Delta h_i^f}{R T_i^f} \left( 1 - \frac{T_i^f}{T} \right) - \frac{\Delta c_{pi}}{R} \left( 1 - \frac{T_i^f}{T} \right) - \frac{\Delta c_{pi}}{R} \ln \left( 1 - \frac{T_i^f}{T} \right) \right] \quad (11.45)$$

where  $\Delta h_i^f$  is the enthalpy of fusion for component  $i$ ,  $\Delta c_{pi}$  is heat capacity of fusion  $i$ ,  $T_i^f$  is the melting point temperature of component  $i$ ,  $f_i^S(p, T)$  is the fugacity of a pure component of  $i$  in the solid phase,  $f_i^L(p, T)$  is the fugacity of a pure component of  $i$  in the liquid phase,  $R$  is the gas constant,  $T$  is temperature, and  $p$  is pressure.

The concept of fugacity for the phase equilibrium calculation is discussed in Chapter 4 (4.4).

In the manipulation of the model, non-PNA components are assigned very high fugacity as they do not form wax.

A wax model can also be formulated as a liquid–solid equilibrium relationship in a similar way to hydrate problem, which was expressed as a gas–solid equilibrium problem.

### 11.5.3. Inorganic Scale Deposition

Inorganic scale deposition occurs mostly due to the formation water mixing with different water with incompatible ions, triggering reactions that cause deposition of inorganic salts such as carbonates and sulfates. Scale deposition causes a reduction in the internal diameter of the flow line and in the flow rate, finally causing blockage if remediation actions are not taken.

Water compatibility tests should always be carried out to evaluate the risk of precipitation of inorganic scale before water injection in a petroleum reservoir. Laboratory analysis should include measurement of inorganic scale precipitation for different mixing ratios of raw water to formation water. This analysis is crucial in understanding the potential for inorganic scale deposition, selection of chemical scale inhibitors, and the required concentration of inhibitor to prevent scale deposition.

### 11.5.4. Sand Production and Fines Migration

The mechanical collapse of the formation can lead to sand grains being produced with the fluid. Where the formation is made of siliceous or clay fines, these may also be produced with hydrocarbons as fines, which can cause plugging in the reservoir and wellbore.

Sand production can be managed using downhole completions, such as sand screens and gravel packing, or *surface wellhead desanders* to capture produced sand at the surface. Wellhead desanders can be used to complement downhole sand control in the case of completion failure. Desanders can be used during workover, well test, or continuous operations. Sand production creates problems such as erosion, sand accumulation in equipment, and collapse of formation due to the creation of voids that make the formation lose its integrity.

### 11.5.5. Corrosion

Corrosion in tubing and producing facilities can be aggravated by the presence of corrosive constituents in reservoir fluid, such as hydrogen sulfide (H<sub>2</sub>S) and carbon dioxide (CO<sub>2</sub>). Chloride ions in produced water and oxygen in injected water can also aid corrosion of tubing, flow lines, and surface facilities. Corrosion, where unchecked, can lead to total equipment failure, loss of fluid, and, possibly, risk to the life of personnel. Corrosion inhibitors absorbed on the metal surface to form a protective film can be used in highly corrosive fluid to reduce corrosion rate. Corrosion inhibitors can be introduced into flow lines via capillary tubes or tubing displacement methods.

### REFERENCES

- API (American Petroleum Institute), 1991. *API Recommended Practice 14E (RP 14E), Recommended Practice for Design and Installation of Offshore Production Platform Piping Systems*. Washington, DC: API.
- API (American Petroleum Institute), 1999. *API Recommended Practice RP 11V6, Recommended Practice For Design Of Continuous Flow Gas Lift Installations Using Injection Pressure Operated Valves*. Washington, DC: API.
- Bradley, H., 1987. *Petroleum Engineering Handbook*. Richardson, TX: Society Of Petroleum Engineers.

### BIBLIOGRAPHY

- Bellarby, J., 2009. *Well Completion Design*, 1st edn. Elsevier.
- Brown, K., 1980. *The Technology of Artificial Lift Methods*, Vol. 2a. Tulsa, OK: PennWell Publishing.
- Brown, K. and Beggs, H., 1977. *The Technology of Artificial Lift Methods*, Vol. 1. Tulsa, OK: PennWell Publishing.
- Clegg, J., Bucaram, S., and Hein, N.J., 1993. Recommendations and comparisons for selecting artificial lift methods. *Journal of Petroleum Technology*, **45**(12), 1128.
- Colebrook, C. and White, C., 1937. Experiments with fluid friction in pipes roughened. *Proceedings of the Royal Society of*

- London, Mathematical and Physical Sciences*, **161**(906), 367–381.
- Coleman, S.B., Clay, H.B., McCurdy, D.G, and Norris, H.L.I., 1991. A new look at predicting gas-well load up. *Journal of Petroleum Technology*, **43**(03), 329–333.
- Gilbert, W., 1954. Flowing and gas-lift well Performance. In *Drilling and Production Practice*, American Petroleum Institute, pp. 126–157.
- Golan, M. and Whitson, C., 1986. *Well Performance*, 2nd edn. Englewood Cliffs, NJ: Prentice Hall.
- Greene, W., 1983. Analyzing the performance of gas wells. *Journal of Petroleum Technology*, **35**(07), 1378–1384.
- Guo, B., Lyons, W., and Ghalambor, A., 2007. *Petroleum Production Engineering, A computer-Assisted Approach*. Elsevier Science & Technology Books.
- Hall, K. and Yarborough, L., 1973. A New equation of state for Z-Factor calculations. *Oil & Gas Journal*, **71**(25), 82.
- Kareem, L., Iwalewa, T., and Al-Marhoun, M., 2016. New explicit correlation for the compressibility factor of natural gas: linearized z-factor isotherms. *Journal of Petroleum Exploration and Production Technology*, **6**(3), 481–492.
- Lea, J., Nickens, H., and Wells, M., 2008. *Gas Well Deliquification*, 2nd edn. Gulf Professional Publishing–Elsevier.
- Mach, J., Proano, E., and Brown, K., 1979. *A Nodal Approach For Applying Systems Analysis To The Flowing And Artificial Lift Oil Or Gas Well*. TX; Society of Petroleum Engineers.
- Serghides, T., 1984. Estimate friction factor Accurately. *Chemical Engineering Journal*, **91**(5), 63–64.
- Stewart, G., 2011. *Wireline Formation Testing and Well Deliverability*. Tulsa, OK: PennWell Corporation.
- Turner, R.G., Hubbard, M.G., and Dukler, A.E., 1969. Analysis and Prediction of Minimum Flow Rate for the Continuous Removal of Liquids from Gas Wells. *Journal of Petroleum Technology*, **21**(11), 1475–1482.
- Winkler, H. and Camp, G., 1987. Dynamic performance testing of single-element unbalanced gas-lift valves. *SPE Production Engineering*, **2**(3), 183–190.
- Winkler, H. and Eads, P., 1993. Applying the basic performance concepts of single-element, unbalanced gas-lift valves for installation design. *SPE Production & Facilities*, **8**(3), 211–216.

# 12

## Reservoir Material Balance

### 12.1. MATERIAL BALANCE

Material balance techniques for reservoir performance prediction involve using cumulative reservoir fluid withdrawal and/or injection with average reservoir pressure to model and predict reservoir performance with or without a geological model. Material balance techniques are useful for reserve calculation, reservoir drive mechanisms characterization, and production forecasting.

Though material balance was originally formulated for primary producing, its application has been extended to secondary production, where water and/or gas is injected to energize the reservoir.

#### 12.1.1. Material Balance as Solution to Inverse Problem

Material balance, like all reservoir characterization techniques, such as well testing and core analysis, uses inversion processes (inverse problem) to determine a system model. In well test analysis (Chapter 8 (8.5)), a system model is a *well test interpretation model*. In *special core analysis* (Chapter 2 (2.6)), system models include *relative permeability* and *capillary pressure models*.

The solution of inverse problems involves defining a system model using the response of the system. In inverse problems, more than one model that matches the system response can be derived. Inverse problems can be ill-posed with nonunique solutions. In material balance, more than one reservoir model (combination of gas cap, oil, and aquifer model) can be used to match a given production history (average pressure and cumulative fluid production).

The response of a reservoir model to a given cumulative volume of oil, gas, and water is a direct problem

(convolution) that gives a unique solution of pressure response (Fig. 12.1a). Also, prediction of the cumulative reservoir fluid for a given pressure history is a direct problem (Fig. 12.1b).

However, defining the reservoir model for a given cumulative volume of gas, oil, water, and average reservoir pressure using material balance techniques can yield more than one combination of gas cap, oil, and aquifer parameters, so making the solution nonunique (Fig. 12.2).

Workflow for material balance calculations, in order to reduce uncertainty due to nonuniqueness, must include:

- *Data preparation processes*, which involve checking that the pressure response is consistent with the cumulative volume reported and removal of outliers.
- *Diagnosis*, which involves extracting information about the reservoir model from measured data.
- *Defining system model and initial model parameter*, which involves defining a material balance model and a valid range of model parameters from diagnosis.
- *Model consistency check*, which involves checking that the model from diagnosis is consistent with any other data, information or reservoir model from other characterization methods.
- *Forward simulation*, which involves using values from initial model parameters to predict response to check for consistency and validity of the model.
- *Regression*, which may be applied to a model to refine simulation model parameters and improve the match of model response with a measured response where required.

Fig. 12.3 summarizes workflow reservoir material balance analysis.

Since material balance in an inverse problem with a nonunique solution, integration and validation of the material balance model with other acquired reservoir data

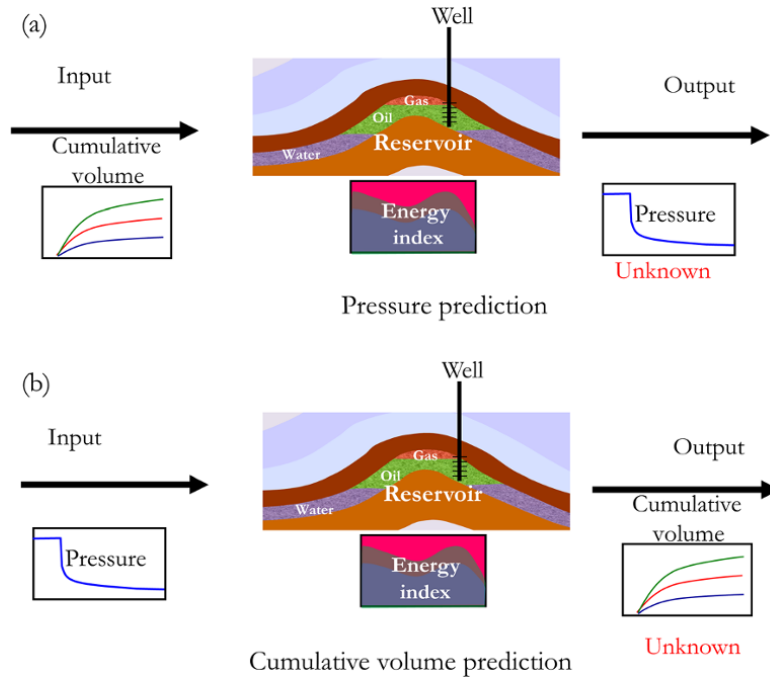


Figure 12.1 Reservoir simulation as a direct problem (convolution).

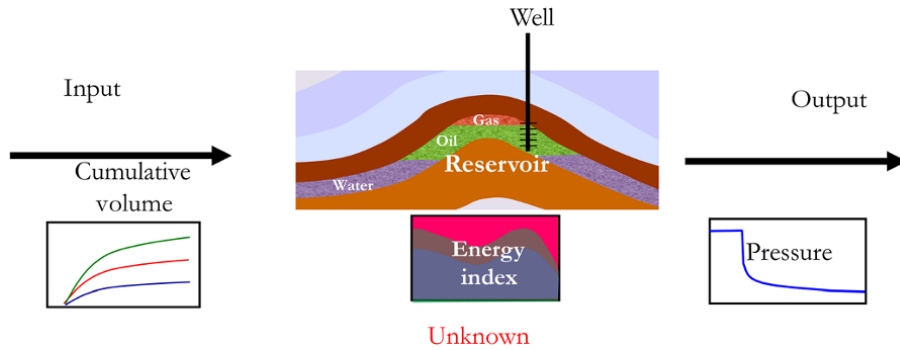


Figure 12.2 Material balance as an inverse problem (deconvolution).

and properties can reduce uncertainties associated with nonuniqueness in solution. For example, in an oil reservoir with gas cap and aquifer support, more than one combination of size of gas cap, oil, and aquifer can match the pressure and cumulative reservoir volume history. Hence, using combined well logs and geophysical model to determine the possible range of gas cap size can help reduce uncertainty in calculated oil in place and aquifer size from the material balance calculation.

### 12.2. OIL RESERVOIR MATERIAL BALANCE (OMB)

The generalized material balance equation that shows the relationship between reservoir pressure, quantity of

reservoir fluid produced, remaining reservoir fluid, and reservoir fluid properties was first presented by *Schilthuis* [1936].

Consider an oil reservoir with gas cap and aquifer support with an initial volume of oil in place at standard conditions defined as  $N$ , and the ratio of initial hydrocarbon volume in the gas cap to initial hydrocarbon volume of oil measured in the reservoir defined as  $m$  (Fig. 12.4).

The initial gas cap volume ( $G_i$ ) at reservoir condition can be defined as:

$$G_i = mNB_{oi} \tag{12.1}$$

and the initial oil and solution gas volume ( $N_{oil+soln}$ ) defined as:

$$N_{oil+soln} = NB_{oi} \tag{12.2}$$



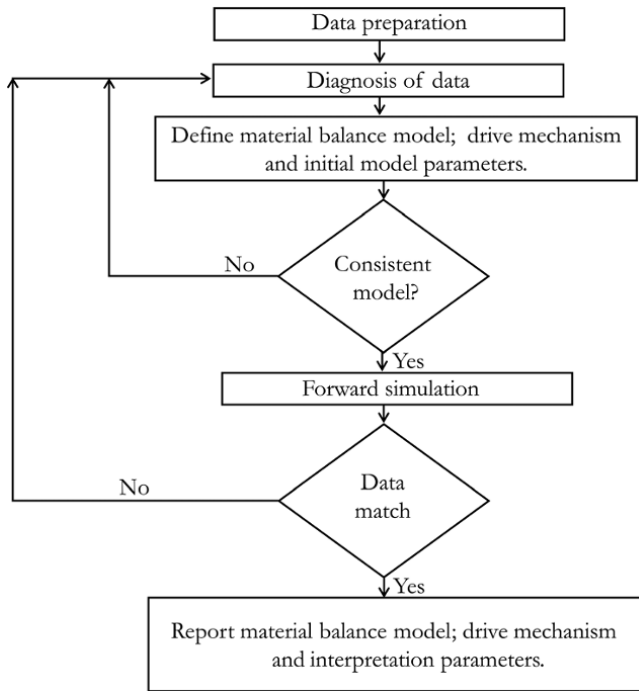


**Figure 12.3** Workflow of reservoir material balance analysis.

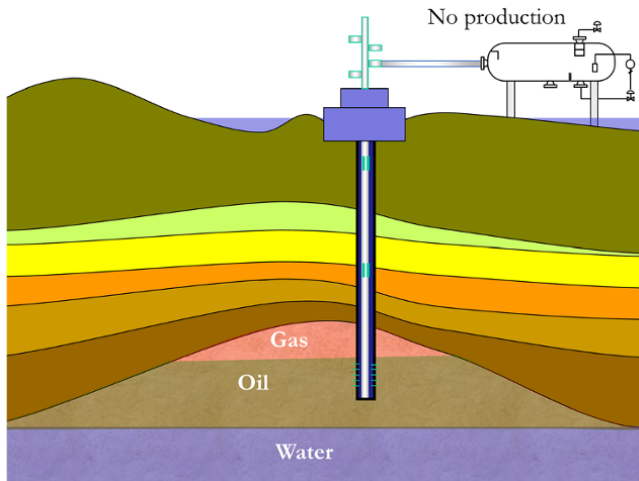


**Figure 12.4** Oil reservoir with gas cap and aquifer support at initial reservoir condition.

where

$$N = \frac{V\phi(1 - S_{wc})}{B_{oi}} \quad (12.3)$$

$V$  is net reservoir rock volume,  $S_{wc}$  is initial connate water saturation,  $B_{oi}$  is initial oil formation volume factor, and  $\phi$  is reservoir porosity.

For measured cumulative oil produced at standard condition ( $N_p$ ) and cumulative gas-to-oil production ratio

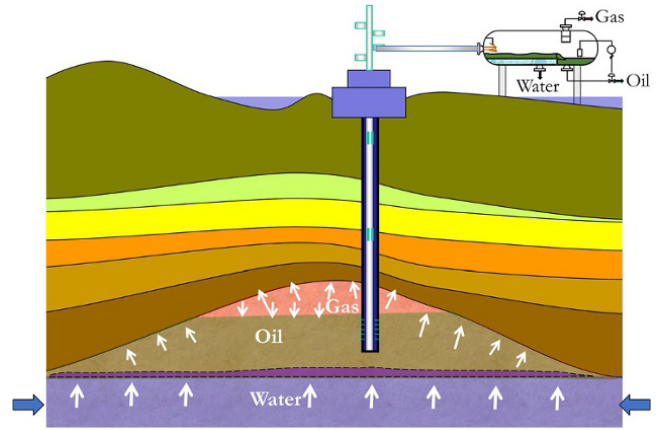


**Figure 12.5** Oil reservoir after oil, gas, and water production.

measured at standard condition ( $R_p$ ), cumulative oil and gas produced at reservoir condition ( $V_{oil+gas}$ ) can be expressed as:

$$V_{oil+gas} = N_p(B_o + (R_p - R_s)B_g) \quad (12.4)$$

and cumulative water produced at reservoir condition ( $V_{water}$ ) can be expressed as:

$$V_{water} = W_p B_w \quad (12.5)$$

where  $B_o$  is oil formation volume factor,  $B_g$  is gas formation volume factor,  $R_s$  is solution gas:oil ratio,  $W_p$  is cumulative water produced at surface condition;  $B_w$  is formation volume factor for water.

For primary production (Fig. 12.5), the fluid produced corresponds to the sum of expansion of oil and solution gas, expansion of gas cap gas, reduction in hydrocarbon pore volume (HCPV) due to connate water expansion, and decrease in porosity and water influx as pressure drops.

Expansion of oil =  $NB_o - NB_{oi} = N(B_o - B_{oi})$ .

Expansion of solution gas when the reservoir is below the bubble point =  $NB_g(R_{si} - R_s)$ .

Hence, the oil expansion term  $\Delta V_o$  can be expressed as:

$$\begin{aligned} \Delta V_o &= N(B_o - B_{oi}) + NB_g(R_{si} - R_s) \\ \Delta V_o &= N((B_o - B_{oi}) + B_g(R_{si} - R_s)) \end{aligned} \quad (12.6)$$

where  $R_{si}$  is the initial solution gas-oil ratio,  $B_{oi}$  is initial oil formation volume factor, and  $B_{gi}$  is initial gas formation volume factor.

Equation (12.6) can be expressed as:

$$\Delta V_o = NE_o \quad (12.7)$$

where

$$E_o = (B_o - B_{oi}) + (R_{si} - R_s)B_g \quad (12.8)$$

Gas cap expansion without gas production is expressed as:

$$\Delta V_g = G_i \left( \frac{B_g - B_{gi}}{B_{gi}} \right) = G_i \left( \frac{B_g}{B_{gi}} - 1 \right)$$

Substituting  $G_i$  from equation (12.1) into the above equation:

$$\Delta V_g = mNB_{oi} \left( \frac{B_g}{B_{gi}} - 1 \right) \quad (12.9)$$

For a slightly compressible system, expansion of connate water can be expressed as:

$$\Delta V_{swc} = \frac{V_{HC}}{1 - S_{wc}} (c_w S_{wc}) \Delta p \quad (12.10)$$

and change in reservoir volume due to rock compressibility expressed as:

$$\Delta V_f = \frac{V_{HC}}{1 - S_{wc}} c_f \Delta p \quad (12.11)$$

where  $c_w$  is the compressibility of water,  $c_f$  is the compressibility of the formation, and  $V_{HC}$  is the total hydrocarbon pore volume, which includes the oil and the gas cap.

Hence, connate water expansion and rock compressibility for  $\Delta p$  pressure change can be defined as:

$$\Delta V_{fw} = \Delta V_{swc} + \Delta V_f$$

Substituting equations (12.10) and (12.11) into the above:

$$\Delta V_{fw} = V_{HC} \left( \frac{c_w S_{wc} + c_f}{1 - S_{wc}} \right) \Delta p \quad (12.12)$$

From equations (12.1) and (12.2):

$$V_{HC} = NB_{oi} + mNB_{oi} \quad (12.13)$$

Substituting equation (12.13) into equation (12.12):

$$\Delta V_{fw} = NB_{oi}(1 + m) \left( \frac{c_w S_{wc} + c_f}{1 - S_{wc}} \right) \Delta p \quad (12.14)$$

The  $\left( \frac{c_w S_{wc} + c_f}{1 - S_{wc}} \right) \Delta p$  term in equation (12.14) represents the combined expansion of connate water and formation per volume of  $V_{HC}$  and is denoted as  $E_{wf}$ :

$$E_{fw} = \left( \frac{c_w S_{wc} + c_f}{1 - S_{wc}} \right) \Delta p \quad (12.15)$$

Hence, equation (12.14) can be written as:

$$\Delta V_{fw} = NB_{oi}(1 + m)E_{fw} \quad (12.16)$$

Summing up all the expansion terms from equations (12.6), (12.9), and (12.14) and including water influx from the aquifer ( $W_e$ ) and equating to cumulative fluid withdrawal from the reservoir, which is equation (12.4) plus equation (12.5):

$$\begin{aligned} & N_p(B_o + (R_p - R_s)B_g) + W_p B_w \\ &= NB_{oi} \left( \frac{(B_o - B_{oi}) + (R_{si} - R_s)B_g}{B_{oi}} \right) + NB_{oi}m \left( \frac{B_g}{B_{gi}} - 1 \right) \\ &+ NB_{oi}(1 + m) \left( \frac{c_w S_{wc} + c_f}{1 - S_{wc}} \right) \Delta p + W_e \end{aligned}$$

$$\begin{aligned} & N_p(B_o + (R_p - R_s)B_g) + W_p B_w \\ &= NB_{oi} \left[ \left( \frac{(B_o - B_{oi}) + (R_{si} - R_s)B_g}{B_{oi}} \right) + m \left( \frac{B_g}{B_{gi}} - 1 \right) \right. \\ &+ (1 + m) \left. \left( \frac{c_w S_{wc} + c_f}{1 - S_{wc}} \right) \Delta p \right] + W_e \quad (12.17) \end{aligned}$$

Equation (12.17) is the generalized material balance equation for oil reservoirs.

When there is gas injection into the gas cap and water into the aquifer to support or energize the reservoir, the energy contribution of the injection fluid is accounted for in the oil reservoir material balance (OMB) equation, hence becoming:

$$\begin{aligned} & N_p(B_o + (R_p - R_s)B_g) + W_p B_w - W_{inj} B_{winj} - G_{inj} B_{ginj} \\ &= NB_{oi} \left[ \left( \frac{(B_o - B_{oi}) + (R_{si} - R_s)B_g}{B_{oi}} \right) + m \left( \frac{B_g}{B_{gi}} - 1 \right) \right. \\ &+ (1 + m) \left. \left( \frac{c_w S_{wc} + c_f}{1 - S_{wc}} \right) \Delta p \right] + W_e \quad (12.18) \end{aligned}$$

where  $W_{inj}$  is the cumulative water injection measured at the surface,  $B_{winj}$  is the formation volume factor of injected water,  $G_{inj}$  is the cumulative gas injection measured at surface, and  $B_{ginj}$  is the formation volume factor of injected gas.

### 12.2.1. Oil Material Balance Model Diagnosis

The *Campbell plot* [Campbell and Campbell, 1978] and *Havlena-Odeh straight-line methods* [Havlena and Odeh, 1963] are important oil reservoir material balance diagnostic plots that can give a good estimate of oil in place and energy support to the oil zone from the gas cap and aquifer.

**12.2.1.1. Campbell Plot.** From the generalized OMB equation (equation (12.17)):

$$\begin{aligned} & N_p(B_o + (R_p - R_s)B_g) + W_p B_w \\ &= N(B_o - B_{oi}) + N(R_{si} - R_s)B_g + NB_{oi}m \left( \frac{B_g}{B_{gi}} - 1 \right) \\ &+ NB_{oi}(1 + m) \left( \frac{c_w S_{wc} + c_f}{1 - S_{wc}} \right) \Delta p + W_e \end{aligned}$$

Rearranging this:

$$\begin{aligned} & N_p(B_o + (R_p - R_s)B_g) + W_p B_w \\ &= NB_{oi} \left[ \frac{(B_o - B_{oi}) + (R_{si} - R_s)B_g}{B_{oi}} + m \left( \frac{B_g}{B_{gi}} - 1 \right) \right. \\ & \quad \left. + (1 + m) \left( \frac{c_w S_{wc} + c_f}{1 - S_{wc}} \right) \Delta p \right] + W_e \end{aligned}$$

The above expression can be presented as:

$$F = NE_t + W_e \quad (12.19)$$

where

$$F = N_p(B_o + (R_p - R_s)B_g) + W_p B_w \quad (12.20)$$

and

$$\begin{aligned} E_t = B_{oi} \left[ \frac{(B_o - B_{oi}) + (R_{si} - R_s)B_g}{B_{oi}} + m \left( \frac{B_g}{B_{gi}} - 1 \right) \right. \\ \left. + (1 + m) \left( \frac{c_w S_{wc} + c_f}{1 - S_{wc}} \right) \Delta p \right] \end{aligned} \quad (12.21)$$

Rearranging equation (12.19):

$$\frac{F}{E_t} = N + \frac{W_e}{E_t} \quad (12.22)$$

When the reservoir is undergoing volumetric depletion, then  $W_e = 0$ . Hence, the first term is constant and independent of oil produced ( $N_p$ ).

When there is aquifer support, there is extra energy support and the energy term increases with  $N_p$  due to this extra energy. For moderate aquifer support, the energy contribution from the aquifer dissipates with increased  $N_p$ . Hence, the initial energy increase is, subsequently, followed by an energy decrease. However, with strong aquifer support, there is no decrease in the energy term.

A *Campbell plot* [Campbell and Campbell, 1978] can be used to identify the presence of water influx. The shape of the plot gives an indication of the strength of the aquifer, as illustrated in Fig. 12.6.

**12.2.1.2. Generalized Havlena–Odeh Diagnostic Method.** This method provides both qualitative and quantitative diagnosis of the material balance model.

From equation (12.22), a plot of  $\frac{F}{E_t}$  against  $\frac{W_e}{E_t}$  for a model with correct gas cap volume and aquifer volume will yield a straight-line with intercept of  $N$  on the vertical  $y$ -axis, as shown in Fig. 12.7.

In order to use the generalized Havlena–Odeh plot for diagnosis of aquifer and initial aquifer parameter calculation, it is important that the estimate of initial volume of gas cap to oil reservoir ( $m$ ) is known. Combined well log and geophysical interpretation techniques can provide a

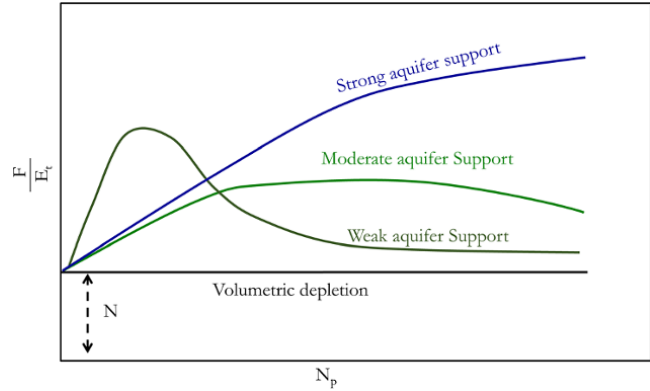


**Figure 12.6** Qualitative and quantitative interpretation of a Campbell plot [Adapted from Campbell and Campbell, 1978].

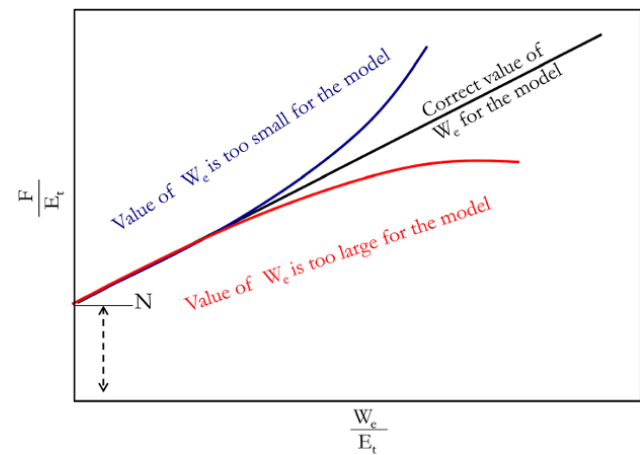


**Figure 12.7** Generalized Havlena–Odeh diagnostic plot [Based on concept by Havlena and Odeh, 1963].

reasonable range of estimate for gas cap size. Diagnosis of oil reservoir with both gas cap and aquifer is always challenging without any additional information due to the nonuniqueness of the material balance solution. However, when the reservoir has one or two fluid zones only, diagnostic models can be used easily to estimate the volume and energy contribution from each reservoir fluid zone and, hence, reduce the uncertainty in material balance calculations. Simplified Havlena–Odeh diagnostic techniques for different reservoir conditions are discussed in the next sections.

**12.2.1.3. Havlena–Odeh Diagnostic Method for Oil Reservoir Without Gas Cap ( $m = 0$ ).** When the oil reservoir has no gas cap ( $m = 0$ ), the use of Havlena–Odeh techniques for aquifer and initial oil in place diagnosis becomes easier than the case of a reservoir with gas cap, oil, and aquifer.

From the  $E_t$  term in equation (12.21):

$$E_t = B_{oi} \left[ \frac{(B_o - B_{oi}) + (R_{si} - R_s)B_g}{B_{oi}} + m \left( \frac{B_g}{B_{gi}} - 1 \right) + (1 + m) \left( \frac{c_w S_{wc} + c_f}{1 - S_{wc}} \right) \Delta p \right]$$

When  $m = 0$ , equation (12.21) becomes:

$$E_t = B_{oi} \left[ \frac{(B_o - B_{oi}) + (R_{si} - R_s)B_g}{B_{oi}} + \left( \frac{c_w S_{wc} + c_f}{1 - S_{wc}} \right) \Delta p \right]$$

$$E_t = ((B_o - B_{oi}) + (R_{si} - R_s)B_g) + B_{oi} \left( \frac{c_w S_{wc} + c_f}{1 - S_{wc}} \right) \Delta p \tag{12.23}$$

Substituting

$$E_o = (B_o - B_{oi}) + (R_{si} - R_s)B_g \text{ from Equation (12.8)}$$

and

$$E_{fw} = \left( \frac{c_w S_{wc} + c_f}{1 - S_{wc}} \right) \Delta p \text{ from equation (12.15), into equation (12.23):}$$

$$E_t = E_o + B_{oi}E_{fw}$$

Substituting  $E_t = E_o + B_{oi}E_{fw}$  into equation (12.19):

$$F = N(E_o + B_{oi}E_{fw}) + W_e \tag{12.24}$$

Equation (12.24) can be rearranged in various ways for plotting and diagnosis

*Option 1:*

Rearranging equation (12.24):

$$F - W_e = N(E_o + B_{oi}E_{fw}) \tag{12.25}$$

Hence, a plot of  $(F - W_e)$  against  $(E_o + B_{oi}E_{fw})$  will yield a straight-line passing through the origin with the slope of the plot giving initial oil in place ( $N$ ), as shown in Fig. 12.8.

*Option 2:*

Rearranging equation (12.24):

$$\frac{F}{(E_o + B_{oi}E_{fw})} = N + \frac{W_e}{(E_o + B_{oi}E_{fw})} \tag{12.26}$$

For option 2, a plot of  $\frac{F}{(E_o + B_{oi}E_{fw})}$  against  $\frac{W_e}{(E_o + B_{oi}E_{fw})}$  will yield a straight-line passing through  $N$  on the vertical  $y$ -axis, as shown in Fig. 12.9.

If connate water expansion and rock compressibility are assumed insignificant compared to oil expansion,  $E_{fw}$  becomes zero and equation (12.26) reduces to:

$$\frac{F}{E_o} = N + \frac{W_e}{E_o} \tag{12.27}$$

Diagnostic plots are shown in Fig. 12.10.

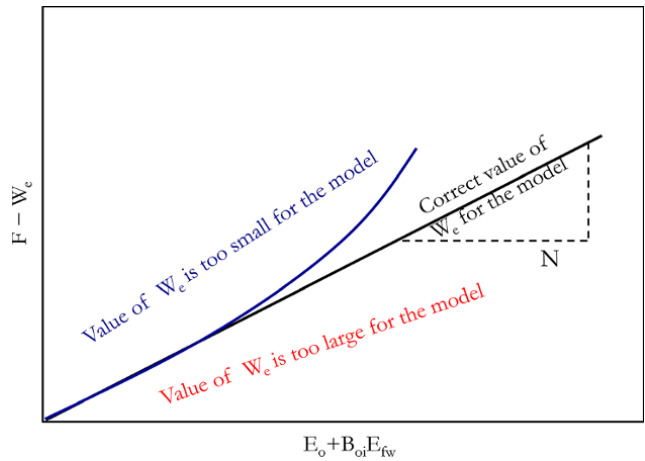


**Figure 12.8** Havlena–Odeh diagnostic plot for a reservoir with  $m = 0$  (option 1)[Based on concept by *Havlena and Odeh, 1963*].

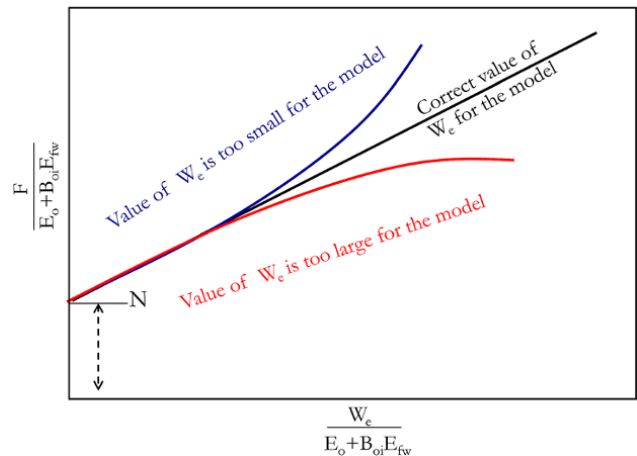


**Figure 12.9** Havlena–Odeh diagnostic plot for a reservoir with  $m = 0$  (option 2)[Based on concept by *Havlena and Odeh, 1963*].

**12.2.1.4. Havlena–Odeh Diagnostic Method for an Oil Reservoir Without Active Aquifer Support ( $W_e = 0$ ).** When reservoir has no active aquifer support ( $W_e = 0$ ), similar to the case in Section 12.2.1.3, use of Havlena–Odeh techniques for gas cap and initial oil in place diagnosis becomes easier than the case with gas cap, oil, and aquifer.

From equation (12.21):

$$E_t = B_{oi} \left[ \frac{(B_o - B_{oi}) + (R_{si} - R_s)B_g}{B_{oi}} + m \left( \frac{B_g}{B_{gi}} - 1 \right) + (1 + m) \left( \frac{c_w S_{wc} + c_f}{1 - S_{wc}} \right) \Delta p \right]$$

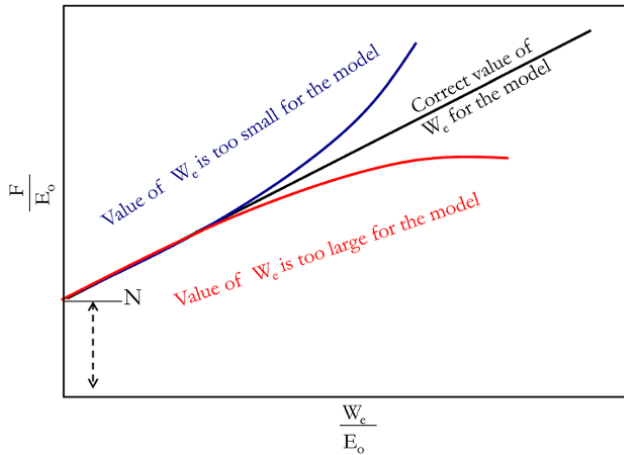


**Figure 12.10** Havlena–Odeh diagnostic plot for a reservoir with  $m = 0$  and  $E_{wf} = 0$  [Based on concept by *Havlena and Odeh, 1963*].

Neglecting connate water expansion and rock compressibility:

$$E_{fw} = \left( \frac{c_w S_{wc} + c_f}{1 - S_{wc}} \right) \Delta p = 0$$

and  $E_t$  becomes:

$$E_t = B_{oi} \left[ \frac{(B_o - B_{oi}) + (R_{si} - R_s) B_g}{B_{oi}} + m \left( \frac{B_g}{B_{gi}} - 1 \right) \right]$$

$$E_t = (B_o - B_{oi}) + (R_{si} - R_s) B_g + B_{oi} m \left( \frac{B_g}{B_{gi}} - 1 \right)$$

Expressing  $E_t$  as:

$$E_t = E_o + mE_g \quad (12.28)$$

where  $E_o = (B_o - B_{oi}) + (R_{si} - R_s) B_g$  and  $E_g = B_{oi} \left( \frac{B_g}{B_{gi}} - 1 \right)$

Substituting  $E_t = E_o + mE_g$  into equation (12.19):

$$F = NE_o + NmE_g + W_e$$

and making  $W_e = 0$  (absence of active aquifer support):

$$F = NE_o + NmE_g$$

$$F = N(E_o + mE_g) \quad (12.29)$$

Hence, a plot of  $F$  against  $(E_o + mE_g)$  will yield a straight-line passing through the origin with the slope of the plot giving initial oil in place ( $N$ ) for the correct value of  $m$  as shown in Fig. 12.11.

### 12.2.2. Oil Material Balance Below Bubble Point Pressure

Below the bubble point pressure, the prediction of  $N_p$  for a given pressure depends on fluid properties and the

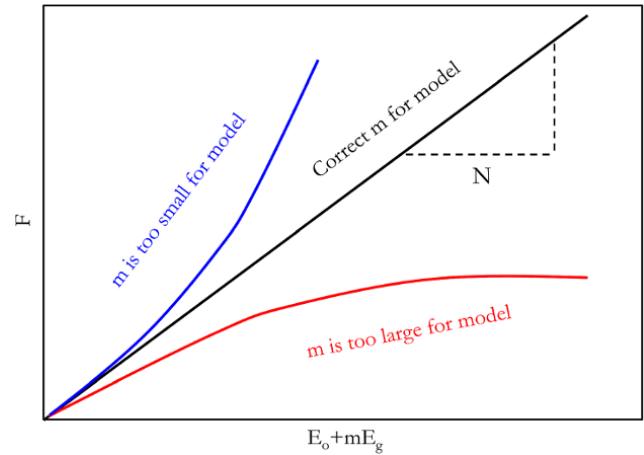


**Figure 12.11** Havlena–Odeh diagnostic plot for reservoir with  $W_e = 0$  [Based on concept by *Havlena and Odeh, 1963*].

relative permeabilities of the phases present. The material balance approach towards oil reservoir performance prediction below the bubble point pressure was described by *Schilthuis [1936]*.

For the case without water production and aquifer water encroachment, the material balance equation from equation (12.17) becomes:

$$N_p (B_o + (R_p - R_s) B_g) = NB_{oi} \left[ \left( \frac{(B_o - B_{oi}) + (R_{si} - R_s) B_g}{B_{oi}} \right) + m \left( \frac{B_g}{B_{gi}} - 1 \right) + (1 + m) \left( \frac{c_w S_{wc} + c_f}{1 - S_{wc}} \right) \Delta p \right]$$

Neglecting water and the rock expansion factor, since this is small compared to expansion of solution gas:

$$N_p (B_o + (R_p - R_s) B_g) = NB_{oi} \left[ \left( \frac{(B_o - B_{oi}) + (R_{si} - R_s) B_g}{B_{oi}} \right) + m \left( \frac{B_g}{B_{gi}} - 1 \right) \right]$$

$$N_p (B_o - R_s B_g) + N_p R_p B_g$$

$$= NB_{oi} \left[ \left( \frac{(B_o - B_{oi}) + (R_{si} - R_s) B_g}{B_{oi}} \right) + m \left( \frac{B_g - B_{gi}}{B_{gi}} \right) \right]$$

Substituting  $G_p = N_p R_p$ :

$$N_p (B_o - R_s B_g) + G_p B_g = NB_{oi} \left[ \left( \frac{(B_o - B_{oi}) + (R_{si} - R_s) B_g}{B_{oi}} \right) + m \left( \frac{B_g - B_{gi}}{B_{gi}} \right) \right]$$

$$N_p (B_o - R_s B_g) + G_p B_g = N \left( (B_o - B_{oi}) + (R_{si} - R_s) B_g \right) + \frac{m N B_{oi}}{B_{gi}} (B_g - B_{gi})$$

$$(12.30)$$

From equation (12.1):

$$G_i = mNB_{oi}$$

where  $G_i$  is the initial free gas at reservoir conditions.

Hence, the initial free gas at surface conditions ( $G$ ) can be defined as:

$$G = \frac{G_i}{B_{gi}} = \frac{mNB_{oi}}{B_{gi}} \quad (12.31)$$

Substituting  $G = \frac{mNB_{oi}}{B_{gi}}$  from equation (12.31) into equation (12.30)

$$N_p(B_o - R_s B_g) + G_p B_g = N((B_o - B_{oi}) + (R_{si} - R_s)B_g) + G(B_g - B_{gi})$$

Making  $N_p$  the subject of the formula:

$$N_p = \frac{N((B_o - B_{oi}) + (R_{si} - R_s)B_g) + G(B_g - B_{gi}) - G_p B_g}{(B_o - R_s B_g)} \quad (12.32)$$

For prediction, the initial reservoir pressure and fluid properties at the initial reservoir pressure ( $B_{oi}$ ;  $B_{gi}$ ;  $R_{si}$ ) should be known. At each prediction time step defined by an average reservoir pressure, other fluid properties ( $B_o$ ,  $B_g$ , and  $R_s$ ) can be determined.

The cumulative gas production can be determined using:

$$G_p = \sum RN_p \quad (12.33)$$

and also

$$G_p = R_p N_p \quad (12.34)$$

where  $R$  is the instantaneous producing gas–oil ratio (GOR) and  $R_p$  is the cumulative production gas–oil ratio.

In order to predict  $N_p$ , the following steps can be used.

*Step 1:* for reservoir pressure of interest, guess a value of  $G_p$

*Step 2:* determine oil saturation ( $S_o$ ) using:

$$S_o = \frac{\text{oil volume}}{\text{pore volume}} = \frac{(N - N_p)B_o}{\left(\frac{NB_{oi}}{1 - S_{wc}}\right)}$$

Rearranging:

$$S_o = \left(1 - \frac{N_p}{N}\right) \left(\frac{B_o}{B_{oi}}\right) (1 - S_{wc}) \quad (12.35)$$

*Step 3:* for  $S_o$  calculated, determine the relative permeability of oil and gas, and then the relative permeability ratio of gas to oil,  $\left(\frac{k_{rg}}{k_{ro}}\right)$ , using the relative permeability model (relative permeability against

saturation). The relative permeability ratio determined, together with the viscosity ratio and formation volume factor ratio, is then used in calculating instantaneous producing gas–oil ratio at the end of the time step of interest, which corresponds to the start of the next time step, as shown in equation (12.36):

$$R = R_s + \left(\frac{B_o}{B_g}\right) \left(\frac{\mu_o}{\mu_g}\right) \left(\frac{k_{rg}}{k_{ro}}\right) \quad (12.36)$$

$G_p$  is then calculated using equation (12.34):

$$G_p = R_p N_p$$

where  $N_p$  is defined in equation (12.32).

*Step 4:* where  $G_p$  from equations (12.33) and (12.34) are equal, then the guessed value of  $G_p$  is correct and, also,  $N_p$  calculated.

Where the value of  $G_p$  from equations (12.33) and (12.34) are not equal, another  $G_p$  is tried until  $G_p$  from equations (12.33) and (12.34) are equal.

*Step 5:* after solving for a given time step defined by an average reservoir pressure, the same process is repeated for the next time step.

The assumptions generally made in the application of this approach to reservoir performance prediction include: uniform reservoir and fluid properties; equilibrium is attained in the reservoir at the end of each time step; and absence of gravity segregation.

Other variations of the Schilthuis approach described here exist in the literature. Fig. 12.12 shows a typical producing gas–oil ratio against average reservoir pressure profile for a solution gas driven oil reservoir.

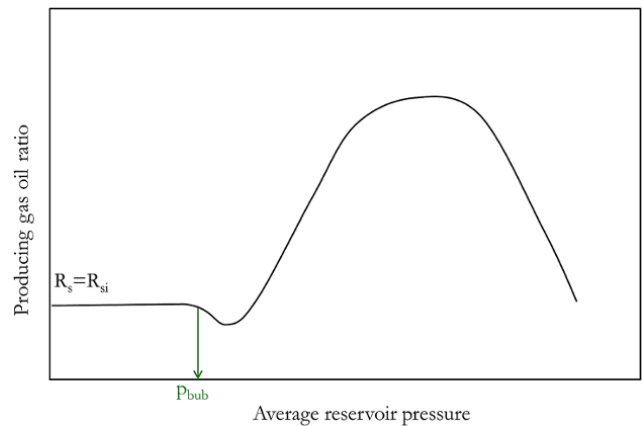


**Figure 12.12** Typical producing gas–oil ratio profile for a solution gas driven oil reservoir.

**12.2.3. Oil Material Balance Drive Index–Energy Plot**

More than one drive mechanism is involved in a producing reservoir (Fig. 12.13). Hence, it is very important to understand the contribution of energy (drive mechanism) to the reservoir and field, and how best to use the existing energy in the reservoir and support the reservoir with more energy to achieve optimum production. Oil reservoir drive energy can be grouped as:

- *Depletion drive*, which is due to oil and solution expansion. Depletion drive derives its name from drive mechanism in the reservoir during depletion without any other drive or support. Overall reservoir deliverability will mainly be due to expansion of dissolved gas and liquid oil when the reservoir pressure drops.

- *Segregating gas-cap drive* (also called *primary gas-cap drive* or *free gas drive*), which is due to expansion of the segregated gas zone. A complex form of gas-cap drive called *nonsegregation-drive gas caps*, which is based on diffusion, can also take place.

- *Compaction drive*, which is due to contraction of porous rock and expansion of the pore fluids when the pressure drops in the reservoir.

- *Water drive*, which is due to the combined effect of natural aquifer and injected water. Typical recoveries for different drive mechanisms are shown in Table 12.1.

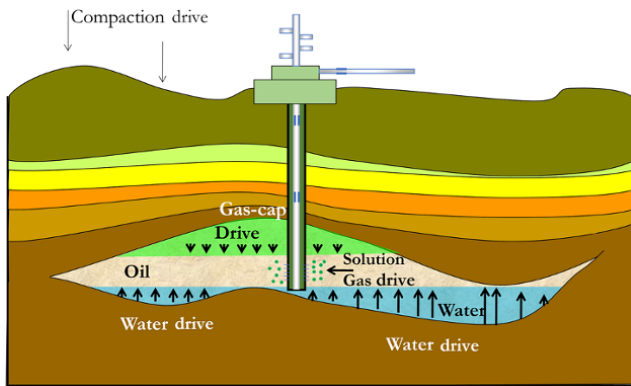


**Figure 12.13** Oil reservoir showing different energy drives.

**Table 12.1** Typical Recoveries for Different Drive Mechanisms.

Drive mechanism	Recovery of original oil (%)
Depletion drive	5–25
Segregated gas-cap drive	15–40
Compaction drive	2–5
Water drive	15–60

From the generalized oil material balance equation (equation (12.17)):

$$\begin{aligned}
 N_p(B_o + (R_p - R_s)B_g) &= \frac{NB_{oi}[(B_o - B_{oi}) + (R_{si} - R_s)B_g]}{B_{oi}} \\
 &+ NB_{oi}m\left(\frac{B_g}{B_{gi}} - 1\right) + NB_{oi}(1 + m)\left(\frac{c_w S_{wc} + c_f}{1 - S_{wc}}\right)\Delta p \\
 &+ (W_e - W_p B_w) \\
 1 &= \frac{N[(B_o - B_{oi}) + (R_{si} - R_s)B_g]}{N_p(B_o + (R_p - R_s)B_g)} + \frac{NB_{oi}m\left(\frac{B_g}{B_{gi}} - 1\right)}{N_p(B_o + (R_p - R_s)B_g)} \\
 &+ \frac{NB_{oi}(1 + m)\left(\frac{c_w S_{wc} + c_f}{1 - S_{wc}}\right)\Delta p}{N_p(B_o + (R_p - R_s)B_g)} + \frac{(W_e - W_p B_w)}{N_p(B_o + (R_p - R_s)B_g)} \\
 1 &= \frac{N[(B_o - B_{oi}) + (R_{si} - R_s)B_g]}{N_p(B_o + (R_p - R_s)B_g)} + \frac{NB_{oi}m\left(\frac{B_g}{B_{gi}} - 1\right)}{N_p(B_o + (R_p - R_s)B_g)} \\
 &\quad \text{Depletion} \qquad \qquad \qquad \text{Segregation} \\
 &\quad \text{Drive Index} \qquad \qquad \qquad \text{Drive Index} \\
 &+ \frac{NB_{oi}(1 + m)\left(\frac{c_w S_{wc} + c_f}{1 - S_{wc}}\right)\Delta p}{N_p(B_o + (R_p - R_s)B_g)} + \frac{(W_e - W_p B_w)}{N_p(B_o + (R_p - R_s)B_g)} \\
 &\quad \text{Compaction} \qquad \qquad \qquad \text{Water Drive} \\
 &\quad \text{Drive Index} \qquad \qquad \qquad \text{Index}
 \end{aligned}
 \tag{12.37}$$

Components on the right-hand side of equation (12.37) define the *drive index* or *energy components* as a fraction of 1.

Though in most reservoirs compaction drive rarely contributes more than 5%, some reservoirs have shown significant compaction drive contribution to oil recovery. In the Bachaquero field in Venezuela, compaction contributes over 50% recovery; in the Valhall reservoir in the Norwegian sector of the North Sea, compaction contributes over 70%.

**Exercise 12.1** Oil Material Balance Calculation for a Model Without a Gas Cap and Aquifer

A reservoir with initial pressure of 5,200 psia and temperature of 123°F has the following properties:  $\phi = 0.2$ ;  $S_{wc} = 0.15$ ;  $c_f = 3.50 \text{ E-}06 \text{ psi}^{-1}$ ; and  $c_w = 7.00\text{E-}06 \text{ psi}^{-1}$ . An oil sample recovered from the reservoir has an API of 30°; solution gas–oil ratio of 800 scf/stb, and gas gravity of 0.8. The production history and fluid properties required for the material balance calculation are shown in Table 12.2.

Formation testing, openhole logs, and geophysical and geological interpretations suggest the absence of a gas cap and active aquifer.

**Table 12.2** Production History and Fluid Properties for Exercise 12.1.

Date (dd/mm/yyyy)	$p_{\text{Avg}}$ (psia)	$N_p$ (MMSTB)	$G_p$ (Bscf)	$B_o$ rb/stb	$R_s$ (Mscf/stb)	$B_g$ (rb/Mscf)	$R_p$ (Mscf/stb)
01/01/2003	5,200	0.00	0.00	1.376	0.800	0.545	0.800
02/04/2003	3,940.89	3.89	3.11	1.389	0.800	0.613	0.800
02/07/2003	3,512.38	6.07	4.85	1.364	0.747	0.651	0.800
01/10/2003	3,322.18	7.74	6.17	1.336	0.696	0.673	0.798
31/12/2003	3,178.82	9.22	7.51	1.316	0.658	0.692	0.814
31/03/2004	3,058.58	10.57	8.98	1.299	0.627	0.709	0.850
30/06/2004	2,952.1	11.79	10.63	1.285	0.600	0.727	0.901
29/09/2004	2,854.95	12.90	12.47	1.272	0.576	0.745	0.966
29/12/2004	2,764.87	13.91	14.50	1.261	0.554	0.763	1.042
30/03/2005	2,680.77	14.83	16.70	1.250	0.533	0.781	1.126
29/06/2005	2,602.16	15.65	19.04	1.241	0.515	0.800	1.216
28/09/2005	2,528.94	16.39	21.47	1.232	0.497	0.820	1.310
28/12/2005	2,461.18	17.05	23.94	1.224	0.482	0.839	1.404
29/03/2006	2,399.03	17.62	26.40	1.216	0.467	0.858	1.498
28/06/2006	2,342.59	18.13	28.79	1.210	0.455	0.877	1.588
27/09/2006	2,291.91	18.56	31.07	1.204	0.443	0.895	1.674
27/12/2006	2,246.93	18.94	33.20	1.199	0.433	0.912	1.753
28/03/2007	2,207.46	19.26	35.14	1.195	0.424	0.928	1.825
27/06/2007	2,173.21	19.53	36.89	1.191	0.417	0.943	1.889
26/09/2007	2,143.79	19.76	38.44	1.188	0.410	0.956	1.945
26/12/2007	2,118.77	19.95	39.79	1.185	0.405	0.967	1.994
26/03/2008	2,097.66	20.11	40.95	1.183	0.400	0.977	2.037
25/06/2008	2,080.00	20.24	41.94	1.181	0.397	0.986	2.072
24/09/2008	2,065.32	20.35	42.77	1.179	0.393	0.993	2.102
24/12/2008	2,053.19	20.43	43.47	1.178	0.391	0.999	2.127
25/03/2009	2,043.21	20.51	44.05	1.177	0.389	1.004	2.148
24/06/2009	2,035.03	20.56	44.52	1.176	0.387	1.008	2.165
23/09/2009	2,028.36	20.61	44.91	1.176	0.385	1.012	2.179
23/12/2009	2,022.92	20.65	45.23	1.175	0.384	1.015	2.190
24/03/2010	2,018.51	20.68	45.50	1.174	0.383	1.017	2.200
23/06/2010	2,014.94	20.71	45.80	1.174	0.383	1.019	2.212

$R_p$  is produced cumulative gas–oil ratio.

$p_{\text{Avg}}$  is average reservoir pressure.

Using the workflow in Fig. 12.3, determine the primary drive mechanism and initial oil in place.

### Solution Steps.

*Step 1:* data preparation.

This involves a quality check of all data supplied. Verification of average pressure is important, as this is often not correctly determined. Also, fluid data should be examined for consistencies. Fluid properties quality check is discussed in Chapter 4 (4.3).

*Step 2:* data diagnosis.

Using equations (12.20), (12.21) and (12.22), create a table of  $\frac{F}{E_t}$ , then create a *Campbell plot* ( $\frac{F}{E_t}$  against  $N_p$ ) (Table 12.3). Inspect if there is additional energy support (gas cap or aquifer) and determine  $N$  from the *Campbell plot* (Fig. 12.14).

If the system has an aquifer, following aquifer identification using a Campbell plot, the generalized Havlena–Odeh diagnostic plot should be used to confirm  $N$  and determine aquifer size before forward simulation.

*Step 3:* define material balance model and initial model parameters based on diagnostic plots.

Based on the diagnosis, the reservoir model is possibly an oil reservoir with no active aquifer or gas cap.

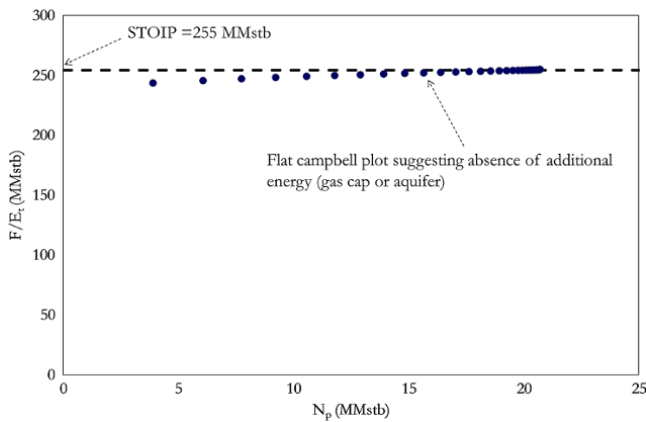
*Step 4:* model consistency checks.

This generally involves checking that the model from diagnosis is consistent with any other data, information or reservoir model from other characterization method. In this case, formation testing, geophysical interpretation, and openhole logs suggest the absence of a gas cap and active aquifer. Hence, the material balance model is consistent with available data.



**Table 12.3**  $F/E_t$  for a Campbell Plot.

F (MMrb)	$E_t$ (rb/stb)	$F/E_t$ (MMstb)	F (MMrb)	$E_t$ (rb/stb)	$F/E_t$ (MMstb)
0.000	0.000	0.000	45.516	0.179	253.676
5.409	0.022	243.468	48.046	0.189	253.846
8.486	0.035	245.487	50.367	0.198	253.985
10.872	0.044	246.998	52.459	0.206	254.101
13.136	0.053	248.145	54.313	0.214	254.194
15.403	0.062	249.062	55.933	0.220	254.280
17.736	0.071	249.799	57.329	0.225	254.351
20.172	0.081	250.451	58.520	0.230	254.404
22.729	0.091	251.016	59.524	0.234	254.445
25.412	0.101	251.520	60.365	0.237	254.485
28.212	0.112	251.965	61.063	0.240	254.514
31.105	0.123	252.354	61.640	0.242	254.535
34.058	0.135	252.700	62.114	0.244	254.558
37.027	0.146	252.995	62.502	0.246	254.569
39.960	0.158	253.263	62.908	0.247	254.941
42.806	0.169	253.485			


**Figure 12.14** Data diagnosis using a Campbell plot.

*Step 5:* forward simulation.

With determined *initial oil in place* ( $N$ ), average reservoir pressure and fluid properties ( $R_s$  against  $p_{Avg}$ ;  $B_g$  against  $p_{Avg}$ ;  $B_o$  against  $p_{Avg}$ ) forward simulation is then carried out to predict  $N_p$  (Fig. 12.1b) and compared with the measured value. Also, the prediction can be  $p_{Avg}$  with  $N_p$  as input (Fig. 12.1a).

Predicting  $N_p$  using equation (12.17):

$$N_p(B_o + (R_p - R_s)B_g) + W_p B_w = NB_{oi} \left[ \frac{(B_o - B_{oi}) + (R_{si} - R_s)B_g}{B_{oi}} + m \left( \frac{B_g}{B_{gi}} - 1 \right) + (1 + m) \left( \frac{c_w S_{wc} + c_f}{1 - S_{wc}} \right) \Delta p \right] + W_e$$

With  $w_p = 0$ ,  $w_e = 0$ , and  $m = 0$ , this equation reduces to:

$$N_p(B_o + (R_p - R_s)B_g) = NB_{oi} \left[ \frac{(B_o - B_{oi}) + (R_{si} - R_s)B_g}{B_{oi}} + \left( \frac{c_w S_{wc} + c_f}{1 - S_{wc}} \right) \Delta p \right]$$

Making  $N_p$  the subject of the formula:

$$N_p = \frac{NB_{oi}}{(B_o + (R_p - R_s)B_g)} \left[ \frac{(B_o - B_{oi}) + (R_{si} - R_s)B_g}{B_{oi}} + \left( \frac{c_w S_{wc} + c_f}{1 - S_{wc}} \right) \Delta p \right] \quad (12.38)$$

$N_p$  prediction is carried out using equation (12.38) and comparing with the measured  $N_p$  as shown in Table 12.4.

The history match of cumulative oil produced is shown in Fig. 12.15.

*Step 6:* data matching.

This involves using regression to improve the match of predicted  $N_p$  compared with measured  $N_p$ . The least square error method using equation (5.112) was used to refine  $N_p$  history match by minimizing the sum of the square of the errors. The improved match has  $N = 258$  MMstb.

*Step 7:* final results.

The final results will include: material balance model, drive indices plot, and interpretation parameters. The material balance model is, therefore, an oil reservoir with no active aquifer or gas cap.

Energy indices are calculated from equation (12.37):

$$I = \frac{N[(B_o - B_{oi}) + (R_{si} - R_s)B_g]}{N_p(B_o + (R_p - R_s)B_g)} + \frac{NB_{oi}m \left( \frac{B_g}{B_{gi}} - 1 \right)}{N_p(B_o + (R_p - R_s)B_g)} + \frac{NB_{oi}(1 + m) \left( \frac{c_w S_{wc} + c_f}{1 - S_{wc}} \right) \Delta p}{N_p(B_o + (R_p - R_s)B_g)} + \frac{(W_e - W_p B_w)}{N_p(B_o + (R_p - R_s)B_g)}$$

in this case,  $m = 0$ ,  $w_p = 0$ , and  $w_e = 0$ . This thus becomes:

$$I = \frac{N[(B_o - B_{oi}) + (R_{si} - R_s)B_g]}{N_p(B_o + (R_p - R_s)B_g)} + \frac{NB_{oi} \left( \frac{c_w S_{wc} + c_f}{1 - S_{wc}} \right) \Delta p}{N_p(B_o + (R_p - R_s)B_g)}$$

where  $\frac{N[(B_o - B_{oi}) + (R_{si} - R_s)B_g]}{N_p(B_o + (R_p - R_s)B_g)}$  is the depletion drive index.

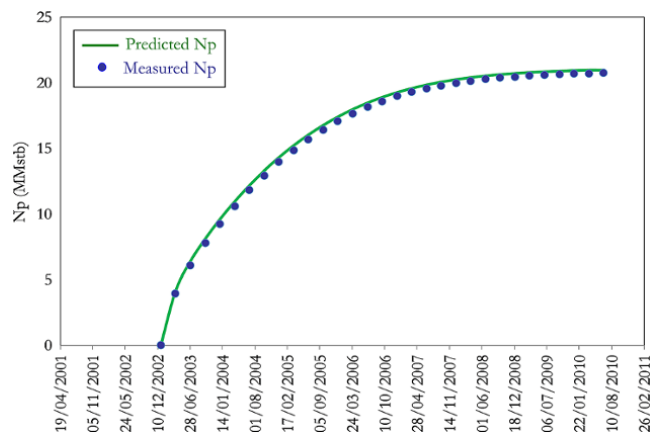
$\frac{NB_{oi} \left( \frac{c_w S_{wc} + c_f}{1 - S_{wc}} \right) \Delta p}{N_p(B_o + (R_p - R_s)B_g)}$  is the compaction drive index.

The calculated energy/drive indices are summarized in Table 12.5.

The drive indices plot or energy plot, which is the plot of drive indices summing up to 1, is shown in Fig. 12.16.

**Table 12.4** Initial Prediction of  $N_p$  Based on Diagnosis Result.

Date (dd/mm/yyyy)	Measured $N_p$ (MMstb)	Predicted $N_p$ (MMstb)	Date (dd/mm/yyyy)	Measured $N_p$ (MMstb)	Predicted $N_p$ (MMstb)
01/01/2003	0.00	0.00	27/12/2006	18.94	19.04
02/04/2003	3.89	4.08	28/03/2007	19.26	19.35
02/07/2003	6.07	6.30	27/06/2007	19.53	19.61
01/10/2003	7.74	7.99	26/09/2007	19.76	19.83
31/12/2003	9.22	9.48	26/12/2007	19.95	20.01
31/03/2004	10.57	10.82	26/03/2008	20.11	20.17
30/06/2004	11.79	12.04	25/06/2008	20.24	20.29
29/09/2004	12.90	13.14	24/09/2008	20.35	20.39
29/12/2004	13.91	14.14	24/12/2008	20.43	20.48
30/03/2005	14.83	15.04	25/03/2009	20.51	20.55
29/06/2005	15.65	15.84	24/06/2009	20.56	20.60
28/09/2005	16.39	16.56	23/09/2009	20.61	20.65
28/12/2005	17.05	17.20	23/12/2009	20.65	20.69
29/03/2006	17.62	17.76	24/03/2010	20.68	20.72
28/06/2006	18.13	18.25	23/06/2010	20.71	20.71
27/09/2006	18.56	18.68			

**Figure 12.15** Cumulative oil produced history match.

Forward simulation/prediction using material balance reservoir models can be a case of pressure determination with known cumulative reservoir withdrawal/injection (Fig. 12.1a) or a case of cumulative withdrawal/injection determination with known average pressure (Fig. 12.1b). The case of pressure determination can be implemented by changing pressure iteratively until a guessed value of cumulative withdrawal/injection is achieved with fluid properties defined as a function of pressure.

The need to estimate and predict pressure rather than cumulative volume withdrawal/injection arises especially when the reservoir pressure response due to fluid withdrawal or injection is of interest. Also, pressure prediction rather than cumulative volume withdrawal/injection is important as profiles gives a better understanding of energy drive and support in a reservoir in response to fluid withdrawal/injection.

### 12.3. AQUIFER MODEL

Aquifers are important components of gas and oil material balance models. Aquifers can be large when compared to the reservoir and, as such, give significant pressure support and drive for reservoir fluid production. When aquifers are small, their effect on reservoir deliverability may be negligible. The ability to predict aquifer response during depletion of a reservoir is important in material balance analysis.

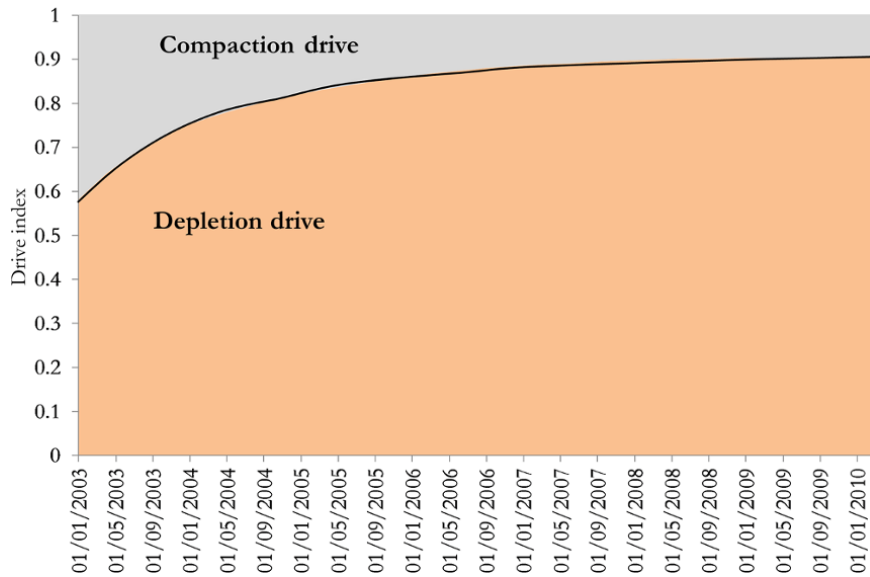
Aquifers come in different geometries (Fig. 12.17), orientation, and sizes. As such, they can be connected to the reservoir in different ways which affect reservoir deliverability.

Fig. 12.17 shows different simplistic representations of aquifer flow geometry. In reality, aquifer geometry may be more complex than those shown in Fig. 12.17; as such, interaction with a geologist and geophysicist on the most likely aquifer geometry is important. Aquifers often present high uncertainty, since the modelling of aquifer influx requires aquifer parameters such as porosity and permeability, which may not be known if aquifer rock properties are not measured.

Aquifer response to pressure diffusion from the hydrocarbon reservoir can be viewed in a similar way as the response of the hydrocarbon reservoir to pressure diffusion from the wellbore. When a steady state has been reached in the reservoir (pressure diffusion from well has reached the reservoir–aquifer interface with constant pressure boundary), the effect of the aquifer begins to manifest in the reservoir response. Though reservoir response is at a steady state, the aquifer response at the beginning is transient (nonsteady state) until the aquifer boundaries are reached. An aquifer model that captures both transient and nontransient aquifer response should

**Table 12.5** Drive Indices.

Date (dd/mm/yyyy)	Depletion drive index	Compaction drive index	Date (dd/mm/yyyy)	Depletion drive index	Compaction drive index
01/01/2003	0.00	0.00	27/12/2006	0.88	0.12
02/04/2003	0.58	0.42	28/03/2007	0.88	0.12
02/07/2003	0.64	0.36	27/06/2007	0.89	0.11
01/10/2003	0.69	0.31	26/09/2007	0.89	0.11
31/12/2003	0.72	0.28	26/12/2007	0.89	0.11
31/03/2004	0.74	0.26	26/03/2008	0.90	0.10
30/06/2004	0.77	0.23	25/06/2008	0.90	0.10
29/09/2004	0.79	0.21	24/09/2008	0.90	0.10
29/12/2004	0.80	0.20	24/12/2008	0.90	0.10
30/03/2005	0.82	0.18	25/03/2009	0.90	0.10
29/06/2005	0.83	0.17	24/06/2009	0.90	0.10
28/09/2005	0.84	0.16	23/09/2009	0.90	0.10
28/12/2005	0.85	0.15	23/12/2009	0.90	0.10
29/03/2006	0.86	0.14	24/03/2010	0.90	0.10
28/06/2006	0.87	0.13	23/06/2010	0.90	0.10
27/09/2006	0.87	0.13			



**Figure 12.16** Energy plot for Exercise 12.1.

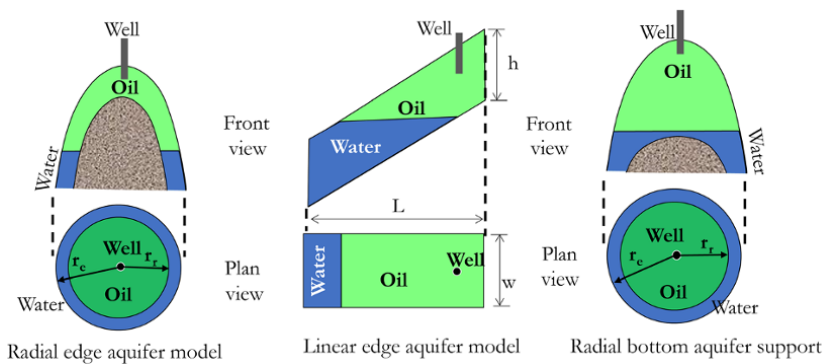


**Figure 12.17** Different aquifer flow geometries.

always be considered in order to characterize the reservoir-aquifer system correctly.

**12.3.1. Small Pot Aquifer Model**

The small plot is the most simplistic aquifer influx model; it is based on linear expansivity of the aquifer to instantaneous change in reservoir pressure. This model is applicable to small aquifers. The small pot aquifer influx model can be expressed as:

$$W_e(t) = (c_f + c_w)W\Delta p \text{ in consistent units} \quad (12.39)$$

and can be expressed in engineering oil field (EOF) units as:

$$W_e(t) = 5.615(c_f + c_w)W\Delta p \quad (12.40)$$

where  $\Delta p = (p_i - p(t))$ ,  $W$  is the initial aquifer water volume,  $c_w$  is the compressibility of water,  $c_f$  is the compressibility of the rock,  $W_e(t)$  is the cumulative water influx at time  $t$ ,  $p_i$  is the initial pressure, and  $p(t)$  is the average reservoir pressure at time  $t$ .

**12.3.2. Hurst-van Everdingen (HVE) Unsteady State Aquifer Model**

This is one of the most rigorous aquifer models derived based on pressure transient response; it does not assume the instantaneous response of the reservoir to aquifer influx. The HVE model is based on a constant terminal pressure solution (Chapter 8 (8.5.1.2)). Hence, due to changing pressure history, the superposition principle is applied in a similar way to the way it is implied in well test analysis (Chapter 8 (8.5.1.4)).

The HVE water influx solution is in dimensionless form ( $W_D$  as a function of  $t_D$  and  $r_{eD}$ ) and is similar to earlier well test analysis type curves. For computational efficiency, an analytical expression for predicting cumulative water influx at any time,  $t$ , for an aquifer is often preferred to type curve matching.

Cumulative water influx ( $W_e(t)$ ) at any given time,  $t$ , can be described by the HVE water influx model as [van Everdingen and Hurst, 1949]:

$$W_e(t) = U \sum_{j=0}^{n-1} \Delta p_j W_D(t_D - t_{Dj}) \quad (12.41)$$

where  $U$  is an aquifer constant and depends on the geometry of the aquifer.

For radial geometry:

$$U = 1.119 \left(\frac{\theta}{360}\right) h \phi_a (c_f + c_w) r_r^2 \text{ in EOF units (bbl/psi)}$$

For linear geometry:

$$U = 0.1781 wLh\phi_a(c_f + c_w)$$

where  $r_r$  is the reservoir radius in ft,  $r_e$  is the aquifer radius in ft,  $L$  is the reservoir length in ft,  $w$  is the reservoir width in ft,  $h$  is the reservoir thickness in ft,  $\phi_a$  is aquifer porosity,  $c_f$  is the formation compressibility ( $\text{psi}^{-1}$ ),  $c_w$  is water compressibility in ( $\text{psi}^{-1}$ ),  $\theta$  is the water influx encroachment angle  $\Delta p_j = \left(\frac{p_{j-1} - p_{j+1}}{2}\right)$  ( $^\circ$ ),  $p_j$  is average reservoir pressure at time step  $j$ ,  $W_e$  is cumulative water influx,  $W_D(t_D)$  is dimensionless cumulative water influx as a function of dimensionless time ( $t_D$ ), and  $t_D$  is dimensionless time which is defines as:

• *Radial Geometry*

$$\begin{aligned} t_D &= \frac{0.00264kt}{\phi\mu c_t r_r^2} \text{ for } t \text{ in hr} \\ t_D &= \frac{0.0063kt}{\phi\mu c_t r_r^2} \text{ for } t \text{ in days} \\ t_D &= \frac{2.309kt}{\phi\mu c_t r_r^2} \text{ for } t \text{ in years} \end{aligned} \quad (12.42)$$

• *Linear Geometry*

$$\begin{aligned} t_D &= \frac{0.00264kt}{\phi\mu c_t L^2} \text{ for } t \text{ in hr} \\ t_D &= \frac{0.0063kt}{\phi\mu c_t L^2} \text{ for } t \text{ in days} \\ t_D &= \frac{2.309kt}{\phi\mu c_t L^2} \text{ for } t \text{ in years} \end{aligned} \quad (12.43)$$

For each time step 1, 2, 3...  $k$ , using equation (12.41):

$$\begin{aligned} W_{e1}(t) &= U\Delta p_1 W_D(t_{D1} - t_{D0}) \\ W_{e2}(t) &= U(\Delta p_1 W_D(t_{D2} - t_{D0}) + \Delta p_2 W_D(t_{D2} - t_{D1})) \\ W_{e3}(t) &= U(\Delta p_1 W_D(t_{D3} - t_{D0}) + \Delta p_2 W_D(t_{D3} - t_{D1}) \\ &\quad + \Delta p_3 W_D(t_{D3} - t_{D2})) \\ W_{ek}(t) &= U(\Delta p_1 W_D(t_{Dk} - t_{D0}) + \Delta p_2 W_D(t_{Dk} - t_{D1}) \\ &\quad + \Delta p_3 W_D(t_{Dk} - t_{D2}) + \dots + \Delta p_k W_D(t_{Dk} - t_{Dk-1})) \end{aligned}$$

Using the series above, equation (12.41) can be expressed as a matrix multiplication operation:

$$[W_e] = U[[W_D] \times [\Delta p]] \quad (12.44)$$

where

$$[W_e] = \begin{pmatrix} W_{e1}(t) \\ W_{e2}(t) \\ W_{e3}(t) \\ \dots \\ W_{ek}(t) \end{pmatrix}$$

$$[W_D] = \begin{pmatrix} W_D(t_{D1} - t_{D0}) \\ W_D(t_{D2} - t_{D0}) & W_D(t_{D2} - t_{D1}) \\ W_D(t_{D3} - t_{D0}) & W_D(t_{D3} - t_{D1}) & W_D(t_{D3} - t_{D2}) \\ \dots & \dots & \dots & \dots & \dots \\ W_D(t_{Dk} - t_{D0}) & W_D(t_{Dk} - t_{D1}) & W_D(t_{Dk} - t_{D2}) & + \dots + & W_D(t_{Dk} - t_{Dk-1}) \end{pmatrix}$$

$$[\Delta p] = (\Delta p_1 \quad \Delta p_2 \quad \Delta p_3 \quad \dots \quad \Delta p_k)$$

For an infinite acting aquifer,  $W_D$  is defined as follows:

$$W_D = 2\sqrt{\frac{t_D}{\pi}} + \frac{t_D}{2} - \frac{t_D}{6}\sqrt{\frac{t_D}{\pi}} + \frac{t_D^2}{16} \text{ for } t_D < 1 [\text{Marshal, 1982}] \quad (12.45)$$

and

$$W_D = a_7 t_D^7 + a_6 t_D^6 + a_5 t_D^5 + a_4 t_D^4 + a_3 t_D^3 + a_2 t_D^2 + a_1 t_D^1 + a_0 \text{ for } 1 < t_D < 100 [\text{Walsh and Lake, 2003}] \quad (12.46)$$

where  $a_7 = 4.8534 \times 10^{-12}$ ,  $a_6 = -1.8436 \times 10^{-9}$ ,  $a_5 = 2.8354 \times 10^{-7}$ ,  $a_4 = -2.2740 \times 10^{-5}$ ,  $a_3 = 1.0284 \times 10^{-3}$ ,  $a_2 = -2.7455 \times 10^{-2}$ ,  $a_1 = 8.5373 \times 10^{-1}$ ,  $a_0 = 8.1638 \times 10^{-1}$ , and

$$W_D = \frac{2t_D}{\ln(t_D)} \text{ for } t_D > 100 [\text{Marshal, 1982}] \quad (12.47)$$

For material balance analysis, a finite size aquifer is what is mainly of interest. Therefore, the effect of the boundary is included into the  $W_D$  function:

$$W_D = 0.5(r_{eD}^2 - 1) \left( 1 - \exp\left(-\frac{2t_D}{J^*}\right) \right) \text{ for } t_D > t_D^* [\text{Marshal, 1982}] \quad (12.48)$$

where

$$r_{eD} = \frac{r_e}{r_r}$$

$$t_D^* = 0.4(r_{eD}^2 - 1)$$

and

$$J^* = \frac{r_{eD}^4 \ln(r_{eD})}{(r_{eD}^2 - 1) + 0.25(1 - 3r_{eD}^2)}$$

$W_D$  calculated for a finite aquifer size if then substituted into equation (12.41) to take care of the superposition time effect.

When  $t_D < t_D^*$ , the equation for an infinite acting aquifer (equation (12.45)–(12.47)) should be used.

### Exercise 12.2 Hurst–van Everdingen (HVE) Unsteady State Aquifer Type Curve

Using equation (12.45)–(12.48), create the Hurst–van Everdingen (HVE) unsteady state aquifer type curve for  $r_{eD} = 5$ ,  $r_{eD} = 6$ ,  $r_{eD} = 7$ ,  $r_{eD} = 8$ ,  $r_{eD} = 9$ ,  $r_{eD} = 10$ , and  $r_{eD} = \infty$  given that  $0 \leq t_D \leq 280$ .

#### Solutions Steps.

Appendix 12A describes the Visual Basic for Applications (VBA) function for calculating  $W_D$  using the call function  $W_D(r_{eD}, t_D)$ .

#### Solution.

Calculate  $W_D$  using the **WD(reD, tD)** function from an Excel spreadsheet after adding the code in Appendix 12A where  $r_{eD}$  in the code is  $r_{eD} = \frac{r_e}{r_r}$  and  $t_D$  in the code is dimensionless time ( $t_D$ ).

Table 12.6 shows a summary of the results for  $0 \leq t_D \leq 280$ .

For the case of  $r_{eD} = \infty$ ,  $r_{eD}$  value greater than 100 is sufficient to give the infinite acting solution as defined in equation (12.47).

The HVE unsteady state aquifer type curve is presented in Fig. 12.18.

### Exercise 12.3 Oil Material Balance with HVE Unsteady State Aquifer Model

An oil reservoir with a thickness of 157.5 ft, radius of 1,033 ft, initial pressure of 6,050 psia, and temperature of 145°F has the following properties: porosity = 0.135,  $S_{wc} = 0.2$ ,  $c_f = 4.20 \text{ E-}06 \text{ psi}^{-1}$ ,  $c_w = 3.5.00\text{E-}06 \text{ psi}^{-1}$ , water viscosity ( $\mu_w$ ) = 0.497 cp, and an aquifer with a permeability of 0.135 mD.

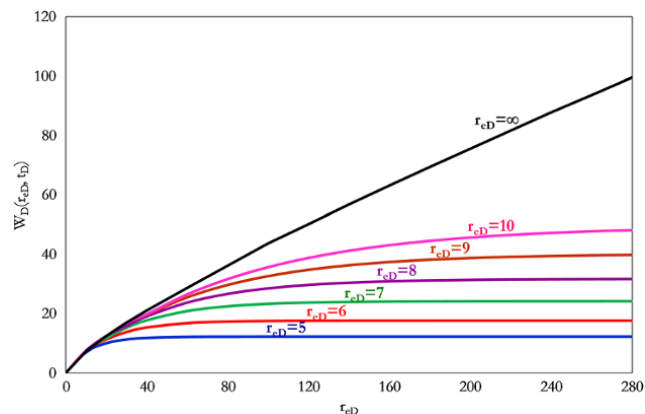
An oil sample from the reservoir has an API of 37°, initial solution gas–oil ratio of 1,100 scf/stb, and gas gravity of 0.79.

Table 12.7 shows the properties of the fluid; Table 12.8 is the production history. Geophysical and geological modelling suggest a radial reservoir–aquifer geometry with a 360° aquifer water encroachment angle and the absence of a gas cap.

Using the workflow in Fig. 12.3, determine the primary drive mechanism and initial oil in place using cumulative volume withdrawal as history match response.

**Table 12.6** HVE Unsteady State Aquifer Type Curve using Equations (12.45)–(12.48).

$t_D$	$r_{eD}$						
	5	6	7	8	9	10	$\infty$
	$W_D(r_{eD}, t_D)$						
0	0.00	0.00	0.00	0.00	0.00	0.00	0.00
10	6.89	7.44	7.44	7.44	7.44	7.44	7.44
20	9.83	11.13	11.56	12.29	12.29	12.29	12.29
30	11.07	13.65	15.05	15.64	16.72	16.72	16.72
40	11.61	15.18	17.56	18.88	19.50	19.68	20.92
60	11.93	16.65	20.66	23.51	25.32	26.36	28.68
80	11.99	17.19	22.27	26.45	29.49	31.54	36.11
100	12.00	17.39	23.10	28.30	32.48	35.56	43.43
120	12.00	17.46	23.54	29.48	34.61	38.68	50.13
140	12.00	17.49	23.76	30.22	36.14	41.10	56.66
160	12.00	17.49	23.88	30.69	37.24	42.98	63.05
180	12.00	17.50	23.94	30.99	38.02	44.44	69.32
200	12.00	17.50	23.97	31.18	38.58	45.57	75.50
220	12.00	17.50	23.98	31.29	38.99	46.45	81.58
240	12.00	17.50	23.99	31.37	39.27	47.13	87.58
260	12.00	17.50	24.00	31.42	39.48	47.66	93.51
280	12.00	17.50	24.00	31.45	39.63	48.08	99.38



**Figure 12.18** HVE unsteady state aquifer type curve using equation (12.45)–(12.48).

Interpolation of the fluid properties will be required to obtain fluid properties at the pressure corresponding to that in the production history.

**Solution.**

*Step 1:* data preparation.

As discussed in Exercise 12.1.

*Step 2:* data diagnosis.

Creating a Campbell plot data using equation (12.20) for  $F$  and equation (12.21) for  $E_t$ , then calculating  $\frac{F}{E_t}$  (Table 12.9).

**Table 12.7** Fluid Properties for Exercise 12.3.

Pressure (psia)	Oil FVF (rb/stb)	Gas–oil ratio (Mscf/stb)	Gas FVF (rb/Mscf)
6,050.00	1.5477	1.1	6.8688
5,736.84	1.5511	1.1	3.6938
5,423.68	1.5550	1.1	2.4422
5,110.53	1.5593	1.1	1.7857
4,797.37	1.5642	1.1	1.3955
4,484.21	1.5698	1.1	1.1488
4,171.05	1.5762	1.1	0.9863
3,857.89	1.5457	1.0397	0.6587
3,544.74	1.4842	0.9301	0.6934
3,231.58	1.4262	0.8260	0.7377
2,918.42	1.3716	0.7274	0.7960
2,605.26	1.3204	0.6338	0.8750
2,292.11	1.2726	0.5451	0.9863
1,978.95	1.2284	0.4611	1.1488
1,665.79	1.1876	0.3815	1.3955
1,352.63	1.1502	0.3060	1.7857
1,039.47	1.1165	0.2343	2.4422
726.32	1.0862	0.1660	3.6938
413.16	1.0593	0.1001	6.8688
100.00	1.0349	0.0324	29.9681

Plot  $\frac{F}{E_t}$  against  $N_p$  as shown in Fig. 12.19.

The Campbell plot in Fig. 12.19 shows moderate aquifer support with an initial estimate of initial oil in place ( $N$ ) of 17 MMstb.

Since the Campbell plot shows the presence of an aquifer and the estimate of  $N$  is known, the Havena–Odeh diagnostic plot for a reservoir with

**Table 12.8** Production History for Exercise 12.3.

Date (dd/mm/yyyy)	$p_{Avg}$ (psia)	$N_p$ (MMstb)	$G_p$ (Bscf)	$W_p$ (MMstb)
01/01/2006	6,050	0	0	0.0000
01/07/2006	5,997.05	0.010	16.95	0.0000
30/12/2006	5,359.06	0.124	223.16	0.0225
30/06/2007	4,912.91	0.227	429.36	0.0450
29/12/2007	4,509.17	0.345	635.57	0.0675
28/06/2008	4,120.93	0.480	841.77	0.0900
27/12/2008	3,806.87	0.633	1,047.98	0.1125
27/06/2009	3,561.13	0.806	1,254.19	0.1350
26/12/2009	3,350.48	0.995	1,460.39	0.1575
26/06/2010	3,166.36	1.195	1,666.60	0.1800
25/12/2010	3,003.56	1.402	1,872.80	0.2025
25/06/2011	2,858.38	1.614	2,079.01	0.2250
24/12/2011	2,727.89	1.829	2,285.22	0.2474

**Table 12.9**  $F/E_t$  for Exercise 12.3.

F (MMrb)	$E_t$ (rb/stb)	$F/E_t$ (MMstb)
0.000	0.000	0.000
0.019	0.001	17.262
0.264	0.015	17.979
0.504	0.025	19.819
0.765	0.036	21.105
1.047	0.048	21.780
1.351	0.061	22.087
1.680	0.077	21.851
2.030	0.095	21.407
2.398	0.115	20.870
2.781	0.137	20.336
3.179	0.160	19.824
3.589	0.185	19.355

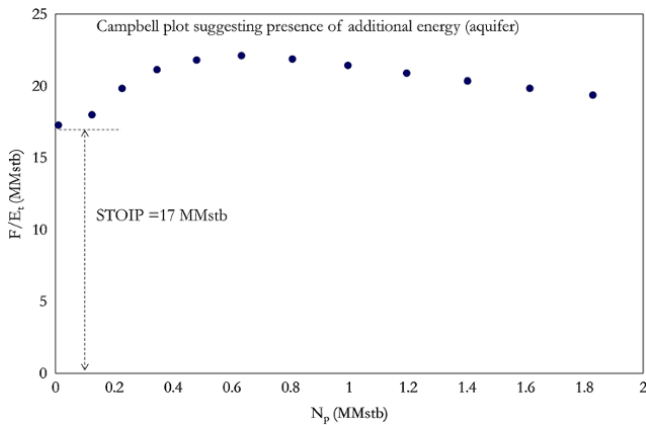


**Figure 12.19** Campbell diagnostic plot for Exercise 12.3.

aquifer and without a gas cap ( $m = 0$ ) is then used to get an initial estimate of aquifer size. The use of a Havlena–Odeh diagnostic plot requires water influx modelling. Equations (12.41)–(12.48) will be used for calculation of  $W_e$  with an initial guess of  $r_{eD} = \frac{r_e}{r_r} = 1.3$

$\Delta p_j$  and  $W_e(t)$  calculations are shown in Table 12.10. The matrix operation  $[W_D] \times [\Delta p]$  can be carried out in Excel using the MMULT function.  $t_D$  and  $[W_D]$  are shown in Table 12.11.

Create a table of  $F - W_e$  and  $E_t = E_o + B_{oi}E_{fw}$  (Table 12.12) then make a Havlena–Odeh diagnostic plot for the oil reservoir without gas cap ( $m = 0$ ) (Fig. 12.20).

Comparison of a straight-line passing through the origin (0,0) with a slope of 17 MMstb (value of  $N$  determined from a Campbell plot) with  $F - W_e$  against the  $E_o + B_{oi}E_{fw}$  trend from Table 12.12 will give an indication if the  $r_{eD}$  value selected is small, large or correct, as discussed in Section 12.2.1.3 and Fig. 12.8.

From Fig. 12.20, the Havlena–Odeh diagnostic plot suggest that the aquifer size used for the calculation is too small. Hence,  $r_{eD} = \frac{r_e}{r_r}$  is changed until the data on the Havlena–Odeh diagnostic plot (taken from Table 12.12) align with the line fit. Iterative change in  $r_{eD}$  is carried out and an improved match of the Havlena–Odeh diagnostic plot was achieved with  $r_{eD} = 2.3$  (Fig. 12.21).

**Step 3:** define the material balance model and initial model parameters based on diagnosis plots.

From diagnosis using the Campbell plot and the Havlena–Odeh plot, the reservoir can be described as a reservoir with oil and a moderate aquifer with initial oil in place of 17 MMstb and radial aquifer with  $r_{eD} = 2.3$ . These parameters will provide initial reservoir model parameters, subject to validation of the model for consistency.

**Step 4:** carry out model consistency checks.

The model described above is consistent with the geophysical and geological information given, which is an oil reservoir with a moderate aquifer and no gas cap.

**Step 5:** data matching.

This involves using regression to improve the match of predicted  $N_p$  (Fig. 12.22) or predicted  $p_{Avg}$  and comparison with actual field value. To do this,  $N_p$  in the material balance equation can be made the subject of the formula ensuring fluid properties are defined as a function of pressure, either by correlation or interpolation from a table of data as done in this example.

**Step 6:** final result.

The final result is summarized in Table 12.13.

**Table 12.10** Calculation of Water Influx by the HEV Method.

$\Delta t$ (Days)	$t_D$	$\Delta p_j = \left(\frac{p_{j-1} - p_{j+1}}{2}\right)$ (psi)	$\sum_{j=0}^{n-1} \Delta p_j W_D(t_D - t_{Dj}) = [W_D] \times [\Delta p]$ (psi)	$W_e(t) = U \sum_{j=0}^{n-1} \Delta p_j W_D(t_D - t_{Dj})_{(rb)}$
0	0.0000	—	—	0.00
181	0.1389	26.475	12.876609	2,519.26
363	0.2786	318.995	164.76424	32,235.54
545	0.4183	223.075	227.99062	44,605.56
727	0.5580	201.870	294.61488	57,640.36
909	0.6977	194.120	360.48116	70,526.87
1,091	0.8374	157.030	409.35769	80,089.39
1,273	0.9771	122.870	446.87056	87,428.65
1,455	1.1167	105.325	480.7042	94,048.08
1,637	1.2564	92.060	510.57131	99,891.48
1,819	1.3961	81.400	537.1325	1,05,088.08
2,001	1.5358	72.590	560.9183	1,09,741.69
2,183	1.6755	65.245	582.37922	1,13,940.44

Exercises 12.1–12.3 show cumulative oil ( $N_p$ ) history matching. Exercise 12.4 describes pressure ( $p_{Avg}$ ) history matching.

**Exercise 12.4** Oil Material Balance with Pressure History Match

Carry out average reservoir pressure ( $p_{Avg}$ ) matching using the information provided in Exercise 12.3.

**Solution.**

This involves calculating pressure ( $p_{Avg}$ ) instead of  $N_p$  to match the material balance model. From the fluid property table, the black oil fluid model or equation of state fluid model, fluid properties ( $B_o$ ,  $R_s$ , and  $B_g$ ) can be defined as a function of pressure such that when pressure changes at each time step, fluid properties change accordingly. Using iterative techniques such as goal seek in a spreadsheet, pressures that match  $N_p$  at the required time steps can then be determined using  $N$  and  $r_{eD}$  from diagnosis plots. Regression can then be used to refine values of  $N$  and  $r_{eD}$  with an improved match. The reservoir pressure ( $p_{Avg}$ ) history match is shown in Table 12.14.

The comparison of measured and predicted  $p_{Avg}$  is shown graphically in Fig.12.23.

**12.3.3. Carter–Tracy Aquifer Model**

The Carter–Tracy model is an approximation of the van Everdingen–Hurst unsteady state aquifer influx model that eliminates the need for superposition in the water influx calculation. The Carter–Tracy aquifer influx model for cumulative water influx at a time ( $t_n$ ) is expressed as [Carter and Tracy, 1960]:

$$W_{en} = W_{e(n-1)} + (t_{Dn} - t_{D(n-1)}) \left( \frac{U p_n - W_{e(n-1)} (p'_{Dn})}{p_{Dn} - t_{D(n-1)} (p'_{Dn})} \right) \tag{12.49}$$

Edwardson *et al.* [1962] presented an approximation for  $p_D$  as:

$$p_D = \frac{370.529\sqrt{t_D} + 137.582t_D + 5.69549(t_D)^{1.5}}{328.834 + 265.488\sqrt{t_D} + 45.2157t_D + (t_D)^{1.5}} \tag{12.50}$$

and  $p'_D$  as:

$$p'_D = \frac{716.441 + 46.7984(t_D)^{0.5} + 270.038t_D + 71.0098 t_D^{1.5}}{1296.86(t_D)^{0.5} + 1204.73t_D + 618.618 t_D^{1.5} + 538.07 t_D^2 + 142.41 t_D^{2.5}} \tag{12.51}$$

where:  $\Delta p_n$  is total pressure drop defined as  $\Delta p_n = p(0) - p(t_{Dn})$ ;  $U$  is the HVE water influx constant, which is same as that in equation (12.41);  $t_D$  is dimensionless time as defined by equations (12.42) and (12.43);  $n$  is the time step;  $p_D$  is dimensionless pressure as a function of  $t_D$  and  $r_{eD}$ ; and  $p'_D$  is the dimensionless pressure derivative.

**12.3.4. Fetkovich Semisteady State Aquifer Model**

This model is based on the pseudosteady state aquifer productivity index (PI) and aquifer compressibility. The model can simply be implemented by eliminating the need for using the superposition principle [Fetkovich, 1971]. This approach, however, neglects the early transient response of the aquifer. The Fetkovich model may slightly under predict water influx when compared to the HVE model. Incremental water influx for the  $n$ th time steps



**Table 12.11**  $t_D$  and  $[W_D]$  Calculation.

$t_D$	$W_D(t_1-t_0)$	$W_D(t_2-t_1)$	$W_D(t_3-t_2)$	$W_D(t_4-t_3)$	$W_D(t_5-t_4)$	$W_D(t_6-t_5)$	$W_D(t_7-t_6)$	$W_D(t_8-t_7)$	$W_D(t_9-t_8)$	$W_D(t_{10}-t_9)$	$W_D(t_{11}-t_{10})$	$W_D(t_{12}-t_{11})$
0.0000	0.0000	0.0000	0.0000	0.0000	0.0000	0.0000	0.0000	0.0000	0.0000	0.0000	0.0000	0.0000
0.1389	0.4864	0.0000	0.0000	0.0000	0.0000	0.0000	0.0000	0.0000	0.0000	0.0000	0.0000	0.0000
0.2786	0.3449	0.4879	0.0000	0.0000	0.0000	0.0000	0.0000	0.0000	0.0000	0.0000	0.0000	0.0000
0.4183	0.3450	0.3449	0.4879	0.0000	0.0000	0.0000	0.0000	0.0000	0.0000	0.0000	0.0000	0.0000
0.5580	0.3450	0.3450	0.3449	0.4879	0.0000	0.0000	0.0000	0.0000	0.0000	0.0000	0.0000	0.0000
0.6977	0.3450	0.3450	0.3450	0.3449	0.4879	0.0000	0.0000	0.0000	0.0000	0.0000	0.0000	0.0000
0.8374	0.3450	0.3450	0.3450	0.3450	0.3449	0.4879	0.0000	0.0000	0.0000	0.0000	0.0000	0.0000
0.9771	0.3450	0.3450	0.3450	0.3450	0.3450	0.3449	0.4879	0.0000	0.0000	0.0000	0.0000	0.0000
1.1167	0.3450	0.3450	0.3450	0.3450	0.3450	0.3450	0.3449	0.4879	0.0000	0.0000	0.0000	0.0000
1.2564	0.3450	0.3450	0.3450	0.3450	0.3450	0.3450	0.3450	0.3449	0.4879	0.0000	0.0000	0.0000
1.3961	0.3450	0.3450	0.3450	0.3450	0.3450	0.3450	0.3450	0.3450	0.3449	0.4879	0.0000	0.0000
1.5358	0.3450	0.3450	0.3450	0.3450	0.3450	0.3450	0.3450	0.3450	0.3450	0.3449	0.4879	0.0000
1.6755	0.3450	0.3450	0.3450	0.3450	0.3450	0.3450	0.3450	0.3450	0.3450	0.3450	0.3449	0.4879

$t_D$  is calculated using  $t_D = \frac{0.0063 \text{ kt}}{\phi \mu c_t r_0^2}$  from equation (12.42).

$[W_D]$  was calculated using  $W_D(r_{eD}, t_D)$  call function (Appendix 12A) for  $r_{eD} = 1.3$ .

**Table 12.12**  $F - W_e$  and  $E_t = E_o + B_{oi}E_{fw}$  Calculations for the Havlena–Odeh Diagnostic Plot.

$F - W_e$ (MMrb)	$E_t = E_o + B_{oi}E_{fw}$ (rb/stb)
0.0000	0.0000
0.0162	0.0011
0.2321	0.0147
0.4597	0.0254
0.7070	0.0362
0.9763	0.0481
1.2708	0.0612
1.5923	0.0769
1.9358	0.0948
2.2979	0.1149
2.6762	0.1368
3.0690	0.1604
3.4754	0.1854

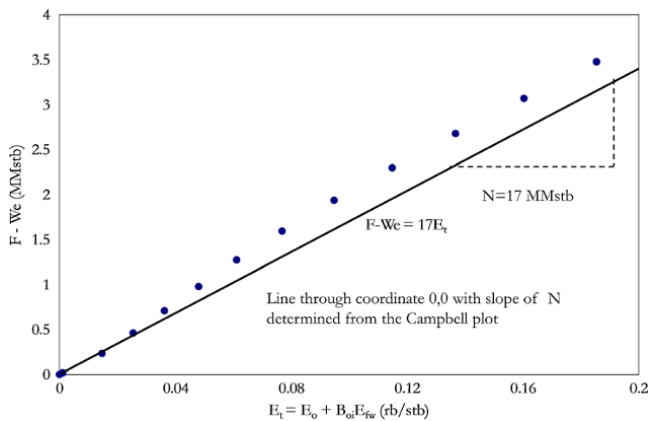


**Figure 12.20** The Havlena–Odeh diagnostic plot for  $r_{eD} = 1.3$ .

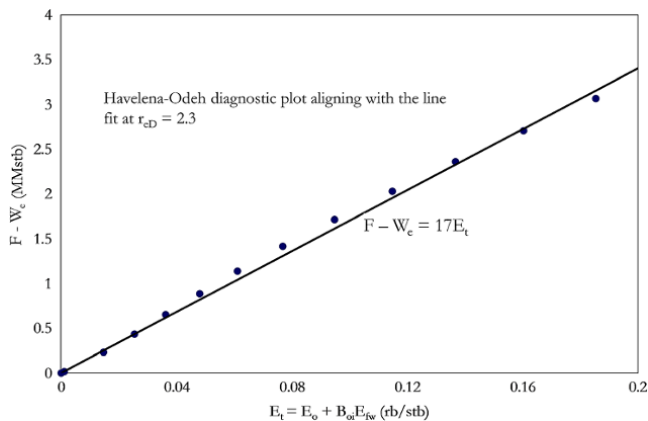


**Figure 12.21** The Havlena–Odeh diagnostic plot for  $r_{eD} = 2.3$ .

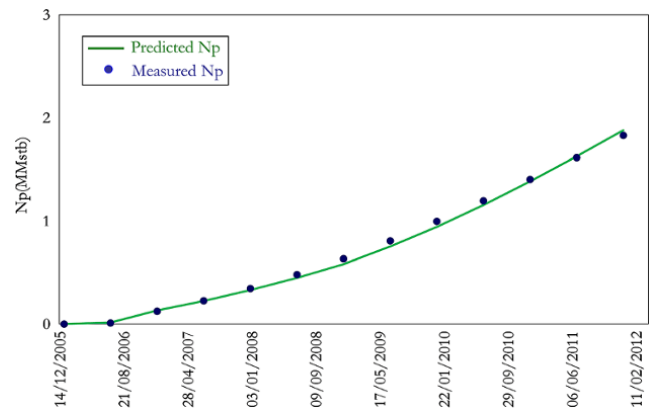


**Figure 12.22** Cumulative oil ( $N_p$ ) history match.

**Table 12.13** Result of material balance analysis.

Reservoir model	Aquifer model
Oil reservoir	Moderate aquifer
$N = 17$ MMstb	$r_{eD} = 2.3$

**Table 12.14** Reservoir Pressure ( $p_{Avg}$ ) History Match Solution.

Date (dd/mm/yyyy)	$N_p$ (given) (MMstb)	Measured	Calculated
		$p_{Avg}$ (psia)	$p_{Avg}$ (psia)
01/01/2006	0	6,050	6,050
01/07/2006	0.010	5,997.05	6,002.71
30/12/2006	0.124	5,359.06	5,403.64
30/06/2007	0.227	4,912.91	4,912.91
29/12/2007	0.345	4,509.17	4,442.39
28/06/2008	0.480	4,120.93	4,014.48
27/12/2008	0.633	3,806.87	3,688.99
27/06/2009	0.806	3,561.13	3,451.83
26/12/2009	0.995	3,350.48	3,262.97
26/06/2010	1.195	3,166.36	3,110.84
25/12/2010	1.402	3,003.56	2,984.91
25/06/2011	1.614	2,858.38	2,879.58
24/12/2011	1.829	2,727.89	2,789.87

using the Fetkovich semisteady state aquifer model can be defined as:

$$\Delta W_{en} = \frac{W_{ei}}{P_{aq,i}} (\bar{p}_{aq,n-1} - \bar{p}_{rn}) \left( 1 - e^{\left\{ -\frac{J_{Paq,i} \Delta t_n}{W_{ei}} \right\}} \right) \quad (12.52)$$

[Fetkovich, 1971]

where  $\bar{p}_{aq,n-1}$  is aquifer pressure at the beginning of the time step and is defined as:

$$\bar{p}_{aq,n-1} = p_{aq,i} \left( 1 - \frac{W_{e,n-1}}{W_{ei}} \right) \quad (12.53)$$

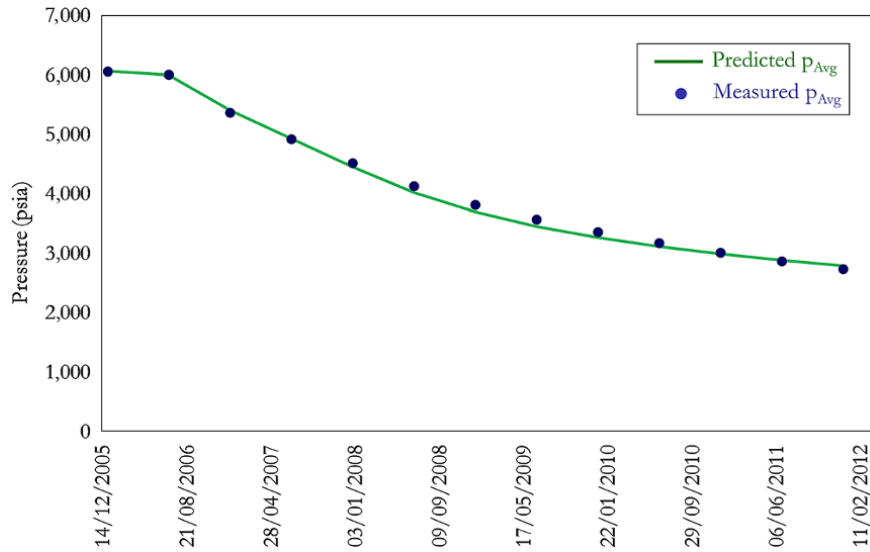


Figure 12.23 Reservoir pressure (p<sub>Avg</sub>) history match.

Table 12.15 Aquifer Productivity for the Fetkovich Semisteady State Aquifer Model.

Type of outer aquifer boundary	J for radial flow (stb/D/psi)	J for linear flow (stb/D/psi)
Finite-no-flow	$J = \frac{0.00708 kh(\theta/360)}{\mu \ln(r_e/r_r) - 0.75}$	$J = \frac{3 \times 0.001127 khw}{\mu L}$
Finite-constant pressure	$J = \frac{0.00708 kh(\theta/360)}{\mu \ln(r_e/r_r)}$	$J = \frac{0.001127 khw}{\mu L}$
Infinite	$J = \frac{0.00708 kh(\theta/360)}{\mu \ln \sqrt{0.0142/k t / \phi \mu c_t r_r^2}}$	$J = \frac{khw}{1000 \mu \sqrt{0.0633 kt / \phi \mu c_t}}$

$\bar{p}_{rn}$  is the average reservoir pressure at the end of the time step and is defined as:

$$\bar{p}_{rn} = \frac{p_{rn-1} + p_{rn}}{2} \quad (12.54)$$

$W_{ei}$  is the initial amount of encroachable water, which characterizes the maximum possible aquifer expansion, and is defined as:

$$W_{ei} = (c_f + c_w) p_{aq} W_i \quad (12.55)$$

$W_i$  is the initial volume of water in the aquifer and for a radial reservoir-aquifer system:

$$W_i = \frac{\pi (r_e^2 - r_o^2) h \phi (\theta/360)}{5.615} \text{ in EOF units} \quad (12.56)$$

where  $W_e$  is the cumulative aquifer influx and J is the aquifer productivity index, which is defined for different geometry and boundary types in Table 12.15 with EOF units.

The HVE model remains the most preferred water influx model, as other are simplifications of the aquifer influx or modification of the HVE model.

**Exercise 12.5** Oil Material Balance with the Fetkovich Semisteady State Aquifer Model

Carry out a forward model prediction of the  $N_p$  in Exercise 12.3 using the Fetkovich semisteady state aquifer model and compare the calculated  $N_p$  with the measured  $N_p$ .

The entire calculation approach is the same as in Exercise 12.3, except that water influx ( $W_e(t)$ ) model changes from HVE to Fetkovich.

**Solution Steps.**

Step 1: calculate  $W_{ei}$  using equation (12.55) and J using a finite-constant pressure aquifer boundary with radial flow (Table 12.15).

Step 2: calculate  $\Delta W_{en}$  incrementally with time steps using equation (12.52).

Step 3: calculate  $W_{en}(t) = \sum_{i=1}^n \Delta W_{ei}$  for each time step.

Step 4: replace the water influx with that in Exercise 12.3 to get a prediction for  $N_p$ .  $W_{ei} = (C_f + c_w) p_{aq} W_i$  from equation (12.55).

with  $W_i = \frac{\pi(r_c^2 - r_o^2) h \phi (\theta/360)}{5.615}$  from equation (12.56)

and

$$\Delta W_{en} = \frac{W_{ei}}{p_{aq,i}} (\bar{p}_{aq,n-1} - \bar{p}_{rm}) \left( 1 - e^{\left\{ -\frac{J p_{aq,i} \Delta t_n}{W_{ei}} \right\}} \right)$$

from equation (12.52).

With aquifer productivity defined by finite-constant pressure with radial flow (Table 12.15):

$$J = \frac{0.00708kh(\theta/360)}{\mu \ln(r_e/r)}$$

**Solution.**

The calculation for the Fetkovich semisteady state water influx is shown in Table 12.16.

Cumulative oil ( $N_p$ ) prediction using the Fetkovich water influx model is shown in Fig. 12.24.

The Fetkovich method assumes a semisteady state flow regime throughout the entire duration of aquifer response to pressure change, which is not true. The method is a

**Table 12.16** Calculation for the Fetkovich Semisteady State Water Influx.

$p_{Avg}$ (psia)	$\bar{p}_{rm}$ (psia)	$\bar{p}_{aq,n-1}$ psia	$\bar{p}_{aq,n-1} - \bar{p}_{rm}$ psi	$\Delta W_{en}$ (rb)	$W_e(t)$ (rb)	$W_e(t)$ (MMrb)
6,050	6,050.00	6,050	0	0	0	0.0000
5,997.05	6,023.53	6.05E+03	2.648E+01	1.609E+03	1.609E+03	0.0016
5,359.06	5,678.06	6.05E+03	3.719E+02	2.272E+04	2.433E+04	0.0243
4,912.91	5,135.99	5.99E+03	9.102E+02	5.559E+04	7.992E+04	0.0799
4,509.17	4,711.04	5.86E+03	1.281E+03	7.824E+04	1.582E+05	0.1582
4,120.93	4,315.05	5.67E+03	1.545E+03	9.434E+04	2.525E+05	0.2525
3,806.87	3,963.90	5.45E+03	1.709E+03	1.044E+05	3.569E+05	0.3569
3,561.13	3,684.00	5.20E+03	1.764E+03	1.078E+05	4.647E+05	0.4647
3,350.48	3,455.81	4.94E+03	1.744E+03	1.065E+05	5.712E+05	0.5712
3,166.36	3,258.42	4.69E+03	1.684E+03	1.029E+05	6.741E+05	0.6741
3,003.56	3,084.96	4.44E+03	1.604E+03	9.797E+04	7.720E+05	0.7720
2,858.38	2,930.97	4.21E+03	1.513E+03	9.241E+04	8.644E+05	0.8644
2,727.89	2,793.14	3.99E+03	1.417E+03	8.656E+04	9.510E+05	0.9510

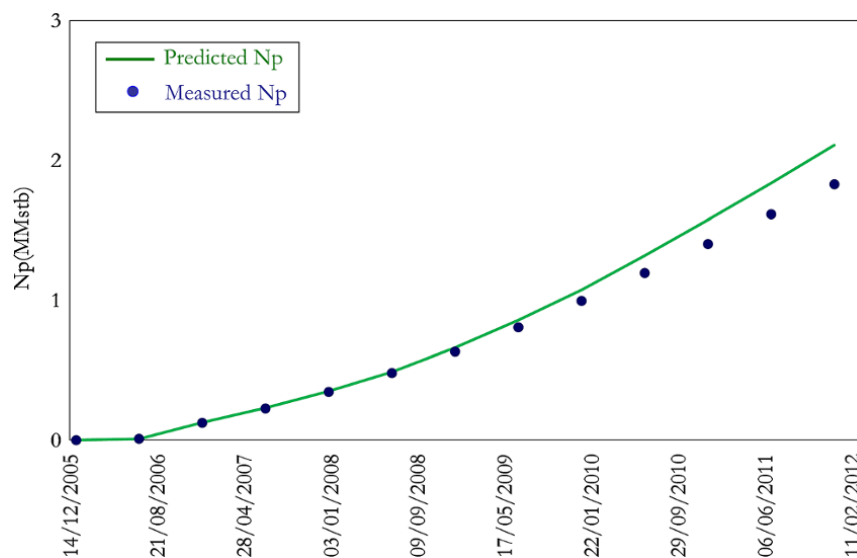


**Figure 12.24** Cumulative oil ( $N_p$ ) prediction using the Fetkovich water influx model.

simplification of the HVE model, formulated to avoid the use of the superposition principle required for the HVE model. As shown in Exercise 12.3, implementing superposition even with spreadsheet is not complicated. Also, computers and software have advanced to handle such problems easily. Hence, the need to use simplified aquifer models like Small pot, Fetkovich, and Carter and Tracey should be avoided. The HVE model (Section 12.3.2) should be used all the time.

Equation (12.57) is the generalized material balance equation for gas where  $G_p$  is the cumulative gas produced,  $B_g$  is the gas formation volume factor,  $B_{gi}$  is the initial formation volume factor,  $W_p$  is the cumulative water produced at surface condition,  $B_w$  is the formation volume factor of water,  $G$  is initial gas in place,  $\Delta p$  is pressure drop,  $S_{wc}$  is initial reservoir connate water saturation,  $c_w$  is the compressibility of water,  $c_f$  is the compressibility of the formation, and  $W_e$  is the water aquifer influx.

### 12.4. GAS RESERVOIR MATERIAL BALANCE (GMB)

Consider a gas reservoir with an aquifer as shown in Fig. 12.25, with initial gas in place,  $G$ .

Cumulative gas and water production (Fig. 12.26) is due to a combination of volumetric gas expansion in the reservoir, expansion of the connate water and formation, and aquifer water influx for a given pressure drop in the reservoir as shown in equation (12.57).

$$\begin{aligned}
 G_p B_g + W_p B_w &= G (B_g - B_{gi}) + \frac{G B_{gi} c_w \Delta p S_{wc}}{(1 - S_{wc})} \\
 \text{Gas Production} + \text{Water Production} &= \text{Gas Expansion} + \text{Water Expansion} \\
 &+ \frac{G B_{gi} c_f \Delta p}{(1 - S_{wc})} + W_e \\
 &+ \text{Formation Expansion} + \text{Water Influx}
 \end{aligned}
 \tag{12.57}$$

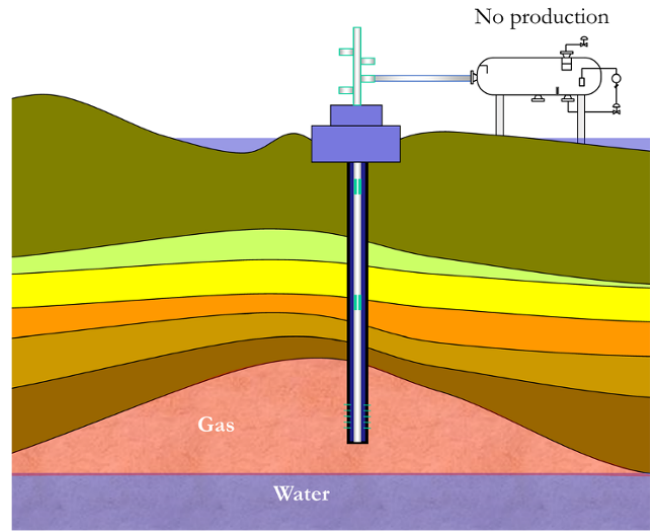


Figure 12.25 Gas reservoir with aquifer support at initial reservoir condition.

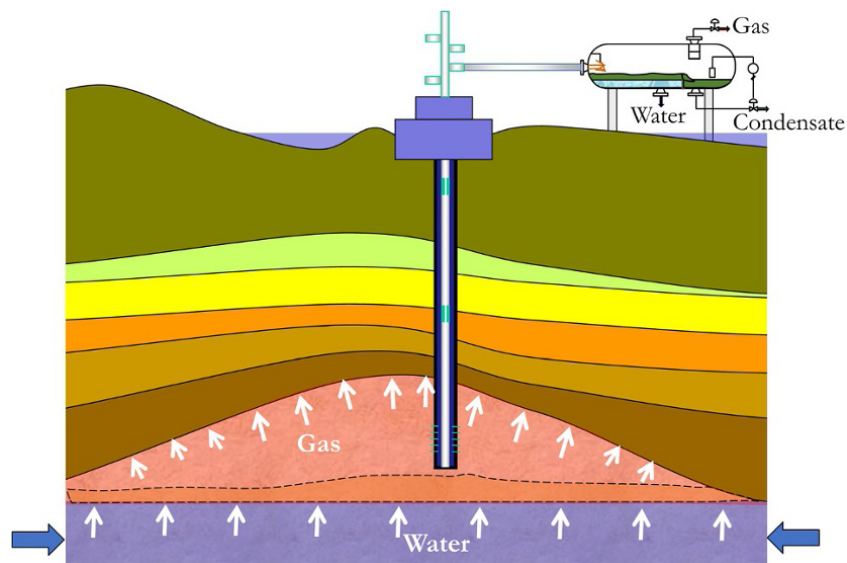


Figure 12.26 Gas reservoir after gas and water production.

**12.4.1. Gas Material Balance (GMB) Model Diagnosis**

Two important material balance diagnostic plots for gas reservoirs are the *Cole plot* and the *GMB straight-line methods*, which can give an estimation of aquifer size or strength and initial gas in place ( $G$ ).

**12.4.1.1. Cole Plot.** The Cole plot is one of the most useful diagnostic plots in GMB analysis. The *Cole plot* for gas, which is similar to the *Campbell plot* (Section 12.2.1.1) for oil, is a material balance diagnostic plot for estimating the strength of the aquifer and initial gas in place [Cole, 1969].

Consider that the effect of water and formation expansion is insignificant compared to the gas volumetric expansion equation (equation (12.57)) can be expressed as:

$$G_p B_g + W_p B_w = G (B_g - B_{gi}) + W_e \tag{12.58}$$

and further rearranged as:

$$\frac{G_p B_g + W_p B_w}{(B_g - B_{gi})} = G + \frac{W_e}{(B_g - B_{gi})} \tag{12.59}$$

The Cole plot is a plot of the left-hand side (LHS) term in equation (12.59),  $\left(\frac{G_p B_g + W_p B_w}{(B_g - B_{gi})}\right)$ , against  $G_p$ , as shown Fig. 12.27.

When the reservoir is undergoing volumetric depletion, then  $W_e = 0$ , and  $\frac{G_p B_g + W_p B_w}{(B_g - B_{gi})}$  in equation (12.59) becomes constant and independent of gas produced ( $G_p$ ). However, when there is an aquifer support, the energy support increases with  $G_p$ . For a moderate aquifer, the energy contribution from the aquifer dissipates with a further increase in  $G_p$  after an initial increase. In strong

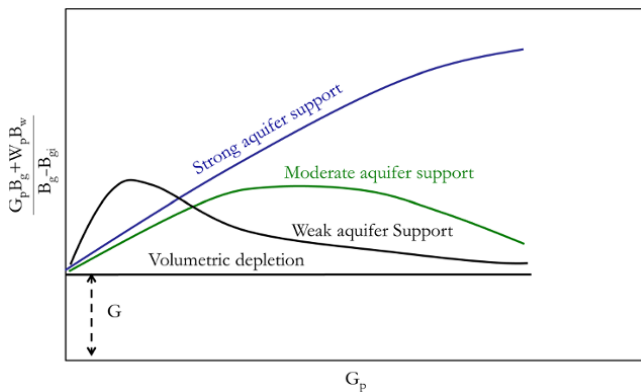


**Figure 12.27** Cole plot for gas material balance diagnosis [Adapted from Cole, 1969]

aquifer support, there is no decrease in the energy, as shown in Fig. 12.27.

**12.4.1.2. GMB Straight-Line Diagnostic Method (Strong Aquifer Drive).** A concept similar to the straight-line diagnosis of OMB using the Havlena–Odeh approach can be extended to GMB. From equation (12.59):

$$\frac{G_p B_g + W_p B_w}{(B_g - B_{gi})} = G + \frac{W_e}{(B_g - B_{gi})}$$

A plot of  $\frac{G_p B_g + W_p B_w}{(B_g - B_{gi})}$  against  $\frac{W_e}{(B_g - B_{gi})}$  would give a straight-line with the intercept on the vertical  $y$ -axis corresponding to  $G$  if the correct aquifer influx  $W_e$  is defined in the model. This method gives qualitative and quantitative diagnoses of the material balance model with initial gas in place ( $G$ ) determination and aquifer fitting capability (Fig. 12.28).

**12.4.1.3. GMB as  $p/Z$  Plot (Case of No Water and Condensate Production).** Equation (12.59) without water production reduces to:

$$\frac{G_p B_g}{(B_g - B_{gi})} = G + \frac{W_e}{(B_g - B_{gi})}$$

Rearranging this:

$$G_p = \frac{G(B_g - B_{gi})}{B_g} + \frac{W_e}{B_g}$$

$$\frac{G_p}{G} = \left(1 - \frac{B_{gi}}{B_g}\right) + \frac{W_e}{GB_g}$$

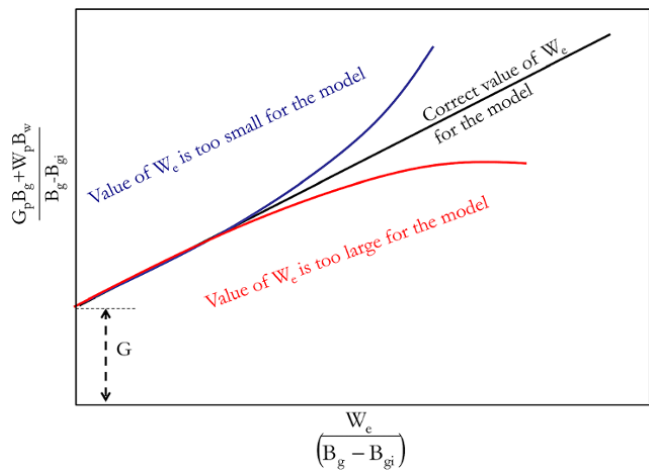


**Figure 12.28** GMB straight-line diagnosis.

$$\begin{aligned}\frac{G_p}{G} &= 1 - \frac{B_{gi}}{B_g} + \frac{W_e}{GB_{gi}} \\ \frac{G_p}{G} &= 1 - \frac{B_{gi}}{B_g} \left(1 - \frac{W_e}{GB_{gi}}\right) \\ \frac{G_p}{G} &= 1 - \left(1 - \frac{W_e}{GB_{gi}}\right) \frac{B_{gi}}{B_g}\end{aligned}\quad (12.60)$$

From equation (3.20), the formation volume factor  $B_g$  for gas is:

$$B_g = \frac{p_{sc} ZT}{T_{sc} p}$$

Hence:

$$B_{gi} = \frac{p_{sc} Z_i T}{T_{sc} p_i}$$

Substituting  $B_g$  and  $B_{gi}$  defined above into Equation (12.60) for reservoir temperature  $T$ :

$$\frac{G_p}{G} = 1 - \left(1 - \frac{W_e}{GB_{gi}}\right) \frac{pZ_i}{p_i Z}$$

Making  $p/Z$  the subject of the formula:

$$\begin{aligned}\left(1 - \frac{W_e}{GB_{gi}}\right) \frac{pZ_i}{p_i Z} &= 1 - \frac{G_p}{G} \\ \frac{p}{Z} &= \frac{p_i}{Z_i} \frac{(1 - G_p/G)}{(1 - W_e/GB_{gi})}\end{aligned}\quad (12.61)$$

where  $\frac{W_e}{GB_{gi}}$  is the fraction of the original hydrocarbon pore volume that has been flooded by water.

When there is no aquifer support,  $W_e = 0$  and equation (12.61) becomes:

$$\begin{aligned}\frac{p}{Z} &= \frac{p_i}{Z_i} \frac{(1 - G_p/G)}{(1 - 0)} \\ \frac{p}{Z} &= \frac{p_i}{Z_i} (1 - G_p/G) \\ \frac{p}{Z} &= -\frac{p_i}{Z_i} \frac{G_p}{G} + \frac{p_i}{Z_i}\end{aligned}\quad (12.62)$$

Therefore, for a dry gas reservoir with no condensate production and no water aquifer influx, a plot of  $\frac{p}{Z}$  against  $G_p$  would give a straight-line.

When  $p = 0$ , equation (12.62) becomes:

$$0 = -\frac{p_i}{Z_i} \frac{G_p}{G} + \frac{p_i}{Z_i}$$

and therefore:

$$\begin{aligned}\frac{G_p}{G} &= 1 \\ G &= G_p\end{aligned}$$

Hence, a plot of  $\frac{p}{Z}$  against  $G_p$  for a dry gas reservoir will have a slope of  $-\frac{p_i}{GZ_i}$  and an intercept at  $p = 0$  corresponding to the value of  $G$ . The presence of an aquifer makes  $\frac{p}{Z}$  against  $G_p$  deviate from a straight-line relationship, as shown in Fig. 12.29.

Gas reservoirs are not depleted to 1 atm (14.7 psia), as this would correspond to 100% recovery of initial gas in place. Even in a dry gas, pressure is required to transport the gas from the bottom of the reservoir to the surface. Hence, the reservoir cannot be depleted to 1 atm. Also, for gas with water production, at low reservoir pressure the well may not be able to lift liquid to the surface if the flowing bottomhole pressure is too low. Finally, at lower wellhead pressure, the cost of compression becomes significantly high to boost pressure for transport and processing.

### Exercise 12.6 Gas Material Balance Using the $p/Z$ Plot

Given the production data for a dry gas in Table 12.17 and the fluid properties in Table 12.18:

1. Calculate the initial gas in place (IGIP), also called the original gas in place (OGIP), represented as  $G$  in the gas material balance equation.
2. Assuming an abandonment pressure of 700 psi, calculate  $G_p$  and *ultimate recovery factor* (URF) at time of abandonment.

### Solution.

Interpolate  $Z$  from Table 12.18 at average reservoir pressures and calculate  $p/Z$  (Table 12.19).

From the calculated  $p/Z$ , a plot of  $p/Z$  against  $G_p$  is created (Fig. 12.30).

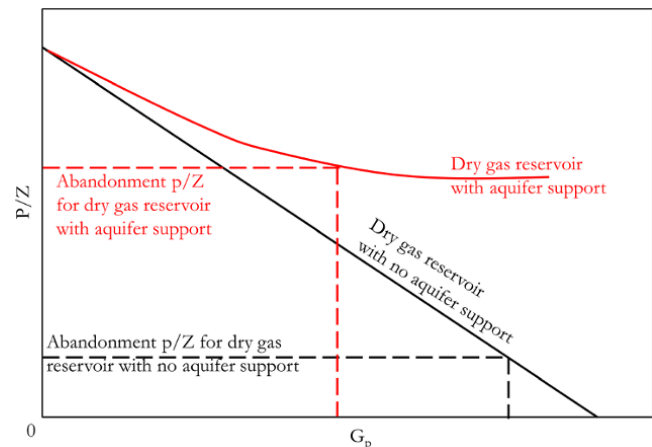


Figure 12.29 GMB using  $\frac{p}{Z}$  against  $G_p$ .

The p/Z plot in Fig. 12.30 can be describe by the relationship:

$$\frac{p}{Z} = -2.3544G_p + 5213.1 \quad (12.63)$$

To determine the initial gas in place (G) – when p = 0, G = G<sub>p</sub>. Thus, substituting p = 0 and G = G<sub>p</sub> into equation (12.63):

$$0 = -2.3544G + 5213.1$$

$$2.3544G = 5213.1$$

$$G = \frac{5213.1}{2.3544}$$

G = 2214.195 MMscf.

G = 2.2 Bscf.

**Table 12.17** Production Data for Exercise 12.6.

Date (dd/mm/yyyy)	Average reservoir pressure (psia)	Cumulative gas produced (MMscf)
03/08/1993	5,010.00	0.00
02/11/1993	4,968.52	8.20
01/02/1994	4,937.34	16.41
03/05/1994	4,896.65	24.61
02/08/1994	4,861.24	32.82
01/11/1994	4,826.19	41.02
31/01/1995	4,796.27	49.23
02/05/1995	4,761.86	57.43
01/08/1995	4,727.78	65.64
31/10/1995	4,689.35	73.84
30/01/1996	4,660.62	82.05
30/04/1996	4,627.52	90.25
30/07/1996	4,590.16	98.46
29/10/1996	4,557.72	106.66
28/01/1997	4,530.12	114.87
29/04/1997	4,493.77	123.07
29/07/1997	4,462.26	131.28
28/10/1997	4,435.47	139.48
27/01/1998	4,404.52	147.69
28/04/1998	4,373.85	155.89
28/07/1998	4,343.47	164.10

**Table 12.18** Fluid Property of Dry Gas for Exercise 12.6.

Pressure (psia)	Z-factor	Pressure (psia)	Z-factor	Pressure (psia)	Z-factor
100	0.9860	2,165	0.7890	4,230	0.8899
395	0.9452	2,460	0.7887	4,525	0.9157
690	0.9061	2,755	0.7953	4,820	0.9428
985	0.8700	3,050	0.8073	5,115	0.9708
1,280	0.8387	3,345	0.8236	5,410	0.9996
1,575	0.8139	3,640	0.8433	5,705	1.0289
1,870	0.7972	3,935	0.8656	6,000	1.0587

At an abandonment pressure of 700 psia – interpolating Z at p = 700 psia, Z = 0.9049. Calculating p/Z at abandonment,  $\left(\frac{p}{Z}\right)_{\text{limit}}$  :

$$\left(\frac{p}{Z}\right)_{\text{limit}} = \frac{700}{0.9049} = 773.592 \text{ psia}$$

Substituting  $\left(\frac{p}{Z}\right)_{\text{limit}}$  psia above into equation (12.63) to calculate the cumulative gas produced at abandonment (G<sub>p\_limit</sub>):

$$773.592 = -2.3544G_{p\_limit} + 5213.1$$

G<sub>p\_limit</sub> = 1885.622 MMscf.

Therefore, the ultimate recovery factor (URF) is:

$$URF = \frac{G_{p\_abandonment}}{G} = \frac{1885.622}{2214.195} = 0.85$$

URF = 85%.

In dry gas reservoirs, recoveries are always very high compared to oil reservoirs, as gas is delivered to the surface by volumetric expansion. The absence of two-phase flow, due to water or condensate production, is also responsible for high gas recoveries in dry gas reservoirs, as the presence of a second phase creates impairment to gas flow.

### 12.4.2. Gas Condensate Material Balance(GCMB)

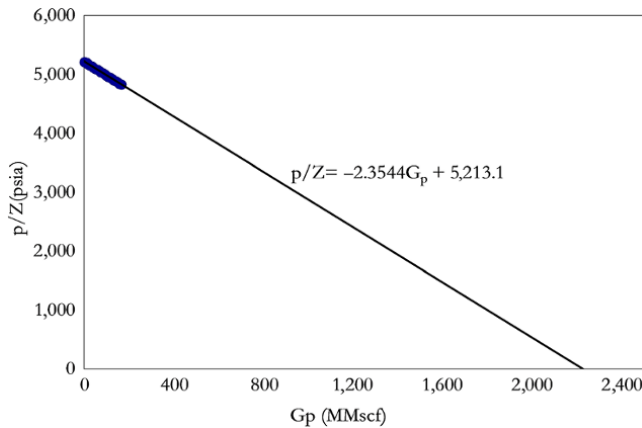
In gas condensate systems below the dew point, gas condensate is formed. Reservoir deliverability in a gas condensate system below the dew point is controlled by many factors, such as relative permeability and wettability, and fluid properties (richness of the gas condensate stream).

**12.4.2.1. Generalized Material Balance for Gas Condensate.** The generalized material balance equation from equation (12.29) can be modified to account for the effects of condensate formation and vaporization on fluid expansion. From the generalized material balance equation (equation (12.29)):



**Table 12.19**  $p/Z$  with Corresponding  $G_p$ .

Date (dd/mm/yyyy)	$p_{Avg}$ (psia)	$G_p$ (MMscf)	Z (by interpolation)	$p/Z$ (psia)
03/08/1993	5,010.00	0.00	0.960863	5,214.07
02/11/1993	4,968.52	8.20	0.956923	5,192.18
01/02/1994	4,937.34	16.41	0.953962	5,175.61
03/05/1994	4,896.65	24.61	0.950098	5,153.84
02/08/1994	4,861.24	32.82	0.946736	5,134.74
01/11/1994	4,826.19	41.02	0.943407	5,115.70
31/01/1995	4,796.27	49.23	0.940641	5,098.94
02/05/1995	4,761.86	57.43	0.937484	5,079.40
01/08/1995	4,727.78	65.64	0.934357	5,059.93
31/10/1995	4,689.35	73.84	0.93083	5,037.81
30/01/1996	4,660.62	82.05	0.928194	5,021.17
30/04/1996	4,627.52	90.25	0.925157	5,001.88
30/07/1996	4,590.16	98.46	0.921728	4,979.95
29/10/1996	4,557.72	106.66	0.918751	4,960.77
28/01/1997	4,530.12	114.87	0.916219	4,944.36
29/04/1997	4,493.77	123.07	0.913012	4,921.92
29/07/1997	4,462.26	131.28	0.91025	4,902.24
28/10/1997	4,435.47	139.48	0.907902	4,885.40
27/01/1998	4,404.52	147.69	0.90519	4,865.85
28/04/1998	4,373.85	155.89	0.902502	4,846.36
28/07/1998	4,343.47	164.10	0.899839	4,826.94


**Figure 12.30**  $p/Z$  Plot for dry gas material balance analysis.

$$F = N(E_o + mE_g)$$

$$F = NE_o + NmE_g$$

where  $G = Nm$

$$F = NE_o + GE_g$$

Adding the expansivity of water and formation rock to the above equation:

$$F = NE_{owf} + GE_{gwf} \quad (12.64)$$

where  $E_{owf}$  is the composite expansion factor for oil with water and rock,  $E_{gwf}$  is the composite expansion factor for gas with water and rock, and  $F$  is defined as:

$$F = N_p \left( \frac{B_o - B_g R_s}{1 - R_v R_s} \right) + G_p \left( \frac{B_g - R_v B_o}{1 - R_v R_s} \right) + W_p B_w - W_{inj} B_{winj} - G_{inj} B_{ginj} \quad (12.65)$$

$E_{owf}$  is defined as:

$$E_{owf} = E_o + \frac{B_{oi}}{(1 - S_{wc})} (c_w S_{wc} + c_f) \Delta p \quad (12.66)$$

$E_{gwf}$  is defined as:

$$E_{gwf} = E_g + \frac{E}{(1 - S_{wc})} (c_w S_{wc} + c_f) \Delta p \quad (12.67)$$

$E_o$  is defined as:

$$E_o = \frac{(B_o - B_{oi}) + B_g (R_{si} - R_s) + R_v (B_{oi} R_s - B_o R_{si})}{1 - R_v R_s} \quad (12.68)$$

$E_g$  is defined as:

$$E_g = \frac{(B_g - B_{gi}) + B_o (R_{vi} - R_v) + R_s (B_{gi} R_v - B_g R_{vi})}{1 - R_v R_s} \quad (12.69)$$

where  $R_v$  is the condensate to gas ratio in the gas phase and  $R_s$  is the gas to condensate ratio in the liquid phase.

The gas condensate material balance equation described by equations (12.64)–(12.69) is also applicable to volatile oil below saturation pressure.

**12.4.2.2. p/Z Material Balance for Gas Condensate.**

The p/Z plot from dry gas has been extended to a gas–condensate system using a two-phase Z-factor.

The use of a two-phase Z-factor assumes that condensate dropout is immobile and is not produced. In practice, though, condensate is produced when the critical oil (condensate) saturation is reached. However, for lean gas condensate, production can be considered not considerable and gas still remains the dominant phase. The use of the two-phase Z-factor for material balance in gas condensate is only an approximation and should only be considered for lean gas condensate where the amount of gas condensate is not significant enough to change the composition of the fluid. This method should not be considered where significant condensate is produced remembering that the method is based on the *two-phase constant volume depletion (CVD) Z-factor*, which describes the condition of immobile condensate.

**12.4.2.3. Determination of Two-Phase Z-factor (Z<sub>2-phase</sub>).** From the *constant volume depletion (CVD) experiment* (Chapter 3 (3.6.1.1)), the two-phase Z-factor can be calculated using:

$$Z_{2-phase} = \frac{p}{\frac{p_i}{Z_i} \left(1 - \frac{V_{gas}}{V_{cell}}\right)} \quad (12.70)$$

where p is cell pressure at each stage during the CVD experiment, V<sub>cell</sub> is the PVT cell of volume, p<sub>i</sub> is the initial cell pressure, which is above saturation pressure, and V<sub>gas</sub> is the volume of gas recovered in stages during the CVD experiment

Z<sub>2-phase</sub> can also be determined from empirical relationships using the Rayes method [Rayes et al., 1992], which is applicable to fluid compositions with a mole percentage of C<sub>7+</sub> greater than 4 mol% and expressed as:

$$Z_{2-phase} = 2.243 - 0.0375(p_r) - 3.56 \left(\frac{1}{T_r}\right) + 0.00083(p_r)^2 + 1.534 \left(\frac{1}{T_r}\right)^2 + 0.132 \left(\frac{p_r}{T_r}\right) \text{ for } y_{C7+} > 4 \text{ mol\%} \quad (12.71)$$

The single-phase Z-factor can be used for fluid with a composition of C<sub>7+</sub> less than 4 mol% with appropriate gas gravity correction. The composition of C<sub>7+</sub> where unknown can be determined using [Rayes et al., 1972]:

$$y_{C7+} = -0.088519 + 0.141013 (\gamma_g) \quad (12.72)$$

The two-phase p/Z is then applied to equation (12.61) when there is an active aquifer and to equation (12.62) when there is no active aquifer.

Considering this limitation of the two-phase p/Z approach, the generalized material balance equation for gas condensate (Chapter 12.4.2.1) should always be used.

**12.4.3. Gas Material Balance Drive Index–Energy Plot**

Using a similar concept to that used with the OMB, the drive index can be determined for the GMB.

From the generalized gas material balance equation in equation (12.57):

$$G_p B_g + W_p B_w = G(B_g - B_{gi}) + \frac{GB_{gi}c_w \Delta p S_w}{(1 - S_w)} + \frac{GB_{gi}c_f \Delta p}{(1 - S_w)} + W_e$$

Making G<sub>p</sub> the subject of the formula:

$$G_p B_g = G(B_g - B_{gi}) + \frac{GB_{gi}c_w \Delta p S_w}{(1 - S_w)} + \frac{GB_{gi}c_f \Delta p}{(1 - S_w)} + W_e - W_p B_w$$

Normalizing the left-hand side and right-hand side with respect to G<sub>p</sub>B<sub>g</sub> so all contributing energy terms sum up to 1:

$$1 = \frac{G(B_g - B_{gi})}{G_p B_g} + \frac{GB_{gi}c_w \Delta p S_w}{G_p B_g (1 - S_w)} + \frac{GB_{gi}c_f \Delta p}{G_p B_g (1 - S_w)} + \frac{(W_e + W_p B_w)}{G_p B_g} \quad (12.73)$$

Gas Expansion Drive Index	+	Water Expansion Drive Index	+	Formation Expansion Drive Index	+	Water Drive Index
Compaction Drive Index						

Equation (12.73) is the energy index equation with the different drive index constituent. The energy index is the fraction of the reservoir drive contributing to production.

**REFERENCES**

Campbell, R. and Campbell, J., 1978. *Mineral Property Economics: Petroleum Property Evaluation*. Norman, OK: Campbell Petroleum Series.

Carter, R. and Tracy, G., 1960. An improved method for calculating water influx. *Transactions of the AIME*, **219**, 415–417.

Cole, F., 1969. *Reservoir Engineering Manual*. Houston, TX: Gulf Publishing.

Edwardson, M., Girner, H.M., Parkison, H.R., and Matthews, C.S., 1962. Calculation of formation temperature disturbances caused by mud circulation. *Journal of Petroleum Technology*, **14**(04), 416–425.

Fetkovich, M., 1971. A simplified approach to water influx calculations – finite aquifer systems. *Journal of Petroleum Technology*, **23**(7), 814–28.

Havlena, D. and Odeh, A., 1963. The material balance as an equation of a straight line. *Journal of Petroleum Technology*, **15**(08), 896–900.

Marsal, D., 1982. *Topics of Reservoir Engineering. Course Notes*. Delft, The Netherlands: Delft University of Technology.

- Rayes, D., Piper, L., McCain Jr, W., and Poston, S., 1992. Two-phase compressibility factors for retrograde gases. *SPE Formation Evaluation*, 7(01), 87–92.
- Schilthuis, R., 1936. Active oil and reservoir energy. *Transactions of the AIME*, 118(1), 33–52.
- van Everdingen, A. and Hurst, W., 1949. The application of the Laplace transformation to flow problems in reservoirs. *Transactions of the AIME*, 1(12), 305–324.
- Walsh, M. and Lake, L., 2003. *A Generalized Approach to Primary Hydrocarbon Recovery*. Amsterdam: Elsevier.

## BIBLIOGRAPHY

- Ahmed, T., 2006. *Reservoir Engineering Handbook*, 3rd edn. Gulf Professional Publishing.
- Amyx, J.W., Bass, D.M., and Whiting, R.L., 1960. *Petroleum Reservoir Engineering: Physical Properties*. McGraw-Hill.
- Archer, J. and Wall, C., 1986. *Petroleum Engineering: Principle and Practice*, 1st edn. Kluwer Academic Publishing.
- Archer, J. and Wall, C., 1999. *Petroleum Engineering Principles and Practice*. Dordrecht/Boston: Kluwer Academic Publishing.
- Buckley, S. and Leverett, M., 1942. Mechanism of fluid displacement in sand. *SPE, Transactions of the AIME*, 146(01), 107–116.

## APPENDIX 12A VBA CODE FOR HURST-VAN EVERDINGEN (HVE) UNSTEADY STATE AQUIFER

Function WDinf(tD)  
"This function describes Water Influx for infinite acting Aquifer

```

a7 = 4.8534E-12
a6 = -0.0000000018436
a5 = 0.00000028354
a4 = -0.00002274
a3 = 0.0010284
a2 = -0.027455
a1 = 0.85373
a0 = 0.81638

If tD < 1 Then
WDinf = 2 * (tD / Excel.WorksheetFunction.Pi()) ^ 0.5 +
(tD / 2) - (tD / 6) * (tD / Excel.WorksheetFunction.Pi())
^ 0.5 + (tD ^ 2) / 16
ElseIf tD < 100 Then
WDinf = a7 * tD ^ 7 + a6 * tD ^ 6 + a5 * tD ^ 5 + a4 * tD ^
4 + a3 * tD ^ 3 + a2 * tD ^ 2 + a1 * tD ^ 1 + a0
Else
WDinf = 2 * tD / Excel.WorksheetFunction.Ln(tD)
End If
End Function

Function WD(reD, tD)
"This function describes Water Influx for finite acting
Aquifer
tDD = 0.4 * (reD ^ 2 - 1)
JJ = (reD ^ 4 * (Excel.WorksheetFunction.Ln(reD)) /
(reD ^ 2 - 1)) + 0.25 * (1 - 3 * reD ^ 2)
If tD > tDD Then
WD = 0.5 * (reD ^ 2 - 1) * (1 - Exp(-2 * tD / JJ))
Else
WD = WDinf(tD)
End If
End Function

```

# 13

## Decline Curve Analysis

The life cycle and production profile of a field, made up of one or more reservoirs, can be characteristically described by Fig. 13.1. The production profile may vary depending on field development strategy, reservoir rock and fluid properties, geology of the field, and reservoir drive mechanism.

The life cycle of a petroleum field involves drilling and managing different types of wells, which include:

*Wildcat wells* – the first wells drilled in the field with minimum or no knowledge of subsurface geology of the region or field.

*Exploratory wells* – drilled in a new field, based on geological and subsurface data.

*Step-out wells* – a special kind of exploration well drilled to determine the extent of the reservoir boundaries or an additional compartment connected to the main reservoir.

*Development wells* – drilled after identification of productive reservoirs for the production of oil and gas.

*Reentry wells* – drilled to re-open existing wells that have been previously plugged and suspended.

The variation in production profile from field to field could be in the rate of buildup, the level of the plateau, the duration of the plateau, and the rate of decline. The period characterized by a production increase due to increasing well count is called *buildup* (not to be confused with buildup in well test analysis, Chapter 8). The buildup reaches a continuous plateau production, after which field production decline sets in. Production decline continues until the economic limit of the field is reached, after which field is abandoned.

### 13.1. PRODUCTION DECLINE CURVE MODELS

Most recovery in the life of the field is during the declining phase of the field life cycle. With limited reservoir properties to build a simulation model or material balance model, production decline curve models provide a simple, but effective, way of predicting reservoir performance with or without production data. Production decline curve models were originally developed based on empirical observation of production data rather than the fundamental physics of flow [Arps, 1945]. Fetkovich [1980] later showed that the *constant terminal pressure solution* (Chapter 8 (8.5.1.2)) with a no-flow boundary reservoir creates an exponential declining rate.

Common production decline curve models include: *exponential decline* (constant fractional decline), *harmonic decline*, and *hyperbolic decline*. For practical application, it is good practice to use more than one model as part of a sensitivity analysis. It is also important to note that moderate forecasts are most likely appropriate in the early production stages, where more factors aid production decline than enhance production. Production decline curve models can be represented by a generalized equation:

$$q = \frac{q_i}{(1 + bD_i t)^{1/b}} \quad (13.1)$$

where  $q_i$  is the initial production rate at onset of production decline,  $t$  is time,  $D_i$  is the initial nominal decline rate (unit of  $\text{time}^{-1}$ ),  $b$  is an empirical constant (Arps' decline-curve exponent), and  $q$  is the production rate at time  $t$ .

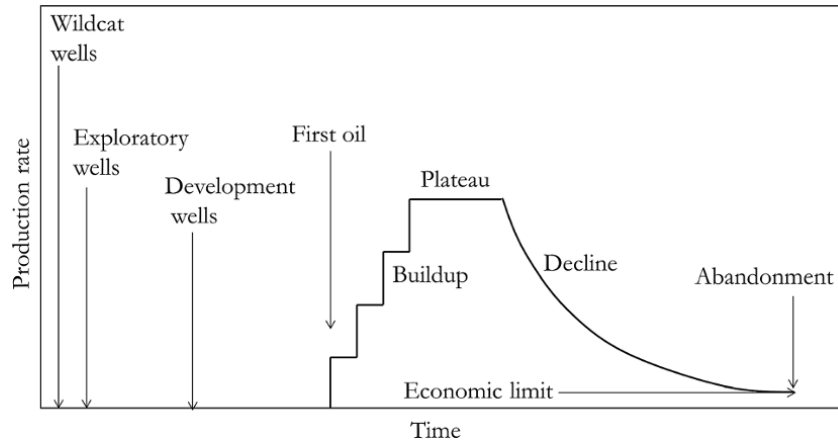


Figure 13.1 Typical production profile of a field.

$b$  and  $D_i$  can be derived from fitting the measured production data with the production decline model or taken from an analogue field.

Production decline models can be presented as a function of *effective decline* (rather than nominal), where *initial effective decline* is defined as:

$$D_{ei} = \frac{q_i - q}{q_i} \tag{13.2}$$

Substituting equation (13.1) into equation (13.2):

$$D_{ei} = \frac{q_i - q_i(1 + bD_it)^{-1/b}}{q_i}$$

$$D_{ei} = 1 - (1 + bD_it)^{-1/b}$$

Making  $D_i$  the subject of the formula and solving for the first time step,  $t = 1$ , to get an initial production decline rate:

$$(1 + bD_it)^{-1/b} = 1 - D_{ei}$$

$$(1 + bD_it) = (1 - D_{ei})^{-b}$$

$$bD_it = (1 - D_{ei})^{-b} - 1$$

$$D_i = \frac{(1 - D_{ei})^{-b} - 1}{bt}$$

at  $t = 1$ , the relationship between *initial nominal decline rate* ( $D_i$ ) and *initial effective decline rate* ( $D_{ei}$ ) can be expressed as:

$$D_i = \frac{(1 - D_{ei})^{-b} - 1}{b} \tag{13.3}$$

Fig. 13.2 shows the rate of decline based on the various production decline models.

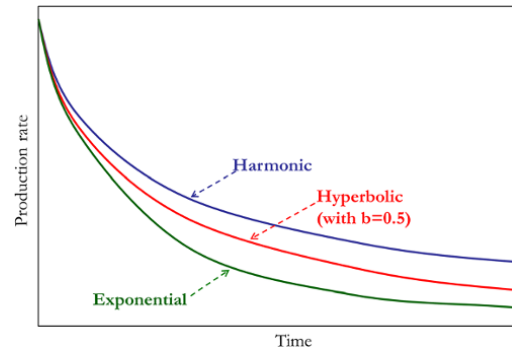


Figure 13.2 Different production decline models.

### 13.1.1. Exponential Production Decline Model

When  $b = 0$ , equation (13.1) reduces to:

$$q = \frac{q_i}{(1 + bD_it)^{1/b}} = \frac{q_i}{(1 + bD_it)^{\frac{1}{b}D_i}}$$

As  $b \rightarrow 0$ ,  $bD_i \rightarrow 0$ :

$$q = \frac{q_i}{\left[ (1 + bD_it)^{\frac{1}{b}D_i} \right]_{bD_i \rightarrow 0}} \tag{13.4}$$

Note that  $(1 + x)^{\frac{1}{x}} = 2.718 = e$  as  $x \rightarrow 0$

Hence, equation (13.4) becomes:

$$q = \frac{q_i}{e^{D_it}} = q_i e^{-D_it} \tag{13.5}$$

Equation (13.5), the exponential decline production model, can be integrated to determine cumulative production:

$$N_p = \int_0^t q dt = \int_0^t q_i e^{-D_i t} dt$$

$$N_p = \frac{q_i}{D_i} (1 - e^{-D_i t}) \tag{13.6}$$

For equation (13.6) to be dimensionally consistent,  $D_i$  in the term  $[D_i t]$  should have the same unit as time ( $t$ ). For instance, if  $t$  has a unit of a year,  $D_i$  in the term  $[D_i t]$  should have a unit of  $\text{year}^{-1}$ . Also,  $D_i$  in the term  $\left[\frac{q_i}{D_i}\right]$  should be in consistent units. For instance, if  $q$  has a unit of  $\text{stb/d}$  then  $D_i$  in the term  $\left[\frac{q_i}{D_i}\right]$  should have a unit of  $\text{d}^{-1}$ , so that the ratio  $\left[\frac{q_i}{D_i}\right]$  gives a unit of  $\text{stb}$ .

Rearranging equation (13.5):

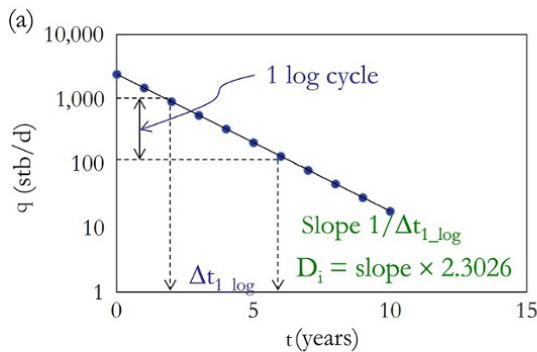
$$\frac{q}{q_i} = e^{-D_i t}$$

Substituting this into equation (13.6), the cumulative production for the exponential production decline model becomes:

$$N_p = \frac{q_i}{D_i} \left(1 - \frac{q}{q_i}\right)$$

$$N_p = \frac{(q_i - q)}{D_i} \tag{13.7}$$

**13.1.1.1. Diagnosis and Determination of Initial Decline Rate for the Exponential Decline Model.** From equation (13.5), production data that honor exponential decline will show a straight-line, semi-log relationship between production rate and time, with the logarithmic of the production rate on the vertical axis (Fig. 13.3).



Exponential production decline diagnosis as a semi-log plot of  $q$  against  $t$

Also, as shown by equation (13.7), production data that honor an exponential decline will show a straight-line relationship between production rate and cumulative production.  $D_i$  can be calculated from the slope of the graph shown in Fig. 13.3:

$$D_i = \text{Slope} \times 2.3026 \tag{13.8}$$

The value of 2.306 in Fig. 13.3 and equation (13.8) is  $\ln(10)$ , which converts slope in *log base 10* to slope in *natural logarithmic (ln)*. The concept of semi-log plots and their slopes was discussed also in Chapter 7 (7.3.2.1).

**13.1.2. Harmonic Production Decline Model**

When  $b = 1$ , equation (13.1) reduces to a harmonic production decline model:

$$q = \frac{q_i}{(1 + D_i t)} \tag{13.9}$$

Integrating the above equation yields a forecast of cumulative production:

$$N_p = \frac{q_i}{D_i} \ln(1 + D_i t) \tag{13.10}$$

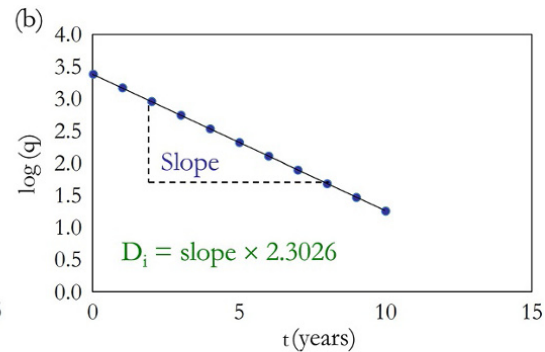
Rearranging equation (13.9)

$$\frac{q}{q_i} = \frac{1}{(1 + D_i t)}$$

Substituting  $\frac{q}{q_i} = \frac{1}{(1 + D_i t)}$  from the above into equation (13.10), the cumulative production for the harmonic decline model becomes:

$$N_p = \frac{q_i}{D_i} \ln\left(\frac{q_i}{q}\right) \tag{13.11}$$

**13.1.2.1. Diagnosis and Determination of Initial Decline Rate for Harmonic Decline Model.** From equation (13.11):



Exponential production decline diagnosis as a cartesian plot of  $\log(q)$  against  $t$

**Figure 13.3** Exponential production decline diagnosis.

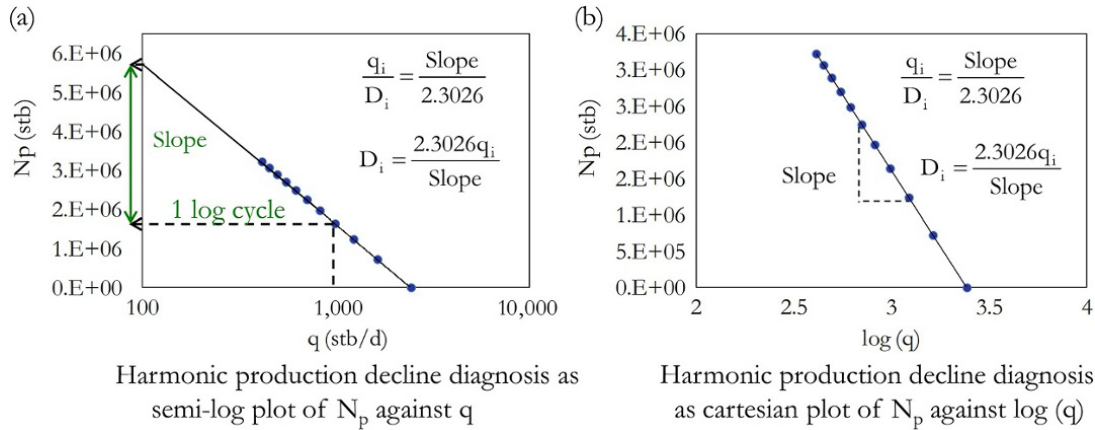


Figure 13.4 Harmonic production decline diagnosis.

$$N_p = \frac{q_i}{D_i} (\ln(q_i) - \ln(q))$$

Production data that honor a harmonic decline model will show a semi-log straight-line relationship between cumulative production and production rate, with the logarithmic of production on horizontal axis (Fig. 13.4).

### 13.1.3. Hyperbolic Production Decline Model

When  $0 < b < 1$ , the generalized hyperbolic production decline curve equation is:

$$q = \frac{q_i}{(1 + bD_i t)^{1/b}} \quad (13.12)$$

Defining  $a = 1/b$ :

$$q = \frac{q_i}{\left(1 + \frac{D_i t}{a}\right)^a}$$

Integrating this equation for  $0 < b < 1$ , and substituting  $b = 1/a$ , the cumulative production is thus expressed as:

$$N_p = \frac{q_i}{bD_i \left(\frac{1}{b} - 1\right)} \left[1 - (1 + bD_i t)^{1-\frac{1}{b}}\right]$$

$$N_p = \frac{q_i}{D_i(1-b)} \left[1 - (1 + bD_i t)^{\frac{b-1}{b}}\right] \quad (13.13)$$

**13.1.3.1. Diagnosis and Determination of Model Parameters for the Hyperbolic Decline Model.** The hyperbolic production decline curve model does not have specialized diagnostic plots. Where data do not fit exponential and harmonic decline models, the hyperbolic decline model should be investigated. Regression can be used to fit production data to the hyperbolic decline model, with  $D_i$  and  $b$  as model match parameters.

### Exercise 13.1 Production Decline Forecast Using Decline Curve Analysis

An oil field is considered to have a hyperbolic production decline profile based on comparison with an analogue field, with nominal decline rate of  $0.6 \text{ year}^{-1}$ , plateau oil production rate of 56,847 stb/d, and  $b = 0.75$ .

1. Calculate the average annual production rate of oil in stb/d, or Mstb/d, over 20 years of the field declining phase.
2. Calculate the cumulative oil production, in stb or MMstb, at the end of each year, over 20 years of the field declining phase.
3. Calculate annual oil production, in stb or MMstb, over 20 years of the field declining phase.
4. If the field is considered uneconomical at a production rate of 1,000 stb/d, determine when the field should be considered for abandonment.
5. Determine recovery, in stb or MMstb, from the onset of production decline to abandonment date.

#### Solution Steps.

*Step 1:*  $q$  is the average annual production rate of oil in stb/d; it is calculated using equation (13.12):

$$q = \frac{56847}{(1 + 0.75 \times 0.6 t)^{1/0.75}}$$

*Step 2:*  $N_p$  is the cumulative oil production at the end of each year in stb; it is calculated using equation (13.13):

$$N_p = \frac{q_i}{D_i(1-b)} \left[1 - (1 + bD_i t)^{\frac{b-1}{b}}\right]$$

For year  $t$ , substituting known parameters,  $N_p(t)$  becomes:

$$N_p(t) = \frac{56847(\text{stb/d})}{\left(\frac{0.6}{365}(\text{d}^{-1})\right)(1-0.75)} \left[1 - (1 + 0.75 \times 0.6t)^{\frac{0.75-1}{0.75}}\right]$$

$$N_p(t) = 138327700 \left[ 1 - (1 + 0.45t)^{-\frac{1}{3}} \right] \quad (13.14)$$

Note that the  $D_i$  in  $\frac{q_i}{D_i(1-b)}$  was divide by 365 to convert to  $d^{-1}$  (days<sup>-1</sup>) since  $q_i$  is in stb/d.

Step 3:  $\Delta N_{p,j}$  is the annual oil production in stb at a given time step,  $j$ , calculated by subtracting the previous year's cumulative oil production from the current year's cumulative oil production.

The annual oil production at time step,  $j$ , is therefore:

$$\Delta N_{p,j} = N_{p,j} - N_{p,j-1} \quad (13.15)$$

**Solution.**

The solutions to questions 1, 2, and 3 are summarized in Table 13.1.

Graphical presentations of the solutions to questions 1, 2, and 3 (Exercise 13.1) are shown in Fig. 13.5.

4. From equation (13.12):

$$q = \frac{q_i}{(1 + bD_it)^{1/b}}$$

At an uneconomic oil production rate ( $q_{limit}$ ), the corresponding abandonment time is defined as  $t_{limit}$ .

Substituting  $q_{limit}$  and  $t_{limit}$  into equation (13.12):

$$q_{limit} = \frac{q_i}{(1 + bD_it_{limit})^{1/b}}$$

where  $q_{limit} = 1000$  stb/d.

Substituting the given parameters into the above equation and making  $t_{limit}$  the subject of the formula:

$$1,000 = \frac{56,847}{(1 + 0.75 \times 0.6t_{limit})^{1/0.75}}$$

$$t_{limit} = \frac{\left(\frac{56,847}{1,000}\right)^{0.75} - 1}{0.45} = 43.8 \text{ years.}$$

$$t_{limit} \approx 44 \text{ years}$$

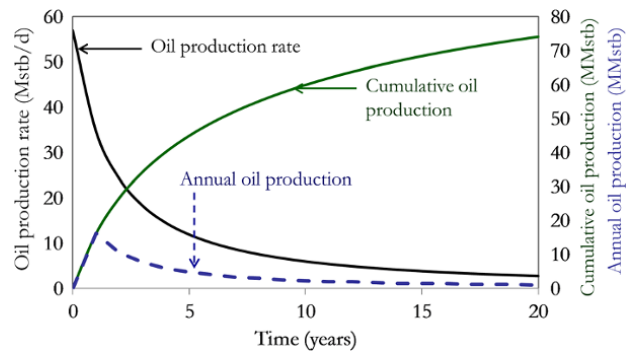


**Figure 13.5** Graphical presentations of solutions to questions 1, 2, and 3 (Exercise 13.1).

**Table 13.1** Solution to Exercise 13.1 (questions 1, 2, and 3).

Year	q (stb/d) using equation (13.12)	$N_p$ (stb) using equation (13.14)	$\Delta N_{p,j}$ (stb) using equation (13.15)
0	5.685E + 04	0.000E + 00	
1	3.464E + 04	1.611E + 07	1.611E + 07
2	2.416E + 04	2.664E + 07	1.053E + 07
3	1.819E + 04	3.428E + 07	7.639E + 06
4	1.440E + 04	4.019E + 07	5.902E + 06
5	1.181E + 04	4.494E + 07	4.756E + 06
6	9.934E + 03	4.889E + 07	3.951E + 06
7	8.524E + 03	5.225E + 07	3.357E + 06
8	7.431E + 03	5.515E + 07	2.904E + 06
9	6.561E + 03	5.770E + 07	2.548E + 06
10	5.855E + 03	5.996E + 07	2.262E + 06
11	5.273E + 03	6.199E + 07	2.028E + 06
12	4.784E + 03	6.382E + 07	1.833E + 06
13	4.370E + 03	6.549E + 07	1.669E + 06
14	4.014E + 03	6.702E + 07	1.528E + 06
15	3.707E + 03	6.843E + 07	1.408E + 06
16	3.438E + 03	6.973E + 07	1.303E + 06
17	3.201E + 03	7.094E + 07	1.211E + 06
18	2.992E + 03	7.207E + 07	1.130E + 06
19	2.806E + 03	7.313E + 07	1.057E + 06
20	2.639E + 03	7.412E + 07	9.930E + 05



Therefore, the field should be abandoned 44 years from the onset of production decline.

5. Using equation (13.14) and substituting abandonment time:

$$N_p(t) = 13,83,27,700 \left[ 1 - (1 + 0.45t)^{-\frac{1}{3}} \right]$$

$$N_p(t) = 13,83,27,700 \left[ 1 - (1 + 0.45 \times 43.8)^{-\frac{1}{3}} \right] = 8.796E + 07$$

$$N_p(t = t_{\text{limit}}) = 88 \text{ MMstb.}$$

Therefore, recovery from the onset of production decline to the abandonment date is 88 MMstb.

**Exercise 13.2** Production Decline Diagnosis and Forecast Using Decline Curve Analysis

Table 13.2 shows oil production data during the declining stage of a field production from the plateau production rate of 20,305 stb/d.

1. Determine the production decline model that best describes the field production performance and calculate the cumulative oil produced using historical data.
2. Predict oil production 13 years from the end of production history.
3. Predict recoverable oil 25 years from the onset of production decline.
4. Plot annual oil production rate and cumulative oil production from both history and prediction over the 25 years from the onset of production decline.

**Solution Steps.**

*Step 1:* using the diagnostic plots in Figs. 13.3 and 13.4, determine if production data honor the exponential or harmonic production decline model. Where data do not fit either the exponential or harmonic decline models, the hyperbolic decline model should be

**Table 13.2** Oil Production Data During the Decline Stage of Field Life.

Time (years)	Average annual oil production rate (stb/d)
0	20,305
1	19,054
2	17,880
3	16,778
4	15,745
5	14,775
6	13,864
7	13,010
8	12,208
9	11,456
10	10,750
11	10,088
12	9,466

considered with regression to match and determine model parameters.

*Step 2:* after model identification, the decline model that best matches the production data should be selected for production rate and oil recovery prediction.

**Solution.**

1. Production decline model diagnosis.

Create a column of log(q) as shown in Table 13.3 and make a diagnostic plot of log (q) against t to examine if production data fit an exponential decline model (Fig. 13.6).

As diagnosis shows that production can be described by an exponential decline model, the parameter  $D_i$  for the exponential decline model can then be determined.

Determining the slope and then  $D_i$  from Fig. 13.6 using the same approach as illustrated in Fig. 13.3.

$$D_i = \text{slope} \times 2.3026$$

$$D_i = 0.0276 \times 2.3026 = 0.06355176 \text{ per year}$$

$$D_i = 0.0636 \text{ per year.}$$

For a period with measured data, it is best to determine the cumulative oil produced from historical/measured

**Table 13.3** log(q) with Corresponding Time.

Time (years)	q (stb/d)	log(q)
0	20,305	4.31
1	19,053.9	4.28
2	17,880	4.25
3	16,778	4.22
4	15,745	4.20
5	14,775	4.17
6	13,864	4.14
7	13,010	4.11
8	12,208	4.09
9	11,456	4.06
10	10,750	4.03
11	10,088	4.00
12	9,466	3.98

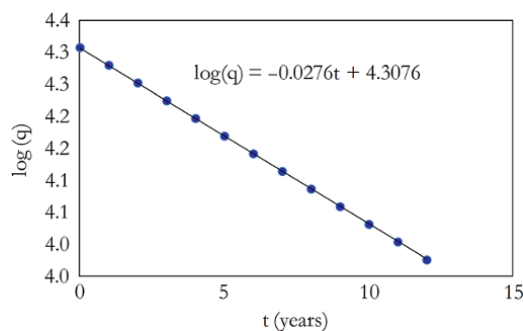


**Figure 13.6** Exponential decline production diagnosis for Exercise 13.2.

**Table 13.4** Cumulative and Annual Oil Production from Historical Data.

Time (years)	q (stb/d)	Annual oil production $\Delta N_{p,j} = q_j \times \Delta t_j$ (stb)	Cumulative oil production $N_{p,j} = \Delta N_{p,j} + N_{p,j-1}$ (stb)
0	2.031E+04	7.411E+06	0.000E+00
1	1.905E+04	6.955E+06	6.955E+06
2	1.788E+04	6.526E+06	1.348E+07
3	1.678E+04	6.124E+06	1.960E+07
4	1.575E+04	5.747E+06	2.535E+07
5	1.478E+04	5.393E+06	3.074E+07
6	1.386E+04	5.060E+06	3.581E+07
7	1.301E+04	4.749E+06	4.055E+07
8	1.221E+04	4.456E+06	4.501E+07
9	1.146E+04	4.181E+06	4.919E+07
10	1.075E+04	3.924E+06	5.311E+07
11	1.009E+04	3.682E+06	5.680E+07
12	9.466E+03	3.455E+06	6.025E+07

**Table 13.5** Production Rate and Cumulative Oil Predictions.

Time (years)	q (stb/d) using equation (13.5)	N <sub>p</sub> (stb) using equation (13.6)
13	8.888E+03	6.562E+07
14	8.341E+03	6.876E+07
15	7.827E+03	7.171E+07
16	7.345E+03	7.448E+07
17	6.893E+03	7.708E+07
18	6.468E+03	7.952E+07
19	6.070E+03	8.181E+07
20	5.696E+03	8.396E+07
21	5.346E+03	8.598E+07
22	5.016E+03	8.787E+07
23	4.708E+03	8.964E+07
24	4.418E+03	9.131E+07
25	4.146E+03	9.287E+07

data by rearranging equation (13.15) to make the cumulative production at time step  $j$  ( $N_{p,j}$ ) the subject of the formula:

$$N_{p,j} = \Delta N_{p,j} + N_{p,j-1} \quad (13.16)$$

where the annual oil production ( $\Delta N_{p,j}$ ) is defined as:

$$\Delta N_{p,j} = q_j \times \Delta t_j$$

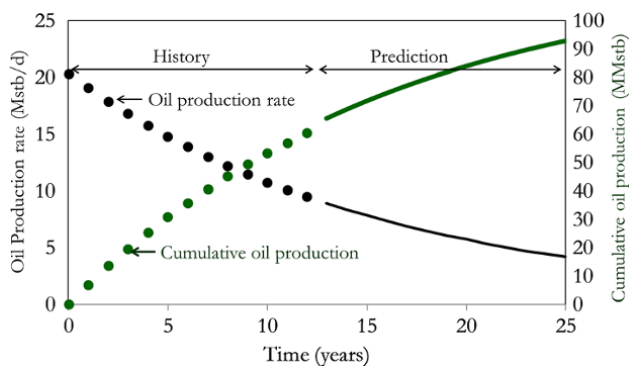
where  $\Delta t_j = t_j - t_{j-1}$

The cumulative oil produced from historical data is summarized in Table 13.4.

2. For the prediction for 13 years from the end of history, the calculation is carried out using the same approach as Exercise 13.1 (Table 13.5).

3. From Table 13.5, the recoverable oil at the end of 25 years from the onset of production decline is 93 MMstb ( $93 \times 10^6$  stb).

4. Combining Table 13.4 (history) and Table 13.5 (prediction) gives the oil production rate and cumulative oil production expected over 25 years from the onset of production decline (Fig. 13.7).

**Figure 13.7** Production rate and cumulative oil profile over 25 years (Exercise 13.2).

## REFERENCES

- Arps, J., 1945. Analysis of decline curves. *Transactions of the AIME*, **160**(01), 228–247.
- Fetkovich, M., 1980. Decline curve analysis using type curves. *Journal of Petroleum Technology*, **32**(06), 1–65.

## BIBLIOGRAPHY

- Ahmed, T., 2006. *Reservoir Engineering Handbook*, 3rd edn. Gulf Professional Publishing.
- Amyx, J.W., Bass, D.M., and Whiting, R.L., 1960. *Petroleum Reservoir Engineering: Physical Properties*. McGraw-Hill.

- Archer, J. and Wall, C., 1999. *Petroleum Engineering Principles and Practice*. Dordrecht/Boston: Kluwer Academic Publishing.
- Craft, B. and Hawkins, M., 1991. *Applied Petroleum Reservoir Engineering*, 2nd edn. Prentice-Hall.
- Craig, F.G. and Morse, R., 1995. Oil recovery performance of pattern gas or water injection operations from model tests. *Petroleum Transactions, AIME*, **204**, 7–15.
- Dake, L., 1998. *Fundamentals of Reservoir Engineering*. 17th edn. Development in Petroleum Science 8, Elsevier.
- Ehlig-Economides, C., 1979. *Well Test Analysis for Wells Produced at a Constant Pressure*. Doctoral dissertation, Stanford, CA: Stanford University.
- Walsh, M. and Lake, L., 2003. *A Generalized Approach to Primary Hydrocarbon Recovery*. Amsterdam: Elsevier.

## Secondary and Tertiary Recovery Methods

Oil recovery methods can be broadly considered as *primary*, *secondary*, and *tertiary (enhanced)* oil recovery. The definition of oil recovery methods can be based on the *stage (time) of recovery* or *energy drive* used in producing oil from the reservoir.

If oil recovery methods are defined based on the stages of recovery, then *primary oil recovery*, also called *primary production*, would include production/recovery at the initial stage of production where oil is produced using natural energy until the economic limit is reached. During the primary oil recovery stage, pressure maintenance using water or gas injection would be generally considered part of the primary oil recovery process. When production using the reservoir's natural energy has reached its economical limit, a second stage called *secondary oil recovery*, also called *secondary production*, may be considered to boost production. Additional recovery to primary recovery during secondary recovery is also referred to as *secondary oil recovery*. When secondary oil recovery reaches its economic limit, recovery methods that can be used to produce some of the remaining mobile and residual oil economically may be considered. This third stage of oil recovery, which involves mostly unconventional recovery methods, is known as *tertiary oil recovery*, and also called *tertiary production*. Additional recovery to primary and secondary oil recoveries is also referred to as *tertiary oil recovery*.

Oil recovery methods based on the production stages are summarized in Fig. 14.1.

If oil recovery methods are defined based on energy drive for producing reservoir fluid, *primary oil recovery* methods would include methods of production that

use natural reservoir energy for production. Since this definition is not based on production stage (time), pressure maintenance methods such as water and gas injection would be termed secondary oil recovery methods. Hence, producing a reservoir with both natural and external energy would be best described as a combination of primary and secondary oil recovery methods. Primary drive mechanisms include: *depletion drive*; *natural segregated gas-cap drive*; *compaction drive*, and *natural water drive*. Primary oil recovery can be combined with an artificial lift system. Secondary oil recovery methods based on energy drive include methods where the reservoir is produced using external energy without alteration of reservoir fluid or rock–fluid properties. Methods under secondary oil recovery methods include *water injection*, *immiscible gas injection*, and *immiscible water alternating gas injection* to energize the reservoir or sweep oil to increase production. Secondary oil recovery methods, like primary oil recovery, can be combined with artificial lift systems.

Tertiary oil recovery methods based on energy drive include methods where production of reservoir oil is enhanced by changing the reservoir fluid properties, such as viscosity, and/or the rock–fluid properties, such as wettability, to make oil production more favorable. Tertiary oil recovery methods where viscosity is reduced to enhanced recovery include thermal processes such as *in situ* combustion, steam injection drive (cyclic and steam-assisted gravity drive), and hot water drive. Other methods that make production favorable by viscosity reduction are miscible gas injection and miscible water alternating gas injection.

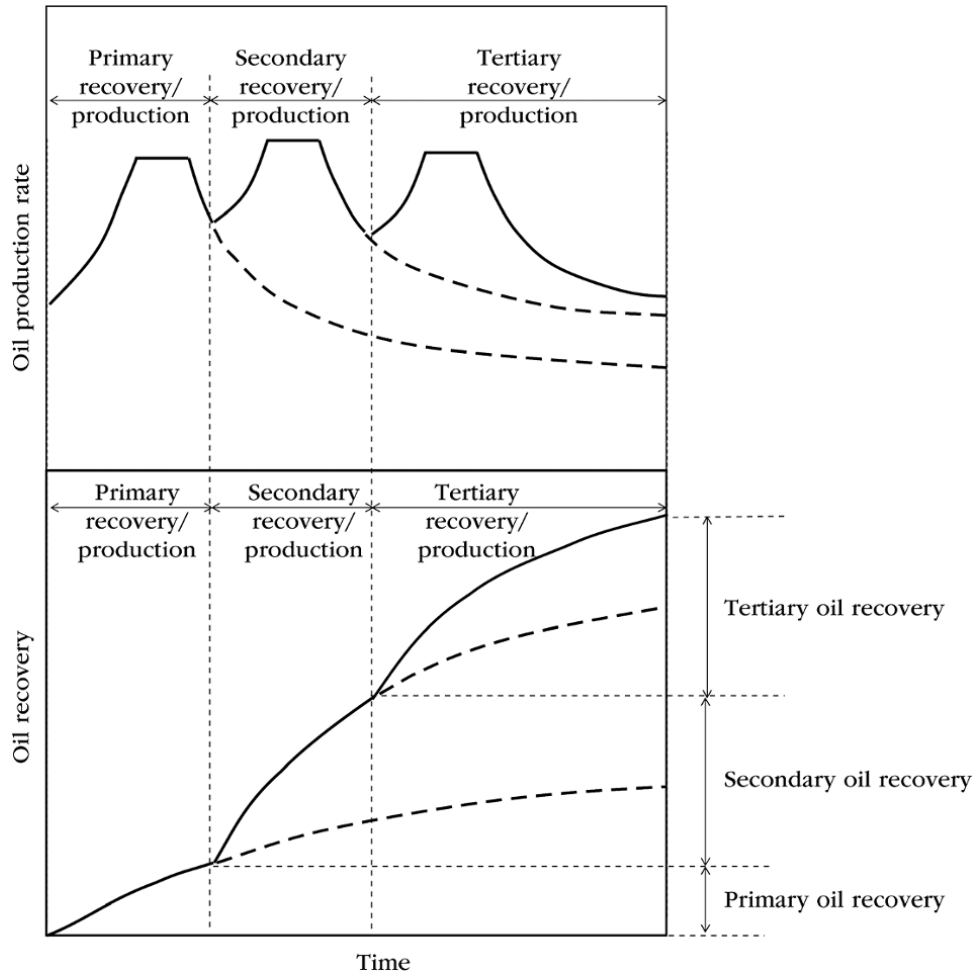


Figure 14.1 Oil recovery based on production stages.

Tertiary oil recovery methods that alter the reservoir rock–fluid properties such as wettability to enhanced production are mostly chemical injection methods. Wettability alteration enhances production by increasing the relative permeability of the oil. Alteration of rock wettability in tertiary oil recovery is achieved through the reduction in interfacial tension. Emerging tertiary oil recovery methods include the use of microbial, ultrasonic vibration, and electromagnetic methods. Tertiary oil recovery methods, as in primary and secondary oil recoveries, can also have artificial lift systems to improve tubing performance.

Secondary and tertiary (enhanced) oil recovery methods can both be defined as *improved oil recovery* (IOR) methods.

Oil recovery methods based on energy drive are summarized in Fig. 14.2.

Typical recoveries from each recovery method are summarized in Fig. 14.3.

### 14.1. PRIMARY OIL RECOVERY

Reservoir performance in primary oil recovery processes has been discussed under material balance models (Chapter 12). The material balance models discussed in Chapter 12 incorporate the effect of reservoir deliverability due to natural (primary) production drives, which include depletion drive; natural segregated gas-cap drive; compaction drive, and natural water drive.

### 14.2. SECONDARY OIL RECOVERY

Secondary oil recovery methods include water injection, immiscible gas injection, and immiscible water alternating gas injection.

The effect of gas injection into a gas cap and/or water into the aquifer to support or energize the reservoir can be handled in reservoir performance prediction by adding

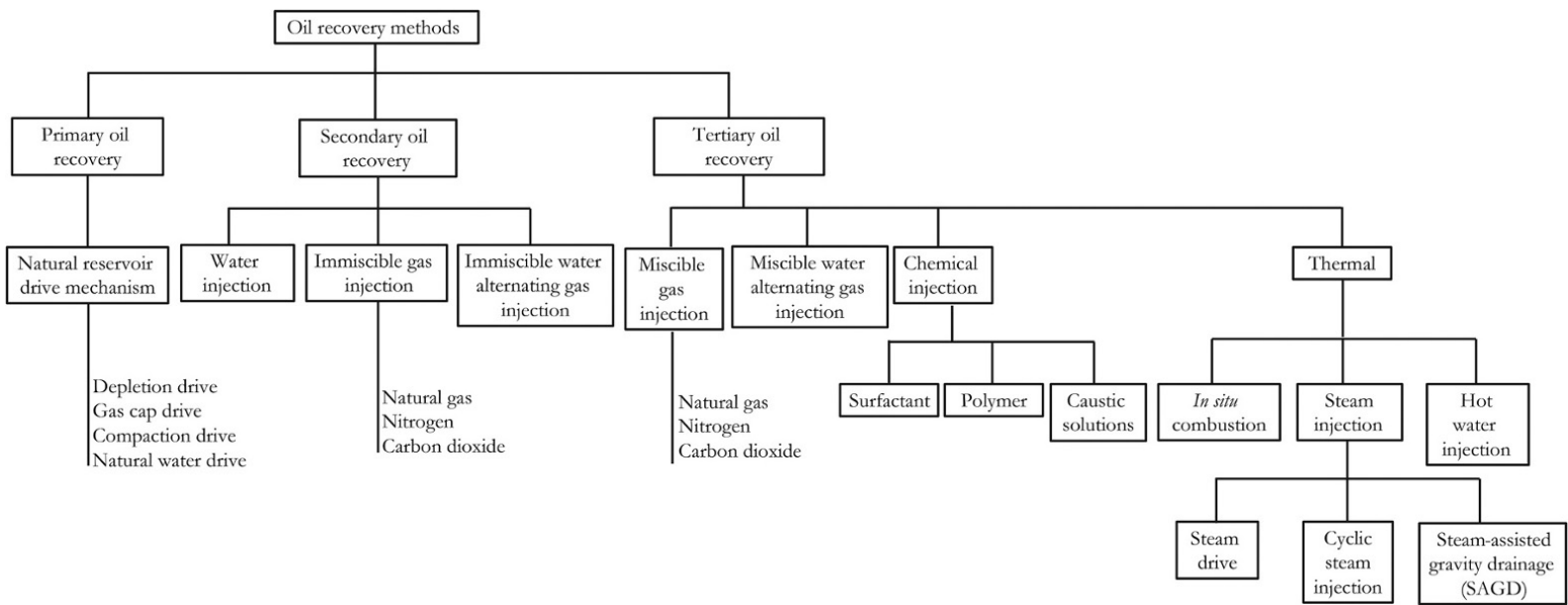


**Figure 14.2** Oil recovery methods based on energy drive.

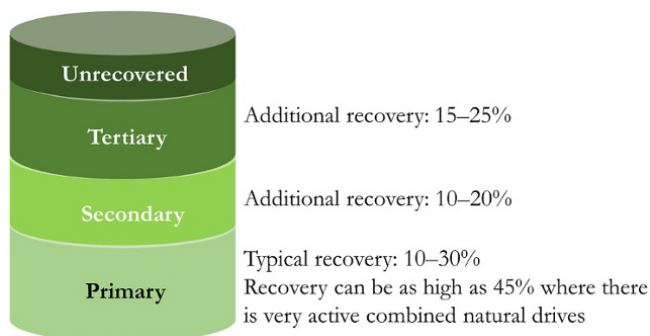


Figure 14.3 Oil recovery for different recovery methods.

gas injection ( $G_{inj}$ ) and water inject ( $W_{inj}$ ) into the oil material balance equation, as shown in equation (12.18).

$$N_p(B_o + (R_p - R_s)B_g) + W_p B_w - W_{inj} B_{winj} - G_{inj} B_{ginj} \\ = NB_{oi} \left[ \left( \frac{(B_o - B_{oi}) + (R_{si} - R_s)B_g}{B_{oi}} \right) + m \left( \frac{B_g}{B_{gi}} - 1 \right) \right. \\ \left. + (1 + m) \left( \frac{c_w S_{wc} + c_f}{1 - S_{wc}} \right) \Delta p \right] + W_e$$

Where the injection of fluid is for displacement rather than energizing the reservoir, methods based on fractional flow should be used.

#### 14.2.1. Water Injection

Water is a common choice of injectant for secondary recovery due to low cost and ready availability. Water injection may be carried out to achieve pressure support (pressure maintenance), reservoir sweeping (water flooding) or both.

Where the objective of water injection is pressure maintenance, it should commence before reservoir depletion or significant reservoir depletion sets in. The effect of water injection for pressure maintenance on reservoir performance can be captured by adding water injection into material balance equation, as shown in equation (12.18).

Water flooding is another objective of water injection and involves injecting water to sweep reservoir hydrocarbon through the displacement process in order to improve hydrocarbon recovery (Fig. 14.4). Water flooding is not strictly for pressure maintenance, as it can be carried out in a depleted reservoir.

It is always preferable to inject water peripherally or basal, near the water leg or in the water leg, away from hydrocarbon-bearing sand (Fig. 14.5).

The effect of gravity ensures that water displacement is from the bottom or edge to the oil-bearing zone to achieve an efficient sweep. Though reservoir response to sweep and pressure from water injected peripherally or basal

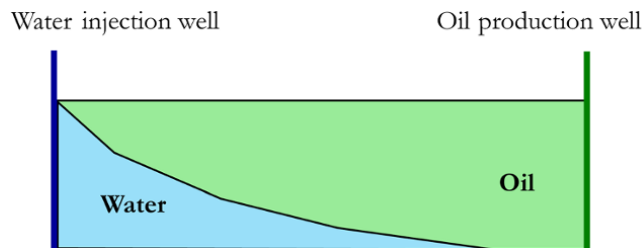


Figure 14.4 Water flooding.

may be slow initially, overall recovery is often higher with a lower water cut than a patterned injection well layout (Fig. 14.6).

Before water injection is considered for flooding or pressure maintenance, it is important that the source of the water is identified; that the water to be injected is compatible with formation water; a reasonable estimate of reservoir permeability and heterogeneity within the area of interest is known; reservoir fluid properties and the effect on displacement are understood; wettability and relative permeability and the effect on displacement are also understood.

It is very important that the proposed injection water is analyzed for compatibility with formation connate water. The *injection water compatibility test* evaluates the risk of precipitation of inorganic scale during water injection by the laboratory measurement of inorganic scale precipitation due to different mixing ratios of raw and formation water. This analysis is essential in the selection of chemical scale inhibitors and the required concentrations of these inhibitors if needed for scale prevention. Prior to injection, water should be: treated to remove oxygen, which accelerates corrosion and bacterial growth; treated to remove bacteria whose growth leads to the production of hydrogen sulfide; and treated to remove sulfates, which can precipitate as scale (calcium sulfate, barium sulfate or strontium sulfate) at conducive temperatures and pressures.

Understanding spatial reservoir permeability variation is very important, as injection fluid will tend to flow through the path of least resistance, which is defined by high permeability. Hence, where there are permeability streaks or fractures, an efficient sweep of oil may not be achieved. Also, knowing aquifer permeability is very important when considering water injection/flooding, as it is advantageous to inject water peripherally or basal for flooding and pressure maintenance where it is possible. Permeability in the aquifer may be significantly less than that in the reservoir due to *diagenesis*. Where the permeability of the aquifer or the edge of the reservoir does not permit the desired injection rate required for

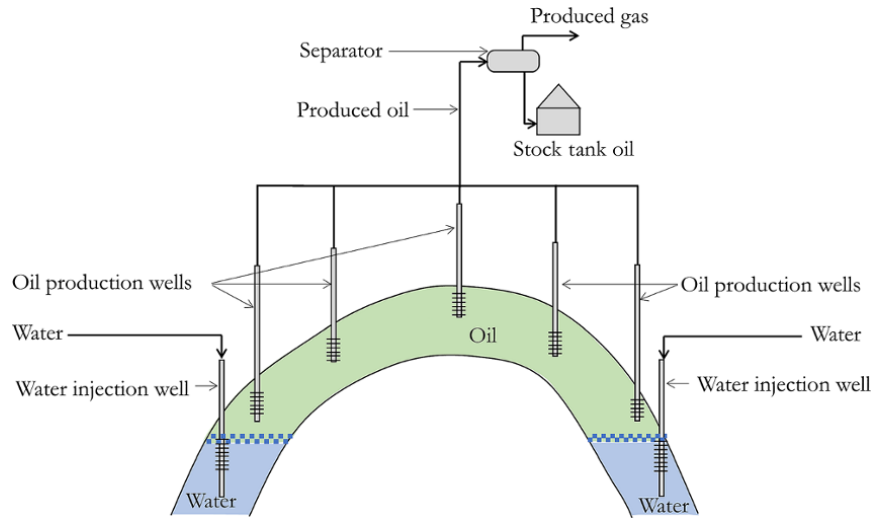


Figure 14.5 Peripheral aquifer water injection for flooding and pressure maintenance.

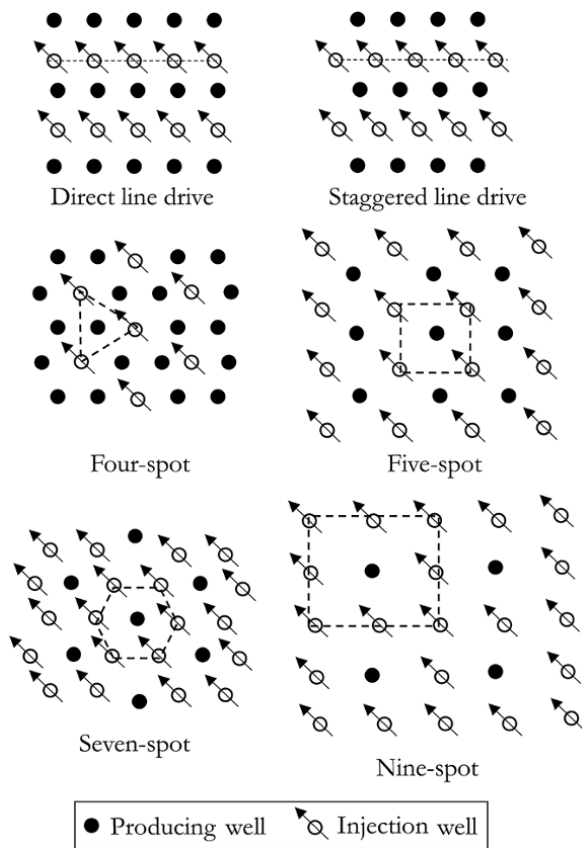


Figure 14.6 Patterned water injection layout [Adapted from Craft and Hawkins, 1991].

flooding or pressure maintenance to be achieved, different options for injection pattern layout may be considered.

Reservoir structure as well plays an important role in water injection as, gravity affects the distribution of

flowing water. If water is injected close to the crest of a high dip reservoir structure, water will slump to the bottom without sweeping most parts of the reservoir towards the top, thereby creating an inefficient vertical sweep and, hence, low recovery.

**14.2.1.1. Fractional Flow Equation.** The fractional flow equation describes the flow of water or polymer and oil in a homogeneous reservoir. It can be used to predict reservoir performance during water flooding.

Consider a reservoir with dip of  $\theta$ , with water displacing oil. From Darcy's equation, the flow rate of the oil phase ( $q_o$ ) and the water phase ( $q_w$ ) during displacement process are, respectively:

$$q_o = -\frac{kk_{ro}A}{\mu_o} \left( \frac{\partial p_o}{\partial x} + \rho_o g \sin\theta \right) \quad (14.1)$$

and

$$q_w = -\frac{kk_{rw}A}{\mu_w} \left( \frac{\partial p_w}{\partial x} + \rho_w g \sin\theta \right) \quad (14.2)$$

where  $k_{ro}$  and  $k_{rw}$  are the relative permeabilities of oil and water, respectively,  $\mu_o$  and  $\mu_w$  are the viscosities of the oil and water, respectively,  $k$  is absolute permeability,  $x$  is linear displacement of fluid,  $p$  is the pressure (with the subscripts  $o$  and  $w$  representing oil and water, respectively, and  $\rho$  is density (with the subscripts  $o$  and  $w$  representing oil and water, respectively).

$$p_{cow} = p_o - p_w$$

where  $p_{cow}$  is capillary pressure.



Making  $p_w$  the subject of the formula:

$$p_w = p_o - p_{cow}$$

Substituting into equation (14.2)

$$q_w = -\frac{kk_{rw}A}{\mu_w} \left( \frac{\partial(p_o - p_{cow})}{\partial x} + \rho_w g \sin \theta \right) - q_w \frac{\mu_w}{kk_{rw}A} = \frac{\partial p_o}{\partial x} - \frac{\partial p_{cow}}{\partial x} + \rho_w g \sin \theta \quad (14.3)$$

From equation (14.1):

$$-q_o \frac{\mu_o}{kk_{ro}A} = \frac{\partial p_o}{\partial x} + \rho_o g \sin \theta \quad (14.4)$$

Equation (14.3) minus equation (14.4):

$$-\frac{1}{kA} \left( \frac{q_w \mu_w}{k_{rw}} - \frac{q_o \mu_o}{k_{ro}} \right) = -\frac{\partial p_{cow}}{\partial x} + (\rho_w - \rho_o) g \sin \theta \quad (14.5)$$

The total liquid rate ( $q_t$ ) is defined as:

$$q_t = q_o + q_w$$

Making  $q_o$  the subject of the formula:

$$q_o = q_t - q_w$$

Substituting  $q_o = q_t - q_w$  into equation (14.5):

$$-\frac{1}{kA} \left( \frac{q_w \mu_w}{k_{rw}} - \frac{\mu_o (q_t - q_w)}{k_{ro}} \right) = -\frac{\partial p_{cow}}{\partial x} + (\rho_w - \rho_o) g \sin \theta \quad (14.6)$$

The fractional flow of water is defined as:

$$f_w = \frac{q_w}{q_o + q_w} = \frac{q_w}{q_t} \quad (14.7)$$

Making  $q_w$  the subject of the formula:

$$q_w = f_w q_t$$

$q_t$  is total flow rate.

Substituting  $q_w = f_w q_t$  into equation (14.6) the fractional flow in consistent unit becomes:

$$-\frac{1}{kA} \left( \frac{f_w q_t \mu_w}{k_{rw}} - \frac{\mu_o (q_t - f_w q_t)}{k_{ro}} \right) = -\frac{\partial p_{cow}}{\partial x} + (\rho_w - \rho_o) g \sin \theta$$

$$-\frac{q_t \mu_o}{kk_{ro}A} \left( \frac{f_w k_{ro} \mu_w}{k_{rw} \mu_o} - (1 - f_w) \right) = -\frac{\partial p_{cow}}{\partial x} + (\rho_w - \rho_o) g \sin \theta$$

$$\frac{q_t \mu_o}{kk_{ro}A} \left( f_w + \frac{f_w k_{ro} \mu_w}{k_{rw} \mu_o} - 1 \right) = \frac{\partial p_{cow}}{\partial x} - (\rho_w - \rho_o) g \sin \theta$$

$$\frac{q_t \mu_o}{kk_{ro}A} \left( f_w + \frac{f_w k_{ro} \mu_w}{k_{rw} \mu_o} \right) = \frac{q_t \mu_o}{kk_{ro}A} + \frac{\partial p_{cow}}{\partial x} - (\rho_w - \rho_o) g \sin \theta$$

$$f_w \frac{q_t \mu_o}{kk_{ro}A} \left( 1 + \frac{k_{ro} \mu_w}{k_{rw} \mu_o} \right) = \frac{q_t \mu_o}{kk_{ro}A} + \frac{\partial p_{cow}}{\partial x} - (\rho_w - \rho_o) g \sin \theta$$

$$f_w = \frac{\frac{q_t \mu_o}{kk_{ro}A} + \frac{\partial p_{cow}}{\partial x} - (\rho_w - \rho_o) g \sin \theta}{\frac{q_t \mu_o}{kk_{ro}A} \left( 1 + \frac{k_{ro} \mu_w}{k_{rw} \mu_o} \right)}$$

$$f_w = \frac{1 + \frac{kk_{ro}A}{q_t \mu_o} \left( \frac{\partial p_{cow}}{\partial x} - (\rho_w - \rho_o) g \sin \theta \right)}{1 + \frac{k_{ro} \mu_w}{k_{rw} \mu_o}} \quad (14.8)$$

Equation (14.8) in engineering oil field (EOF) units is expressed as:

$$f_w = \frac{1 + \left( \frac{0.001127 k k_{ro} A}{q_t \mu_o} \right) \left( \frac{\partial p_{cow}}{\partial x} - 0.433 (\rho_w - \rho_o) \sin \theta \right)}{1 + \frac{k_{ro} \mu_w}{k_{rw} \mu_o}} \quad (14.9)$$

where  $A$  is the area ( $\text{ft}^2$ ),  $f_w$  is the fractional water flow,  $k$  is the absolute permeability (mD),  $k_{ro}$  is the relative permeability of oil phase,  $k_{rw}$  is the relative permeability of the water phase,  $\mu_o$  is oil viscosity,  $\mu_w$  is water viscosity,  $p_{cow}$  is capillary pressure (psi),  $q_t$  is total flow rate (bbl/d),  $\rho_w$  is the specific gravity of water,  $\rho_o$  is the specific gravity of oil, and  $\theta$  is the angle of dip of the reservoir to the horizon in degrees

Neglecting the effect of capillary pressure and gravity, equation (14.8) becomes:

$$f_w = \frac{1}{1 + \frac{k_{ro} \mu_w}{k_{rw} \mu_o}} \quad (14.10)$$

Defining the mobility ratio ( $M$ ) as  $M = \frac{k_{rw} \mu_o}{k_{ro} \mu_w}$  equation (14.10) becomes:

$$f_w = \frac{1}{1 + \frac{1}{M}} \quad (14.11)$$

**Exercise 14.1** Effect of the Mobility Ratio on Fractional Flow

A reservoir has a relative permeability  $K_{rw} = 0.2(S_w - 0.2)^2$  and  $K_{ro} = 0.4(S_o - 0.25)^2$ , plot the fractional flow plot ( $f_w$  against  $S_w$ ) for water–oil viscosity ratios  $\left( \frac{\mu_w}{\mu_o} \right)$  of 0.05, 0.2, 0.6, 1.4, 5, 10, and 20.

The end point (maximum) relative permeability of water ( $k'_{rw}$ ) is 0.2 as shown in the relative permeability model.

**Table 14.1**  $f_w$  Calculation for  $\frac{\mu_w}{\mu_o}$  of 0.05, 0.2, 0.6, 1.4, 5, 10, and 20.

$S_w$	$\frac{\mu_w}{\mu_o} = 0.05$	$\frac{\mu_w}{\mu_o} = 0.2$	$\frac{\mu_w}{\mu_o} = 0.6$	$\frac{\mu_w}{\mu_o} = 1.4$	$\frac{\mu_w}{\mu_o} = 5$	$\frac{\mu_w}{\mu_o} = 10$	$\frac{\mu_w}{\mu_o} = 20$
0.20	0	0	0	0	0	0	0
0.25	0.091	0.024	0.008	0.004	0.001	0.000	0.000
0.30	0.331	0.110	0.040	0.017	0.005	0.002	0.001
0.35	0.584	0.260	0.105	0.048	0.014	0.007	0.004
0.40	0.766	0.449	0.214	0.104	0.032	0.016	0.008
0.45	0.874	0.635	0.367	0.199	0.065	0.034	0.017
0.50	0.935	0.783	0.545	0.340	0.126	0.067	0.035
0.55	0.968	0.884	0.718	0.522	0.234	0.133	0.071
0.60	0.986	0.947	0.856	0.717	0.416	0.262	0.151
0.65	0.995	0.981	0.944	0.879	0.669	0.503	0.336
0.70	0.999	0.996	0.988	0.973	0.909	0.833	0.714
0.75	1	1	1	1	1	1	1

End point (maximum) relative permeability of oil ( $k'_{rw}$ ) is 0.4, as shown in the relative permeability model.

**Solution.**

From equation (14.10):

$$f_w = \frac{1}{1 + \frac{k_{ro}\mu_w}{k_{rw}\mu_o}} = \frac{1}{1 + \frac{1}{\left(\frac{k_{rw}\mu_o}{k_{ro}\mu_w}\right)}}$$

Substituting the relative permeability into the above:

$$f_w = \frac{1}{1 + \frac{2(S_o - 0.25)^2 \mu_w}{(S_w - 0.2)^2 \mu_o}} = \frac{1}{1 + \frac{2((1 - S_w) - 0.25)^2 \mu_w}{(S_w - 0.2)^2 \mu_o}} \tag{14.12}$$

Create a table of  $f_w$  for different values of  $\frac{\mu_w}{\mu_o}$  using equation (14.12) with values of  $S_w$  from  $S_{wc}$  (0.2) to  $1 - S_{or}$  ( $1 - 0.25 = 0.75$ ) (Table 14.1).

Fig. 14.7 shows a plot of  $f_w$  against  $S_w$  for  $\frac{\mu_w}{\mu_o} = 0.05, 0.2, 0.6, 1.4, 5, 10,$  and  $20$ .

The *end-point mobility*, defined as  $M_{end} = \frac{k'_{rw}\mu_o}{k'_{ro}\mu_w}$ , for given values of the  $\frac{\mu_w}{\mu_o}$  ratio are summarized in Table 14.2.

*Case 1* ( $\frac{\mu_w}{\mu_o} = 0.05$ ), with an end-point mobility ratio greater than 1 (Table 14.2), shows a fractional flow curve characterized by unstable displacement, as shown by the downward concave shape of the fractional flow curve (Fig. 14.7). This unfavorable displacement is due to low

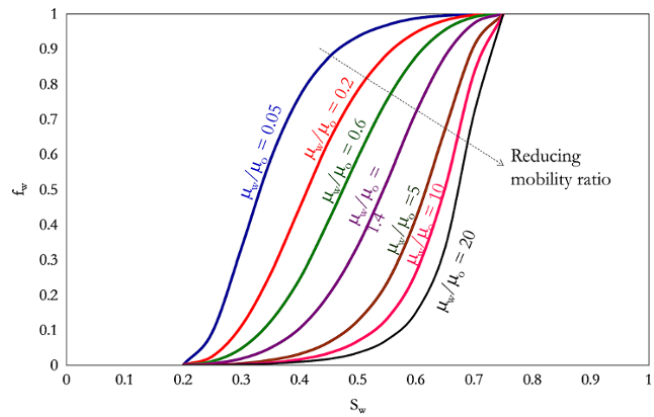


**Figure 14.7** Fractional flow plot for Exercise 14.1.

$\frac{\mu_w}{\mu_o}$  (high  $\frac{\mu_o}{\mu_w}$ ), which can occur in a high viscosity oil reservoir under water flooding. In this situation, the injected water will bypass a significant amount of oil in the reservoir with low recovery at water breakthrough. Reservoirs with high oil viscosity are not good candidates for water flooding.

The end-point mobility ratio can be reduced by addition of polymer to the injection water to increase the viscosity of the displacing fluid, thereby achieving the mobility ratio required for favorable displacement of oil as shown in Case 4. Use of polymer to improve oil recovery is discussed in Section 14.3.3.1.

*Case 2* ( $\frac{\mu_w}{\mu_o} = 0.2$ ), with an end-point mobility ratio greater than 1 (Table 14.2), shows a fractional flow curve with inflexion; however, it is not well pronounced (Fig. 14.7). Hence, Case 2 may not be the best case for efficient oil recovery with water flooding.

**Table 14.2** End-point Mobility Ratio for  $\frac{\mu_w}{\mu_o}$  Values of 0.05, 0.2, 0.6, 1.4, 5, 10, and 20.

$\frac{\mu_w}{\mu_o}$	0.05	0.2	0.6	1.4	5	10	20
$M_{end} = \frac{k'_{rw}\mu_o}{k'_{ro}\mu_w}$	10	2.5	0.83	0.36	0.1	0.05	0.025

Case 3 ( $\frac{\mu_w}{\mu_o} = 0.6$  and 1.4), with end-point mobility ratios less than 1 (Table 14.2), shows a fractional flow curve with a well-developed inflection shape (Fig. 14.7), which characterizes favorable displacement, and such reservoirs can be considered good candidates for water flooding.

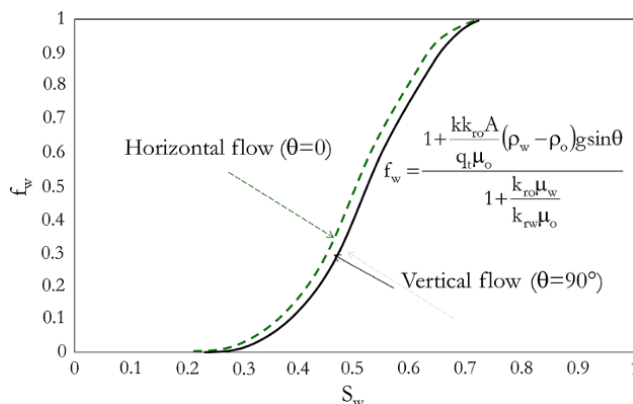
Case 4 ( $\frac{\mu_w}{\mu_o} = 5, 10, 20$ ), with end-point mobility ratios less than or equal to 0.1, show fractional flow curves with totally upward, concave fractional flow curves (Fig. 14.7), which characterize a highly favorable displacement.

#### Effect of Gravity on Fractional Flow Curve

The typical fractional flow curves for horizontal ( $\theta = 0$ ) and vertical flow ( $\theta = 90$ ) are shown in Fig. 14.8. The gravitation component in the fractional flow equation adds extra force to the injectant, which improves the sweep of oil by water.

**14.2.1.2. Buckley–Leverett (BL) Equation.** The Buckley–Leverett (BL) equation [Buckley and Leverett, 1942] describes one-dimensional (1D), piston-like displacement of two-phase immiscible, incompressible fluids in a single layered homogeneous reservoir (Fig. 14.9). The use of the BL equation is most common for the prediction of reservoir performance during water flooding. This method has also been extended to polymer and chemical injection. In the case of polymer and chemical injection, the effect of a change in wettability is captured by modifying the relative permeability model in the fractional flow equation to reflect this change, while the effect of viscosity is captured by adjusting the viscosity of the displacing fluid appropriately in the fractional flow equation.

The formulation of the BL equation is based on the assumption of the 1D piston-like displacement of an immiscible fluid. Hence, the BL equation is not applicable to segregated flow where the effect of gravity is dominant and in heterogeneous reservoirs where piston-like displacement may not be achievable. The assumption of piston-like displacement is valid for flooding with end-point mobility ratios (mobility of injectant divided by the displaced fluid) of less than one, but is invalid for end-point mobility ratios greater than 10 due to possible effects of viscous fingering (Fig. 14.10).

**Figure 14.8** The effect of gravity on the fractional flow curve.

The BL equation can be used for solving a wide range of reservoir and field management problems during water flooding, some of which are highlighted here.

#### • Water Saturation Distribution in the Reservoir

The BL equation can be used during water flooding to predict: water saturation at the flood front, average water saturation behind the flood front, the speed of the water front and the time water breaks through.

#### • Oil Recovery Prediction

During water flooding, the BL equation can be used to predict the amount of oil swept/oil recovery by displacing water; sweep/recovery efficiency before and after water breakthrough.

#### • Water Production and Injection Management

The BL equation can be used to predict the water–oil ratio (WOR), the water cut after injection water breakthrough, and the amount of water required to achieve a given oil recovery.

#### • Developing the BL Equation

The BL equation is a combination of the mass continuity equation (equation (14.13)) and the fractional flow equation (equation (14.10)).

Carrying out the mass balance over the volume element with cross-sectional area of  $A$  and thickness of  $dx$  (Fig. 14.11) to develop mass continuity equation.

mass in – mass out = change in mass

$$(q_w \rho_w|_x - q_w \rho_w|_{x+dx}) \Delta t = A \phi (S_w \rho_w|_{t+\Delta t} - S_w \rho_w|_t) \Delta x$$

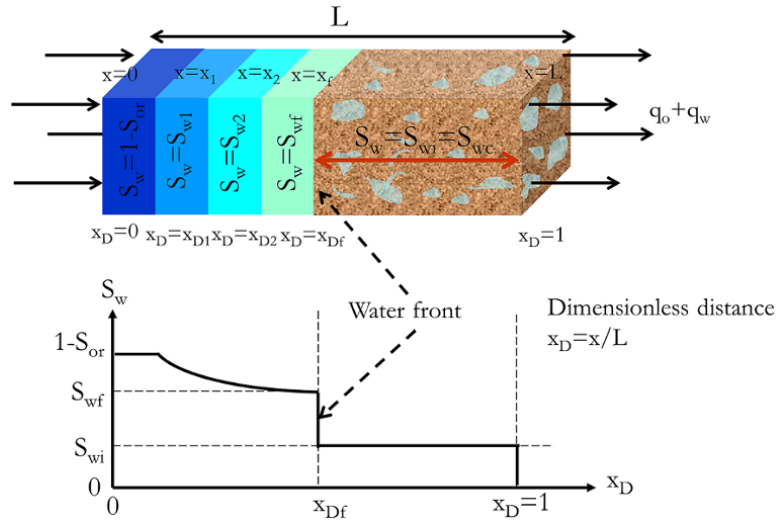


Figure 14.9 One-dimensional piston-like displacement showing water front.

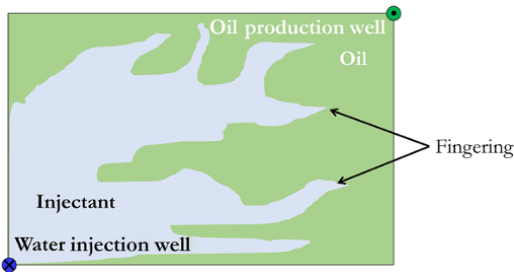


Figure 14.10 Viscous fingering.

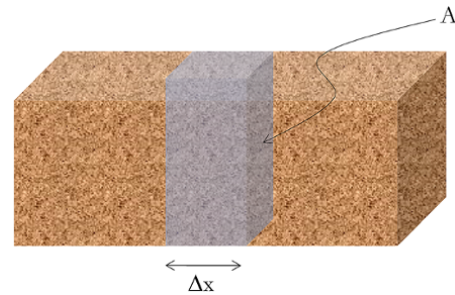


Figure 14.11 Flow through element volume of  $A\Delta x$ .

where  $q_w$  is the flow rate of water,  $\rho_w$  is the density of water,  $S_w$  is water saturation,  $\Delta t$  is the time interval,  $A$  is the cross-sectional area of the flow, and  $x$  is the linear displacement of the fluid.

Taking limits  $\Delta x \rightarrow 0$ ,  $\Delta t \rightarrow 0$ :

$$-\frac{\partial}{\partial x}(q_w \rho_w) = A\phi \frac{\partial}{\partial t}(S_w \rho_w)$$

$$A\phi \frac{\partial}{\partial t}(S_w \rho_w) - \frac{\partial}{\partial x}(q_w \rho_w) = 0 \quad (14.13)$$

Equation (14.13) is the *mass continuity equation*. With constant density, equation (14.13) reduces to:

$$A\phi \frac{\partial}{\partial t}(S_w) - \frac{\partial}{\partial x}(q_w) = 0 \quad (14.14)$$

The fractional flow of water is expressed as:

$$f_w = \frac{q_w}{q_o + q_w} = \frac{q_w}{q_t}$$

At a steady state, the rate of injection ( $q_{in}$ ) equals the total displacement of oil and water ( $q_t$ ):

$$q_t = q_{in}$$

Hence:

$$f_w = \frac{q_w}{q_o + q_w} = \frac{q_w}{q_{in}}$$

$$q_w = f_w q_{in}$$

Substituting  $q_w$  above into the mass continuity equation, equation (14.14):

$$A\phi \frac{\partial}{\partial t}(S_w) - \frac{\partial}{\partial x}(f_w q_{in}) = 0 \quad (14.15)$$

Since  $f_w = f_w(S_w)$ :

$$\frac{\partial f_w}{\partial x} = \frac{\partial f_w}{\partial S_w} \frac{\partial S_w}{\partial x}$$

Substituting  $\frac{\partial f_w}{\partial x}$  above into equation (14.15) gives the *Buckley–Leverett equation* [Buckley and Leverett, 1942]:

$$\frac{A\phi}{q_{in}} \frac{\partial S_w}{\partial t} - \frac{\partial f_w}{\partial S_w} \frac{\partial S_w}{\partial x} = 0 \quad (14.16)$$

*Frontal Advance Equation*

During immiscible water displacement of oil, water saturation is a function of location and time:

$$S_w = S_w(x, t)$$

Hence

$$dS_w = \frac{\partial S_w}{\partial x} dx + \frac{\partial S_w}{\partial t} dt$$

Since the water front is at constant saturation during immiscible water displacement of oil:

$$dS_w = 0 = \frac{\partial S_w}{\partial x} dx + \frac{\partial S_w}{\partial t} dt$$

Rearranging this equation:

$$\frac{\partial S_w}{\partial t} = - \frac{\partial S_w}{\partial x} \frac{dx}{dt}$$

Substituting  $\frac{\partial S_w}{\partial t}$  from above into equation (14.16) and rearranging:

$$- \frac{\partial f_w}{\partial S_w} \frac{\partial S_w}{\partial x} = - \frac{A\phi}{q_{in}} \frac{\partial S_w}{\partial x} \frac{dx}{dt}$$

Making  $\frac{dx}{dt}$  the subject of the formula gives the *velocity flood front*, or *velocity shock front*:

$$\frac{dx}{dt} = \frac{q_{in}}{A\phi} \left( \frac{\partial f_w}{\partial S_w} \right) \tag{14.17}$$

Therefore, the velocity of a given  $S_w$  is:

$$\left( \frac{dx}{dt} \right)_{S_w} = \frac{q_{in}}{A\phi} \left( \frac{\partial f_w}{\partial S_w} \right)_{S_w}$$

In engineering oil field (EOF) units this is:

$$\left( \frac{dx}{dt} \right)_{S_w} = \frac{5.615q_{in}}{A\phi} \left( \frac{\partial f_w}{\partial S_w} \right)_{S_w} \tag{14.18}$$

where  $\left( \frac{\partial f_w}{\partial S_w} \right)_{S_w}$  is the slope of the fractional flow curve ( $f_w$  against  $S_w$ ) at  $S_w$  and  $q_{in}$  is the rate of injection (bbl/d).

Integrating equation (14.17) to determine the distance  $x$  for a given  $S_w$  from the injector:

$$\int_0^x dx = \frac{q_{in}}{A\phi} \left( \frac{\partial f_w}{\partial S_w} \right)_f \int_0^t dt$$

This gives:

$$(x)_{S_w} = \frac{q_{in}t}{A\phi} \left( \frac{\partial f_w}{\partial S_w} \right)_{S_w} \tag{14.19}$$

In EOF units:

$$(x)_{S_w} = \frac{5.615q_{in}t}{A\phi} \left( \frac{\partial f_w}{\partial S_w} \right)_{S_w} \tag{14.20}$$

where  $(x)_{S_w}$  is the distance of any given saturation  $S_w$  from the injector in feet.

The advancement of the shock front can also be determined by integrating equation (14.17) between the limits of  $x_f$  (location of front) and 0 (injector):

$$\int_0^{x_f} dx = \frac{q_{in}}{A\phi} \left( \frac{\partial f_w}{\partial S_w} \right)_f \int_0^t dt$$

$$x_f = \frac{q_{in}t}{A\phi} \left( \frac{\partial f_w}{\partial S_w} \right)_f \tag{14.21}$$

Equation (14.21) is the *frontal advance equation* and can be expressed in engineering oil field (EOF) units as:

$$x_f = \frac{5.615q_{in}t}{A\phi} \left( \frac{\partial f_w}{\partial S_w} \right)_f \tag{14.22}$$

In EOF units,  $t$  is in days,  $q$  is in bbl/d,  $A$  is in  $ft^2$ , and  $x$  is in ft.

*Buckley–Leverett Solution*

From equation (14.19), the distance of any given saturation,  $S_w$ , from the injector at a given time,  $t$ , is proportional to the slope of the fractional flow curve ( $f_w$  against  $S_w$ ) at  $S_w$ .

From Fig. 14.12, the saturation distribution is shown in Fig. 14.13.

Fig. 14.13 suggests the existent of two different saturations ( $S_{w1}$  and  $S_{w2}$ ) at a given position,  $x$ , for a 1D displacement, which is physically impossible. This is

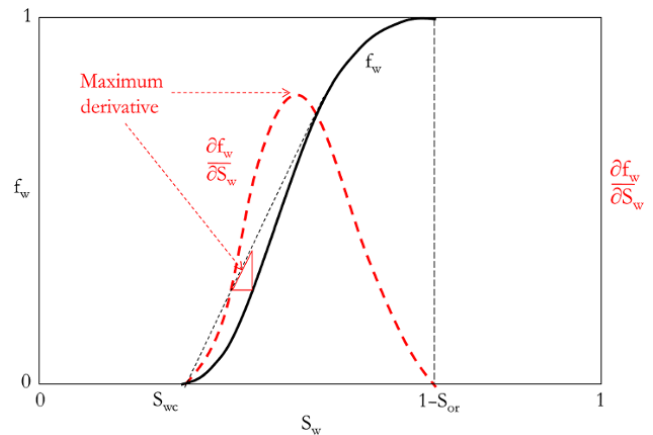


**Figure 14.12**  $f_w$  and  $\frac{\partial f_w}{\partial S_w}$  curve without capillary pressure gradient effect.

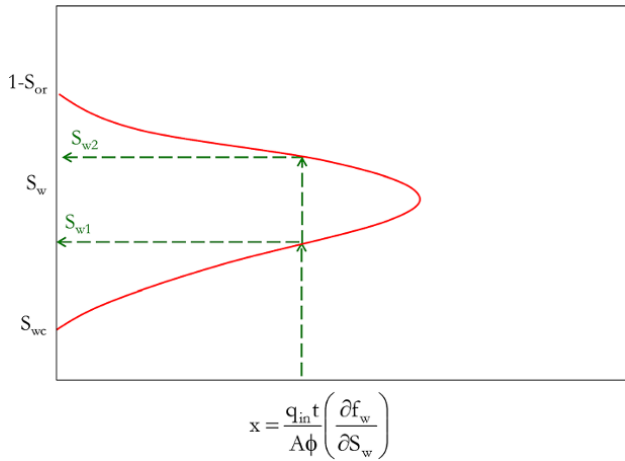


**Figure 14.13**  $S_w$  profile as a function of location without capillary pressure gradient effect.

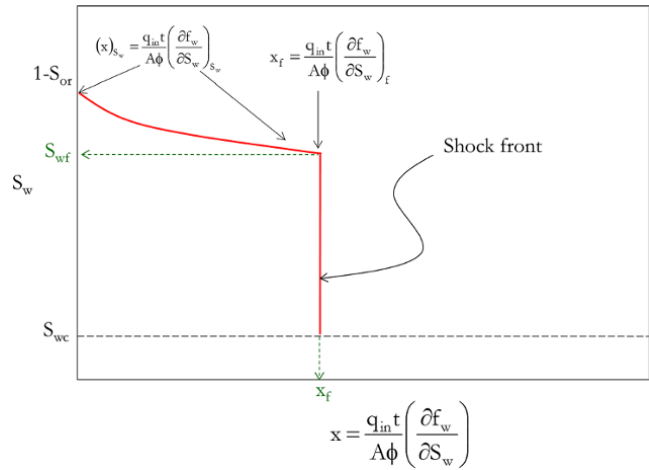


**Figure 14.15**  $S_w$  profile as a function of location with capillary pressure gradient effect.

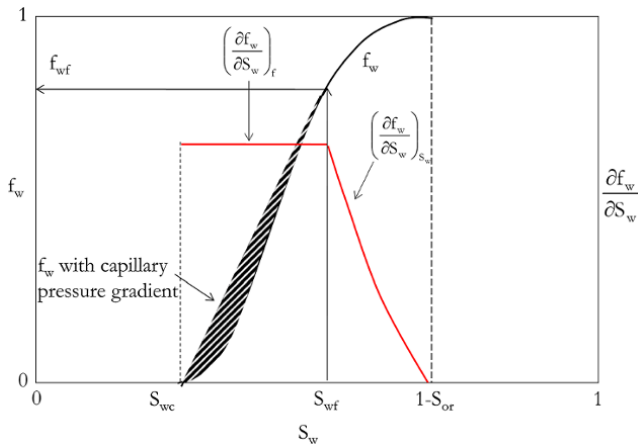


**Figure 14.14**  $f_w$  and  $\frac{\partial f_w}{\partial S_w}$  curve with capillary pressure gradient effect.

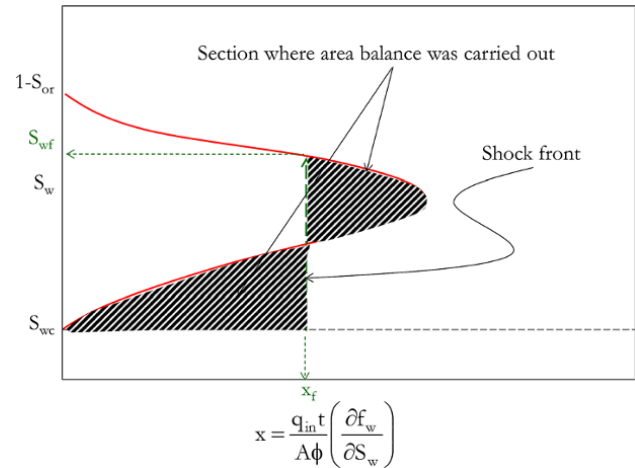


**Figure 14.16**  $S_w$  profile as a function of location showing area balancing.

due to neglecting the capillary pressure term in the fractional flow equation. The inclusion of the capillary pressure gradient modifies the  $f_w$  curve as shown in Fig. 14.14.

From Fig. 14.14, the  $f_w$  and  $\frac{\partial f_w}{\partial S_w}$  curve consists of two important sections:

- (i) between  $S_{wc}$  and  $S_{wf}$ , where the gradient is constant and defined as  $\left(\frac{\partial f_w}{\partial S_w}\right)_f$ ;
- (ii) between  $S_{wf}$  and  $1 - S_{or}$ , where the gradient is decreasing from  $S_{wf}$  to  $1 - S_{or}$  and defined as  $\left(\frac{\partial f_w}{\partial S_w}\right)_{S_w}$ .

Therefore, the location of the shock front can be correctly illustrated by Fig. 14.15.

The  $S_w$  profile in Fig. 14.15 can be created by transferring areas from the section ahead of the shock to sections below the curve for the case without capillary pressure gradient, as illustrated in Fig. 14.16.

The approach of area transfer (Fig. 14.16) is a convenient way of determining water saturation distribution in the reservoir and shock front movement during water flooding.

With  $\frac{\partial f_w}{\partial S_w}$  determined correctly, saturation distribution and movement of shock front with time can be calculated using equations (14.19) and (14.21), as illustrated in Fig. 14.17.

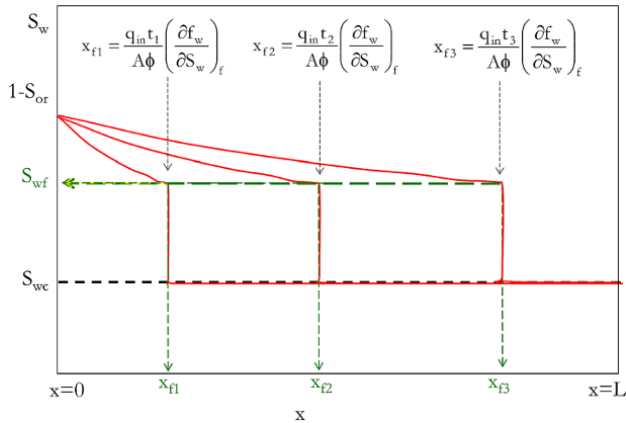


Figure 14.17 Movement of shock at different times.

As shown in Fig. 14.17, injection water breakthrough at a production well will occur when  $x_f = L$ .

Shocks are discontinuities in saturation, therefore differential equations are not applicable at the point of discontinuity.

*Breakthrough Time*

From the frontal advance equation in EOF units (equation (14.22)):

$$x_f = \frac{5.615q_{in}t}{A\phi} \left( \frac{\partial f_w}{\partial S_w} \right)_f$$

At water breakthrough,  $x_f = L$ , where  $L$  is the distance between the injector and the producer and  $t_b$  is the breakthrough time. Therefore:

$$t_b = \frac{A\phi L}{5.615q_{in}} \left( 1 / \left( \frac{\partial f_w}{\partial S_w} \right)_f \right) \text{ in EOF units} \quad (14.23)$$

Defining pore volume, PV, as:

$$PV = A\phi L \text{ in consistent units}$$

and

$$PV = \frac{A\phi L}{5.615} \text{ in EOF units} \quad (14.24)$$

where  $PV = \text{bbbl}$ ,  $q_{in} = \text{bbl/d}$ , and  $t_b = \text{days}$ .

Making  $A\phi L$  the subject of the formula in equation (14.24) and substituting into equation (14.22) to get *breakthrough time* ( $t_b$ ) in terms of PV:

$$t_b = \frac{PV}{q_{in}} \left( 1 / \left( \frac{\partial f_w}{\partial S_w} \right)_f \right) \quad (14.25)$$

**14.2.1.3. Water Distribution in the Reservoir using the Buckley–Leverette Equation. Average Water Saturation Behind Front**

The average water saturation behind the front can be defined as:

$$S_{wAvg} = \frac{\int_{x=0}^{x=x_f} S_w dx}{x_f}$$

Using integration by parts:

$$S_{wAvg} = \frac{xS_w \Big|_{x=0}^{x=x_f} - \int_{S_w=1}^{S_w=S_{wf}} x dS_w}{x_f} \quad (14.26)$$

From the frontal advance equation (equation (14.21)):

$$x = \frac{q_{in}t}{A\phi} \left( \frac{\partial f_w}{\partial S_w} \right)$$

and

$$x_f = \frac{q_{in}t}{A\phi} \left( \frac{\partial f_w}{\partial S_w} \right)_f$$

Substituting  $x$  and  $x_f$  into equation (14.26) [Welge, 1952]:

$$S_{wAvg} = S_{wf} - \frac{\int_{S_w=1}^{S_w=S_{wf}} \frac{q_{in}t}{A\phi} \left( \frac{df_w}{dS_w} \right) dS_w}{\frac{q_{in}t}{A\phi} \left( \frac{\partial f_w}{\partial S_w} \right)_f}$$

$$S_{wAvg} = S_{wf} - \frac{\int_{f_w=1}^{f_w=f_{wf}} df_w}{\left( \frac{\partial f_w}{\partial S_w} \right)_f}$$

$$S_{wAvg} = S_{wf} - \frac{(f_{wf} - 1)}{\left( \frac{\partial f_w}{\partial S_w} \right)_f}$$

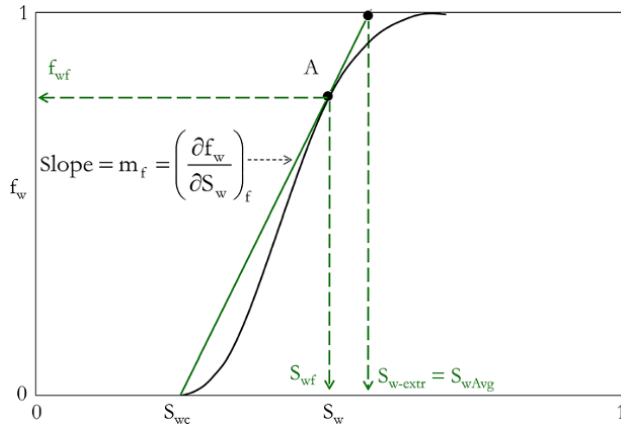


**Figure 14.18** Graphical calculation of  $S_{wAvg}$  behind the front.

$$S_{wAvg} = S_{wf} + \frac{(1 - f_{wf})}{\left(\frac{\partial f_w}{\partial S_w}\right)_f} \quad (14.27)$$

Graphically,  $S_{wAvg}$  can be determined by extending the gradient line  $\left(\frac{\partial f_w}{\partial S_w}\right)_f$  to  $f_w = 1$  and reading the corresponding value of  $S_w$  (Fig. 14.18) [Welge, 1952].  $f_{wf}$  is the fractional flow of water at the front and  $S_{wf}$  is the saturation of water at the front.

As shown in Fig. 14.18, the slope of the straight line extrapolated to  $f_w = 1$  is still  $\left(\frac{\partial f_w}{\partial S_w}\right)_f$  and can be expressed as:

$$\left(\frac{\partial f_w}{\partial S_w}\right)_f = \frac{(1 - f_{wf})}{(S_{w\_extra} - S_{wf})}$$

Making  $S_{w\_extra}$  the subject of the formula:

$$S_{w\_extra} = S_{wf} + \frac{(1 - f_{wf})}{\left(\frac{\partial f_w}{\partial S_w}\right)_f} \quad (14.28)$$

Comparing equation (14.28) and equation (14.27)

$$S_{w\_extra} = S_{wf} + \frac{(1 - f_{wf})}{\left(\frac{\partial f_w}{\partial S_w}\right)_f} = S_{wAvg} = S_{wf} + \frac{(1 - f_{wf})}{\left(\frac{\partial f_w}{\partial S_w}\right)_f}$$

$$S_{wAvg} = S_{extra}$$

*Average Water Saturation in the Reservoir After Breakthrough*

Average water saturation in the reservoir after breakthrough can be determine in a similar way as average water saturation behind the front. Average water saturation in the reservoir after breakthrough is expressed as:

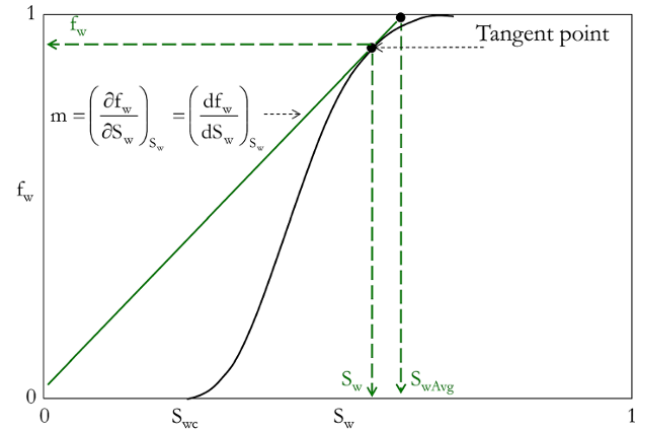


**Figure 14.19** Graphical calculation of  $S_{wAvg}$  after breakthrough.

$$S_{wAvg} = S_w + \frac{(1 - f_w)}{\left(\frac{df_w}{dS_w}\right)_{S_w}} \quad (14.29)$$

After breakthrough  $\frac{df_w}{dS_w}$  is taken directly on the  $f_w$  curve as shown in Figures 14.14 and 14.19.

In order to determine  $S_{wAvg}$  graphically after breakthrough,  $S_{wAvg}$  is read at  $f_w = 1$  on the tangential line through  $S_w$  of interest as shown in Fig. 14.19.

**14.2.1.4. Reservoir Performance Prediction using the Buckley–Leverett Equation.** Original oil in place (OOIP) at reservoir conditions can be defined as:

$$OOIP = AL\phi(1 - S_{wc}) \text{ in consistent units} \quad (14.30)$$

and

$$OOIP = \frac{AL\phi}{5.615}(1 - S_{wc}) \text{ in EOF units} \quad (14.31)$$

where OOIP is in bbl; A is in  $\text{ft}^2$ , and L is in ft.

Or, in terms of pore volume (PV):

$$OOIP = PV(1 - S_{wc}) \quad (14.32)$$

*Oil Swept*

From equation (14.30), the oil swept during water flooding at reservoir conditions ( $V_{oil\_Swept}$ ) can be determined from the difference between the original oil in place and the oil left at a given time and expressed as:

$$V_{oil\_Swept} = AL\phi(1 - S_{wc}) - AL\phi(1 - S_{wAvg})$$

$$V_{oil\_Swept} = AL\phi(S_{wAvg} - S_{wc})$$

or

$$V_{oil\_Swept} = PV(S_{wAvg} - S_{wc}) \text{ in terms of pore volume.}$$



$$V_{oil\_swept} = \frac{AL\phi}{5.615} (S_{wAvg} - S_{wc}) \text{ in EOF} \quad (14.33)$$

*Displacement/Sweep Efficiency*

Displacement/sweep efficiency can be defined as:

$$E_D = \frac{\text{Oil Swept}}{\text{OOIP}}$$

$$E_D = \frac{PV(S_{wAvg} - S_{wc})}{PV(1 - S_{wc})}$$

$$E_D = \frac{S_{wAvg} - S_{wc}}{1 - S_{wc}} \quad (14.34)$$

*Cumulative Oil Produced*

For a full areal and vertical sweep of the reservoir, oil swept ( $V_{oil\_swept}$ ) is equal to oil produced ( $V_{oil\_produced}$ ):

$$V_{oil\_produced} = V_{oil\_swept} = PV(S_{wAvg} - S_{wc})$$

Substituting  $S_{wAvg} - S_{wc} = E_D(1 - S_{wc})$  from equation (14.34) into the above:

$$V_{oil\_produced} = E_D \times PV(1 - S_{wc}) \quad (14.35)$$

The objective of water flooding is to sweep as a wide volume of the reservoir as possible. Factors that affect the fraction of the reservoir swept by injected water include the number of injection wells, the well injection patterns, and the reservoir geometry. Area and vertical sweep efficiency ( $E_A$  and  $E_V$ ) are always less than 100%, as all areal and vertical sections of the reservoir cannot be completely swept by flooding water (Fig. 14.20). When area and vertical sweep efficiencies are included in the oil produced, equation (14.35) becomes:

$$V_{oil\_produced} = E_D \times E_A \times E_V \times PV(1 - S_{wc}) \quad (14.36)$$

or

$$V_{oil\_produced} = E_D \times E_A \times E_V \times V_{oil\_swept} \quad (14.37)$$

**14.2.1.5. Water Production and Injection Management using the Buckley–Leverett Equation.** For surface facility design, prediction of surface water production is important and can be determined using fractional flow and BL equation.

*Water Cut at Surface*

The water cut at surface conditions can be defined as:

$$WC_{Surface} = f_{w\_surface} = \frac{q_{ws}}{q_{ws} + q_{os}}$$

where  $q_{ws}$  and  $q_{os}$  represent, respectively, the water and oil production rates at surface condition.

$$WC_{Surface} = \frac{q_w / B_w}{q_w / B_w + q_o / B_o}$$

where  $B_w$  and  $B_o$  represent, respectively, the water and oil formation volume factors, and  $q_w$  and  $q_o$  represent water and oil production rates, respectively, at reservoir conditions.

$$WC_{Surface} = \frac{1}{1 + \frac{q_o B_w}{q_w B_o}}$$

$$WC_{Surface} = \frac{1}{1 + \frac{(q_{inj} - q_w) B_w}{q_w B_o}}$$

where  $q_{inj}$  is rate of injection.

$$WC_{Surface} = \frac{1}{1 + \frac{1 - f_w B_w}{f_w B_o}} \quad (14.38)$$

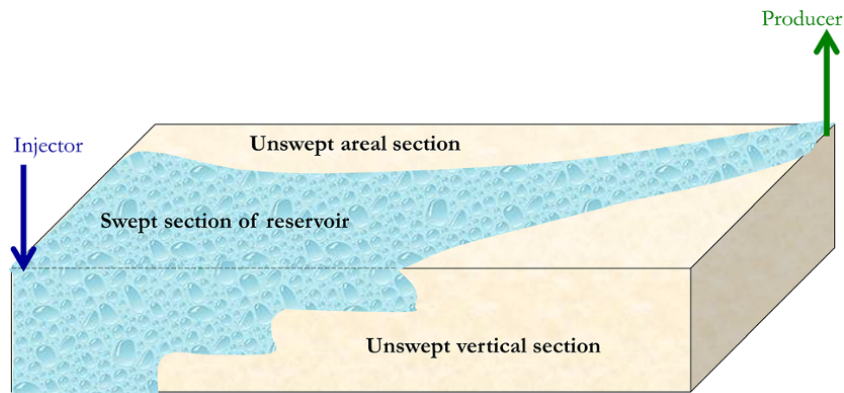


**Figure 14.20** Illustration of swept and unswept reservoir during water flooding.

*Surface Water–Oil Ratio*

In a similar way to the surface water cut, the surface water–oil ratio ( $WOR_{\text{Surface}}$ ) can be calculated:

$$\begin{aligned} WOR_{\text{Surface}} &= \frac{f_w / B_w}{(1-f_w) / B_o} \\ WOR_{\text{Surface}} &= \frac{B_o f_w}{B_w (1-f_w)} \\ WOR_{\text{Surface}} &= \frac{B_o}{B_w (1-f_w) / f_w} \\ WOR_{\text{Surface}} &= \frac{B_o}{(1/f_w - 1) B_w} \end{aligned} \quad (14.39)$$

*Amount of Water Injected (or required for injection)*

From equation (14.22):

$$x_f = \frac{5.615 q_{\text{in}} t}{A \phi} \left( \frac{\partial f_w}{\partial S_w} \right)_f \text{ in EOF units.}$$

Making  $t$  the subject of the formula

$$t = \frac{A \phi x_f}{5.615 q_{\text{in}}} \left( 1 / \left( \frac{\partial f_w}{\partial S_w} \right)_f \right)$$

Multiplying the above equation by  $q_{\text{in}}$  to get the cumulative water injected at reservoir conditions ( $V_{w_{\text{in}}}$ ):

$$V_{w_{\text{in}}} = q_{\text{in}} t = \frac{A \phi x_f}{5.615} \left( 1 / \left( \frac{\partial f_w}{\partial S_w} \right)_f \right) \quad (14.40)$$

At breakthrough time  $t = t_b$  and  $x = L$ .

Substituting  $t = t_b$  and  $x_f = L$  into equation (14.40):

$$V_{w_{\text{in}}} = q_{\text{in}} t_b = \frac{A \phi L}{5.615} \left( 1 / \left( \frac{\partial f_w}{\partial S_w} \right)_f \right) \text{ in EOF units} \quad (14.41)$$

In terms of pore volume (PV):

$$PV = \frac{A \phi L}{5.615} \text{ in EOF units from equation (14.24), hence:}$$

$$V_{w_{\text{in}}} = PV \left( 1 / \left( \frac{\partial f_w}{\partial S_w} \right)_f \right)$$

$$V_{w_{\text{in}}} = 1 / \left( \frac{\partial f_w}{\partial S_w} \right)_f \text{ in terms of pore volume} \quad (14.42)$$

After breakthrough:

$$V_{w_{\text{in}}} = \frac{A \phi L}{5.615} \left( 1 / \left( \frac{\partial f_w}{\partial S_w} \right)_f \right) \text{ in EOF units} \quad (14.43)$$

*Amount of Water Produced*

Cumulative water produced at reservoir conditions ( $V_{w_{\text{prod}}}$ ) = cumulative water injected – cumulative oil produced

$$V_{w_{\text{prod}}} = V_{w_{\text{in}}} - PV(S_{w_{\text{Avg}}} - S_{w_c}) E_A \times E_V \quad (14.44)$$

Hence, the amount of water produced at surface conditions is:

$$V_{w_{\text{prod-sur}}} = \frac{V_{w_{\text{prod}}}}{B_w} \quad (14.45)$$

**Exercise 14.2** Reservoir Management Using Fractional Flow and Advanced Frontal Equation

A reservoir with the following relative permeability  $k_{rw} = 0.4(S_w - 0.2)^2$  and  $k_{ro} = 0.9(S_o - 0.25)^2$  has the reservoir, fluid, and injection data shown in Table 14.3.

The critical water saturation is equal to the connate water saturation given in Table 14.3.

1. Plot the fractional flow curve annotating important features of the plot.

2. Plot the water saturation profile in the reservoir after 80, 160, and 204 days indicating clearly shock front saturation.

3. Calculate average water saturation behind the front at times given in Q2.

4. Calculate average water saturation behind the front at breakthrough.

5. Calculate the time for water breakthrough.

6. Calculate the amount of water injected at breakthrough time.

7. Plot the water saturation profile at 100, 200, and 300 days after water breakthrough.

8. Plot average water saturation after breakthrough against time.

9. Plot the volume of oil swept against time.

10. Plot the water cut at reservoir conditions against time after water breakthrough.

11. Plot the water cut at surface conditions against time after water breakthrough.

12. Calculate sweep efficiency against time after water breakthrough.

13. Plot oil recovered against time ( $E_A = 80$ ;  $E_V = 60\%$ ) after water breakthrough

14. Plot the surface water–oil ratio against time after water breakthrough.

**Table 14.3** Reservoir, Fluid and Injection Rate Data for Exercise 14.2.

Parameter	Value
$B_o$ (bbl/stb)	2.3
$B_w$ (bbl/stb)	1.01
$\mu_o$ (cp)	4.01
$\mu_w$ (cp)	1.02
$A$ (ft <sup>2</sup> )	6,724
$L$ (ft)	723
$\phi$	0.2
$q_{\text{inj}}$ (bbl/day)	350
$S_{w_c}$	0.20

15. Plot water injected against time after water breakthrough.

16. Plot water produced at reservoir conditions against time after water breakthrough.

17. Plot water produced at surface conditions against time after water breakthrough.

18. Determine when the reservoir will have been swept of recoverable oil.

**Solution.**

1. From equation (14.10),  $f_w = \frac{1}{1 + \frac{\mu_w k_{ro}}{\mu_o k_{rw}}}$

Substituting fluid viscosities and relative permeability models:

$$f_w = \frac{1}{1 + \frac{1.02 \times 0.9((1 - S_w) - 0.25)}{4.01 \times 0.4(S_w - 0.2)}}$$

$$f_w = \frac{1}{1 + \frac{0.5723192 \times ((1 - S_w) - 0.25)}{(S_w - 0.2)}} \tag{14.46}$$

Create a table of  $f_w$  against  $S_w$  using equation (14.46) as shown in Table 14.4.

Fig. 14.21 is the fractional flow plot showing critical water saturation, which equals initial connate water saturation ( $S_{wc}$ ), average water saturation behind the front ( $S_{wAvg}$ ), fractional flow of water at the front ( $f_{wf}$ ), and saturation of water at the front ( $S_{wf}$ ).

2. As shown in Fig. 14.14, up to  $S_w = S_{wf}$ , the derivative is taken as  $(\frac{\partial f_w}{\partial S_w})_f$ , after which the derivative is  $(\frac{\partial f_w}{\partial S_w})_{S_w}$  up to  $S_w = 1 - S_{or}$ . Derivative  $(\frac{\partial f_w}{\partial S_w})_{S_w}$  will be taken from  $S_{wf}$  ( $S_w = 0.53$ ) to  $1 - S_{or}$  (0.75).

With  $\frac{\partial f_w}{\partial S_w}$  determined at each  $S_w$  between  $S_{wf}$  and  $1 - S_{or}$ ,  $x(t)$  is then determined using equation (14.20):

**Table 14.4** Calculation of Saturation Behind Shock Front.

	$S_w$	$f_w$	$(\frac{\partial f_w}{\partial S_w})_{S_w}$	$x$ ( $t = 80$ )	$x$ ( $t = 160$ )	$x$ ( $t = 240$ )
$S_{wf} \rightarrow$	0.53	0.80	2.42	283.42	566.83	723.07
	0.56	0.86	2.20	257.04	514.07	655.76
	0.59	0.90	1.72	200.66	401.33	511.95
	0.61	0.94	1.28	150.20	300.41	383.21
	0.64	0.97	0.92	107.36	214.73	273.91
	0.67	0.98	0.62	72.37	144.74	184.64
	0.70	0.99	0.38	44.62	89.23	113.83
	0.72	1.00	0.20	23.10	46.20	58.93
$1 - S_{or} \rightarrow$	0.75	1.00	0.06	0.00	0.00	0.00

$$(x)_{S_w} = \frac{5.615 q_{in} t}{A \phi} \left( \frac{\partial f_w}{\partial S_w} \right)_{S_w}$$

By substituting a given  $t$  (80, 160, and 204 days) and  $(\frac{\partial f_w}{\partial S_w})_{S_w}$  into equation (14.20) for  $S_w$  between  $S_{wf}$  and  $1 - S_{or}$  as shown in Table 14.4, the water saturation profile behind the shock front is created (Fig. 14.22).

At  $S_w = 1 - S_{or}$ ,  $x(t) = 0$  as  $\frac{\partial f_w}{\partial S_w} \rightarrow 0$ . This is shown by the  $f_w$  curves flattening out.

The  $S_w$  profile for the entire reservoir (which includes the positions behind the front and ahead of the front) is then created by adding a discontinuous front at a location corresponding to  $S_{wf}$  and saturation ahead of the front having a constant  $S_w$  value that is equal to  $S_{wc}$  as shown in Fig. 14.23.

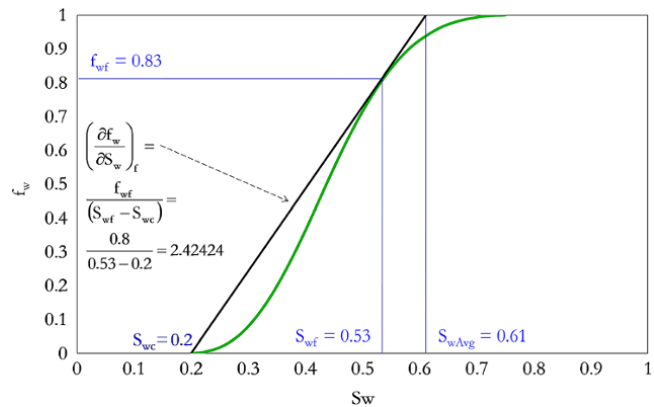


**Figure 14.21** Fractional flow curve showing  $S_{wcr}$ ,  $S_{wAvg}$ ,  $f_{wf}$ , and  $S_{wf}$ .

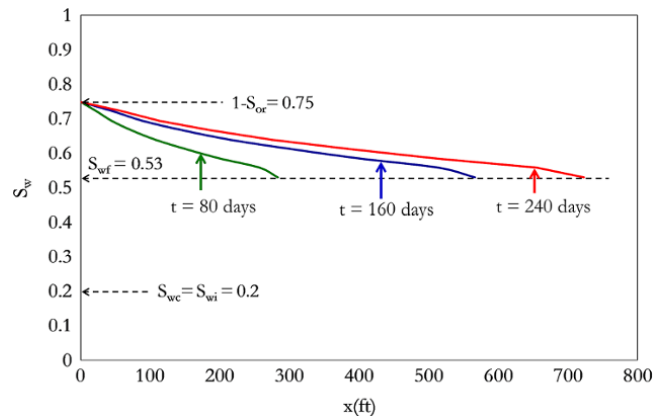


**Figure 14.22** Saturation profile behind the shock front.

3. Graphically,  $S_{wAvg}$  behind the front can be determined by extending  $\left(\frac{\partial f_w}{\partial S_w}\right)_f$  to  $f_w=1$  on the fractional flow curve and reading the corresponding value of  $S_w$  to get

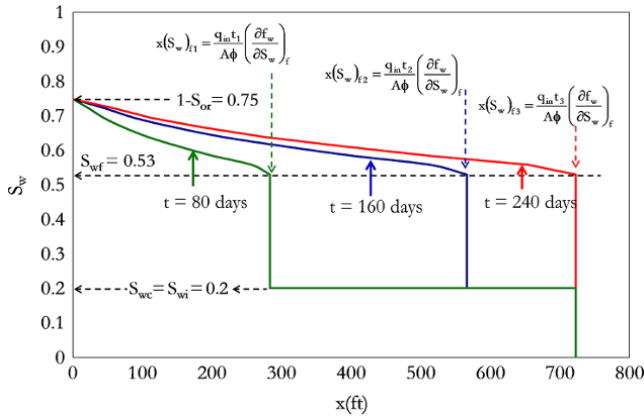


Figure 14.23 Saturation profile for the entire reservoir.

$S_{wAvg}$ . As shown in Fig. 14.21, the value of  $S_{wAvg}$  is 0.61.

$S_{wAvg} = 0.61$  up to breakthrough time.

The average saturation behind the front can also be determined by integration, as shown by Fig. 14.24.

$$S_{wAvg} = \frac{\int_{x=0}^{x=x_f} S_w dx}{x_f} = \frac{\text{Area 1} + \text{Area 2}}{x_f}$$

Area 2 are shown in Fig. 14.24a for  $t = 80$ , in Fig. 14.24b for 160, and in Fig. 14.24c for 204 days.

4. Integration in Q3 for  $t = 80, 160,$  and  $204$  days, shows that average saturation behind the front up to breakthrough time is the same with a value of 0.61.

Hence,  $S_{wAvg} = 0.61$

5. From equation (14.23):

$$t_b = \frac{A\phi L}{5.615q_{in}} \left( 1 / \left( \frac{\partial f_w}{\partial S_w} \right)_f \right)$$

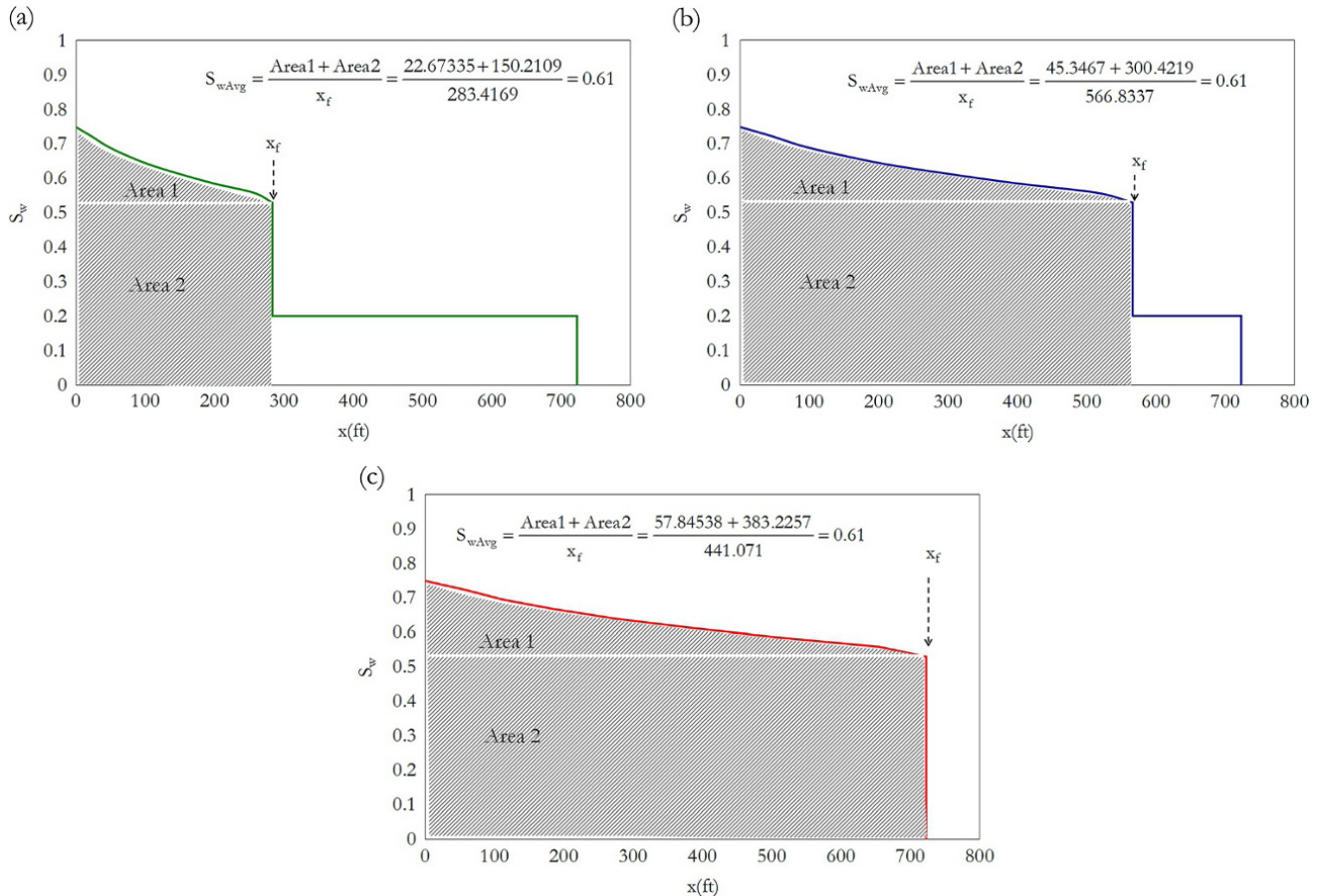


Figure 14.24 Determination of  $S_{wAvg}$  using integration for (a)  $t = 80$ , (b)  $t = 160$ , and (c)  $t = 204$  days.

Substituting the parameters given:

$$t_b = \frac{6724 \times 0.2 \times 723}{5.615 \times 350} \left( \frac{1}{2.424242} \right) = 204.1 \text{ Days}$$

6. The amount of water injected at time of breakthrough:

$$V_{w\_in} = q_{in} t_b = 350 \times 204.1 = 71435 \text{ bbl}$$

Therefore, the amount of water injected at surface conditions is:

$$V_{w\_in\_surface} = \frac{V_{w\_in}}{B_w} = \frac{71435}{1.01} = 70728 \text{ stb}$$

7. Following the steps in Q2 and extending the profile as far as the distance between injector and producer (723 ft), the plot is shown in Fig. 14.25.

8. –18.

The solutions to questions 8–18 are summarized in Tables 14.5 and 14.6.

Q8, using equation (14.29):  $S_{wAvg} = S_w + \frac{(1 - f_w)}{\left( \frac{df_w}{dS_w} \right)}$

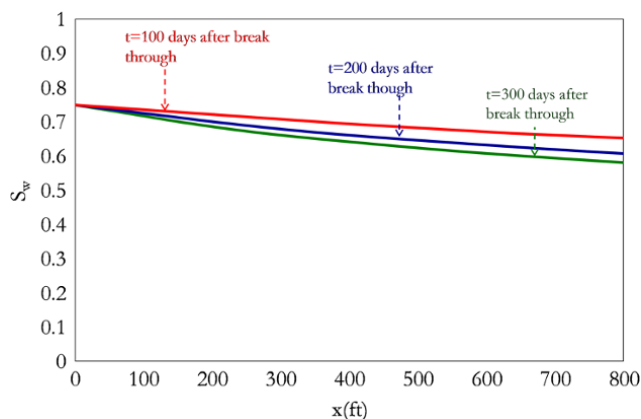


Figure 14.25 Saturation profile after breakthrough.

Table 14.5 Solutions to Q8–13 of Exercise 14.2.

		Q8	Q9	Q10	Q11	Q12	Q13	
$S_w$	$f_w$	$\frac{\partial f_w}{\partial S_w}$	$S_{wAvg}$ after breakthrough	$V_{Oil\_Swept}$ (rb)	$WC_{Res}=f_w$	$WC_{Surface}$	ED (fraction)	$V_{Oil\_produced}$ (rb)
0.53	0.80	2.42	0.61	71,627.10	0.80	0.90	0.52	17,777.05
0.56	0.86	2.20	0.62	73,113.67	0.86	0.93	0.53	18,522.61
0.59	0.90	1.72	0.64	76,262.64	0.90	0.96	0.55	20,152.49
0.61	0.94	1.28	0.66	79,486.41	0.94	0.97	0.57	21,892.27
0.64	0.97	0.92	0.68	82,701.92	0.97	0.98	0.60	23,699.34
0.67	0.98	0.62	0.70	85,850.25	0.98	0.99	0.62	25,538.08
0.70	0.99	0.38	0.71	88,897.37	0.99	1.00	0.64	27,383.12
0.72	1.00	0.20	0.73	91,863.10	1.00	1.00	0.66	29,240.66
0.75	1.00	0.06	0.75	95,237.71	1.00	1.00	0.69	31,428.44

Q9, using equation (14.33).

Q10, using  $WC_{Res} = f_w$ .

Q11 using equation (14.38).

Q12, using equation (14.34).

Q13, using equation (14.36).

Q14, using equation (14.39).

Q15, using equation (14.43).

Q16, using equation (14.44).

Q17, using equation (14.45).

Q18 using  $t = \frac{V_{inj}}{q_{inj}}$ . The time required to sweep the entire

reservoir when  $S_w = 1 - S_{or}$  ( $f_w = 1$ ) and from Table 14.6 is **8595 days (23.5 years)**.

A reservoir simulator, can be used to validate the BL solution to Exercise 14.2. Fig. 14.26, shows a 1D simulation of water displacement of oil using a reservoir simulator, for Exercise 14.2.

**14.2.1.6. Determining the Relative Permeability from Flood Experiment or Field Data.** It is important to carry out a water flood experiment on core samples in order to understand how the reservoir will respond to water flooding at the field scale. Water flood experiments generate fractional flow relationships similar to that in Fig. 14.7. Relative permeability, which is an intrinsic part of the fractional flow data, can also be calculated from flood experiments using techniques similar to Buckley–Leverett analysis. Deriving a relative permeability model from fractional flow data, like most reservoir engineer problems, is an inverse problem and there may exist more than one possible relative permeability model that may match the flooding experiment, often due to the limitation of experimental methods and quality of data as discussed in Chapter 2 (2.6). Therefore, it is important to refine calculated relative permeability data using the approach discussed in Exercises 2.13 and 2.14, validate the final relative permeability with other information, such as analogues, and also ensure that the relative permeability

**Table 14.6** Solutions to Q14–18 of Exercise 14.2.

$S_w$	$f_w$	$\frac{\partial f_w}{\partial S_w}$	Q14	Q15	Q16	Q17	Q18 (see last row)	
			$WOR_{Surface}$	$V_{w\_in}$ (rb)	$V_{w\_prod}$ (rb)	$V_{w\_prod\_surface}$ (stb)	$t$ (day)	
0.53	0.80	2.42	8.95	71,428.35	53,651.30	53,120.10	204.08	← Breakthrough time
0.56	0.86	2.20	13.72	78,759.20	60,236.59	59,640.19	225.03	
0.59	0.90	1.72	21.66	1,00,884.82	80,732.33	79,933.00	288.24	
0.61	0.94	1.28	35.81	1,34,776.22	1,12,883.95	1,11,766.29	385.07	
0.64	0.97	0.92	63.66	1,88,557.16	1,64,857.83	1,63,225.57	538.73	
0.67	0.98	0.62	127.77	2,79,721.63	2,54,183.55	2,51,666.88	799.20	
0.70	0.99	0.38	322.29	4,53,733.55	4,26,350.43	4,22,129.14	1,296.38	
0.72	1.00	0.20	1,436.40	8,76,436.72	8,47,196.06	8,38,807.98	2,504.10	
0.75	1.00	0.06	—	30,08,401.45	29,76,973.00	29,47,498.02	8,595.43	← Time to sweep entire reservoir (Q18)

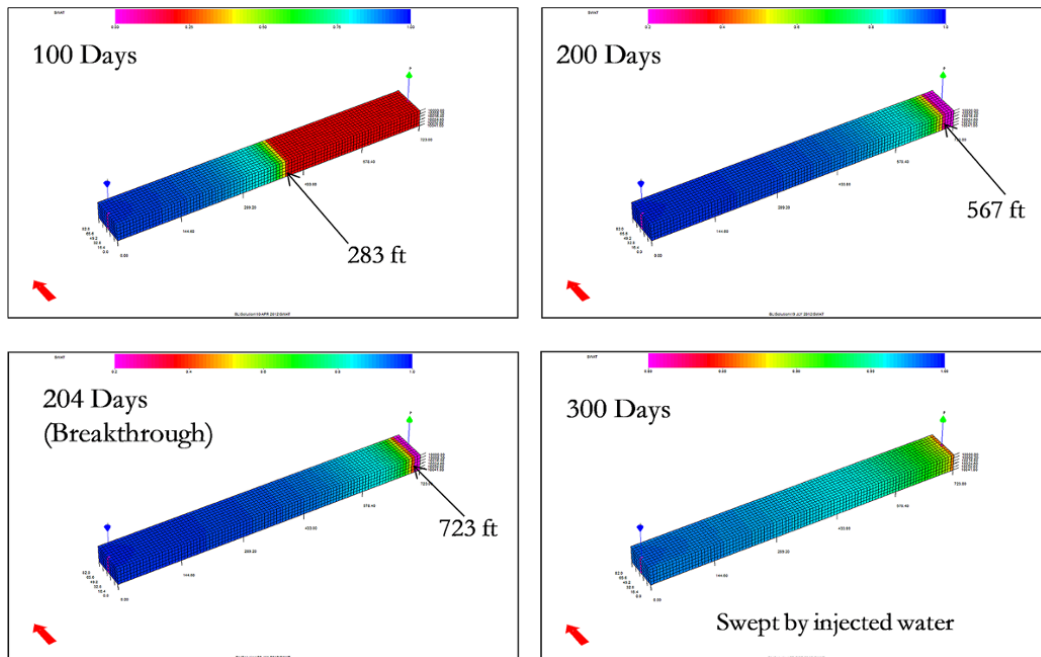


**Figure 14.26** 1D Simulation of water displacement of oil using a reservoir simulator.

model is consistent with other rock properties, such as wettability if available.

The Johnson Bossler and Nauman (JBN) method [Johnson *et al.*, 1959] is based on the Welge approach [Welge, 1952] of solving fractional flow equation discussed in Section 14.2.1.3. The JBN method is a widely used approach for calculating relative permeability from flood experiments.

Given the following parameters:

$V_{in}$  is the amount of injected displacing water/brine in pore volume.

$V_o$  is the volume of produced oil in pore volume.

$V_w$  is the volume of produced water in pore volume.

$\Delta p$  is measured pressure differential across core sample during fluid displacement in atm.

the formulae and calculations required to calculate relative permeability from a flood experiment using the JBN method are summarized below with units of parameters in Darcy’s units, and defined as follows: permeability in Darcy, pressure in atm, viscosity in cp, length in cm, volume in  $cm^3$ , and flow rate in  $cm^3/s$ .

1: calculating  $\frac{k_{rw}}{k_{ro}}$  from fractional flow of oil at core outlet.

Define the fractional flow of oil at the core outlet as:

$$f_o = \frac{dV_o}{dV_t} = \frac{dV_o}{dV_{in}} \quad (14.47)$$

where the amount of fluid injected ( $V_{in}$ ) equals the total amount of fluid produced ( $V_t$ ) under steady state conditions.

Also:

$$S_{wAvg} = S_{wi} + V_o \quad (14.48)$$

where  $S_{wAvg}$  is average water saturation and  $S_{wi}$  is initial water saturation.

Making  $V_o$  in equation (14.48) the subject of the formula and substituting into equation (14.47):

$$f_o = \frac{dV_o}{dV_{in}} = \frac{d(S_{wAvg} - S_{wi})}{dV_{in}} = \frac{dS_{wAvg}}{dV_{in}} \quad (14.49)$$

$\frac{dS_{wAvg}}{dV_{in}}$  can be determined from the semi-log plot slope defined as  $\frac{dS_{wAvg}}{d(\log V_{in})}$  based on the relationship between  $\frac{dS_{wAvg}}{dV_{in}}$  and  $\frac{dS_{wAvg}}{d(\log V_{in})}$ .

Starting from  $\frac{dS_{wAvg}}{d(\log V_{in})}$ :

$$\frac{dS_{wAvg}}{d(\log V_{in})} = \frac{dS_{wAvg}}{dV_{in}} \times \frac{dV_{in}}{d(\log V_{in})}$$

$$\frac{dS_{wAvg}}{d(\log V_{in})} = \frac{dS_{wAvg}}{dV_{in}} \times \frac{\ln 10}{\frac{d(\ln V_{in})}{dV_{in}}}$$

$$\frac{dS_{wAvg}}{d(\log V_{in})} = \frac{dS_{wAvg}}{dV_{in}} \times \frac{\ln 10}{\frac{1}{V_{in}}}$$

$$\frac{dS_{wAvg}}{d(\log V_{in})} = \frac{dS_{wAvg}}{dV_{in}} \times V_{in} \ln 10$$

Making  $\frac{dS_{wAvg}}{dV_{in}}$  the subject of the formula

$$\frac{dS_{wAvg}}{dV_{in}} = \frac{\frac{dS_{wAvg}}{d(\log V_{in})}}{2.303 V_{in}} \quad (14.50)$$

$\frac{dS_{wAvg}}{d(\log V_{in})}$  in equation (14.50) is the slope of the semi-log plot of  $S_{wAvg}$  against  $V_{in}$  and can be defined as the change in  $S_{wAvg}$  over one cycle change in  $V_{in}$  and represented as

$\Delta S_{wAvg}$ . Calculation of the slope on semi-log plot is also discussed in Chapter 7 (7.3.2.1) in Exercise 7.5.

With the semi-log slope of  $S_{wAvg}$  against  $V_{in}$  defined as  $\Delta S_{wAvg}$ , equation (14.50) becomes:

$$\frac{dS_{wAvg}}{dV_{in}} = \frac{\Delta S_{wAvg}}{2.303 V_{in}} \quad (14.51)$$

Substituting  $\frac{dS_{wAvg}}{dV_{in}} = \frac{\Delta S_{wAvg}}{2.303 V_{in}}$  from equation (14.51) into equation (14.49), gives the fractional flow of oil at core outlet as:

$$f_o = \frac{\Delta S_{wAvg}}{2.303 V_{in}} \quad (14.52)$$

The fractional flow of oil, based on the fractional flow equation, discussed in Section 14.2.1.1 can be expressed as:

$$f_o = \frac{1}{1 + \left( \frac{k_{rw} \mu_o}{k_{ro} \mu_w} \right)} \quad (14.53)$$

where  $k_{ro}$  and  $k_{rw}$  are the relative permeabilities of oil and water, respectively, and  $\mu_o$  and  $\mu_w$  are the viscosity of oil and water, respectively.

Rearranging equation (14.53),  $\frac{k_{rw}}{k_{ro}}$  can then be determined using known  $\frac{\mu_o}{\mu_w}$  and  $f_o$  from equation (14.52):

$$\frac{k_{rw}}{k_{ro}} = \frac{(1 - f_o)}{\left( f_o \times \frac{\mu_o}{\mu_w} \right)} \quad (14.54)$$

2: Calculating  $k_{ro}$  from relative injectivity.

Determining  $k_{ro}$  requires the relative injectivity ratio ( $I_{rr}$ ), which is defined as:

$$I_{rr} = \frac{\Delta p_i V}{\Delta p V_{in}} = \frac{\Delta p_i u}{\Delta p u_{in}} \quad (14.55)$$

where  $\Delta p_i$  is the initial pressure differential in atm across the sample at the start of injection,  $\Delta p$  is the pressure difference across the sample in atm,  $u$  is the average velocity of the the displacing phase approaching the inlet face of the sample cm/s, and  $u_{in}$  is the average velocity in cm/s of the displacing phase approaching the inlet face of sample at the start of displacement.

Using the relative injectivity ratio defined by equation (14.55):

$$I_{rr} = \frac{\Delta p_i u}{\Delta p u_{in}} = \frac{\frac{u}{\Delta p}}{\frac{u_{in}}{\Delta p_i}} = \frac{\left( \frac{q}{A} \right) / \Delta p}{\left( \frac{k_{eo} \Delta p_i}{\mu_o L} \right) / \Delta p_i} = \frac{\mu_o L / A q}{k_{eo} \Delta p}$$

$$\frac{1}{I_{rr}} = \frac{k_{eo}\Delta p}{\mu_o^L/Aq} \text{ for an oil-water system} \quad (14.56)$$

In a similar approach:

$$\frac{1}{I_{rr}} = \frac{k_{eg}\Delta p}{\mu_g^L/Aq} \text{ for a gas-oil system} \quad (14.57)$$

where  $k_{eo}$  and  $k_{eg}$  are the effective permeabilities of oil and gas, respectively,  $q$  is the rate of injection in  $\text{cm}^3/\text{s}$ ,  $L$  is the length of the sample in  $\text{cm}$ , and  $A$  is the cross-sectional area of flow in  $\text{cm}^2$ .

The relationship between  $k_{ro}$  and  $I_{rr}$  can be expressed as [Johnson *et al.*, 1959]:

$$\frac{f_o}{k_{ro}} = \left( \frac{d\left(\frac{1}{V_{in}I_{rr}}\right)}{d\left(\frac{1}{V_{in}}\right)} \right)$$

Making  $k_{ro}$  the subject of the formula:

$$k_{ro} = f_o \frac{1}{\left( \frac{d\left(\frac{1}{V_{in}I_{rr}}\right)}{d\left(\frac{1}{V_{in}}\right)} \right)} \quad (14.58)$$

$$\frac{d\left(\frac{1}{V_{in}I_{rr}}\right)}{d\left(\frac{1}{V_{in}}\right)}$$

required for  $k_{ro}$  calculation in equation (14.58) can be determined from a plot of  $\left(\frac{1}{V_{in}I_{rr}}\right)$  against  $\left(\frac{1}{V_{in}}\right)$  on a log-log scale.

Derive the relationship between  $\frac{d\left(\frac{1}{V_{in}I_{rr}}\right)}{d\left(\frac{1}{V_{in}}\right)}$  and the log-

$$\text{log slope defined as } \frac{d \log\left(\frac{1}{V_{in}I_{rr}}\right)}{d \log\left(\frac{1}{V_{in}}\right)}$$

$$\text{Starting from } \frac{d \log\left(\frac{1}{V_{in}I_{rr}}\right)}{d \log\left(\frac{1}{V_{in}}\right)}$$

$$\frac{d \log\left(\frac{1}{V_{in}I_{rr}}\right)}{d \log\left(\frac{1}{V_{in}}\right)} = \frac{d \log(ab)}{d \log(a)}, \text{ where } a = \frac{1}{V_{in}} \text{ and } b = \frac{1}{I_{rr}}$$

$$\frac{d \log(ab)}{d \log(a)} = \frac{d \log(ab)}{d \log(ab)} \times \frac{d(a)}{d \log(a)} \times \frac{d(ab)}{d(a)}$$

$$\frac{d \log(ab)}{d \log(a)} = \frac{d \ln(ab)}{d \ln(ab)} \times \frac{d(a)}{d \ln(a)} \times \frac{d(ab)}{d(a)}$$

$$\frac{d \log(ab)}{d \log(a)} = \frac{d \ln(ab)}{d \ln(ab)} \times \frac{1}{\frac{d \ln(a)}{d(a)}} \times \frac{d(ab)}{d(a)}$$

$$\frac{d \log(ab)}{d \log(a)} = \frac{1}{ab} \times \frac{1}{\frac{1}{a}} \times \frac{d(ab)}{d(a)}$$

$$\frac{d \log(ab)}{d \log(a)} = \frac{1}{b} \frac{d(ab)}{d(a)}$$

Making  $\frac{d(ab)}{d(a)}$  the subject of the formula:

$$\frac{d(ab)}{d(a)} = \frac{b \times d \log(ab)}{d \log(a)}$$

Substituting  $a$  and  $b$ :

$$\frac{d\left(\frac{1}{V_{in}I_{rr}}\right)}{d\left(\frac{1}{V_{in}}\right)} = \frac{\frac{1}{I_{rr}} d \log\left(\frac{1}{V_{in}I_{rr}}\right)}{d \log\left(\frac{1}{V_{in}}\right)} \quad (14.59)$$

A plot of  $\log\left(\frac{1}{V_{in}I_{rr}}\right)$  against  $\log\left(\frac{1}{V_{in}}\right)$  can be represented by directly plotting  $\left(\frac{1}{V_{in}I_{rr}}\right)$  against  $\left(\frac{1}{V_{in}}\right)$  on a log-log scale. One log cycle change in  $\left(\frac{1}{V_{in}}\right)$ , which is  $\log\left(\frac{1}{V_{in}}\right)_2 - \log\left(\frac{1}{V_{in}}\right)_1$ , is always, one as shown by the following examples:

$$\log(1) - \log(0.1) = \log\left(\frac{1}{0.1}\right) - \log(10)$$

$$= 1 \text{ and } \log(0.1) - \log(0.01) = \log\left(\frac{0.1}{0.01}\right) - \log(10) = 1$$

The slope of  $\log\left(\frac{1}{V_{in}I_{rr}}\right)$  against  $\log\left(\frac{1}{V_{in}}\right)$  can thus be determined by reading the change in  $\log\left(\frac{1}{V_{in}I_{rr}}\right)$ , which is  $\log\left(\frac{1}{V_{in}I_{rr}}\right)_2 - \log\left(\frac{1}{V_{in}I_{rr}}\right)_1$ , over one log-cycle of  $\log\left(\frac{1}{V_{in}}\right)$ . This slope is then substituted into equation

$$(14.59) \text{ to determine } \frac{d\left(\frac{1}{V_{in}I_{rr}}\right)}{d\left(\frac{1}{V_{in}}\right)}.$$



3: Calculating terminal water saturation ( $S_{w2}$ ).

Terminal water saturation can be determined using:

$$S_{w2} = S_{av} - f_o V_{in} \tag{14.60}$$

**Exercise 14.3** Using the JBN Method to Calculate Relative Permeability from a Flood Experiment

A core plug sample was drilled using formation brine as the drill bit lubricant. The sample was trimmed, cleaned, and dried. Porosity and permeability were determined. The core sample has an effective oil permeability of 12 mD at irreducible water saturation, a porosity of 0.22, and irreducible water saturation  $S_{wir}$  of 0.255. Synthetic oil with a viscosity of 22 cp and brine with a viscosity of 0.97 cp were used for the unsteady state water flood experiment with brine a injection rate of 0.02 cm<sup>3</sup>/s. The core sample has a diameter of 1.5 inches and length of 5 inches.

1. Using the JBN method, determine the relative permeability model that best represents the core sample.

2. Fit the relative permeability model to a Corey’s model using the approach discussed in Exercise 2.13.

Data from the flooding experiment are shown in Table 14.7.

**Solution.**

1. Core diameter,  $D = 1.5 \text{ in} = 1.5 \times 2.54 \text{ cm} = 3.81 \text{ cm}$ .

Core length,  $L = 5 \text{ in} = 5 \times 2.54 \text{ cm} = 12.7 \text{ cm}$ .

Core cross-sectional area,  $A = \frac{\pi D^2}{4} = \frac{\pi(3.81)^2}{4} = 11.401 \text{ cm}^2$ .

Pore volume (PV) in cm<sup>3</sup> is:

$$PV = A\phi L = 11.401 \times 0.22 \times 12.7 = 31.854 \text{ cm}^3$$

$$\frac{L}{A} = \frac{12.7}{11.401} = 1.114 \text{ cm}^{-1}$$

The viscosity ratio,  $\frac{\mu_o}{\mu_w}$  is:

$$\frac{\mu_o}{\mu_w} = \frac{22}{0.97} = 22.68$$

**Table 14.7** Data from the Flooding Experiment.

$V_o \text{ (cm}^3\text{)}$	$V_{in} \text{ (cm}^3\text{)}$	$\Delta p \text{ (psi)}$
5.89	7.13	231.81
7.64	15.14	131.33
8.94	29.19	95.6
11.08	92.2	68.56
13.39	357.26	54.68
13.97	723.28	48.17

$\Delta p$  is the pressure differential across the core sample during flooding

A graphical calculation of  $\Delta S_{wAvg}$ , which is the slope of  $S_{wAvg}$  against  $\log(V_{in})$ , for the first data point is shown in Fig. 14.27.

The relationship between  $\frac{1}{I_{rr}}$  and  $\Delta p$  based on equation (14.56) is:

$$\frac{1}{I_{rr}} = \frac{k_{eo} \Delta p}{\mu_o L / A q}$$

$$k_{eo} = 12 \text{ mD} = 0.012 \text{ D}$$

$$\frac{1}{I_{rr}} = \frac{0.012 \times \Delta p}{22 \times 1.114 \times 0.02} = 0.024483$$

$$\frac{1}{I_{rr}} = 0.024483 \Delta p \tag{14.61}$$

Calculate  $\frac{d\left(\frac{1}{V_{in} I_{rr}}\right)}{d\left(\frac{1}{V_{in}}\right)}$  using equation (14.59).

Fig. 14.28 illustrates the readings  $\left(\frac{1}{V_{in} I_{rr}}\right)_1$  and  $\left(\frac{1}{V_{in} I_{rr}}\right)_2$  over one log cycle change in  $\left(\frac{1}{V_{in}}\right)$  for the first data point.

$$\left(\frac{1}{V_{in} I_{rr}}\right)_2 = 1.084$$

$$\left(\frac{1}{V_{in} I_{rr}}\right)_1 = 0.017$$

Hence,  $\frac{d \log\left(\frac{1}{V_{in} I_{rr}}\right)}{d \log\left(\frac{1}{V_{in}}\right)}$  for the first point shown in

Fig. 14.28 is:

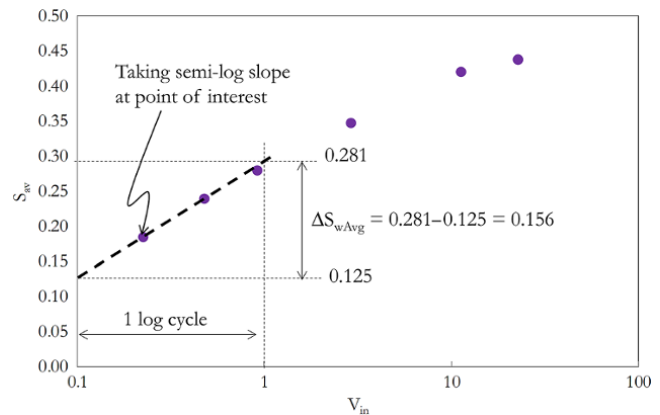


**Figure 14.27** Determination of  $\Delta S_{wAvg}$  from semi-log plot of  $S_{wAvg}$  against  $V_{in}$ .

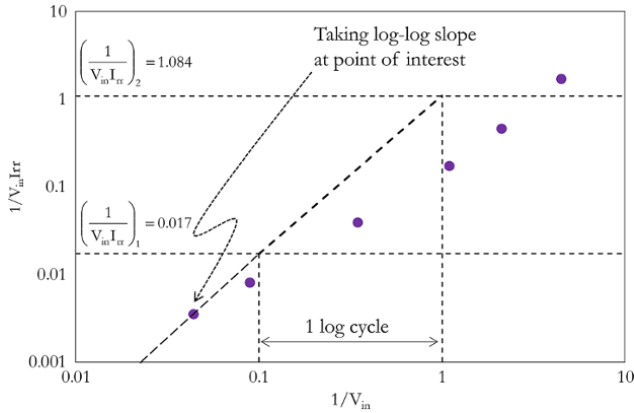


**Figure 14.28** Log-log plot of  $1/V_{in,Irr}$  against  $1/V_{in}$ .

$$\begin{aligned} \frac{d \log \left( \frac{1}{V_{in,Irr}} \right)}{d \log \left( \frac{1}{V_{in}} \right)} &= \log \left( \frac{1}{V_{in,Irr}} \right)_2 - \log \left( \frac{1}{V_{in,Irr}} \right)_1 \\ &= \log \left( \frac{\left( \frac{1}{V_{in,Irr}} \right)_2}{\left( \frac{1}{V_{in,Irr}} \right)_1} \right) = \log \left( \frac{1.084}{0.017} \right) = 1.8046 \end{aligned}$$

Also from equation (14.61):

$$\frac{1}{I_{rr}} = 0.024483 \Delta p$$

For the first data point,  $\Delta p = 231.81 \text{ psi} = 15.77 \text{ atm}$ . Hence:

$$\frac{1}{I_{rr}} = 0.024483 \Delta p = 0.024483 \times 15.77 = 0.386$$

Thus, from equation (14.59):

$$\frac{d \left( \frac{1}{V_{in,Irr}} \right)}{d \left( \frac{1}{V_{in}} \right)} = \frac{1}{I_{rr}} \frac{d \log \left( \frac{1}{V_{in,Irr}} \right)}{d \log \left( \frac{1}{V_{in}} \right)} = 0.386 \times 1.8046 = 0.697$$

This calculation is repeated for each data point. The solution to Exercise 14.3 is summarized in Table 14.8.

The calculated relative permeability model is shown graphically in Fig. 14.29.

2. Refining the relative permeability data model and fitting the relative permeability data to Corey's model are discussed in Chapter 2 (2.6).

### 14.2.2. Immiscible Gas Injection

The immiscible gas injection process to displace oil can be described by the fractional flow equation for gas, in a similar way to that of water, and expressed as:

$$f_g = \frac{1 + \left( \frac{0.044 k k_{ro} A}{q_t \mu_o} \right) (\rho_g - \rho_o) \sin \theta}{1 + \frac{k_{ro} \mu_g}{k_{rg} \mu_o}} \quad (14.62)$$

where  $q_t$  is total flow rate ( $\text{ft}^3/\text{d}$ ),  $\mu_o$  is oil viscosity (cp),  $\mu_g$  is gas viscosity (cp),  $A$  is cross-sectional area ( $\text{ft}^2$ ),  $f_g$  is the fraction of flowing gas,  $\rho_g$  is gas density ( $\text{lbm}/\text{ft}^3$ ), and  $\rho_o$  is oil density ( $\text{lbm}/\text{ft}^3$ ).

Gas displacement of oil is generally an inefficient displacement process, as the viscosity of gas is always far lower than that of oil. The fractional flow curve of gas displacing oil will generally be characterized by unstable displacement due to low  $\frac{\mu_g}{\mu_o}$  (high  $\frac{\mu_o}{\mu_g}$ ). The effect of the

low viscosity of the displacing fluid relative to the oil viscosity is discussed in Case 1 of Exercise 14.1. Significant difference in density between gas and oil causes gas to migrate to the top of reservoir with oil sinking to the bottom, thereby increasing the chance of the gas bypassing the oil and not achieving an efficient sweep/displacement. Also, in gas displacement of oil, gas is always the nonwetting phase, hence there is always a preferential flow of gas relative to the oil, thus making gas bypass oil.

A common and preferable way of implementing immiscible gas injection is to inject gas in the reservoir gas cap, where it exists to arrest pressure decline and further enhance gas gravity drainage (Fig. 14.30). The gas cap can exist naturally as a *primary gas cap*. The gas cap can also be created by migration of injected gas or solution gas to the top of the reservoir, thereby forming a *secondary gas cap*, above the oil zone.

A high dip reservoir structure is important in immiscible gas injection, as gas will preferentially occupy the top of the reservoir above the oil zone, unlike when the reservoir structure is flat.

Gas cap injection, due to specific density difference, ensures gas displacement is from the top downwards towards the oil column, creating a better sweep of oil. It is also important that for immiscible gas injection consideration, the oil column should be thick enough with oil production wells perforated far away from the gas cap to reduce the risk of early gas breakthrough. Perforating the oil producing wells at the base of a thick oil column also ensures room for shutting zones where there is gas cap breakthrough. It is important for the reservoir to have a reasonable vertical permeability for gas cap injection, to ensure that efficient gas displacement of oil can be achieved.

Immiscible gas injection can be combined with water injection to give improved recovery compared to water injection only or immiscible gas injection only. Fig. 14.31 shows combined gas and water injection with gas injection at the crest and water injection at an edge in the aquifer.

**Table 14.8** Solution to Exercise 14.3.

$V_o$ (PV) = $V_o(\text{cm}^3)/\text{PV}(\text{cm}^3)$	$V_{in}$ (PV) = $V_{in}(\text{cm}^3)/\text{PV}(\text{cm}^3)$	$S_{wAvg} = S_{wi} + V_o$	$\Delta S_{wAvg} =$ Slope of $S_{wAvg}$ vs $\log(V_{in})$
0.185	0.224	0.440	0.1560
0.240	0.475	0.495	0.1551
0.281	0.916	0.536	0.1496
0.348	2.894	0.603	0.1299
0.420	11.215	0.675	0.0900
0.439	22.706	0.694	0.0621

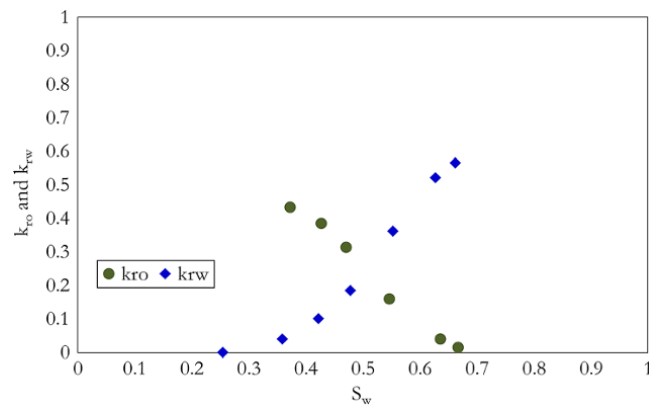
$f_o = \frac{\Delta S_{wAvg}}{2.303V_{in}}$ equation (14.52)	$S_{w2}$ (terminal water saturation) = $S_{wAvg} - f_o V_{in}$	$\Delta p$ (atm)	$I_{rr} = 0.024483 \Delta p$ (equation 14.61)
0.303	0.372	15.77	0.386
0.142	0.428	8.94	0.219
0.071	0.471	6.51	0.159
0.019	0.546	4.67	0.114
0.003	0.636	3.72	0.091
0.001	0.667	3.28	0.080

$I/V_{in}$	$I/V_{in} I_{RR}$	$m = d\left(\frac{1}{V_{in} I_{RR}}\right) / d\left(\frac{1}{V_{in}}\right)$	$k_{ro} = f_o / m$
4.468	1.725	0.697	0.434
2.104	0.460	0.367	0.386
1.091	0.174	0.226	0.314
0.345	0.039	0.122	0.160
0.089	0.008	0.086	0.041
0.044	0.004	0.079	0.015

$\frac{k_{rw}}{k_{ro}} = \frac{(1-f_o)}{\left(f_o \times \frac{\mu_o}{\mu_w}\right)}$	$k_{rw} = \left(\frac{k_{rw}}{k_{ro}}\right) \times k_{ro}$
0.102	0.044
0.267	0.103
0.578	0.182
2.218	0.356
12.607	0.512
37.092	0.554



**Figure 14.29** Relative permeability from water flood experiment.

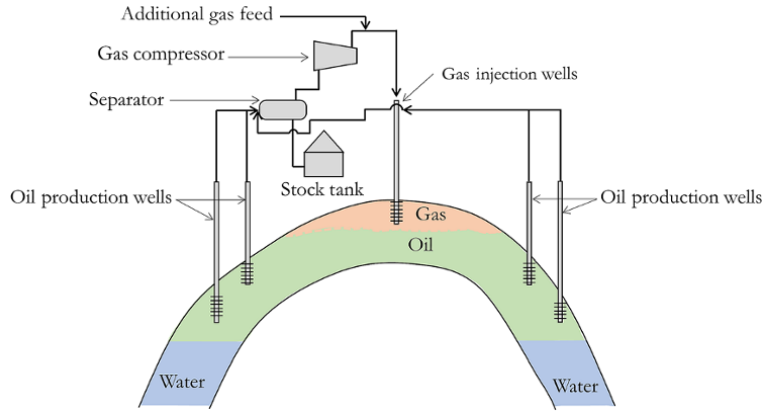


Figure 14.30 Crestal gas injection for gas cap pressure support and displacement of oil.

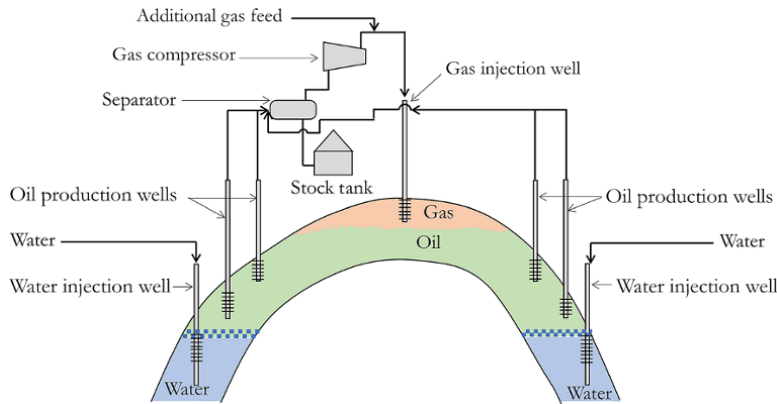


Figure 14.31 Crestal gas injection and peripheral water injection.

**14.2.3. Immiscible Water Alternating Gas Injection (IWAG)**

One approach for controlling gas mobility is injecting water alternately with gas, thereby creating a slug of liquid between a discontinuous gas phase (Fig. 14.32). This concept can be applied to immiscible and miscible water alternating with a gas injection process. IWAG has a higher recovery efficiency than water alone due to the reduced relative permeability of water as a result of the presence of three phases rather than two. This reduced relative permeability of water increases the chances that water will be diverted, thereby increasing the sweep. The presence of gas in IWAG causes reduced interfacial tension (IFT) since gas–oil IFT is lower than water–oil IFT, thereby enhancing the displacement of oil in pore spaces inaccessible by the water phase only. In water-wet rocks, trapping of gas enhances the mobility of oil, including residual oil. The difference in density between water and gas also creates segregation during

flow, which allows water to sweep the bottom and the gas the top of the reservoir, so increasing the vertical sweep.

The fractional flow equation and frontal advance equation used in water flooding (Section 14.2.1) can also be used for the analysis of WAG injection. In using the fractional flow equation for WAG analysis, the fractional flow curve for oil–water and gas–water are created and plotted together, as shown in Fig. 14.33.

The WAG ratio, which is the ratio of the volume of water to gas injected (water-to-gas ratio) into the reservoir, can be expressed as:

$$\text{WAG ratio} = \frac{q_w}{q_g} \tag{14.63}$$

Expressing the WAG in terms of the fractional water flow relative to gas phase ( $f_{wg}$ ):

$$f_{wg} = \frac{q_w}{q_g + q_w} \tag{14.64}$$

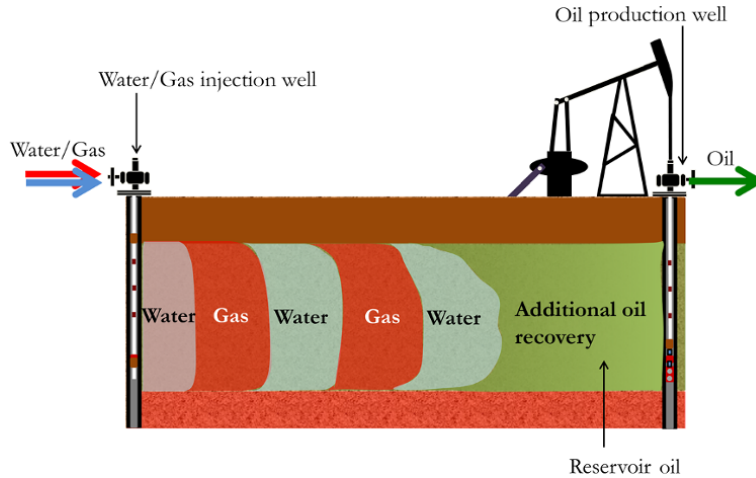


Figure 14.32 Immiscible water alternating gas injection (IWAG).

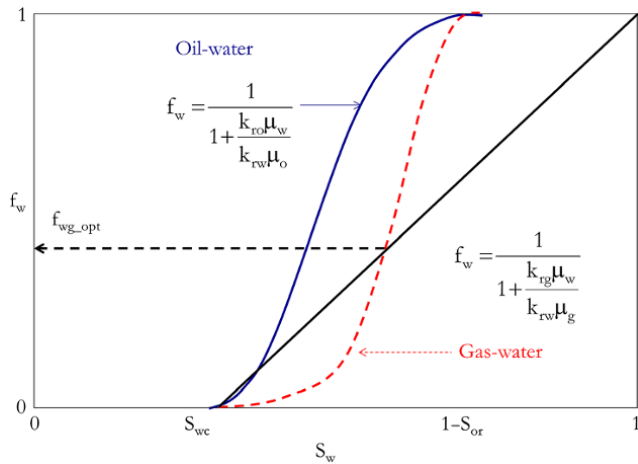


Figure 14.33 Fractional flow for WAG showing optimum fractional flow.

Combining equations (14.63) and (14.64) to derive WAG ratio in terms of  $f_{wg}$ :

$$\text{WAG ratio} = \frac{f_{wg}}{1 - f_{wg}} \quad (14.65)$$

It is important to optimize the WAG injection operation. Determination of the optimum WAG ratio ( $\text{WAG}_{\text{opt}}$ ), which is the WAG ratio that gives the optimum recovery factor, is shown in Fig. 14.33.

As shown in Fig. 14.33, a straight-line from  $[S_{wc}, 0]$  to  $[1, 1]$  and fractional flow curve for the gas–water can be used to determine the fractional flow of injected gas that corresponds to the optimum WAG ratio.

Substituting determined  $f_{g\_opt}$  at optimum WAG conditions from Fig. 14.33 into equation (14.64) would give the optimum WAG ratio ( $\text{WAG}_{\text{opt}}$ ):

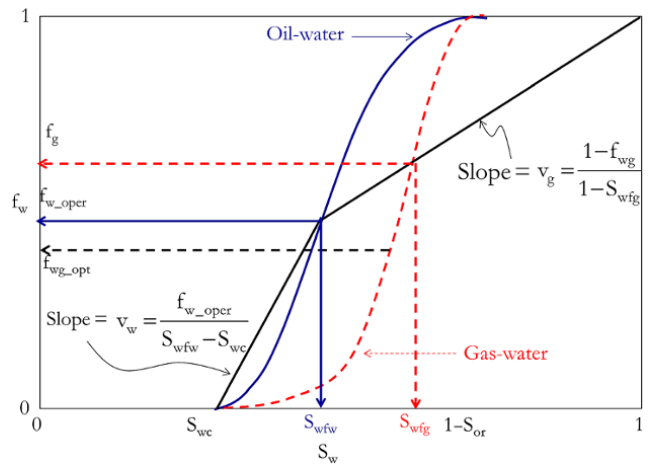


Figure 14.34 Determination of the speed of the front.

$$\text{WAG}_{\text{opt}} = \frac{f_{wg\_opt}}{1 - f_{wg\_opt}} \quad (14.66)$$

For a given operating or proposed WAG ratio ( $f_{w\_oper}$ ), the speed of the gas and water front can be calculated using, respectively:

$$v_g = \frac{1 - f_{wg}}{1 - S_{wfg}} \quad (14.67)$$

and

$$v_w = \frac{f_{w\_oper}}{S_{wfw} - S_{wc}} \quad (14.68)$$

From the determined speed of gas and water, the displacement of each front is calculated using the frontal advance equation (equation (14.21)). Using the determined frontal displacement of gas and water and their corresponding saturations as shown in Fig. 14.34, the saturation profile can then be created, as shown in Fig. 14.35.

### 14.3. TERTIARY (ENHANCED) OIL RECOVERY

Important tertiary oil recovery methods include: miscible gas injection; miscible water alternating gas injection; chemical injection, and thermal recovery (Fig. 14.2).

#### 14.3.1. Miscible Gas Injection

A broader definition for miscible gas injection is solvent injection considering that other nongaseous fluids such as condensate may be injected to increase recovery in similar way to miscible gas injection. The miscible gas injection process is an enhanced oil recovery (EOR) process involving phase changes and multiphase interaction

between the injection gas (solvent) and crude oil, leading to one or more of dissolution, vaporization, or condensation to improve recovery of oil in the reservoir. During miscible gas or solvent injection in an oil reservoir, one or more of oil viscosity reduction, oil swelling, and solution gas drive helps to increase oil production. Gases used for miscible gas injection/flooding include: nitrogen, carbon dioxide, and methane. Liquid solvent commonly used for enhanced oil recovery is condensate. Where condensate is to be added to dry gas to meet the composition of the injecting gas, the condensate will be added downstream of the compressor after compression of the dry gas.

Miscible gas injection enhances significant recovery of residual oil after primary and secondary recovery through miscibility. Gas-oil miscibility in the reservoir depends on the equation of state (EOS) properties, which include pressure, temperature, and fluid composition. Other factors that affect miscibility include reservoir properties such as mobility ratio and reservoir anisotropy. Fig. 14.36 shows a schematic of a miscible gas injection process.

Miscible gas injection is carried out at reservoir pressure above *minimum miscibility pressure (MMP)*, which is the lowest pressure at a given temperature for which a gas with a given composition would achieve first or multiple-contact miscibility (Chapter 3 (3.6.3.2)). Miscibility is achieved when there is no interfacial tension between mixing fluids.

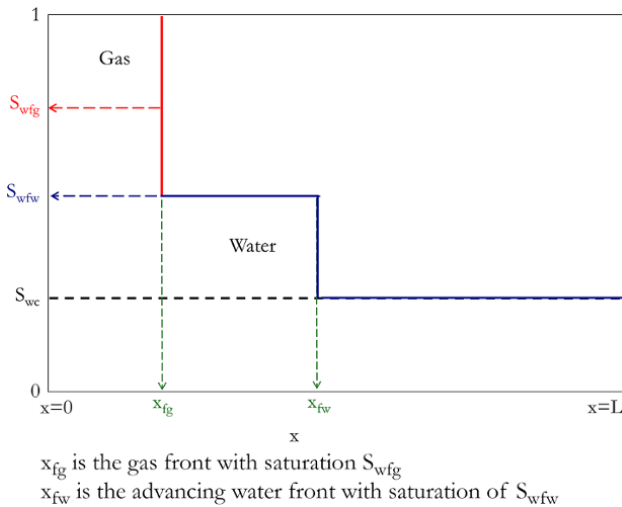


Figure 14.35 Saturation profile for WAG.

**14.3.1.1. Ternary Diagram.** A ternary diagram/plot/chart is a convenient way of presenting the phase behavior of a three-component (or pseudocomponent) system at a given temperature and pressure. To use a ternary diagram

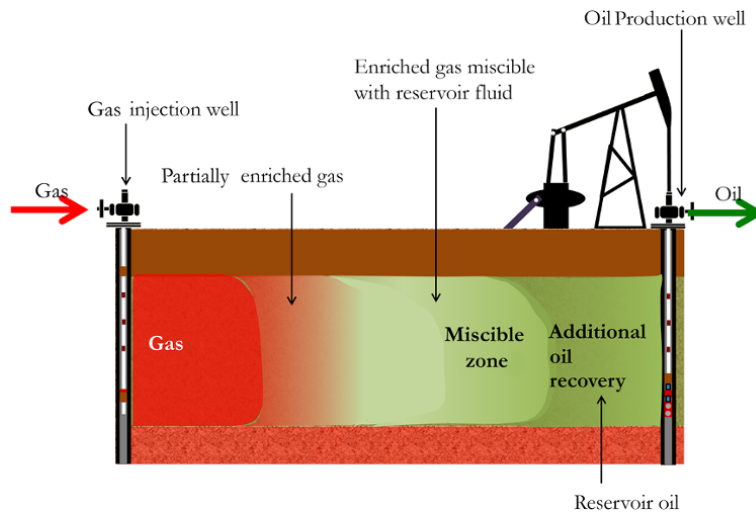
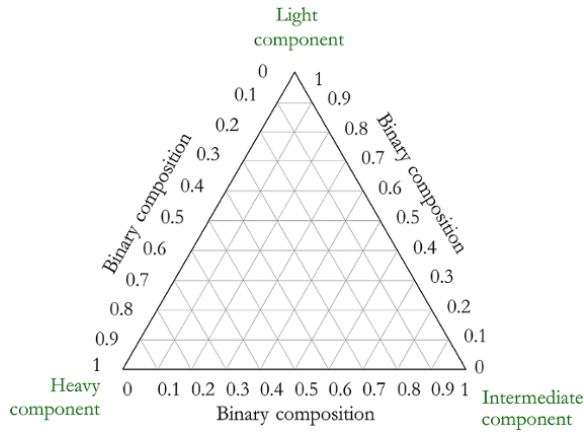
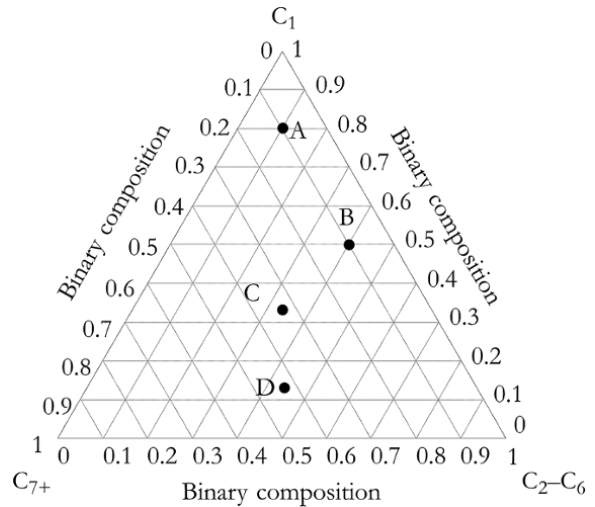


Figure 14.36 Miscible gas injection.



**Figure 14.37** A ternary diagram showing a three-component system.



**Figure 14.39** Ternary diagram for Exercise 14.4.

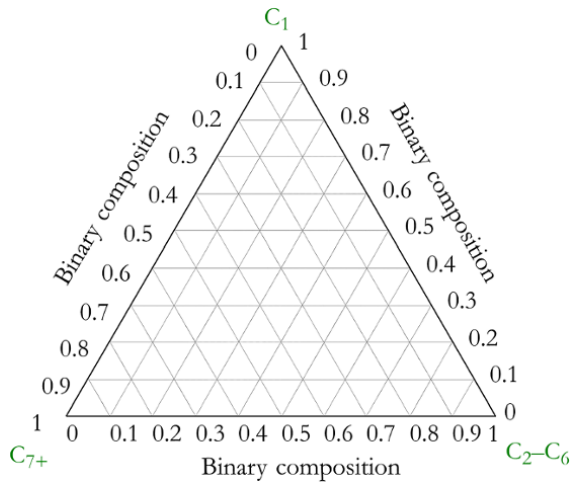


**Figure 14.38** A ternary diagram showing grouped hydrocarbon composition.

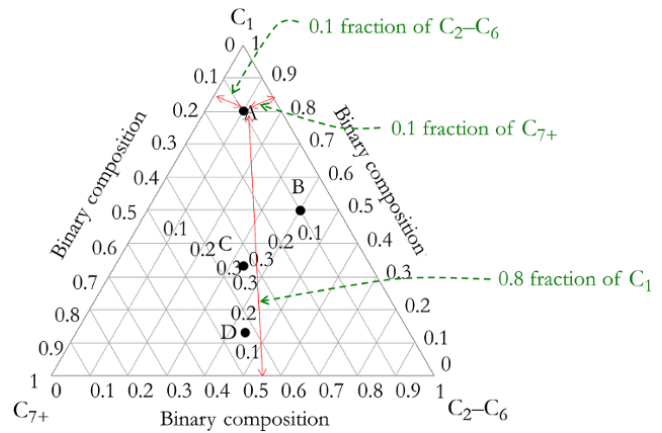


**Figure 14.40** Diagram showing the determination of the composition of A.

to describe the solvent/gas injection process in a reservoir, the entire constituents of the gas/solvent and reservoir must be grouped into three pseudocomponents. In a *ternary diagram* (Figs. 14.37 and 14.38), the mole fraction of a three-component (or pseudocomponent) system can be read at any given point, with composition of the three constituents summing up to 1.

*Ternary phase diagrams* (phase diagrams on a ternary chart) can be used to characterize the miscible gas/solvent injection processes in a reservoir, as they outline compositional boundaries that separate single-phase gas, single-phase oil, and two-phase oil and gas during the gas/solvent injection process, hence easily describing the effect of composition on miscibility during the gas/solvent injection process.

**Exercise 14.4** Reading Composition on the Ternary Diagram

Determine the composition of A, B, C, and D in the ternary diagram shown in Fig. 14.39.

**Solution Steps.**

Read the composition along the marked grids towards the apex of the triangle with the side of the triangle read as 0 and the apex as 1.

**Solution.**

At A, as shown in (Fig. 14.40), the composition is:  $C_1 = 0.8$ ,  $C_2-C_6 = 0.1$ , and  $C_{7+} = 0.1$ .

In similar way to the composition of A, the composition of B, C, and D are determined.

Composition of A: ( $C_1 = 0.8$ ;  $C_2-C_6 = 0.1$ ;  $C_{7+} = 0.1$ ).

Composition of B: ( $C_1 = 0.5$ ;  $C_2-C_6 = 0.4$ ;  $C_{7+} = 0.1$ ).  
 Composition of C: ( $C_1 = 0.33$ ;  $C_2-C_6 = 0.33$ ;  $C_{7+} = 0.33$ ).  
 Composition of D: ( $C_1 = 0.133$ ;  $C_2-C_6 = 0.433$ ;  $C_{7+} = 0.433$ ).

#### 14.3.1.2. Phase Equilibria in Ternary Fluid Mixture.

The two-phase region (phase envelope) in a ternary phase diagram describes the compositional boundary, within which liquid and vapor can exist in equilibrium at a given temperature and pressure for a three-component (or pseudocomponent) system (Fig. 14.41). The compositions of the equilibrium phase (liquid and vapor) are joined by *tie lines* within the two-phase region bounded by the phase envelope. Tie lines reduces to a *critical point* where the liquid and vapor (gas) phases become indistinguishable.

The fraction of the phase in a liquid–vapor mixture in equilibrium can be determined using the *Lever Rule*.

**14.3.1.3. Lever Rule.** Consider a hydrocarbon mixture with the *ternary phase diagram* shown in Fig. 14.42.

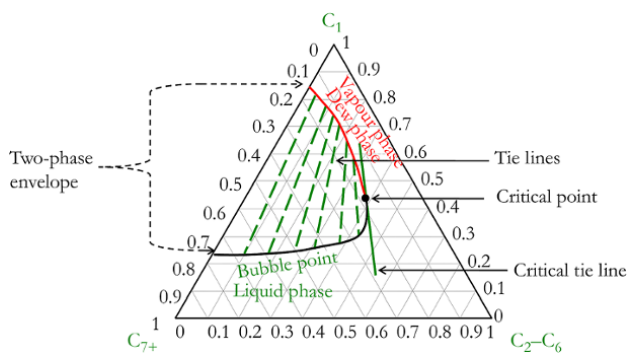


Figure 14.41 Ternary phase diagram.

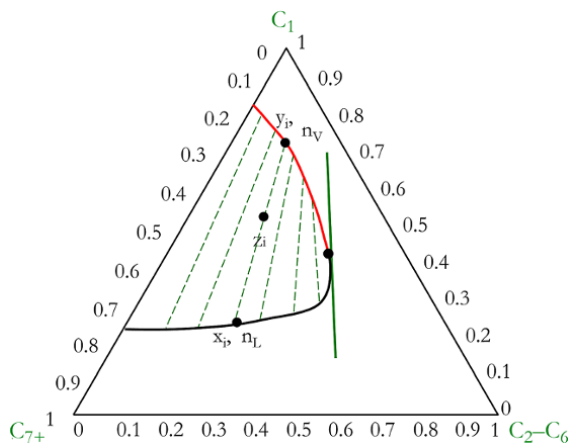


Figure 14.42 Hydrocarbon ternary phase diagram for vapor–liquid equilibrium calculation.

For this mixture,  $n_v$  is the mole fraction of vapor in equilibrium (gas phase fraction),  $n_L$  is the mole fraction of liquid in equilibrium (liquid phase fraction),  $x_i$  is the mole fraction of component  $i$  in the liquid phase,  $y_i$  is the mole fraction of component  $i$  in the vapor phase, and  $z_i$  is the mole fraction of component  $i$  in the original hydrocarbon mixture.

From material balance, the phase fraction will add up to 1 (phase material balance); hence:

$$n_L + n_V = 1 \quad (14.69)$$

The material balance of the individual component  $i$  is:

$$x_i n_L + y_i n_V = z_i \quad (14.70)$$

Making  $n_L$  the subject of formula in equation (14.69) and substituting into equation (14.70):

$$x_i(1 - n_V) + y_i n_V = z_i$$

Making  $n_V$  the subject of the formula:

$$x_i - x_i n_V + y_i n_V = z_i$$

$$y_i n_V - x_i n_V = z_i - x_i$$

The vapor fraction is thus:

$$n_V = \frac{z_i - x_i}{y_i - x_i} \quad (14.71)$$

Making  $n_V$  the subject of the formula in equation (14.69) and substituting into equation (14.70):

$$x_i n_L + y_i(1 - n_L) = z_i$$

$$x_i n_L + y_i - y_i n_L = z_i$$

$$x_i n_L - y_i n_L = z_i - y_i$$

The liquid fraction is thus:

$$n_L = \frac{z_i - y_i}{x_i - y_i} \quad (14.72)$$

Equations (14.71) and (14.72) represent the *lever rule*, which shows that the fraction of length of tie line from  $z_i$  to the dew point curve is the liquid phase fraction while the fraction of length of tie line from  $z_i$  to the bubble point curve is the vapor phase fraction.

**Exercise 14.5** Lever Rule and Reading Composition on the Ternary Diagram

Determine the fraction of the phase and composition for the mixture A, B, and C shown in Fig. 14.43.

**Solution.**

The vapor and liquid split for mixture B is shown in Fig. 14.44.

*Hydrocarbon Mixture A*

A is all in the vapor phase because it is on the gas phase area (outside the phase envelope away from dew point line).



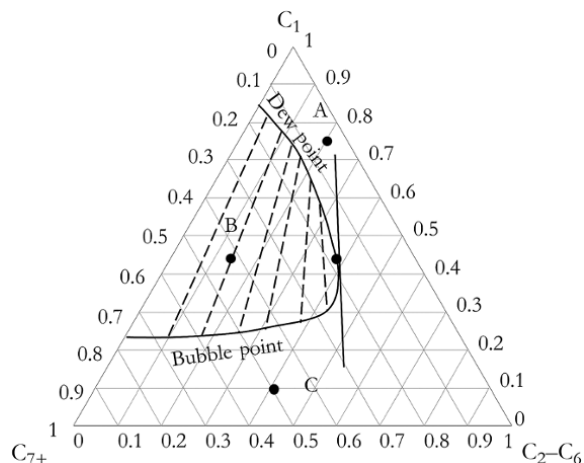


Figure 14.43 Ternary phase diagram for Exercise 14.5.

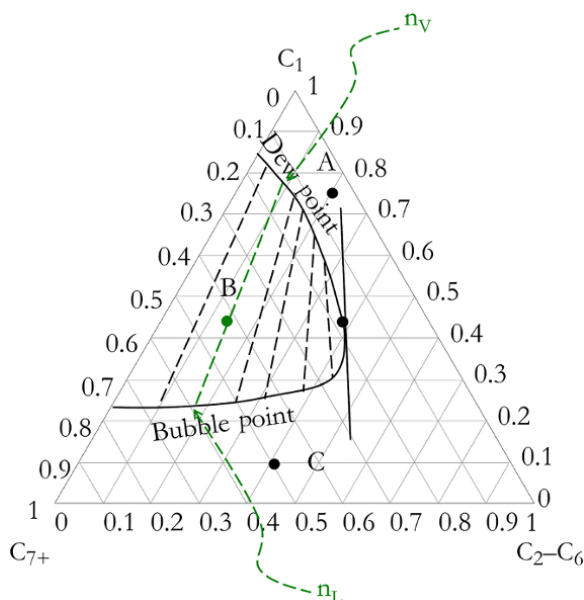


Figure 14.44 Vapor and liquid split for mixture B.

The composition of A is:  $C_1 = 0.75$ ;  $C_2-C_6 = 0.2$  and  $C_{7+} = 0.05$

*Composition of Hydrocarbon Mixture B*

B lies within the phase envelope section of the ternary diagram, hence mixture B has the vapor and liquid phase in equilibrium.

Composition of B in the vapor phase is read from the point labeled  $n_V$  in Fig. 14.44:

Composition of B in the vapor phase:  $C_1 = 0.78$ ;  $C_2-C_6 = 0.09$  and  $C_{7+} = 0.13$

Composition of B in the liquid phase is read from the point labeled  $n_L$  in Fig. 14.44.

Composition of B in the liquid phase:  $C_1 = 0.23$ ;  $C_2-C_6 = 0.17$  and  $C_{7+} = 0.6$ .

*Mole Fraction of Phase in Equilibrium for Hydrocarbon Mixture B*

The mole fraction of vapor in equilibrium (gas phase fraction),  $n_V$ , can be determined using equation (14.71):

$$n_V = \frac{z_i - x_i}{y_i - x_i}$$

Any of the components can be used to determine  $n_V$

Using  $C_1$ :  $n_V = \frac{0.44 - 0.23}{0.78 - 0.23} = 0.38$

Using  $C_2-C_6$ :  $n_V = \frac{0.14 - 0.17}{0.09 - 0.17} = 0.38$

Using  $C_{7+}$ :  $n_V = \frac{0.42 - 0.60}{0.13 - 0.60} = 0.38$

Hence, the mole fraction of B in the vapor phase ( $n_V$ ) is 0.38.

The mole fraction of liquid in equilibrium (liquid phase fraction),  $n_L$ , can be determined using equation (14.72):

$$n_L = \frac{z_i - y_i}{x_i - y_i}$$

Any of the components can be used to determine  $n_L$

Using  $C_1$ :  $n_L = \frac{0.44 - 0.78}{0.23 - 0.78} = 0.62$

Using  $C_2-C_6$ :  $n_L = \frac{0.14 - 0.09}{0.17 - 0.09} = 0.62$

Using  $C_{7+}$ :  $n_L = \frac{0.42 - 0.13}{0.60 - 0.13} = 0.62$

Hence, the mole fraction of B in the liquid phase ( $n_L$ ) is 0.62.

*Hydrocarbon Mixture C*

C is all in the liquid phase because it is on the liquid phase area (outside the phase envelope away from bubble point line).

Composition of C:  $C_1 = 0.1$ ;  $C_2-C_6 = 0.4$ , and  $C_{7+} = 0.5$ .

**14.3.1.4. Creating a Ternary Phase Diagram.** For any given composition (point on the ternary diagram), the phase fraction and phase composition can be determined using either VLE methods in Chapter 3 (3.4 or 4.4). From the determined vapor saturation (dew) points and liquid saturation (bubble) points, the loci of points created by vapor saturation (dew point) and loci of points created by liquid saturation (bubble point) can be traced. Dew point and bubble point locus are extrapolated to meet at critical point.

**Exercise 14.6** Ternary Phase Diagram in the EOR Process

A reservoir fluid is characterized as a mixture of light ( $C_{L1}$ ), intermediate ( $C_{Int}$ ) and heavy component ( $C_{HV}$ ). The intermediate component is desired to be extracted

**Table 14.9**  $C_{HV}$ ,  $C_{Int}$ , and  $C_{Lt}$  Compositions in the liquid and vapor phases.

Liquid phase			Vapor phase		
$C_{HV}$	$C_{Int}$	$C_{Lt}$	$C_{HV}$	$C_{Int}$	$C_{Lt}$
0.76	0	0.24	0.16	0	0.84
0.67	0.09	0.24	0.16	0.02	0.82
0.59	0.17	0.24	0.14	0.08	0.78
0.51	0.24	0.25	0.14	0.12	0.74
0.44	0.3	0.26	0.14	0.16	0.7
0.36	0.37	0.27	0.14	0.21	0.65
0.28	0.42	0.3	0.17	0.30	0.53
0.19	0.36	0.45	0.19	0.36	0.45

with solvent  $C_{Lt}$ . Equilibrium data showing the composition of constituents are shown in Table 14.9.

1. Draw a ternary phase diagram for the above system showing important features of the ternary diagram.

2. Determine the  $C_{Lt}$ ,  $C_{Int}$ , and  $C_{HV}$  mole fractions in the liquid and vapor phases in equilibrium following injection of  $C_{Lt}$  to get a final composition of  $C_{Lt} = 0.400$ ,  $C_{Int} = 0.215$ , and  $C_{HV} = 0.385$  in the extraction region of the reservoir.

3. Determine the mole fraction split of the final mixture into the liquid and vapor phases.

### Solution.

1. The ternary phase diagram for Exercise 14.6 is shown in Fig. 14.45.

2. The final composition of the extraction region is shown in the ternary phase equilibria in Fig. 14.46.

The molar fractions of  $C_{Lt}$ ,  $C_{Int}$ , and  $C_{HV}$  in liquid and vapor phase in equilibrium is calculated using same approach as in Exercise 14.5.

#### Composition of Hydrocarbon Mixture in Extraction Region

Since the mixture lies within the phase envelope of the ternary diagram, the mixture has vapor and liquid phases in equilibrium.

Composition of the mixture in the vapor phase is read from the point labeled  $n_V$  in Fig. 14.46:

Composition of the mixture in the vapor phase:  $C_{Lt} = 0.720$ ,  $C_{Int} = 0.130$ , and  $C_{HV} = 0.150$

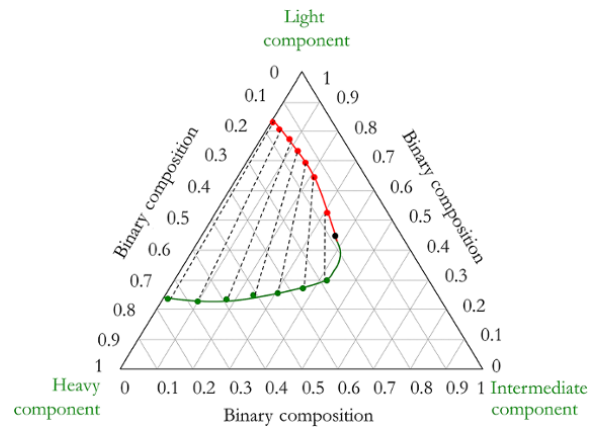
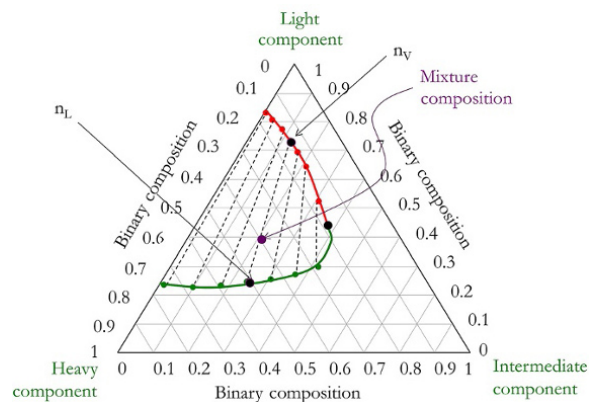
Composition of the mixture in the liquid phase is read from the point labeled  $n_L$  in Fig. 14.46.

Composition of the mixture in the liquid phase:  $C_{Lt} = 0.240$ ;  $C_{Int} = 0.260$  and  $C_{HV} = 0.500$

3. Mole fraction split of the final mixture into the liquid and vapor phases.

The mole fraction of vapor in equilibrium (gas phase fraction),  $n_V$ , can be determined using equation (14.71):

$$n_V = \frac{z_i - x_i}{y_i - x_i}$$


**Figure 14.45** Ternary phase diagram for Exercise 14.6.

**Figure 14.46** Ternary phase diagram showing the final mixture of the extraction region.

Any of the components can be used to determine  $n_V$ .

$$\text{Using } C_{Lt}: n_V = \frac{0.400 - 0.240}{0.720 - 0.240} = 0.33$$

$$\text{Using } C_{Int}: n_V = \frac{0.215 - 0.260}{0.130 - 0.260} = 0.33$$

$$\text{Using } C_{HV}: n_V = \frac{0.385 - 0.500}{0.150 - 0.500} = 0.33$$

Hence, the mole fraction of B in the vapor phase ( $n_V$ ) is 0.33.

The mole fraction of liquid in equilibrium (liquid phase fraction),  $n_L$ , can be determined using equation (14.72):

$$n_L = \frac{z_i - y_i}{x_i - y_i}$$

Any of the components can be used to determine  $n_L$

$$\text{Using } C_{Lt}: n_L = \frac{0.400 - 0.720}{0.240 - 0.720} = 0.66$$

$$\text{Using } C_{Int}: n_L = \frac{0.215 - 0.130}{0.260 - 0.130} = 0.66$$

**Table 14.10** Component Properties for Exercise 14.7.

Component	$T_{ci}$ (R)	$p_{ci}$ (psi)	$\omega_i$
$C_1$	343.37	667.8	0.0104
$C_2-C_6$	757	545.71	0.099
$C_{7+}$	1,044	348.75	0.36

$$\text{Using } C_{Hv}: n_L = \frac{0.385 - 0.150}{0.500 - 0.150} = 0.66$$

Hence, the mole fraction of the mixture in the liquid phase ( $n_L$ ) is 0.66.

**Exercise 14.7** Creating the Ternary Phase Diagram

Create the phase equilibrium data for a ternary system of  $C_1$ ,  $C_2-C_6$  and  $C_{7+}$  using the properties provided in Table 14.10 with Wilson's correlation. Plot the equilibrium phase diagram on a ternary chart for the system at 500 psi given that the system temperature is 189°F.

**Solution Steps.**

Carrying out the VLE calculations using Wilson's correlation (Chapter 3 (3.4.2.1)) to determine the fractions of  $C_1$ ,  $C_2-C_6$  and  $C_{7+}$  in the different phases at equilibrium. The limitation of Wilson's correlation is discussed in Chapter 3 (3.4.2.1).

Plot the composition of multiple flash calculations.

Extrapolate the liquid saturation curve and vapor saturation line to meet at the critical point.

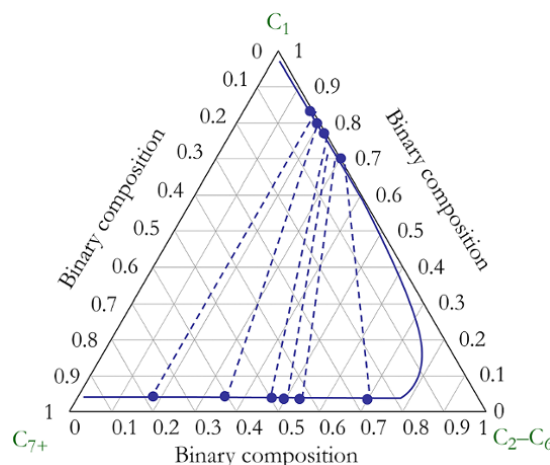
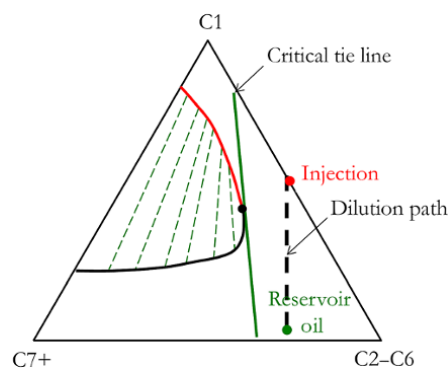
**Solution.**

The solution using Wilson's correlation is shown in Fig. 14.47.

Fig. 14.47 shows a ternary phase diagram with almost all of the ternary chart within the phase envelope (two-phase region) and, hence, the reservoir is unlikely to achieve miscibility for a wide range of injected gas compositions at this pressure. Reservoir pressure can be increased above the minimum miscibility pressure, to shrink the phase envelope, hence ensuring the miscible gas injection is achievable.

Wilson's correlation is only applicable up to a pressure of 500 psia. Hence, at higher pressure, VLE calculations using EOS models, as discussed in Chapter 4 (4.4.1), should be used. Wilson's correlation also has convergence difficulties near critical regions. Therefore, it is difficult to use to construct ternary phase diagrams.

**14.3.1.5. Miscible Gas/Solvent Injection Characterization using Ternary Phase Diagrams.** Ternary phase diagrams are a useful way of describing the miscibility drive mechanism in EOR. For a given fluid composition, the phase behavior will vary depending on the temperature and pressure of the system.

**Figure 14.47** Ternary phase diagram using Wilson's correlation for VLE calculations.**Figure 14.48** Single contact miscibility.**First Contact Miscible Gas/Solvent Injection**

In the process of *single contact miscibility*, injected gas/solvent forms a single homogeneous fluid with the reservoir oil on contact. The mobility of the oil is improved at the mixing boundary due to dilution with solvent/gas. A simple way of identifying this process using the ternary phase diagram is that the dilution path between the gas/solvent and the crude oil must be on the side of the critical tie line away from the  $C_1$  apex ( $C_1 = 1$ ) or light component (single-phase region) with dilution path not intersecting the two-phase region as shown in Fig. 14.48.

There are situations where the gas or solvent injected do not achieve miscibility with the reservoir oil on first contact and depend on the process of mass transfer (*multiple contact*) between phases to *develop miscibility*. Two processes that fall into this category of *multiple contact miscibility* or developed miscibility are *vaporizing gas drive injection* and *condensing gas drive injection*.

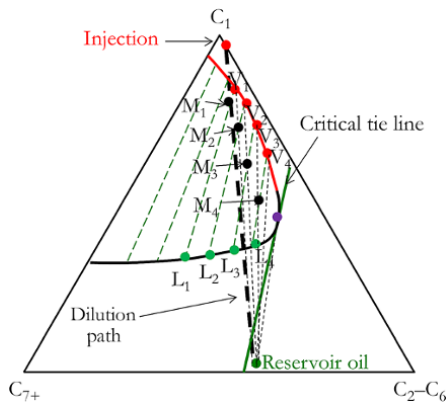


Figure 14.49 Vaporizing gas/solvent drive injection.

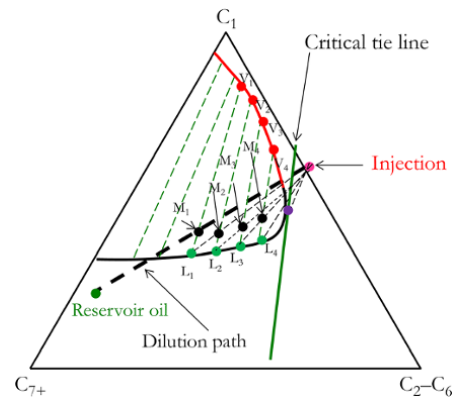


Figure 14.50 Condensing gas/solvent drive injection.

#### Vaporizing Gas/Solvent Drive Injection

The process involves mixing of injection gas/solvent with crude oil in the first stage to create composition  $M_1$  (Fig. 14.49). The mixture in phase equilibrium will then separate into vapor and liquid phases,  $L_1$  and  $V_1$ . The vapor phase formed from phase equilibrium separation is richer in intermediates than the original gas injected. Considering that vapor (gas) is more mobile than liquid, the vapor phase moves to next stage where it forms new mixture  $M_2$ , which is also separated into  $L_2$  and  $V_2$  with  $V_2$  richer in intermediates than  $V_1$  (Fig. 14.49). This process continues until full miscibility is achieved, so leading to extra recovery. Full miscibility is characterized by a final dilution path that does not cross the two-phase region but is rather a tangent line passing through the critical point (Fig. 14.49). A very simple approach for identifying vaporization drive from the ternary phase diagram is that injection gas/solvent and crude oil must be on different sides of the critical tie line, with gas/solvent on the side closer to the  $C_1$  apex ( $C_1 = 1$ ) or light component as shown in Fig. 14.49.

#### Condensing Gas/Solvent Drive Injection

In this process, at the first stage when the solvent comes in contact with the reservoir, phase separation occurs with the formation of  $L_1$  and  $V_1$ . The  $V_1$  created then moves to the next stage and  $L_1$ , which is richer in intermediates than the original reservoir oil composition, is further diluted with solvent to form a new mixture,  $M_2$ , which is separated into  $L_2$  and  $V_2$  (Fig. 14.50). The liquid phase is continuously enriched along the bubble point curve until the critical point is reached and miscibility attained. When the composition required to form a single phase is reached, the liquid forms single-phase mixture with solvent directly. Considering that gas is more mobile, the miscible front will be behind the gas phase flowing through the reservoir, which is in two-phases with reservoir oil. In this case, the miscibility is achieved through

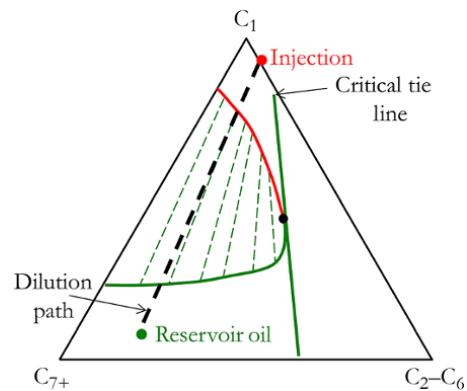


Figure 14.51 Immiscible gas injection.

enrichment of the oil with lighter hydrocarbons or solvent until miscibility is achieved. This process is also called *rich gas drive*. A simple approach for identifying a condensing gas/solvent drive from the ternary phase diagram is that injection gas/solvent and crude oil must be on different sides of the critical tie line, with solvent on the side away from the  $C_1$  apex ( $C_1 = 1$ ) or light component (Fig. 14.50).

#### Immiscible Gas Injection

In this process, on the ternary phase diagram, the dilution path between the gas/solvent and crude oil are on the same side of the critical tie line, with the dilution path intersecting the phase envelope, as shown in Fig. 14.51. Since there is no miscibility between the injected gas and the reservoir oil, the recovery process is an *immiscible gas displacement* process, as discussed in Section 14.2.2.

Miscibility can be achieved by increasing the pressure above the minimum miscibility pressure (MMP), where the limiting tie line matches with the critical tie line.

### 14.3.2. Miscible Water Alternating Gas Injection (MWAG)

The difference between *immiscible water alternating gas* (IWAG) injection and *miscible water alternating gas* (MWAG) injection is that MWAG is carried out at reservoir pressure above the *minimum miscibility pressure* (MMP) to ensure miscibility between gas and oil is achieved. MWAG gives a better recovery than IWAG due to the effect of miscibility on viscosity reduction, oil swelling, and solution gas drive.

In IWAG, due to the absence of miscibility between the gas and oil, combined with high density and viscosity contrast, there is the possibility of early gas breakthrough when compared with MWAG.

In field implementation of MWAG, it may be challenging to maintain minimum miscibility pressure throughout the WAG process, hence WAG may alternate from IMWAG to MWAG.

The fractional flow approach used in Exercise 14.2 can be used for analysis of MWAG by adjusting the relative permeability and viscosity in the fractional flow model to account for changes due to miscibility. Typical additional recovery from WAG is generally between 5 and 15% of original oil in place.

Miscible water alternate gas injection (MWAG) is illustrated in Fig. 14.52.

### 14.3.3. Chemical Injection

The chemical injection process involves the addition of *polymers*, *surfactants* or *caustic* to the water used for flooding.

**14.3.3.1. Polymer Flooding.** Polymers are long chain molecules that can be added to the water used for flooding to increase the viscosity of the injected water to achieve the mobility ratio required for vertical and area sweep, thereby increasing the oil recovery rate. Polymers are generally expensive, hence only a slug may be injected ahead of water flooding.

**14.3.3.2. Surface Active Agent (Surfactant).** Surfactants can be added to flood water solution to reduce interfacial tension between the oil and water, reduce residual oil saturation, and improve the displacement efficiency of oil by water. Surfactants, like most chemical EOR methods, are injected as slugs then followed by conventional flood water. Slugs of polymer may be injected after the surfactant prior to flood water to improve sweep efficiency.

**14.3.3.3. Caustic Solutions.** Caustic soda (sodium hydroxide) can react with natural organic acids, such as *naphthenic acids*, which are found predominantly in low mature heavy crude oils to form soap (surfactants). Surfactants formed *in situ*, in turn reduce interfacial tension and improve displacement efficiency, thereby enhancing oil recovery.

### 14.3.4. Thermal Recovery

Thermal recovery processes enhance oil production by heating reservoir rock and oil in the rock to reduce oil viscosity, reduce interfacial tension, alter wettability in ways that improve relative permeability of oil, and vaporize mobile and residual oil, thereby adding gas drive to oil recovery. The sources of heat for thermal EOR include *in situ combustion*, *steam injection*, or *hot water injection*.

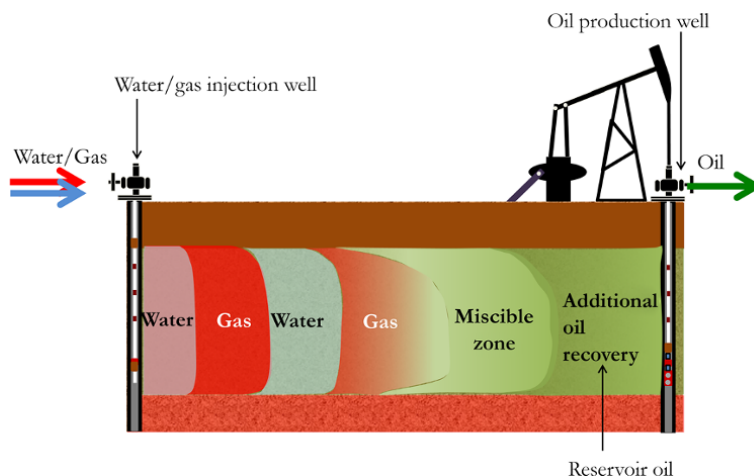


Figure 14.52 Miscible water alternate gas injection (MWAG).

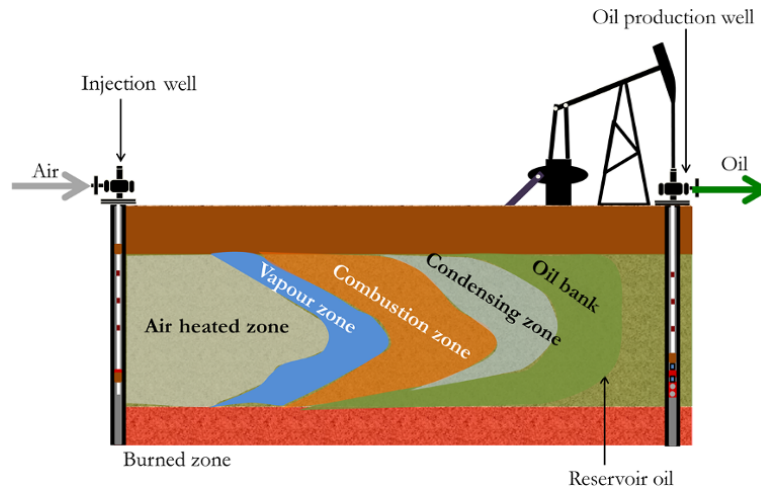


Figure 14.53 *In situ* combustion.

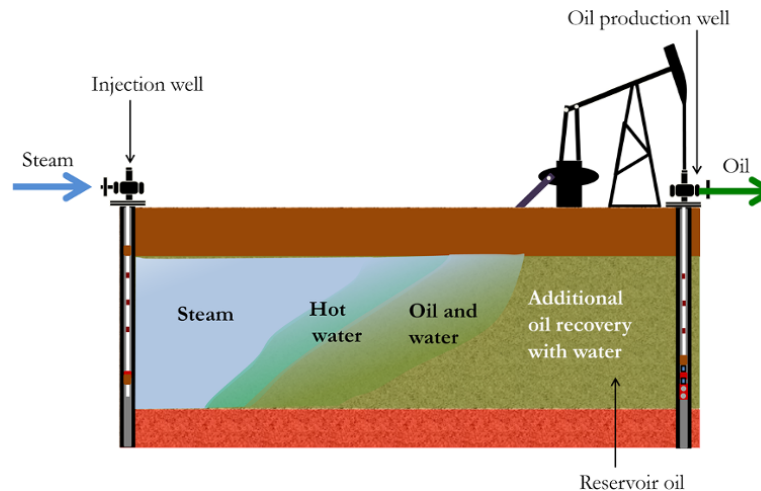


Figure 14.54 Steam flooding

**14.3.4.1. *In Situ Combustion.*** *In situ* combustion involves generating the heat required to improve oil mobility *in situ* via combustion (Fig. 14.53). Air is injected into the reservoir using high pressure compressors. The crude oil at the wellbore is then ignited at the wellbore. This is followed by continuous injection of air, which causes the combustion zone to spread into the reservoir and heat the oil ahead of it. The traveling combustion zone creates a vapor and condensing zone. The condensing zone, with hot water, pushes the oil bank towards the production well (Fig. 14.53).

**14.3.4.2. *Steam Injection.*** Steam injection can be in the form of *steam flooding/drive*, *cyclic steam injection* or *steam-assisted gravity drainage*.

#### *Steam Flooding*

Steam flooding involves the continuous injection of steam from an injection well to recover oil from a production well (Fig. 14.54). As the steam travels through the reservoir, it loses energy and its temperature drops creating a hot water zone. The hot water heats oil ahead of it, reducing its viscosity (Fig. 14.54). Reduction in residual oil saturation and in interfacial tension improve the relative permeability of the heated oil; this enhances oil recovery. In steam zone where oil is vaporized, the gas drive created also helps to enhance oil recovery.

Reservoir performance during steam flooding can be represented by a set of steady-state flow equations, as steam flooding, when equilibrium is reached, will be producing at a steady state during a considerable part of its

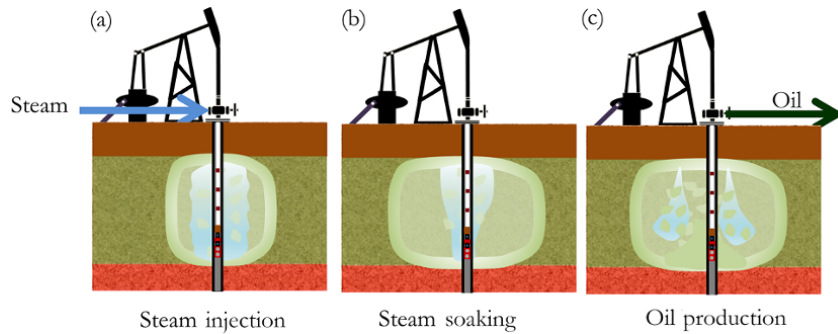


Figure 14.55 Cyclic steam injection.

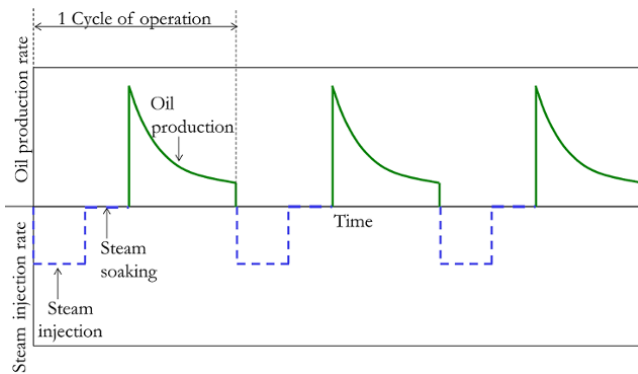


Figure 14.56 Cycles of cyclic steam injection production.

life. The steady-state reservoir flow equation was discussed in Chapter 9 (9.1).

*Cyclic Steam Injection*

Cyclic steam injection (CSI) also called “huff and puff” is an effective thermal method common for stimulating heavy oil reservoirs. This method enhances oil recovery through viscosity reduction, gas expansion, and alteration of the wettability. The process involves injecting steam at a temperature of about 200–300°C, then allowing the injected steam to soak for few days. After the soaking period, the well is opened for production through a natural tubing flow or with artificial lift systems. A cycle of steam injection is shown in Fig. 14.55.

During the CSI production of oil, cycles of injection, soaking, and production are repeated when the rate declines to an economic limit (Fig. 14.56).

Well injectivity is very important to ensure that sufficient steam can be injected to create the desired volume of heated oil. Improvements that may be considered in CSI to further improve the effectiveness of the method include: well fracturing, where well–reservoir injectivity and deliverability are low; using horizontal wells to

increase the contact surface area of the well with the formation, thereby enhancing injectivity and productivity; and the use of chemical additives to alter wettability to further enhance oil mobility.

Due to the high steam temperature, chemical reactions occur and produce carbon dioxide, carbon monoxide, methane, hydrogen, and hydrogen sulfide. These gasses produce an additional gas drive that enhances oil recovery.

CSI is a transient flow problem involving cycles of injection, soaking then production. Various assumptions can be applied to CSI production to simplify analysis. The heated area can be described as not having flow from a cold zone (no-flow boundary, as shown in Fig. 14.57, or with flow from a cold zone (boundary defined by known pressure or flux), as shown in Fig. 14.58.

The Laplace solution for radial flow in an homogeneous reservoir for different reservoir boundaries is summarized in Table 8.4. Also,  $f(s)$  functions that can be substituted into homogeneous reservoir models to convert them to appropriate heterogeneous models were summarized in Fig. 8.76.

The volume of the steam-stimulated region ( $V_s$ ) can be expressed as [Aziz and Gontijo, 1984]:

$$V_s = \frac{Q_s t_{inj} \rho_s Q_i + H_{last}}{(\rho C)_{total} (T_s - T_R)} \quad (14.73)$$

where  $Q_s$  is the rate of steam injection ( $ft^3/d$ ),  $t_{inj}$  is steam injection time (days),  $Q_s t_{inj}$  is the cumulative volume of steam injected ( $ft^3$ ),  $\rho_s$  is the density of the steam ( $lb/ft^3$ ),  $(\rho C)_{total}$  is the volumetric heat capacity of reservoir ( $btu/ft^3/^\circ F$ ), and  $Q_i$  is the heat injected into the reservoir per unit mass of steam ( $btu/lb$ ), and is expressed as:

$$Q_i = C_w (T_s - T_R) + L_{vdh} f_{sdh} \quad (14.74)$$

$C_w$  is the average specific heat of water ( $btu/lb/^\circ F$ ),  $T_s$  is steam temperature ( $^\circ F$ ),  $L_{vdh}$  is the latent heat of vaporization ( $btu/lb$ ),  $f_{sdh}$  is the steam quality at downhole

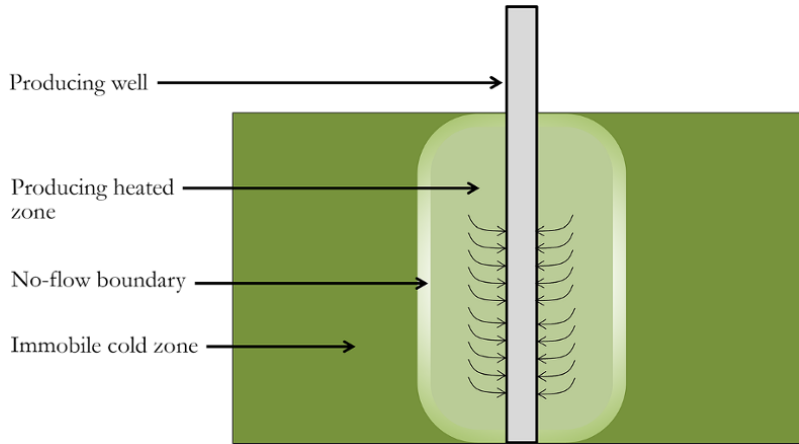


Figure 14.57 Steam-stimulated reservoir with immobile cold zone.

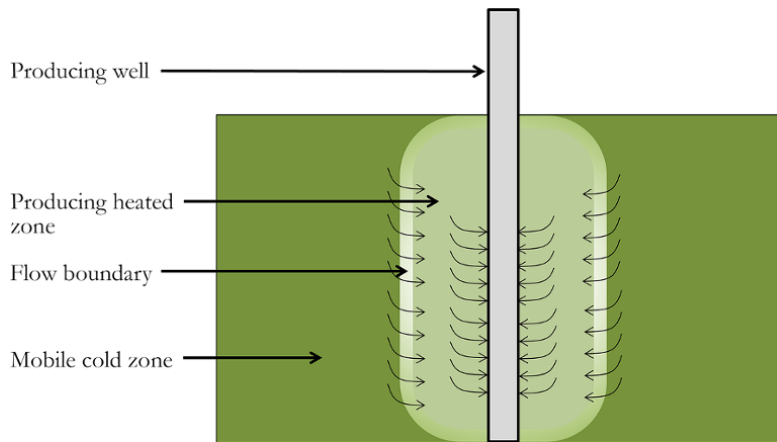


Figure 14.58 Steam-stimulated reservoir with mobile cold zone.

conditions, and  $H_{last}$  is the heat remaining after each cycle (btu/lb), and is expressed as:

$$H_{last} = V_s(\rho C)_{total} (T_{avg} - T_R) \quad (14.75)$$

where  $T_R$  is the initial reservoir temperature (°F) and  $T_{avg}$  is the average temperature of the steam-stimulated zone (°F).

Considering radial steam injection to form a cylindrical steam-stimulated zone, the radius of the steam-stimulated zone ( $r_o$ ), in feet, can be expressed as:

$$r_o = \sqrt{\frac{V_s}{\pi h}} \quad (14.76)$$

where  $h$  is the reservoir thickness (ft).

The properties of the fluid in the stimulated zone are computed at the average steam zone temperature ( $T_{avg}$ ) determined using:

$$\frac{T_{avg} - T_R}{T_s - T_R} = f_{HD}f_{VD}(1 - f_{PD}) - f_{PD} \quad (14.77)$$

where  $f_{HD}$ ,  $f_{VD}$ , and  $f_{PD}$  are dimensionless parameters that characterize the horizontal, vertical, and production heat losses, respectively, defined as [Aziz and Gontijo, 1984]:

$$f_{HD} = \frac{1}{1 + 5t_{DH}} \quad (14.78)$$

where

$$t_{DH} = \frac{\alpha(t - t_{inj})}{R_h^2}$$

where  $\alpha$  is the reservoir thermal diffusivity,  $R_h$  is the heated zone in the horizontal range, and  $h_i$  is total reservoir thickness.



**Table 14.11** CSI Operating Parameters.

Cycle	Steam injection rate (ft <sup>3</sup> /d)	Injection pressure (psia)	Injection time (days)	Soaking time (days)	Production time (days)	Sandface flowing pressure (psia)
1	5,615	536	27.5	20	250	154
2	5,615	536	27.5	20	250	154
3	5,615	536	27.5	20	250	154

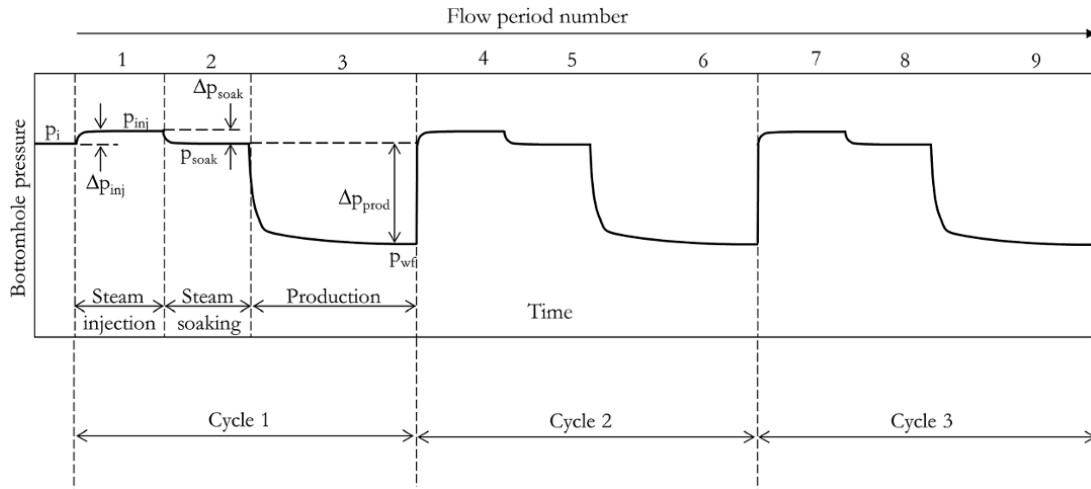


**Figure 14.59** Simplified sandface pressure history for CSI operation.

$$f_{VD} = \frac{1}{\sqrt{1 + 5t_{DV}}} \quad (14.79)$$

where

$$t_{DV} = \frac{4\alpha(t_{inj})}{h_t^2}$$

$$f_{PD} = \frac{1}{2Q} \int_0^t Q_p dt \quad (14.80)$$

where  $Q_p$  is the rate of heat withdrawal from the reservoir with produced fluids in btu/d and expressed as:

$$Q_p = 5.615 (q_o M_o + q_w M_w) (T_{avg} - T_R) \quad (14.81)$$

where  $q_o$  and  $q_w$  are the production rates (bbl/d) of oil and water, respectively,  $M_o$  and  $M_w$  are the volumetric heat capacities (btu/ft<sup>3</sup>/°F) of oil and water, respectively, and  $Q$  is the maximum heat added to the reservoir in one cycle (btu).

**Exercise 14.8** Cyclic Steam Injection (CSI) Production Prediction

A heavy oil reservoir is to be produced by CSI using a well with a sucker-rod pump (SRP) artificial lift. Analysis of the fluid level in the wellbore using acoustic well

sounders (AWS) suggests that the well can be considered as producing at constant pressure. Most of the heat injected is assumed lost during production of the oil and to the surrounding formation in each cycle. The boundary between the steam-stimulated zone and the cold zone is best described as a no-flow boundary system, as the reservoir could not produce into the wellbore without steam stimulation and recharge from cold zone to steam-stimulated zone during production is considered insignificant.

Predict the oil production profile given that the pressure dissipates during soaking to bring the reservoir to equilibrium average reservoir pressure.

The latent heat of vaporization ( $L_{vdh}$ ) is 1,984.54 btu/lb, the average specific heat of water ( $C_w$ ) is 1.0749 btu/lb/°F, and steam quality at downhole condition ( $f_{sdh}$ ) is 0.7.

CSI operating parameters are shown in Table 14.11.

Fig. 14.59 shows a schematic of the sandface pressure for the entire operation.

Reservoir and fluid properties are summarized in Table 14.12.

**Solution.**

The entire cycle of operation, which involves steam injection, soaking, and production, can be described using the constant terminal pressure (CTP) solution with a no-flow boundary as suggested by the problem definition.

**Table 14.12** Reservoir and Fluid Properties for Exercise 14.8.

Average initial reservoir pressure (psia)	456
Initial reservoir temperature, $T_R$ (°F)	125.6
Reservoir permeability, $k$ (mD)	20
Reservoir porosity, $\phi$	0.4
Total reservoir thickness, $h_t$ (ft)	75
Total reservoir compressibility during production ( $\text{psi}^{-1}$ )	2.61E-05
Total reservoir compressibility during injection and soaking ( $\text{psi}^{-1}$ )	2.19E-03
Well radius, $r_w$ (ft)	0.4
Steam temperature, $T_s$ (°F)	449
Oil viscosity during production, $\mu_o$ (cp)	2.75
Effective steam viscosity during injection, $\mu_s$ (cp)	0.017
Average steam density, $\rho_s$ ( $\text{lb}/\text{ft}^3$ )	0.827
Total volumetric heat capacity of reservoir, $(\rho C)_{\text{Total}}$ ( $\text{btu}/\text{ft}^3/^\circ\text{F}$ )	35.8
Relative permeability of oil during production, $k_{ro}$	0.25
Relative permeability of steam during injection, $k_{rs}$	0.1

The *constant terminal rate* (CTR) solution for an homogeneous reservoir with no flow boundary is, from Table 8.4:

$$\bar{p}_{wD}(s, r_D) = \frac{1}{s^{3/2}} \frac{K_0(r_D \sqrt{s}) I_1(r_{eD} \sqrt{s}) + K_1(r_{eD} \sqrt{s}) I_0(r_D \sqrt{s})}{[K_1(\sqrt{s}) I_1(r_{eD} \sqrt{s}) - K_1(r_{eD} \sqrt{s}) I_1(\sqrt{s})]}$$

CTR can be converted to CTP using the transform in equation (8.70) given as:

$$\bar{q}_D(s) = \frac{1}{s^2 \bar{p}_{wD}(s)}$$

$$\bar{q}_D(s) = \frac{1}{s^{2-3/2}} \frac{K_1(\sqrt{s}) I_1(r_{eD} \sqrt{s}) - K_1(r_{eD} \sqrt{s}) I_1(\sqrt{s})}{[K_0(r_D \sqrt{s}) I_1(r_{eD} \sqrt{s}) + K_1(r_{eD} \sqrt{s}) I_0(r_D \sqrt{s})]}$$

$$\bar{q}_D(s) = \frac{1}{\sqrt{s}} \frac{K_1(\sqrt{s}) I_1(r_{eD} \sqrt{s}) - K_1(r_{eD} \sqrt{s}) I_1(\sqrt{s})}{[K_0(r_D \sqrt{s}) I_1(r_{eD} \sqrt{s}) + K_1(r_{eD} \sqrt{s}) I_0(r_D \sqrt{s})]} \quad (14.82)$$

Equation (14.82) is the CTP solution for an homogeneous reservoir with no-flow boundary.

$$\text{Where } q_D = \frac{141.2B\mu}{k_{\text{eff}} h \Delta p} q$$

Since oil rates in this problem are requested to be calculated at downhole condition, the formation volume factor (B)  $q_D$  function above will be equal to 1.

$$t_D = \frac{0.000264k}{\phi \mu c_t r_w^2} \Delta t \text{ in hours}$$

$$t_D = \frac{0.0063k}{\phi \mu c_t r_w^2} \Delta t \text{ in days}$$

$$r_D = \frac{r}{r_w}$$

$$r_{eD} = \frac{r_o}{r_w}$$

For pressure measurement at wellbore,  $r = r_w$

$$\text{And } r_D = \frac{r_w}{r_w} = 1$$

Hence, for the pressure measured at wellbore, equation (14.82) becomes:

$$\bar{q}_D(s) = \frac{1}{\sqrt{s}} \frac{K_1(\sqrt{s}) I_1(r_{eD} \sqrt{s}) - K_1(r_{eD} \sqrt{s}) I_1(\sqrt{s})}{[K_0(\sqrt{s}) I_1(r_{eD} \sqrt{s}) + K_1(r_{eD} \sqrt{s}) I_0(\sqrt{s})]} \quad (14.83)$$

The numerical Laplace inversion equation (equation (8.73)) can be used to convert  $\bar{q}_D(s)$  to  $q_D(t-t_j)_D$ . Since the entire operation can be considered as multipressure change, the solution for the entire CSI operation is a convolution (superposition) of each of the rate signals  $q(t-t_j)$ .

The concept of superposition in this problem is similar to that discussed in Chapter 7 (7.3.2.1) and Chapter 8 (8.5.1.4) for the *constant terminal rate* (CTR) solution.

Using the superposition principle with constant  $\frac{k_{\text{eff}} h}{B\mu}$ , the solution to equation (14.83) can be expressed as [van Everdingen and Hurst, 1949]:

$$q_o(t) = \frac{k_{\text{eff}} h}{141.2B\mu} \sum_{j=0}^{n-1} \Delta p_j q_D(t-t_j)_D \quad (14.84)$$

When  $\frac{k_{\text{eff}} h}{B\mu}$  is the changing per flow period, equation (14.84) can be expressed as:

$$q_o(t) = \sum_{j=0}^{n-1} \left[ \frac{k_{\text{eff}} h}{141.2B\mu} \right]_j \left[ \Delta p_j q_D(t-t_j)_D \right] \quad (14.85)$$

From equation (14.74):

$$Q_i = C_w(T_s - T_R) + L_{vdh} f_{sdh}$$

Substituting the parameters given to get  $Q_i$ :

$$Q_i = 1.0749 (449 - 125.6) + 1984.54 \times 0.7$$

$$Q_i = 1736.8 \text{ btu}/\text{lb}$$

Calculating the volume of the steam-stimulated region using equation (14.73):

$$V_s = \frac{Q_s t_{\text{inj}} \rho_s Q_i + H_{\text{last}}}{(\rho C)_{\text{total}} (T_s - T_R)}$$

For the first cycle  $H_{last} = 0$ .  
 Substituting the given parameters into equation (14.73):

$$V_s = \frac{5615 \times 27.5 \times 0.827 \times 1736.8 + 0}{35.8 \times (449 - 125.6)}$$

$$V_s = 19155 \text{ft}^3$$

Determining the radius of steam-stimulated zone using equation (14.76):

$$r_o = \sqrt{\frac{V_s}{\pi h}}$$

$$r_o = \sqrt{\frac{19155}{\pi \times 75}}$$

$$r_o = 9.017 \text{ft}$$

Time steps can be created as shown in Table 14.13. The injection and soaking periods are defined as single time steps while, for simplification, the production period of 250 days is divided into five time steps for each cycle. Time steps for the entire operation can be made smaller.

The properties required to calculate  $\bar{q}_D(s)$  and the superposition principle are shown in Table 14.14.

In this problem, it is assumed that most heat is lost during production and to the formation; hence,  $r_o$  can be assumed constant for all cycle.

In order to solve equations (14.83) and (14.84),  $(t - t_j)$  is calculated for each flow period (Table 14.15).  $t_j$  is taken from Table 14.14 and  $t$  is shown in Table 14.13.

$(t - t_j)$  is converted to dimensionless time,  $(t - t_j)_D$ , by multiplying by  $\frac{0.0063k}{\phi \mu c_t r_w^2}$  (equation (12.42)) for each flow period.  $(t - t_j)_D$  calculations are summarized in Table 14.16.

Using  $(t - t_j)_D$ ,  $q_D(t - t_j)_D$  is calculated using the call function  $q_D(t_D, r_{eD})$  with VBA script in Appendix 14A. The VBA code handles the calculation of  $\bar{q}_D(s)$  and then

numerical inversion to  $q_D(t - t_j)_D$ . Calculated  $q_D(t - t_j)_D$  are shown in Table 14.17.

The results of  $\Delta p_j q_D(t - t_j)_D$  are shown in Table 14.18 and  $q_o$  in Table 14.19.

$$q(t - t_j) = \left[ \frac{k_{eff} h}{141.2 B \mu} \right]_j [\Delta p_j q_D(t - t_j)_D] \text{ and}$$

$$q_o(t) = \sum_{j=0}^{n-1} \left[ \frac{k_{eff} h}{141.2 B \mu} \right]_j [\Delta p_j q_D(t - t_j)_D]$$

A plot of  $q_o$  (bbl/d) in Table 14.19 against  $t$  (days) in Table 14.13 gives a production profile for oil

**Table 14.13** Time Steps for the Entire Operation.

Cycle number	Flow period	Operation	Time, t (days)
0	0	start	0
1	1	injection	27.5
	2	soaking	47.5
	3	producing	97.5
		producing	147.5
		producing	197.5
2	4	injection	325
	5	soaking	345
	6	producing	395
		producing	445
		producing	495
3	7	injection	622.5
	8	soaking	642.5
	9	producing	692.5
		producing	742.5
		producing	792.5
	producing	842.5	
	producing	892.5	
	producing	942.5	

**Table 14.14** Properties for Each Flow Period.

Operation	Flow period	$t_j$	$p_j$	$\Delta p_j = p_j - p_{j-1}$	$r_o$ (calculated)	$r_{oD} = \frac{r_o}{r_w}$	$k_{eff} = k_r \times k$	$\mu_o$ (cp)	$c_t$ (psi <sup>-1</sup> )	$\frac{t_D}{t} = \frac{0.0063 k_{eff}}{\phi \mu c_t r_o^2}$	$\frac{q_D}{q} = \frac{141.2 \mu}{k_{eff} h \Delta p}$
injection	1	0.0	536	-80	9.017	22.54	2	0.017	2.19E-03	104.0623	62.4896
soaking	2	27.5	456	80	9.017	22.54	2	0.017	2.19E-03	104.0623	62.4896
production	3	47.5	154	302	9.017	22.54	5	2.75	2.61E-05	134.9439	0.9657
injection	4	325.0	536	-80	9.017	22.54	2	0.017	2.19E-03	104.0623	62.4896
soaking	5	345.0	456	80	9.017	22.54	2	0.017	2.19E-03	104.0623	62.4896
production	6	395.0	154	302	9.017	22.54	5	2.75	2.60E-05	134.9439	0.9657
injection	7	622.5	536	-80	9.017	22.54	2	0.017	2.19E-03	104.0623	62.4896
soaking	8	642.5	456	80	9.017	22.54	2	0.017	2.19E-03	104.0623	62.4896
production	9	692.5	154	302	9.017	22.54	5	2.75	2.61E-05	134.9439	0.9657

**Table 14.15** Calculation of  $(t - t_i)$  for all Flow Periods.

t (days)	$(t - t_1)$	$(t - t_2)$	$(t - t_3)$	$(t - t_4)$	$(t - t_5)$	$(t - t_6)$	$(t - t_7)$	$(t - t_8)$	$(t - t_9)$
0	0								
27.5	27.5	0							
47.5	47.5	20	0						
97.5	97.5	70	50						
147.5	147.5	120	100						
197.5	197.5	170	150						
247.5	247.5	220	200						
297.5	297.5	270	250						
325	325	297.5	277.5	0					
345	345	317.5	297.5	20	0				
395	395	367.5	347.5	70	50	0			
445	445	417.5	397.5	120	100	50			
495	495	467.5	447.5	170	150	100			
545	545	517.5	497.5	220	200	150			
595	595	567.5	547.5	270	250	200			
622.5	622.5	595	575	297.5	277.5	227.5	0		
642.5	642.5	615	595	317.5	297.5	247.5	20	0	
692.5	692.5	665	645	367.5	347.5	297.5	70	50	0
742.5	742.5	715	695	417.5	397.5	347.5	120	100	50
792.5	792.5	765	745	467.5	447.5	397.5	170	150	100
842.5	842.5	815	795	517.5	497.5	447.5	220	200	150
892.5	892.5	865	845	567.5	547.5	497.5	270	250	200
942.5	942.5	915	895	617.5	597.5	547.5	320	300	250

**Table 14.16** Calculation of  $(t - t_i)_D$ .

$(t - t_1)_D$	$(t - t_2)_D$	$(t - t_3)_D$	$(t - t_4)_D$	$(t - t_5)_D$	$(t - t_6)_D$	$(t - t_7)_D$	$(t - t_8)_D$	$(t - t_9)_D$
0.00								
2,861.71	0.00							
4,942.96	2,081.25	0.00						
10,146.07	7,284.36	6,747.19						
15,349.19	12,487.47	13,494.39						
20,552.30	17,690.59	20,241.58						
25,755.42	22,893.70	26,988.78						
30,958.53	28,096.82	33,735.97						
33,820.24	30,958.53	37,446.93	0.00					
35,901.49	33,039.78	40,145.81	2,081.25	0.00				
41,104.60	38,242.89	46,893.00	7,284.36	5,203.11	0.00			
46,307.72	43,446.01	53,640.20	12,487.47	10,406.23	6,747.19			
51,510.83	48,649.12	60,387.39	17,690.59	15,609.34	13,494.39			
56,713.95	53,852.24	67,134.58	22,893.70	20,812.46	20,241.58			
61,917.06	59,055.35	73,881.78	28,096.82	26,015.57	26,988.78			
64,778.78	61,917.06	77,592.74	30,958.53	28,877.29	30,699.73	0.00		
66,860.02	63,998.31	80,291.61	33,039.78	30,958.53	33,398.61	2,081.25	0.00	
72,063.14	69,201.42	87,038.81	38,242.89	36,161.65	40,145.81	7,284.36	5,203.11	0.00
77,266.25	74,404.54	93,786.00	43,446.01	41,364.76	46,893.00	12,487.47	10,406.23	6,747.19
82,469.36	79,607.65	1,00,533.20	48,649.12	46,567.87	53,640.20	17,690.59	15,609.34	13,494.39
87,672.48	84,810.77	1,07,280.39	53,852.24	51,770.99	60,387.39	22,893.70	20,812.46	20,241.58
92,875.59	90,013.88	1,14,027.59	59,055.35	56,974.10	67,134.58	28,096.82	26,015.57	26,988.78
98,078.71	95,217.00	1,20,774.78	64,258.46	62,177.22	73,881.78	33,299.93	31,218.69	33,735.97

**Table 14.17** Calculation of  $q_D(t - t_j)_D$  using VBA script in Appendix 14A.

$q_D(t - t_1)_D$	$q_D(t - t_2)_D$	$q_D(t - t_3)_D$	$q_D(t - t_4)_D$	$q_D(t - t_5)_D$	$q_D(t - t_6)_D$	$q_D(t - t_7)_D$	$q_D(t - t_8)_D$	$q_D(t - t_9)_D$
0.000								
1.389	0.000							
1.029	1.613	0.000						
0.629	0.799	0.842						
0.453	0.535	0.503						
0.354	0.402	0.359						
0.291	0.322	0.279						
0.246	0.269	0.228						
0.227	0.246	0.207	0.000					
0.215	0.232	0.194	1.613	0.000				
0.190	0.203	0.168	0.799	0.997	0.000			
0.170	0.181	0.148	0.535	0.617	0.842			
0.154	0.162	0.132	0.402	0.447	0.503			
0.141	0.148	0.120	0.322	0.350	0.359			
0.129	0.135	0.109	0.269	0.288	0.279			
0.124	0.129	0.104	0.246	0.262	0.248	0.000		
0.120	0.125	0.101	0.232	0.246	0.230	1.613	0.000	
0.112	0.116	0.093	0.203	0.214	0.194	0.799	0.997	0.000
0.105	0.109	0.087	0.181	0.189	0.168	0.535	0.617	0.842
0.098	0.102	0.081	0.162	0.169	0.148	0.402	0.447	0.503
0.093	0.096	0.076	0.148	0.153	0.132	0.322	0.350	0.359
0.088	0.090	0.072	0.135	0.140	0.120	0.269	0.288	0.279
0.083	0.086	0.068	0.125	0.129	0.109	0.231	0.245	0.228

**Table 14.18** Calculation of  $\Delta p_1 q_D(t - t_j)_D$ .

$\Delta p_1 q_D(t - t_1)_D$	$\Delta p_1 q_D(t - t_2)_D$	$\Delta p_1 q_D(t - t_3)_D$	$\Delta p_1 q_D(t - t_4)_D$	$\Delta p_1 q_D(t - t_5)_D$	$\Delta p_6 q_D(t - t_6)_D$	$\Delta p_7 q_D(t - t_7)_D$	$\Delta p_8 q_D(t - t_8)_D$	$\Delta p_9 q_D(t - t_9)_D$
0.000								
-111.158	0.000							
-82.292	129.002							
-50.292	63.950	254.394						
-36.233	42.815	151.916						
-28.318	32.185	108.314						
-23.242	25.784	84.163						
-19.709	21.507	68.819						
-18.189	19.709	62.547	0.000					
-17.222	18.580	58.660	-129.002	0.000				
-15.203	16.251	50.770	-63.950	79.742	0.000			
-13.608	14.441	44.752	-42.815	49.335	254.394			
-12.316	12.994	40.009	-32.185	35.733	151.916			
-11.247	11.811	36.175	-25.784	28.012	108.314			
-10.350	10.825	33.012	-21.507	23.036	84.163			
-9.914	10.350	31.497	-19.709	20.985	74.969	0.000		
-9.620	10.030	30.480	-18.580	19.709	69.452	-129.002	0.000	
-8.956	9.310	28.202	-16.251	17.109	58.660	-63.950	79.742	0.000
-8.377	8.686	26.242	-14.441	15.115	50.770	-42.815	49.335	254.394
-7.869	8.141	24.536	-12.994	13.537	44.752	-32.185	35.733	151.916
-7.419	7.660	23.039	-11.811	12.257	40.009	-25.784	28.012	108.314
-7.017	7.233	21.714	-10.825	11.199	36.175	-21.507	23.036	84.163
-6.657	6.851	20.533	-9.991	10.309	33.012	-18.448	19.561	68.819

**Table 14.19** Calculation of  $q(t-t_j)$  and  $q_o(t)$ .

$q(t - t_1)$	$q(t - t_2)$	$q(t - t_3)$	$q(t - t_4)$	$q(t - t_5)$	$q(t - t_6)$	$q(t - t_7)$	$q(t - t_8)$	$q(t - t_9)$	$q_o = \sum q(t - t_j)$ (bbl/d)
0.00									0.00E+00
-6,946.24									-6.95E+03
-5,142.41									-5.14E+03
-3,142.74	3,996.22	245.68							1.10E+03
-2,264.17	2,675.51	146.71							5.58E+02
-1,769.60	2,011.22	104.60							3.46E+02
-1,452.39	1,611.24	81.28							2.40E+02
-1,231.62	1,343.98	66.46							1.79E+02
-1,136.61	1,231.62	60.41	0.00						1.55E+02
-1,076.22	1,161.04	56.65	-8,061.28	0.00					-7.92E+03
-950.05	1,015.53	49.03	-3,996.22	4,983.05	0.00				1.10E+03
-850.35	902.43	43.22	-2,675.51	3,082.92	245.68				7.48E+02
-769.59	812.01	38.64	-2,011.22	2,232.97	146.71				4.50E+02
-702.84	738.05	34.94	-1,611.24	1,750.48	104.60				3.14E+02
-646.75	676.44	31.88	-1,343.98	1,439.49	81.28				2.38E+02
-619.55	646.75	30.42	-1,231.62	1,311.35	72.40	0.00			2.10E+02
-601.17	626.74	29.44	-1,161.04	1,231.62	67.07	-8,061.28	0.00		-7.87E+03
-559.65	581.75	27.24	-1,015.53	1,069.12	56.65	-3,996.22	4,983.05	0.00	1.15E+03
-523.50	542.78	25.34	-902.43	944.51	49.03	-2,675.51	3,082.92	245.68	7.89E+02
-491.73	508.71	23.70	-812.01	845.91	43.22	-2,011.22	2,232.97	146.71	4.86E+02
-463.60	478.66	22.25	-738.05	765.95	38.64	-1,611.24	1,750.48	104.60	3.48E+02
-438.51	451.96	20.97	-676.44	699.81	34.94	-1,343.98	1,439.49	81.28	2.70E+02
-416.00	428.09	19.83	-624.33	644.18	31.88	-1,152.78	1,222.34	66.46	2.20E+02

(Fig. 14.60). The plot is scaled with a minimum of zero, as negative values indicate water injection.

Exercise 14.8 demonstrates the tedium of using analytical models for CSI production prediction, even with simplifications, such as neglecting  $H_{last}$  and using a reduced number of multipressure changes.

A more rigorous analytical calculation would include the effect of  $H_{last}$  from the previous cycle, more refined time steps to capture subtle changes in pressure, and the effect of changing  $T_{avg}$  with time.

Equation (14.77) is an implicit function in terms of  $T_{avg}$ , where  $f_{pD}$  is also a function of  $T_{avg}$ , as shown in combination of equations (14.80) and (14.81). Calculation of  $T_{avg}$  is, therefore, iterative. Due to the tedium of analytical calculations in CSI, numerical simulation is commonly used for CSI production prediction.

*Steam-Assisted Gravity Drive (SAGD)*

SAGD is an advanced form of steam injection that involves using two horizontal wells drilled a few meters vertically apart. High-pressure steam is continuously injected from the upper horizontal well to reduce the viscosity of oil around both wells. Heated oil with reduced viscosity then drains due to gravity and reduced viscosity

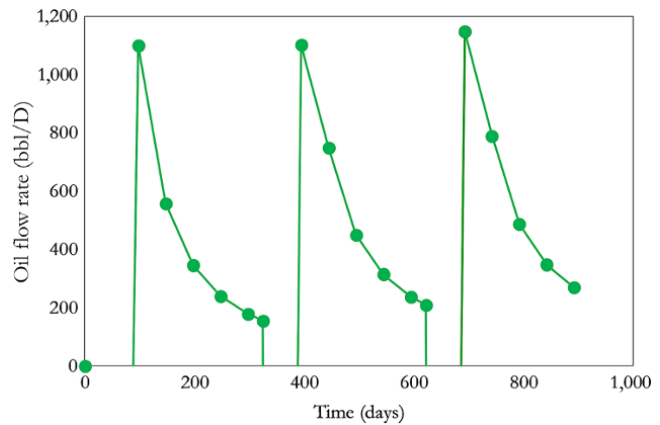


**Figure 14.60** Oil production profile from cyclic steam injection.

to the lower horizontal well. This method is used in the production of extra heavy oil and bitumen.

**14.3.4.3. Hot Water Injection.** Hot water injection is also called *hot water flooding*. This involves injecting hot water from an injection well and producing oil from another well. The injected hot water reduces the viscosity

of the oil, thereby creating a bank of heated oil that is pushed towards the producing well. Hot water injection is generally less effective than steam injection due to lower heat per unit volume.

## REFERENCES

- Aziz, K. and Gontijo, J., 1984. *A Simple Analytical Model for Simulating Heavy Oil Recovery by Cyclic Steam in Pressure-Depleted Reservoirs*. SPE paper 13037, 59th Annual Technical Conference and Exhibition, 16–19 September, Houston, TX.
- Buckley, S. and Leverett, M., 1942. Mechanism of fluid displacement in sand. *SPE, Transactions of the AIME*, **146**(01), 107–116.
- Craft, B. and Hawkins, M., 1991. *Applied Petroleum Reservoir Engineering*, 2nd edn. Prentice-Hall.
- Johnson, E., Bossler, D., and Naumann Bossler, V., 1959. *Calculation of Relative Permeability from Displacement Experiments*. American Institute of Mining, Metallurgical, and Petroleum Engineers.
- van Everdingen, A. and Hurst, W., 1949. The Application of the Laplace Transformation to Flow Problems in Reservoirs. *Transactions of the AIME*, **1**(12), 305–324.
- Welge, H., 1952. A simplified method for computing oil recovery by gas or water drive. *SPE-Journal of Petroleum Technology*, **4**(04), 91–98.

## BIBLIOGRAPHY

- Ahmed, T., 2006. *Reservoir Engineering Handbook*, 3rd edn. Gulf Professional Publishing.
- Amyx, J.W., Bass, D.M., and Whiting, R.L., 1960. *Petroleum Reservoir Engineering: Physical Properties*. McGraw-Hill.
- Archer, J. and Wall, C., 1999. *Petroleum Engineering Principles and Practice*. Dordrecht/Boston: Kluwer Academic Publishing.
- Boberg, T. and Lantz, R., 1966. Calculation of the Production Rate of a Thermally Stimulated Well. *Journal of Petroleum Technology*, **18**(12), 1613–1623.
- Campbell, R. and Campbell, J., 1978. *Mineral Property Economics: Petroleum Property Evaluation*. Norman, OK: Campbell Petroleum Series.
- Carter, R. and Tracy, G., 1960. An improved method for calculating water influx. *Transactions of the AIME*, **219**, 415–417.
- Cole, F., 1969. *Reservoir Engineering Manual*. Houston, TX: Gulf Publishing.
- Craig, F.G. and Morse, R., 1995. Oil recovery performance of pattern gas or water injection operations from model tests. *Petroleum Transactions, AIME*, **204**, 7–15.
- Dake, L., 1998. *Fundamentals of Reservoir Engineering*, 17th edn. Development in Petroleum Science 8, Elsevier.
- Fetkovich, M., 1971. A simplified approach to water influx calculations – finite aquifer systems. *Journal of Petroleum Technology*, **23**(7), 814–828.
- Havlena, D. and Odeh, A., 1963. The material balance as an equation of a straight line. *Journal of Petroleum Technology*, **15**(08), 896–900.

- Holtz, M., 2016. *Immiscible Water Alternating Gas (IWAG) EOR: Current State of the Art*. Tulsa, OK: Society of Petroleum Engineers.
- Jones, J., 1977. *Cyclic Steam Reservoir Model for Viscous Oil, Pressure Depleted Gravity Drainage Reservoirs*. SPE paper 6544, 47th Annual California Regional Meeting of the SPE of AIME, 13–18 April, Bakersfield, CA.
- Marsal, D., 1982. *Topics of Reservoir Engineering. Course Notes*. Delft University of Technology, Delft, The Netherlands.
- Schilthuis, R., 1936. Active Oil and Reservoir Energy. *Transactions of the AIME*, **118**(1), 33–52.
- Walsh, M. and Lake, L., 2003. *A Generalized Approach to Primary Hydrocarbon Recovery*. Amsterdam: Elsevier.
- Willhite, G., 1986. *Waterflooding*. Text Book Series, Vol.3, Society of Petroleum Engineer.

## APPENDIX 14A VBA SCRIPT FOR EXERCISE 14.8

```
Function LaplaceQD(i, td, reD)
constant terminal pressure solution function
lns = WorksheetFunction.Ln(2) / td
Srts = (i * lns) ^ 0.5
"upper is numerator of constant terminal pressure solution
"lower is denominator of constant terminal pressure solution
upper = WorksheetFunction.BesselI(reD * Srts, 1)
* WorksheetFunction.BesselK(Srts, 1) - Worksheet
Function.BesselK(reD * Srts, 1) * Worksheet
Function.BesselI(Srts, 1)
lower = Srts * (WorksheetFunction.BesselI(Srts, 0)
* WorksheetFunction.BesselK(reD * Srts, 1) +
WorksheetFunction.BesselK(Srts, 0) *
WorksheetFunction.BesselI(reD * Srts, 1))
LaplaceQD = upper / lower
End Function
Function QD(td, reD)
"Stehfest Numerical Laplace inversion using N= 10
QD = (WorksheetFunction.Ln(2) / td) * (0.0833 *
LaplaceQD(1, td, reD) - 32.1 * LaplaceQD(2, td, reD)
+ 1280# * LaplaceQD(3, td, reD) - 15600# *
LaplaceQD(4, td, reD) + 84200# * LaplaceQD
(5, td, reD) - 237000# * LaplaceQD(6, td, reD) +
376000# * LaplaceQD(7, td, reD) - 340000# *
LaplaceQD(8, td, reD) + 164000# * LaplaceQD
(9, td, reD) - 32800# * LaplaceQD(10, td, reD))
End Function
```

# INDEX

---

- absolute openhole flow potential, 333
- acid fracturing, 381
- acidizing, 3, 223, 381
- active probe, 184, 196, 197, 321
- Amott–Harvey technique, 32–34, 37
- Antoine equation, 83
- apparent mobility-thickness (apparent transmissibility), 288
- apparent skin effect, 274, 279, 311, 315, 316
  
- bilinear flow, 225, 232
- binary interaction coefficient, 105, 106, 110
- bottomhole sampling, 88
- bubble point pressure, 65, 66, 78–80, 87, 93–95, 115
- Buckles constant, 163
- Buckley–Leverett equation, 466–472, 476
- buildup
  - development stage, 15, 451, 452
- buildup test, 186, 227, 230, 243, 244, 253, 277
- bulk density, 137, 138, 141–143
  
- Campbell plot, 424, 425, 431, 437
- c and n equation, 350
- capillary pressure, 17, 36–44
- capillary pressure measurement
  - centrifuge method, 43
  - dynamic method, 43
  - mercury injection method, 43
  - porous diaphragm method, 43
- cap rock, 3, 36
- Cardano’s method, 75, 106, 112
- Carter–Tracy aquifer model, 438
- casing head spool, 374
- casing pressure gauges, 373
- casings, 369
- casing valves, 374
- changing wellbore storage, 307
- Christmas tree, 365, 372–374
- closed chamber testing, 264
- cokriging, 13
- Colebrook–White equation, 385
- Cole plot, 444
- commingled tubing production, 289, 291, 292, 366–368
- Compton effect, 137
- Compton scattering, 199
- computed gamma ray, 129, 175
- condensate bank(ing), 287, 288
- condensate dropout, 32, 69, 90, 91, 108, 109
- conductor pipe, 369
- connate water saturation, 13, 32, 36, 163, 164, 423
- constant compositional expansion experiment (CCE), 91
- constant mass expansion, 91
- constant terminal pressure solution, 267, 434, 451
  
- constant terminal rate, 267, 497
- constant volume depletion (CVD) experiment, 89
- contact angle, 31, 32, 37, 43, 44
- continuous gas lift, 406, 411, 413
- conventional back pressure equation for gas, 351
- conventional gas lift valves, 406
- coriolis effect, 199
- corrosion, 382, 420
- Craig’s wettability criteria, 32, 35–37
- cricondenbar, 65
- cricondentherm, 65, 69
- critical point, 65, 66, 69, 110, 487, 488, 490, 491
- cross-plot
  - neutron-density, 143, 157
  - permeability-porosity, 166, 168
  - sonic-density, 148, 149
- crown valve, 374
- cubic equation of states, 74, 103, 106, 107, 112, 118
- cycle skipping, 148
- cyclic steam injection, 494, 496, 501
  - convolution, 497
  
- Darcy’s law, 21–24
- datum pressure correction, 398
- deep resistivity log, 144, 149, 151, 154, 176
- derivative end effect, 308, 310
- developed reserves, 12
- deviation survey, 122, 123, 205
- dew point pressure, 85–87, 91, 114, 115, 117, 287, 288, 319
- diagenesis, 121, 462
- Dietz shape factor, 338, 340
- differential liberation experiment, 94
- differential vaporization experiment, 94
- diffusivity equation, 211–213, 215, 246
  - gas diffusivity equation, 213, 215, 310, 318
  - solution to diffusivity equation, 216, 265
- drawdown test, 226, 243, 252
- drill stem test(ing), 89, 117, 245, 307
- drive pipe, 369
- dry tree system/completion, 374
- dual laterolog, 151, 152
- dual water model, 157, 158
- Duhamel’s principle, 262
  
- Economides horizontal well IPR model, 361
- effective decline, 452
- effective wellbore radius, 274–276, 376
- electrical submersible pump, 401, 404
- end point mobility ratio, 465, 466
- enhanced oil recovery, 9, 459, 485
- equation of state (EOS), 69, 73, 74, 76, 83, 89, 103, 107
  - Peng Robinson, 74, 103, 104



- equation of state (EOS) (*cont'd*)  
 Redlich–Kwong, 73, 103, 104  
 Soave–Redlich–Kwong, 73, 103, 104  
 van der Waals, 74, 76
- erosion velocity, 400
- excess pressure, 206, 208
- exponential law  
 permeability dependence on pressure, 31  
 porosity dependence on pressure, 1
- extended well test, 14
- facies, 13, 121, 168, 170  
 biofacies, 121  
 depositional facies, 121  
 diagenetic facies, 121  
 lithological facies, 121
- fall-off test, 244
- Fetkovich semisteady state aquifer model, 438
- flash expansion, 91, 93
- flash liberation experiment, 91, 93
- flash vaporization, 91, 93
- flow assurance, 88, 196, 412
- flowing pressure gradient  
 acceleration pressure gradient, 383, 389  
 frictional pressure gradient, 383, 385, 407  
 hydrostatic pressure gradient, 383, 388, 407
- flowline storage effect, 183, 184, 319
- Forchheimer equation, 26
- Forchheimer IPR, 345
- formation pressure log, 181, 184, 186, 199–209
- formation resistivity, 148, 149, 151, 154
- formation test(ing), 184–186, 189, 196–200, 244
- formation volume factor  
 gas formation volume factor, 7, 72, 95, 107  
 oil formation volume factor, 8, 78–80, 95, 107
- frac packing, 381, 382
- fractional flow equation, 463, 466, 469, 478
- fracture conductivity, 275
- fractured well, 274–276
- fracture half-length, 224, 247, 275, 278
- fugacity, 112, 113, 115
- fugacity coefficient, 112–114
- gamma ray index, 126, 127
- gamma ray log, 125, 126, 128, 130
- gas bank(ing), 223, 287, 288
- gas breakthrough, 98
- gas condensate, 68  
 experiment, 89, 91–93  
 fluid behavior, 68, 69, 77, 81  
 inflow performance relationship, 344, 352  
 reservoir material balance, 446–448  
 well test behavior, 223, 287, 288, 319
- gas crossover  
 neutron-density well log, 141, 142, 175
- gas expansion factor, 72
- gas hydrate, 413  
 anti-agglomerants, 418, 419  
 formation, 413  
 kinetic hydrate inhibitors, 418  
 low dosage hydrate inhibitors, 416, 418  
 prediction, 414  
 prevention and inhibition, 416  
 types, 413
- gas lift, 401, 402, 405, 406, 408  
 gas lift design, 411, 412  
 gas lift valves, 405, 408, 410  
 gas oil ratio, 68–69, 79, 80  
 gas solubility, 78  
 gas specific gravity, 70, 77, 79–80  
 gauge noise, 308  
 gauge pressure correction, 398  
 generalized material balance for gas  
 geometric factor, 187, 188, 192  
 geothermal gradient, 3, 132  
 gradient reversal point, 407  
 gross rock volume, 7, 8, 10
- Hammerschmidt equation, 417
- Havlena–Odeh material balance method, 425–427, 444
- Hoffmann quality plot, 90, 92, 109, 110
- homogeneous tubing flow, 383
- horizontal interference test, 195
- horizontal well test behavior, 285
- Horner  
 buildup equation, 228  
 plot, 232, 237–239, 302  
 time, 228, 229
- hot water injection, 492, 501–502
- Hurst–van Everdingen (HVE) unsteady State aquifer model, 434
- hydrate *see* gas hydrate
- hydraulic diffusivity, 213, 216, 231, 287
- hydraulic fracture, 223, 224, 275, 382
- hydraulic jet, 401
- hydraulic piston, 401
- hydrogen index, 140, 175
- imbibition, 32–34, 40
- immiscible gas injection, 459, 460, 481, 491
- immiscible water alternating gas injection, 459, 460, 483, 484
- improved oil recovery, 460
- impulse test, 244
- index of oil movability, 154
- Indonesia equation, 157, 158
- induction logs, 149, 151, 153
- induction tools, 149, 151–153
- infinite conductivity fracture, 224, 255, 257, 278
- inflow performance relationship  
 Fetkovich, 351, 352, 354  
 gas, 343–346, 351  
 two-phase, 344, 351, 352  
 Vogel, 315–354
- initial gas in place *see* original gas in place
- injection test, 244
- inorganic scale deposition, 419
- in-place hydrocarbon volume calculation  
 deterministic, 8, 9, 12  
 stochastic, 8, 12
- in-situ combustion, 459, 492, 493
- interfacial tension, 31, 32, 37, 43, 82, 97, 483, 485, 492, 493
- interference test, 244
- interlayer cross flow coefficient, 292
- intermediate casing, 370
- intermittent gas lift, 405, 406
- interporosity flow coefficient, 236, 237, 286
- irreducible water saturation, 32, 162, 163, 174
- isothermal compressibility, 71, 80, 99, 318
- jet perforator(perforation), 370, 373
- Jones and Raghavan pseudo-pressure transformation, 319, 344

- Jones IPR for gas, 346
- Jones IPR for oil, 346
- Joshi IPR model, 360
  
- Kay's rules, 71
- Kerogen(s), 2, 3
- kill wing valve, 374
- kinetic hydrate inhibitors
- Klinkenberg correction (and Klinkenberg effect), 25, 26
- Kozeny–Carman, 161, 162
- kriging, 13
  
- laminar clay (and laminar model), 155, 156, 158
- Laplace's equation, 38
- laterolog, 149, 151, 152, 158
- leaky fault, 275, 296
- Leverett J-function, 44, 45
- lever rule, 487
- limestone compatible scale, 142, 143
- limestone porosity unit, 141
- limited entry well, 184, 195, 218, 223, 225, 258, 259, 273, 274
- linear composite reservoir, 239, 288
- linear flow regime, 224, 232, 259, 284
- liner completions, 375
- liquid holdup, 383, 384
- liquid-junction potential, 130
- liquid permeability, 22, 25
- lithification, 2
- lithofacies, 121, 168
- lithology, 121
- logging depth, 122
- logging while drilling, 124
- Lohrenz–Bray–Clark viscosity model, 81
- lower master valve, 374
- lower well completion, 375
  - openhole completion, 375
  - perforated casing completions, 376
  - perforation skin effect, 376
  - tubingless or reduced diameter completions, 376
  
- mass continuity equation, 467
- material balance correction
  - well test analysis, 318
- matrix acidizing, 3, 223, 381
- matrix concentration, 236
- measured depth, 122, 205
- mechanical skin, 222, 223, 279, 281, 315, 316
- mercury injection method
  - capillary pressure measurement, 43
- microlog, 151
- microresistivity, 151
- minimum connected volume, 13, 14, 264
- minimum miscibility pressure, 97, 485, 490–492
- miscible gas injection, 97, 459, 460, 481, 485, 490, 491
- miscible water alternating gas injection, 459, 460, 483–485, 492
- mobility ratio
  - fraction flow equation, 464–466, 485, 492
  - well test analysis, 287, 289, 292
- modified Simandoux equation, 156–158
- Monte Carlo methods, 8
- Moody friction factor chart, 385, 388
- movable hydrocarbon, 154
- mud acid, 382
- mud hydrostatic pressure, 195
  
- multilateral well completion, 381, 382
- multilayered reservoirs, 289, 291, 292, 365, 366
- multilayered reservoir with crossflow, 289, 292, 365, 366
- multilayered reservoir without crossflow, 289, 291, 292, 365, 366
- multiphase flow regimes
  - annular/mist flow, 386
  - bubble/dispersed flow, 386
  - slug flow, 386
  - transition flow, 386
- multiple contact miscibility, 97, 99, 485, 490
  
- naphthenic acids, 492
- naphthenic hydrocarbons, 419
- natural gamma ray, 125, 128, 175
- natural segregated gas cap drive, 459, 460
- natural water drive, 459, 460
- near critical fluids, 104, 116, 288, 490
- near wellbore effects, 218
- net rock volume, 7
- net to gross ratio, 7, 10, 11, 13
- neutron log, 140, 141, 144, 148, 175
- neutron porosity, 140–143, 175
- Nielsen–Bucklin equation, 417
- non-Darcy coefficient, 26, 316
- non-Darcy skin coefficient, 311, 315
- nonproducing reserve, 12
- nonsegregation-drive gas caps, 429
- normalized pseudopressure, 215, 310, 312, 314, 343, 344, 348
- normalized pseudotime, 318
- normally pressured, 5–7, 219, 318
- nuclear magnetic resonance, 161, 164, 174
  
- observation probe, 184, 197, 321, 322
- oil compressibility, 80, 219
- oil density, 77–80
- oil viscosity, 79, 80, 465
- openhole completion, 375
- openhole gravel pack, 375
- openhole sand control, 375
- optical spectroscopy
  - contamination monitoring, 198, 199
  - downhole fluid analysis, 198, 199
- organic acids, 382, 492
- original gas in place, 7, 318, 443, 444, 446
- original oil in place, 7, 422, 424–427, 471
- overburden pressure, 3, 4, 21
- overpressured, 5, 6
  
- paraffin wax, 419
- partially penetrating well *see* limited entry well
- pay net-to-gross ratio, 10
- perforated casing completions, 376
- perforated liner completion, 375
- perforating gun(s), 370–373
- perforation skin effect, 376
- peripheral water injection, 483
- permeability, 3, 10, 13, 21
  - absolute, 48, 49
  - anisotropy, 187, 360
  - averaging, 27–30
  - core, 159, 161
  - crushed zone, 377
  - effective, 48, 49
  - effect of confining pressure, 30, 31

- permeability (*cont'd*)  
 fissure, 36  
 formation logs, 159, 161  
 formation testing, 182, 184–186, 194  
 gas, 22  
 horizontal, 226, 265  
 liquid, 22  
 log prediction, 162–174  
 logs, 159, 161, 162, 164, 166, 167, 170, 172, 174  
 matrix, 236  
 measurement, 22–25  
 radial, 226, 228, 265, 301, 321  
 reduction, 222  
 relative, 13, 14, 17, 48  
 spherical, 225, 226  
 stress-dependent, 31  
 vertical, 194, 226, 321  
 well testing, 161
- petroleum resources classification  
 contingent, 11, 12, 14, 15  
 prospective, 11, 12, 14  
 reserves, 11, 12, 14
- photoelectric absorption, 137, 139
- planktons, 2
- plunger lift system, 401, 402
- polymer flooding, 492
- pore pressure, 186
- porosimeter, 19, 20
- porosity, 3, 13, 17  
 absolute, 18, 19  
 core, 20  
 density log (density porosity), 137–139  
 effective, 18, 20, 21, 139, 143, 154  
 effect of confining pressure, 30  
 neutron-density, 143  
 neutron log (neutron porosity), 140, 141  
 stressed, 30  
 total, 154  
 true porosity, 143  
 unconnected, 21
- power law  
 permeability dependence on pressure, 31  
 permeability model, 162, 164, 167  
 porosity dependence on pressure, 31  
 relative permeability model, 51
- pretest chamber, 181–184, 189, 192
- primary drainage, 31, 32
- primary migration, 3
- primary oil recovery, 459, 460
- primary production, 423, 459, 460
- prismoidal method for gross rock volume calculation, 9, 10
- probe–packer configuration, 184, 195, 196, 319–322
- probe–probe configuration, 184, 195, 196, 319–322
- producing reserve, 12
- production casing, 370, 374–376
- production decline model, 13, 267, 451  
 exponential production decline model, 13, 267, 451  
 harmonic production decline, 451, 453  
 hyperbolic production decline, 451, 454
- production packer, 370
- production system plot, 397–399, 404
- production tubing, 370, 373, 376, 379
- production well test, 243, 268
- production wing valve, 374
- productivity index, 333, 334, 363, 366, 438, 441
- progressing cavity pump, 401, 402
- propped hydraulic fracturing, 381, 382
- pseudocomponent(s), 82, 84, 85, 108, 109
- pseudocritical properties (density, pressure and temperature), 71, 75, 77
- pseudopressure, 214, 215, 310, 312, 343, 344, 348
- pseudoradial flow, 284
- pseudo-reduced properties, 72
- pseudo-steady state flow regime, 91, 216, 240, 267, 291, 292, 317, 318, 327, 334, 337, 338, 361, 368, 438
- pseudotime, 317, 318
- pumpout module, 181
- p/z plot  
 depletion effect during well test, 317, 318  
 gas condensate material balance, 448  
 gas material balance, 444, 445, 447
- radial composite model, 286–288
- radial superposition function, 251, 252, 313
- Raghavan's pseudopressure transform, 319
- Raoult's law, 83
- rate dependent skin, 223, 279, 310, 344–346, 348, 349
- reduced diameter completions, 376
- relative permeability  
 calculating, 477, 480–481  
 capillary end effect, 52  
 denormalizing, 51, 52  
 end point, 464, 465  
 gas-oil, 50, 53  
 models, 51  
 normalizing, 51, 52  
 quality control, 52  
 refining, 52, 55  
 three-phase, 51, 61, 63  
 two-phase, 51, 61  
 unstable flood, 52  
 water flood, 50, 476, 482  
 water-gas, 51  
 water-oil, 50, 52
- relative volume, 91, 93–95, 97, 107
- reservoir compartment volume, 264
- reservoir drive mechanism  
 compaction drive, 429, 448  
 depletion drive, 429, 448  
 segregating gas-cap drive, 429, 448  
 water drive, 429, 448
- reservoir material balance  
 convolution, 421, 422  
 deconvolution, 422
- reservoir net-to-gross ratio, 10
- reservoir pressure  
 abnormally pressured, 5–7  
 normally pressured, 5–7
- reservoir quality index, 45, 59, 168
- residual oil saturation, 32, 63, 492, 493
- residual plots, 204, 207
- resistivity logs, 148–151, 153, 154, 157, 158
- retort method, 20
- Reynolds number, 385, 388
- rod pump, 401, 496
- rotational viscometer, 198
- routine core analysis, 17

- sand net-to-gross ratio, 10
- sand production, 419
- sandstone compatible scale, 142
- sandstone porosity unit, 142
- saturation-height function, 13, 48
- secondary migration, 3
- secondary oil recovery, 459, 460
- segregated gas-cap drive, 429, 459, 460
- separated tubing flow, 383
- shape factor
  - Dietz shape factor, 338, 340
  - grain shape factor, 162
  - horizontal well shape factor, 364
- shift parameter *see* volume shift parameter
- Simandoux equation, 156–158
- simple mixing rule, 104, 105
- slant well, 279, 284
- slip velocity, 384
- slug test(ing) 244, 264
- slumping effect, 201
- small pot aquifer model, 434
- solubility swelling test, 97
- solvent drive injection, 491
- solvent injection, 485, 486, 490
- sonic cross-plot, 148
  - Wyllie time-average, 147
  - compaction factor, 147
  - Raymer–Hunt, 148
- sonic porosity calculation, 148
- sonic travel time logs, 144, 147
- special core analysis, 17
- spectrometry gamma ray log, 129
- spherical flow, 185, 187, 225, 232, 274, 319
- spherical permeability, 225, 226, 319
- spontaneous potential log, 129, 130
- standard gamma ray log, 128–130
- static fluid pore pressure, 186
- static spontaneous potential, 130
- steady state pretest analysis, 184, 186
- steam assisted gravity drainage (SAGD), 501
- steam flooding, 493
- steam injection, 459, 492, 493
- Stehfest numerical Laplace inversion, 216, 267–269
- stock tank oil initially in place *see* original oil in place
- storativity ratio, 236, 237, 286, 288, 292
- straddle/dual packer, 195, 196
- stratigraphic traps, 4
- structural traps, 3, 4
- subsea wellhead, 374
- superposition function, 230–232, 249–254, 262, 434, 435, 438, 497
  - bilinear flow superposition function, 232
  - linear flow superposition function, 232
  - radial flow superposition function, 232, 251, 252, 313
  - spherical flow superposition function, 232
- superposition principle, 228, 230, 232, 262, 268, 303, 304, 307, 434, 497, 498
- surface active agent, 492
- surface casing, 369
- surface equipment, 369, 373
- surface sampling, 89
- surface wellhead desanders, 419
- sustained casing pressure, 373
- swab valve, 374
- swelling test, 97
- system plot, 327, 397, 398, 404
- ternary diagram
  - for enhanced oil recovery, 485, 486
  - for three-phase relative permeability, 63
- ternary phase diagram, 486
- tertiary oil recovery, 459, 460, 485
- tertiary production, 459
- thermodynamic inhibitors, 416, 419
- three-phase relative permeability calculation
  - saturated-weighted interpolation, 61, 63
  - Stone I model, 61
  - Stone II model, 61, 63
- through tubing guns, 372
- tortuosity, 162
- tortuosity factor, 149, 154
- total equivalent rate, 319, 359, 360
- total flowing fluid gradient, 383, 386, 407
- total mobility, 319
- total organic content, 2
- total petroleum initially-in-place, 11
- tough logging condition, 124
- transient well test, 195, 243
- trapezoidal method for gross rock volume calculation, 8–10
- true vertical depth, 122, 205
- tubing completion type, 379
  - dual completion, 380
  - horizontal well completion, 381
  - multilateral well completion, 381
  - single string commingled completions, 379
  - single string selective zone completion, 380
  - single string sequential completions, 379
- tubing conveyed perforating gun, 372, 373
- tubing head spool, 374
- tubing performance relationship
  - Beggs and Brill, 391
  - Duns and Ros, 391
  - Fancher Brown, 391
  - Griffith and Wallis, 391
  - Hagedorn and Brown, 391
  - Orkiszewski, 391
- tubing pressure gauge, 374
- turner critical velocity *see* turner velocity
- turner velocity, 400
- two-phase Z-factor, 448
- type curves
  - Bourdet type curves, 248
  - Cinco-Ley type curve, 275
  - Gringarten type curves, 247
  - Hurst–van Everdingen type curves, 434
- underpressured, 5
- undeveloped reserves, 12
- unstable flood, 52
- upper master valve, 374
- uranium free gamma ray, 129, 130
- USBM wettability technique, 32, 34, 35
- van der Waals and Platteeuw hydrate model, 414
- van der Waals mixing rule, 105
- vapor equivalent of stock of the stock tank liquid, 358
- variable-rate test, 228, 230, 251, 252, 307, 308
- vertical convergence skin effect, 377, 378

- vertical interference test(ing), 184, 195, 196, 319, 321
- vertical radial flow, 259, 281, 284, 285
- vibrational viscometers, 198
- volatile oil, 68
  - experiment, 91, 94, 95, 97
  - fluid behavior, 68, 77, 81
  - reservoir material balance, 447
  - well test behavior, 223, 287, 288
- volume shift parameter, 106
  
- WAG ratio, 483, 484
- water breakthrough, 397, 465, 466, 470
- water compatibility test (injection water compatibility test), 419, 462
- water drive, 429, 448, 459, 460
- water injection, 459, 460, 462, 463, 483
- water saturation calculation
  - Archie equation, 149, 153, 154, 156, 158
  - Pickett plot, 154
  - ratio method, 153
- wax, 419
  - formation and deposition, 419
- Waxman–Smits method, 157, 158
- Welge method, 470, 477
- wellbore damage, 274, 376, 381
- wellbore skin effect, 226, 228, 274, 377, 378, 398
- wellbore storage effect, 218–221, 246, 247, 254, 264–266, 268, 273
- wellhead, 369, 373, 397
- wellhead choke, 374
- well loading, 220, 308, 310, 389
- well perforations, 370
- well stimulation, 218, 223, 345, 381, 382
- well test analysis
  - convolution, 246, 261–262
  - deconvolution, 246, 261–264, 308
- well test boundaries
  - channel boundary (parallel boundary), 259, 261, 296
  - closed rectangular boundary, 297, 298
  - closed reservoir boundary, 240, 261, 264, 334
  - constant pressure boundary, 186, 216, 238, 239, 259, 261, 267, 279, 293, 297, 299, 339
  - leaky fault, 245, 295, 296
  - open rectangle, 240, 296, 297
  - single linear boundary, 293
  - single no-flow boundary, 259, 261
  - single sealing fault, 238, 239, 293, 301, 302, 306
  - wedge boundary, 239, 259, 261, 293–295
- well test derivative
  - derivative calculation, 251, 254, 255
  - derivative plot, 248, 250, 252, 253, 259–263, 286, 299, 315
- well test design, 323
- well test reservoir models/behavior
  - double permeability model, 291, 292
  - double porosity model, 235, 236, 248, 259, 260, 285
  - homogeneous, 214, 226, 248, 264, 266, 269, 277
  - linear composite, 288
  - multilayered, 289, 291, 292
  - radial composite, 286–288
- well types
  - development wells, 451
  - exploratory wells, 451
  - reentry wells, 451
  - step-out wells, 451
  - wildcat wells, 451
- Wenner array, 199
- wet gas, 69, 70, 77, 81
- wettability, 17, 31, 32, 37, 201, 459, 460, 462, 466, 492, 494
- wet tree system/completion, 374
- Whitson and Torp correlation, 83
- Wilson’s correlation, 83–85, 88, 113, 115, 490
- wireline-retrievable gas lift valve, 406